University of Oxford

College of Computer Science

Elzein Salah Elzein

22/12/2021

PHD Report Draft

Written By Elzein Salah Elzein

Characterization of Hydrogen Explosion Safety

Contents (Section)	Page
1. Introduction	2
2. Literature Review	157
3. Hydrogen Generation and Explosion Safety	382
4. Research Overview	570
5. Methodology	607
6. Related Work	654
7. Discussion	883
8. Conclusion and Future Work	975
9. References	1030

1. Introduction

1

Hydrogen Economy

S.A. Sherif
University of Florida

Frano Barbir
University of Split

T. Nejat Veziroglu
International Association for Hydrogen Energy

CONTENTS

1.1 Introduction 2
1.2 Hydrogen Production 3
1.2.1 Electrolysis 3
1.2.2 Direct Thermal Decomposition of Water (Thermolysis) 4
1.2.3 Thermochemical Cycles 4
1.2.4 Photolysis 4
1.2.5 Hydrogen Production from Biomass 4
1.3 Hydrogen Storage 5
1.3.1 Gaseous Hydrogen Storage 5
1.3.2 Metal Hydride Storage 5
1.3.3 Novel Hydrogen Storage Methods 5
1.3.4 Liquid Hydrogen Storage 6
1.3.4.1 Hydrogen Liquefaction 6
1.3.4.2 Liquid Hydrogen Storage 7
1.3.5 Slush Hydrogen Storage 8
1.4 Hydrogen Transport 9
1.5 Hydrogen Conversion 9
1.5.1 Combustion in Internal Combustion, Jet, and Rocket Engines 9
1.5.2 Steam Generation by Hydrogen/Oxygen Combustion 10
1.5.3 Catalytic Combustion of Hydrogen 10
1.5.4 Electrochemical Conversion (Fuel Cells) 11
1.5.5 Energy Conversions Involving Metal Hydrides 11
1.6 Hydrogen Safety 12
1.7 Conclusions 13
References 14

1

This chapter presents an overview of how a hydrogen economy can be realized. We will give an overview of the principles of hydrogen energy production, storage, and utilization. We will also discuss different aspects of hydrogen safety. Hydrogen production will cover a whole array of methods including electrolysis, thermolysis, photolysis, thermochemical cycles, and production from biomass. Hydrogen storage will cover all modes of gaseous, liquid, slush, and metal hydride storage. Hydrogen utilization will focus on a large cross section of applications such as fuel cells and catalytic combustion of hydrogen. Details of many of these topics will be presented in the rest of the handbook.

1.1 Introduction

A hydrogen economy is one in which hydrogen is the main energy carrier along with electricity. Hydrogen would be produced from renewable energy sources such as solar or wind energy through water electrolysis. While this is considered an ideal scenario for a hydrogen economy, other possibilities exist. In theory, hydrogen and electricity can satisfy all the energy needs of humankind and form an energy system that would be permanent and independent of energy sources [1–3]. Hydrogen has unique characteristics that make it an ideal energy carrier [4]. These include the fact that (1) it can be produced from and converted into electricity at relatively high efficiencies; (2) its raw material for production is water, which is available in abundance; (3) it is a completely renewable fuel; (4) it can be stored in gaseous form (convenient for large-scale storage), in liquid form (convenient for air and space transportation), or in the form of metal hydrides (convenient for surface vehicles and other relatively small-scale storage requirements); (5) it can be transported over large distances through pipelines or via tankers; (6) it can be converted into other forms of energy in more ways and more efficiently than any other fuel (such as catalytic combustion, electrochemical conversion, and hydriding); and (7) it is environmentally compatible since its production, storage, transportation, and end use do not produce any pollutants (except for small amounts of nitrogen oxides), greenhouse gases, or any other harmful effects on the environment.

In a hydrogen economy, electricity and hydrogen would be produced in large quantities from available energy sources and used in every application where fossil fuels are being used today. This includes large industrial plants as well as small, decentralized units, wherever the primary energy source (solar, nuclear, and even fossil) is available. Electricity would be used directly or transformed into hydrogen. For large-scale storage, hydrogen can be stored underground in ex-mines, caverns, and/or aquifers. Energy transport to the end users, depending on distance and overall economics, would either be in the form of electricity or in the form of hydrogen. Hydrogen would be transported by means of pipelines or supertankers. It would then be used in transportation and industrial, residential, and commercial sectors as a fuel. Some of it would be used to generate electricity (via fuel cells), depending on demand, geographical location, or time of the day.

1.2 Hydrogen Production

Hydrogen is usually found in small amounts mixed with natural gas in crustal reservoirs. However, a few wells have been found to contain large amounts of hydrogen, such as some wells in Kansas that contain 40% hydrogen, 60% nitrogen, and trace amounts of hydrocarbons [5]. Logical sources of hydrogen are hydrocarbon (fossil) fuels (C_XH_Y) and water (H_2O). Presently, hydrogen is mostly being produced from fossil fuels (natural gas, oil, and coal). However, except for the space program, hydrogen is not being used directly as a fuel or an energy carrier. It is being used in refineries to upgrade crude oil (hydrotreating and hydrocracking), in the chemical industry to synthesize various chemical compounds (such as ammonia and methanol), and in metallurgical processes (as a reduction or protection gas). The total annual hydrogen production worldwide in 1996 was about 40 million tons (5.6 EJ) [6]. Less than 10% of that amount was supplied by industrial gas companies; the rest is being produced at consumer-owned and consumer-operated plants (the so-called captive production), such as refineries, and by ammonia and methanol producers. Production of hydrogen as an energy carrier would require an increase in production rates by several orders of magnitude.

To help speed up the introduction of fuel cell–powered vehicles, car manufacturers in collaboration with oil- and fuel-processing companies are intensively working on the development of onboard fuel processors. These devices would enable the use of conventional fuels such as gasoline and diesel, as well as methanol. This would allow the car companies to plan to overcome nonexistence of a hydrogen refueling infrastructure and the difficulties of onboard hydrogen storage. However, development of such compact fuel processors poses several engineering challenges, such as rapid start-up, high efficiency, and very high purity of the produced gas (<100 ppm CO).

The most logical source for large-scale hydrogen production is water. Methods of hydrogen production from water include electrolysis, direct thermal decomposition or thermolysis, thermochemical processes, and photolysis.

1.2.1 Electrolysis

The production of hydrogen by water electrolysis is a mature technology, based on a fundamentally simple process, is very efficient, and does not involve moving parts. It is suitable for large-scale hydrogen production. Typical efficiencies are 72%–82%. Several advanced electrolyzer technologies are being developed such as the advanced alkaline electrolysis (which employs new materials for membranes and electrodes that allow further improvement in efficiency—up to 90% [7,8]), the solid polymer electrolytic (SPE) process (which employs a proton-conducting ion exchange membrane as an electrolyte and as a membrane that separates the electrolysis cell [8,9]), and high-temperature steam electrolysis (which operates between 700°C and 1000°C and which employs oxygen ion–conducting ceramics as electrolyte [10]). An electrolysis plant can operate over a wide range of capacity factors and is convenient for a wide range of operating capacities, which makes this process interesting for coupling with renewable energy sources, particularly with photovoltaics (PVs). The latter generate low-voltage direct current, which is exactly what is required for the electrolysis process. Theoretical and experimental studies on the performance of PV-electrolyzer systems have been performed [11–14]. Examples of experimental PV-electrolysis plants

that are currently in operation worldwide include the Solar-Wasserstoff-Bayern pilot plant (Neunburg vorm Wald, Germany) [15], the HYSOLAR project (Saudi Arabia) [16], Schatz Energy Center (Humboldt State University, Arcata, California) [17], Helsinki University of Technology (Helsinki, Finland) [18], and INTA Energy Laboratory (Huelva, Spain) [19].

1.2.2 Direct Thermal Decomposition of Water (Thermolysis)

Water can be split thermally at temperatures above 2000 K [20]. The degree of dissociation is a function of temperature: only 1% at 2000 K, 8.5% at 2500 K, and 34% at 3000 K. The product is a mixture of gases at extremely high temperatures. The main problems in connection with this method are related to materials required for extremely high temperatures, recombination of the reaction products at high temperatures, and separation of hydrogen from the mixture.

1.2.3 Thermochemical Cycles

Production of hydrogen employing thermochemical cycles involves the chemical split- ting of water at temperatures lower than those needed for thermolysis, through a series of cyclical chemical reactions that ultimately release hydrogen. Some of the more thoroughly investigated thermochemical process cycles include the following [9,21,22]: sulfuric acid–iodine cycle, hybrid sulfuric acid cycle, hybrid sulfuric acid–hydrogen bromide cycle, calcium bromide–iron oxide cycle (UT-3), and iron–chlorine cycle. Depending on the temperatures at which these processes are occurring, relatively high efficiencies are achievable (40%–50%). However, the problems related to movement of a large mass of materials in chemical reactions, toxicity of some of the chemicals involved, and corrosion at high temperatures remain to be solved in order for these methods to become practical.

1.2.4 Photolysis

Photolysis (or direct extraction of hydrogen from water using only sunlight as an energy source) can be accomplished by employing photobiological systems, photochemical assemblies, or photoelectrochemical cells [23,24]. Intensive research activities are opening new perspectives for photoconversion, where new redox catalysts, colloidal semiconductors, immobilized enzymes, and selected microorganisms could provide means of large-scale solar energy harvesting and conversion into hydrogen.

1.2.5 Hydrogen Production from Biomass

Hydrogen can be obtained from biomass by a pyrolysis/gasification process [25]. The biomass preparation step involves heating of the biomass/water slurry to high temper- atures under pressure in a reactor. This process decomposes and partially oxidizes the biomass, producing a gas product consisting of hydrogen, methane, CO_2, CO, and nitro- gen. Mineral matter is removed from the bottom of the reactor. The gas stream goes to a high-temperature shift reactor where the hydrogen content is increased. Relatively high- purity hydrogen is produced in the subsequent pressure swing adsorption unit. The whole system is very much similar to a coal gasification plant, with the exception of the unit for pretreatment of the biomass and the design of the reactor. Because of the lower calorific value per unit mass of biomass as compared to coal, the processing facility is larger than that of a comparably sized coal gasification plant.

1.3 Hydrogen Storage

Once hydrogen is produced, it needs to be stored in order to overcome daily and seasonal discrepancies between energy source availability and demand. Several forms of storage are discussed briefly in the following.

1.3.1 Gaseous Hydrogen Storage

Depending on storage size and application, several types of hydrogen storage systems may be available. This includes stationary large storage systems and stationary small storage systems at the distribution, or final user level; mobile storage systems for transport and distribution including both large-capacity devices (such as a liquid hydrogen tanker—bulk carrier) and small systems (such as a gaseous or liquid hydrogen truck trailer); and vehicle tanks to store hydrogen used as fuel for road vehicles. Because of hydrogen's low den- sity, its storage always requires relatively large volumes and is associated with either high pressures (thus requiring heavy vessels) or extremely low temperatures, and/or combination with other materials (much heavier than hydrogen itself). Studies dealing with large underground storage of hydrogen include those reported in Refs. [26–28]. Pressurized gas storage systems are used today in the natural gas business in various sizes and pressure ranges from standard pressure cylinders (50 L, 200 bar) to stationary high-pressure containers (over 200 bar) or low-pressure spherical containers (>30,000 m^3, 12–16 bar). This application range will be similar for hydrogen storage. Storage in vehicular pressurized hydrogen tanks are discussed in Ref. [29].

1.3.2 Metal Hydride Storage

In the presence of some metals and alloys, hydrogen can form metal hydrides. During that process, hydrogen molecules are split and hydrogen atoms are inserted in spaces inside the lattice of the metal or alloy. This creates effective storage comparable to the density of liquid hydrogen. However, when the mass of the metal or alloy is taken into account, then the metal hydride gravimetric storage density becomes comparable to storage of pressurized hydrogen. The best achievable gravimetric storage density is about 0.07 kg of H_2/kg of metal, for a high-temperature hydride such as MgH_2 [30]. During the storage process (charging or absorption), heat is released, which must be removed in order to achieve the continuity of the reaction. During the hydrogen release process (discharging or desorption), heat must be supplied to the storage tank. An advantage of storing hydrogen in hydriding substances is the safety aspect. A serious damage to a hydride tank (such as one that could be caused by a collision) would not pose a fire hazard since hydrogen would remain in the metal structure.

1.3.3 Novel Hydrogen Storage Methods

There are several emerging methods of storing hydrogen that are still under investigation. For example, hydrogen can be physically adsorbed on activated carbon and be *packed* on the surface and inside the carbon structure more densely than if it has been just compressed. Amounts of up to 48 g H_2 per kg of carbon have been reported at 6.0 MPa and 87 K [31]. The adsorption capacity is a function of pressure and temperature; therefore, at higher pressures and/or lower temperatures, even larger amounts of hydrogen can be adsorbed.

For any practical use, relatively low temperatures are needed (less than 100 K). Since the adsorption is a surface process, the adsorption capacity of hydrogen on activated carbon is largely due to the high surface area of the activated carbon, although there are some other carbon properties that affect the ability of activated carbon to adsorb hydrogen. Researchers at the Northeastern University developed a carbon nanotube capable of stor- ing up to 75% of hydrogen by weight [32]. This material is being researched in several laboratories including the National Renewable Energy Laboratory, which is claiming a storage density corresponding to about 10% of the nanotube weight [33]. Hydrogen can also be stored in glass microspheres of approximately 50 μm diameter. The microspheres can be filled with hydrogen by heating them to increase the glass permeability to hydro- gen. At room temperature, a pressure of approximately 25 MPa is achieved resulting in storage density of 14% mass fraction and 10 kg H_2/m^3 [34]. At 62 MPa, a bed of glass micro- spheres can store 20 kg H_2/m^3. The release of hydrogen occurs by reheating the spheres to again increase the permeability. Researchers at the University of Hawaii are investigating hydrogen storage via polyhydride complexes. Complexes have been found that catalyze the reversible hydrogenation of unsaturated hydrocarbons. This catalytic reaction could be the basis for a low-temperature hydrogen storage system with an available hydrogen density greater than 7% [35].

1.3.4 Liquid Hydrogen Storage

Liquid hydrogen's favorable characteristics include its high heating value per unit mass and large cooling capacity due to its high specific heat [36,37]. Liquid hydrogen has some important uses such as in the space program, in high-energy nuclear physics, and in bubble chambers. The transport of hydrogen is vastly more economical when it is in liquid form even though cryogenic refrigeration and special Dewar vessels are required. Although liquid hydrogen can provide a lot of advantages, its uses are restricted in part because liq- uefying hydrogen by existing conventional methods consumes a large amount of energy (around 30% of its heating value). Liquefying 1 kg of hydrogen in a medium-size plant requires 10–13 kWh of energy (electricity) [37]. In addition, boil-off losses associated with the storage, transportation, and handling of liquid hydrogen can consume up to 40% of its available combustion energy. It is therefore important to search for ways that can improve the efficiency of the liquefiers and diminish the boil-off losses.

1.3.4.1 Hydrogen Liquefaction

The production of liquid hydrogen requires the use of liquefiers that utilize different prin- ciples of cooling. In general, hydrogen liquefiers may be classified as conventional, mag- netic, or hybrid. Many types of conventional liquefiers exist such as the Linde–Hampson liquefiers, the Linde dual-pressure liquefiers, the Claude liquefiers, the Kapitza liquefi- ers, the Heylandt liquefiers, and the Collins liquefiers. Conventional liquefiers generally comprise compressors, expanders, heat exchangers, and Joule–Thomson valves. Magnetic liquefiers, on the other hand, utilize the magnetocaloric effect. This effect is based on the principle that some magnetic materials experience a temperature increase upon the application of a magnetic field and a temperature drop upon lifting the magnetic field. The magnetic analog of several conventional liquefiers includes the Brayton liquefiers, the Stirling liquefiers, and the active magnetic regenerative (AMR) liquefier. Additional infor- mation on liquid hydrogen production methods can be found in Sherif et al. [39].

1.3.4.2 Liquid Hydrogen Storage

The need for liquid hydrogen is highest in the transportation sector and the space pro- gram. Transport of large quantities of hydrogen is usually accomplished by truck tank- ers of 30–60 m^3 capacity, by rail tank cars of 115 m^3 capacity, and by barge containers of 950 m^3 capacity [39]. Liquid hydrogen storage vessels are usually available in sizes ranging from 1 L Dewar flasks used in laboratory applications to large tanks of 5000 m^3 capacity. The National Aeronautics and Space Administration (NASA) typically uses large tanks of 3800 m^3 capacity (25 m in diameter) [26]. The total boil-off rate from such Dewars is approximately 600,000 LPY (liters per year), which is vented to a burn pond. The contributing mechanisms to boil-off losses in cryogenic hydrogen storage systems are as follows: (1) ortho–para conversion, (2) heat leak (shape and size effect, thermal stratification, thermal overfill, insulation, conduction, radiation, cooldown), (3) sloshing, and (4) flashing. In order to minimize the storage boil-off losses, the conversion rate of ortho-to-para hydrogen should be accelerated with a catalyst that converts the hydrogen during the liquefaction process [40–43]. The use of a catalyst usually results in a larger refrigeration load and consequently in an efficiency penalty primarily because the heat of conversion must be removed. The time for which hydrogen is to be stored usually determines the optimum amount of conversion. For use within a few hours, no conversion is necessary. For example, large-scale use of liquid hydrogen as a fuel for jet aircraft is one of those cases where conversion is not necessary since utilization of the liquid is almost a continuous process and long-term storage is therefore not needed [43]. For some other uses, a partial conversion might be required to create more favorable conditions. It should be noted that for every initial ortho concentration, there exists a unique curve for boil-off of hydrogen with respect to time.

The heat leakage losses are generally proportional to the ratio of surface area to the volume (S/V) of the storage vessel. The most favorable shape is therefore spherical since it has the least S/V ratio. Spherical shape containers have another advantage. They have good mechanical strength since stresses and strains are distributed uniformly. Storage vessels may also be constructed in other shapes such as cylindrical, conical, or any combination of these shapes. Cylindrical vessels are usually required for transportation of liquid hydrogen by trailers or railway cars because of limitations imposed on the maximum allowable diameter of the vessel. For normal highway transportation, the outside diameter of the vessel cannot exceed 2.44 m. From an economics standpoint, cylindrical vessels with either dish, elliptical, or hemispherical heads are very good, and their S/V ratios are only about 10% greater than that of the sphere [44]. Since boil-off losses due to heat leak are proportional to the S/V ratio, the evaporation rate will diminish drastically as the storage tank size is increased. For double-walled, vacuum-insulated, spherical Dewars, boil-off losses are typically 0.3%–0.5% per day for containers having a storage volume of 50 m^3, 0.2% for 103 m^3 tanks, and about 0.06% for 19,000 m^3 tanks [45].

Additional boil-off may be caused by thermal stratification in liquid hydrogen in which case the warmer upper layers evaporate much faster than the bulk liquid [44]. One way of decreasing boil-off losses due to stratification and thermal overfill is by employing high-conductivity plates (conductors) installed vertically in the vessel. The plates produce heat paths of low resistance between the bottom and top of the vessel and can operate most satisfactorily in eliminating temperature gradients and excessive pressures. Another way is to pump the heat out and maintain the liquid at subcooled or saturated conditions. An ideal refrigeration system to perform this task can be an efficient magnetic refrigerator.

The magnetic refrigerator is very suitable for this job because of its relatively higher efficiency, compactness, lower price, and reliability [46–53].

Liquid hydrogen containers are usually of three types: double-jacketed vessels with liquid nitrogen in the outer jacket, superinsulated vessels with either a reflecting powder or multilayer insulation (MLI), and containers with vapor-cooled shields (VCSs) employing superinsulation. Although MLI provides for a low boil-off rate, the addition of a VCS will lower the boil-off losses even further. A VCS is a type of insulation that takes the vapor boil-off and passes it past the tank before being reliquefied or vented. Published data indicate that a reduction of more than 50% in boil-off losses may be achieved for a 100,000 lb liquid hydrogen cryogenic facility with a VCS than without one. Brown [54] showed that locating the VCS at half the distance from the tank to the outer surface of a 4 in. MLI of a 100,000 lb facility would reduce the boil-off by 10%. A dual VCS system on the tank would improve the performance by 40% over a single VCS. Brown [54] also showed that the preferred locations for the inner and outer shields in a dual VCS system are 30% and 66% of the distance from the tank to the outer surface of the MLI.

Another process that leads to boil-off during liquid hydrogen transportation by tankers is sloshing. Sloshing is the motion of liquid in a vessel due to acceleration or deceleration. Due to different types of acceleration and deceleration, there exist different types of sloshing. Acceleration causes the liquid to move to one end and then reflect from that end, thus producing a hydraulic jump. The latter then travels to the other end, thus transforming some of its impact energy to thermal energy. The thermal energy dissipated eventually leads to an increase in the evaporation rate of the liquid [40,44]. The insertion of traverse or antislosh baffles not only restrains the motion of the liquid, thus reducing the impact forces, but also increases the frequency above the natural frequency of the tanker [40,55].

Another source of boil-off is flashing. This problem occurs when liquid hydrogen, at a high pressure (2.4–2.7 atm), is transferred from trucks and railcars to a low-pressure Dewar (1.17 atm). This problem can be reduced if transportation of liquid hydrogen is car- ried out at atmospheric pressures. Furthermore, some of the low-pressure hydrogen can be captured and reliquefied.

1.3.5 Slush Hydrogen Storage

Slush hydrogen is a mixture of liquid and frozen hydrogen in equilibrium with the gas at the triple point, 13.8 K. The density of the icelike form is about 20% higher than that of the boiling liquid. To obtain the icelike form, one has to remove the heat content of the liquid at 20.3 K until the triple point is reached and then remove the latent heat of fusion. The *cold content* of the icelike form of hydrogen is some 25% higher than that of the saturated vapor at 20.3 K.

Slush hydrogen is of great interest for the space program because of its potential in reducing its physical size and significantly cutting the projected gross liftoff weight [56]. Some of the problems related to liquid hydrogen storage, such as low density, temperature stratification, short holding time due to its low latent heat, hazards associated with high vent rates, and unstable flight conditions caused by sloshing of the liquid in the fuel tank, may be eliminated or reduced if slush hydrogen is used. It is apparent that the use of slush hydrogen should be considered only for cases in which higher density and greater solid content are really needed. This is mainly because the production costs of slush hydrogen now and in the near future are greater than the liquefaction costs of hydrogen due to the larger energy use involved. For additional information on slush hydrogen properties, its production methods, and its applications, the reader is referred to Baker and Matsch [57], Sindt [58], and Voth [59].

1.4 Hydrogen Transport

In a hydrogen economy, it is envisaged that from the production plants and/or storage, hydrogen will be transmitted to consumers by means of underground pipelines (gaseous hydrogen) and/or supertankers (liquid hydrogen). Presently, hydrogen transportation through pipelines is used either in links between nearby production and utilization sites (up to 10 km) or in more extensive networks (roughly 200 km) [60]. Future developments will certainly entail greater flow rates and distances. However, it would be possible to use the existing natural gas pipelines with some modifications. For hydrogen pipelines, it is necessary to use steel less prone to embrittlement by hydrogen under pressure (particularly for very pure hydrogen [>99.5% purity]). Reciprocating compressors used for natural gas can be used for hydrogen without major design modifications. However, special attention must be given to sealing (to avoid hydrogen leaks) and to materials selection for the parts subject to fatigue stress. The use of centrifugal compressors for hydrogen creates more problems due to hydrogen's exceptional lightness.

As a rule, hydrogen transmission through pipelines requires larger-diameter piping and more compression power than natural gas for the same energy throughput. However, due to lower pressure losses in the case of hydrogen, the recompression stations would need to be spaced twice as far apart. In economic terms, most of the studies found that the cost of large-scale transmission of hydrogen is about 1.5–1.8 times that of natural gas transmission. However, transportation of hydrogen over distances greater than 1000 km is more economical than transmission of electricity [61]. Hydrogen in the gas phase is generally transported in pressurized cylindrical vessels (typically at 200 bar) arranged in frames adapted to road transport. The unit capacity of these frames or skids can be as great as 3000 m^3. Hydrogen gas distribution companies also install such frames at the user site to serve as a stationary storage.

1.5 Hydrogen Conversion

Hydrogen as an energy carrier can be converted into useful forms of energy in several ways including combustion in internal combustion engines and jet and rocket engines, combustion with pure oxygen to generate steam, catalytic combustion to generate heat, electrochemical conversion to electricity, and metal hydride conversions.

1.5.1 Combustion in Internal Combustion, Jet, and Rocket Engines

Hydrogen-powered internal combustion engines are on average about 20% more efficient than comparable gasoline engines. The thermal efficiency of an internal combustion engine can be improved by increasing either the compression ratio or the specific heat ratio or both. In hydrogen engines, both ratios are higher than in a comparable gasoline engine due to hydrogen's lower self-ignition temperature and ability to burn in lean mixtures. However, the use of hydrogen in internal combustion engines results in loss of power due to the lower energy content in a stoichiometric mixture in the engine's cylinder. A stoichiometric mixture of gasoline and air, and gaseous hydrogen and air, premixed externally, occupies ~2% and 30% of the cylinder volume, respectively. Under these conditions, the energy of

the hydrogen mixture is only 85% of the gasoline mixture, thus resulting in about 15% reduction in power. The power output of a hydrogen engine can be improved by using more advanced fuel injection techniques or liquid hydrogen. For example, if liquid hydro- gen is premixed with air, the amount of hydrogen that can be introduced into the combus- tion chamber can be increased by approximately one-third [62]. One major advantage of hydrogen-powered engines is that they emit far fewer pollutants than comparable gaso- line engines. Basically, the only products of hydrogen combustion in air are water vapor and small amounts of nitrogen oxides. Hydrogen has a wide flammability range in air (4%–75% vol.), and therefore high excess air can be utilized more effectively. The formation of nitrogen oxides in hydrogen/air combustion can be minimized with excess air. NO_x emissions can also be lowered by cooling the combustion environment using techniques such as water injection, exhaust gas recirculation, or using liquid hydrogen. The emissions of NO_x in hydrogen engines are typically one order of magnitude smaller than the emis- sions from comparable gasoline engines primarily because the former run leaner than the latter. Small amounts of unburned hydrocarbons, CO_2, and CO have been detected in hydrogen engines due to lubrication oil [62].

1.5.2 Steam Generation by Hydrogen/Oxygen Combustion

Hydrogen combusted with pure oxygen results in pure steam. This creates temperatures in the flame zone above 3000°C; therefore, additional water has to be injected so that the steam temperature can be regulated at a desired level. Both saturated and superheated vapor can be produced.

A compact hydrogen/oxygen steam generator has been commercially developed by the German Aerospace Research Establishment (DLR) [63]. This generator consists of the igni- tion, combustion, and evaporation chambers. In the ignition chamber, a combustible mix- ture of hydrogen and oxygen at a low oxidant/fuel ratio is ignited by means of a spark plug. The rest of the oxygen is added in the combustion chamber to adjust the oxidant/fuel ratio exactly to the stoichiometric one. Water is also injected in the combustion chamber after it has passed through the double walls of the combustion chamber. The evapora- tion chamber serves to homogenize the steam. The steam's temperature is monitored and controlled. Such a device is close to 100% efficient, since there are no emissions other than steam and little or no thermal losses. Hydrogen steam generators can be used to generate steam for spinning reserve in power plants, for peak-load electricity generation, for indus- trial steam supply networks, and as a micro steam generator in medical technology and biotechnology [63].

1.5.3 Catalytic Combustion of Hydrogen

Hydrogen and oxygen in the presence of a suitable catalyst may be combined at tempera- tures significantly lower than flame combustion (from ambient to 500°C). This principle can be used to design catalytic burners and heaters. Catalytic burners require consider- ably more surface area than conventional flame burners. Therefore, the catalyst is typi- cally dispersed in a porous structure. The reaction rate and resulting temperature are easily controlled by controlling the hydrogen flow rate. The reaction takes place in a reac- tion zone of the porous catalytic sintered metal cylinders or plates in which hydrogen and oxygen are mixed by diffusion from opposite sides. A combustible mixture is formed only in the reaction zone and assisted with a catalyst (platinum) to burn at low tempera- tures. The only product of catalytic combustion of hydrogen is water vapor. Due to low

temperatures, there are no nitrogen oxides formed. The reaction cannot migrate into the hydrogen supply, since there is no flame and hydrogen concentration is above the higher flammable limit (75%). Possible applications of catalytic burners are in household appliances such as cooking ranges and space heaters. The same principle is also used in hydrogen sensors.

1.5.4 Electrochemical Conversion (Fuel Cells)

Hydrogen can be combined with oxygen without combustion in an electrochemical reaction (reverse electrolysis) and produce direct-current electricity. The device where such a reaction takes place is called a fuel cell. Depending on the type of electrolyte used, there are several types of fuel cells:

- Alkaline fuel cells (AFCs) use concentrated (85 wt.%) KOH as the electrolyte for high-temperature operation (250°C) and less concentrated (35–50 wt.%) for low- temperature operation (<120°C). The electrolyte is retained in a matrix (usually asbestos), and a wide range of electrocatalysts can be used (such as Ni, Ag, metal oxides, and noble metals). This fuel cell is intolerant to CO_2 present in either the fuel or the oxidant [64].
- Polymer electrolyte membrane or proton exchange membrane fuel cells (PEMFCs) use a thin polymer membrane (such as perfluorosulfonated acid polymer) as the electrolyte. The membranes as thin as 12–20 μm have been developed, which are excellent proton conductors. The catalyst is typically platinum with loadings about 0.3 mg/cm^2, or if the hydrogen feed contains minute amounts of CO, Pt–Ru alloys are used. The operating temperature is usually below 100°C, more typically between 60°C and 80°C.
- Phosphoric acid fuel cells (PAFCs) use concentrated phosphoric acid (~100%) as the electrolyte. The matrix used to retain the acid is usually SiC, and the electrocata- lyst in both the anode and cathode is platinum black. The operating temperature is typically between 150°C and 220°C [64,65].
- Molten carbonate fuel cells (MCFCs) have the electrolyte composed of a combi- nation of alkali (Li, Na, K) carbonates, which is retained in a ceramic matrix of $LiAlO_2$. Operating temperatures are between 600°C and 700°C where the carbon- ates form a highly conductive molten salt, with carbonate ions providing ionic conduction. At such high operating temperatures, noble metal catalysts are typi- cally not required [64,65].
- Solid oxide fuel cells (SOFCs) use a solid, nonporous metal oxide, usually Y_2O_3- stabilized ZrO_2, as the electrolyte. The cell operates at 900°C–1000°C where ionic conduction by oxygen ions takes place [64,65].

1.5.5 Energy Conversions Involving Metal Hydrides

Hydrogen's property to form metal hydrides may be used not only for hydrogen stor- age but also for various energy conversions. When a hydride is formed by the chemical combination of hydrogen with a metal, an element, or an alloy, heat is generated, that is, the process is exothermic. Conversely, in order to release hydrogen from a metal hydride, heat must be supplied. The rate of these reactions increases with an increase in the surface area. Therefore, in general, the hydriding substances are used in powdered form to

speed up the reactions. Elements or metals with unfilled shells or subshells are suitable hydriding substances. Metal and hydrogen atoms form chemical compounds by sharing their electrons in the unfilled subshells of the metal atom and the K shells of the hydrogen atoms.

Ideally, for a given temperature, the charging or absorption process and the discharging or desorption process take place at the same constant pressure. However, actually, there is a hysteresis effect, and the pressure is not absolutely constant—for a given temperature, charging pressures are higher than the discharging pressures. The heat generated during the charging process and the heat needed for discharging are functions of the hydriding substance, the hydrogen pressure, and the temperature at which the heat is supplied or extracted. Using different metals and by forming different alloys, dif- ferent hydriding characteristics can be obtained. In other words, it is possible to make or find hydriding substances that are more suitable for a given application, such as waste heat storage, electricity generation, pumping, hydrogen purification, and isotope separation.

Hydriding substances can be used for electricity storage in two ways. In one of the methods, electricity (direct current) is used to electrolyze the water, and the hydrogen produced is stored in a hydriding substance. When electricity is needed, the hydrogen is released from the hydriding substance by adding heat and used in a fuel cell to produce direct-current electricity. Heat from a fuel cell can be used to release hydrogen from the metal hydride. In the second method, one electrode is covered with a hydriding substance (e.g., titanium–nickel alloy). During the electrolysis of water, the hydriding substance covering the electrode immediately absorbs the hydrogen produced on the surface of the electrode. Then, when electricity is needed, the electrolyzer operates in a reverse mode as a fuel cell producing electricity using the hydrogen released from the metal hydride.

1.6 Hydrogen Safety

Since hydrogen has the smallest molecule, it has a greater tendency to escape through small openings than other liquid or gaseous fuels. Based on properties of hydrogen such as density, viscosity, and diffusion coefficient in air, the propensity of hydrogen to leak through holes or joints of low-pressure fuel lines may be only 1.26–2.8 times faster than a natural gas leak through the same hole (and not 3.8 times faster as frequently assumed based solely on diffusion coefficients). Experiments have indicated that most leaks from residential natural gas lines are laminar [66]. Since natural gas has over three times the energy density per unit volume, the natural gas leak would result in more energy release than a hydrogen leak. For very large leaks from high-pressure storage tanks, the leak rate is limited by the sonic speed. Due to higher sonic velocity (1308 m/s), hydrogen would initially escape much faster than natural gas (sonic velocity of natural gas is 449 m/s).

Some high-strength steels are prone to hydrogen embrittlement. Prolonged exposure to hydrogen, particularly at high temperatures and pressures, can cause the steel to lose strength, eventually leading to failure. However, most other construction, tank, and pipe materials are not prone to hydrogen embrittlement. Therefore, with proper choice of materials, hydrogen embrittlement should not contribute to hydrogen safety risks.

If a leak should occur for whatever reason, hydrogen will disperse much faster than any other fuel, thus reducing the hazard levels. Hydrogen is both more buoyant and more diffusive than gasoline, propane, or natural gas. A hydrogen/air mixture can burn in relatively wide volume ratios, between 4% and 75% of hydrogen in air. The other fuels have much lower flammability ranges, namely, natural gas 5.3%–15%, propane 2.1%–10%, and gasoline 1%–7.8%. However, the range has little practical value. In many actual leak situations, the key parameter that determines if a leak would ignite is the lower flammability limit, and hydrogen's lower flammability limit is four times higher than that of gasoline, 1.9 times higher than that of propane, and slightly lower than that of natural gas. It also has a very low ignition energy (0.02 mJ), about one order of magnitude lower than other fuels. The ignition energy is a function of fuel/air ratio, and for hydrogen, it reaches a minimum at about 25%–30%. At the lower flammability limit, hydrogen ignition energy is comparable with that of natural gas [67]. Its flame velocity is seven times faster than that of natural gas or gasoline. A hydrogen flame would therefore be more likely to progress to a deflagration or even a detonation than other fuels. However, the likelihood of a detonation depends in a complex manner on the exact fuel/air ratio, the temperature, and, particularly, the geometry of the confined space. Hydrogen detonation in the open atmosphere is highly unlikely.

The lower detonability fuel/air ratio for hydrogen is 13%–18%, which is two times higher than that of natural gas and 12 times higher than that of gasoline. Since the lower flammability limit is 4%, an explosion is possible only under the most unusual scenarios; for example, hydrogen would first have to accumulate and reach 13% concentration in a closed space without ignition, and only then an ignition source would have to be triggered. Should an explosion occur, hydrogen has the lowest explosive energy per unit stored energy in the fuel, and a given volume of hydrogen would have 22 times less explosive energy than the same volume filled with gasoline vapor.

A hydrogen flame is nearly invisible, which may be dangerous, because people in the vicinity of a hydrogen flame may not even know there is a fire. This may be remedied by adding some chemicals that will provide the necessary luminosity. The low emissivity of hydrogen flames means that nearby materials and people will be much less likely to ignite and/or be hurt by radiant heat transfer. The fumes and soot from a gasoline fire pose a risk to anyone inhaling the smoke, while hydrogen fires produce only water vapor (unless secondary materials begin to burn).

Liquid hydrogen presents another set of safety issues, such as risk of cold burns and the increased duration of leaked cryogenic fuel. A large spill of liquid hydrogen has some characteristics of a gasoline spill; however, it will dissipate much faster. Another potential danger is a violent explosion of a boiling liquid/expanding vapor in case of a pressure relief valve failure.

In conclusion, hydrogen appears to pose safety risks of the same order of magnitude as gasoline or natural gas. The perception that hydrogen is an unsafe fuel needs to be addressed if a hydrogen economy is to replace the existing fossil fuel–based economy.

1.7 Conclusions

In this chapter, an overview of the hydrogen economy was presented. Many of the aforementioned topics are discussed in much greater detail in the remainder of the handbook.

References

1. Bockris, J.O'M., *Energy: The Solar-Hydrogen Alternative*, Halsted Press, New York, 1975.
2. Bockris, J.O'M. and Veziroglu, T.N., A solar-hydrogen energy system for environmental com- patibility, *Environ. Conserv*., 12(2), 105–118, 1985.
3. Bockris, J.O'M., Veziroglu, T.N., and Smith, D., *Solar Hydrogen Energy: The Power to Save the Earth*, Optima, London, U.K., 1991.
4. Veziroglu, T.N. and Barbir, F., Hydrogen: The wonder fuel, *Int. J. Hydrogen Energy*, 17(6), 391–404, 1992.
5. Goebel, E., Coveney, Jr., R.M., Angino, E.E., Zeller, E.J., and Dreschoff, G.A.M., Geology, com- position, isotopes of naturally occurring H_2/N_2 rich gas from wells near Junction City, Kansas, *Oil Gas J*., 217–222, May 1994.
6. Heydorn, B., *SRI Consulting Chemical Economics Handbook*, SRI, Menlo Park, CA, 1998.
7. Bonner, M., Botts, T., McBreen, J., Mezzina, A., Salzano, F., and Yang, C., Status of advanced electrolytic hydrogen production in the United States and Abroad, *Int. J. Hydrogen Energy*, 9(4), 269–275, 1984.
8. Dutta, S., Technology assessment of advanced electrolytic hydrogen production, *Int. J. Hydrogen Energy*, 15(6), 379–386, 1990.
9. Wendt, H., Water splitting methods, in C.-J. Winter and J. Nitsch (eds.), *Hydrogen as an Energy Carrier*, Springer-Verlag, Berlin/Heidelberg, Germany, pp. 166–238, 1988.
10. Liepa, M.A. and Borhan, A., High-temperature steam electrolysis: Technical and economic evaluation of alternative process designs, *Int. J. Hydrogen Energy*, 11(7), 435–442, 1986.
11. Hancock, Jr., O.G., A photovoltaic-powered water electrolyzer: Its performance and economics, in T.N. Veziroglu and J.B. Taylor (eds.), *Hydrogen Energy Progress V*, Pergamon Press, New York, pp. 335–344, 1984.
12. Carpetis, C., An assessment of electrolytic hydrogen production by means of photovoltaic energy conversion, *Int. J. Hydrogen Energy*, 9(12), 969–992, 1984.
13. Siegel, A. and Schott, T., Optimization of photovoltaic hydrogen production, *Int. J. Hydrogen Energy*, 13(11), 659–678, 1988.
14. Steeb, H., Brinner, A., Bubmann, H., and Seeger, W., Operation experience of a 10 kW PV-electrolysis system in different power matching modes, in T.N. Veziroglu and P.K. Takahashi (eds.), *Hydrogen Energy Progress VIII*, Vol. 2, Pergamon Press, New York, pp. 691–700, 1990.
15. Blank, H. and Szyszka, A., Solar hydrogen demonstration plant in Neunburg vorm Wald, in T.N. Veziroglu, C. Derive, and J. Pottier (eds.), *Hydrogen Energy Progress IX*, Vol. 2, M.C.I., Paris, France, pp. 677–686, 1992.
16. Grasse, W., Oster, F., and Aba-Oud, H., HYSOLAR: The German-Saudi Arabian program on solar hydrogen—5 years of experience, *Int. J. Hydrogen Energy*, 17(1), 1–8, 1992.
17. Lehman, P. and Chamberlain, C.E., Design of a photovoltaic-hydrogen-fuel cell energy system, *Int. J. Hydrogen Energy*, 16(5), 349–352, 1991.
18. Lund, P.D., Optimization of stand-alone photovoltaic system with hydrogen storage for total energy self-sufficiency, *Int. J. Hydrogen Energy*, 16(11), 735–740, 1991.
19. Garcia-Conde, A.G. and Rosa, F., Solar hydrogen production: A Spanish experience, in T.N. Veziroglu, C. Derive, and J. Pottier (eds.), *Hydrogen Energy Progress IX*, Vol. 2, M.C.I., Paris, France, pp. 723–732, 1992.
20. Baykara, S.Z. and Bilgen, E., An overall assessment of hydrogen production by solar water thermolysis, *Int. J. Hydrogen Energy*, 14(12), 881–889, 1989.
21. Engels, H. et al., Thermochemical hydrogen production, *Int. J. Hydrogen Energy*, 12(5), 291–295, 1987.
22. Yalcin, S., A review of nuclear hydrogen production, *Int. J. Hydrogen Energy*, 14(8), 551–561, 1989.
23. Bull, S.R., Hydrogen production by photoprocesses, *Proceedings of International Renewable Energy Conference*, Honolulu, HI, pp. 413–426, 1988.

Free ebooks ==> www.Ebook777.com

24. Willner, I. and Steinberger-Willner, B., Solar hydrogen production through photo-biological, photochemical and photoelectrochemical assemblies, *Int. J. Hydrogen Energy*, 13(10), 593–604, 1988.
25. National Hydrogen Association, The hydrogen technology assessment, phase I. A report for NASA, Washington, DC, 1991.
26. Taylor, J.B., Alderson, J.E.A., Kalyanam, K.M., Lyle, A.B., and Phillips, L.A. Technical and economic assessment of methods for the storage of large quantities of hydrogen, *Int. J. Hydrogen Energy*, 11(1), 5–22, 1986.
27. Carpetis, C., Storage, transport and distribution of hydrogen, in C.-J. Winter and J. Nitsch (eds.), *Hydrogen as an Energy Carrier*, Springer-Verlag, Berlin, Germany, pp. 249–289, 1988.
28. Pottier, J.D. and Blondin, E., Mass storage of hydrogen, in Y. Yurum (ed.), *Hydrogen Energy System: Production and Utilization of Hydrogen and Future Aspects*, NATO ASI Series E-295, Kluwer Academic Publishers, Dordrecht, the Netherlands, pp. 167–180, 1995.
29. Mitlitsky, F., Development of an advanced, composite, lightweight, high pressure stor- age tank for on-board storage of compressed hydrogen, *Proceedings of the Fuel Cells for Transportation TOPTEC: Addressing the Fuel Infrastructure Issue*, Alexandria, VA, SAE, Warrendale, PA, 1996.
30. Veziroglu, T.N., Hydrogen technology for energy needs of human settlements, *Int. J. Hydrogen Energy*, 12(2), 99–129, 1987.
31. Schwartz, J.A. and Amankwah, K.A.G., Hydrogen storage systems, in D.G. Howell (ed.), *The Future of Energy Gases*, U.S. Geological Survey Professional Paper 1570, U.S. Government Printing Office, Washington, DC, pp. 725–736, 1993.
32. Chambers, A., Park, C., Baker, R.T.K., and Rodriguez, N.M., Hydrogen storage in graphite nanofibers, *J. Phys. Chem. B*, 102(22), 4253–4259, 1998.
33. Dillon, A.C., Jones, K.M., and Heben, M.J., Carbon nanotube materials for hydrogen storage, *Proceedings of the 1996 U.S. DOE Hydrogen Program Review*, Vol. II, National Renewable Energy Laboratory, Golden, CO, pp. 747–763, 1996.
34. Rambach, G. and Hendricks, C., Hydrogen transport and storage in engineered glass micro- spheres, *Proceedings of the 1996 U.S. DOE Hydrogen Program Review*, Vol. II, National Renewable Energy Laboratory, Golden, CO, pp. 765–772, 1996.
35. Jensen, C., Hydrogen storage via polyhydride complexes, *Proceedings of the 1996 U.S. DOE Hydrogen Program Review*, Vol. II, National Renewable Energy Laboratory, Golden, CO, pp. 787–794, 1996.
36. Brewer, G.D., The prospects for liquid hydrogen fueled aircraft, *Int. J. Hydrogen Energy*, 7, 21–41, 1982.
37. Winter, C.J. and Nitsch, J., *Hydrogen as an Energy Carrier*, Springer-Verlag, Berlin, Germany, 1988.
38. Huston, E.L., Liquid and solid storage of hydrogen, *Hydrogen Energy Progress V*, Toronto, Ontario, Canada, 1984.
39. Sherif, S.A., Lordgooei, M., and Syed, M.T., Hydrogen liquefaction, in T.N. Veziroglu (ed.), *Solar Hydrogen Energy System*, Final Technical Report, Clean Energy Research Institute, University of Miami, Coral Gables, FL, pp. C1–C199, August 1989.
40. Hands, B.A., *Cryogenic Engineering*, Academic Press, New York, 1986.
41. Newton, C.L., Hydrogen production, liquefaction and use, *Cryogen. Eng. News*, Part I(8), 50–60, 1967.
42. Newton, C.L., Hydrogen production, liquefaction and use, *Cryogen. Eng. News*, Part II(9), 24–29, 1967.
43. Baker, C.R. and Shaner, R.L., A study of the efficiency of hydrogen liquefaction, *Int. J. Hydrogen Energy*, 3, 321–334, 1978.
44. Scott, R.B., *Cryogenic Engineering*, Van Nostrand Company, Inc., Princeton, NJ, 1962.
45. Ewe, H.H. and Selbach, H.J., The storage of hydrogen, in W.E. Justi (ed.), *A Solar Hydrogen Energy System*, Plenum Press, London, U.K., 1987.

www.Ebook777.com

46. Barclay, J.A., Magnetic refrigeration for low-temperature applications, *Proceedings of the Cryocooler Conference*, Boulder, CO, September 1984.
47. Barclay, J.A., Overton, Jr., W.C., and Stewart, W.F., Phase I final report: Magnetic reliquefication of LH_2 storage tank boil-off, Kennedy Space Center, Ref. No. PT-SPD/6037/2511C/000000/04/82, (NASA-Defense Purchase Req. CC-22163B), NASA, Washington, DC, 1983.
48. Barclay, J.A., The theory of an active magnetic regenerative refrigerator, NASA-R-2287, NASA, Washington, DC, 1983.
49. Barclay, J.A. and Steyert, W.A., Materials for magnetic refrigeration between 2 K and 20 K, *Cryogenics*, 22, 73–79, February 1982.
50. Barclay, J.A. and Stewart, W.F., The effect of parasitic refrigeration on the efficiency of magnetic liquefiers, *Proceedings IECEC '82: 17th Intersociety Energy Conversion Engineering Conference*, Los Angeles, CA, p. 1166, August 1982.
51. Barclay, J.A., Use of a ferrofluid as the heat-exchange fluid in a magnetic refrigerator, *J. Appl. Phys.*, 53(4), 2887, 1982.
52. Barclay, J.A. and Sarangi, S., Selection of regenerator geometry for magnetic refrigerator appli- cations, *Proceedings of the ASME Winter Annual Meeting*, New Orleans, LA, December 1984.
53. Barclay, J.A., Stewart, W.F., Overton, W.C., Candler, R.C., and Harkleroad, O.D., Experimental results on a low-temperature magnetic refrigerator, *Cryogenic Engineering Conference*, Boston, MA, August 1985.
54. Brown, N.S., Advanced long term cryogenic storage systems, NASA Marshall Space Flight Center, Huntsville, AL, NASA Conference Publication 2465P, Washington, DC, pp. 7–16, 1986.
55. Barron, R.F., *Cryogenic Systems*, Oxford University Press, Oxford, U.K., 1985.
56. Kandebo, S.W., Researchers explore slush hydrogen as fuel for national aerospace plane, *Aviation Week Space and Technology*, pp. 37–38, June 26, 1989.
57. Baker, C.R. and Matsch, L.C., Production and distribution of liquid hydrogen, *Adv. Pet. Chem. Refin.*, 10, 37–81, 1965.
58. Sindt, C.F., A summary of the characterization study of slush hydrogen, *Cryogenics*, 10, 372–380, October 1970.
59. Voth, R.O., Producing liquid-solid mixtures (slushes) of oxygen or hydrogen using an auger, *Cryogenics*, 25, 511–517, September 1985.
60. Pottier, J.D., Hydrogen transmission for future energy systems, in Y. Yurum (ed.), *Hydrogen Energy System, Utilization of Hydrogen and Future Aspects*, NATO ASI Series E-295, Kluwer Academic Publishers, Dordrecht, the Netherlands, pp. 181–194, 1995.
61. Oney, F., The comparison of pipelines transportation of hydrogen and natural gas, MS thesis, University of Miami, Coral Gables, FL, 1991.
62. Norbeck, J.M., Heffel, J.W., Durbin, T.D., Tabbara, B., Bowden, J.M., and Montano, M.C., *Hydrogen Fuel for Surface Transportation*, SAE, Warrendale, PA, 1996.
63. Sternfeld, H.J. and Heinrich, P., A demonstration plant for the hydrogen/oxygen spinning reserve, *Int. J. Hydrogen Energy*, 14, 703–716, 1989.
64. Kinoshita, K., McLarnon, F.R., and Cairns, E.J., *Fuel Cells: A Handbook*, U.S. Department of Energy, DOE/METC88/6069, Morgantown, WV, 1988.
65. Blumen, L.J.M.J. and Mugerwa, M.N. (eds.), *Fuel Cell Systems*, Plenum Press, New York, 1993.
66. Thomas, C.E., Preliminary hydrogen vehicle safety report, The Ford Motor Company, Contract. No. DE-AC02-94CE50389, U.S. Department of Energy, Washington, DC, 1996.
67. Swain, M.R. and Swain, M.N., A comparison of H_2, CH_4, and C_3H_8 fuel leakage in residential settings, *Int. J. Hydrogen Energy*, 17(10), 807–815, 1992.

Section I

Hydrogen Production Overview

2

Overview of Hydrogen Production

Aldo Steinfeld

ETH Zurich

Paul Scherrer Institute

Pure hydrogen is not found free in nature, but bounded mainly as water and natural gas, and in lower concentration as biomass, fossil fuels, and other hydrogen-containing compounds. Its production from these natural raw materials requires energy-intensive processes. Thus, two crucial aspects are pertinent to the selection of a production methodology, namely, the raw material and the energy source. Both aspects ultimately determine the carbon footprint of hydrogen production.

The production processes can be grouped into electrochemical, thermochemical, photochemical, and their combinations. In electrochemical processes, the energy input is given as electricity, which in turn is generated from various energy sources such as renewables (e.g., wind, solar, geothermal, hydro, biomass) and nonrenewables (e.g., fossil fuels, nuclear). In thermochemical processes, the energy input is given as high-temperature heat, which in turn is generated from various energy sources such as renewables (e.g., concentrated solar thermal, biomass combustion) and nonrenewables (e.g., fossil fuel combustion, nuclear heat). In photochemical processes, the energy input is by the direct absorption of photons of light. Combinations of these energy-intensive processes include photoelectrochemical (e.g., artificial catalytic photosynthesis), photobiological (e.g., photosynthesis by microbial metabolic systems), thermoelectrochemical (e.g., high-temperature electrolysis), and hybrid methods involving multiple steps of the aforementioned processes (e.g., thermochemical and electrochemical splitting cycles).

The carbon footprint of hydrogen production is of utmost importance for its use as a sustainable fuel. The plurality of production processes and associated energy sources is further complicated by the plurality of raw materials. Figure 2.1 lists examples of production processes along with their associated raw materials and energy sources. For the raw materials, the key attribute is the ability to close the material cycle, that is, to regenerate the starting material without emissions discharge to the environment. For the energy sources, the key attribute is renewable or nonrenewable. A most cited example of a production process theoretically approaching zero carbon footprint is the electrolysis of water (Chapter 7) driven by solar, wind, hydropower, or any other renewable electricity source. Competing production processes that also use water as a raw material and a renewable energy resource are solar thermochemical cycles (Chapter 12) and solar photosynthesis (Chapter 13). Thermochemical cycles may also be driven by nuclear process heat (Chapter 8). An example of a production process with a relatively large carbon footprint is the reforming of natural gas driven by heat from fossil fuel combustion (Chapter 3), which presently is the most practiced manufacturing process at an industrial scale because of its economic feasibility. Given the future importance of solid carbonaceous feedstocks such as coal, coke, biomass,

Free ebooks ==> www.Ebook777.com

	Processes	Raw Materials	Source of Energy
Electrochemical	Electrolysis	• Water	• Electricity from renewable energy sources (e.g., wind, geothermal, solar, hydro) • Electricity from nonrenewables (e.g., fossil fuels, nuclear)
Thermochemical	Reforming	• Natural gas • Hydrocarbons • + Water	• Combustion of natural gas/syngas • Concentrating solar thermal
	Gasification	• Coal • Carbonaceous materials • Biomass • + Water	• Combustion of coal/biomass/carbonaceous materials/syngas • Concentrating solar thermal
	Decomposition	• Natural gas • Fossil fuel hydrocarbons • Biomethane • Biohydrocarbons	• Natural gas combustion • Concentrating solar thermal
	Thermolysis	• Water	• Concentrating solar thermal
	Thermochemical cycles	• Water	• Concentrating solar thermal • Nuclear heat
Photochemical	Photosynthesis	• Water	• Solar radiation, artificial light
	Photobiological	• Microbial (e.g., algae) • + Water	• Solar radiation

FIGURE 2.1

Production processes, raw materials, and sources of energy.

bitumen, and carbon-containing wastes, gasification technologies are developing rapidly. An example of this category of thermochemical processes with a low carbon footprint is the gasification of biomass driven by heat from biomass combustion (Chapter 5) or from concentrated solar energy (Chapter 12). Alternatively, when coal is the raw material and coal combustion the source of process heat, the large carbon footprint may be mitigated by implementing CO_2 capture technologies (Chapter 4). Ultimately, the carbon footprint of hydrogen production is determined via a life cycle assessment (Chapter 14), which evaluates the environmental burdens associated with the production process by identifying and quantifying the energy and materials used and wastes released to the environment and accounts for the entire life cycle of the process encompassing extraction and processing of raw materials, manufacturing, transportation, distribution, recycling, and final disposal.

Sections II through VI present the fundamental principles of the various hydrogen production processes and their associated technologies and systems. It recognizes that transitioning from a fossil fuel–based economy to a sustainable hydrogen-based economy

imposes scientific and technical challenges. Further R&D aimed at near-zero carbon footprint is warranted, while emphasizing the interrelation between the production, storage, and final use of hydrogen as a fuel, along with the social and environmental aspects of energy sustainability.

www.Ebook777.com

Section II

Hydrogen Production: Fossil Fuels and Biomass

3

Reformation of Hydrocarbon Fuels

Paul A. Erickson
University of California, Davis

Hong-Yue (Ray) Tang
University of California, Davis

David R. Vernon
Humboldt State University

CONTENTS

3.1 Introduction 24
3.2 What Is Reformation? 25
3.3 History of Reformation 26
3.4 Modern Reformation: State of the Art and Technological Barriers 27
3.5 Quantifying Reactor Performance and Parameters 28
3.5.1 Flow Rate 29
3.5.2 Stoichiometry 29
3.5.3 Output and Analysis 30
3.5.4 Reformer Characterization 30
3.6 Catalyst Selection 32
3.7 Types of Reformation 34
3.8 Steam Reformation 34
3.9 Partial Oxidation 37
3.10 Autothermal Reforming 38
3.11 ATR of Different Fuels 41
3.12 Limiting Mechanisms in the Reformation Processes 44
3.12.1 Chemical Kinetics 44
3.12.2 Mass Transfer 44
3.12.3 Heat Transfer 45
3.12.4 Degradation Mechanisms 46
3.12.5 Controls 47
3.13 Comparison of the Reforming Methods 48
3.14 Fuel Selection 49
3.15 Internal Reforming in High-Temperature Fuel Cells 51
3.16 Reactor Design 51
3.17 Reformer Control Issues 53
3.18 Summary 53
References 54

3.1 Introduction

Hydrogen is not readily available in nature in the unbound molecular form. Thus, hydrogen is not a primary energy source but, like electricity, is an energy carrier and must be converted from other sources of energy. While hydrogen as an energy carrier has low environmental impact at the point of use, there may be significant impacts from the production and distribution of hydrogen. There are many hydrogen production methods ranging from well-developed industrial processes to emerging pathways in both biological and thermochemical pathways. The most commonly used process to generate hydrogen is reformation of fossil fuels. This chapter will discuss the basic principles and state of the art of steam and autothermal reformation (ATR) processes.

Figure 3.1 shows the energy density of some fuels on both mass and volumetric bases. Note that for Figure 3.1, these values include only the fuel itself and not the tank required to hold such a fuel. The low volumetric energy content of hydrogen and the lack of infrastructure for hydrogen refueling present a significant obstacle for enabling hydrogen-fueled systems for power generation. Producing hydrogen via reformation of a liquid fuel for onboard mobile hydrogen applications shows the potential of using hydrogen technologies while avoiding storage difficulties by allowing the storage and transport of a higher-energy-density liquid. While significant progress has been made recently in hydrogen storage issues, reforming high-energy-density liquid hydrocarbons allows for fast refueling, ambient pressure storage, and potentially higher total energy storage capacity in a given volume. For stationary

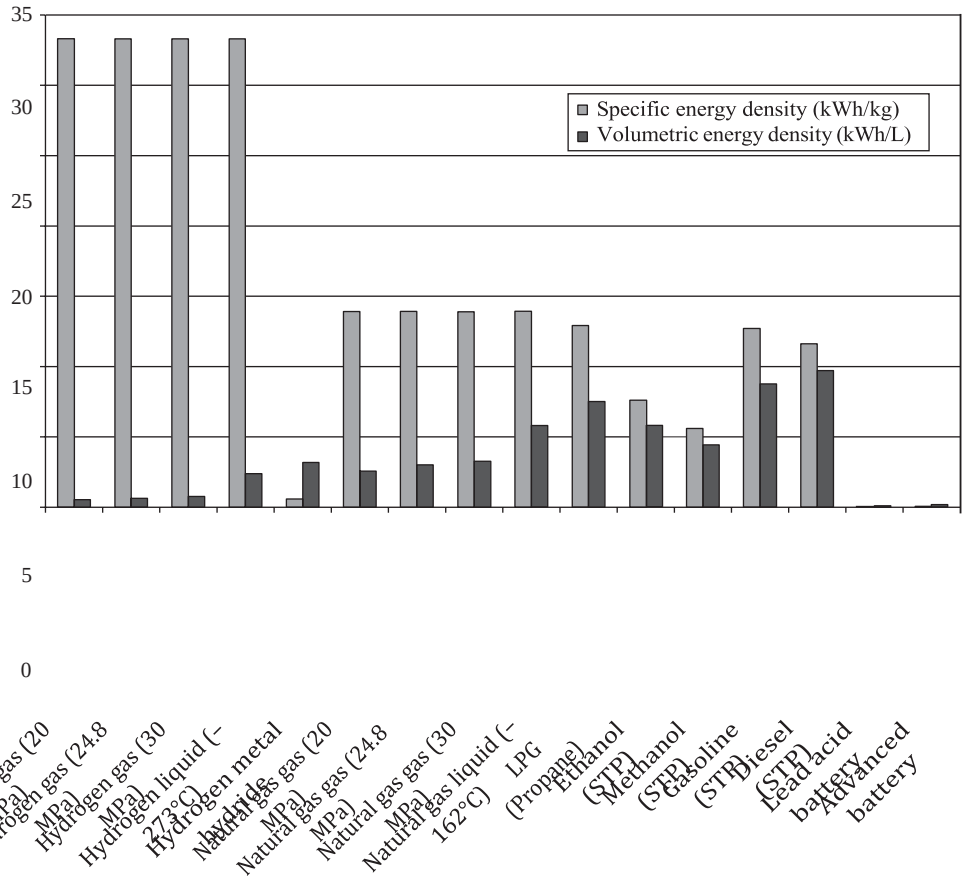


FIGURE 3.1

A comparison of various fuels. Hydrogen has the highest energy per unit weight but the lowest energy per unit volume. Currently, diesel, gasoline, and LPG are common fuel for transportation application.

Free ebooks ==> www.Ebook777.com

applications, catalytic reforming of a hydrocarbon feedstock can potentially be combined with carbon dioxide capture and sequestration systems to reduce greenhouse gas emissions.

For about a century, stationary large-scale hydrogen production plants have been providing hydrogen for industrial processes such as for refinery hydrogenation, ammonia production, and gas-to-liquid (GTL) plants, that is, converting methane to methanol.

While large-scale hydrogen production plants are well established, small-scale fuel processors are not as established and are found in the research and development field or in niche markets [1–6]. These potential hydrogen applications include standby and auxiliary power systems, mobile power generation (i.e., auxiliary power units, forklift applications), and stationary distributed power generation.

3.2 What Is Reformation?

Reformation is a chemical process that breaks hydrocarbon molecules into hydrogen from a compounded element to its elemental form. Equation 3.1 represents the typical overall reaction in steam reformation (SR) of a hydrocarbon. In a pure definition, reformation is when the characteristics of a certain fuel

$$C_nH_m + n\,H_2O \rightarrow n\,CO + \frac{n+m}{2}H_2 \qquad \Delta H\,(298\ K) > 0 \tag{3.1}$$

are reformed into a desirable trait. The SR process shown in Equation 3.1 and other processes like it can be used to change the characteristics of fuels.

Reformation is typically an endothermic reaction due to the hydrogen product having a higher energy state than the hydrocarbon fuel or fuel–water mixture. Thus, energy is needed to volatilize the hydrocarbons and break the C–C and H–C bonds. A heat source, such as an external burner, is used to provide the energy in a typical system. Internal heat sources can also be used by introducing an oxidizer into the fuel–water stream, but this typically will dilute the output stream purity with nitrogen when air is used. A variety of hydrocarbon fuels have been used in reformation studies and have been successfully used in some prototypes and commercial applications: gasoline [7,8], ethanol [4,9], methanol [10–12], dimethyl ether, propane, butane, methane (natural gas), diesel [1,13,14], isooctane, and jet fuel such as JP-8 [15] are some of the examples [5–7,12,16–18]. The reassembly of the elemental hydrocarbon constituents with oxygen, either supplied with the fuel–water mixture or externally added in small amounts, is thermodynamically favored as being exothermic. Thus, with typical reformation of hydrocarbon feedstocks, one has a highly endothermic and rate-limiting fuel steam breakdown followed by a moderately exothermic reassembly through the water–gas shift reaction with the total reaction being endothermic.

Although reformation can proceed unaided by using solely thermal processes at high temperature, the typical reformation system uses a catalyst bed or a series of catalyst beds to shift selectivity toward the desired products (H_2 and CO_2). Inside the fuel processor, the catalyst aids the reformation of the hydrocarbon fuel into a hydrogen-rich gas mixture. The main reformer can be followed by numerous catalytic water–gas shift reactors that bring the H_2 concentrations up and minimize problematic compounds. The conversion,

www.Ebook777.com

efficiencies, cost, and usable life of the catalysts are strongly dependent on the temperature at which the catalyst is operated; thus, temperature is an important aspect of the control of the fuel processor.

For complex hydrocarbons, dry reforming (or partial oxidation [POX]) is used in prereformers to break apart long-chain hydrocarbons prior to SR. If water or steam is added to the process, then part of the water will be consumed to produce additional hydrogen via the water–gas shift reaction. POX and ATR can use either oxygen or air to produce heat in the overall process. This improves the heat and mass transfer of the catalyst bed by trading off reformate stream purity and results in product dilution when using air as the oxidizer.

3.3 History of Reformation

Historically speaking, reformation is as old as flame itself and is not independent of combustion especially regarding solid or liquid fuel combustion. It is well known that a typical solid or liquid fuel does not burn directly but only in gaseous phase. Thus, the endothermic heating and vaporization as seen with most diffusion flames lead to a local gasification or reformation of the fuel. This gaseous fuel then diffuses until it reaches the oxidizer and then burns to the end products.

Reformation is then an effective short-circuiting of the combustion process and is usually classified in the combustion field as gasification. While it can be argued that reformation has always occurred with combustion and it is not an independent field, reformation as known in literature as a deliberate action had its roots in the late 1700s in solving England's early street lighting problems.

Table 3.1 shows early milestones in the uses of reformation or gasification. In the late 1700s, coal and biomass fuels were not readily applicable to distributed lighting systems because of their traits regarding solid transportability. With the price of whale oil skyrocketing with resource depletion, a crisis in the lighting systems of London was developing. William Murdoch is attributed with devising ways of changing solid fuels such as wood and coal into distributable gaseous fuels by POX or gasification of the solid fuel. One of the early commercial uses of reformation was deriving *town gas* or *syngas* from coal in the early 1800s. This was used for lighting and cooking before natural gas and electricity became more available in the mid-1900s.

TABLE 3.1

Early Milestones of Gasification

Date	Milestone
1792–1794	Scottish scientist William Murdoch produced gas from heating coal for lighting. 1804 Coal gas first patented for lighting.
1813	London and Westminster Gas Light and Coke Company, Great Peter Street, illuminates Westminster Bridge with town gas lights on New Year's Eve using wooden pipes.
1816	Baltimore, Maryland, becomes the first US city to light streets with town gas. 1959 British Gas Council started to replace coal gas with liquid natural gas.

Source: http://www.netl.doe.gov/technologies/coalpower/gasification/basics/3.html.

3.4 Modern Reformation: State of the Art and Technological Barriers

The use of town gas was essentially that of converting a fuel from a solid form to a form that had desirable transport characteristics. Modern reformation also converts liquid, solid, or gaseous fuels into hydrogen that has desirable environmental point-of-use characteristics or allows hydrogen to be used in chemical processing. Reformation can also be used to convert marginally usable low-energy fuels as is found with some biomass sources into a hydrogen gas with benefits in transportability and energy intensity.

The dominant use of hydrogen is in the chemical industry [20]. The primary use of hydrogen is for the production of ammonia and methanol, for hydrotreatment in refineries, and for hydrogenation of unsaturated hydrocarbons. Approximately 90% of the hydrogen used is produced by SR of natural gas and other light refinery hydrocarbons. Other production methods used include gasification and reforming of heavier hydrocarbon fuels, electrolysis, and biological methods.

In a modern reformation facility, natural gas is joined with steam and fed across a catalyst bed. Product gas is collected and fed into various purification steps. The product gas typically carries more chemical energy than the input fuel and steam; thus, the reformation is endothermic, and heat is supplied externally from a combusted fuel.

In a typical methane steam reformer, the reforming process typically requires a temperature from 500°C to 950°C. The reformate, or the product of hydrocarbon reformation, is usually fed into high-temperature and low-temperature water–gas shift reactors to increase the hydrogen concentration and decrease the CO content. The output stream of the water–gas shift reactors is fed into a pressure swing adsorption (PSA) system for purification that gives 99.9% or higher purity. While large-scale hydrogen production has been commercialized for many decades, the current gap to make hydrogen readily available for distributed power generation and transportation applications is dependent on decentralized hydrogen production [21]. Smaller fuel processors for point-of-use application are now actively studied.

In commercial large-scale hydrogen production systems, the steam reformer operates with the catalyst bed temperature typically at 450°C–800°C at 30–45 bar using a Ni-based catalyst held on a ceramic pellet substrate. Cobalt and other noble metals can also be used as catalysts but are generally more expensive. The selection of the catalyst is typically a trade-off in the costs associated with operational life and avoidance of solid carbon (coke) formation, which is also affected by the steam-to-carbon (S/C) ratio. Along with the S/C ratio, other cost factors include flow throughput and pressure drop that reflect operational costs. The catalyst is loaded into high-strength alloy tubes with an outer diameter that ranges from 100 to 150 mm and the length ranges from 10 to 13 m. These tubes must have long creep life and high creep rupture strength due to the high-temperature and high-pressure operation inside the reformer. Central external burners operating at slightly negative gauge pressure provide heat to arrays of steam reformer tubes that can have over 1000°C external wall temperatures. Furnaces holding hundreds of reformer tubes are not unheard of and even small plants might have a 72-tube array in a single furnace. The standard reformer tube is mechanically simple with a header and an orifice at each tube entrance to ensure similar flows in each tube. Temperature for the entire reformate stream is typically monitored by a single temperature sensor at the merged reformate exit. Some operators will monitor tube temperature down the center line of each tube with a multijunction device. Areas of high heat flux can also be noted by observing the dark or cooler regions of the tube from observation points within the furnace. Lifetimes on the



FIGURE 3.2

Georgetown's Test Bed Bus-1 at University of Davis. First demonstrated in April 1994.

order of years with continuous use are expected with the commercial system catalysts and reformer apparatus. Other than methane, various heavy hydrocarbon feedstocks can be used with additional prereforming and suitable catalysts as longer-chain molecules as fuels have the tendency to form carbon at hot spots on the Ni-based catalyst. Ammonia formation and other minor species can also be problematic.

For small-scale hydrogen production, adopting technology from well-understood industrial processes and scale down shows unique challenges [22–24], such as optimizing catalyst operation life and reformer design. In recent years, detailed studies of small-scale reformers for hydrogen production have been published [15,25–27]. Unlike large-scale reformers, small-scale reformers are expected to experience significant transients in normal operation. Frequent start-up and shutdown of reformers can degrade the catalyst and apparatus reducing the life and performance of the system. Reformation systems have been adapted to mobile applications including several iterations of the Georgetown fuel cell buses (1994–2000). The earliest system (1994) is shown in Figure 3.2. Reformation was also used by early fuel cell vehicles including those demonstrated by Daimler (NECAR 3), Toyota (fuel cell electric vehicle [FCEV]), General Motors, and Hyundai motors. An excellent review of small-scale fuel processing for fuel cells and fuel cell vehicles is given in Gunther Kolbs' recent book [28].

3.5 Quantifying Reactor Performance and Parameters

A somewhat standard set of terms and language is used in the reformation industry. Typical parlance includes flow rate in terms of space velocity, stoichiometric terms such as oxygen-to-carbon (O_2/C) ratio and S/C ratio, and output and analysis terms such as conversion, selectivity, and yield.

3.5.1 Flow Rate

Flow rate is typically normalized to an inverse residence time parameter known as space velocity, which can be further distinguished to indicate gaseous species or equivalent liquid species if applicable. Space velocity (sv) is a quasi-nondimensional term that is defined as the reactor volumetric flow rate divided by the reactor volume. This is shown in the following:

$$\mathrm{SV} = \frac{\dot{V}}{V} \tag{3.2}$$

where
$\dot{V}$ is the volumetric flow rate
V is the reactor volume

The units are inverse time so as flow rate increases so does space velocity. The units can be done in any time unit but hourly space velocity is commonly used. For gas space velocity, the species temperature and pressure can change the volumetric flow rate at any location in the reactor; thus, nonreacted reactor inlet conditions are often used. Standard temperature and pressure can also be used for normalization. S/C ratio can often change, but as the fuel stream is often the only reactant supplying energy, the space velocity can remove the steam-to-carbon dependence by stating just the volumetric flow rate of the fuel and not the water or steam flow. For fuels that are liquids under standard temperature and pressure, liquid space velocities can be used although the reactants are vaporized and are certainly not reacting in liquid phase. A denotation of LHSV-M would represent a liquid hourly space velocity of methanol, whereas liquid hourly space velocity (LHSV) might be methanol or a premix of methanol and water. GHSV could also be used to represent this flow as gas hourly space velocity at specified inlet conditions and S/C. GHSV-MSTP would mean gas hourly space velocity of methane at standard temperature and pressure, whereas GHSV could mean any or all reactants at standard or another given inlet condition. Another issue with all space velocity terms is the definition of the reactor volume. Those in industry generally prefer to indicate the entire tube including empty locations as it indicates the true length and volume required by the reactor, while those in academic studies typically will only include the volume displaced by the catalyst because the typical research reactor housing is not filled to its full capacity with the catalyst. Those reporting flow values in space velocity should be careful to include a full description of their values to avoid ambiguity or mistranslation of the values.

3.5.2 Stoichiometry

O_2/C ratio and S/C ratio are parameters used to describe the stoichiometry in reformation processes. Those reporting values should clearly define O_2/C ratio nomenclature especially when using air as the oxidizer and/or using fuels with oxygen contained therein (i.e., alcohols). S/C ratio and stoichiometry can also be potentially confused in the O_2/C ratio. Typically, oxygen bound up in compounds will not be counted in the O_2/C ratio, and oxygen is counted in its bound O_2 form and not as an oxygen radical. When using alcohols, it is helpful to note the oxygen–alcohol ratio (i.e., oxygen to methanol [O_2: CH_3OH]) rather than just O_2/C to avoid mistranslation.

Free ebooks ==> www.Ebook777.com

3.5.3 Output and Analysis

Outputs of reformation reactors can be equally ambiguous and many output metrics can include all or selected species. Typical output nomenclature includes conversion, selectivity, and yield. These outputs should also be defined carefully for a system as some outputs can be defined by the user and most are specific to a certain reactant or a certain product.

Conversion is defined as the reactant consumed divided by the reactant fed as shown in the following:

$$\text{Conversion} \quad \frac{\text{Reactant consumed}}{\text{Reactant fed}} \tag{3.3}$$

Conversion is typically given in percent and only indicates how much reactant was consumed. For a single pathway system, this does give insight of the fuel consumption and reactant progression. It does not however give any indication of the product produced. This is an important distinction because in reformation systems, the hydrogen product is typically what is desired. Thus, even though conversion may be high, the hydrogen output could be nonexistent especially with POX reforming or ATR systems that employ an oxidation step. For example, complete combustion implies complete conversion but no hydrogen production.

The selectivity has at least two potential definitions. These are shown in the following:

$$\text{Selectivity} \quad \frac{\text{Desired product produced}}{\text{Undesired product produced}} \tag{3.4}$$

and

$$\text{Selectivity} = \frac{\text{Desired product produced}}{\text{Reactant consumed}} \times \tag{3.5}$$

where the stoichiometric factor (SF) is used to normalize the selectivity to 100%.

For example, in methanol reformation, the stoichiometric equation is shown in the following:

$$CH_3OH + H_2O \rightarrow CO_2 + 3H_2 \tag{3.6}$$

In this case, if the desired product is hydrogen and the reactant is methanol (CH_3OH), the SF would be 1/3 as 3 mol of hydrogen H_2 is produced per 1 mol CH_3OH reactant. This factor allows normalization to 100%.

The yield shown in the following also uses a similar SF:

$$\text{Yield} = \frac{\text{Desired product produced}}{\text{Reactant fed}} \times \tag{3.7}$$

3.5.4 Reformer Characterization

Space velocity describes the fuel-processing capacity and the volume of the reactor but is insufficient to quantify the properties of the reactor. However inadequate, reactors are often compared using space velocity as a metric. Many researchers speak of a break point in space velocity where the reactor begins to break away from the 100% or previously

www.Ebook777.com

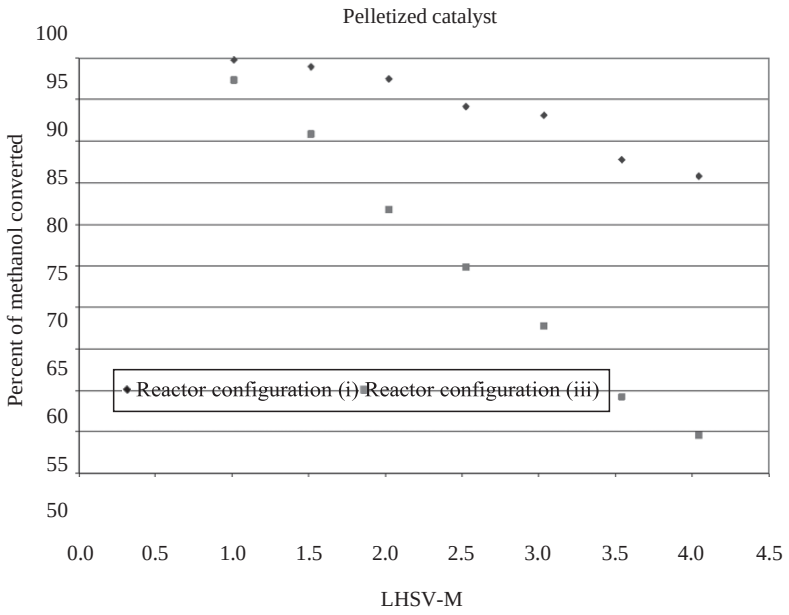


FIGURE 3.3

Two similar reactors with different aspect ratios. (From Davieau, D.D. and Erickson, P.A., *Int. J. Hydrogen Energy*, 32(9), 1192, 2007.)

defined percent conversion or yield. While this is useful to know the limits of performance, the first-order behavior of the reactor is not captured by such characterization. As seen in Figure 3.3 [29], performance can vary greatly for reactors that have the same space velocity. In this figure, the catalyst, flow rate, reactor set point temperature, control scheme, and reactor volumes are identical. The only difference between these data is that the reactor radius of configuration (i) is 0.635 cm (¼ in.) less than that of configuration (iii). This clearly shows that reactor performance cannot be described by space velocity alone.

A better metric is to use the characteristic time constant, which factors additional information such as geometric conditions, heat and mass transfer characteristics, and flow condition and describes the performance directly from the residence time. In addition, the chemical kinetic properties are indirectly captured by the reaction rate coefficient in the residence time distribution (RTD). This is especially important in describing steam reformers as their performances are dependent on the heat transfer characteristic. Since the characteristic time embodies the geometric effect and chemical kinetics, it is more descriptive than using space velocity (SV) [30].

The characteristic time is a modification of the RTD. The overall reformation process based on fuel conversion can be simplified to a first-order reaction. Taking methanol SR as example, using the Arrhenius mechanism, the reaction rate coefficient can be expressed as shown in the following:

$$k(T) = Ae^{E_a/RT} \tag{3.8}$$

Following Fogler's formulation of a segregation model for packed-bed reactors [31], by knowing the reactor's RTD function, $E(t)$, and the reaction rate coefficient from Equation 3.8, the theoretical conversion is shown in the following:

$$\bar{X} = 1 - \int_0^\infty e^{-k(T)t} E(t)\,dt$$

(3.9)

By assuming an ideal plug flow reactor (PFR) RTD function as a Dirac function, $E(t) = \partial(t - t_r)$, with an identical residence time t_r for every molecule in the reactor, and substituted into Equation 3.9 yields the following:

$$X = 1 - e^{-k(T)t_r} = 1 - e^{\frac{-t_r}{\tau}} \tag{3.10}$$

The first-order characteristic time, τ, represents the time needed to convert 63.2% of the fuel or produce 63.2% of the possible desired product in a particular reactor. Like all first-order systems after five time constants, the reactor should produce near 100% conversion or yield and this characterization captures this behavior. Unlike SV, LHSV-M, or GHSV, characteristic time is descriptive of the actual performance and takes into account catalyst particle size, flow conditions, and other passive enhancements such as baffles and acoustic waves. As characteristic time is based on conversion or yield performance, reactors with the same characteristic time will have the same performance, regardless of temperature, geometry, catalyst, pressure, etc. In other words, given the required characteristic time, there are multiple ways to optimize the reactor design.

3.6 Catalyst Selection

By introducing a catalyst into the reaction, new pathways and acceleration of the reaction occur. An ideal catalyst would not be consumed, but in practice, catalysts do undergo physical and chemical changes. There are three modes of action of catalyst [32]: activity, selectivity, and stability (or degradation behavior).

Activity is a measure of how fast the reaction(s) proceeds in the presence of the catalyst. It is influenced by temperature, concentration of the chemical species, pressure, residence time, and other factors. In reformation, the limiting mechanisms are mass and heat transfer and chemical kinetics and are discussed in a later section. They are fully coupled with one another, and improving the control of the catalyst temperature helps to improve catalyst activity and the overall performance.

The selectivity of the catalyst is the measure of desirable product to the reacted quantity of the feedstock. The realistic selectivity is often less than ideal because of a secondary reaction creating an undesirable by-product that reduces efficiencies. Additional cleanup or removal steps are needed to ensure purity of the output stream. In reformation, CO is undesirable because it can poison the electrode of a proton exchange membrane fuel cell (PEMFC). Carbon formation or coke can also degrade the catalyst, which is the third mode of action of catalysts.

Catalysts help introduce new pathways to reduce the activation energy required to reform a hydrocarbon, provided that the catalyst is active by having sufficient tempera- ture. The reformation is typically an endothermic process; thus, the limiting mecha- nisms are heat and mass transfer. When a hydrocarbon finds an active site on a catalyst, it breaks down the chemical bonds and reassembles, and it consumes heat and reduces the catalyst and fuel temperature in the process. Heat is added to the system to ensure high catalyst activity to sustain the operation. If the catalyst is highly active, the refor- mation continues to go forward as long as fuel can find an active site on the catalyst. The porous structure of the catalyst allows fuel to diffuse into the catalyst. After the

reactants diffuse into the catalyst and reform, products need to diffuse out from the catalyst to allow the active site to reform the next reactant.

Catalyst degradation is an important issue in catalytic reformation. The chemical, thermal, and mechanical stability of the catalyst determine the operation life of the reactor [32]. Desulfurization is often necessary with most fossil-fuel-based liquids. Care must be taken in controlling the temperature because of the poor heat transfer property of the catalyst or the catalyst bed. A Ni-based catalyst is often used in the high-temperature reformers because it is cheap, active at elevated temperature, and stable. On the other hand, Cu-based catalysts cannot operate at high temperature but have high selectivity toward hydrogen. Care is taken when using a Cu-based catalyst with an exothermic reaction to ensure the integrity of the catalyst. Additionally, other operating conditions such as S:C and O_2:C, where appropriate, should be controlled to minimize carbon formation. The two general types of catalyst substrates are pellets and monolith structures shown in Figure 3.4.

The choice of catalyst depends on the feedstock used. There are wide selections of catalyst formulations for reforming hydrocarbon fuels, and many more are in development. In general, monolith catalysts produce less pressure drop than do pellets. A small amount of catalyst material is washcoated onto a monolith substrate to form the monolithic catalyst. Pellets are usually porous alumina structures with open sites for the catalyst. The advantage of pelletized catalyst over the monolith catalyst is their resistance to poisoning and high amounts of internal surface area.

The reforming catalyst is usually based on nickel/nickel oxide or cobalt composite. They require high temperature to become active and are generally suitable for higher-order hydrocarbon reformation. Lighter hydrocarbons, such as methanol, can be reformed using copper-based medium temperature shift (MTS) [20] catalysts. Many of these formulations used for methanol and ethanol reformation have been used as water–gas shift catalysts for the natural gas reforming industry because of their high selectivity toward hydro- gen and CO_2. The catalyst system of copper (Cu) in the presence of zinc oxide (ZnO) sup- ported by alumina (Al_2O_3), derived from industrial catalysts, is the most popular. There have been other catalysts proposed [33–42], but $Cu/ZnO/Al_2O_3$ remains the primary inter- est [10,34,43–46]. The low-temperature catalyst allows a less complex heat exchanger and is potentially compatible with phosphoric acid fuel cell (PAFC) or PEMFC applications. Another advantage for reforming at low temperature is the low level of CO formation. The high temperature allows the reverse water–gas shift reaction to consume hydrogen

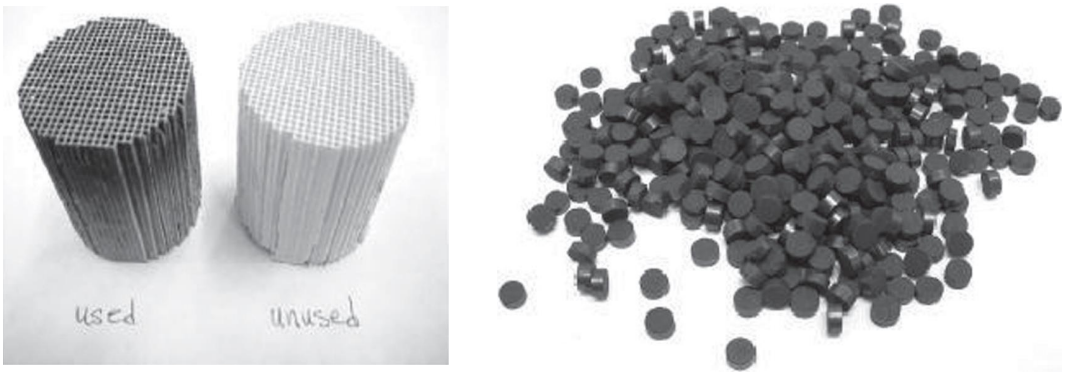


FIGURE 3.4

Variations of catalysts for steam and ATR. On the left are examples of monolith catalysts. On the right are examples of pelletized catalyst. (Courtesy University of California, Davis, CA.)

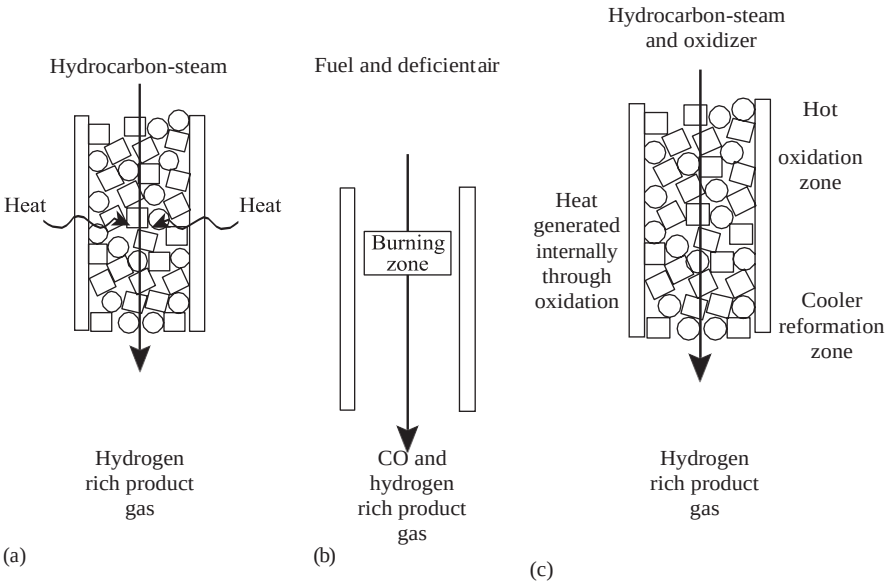


FIGURE 3.5

Graphic representation of (a) SR, (b) POX, and (c) ATR.

even if the catalyst has high selectivity for CO_2 over CO. Other expensive precious metal catalysts are used in high-temperature steam reformers. Rh, Ru, Pt, Pd, and Re supported by porous alumina or magnesium alumina spinel structures are highly active at elevated temperature [47,48]. Current catalyst development is targeting ways to improve selectivity and resistance to degradation by incorporating various oxides and compounds [49], as well as micromachining techniques in fabrication [50–53].

3.7 Types of Reformation

There are currently three major methods for reforming hydrocarbon fuels into hydrogen-rich gas. These are SR, POX reforming, and ATR. Figure 3.5 shows a graphical representation of each process. Today, in large-scale plants, SR is the most common method to obtain hydrogen from a hydrocarbon fuel.

3.8 Steam Reformation

SR is the most widely used method to reform hydrocarbons in large-scale hydrogen production plants. A typical reformer schematic is given in Figure 3.6. This system would be coupled with significantly complex water–gas shift and cleanup devices as well as heat exchangers and preheaters. Specific catalysts are used depending on the hydrocar- bon feedstock. The general SR steps are described as fuel breakdown and the water–gas shift reaction and are sometimes followed by methanation as shown in Equations 3.11 through 3.13. All of these reactions can happen at the same physical location, or these may be separated into individual reactors with different catalysts to promote one reaction or

another. Higher temperature typically speeds up the rate-limiting steps of fuel breakdown,

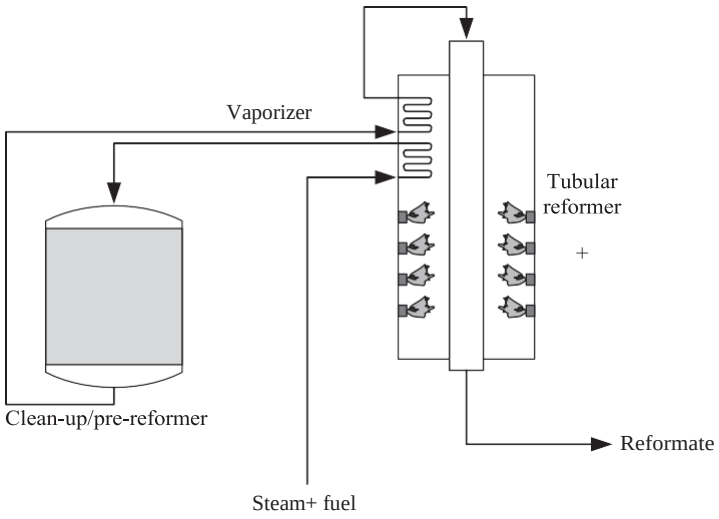


FIGURE 3.6

Schematic of a typical steam reformer.

but higher temperature typically promotes CO and CH_4 production. It is thus typical to have multiple reactors in series each operating at a different temperature with increasing hydrogen purity as the gas progresses through the plant. With heavy hydrocarbons, intermediate species and radicals often are produced and these potentially have carbon or coke formation difficulties:

$$C_nH_m + n\,H_2O \rightarrow n\,CO + \frac{n+m}{2}H_2 \qquad \Delta H\,(298\ K) > 0 \qquad (3.11)$$

$$CO + H_2O \leftrightarrow CO_2 + \qquad \Delta H\,(298\ K) = -41\ kJ/mol \qquad (3.12)$$

$$H_2\ CO + 3H_2 \rightarrow CH_4 + \qquad \Delta H\,(298\ K) = -206.2\ kJ/mol \qquad (3.13)$$

$$H_2O$$

Many hydrocarbons have been used as feedstock for SR. To illustrate some of the key parameters in SR, methanol and ethanol will be described here as examples. The SR kinetics of methanol on a Cu-based catalyst are available in the literature [10,36,54,55]. The exact mechanism of SR is still debated [10,56,57]. As commonly understood, different catalyst formulations promote the reaction in favor of certain pathways that is manifested as selectivity. However complex in application, a simplified reformation process can be expressed for methanol as the overall reaction consisting of methanol decomposition and the water–gas shift reaction. These are shown in Equations 3.4 through 3.6:

$$CH_3OH + H_2O \rightarrow CO_2 + 3H_2 \qquad \Delta H\,(298\ K) = +49\ kJ/mol \qquad (3.14)$$

$$CH_3OH \rightarrow CO + 2H_2 \qquad \Delta H\ (298\ K) = +90.1\ kJ/mol \tag{3.15}$$

$$CO + H_2O \leftrightarrow CO_2 + H_2 \qquad \Delta H\ (298\ K) = -41\ kJ/mol \tag{3.16}$$

While the overall reaction is endothermic, the methanol decomposition reaction is endothermic and the faster water–gas shift reaction is exothermic. For methanol SR, 75% dry hydrogen concentration can be produced based on 100% carbon dioxide selectivity as shown in the following:

$$\%H_2 \text{ selectivity} = \frac{\text{mole } H_2}{\text{mole of } H_2 + \text{mole of } CO_2} = \frac{3 \text{ mol}}{3 \text{ mol} + 1 \text{ mol}} = 75\% \quad (3.17)$$

In practice, dry hydrogen concentration is less than 75%. The conversion is strongly dependent on temperature and hence the activity and selectivity of the catalyst used. For a reformer operating at less than ~250 PSI, the pressure effect has been found as less significant [30]. Higher-pressure operation typically allows for higher throughput and bet- ter integration with either feedstock or end use such as high-pressure hydrocracking. It should be noted that Equation 3.16 also has a significant backward component that can form CO from the desired products. In the reverse water–gas shift reaction, hydrogen may be consumed to produce CO if the reactor temperature is too high. CO is typically an undesirable by-product when considering operation of a fuel cell system. On the other hand, sufficient heat is needed to obtain high fuel conversion and to assist the forward reaction considering fuel breakdown.

Another key parameter in methanol SR is the S/C ratio (H_2O/CH_3OH, in the case of methanol) [54]. This parameter impacts fuel utilization, efficiencies, and life of the reactor. Sufficient steam is required to achieve full conversion and suppress CO and solid carbon formation. Excessive steam will reduce energy efficiencies because it must be vaporized with the fuel without adding to the hydrogen product. High-temperature steam may also sinter Cu-based catalysts. Insufficient steam results in carbon formation and degraded catalyst performance by means of coking. Experimental work by many researchers has found that an S/C ratio between 1.3 and 1.6 for methanol steam reforming results in higher dry hydrogen yield at the reformer outlet.

Ethanol SR can be carried out with a Ni-based catalyst at about 550°C–650°C. Relatively higher temperature is needed to break the carbon–carbon bond in the fuel. The use of ethanol can favor carbon formation inside the reactor that potentially will degrade catalyst performance. Solid carbon fouls the catalyst by blocking fuel from contacting the active site inside the catalyst structure. The effect of fouling is more pronounced at low tempera- ture or low S/C. It has been reported that an S/C ratio > 1.5 reduces carbon formation but added water has a trade-off in the energy needed for fuel vaporization [58]. In this respect, the ethanol process is quite similar to methanol SR. The following equations show the simplified reactions:

$$CH_3CH_2OH + 3H_2O \rightarrow 2CO_2 + 6H_2 \qquad \Delta H\,(298\text{ K}) = 347 \text{ kJ/mol} \quad (3.18)$$

$$CH_3CH_2OH + H_2O \rightarrow 2CO + 4H_2 \qquad \Delta H\,(298\text{ K}) = 298 \text{ kJ/mol} \quad (3.19)$$

$$CO + H_2O \leftrightarrow CO_2 + H_2 \qquad \Delta H\,(298\text{ K}) = -41 \text{ kJ/mol} \quad (3.20)$$

3.9 Partial Oxidation

POX is an alternative to SR and is generally employed with higher hydrocarbons or if pure oxygen is available [59]. With a lower product concentration of hydrogen, this process sacrifices some efficiency relative to SR but offers rapid dynamic response and compactness. Unfortunately, this process is susceptible to coke formation and must be carried out at high temperatures. POX can be performed with or without a catalyst, but using a catalyst allows for a lower reaction temperature. The POX of methane is described by the chemical reaction shown in the following:

$$CH_4 + \frac{1}{2}O_2 \rightarrow CO + 2H_2 \qquad (\Delta H = -36 \text{ kJ/mol}) \tag{3.21}$$

If the oxygen-to-fuel ratio is increased, then the reaction becomes even more exothermic as shown in the following:

$$CH_4 + O_2 \rightarrow CO_2 + 2H_2 \qquad (\Delta H = -319 \text{ kJ/mol}) \tag{3.22}$$

These equations illustrate how the amount of heat generated from the POX of methane can be quickly increased from −36 to −319 kJ/mol by simply increasing the amount of oxygen in the reaction, that is, increasing the air flow rate and combusting additional fuel. Therefore, it is possible to reduce reformer start-up times by increasing the temperature rapidly; that is achieved by increasing the air (or oxidant)-to-fuel ratio.

The fast response time of the POX reformer is typically inhibited by the low hydrogen concentration and high CO levels that result. This implies a lagging hydrogen response time because of the potentially necessary water–gas shift and other cleanup systems put in place to clean up the high levels of CO that result from the POX reformer.

POX and catalytic partial oxidation (CPO or CPOX) is similar to a combustion process. With catalyst, CPOX can be carried out at lower temperature. Without catalyst, POX is typically carried out at 1300°C–1500°C to ensure complete conversion. As compared to SR, CPOX has the advantage of short start-up time because of the fast exothermic nature of the reaction. On the other hand, the exothermic nature of the reaction and the heat transfer limitation within the catalyst make it difficult to control the catalyst tempera- ture and reformate composition. Localized hot spots can overheat and sinter the catalyst if present. The product stream is influenced by the process conditions. Temperature, pressure, and O_2/C ratio are some of the process variables. For example, increasing reformer pressure will reduce the hydrogen yield in POX. A POX or CPOX reformer is comparatively compact because it doesn't require external heating to sustain the reaction and lowers the energy required to vaporize the fuel, but it is relatively less efficient than SR and ATR. Experiments on CPOX of various liquid hydrocarbon fuels have been reported by Cheekatamarla [60].

A general equation for POX is shown in the following:

$$C_nH_m + nO_2 \rightarrow nCO + \frac{m}{2}H_2 \qquad \Delta H\,(298\text{ K}) < 0 \text{ kJ/mol} \tag{3.23}$$

POX and CPOX have complex reaction systems. The reaction produces various intermediate species and radicals that decrease the purity of the output stream. They are also potentially coke precursors that cause catalyst deactivation for both precious and nonprecious metal catalysts. Pure oxygen and air have been used as oxidizer in these systems. However, the effect of inert gases such as nitrogen in the POX process can reduce the efficiency of the reformer by lowering the output stream hydrogen concentration. In general, other than O_2/C ratio, there is no control over the chemical species in POX or CPOX. Equations 3.24 and 3.25 show the POX of ethanol, and Equation 3.26 shows the complete oxidation:

$$CH_3CH_2OH + 0.5O_2 \rightarrow 2CO + 3H_2 \uparrow \qquad \Delta H\ (298\ K) = 57\ kJ/mol \qquad (3.24)$$

$$CH_3CH_2OH + O_2 \rightarrow CO_2 + CO + 3H_2 \qquad \Delta H\ (298\ K) = -226\ kJ/mol \qquad (3.25)$$

$$CH_3CH_2OH + 1.5O_2 \rightarrow 2CO_2 + 3H_2 \qquad \Delta H\ (298\ K) = -509\ kJ/mol \qquad (3.26)$$

In POX or CPOX, CO is one of the products in the reformate stream. This is especially problematic for low-temperature fuel cell applications because the high concentration of CO will poison the electrode. An additional CO oxidation reactor, water–gas shift reac- tor, or preferential oxidation (PROX) reactor can be used for CO removal. On the other hand, with high-temperature fuel cells, solid oxide fuel cell (SOFC) can utilize CO as a fuel source and it is less sensitive to impurities. Moreover, SOFC operation temperature is near 800°C, which is the typical POX reformate stream temperature. This makes POX and SOFC a good combination for fuel cell power system integration. It should be noted that it is not typically economical to use pure oxygen as oxidizer; thus, air is used.

3.10 Autothermal Reforming

ATR is essentially a combination between SR and CPOX. This is done by bringing the two reforming reactions into close thermal contact or by placing them into a single catalytic reactor. The single catalytic reactor is the most efficient means of heat transfer. ATR has advantages of both SR and POX in that it has potentially high hydrogen product concentration and adequate response to dynamic loads. Ideally, the heat generated from the exothermic POX reaction is used for rapid start-up and supplying the heat needed for the endothermic SR reaction during operation. Once the reactor is at operating temperature, the fuel, steam, and air are all fed into the reactor in the same step. The reactants ignite and form the ideal products of hydrogen and carbon dioxide. It has been found that on noble metal–based catalysts, ATR generally follows equilibrium concentrations in the output gas based on reaction temperature.

With a higher temperature due to the oxidation step, ATR is also capable of reform- ing multiple fuels, a necessary characteristic if alternative hydrocarbon feedstocks are reformed. Liquid fuels like methanol produced from coal or biomass may contain higher

hydrocarbons. For example, at a pulp mill under investigation for hydrogen production from waste, it was found that small amounts of pinenes existed in the methanol fuel used.

In SR systems, the pinenes and other compounds tend to overwhelm any catalyst site until they are reacted. The higher temperatures and oxidation found in ATR may allow faster treatment of the trace levels of higher hydrocarbons. Although the pinenes are relatively small in quantity (about one-tenth of a percent volumetrically for this fuel), their effect on the catalyst can be significant. Similar studies found that trace amounts of heavier oils as found with methanol derived from coal had similar effects in SR [61,62] but could be acceptably dealt with in ATR [63].

ATR is similar to SR with an additional CPOX step. These exothermic steps are fast, and the resulting heat can be used to sustain the SR steps; thus, ATR is termed *autothermal* or thermal neutral. The typical ATR equation of a hydrocarbon is shown in the following:

$$C_nH_m + 0.5mO_2 + 0.5mH_2O \rightarrow mCO + (0.5m + 0.5n)H_2 \quad \Delta H\ (298\ \text{K}) = 0\ \text{kJ/mol} \tag{3.27}$$

The steps in an ATR process of using methanol as feedstock are shown in Equations 3.28 through 3.33. Equation 3.28 shows the CPOX steps, and combined with the carbon monoxide oxidation step in Equation 3.29, much of the CO will be consumed in these steps:

$$CH_3OH + 0.5O_2 \rightarrow CO + 2H_2 \quad \Delta H\ (298\ \text{K}) = -192\ \text{kJ/mol} \tag{3.28}$$

$$CO + 0.5O_2 \rightarrow CO_2 \quad \Delta H\ (298\ \text{K}) = -283\ \text{kJ/mol} \tag{3.29}$$

Another CPOX formulation is by substituting combustion/methanol oxidation steps shown in Equation 3.30. The remaining steps in Equations 3.31 through 3.33 are identical SR steps from the previous section:

$$CH_3OH + 1.5O_2 \rightarrow CO_2 + 2H_2O \quad \Delta H(298\ \text{K}) = -675.4\ \text{kJ/mol} \tag{3.30}$$

$$CH_3OH + H_2O \rightarrow CO_2 + 3H_2 \quad \Delta H\ (298\ \text{K}) = 50\ \text{kJ/mol} \tag{3.31}$$

$$CH_3OH \rightarrow CO + 2H_2 \quad \Delta H\ (298\ \text{K}) = 90.1\ \text{kJ/mol} \tag{3.32}$$

$$CO + H_2O \leftrightarrow CO_2 + H_2 \quad \Delta H\ (298\ \text{K}) = -41\ \text{kJ/mol} \tag{3.33}$$

The amount of heat generated in the reaction is directly related to the available oxygen in the fuel. If the proper stoichiometry fuel mixture is used, it will result in a thermoneutral condition: a self-sustaining operation as shown in the following:

$$CH_3OH + 0.1O_2 + 0.8H_2O \rightarrow CO_2 + 2.8H_2 \quad \Delta H\ (298\ \text{K}) = 0\ \text{kJ/mol}$$

However, in a typical reactor, heat lost due to conduction is unavoidable. It is necessary to allow additional oxygen to account for this heat lost, as shown in the following:

$$CH_3OH + 0.27O_2 + 1.5H_2O \rightarrow CO_2 + 2.46H_2 + 1.04H_2O \qquad \Delta H\,(298\ K) = -81\ kJ/mol \tag{3.35}$$

The O_2/C ratio, or O_2/C, is an important parameter in ATR. Researchers have found O_2/C = 0.2–0.3 to be optimum using a Cu-based catalyst [54,64]. Higher O_2/C ratios will

Free ebooks ==> www.Ebook777.com

reduce the amount of hydrogen in the output stream and increase the temperature inside the reactor, while lower O_2/C ratios will result in low conversion due to insufficient heat.

The steps in an ATR process of using ethanol as feedstock are described by Equations 3.18 through 3.20, 3.24, and 3.25. The case of complete oxidation of ethanol is described in the following:

$$CH_3CH_2OH + 3O_2 \rightarrow 2CO_2 + 3H_2O \qquad \Delta H\ (298\ K) = -1368\ kJ/mol \tag{3.36}$$

In a small fuel processor design, an ATR reactor is compact and has higher heat and power efficiencies when compared to a steam reformer reactor. A typical schematic of the ATR reactor is found in Figure 3.7. The exothermic reactions take place on the surface of the catalyst; thus, they help shorten the warm-up time of the reactor. However, air is typically used to feed into the autothermal reformer; thus, nitrogen dilution will reduce the thermal efficiency and concentration of hydrogen in the reformate output stream. The fast start-up feature has been studied [65,66] for the potential use on fuel cell vehicle [67].

ATR also suffers from mass and heat transfer limitations as in SR but in a different manner. The rate of the exothermic reaction occurring on the catalyst surface is dependent on the rate of reactants mass transfer to and away from active catalyst sites [68,69]. In the case of reforming methanol on Cu-based catalyst, the rate of exothermic reaction is at least two orders of magnitude faster than the endothermic reaction [66,70–72], the heat generated is localized, and a hot spot is created by the heat transfer limitations of the catalyst. This is common in catalytic combustion and often degrades the catalyst by means of sintering. However, a well-designed ATR can take advantage of the exothermic reaction to overcome the heat transfer limitation of the SR step. This reduces the size of the overall reformer while maintaining high H_2 concentration. In addition, the nonlinear relationship between the reaction rate and catalyst temperature has a sharp transition known as the light-off

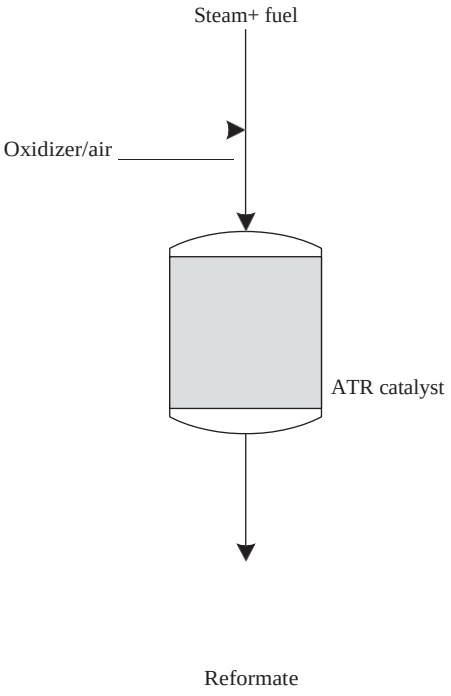


FIGURE 3.7

Schematic of a typical autothermal reformer.

www.Ebook777.com

temperature. Operating below the light-off temperature will result in extinction in the combustion process because it is unable to sustain the reaction [31].

The light-off temperature has the following implications. First, selection of a proper O_2/C ratio is based on both stoichiometry and reactor design. Not only sufficient oxygen is needed to sustain the reaction, but it must have excess oxidizer to account for heat lost by the reactor design. Balancing between S/C and O_2/C ratios for a specific catalyst selection can be difficult [65]. Second, if heat lost is significant, excessive oxygen required to sustain the reaction will potentially sinter the catalyst by overheating away from the heat sink. Poor heat transfer of the catalyst will create large temperature gradients, thus degrading (and possibly destroying) the catalyst. Various autothermal methanol reforming reactors have been studied [73,74].

3.11 ATR of Different Fuels

Gasoline and heavy hydrocarbons are typically considered for ATR to produce hydro- gen for fuel cells. The advantages of gasoline are its existing fuel infrastructure and high energy density (32.3 MJ/L, based on LHV). However, using gasoline or other fos- sil petroleum products will not solve the long-term problem of fossil fuel dependence. For theoretical calculations, the optimal temperature to reform gasoline into hydrogen is around 400°C [75]. However, in other studies of gasoline and diesel ATR, temperatures of 600°C–800°C have been used [76,77]. From Sandakane, Saitoh, and Oyama's research [78], a fuel conversion of greater than 97% can be obtained at temperatures in excess of 800°C. High temperatures require expensive materials and longer start-up times for automotive scale reformer systems. The high temperatures required for ATR of gasoline and other higher hydrocarbons make them less than optimal for automotive applications.

Although most work is done on ATR with higher hydrocarbons, focusing on renewably produced alcohols provides a basic understanding of the process. The general form of the ATR reaction of an alcohol fuel using air as the oxidizer, assuming complete conversion of the reactants, is shown in the following:

$$C_nH_mO_p + (2n - 2x - p)H_2O + x\left(O_2 + 3.76N_2\right) \rightarrow (2n - 2x - p + m/2)H_2 + nCO_2 + 3.76xN_2 \tag{3.37}$$

where $(2n - 2x - p)$ represents the minimum amount of water required in the reaction, and x represents the air-to-fuel ratio. The air-to-fuel ratio and O_2/C are related by a factor of n, the number of carbon atoms in the fuel. The heat of reaction is dependent on the O_2/C and S/C. Note that $(2n - 2x - p)$ is the minimum amount of water required for the reaction and the S/C ratio in practical applications is typically much higher in order to inhibit coke formation. Methanol is a very attractive fuel for hydrogen production. Like hydrogen, methanol can be produced from multiple feedstocks. Ideally, methanol would be produced renewably, but it may also be produced from abundant coal resources and natural gas. Because it is an oxygenated fuel, it requires lower operating temperatures for effective reformation [75]. Ethanol and higher alcohols have longer carbon chains (two or more carbon atoms) and therefore require higher temperatures and more energy to be reformed. Methanol can be reformed at relatively low temperatures, around 250°C. According to one ATR study, con- versions of greater than 90% are possible at temperatures just above 250°C, [79]. Based on

Free ebooks ==> www.Ebook777.com

thermodynamic equilibrium, the lower the reaction temperature, the lower the CO concentration that can be achieved [80]. This translates into less reformate cleanup and, therefore, a smaller and less complicated fuel-processing system. The lower temperatures also mean that less energy is required to heat the reforming system to operating temperature, so shorter start-up times are possible. It also means that the reformer can be made from a larger variety of materials that potentially reduces manufacturing costs.

In addition to the ease of reformation, methanol can be produced renewably through gasification of biomass or from coal resources. The different feedstocks of methanol result in different methanol purities. For example, coal-derived methanol may include higher hydrocarbons as an impurity [61]. Fortunately, ATR is a proven method of reforming higher hydrocarbons and should be able to cope with varying purities of fuel, depending on the feedstock [62].

The heat of reaction indicates whether a reaction is exothermic (releasing energy) or endothermic (requiring energy) and is defined as the heat of formation of the products minus the heat of formation of the reactants. Since the heat of formation for the oxygen, nitrogen, and hydrogen reactants and products are all zero, the heat of reaction for methanol ATR is simplified as shown in Equation 3.38:

$$\Delta H_r = \Delta H_{f,CO_2} - (1 - 2x)\Delta H_{f,H_2O(l)} - \Delta H_{f,fuel(l)} \quad (3.38)$$

By evaluating the heat of reaction as a function of O_2/C, x, it is possible to find x_0, the thermoneutral point that produces a net enthalpy change of zero. Plotting the heat of reaction for methanol as a function of x, from $x = 0$ (SR) to $x = 1.5$ (complete combustion), and assuming an ideal reaction, yields Figure 3.8. The stoichiometry of the reaction is simply an $O_2/C = x$ and $S/C = 1-2x$, until $x > 0.5$. At this point, water is no longer consumed in the reaction but rather produced as a product of combustion. It is easy to pinpoint the thermoneutral point that occurs at $x_0 = 0.230$.

The efficiency of a reforming process is defined as the lower heating value of hydrogen produced divided by the lower heating value of fuel consumed as shown in Equation 3.38:

$$\eta = \frac{\text{LHV } H_{2\text{output}}}{\text{LHV fuel}_{\text{input}}} \quad (3.39)$$

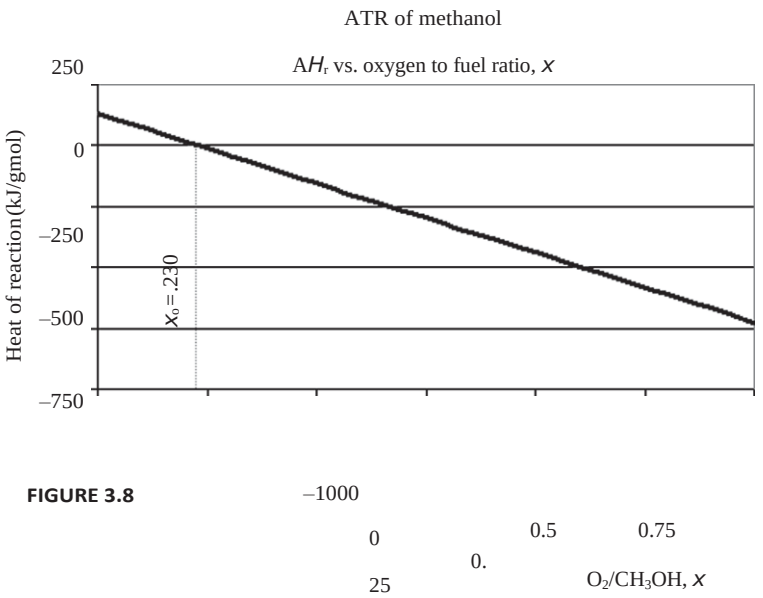


FIGURE 3.8

1 1.25
1.5

ATR of methanol, heat of reaction vs. O_2/C. (From Dorr, J.L., Methanol autothermal reformation: Oxygen-to-carbon ratio and reaction progression, Master thesis, University of California, Davis, CA, 2004.)

www.Ebook777.com

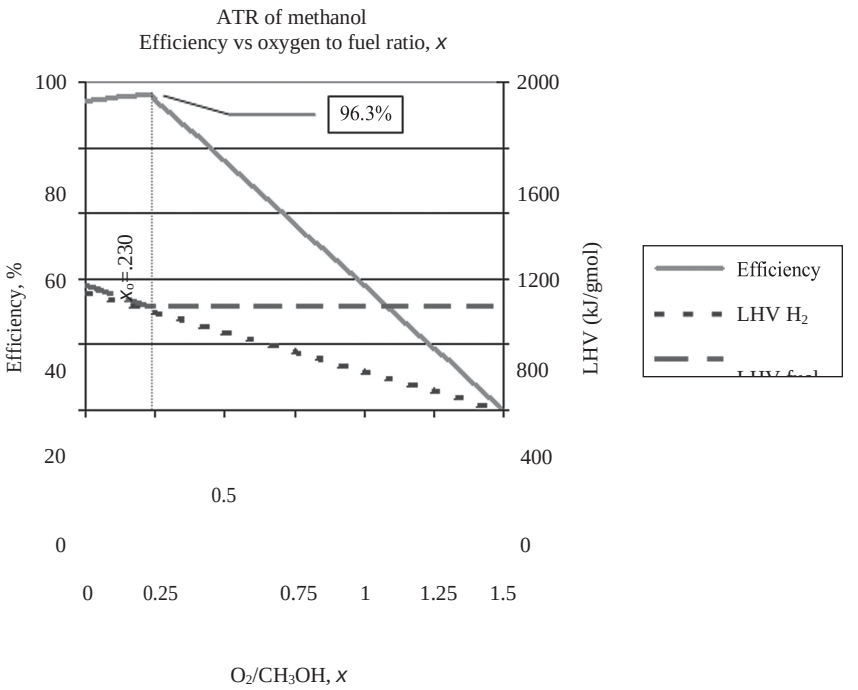


FIGURE 3.9

ATR of methanol, efficiency vs. O_2/C. (From Dorr, J.L., Methanol autothermal reformation: Oxygen-to-carbon ratio and reaction progression, Master thesis, University of California, Davis, CA, 2004.)

Further evaluation of this simple model reveals that the peak efficiency of ATR of metha- nol occurs at the thermoneutral point, as seen in Figure 3.9. The peak efficiency of ATR of methanol at the thermoneutral point x_o = 0.230 is 96.3%, which is one of the highest theoretical efficiencies of ATR of various hydrocarbon fuels [80]. Therefore, it seems most desirable to operate as close to the thermoneutral point as possible if efficiency is a priority. It is important to note that below the thermoneutral point ($x < x_o$), the reaction is endo- thermic and thus requires a heat input. This heat input is assumed to be provided by combusting additional fuel. Also, the amount of energy required to heat the reactants is not included in this efficiency. The amount of excess water in the reaction does play a great role in the amount of heat required to increase the temperature of the reactants. It is also possible to utilize waste heat from the fuel cell, which would effectively increase the effi- ciency at lower O_2/C ratios, moving the balance toward an SR reaction.

To maximize the overall benefit of hydrogen, renewable energy sources are desired as feedstock. Methanol, although not currently derived from renewable sources but from natural gas, has the potential to be sourced from renewables. Methanol is an attractive choice for many reasons including the basis of carbon-to-hydrogen ratio, fuel processor start-up and operation energies, availability of biorenewable sources, and overall system complexity [62,82–85]. It has been considered as one of the possible feedstocks for hydrogen fuel cells as it can be stored and transported in a liquid form using the existing energy infrastructure and technology with only slight modification [4,9]. Indeed presently, some methanol refueling stations exist for supplying racing fuel across the United States. Methanol can be reformed at relatively low temperatures as compared to other fuels, and the reaction mechanism for carbon formation is less active, which helps to prolong catalyst

operation life. An extensive review of methanol SR was done by Palo et al [86]. Ethanol is another promising fuel candidate based on its potential to be carbon neutral [87–90]. Although much debate surrounds the actual carbon neutrality of the fuel, ethanol can be produced through the fermentation of biomass or organic waste materials from agroindustries, forestry residue, and municipal solid waste. Bioethanol is recognized by the automobile industries as an alternative fuel with near-established infrastructure. Hydrogen from ethanol is likewise considered potentially beneficial.

3.12 Limiting Mechanisms in the Reformation Processes

The conversion of fuel and yield of hydrogen are limited by the presence of the physical mechanisms. Heat and mass transfer and chemical kinetics are the major limiting mechanisms in reformation. The effect of these mechanisms is discussed individually in the following sections. A conventional steam reformer has temperature and concentration gradients inside the catalyst bed. Efforts to improve the reactors limiting mechanisms can have significant cost and flow through improvements.

3.12.1 Chemical Kinetics

Catalyst temperature impacts the catalyst activity. Arrhenius behavior as shown in Figure 3.10 for a methanol SR catalyst indicates that activity is exponential with tempera- ture. As typical reformation systems are endothermic, the presence of activity limits is an indication of insufficient heat transfer.

Increasing activity through increased temperature can also damage the catalyst; thus, rugged low activity catalysts may be desired. For example, Ni-based catalysts are typically most active above 800°C. This high-temperature requirement makes a Ni-based catalyst bed difficult to implement for mobile devices because of the long start-up times required. Cu-based catalysts are attractive because they are active at about 260°C. Since the conventional catalyst effectiveness factor is typically less than 5%, being able to control the catalyst bed temperature can potentially improve the overall performance.

3.12.2 Mass Transfer

SR is typically limited by mass and heat transfer [91]; thus, low-cost catalysts are used. Mass transfer includes both external and internal diffusions. Reactant diffusion through the catalyst bed onto a catalyst is known as the external diffusion. Diffusion inside the catalyst pore onto an active site is known as internal diffusion. To improve diffusion, one can increase the catalyst loading and/or use smaller catalyst pellets. Using crushed cata- lysts is a common practice although this typically increases limitations in heat transfer and

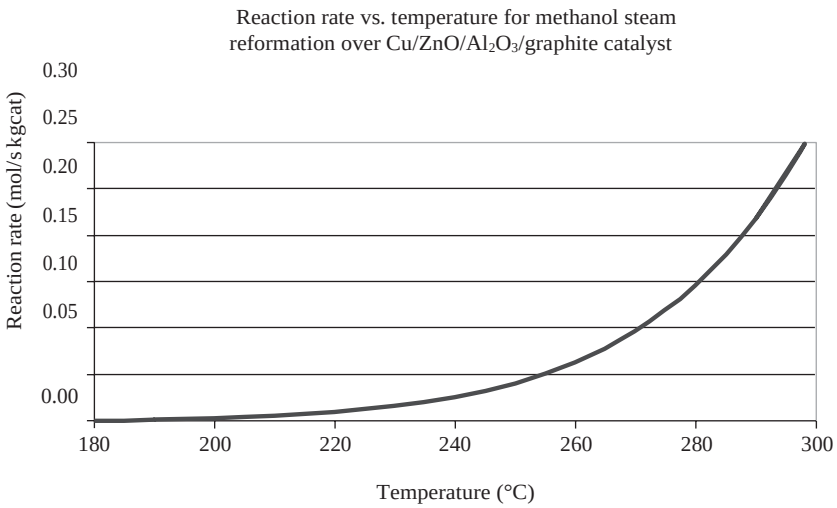


FIGURE 3.10

Reaction rate versus temperature.

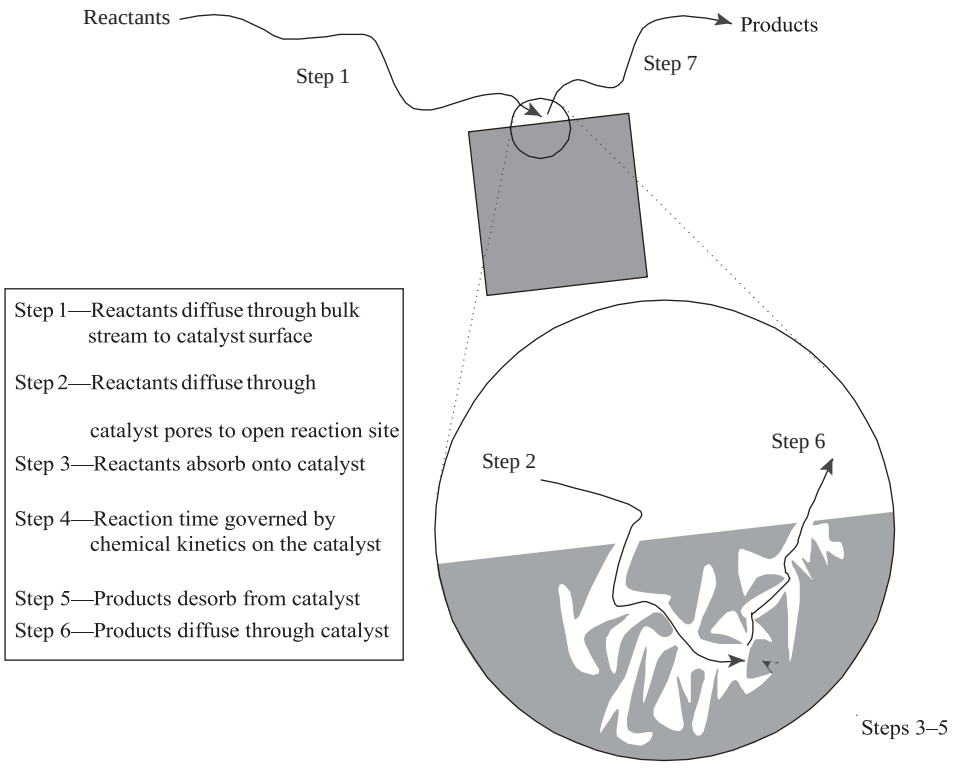


FIGURE 3.11

Mass transfer steps in a typical steam reformer. (From Erickson, P., Enhancing the steam-reformation process with acoustics: An investigation for fuel cell vehicle applications, PhD dissertation, University of Florida, Gainesville, FL, 2002.)

increases pressure drop. Increased catalyst loading will increase the weight of the reactor, while using smaller catalyst pellets will increase flow resistance.

Typical mass transfer steps are given in Figure 3.11.

3.12.3 Heat Transfer

External heat is required by SR as the overall process is endothermic. Inside the reactor, pelletized or crushed catalyst particles are packed randomly with point-to-point contact with each other. Convection is the dominating mode of heat transfer within the reactor. As a consequence, large temperature gradients exist in the region near the reactor wall. Unreacted fuel can potentially flow past in the center region reducing overall fuel conversion. Unreacted fuel may also deactivate the catalyst by accumulating on the catalyst pores blocking active sites causing fouling. Using a small radius reactor can improve heat transfer to the centerline. However, as reactor radius decreases, the reactor-to-catalyst weight ratio increases, and the pressure drop increases rendering inefficient reactor design. Figure 3.12 shows experimental temperature gradients encountered with SR of metha- nol [93]. Although conduction errors are evident in this figure, experimentation shows that 100°C/cm temperature gradients are frequently encountered near the wall. This result implies that a catalyst might be degraded by sintering at the wall yet simultaneously experience fouling due to relatively cold condensed species forming at the centerline.

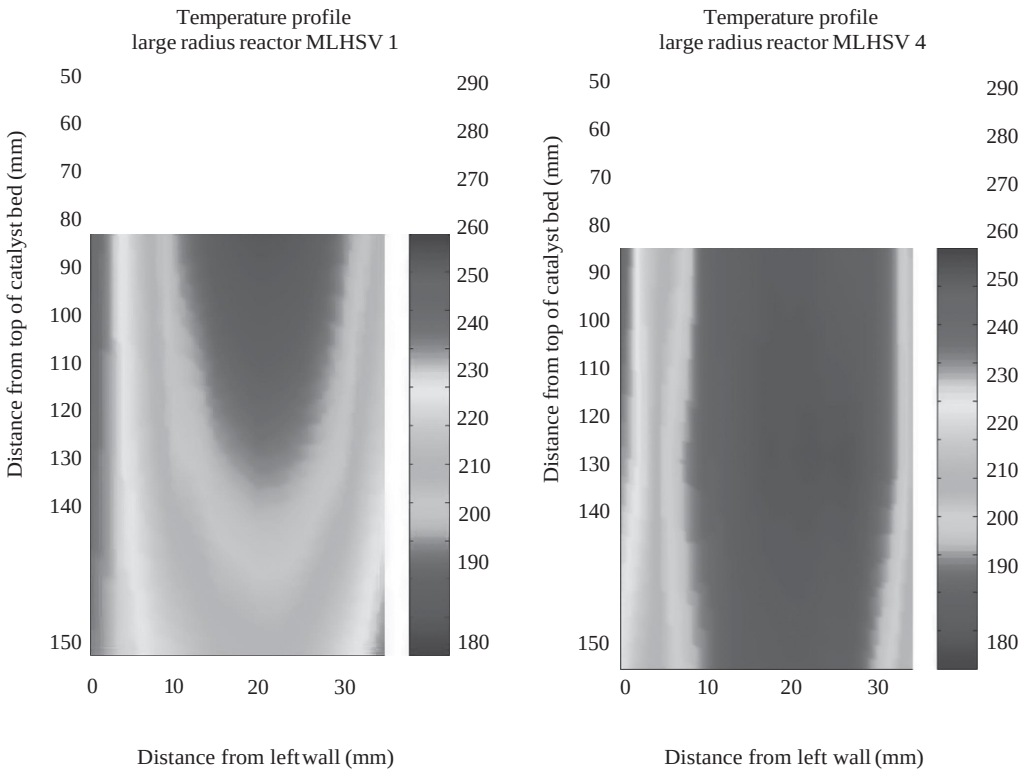


FIGURE 3.12

Example of large temperature gradients in a methanol steam reformer. The temperature differences is 46.4°C from interior wall to centerline, which is a 17.5 mm distance. (From Vernon, D., Understanding the effects of reactor geometry and scaling through temperature profiles in steam-reforming hydrogen production reactors. Master thesis, University of California, Davis, CA, 2006.)

TABLE 3.2

Limiting Mechanisms and Their Effect on Reaction Rate

	Variation of Reaction Rate with:		
Type of Limitation	**Velocity**	**Particle Size**	**Temperature**
External diffusion	$U^{1/2}$	$(dp)^{-3/2}$	~Linear
Internal diffusion	Independent	$(dp)^{-1}$	Exponential
Surface reaction	Independent	Independent	Exponential

Source: Fogler, H.S., *Elements of Chemical Reaction Engineering*, 4th edn., Pearson Education, Inc, 2006.

Table 3.2 shows the overall effects of each limitation and the effect of velocity particle size and temperature on the reaction rate.

3.12.4 Degradation Mechanisms

Reformation can also be limited by catalyst degradation. Degradation is typically classified as attrition, poisoning, fouling, and sintering.

Attrition occurs when the catalyst material is broken off of the substrate and is removed

from the reactor. Catalyst and substrate attrition can also lead to physical flow restrictions in the reactor system. This phenomenon is common with frequent temperature cycling in metal housings where the thermal coefficient of expansion and resultant displacement of the housing crushes a pelletized catalyst resulting in a large pressure drop over time.

Poisoning occurs in reformation when a species binds to the reaction site blocking the reaction site from the reactants. Poisoning can be either reversible or nonreversible and may have a temperature effect with higher temperatures inhibiting the poisoning of the

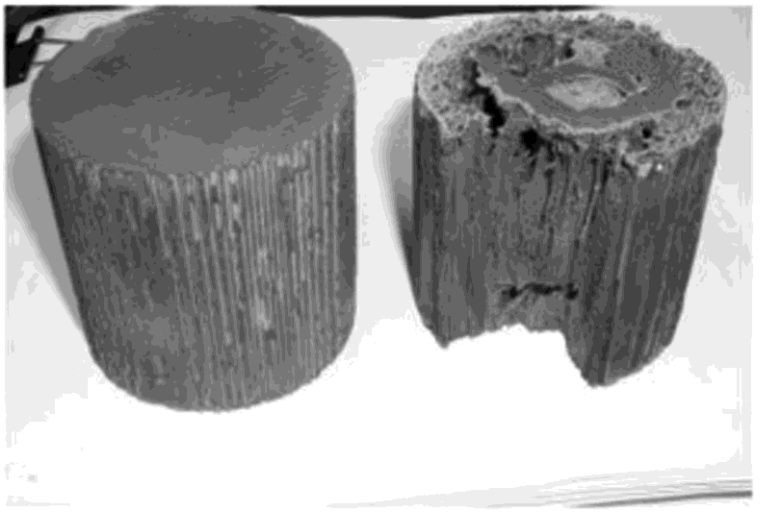


FIGURE 3.13

New monolithic ATR catalyst is shown on the left and a similar cut-away sintered catalyst is shown on the right in this grayscale image.

catalyst. Sulfur and sulfur-containing compounds are especially problematic for typical reformer catalysts and poisoning agents. Deactivation of the catalyst by poisoning can typically be seen as the endothermic active zone of catalyst progresses through the reformer following the flow pattern. Zinc and related species can be used in a sacrificial manner to slow down the poisoning effect in reformers.

Fouling occurs when the active area of a catalyst is physically blocked by species forming on the external or internal surface of the catalyst. When the entrance and exit pores become blocked by condensed species or coke formation, reformer performance can drop significantly due to the induced mass transfer limitation. Because the internal area can be as high as 1600 m^2/g of the catalyst in pelletized catalyst, it is important to keep pore areas clear to avoid mass transfer limitations. Any gas–liquid or gas–solid phase transformations can induce fouling as the liquid or solid blocks the gas reactants from reaching the reaction surface.

Sintering can occur when the catalyst or the substrate changes form. Sintering is typically due to exothermic reactions driving the temperature above the melting point of either the substrate or the catalyst material. In many reformation processes, a ceria substrate is used with a washcoated metal acting as the catalyst material. Typical ceria will melt at 1450°C; thus, high temperatures can lead to pore blocking and absorption of the catalyst through melting of the substrate. It is also important to note that metallic phase transformation and changes can occur far below the melting point of the metal and this phase transformation can change the activity and selectivity of the catalyst. A common rule of thumb is that a certain metal can be used up to 1/3 of its melting point temperature. Structural integrity can also be compromised in extreme sintering cases as shown in Figure 3.13. The need to have fast reactions with heavy complex fuels can be limited by the catalyst's ability to withstand high temperatures and high heat flux.

3.12.5 Controls

Researchers have modeled the SR process [13,83,95,96] and the reformer [82,97–99] in vari- ous literature and have also proposed control algorithms [23,100,101] to better control the

temperature, but the issue of controlling catalyst temperature has not been fully addressed. A high-level control algorithm sends manipulated inputs to control fuel flow rate and heater power for a given reformer, and the means of getting the heater power to the cata- lyst is limited by the design of the reformer. It should be noted that these concerns are only dealing with the steady-state control of the reformer temperature and do not address the transients encountered with large flow changes or start-up of the reactor. Slow transient response is a large hurdle for SR. While most current large-scale reformers run continu- ously for over 12,000 h [20], small-scale reformers will experience frequent fuel rate tran- sients due to changes of demand. Optimizing reactor geometry is one approach to enhance reformer dynamics [102]. However, reformer geometry can impact the characteristic of the heat transfer, thus impacting the control algorithm design. A better approach is to design both the control algorithm and the reformer in parallel.

3.13 Comparison of the Reforming Methods

End use of the hydrogen is perhaps the important aspect when considering types of reformation systems. For example, in combustion applications, high concentrations of CO and unconverted fuel are not typically problematic, yet in fuel cell applications, there are significant requirements for fuel purity. Lower operating temperature fuel cell stacks usually have stricter requirements. Impurity in the hydrogen stream will slowly poison the fuel cell anode over time. CO poisoning is an important issue for PEMFC. High-temperature fuel cell stacks such as molten carbonate fuel cell (MCFC) and SOFC have higher impurity tolerance. They are capable of internal reforming and use CO and some volatile organic compounds (VOCs) as fuel. Selecting a proper fuel cell for a specific application can significantly impact the reformer's technical specifications.

SR has the advantage of a relatively high hydrogen concentration in the product gas, which leads to better utilization by a fuel cell. For example, for SR of methanol, the maxi- mum hydrogen concentration is 75%. The efficiency of the process is also very high, which is desirable for transportation applications. It also has the advantage of a high S/C ratio, which leads to a low instance of coking (solid carbon deposits) without having to raise the reactor temperature. For an onboard steam reformer, the external heat needed for the endo- thermic reaction is most conveniently provided by simply combusting a portion of the fuel. Therefore, only a fraction of the total fuel used, Y, actually enters the reformer. The remain- ing fuel, $1 - Y$, is fully combusted to provide the energy required for the desired SR reaction. In an ideal reactor, there would be 100% heat transfer from the combustion reaction to the SR reaction. However, there are limitations to the efficiency of the heat transfer process and this should be considered when selecting a reforming method. SR is endothermic and therefore an inherently slow process. An SR reactor is most commonly heated exter- nally and has slow dynamic responses that may lead to system degradation. If the load is suddenly decreased and the reactant flow rates are decreased, the reformer heats up and can potentially sinter the catalyst. Alternatively, if the load is suddenly increased, the reformer cannot supply the required hydrogen to the fuel cell stack; consequently, the fuel cell extracts protons from the electrolyte membrane causing irreversible damage. This, coupled with a long start-up time, makes SR a less than optimal choice for onboard reforming or small-scale on-site reforming. It is still a good choice for centralized production of hydrogen on a large scale.

A POX reactor can heat up quickly by simply increasing the flow rate of oxygen to increase the combustion of the incoming fuel; this results in a fast start-up. For the same reason, it is extremely well equipped to handle transient loads. The reactor is much smaller and reformers can be made compact. However, POX produces excess CO and must therefore be accompanied by additional cleanup of the product gas. This increases the size and mass of the fuel-processing system. POX reforming is an exothermic reaction that operates at high temperatures usually above 1000°C. Because there is an absence of water (an S/C ratio of zero), reactors must operate at significantly higher temperatures (1180°C for 2,2,4-trimethylpentane) to avoid coking [103]. The system design must also include a heat exchanger that transfers excess heat to the surroundings. Hot spots may develop as a result of nonuniform mixing and can cause catalyst sintering. Most importantly, the major drawback of POX is the low concentration of hydrogen in the product gas. The addition of air into the reaction dilutes the product gases with nitrogen. For example, when POX is used to reform methanol, the highest theoretical concentration of hydrogen is only 41% (when using air as the source of oxygen), compared to 75% for SR [104]. This directly affects the efficiency of the PEM fuel cell and thus decreases the overall system efficiency, an especially undesirable characteristic for automotive applications.

One potential solution to the drawbacks of SR and POX is to combine the two into ATR. ATR operates ideally at a thermoneutral point, neither consuming nor releasing external energy. This gives ATR a higher efficiency and hydrogen concentration than POX and, at the same time, a better dynamic response than SR and the flexibility to accommodate multiple fuels. Rapid start-up is possible because of the ability to produce heat within the catalyst bed rather than transferring heat from the surroundings. Hot spots are reduced because of the addition of steam in the reforming reaction. This thermal integration lowers the temperature rise potential that is caused by the POX of the fuel and thereby reduces the potential for catalyst sintering. ATR has great potential in applications that require a lightweight, compact reactor capable of reforming multiple fuels [103]. These criteria fit into the needs of the automotive industry, whether for onboard or on-site reforming, and therefore ATR should be considered for transportation applications. ATR can provide a rapid response to hydrogen demand with short start-up times, high efficiencies, and fuel flexibility.

It should be noted that reactant mixing is an important consideration for ATR. Possible mixing schemes include the use of bluff bodies, swirling, and acoustic enhancement. Acoustic enhancement has been proven to improve the capabilities of SR, and there is a reason to believe that it may also be beneficial to ATR. These results have yet to be tested. Other reactant mixing schemes may also enhance ATR reactor performance. Should reactant mixing prove to be beneficial to ATR, it will further reduce the size and weight of the reformer. This in turn would decrease start-up time of the reforming system, one of the most critical aspects of a small-scale reformer.

3.14 Fuel Selection

Cost and environmental reasons are factors in deciding the choice of fuel. Many researchers have built small fuel processors for various hydrocarbon feedstocks [3,4,7,11]. They have shown competitive advantage in implementation, flexibility, and efficiencies [105–108]. Insulation and heat recirculation are important for these reformers to maintain high

Free ebooks ==> www.Ebook777.com

efficiencies. Coupled with PEMFC, they have demonstrated functional stationary [4,107] and onboard [3,106,109] fuel cell power systems. Although they have presented workable solutions to reform hydrocarbon feedstock, there are a range of issues to be addressed. For example, PEMFCs generally have low CO tolerance at <50 ppm [110–112]; thus, a cleanup system, such as PSA, is necessary to purify the reformed hydrogen stream [3,113–116]. High CO-tolerant electrodes and high-temperature fuel cell operation are also under development to overcome this limitation. Water management [4,105,112] and temperature are also critical to the life and performance of the PEMFC; thus, the temperature and humidity of the hydrogen stream must be regulated [23,24,101,117].

Table 3.3 is an estimate of the hydrogen yield by reforming various hydrocarbons.

Comparing the weight of hydrogen produced per liter of fuel, methanol and ethanol are clearly not competitive with gasoline and diesel. However, both alcohols can be reformed at relatively low temperature and can be made from renewable fuels. The low-temperature reformation process allows less complex reformer design, lower CO selectivity, and good compatibility with low-temperature fuel cell applications. Typical reformer temperatures and catalysts are shown in Table 3.4.

Other fuels such as diesel, gasoline, propane, and logistic fuels such as kerosene and jet fuel have also been used as feedstock. Typically, heavier hydrocarbons will require higher temperature and additional cleanup prior to or after reforming. Desulfurization and prereformers are used to ensure high-purity fuel is fed into the fuel processor. Gasoline and

TABLE 3.3

Hydrogen Yield by Reforming Various Hydrocarbons

		SR		POX	
Fuel	**Formula**	**Wt.% H_2**	**g H_2 per L_{fuel}**	**Wt.% H_2**	**g H_2 per L_{fuel}**
Methanol	CH_3OH	19%	150	13%	100
Ethanol	C_2H_5OH	26%	209	22%	168
Methane (LNG)	CH_4	52%	205	38%	151
Gasoline	$C_8H_{15.4}$	43%	301	28%	200
Diesel fuel	$C_{14}H_{25.5}$	42%	357	28%	231

Source: Spiegel, C., *Designing and Building Fuel Cells*, 1st edn., McGraw-Hill, 2007.

TABLE 3.4

Typical Reforming Temperature of Various Hydrocarbons

Fuel	**Reformation Temperature (°C)**	**Catalyst**
Glycerol	650–900	Pt
Isooctane/gasoline	650–800	Ru, Ni
Hexadecane/diesel	700–800	Ru, Ni
Natural gas	650–800	Ru, Ni
Methanol	200–300	Cu, Zn, Cr
Ethanol	200–300	Cu, Zn, Cr
Dodecane	450–550	Ni, Rh, Ce
JP-8	>520	Mn, Ni
Propane/*n*-butane	600–800	Pd, Cu, Ni
Methane	>500	Ni
Kerosene/*n*-octane	>500	Ni

www.Ebook777.com

diesel have a well-established infrastructure and higher energy storage density for hydrogen. A gasoline reformer can be started and deliver 90% rated hydrogen capacity with less than 50 ppm CO in 60 s [7]. Natural gas or methane is abundant in many parts of the world and is used as feedstock for hydrogen production in industrial settings. It can also be converted to methanol and transported using existing infrastructure. Liquefied petro- leum gas (LPG), which has been widely used for cars and buses, is also a potential fuel for mobile reformer systems.

3.15 Internal Reforming in High-Temperature Fuel Cells

Internal reforming refers to reformation taking place at or near the anode of the fuel cell. With SOFC and MCFC, the stack temperature is sufficient to reform low–molecular weight hydrocarbons [119]. Internal reforming has the advantage of reducing cost and complexity since a separated reformer and heat exchangers are not necessary. It is also more energy efficient since less steam is required and heat loss is minimized. The anode catalyst must be able to reform the hydrocarbon fuel and catalyze the oxidation reaction in the high-temperature anode of these fuel cells. The internal reforming systems are favored by Le Chatelier's principle that drives the reaction toward the product side at high tempera- tures and pressures as the hydrogen produced by reformation is immediately consumed by the fuel cell oxidation reaction.

3.16 Reactor Design

In SR, CPOX, and ATR, maintaining chemical reaction kinetics by activating the catalyst becomes the important aspect in controlling the reformation process. In order to activate the catalyst, sufficient heat must be available for the reaction. Insufficient temperature will deactivate the catalyst, thus reducing efficiencies. It is important to address the need for maintaining proper temperature in reformation processes. For MTS catalysts containing copper, exceeding 300°C generally will make the catalyst unstable and degrade by sintering [35,42,120]. Ni-based catalyst is stable at higher temperatures, but this becomes a trade-off with the material and operating cost of a high-temperature reformer. Maintaining a uniform temperature profile inside the reactor is ideal but is difficult to achieve. Heat distribution is limited by convection; thus, high-temperature gradients exist inside the catalyst bed. Modifying the reactor design to improve the heat and mass transfer limitation is one possible solution [121–123].

Inside the steam reformer catalyst bed, convection is the primary means to transfer heat from the reactor wall to the catalyst; thus, a small diameter tubular configuration is advantageous. Passive flow baffles can be used inside the reactor to enhance heat transfer [124]. Structured catalysts have also been employed [125]. Figure 3.14 shows how passive flow disturbance can be used to enhance the heat distribution.

Inside the autothermal reformer, an exothermic reaction occurs on the surface of the catalyst in the presence of oxygen; thus, controlling the flow of oxygen can control heat generation. Employing a porous membrane within the catalyst bed to distribute air inside the

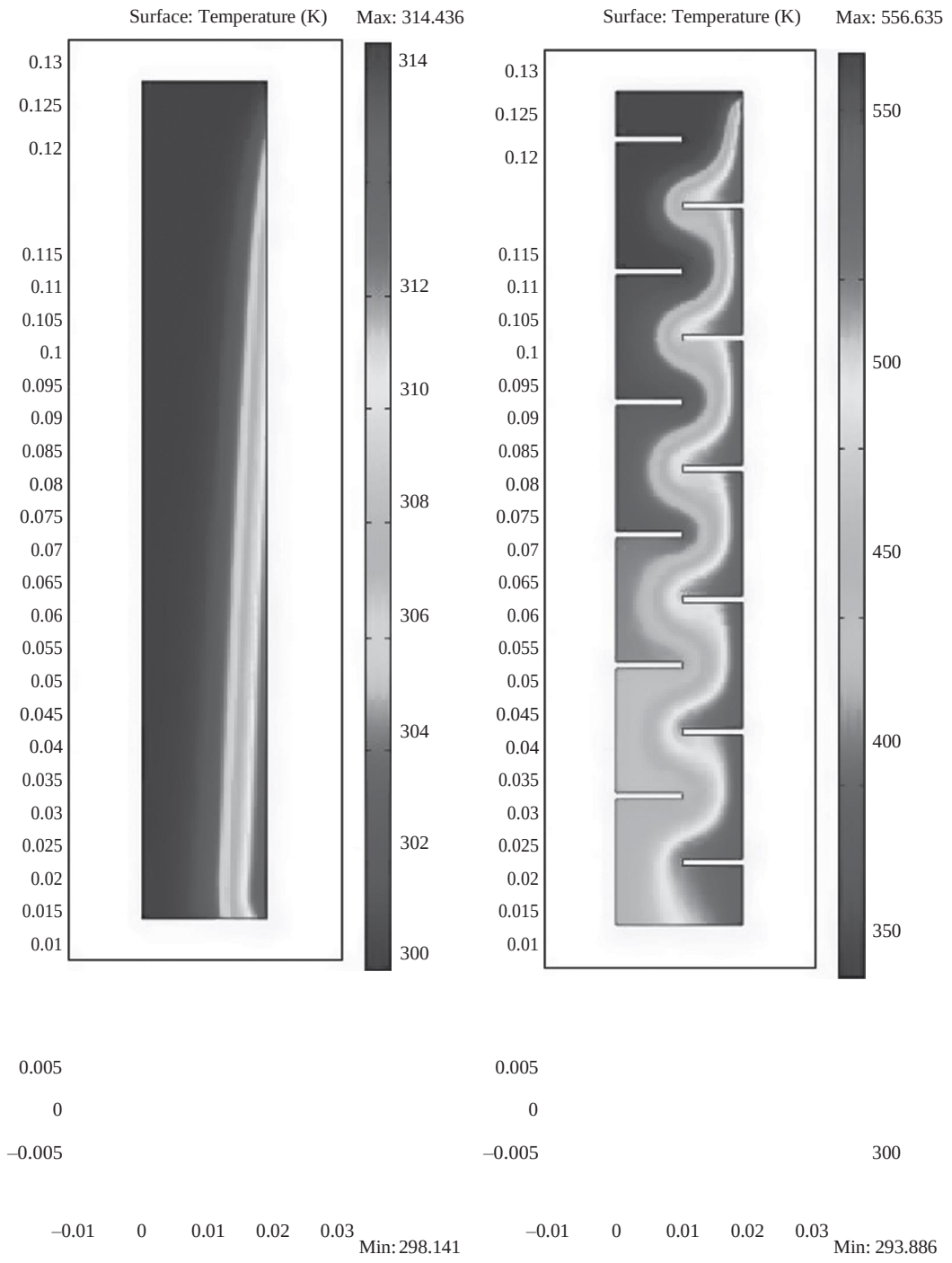


FIGURE 3.14

Simulation of the convective heat transfer inside a large radius cylindrical reactor with and without baffles. The axis of symmetry is on the left side of the domain and heat flux is applied on the right. These two reactors have the same space velocity, but one has dramatically better heat transfer properties. (From Tang, H.-Y., Reactor controller design for steam and autothermal reforming for fuel cell applications, PhD dissertation, University of California, Davis, CA, 2009.)

reactor has been investigated by Lattner [25] and Liu et al. [126]. Other variations of using multiple heating zones [67], dual catalysts [127], and coupling exothermic to endothermic regions of the reactor [128] have also been proposed. These passive methods all intend to optimize energy efficiencies by moving heat from the exothermic reaction region or exhaust to the endothermic reaction region. The various operation conditions can be incorporated into a control algorithm. However, these efforts reduce the flexibility in designing the control algorithm. The best approach is the combination of active control and passive reactor enhancement.

Free ebooks ==> www.Ebook777.com

3.17 Reformer Control Issues

Temperature control of the reformer influences fuel conversion and catalyst degradation. The poor heat transfer properties of the catalyst make transferring heat in and out of the catalyst bed difficult as shown in Figure 3.14. In ATR, if excess heat is produced on the catalyst, it will sinter and melt the catalyst. In SR, if insufficient heat is available, unreacted fuel may poison or foul the catalyst. In implementing feedback control, the feedback or the sensor placement location and control variables are not obvious. In ATR, the exother- mic reaction typically takes place near the top of the catalyst bed. To control the catalyst temperature, it is necessary to control the available oxidizer in the fuel stream. In SR, the centerline usually is the region with the lowest temperature because convection is the primary mode of heat transfer from the reactor wall to the center. However, using the centerline as the feedback location can produce oscillations in temperature inside the reformer. The high thermal resistance of the catalyst bed potentially creates a long lag in temperature response. Using strictly temperature control can lead to sintering of the catalyst near the reactor wall by excessive heating from the external burner. The situation is more problematic during transients. By the time the centerline temperature has increased, the reactor wall temperature may reach a much higher temperature creating a large temperature gradient. This could reduce the overall efficiencies as heat is not effectively utilized, and the catalyst can be degraded by multiple high-amplitude thermal cycles. A possible solution is to regulate heat flux in the steam reformer to avoid such problems. This is done by combining the ability to control the fuel feed rate and external burner input. The controller will incorporate the heat transfer properties of the reactor and the chemical kinetics of the reformation process to adjust the fuel feed rate and the external heater temperature. This concept allows maintenance of the catalyst in a certain temperature range during transient ramps [129].

3.18 Summary

Direct transport and storage of hydrogen is costly. Hydrogen production at the point of use may be a viable near-term solution. Reforming liquid hydrocarbon fuels for hydrogen production has several advantages for transportation applications: the existing infrastructure for transporting hydrocarbon fuel is well developed; refueling liquid fuel is faster and much more familiar and intuitive than recharging gaseous fuels; and there are wide ranges of possible hydrocarbon feedstocks. SR is the most widely used method of gener- ating hydrogen and produces the highest-quality reformate. POX can respond quickly to transient demand but is associated with low-quality hydrogen. ATR generally combines a higher output gas purity, similar to though not attaining that of SR, with a fast response time, similar to but not attaining that of POX. All of the methods are presently studied in earnest for the small-scale reformers required in mobile and distributed generation appli- cations. In the known and practiced reformation techniques, the resultant reformate is not a pure hydrogen stream; thus, additional cleanup steps are needed for stringent purity applications. If an inert gas, such as nitrogen, is present, it will lower the hydrogen concen- tration. End use of the hydrogen may change the reformate requirements and hence the fuel processor.

www.Ebook777.com

References

1. Amphlett, J.C., Mann, R.F., Peppley, B.A., Roberge, P.R., Rodrigues, A., and Salvador, J.P.: Simulation of a 250 kW diesel fuel processor/PEM fuel cell system, *Journal of Power Sources*, 1998, 71(1–2), 179–184.
2. Han, J., Lee, S.-M., and Chang, H.: Metal membrane-type 25-kW methanol fuel processor for fuel-cell hybrid vehicle, *Journal of Power Sources*, 2002, 112(2), 484–490.
3. Lee, S.H., Han, J., and Lee, K.-Y.: Development of 10-kWe preferential oxidation system for fuel cell vehicles, *Journal of Power Sources*, 2002, 109(2), 394–402.
4. Mathiak, J., Heinzel, A., Roes, J., Kalk, T., Kraus, H., and Brandt, H.: Coupling of a 2.5 kW steam reformer with a 1 kWel PEM fuel cell, *Journal of Power Sources*, 2004, 131(1–2), 112–119.
5. Sopeña, D., Melgar, A., Briceño, Y., Navarro, R.M., Álvarez-Galván, M.C., and Rosa, F.: Diesel fuel processor for hydrogen production for 5 kW fuel cell application, *International Journal of Hydrogen Energy*, 2007, 32(10–11), 1429–1436.
6. Yan, X., Wang, S., Li, X., Hou, M., Yuan, Z., Li, D., Pan, L., Zhang, C., Liu, J., Ming, P., and Yi, B.: A 75-kW methanol reforming fuel cell system, *Journal of Power Sources*, 2006, 162(2), 1265–1269.
7. Ahmed, S., Ahluwalia, R., Lee, S.H.D., and Lottes, S.: A gasoline fuel processor designed to study quick-start performance, *Journal of Power Sources*, 2006, 154(1), 214–222.
8. Docter, A. and Lamm, A.: Gasoline fuel cell systems, *Journal of Power Sources*, 1999, 84(2), 194–200
9. Amphlett, J.C., Creber, K.A.M., Davis, J.M., Mann, R.F., Peppley, B.A., and Stokes, D.M.: Hydrogen production by steam reforming of methanol for polymer electrolyte fuel cells, *International Journal of Hydrogen Energy*, 1994, 19(2), 131–137.
10. Agarwal, V., Patel, S., and Pant, K.K.: H_2 production by steam reforming of methanol over $Cu/ZnO/Al_2O_3$ catalysts: Transient deactivation kinetics modeling, *Applied Catalysis A: General*, 2005, 279(1–2), 155–164.
11. Breen, J.P. and Ross, J.R.H.: Methanol reforming for fuel-cell applications: Development of zirconia-containing Cu-Zn-Al catalysts, *Catalysis Today*, 1999, 51(3–4), 521–533.
12. Palo, D.R., Dagle, R.A., and Holladay, J.D.: Methanol steam reforming for hydrogen produc- tion, *Chemical Reviews*, 2007, 107(10), 3992–4021.
13. Ming, Q., Healey, T., Allen, L., and Irving, P.: Steam reforming of hydrocarbon fuels, *Catalysis Today*, 2002, 77(1–2), 51–64.
14. Rosa, F., López, E., Briceño, Y., Sopeña, D., Navarro, R.M., Alvarez-Galván, M.C., Fierro, J.L.G., and Bordons, C.: Design of a diesel reformer coupled to a PEMFC, *Catalysis Today*, 2006, 116(3), 324–333.
15. Roychoudhury, S., Lyubovsky, M., Walsh, D., Chu, D., and Kallio, E.: Design and development of a diesel and JP-8 logistic fuel processor, *Journal of Power Sources*, 2006, 160(1), 510–513.
16. Cutillo, A., Specchia, S., Antonini, M., Saracco, G., and Specchia, V.: Diesel fuel processor for PEM fuel cells: Two possible alternatives (ATR versus SR), *Journal of Power Sources*, 2006, 154(2), 379–385.
17. Hu, J., Wang, Y., VanderWiel, D., Chin, C., Palo, D., Rozmiarek, R., Dagle, R., Cao, J., Holladay, J., and Baker, E.: Fuel processing for portable power applications, *Chemical Engineering Journal*, 2003, 93(1), 55–60.
18. Liu, Z., Mao, Z., Xu, J., Hess-Mohr, N., and Schmidt, V.M.: Modelling of a PEM fuel cell system with propane ATR reforming, *Fuel Cells*, 2006, 6(5), 376–386.
19. National Energy Technology Laboratory, Gasification Systems Technologies; Gasification Basics http://www.netl.doe.gov/technologies/coalpower/gasification/basics/3.html. Accessed on December 7, 2013.
20. Rostrup-Nielsen, J.R. and Rostrup-Nielsen, T.: Large-scale hydrogen production, *CATTECH*, 2002, 6(4), 150–159.
21. *Risø Energy Report 3 – Hydrogen and Its Competitors*, Larsen, H., Feidenhans'l and Petersen, L.S. (Eds), Technical University of Denmark, Risø National Laboratory for Sustainable Energy, Holmen Center-Tryk, Holbæk, Denmark, 2004, p. 76.

22. Borup, R.L., Inbody, M.A., Semelsberger, T.A., Tafoya, J.I., and Guidry, D.R.: Fuel composition effects on transportation fuel cell reforming, *Catalysis Today*, 2005, 99(3–4), 263–270.
23. Chen, Y.-H., Yu, C.-C., Liu, Y.-C., and Lee, C.-H.: Start-up strategies of an experimental fuel processor, *Journal of Power Sources*, 2006, 160(2), 1275–1286.
24. Horng, R.-F., Chen, C.-R., Wu, T.-S., and Chan, C.-H.: Cold start response of a small methanol reformer by partial oxidation reforming of hydrogen for fuel cell, *Applied Thermal Engineering*, 2006, 26(11–12), 1115–1124.
25. Lattner, J.R. and Harold, M.P.: Autothermal reforming of methanol: Experiments and model- ing, *Catalysis Today*, 2007, 120(1), 78–89.
26. Dams, R.A.J., Hayter, P.R., and Moore, S.C.: *Book Continued Development of Mathematical Model for a Methanol Reformer*, Crown, London, UK, 2001.
27. Radu, R. and Taccani, R.: SIMULINK-FEMLAB integrated dynamic simulation model for a PEM fuel cell system, *Journal of Fuel Cell Science and Technology*, 2006, 3(4), 452–458.
28. Kolb, G.: *Fuel Processing: For Fuel Cells*, Wiley-VCH Verlag GmbH & Co. KGaA, Weinheim, Germany, 2008.
29. Davieau, D.D. and Erickson, P.A.: The effect of geometry on reactor performance in the steam-reformation process, *International Journal of Hydrogen Energy*, 2007, 32(9), 1192–1200.
30. Liao, C.-H. and Erickson, P.A.: Characteristic time as a descriptive parameter in steam refor- mation hydrogen production processes, *International Journal of Hydrogen Energy*, 2008, 33(6), 1652–1660.
31. Fogler, H.S.: *Elements of Chemical Reaction Engineering*, Pearson Education, Inc, Boston, MA, 4th edn., 2006.
32. Hagen, J.: *Industrial Catalysis – A Practical Approach*, Wiley-VCH Verlag GmbH & Co. KGaA, Weinheim, Germany, 2nd edn., 2006.
33. Catillon, S., Louis, C., and Rouget, R.: Development of new CuO–ZnII/Al_2O_3 catalyst sup- ported on copper metallic foam for the production of hydrogen by methanol steam reforming, *Topics in Catalysis*, 2004, 30–31(1), 463–467.
34. Lindström, B., Pettersson, L.J., and Govind Menon, P.: Activity and characterization of Cu/Zn, Cu/Cr and Cu/Zr on [gamma]-alumina for methanol reforming for fuel cell vehicles, *Applied Catalysis A: General*, 2002, 234(1–2), 111–125.
35. Liu, S., Takahashi, K., Uematsu, K., and Ayabe, M.: Hydrogen production by oxidative metha- nol reforming on Pd/ZnO, *Applied Catalysis A: General*, 2005, 283(1–2), 125–135.
36. Mastalir, A., Frank, B., Szizybalski, A., Soerijanto, H., Deshpande, A., Niederberger, M., Schomäcker, R., Schlögl, R., and Ressler, T.: Steam reforming of methanol over Cu/ZrO_2/CeO_2 catalysts: A kinetic study, *Journal of Catalysis*, 2005, 230(2), 464–475.
37. Matter, P.H., Braden, D.J., and Ozkan, U.S.: Steam reforming of methanol to H_2 over nonre- duced Zr-containing CuO/ZnO catalysts, *Journal of Catalysis*, 2004, 223(2), 340–351.
38. Oguchi, H., Nishiguchi, T., Matsumoto, T., Kanai, H., Utani, K., Matsumura, Y., and Imamura, S.: Steam reforming of methanol over Cu/CeO_2/ZrO_2 catalysts, *Applied Catalysis A: General*, 2005, 281(1–2), 69–73.
39. Papavasiliou, J., Avgouropoulos, G., and Ioannides, T.: Effect of dopants on the performance of CuO-CeO_2 catalysts in methanol steam reforming, *Applied Catalysis B: Environmental*, 2007, 69(3–4), 226–234.
40. Purnama, H., Girgsdies, F., Ressler, T., Schattka, J.H., Caruso, R.A., Schomäcker, R., and Schlögl, R.: Activity and selectivity of a nanostructured CuO/ZrO_2 catalyst in the steam reforming of methanol, *Catalysis Letters*, 2004, 94(1), 61–68.
41. Shan, W., Feng, Z., Li, Z., Zhang, J., Shen, W., and Li, C.: Oxidative steam reforming of meth- anol on $Ce_{0.9}Cu_{0.1}OY$ catalysts prepared by deposition-precipitation, coprecipitation, and complexation-combustion methods, *Journal of Catalysis*, 2004, 228(1), 206–217.
42. Wang, Z., Wang, W., and Lu, G.: Studies on the active species and on dispersion of Cu in Cu/SiO_2 and Cu/Zn/SiO_2 for hydrogen production via methanol partial oxidation, *International Journal of Hydrogen Energy*, 2003, 28(2), 151–158.

43. Agrell, J., Birgersson, H., Boutonnet, M., Melián-Cabrera, I., Navarro, R.M., and Fierro, J.L.G.: Production of hydrogen from methanol over Cu/ZnO catalysts promoted by ZrO_2 and Al_2O_3, *Journal of Catalysis*, 2003, 219(2), 389–403.
44. Choi, Y. and Stenger, H.G.: Fuel cell grade hydrogen from methanol on a commercial $Cu/ZnO/Al_2O_3$ catalyst, *Applied Catalysis B: Environmental*, 2002, 38(4), 259–269.
45. Costantino, U., Marmottini, F., Sisani, M., Montanari, T., Ramis, G., Busca, G., Turco, M., and Bagnasco, G.: Cu-Zn-Al hydrotalcites as precursors of catalysts for the production of hydrogen from methanol, *Solid State Ionics*, 2005, 176(39–40), 2917–2922.
46. Agrell, J., Boutonnet, M., Melián-Cabrera, I., and Fierro, J.L.G.: Production of hydrogen from methanol over binary Cu/ZnO catalysts: Part I. Catalyst preparation and characterisation, *Applied Catalysis A: General*, 2003, 253(1), 201–211.
47. Faur Ghenciu, A.: Review of fuel processing catalysts for hydrogen production in PEM fuel cell systems, *Current Opinion in Solid State and Materials Science*, 2002, 6(5), 389–399.
48. Auprêtre, F., Descorme, C., and Duprez, D.: Bio-ethanol catalytic steam reforming over sup- ported metal catalysts, *Catalysis Communications*, 2002, 3(6), 263–267.
49. De Rogatis, L., Montini, T., Casula, M.F., and Fornasiero, P.: Design of $Rh@Ce_{0.2}Zr_{0.8}O_2$-Al_2O_3 nanocomposite for ethanol steam reforming, *Journal of Alloys and Compounds*, 2008, 451(1–2), 516–520.
50. Ha, J.W., Kundu, A., and Jang, J.H.: Poly-dimethylsiloxane (PDMS) based micro-reactors for steam reforming of methanol, *Fuel Processing Technology*, 91(11), 1725–1730.
51. Hwang, S.-M., Kwon, O.J., and Kim, J.J.: Method of catalyst coating in micro-reactors for meth- anol steam reforming, *Applied Catalysis A: General*, 2007, 316(1), 83–89.
52. Kawamura, Y., Ogura, N., Yamamoto, T., and Igarashi, A.: A miniaturized methanol reformer with Si-based microreactor for a small PEMFC, *Chemical Engineering Science*, 2006, 61(4), 1092–1101.
53. Moreno, A.M. and Wilhite, B.A.: Autothermal hydrogen generation from methanol in a ceramic microchannel network, *Journal of Power Sources*, 195(7), 1964–1970.
54. Agrell, J., Birgersson, H., and Boutonnet, M.: Steam reforming of methanol over a $Cu/ZnO/Al_2O_3$ catalyst: A kinetic analysis and strategies for suppression of CO formation, *Journal of Power Sources*, 2002, 106(1–2), 249–257.
55. Sahoo, D.R., Vajpai, S., Patel, S., and Pant, K.K.: Kinetic modeling of steam reforming of etha- nol for the production of hydrogen over Co/Al_2O_3 catalyst, *Chemical Engineering Journal*, 2007, 125(3), 139–147.
56. Peppley, B.A., Amphlett, J.C., Kearns, L.M., and Mann, R.F.: Methanol-steam reforming on $Cu/ZnO/Al_2O_3$. Part 1: The reaction network, *Applied Catalysis A: General*, 1999, 179(1–2), 21–29.
57. Choi, Y. and Stenger, H.G.: Kinetics, simulation and optimization of methanol steam reformer for fuel cell applications, *Journal of Power Sources*, 2005, 142(1–2), 81–91.
58. Rabenstein, G. and Hacker, V.: Hydrogen for fuel cells from ethanol by steam-reforming, partial-oxidation and combined auto-thermal reforming: A thermodynamic analysis, *Journal of Power Sources*, 2008, 185(2), 1293–1304.
59. Hoogers, G.: *Fuel Cell Technology Handbook*, CRC Press, Boca Raton, FL, 2003.
60. Cheekatamarla, P.K. and Finnerty, C.M.: Synthesis gas production via catalytic partial oxida- tion reforming of liquid fuels, *International Journal of Hydrogen Energy*, 2008, 33(19), 5012–5019.
61. Sterchi, P.: The effect of hydrocarbon impurities on the methanol steam-reforming process for fuel cell applications. PhD dissertation, University of Florida, Gainesville, FL, 2001.
62. Yoon, H.C. and Erickson, P.A.: Hydrogen from coal-derived methanol via autothermal reform- ing processes, *International Journal of Hydrogen Energy*, 2008, 33(1), 57–63.
63. Yoon, H.C.: Comparison of steam and autothermal reforming of methanol for fuel cell applica- tions. PhD dissertation, University of California, Davis, CA, 2008.
64. Velu, S., Suzuki, K., Okazaki, M., Kapoor, M.P., Osaki, T., and Ohashi, F.: Oxidative steam reforming of methanol over CuZnAl(Zr)-oxide catalysts for the selective production of hydro- gen for fuel cells: Catalyst characterization and performance evaluation, *Journal of Catalysis*, 2000, 194(2), 373–384.

65. Chan, S.H. and Wang, H.M.: Thermodynamic and kinetic modelling of an autothermal metha- nol reformer, *Journal of Power Sources*, 2004, 126(1–2), 8–15.
66. Turco, M., Bagnasco, G., Cammarano, C., Senese, P., Costantino, U., and Sisani, M.: Cu/ZnO/ Al_2O_3 catalysts for oxidative steam reforming of methanol: The role of Cu and the dispersing oxide matrix, *Applied Catalysis B: Environmental*, 2007, 77(1–2), 46–57.
67. Sundaresan, M., Ramaswamy, S., Moore, R.M., and Hoffman, M.A.: Catalytic burner for an indirect methanol fuel cell vehicle fuel processor, *Journal of Power Sources*, 2003, 113(1), 19–36.
68. Pfefferle, W.C. and Pfefferle, L.D.: Catalytically stabilized combustion, *Progress in Energy and Combustion Science*, 1986, 12(1), 25–41.
69. Pfefferle, L.D. and Pfefferle, W.C.: Catalysis in combustion, *Catalysis Reviews*, 1987, 29(2), 219–267.
70. Otsuka, K., Ina, T., and Yamanaka, I.: The partial oxidation of methanol using a fuel cell reactor, *Applied Catalysis A: General*, 2003, 247(2), 219–229.
71. Sakong, S., Sendner, C., and Groß, A.: Partial oxidation of methanol on Cu(110): Energetics and kinetics, *Journal of Molecular Structure: THEOCHEM*, 2006, 771(1–3), 117–122.
72. Zhou, L., Günther, S., and Imbihl, R.: Low-pressure methanol oxidation over a Cu(110) surface under stationary conditions: (I) reaction kinetics, *Journal of Catalysis*, 2005, 230(1), 166–172.
73. Mu, X., Pan, L., Liu, N., Zhang, C., Li, S., Sun, G., and Wang, S.: Autothermal reforming of methanol in a mini-reactor for a miniature fuel cell, *International Journal of Hydrogen Energy*, 2007, 32(15), 3327–3334.
74. Schildhauer, T.J. and Geissler, K.: Reactor concept for improved heat integration in autothermal methanol reforming, *International Journal of Hydrogen Energy*, 2007, 32(12), 1806–1810.
75. Semelsberger, T.A., Brown, L.F., Borup, R.L., and Inbody, M.A.M.A.: Equilibrium products from autothermal processes for generating hydrogen-rich fuel-cell feeds, *International Journal of Hydrogen Energy*, 2004, 29(10), 1047–1064.
76. Liu, Y., Hayakawa, T., Tsunoda, T., Suzuki, K., Hamakawa, S., Murata, K., Shiozaki, R., Ishii, T., and Kumagai, M.: Steam reforming of methanol over Cu/CeO_2 catalysts studied in comparison with Cu/ZnO and Cu/Zn(Al)O catalysts, *Topics in Catalysis*, 2003, 22(3), 205–213.
77. Simmons, T.: Characteristics of autothermal reforming of a hydrocarbon fuel for hydrogen for fuel cell vehicles. PhD dissertation, University of Florida, Gainesville, FL, 2003.
78. Sadakane, O., Saitoh, K., Oyama, K., Yamauchi, N., and Komatsu, H.: Fuel-cell vehicle fuels: Evaluating the reforming performance of gasoline components, SAE, 2003, 2003-01-0414.
79. Lindström, B., Agrell, J., and Pettersson, L.J.: Combining methanol reforming for hydrogen generation over monolithic catalysts, *Chemical Engineering Journal*, 2003, 93(1), 91–101.
80. Krumpelt, M., Krause, T.R., Carter, J.D., Kopasz, J.P., and Ahmed, S.: Fuel processing for fuel cell systems in transportation and portable power applications, *Catalysis Today*, 2002, 77(1–2), 3–16.
81. Dorr, J.L.: Methanol autothermal reformation: Oxygen-to-carbon ratio and reaction progres- sion. Master thesis, University of California, Davis, CA, 2004.
82. Fukahori, S., Kitaoka, T., Tomoda, A., Suzuki, R., and Wariishi, H.: Methanol steam reforming over paper-like composites of Cu/ZnO catalyst and ceramic fiber, *Applied Catalysis A: General*, 2006, 300(2), 155–161.
83. Patel, S. and Pant, K.K.: Production of hydrogen with low carbon monoxide formation via catalytic steam reforming of methanol, *Journal of Fuel Cell Science and Technology*, 2006, 3(4), 369–374.
84. Wang, J., Li, C.-H., and Huang, T.-J.: Study of partial oxidative steam reforming of methanol over Cu–ZnO/samaria-doped ceria catalyst, *Catalysis Letters*, 2005, 103(3), 239–247.
85. Zhou, S., Yuan, Z., and Wang, S.: Selective CO oxidation with real methanol reformate over monolithic Pt group catalysts: PEMFC applications. *International Journal of Hydrogen Energy*, 2006, 31(7), 924–933.
86. Palo, D.R., Dagle, R.A., and Holladay, J.D.: Methanol steam reforming for hydrogen produc- tion, *Chemical Reviews*, 2007, 107(10), 3992–4021.
87. Comas, J., Mariño, F., Laborde, M., and Amadeo, N.: Bio-ethanol steam reforming on Ni/Al_2O_3 catalyst, *Chemical Engineering Journal*, 2004, 98(1–2), 61–68.

88. Giunta, P., Amadeo, N., and Laborde, M.: Simulation of a low temperature water gas shift reactor using the heterogeneous model/application to a PEM fuel cell, *Journal of Power Sources*, 2006, 156(2), 489–496.
89. Mas, V., Kipreos, R., Amadeo, N., and Laborde, M.: Thermodynamic analysis of ethanol/water system with the stoichiometric method, *International Journal of Hydrogen Energy*, 2006, 31(1), 21–28.
90. Wang, W. and Wang, Y.: Thermodynamic analysis of hydrogen production via partial oxidation of ethanol, *International Journal of Hydrogen Energy*, 2008, 33(19), 5035–5044.
91. Yoon, H.C., Otero, J., and Erickson, P.A.: Reactor design limitations for the steam reforming of methanol, *Applied Catalysis B: Environmental*, 2007, 75(3–4), 264–271.
92. Erickson, P.: Enhancing the steam-reformation process with acoustics: An investigation for fuel cell vehicle applications. PhD dissertation, University of Florida, Gainesville, FL, 2002.
93. Vernon, D.: Hydrogen enrichment and thermochemical recuperation in internal combustion engines: An investigation of dilution and inlet temperature effects in the autothermal reforma- tion of ethanol. PhD dissertation, University of California, Davis, CA, 2010.
94. Vernon, D.: Understanding the effects of reactor geometry and scaling through tempera- ture profiles in steam-reforming hydrogen production reactors. Master thesis, University of California, Davis, CA, 2006.
95. Al-Ubaid, A. and Wolf, E.E.: Steam reforming of methane on reduced non-stoichiometric nickel aluminate catalysts, *Applied Catalysis*, 1988, 40, 73–85.
96. Patel, S. and Pant, K.K.: Selective production of hydrogen via oxidative steam reforming of methanol using Cu-Zn-Ce-Al oxide catalysts, *Chemical Engineering Science*, 2007, 62(18–20), 5436–5443.
97. Kundu, A., Shul, Y.G., Kim, D.H., T.S. Zhao, K.D.K., and Trung Van, N.: *Chapter Seven Methanol Reforming Processes: Advances in Fuel Cells*, Elsevier Science, 2007, pp. 419–472.
98. Turco, M., Bagnasco, G., Costantino, U., Marmottini, F., Montanari, T., Ramis, G., and Busca, G.: Production of hydrogen from oxidative steam reforming of methanol: I. Preparation and char- acterization of $Cu/ZnO/Al_2O_3$ catalysts from a hydrotalcite-like LDH precursor, *Journal of Catalysis*, 2004, 228(1), 43–55.
99. Turco, M., Bagnasco, G., Costantino, U., Marmottini, F., Montanari, T., Ramis, G., and Busca, G.: Production of hydrogen from oxidative steam reforming of methanol: II. Catalytic activity and reaction mechanism on $Cu/ZnO/Al_2O_3$ hydrotalcite-derived catalysts, *Journal of Catalysis*, 2004, 228(1), 56–65.
100. Arcak, M., Gorgun, H., Pedersen, L.M., and Varigonda, S.A.V.S.: A nonlinear observer design for fuel cell hydrogen estimation, *IEEE Transactions on Control Systems Technology*, 2004, 12(1), 101–110.
101. Gorgun, H., Arcak, M., Varigonda, S., and Bortoff, S.A.: Observer designs for fuel processing reactors in fuel cell power systems, *International Journal of Hydrogen Energy*, 2005, 30(4), 447–457.
102. Nummedal, L., Røsjorde, A., Johannessen, E., and Kjelstrup, S.: Second law optimization of a tubular steam reformer, *Chemical Engineering and Processing*, 2005, 44(4), 429–440.
103. Ahmed, S. and Krumpelt, M.: Hydrogen from hydrocarbon fuels for fuel cells, *International Journal of Hydrogen Energy*, 2001, 26(4), 291–301.
104 Lindström, B. and Pettersson, L.J.: Catalytic oxidation of liquid methanol as a heat source for an automotive reformer, *Chemical Engineering and Technology*, 2003, 26(4), 473–478. April 2003. doi:10.1002/ceat.200390071.
105. Lattner, J.R. and Harold, M.P.: Comparison of methanol-based fuel processors for PEM fuel cell systems, *Applied Catalysis B: Environmental*, 2005, 56(1–2), 149–169.
106. Mitchell, W., Bowers, B.J., Garnier, C., and Boudjemaa, F.: Dynamic behavior of gasoline fuel cell electric vehicles, *Journal of Power Sources*, 2006, 154(2), 489–496.
107. Pan, L. and Wang, S.: A compact integrated fuel-processing system for proton exchange mem- brane fuel cells, *International Journal of Hydrogen Energy*, 2006, 31(4), 447–454.
108. Lattner, J.R. and Harold, M.P.: Comparison of conventional and membrane reactor fuel pro- cessors for hydrocarbon-based PEM fuel cell systems, *International Journal of Hydrogen Energy*, 2004, 29(4), 393–417.

109. Bowers, B.J., Zhao, J.L., Ruffo, M., Khan, R., Dattatraya, D., Dushman, N., Beziat, J.-C., and Boudjemaa, F.: Onboard fuel processor for PEM fuel cell vehicles, *International Journal of Hydrogen Energy*, 2007, 32(10–11), 1437–1442.
110. Ahluwalia, R.K., Zhang, Q., Chmielewski, D.J., Lauzze, K.C., and Inbody, M.A.: Performance of CO preferential oxidation reactor with noble-metal catalyst coated on ceramic monolith for on-board fuel processing applications, *Catalysis Today*, 2005, 99(3–4), 271–283.
111. Jiménez, S., Soler, J., Valenzuela, R.X., and Daza, L.: Assessment of the performance of a PEMFC in the presence of CO, *Journal of Power Sources*, 2005, 151, 69–73.
112. Kim, J.-D., Park, Y.-I., Kobayashi, K., Nagai, M., and Kunimatsu, M.: Characterization of CO tolerance of PEMFC by AC impedance spectroscopy, *Solid State Ionics*, 2001, 140(3–4),313–325.
113. Kim, J.-D., Park, Y.-I., Kobayashi, K., and Nagai, M.: Effect of CO gas and anode-metal loading on H_2 oxidation in proton exchange membrane fuel cell, *Journal of Power Sources*, 2001, 103(1), 127–133.
114. Lee, S.J., Mukerjee, S., Ticianelli, E.A., and McBreen, J.: Electrocatalysis of CO tolerance in hydrogen oxidation reaction in PEM fuel cells, *Electrochimica Acta*, 1999, 44(19), 3283–3293.
115. Pereira, L.G.S., dos Santos, F.R., Pereira, M.E., Paganin, V.A., and Ticianelli, E.A.: CO tolerance effects of tungsten-based PEMFC anodes, *Electrochimica Acta*, 2006, 51(19), 4061–4066.
116. Wagner, N. and Gülzow, E.: Change of electrochemical impedance spectra (EIS) with time during CO-poisoning of the Pt-anode in a membrane fuel cell, *Journal of Power Sources*, 2004, 127(1–2), 341–347.
117. Auckenthaler, T.S.: *Modelling and Control of Three-Way Catalytic Converters*, Swiss Federal Institute of Technology (ETH), Zürich, Switzerland, 2005.
118. Spiegel, C.: *Designing and Building Fuel Cells*, McGraw-Hill Professional Publishing, 1st edn., 2007.
119. Laosiripojana, N. and Assabumrungrat, S.: Catalytic steam reforming of methane, methanol, and ethanol over Ni/YSZ: The possible use of these fuels in internal reforming SOFC, *Journal of Power Sources*, 2007, 163(2), 943–951.
120. Liu, S., Takahashi, K., Uematsu, K., and Ayabe, M.: Hydrogen production by oxidative metha- nol reforming on Pd/ZnO catalyst: Effects of the addition of a third metal component, *Applied Catalysis A: General*, 2004, 277(1–2), 265–270.
121. Polman, E.A., Der Kinderen, J.M., and Thuis, F.M.A.: Novel compact steam reformer for fuel cells with heat generation by catalytic combustion augmented by induction heating, *Catalysis Today*, 1999, 47(1–4), 347–351.
122. Smith, T.G. and Carberry, J.J.: Design and optimization of a tube-wall reactor, *Chemical Engineering Science*, 1975, 30(2), 221–227.
123. Zanfir, M. and Gavriilidis, A.: Modelling of a catalytic plate reactor for dehydrogenation- combustion coupling, *Chemical Engineering Science*, 2001, 56(8), 2671–2683.
124. Erickson, P.A. and Liao, C.-h.: Statistical validation and an empirical model of hydrogen pro- duction enhancement found by utilizing passive flow disturbance in the steam-reformation process, *Experimental Thermal and Fluid Science*, 2007, 32(2), 467–474.
125. Erickson, P.A., Feinstein, J.J., Ralston, M.P., Davieau, D.D., and Sit, I.K.: *Testing of Methane Steam Reforming in a Novel Structured Catalytic Reactor Providing Flow Impingement Heat Transfer*, Proceedings of the AIChe 2010 Annual Meeting, Salt Lake City, Utah, 2010.
126. Liu, S., Li, W., Wang, Y., and Xu, H.: Catalytic partial oxidation of methane to syngas in a fixed- bed reactor with an O_2-distributor: The axial temperature profile and species profile study, *Fuel Processing Technology*, 2008, 89(12), 1345–1350.
127. Zhu, J., Rahuman, M.S.M.M., van Ommen, J.G., and Lefferts, L.: Dual catalyst bed concept for catalytic partial oxidation of methane to synthesis gas, *Applied Catalysis A: General*, 2004, 259(1), 95–100.
128. Patel, K.S. and Sunol, A.K.: Modeling and simulation of methane steam reforming in a thermally coupled membrane reactor, *International Journal of Hydrogen Energy*, 2007, 32(13), 2344–2358.
129. Tang, H.-Y.: Reactor controller design for steam and autothermal reforming for fuel cell applica- tions. PhD dissertation, University of California, Davis, CA, 2009.

Free ebooks ==> www.Ebook777.com

www.Ebook777.com

4

Hydrogen Production Using Solid Fuels

Nirmal V. Gnanapragasam
University of Ontario Institute of Technology

Bale V. Reddy
University of Ontario Institute of Technology

Marc A. Rosen
University of Ontario Institute of Technology

CONTENTS

4.1 Solid Fuels 64
4.1.1 Supply and Utilization 64
4.1.2 Issues Associated with Solid Fuels 67
4.2 Utility Processes 68
4.2.1 Upstream Processes 68
4.2.2 Fuel Handling and Air Separation Unit 68
4.2.3 Steam and Electricity: Pressurized Fluidized Bed Combustion 69
4.3 Energy Conversion Processes 70
4.3.1 Gasification 71
4.3.1.1 Gasification Process Design 72
4.3.1.2 Gasifier Process Optimization 74
4.3.1.3 Fluidized Bed Gasifier 74
4.3.1.4 Ultrasuperheated Steam Gasification 75
4.3.1.5 Supercritical Water Gasification 77
4.3.1.6 Plasma Gasification 79
4.3.2 Anaerobic Digestion 80
4.3.3 Chemical Looping Processes 83
4.3.3.1 Syngas Chemical Looping 83
4.3.3.2 Direct Chemical Looping 85
4.3.4 Autothermal Reforming 88
4.3.5 Hydrogen Separation and Purification Processes 90
4.3.5.1 Water–Gas Shift Process 90
4.3.5.2 Gas Separation Membranes 91
4.3.5.3 Pressure Swing Adsorption for Hydrogen Purification 93
4.4 Environment Protection Processes 93
4.4.1 Acid Gas Removal: Sulfur Removal 94
4.4.2 Claus and SCOT Processes: Sulfur Recovery 95
4.3 Tar, Ash, and Soot Removal 95
4.4 CO_2 Capture and Storage 97

Free ebooks ==> www.Ebook777.com

4.5 Economic Benefits through Process Integration 99
4.5.1 Integration of Energy Conversion and Waste Management Processes 99
4.5.1.1 Benefits of Process Integration 100
4.5.1.2 Challenges in Large-Scale Process Integration 100
4.5.1.3 Economics of Process Integration 101
4.5.2 Cost of Hydrogen Production: Impact of CO_2 Capture on Various Technologies 101
4.5.3 Comparison of Hydrogen Production: Efficiency and Overall Costs 102
4.5.4 Cost of Hydrogen in World Markets 104
4.6 Summary 104
Acknowledgment 105
References 105

Hydrogen is an energy carrier like electricity but with advantageous applications, especially in transportation (through engines and fuel cells). Hydrogen does not occur naturally in large quantities or in high concentrations on Earth. It must be produced from other compounds such as water and hydrocarbons (coal, biomass, solid wastes, natural gas, heavy oils, oil sands, etc).

Solid fuels such as coal, biomass, and solid wastes are increasingly used with water to produce hydrogen, and the energy transfer/conversion processes have been enhanced through recent developments (Gnanapragasam et al., 2010). The search for better uses for solid fuels is gaining prominence rapidly due to environmental imbalances caused by excessive CO_2 emissions from solid fossil fuels in energy conversion processes (IPCC, 2008). The impact of global warming has focused efforts on reducing or capturing emissions of CO_2 and other greenhouse gases from all energy sources.

Producing hydrogen from solid fuels increases their commercial value, especially for coal in the transportation sector. By converting solid fuels into gases and liquids, two major problems associated with solid fuels are addressed: (1) increasing adaptability to gas/liquid intake processes and (2) enabling cost-effective capture of various pollutants during the solid-to-gas/liquid conversion. A third advantage pertaining to certain solid fuels such as solid wastes is their safe and effective disposal (IEA, 2008b). Collective information on these hydrogen production processes is required to assess the expected outcomes of research and development and other improvement efforts now in place and required in the future.

An extended review of selected technological advances in hydrogen production using solid fuels is presented in this chapter, focusing on energy, environment, and economic sustainability. The advantages and problems associated with new developments are assessed based on research and development involving design, integration, and economics.

The process of producing hydrogen from various solid fuels follows several stages of processes, and the sequence is outlined in Figure 4.1. Solid fuels, depending on their natural occurrence and characteristics, are processed (sometimes with water) to use their exergy for deriving hydrogen through various high- and low-temperature processes. Utility processes involve those that pretreat solid fuels in cleaning, drying, and storing before being used in energy conversion processes. Any system that uses solid fuels in producing hydrogen needs oxygen, steam, and electricity for various stages of hydrogen production, and generating them becomes part of the utility processes.

Energy conversion processes primarily involve converting solid fuels into gaseous and liquid forms for further transformation into hydrogen. As listed in section 3 in Figure 4.1,

www.Ebook777.com

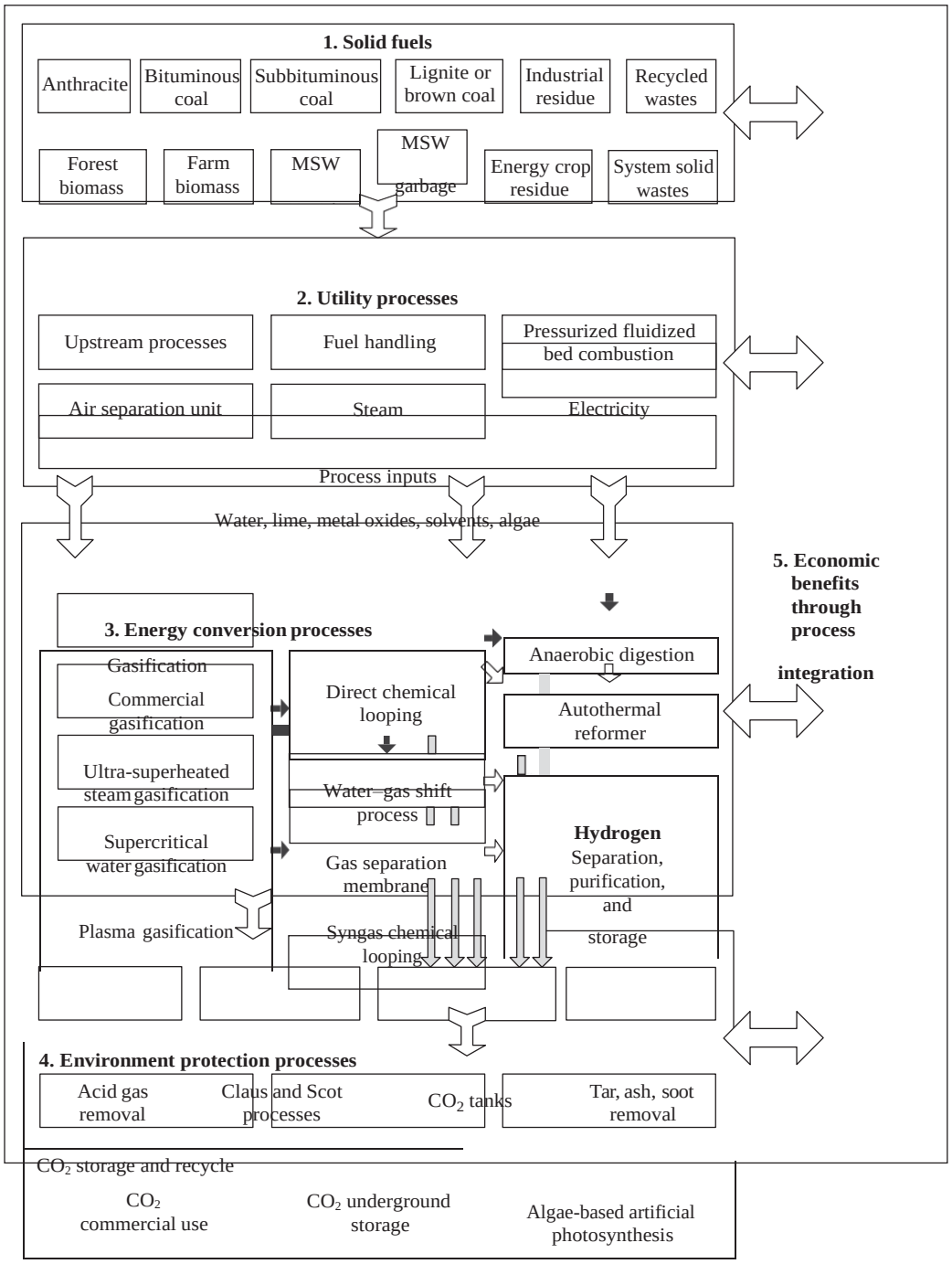


FIGURE 4.1

Organizational flowchart of various processes involved in hydrogen production from solid fuels, representing an outline of subject matter discussed in this chapter.

gasification, chemical looping, and anaerobic digestion are the primary processes that are discussed in this chapter. Although hydrogen storage is listed as part of energy con- version

processes it is of a different nature that involves issues associated with storing hydrogen for longer periods of time. Hydrogen storage is not discussed here but is cov- ered in another chapter of this book.

Processes that enable environmental protection by capturing, controlling, and reducing releases of harmful gaseous and solid elements are discussed to provide an understand- ing of the energy and costs involved in these processes, which can hinder developments of certain technologies for producing hydrogen using solid fuels. To achieve environmental and economic benefits, energy-coordinated process integration is necessary and is discussed toward the end of this chapter.

4.1 Solid Fuels

Solid fuels supply the energy required to split hydrogen from water through various conversion processes, sometimes yielding additional products. Solid fuels as shown in Figure 4.2 include such hydrocarbons as coal, tar sands, oil shale, and bitumen; renewable organic materials such as biomass/charcoal, agricultural residue, and forest residue; and renewable inorganic materials such as municipal and industrial solid wastes.

4.1.1 Supply and Utilization

Reserves of solid fuels are significantly higher than those for other fossil fuels. Of the cur- rent global energy use, 80% is supplied by fossil fuels; 13.5% by renewable sources like solar, wind, and geothermal energy; and 6.5% by nuclear energy (Asif and Muneer, 2007). Coal is the most significant contributor among fossil fuels to the current global elec- tricity generation, accounting for 40% (IEA, 2008b). The most abundant fossil fuel on the planet, current estimates of global recoverable coal reserves range from 216 years to over 500 years (British Petroleum, 2003) at present usage rates. By the year 2025, it is expected that the United States will require over 250 GW of new electrical generation

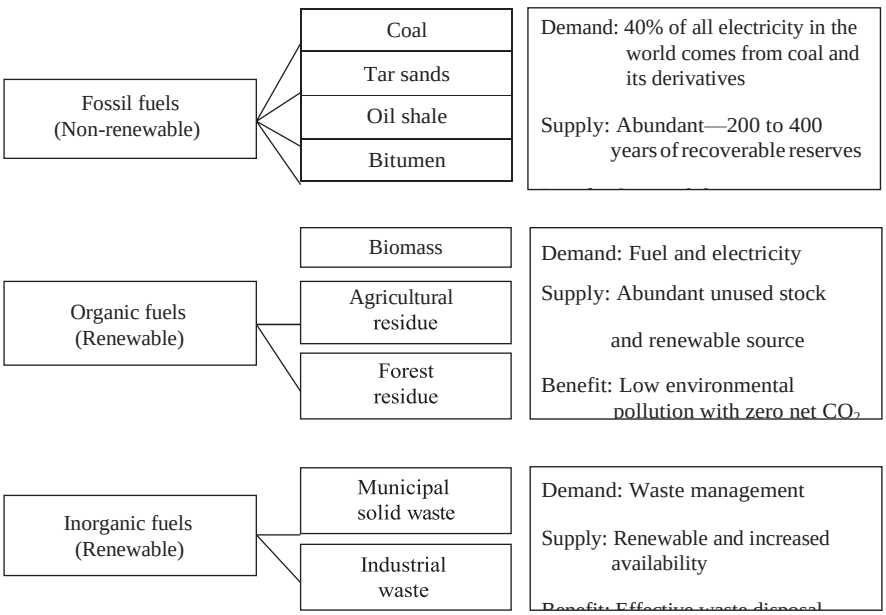


FIGURE 4.2

Types of primary solid fuels with an overview of the demand, supply, and benefit of each.

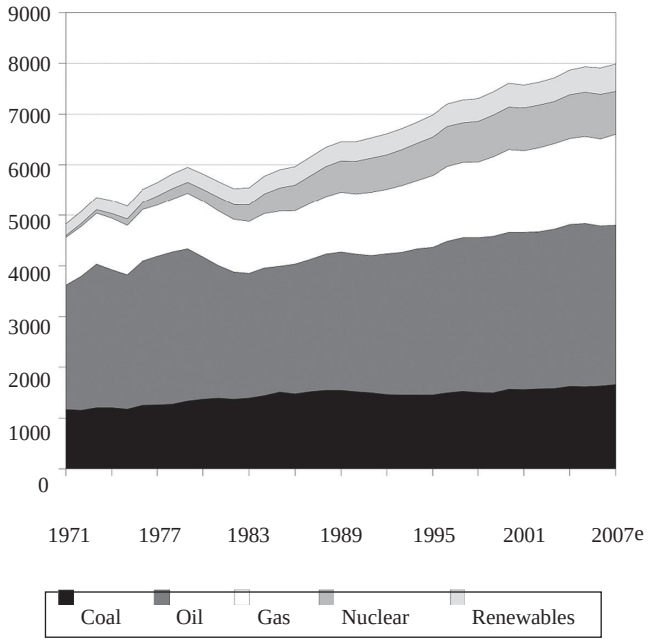


FIGURE 4.3

TPES by fuel in million tons of coal equivalent (Mtce) for member countries of the OECD. (Reprinted from IEA, World energy outlook 2008, International Energy Agency Report, Paris, France, 2008a; IEA, Energy technology perspectives 2008: Scenarios and strategies to 2050, International Energy Agency Report, Paris, France, 2008b.)

capacity even without considering replacing old plants (DOE, 2005). Of this new capacity, the International Energy Agency (IEA) estimates that 80 GW will be met through the construction of coal-based power plants, through advanced cocombustion and cogasification processes. Worldwide installed capacity of coal-based plants is expected to increase by over 40% in the next 20 years, exceeding 1400 GW by 2025 (DOE, 2005). When the hydrogen demand becomes equal to that of oil in the transportation sector or electricity in the power sector, solid fuels especially coal will likely have an important role to play owing to their abundance and low market price (IEA, 2008a). Within the member countries of the Organization for Economic Co-operation and Development (OECD), the nature of coal use relative to other energy sources for the last four decades is shown in Figure 4.3. The rapid increase in nuclear and renewable energy in recent years (after 2001 in Figure 4.3) shows the significant efforts of these countries in curbing greenhouse gas emissions.

Only nonagglomerating coal is considered for the purpose of hydrogen production, especially when using gasification as the primary conversion process. In 2007, hard coal (anthracite and bituminous coal) production increased by 6.5% (or 338.0 Mt) to 5542.9 Mt. Brown coal (subbituminous coal) production increased by 0.9% (or 7.9 Mt) to 945.2 Mt, a little above its 1994 level (IEA, 2008a). Total global coal production increased by 5.6%, well above the 10-year average growth trend of 3.4%. Total global coal consumption increased by 6.2% or 271.7 Mtce in 2007, which follows a 4-year trend of annual increases averaging 6.6%. These numbers suggest an increase in worldwide demand for electricity (which is the largest end use for coal), largely due to the migration of vast numbers of potential consumers to the OECD countries, an increase in living standards across the planet and an increase in global population (IEA, 2008b). The total primary energy supply (TPES) by fuel shares for the year 2007 is shown in Figure 4.4, where it is observed that coal delivers up to 26.4% and still maintains the lead role in electricity generation (IEA, 2009). The calorific values of various coals and biomass based on proximate and ultimate analyses are available elsewhere (Parikh et al., 2007).

Free ebooks ==> www.Ebook777.com

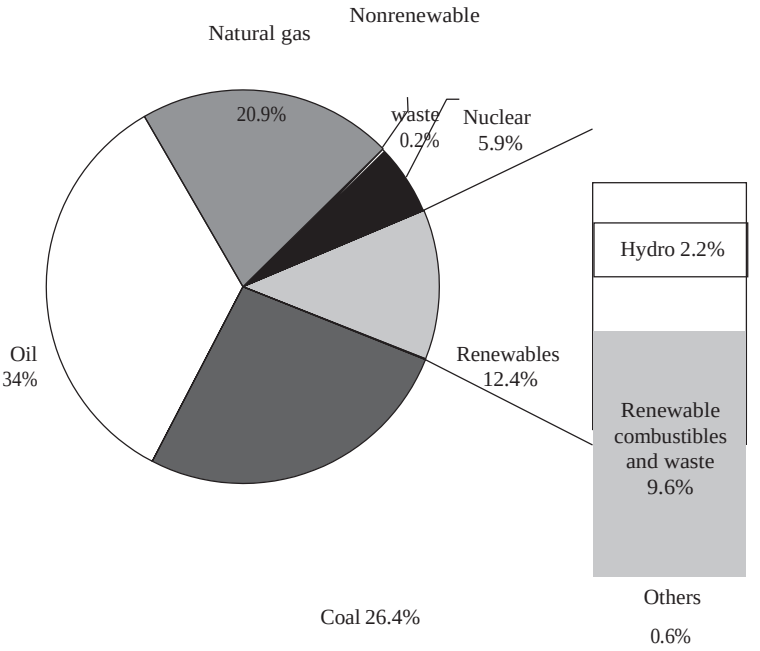


FIGURE 4.4

Breakdown of energy form from the 2007 world TPES. (From International Energy Agency, Renewables infor- mation 2009 with 2008 data, 2009. Available at www.iadb.org/intal/intalcdi/PE/2009/03711.pdf, Accessed on December 5, 2013.)

Biomass capable of use in hydrogen production includes agricultural residues, forest residues, energy crop residues, organic solid wastes, and firewood (charcoal). From data gathered by the IEA (2009) shown in Figure 4.4, only 12.4% is contributed by all renewable resources to the TPES in the world. A contribution of 9.6% is directly from renewable solid fuels such as biomass, residues, and municipal solid waste (MSW).

A total of about 36% of energy contributions are from solid fuels in recent years, providing ample opportunity for producing hydrogen using the energy from these solid fuels. Of the 12.4% renewables in Figure 4.4, 77.3% is shown in Figure 4.5 to be from solid biomass, charcoal, and MSW except for 1.1% from landfill gas, far more than any other renewable energy resources. But biomass tends to be bulky, to deteriorate over time, and to be difficult to store and handle. Compared to coal and oil, biomass has a lower energy density (GJ per unit of weight or volume), which makes handling, transport, storage, and combustion more difficult (IEA, 2006). Although the contribution of solid renewables to the TPES has increased by 9% compared to 1990 levels (IEA, 2009), much of it is used for combustion-based energy systems.

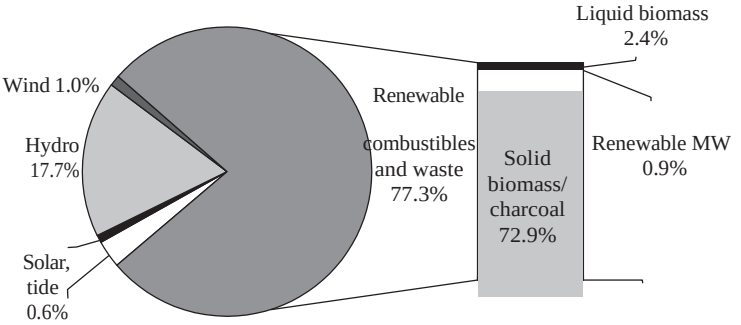




FIGURE 4.5

The 2007 product shares in world renewable energy supply (within the 12.4% in Figure 4.4). (From International Energy Agency, Renewables information 2009 with 2008 data, 2009. Available at www.iadb.org/intal/intalcdi/ PE/2009/03711.pdf, Accessed on December 5, 2013.)

www.Ebook777.com

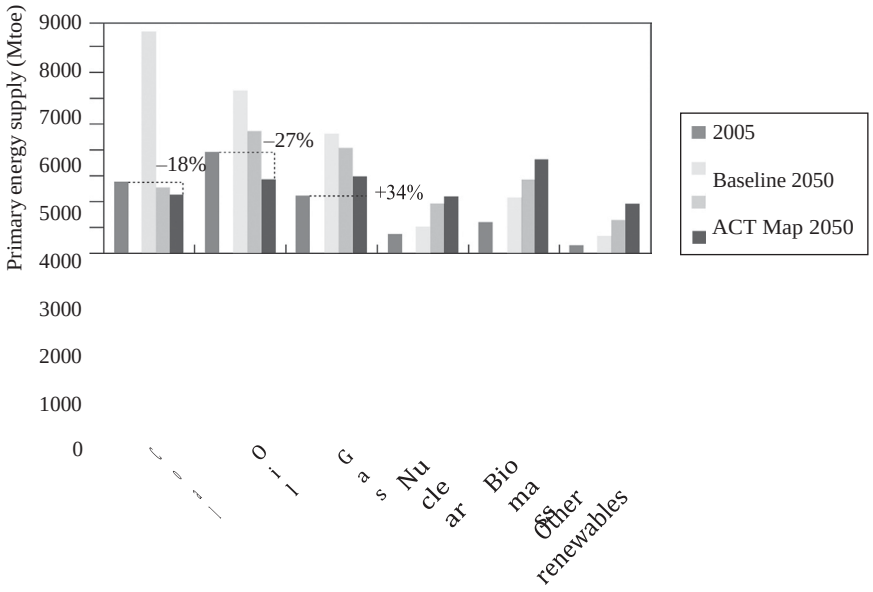


FIGURE 4.6

Comparison of world primary energy supply for year 2005 with values for 2050 using the baseline, ACT map, and BLUE map projections. (Reprinted from IEA, Energy technology perspectives 2008: Scenarios and strate- gies to 2050, International Energy Agency Report, Paris, France, 2008b.)

The IEA (2008b) recently compared energy resource types, conversion technologies, and associated policies based on three scenarios (used in Figure 4.6) scaled to the year 2050: (1) the ACT map scenario of the IEA, which implies adoption of a *wide range of technologies* with marginal costs of up to USD 50/ton of CO_2 saved when fully commercialized; (2) the BLUE map scenario, which requires deployment of *all technologies* involving costs of up to USD 200/ton of CO_2 saved when fully commercialized; and (3) the baseline scenario, which reflects developments likely to occur with energy and climate policies implemented to date. While the ACT scenarios are demanding, the BLUE scenarios depend on rapid implementation of unprecedented and far-reaching new policies in the energy sector (IEA, 2008b), which will take more time and effort to implement than the ACT scenarios.

From the data in Figure 4.6, coal appears to be the least favorable fuel for the future owing to its CO_2 emissions based on existing commercial-level combustion technologies, which mostly generate electricity. But this trend will change when coal is used for pro- ducing hydrogen (Gnanapragasam et al., 2009b), since the downstream processes enable easier capture of CO_2 and, when combined with biomass, can also help in reducing overall CO_2 emissions. Biomass has tremendous potential (as seen from Figure 4.6) for delivering more energy than coal and other resources by 2050 when the BLUE map is implemented effectively. Thus, it appears to be promising to use biomass for hydrogen production along with high-energy-intensity fuels such as coal.

Industrial inorganic solid wastes such as scrap tires (Stringfellow and Beaumant, 2008) and plastics (Aznar et al., 2006) are also being considered as *alternative* fuels through effective gasification processes. The supply and utilization of other solid fuels are discussed in detail elsewhere (IEA, 2006, 2007, 2008c; Asif and Muneer, 2007).

4.1.2 Issues Associated with Solid Fuels

Solid fuels contain carbon and their use in producing hydrogen results in emissions of CO_2, which is currently the most significant greenhouse gas and to which increasing temperatures in the lower atmosphere are attributed (USEPA, 2008). The carbon from solid fossil fuels (shown in Figure 4.2) is of higher concern and requires measures to capture and store underground. Due to the recent necessity to curb CO_2 emissions, combustion processes are becoming of decreasing interest to the energy sector (IPCC, 2008). One option to avoid CO_2

emissions is the use of renewables, but renewable energy sources that can provide base-load electricity—hydro, biomass, and geothermal—together are not anticipated to be able to satisfy even existing electricity demands and are not climate-neutral when operating continuously (Moriarty and Honnery, 2007). Another possible option, coal gasification with carbon capture and sequestration/storage (CCS), entails large energy and cost penalties using commercially proven methods of CO_2 separation (Muradov and Veziroglu, 2008).

In an effort to demonstrate the potential of CO_2-free coal-based power generation, a company in Germany has commissioned and is operating a power plant incorporating a complete CO_2 capture and sequestration facility (Harrabin, 2008). CO_2 capture and separation for gasification (Pennline et al., 2008) involves novel concepts in wet scrubbing with physical sorption, chemical sorption with solid sorbents, and separation by membranes.

Energy crops such as biomass resources are a risk for a sustainable future, since the carbon debt arising from land-use changes can take many years, even centuries, to pay back by using the biomass produced to displace fossil fuels (Fargione et al., 2008). Producing biomass for energy purposes at the expense of either food or fiber supplies, or by increasing deforestation, is of little global benefit (IEA, 2008b).

Other issues regarding solid fuels such as washing, drying, ash removal, and solid pollutant removal are well understood and managed in existing solid fuel–based energy systems and are discussed further elsewhere (de Souza-Santos, 2004; Rezaiyan and Cheremisinoff, 2005; Higman and Burgt, 2008).

4.2 Utility Processes

Utility processes are those that involve preparing solid fuels for actual energy conversion processes where hydrogen production begins in gaseous or liquid forms.

4.2.1 Upstream Processes

Upstream processes (in Figure 4.1) involve cleaning, blending, and upgrading solid fuels to enhance the quality of feedstock, thus improving the efficiency of various downstream conversion processes (CanmetENERGY, 2005) and also simplifying the separation of pollutants associated with solid fuels (NEDO, 2004). Some of the upstream cleaning processes that are in use in Japan and other larger importers of coal include (1) using a cartridge system, where all solid feedstocks are blended to form a uniform mixture containing a standardized composition; (2) treating the feedstock with solvents to clean the fuel of unusable residue; (3) blending of high-sulfur, high-grade coals with low-sulfur, low-grade coals and high-ash biomass (to avoid sintering); and (4) upgrading low-grade solid fuels with pretreatment using heavy oils (NEDO, 2004). These upstream processes likely will eventually be part of every energy conversion facility in the world, due to the long-term environmental and economic benefits and the desire of governments to implement energy efficiency policies (Eldridge et al., 2009) for improving the sustainability of operating existing and future energy systems.

4.2.2 Fuel Handling and Air Separation Unit

Solid fuels arriving at energy transfer plants need temporary storage, drying, crushing/milling, and internal transportation mechanisms. The handling of solid fuels consumes

some energy with operation and maintenance costs and is vital to the functioning of systems that produce hydrogen using energy from solid fuels. Due to their availability and widespread use (de Souza-Santos, 2004), solid fuel handling is mature and is not discussed in detail here. Commercially, ProcessBarron (www.processbarron.com) is one of several private companies that specializes in design, manufacture, and commissioning of integrated solid fuel handling equipment for a given energy conversion system.

The nature of integration of such fuel handling equipment within the system should entail limited wastes in all forms (energy, material, and cost). For example, storing the right type of fuel in a feasible environment reduces energy requirements for drying and transportation. Using waste heat from various processes within the system, to dry high-moisture feedstocks before crushing, increases the specific energy output of the fuel and overall system energy efficiency.

Air separation (Kerry, 2006) is crucial to enable both oxyfuel combustion and oxyfuel gasification processes that result in gaseous CO_2 only at the exhaust (after hydrogen separation). This makes the CO_2 underground storage much easier by compressing only CO_2. Removing N_2 from air also increases the residence time of high-temperature synthetic gas (syngas) within the gasifier. When N_2 is not removed from air, the high nitrogen con- tent in the gasifier yields syngas with a low heating value, 4–6 MJ/Nm^3 based on HHV (McKendry, 2002). Oxygen and steam gasification on the other hand may produce a gas with a medium heating value, 10–18 MJ/Nm^3 based on HHV (Hofbauer et al., 2003).

Air separation units (ASUs) consume a considerable amount of electric power, up to 10% of that for the entire system, especially in larger systems using cryogenic separation (Li, 2007), thus requiring a careful assessment of the need for only high-quality processes (Kerry, 2006). Membrane-based gas separation units (ion transport membranes [ITMs]) have been proven to be cheaper to install than cryogenic-based air separation by about 8% (Stiegel, 1999), and they also consume less power and are likely to prevail in most hydrogen-producing systems in the future.

4.2.3 Steam and Electricity: Pressurized Fluidized Bed Combustion

Circulating fluidized bed (CFB) combustors operating at atmospheric pressure are commercially established globally, that is, more than 400 power units are in operation around the world (Kavidass et al., 2000), with approximately 3000 operating CFB boilers in China alone (Yue et al., 2009). Fluidized beds are particularly suited to the combustion of low-quality coals, and most existing circulating fluidized bed combustion/combustor (CFBC) plants burn such materials along with biomass in cofiring mode. Moving to supercritical cycles is a logical step for very large CFB units (IEA, 2008b). A 460 MW supercritical unit is under construction at Lagisza, Poland, with start-up anticipated in 2009. This unit is expected to have a thermal efficiency of 70%. CFB combustor-based power plants using oxygen instead of air (known as oxy fuel combustion) are advantageous for CO_2 capture (Anthony, 2008; Manovic et al., 2008). There are hundreds of atmospheric CFB combustors operating world- wide, including a number of plants as large as 250–300 MW. Designs for larger supercritical CFBC units (600 MW capacity) are being developed (IEA, 2008b) with still higher efficiencies. Any system that produces hydrogen involves processes that need high-quality steam and electricity, which may be produced on-site with a pressurized fluidized bed combustion unit. This process is of particular interest when considering the energy, environment, and economic benefits through integration and was devel- oped by the US Department of Energy and industry partners (Weinstein and Travers, 2002). The process is still under development but is moving into demonstration

Free ebooks ==> www.Ebook777.com

and commercial stages owing to its small- and medium-scale capacities and higher operating efficiencies, above 70% (IEA, 2008b).

Pressurized fluidized bed combustion is employed at high pressures in combined cycles, with the boiler exhaust gases routed to generate additional power through heat recovered from the gas turbine exhaust. The combined gas and steam cycle achieves efficiencies up to approximately 44% (DOE, 2007). The first of such units had a capacity of about 80 MW, but two larger units are operating in Karita and Osaki, Japan, the former using supercritical steam (IEA, 2008b).

Incorporating advanced pressurized fluidized bed combustion/combustor (PFBC), with a thermal efficiency exceeding 70%, would enhance the use of nongasifiable solid feedstock, such as certain types of biomass, which then may be cofired with coal in the advanced PFBC to produce process steam and electricity.

4.3 Energy Conversion Processes

Much research on converting solid fuels to hydrogen is in early stages, but developments are expected to accelerate in the near future as the demand for hydrogen increases in various applications. Recent research into processes for converting solid fuels to gaseous forms indicates that such processes have a significant potential for commercialization and should be able to achieve industrial-scale production levels (Gnanapragasam et al., 2010).

Hydrogen derived from coal is slated to be the primary objective in the fuel program of the US Department of Energy (Lior, 2008), and research is ongoing to develop modules for coproducing hydrogen from coal via systems integrated with advanced coal power plants at prices competitive with crude oil (DOE, 2007).

Primary conversion processes in producing hydrogen from solid fuels include direct processes such as gasification, anaerobic digestion, fermentation, and liquefaction (Chmielniak and Sciazko, 2003). There are also direct chemical looping (DCL) processes such as the iron oxide cycle and indirect thermochemical cycles based on copper–chloride and sulfur–iodine. Some of these processes (copper–chloride and sulfur–iodine cycles) are undergoing exten- sive research for commercial development and implementation (IEA, 2008b) and thus are not discussed here. The process diagrams in this chapter are wherever possible self-explanatory. Coal, biomass, solid wastes, and oil sand coke (Furimsky, 1998) are potential gasifica- tion fuels for syngas production and methanol synthesis (Chmielniak and Sciazko, 2003). Applications of these processes depend on feedstock characteristics, volume of produc- tion, and postconversion processes to manage wastes and by-products (Higman and Burgt, 2008). A review of decarbonization processes for fossil fuels ranging from natural gas to coal (Muradov and Veziroglu, 2008) has identified the commercial potential of new technologies, which suggests various uses for solid carbon after CO_2 sequestration.

The average energy and exergy conversion efficiencies of syngas from solid fuel gasification (76% and 75%, respectively) are found to be higher than those for hydrogen (64% and 55%) production from gasification (Bargigli et al., 2004). However, coal-to-syngas conversion generates a significant amount of solid waste, and the material intensity is much higher for syngas than for natural gas and hydrogen (21 and 39 g/g, respectively), indicating a higher load on the environment that should be dealt with carefully.

Technoeconomic comparisons of hydrogen production via steam–CH_4 reforming (SMR), coal and biomass gasification, and water electrolysis have been reported (Langer et al., 2007).

www.Ebook777.com

Increases in natural gas prices are observed to make coal gasification as well as biomass gasification competitive, provided its technological barriers are overcome (including feedstock processing and postconversion of products). A comparison of electricity and hydrogen production processes, from coal and natural gas with CO_2 capture, for various technologies and for large-scale and decentralized systems (Damen et al., 2006, 2007), demonstrated that a short-term net power efficiency of 32%–40% is achieved by an integrated gasification combined cycle (IGCC) system with production costs of 4.7–6.3 €ct/kWh.

Coal gasification forms the central element of IGCC systems and has the greatest fuel flexibility of advanced technologies for power generation (Beer, 2007). Current commercial gasification technologies are also well adapted to using biomass and other low-value feedstocks that have high ash residues (Liu and Niksa, 2004). Gasification also permits the control and reduction of gaseous pollutant emissions (Trapp, 2005) and a possible low- cost approach to concentrate CO_2 emissions at high pressure to facilitate underground sequestration.

4.3.1 Gasification

Presently, gasification is the only commercial, large-scale option for converting solids to gases (Rezaiyan and Cheremisinoff, 2005) and one of the cleanest conversion technologies for solid fuels. Academic and industrial research has improved production capabilities and operating efficiencies in recent years. The gasification of carbonaceous, hydrogen-contain- ing fuels is an effective method for thermal hydrogen production (Stiegel and Ramezan, 2006) and is considered a key technology in the transition to a hydrogen economy (Collot, 2006). Gasification converts solid fuels into a syngas comprised mainly of CO, CO_2, H_2, CH_4, H_2O, and other constituents in minor concentrations (Higman and Burgt, 2008). Syngas pro- duction offers the possibility of obtaining multiple products that can be used for different applications. Gasification has the highest energy conversion efficiency relative to other solid fuel conversion technologies (Beer, 2000). One particular version of a commercial gasifica- tion process is shown in Figure 4.7, as an example of the initial stage of solid fuel conversion. Producing hydrogen from syngas is a significant step in the clean coal technology road- map as realized by many countries including Canada (CanmetENERGY, 2005), Japan (NEDO, 2004), and the United States (DEO, 2002). Gasification carries great significance for coal and dry biomass, while for wet biomass and sewage, other conversion processes such as anaerobic digestion and supercritical water gasification (SCWG), respectively, appear advantageous due to the higher moisture content in the feedstock (Mozaffarian et al., 2004). The British Gas–Lurgi (BGL) gasifier shown in Figure 4.7 is a countercurrent, moving- bed, slagging gasifier operating at pressures of 25 bar or higher (NETL, 2000). The reactor vessel is water cooled and refractory lined. The coal and/or biomass mixture is fed into the top of the gasifier via a lock-hopper system and reacts while moving downward through the gasifier. The coal's ash/mineral matter is removed from the bottom of the gasifier as molten slag through a slag tap, then quenched in water, and removed. Steam and oxygen are injected through tuyere nozzles near the base of the gasifier and react with the coal as the gases move up. This countercurrent action results in a wide temperature difference between the top and the bottom of the gasifier. After gas conversion, the ash and unconverted char from coal/biomass end up as slag and get collected at the bottom of slag lock after cooling. The typical operating temperature for this type of gasifier is from 600°C to 1900°C (Higman and Burgt, 2008). The gasifier can be characterized due to this tempera- ture profile as being divided into drying, devolatilization, gasification, and combustion zones from top to bottom, respectively.

Free ebooks ==> www.Ebook777.com

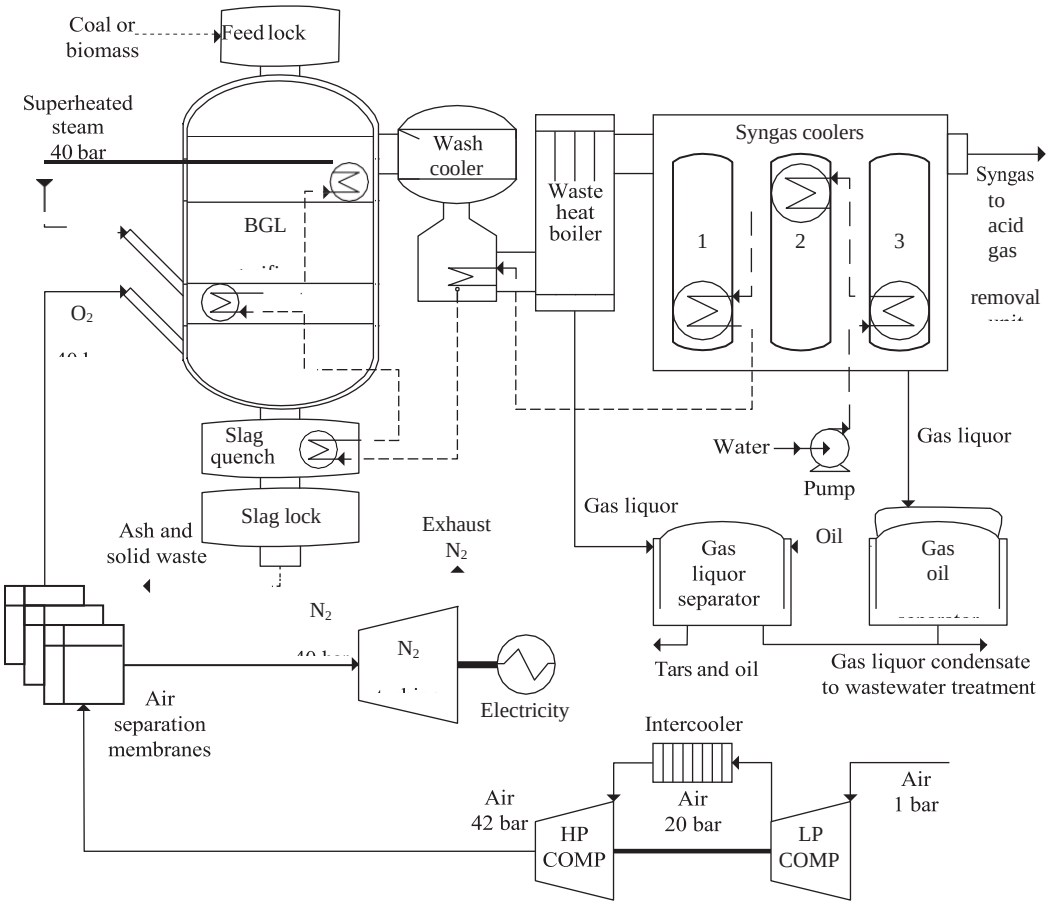


FIGURE 4.7

Industrial-scale gasification process with BGL downdraft gasifier. (Adapted from DOE, Gasification: Reference shelf—System studies, National Energy Technology Laboratory, U.S. Department of Energy, Washington, DC, accessible at: http://www.netl.doe.gov/technologies/coalpower/gasification/pubs/system-studies.html, 2000.)

Experimental and modeling investigations of long-stick wood gasification in a top-lit updraft fixed-bed gasifier describe common problems of many gasifier designs (Saravanakumar et al., 2007). They produce so much tar that the gas cleanup equipment cost is several times the gasifier cost. Fluidized beds typically produce 0.5%–4% tars, while updraft biomass gasifiers produce 10% tars. Both stratified downdraft and top-lit updraft gas- ifiers produce much lower tar levels, typically 0.1%. For the gasifier, the top-lit updraft mode is found to provide more satisfactory overall performance (NETL, 2000); the BGL gasifier (Figure 4.7) belongs to this category.

4.3.1.1 Gasification Process Design

The two combustion-related factors of greatest impact on gasifier design and operation have been reported to be (1) fuel reactivity and (2) slag flow as it runs down the refractory walls and out of the bottom of the reactor under gravity (Wall, 2007). A gasification product gas with tar content below the targeted limit of 2 g/m^{3}can be achieved only under special conditions in terms of gasifier design and operation as well as feedstock characteristics (Corella et al., 2006).

www.Ebook777.com

The main chemical reactions that occur inside the gasifier with appropriate energy conditions (Ptasinski et al., 2007; Mountouris et al., 2008) are as follows:

Exothermic combustion reaction:

$$C + O_2 \rightarrow CO_2; \quad \Delta H = -393.5 \text{ kJ/mol} \tag{4.1}$$

Endothermic Boudouard equilibrium process:

$$C + CO_2 \rightarrow 2CO; \quad \Delta H = 172.6 \text{ kJ/mol} \tag{4.2}$$

Endothermic heterogeneous water–gas shift (WGS) reaction:

$$C + H_2O_{(g)} \rightarrow CO + H_2; \quad \Delta H = 131.4 \text{ kJ/mol} \tag{4.3}$$

Exothermic hydrogenation gasification:

$$C + 2H_2 \rightarrow 2CH_4; \quad \Delta H = -74.9 \text{ kJ/mol} \tag{4.4}$$

After formation, these gases tend to react based on local temperature and pressure gradients and nonequilibrium conditions. Depending on the amount of steam available, the following reactions may occur within the gasifier and in the WGS reactors in the H_2 system:
Endothermic CH_4 decomposition:

$$CH_4 + H_2O \rightarrow CO + 3H_2; \quad \Delta H = 206.12 \text{ kJ/mol} \tag{4.5}$$

Exothermic WGS reaction:

$$CO + H_2O \rightarrow CO_2 + H_2; \quad \Delta H = -41.2 \text{ kJ/mol} \tag{4.6}$$

At high gasifier temperatures, the sulfur in coal reacts with CH_4 and steam to form H_2S in a two-step process (Patnaik, 2002) as shown in the following discussion; this is removed using stages of separation processes, the descriptions for which can be found in the literature (Garcia et al., 2006):

$$CH_4 + 2S \rightarrow CS_2 + 2H_2 \tag{4.7}$$

$$CS_2 + 2H_2O \rightarrow 2H_2S + CO_2 \tag{4.8}$$

The overall reaction in the gasifier, considering the use of CO_2 as a coal carrier gas and using oxygen instead of air for gasification, may be represented as

$$\underbrace{\dot{n}_{coal}(y_C C + y_{H_2}H_2 + y_{N_2}N_2 + y_{O_2}O_2 + y_S S + y_{ash})}_{\text{coal}} + \dot{n}_{O_2}O_2 + \dot{n}_{CO_2}CO_2 + \underbrace{\dot{n}_{st}(H_2O)}_{\text{steam}} \rightarrow$$

$$\dot{n}_{syn}(y_{CO}\ CO_2 + y_{CO}CO + y_{pH_2}\ H_2 + y_{CH}\ CH_4 + y_{H\ O}H_2O + y_{pN}\ N_2) + \dot{n}_{H\ S}H_2S + \dot{n}_{ash} \quad (4.9)$$

Syngas

where

y is the molar fraction
n is the molar flow rate
p denotes the product

4.3.1.2 Gasifier Process Optimization

An assessment of the performance of a gasifier operating without air preheating and using a higher-moisture-content fuel (over 10% moisture by weight) demonstrates the benefits of high-temperature air preheat (Young and Pian, 2003). Performance was observed to improve minimally by drying a manure–waste fuel to below 10% moisture. An investigation of the selection of IGCC candidate coals using a pilot-scale gasifier operation showed that high-ash coal (about 17% by weight) yields less than 60% cold-gas efficiency (Yun et al., 2007). To improve the efficiency for such low-reactivity coal, it is suggested that the gasifier design should permit increased reaction time and the option of char recycling and that methods of inducing higher mixing of coal powder with reacting gases be considered. Since all types of coal can be gasified, gasification appears promising for the production of hydrogen from coal. Gasification plants are also advantageous, compared to other coal-based alternatives, for CO_2 capture (Collot, 2006) as mentioned earlier.

An optimization of catalytic steam gasification of biomass at low temperatures for hydrogen production suggests that higher temperatures and steam flow rates increase syngas yield (Moghtaderi, 2007). At 600°C and high steam content (about 90%), hydrogen production can be optimized with the help of a catalyst when using biomass. The status of catalytic gasification of biomass, similarities and differences between dry and wet processes, and challenges for future research and development from both catalysis and process viewpoints have been discussed (van Rossum et al., 2008).

The influences on hydrogen production of gasifier operating temperature, pressure and coal type, and steam-to-carbon ratio that have been examined based on chemical equilibrium (Wang et al., 2006) suggest that the operating pressure in the gasifier be maintained at 20–30 bar for enhanced CO_2 partial pressure and capture efficiency. The appropriate gasifier temperature is between 625°C and 850°C, for which more than 70% hydrogen can be obtained with a production efficiency of 46.45%. The overall system also cogenerates hydrogen and power with near-zero emissions.

An energy analysis of the biomass gasifier showed (Mahishi and Goswami, 2007) that the optimum conditions for hydrogen production occurred at a gasification temperature of 1000 K, a steam–biomass ratio of 3 and an equivalence ratio of 0.1, achieving a 54% energy efficiency for the gasifier. A similar thermodynamic analysis (Gnanapragasam et al., 2009a) of the performance of a gasification process under varying steam-to-coal (S/C) and oxygen-to-coal (O/C) ratios in the gasifier yielded a range of syngas compositions as given in Table 4.1. These values are based on a Gibbs free energy minimization equilib- rium model for the gasifier when using anthracite coal with an HHV of 32.85 MJ. From Table 4.1, it is evident that, when 80% S/C and 70% O/C are used, the hydrogen produced is the highest (37 vol.%) and that the remaining CO will be converted to hydrogen and CO_2 during the WGS reaction stage. The amount of CO_2 emission is directly proportional to the carbon in the feedstock.

4.3.1.3 Fluidized Bed Gasifier

A novel fluidized bed gasifier fitted with water-cooled sampling probes for measuring the axial gas concentrations at various gasifier heights has been reported (Ross et al., 2007). Three distinct zones are observed in the gasifier. In the first zone (the bottom third of the distance from the distributor), with a temperature below 950°C, char combustion and gasification reactions dominate. In the second zone, with a temperature between 800°C and 900°C, the devolatilization products from the biomass combine with the char

Free ebooks ==> www.Ebook777.com

TABLE 4.1

Simulated Syngas Volumetric Composition

(without Nitrogen) for Four S/C Inlet Ratios and Five O/C Inlet Ratios, Considering an Anthracite Feedstock When Gasifier Operates at 20 bar, 1173 K

	Syngas Composition (Volume Fraction)							
S/C (%)	**20**	**40**	**60**	**80**	**40**	**40**	**40**	**40**
O/C (%)	**70**	**70**	**70**	**70**	**60**	**80**	**90**	**100**
H_2	0.19	0.31	0.35	0.37	0.25	0.31	0.28	0.24
CO	0.74	0.61	0.52	0.46	0.63	0.6	0.59	0.58
CO_2	0	0.05	0.09	0.12	0.04	0.06	0.09	0.12
CH_4	0.07	0.03	0.02	0.01	0.08	0	0	0
H_2O (g)	0	0.01	0.03	0.04	0.01	0.02	0.04	0.05

Source: Adapted from Gnanapragasam, N.V. et al., *Energy Conserv. Manage.*, 50, 1915, 2009a.

gasification reactions. The third zone is the freeboard with a temperature of 800°C and below, where variations in the main gas components occur due to the WGS reaction.

In the case of a fluidized bed gasifier, the fuel is gasified in a bed of small particles fluidized by a suitable gasification medium such as air or steam. The concern for climate change has increased the interest in biomass gasification for which fluidized bed gasifiers are particularly popular, occupying nearly 20% of the market (Basu, 2006). Fluidized bed gasifiers are divided into the following two major types: (1) bubbling and (2) circulating. Depending on the fuel and the application, the gasifier operates at a temperature within the range of 800°C–1000°C and at atmospheric and pressurized conditions. The hot gas from the gasifier passes through a cyclone, which separates most of the solid particles associated with the gas and returns them to the bottom of the gasifier for recirculation. An air preheater located below the cyclone raises the temperature of the gasification air and indirectly controls the temperature inside the gasifier.

4.3.1.4 Ultrasuperheated Steam Gasification

A new method for gasifying carbonaceous materials to syngas comprises the formation of an ultrasuperheated steam (USS) composition containing mainly water vapor, CO_2, and highly reactive free radicals (Lewis, 2007). The USS at temperatures ranging from 1316°C to 2760°C is a clear colorless flame; when it comes into contact with carbonaceous materials (feedstock), rapid gasification occurs to form a syngas. The syngas generated from USS gasification has a higher hydrogen fraction (more than 50%) than other gasification processes (Pei and Kulkarni, 2008). When used within an IGCC system, the overall efficiency is found to be lower, suggesting that USS gasification is more suitable for hydrogen production than power generation.

The USS gasifier is a long cylindrical reactor with a steel casing for the high-pressure (above 30 bar) operation and a ceramic lining (Lewis et al., 2002; Ryu, 2004) to resist the high temperatures of up to 2500°C. The pulverized coal or biomass is fed from the top into a pilot burner as shown in Figure 4.8, which initiates with some propane aided by synthetic air the high-temperature flame, which is a combination of 79% steam and 21% oxygen. The flame disintegrates hydrogen from steam, allowing the syngas to have a higher hydrogen fraction (more than 50%) than other gasification processes (shown in Table 4.1). The reactor

www.Ebook777.com

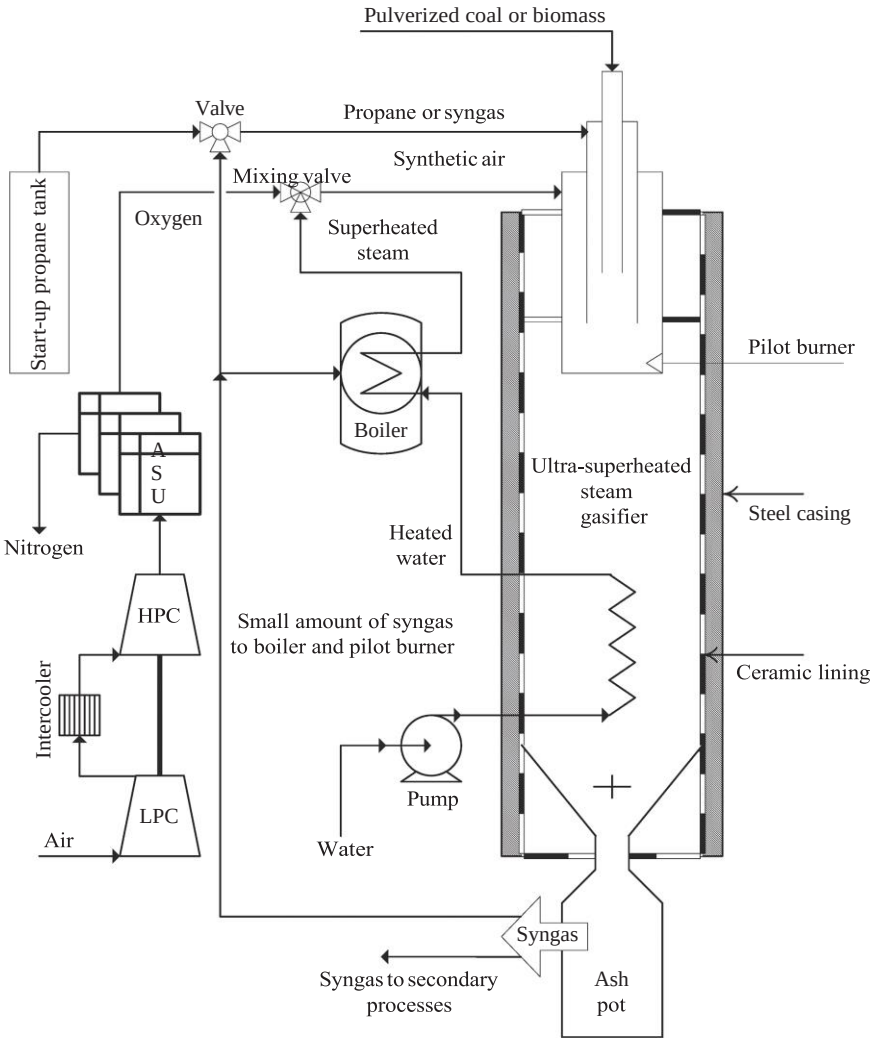


FIGURE 4.8

USS gasification. (Adapted from Lewis, F.M., Generation of an ultra-superheated steam composition and gasifi- cation therewith, US Patent No. US 7,229,483 B2, June 12, 2007.)

also generates a tremendous amount of heat, thus enabling self steam generation. The flame is maintained by using some portion of the syngas generated.

The ASU is mandatory for this type of gasifier, since the higher hydrogen percentage depends on the synthetic air composition; thus, oxygen becomes important for high-temperature combustion. This adds to the power requirement for the compressors unless membrane-based separation is used (Stiegel, 1999). The USS process is burner-based, not reaction-based, offering the end user a wide choice of reactor designs. There are no exothermic oxidization reactions within the reactor. Downstream of the USS steam envelope, gasification becomes a steam-only gasification and/or steam reforming process inherently

resistant to the production of tars (Sieger and Donovon, 2002). No ash slagging occurs despite very high temperatures (Ryu et al., 2004), which makes the USS process ideal for small-scale hydrogen production.

TABLE 4.2

Experimental Syngas Volumetric Composition for Four Test Cases Involving Two Different USS Compositions with Char and Coal

	Syngas Composition (Volume Fraction of Dry Gas)			
Test Cases	**Wood Char**		**Anthracite Coal**	
Fuel composition (%)	Moisture—1.6 Volatile matter—21.8 Fixed carbon—78.2 Ash—1.4		Moisture—0.9 Volatile matter—11.6 Fixed carbon—81.5 Ash—6.0	
Fuel feed rate (g/s)	2.5		4	
USS composition	**70% H_2O, 30% CO_2**	**80% H_2O, 20% CO_2**	**70% H_2O, 30% CO_2**	**80% H_2O, 20% CO_2**
H_2	0.323	0.37	0.321	0.367
CO	0.254	0.236	0.243	0.203
CO_2	0.4	0.373	0.409	0.402
CH_4	0.02	0.019	0.019	0.014

Source: Adapted from Ryu, C. et al., *J. Energy Inst.*, 77, 46, 2004.

Wood char with a lower higher heating value than that of anthracite (about 2–3 MJ/kg) still is able to produce about 37% hydrogen for about 63% of its weight compared to anthracite, as can be seen from Table 4.2 when USS composition is at 80% steam and 20% CO_2. The data in Table 4.2 are mainly for steam gasification since no oxygen is supplied, thus belonging to a second type of USS process with temperatures ranging from 300°C to 700°C. This particular USS process does not require an ASU, reducing the penalty on the overall energy efficiency.

4.3.1.5 Supercritical Water Gasification

This process is aimed at generating hydrogen from the biogenic feedstock sewage sludge (Gasafi et al., 2007; Li et al., 2009). The process exploits the specific physical and chemical properties of water above its critical point (T = 374°C, P = 221 bar). These properties allow for a nearly complete conversion of the organic substance contained in the feed mate- rial to an energy-rich fuel gas containing hydrogen, CO_2, and CH_4. The characteristics of SCWG are examined and compared to other energy conversion technologies by modeling an overall energy system (Yoshida et al., 2003). A SCWG combined cycle is determined to be the most efficient conversion process for biomass with high moisture content. The breakeven point between thermal gasification and SCWG is approximately 40% biomass moisture content.

Gas yields, carbon gasification efficiency, and the total gasification efficiency increase with increasing temperature and reaction time and decreasing feed concentration (Yamaguchi et al., 2009). Hydrogen yield increases from 7% mole fraction to over 30% for an increase of reaction temperature from 600°C to 800°C for the gasifier shown in Figure 4.9. Among the parameters varied, temperature and feed concentration are found to have the most significant effect on the SCWG reaction behaviors. Higher temperatures and lower feed concentrations favor coal utilization for hydrogen production, promoting the reforming reaction of CH_4 and CO (Lu et al., 2008). The SCWG of brown coal requires

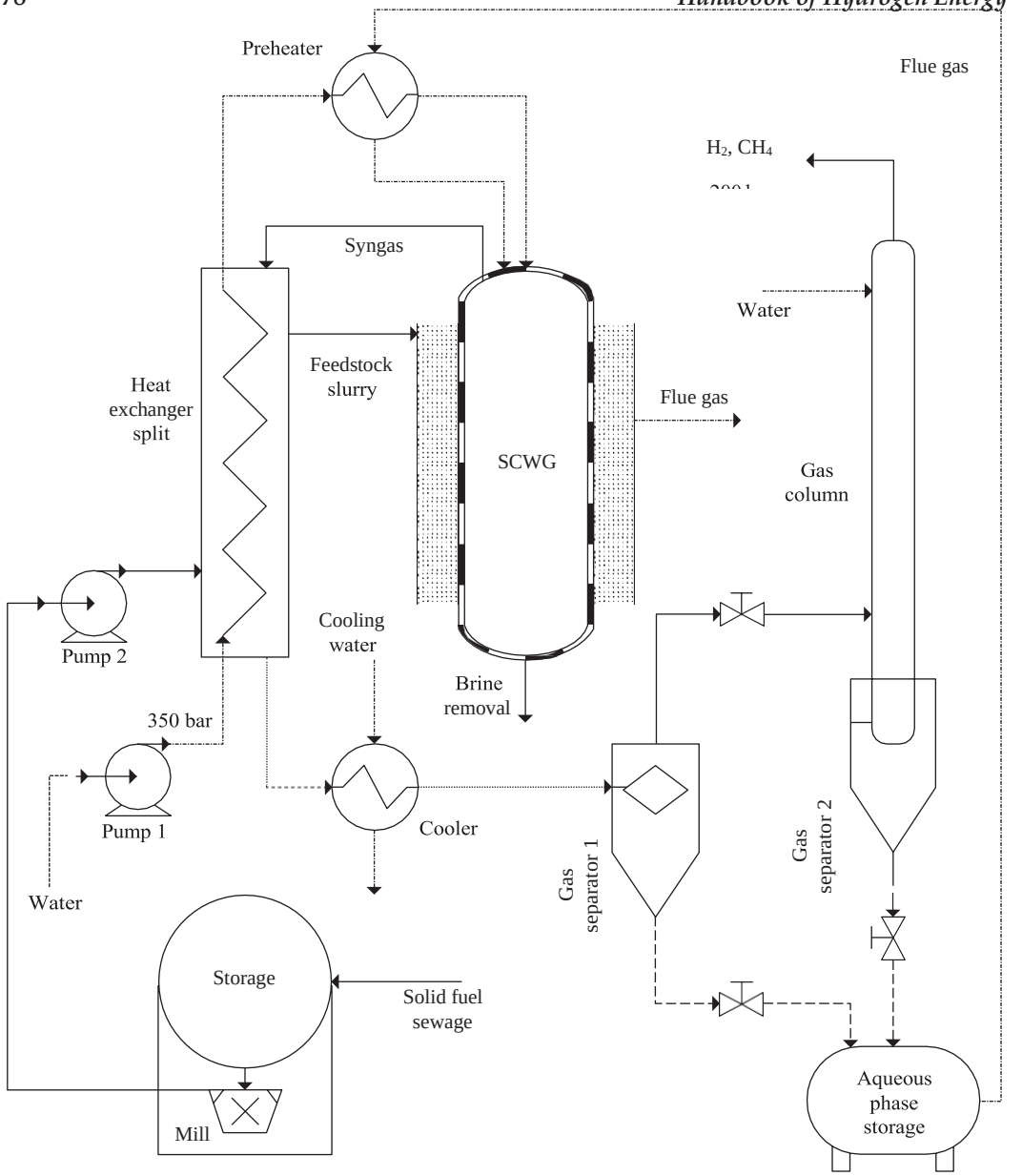


FIGURE 4.9

SCW gasification process. (Adapted from Gasafi, E. et al., *Int. J. Energy Res.*, 31, 346, 2007.)

a catalyst for achieving a high utilization efficiency that leads to a high hydrogen production closer to the theoretical limit.

To improve hydrogen production when using SCWG with biomass, an alkali, such as NaOH, KOH, Na_2CO_3, K_2CO_3, and $Ca(OH)_2$, is used as a catalyst or promoter. Of these, potassium carbonate (K_2CO_3) is found to catalyze gasification of the cellulose (in biomass) with the formation of more hydrogen and less CO (Guo et al., 2007). The activity of K_2CO_3 is higher than that of $Ca(OH)_2$ and K_2CO_3 cannot capture CO_2. A summary of the catalytic

mechanism of K_2CO_3 for biomass gasification in supercritical water (SCW) occurs as given in the following (Sinag et al., 2003):

$$K_2CO_3 + H_2O \rightarrow KHCO_3 + \quad (4.10)$$

$$KOH\ KOH + CO \rightarrow \quad (4.11)$$

$$HCOOK$$

$$HCOOK + H_2O \rightarrow KHCO_3 + H_2 \quad (4.12)$$

$$2KHCO_3 \rightarrow H_2O + K_2CO_3 + CO_2 \quad (4.13)$$

$$H_2O + CO \leftrightarrow HCOOH \leftrightarrow H_2 + CO_2 \quad (4.14)$$

More hydrogen was also obtained for cellulose gasification with the mixture of K_2CO_3 and $Ca(OH)_2$, and the CO_2 capture is enabled in this particular case. The processes within the SCWG system provide opportunities for waste energy integration, thus enabling a self-sustained process with feedstock delivering the corresponding product of syngas with a higher hydrogen fraction.

4.3.1.6 Plasma Gasification

Plasma gasification is another process for producing a hydrogen-rich syngas. The pro- cess has no limitation on feedstock characteristics and smaller requirements of air/oxygen and is a pyrolysis process becoming commercially popular in solid waste management facilities around the world (especially in Canada, Europe, Japan, and the United States). It is mostly used for efficient and clean disposal of municipal solid wastes and garbage (Carabin and Gagnon, 2007). When coal is gasified in a steam and air environment under arc plasma conditions, hydrogen production is enhanced (Galvita et al., 2007). The steam environment is estimated to increase syngas output by 30%–40% for plasma gasification compared to an air environment.

Efforts on process development and energy optimization for plasma gasification of sewage sludge have suggested (Mountouris et al., 2006) that a moisture content (w/w) of about 0.4 produces maximum hydrogen with lower CO, for 0.3 mol/mol of dry waste at a temperature of 1273 K. But at lower moisture content (about 0.1) for almost the same amount of hydrogen produced, an equal amount of CO is also produced, thus enabling higher overall hydrogen production, through the WGS process. Sewage treatment using plasma gasification indicates (Mountouris et al., 2008) that integration of predrying and electri- cal energy production processes (or hydrogen) not only is self-sufficient from an energy point of view but leads to the availability of additional electrical energy for distribution. The primary roadblock to performance of plasma gasification is the amount of moisture in the feedstock, and the sensitivity is shown in Table 4.3. Correlating with the data from Mountouris et al. (2006), the moisture content of feedstock is not critical for hydrogen production although it is for electricity generation, as seen from the data in Table 4.3. The equilibrium model based on plasma gasification demonstrates that an input of 250 tons/day of sewage sludge with 68% moisture yields a net electric power output of 2.85 MW.

From an energy viewpoint, the ratio of power available for material treatment (after all power losses are subtracted from the arc power) to the total arc power (as shown in

Free ebooks ==> www.Ebook777.com

TABLE 4.3

Effect of Feed Moisture Content on Required Oxygen Amount, Energy Values, and Quality of Synthesis Gas

Moisture Content (% w/w)	Oxygen (mol/mol)	Net Thermal (MW)	Net Electrical (MW)	Syngas Heating Value (kWh/Nm^3)
Zero gasification energy (when the energy for gasification is self-sustained)				
5.2	0.53	−1.07	4.17	1.12
10.23	0.55	−0.92	4.04	1.03
14.68	0.57	−0.77	3.90	0.96
20.50	0.60	−0.54	3.71	0.86
27.04	0.64	−0.25	3.45	0.74
29.88	0.66	−0.10	3.33	0.69
34.92	0.70	0.19	3.07	0.60
Zero net thermal energy (when net thermal energy is self-sustained)				
Moisture Content (% w/w)	**Oxygen (mol/mol)**	**Gasification Energy (MW)**	**Net Electrical (MW)**	**Syngas Heating Value (kWh/Nm^3)**
14.68	0.213	−3.92	2.12	2.14
20.50	0.348	−2.77	2.45	1.52
27.04	0.535	−1.18	2.90	0.95
29.88	0.613	−0.52	3.09	0.78

Source: Adapted from Mountouris, A. et al., *Energy Convers. Manage.*, 49, 2264, 2008.

Figure 4.10) increased with increasing arc power from 0.35–0.41 at arc power 95–100 kW to 0.41–0.46 for arc power higher than 130 kW for wall temperatures of 1100°C–1200°C. The ratio is lower for higher wall temperatures (Van Oost et al., 2009).

Plasma gasification above 1300 K when using biomass appears to produce higher fractions of hydrogen in syngas (Van Oost et al., 2009) than at 800 K, ranging from 28% to 46% by volume. Due to their high costs, plasma systems have been used primarily for the vitrification of high-toxicity waste and mainly at the pilot scale (Moustakas et al., 2008).

As these systems become more accepted and their designs simpler, their use will likely be more extensive. Plasma gas used in gasifiers for vitrification also belongs to this category and can result in a significant waste reduction volume, ranging from about 5:1 for ash input to maximum 50:1 for solid waste (Minutillo et al., 2009). A better solution can be achieved using air as the plasma gas and adding oxygen to sustain the waste gasification. Then, the plasma gasification efficiency is 69%.

4.3.2 Anaerobic Digestion

Anaerobic digestion is similar to SCWG for producing syngas and substitute natural gas (SNG) by converting wet biomass with moisture of about 70–95 wt.% (Mozaffarian et al., 2004). Anaerobic digestion is a biological process that occurs in the absence of air and has been used to convert organic wastes to biogas, that is, a mixture of CH_4 (55–75 vol.%) and CO_2 (25–45 vol.%). During anaerobic digestion, typically 30%–60% of the solid input is converted to biogas. The by-products consist of an undigested residue and various water-soluble substances that may act as nutrients for algae growth and other biodigesters. Depending on the digestion system (wet or dry), the average residence time is between 10 days and 4 weeks. The anaerobic digestion of biomass and organic waste streams has the potential to facilitate energy recovery and sustainability from biodegradable waste (Duerr et al., 2007). With current developments in reformer technologies, hydrogen can be

www.Ebook777.com

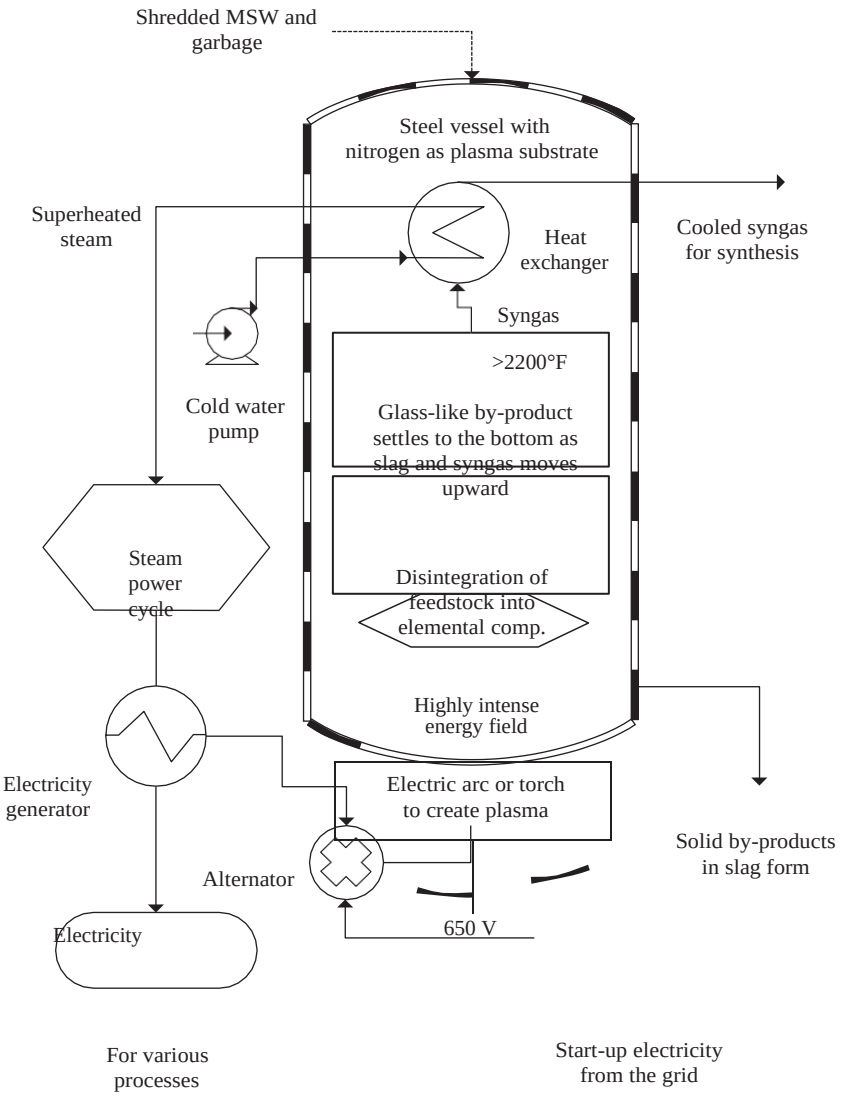


FIGURE 4.10

Plasma gasification process. (Adapted from Mountouris, A. et al., *Energy Convers. Manage*., 49, 2264, 2008.)

produced from CH_4-derived anaerobic digestion of organic waste material, much of which is currently landfilled through autothermal reforming (ATR).

Factors affecting anaerobic digestion operation and performance of such system as shown in Figure 4.11 include physical composition of the manure, manure type and manure collection method, and frequency of feeding the digester, along with suit- able conditions for bacteria growth, for biogas energy production (Brown et al., 2007). Anaerobic bacteria grows and performs best under optimal temperatures in the range of 951°F–1051°F, which has an optimal retention time range of 10–30 days and an optimal pH range of 7–8.5.

The production of biogas through anaerobic digestion offers significant advantages over

other waste treatment processes (Ward et al., 2008), including the following:

- Production of less biomass sludge compared to aerobic treatment technologies.
- Success in treating wet wastes of less than 40% dry matter.

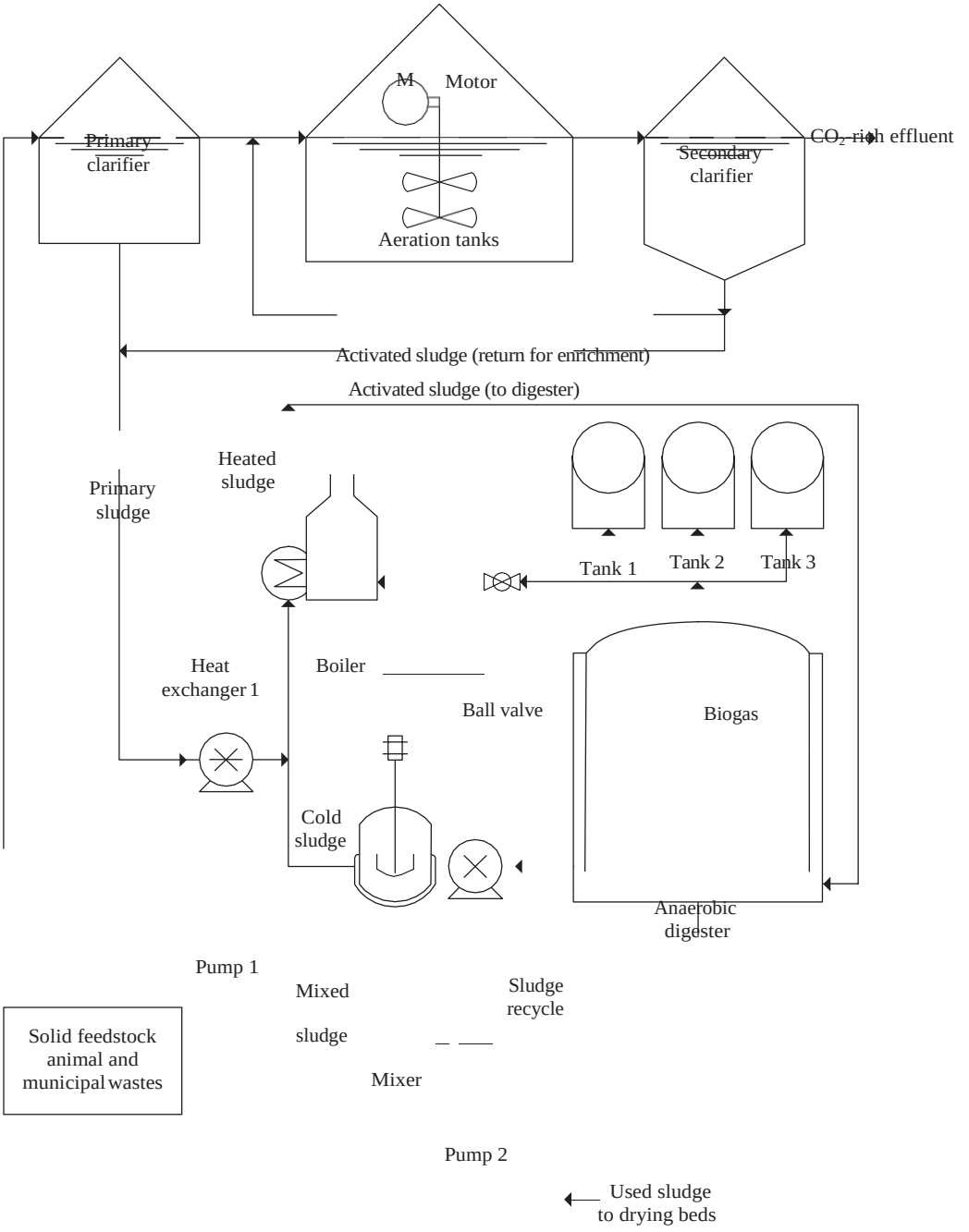


FIGURE 4.11

Anaerobic digestion system and processes. (Adapted from Goodman, B.L., Stabilization: Anaerobic digestion, chapter 7, in *Environmental Engineer's Handbook*, CRC Press/Taylor & Francis Group, LLC, Boca Raton, FL, 1999.)

- More effective pathogen removal. This is especially true for multistage digesters or if a pasteurization step is included in the process.
- Minimal odor emissions, as 99% of volatile compounds are oxidatively decom- posed upon combustion, for example, H_2S forms SO_2.
- A high degree of compliance with many national waste strategies, implemented to reduce the amount of biodegradable waste entering landfills.
- A slurry is produced (digestate), which is an improved fertilizer in terms of both its availability to plants and its rheology.
- A source of carbon-neutral energy in the form of biogas.

There are four important biological and chemical stages of anaerobic digestion (Gerardi, 2003):

- Hydrolysis: A chemical reaction where particulates are solubilized and large poly- mers converted into simpler monomers, when one or more water molecules are split into hydrogen and hydroxide ions.
- Acidogenesis: A biological reaction where simple monomers are converted into volatile fatty acids.
- Acetogenesis: A biological reaction where volatile fatty acids are converted into acetic acid, CO_2, and hydrogen. The acetate is produced by anaerobic bacteria from a variety of energy sources such as hydrogen and carbon.
- Methanogenesis: A biological reaction where acetates are converted into CH_4 and CO_2, while hydrogen is consumed by the formation of CH_4 by microbes known as methanogens.

The material drawn from the anaerobic digester is called sludge or effluent. It is rich in nutrients (ammonia, phosphorus, potassium, and more than a dozen trace elements) and is an excellent soil conditioner and feed for algae growth (Goodman, 1999). Digester sizing and process details are available elsewhere (Goodman, 1999; Gerardi, 2003; Pandey, 2004).

4.3.3 Chemical Looping Processes

Chemical looping combustion (CLC), developed in the mid-1990s, uses metallic oxide as an oxygen carrier for combustion (Ishida and Jin, 1995). The fuel, mostly gases similar in composition to syngas, reduces the metal oxide to the corresponding metal at low temperature in the first reactor. In a second reactor, the metal is oxidized using oxygen in moistened air at high temperature to form the metal oxide, which is recycled to the first reactor. Hydrogen is produced from water in the second reactor. During the reaction in the first reactor, the oxygen in the metal is transferred to the carbon in the fuel forming CO_2 and water (Yu et al., 2003; Jin and Ishida, 2004; Fan et al., 2008). The water is condensed to separate CO_2 and send it to storage. This process exhibits a greater potential for CO_2 separation compared to membrane separation of CO_2.

Experimentation and process modeling and simulation suggest that a maximum coal-to-hydrogen conversion efficiency of 80% can be achieved using coal DCL (Fan et al., 2008; Gnanapragasam et al., 2009b). Some problems with this process include temperature issues relating to metal oxide (very high temperatures destabilize the structure) and sizing the reactor to control reaction rates (Fan et al., 2008).

Exergy analysis allows meaningful efficiencies and losses to be evaluated for energy systems and corresponding design improvements to be identified (Dincer and Rosen, 2007). Such an analysis suggests that the net power efficiency of a power generation system incorporating CLC exceeds that of a conventional power system by reducing combustion irreversibilities (Anheden and Svedberg, 1998). Of the various metal oxides that can be used for the syngas redox process, iron oxide (Fe_2O_3) has been identified as permitting the highest conversion of syngas to combustion products (CO_2 and water) along with a high conversion of steam to hydrogen (Gupta et al., 2007).

4.3.3.1 Syngas Chemical Looping

4.3.3.1.1 Reduction Reactor

The syngas produced from the gasifier contains mostly CO, H_2, CO_2, and CH_4 (Li et al., 2001), and it reduces the metal oxide (Fe_2O_3) to the constituent metal (Fe and FeO). The advantage

of using iron oxide (Fe_2O_3) as the oxygen carrier is that it does not involve catalytically dependent reactions (Gupta et al., 2007). The gaseous products are CO_2 and steam. The steam is condensed to obtain sequestration-ready CO_2. The reactions of CO in the syngas with iron oxide and wustite (FeO) are given as follows:

$$Fe_2O_3 + CO \rightarrow 2FeO + CO_2 \tag{4.15}$$

$$FeO + CO \rightarrow Fe + CO_2 \tag{4.16}$$

Similarly, the reactions of hydrogen in the syngas with iron oxide and wustite (FeO) are as follows:

$$Fe_2O_3 + H_2 \rightarrow 2FeO + H_2O \tag{4.17}$$

$$FeO + H_2 \rightarrow Fe + H_2O \tag{4.18}$$

The reactions in Equations 4.15 through 4.18 occur at a pressure of 30 atm and a temperature ranging from 750°C to 900°C within the process shown in Figure 4.12. The particle size for the iron oxide is 2–10 mm. The reduction reactors in the syngas chemical looping (SCL) system are set with inert conditions for CH_4 since the model does not allow CH_4 to react with the iron oxide, thus completing the reactions in Equations 4.15 through 4.18 and enabling the production of hydrogen (Hoffman, 2005). In the SCL system, therefore, the CO_2 stream contains the unreacted CH_4, depending on the inlet conditions. These data are included in the results.

4.3.3.1.2 Oxidation Reactor

This reactor operates at 30 atm and 500°C–700°C to oxidize the metal produced in the reduction reactor using steam. The products are 99% pure hydrogen and magnetite (Fe_3O_4). The reactions are as follows:

$$Fe + H_2O_{(g)} \rightarrow FeO + H_2 \tag{4.19}$$

$$3FeO + H_2O_{(g)} \rightarrow Fe_3O_4 + H_2 \tag{4.20}$$

Both reactions are slightly exothermic and some of the heat may be used for preheating the feedwater to make steam. Hydrogen production using CLC of the syngas is indirect with the use of iron oxide. The actual hydrogen in the syngas is converted to water (Equations 4.17 and 4.18). These oxidation reactions are similar with a principal purpose as that of the SCL system to produce hydrogen as in the case of the DCL system in Figure 4.14.

4.3.3.1.3 Combustion Reactor

The magnetite formed in the oxidation reactor enters the combustion reactor where it reacts with oxygen to form a more stable form of iron oxide III (Fe_2O_3). A significant amount of heat is produced during the oxidation of Fe_3O_4 to Fe_2O_3. The reaction is

$$4Fe_3O_4 + O_2 \rightarrow 6Fe_2O_3 \tag{4.21}$$

The gas composition of exhaust ($N_2 + O_2$ in Figures 4.12 and 4.14) includes the remaining

oxygen after the reaction in Equation 4.21 and the corresponding nitrogen

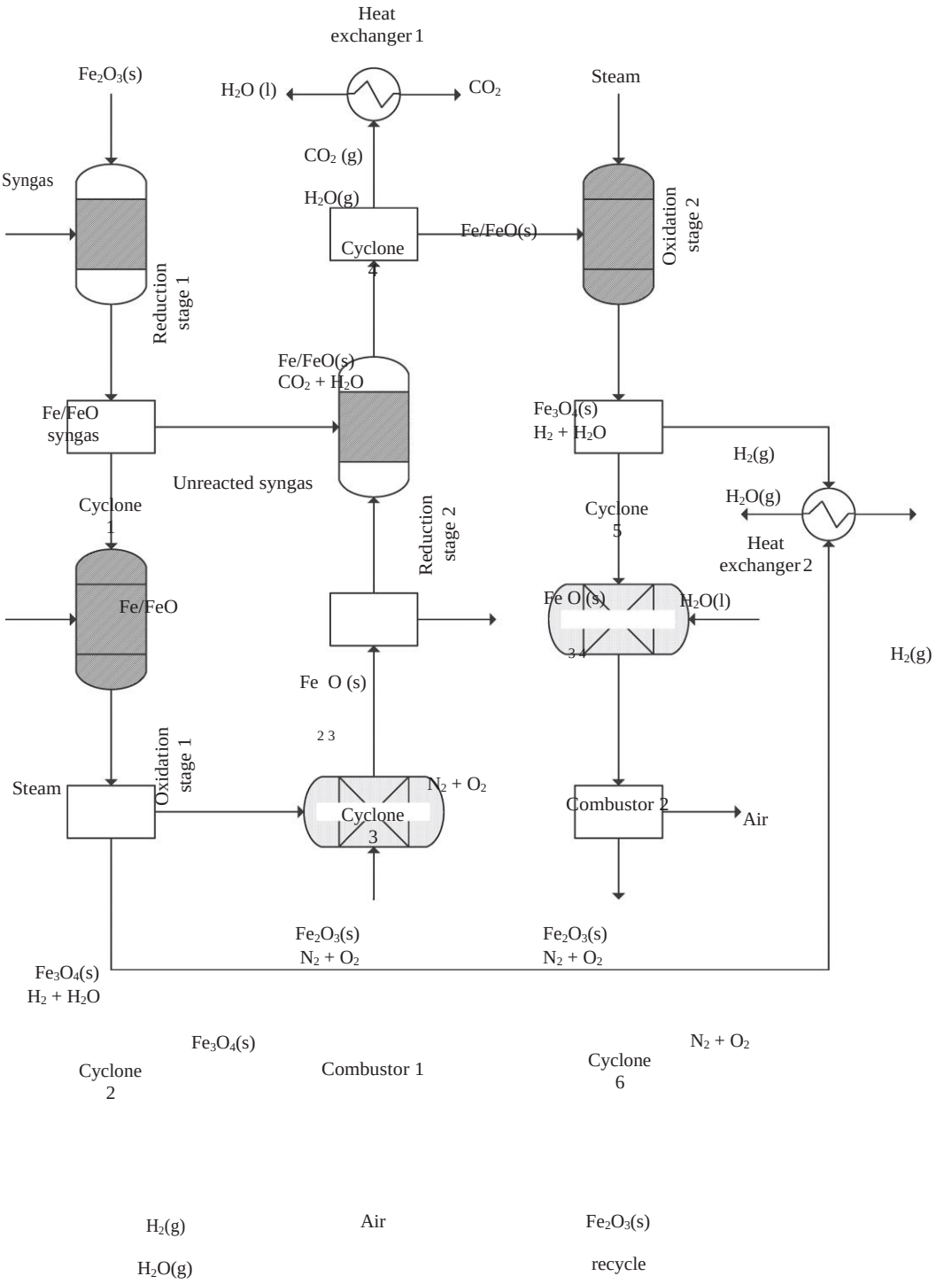


FIGURE 4.12

Syngas-based chemical looping process (SCL). (Adapted from Gnanapragasam, N.V. et al., *Int. J. Hydrogen Energy*, 34, 2606, 2009b.)

Chemical looping with oxygen uncoupling (CLOU) is a novel method to burn solid fuels in gaseous oxygen without the need for an energy-intensive ASU (Mattison et al., 2008). The CO_2 from combustion is inherently separated from the rest of the flue gases. The reaction rate of petroleum coke was found to be approximately 50 times higher when using CLOU compared to the reaction rate of the same fuel with an iron-based oxygen carrier in conventional CLC.

4.3.3.2 Direct Chemical Looping

The DCL process removes the gasification process from the hydrogen production route. Rather, it has a fuel reactor that first combusts some feedstock to generate the temperature required for the endothermic reactions as described in Equations 4.24 through 4.28.

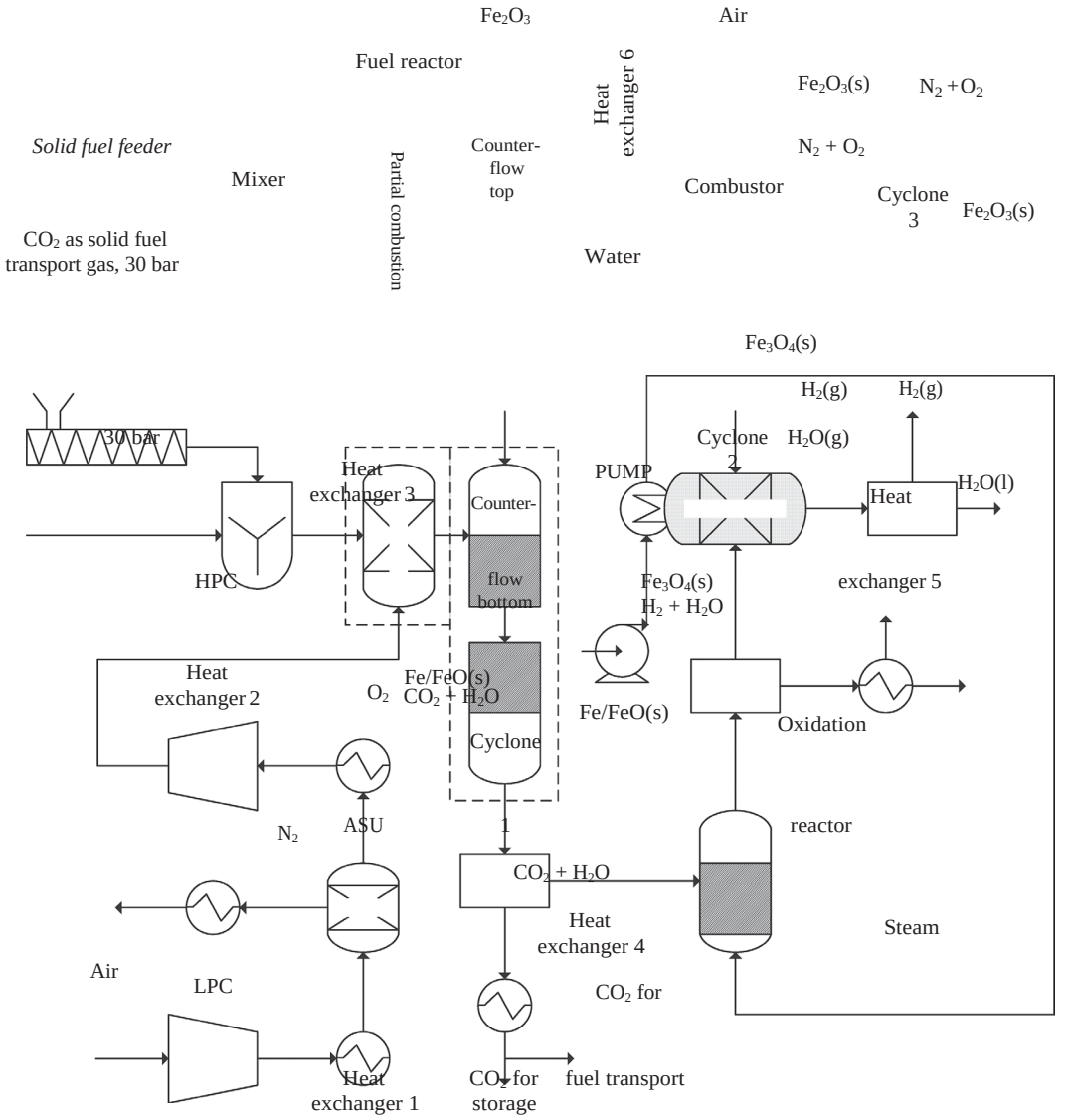


FIGURE 4.13

DCL process without gasification. (Adapted from Gnanapragasam, N.V. et al., *Int. J. Hydrogen Energy*, 34, 2606, 2009b.)

4.3.3.2.1 Fuel Reactor

The principal difference in the DCL system (Figure 4.13) relative to the SCL system (Figure 4.12) is the absence of the gasifier and the addition of a fuel reactor. The latter is an extended form of reduction reactor, and its chemical reactions are discussed as fol- lows. The fuel reactor can be modeled as three separate *RGibbs* reactors (rigorous reaction and multiphase equilibrium based on Gibbs free energy minimization) linked together by restricting products from each of the three reactors: partial combustion, fuel reactor top, and fuel reactor bottom (see Figure 4.13). The reactions and conditions in the fuel reactor, based on Fan et al. (2008) and Mattison et al. (2008), are as follows:

- *Partial combustion*: Coal devolatilization and partial combustion occur (where the formula

for coal used here represents Pittsburgh #8 coal, although a different coal similar in composition is used in the calculations) as follows:

$$C_{11}H_{10}O \rightarrow C + CH_4 \quad (4.22)$$

$$C + O_2 \rightarrow CO_2 \quad (4.23)$$

- *Fuel reactor top*: Char gasification and iron oxide reduction occur as follows:

$$2C + O_2 \rightarrow \quad (4.24)$$

$$2CO\ C + CO_2 \rightarrow 2CO \quad (4.25)$$

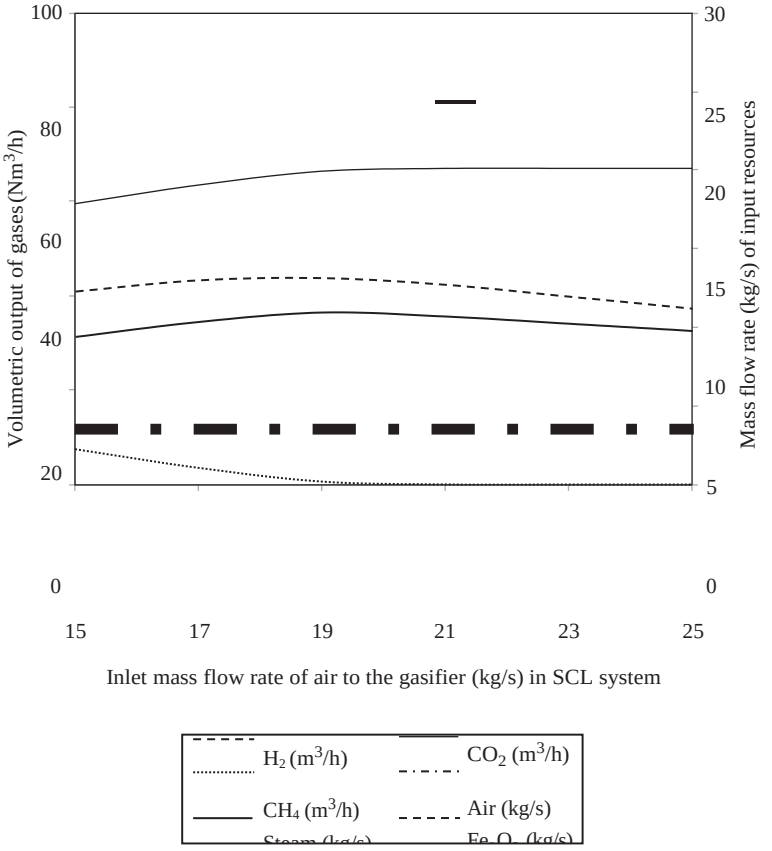


FIGURE 4.14

Variation in gas outputs from the SCL system with inlet mass flow rate of air to the gasifier. The input variations of steam and iron oxide (Fe_2O_3) are also provided. (Adapted from Gnanapragasam, N.V. et al., *Int. J. Hydrogen Energy*, 34, 2606, 2009b.)

$$2C + H_2O \rightarrow CO + H_2 \tag{4.26}$$

$$CH_4 + 4Fe_2O_3 \rightarrow CO_2 + 2H_2O + 8FeO \tag{4.27}$$

- *Fuel reactor bottom*: Wustite (FeO) reduction occurs, following the reactions in Equations 4.15 and 4.16.

The overall chemical reaction within the fuel reactor (Fan et al., 2008) is

$$C_{11}H_{10}O + 6.44Fe_2O_3 + 3.34O_2 \rightarrow 11CO_2 + 5H_2O + 12.88Fe \tag{4.28}$$

The residence time for the coal char in the fuel reactor is between 30 and 90 min (Fan et al., 2008), depending on operating temperature (750°C–900°C) and pressure (1–30 atm). The reaction in Equation 4.27 enables the conversion of CH_4 in the gas stream to CO_2 and H_2 while reducing iron oxide (Fe_2O_3). Thus, in the DCL system, the CO_2 stream may not con-

tain CH_4, unlike the SCL system.

Figures 4.14 and 4.15 show the range (from 15 to 25 kg/s) of air mass flow rate into the gasifier for the SCL system and into the fuel reactor for the DCL system, on the horizontal axis. The distributions of the production of H_2, CO_2, and CH_4 are plotted in Figure 4.14 for the corresponding change in inlet air mass flow rate to the gasifier in the SCL system. In Figure 4.15, a similar distribution is shown for the DCL system, except for CH_4 since

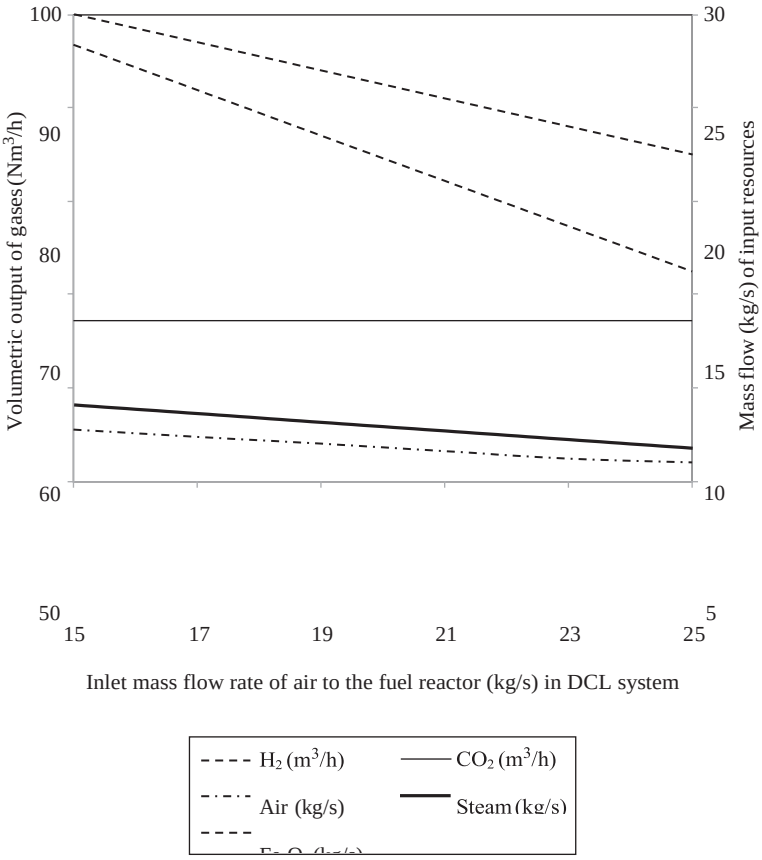


FIGURE 4.15

Variation in gas outputs from the DCL system with inlet mass flow rate of air to the fuel reactor. The input variations of steam and iron oxide (Fe_2O_3) are also provided. (Adapted from Gnanapragasam, N.V. et al., *Int. J. Hydrogen Energy*, 34, 2606, 2009b.)

it is consumed within the process (Equation 4.27) and not produced along with H_2 and CO_2 as in the SCL system. Since CH_4 is not converted to hydrogen or any other form in the SCL system, the H_2 output rate in Figure 4.14 increases with air inlet flow rate until the air inlet flow rate reaches 19 kg/s, when CH_4 is no longer produced in the gasifier of the SCL system. The results in Figures 4.14 and 4.15 are based on simulations of the SCL and DCL systems when anthracite coal is used at a rate of 5 kg/s. Theoretically, the DCL system is better than the SCL system in producing more hydrogen at low oxygen input (Gnanapragasam et al., 2009b), but this observation has not been confirmed at large scales.

4.3.4 Autothermal Reforming

Hydrogen production from coal-derived methanol via ATR has been reported to have fewer trace impurities than other coal-based hydrogen production processes, mainly due to higher operating temperature generated by the partial oxidation step (Yoon and Erickson, 2008) as shown in Figure 4.16. Coal-based methanol has been shown to have higher amounts of trace hydrocarbons than chemical-grade methanol derived from natu- ral gas, so hydrogen production from coal-derived methanol via ATR is feasible consider- ing fuel cell applications.

Natural gas and the thermolysis gases from petroleum and coal can be thermally decom-

posed to manufacture hydrogen and vapor-deposited carbon materials, in the form of nanoparticles, fibrous materials, or pyrolytic carbon solids (Halloran, 2008). Coal thermolysis can produce hydrogen from coke oven gas and carbon materials from fabricated cokes.

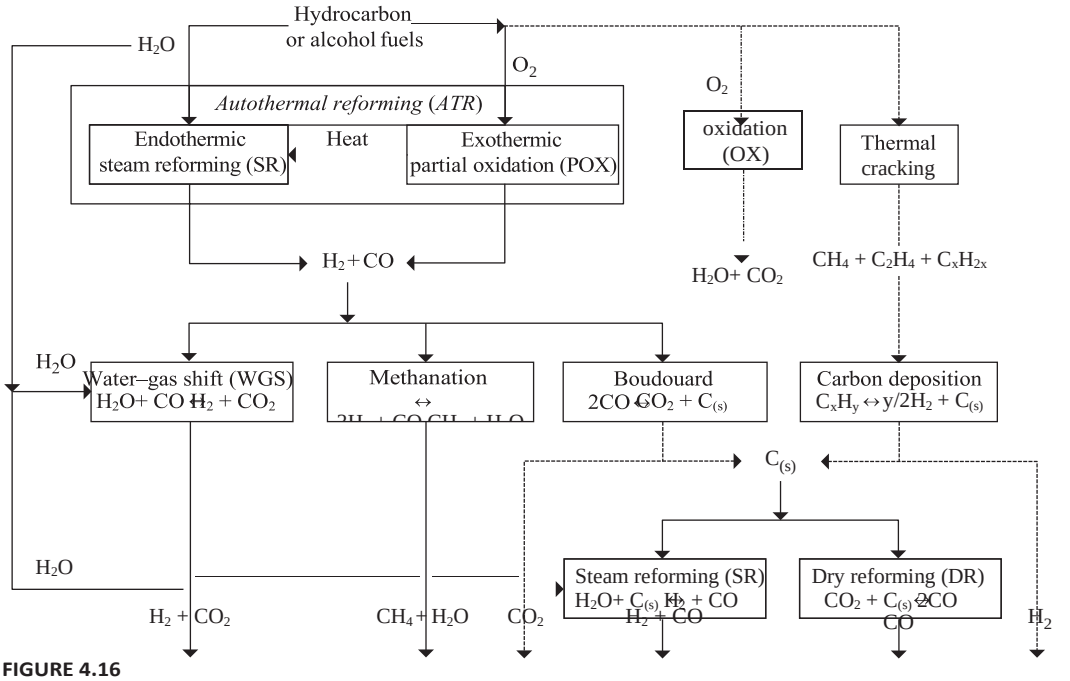


FIGURE 4.16

Flow scheme of possible reactions taking place within ATR process. (From Chen, Y. et al., *Catal. Today*, 116, 334, 2006.)

The combined manufacture of hydrogen and carbon materials would be economical if the market value of the hydrogen and solid carbon materials were greater than the value of coal as a fuel.

ATR uses oxygen and CO_2 or steam in a reaction with CH_4 to form syngas (Xuan et al., 2009). The reaction takes place in a single chamber where the CH_4 is partially oxidized. The reaction is exothermic due to the oxidation. When the ATR uses CO_2, the H_2/CO ratio produced is 1:1; when the ATR uses steam, the H_2/CO ratio produced is 2.5:1.

The exothermic reaction in the ATR process when using CO_2 is

$$2CH_4 + O_2 + CO_2 \rightarrow 3H_2 + 3CO + H_2O \quad (4.29)$$

and when using steam is

$$4CH_4 + O_2 + 2H_2O \rightarrow 10H_2 + 4CO \quad (4.30)$$

The outlet temperature of the syngas is between 950°C and 1100°C, and the outlet pressure can be as high as 100 bar (Mahecha-Botero et al., 2008). The main difference between SMR and ATR is that SMR uses no oxygen. The advantage of ATR is that the H_2/CO can be varied, which is particularly useful for producing some second-generation biofuels, such as dimethyl ether (DME, CH_3OCH_3) that requires a 1:1 H_2/CO ratio. For the genera- tion of hydrogen, the use of steam in the flow of processes in the ATR system is shown in Figure 4.16. The broken lines in Figure 4.16 denote SMR, while the solid lines denote the ATR process.

4.3.5 Hydrogen Separation and Purification Processes

Hydrogen is generated from the gasification process and available in the syngas, but it needs to be separated before and after WGS reaction. Chemical looping does not require physical hydrogen separation since it is a thermochemical process and enables cheaper separation (Andrus, 2009). After hydrogen is separated, it still contains other gaseous elements in smaller amounts that need to be removed for highly purified hydrogen.

4.3.5.1 Water–Gas Shift Process

WGS catalysts have been commercially developed for use by the petrochemical industry (Leach, 1984; Twigg, 1996). Presently, there is renewed interest in the WGS reaction because of its importance in reforming fuels to hydrogen for use in fuel cells. Since biomass gasification yields relatively high CO/H_2 ratios, higher hydrogen contents can be achieved using commer- cial CO shift catalysts in two fixed-bed reactors operated in series: a high-temperature shift reactor (HTSR) for rapid reaction and a low-temperature shift reactor (LTSR) to shift ther- modynamic equilibrium to very low levels of CO (Zhang et al., 2005). The high-temperature shift reaction takes advantage of faster kinetics at elevated temperatures to convert about 75% of the CO into H_2. Conversion is, however, limited by thermodynamic equilibrium, which favors hydrogen formation at low temperatures. Accordingly, the gas is slightly cooled and passed through a second LTSR to convert most of the remaining CO to H_2.

The WGS reactors in Figure 4.17 are arranged to obtain the maximum hydrogen production. The WGS reaction, Equation 4.6, is carried out in two reactors placed in series, including a HTSR and LTSR. These reactors operate at temperatures of about 350°C–400°C

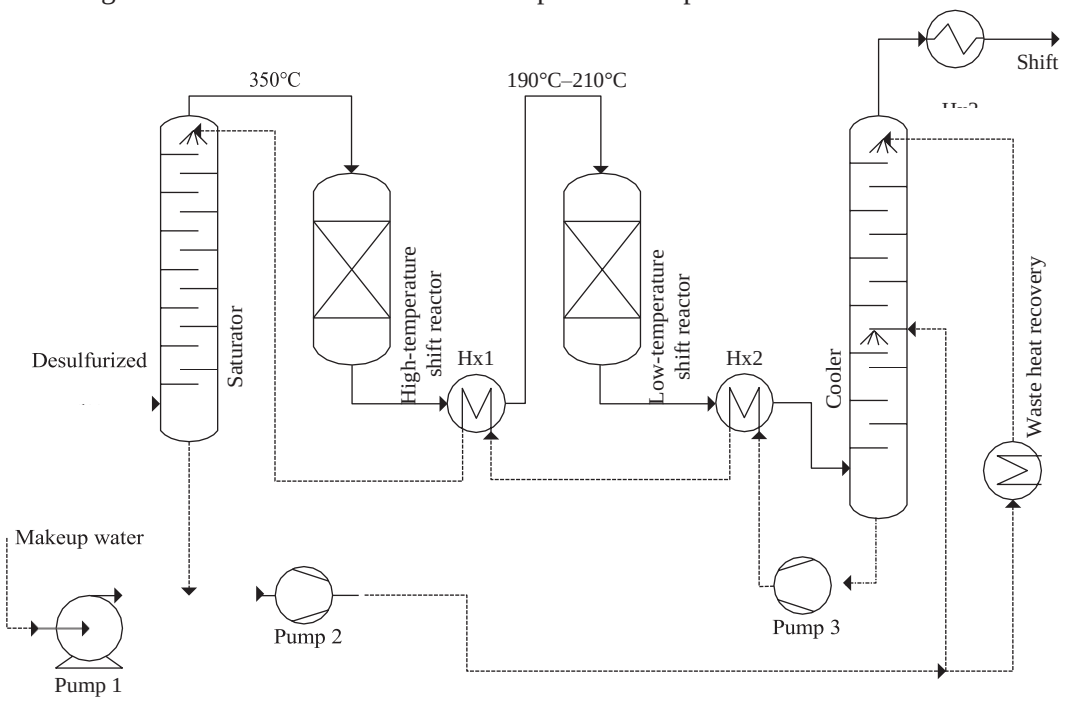


FIGURE 4.17

WGS process. (Adapted from Zhang, R. et al., *Fuel Process. Technol*., 86, 861, 2005.)

TABLE 4.4

Characteristics of the Syngas from LTSR at Different S_{SHIFT}/C Ratios in the Conditions of Maximum Hydrogen Production

S_{SHIFT}/C	0.6	0.8	1	1.2
S/C	0.7	0.6	0.4	0.2
Molar Composition (%)				
H_2	49.95	48.92	49.58	50.15
CO_2	33.28	32.44	32.39	32.28
CO	0.89	0.55	0.61	0.72
H_2O	14.34	16.61	15.96	15.4
H_2S	0.5	0.49	0.49	0.49
CH_4	0	0	0	0.01
N_2 + Ar	1	1	1	1
Hydrogen Flow Rate (kg/kg coal)				
H_2	0.156	0.159	0.161	0.162

Source: Adapted from Perna, A., *Int. J. Hydrogen Energy*, 33, 2957, 2008.

and 190°C–210°C, respectively (Perna, 2008). The catalysts employed to improve the reaction rate are sulfur tolerant, thus enabling the sulfur removal unit to be downstream of the shift units (Chiesa et al., 2005). The syngas exiting the LTSR is cooled at the operating temperature of the acid gas removal (AGR) unit.

The steam-to-carbon ratio (S_{SHIFT}/C) in the WGS reactors in Table 4.4 is defined as the ratio of the mass flow rate of the feed coal to the mass flow rate of the water input to the shift units, in the range 0.6–1.2. It is assumed that the mass fraction input to the HTSR is 0.67. The syngas converted after the WGS process is similar in composition to Table 4.4.

The catalytic tar process in combination with high- and low-temperature WGS reactors upgrades hydrogen in the raw gas from 5.8–8.8 vol.% to as high as 27–29 vol.% (Zhang et al., 2005). The CO concentration of 13–15 vol.% in the raw gas is reduced to less than 0.5 vol.%. The conversion of CO in the high-temperature WGS reaches 75%–80%, while the CO conversion by the combination of high- and low-temperature WGS reactors exceeds 95% (Mahecha-Boteroa et al., 2009).

4.3.5.2 Gas Separation Membranes

Gas separation using membranes of various kinds, primarily differentiated by the membrane material, is a rapidly evolving field (Li, 2007). The most common commercial materials for membranes include metallic, ceramic, and polymeric substances and, recently, carbon-based nanotubes or pores in compact grid arrangements (Kerry, 2006). It was reported in 2004 that membrane use in power cycles and fuel produc- tion using fossil fuels through the integration of membrane technologies has not been fully explored (Bredesen et al., 2004). Since then, several integration works have been reported, including design optimization and feasibility assessments using technoeco- nomic analyses of the membranes for power and fuel production systems (Amelio et al., 2007; Rezvani et al., 2009). New combustion processes with porous membrane integra- tion have also been recently reviewed (Mujeebu et al., 2009), providing a broader picture of membrane applications in energy conversion processes: mainly air separation and CO_2 and H_2 separation.

Of the current noncryogenic technologies for oxygen separation, membranes such as the ITM provide clean, efficient, and economic means of producing oxygen (Li, 2007). Ionic conducting or ionic and electronic conducting ceramic dense membranes are of particular interest due to their 100% selectivity for oxygen, with three to four orders of magnitude higher flux than the best organic membranes.

Carbon separation membranes (CSMs) are ceramic hollow fiber membranes that provide a good alternative. Ceramic hollow fiber membranes are not commercially available at present, mainly due to the lack of techniques to produce the ceramic membrane with a thin and dense separation layer in a hollow fiber form (Li, 2007). Hollow fiber membranes are frequently produced from polymeric materials and can provide the highest membrane area per unit packing volume, achieving densities as high as 8,000–10,000 m^2/m^3 (Li, 2007). However, this configuration is seldom used in ceramic membranes because of its poor mechanical strength. An early effort at gas separation, via the development of glass hollow fiber membranes (Way and Roberts, 1992), yielded membranes that were too fragile for industrial uses. Many other attempts have been made to develop fabrication techniques for hollow fiber ceramic membranes (Smid et al., 1996; Brinkman et al., 2000; Luyten et al., 2000; Tan et al., 2001; de Jong et al., 2004; Xu et al., 2004; Liu et al., 2006).

A fundamental process for noncryogenic separation of industrial gases is permeation (Kerry, 2006), which involves the diffusion of a substance in solution through a barrier or membrane. Permeability is the capacity of a porous material (membrane) for transmitting a fluid. The membranes used for permeation simulation in this work may be one or a combination of thin, dense, and continuous films formed from cellulose acetate or polymers.

The separation of a component in a gas mixture is carried out in three steps, in which the component dissolves in the membrane wall, diffuses through the membrane material, and is desorbed on the opposite side of the membrane wall. This procedure can be defined by Henry's law of solubility and by Fick's law of diffusivity, while noting that the solubil- ity of a gas in a liquid is proportional to the partial pressure of the gas. These laws can be expressed as follows:

Feed gas solubility in the polymer:

$$z_{iF} = S_i P_F x_i \tag{4.31}$$

Fick's law inside membrane material:

$$\frac{Q_i}{A} = \frac{D_i\left(x_i - y_i\right)}{L_p} \tag{4.32}$$

Permeate solubility in the polymer:

$$z_{iP} = S_i P_P y_i \tag{4.33}$$

The operating performance of any polymeric membrane is characterized by two factors: (1) permeability (which defines productivity, the transport rate for a given species in the feed stream, and, therefore, the cost of the system) and (2) selectivity (which in turn defines recovery or purity of the selected stream). Expressions for permeability and selectivity can be derived from Equations 4.31 through 4.33 (Fleming and Dupuis, 1993). For oxygen separation from air, N_2 is more permeable than O_2 due to the higher molar fraction of N_2 in air, whereas H_2 is more permeable than CO_2 due to the lower molar fraction of CO_2 in the exhaust gas stream after WGS reaction.

4.3.5.3 Pressure Swing Adsorption for Hydrogen Purification

The quality of the hydrogen produced can be a major issue for automotive applications. The pressure swing adsorption (PSA) unit produces hydrogen with 99.999% of purity, operates at above 20 bar, and reaches H_2 separation efficiencies in the range 85%–90%. The PSA purge gas (waste gas) can be used to superheat steam or can be combusted for power generation in a gas turbine combined cycle (Perna, 2008). New hydrogen plants are almost invariably designed using PSA for final hydrogen purification (Hamelinck and Faaij, 2002). PSA is based on the difference in adsorption behavior between different molecules (Katofsky, 1993). The process separates components of a gas stream by selective adsorption to a solid at high pressure and subsequent desorption at low pressure. This adsorption/ desorption is a batch process, but by placing two beds in parallel, it operates nearly con- tinuously. While adsorption takes place in one bed, the other is desorbed (LaCava et al., 1998). First, activated carbon in the set of beds *A* selectively adsorbs nearly all CO_2 and all H_2O. The remaining gas then passes to the second set of beds *B* containing a zeolite molecular sieve, which selectively adsorbs essentially all the remaining compounds and some hydrogen. The overall recovery of hydrogen is increased by recycling some of the desorbed gas from the *B* beds (LaCava et al., 1998). There is a trade-off in that the recycled gas must be recompressed and cooled to near-ambient temperature, adding to capital and operating costs, and a slightly larger PSA unit will also be needed. As with the methanol synthesis loop, some of the recycled gas must be purged to prevent the buildup of CH_4 and other nonhydrogen gases. Recovery rates of over 90% are achievable, and the product purity is extremely high: 99.999%.

In PSA, species other than hydrogen are selectively adsorbed on a solid adsorbent, for example, activated carbon and 5A zeolite (Ruthven et al., 1994), at a relatively high pressure by contacting the gas with the solid in a packed column in order to produce a hydrogen-rich gas stream. The adsorbed species are then desorbed from the solid by lowering the pressure and purging with high-purity product hydrogen, and the PSA waste gas is generated. Continuous flow of product is maintained by using multiple, properly synchronized adsorption beds.

In a pressure swing adsorption (PSA) facility for H_2 purification, the impurities are adsorbed at high pressure, while H_2 passes through the adsorber vessel. When the vessel is full, it is disconnected from the process and the pressure is decreased, thus releasing most of the impurities (Rydén and Lyngfelt, 2006). A small fraction of the produced H_2 is needed for purging and regeneration of the adsorbers, so the H_2 recovery is limited to about 90%. The off-gas from the adsorber vessel consists of CO_2, purge H_2, unreformed CH_4, some CO, and minor fractions of other impurities. PSA is a batch process, but by using multiple adsorbers, it is possible to provide constant flows. The pressure drop for H_2 is usually about 0.5 bar. There is no need for power, heating, or chemicals.

4.4 Environment Protection Processes

When producing hydrogen from coal, pollutants of various forms are released at various conversion stages to the Earth's surface and lower atmosphere. Only gases that form in large quantities, such as H_2S, carbonyl sulfide (COS), and CO_2, and solids, such as ash, tars, and other nonenergy solid wastes, are discussed as part of pollution-control processes. These have to be managed for a sustainable environment without long-term damage to the

balance in the ecosystem. This section discusses some of the primary measures in managing these hazardous wastes that result in using coal and other solid fossil fuels. These processes improve the sustainability of hydrogen production systems that use solid fuels.

4.4.1 Acid Gas Removal: Sulfur Removal

Sulfur appears as SO_2 (only in combustion processes), H_2S, and COS in syngas after the energy conversion of sulfur-rich solid fuels (all solid fossil fuels). Sulfur in raw coal is converted to H_2S and COS in the gasifier, and most of the COS is converted to H_2S in the WGS reactors. In systems without the WGS process and CO_2 removal (Kohl, 1997), COS is typically hydrolyzed to H_2S in a catalytic bed at about 200°C.

AGR units (shown in Figure 4.18) are based on chemical absorption and physical absorption for atmospheric and pressurized configurations, respectively (Perna, 2008). AGR removes 99.9% of the H_2S, which is converted to elemental sulfur via Claus and shell claus

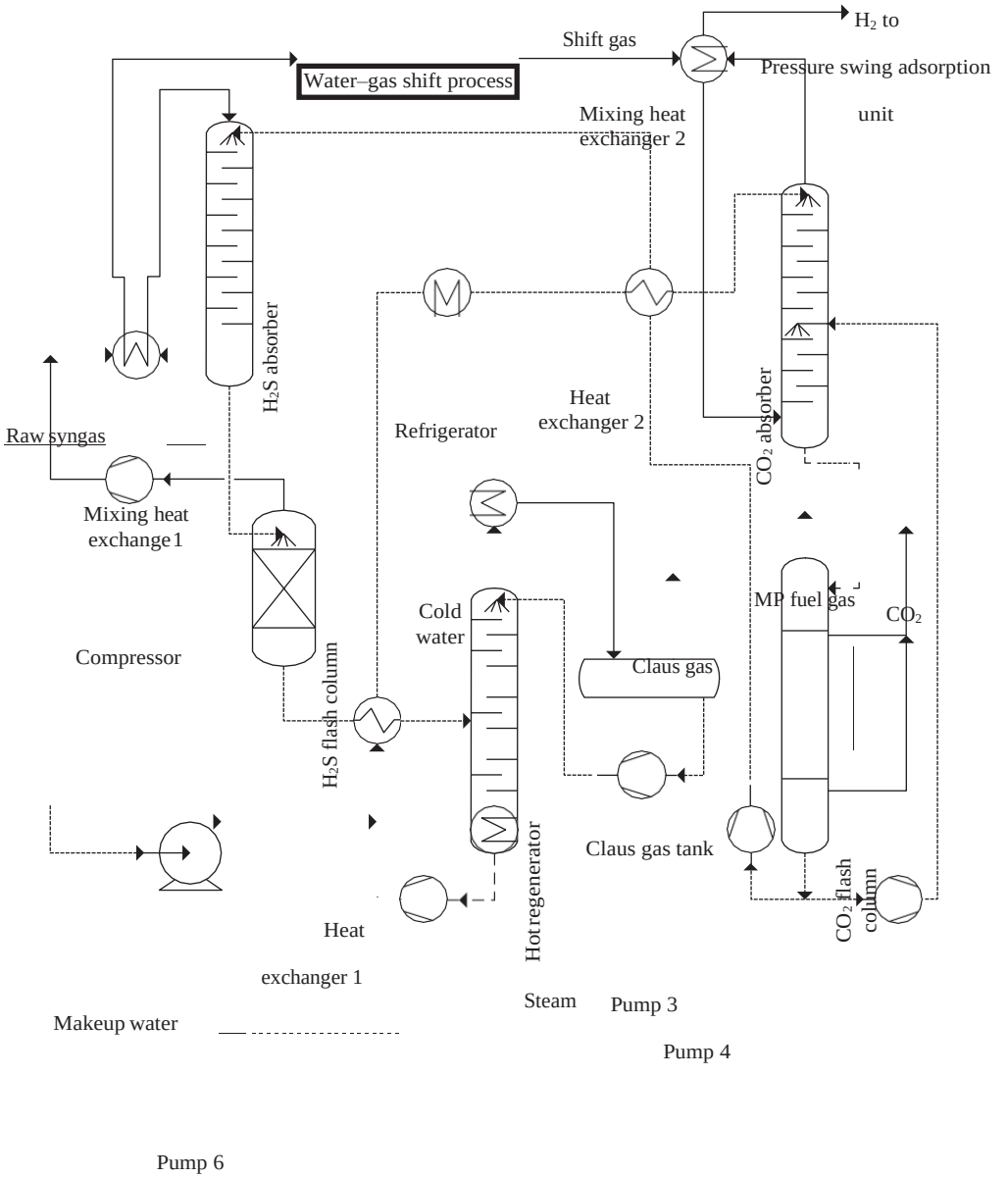


FIGURE 4.18

AGR process. (From Korens, N. et al., Process screening analysis of alternative gas treating and sulfur removal for gasification, Report for US Department of Energy by SFA Pacific, Inc., Engineering and Economic Consultants, 2002. Available at http://www.netl.doe.gov/technologies/coalpower/gasification/pubs/pdf/SFA%20Pacific_Process%20Screening%20Analysis_Dec%202002.pdf, Accessed on December 5, 2013.)

off-gas treating (SCOT) plants. The efficiency of the CO_2 capture unit is assumed equal to 95%. Prior to CO_2 capture, H_2S is removed from the syngas (containing 0.6% H_2S by volume) by physical absorption in CH_3OCH_3 of polyethylene glycol (Selexol). The WGS reactors included in H_2 plants and electricity plants with CO_2 capture greatly elevate (relative to electricity plants with CO_2 venting) the CO_2/H_2S ratio in the syngas and thus promote significant cocapture of CO_2 along with H_2S in the H_2S absorption tower.

Since essentially all of the sulfur in the gasifier feedstock is converted to H_2S, the amount of H_2S produced is totally dependent on the sulfur content of the feedstock. Note that coal has a relatively high sulfur content, while biomass has a relatively low sulfur content. Generally, the AGR processes lower the H_2S content of the syngas to less than 4 ppm, which means that, in essence, all of the H_2S produced in the gasifier must be processed in the sulfur recovery system.

4.4.2 Claus and SCOT Processes: Sulfur Recovery

The type of sulfur recovery system required is dependent on the required sulfur recovery efficiency, the quantity of sulfur to be removed, and the concentration of the H_2S in the acid gas. The required sulfur removal/recovery efficiency will vary depending on location; however, the gasification industry claims that the technology has *near-zero* pollution, so it necessitates the industry to install the best available control technology. Currently, H_2S removal efficiencies of 99.9% can be economically achieved (Nagl, 2005).

The Claus process has been the main sulfur recovery process for applications with large amounts of sulfur (greater than 20 long tons per day), relatively high H_2S concentrations (greater than 15%), and consistent inlet conditions. However, the Claus process is limited by chemical equilibrium to removal efficiencies of approximately 98% if three catalytic reactor stages are employed. To achieve higher removal efficiencies, a tail gas treating unit is required. For over 30 years, the preferred tail gas treating process has been the SCOT process. In that process, the tail gas from the Claus unit is heated to approximately 300°C in an in-line burner, which serves the dual purpose of heating the gas stream and producing a reduc- ing gas, which is needed in the downstream reactor. The effluent from the burner is then passed over a cobalt–molybdenum catalyst. In the reactor, all of the SO_2, COS, and CS_2 are converted to H_2S by a combination of hydrogenation and hydrolysis reactions. The reactor effluent gas is then cooled and processed through a typical amine unit, which is selective to the absorption of H_2S. The recovered H_2S is then recycled back to the Claus unit, and the remaining gas is sent to an incinerator prior to exhausting to the atmosphere.

Although many of these processes are mature, when integrated with hydrogen production, process optimization becomes essential for improving the overall energy efficiency.

4.3 Tar, Ash, and Soot Removal

The presence of tars in the product gas is a significant challenge in the commercial utilization of coal and biomass product gas (syngas) as a source of sustainable energy. Tar is formed in the gasifier and comprises a wide spectrum of organic compounds, generally consist- ing of several aromatic rings. Simplified tars can be separated into heavy and light tars (Higman and Burgt, 2008). Heavy tars condense as gas temperature drops and cause notable fouling, efficiency loss, and unscheduled plant shutdowns. The tar dew point, that is, the temperature at which tars start to condense, is a critical factor. Light tars like phenol or naphthalene have limited influence on the tar dew point but are not less problematic.

Light tars like phenol chemically pollute the bleed water of downstream condensers and aqueous scrubbers. Naphthalene is important as it is known to crystallize at the inlet of gas engines increasing needs for maintenance and service.

Conventional gas tar cleaning is based on wet scrubbing and on a wet cleaning with an electrostatic precipitator (ESP). In some new processes (Zwart et al., 2008), the tar removal principle is based on a multiple-stage scrubber in which gas is cleaned by a special scrubbing oil. In the first stage, the gas is cooled with scrubbing oil. Heavy tar particles condense and are collected, after which they are separated from the scrubbing oil and can be recycled to the gasifier, together with a small bleed. In the second stage, lighter gaseous tars are absorbed with scrubbing oil. In the absorber column, the scrubbing oil is saturated by these light tars. This saturated oil is regenerated in a stripper. Hot air or steam is used to strip the tars of the scrubbing oil. All heavy and light tars can be recycled to the gasifier where they are destroyed and contribute to the energy efficiency. Tar waste streams are efficiently recycled this way.

The raw syngas generated in a partial oxidation gasifier also includes carbon soot that is removed and recovered from the syngas by scrubbing with water (as shown in Figure 4.19). The scrubbing water contains one or more high-temperature surfactants that allow greater soot concentrations in the water-scrubbing quench zone of the gasifier. The carbon soot is separated from the scrubbing water with the aid of scrubbing oil. The separation of the carbon soot from the scrubbing water is enhanced with the aid of one or more surfactants that render the soot particles hydrophobic and oleophilic (Jahnke, 2003). The recovered carbon soot is ultimately recycled to the gasifier to recover the energy value of the carbon during the partial oxidation reaction. The overall energy efficiency of the gasification process can be

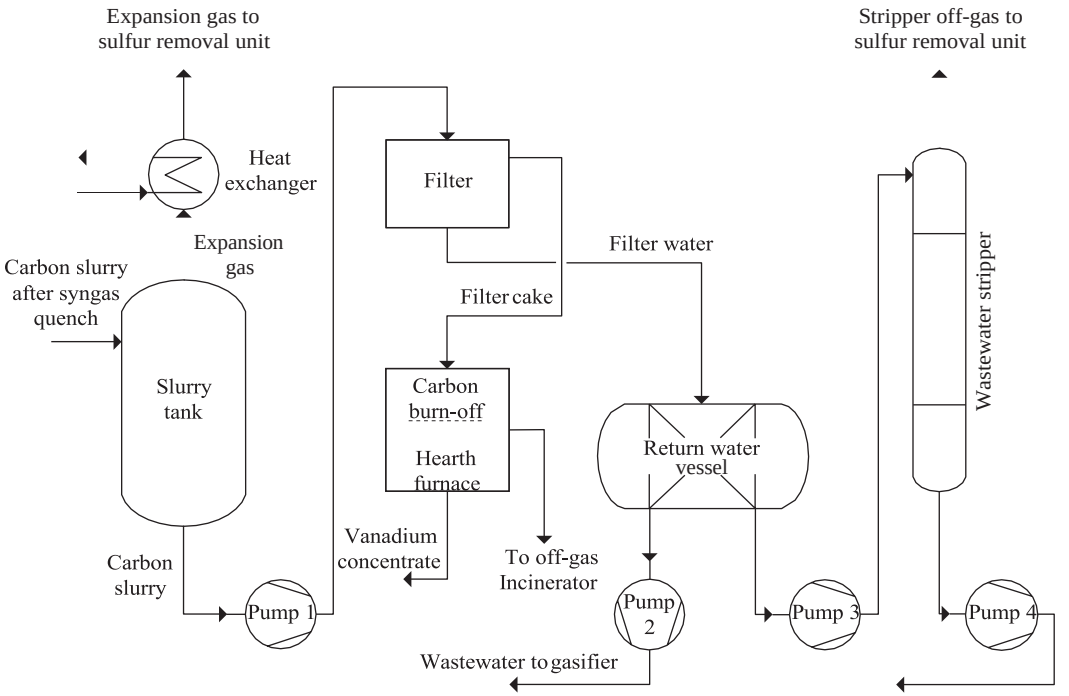


FIGURE 4.19

Syngas carbon soot removal unit. (Adapted from *Gasification*, 2nd edn., Higman, C. and van der Burgt, M., Copyright 2008, with permission from Elsevier.)

increased by removing all or a significant portion of the water from the soot mixture before recycling the soot. Separating the soot from the water allows for independent regulation of the soot and water recycle streams, depending on the reaction conditions in the gasifier.

Other solid particles from mostly syngas are removed at several stages. Char particles are collected in a syngas cooler and cyclones and recycled to the gasifier. Slag from the gasifier is water quenched and removed through a lock hopper (Collot, 2006). Syngas is quenched with recycled cleaned cooled water. Raw syngas is then dedusted in ceramic candle filters. Molten ash is tapped off and quenched with water in the bottom of most types of gasifiers. Ash is commonly removed from the gasifier by a revolving grate and depressurized in a lock hopper.

4.4 CO_2 Capture and Storage

The current challenge for using carbonaceous solid fuels in producing hydrogen is the capture and disposal/storage of CO_2 in an environmentally feasible manner (EcoEnergy, 2008). Based on a performance evaluation of state-of-the-art commercial technology for hydrogen coproduction (Chiesa et al., 2005), a system that converts 57%–58% of the coal lower heating value (LHV) to hydrogen while exporting to the grid electricity amounting to 2%–6% of the coal LHV, in contrast to decarbonizing coal in IGCC electricity generation (which entails a loss of 6%–8% points of electricity conversion when capturing CO_2 as an alternative to venting it), CO_2 capture for hydrogen production incurs a minor energy penalty (2% points of export electricity). Some of these losses are attributable to the number of intermediate processes involved in producing hydrogen from coal, including several for pollution control.

The hydrogen from various gas streams, subsequent to cleaning and particle separa- tion, is accompanied by CO_2, which can be stored (Damen et al., 2007) and used for dif- ferent applications. After further cooling of syngas from gasifiers, H_2S is removed from the syngas using a physical solvent (Selexol) and CO_2 is removed from the syngas (again using Selexol). After being stripped from the solvent, the CO_2 is dried and compressed to 150 bar for pipeline transport and underground storage (Higman and Burgt, 2008). Three paths for the CO_2 are possible, as shown in Figure 4.1. The commercial route is already applied by several industries for using and storing CO_2 in various forms. The current com- mercial applications include industrial use of CO_2 in large refrigeration systems making dry ice, enhanced oil recovery, and manufacturing of various chemicals. Also some CO_2 produced within the hydrogen production system may be used for transporting solid fuels into high-pressure reactors.

The second option of storage involves sending the remaining CO_2 for large-scale underground storage (IEA, 2008b). Such processes are being implemented commercially in recent years through a process known as geological sequestration (GS), where the CO_2 is com- pressed and placed in deep underground aquifers, depleted oil and gas reservoirs, and dried underground coal beds. Some large-scale CO_2 storage projects are already in opera- tion and under construction, while others are the subject of feasibility studies (NETL, 2009). There is an upcoming and promising third option of disposing CO_2, converting CO_2 into microalgae using sunlight and water, via algae-based artificial photosynthesis (in Figure 4.1). Microalgae are microscopic photosynthetic organisms. They generally produce more of the kinds of natural oils needed for biodiesel extraction (Sheehan et al., 1998). Autotrophic

algae enable the photosynthesis process by utilizing light, CO_2, and water to grow the candidate algae (depending on the conditions available for growth). Heterotrophic algae use thermal energy from waste heat applications, CO_2, and nutrients derived from biogas effluents, leachate in landfills, and wastewater from fermenting processes. Some of the advantages of algae include (Sheehan et al., 1998) the following:

- Use of far less water than traditional oilseed crops.
- More efficient conversion of solar energy because of their simple cellular structure.
- Capable of producing 30 times the amount of oil per unit area of land, compared to terrestrial oilseed crops.
- Capable of taking the waste (zero-energy) form of carbon (CO_2) and converting it to a high-density liquid form of energy (natural oil).
- Growth that is directly proportional to the surface area and the area of exposure to sunlight (only for autotrophs).
- Use of optical fiber–based reactor systems (only for autotrophs) developed by Japanese researchers that could dramatically reduce the amount of surface area required for algae production.
- Three main ingredients of microalgae: carbohydrates, protein, and natural oils.
- Fuel production concepts:
  - Production of CH_4 gas through biological or thermal gasification: breakdown of any form or organic carbon into CH_4
  - Production of ethanol through fermentation: most effective for conversion of carbohydrate portion of algae
  - Production of biodiesel: applies exclusively to the natural oil fraction of the microalgae
- Ability to produce up to 60% of their body weight in the form of triacylglycerols (TAGs), making it an alternative source for biodiesel than the oilseeds.
- Transesterification: reacting TAGs with simple alcohols creates a chemical com- pound known as alkyl ester or, more commonly, biodiesel.
- Not dependent on land area if algae are grown in large existing aquatic environ- ments, although for large-scale production, a sizable portion of the land (nonagri- cultural land) area is needed.

There is also a fourth option not denoted in Figure 4.1, which is the mineral stor- age of CO_2, in which CO_2 is reacted with naturally occurring magnesium (Mg)- and calcium (Ca)-containing minerals to form carbonates. This process has several advan- tages, the most significant of which is the fact that carbonates have a lower energy state than CO_2, which is why mineral carbonation is thermodynamically favorable and occurs naturally (Shackley and Gough, 2006). Thus, the carbonates are stable and are unlikely to convert back to CO_2 under standard conditions. On the same basis, CO_2 recycle or reuse is another option that involves metal oxides such as Fe_2O_3, ZnO, and CaO to split CO_2 into CO and oxygen, for use in various processes (Kodama and Gokon, 2007). The latter option, in which CO_2 is split into CO and oxygen is an artificial photosynthesis process; it is a greenhouse-type concept for controlled feeding of biologically engineered plants that can consume, in a controlled environment, high volumes of CO_2 to store carbon and emit oxygen (Collings and Critchley, 2005).

4.5 Economic Benefits through Process Integration

Several paths exist to obtain hydrogen from water using energy from solid fuels, but the sustainability of these paths remains partly dependent on the economics of the overall system. This section presents an overview of the benefits of appropriate process integration toward economic sustainability of hydrogen production using solid fuels as the energy source.

Biomass is likely to remain a major solid fuel in driving the hydrogen economy. By the year 2050, according to the VTT report estimates (IEA, 2008b), agricultural and forestry residues and wastes will be the most cost-competitive types of biomass, with only around 30% of total bioenergy coming from specialized energy crops. Only current technologies and crop yields are used in this assessment, and population growth is taken to be zero. Larger biomass-based plants can achieve economies of scale, but this can be more than offset by the increased transport distances needed to obtain the required volume of biomass. The costs of delivered biomass vary with country and region due to factors including variations in terrain, labor costs, and crop yields. On average in Europe, the cost of operating a forwarder is USD 67–104/h, chipping costs USD 148–213/h, transport costs USD 91–143/h, and loading/unloading costs USD 40–83/h.

The coal sector is well established from mining to transportation to distribution and utilization, enabling economic development in several countries around the world (IEA, 2008a). Some current and possible future integration benefits are given in the following.

4.5.1 Integration of Energy Conversion and Waste Management Processes

Integrated processes, such as the one shown in Figure 4.20, create opportunities to improve the use of solid fuels, thereby reducing the associated environmental pollution and helping meet growing energy demands (Gnanapragasam et al., 2010). Numerous small-scale integrated projects for end users, such as combined power generation with hydrogen production and CO_2 capture, and their benefits have been investigated (Chiesa et al., 2005;

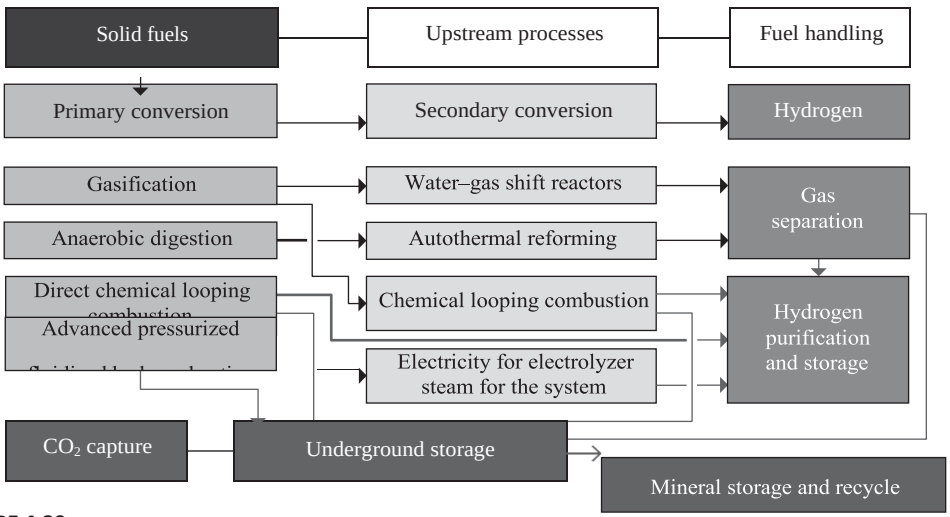


FIGURE 4.20

Example of process integration aimed at centralized hydrogen production for energy, environment, and eco- nomic benefits.

Damen et al., 2006; Shoko et al., 2006; Stiegel and Ramezan, 2006; Turner et al., 2008). New energy conversion technologies are also being developed and adopted due to the potential markets for efficient processes. Gasification as shown in Figure 4.7 is a promising conver- sion process that is expected to achieve significantly higher efficiencies for coal/biomass conversion to electricity and transport fuels (Beer, 2000).

4.5.1.1 Benefits of Process Integration

In large-scale process integration, solid fuels are converted via various industrial-scale integrated processes to convenient energy forms and ultimately to hydrogen. The benefits of such systems include the following:

1. *Multiple uses of feedstock*: Input solid fuels are converted to hydrogen, increasing efficiency and decreasing waste generation.
2. *Demand-based production*: Since each feedstock has a different market value, a proper blend of the cheapest and most efficiently used feedstocks can be used to reduce operating costs as well as to conserve rare fuels.
3. *Process applicability*: Based on the market value and demand for hydrogen, some of the processes are used for producing other products such as chemicals, reducing operating costs while utilizing the full potential of the facility.
4. *Resource availability*: Proven coal reserves and potentially consistent biomass sup- plies (IEA, 2006, 2007, 2008; Asif and Muneer, 2007), as well as the challenges asso- ciated with solid waste disposal (e.g., lack of landfills, special needs depending on the nature of waste), contribute to sustainability by being flexible in terms of allowable feedstocks.
5. *Proven technologies*: The processes considered have been tested or proven in indus- try so as to ensure high efficiency and low pollution with optimized performance.
6. *Opportunities*: When combining several processes for multiple products, new opportunities are provided for improving and developing these processes.
7. *Centralized pollution control*: Integration provides a major advantage by permitting centralized pollution control (reducing the overall energy consumption), which increases the capture efficiency for many pollutants, for example, SO_2, H_2S, COS, NO_x, and CO_2.

4.5.1.2 Challenges in Large-Scale Process Integration

Integration poses several challenges including potential incompatibility of processes and the need for additional accessory units that increase costs and reduce overall system effi- ciency. The demand for hydrogen energy is not yet large, in part because infrastructure for hydrogen is not yet widely available. Much of the public and the media view coal as *dirty* based on data from existing power plants, which lack the pollution-control technolo- gies capable of achieving near-zero emissions, confusing information and lack of aware- ness about cleaner technologies for using solid fuels. The project in Figure 4.6 has various stages of analysis, including thermodynamic, material, economic, environmental, market, and optimization. These stages should detail the benefits of implementing such a system into the existing energy infrastructure. The multiproduct and integrated nature of the system enables efficient use of coal, biomass, and municipal solid waste in producing elec- tricity, hydrogen, and chemicals simultaneously, thereby contributing to making energy systems more sustainable.

4.5.1.3 Economics of Process Integration

Gasification appears to be a more advantageous use of biomass than combustion, but a comprehensive economic analysis of biomass gasification systems suggests that the costs of plant construction are high compared with conventional plants while there are environmental benefits (Dowaki et al., 2005). Hence, an appropriate business model may be available in the future. Gasification has been proven to be the most advantageous conversion process for the initial stages of a hydrogen production facility. However, for gasification to play a major role in the near future, capital and operating cost must be reduced and reliability and performance improved (Collot, 2006).

There are currently several research and industrial development projects worldwide on IGCC and integrated gasification fuel cell (IGFC) systems (Shoko et al., 2006). In such systems, there is a need to integrate complex unit operations including gasifiers, gas separation and cleaning units, WGS reactors, turbines, heat exchangers, steam generators, and fuel cells. The IGFC systems tested in the United States, Europe, and Japan employing gasifiers (types include Texaco, Lurgi, and Eagle) and fuel cells have resulted in energy conversion efficiencies of 47.5% (HHV), which is much higher than the 30%–35% efficiency of conventional coal-fired power generation. IGCC and IGFC are currently not viable economically compared with current coal-utilization technologies, but further efficiency improvements and reductions in gaseous pollutant emissions could render the technolo- gies more competitive. Hydrogen produced from coal-based gasification has recently been shown to be competitive with production from natural gas provided the cost of natural gas remains above \$4/10^6 Btu, and the reliability of gasification-based processes can be demonstrated to be high (Stiegel and Ramezan, 2006). These authors suggest that the cost of producing hydrogen from coal could be reduced by 25%–50%, even with the capture and sequestration of CO_2.

Energy conversion efficiencies are greatest for natural gas–based systems due to the fuel characteristics. The costs of hydrogen production for natural gas and coal/biomass are much lower than for electrolysis (which presently has only a 4% market share) due to the volume of production (which is much higher for hydrogen from fossil fuels) and the mature state of the technology. A comparison of efficiencies and costs for various hydro- gen production methods (Shoko et al., 2006) shows steam reforming of natural gas to be the most beneficial, with high efficiencies (65%–75% based on LHV) and low production costs (USD 5–8/GJ). Gasification of biomass and coal has an overall efficiency of 42%–47% (LHV) with an average production cost at USD 9–13/GJ, while water electrolysis has the lowest efficiency (35%–42% HHV) and the highest production cost (on average USD 20/GJ).

4.5.2 Cost of Hydrogen Production: Impact of CO_2 Capture on Various Technologies

The costs of hydrogen production with coal-based technologies are compared with those for established technologies in Figure 4.21. With current technologies, large-scale hydrogen production can be attained with SMR and coal gasification with CO_2 capture from the shifted syngas, resulting in a CO_2 capture efficiency of 85%–90% (Damen et al., 2006, 2007). The conversion efficiency, including electricity inputs and outputs in primary terms, is 73% for SMR and 59%–62% for coal gasification. Investment costs are approximately 550 and 840 €/kWh for 1000 MWh SMR and coal gasification plants, respectively. The costs of hydrogen produced by SMR are dominated by fuel and feed costs, which makes coal gasification more favorable, especially if energy prices rise increasingly. Hydrogen produc- tion costs for SMR are estimated at 9.5 €/GJ and an optimally designed coal gasification

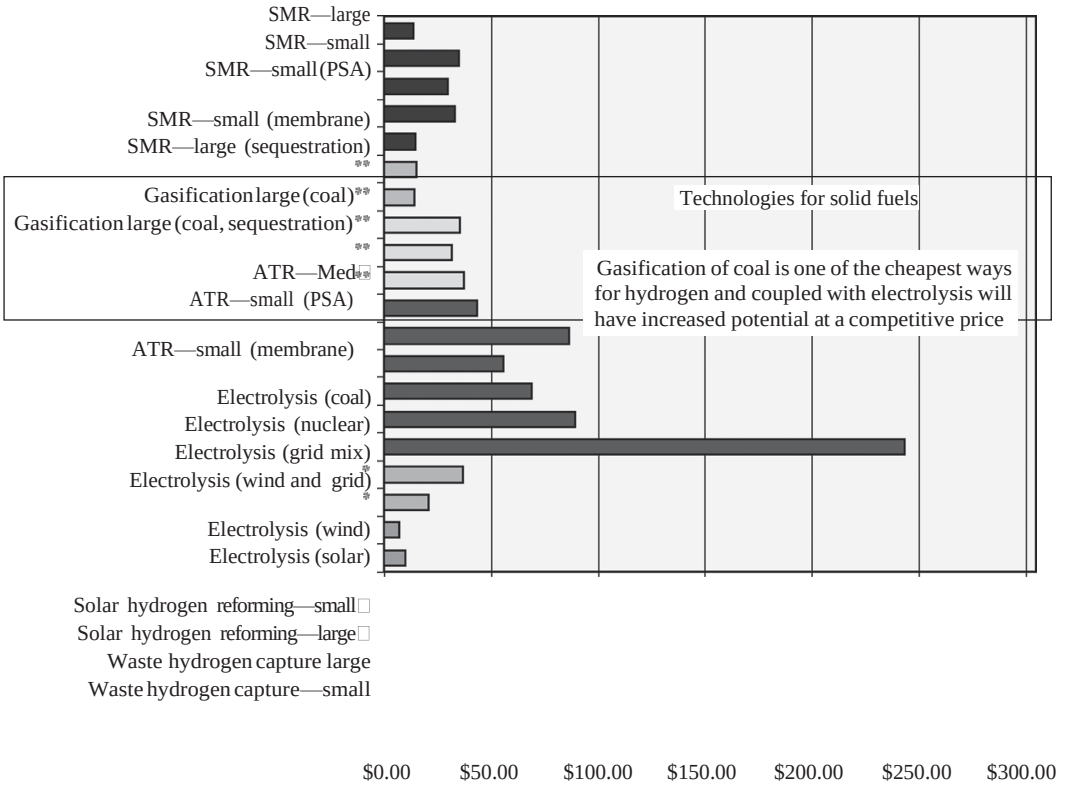


FIGURE 4.21

Total costs in $ per GJ of hydrogen produced with CO_2 valued at $15/ton, for various production processes. (SDTC, Renewable fuel—Hydrogen, SD Business Case, Version 1, Sustainable Development Technology Canada, Report BC_RFH_V7.12.1_EG_061123, 2006. Available at http://www.sdtc.ca/uploads/documents/en/ RenewableFuel-Hydrogen.pdf, Accessed on December 5, 2013.)

plant with electricity export may reach 7 €/GJ. CO_2 avoidance costs compared to identical plants without CO_2 capture are 23 and 5 €/ton of CO_2 for SMR and coal gasification, respectively. The penalty for CO_2 capture is compared in Figure 4.22 with other hydrogen production technologies, based on data compiled by SDTC (2006). The rectangular boxes in Figures 4.21 and 4.22 identify processes relating to hydrogen production using solid fuels.

Advanced large-scale ATR and coal gasification systems with ion-transfer membranes enable hydrogen production with 90% CO_2 capture at efficiencies of 73% for ATR and 69% for coal gasification (Damen et al., 2006, 2007). Investment costs for these systems are estimated at nearly 300 and 600 €/kWh, resulting in hydrogen costs of 8.1 and 6.4 €/GJ and CO_2 avoidance costs of 13 and 5 €/ton CO_2 for ATR and coal gasification, respectively.

A membrane reformer enables small-scale hydrogen production with relatively low-cost CO_2 capture. A 2 MWh plant may achieve efficiencies of 65% and investment costs of around 600 €/kWh (including hydrogen compression to 480 bar), resulting in a hydrogen cost of nearly 17 €/GJ, considering gas and electricity prices for small industrial users. Although the desire to reduce CO_2 emissions and capture emitted CO_2 is growing, the investment cost for solid fuel–based hydrogen production will likely remain the main hurdle.

4.5.3 Comparison of Hydrogen Production: Efficiency and Overall Costs

When carbon sequestration is coupled with natural gas steam reforming or coal gasification for hydrogen production, there is 14%–16% expected increase in the production cost of hydrogen (Tzimas and Peteves, 2005). Hydrogen production costs will decrease for coal and biomass once a market is established, likely as shown in Table 4.5, in which current data are compared with data for the year 2020. Natural gas is presently the most

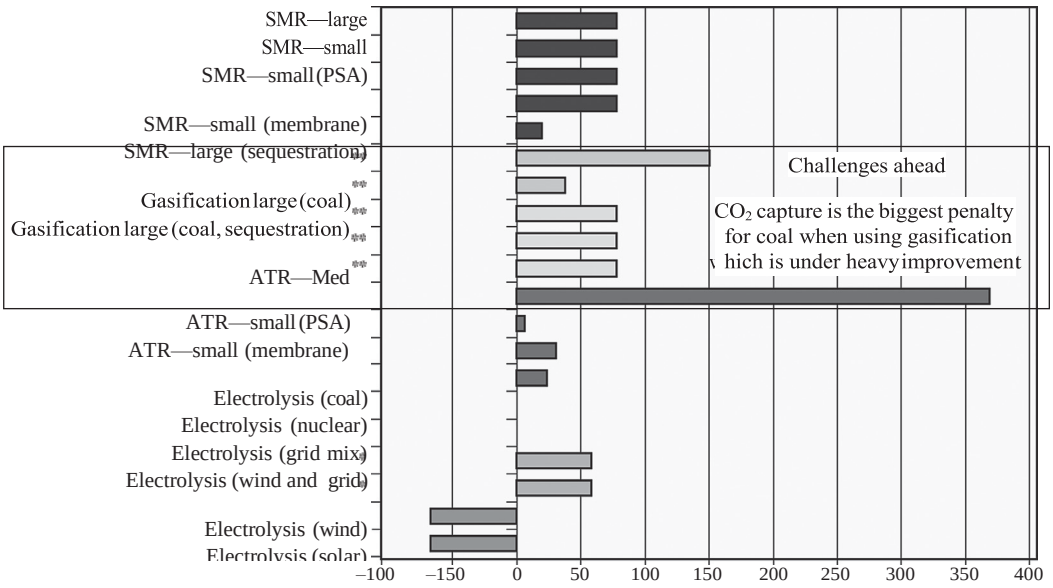


FIGURE 4.22

CO_2 emissions in kg per GJ of hydrogen produced, for various production processes. (SDTC, Renewable fuel— Hydrogen, SD Business Case, Version 1, Sustainable Development Technology Canada, Report BC_RFH_ V7.12.1_EG_061123, 2006. Available at http://www.sdtc.ca/uploads/documents/en/RenewableFuel-Hydrogen. pdf, Accessed on December 5, 2013.)

TABLE 4.5

Comparison of Hydrogen Production for Different Feedstocks[a]

Parameter	Natural Gas to H_2	Natural Gas to H_2 with CO_2 Capture	Coal to H_2	Coal to H_2 with CO_2 Capture	Biomass to H_2
Overall efficiency (%)	80	75	55	65	55
Specific capital investment (€/MW_{th})	333,000	380,000	834,000	745,000	932,000
Specific operation and maintenance costs (€/MW_{th})	18,000	43,000	38,000	79,000	39,000
Feedstock costs (€/GJ)	5.4	5.4	2.1	2.1	4.27
H_2 production costs: present (€/GJ)	8.6	10.0	8.6	10.5	12.0
H_2 production costs: 2020 (€/GJ)	10.1	11.1	8.4	8.7	10.2

Source: Data are compiled from Mueller-Langer, F. et al., *Int. J. Hydrogen Energy*, 32(16), 3797, 2007.

[a] Conversion of coal and biomass to hydrogen is via gasification.

advantageous feedstock in terms of efficiency, CO_2 capture, hydrogen production costs, capital investment and specific operation, and maintenance costs (Langer et al., 2007).

Coal is superior to biomass, with lower capital costs, feedstock costs and availability, and hydrogen production costs. But coal has higher operating costs when coupled with CO_2 capture. With CO_2 capture, the investment cost decreases for coal due to the integration of various processes. Hydrogen production costs based on direct conversion concepts have been projected for 2020 (Langer et al., 2007). The comparison is made for the following processes: natural gas steam reforming, conventional small scale (NGSRS) at 22 €/GJ; natural gas steam

reforming, conventional large scale with carbon capture (NGSTLCC) at 11 €/GJ; conventional

coal gasification, large scale (CCGL) at 10 €/GJ; conventional coal gasification, large scale with carbon capture (CCGLCC) at 11 €/GJ; advanced coal gasification, large scale with carbon capture (ACGLCC) at 9 €/GJ; and biomass gasification, large scale (BGL) at 10 €/GJ.

4.5.4 Cost of Hydrogen in World Markets

Current decentralized hydrogen production costs more than USD 50/GJ, but various centralized production options similar to the process integration shown in Figure 4.20 promise, in the long run, hydrogen prices between USD 10/GJ and USD 15/GJ. While retail hydrogen prices are sensitive to prices of feedstocks (e.g., natural gas and electricity), the cost of hydrogen through natural gas reforming may decrease to less than USD 15/GJ of H_2 by 2030, and through electrolysis, it may decrease to less than USD 20/GJ of H_2. The projected cost of hydrogen from coal gasification in centralized IGCC plants with CCS is even lower—below USD 10/GJ (IEA, 2008b). Long-term costs for high-temperature water splitting could range from USD 10/GJ (using nuclear) to USD 20/GJ (using solar heat). Higher costs are projected for other technologies.

In addition to production facilities, infrastructure needs to be developed to distribute, store, and deliver hydrogen to vehicles. The overall investment cost for this infrastructure, worldwide, is likely to be in the trillions of US dollars (DOE, 2008). Overall, the retail price of hydrogen for transportation users, reflecting all feedstock-related, capital (infrastructure), and operating costs, appears likely to remain well above USD 1.00/L of gasoline equivalent, for the foreseeable future.

4.6 Summary

This review of various stages for obtaining hydrogen using solid fuels, through selected research and development efforts on aspects of hydrogen production from solid fuels, indicates the potential for significant improvements in applications of existing processes in different ways:

- Gasification is an established primary conversion process for producing hydrogen from solid fuels, and research is ongoing in terms of design, modeling, optimiza- tion, and market applications.
- Some processes have significant applications in energy markets, including those that use plasma for gasification, SCW for gasification, and USS for gasification, as well as a solar-thermal process for direct dissociation of carbon and hydrogen from solid fuels.
- Several system-integration projects have been proposed and tested based on the applicability of associated processes to increase hydrogen production and improve overall system productivity with additional products.
- Breakthrough conversion technologies or processes that differ fundamentally from those used at present and that can increase efficiency by more than 10%–15% do not exist presently at research or commercial levels. The reason for this obser- vation is that energy research efforts are widespread, with the focus on core tech- nologies driven by market interests and demand.

- The requirements for alternative transportation fuel sources for clean and sus- tainable energy sources for power generation and less dependence on outside markets will in the near future likely drive increased research and development on new conversion processes. Circumstances at the present time appear adequate for promoting the rapid development of fundamentally different technologies for the conversion of solid fuels to hydrogen. Pressure is increasing on governments, industry, investors, and researchers to find alternatives.

A major shift is expected over the next few years in the way research is performed on the conversion of solid fuels into various energy forms, and hydrogen will likely receive the highest priority. Some research directions for converting solid fuels to hydrogen likely to receive attention include the following:

- Direct conversion of solid fuels to hydrogen and determining ways to reduce the number of steps in the processes
- Decreasing exergy losses for processes and systems and finding ways in process designs to make exergy use more efficient
- Sizing process units to reduce waste heat and entropy creation while maintaining performance
- Improving or optimizing system integration, accounting for convenient installa- tion (closeness to resource location is preferred for municipal solid waste and land- fills), low capital costs, low operating and maintenance costs, low emissions, and comparable overall efficiencies (although higher than existing plants is preferred)

The cost of hydrogen from solid fuels is expected to become competitive and may become lower than other sources, based on an adequate hydrogen infrastructure and combined research efforts from the academic and industrial workforce.

The information amalgamated here is intended to provide a useful resource that can aid researchers pursuing advanced methods for hydrogen production using solid fuels.

Acknowledgment

The authors kindly acknowledge the financial support provided by the Natural Sciences and Engineering Research Council of Canada through its Discovery Grant Program.

References

Amelio M, Marrone P, Gallucci F, Basile A. 2007. Integrated gasification gas combined cycle plant with membrane reactors: Technological and economical analysis. *Energy Conversion and Management* 48:2680–2693.

Andrus H. 2009. Chemical looping combustion coal power technology development prototype. *CO_2 Capture Technology Conference*, Pittsburgh, PA, March 24–26, 2009, US DOE/NETL.

Anheden M, Svedberg G. 1998. Exergy analysis of chemical-looping combustion systems. *Energy Conversion and Management* 39(16–18):1967–1980.

Anthony EJ. 2008. Solid looping cycles: A new technology for coal conversion. *Industrial Engineering Chemical Research* 47:1747–1754.

Asif M, Muneer T. 2007. Energy supply, its demand and security issues for developed and emerging economies. *Renewable and Sustainable Energy Reviews* 11:1388–1413.

Aznar MP, Caballero MA, Sancho JA, Frances E. 2006. Plastic waste elimination by co-gasification with coal and biomass in fluidized bed with air in pilot plant. *Fuel Processing Technology* 87:409–420.

Bargigli S, Raugei M, Ulgiati S. 2004. Comparison of thermodynamic and environmental indexes of natural gas, syngas and hydrogen production processes. *Energy* 29:2145–2159.

Basu P. 2006. *Combustion and Gasification in Fluidized Beds*. CRC Press/Taylor & Francis Group, LLC, Boca Raton, FL.

Bates BC, Kundzewicz ZW, Wu S, Palutikof JP (eds.). 2008. Climate change and water. Technical paper of the Intergovernmental Panel on Climate Change. IPCC Secretariat, Geneva, Switzerland.

Beer JM. 2000. Combustion technology developments in power generation in response to environ- mental challenges. *Progress in Energy and Combustion Science* 26:301–327.

Beer JM. 2007. High efficiency electric power generation: The environmental role. *Progress in Energy and Combustion Science* 33:107–134.

Bredesen R, Jordal K, Bolland O. 2004. High-temperature membranes in power generation with CO_2 capture. *Chemical Engineering and Processing* 43:1129–1158.

Brinkman HW, Van Eijk JPGM, Meinema HA, Terpstra RA. 2000. Processing and characteristics of TNO's hollow fibre ceramic membranes. *International Ceramics* 1:45–47.

British Petroleum. 2003. *BP Statistical Review of World Energy*. British Petroleum, London, U.K.

Brown BB, Yiridoea EK, Gordon R. 2007. Impact of single versus multiple policy options on the economic feasibility of biogas energy production: Swine and dairy operations in Nova Scotia. *Energy Policy* 35:4597–4610.

CanmetENERGY. 2005. Canada's Clean Coal Technology Roadmap. Report, CANMET Energy Technology Center, Natural Resources Canada. Ottawa, Ontario, Canada. Available at: http://canmetenergy.nrcan.gc.ca/clean-fossils-fuels/clean-coal/1806. Accessed on December 5, 2013. Carabin P, Gagnon J-R. 2007. Plasma gasification and vitrification of ash-conversion of ash into glass-like products and syngas. *2007 World of Coal Ash (WOCA)*, Covington, KY, May 7–10, 2007. Available at:

http://www.worldofcoalash.org/2007/ashpdf/148carabin.pdf. Accessed on December 5, 2013.

Chen Y, Xu H, Jin X, Xiong G. 2006. Integration of gasoline prereforming into autothermal reforming for hydrogen production. *Catalysis Today* 116:334–340.

Chiesa P, Consonni S, Kreutz T, Williams R. 2005. Co-production of hydrogen, electricity and CO_2 from coal with commercially ready technology. Part A: Performance and emissions. *International Journal of Hydrogen Energy* 30:747–767.

Chmielniak T, Sciazko M. 2003. Co-gasification of biomass and coal for methanol synthesis. *Applied Energy* 74:393–403.

Collings AF, Critchley C. 2005. *Artificial Photosynthesis: From Basic Biology to Industrial Application*.

Wiley, Weinheim, Germany.

Collot AG. 2006. Matching gasification technologies to coal properties. *International Journal of Coal Geology* 65:191–212.

Corella J, Toledo JM, Molina G. 2006. Calculation of the conditions to get less than 2 g tar/m^3 in a n

fluidized bed biomass gasifier. *Fuel Processing Technology* 87:841–846.

Damen K, van Troost M, Faaij A, Turkenberg W. 2006. A comparison of electricity and hydrogen production systems with CO_2 capture and storage. Part A: Review and selection of promising conversion and capture technologies. *Progress in Energy and Combustion Science* 32:215–246.

Damen K, van Troost M, Faaij A, Turkenberg W. 2007. A comparison of electricity and hydrogen production systems with CO_2 capture and storage. Part B: Chain analysis of promising CCS options. *Progress in Energy and Combustion Science* 33:580–609.

Dincer I, Rosen MA. 2007. *Exergy: Energy, Environment and Sustainable Development*. Elsevier, Oxford, U.K.

DOE. 2000. Gasification: Reference shelf—System studies. National Energy Technology Laboratory,

U.S. Department of Energy, Washington, DC. Accessible at: http://www.netl.doe.gov/technologies/coalpower/gasification/ref-shelf.html. Accessed on December 5, 2013.

DOE. 2005. International energy outlook. Energy Information Agency, U.S. Department of Energy, Washington, DC. Accessible at: www.eia.doe.gov/oiaf/ieo/index.html. Accessed on December 5, 2013.

DOE. April 2007. Industrial size gasification for syngas, substitute natural gas and power production. Report no. DOE/NETL-401/040607, National Energy Technology Laboratory, U.S. Department of Energy, Washington, DC.

DOE. September 2007. Hydrogen from Coal Program: Research, development and demonstration plan for the period 2007 through 2016. External Report, U.S. Department of Energy, Washington, DC. Available at: http://www.netl.doe.gov/technologies/hydrogen_clean_fuels/refshelf/pubs/External_H2_from_Coal_RDD_Plan_September_13.pdf. Accessed on December 5, 2013.

Dowaki K, Mori S, Fukushima C, Asai N. 2005. A comprehensive economic analysis of biomass gas- ification systems. *Electrical Engineering in Japan* 153(3):52–63.

Duerr M, Gair S, Cruden A. 2007. Hydrogen and electrical energy from organic waste treatment.

International Journal of Hydrogen Energy 32:705–709.

EcoEnergy. 2008. Canada's fossil energy future: The way forward on carbon capture and storage. ecoENERGY Carbon Capture and Storage Task Force Report, Government of Alberta, Calgary, Alberta, Canada, January 9, 2008. Available at: http://www.energy.gov.ab.ca/Org/pdfs/Fossil_ energy_e.pdf. Accessed on December 5, 2013.

Eldridge M, Sciortino M, Furrey L, Nowak S, Vaidyanathan S, Neubauer M, Kaufman N, Chittum A, Black S. 2009. The 2009 State Energy Efficiency Scorecard. ACEEE; Colin Sheppard, Charles Chamberlin, and Arne Jacobson, Humboldt State University; Yerina Mugica and Dale Bryk, Natural Resources Defense Council (NRDC). Report available at: http://aceee.org/research- report/e097.htm. Accessed on December 5, 2013.

Fan L, Li F, Ramkumar S. 2008. Utilization of chemical looping strategy in coal gasification processes.

Particuology 6:131–142.

Fargione J, Hill J, Tilman D, Polasky S, Hawthorne P. 2008. Land clearing and the biofuel carbon debt.

Science 319(5867):235–238.

Fleming GK, Dupuis GE. 1993. Hydrogen membrane recovery estimates. *Hydrocarbon Processing*.

Gulf Publishing Company, Houston, TX, pp. 83–86.

Furimsky E. 1998. Gasification of oil sand coke: Review. *Fuel Processing Technology* 56:263–290.

Galvita V, Messerle VE, Ustimenko AB. 2007. Hydrogen production by coal plasma gasification for fuel cell technology. *International Journal of Hydrogen Energy* 32:3899–3906.

Garcia GO, Douglas P, Croiset E, Zheng L. 2006. Technoeconomic evaluation of IGCC power plants for CO_2 avoidance. *Energy Conversion and Management* 47:2250–2259.

Gasafi E, Meyer L, Schebek L. 2007. Exergetic efficiency and options for improving sewage sludge gasification in supercritical water. *International Journal of Energy Research* 31:346–363.

Gerardi MH. 2003. *The Microbiology of Anaerobic Digesters*. John Wiley & Sons, Inc., Hoboken, NJ.

Gnanapragasam NV, Reddy BV, Rosen MA. 2009a. Reducing CO_2 emissions for an IGCC power generation system: Effect of variations in gasifier and system operating conditions. *Energy Conservation and Management* 50:1915–1923.

Gnanapragasam NV, Reddy BV, Rosen MA. 2009b. Hydrogen production from coal using coal direct chemical looping and syngas chemical looping combustion systems: Assessment of system operation and resource requirements. *International Journal of Hydrogen Energy* 34:2606–2615.

Gnanapragasam NV, Reddy BV, Rosen MA. 2010. Feasibility of an energy conversion system in Canada involving large-scale integrated hydrogen production using solid fuels. *International Journal of Hydrogen Energy* 35(10):4788–4807. doi:10.1016/j.ijhydene.2009.10.047.

Goodman BL. 1999. Stabilization: Anaerobic digestion, Chapter 7. In *Environmental Engineer's Handbook*, CRC Press/Taylor & Francis Group, LLC, Boca Raton, FL.

Guo LJ, Lu YJ, Zhang XM, Ji CM, Guan Y, Pei AX. 2007. Hydrogen production by biomass gasification in supercritical water: A systematic experimental and analytical study. *Catalysis Today* 129:275–286.

Gupta P, Velazquez-Vargas LG, Fan L-S. 2007. Syngas redox (SGR) process to produce hydrogen from coal derived syngas. *Energy and Fuels* 21:2900–2908.

Halloran JW. 2008. Extraction of hydrogen from fossil fuels with production of solid carbon materi- als. *International Journal of Hydrogen Energy* 33(9):2218–2224.

Hamelinck CN, Faaij APC. 2002. Future prospects for production of methanol and hydrogen from biomass. *Journal of Power Sciences* 111:1–22.

Harrabin R. Germany leads 'clean coal' pilot. *BBC News*, September 3, 2008. Available at: http://news.bbc.co.uk/2/hi/science/nature/7584151.stm. Accessed on December 5, 2013.

Higman C, van der Burgt M. 2008. *Gasification*, 2nd edn. Elsevier Science, Oxford, U.K.

Hofbauer H, Rauch R, Bosch K, Koch R, Aichernig C. 2003. Biomass CHP plant Gussing—A success story. In Bridgewater, A.V., ed., *Pyrolysis and Gasification of Biomass and Waste*. CPL Press, Newbury, U.K., pp. 527–536.

Hoffman Z. 2005. Simulation and economic evaluation of coal gasification with SETS reforming pro- cess for power production. MS thesis, Louisiana State University, Baton Rouge, LA.

IEA. 2006. World energy outlook 2006. International Energy Agency Report, Paris, France. IEA. 2008a. World energy outlook 2008. International Energy Agency Report, Paris, France.

IEA. 2008b. Energy technology perspectives 2008: Scenarios and strategies to 2050. International Energy Agency Report, Paris, France.

IEA. 2009. Renewables information 2009 with 2008 data. Available at www.iadb.org/intal/intalcdi/PE/2009/03711.pdf, Accessed on December 5, 2013.

International Energy Agency. 2009. Renewables Information 2009 with 2008 data. Available at www.iadb.org/intal/intalcdi/PE/2009/03711.pdf. Accessed on December 5, 2013.

Ishida M, Jin H. 1995. Chemical-looping combustion power generation plant system. US Patent No. 5,447,024. September 5, 1995.

Jahnke FC. 2003. Removal of soot in gasification system. US Patent No. 6623537.

Jin H, Ishida M. 2004. Anew type of coal gas fueled chemical-looping combustion. *Fuel* 83:2411–2417. de Jong J, Benes NE, Koops GH, Wessling M. 2004. Toward single step production of multilayer inorganic hollow fibres. *Journal of Membrane Science* 239:2656–2669.

Katofsky RE. 1993. The production of fluid fuels from biomass. Center for Energy and Environmental Studies, Princeton University, Princeton, NJ.

Kavidass S, Anderson GL, Norton GS. 2000. Why build a circulating fluidized bed boiler to generate steam and electric power. Report by the Babcock & Wilcox Company, Barberton, OH. Report No. BR-1708.

Kerry FG. 2006. *Industrial Gas Handbook: Gas Separation and Purification*. CRC Press/Taylor & Francis Group, LLC, Boca Raton, FL.

Kodama T, Gokon N. 2007. Thermochemical cycles for high-temperature solar hydrogen production. *Chemistry Review* 107:4048–4077.

Kohl AL. 1997. *Gas Purification*, 5th edn. Gulf Professional Publishing, Houston, TX.

Korens N, Simbeck DR, Wilhelm DJ. 2002. Process screening analysis of alternative gas treating and sulfur removal for gasification. Report for US Department of Energy by SFA Pacific, Inc., Engineering and Economic Consultants. Available at http://www.netl.doe.gov/technologies/coalpower/gasification/pubs/pdf/SFA%20Pacific_Process%20Screening%20Analysis_Dec%202002.pdf, Accessed on December 5, 2013.

LaCava AI, Shirley AI, Ramachandran R. 1998. How to specify pressure-swing adsorption units— Key components of PSA units. *Chemical Engineering* 105(6):110–118.

Leach BE. 1984. *Applied Industrial Catalysis*, vol. 3. Academic Press, New York.

Leung DYC, Wang CL. 2003. Fluidized-bed gasification of waste tire powders. *Fuel Processing Technology* 84(1–3):175–196.

Lewis FM. 2007. Generation of an ultra-superheated steam composition and gasification therewith.

US Patent No. US 7,229,483 B2. June 12, 2007.

Lewis FM, Swithenbank J, Hoecke DA, Russell NV, Shabangu SV. September 2002. High temperature steam-only gasification and steam reforming with ultra-superheated steam. *5th International Symposium on High Temperature Air Combustion and Gasification*, Tokyo, Japan.

Li K. 2007. *Ceramic Membranes for Separation and Reaction*. John Wiley & Sons, Ltd., West Sussex, England. Li X, Grace JR, Watkinson AP, Lim CJ, Èdenler AE. 2001. Equilibrium modeling of gasification: A free energy minimization approach and its application to a circulating fluidized bed coal gasifier.

Fuel 80:195–207.

Li Y, Guo L, Zhang X, Jin H, Lu Y. 2009. Hydrogen production from coal gasification in supercritical water with a continuous flowing system. *International Journal of Hydrogen Energy* 35(7):3036–3045. doi:10.1016/j.ijhydene.2009.07.023.

Lior N. 2008. Energy resources and use: The present situation and possible paths to the future. *Energy*

33(6):842–857.

Liu G-S, Niksa S. 2004. Coal conversion sub-models for design applications at elevated pressures.

Part II. Char gasification. *Progress in Energy and Combustion Science* 30:679–717.

Liu L, Tan X, Liu S. 2006. Yttria stabilized zirconia hollow fibre membranes. *Journal of the American Ceramic Society* 89(3):1156–1159.

Lu YJ, Jin H, Guo LJ, Zhang XM, Cao CQ, Guo X. 2008. Hydrogen production by biomass gasifica- tion in supercritical water with a fluidized bed reactor. *International Journal of Hydrogen Energy* 33:6066–6075.

Luyten J, Buekenhoudt A, Adriansens W, Cooymans J, Weyten H, Servaes F, Leysen R. 2000.

Preparation of $LaSrCoFeO_{3-x}$ membranes. *Solid State Ionics* 135:637–642.

Mahecha-Botero A, Boyd T, Gulamhusein A, Comyn N, Lima CJ, Gracea JR, Shirasakic Y, Yasudac I. 2008. Pure hydrogen generation in a fluidized-bed membrane reactor: Experimental findings. *Chemical Engineering Science* 63:2752–2762.

Mahecha-Boteroa A, Grace JR, Lim CJ, Elnashaiec SSEH, Boyd T, Gulamhusein A. 2009. Pure hydro- gen generation in a fluidized bed membrane reactor: Application of the generalized compre- hensive reactor model. *Chemical Engineering Science* 64:3826–3846.

Mahishi MR, Goswami DY. 2007. Thermodynamic optimization of biomass gasifier for hydrogen production. *International Journal of Hydrogen Energy* 32(16):3831–3840.

Manovic V, Anthony EJ, Lu DY. 2008. Sulphation and carbonation properties of hydrated sorbents from a fluidized bed CO_2 looping cycle reactor. *Fuel* 87:2923–2931.

Mattisson T, Lyngfelt A, Leion H. 2009. Chemical-looping with oxygen uncoupling for combustion of solid fuels. *International Journal of Greenhouse Gas Control* 3(1):11–19.

McKendry P. 2002. Energy production from biomass (part 3): Gasification technologies. *Bio-Resource Technology* 83:55–63.

Moghtaderi B. 2007. Effects of controlling parameters on production of hydrogen by catalytic steam gasification of biomass at low temperatures. *Fuel* 86(15):2422–2430.

Minutillo M, Perna A, Di Bona D. 2009. Modelling and performance analysis of an integrated plasma gasification combined cycle (IPGCC) power plant. *Energy Conversion and Management* 50:2837–2842.

Moriarty P, Honnery D. 2007. Intermittent renewable energy: The only future source of hydrogen?

International Journal of Hydrogen Energy 32(12):1616–1624.

Mountouris A, Voutsas E, Tassios D. 2006. Solid waste plasma gasification: Equilibrium model devel- opment and exergy analysis. *Energy Conversion and Management* 47:1723–1737.

Mountouris A, Voutsas E, Tassios E. 2008. Plasma gasification of sewage sludge: Process develop- ment and energy optimization. *Energy Conversion and Management* 49:2264–2271.

Moustakas K, Xydis G, Malamis S, Haralambous KJ, Loizidou M. 2008. Analysis of results from the operation of a pilot plasma gasification/vitrification unit for optimizing its performance. *Journal of Hazardous Materials* 151:473–480.

Mozaffarian M, Zwart RWR, Boerrigter H, Deurwaarder EP, Kersten SRA. 2004. "Green gas" as SNG (synthetic natural gas): Arenewable fuel with conventional quality. *Proceedings of the International Conference on Science in Thermal and Chemical Biomass Conversion*, August 30–September 2, Victoria, British Columbia, Canada. Paper no. ECN-RX-04-085, 17.

Mueller-Langer F, Tzimas E, Kaltschmitt M, Peteves S. 2007. Techno-economic assessment of hydrogen production processes for the hydrogen economy for the short and medium term. *International Journal of Hydrogen Energy* 32(16):3797–3810.

Mujeebu MA, Abdullah MZ, Bakar MZA, Mohamad AA, Abdullah MK. 2009. Applications of porous media combustion technology—A review. *Applied Energy* 86:1365–1375.

Muradov NZ, Veziroglu TN. 2008. "Green" path from fossil-based to hydrogen economy: An over- view of carbon-neutral technologies. *International Journal of Hydrogen Energy* 33:6804–6839.

Nagl GJ. 2005. Cleaning up gasification syngas. Technical article. Available at: http://www. gtp-merichem.com/company/overview/technical-lit/tech-papers/syngas. Accessed on December 5, 2013.

NEDO. 2004. Clean Coal Technologies in Japan, technological innovation in the coal indus- try. Technical report, New Energy and Industrial Technology Development Organization (NEDO), Kawasaki, Japan. Available at: www.nedo.go.jp/content/100079772.pdf. Accessed on December 5, 2013.

NETL. 2000. British Gas/Lurgi gasifier IGCC base cases. Report, Process Engineering Division, National Energy Technology Laboratory, US Department of Energy, Washington, DC. Report No. PED-IGCC-98-004, June.

NETL. 2009. Worldwide CO_2 capture and geologic storage Projects. Report, National Energy Technology Laboratory, US Department of Energy, Washington, DC. Available at: http://www. netl.doe.gov/technologies/carbon_seq/corerd/storage.html. Accessed on December 5, 2013.

Pandey A. 2004. *Concise Encyclopaedia of Bioresource Technology*. Haworth Press Inc., New York. Parikha J, Channiwala SA, Ghosal GK. 2005. A correlation for calculating HHV from proximate anal-

ysis of solid fuels. *Fuel* 84:487–494.

Patnaik P. 2002. *Handbook of Inorganic Chemicals*. McGraw Hill, New York.

Pei P, Kulkarni M. 2008. Modeling of ultra superheated steam gasification in integrated gasification combined cycle power plant with carbon dioxide capture. *Proceedings of Energy Sustainability*, Jacksonville, FL, August 10–14, 2008. Paper No. 54325, pp. 763–774.

Pennline HW, Luebke DR, Jones KL, Myers CR, Morsi BI, Heintz YJ, Ilconich JB. 2008. Progress in carbon dioxide capture and separation research for gasification-based power generation point sources. *Fuel Processing Technology* 89(9):897–907.

Perna A. 2008. Combined power and hydrogen production from coal: Part A—Analysis of IGHP plants. *International Journal of Hydrogen Energy* 33:2957–2964.

Ptasinski KJ, Prins MJ, Pierik A. 2007. Exergetic evaluation of biomass gasification. *Energy* 32:568–574.
Rezaiyan J, Cheremisinoff NP. 2005. *Gasification Technologies: A Primer for Engineers and Scientists*. CRC

Press, Boca Raton, FL.

Rezvani S, Huang Y, Wright DM, Hewitt N, Mondol JD. 2009. Comparative assessment of coal fired IGCC system with CO_2 capture using physical absorption, membrane reactors and chemical looping. *Fuel*. 88(12):2463–2472. doi:10.1016/j.fuel.2009.04.021.

Ross D, Noda R, Horio M, Kosminski A, Ashman P, Mullinger P. 2007. Axial gas profiles in a bubbling fluidised bed biomass gasifier. *Fuel* 86(10–11):1417–1429.

Ruthven DM, Farooq S, Knaebel KS. 1994. *Pressure Swing Adsorption*. John Wiley & Sons, New York. Rydén M, Lyngfelt A. 2006. Using steam reforming to produce hydrogen with carbon diox- ide capture by chemical-looping combustion. *International Journal of Hydrogen Energy*

31:1271–1283.

Ryu C, Nasserzadeh V, Swithenbank J. 2004. Gasification of wood char by ultra-superheated steam in an entrained flow reactor. *Journal of Energy Institute* 77:46–52.

Ryu J-S, Lee K-W, Choi M-J, Yoo H-S. 2004. The synthesis of clean fuels by F-T reaction from CO_2 rich biosyngas. *Studies in Surface Science and Catalysis* 153:47–54.

Saravanakumar A, Haridasan TM, Reed TB, Bai RK. 2007. Experimental investigations of long stick wood gasification in a bottom lit updraft fixed bed gasifier. *Fuel Processing Technology* 88(6):617–622.

SDTC. 2006. Renewable fuel—Hydrogen. SD Business Case, Version 1, Sustainable Development Technology Canada. Report BC_RFH_V7.12.1_EG_061123. Available at http://www.sdtc.ca/uploads/documents/en/RenewableFuel-Hydrogen.pdf. Accessed on December 5, 2013.

Shackley S, Gough C. 2006. *Carbon Capture and Its Storage: An Integrated Assessment*, Illustrated Edition (November). Ashgate Publishing, Aldershot, U.K.

Sheehan J, Dunahay T, Benemann J, Roessler P. 1998. A look back at the U.S. Department of Energy's Aquatic Species Program: Biodiesel from algae. National Energy Technology Laboratory, US Department of Energy, Washington, DC. Report No. NREL/TP-580-24190.

Shoko E, McLellan B, Costa D. 2006. Hydrogen from coal: Production and utilisation technologies.

International Journal of Coal Geology 65:213–222.

Sieger R, Donovon J. 2002. Biogasification and other conversion technologies. White Paper, Bioenergy Subcommittee, Water Environment Federation, Alexandria, VA. Available at: http://www.wef.org/WorkArea/DownloadAsset.aspx?id=2253. Accessed on December 5, 2013.

Sinag A, Kruse A, Schwarzkopf V. 2003. Key compounds of the hydropyrolysis of glucose in super- critical water in the presence of K_2CO_3. *Industrial Engineering Chemical Research* 42:3516–3521.

Smid J, Avci CG, Gunay V, Terstra RA, van Eijk JPGM. 1996. Preparation and characterization of microporous ceramic hollow fibre membranes. *Journal of Membrane Science* 112:85–90.

de Souza-Santos ML. 2004. *Solid Fuels Combustion and Gasification: Modeling, Simulation, and Equipment Operations*. CRC Press/Taylor & Francis Group, LLC, Boca Raton, FL.

Stiegel G. 1999. Mixed conducting ceramic membranes for gas separation and reaction. *Membrane Technology* 110:5–7.

Stiegel GJ, Ramezan M. 2006. Hydrogen from coal gasification: An economical pathway to a sustain- able energy future. *International Journal of Coal Geology* 65:173–190.

Tan X, Liu S, Li K. 2001. Preparation and characterization of inorganic hollow fibre membranes.

Journal of Membrane Science 188:87–95.

Trapp B. 2005. Coal gasification: When does it make sense? *Process PowerGen Conference*, IGCC Session, Las Vegas, NV. http://www.gasification.org/Docs/Penwell%202005/Eastman.pdf

Turner J, Sverdrup G, Mann MK, Maness P-C, Kroposki B, Ghirardi M, Evans RJ, Blake D. 2008.

Renewable hydrogen production. *International Journal of Energy Research* 32:379–407.

Twigg MV. 1996. *Catalyst Handbook*, 2nd edn. Wolfe Publishing, London, U.K., pp. 284–290.

Tzimas E, Peteves SD. 2005. The impact of carbon sequestration on the production cost of electricity and hydrogen from coal and natural-gas technologies in Europe in the medium term. *Energy* 30(14):2672–2689.

USEPA. 2008. Inventory of U.S. Greenhouse Gas Emissions and Sinks: 1990–2011. Report, US Environmental Protection Agency, Washington, DC. Available at: http://www.epa.gov/climatechange/ghgemissions/usinventoryreport.html. Accessed on December 5, 2013.

Van Oost G, Hrabovsky M, Kopecky V, Konrad M, Hlina M, Kavka T. 2009. Pyrolysis/gasification of biomass for synthetic fuel production using a hybrid gas–water stabilized plasma torch. *Vacuum* 83:209–212.

van Rossum G, Potic B, Kersten SRA, van Swaaij WPM. 2009. Catalytic gasification of dry and wet biomass. *Catalysis Today* 145(1–2):10–18.

Wall TF. 2007. Combustion processes for carbon capture. *Process Combustion Institute* 31:31–47. Wang Z, Zhou J, Wang Q, Fan J, Cen K. 2006. Thermodynamic equilibrium analysis of hydrogen pro-

duction by coal based on Coal/CaO/H_2O gasification system. *International Journal of Hydrogen Energy* 31(7):945–952.

Ward AJ, Hobbs PJ, Holliman PJ, Jones DL. 2008. Optimisation of the anaerobic digestion of agricul- tural resources. *Bioresource Technology* 99:7928–7940.

Way JD, Roberts DL. 1992. Hollow fibre inorganic membranes for gas separations. *Separation Science and Technology* 27(1):29–41.

Weinstein RE, Travers RW. 2002. Advanced Circulating Pressurized Fluidized Bed Combustion (APFBC) repowering considerations. National Energy Technology Laboratory, US Department of Energy, Washington, DC. Paper No. 970563.

Xiao G, Ni MJ, Chi Y, Cen KF. 2008. Low-temperature gasification of waste tire in a fluidized bed.

Energy Conversion and Management 49(8):2078–2082.

Xu X, Yang W, Lui J, Lin L, Stron N, Brunner H. 2004. Synthesis of NaA zeolite membrane on a ceramic hollow fibre. *Journal of Membrane Science* 229:81–85.

Xuan J, Leung MKH, Leung DYC, Ni M. 2009. A review of biomass-derived fuel processors for fuel cell systems. *Renewable and Sustainable Energy Reviews* 13:1301–1313.

Yamaguchi D, Sanderson PJ, Lim S, Aye Lu. 2009. Supercritical water gasification of Victorian brown coal: Experimental characterisation. *International Journal of Hydrogen Energy* 34:3342–3350.

Yoon HC, Erickson PA. 2008. Hydrogen from coal-derived methanol via auto-thermal reforming processes. *International Journal of Hydrogen Energy* 33:57–63.

Yoshida Y, Dowaki K, Matsumura Y, Matsuhashi R, Li D, Ishitani H, Komiyama H. 2003. Comprehensive comparison of efficiency and CO_2 emissions between biomass energy conver- sion technologies—Position of supercritical water gasification in biomass technologies. *Biomass and Bioenergy* 25:257–272.

Young L, Pian CCP. 2003. High-temperature, air-blown gasification of dairy-farm wastes for energy production. *Energy* 28(7):655–672.

Yu J, Corripio AB, Harrison DP, Copeland RJ. 2003. Analysis of the sorbent energy transfer system (SETS) for power generation and CO_2 capture. *Advances in Environmental Research* 7:335–345.

Yue GX, Yang HR, Lu JF, Zhang H. 2009. Latest development of CFB boilers in China. *20th International Conference on Circulating Fluidized Bed Combustion*. Keynote Speech, May 18–20, Xian City, China.

Yun Y, Yoo YD, Chung SW. 2007. Selection of IGCC candidate coals by pilot-scale gasifier operation.

Fuel Process Technology 88:107–116.

Zhang R, Cummer K, Suby A, Brown RC. 2005. Biomass-derived hydrogen from an air-blown gas- ifier. *Fuel Processing Technology* 86:861–874.

Zwart RWR, Bos A, Kuipers J. 2008. Principle of OLGA tar removal system. Report. Available at: https://www.ecn.nl/fileadmin/ecn/units/bio/Leaflets/b-08-022_OLGA_principles.pdf. Accessed on December 5, 2013.

2. Literature Review

Section V

Biological Hydrogen Production

9

Biological Hydrogen Production:
Dark Fermentation

Kuo-Shing Lee
Central Taiwan University of Science and Technology

Liang-Ming Whang
National Cheng Kung University

Ganesh D. Saratale
National Cheng Kung University

Shing-Der Chen
National Cheng Kung University

Jo-Shu Chang
National Cheng Kung University

Hisham Hafez
University of Western Ontario
Greenfield Specialty Alcohols

George Nakhla

University of Western Ontario

Hesham El Naggar
University of Western Ontario

CONTENTS

9.1 Introduction 250
9.2 Hydrogen Energy: Importance and Production 251
9.2.1 Features of Hydrogen Energy and Methods of Hydrogen Production 251
9.2.2 Hydrogen Production Using Dark Fermentation Process 254
9.3 Kinetics of Anaerobic Biohydrogen Production 257
9.4 Effects of Physicochemical Factors on Anaerobic Biohydrogen Production 259
9.4.1 Substrate and Microorganism Species 279
9.4.1.1 Pure Culture 279
9.4.1.2 Mixed Culture 281
9.4.1.3 Potential of Simple and Complex Substrates for Biohydrogen Production 281
9.4.2 Substrate/Product Concentration 284

9.4.3 Hydraulic Retention Time 285
9.4.4 pH..... 286

9.4.5 Temperature 287
9.4.6 Oxidation–Reduction Potential 289
9.4.7 Inorganic Nutrients 289
9.4.8 Trace Metal Elements 290
9.4.9 Hydrogen Partial Pressure (P_{H_2}) 291
9.5 Bioreactor Configuration 293
9.5.1 Continuous-Flow Stirred-Tank Reactor 293
9.5.2 Anaerobic Sequencing Batch Reactor 294
9.5.3 Membrane Bioreactor 295
9.5.4 Packed-Bed Reactor 295
9.5.5 Fluidized-Bed Reactor 296
9.5.6 Granular Sludge Reactors 297
9.6 Molecular Techniques for Microbial Community Characterization 301
9.6.1 Phylogenetic Analysis of Microbial Community in Biohydrogen Reactors 303
9.6.2 Fingerprint Methods 304
9.6.2.1 Denaturing Gradient Gel Electrophoresis 305
9.6.2.2 Terminal Restriction Fragment Length Polymorphism 305
9.7 Conclusions 307
References 308

9.1 Introduction

Over the past few decades, the global population and the demand for energy have been growing at an exponential rate. Fossil fuels are the major source of energy (about 80%) in modern society (Demirbas, 2007). On the basis of the current consumption rate, it is estimated that the present known reserves of fossil fuels will last from 41 to 700 years (Goldemberg and Johansson, 2004; Goldemberg, 2007). The limited life and the unfettered use of fossil fuels and concerns about energy security have had a negative impact on the environment because of the emission of greenhouse gases (CO_2, CH_4, and CO), which has resulted in global warming and environmental pollution (Koh and Ghazoul, 2008; Saratale et al., 2008). For these reasons, in the present century, significant efforts are being made globally toward the development of technologies that generate clean, sustainable energy sources that can be a substitute for fossil fuels. One of these is biofuel (Gong et al., 1999; Ragauskas et al., 2006). Biofuels are part of the CO_2 cycle, and their ecofriendly and sustainable nature makes them an important and promising alternative energy source for fossil fuels to protect the biosphere and prevent more localized forms of pollution (Puppan, 2002; Schubert, 2006). Due to these advantages, the worldwide production of biofuels has increased from 4.4 to 50.1 billion liters in the past few years. However, political and public support for biofuels has been shaky regarding less carbon emission of biofuel after combustion (Licht, 2008). Also, the cultivation of food crops for, and croplands dedicated to, biofuel production has resulted in food shortages and associated increasing costs of staple food crops such as maize and rice (James et al., 2008; Keeney and Hertel, 2008). Nevertheless, some scientists remain optimistic that biological processes such as H_2 and methane pro- duction under anaerobic conditions and ethanol fermentation using renewable carbon sources (waste biomass) will minimize the negative environmental and social impacts

and that these resources will not compete directly with food production, or with land that may be needed for food production (Slade et al., 2009). Some also assume that bio- mass energy will play a pivotal role in future energy supply for there are large amounts of waste biomass available in the form of organic residues such as municipal wastes, manure, and forest and agricultural residues (Kapdan and Kargi, 2006; Ragauskas et al., 2006; Field et al., 2008).

Among the processes mentioned earlier, H_2 is considered a clean and renewable energy resource, not contributing to the greenhouse effect because it produces water instead of greenhouse gases after undergoing combustion, with a high energy yield of 122 MJ/kg, which is up to three times greater than that of hydrocarbon fuels (Kapdan and Kargi, 2006; Lo et al., 2008b). Moreover, H_2 has a heating value of 61,100 Btu/lb, almost three times that of methane (23,879 Btu/lb) (Bossel, 2003). Thus, it has been predicted that H_2 will be the main source of energy and a potential substitute for fossil fuels by the year 2100 (Dunn, 2002). Conventional physicochemical methods for H_2 gas production do not accomplish the dual goals of waste reduction and energy production. Furthermore, these methods require such large inputs of energy derived from fossil fuel combustion that they do not qualify as alternative renewable energy sources (Vijayaraghavan and Soom, 2007; Das and Veziroglu, 2008). For global environmental considerations, microbial H_2 production represents an important area of bioenergy production.

Over the past quarter century, many hundreds of publications have focused on microbial H_2 production, but advances toward practical applications have been minimal (Hallenbeck and Benemann, 2002; Show et al., 2008). From an economic point of view, it cannot be expected that biohydrogen production will compete with chemically synthesized H_2 in the next few decades (Akkerman et al., 2002; Kotay and Das, 2008). However, H_2 production from waste materials through dark fermentation by using specific microorganisms is an economically feasible process and is expected to become important in bioenergy production. In the past, the microbial communities in the bioreactor were usually regarded as a *black box*. Many reviews focusing on the fundamentals of biohydrogen production (Hallenbeck and Benemann, 2002; Vijayaraghavan and Soom, 2007; Kotay and Das, 2008; Saratale et al., 2008; Wang and Wan, 2009), metabolism, and bioreactor design for photofermentation (Akkerman et al., 2002; Koku et al., 2002) have been published of late. Nevertheless, there are only few studies on how molecular biotechnology is related to the dark fermentation process. In this chapter, we assess the effect of various factors influencing biohydrogen production, kinetics, and types of reactors for dark fermentation. We also discuss the existing molecular tools for improving microbial H_2 production under dark fermentation.

9.2 Hydrogen Energy: Importance and Production

9.2.1 Features of Hydrogen Energy and Methods of Hydrogen Production

Present-day energy consumption is unsustainable because of equity issues, geopolitical concerns, and the energy paradigm based on fossil fuel dependency that is contributing toward economic and environmental challenges (UNDP, 2000). H_2 is strategically important because of its low emission, representing a cleaner and more sustainable energy

system and having many social, economic, and environmental benefits (Bockris, 2002; Maddy et al., 2003). H_2 acts as a versatile energy carrier with the potential for extensive use in power generation and in many other applications. H_2 gas is widely used as a feedstock for the production of chemicals (ammonia and methanol), in oil refineries for removing impurities or for upgrading heavier oil fractions into lighter and more valuable products, for the production of electronic devices, and for processing steel, desulfurization, and the reformulation of gasoline in refineries; it is also used in the world's space programs (1%) (Elam et al., 2003; Vijayaraghavan and Soom, 2007). The concept of H_2 economy has been presented as a clean and efficient replacement for the petroleum-based economy and recognized by many national and international bodies, for example, the US Department of Energy (US-DOE), the International Partnership for the H_2 Economy (IPHE), and the European H_2 Association (EHA) (Kyazze et al., 2008). Based on the National H_2 Program of the United States, the contribution of H_2 to the total energy market is expected to be 8%–10% by 2025 (Armor, 1999). Technical chal- lenges in attaining a H_2 economy are the cost-effective process for H_2 production, stor- age, delivery, and their practical applications. Conventional physicochemical methods for H_2 production were based on steam reforming of natural gas (methane and other hydrocarbons), partial oxidation of heavier hydrocarbons, coal gasification, electroly- sis of water, and pyrolysis or gasification. However, all these methods usually involve complicated procedures and require a source of energy derived from fossil fuels. This makes them economically unfeasible and not always environmentally benign (Das and Veziroglu, 2001; Momirlan and Veziroglu, 2002).

H_2 has attracted worldwide attention as a clean energy source. However, due to its unavailability in nature, there has been focus on the development of cost-effective and efficient H_2 production technologies in recent years (Kapdan and Kargi, 2006; Gustavo et al., 2009). Biological H_2 production has assumed importance as an alternative and renewable bioenergy resource because of certain advantages such as mild reaction conditions, low cost, low energy requirement; also, it is well suited for decentralized energy production in small-scale installations in locations where biomass or wastes are available, thus avoiding energy expenditure and transport costs (Saratale et al., 2008; Wang and Wan, 2009). Biohydrogen production also provides a feasible means for the sustainable supply of H_2 with low energy and high efficiency, and is there- fore being considered for producing H_2 (Hallenbeck, 2005). In addition, biohydrogen production is important for energy security reasons, environmental concerns, foreign exchange savings, and socioeconomic issues related to the rural sector of all countries in the world (Hallenbeck, 2009). In the past few decades, research on biological H_2 pro- duction has been carried out and a broad spectrum of biological H_2 production pro- cesses has been investigated. Methods adopted to produce H_2 from biological methods can be classified into the following groups: (1) biophotolysis of water using algae/ cyanobacteria, (2) photodecomposition (photofermentation) of organic compounds using photosynthetic bacteria, (3) dark fermentative H_2 production using anaerobic or facultative anaerobic bacteria, (4) bioelectrohydrogenesis or microbial fuel cell (MFC) (Asada and Miyake, 1999; Ghirardi et al., 2000; Das and Veziroğlu, 2001; Koku et al., 2002; Chen et al., 2008b).

Among the processes mentioned earlier, biohydrogen production by anaerobic dark fermentation has the best potential for practical applications (Levin et al., 2004) (Table 9.1). After the mid-1990s, significant attention has been paid to H_2 production by anaerobic

TABLE 9.1

Comparison of Important Biological Hydrogen Production Processes

Biological Process	Advantages	Disadvantages
Direct and indirect biophotolysis	Can produce H_2 directly from water and sunlight Solar conversion energy increased by 10-fold as compared to trees, crops, can produce H_2 from water, and has the ability to fix N_2 from atmosphere	Natural-borne organisms of these species examined so far show rather low rates of H_2 production due to the complicated reaction systems and inhibition of the hydrogenase enzyme by oxygen. Another drawback encountered is the requirement of a carrier gas to collect the evolved gas from the culture.
Photofermentation	A wide spectral light energy can be used by these bacteria Can use different waste materials like distillery effluents and waste	This process requires high activation energy to drive nitrogenase, which is the enzyme responsible for H_2 production in photosynthetic bacteria. Low solar conversion efficiencies, typically not much higher than that for algal biophotolysis systems. In addition, phototrophic H_2 production with photosynthetic bacteria is extremely doubtful due to ammonia and oxygen contents, making it difficult in practical applications.
Dark fermentation	Some basic advantages relative to other processes include process simplicity on technical grounds, low energy requirements, higher rates of H_2 production, economically feasible or better process economy, and the ability to generate H_2 from a large number of carbohydrates (or other organic materials) frequently obtained as refuse or waste products. It can produce H_2 all day long without light It produces valuable metabolites such as butyric, lactic, and acetic acids as by-products It is an anaerobic process, so there is no O_2 limitation problem	Low H_2 yield compared to physicochemical methods. The major drawback is that these bacteria are unable to overcome the inherent thermodynamic energy barrier to full substrate decomposition due to which low H_2 yields was observed.

dark fermentation (Levin et al., 2004). Compared to other biological processes, dark fermentation has some basic advantages such as the simplicity of the process on technical grounds, low energy requirements, higher rates of stable H_2 production, economically more feasible or better process economy, and the production of H_2 from a large number of carbohydrates frequently obtained as refuse or waste products (Benemann, 1996; Nandi and Sengupta, 1998; Levin et al., 2004; Hallenbeck et al., 2009; Wang and Wan, 2009). Dark fermentation normally achieves a much higher H_2 production rate than photolysis and photofermentation, and this higher rate depends upon various factors such as the fermentation metabolic pathway, hydrogenase activity, substrate types. The theoretical maximum H_2 production yield (12 mol H_2/mol glucose) can be engineered by using suitable organisms, but it seems to be difficult to carry out in living cells (Woodward, 2000). To achieve this yield, most of the research has focused on biohydrogen produc- tion from organic wastes by using photosynthetic bacteria over the past two decades (Sasikala et al., 1993). Recent studies show that biohydrogen production using negative- value organic waste streams under dark fermentation is a more promising approach than the use of photosynthetic bacteria (Ueno et al., 1995; Benemann, 1998; Chen et al., 2001; Lo et al., 2009). However, in dark H_2 fermentation, the major drawback is that these bacteria are unable to overcome the inherent thermodynamic energy barrier to full sub- strate decomposition due to which low H_2 yields are observed (Hallenbeck, 2005; Kotay and Das 2008).

9.2.2 Hydrogen Production Using Dark Fermentation Process

Fermentative conversion of substrates to H_2 is a complex biochemical process manifested by diverse groups of bacteria by a series of biochemical reactions under anoxic conditions (i.e., no oxygen present as an electron acceptor) (Valdez-Vazquez and Poggi-Varaldo, 2009). In case of complex organic polymers, bacteria grow on these organic substrates (heterotrophic growth), which are degraded by oxidation to yield monomer units and metabolic energy for growth. It is also noteworthy that when bacteria degrade organic substrates, electrons needed to be disposed to maintain electrical balance are produced. In aerobic environments, reduction of oxygen yields water as the product, whereas in anaerobic environments, protons (H^+) derived from water are reduced to molecular H_2 (H_2) (Das and Veziroglu, 2001; Levin et al., 2004). In general, hydrogen-producing acidogenic bacteria oxidize fermentation products to acid intermediates and H_2 (e.g., production of H_2 and CO_2 by acetogens and homoacetogens), and finally acetoclastic methanogens convert the acid intermediates into methane and CO_2 (Liu et al., 2008; Hallenbeck et al., 2009) (Figure 9.1). In addition, when sulfates or nitrates are present, sulfate-reducing bacteria (SRB) and nitrate-reducing bacteria (NRB) are capable of using H_2 as an elec- tron donor and generating sulfides and ammonia, respectively (Valdez-Vazquez and Poggi-Varaldo, 2009).

When glucose is used as the model substrate for fermentative H_2 production, it is first converted by hydrogen-producing bacteria to pyruvate, via the Embden–Meyerhof– Parnas or glycolytic pathway, producing the reduced form of nicotinamide adenine dinucleotide (NADH). In most *Clostridial* fermentation, pyruvate is then converted to acetyl-CoA and CO_2 by pyruvate:ferredoxin oxidoreductase. In addition to the forma- tion of acetyl-CoA and CO_2, an iron–sulfur protein called ferredoxin, which acts as elec- tron carrier of low redox potential, is also reduced in this reaction. As described earlier,

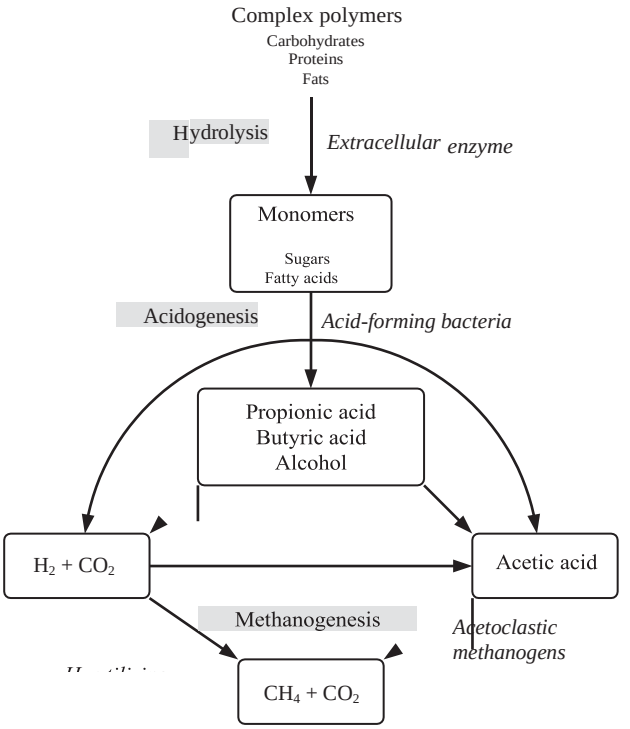


FIGURE 9.1

Schematic description of anaerobic digestion process. (Adapted from Malina, J.F. and Pohland, J.F.G., *Design of Anaerobic Processes for the Treatment of Industrial and Municipal Wastes*, Technomic Pub Co, Lancaster, PA, 1992.)

electrons from the reduced ferredoxin are transferred via hydrogenase to H^+, so that molecular H_2 is formed (Equations 9.1 and 9.2). Pyruvate may also be converted to acetyl-CoA and formate, which may readily be converted to H_2 and carbon dioxide (Nath and Das, 2003; Lee et al., 2004a; Turner et al., 2008). The transfer of electrons from ferredoxin to H^+ is catalyzed by the enzyme called hydrogenase, as illustrated in Figure 9.2 (Brock et al., 1994).

$$\text{Pyruvate} + \text{CoA} + 2\text{Fd (ox)} \rightarrow \text{acetyl-CoA} + 2\text{Fd (red)} + \text{CO}_2 \tag{9.1}$$

$$2\text{H}^+ + \text{Fd (red)} \rightarrow \text{H}_2 + \text{Fd (ox)} \tag{9.2}$$

The fate of acetyl-CoA varies among different *Clostridial* species. It can be converted into some soluble metabolites such as ethanol, acetate, butyrate, and lactate. The amount of H_2 evolved depends on the ratio of the end products formed (Das, 2009). Theoretically, the maximum H_2 yield is 4 mol H_2/mol glucose when glucose is completely metabolized to

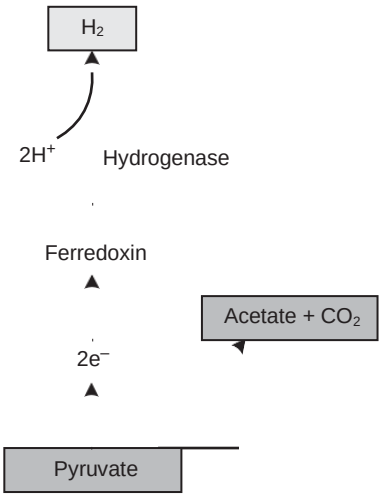


FIGURE 9.2

Production of molecular H_2 from pyruvate. (From Brock, T.D. et al., *Biology of Microorganisms*, 7th edn., Prentice- Hall, Englewood Cliffs, NJ, 1994.)

acetate. The overall stoichiometry is indicated by Equation 9.3 (Ueno et al., 1995; Hawkes et al., 2002; Levin et al., 2004):

$$C_6H_{12}O_6 + 2H_2O \rightarrow 2CH_3COOH + 4H_2 + 2CO_2 \quad (9.3)$$

And according to Equation 9.4, half of this H_2 yield (2 mol H_2/mol glucose) is obtained when butyrate is the fermentation end product:

$$C_6H_{12}O_6 \rightarrow C_3H_7COOH + 2H_2 + 2CO_2 \quad (9.4)$$

The reactions involved in dark fermentative H_2 production (Equations 9.3 and 9.4) are faster and do not rely on the availability of light sources, making them useful for treating a wide spectrum of potentially utilizable substrates, including refuse and waste products, by using appropriate fermenters. Strictly anaerobic bacteria give 4 mol H_2 mole of glucose, whereas facultative anaerobic bacteria give 2 mol of H_2/mole of glucose. Facultative anaerobes were found to be less sensitive to oxygen and were able to recover H_2 production activity after accidental oxygen damage to them by rapidly consuming oxygen present in the broth. Thus, facultative anaerobes are considered to be better than strict anaerobes for the fermentative H_2 production process. However, one of the main constraints in the practical application of anaerobic fermentation is a H_2 yield lower than 4 mol H_2/mol glucose (usually in the range of 0–2 mol H_2/mol glu- cose). This might be due to the formation of mixed acidogenic (VFA) and alcoholic fer- mentation end products. Reduced fermentation end products, such as ethanol, butanol, and lactate, contain H_2 that has not been liberated as gas. It was assumed that by modi- fying the fermentation pathways, a maximum of 4 mol H_2/mol glucose can be expected from ideal acetate fermentation. However, this yield is still low compared to existing chemical or electrochemical processes of H_2 generation (Hallenbeck and Benemann, 2002) and makes biological H_2 production economically unfeasible. Therefore, in this

chapter, we will focus on research and development of dark fermentative H_2 production as well as on a critical discussion of the various practical and theoretical approaches toward improvement of overall H_2 production in a dark fermentative process.

9.3 Kinetics of Anaerobic Biohydrogen Production

Reaction kinetic study provides a rational basis for process analysis, control, and design. The kinetic constants obtained are important to develop H_2-producing processes. Most popularly, the modified Gompertz equation (Equation 9.5) has been used to describe the cumulative H_2 production process obtained from a batch experiment (Lay et al., 1999; Van Ginkel et al., 2001; Chen et al., 2002; Khanal et al., 2004; Lin and Lay, 2004b; Lin and Lay, 2005; Fang et al., 2006; Mu et al., 2006a). In this model, the population of bacteria is expressed as a function of the reaction time, and the overall stoichiometry of the model (Equation 9.5) is as follows:

$$H = P \cdot \exp\left\{-\exp\left[\frac{R_m \cdot e}{P}(\lambda - t) + 1\right]\right\} \tag{9.5}$$

where

H (mL) is the total amount of H_2 produced at incubation time t (h)
P (mL) is the potential maximal amount of H_2 produced
R_m (mL/h) is the maximal H_2 production rate
λ (h) is the lag time to exponential H_2 production
e = 2.71828

Lin and Lay (2004b) checked the effects of carbonate and phosphate concentrations on biological H_2 production obtained from the Taguchi orthogonal array by fitting the cumulative H_2 production data with the modified Gompertz equation. The correlation coefficient values ranged over 0.996–0.999. Recently, the kinetic parameters of H_2 production from rice slurry with acidophilic hydrogen-producing sludge at feedstock concentrations from 2.7 to 22.1 g carbohydrate/L were determined by using the modified Gompertz equation (Fang et al., 2006). In this study, the highest H_2 yield (346 mL/g carbohydrate) was obtained at a concentration of 5.5 g carbohydrate/L. In addition, the individual and interactive effects of pH, temperature, and substrate concentration on biohydrogen production from sucrose by mixed anaerobic cultures were determined by combining the modified Gompertz equation with response surface methodology (RSM) (Mu et al., 2006b). The results showed that pH, temperature, and sucrose concentration have a significant impact on the specific H_2 production potential. The maximum sucrose yield of 252 mL H_2/g was estimated under the optimum conditions of pH 5.5, temperature 34.8°C, and sucrose concentration 24.8 g/L, while R_{max} of 504 mL H_2/h/L was calculated under the optimum conditions of pH 5.5, temperature 35.5°C, and sucrose concentration 25.4 g/L.

The Monod model is also useful and employed most frequently to describe the kinetics of anaerobic biohydrogen production (Bailey and Ollis, 1986). The overall stoichiometry of the Monod model (Equation 9.6) is as follows:

$$\mu = \frac{\mu_{max} S}{K_s + S} \tag{9.6}$$

where

μ is the specific growth rate

μ_{max} is the maximum specific growth rate

S is the substrate concentration

K_s is the Monod constant, the concentration of the limiting nutrient at which the specific growth rate is half of its maximum value

Chen et al. (2001) used the Monod model to describe and predict the kinetic proper- ties of H_2 production from sucrose in the anaerobic mixed culture. The μ_{max}, K_s, and yield coefficient for cell growth ($Y_{x/s}$) were estimated as 0.172 h^{-1}, 68 mg COD/L, and 0.1 g/g, respectively. In addition, the Michaelis–Menten equation (Bailey and Ollis, 1986) was also employed to describe the kinetics of many anaerobic biohydrogen productions. The over- all stoichiometry (Equation 9.7) is as follows:

$$v = \frac{v_{max} S}{K_m + S} \tag{9.7}$$

where

v is the H_2 production rate

v_{max} is the maximum H_2 production rate

K_m is the half-saturation constant

S is the concentration of the substrate

The Michaelis–Menten equation was used to determine the growth kinetics of hydrogen- producing bacteria and the H_2 production rate using different substrates and concentrations, namely, sucrose, nonfat dry milk (NFDM), and food waste, under dark fermentation in batch mode. Results showed that the H_2 production potential and H_2 production rate increased with increasing substrate concentration. The maximum H_2 yields from sucrose, NFDM, and food waste were 234, 119, and 101 mL/g COD, respec- tively (Chen et al., 2006).

Wu et al. (2002) studied the kinetic performance of H_2 fermentation from sucrose using a variety of immobilized-cell systems, activated carbon (AC), polyurethane (PU), and acrylic latex plus silicone (ALSC). The dependence of the specific H_2 pro- duction rate (v_s) of the three types of immobilized cells on sucrose concentration was interpreted with Michaelis–Menten kinetics. In this study, the $v_{s,max}$ and K_m val- ues were estimated from the experimental data via numerical simulation. Results showed that CA/AC (addition of activated carbon into alginate gel) cells have con- siderably higher $v_{s,max}$ and K_m values than those obtained from the other two types of immobilized cells. In the Michaelis–Menten model, the maximal rate (e.g., $v_{s,max}$) is considered a linear function of total active biocatalyst concentration, while the K_m

value is inversely proportional to the affinity between the biocatalyst and the sub- strate (Bailey and Ollis, 1986). Thus, the higher $v_{s,max}$ value of CA/AC cells represents a higher concentration of *active* biocatalyst than that of PU and ALSC cells. The H_2 production by EVA (ethylene–vinyl acetate copolymer)–immobilized acclimated sewage sludge using sucrose as the sole carbon substrate was reported earlier (Wu et al., 2005). Kinetic studies show that the Michaelis–Menten equation is able to describe the dependence of specific H_2 production rate on sucrose concentration. The EVA-immobilized cells achieved an optimal specific H_2 production rate of 488 mL H_2/g VSS/h (sucrose concentration = 40 g COD/L) and the highest H_2 yield of 1.74 mol H_2/mol (sucrose concentration = 20 g COD/L).

Some scientists developed a new least-squares method to describe the kinetics and to estimate the kinetic parameters (Y_g and k_d) (Equation 9.8) for H_2 production from sucrose in an upflow anaerobic sludge blanket (UASB) (Yu and Mu, 2006). These two parameters could provide useful information for designing an effective granule-based UASB system for H_2 production. The parameters Y_g and k_d could be estimated using the least-squares method by plotting $R_{S/X}$ versus (1/HRT). The Y_g and k_d of the H_2-producing granules were estimated to be 0.334 g VSS/g COD and 0.004 h^{-1}, respectively. In some reports, the sludge yield in CSTR (ranging from 0.116 to 0.240 g VSS/g COD) was higher than that of the H_2-producing granule using sucrose as substrate (Liu and Fang, 2002). The kinetic parameters of biological H_2 production in the literature are summarized in Table 9.2.

$$R_{S/X} = \frac{1}{Y_g} \times \frac{1}{\text{HRT}} + \frac{k_d}{Y_g} \tag{9.8}$$

where

$R_{S/X}$ (g COD/g VSS/h) is the specific substrate utilization rate
Y_g (g VSS/g COD) is the sludge yield, expressing the cell mass produced per unit substrate consumed
k_d (h^{-1}) is the endogenous decay coefficient

9.4 *Effects of Physicochemical Factors on Anaerobic Biohydrogen Production*

Biohydrogen production is a complex process and is greatly influenced by many factors. These include microorganism seeding, substrate specificity, organic loading rate (OLR), hydraulic retention time (HRT), pH, temperature, metal ion, oxidation–reduction potential (ORP), nutritional requirements, H_2 partial pressure in the reactor, and reactor configuration. The effects of these factors on fermentative H_2 production have been reported by a number of studies worldwide in the past few years (Hawkes et al., 2002, 2007; Nishio and Nakashimada, 2004; Kapdan and Kargi, 2006; Kraemer and Bagley, 2008; Li and Fang 2007a; Das and Veziroglu, 2008; Wang and Wan, 2009). The literature reviews regarding the effects of these factors on biohydrogen production are summarized in Tables 9.3 through 9.8.

Free ebooks ==> www.Ebook777.com

TABLE 9.2

Comparison of Kinetic Parameters for H_2 Fermentation in Different H_2-Producing Systems

Hydrogen Producer	Culture Type	Substrate	Temperature (°C)	μ_{max}[a] (h^{-1})	v_{max}[b] (mL/h/L)	v_s[b] (mL/h/g VSS)	K^a/K^b (g COD/L)	Y (g Biomass/g Substrate)	References
Sewage sludge	CSTR	Sucrose	35	0.172	NA		0.068	0.1	Chen et al. (2001)
Anaerobically	Batch	Sucrose	36	ND	92.7		1.446	ND	Chen et al. (2006)
digested sludge	Batch	Nonfat dry milk	36	ND	170.7		6.616	ND	
	Batch	Food waste	36	ND	199.3		8.692	ND	
Anaerobically	CSTR	Glucose	37	0.33	NA		NA	0.26	Horiuchi et al.
digested sludge									(2002)
Sewage sludge	Batch								Wu et al. (2002)
(immobilized	CA/AC	Sucrose	35			8033	8.962		
cells)	PU	Sucrose	35			1225	4.279		
	ALSC	Sucrose	35			2640	9.46		
Sewage sludge	Batch/ without acclimation	Sucrose	40			278	20.0		Wu et al. (2005)
(EVA-immobilized cells)		Sucrose	40			468	10.0		
	acclimation								

Note: VSS, volatile suspended solid; COD, chemical oxygen demand; ND, not determined.

[a] For Monod equation: $\mu = \frac{\mu_{max} S}{K_s + S}$.

www.Ebook777.com

[b] For Michaelis–Menten equation: $v = \frac{v_{max} S}{K_m + S}$, $v_s = \frac{v_{s,max} S}{K_m + S}$.

TABLE 9.3

Hydrogen Production Rates and Yield Coefficients from Pure and Complex Substrates Using Pure and Mixed Culture under Batch Operation

Substrate (Concentration, g/L)	H_2 Producer	Temperature (°C)	pH	H_2 Yield (mol H_2/mol Hexose)	H_2 Production Rate (mol H_2/L/day)	References
Glucose (4)	*Escherichia coli* strains	37	7.0	2	NA	Bisaillon et al. (2006)
Raw sludge (11.5 g COD/L)	Raw sludge	36	11 (initial)	0.45 mmol H_2/g COD	NA	Cai et al. (2004)
Alkaline-treated sludge (11.5 g COD/L)	Alkaline-treated sludge	36	11 (initial)	0.83 mmol H_2/g COD		
Sucrose (4.5 g COD/L)	Anaerobic digester	36	5.5 (initial)	9.55 mmol H_2/g COD	NA	Chen et al. (2006)
Nonfat dry milk (4.0 g COD/L)	Sludge	36	5.5 (initial)	4.86 mmol H_2/g COD		
Food waste (4.6 g COD/L)		36	5.5 (initial)	4.12 mmol H_2/g COD		
Sucrose (17.8)	*Clostridium butyricum* CGS5	37	5.5	1.39	0.160	Chen et al. (2005)
			6.0	0.73	0.205	
Hydrolyzed starch (26.7 g COD/L)	*Clostridium butyricum* CGS2	37	7.5 (initial)	1.23	0.162	Chen et al. (2008b)
	Clostridium butyricum CH5			1.25	0.171	
Glucose (21.3)	Anaerobic sludge (acid treatment)	35	5.7	0.98	0.214	Cheong and Hansen (2006)
Glucose (20)	*Clostridium acetobutylicum*	37	6.0	2.0	NA	Chin et al. (2003)
Hydrolyzed corn stover biomass (glucose 138 mM)	Dried mixed sludge	35	5.5	2.86	0.567	Datar et al. (2007)
N-acetyl-v-glucosamine (GlcNAc) (10)	*Clostridium paraputrificum* M-21	45	6.0	2.2 mol/mol GlcNAc	NA	Evvyernie et al. (2001)
Starch hydrolysate (20)	*Enterobacter aerogenes*	40	6.5	1.09	0.417	Fabiano et al. (2002)
HCl pretreated wheat straw (25)	Microflora from a cow dung compost (heat treatment)	36	7.0 (initial)	2.78 mmol H_2/g TVS/h	NA	Fan et al. (2006b)

(*continued*)

TABLE 9.3 (continued)

Hydrogen Production Rates and Yield Coefficients from Pure and Complex Substrates Using Pure and Mixed Culture under Batch Operation

Substrate (Concentration, g/L)	H_2 Producer	Temperature (°C)	pH	H_2 Yield (mol H_2/mol Hexose)	H_2 Production Rate (mol H_2/L/day)	References
Rice slurry (5.5 g-carbohydrate/L)	Anaerobic digester sludge	37	4.5	346 mL/g carbohydrate	NA	Fang et al. (2006)
			6.5	223 mL/g carbohydrate		
Xylose (3.2)	*Thermoanaerobacter finnii*	60	6.4	0.49 mol/mol xylose	0.14 mL/h/L	Fardeau et al. (1996)
Crude cheese whey (ca. 41.4 g lactose/L)	*Clostridium saccharoperbutylacetonicu* ATCC 27021	30	6.0 (initial)	2.7 mol H_2/mol lactose	0.139	Ferchichi et al. (2005)
Sterilized waste sludge (16 g TOCD/L)	*Pseudomonas* sp. GZ1	35	7.38	15.02 mL/g TCOD	NA	Guo et al. (2008)
Glucose (118 mM)	*Enterobacter aerogenes*	38	6.13	NA	425.8 mL H_2/g dry cell/h	Jo et al. (2008)
Glucose (10)	*Caldicellulosiruptor saccharolyticus*	70	6.4	2.53 mol/mol glucose	0.257	Kadar et al. (2004)
Xylose (10)				2.24 mol/mol xylose	0.273	
Glucose (20)	Aerobic and anaerobic sludges, soil and lake sediment (acid and heat conditioned)	35	6.0	1.4	NA	Kawagoshi et al. (2005)
Sucrose (10)	Compost material	37	4.5	214 mL H_2/g COD	NA	Khanal et al. (2004)
Starch (10)			4.5	125 mL H_2/g COD		
Glucose (10)	Defined consortium (1:1:1, and separately tested): *Enterobacter cloacae* IIT-BT 08, *Citrobacter freundii* IIT-BT L139, *Bacillus coagulans*	37	6.0	41.23 mL H_2/g $COD_{removed}$	NA	Kotay and Das (2006)

Cellobiose (10)	*Enterobacter cloacae*	36	6.0	2.7 mol H_2/mol hexose	0.637	Kumar and Das (2000)
l-Arabinose (10)	IIT-BT 08			1.5 mol H_2/mol arabinose	0.353	
Fructose (10)				1.6 mol H_2/mol hexose	0.431	
Maltose (10)				0.7 mol H_2/mol hexose	0.176	
Potato starch (10)				NA	0.196	
C.M. cellulose (10)				NA	0.086	
d-Xylose (10)				0.95 mol H_2/mol xylose	0.341	
Dextrose (10)				2.2 mol H_2/mol hexose	0.438	
Sucrose (10)				3.0 mol H_2/mol hexose	0.647	
Fodder maize Chicory Fructooligosaccharides Perennial ryegrass (*Lolium perenne*)	Heat-treated anaerobically digested sludge	35	5.2–5.3	62.4 mL/g dry matter of fodder maize 218 mL/g chicory fructooligosaccharides 75.6 mL H_2/g dry matter of wilted perennial ryegrass 21.8 mL H_2/g dry matter of fresh perennial ryegrass	NA	Kyazze et al. (2008)
Microcrystalline cellulose (12.5) Microcrystalline cellulose (25)	Anaerobic digested sludge	37	7.0 (initial)	2.18 mmol H_2/g cellulose 1.60 mmol H_2/g cellulose	NA	Lay (2001)
Sucrose (10)	Mixed microbial flora	37	9	1.77	NA	Lee et al. (2002)
Cassava starch (20.3)	Municipal sewage sludge	37	6.0	9.47 mmol H_2/g starch	1.10	Lee et al. (2008)
Cassava starch (20.3)			(initial)	11.25 mmol H_2/g starch	1.05	
α-Cellulose (0.1) Filter paper (0.1) Delignified wood (0.1) Cellobiose (0.1)	*Clostridium thermocellum* 27405	60	7.0	1.9 1.7 2.3 1.6	NA	Levin et al. (2006)

(*continued*)

TABLE 9.3 (continued)

Hydrogen Production Rates and Yield Coefficients from Pure and Complex Substrates Using Pure and Mixed Culture under Batch Operation

Substrate (Concentration, g/L)	H_2 Producer	Temperature (°C)	pH	H_2 Yield (mol H_2/mol Hexose)	H_2 Production Rate (mol H_2/L/day)	References
Peptone (0.1)	Anaerobic sludge	35	7.0	1.7 mmol H_2/g peptone	NA	Liang (2003)
Peptone (0.3)			(initial)	2.2 mmol H_2/g peptone		
Peptone (0.6)				2.1 mmol H_2/g peptone		
Xylose (18.75)	Sludge	35	6.5	2.25	0.086	Lin and Cheng (2006)
Cellulose (3)	Anaerobic cow dung microflora	55	7.0	2.8 mmol H_2/g cellulose	NA	Lin and Hung (2008)
Sucrose (8.9) (C/N ratio = 47)	Sewage sludge	35	6.8	2.4	NA	Lin and Lay (2004a)
Sucrose (8.9)	Sewage sludge	35	6.8	1.72	NA	Lin and Lay (2005)
Starch (20 g COD/L)	Anaerobic sludge	35	5.5	1.1	0.250	Lin et al. (2008a)
Microcrystalline cellulose (5)	*Clostridium thermocellum* JN4 + *Thermoanaerobacterium thermosaccharolyticum* GD17	60	7.0	1.8	NA	Liu et al. (2008)
Xylose (18.75)	*Clostridium butyricum* CGS5	37	7.5 (initial)	0.73 mol/mol xylose	0.208	Lo et al. (2008b)
Xylose (37.5)	*Clostridium butyricum* CGS5	37	7.5 (initial)	0.68 mol/mol xylose	0.264	
Sucrose (35.6)	*Clostridium pasteurianum* CH_4	37	7.5 (initial)	1.04 mol/mol hexose	0.557	
Hydrolyzed carboxymethyl cellulose (10)	*Clostridium pasteurianum*	35	7.0	1.09 mmol H_2/g cellulose	NA	Lo et al. (2008a)
Rice husk hydrolysate (10)	*Clostridium butyricum* CGS5	35	7.0	17.24 mmol H_2/g rice husk hydrolysate	NA	Lo et al. (2009)
Glucose (4 g COD/L)	Heat-shocked mixed cultures	26	6.0	125 mL H_2/g COD	NA	Logan et al. (2002)
Sucrose (4 g COD/L)				131 mL H_2/g COD		

Molasses (4 g COD/L)	134 mL H_2/g COD

Potato starch (4 g COD/L) Sodium lactate (4 g COD/L) Cellulose (4 g COD/L) Xylose (1.26)				90 mL H_2/g COD 2.3 mL H_2/g COD 0.6 mL H_2/g COD 26.7 mol/mol xylose		
	Clostridium uliginosum sp. nov.	20	6.5		2.59 mL/h/L	Matthies et al. (2001)
Sucrose (30)	Anaerobic sludge	35	5.5	1.01	0.20	Mu et al. (2006a)
Sucrose (24.8)	Anaerobic sludge	34.8	5.5	1.76	NA	Mu et al. (2006b)
Sucrose (25.4)		35.5	5.5	NA	0.49	
Glucose (10)	Sewage sludge	41	5.5	1.67	0.42	Mu et al. (2006c)
Potassium gluconate (10)	*Enterobacter aerogene* HU-101	37	7.0	1.44 mmol/g substrate	NA	Nakashimada et al. (2002)
Glucose (10)				1.97 mmol/g substrate		
Fructose (10)				2.17 mmol/g substrate		
Galactose (10)				1.90 mmol/g substrate		
Sorbitol (10)				4.96 mmol/g substrate		
Mannitol (10)				5.20 mmol/g substrate		
Glycerol (10)				6.69 mmol/g substrate		
Cellulose (5)	*Thermotoga maritima* (DSM 3109)	80	6.5	0.96 mmol/g cellulose	NA	Nguyen et al. (2008)
CMC (5)				3.29 mmol/g cellulose		
Cellulose (5)	*Thermotoga neapolitana* (DSM 4359)	75	7.0	1.07 mmol/g cellulose	NA	Nguyen et al. (2008)
CMC (5)				3.37 mmol/g cellulose		
Glucose (5)	*Ruminococcus albus*	37	NR	2.76	NA	Ntaikou et al. (2008)
Sorghum extract (3)		37	6.4–6.5	2.61		
Sorghum stalks (3)		37	6.4–6.5	3.15		
Sorghum residues (3)		37	6.4–6.5	2.59		
Glucose (23.75)	*Clostridium* sp. Fanp2	36	6.47	2.53	0.306	Pan et al. (2008)
Glucose (2)	Aerobic sludge (heat conditioned)	30	6.2	2.0	NA	Park et al. (2005)

(*continued*)

TABLE 9.3 (continued)

Hydrogen Production Rates and Yield Coefficients from Pure and Complex Substrates Using Pure and Mixed Culture under Batch Operation

Substrate (Concentration, g/L)	H_2 Producer	Temperature (°C)	pH	H_2 Yield (mol H_2/mol Hexose)	H_2 Production Rate (mol H_2/L/day)	References
Glucose (3.76)	Anaerobic sludge (heat treated)	30	6.2	1.9	NA	Salerno et al. (2006)
Glucose (3)	*Clostridium* sp. strain No. 2	36	6.8	14.6 mmol H_2/g substrate	NA	Taguchi et al. (1995)
Xylose (3)				16.1 mmol H_2/g substrate		
Avicel hydrolysate (3)				19.6 mmol H_2/g substrate		
Xylan hydrolysate (3)				18.6 mmol H_2/g substrate		
Cellulose (10)	Sludge compost	60	NA	2.4	NA	Ueno et al. (1995)
Cellulose (10)	Anaerobic digestion sludge			0.9		
Glucose (10)	*Thermoanaerobacterium thermosaccharolyticum* KU001	60	6.6	2.4	NA	Ueno et al. (2001a)
Glucose (10)	Thermophilic anaerobic microflora enriched from sludge compost	60	NA	2	NA	Ueno et al. (2001b)
Sucrose (6.68)	Mixed bacteria	37	5.5	2.05	0.073	Van Ginkel et al.

(initial) (2001)

Sucrose (10)	*Caldicellulosiruptor saccharolyticus*	70	7.0	3.3	0.202	van Niel et al. (2002a)
Glucose (10)	*Thermotoga elfiii*	65	7.4	3.3	0.065–0.108	
Glucose (10)	Hydrogen-producing bacterial B49	35	6.0 (initial)	1.73	NA	Wang et al. (2007)
Microcrystalline cellulose (10)	*Clostridium acetobutylicum* X_9 and *Ethanoigenens harbinense* B49	37	5.0	8.1 mmol H_2/g cellulose	NA	Wang et al. (2008)
Sucrose (17.8)	Immobilized sewage sludge	35		1.98	NA	Wu et al. (2002)
Sucrose (17.8)	Immobilized sewage sludge	40	6.7	0.87	NA	Wu et al. (2005)
Sucrose (35.6)		40	6.7	0.72		
Sucrose (25)	Mixed bacteria	35	8.0 (initial)	1.30	NA	Zhang and Shen (2006)
Starch (4.6)	Hydrogen-producing sludge	37	7.0	47 mL H_2/g starch	NA	Zhang et al. (2003)
Starch (4.6)		55	7.0	78 mL H_2/g starch		
Starch (4.6)		55	6.0	92 mL H_2/g starch		
Starch (9.2)		55	6.0	67 mL H_2/g starch		
Sucrose (44)	Mixed bacteria	35	7.5	1.37	NA	Zhang et al. (2005)
Glucose (10)	Anaerobic sludge (heat conditioned)	37	6.0 (initial)	1.75	NA	Zheng and Yu (2005)
Xylose (28.0)	*Clostridium tyrobutyricu* ATCC 25755	37	6.3	187 mol/mol xylose	0.77 mL/h/L	Zhu and Yang (2004)

TABLE 9.4

Hydrogen Production Rates and Yield Coefficients from Pure and Complex Substrates Using Pure and Mixed Culture under Semicontinuous and Continuous Operation

Substrate (Concentration, g/L)	H_2 Producer	Culture Type	HRT (h)	Temp. (°C)	pH	H_2 Yield (mol/mol Hexose)	H_2 Production Rate (mol/L/day)	References
Starch (20 g COD/L)	Anaerobic digester sludge	CSTR	12	35	5.3	0.92	0.175	Arooj et al. (2008)
Palm oil mill effluent (POME)	Mixed microflora	Fed batch	60	60	5.5	2382 mL H_2/L POME	0.307	Atif et al. (2005)
			20			1597 mL H_2/L POME	0.427	
Glucose (2)	Windrow yard waste compost	Fed batch	76	55	5.4	1.75	0.179	Calli et al. (2006)
Starch (10) and xylose (1:1 w/w)	Mixed culture	CSTR and UASB	32.9	35	7	NA	0.108	Camilli and Pedroni (2005)
			6.7	35	7		0.114	
			20.5	35	7		0.061	
Sucrose (17.8)	Mixed culture	UASB	8	35	6.7	0.92	0.274	Chang and Lin (2004)
Sucrose (17.8)	Sewage sludge	Packed-bed	1	35	6.7	1.19	1.29	Chang et al. (2002)
Glucose (18.7)	Sewage sludge	CSTR	13.3	35	6.7	1.63	NA	Chen and Lin (2001)
Sucrose (17.8)			13.3	35	6.7	2.225		
Sucrose (17.8)	Municipal sewage sludge	CSTR	8	35	7.0	2.26	0.649	Chen and Lin (2003)
			3	35	6.9	1.44	1.096	
Sucrose (17.8)	Sewage sludge	CSTR	8	35	6.7	1.735	0.630	Chen et al. (2001)
Sucrose (17.8)	Municipal sewage sludge	CSTR	4	35	5.5	2.35	0.874	Chen et al. (2008a)
Hydrolyzed starch	*Clostridium butyricum*	CSTR	12	37	NA	2.03	ca.0.5	Chen et al.

(29.1 g COD/L)	CGS2.	2	37	1.50	1.47	(2008b)

Broken kitchen wastes (10 kg COD/m^3-day) and corn starch (10 kg COD/m^3-day)	Mixed culture	CSTR	96	35	5.3–5.6	NA	0.041	Cheng et al. (2006)
Lactose (10)	*Clostridium thermolacticum*	CSTR	17.9	58	7.0	2.7 mol/mol lactose	0.060	Collet et al. (2004)
Brewery waste (50 g COD/L)	Cattle dung compost	CSTR	18	37	5.5	1.76 mmol/g COD	0.124	Fan et al. (2006a)
Glucose (7)	Sludge	CSTR	6	36	5.5	2.1	NA	Fang and Liu (2002)
Sucrose (12.15)	Sludge	CSTR (granular sludge)	6	26	5.5	1.96	0.529	Fang et al. (2002)
Glucose (10)	Anaerobic sludge	CSTR	2	35	6.0	1.26	0.185	Gavala et al. (2006)
Glucose (10)		CSTR	2	55	6.4	1.16	0.163	
Glucose (10)		UASB	2	35	4.4	0.79	0.418	
Glucose (8)	Sludge	CSTR	5.4	37	6.0	NA	0.169	Horiuchi et al. (2002)
Wheat starch (10)	Sewage sludge	CSTR						Hussy et al. (2003)
Without N_2 sparging			18	30	5.2	1.3	0.071	
With N_2 sparging			15	30	5.2	1.9	0.120	
Sucrose (without N_2 sparging)	Mixed microflora	CSTR	14–15	32	5.2	1.0	NA	Hussy et al. (2005)
Sucrose (with N_2 sparging)						1.9		
Sugarbeet juice (without N_2 sparging)						0.9		
Sugarbeet juice (with N_2 sparging) (OLR = 16 kg total sugar/m^3/day)						1.7		

(*continued*)

TABLE 9.4 (continued)

Hydrogen Production Rates and Yield Coefficients from Pure and Complex Substrates Using Pure and Mixed Culture under Semicontinuous and Continuous Operation

Substrate (Concentration, g/L)	H_2 Producer	Culture Type	HRT (h)	Temp. (°C)	pH	H_2 Yield (mol/mol Hexose)	H_2 Production Rate (mol/L/day)	References
Glucose (20)	Sewage digester	Biofilm system	20	37	5.0	NA	0.049	Kim et al.
Glucose (20)	sludge	Granular sludge system (stirred reactor)	20	37	5.0		0.118	(2005)
Glucose (10)	Mixed culture	MBR	0.79	37	5.5	1.1	1.71	Kim et al. (2006)
Glucose (10)	Mixed culture	UASB	26.7	70	4.8–5.5	2.47	0.051	Kotsopoulos et al. (2006)
Glucose (10)	*Enterobacter cloace* IIT-BT 08	Packed bed (lignocellulosic agroresidue)	1.1	37	NA	2.04	1.81	Kumar and Das (2001)
Soluble starch (4.25)	Anaerobic digested sludge	CSTR	17	37	5.2	1.29 L H_2/g starch-COD	0.066	Lay (2000)
Sucrose (17.8)	Municipal sewage sludge	Packed bed	0.5	35	6.7	1.44	7.20	Lee et al. (2003)
Sucrose (17.8)	Municipal sewage sludge	CIGSB	0.5	35	6.7	1.52	7.18	Lee et al. (2004a)
Sucrose (17.8)	Municipal sewage sludge	CIGSB	1	35	6.7	2.01	4.97	Lee et al. (2006a)
			0.5			1.96	9.12	
Sucrose (17.8)	Municipal sewage sludge	CIGSB	1	40	6.7	1.94	4.65	Lee et al. (2006b)
			0.5			1.58	7.50	
Glucose (18.75)	Municipal sewage sludge	CSTR	8	35	6.7	1.23	0.362	Lee et al. (2007)
Glucose (18.75)		MBR	1			1.27	1.450	

Sucrose (17.8)	CSTR	4	1.49	0.686

Sucrose (17.8)		MBR	1			1.39	2.028	
Fructose (18.75)		CSTR	4			1.59	0.823	
Fructose (18.75)		MBR	1			1.36	2.694	
Glucose (17.8)	Sewage sludge	CSTR	6	35	5.7	1.71	0.711	Lin and Chang (1999)
				35	6.4	1.66	0.574	
Glucose (17.8)	Sewage sludge	CSTR	6	30–34	6.2	1.15	0.359	Lin and Chang (2004)
Xylose (18.75)	Sludge	CSTR	12	35	6–7	0.7 mol H_2/mol xylose	0.247	Lin and Cheng (2006)
Sucrose (17.8)	Sewage sludge	CSTR	4	35	7.1	1.75	0.408	Lin et al. (2006)
Starch (20 g COD/L)	Anaerobic sludge	CSTR	4	35	5.5	1.5	0.450	Lin et al. (2008a)
Sucrose (14.3)	Sludge	CSTR (granular sludge)	13.7	26	5.5	1.89	0.274	Liu and Fang (2002)
Glucose (10)	Anaerobic microflora (predominantly *Clostridium* sp.)	CSTR (N_2 sparging)	5	35	6	1.43	0.196	Mizuno et al. (2000)
Sucrose (4.75)	Mixed culture	UASB	18	38	4.5	1.44	0.049	Mu and Yu (2006)
Glucose (8.9)	Heat-treated soil	CSTR	3.3	—	5.5	0.88	0.294	Oh et al. (2004)
Glucose (8.9)		MBR	3.3	—	5.5	1.00	0.372	
Molasses (3 g COD/L)	Sewage sludge	CSTR (pilot)	3.9	35	4–5	26.13 mmol/g COD	0.225	Ren et al. (2006)
Food waste (6 g VSS/L)	Thermophilic acidogenesis	Semicontinuous operation	5	55	5.6	1.80	NA	Shin et al. (2004)
Molasses (20)	*Enterobacter aerogenes* E 82005	Continuous fermentor (packing urethane foam)	5	NA	6	1.75	0.313	Tanisho and Ishiwata (1994)

(*continued*)

TABLE 9.4 (continued)

Hydrogen Production Rates and Yield Coefficients from Pure and Complex Substrates Using Pure and Mixed Culture under Semicontinuous and Continuous Operation

Substrate (Concentration, g/L)	H_2 Producer	Culture Type	HRT (h)	Temperature (°C)	pH	H_2 Yield (mol/mol Hexose)	H_2 Production Rate (mol/L/day)	References
Sugary wastewater (carbohydrates 9.847 g/L; COD 31.85 g/L)	Sludge compost	CSTR	12	60	NA	2.52	0.028	Ueno et al. (1996)
Cellulose (10) (peptone 5 g/L)	Thermophilic anaerobic microflora enriched from sludge compost	CSTR	72	60	6.4	2	0.029	Ueno et al. (2001)
Municipal solid waste (Fruit+vegetable+office paper, TS 35%, VS 21%)	Mixed culture	Fed batch	21 day	37	5.5	6.73 mmol/g $VS_{removed}$	NA	Valdez-Vazquez et al. (2005)
				55	6.4	14.7 mmol/g $VS_{removed}$		
Glucose (10)	Agricultural soil	CSTR	1	30	5.5	1.7	2.126	Van Ginkel and Logan (2005)
Glucose (2.5)			10	30	5.5	2.8	0.079	
Palm oil mill effluent (20 g COD/L)	Cow dung	UACF	7 day	NA	5	9.77 mmol/g $COD_{destroyed}$	NA	Vijayaraghavan and Ahmad (2006)
Jackfruit peel (33 g VS/L)	Cow dung	UACF	12 day	NA	5.1	16.2 mmol/g $VS_{destroyed}$	0.024	Vijayaraghavan et al. (2006)
Mixed fruit peelwaste (46–84 g VS/L)	Cow dung	UACF	>5 day	NA	5.4–5.7	18.8 mmol H_2/g $VS_{destroyed}$	NA	Vijayaraghavan et al. (2007)
Organic wastewater	Mixed culture	CSTR	12	30	4.4	NA	0.120	Wang et al.

from a beet sugar refinery (4 g COD/L)		(2006)

Sucrose (17.8)	Immobilized sewage sludge	Fluidized bed	2	35	5.8–6.8	1.34	0.911	Wu et al. (2003)
Glucose (18.75)	Municipal anaerobic sludge	CSTR	10	35	6.5	1.63	0.411	Wu et al. (2008b)
		CSTR	6	35	6.6	0.75	0.588	
		IC-CSABR	4	35	6.3	0.87	0.520	
		AGSB	4	35	6.6	1.57	0.950	
Xylose (18.75)	Municipal sewage sludge	CSTR	12	50	6.5	0.95 mol/mol xylose	0.183	Wu et al. (2008c)
		IC-CSABR	2	40	5.8	0.80 mol/mol xylose	1.060	
		AGSB	2	40	6.5	0.61 mol/mol xylose	0.852	
Sucrose (17.8)	Municipal sewage sludge	IC-CSABR	0.5	40	6.6	1.05	4.79	Wu et al. (2006)
Sucrose (26.7)			0.5	40	6.6	1.93	14.2	
Sucrose (35.6)			0.5	40	6.6	1.59	14.8	
Citric acid wastewater (18 kg COD/L)	Mixed culture	UASB	12	35–38	6.8–7.2	0.84	0.029	Yang et al. (2006)
Sweet potato starch residue (5–20 g/L) + 0.1% Polypeptone	Two-step cultures (by a mixed culture of *C. butyricum* and *E. aerogenes* and by *Rhodobacter* sp. M-19)	Repeated batch		37 (dark), 35 (photo)	5.25 (dark), 7.5 (photo)	7.0 (2.4 + 4.6)		Yokoi et al. (2001b)
Sweet potato starch residue (10 g/L) + 0.5% corn steep liquor as nitrogen source	Mixed culture of *C. butyricum* and *E. aerogenes*	Repeated batch		37	5.25	2.7		Yokoi et al. (2002)
	Two-step cultures (by a mixed culture of *C. butyricum* and *E. aerogenes* and by *Rhodobacter* sp. M-19)	Repeated batch		37 (dark), 35 (photo)	5.25 (dark), 7.5 (photo)	7.2		

(*continued*)

TABLE 9.4 (continued)

Hydrogen Production Rates and Yield Coefficients from Pure and Complex Substrates Using Pure and Mixed Culture under Semicontinuous and Continuous Operation

Substrate (Concentration, g/L)	H_2 Producer	Culture Type	HRT (h)	Temperature (°C)	pH	H_2 Yield (mol/mol Hexose)	H_2 Production Rate (mol/L/day)	References
Rice winery wastewater (34)	Mixed bacterial flora	Upflow anaerobic reactor	24	35	5.5	2.14		Yu et al. (2002)
Rice winery wastewater (34)			2	35		1.74		
Rice winery wastewater (13)			2	35		1.89		
Rice winery wastewater (36)			2	35		1.79	0.156	
Rice winery wastewater (34)			2	55		1.37–2.14		
Glucose (10)	Anaerobically digested sludge	CSTR	10	37	5.5	1.95	0.249	Zhang et al. (2006)
			6	37	5.5	1.88	0.317	
Glucose (10)	Municipal sewage sludge	CSTR (granular sludge)	0.5	37	5.5	1.81	3.135	Zhang et al. (2007)
Glucose	Anaerobically digested sludge	Anaerobic biofilm fluidized bed reactors	0.25	37	5.5	1.7	7.45	Zhang et al. (2008)
		Anaerobic granule fluidized bed reactors				1.6	6.47	

CIGSB, carrier induced granular sludge bed; IC-CSABR, immobilized cell continuously stirred anaerobic bioreactor; CSTR, continuous flow stirred tank reactor; MBR, membrane bioreactor; UASB, upflow anaerobic sludge blanket; UACF, upflow anaerobic contact filter; AGSB, agitated granular sludge bed.

TABLE 9.5

Comparison of Optimal pH for H_2 Fermentation in Different H_2-Producing Systems

Authors	Microorganism	Culture Type	Substrate	Operation Temperature (°C)	Examined pH	Optimal pH for Maximum HY	Optimal pH for Maximum HPR	Optimal pH for Maximum SHPR
Chen et al. (2005)	*Clostridium butyricum* CGS5	Batch	Sucrose	37	5.0–6.5	5.5	6.0	
Cheong and Hansen (2006)	Anaerobic digester sludge	Batch	Glucose	35	4.6, 5.7, 6.8	5.7		
Fan et al. (2006a)	Cattle dung compost	CSTR	Brewery waste	37	5.0–6.5	5.5	5.5	
Fan et al. (2006b)	Cow dung compost	Batch	HCl pretreated wheat straw	36	4.0–9.0	6.0–8.0		
Fang and Liu (2002)	Sludge	CSTR	Glucose	36	4.0–7.0	5.5		
Fang et al. (2006)	Anaerobic digester sludge	Batch	Rice slurry	37	4.0–7.0	4.5		6.5
Horiuchi et al. (2002)	Anaerobic digester sludge	CSTR	Glucose	37	5.0–7.0		6.0	
Khanal et al. (2004)	Compost material	Batch	Sucrose/ starch	37	4.5–6.5	4.5		5.5
Lay (2000)	Sludge	CSTR	Soluble starch	37	4.0–7.0		5.2	
Lee et al. (2002)	Mixed microbial flora	Batch	Sucrose	37	5.5–10.0	9.0	9.0	
Lin and Cheng (2006)	Sewage sludge	Batch	Xylose	35	5.0–9.5	6.5	6.5	

(*continued*)

TABLE 9.5 (continued)

Comparison of Optimal pH for H_2 Fermentation in Different H_2-Producing Systems

Authors	Microorganism	Culture Type	Substrate	Operation Temperature (°C)	Examined pH	Optimal pH for Maximum HY	Optimal pH for Maximum HPR	Optimal pH for Maximum SHPR
Lin and Hung (2008)	Cow dung sludge	Batch	Cellulose	55	5.5–9.0	7.0		
Lin et al. (2008a)	Anaerobic sludge	Batch	Starch	35	5.0–7.0	5.0	5.5	
Liu and Shen (2004)	Cracked cereals	Batch	Starch	35	4.0–9.0	8.0	8.0	
Mu et al. (2006b)	Anaerobic sludge	Batch (RSM)	Sucrose	35	4.5–6.5	5.5	5.5	
O-Thong et al. (2008b)	*Thermoanaerobacterium thermosaccharolyticum* PSU-2	Batch	Sucrose	60	4.0–8.5	6.25	6.25	
Ren et al. (1997)	Sludge	CSTR	Molasses	30	3.0–5.5		4.5	
Wu and Lin (2004)	Waste-activated sludge	Batch	Food wastewater	35	4.0–8.0	6.0	6.0	
Yu et al. (2002)	Mixed bacterial flora	Upflow reactor	Rice winery wastewater	35	4.5–6.0	5.5	5.5	
Zhang et al. (2003)	Sludge	Batch	Starch	55	4.0–9.0	6.0		7.0

HY, H_2 yield; HPR, H_2 production rate; SHPR, specific H_2 production rate; RSM, response surface methodology.

TABLE 9.6

Comparison of Optimal Temperature for H_2 Fermentation in Different H_2-Producing Systems

Authors	Microorganism	Culture Type	Substrate	Examined Temperature (°C)	Optimal H_2-Producing Temperature (°C)
Chin et al. (2003)	*Clostridium acetobutylicum* ATCC824	Fedbatch	Glucose	30, 33, 37, 40	37
Evvyernie et al. (2000)	*Clostridium paraputrificum* M-21	Batch	*N*-Acetyl-d-glucosamine (GlcNAc)	30, 35, 40, 45, 50	45
Fang et al. (2006)	Anaerobic digester sludge	Batch	Rice slurry	37, 55	37
Gavala et al. (2006)	Anaerobic sludge	CSTR	Glucose	35, 55	35
Lee et al. (2006b)	Municipal sewage sludge	CIGSB	Sucrose	30, 35, 40, 45	40
Lee et al. (2008)	Municipal sewage sludge	Batch	Starch	37–55	55
Lin et al. (2008a)	Municipal sewage sludge	Continuous	Xylose	30–55	50
Mu et al. (2006b)	Anaerobic sludge	Batch (RSM)	Sucrose	25, 30, 35, 40, 45	35.5
Mu et al. (2006c)	Sewage sludge	Batch	Glucose	33, 35, 37, 39, 41	41
O-Thong et al. (2008b)	*Thermoanaerobacterium thermosaccharolyticum* PSU-2	Batch	Sucrose	40–80	60
Tanisho et al. (1994)	*Enterobacter aerogenes* E. 82005	Batch	Glucose	32, 35, 37.5, 40.5, 44	40.5
Valdez-Vazquez et al. (2005)	Anaerobic digester sludge	Semicontinuous	Organic waste	37–55	55

(*continued*)

TABLE 9.6 (continued)

Comparison of Optimal Temperature for H_2 Fermentation in Different H_2-Producing Systems

Authors	Microorganism	Culture Type	Substrate	Examined Temperature (°C)	Optimal H_2-Producing Temperature (°C)
Wang and Wan (2008)	Anaerobic sludge	Batch	Glucose	25–55	40
Wang et al. (2005)	Anaerobic sludge	Batch	Sucrose	25–45	35.1
Wu et al. (2005)	Immobilized sewage sludge	Batch	Sucrose	30, 35, 40, 45	40
Xing et al. (2008)	*Ethanoligenens harbinense* YUAN-3	Batch	Glucose	20–44	37
Yokoi et al. (1995)	*Enterobacter aerogenes* HO-39	Batch	Glucose	30, 33, 35, 38, 40, 43	38
Yokoi et al. (2001a)	*Enterobacter* sp. BY-29	Batch	Glucose	30, 35, 40, 45	37
Yokoyama et al. (2007b)	Cow waste slurry	Batch	Cow waste slurry	37–85	60
Yu et al. (2002)	Mixed bacterial flora	Upflow anaerobic reactor	Rice winery wastewater	20, 30, 35, 55	55
Zhang and Shen (2006)	Mixed bacteria	Batch	Sucrose	25, 35, 40, 45	35
Zhang et al. (2003)	Hydrogen-producing sludge	Batch	Starch	37, 55	55

CIGSB, carrier induced granular sludge bed; RSM, response surface methodology.

TABLE 9.7

Effect of Different Nitrogen Concentrations on Fermentative Hydrogen Production

H_2 Producer	Substrates	Culture Type	Nitrogen Source	Optimum Nitrogen Concentration	Hydrogen Yield (mol H_2/mol Glucose)	References
Escherichia coli	Glucose	Batch	NH_4Cl	0.01 g N/L	1.7	Bisaillon et al. (2006)
Grass compost	Food wastes	Batch	NH_4HCO_3	0.4 g N/L	77 mL/g TVS	Lay et al. (2005)
Cracked cereals	Starch	Batch	NH_4HCO_3	1 g N/L	146 mL/g starch	Liu and Shen (2004)
Compost	Glucose	Batch	Yeast extract	4% yeast extract	2.1	Morimoto et al. (2004)
Dewatered and thickened sludge	Glucose	Batch	NH_4Cl	7 g N/L	1.17	Salerno et al. (2006)
Enterobacter aerogenes HO-39	Glucose	Batch	Polypeptone	2% Polypeptone	1.0	Yokoi et al. (1995)

9.4.1 Substrate and Microorganism Species

9.4.1.1 Pure Culture

The literature survey suggests that dark fermentative H_2 production is undertaken by a diverse group of bacteria including facultative anaerobes, facultative aerobes, and obligate anaerobes. Mainly the obligate anaerobes and spore-forming organisms such as *Clostridium buytricum* (sweet potato starch) (Yokoi et al., 2001), *C. thermolacticum* (lactose) (Collet et al., 2004), *C. pasteurianum* (starch) (Liu and Shen, 2004) and *C. paraputrificum* M-21 (chitinous waste) (Evvyernie et al., 2001), *C. butyricum* CGS5 (rice husk hydrolysate) (Lo et al., 2009), and *C. bifermentants* (wastewater sludge) (Wang et al., 2003b) demonstrate maximum H_2 production during the exponential growth phase. *Clostridium* sp. can form endospores in response to unfavorable environmental conditions such as lack of nutri- ents or elevation of temperature and can be activated when required environmental con- ditions are provided for H_2 production (Mallette et al., 1974; Lay, 2000; Wu et al., 2006). A study on the microbial community of mesophilic hydrogen-producing sludge showed the presence of *Clostridia* species up to 64.6%, indicating that these species are dominant microbes for H_2 production (Fang et al., 2002). H_2 production by *Thermotogales* sp. and *Bacillus* sp. were detected in mesophilic acidogenic cultures (Shin et al., 2004). In anaero- bic granular sludge, some anaerobic cultures like *Actinomyces* sp. and *Porphyromonos* sp. have been detected along with *Clostridium* sp., and these strains showed H_2 yields between 1 and 1.2 mmol H_2/mol glucose when cultivated under anaerobic conditions (Oh et al., 2003) (Tables 9.3 and 9.4). Facultative anaerobes such as *Enterobacter* species have the abil- ity to metabolize carbohydrates and produce some valuable products like gaseous H_2 and CO_2 and a mixture of acids, ethanol, and 2,3-butanediol. The capacity of H_2 production associated with *Enterobacter aerogenes* using different substrates has been widely studied (Tanisho and Ishiwata, 1994; Yokoi et al., 1997; Rachman et al., 1998; Palazzi et al., 2000; Fabiano and Perego, 2002). Enhancement of H_2 production (2.2 mol H_2/mol glucose) by

Free ebooks ==> www.Ebook777.com

TABLE 9.8

Effect of Metal Ion Concentrations on Fermentative Hydrogen Production

Inoculum	Substrates	Reactor Type	Metal Ion	Concentration (mg/L)		Hydrogen Yield	References
				Examined Concentration	Optimal Concentration	(mol H_2/mol Hexose)	
Digested sludge	Sucrose	Continuous	Ca^{2+}	0–300	150	1.8	Chang and Lin (2006)
Grass compost	Food wastes	Batch	Fe^{2+}	0–250	132	77 mL/g TVS	Lay et al. (2005)
Anaerobic sludge	Sucrose	Batch	Fe^{2+}	0–1763.8	352.8	1.84	Lee et al. (2001)
Municipal sewage sludge	Sucrose	Continuous	Ca^{2+}	0–27.2	27.2	1.10	Lee et al. (2004)
Anaerobic sludge	Palm oil mill effluent	Batch	Fe^{2+}	2–400	257	6.33 L/L substrate	Thong et al. (2008)
Digested sludge	Glucose	Batch	Fe^{2+}	0–1500	350	2.29	Wang and Wan (2008)
Digested sludge	Glucose	Batch	Ni^{2+}	0–50	0.1	2.18	Wang and wan (2008)
Hydrogen-producing bacterial B49	Glucose	Batch	Mg^{2+}	1.2–23.6	23.6	2360.5 mL/L culture	Wang et al. (2007)
Anaerobic sludge	Starch	Batch	Fe^{2+}	0–1473.7	55.3	296.2 mL/g starch	Yang and Shen (2006)
Anaerobic sludge	Glucose	Batch	Cu^{2+}	0–400	400	1.74	Zheng and Yu (2004)
Anaerobic sludge	Glucose	Batch	Zn^{2+}	0–500	250	1.73	Zheng and Yu (2004)

www.Ebook777.com

using *Enterobacter cloacae* ITT-BY 08 has been reported earlier (Kumar and Das, 2000). H_2 production from glucose by *E. coli* and *Hafnia alvei* was studied by Podestá et al. (1997), and a trace amount of H_2 yield was detected. Some thermophilic anaerobic organisms belong- ing to the genus *Thermoanaerobacterium*, viz. *T. thermosaccharolyticum* and *Desulfotomaculum geothermicum*, have the ability to produce H_2 gas in a thermophilic acidogenic culture (Shin et al., 2004). The *Thermococcus kodakaraensis* KOD1 and *Clostridium thermolacticum* strains can produce H_2 at 85°C and 58°C (Kanai et al., 2005), respectively, whereas *Klebisalle oxytoca* HP1 shows maximal H_2 production rate at 35°C reported earlier (Minnan et al., 2005). In a recent study, isolated *Klebsiella* sp. HE1 demonstrated the ability to produce 2,3-butanediol, ethanol, and H_2 using sucrose as substrate under the dark fermentation process (Wu et al., 2008a). Some studies show that aerobic cultures such as *Aeromonos* spp., *Pseudomonos* spp., and *Vibrio* spp. can produce H_2. *Thermotogales* species and *Bacillus* sp. can produce H_2 under mesophilic acidogenic cultures according to a recent report (Shin et al., 2004).

9.4.1.2 Mixed Culture

Increasing industrialization and urbanization of modern society have resulted in mas- sive amounts of organic wastes being generated, and it would be desirable to turn these wastes into a useful product, such as a biohydrogen. The major criteria for the selection of waste materials for biohydrogen production are the availability, cost, carbohydrate con- tent, and biodegradability (Kapdan and Kargi, 2006). These waste materials can be ideal inexpensive feedstocks for biological H_2 production. Literature survey suggests that a single microorganism has limited hydrolytic potential in degrading complex wastes for biohydrogen production. The degradation of organic matter in anaerobic environments by microbial consortia involves the cooperation of different species existing in the system and synergistic metabolic activity, which generate a stable, self-regulating fermentation. For this purpose, worldwide efforts are under way to design a suitable mixed microbial consortium capable of decomposing various organic waste streams and to improve the H_2 production yields and rates by using these cultures. The mixed microbial consortia presenting in anaerobic digester sludge, sludge compost, soil, animal feces, and so on may be useful for the direct utilization of starch- and cellulose-containing agricultural wastes, food industry wastes, carbohydrate-rich industrial wastewaters, and organic wastewater for biohydrogen production (details are given in the next section) (Kapdan and Kargi, 2006; Datar et al., 2007). Before preparation of the inoculum of various sludges, differ- ent pretreatment methods such as incubation at high temperatures or acidic conditions or combination of these are necessary to remove the methanogens (Valdez-Vazquez and Poggi-Varaldo, 2009). These methods favor the survival of spore-forming *Clostridia* and are found to be effective in enriching for H_2 producers (Tables 9.3 and 9.4). In general, anaero- bic activated sludge is used for the production of H_2 from cellulose and biomass. A recent study about H_2 production from chemical wastewater, using anaerobic mixed consortia in a biofilm-configured reactor operated in periodic discontinuous batch mode, suggests that reactor configuration and mode of operation also affect the composition of the microbial consortia (Mohan et al., 2007) (Tables 9.3 and 9.4).

9.4.1.3 Potential of Simple and Complex Substrates for Biohydrogen Production

Many studies have investigated the potential of various substrates, from simple sugars (glucose) to more complex substrates such as biomass, for dark fermentation H_2 produc- tion. A brief summary of the H_2 production yields and rates (batch and continuous) with

various substrates is given in Tables 9.3 and 9.4. Glucose and sucrose are the most common pure substrates used in both batch and continuous processes because of their relatively simple structures, ease of biodegradability, and presence in several industrial effluents (Kapdan and Kargi, 2006) and different agricultural and biomass wastes in polymeric form. Theoretically, bioconversion of 1 mol of glucose yields 12 mol of H_2, but the highest H_2 yield from glucose in recent studies is only around 2.0–2.4 mol H_2/mol glucose (Ueno et al., 2001b; Morimoto et al., 2004). This lower H_2 yield may be the result of the utilization of glucose as an energy source for bacterial growth. The highest H_2 yield (2.76 mol H_2/mol glucose) from glucose was observed in *Ruminococcus albus* (Ntaikou et al., 2008). In the presence of sucrose, a higher yield was obtained (4.52 mol H_2/mol sucrose) by employing CSTR operation at 8 h HRT (Chen and Lin, 2003). Collet et al. (2004) reported a maximum H_2 yield of 3 mol H_2/mol lactose from lactose, although the theoretical yield is 8 mol H_2/mol lactose. The results indicate that sucrose gives a higher yield compared to other simple sugars. However, the yield per mole of hexose remains almost the same. Starch is abundant in nature and has great potential to be used as a carbohydrate source for H_2 pro- duction. Studies for both batch and continuous operations have been done in recent years. According to the reaction stoichiometry, 1 g of starch yields 553 mL H_2 gas with acetate as the by-product (Zhang et al., 2003). However, the actual yield is lower than the theoreti- cal value because of the utilization of substrate for cell synthesis. The maximum specific H_2 production rate was observed in *C. pasteurianum* (237 mL H_2/g VSS/day from 24 g/L edible corn starch) (Liu and Shen, 2004) and *Thermoanaerobacterium* (365 mL H_2/g VSS/day at 55°C) (Zhang et al., 2003). Mixed culture of *C. butyricum* and *E. aerogenes*, obtained in long-term repeated batch operations with starch residue (2.0%) containing wastewater as substrate, gives better H_2 yield (2.4 mol H_2/mol glucose) (Yokoi et al., 2001). Lay (2000) used anaerobic digested sludge to ferment substrate containing 4.25 g/L soluble starch, attaining a rate of 66.7 mL H_2/h/L. Lin and Cheng (2006) demonstrated H_2 production from xylose (20 g COD/L) by mesophilic sewage sludge in a chemostat anaerobic bioreac- tor at an HRT of 12 h. Each mole of xylose yields 0.7 mol of H_2 and each gram of biomass produces 0.038 mol H_2 day. Some researchers have studied H_2 fermentation using protein as substrate by anaerobic sludge (Bai et al., 2001; Liang et al., 2001; Liang, 2003). Liang (2003) showed a H_2 yield of 2.2 mmol H_2/g peptone with anaerobic sludge in batch cul- ture and noted that H_2 fermentation of peptone has a lower H_2 yield but a higher growth yield than glucose based on 1 g of substrate. In H_2 fermentation of peptone using mixed culture, H_2 consumption was always observed after H_2 production reached a peak value (Bai et al., 2001; Liang, 2003).

The literature survey suggests that some nontoxic carbohydrate-rich industrial effluents such as food industry, dairy industry, olive mill, baker's yeast, and brewery wastewaters can be used as raw material for biohydrogen production. In addition, biologically derived organic materials and residues currently constitute a large source of waste biomass (Giallo et al., 1985). Bioenergy derived from water containing biomass (sewage sludge, agricultural and livestock effluents, as well as animal excreta) was mainly produced by microbial fermentation. However, only limited data on H_2 yield from wastewater sludge have been reported (Wang et al., 2003b; Chang and Yang, 2006).

Lignocellulosic products such as agricultural crops and their waste by-products, effluents from the paper industry, wood and wood waste, food, aquatic plants, and algae are the major biomass resources. Use of these biomass-rich resources for bioenergy and related bioproducts can contribute to the displacement of fossil fuels as our primary energy source and reduce greenhouse gas emissions. Thus, biomass acts as an energy source and is

characterized in the form of both flow and stock. Production of biohydrogen from renewable resources such as lignocellulosic wastes is expected to become an attractive and major source of energy in the future (Kapdan and Kargi, 2006; Saratale et al., 2008). Bioconversion of biomass utilizing anaerobic fermentation to produce H_2 has been demonstrated in many studies (Lin and Chang, 1999; Lay, 2000; Ren et al., 2006; Wu et al., 2006; Lo et al., 2008a). The main source of H_2 production during a biological fermentative process is carbohydrates, which are very common in plant tissues, in the form of either oligosaccharides or poly- mers (e.g., cellulose, hemicellulose, and starch). Among the polymeric forms, cellulose is the predominant constituent and is widely available in agricultural wastes and industrial effluents such as pulp/paper and food industries (Nowak et al., 2005; Lo et al., 2009); it is considered as a very promising feedstock for biohydrogen production. Significant amounts of H_2 may be produced from cellulosic feedstocks (straw, woodchips, grass residue, paper waste, sawdust, etc.) using conventional anaerobic dark fermentation technology and natu- ral mixed microflora under conditions that favor hydrogen-producing acetogenic bacte- ria and inhibit methanogens (Sparling et al., 1997; Valdez-Vazquez et al., 2005). However, depending on the metabolic shift used by the organisms within the consortium, H_2 yields may be variable (Benemann, 1996; Hallenbeck and Benemann, 2002). Some recent studies reported effective H_2 production from agricultural waste using *Ruminococcus albus* (sor- ghum extract) (Ntaikou et al., 2008), heat-treated anaerobically digested sludge (fodder maize, chicory fructooligosaccharides, perennial ryegrass) (Kyazze et al., 2008), *Clostridium butyricum* CGS5 (rice husk hydrolysate) (Lo et al., 2009), and *Clostridium paraputrificum* M-2; (chitinous wastes) (Evvyernie et al., 2001). To get a higher H_2 yield directly from cellulose materials using dark fermentation, pretreatment processes for delignification and hydro- lysis of cellulose are required. Cellulolytic microorganisms or cellulase complexes are usually used to accomplish this (Taguchi et al., 1995, 1996; DeVrije et al., 2002). Recently, Fan et al. (2006b) conducted some batch tests to compare the efficiency of H_2 production from raw wheat straw and HCl-pretreated wheat straw, using cow dung compost as seed- ing. Results showed that acid pretreatment of the substrate played a key role in efficient conversion of the wheat straw wastes into H_2 gas. The maximum cumulative H_2 yield of 68.1 mL H_2/g TVS was observed from the pretreated wheat straw. This value is about 136 times higher than that from raw wheat straw wastes. Ueno et al. (1996) obtained a yield of 2.52 mol H_2/mol glucose with a laboratory-scale continuous mixed-culture flora chemostat reactor. In addition, effective H_2 production using mixed cultures under CSTR operation has been reported. The combinations of mixed-culture type versus the substrate used are as follows: broken kitchen wastes versus corn starch (Cheng et al., 2006), mixed culture versus organic wastewater (Wang et al., 2003b), sewage sludge versus molasses (Ren et al., 2006). Moreover, Yu et al. (2002) constructed a mixed-culture upflow anaerobic reactor, using high-strength rice winery wastewater as substrate, to investigate individual effects of HRT, chemical oxygen demand (COD) concentration, pH, and temperature on biohydro- gen production. The optimal H_2 production rate was achieved at an HRT of 2 h, a COD of 34 g/L, a pH of 5.5, and a temperature of 55°C. The H_2 yield was in the range of 1.37–2.14 mol/mol hexose. Some studies also used solid waste containing jackfruit peel as substrate of H_2 with microflora isolated from cow dung. This sucrose-rich wastewater under UASB operation gave a H_2 yield of 16.2 mmol H_2/g VS destroyed and 1.61 mol H_2/mol glucose, respectively (Mu and Yu, 2006; Vijayaraghavan et al., 2006).

On the other hand, several studies have focused on H_2 production from sludge by anaerobic fermentation, since the sludge contains large quantities of polysaccharides and proteins (Wang et al., 2003a,b; Cai et al., 2004). Wang et al. (2003b) examined the effects of

five pretreatment processes (namely, ultrasonication, acidification, sterilization, freezing/thawing, and adding a methanogenic inhibitor) on the production of H_2 from wastewater sludge by *Clostridium bifermentans*. Results showed that freezing/thawing and sterilization increased the H_2 yield from 0.6, for the original sludge, to 1.5–2.1 mmol H_2/g COD. However, fast consumption of H_2 and interference of methanogens still hamper H_2 production from sludge (Liang, 2003; Wang et al., 2003a,b; Cai et al., 2004). This makes it difficult to maintain high and stable H_2 production and limits the application of biohydrogen production from sludge. Cai et al. (2004) showed that biohydrogen production from sludge could be enhanced and stably maintained by the combination of high initial pH and alkaline pretreatment (Tables 9.3 and 9.4).

9.4.2 Substrate/Product Concentration

Some studies suggested that concentration of carbon substrates (or organic load- ing) in wastewater had a slightly negative effect on the H_2 yield (Yu et al., 2002). It was also observed that the specific H_2 production rate substantially increased with increasing substrate concentration (Lo et al., 2008b). However, in some cases, high sub- strate concentration may be unfavorable for H_2 production due to substrate inhibition (Lay, 2001; van Ginkel et al., 2001). Lay (2001) performed batch studies on convert- ing microcrystalline cellulose into H_2 at 12.5 and 25 g cellulose/L and a H_2 yield of 2.18 mmol H_2/g cellulose and 1.60 mmol H_2/g cellulose, respectively. This decrease in H_2 production at higher substrate concentration might be due to substrate inhibition. It was also reported that higher substrate concentrations may quickly become inhibitory through pH depletion, acid production, or increased H_2 partial pressures (van Ginkel et al., 2001). Hence, the removal of these inhibitory mechanisms may be necessary to achieve high H_2 conversion efficiencies and production rates at higher substrate concentrations.

During dark fermentation, anaerobic bacteria have the ability to produce H_2 while converting organic substrates into soluble metabolites such as volatile fatty acids (e.g., acetic acid, butyric acid) and alcohols. The unstable and low H_2 production is possibly attributed to the different metabolic shift of hydrogen-producing bacteria under dark fermentation. Recently, Fang et al. (2006) investigated the effect of feedstock concentration on H_2 production from rice slurry with acidophilic hydrogen-producing sludge. The results showed that the concentration of 5.5 g carbohydrate/L gave the highest H_2 yield of 346 mL/g carbohydrate, and above this concentration the H_2 yield decreased steadily. The authors mentioned that this may be due to the increased concentration of VFA and alcohols. Similarly, Cheng et al. (2002) also pointed out that high VFA content in the system sped up the consumption of H_2 gas. To study the effect of VFA, some scientists determined the inhibitory effects of butyrate addition on H_2 production from glucose by using anaerobic mixed cultures in batch experiments (Zheng and Yu, 2005). Experimental results showed that addition of butyrate at 25.08 g/L had a strong inhibitory effect on substrate degradation and H_2 production. They employed a noncompetitive and nonlinear inhibition model to describe the inhibition of butyrate addition on H_2 production. The $C_{I,50}$ values (the butyrate concentration at which bioactivity is reduced by 50%) for H_2 production rate and yield were estimated as 19.39 and 20.78 g/L of butyrate added, respectively. Ren et al. (2006) undertook a study on biohydrogen production from molasses in a pilot-scale CSTR (with an available volume of 1.48 m^3) for over 200 days. They reported that the H_2 yield was affected by the presence of ethanol and acetate in the liquid phase, and the maximum H_2 production rate occurred while the

ratio of ethanol to acetate was close to 1, due to the adjustment of $NAD^+/(NADH+H^+)$ through fermentation pathways. The H_2 yield reached 26.13 mol/kg $COD_{removed}$ within an OLR range of 35–55 kg COD/m^3reactor/day. (The value of 26.13 mol H_2/kg COD does not seem to be correct as it is equivalent to 5.02 mol H_2/mol hexose, higher than the theoretical 4 mol H_2/mol hexose.)

9.4.3 Hydraulic Retention Time

Hydraulic retention time (HRT), also known as the inverse of the dilution rate (*D*), is defined as the volume of the reactor/volumetric flow. Continuous-flow stirred-tank reactor (CSTR) is used to select microbial populations whose growth rates are able to catch up to the dilution caused by continuous volumetric flow. The effects of HRT on H_2 production are summarized in Table 9.4. In continuous cultures, microbial populations with growth rates higher than the dilution rate can remain in the reactor ($\mu_{max} > D$). Methanogenesis can be limited by operating at a short HRT (high dilution rate) to cause the washout of slowly growing methanogens and/or operating under acidic environ- ment to inhibit the pH-sensitive methanogens (Lin and Chang, 1999; Chen et al., 2001). The specific growth rates of methanogens are much shorter than those of H_2-producing bacteria (0.0167 and 0.083 h^{-1}, respectively) (Wang and Wan, 2009). Chen et al. (2001) operated a CSTR seeding with nonpretreated sewage sludge to convert sucrose to H_2 with a gradual decrease of HRT. They observed that the H_2 production rate was dra- matically enhanced by a shift of HRT from 5 to 13.3 h and that the H_2 production rate continued to increase when HRT was shifted down further to 8 h. It is likely that an HRT of 13.3 h was short enough to cause the complete washout of methane-producing bacteria, while the H_2-producing population remained in the culture. Fan et al. (2006a) investigated the HRT (from 48 to 8 h) effect on H_2 production from brewery waste by cattle dung compost in a CSTR system at pH 5.5 in which maximum H_2 production rate and H_2 yield were obtained at an HRT of 18 h. In these studies, they expressed that the lower yield at high HRT was probably due to the interference of methanogens and inhibition via major intermediates of acidogenic and alcoholic products. Lin et al. (2006) used a base-enriched anaerobic mixed microflora to perform H_2 fermentation from sucrose in a CSTR bioreactor operating the HRT from 12 to 2 h at 35°C. The results showed that H_2 yield and H_2 production rate were HRT-dependent, and their values ranged from 0.9 to 3.5 mol H_2/mol sucrose and from 263 to 408 mmol H_2/L/day, respec- tively, with an HRT of 4 h having peak H_2 production. The biomass activity was also HRT-dependent, with each gram of biomass producing 65–145 mmol H_2/day. Further analysis by using denaturing gradient gel electrophoresis (DGGE) showed that micro- bial species shifted during the HRT reduction operation, but *Clostridium ramosum* was dominant throughout the experiments. One important hydrogenic organism, namely,
C. pasteurinum, disappeared at an HRT of 2 h. It was observed that the H_2 fermentation pattern may shift to methanogenic fermentation if the HRT increased (Wang and Wan, 2009). Moreover, to understand the effect of glucose loading rate on H_2 production, van Ginkel and Logan (2005) performed the experiments with a combination of different glucose concentrations and HRTs in chemostat reactors seeding a heat-shocked agricultural soil. The results showed that the H_2 production rate increased with increasing glucose loading rate (high HRT or low glucose concentration), but the H_2 yield decreased with increasing glucose loading rate. They observed that the decrease in yield resulted from inhibition of H_2 supersaturation in the liquid phase due to a high H_2 production rate at a higher feeding rate.

Liu and Fang (2002) investigated the influence of HRT and sucrose concentration on H_2 production by the acidogenic granular sludge in a CSTR reactor at a constant loading rate of 25 g sucrose/L/day. The results show that the H_2 yield was highly dependent on HRT and sucrose concentration. The H_2 yield ranged from 0.19 to 0.27 L H_2/g sucrose (2.65–3.77 mol H_2/mol sucrose), with the maximum occurring at a higher HRT of 13.7 h and with a sucrose concentration of 14.3 g/L in the wastewater. Similarly, Yu et al. (2002) operated an upflow reactor for H_2 production from rice winery wastewater under differ- ent HRTs (2–24 h) in which the specific H_2 production rate increased as HRT decreased, but the H_2 yield decreased with decreasing HRT. The results suggest that more carbohy- drates in the wastewater were converted into H_2 at longer HRT. The findings obtained from these studies demonstrate that a decrease in HRT can achieve a methanogen wash- out, although this method can be applied only when noncomplex or soluble substrates are used.

9.4.4 pH

One of the major factors affecting dark fermentative H_2 production is pH. Most investigators reported that the maximum H_2 yield or specific H_2 production rate was obtained at pH between 5.0 and 6.0 (Lay et al., 1999; Chen et al., 2001; Lay, 2001; Fang and Liu, 2002), whereas some reported a pH range between 6.8 and 8.0 (Lay, 2001; Fabiano and Perego, 2002; Collet et al., 2004; Liu and Shen, 2004; Lin and Cheng, 2006) (Table 9.5). During dark fermentative H_2 production, formation of organic acids depletes the buffering capacity of the medium and results in low final pH. This lower pH inhibits H_2 production since pH affects the activity of the iron-containing hydrogenase enzyme and metabolic path- way (Dabrock et al., 1992). Horiuchi et al. (2002) showed that the product spectrum in the CSTR reactor strongly depended on the culture pH. Under acidic and neutral condi- tions, the main product was butyric acid, while acetic and propionic acids were the main products under basic conditions. This phenomenon was reversible between the acidic and basic conditions and was caused by the change in the dominant microbial populations as a pH shift led to transition of the dominant population in the reactor from butyric acid–producing bacteria to propionic acid–producing bacteria. Medium pH also affects H_2 production yield, biogas content, types of organic acids produced, and the specific H_2 production rate (Khanal et al., 2004). Therefore, control of pH at the optimum level may be useful for getting better yield. Since pH affects the growth rate of microorganisms, pH changes may cause drastic shifts in the relative numbers of different species in a hetero- geneous population present in the hydrogen-producing reactors (Horiuchi et al., 1999). Many aspects of microbial metabolism are greatly influenced by pH variations over the range within which the microorganisms can grow. These aspects include utilization of carbon and energy sources, efficiency of substrate degradation, synthesis of proteins and various types of storage materials, and release of metabolic products from cells (Baily and Ollis, 1986). Thus the foregoing results suggest that, in an appropriate range, increasing pH could increase the ability of hydrogen-producing bacteria to produce H_2 during fermenta- tive H_2 production, but pH at much higher levels could reduce production. A number of studies were conducted in batch mode without pH control; only the effect of initial pH on fermentative H_2 production was investigated in these studies. Table 9.5 summarizes sev- eral studies investigating the effect of initial pH on fermentative H_2 production in batch mode. In batch systems, the final pH is around 4–5 regardless of the initial pH. This is due to the production of organic acids, which decreases the buffering capacity of the medium, resulting in a low final pH.

Table 9.5 also shows the reported optimal pH range for fermentation of carbohydrates by mixed-culture microorganisms. Zhang et al. (2003) examined the effect of pH (from 4.0 to 9.0) on starch conversion into H_2 with sludge at 55°C. The maximum H_2 yield of 92 mL/g of starch added (17% of the theoretical value) was found at pH 6.0, and the maximum specific H_2 production rate of 365 mL/day/g VSS occurred at pH 7.0. Zoetemeyer et al. (1982b) obtained an optimum H_2 production rate at a pH of 5.7 and HRT of 4 h with glucose as substrate. Acetate and butyrate with negligible propionate was produced in this batch. Fang and Liu (2002) systematically investigated the optimum pH (from 4.0 to 7.0) for H_2 production from glucose by a mixed culture at an HRT of 6 h and found the optimum yield at pH 5.5. Lay (2000) considered the pH effect on H_2 production from soluble starch by anaerobic digested sludge in a chemostat reactor. Experimental results indicated that the maximum H_2 production rate was obtained at pH = 5.2 and HRT = 17 h, while the culture favored alcohol production when the pH was lower than 4.1. This implies that the metabolism shifted from hydrogen/VFA production to alcohol production at pH < 4.1. Similarly, Mu et al. (2006c) showed that volatile fatty acids (VFA) and ethanol formation was pH-dependent. Ethanol production decreased when pH was decreased from 4.2 to 3.4. In contrast, butyrate concentration decreased when pH was increased from 4.2 to 6.3. It has been reported that high VHPR is associated with butyrate and acetate production and that inhibition of H_2 production is associated with propionic acid formation (Oh et al., 2004; Wang et al., 2006).

Yu et al. (2002) suggested that the optimum pH level was 5.5 for continuous H_2 production from rice winery wastewater by a mixed bacterial flora using an upflow reactor. However, Ren et al. (1997) indicated that the operating pH must be maintained at about 4.5 in an anaerobic sludge system, a CSTR reactor receiving molasses as the feed, to avoid onset of propionic fermentation and to gain a maximum fermentation rate. Cheong and Hansen (2006) stud- ied H_2 production from glucose by mixed anaerobic bacteria in batch culture with pH controlled at 4.6, 5.7, and 6.8. The results showed that higher H_2 yield was significantly related to butyric acid formation. The reactor operated at a pH controlled at 5.7 showed higher H_2 yield than those operated at other pH values, where butyric acid (as 50.8%–75.8% of total acidogenic liquid products) was dominant. The presence of propionic acid and ethanol indicated a decrease in H_2 production. Fan et al. (2006a) investigated the pH effect on H_2 production from brewery waste by cattle dung compost in a CSTR system at HRT = 18 h. The results indicated that maximum H_2 production (47% H_2 concentration, 43 mL H_2/g COD_{added}, and 3.1 L H_2/L reactor/day) was achieved at pH = 5.5.

There is still some disagreement on the optimal initial pH for fermentative H_2 production. For example, batch operation with a mixed culture (using sucrose and starch as substrate) and hydrogen-producing sludge (using rice slurry as substrate) obtained the highest H_2 production yield at a pH of 4.5 (Khanal et al., 2004; Fang et al., 2006). However, Lee et al. (2002) reported an unusual result in which the optimal pH was 9.0 for the batch biohydrogen fermentation of sucrose. The possible reason for this disagreement was the difference among these studies in terms of inoculum, substrate, and initial pH range studied. The foregoing results suggest that a proper control of pH appears to be essential for successful operation of biohydrogen-producing reactors.

9.4.5 Temperature

Temperature is an important environmental factor that influences the growth rate and metabolic activities of hydrogen-producing bacteria and fermentative H_2 production (Bailey and Ollis, 1986). Fermentation reactions can be operated at mesophilic (25°C–40°C),

thermophilic (40°C–65°C), extreme thermophilic (65°C–80°C), or hyperthermophilic (>80°C) temperatures. Most of the biohydrogen-producing studies were performed under mesophilic conditions and some under thermophilic conditions at a constant temperature. In comparable studies reported in the literature, the optimal temperature for H_2 production via dark fermentation varied widely, mainly depending on the type of H_2 producers and carbon substrates (Table 9.6). Nevertheless, the optimal temperatures were in the range of 37°C–45°C for pure culture *Clostridium* or *Enterobacter* species, whereas the mixed bacterial flora gave distinct optimal temperatures and were more effective at thermophilic conditions (Table 9.6).

Recently, semicontinuous H_2 production at mesophilic and thermophilic conditions was studied by Valdez-Vazquez et al. (2005). They found that volumetric H_2 production rate (VHPR) was 60% greater at thermophilic than at mesophilic conditions. The result suggests that this behavior might be due to the optimal temperature for the enzyme hydrogenase (50°C and 70°C) present in thermophilic *Clostridia* sp. Yu et al. (2002) studied the effect of temperature (20°C–55°C) on H_2 production from rice winery wastewater by mixed anaerobic cultures in an upflow anaerobic reactor. The results showed that the partial pressure of H_2, H_2 yield, and specific H_2 production rate increased with temperature. Wu et al. (2005) utilized ethylene–vinyl acetate copolymer (EVA) to immobilize acclimated sewage sludge for investigating the effect of temperature on H_2 production from sucrose in a batch test. The results showed that operation at 40°C attained the best specific H_2 production rate, with a H_2 yield of 389 mL/g VSS/h and 1.41 mol H_2/mol sucrose, respectively. Thermophilic continuous operation on glucose had been reported by Zoetemeyer et al. (1982a) with an optimum temperature of 52°C. It was also reported that shorter retention times may be used under thermophilic conditions. However, the process could become less stable and more sensitive to small changes in HRT or organic load, highlighting the need for sound online monitoring and control (Hawkes et al., 2002). It was observed that fermentation at temperatures above 37°C may be useful in inhibiting the activity of H_2 consumers (Lay et al., 1999) and suppressing lactate-forming bacteria (Oh et al., 2004), resulting in higher yield in both cases. Moreover, Lee et al. (2006b) studied the effect of temperature on H_2 production in a carrier-induced granular sludge bed bioreactor (CIGSB) and found that increasing the temperature from 35°C to 45°C inhibits cell growth or granular sludge formation due primarily to denaturation of essential enzymes to paralyze nor- mal metabolic functions or to the decrease in production of extracellular polymeric substances. Another potential disadvantage of thermophilic processes is the increased energy costs.

Zhang et al. (2003) compared the H_2 production from starch at 37°C and 55°C by mesophilic sludge with batch experiments. The results showed that more starch was converted into H_2 at 55°C, although the sludge required a longer lag time for H_2 production. On the other hand, Fang et al. (2006) compared H_2 production from rice slurry at 37°C and 55°C by anaerobic digester sludge with batch experiments. The results showed that the mesophilic sludge was more effective than the thermophilic sludge in treating rice slurry. The maximum specific H_2 production rate and H_2 yield at 37°C were calculated as 2.1 L/g VSS/day and 346 mL/g carbohydrate. Also, the biohydrogen production from glucose in the CSTR at the mesophilic and thermophilic temperature ranges was studied and com- pared (Gavala et al., 2006). In this study, Gavala et al. found that the thermophilic condi- tions resulted in low volumetric H_2 production rate with poor microbial mass production, whereas they gave a higher specific H_2 production rate compared to mesophilic conditions at 6–12 h HRT.

Mu et al. (2006c) investigated H_2 production from glucose by mixed-culture anaerobes at various temperatures in the mesophilic range (33°C–41°C). Results showed that glucose degradation rate and efficiency, H_2 yield, and growth rate of H_2-producing bacteria all increased as the temperature increased from 33°C to 41°C. However, the specific H_2 production rate increased with increasing temperature from 33°C to 39°C, then decreased as the temperature was further increased to 41°C (Mu et al., 2006c). Through thermodynamic analysis, the activation energies for H_2 production and microbial growth were estimated as 107.66 and 204.77 kJ/mol, respectively. It has been demonstrated that within an appropriate range, increasing temperature could enhance the ability of hydrogen-producing bacteria to produce H_2 during fermentative H_2 production. However, at a higher temperature, decrease in H_2 yield was observed. The literature survey for the effect of temperature on fermentative H_2 production indicates that glucose and sucrose are the most widely used substrates and that most of the reviewed studies were con- ducted in batch mode (Table 9.6). Thus, investigations on the effect of temperature on fermentative H_2 production using organic wastes as substrate and conducted in continu- ous mode are recommended.

9.4.6 Oxidation–Reduction Potential

The oxidation–reduction potential is a good indicator to determine the anaerobic conditions useful for higher H_2 production. The value of ORP depends upon the strain as well as the substrate used during the study. Cohen et al. (1984) showed a strong linear inverse correlation between ORP and butyrate production over the range of −300 mV (maximum butyrate) and −100 mV (zero butyrate) using activated sludge inoculum and continuous operation on a glucose–mineral salts medium. This was likely due to the selection of propionate-producing species as the ORP rose. It is thus important to maintain the ORP near −300 mV to attain maximal H_2 yield for the culture. Ren et al. (2001) studied the effects of pH and ORP on fermentation types in continuous flow acidogenic reactors using molasses as substrate. They indicated that higher ORP (> −100 mV) would lead to propionic-type fermentation because propionogens are facultative anaerobic bacteria. When ORP came down to −200 mV, typical butyric-type fermentation occurred.

9.4.7 Inorganic Nutrients

The carbon-to-nitrogen (C/N) ratio is important for biological processes since nitrogen is an important component in proteins, nucleic acids, and enzymes and one of the most essential nutrients needed for the growth of hydrogen-producing bacteria. Thus, providing an appropriate level of nitrogen is beneficial for the growth of hydrogen-producing bacteria and for fermentative H_2 production (Bisaillon et al., 2006). The optimum C/N ratio at 47 provided efficient conversion of sucrose to H_2 gas by using acclimated anaero- bic sewage sludge with a yield of 4.8 mol H_2/mol sucrose in batch experiments reported earlier (Lin and Lay, 2004a). Experimental results indicated that the H_2 production ability depended on the influent C/N ratio. Under optimum C/N ratio, H_2 production increased by 500% and 80%, respectively, when compared with that obtained from the blank experiments. In addition, Cheng et al. (2002) demonstrated that the use of a proteinaceous substrate, that is, peptone, could avoid the abrupt pH drops in the H_2 fermentation system due to the production of ammonia from fermenting peptone. Thus, with the addition of pep- tone in the feed, their H_2 fermentation system can be stably maintained without additional pH control. They also investigated the concentration effects of carbonate and phosphate

on biological H_2 production using a Taguchi orthogonal array (Lin and Lay, 2004b). Experimental results indicated that the H_2 production ability of the anaerobic microflora in sewage sludge was affected by NH_4HCO_3, Na_2HPO_4, and Na_2CO_3, with Na_2HPO_4 being the most significant supplement. Optimal H_2 production was observed with the addition of 600 mg/L Na_2HPO_4. When proper carbonate and phosphate concentration formulation was used, the H_2 production rate was enhanced 1.9 times compared with an acidogenic nutrient formulation. Ueno et al. (2001b) used a continuous reactor for H_2 production from cellulose powder with thermophilic anaerobic microflora enriched from sludge compost. The H_2 production yield was 2.0 mol/mol hexose when the medium contained both NH_4Cl as an inorganic nitrogen source and peptone as an organic nitrogen source. However, the medium without peptone demonstrated a lower H_2 production yield of 1.0 mol/mol hex- ose, while a lesser amount of butyrate was formed. This implies the need for an appropri- ate organic nitrogen source in media rich in starch, cellulose, or hemicellulose products. Table 9.7 summarizes several studies investigating the effect of nitrogen concentration on fermentative H_2 production. The results show some disagreement on the optimal ammonia nitrogen concentration for fermentative H_2 production. For example, Bisaillon et al. (2006) and Salerno et al. (2006) reported the optimal ammonia nitrogen concentration for fermentative H_2 production to be 0.01 and 7.0 g N/L, respectively. The possible reason for this variation may be due to the differences among these studies in terms of the inoculum and ammonia nitrogen concentration range studied. However, this type of study is most widely carried out using glucose as substrate and ammonia as nitrogen source in batch mode. Further investigation should be done using more complex organic waste and different nitrogen sources under chemostat operation.

Phosphate is also needed for H_2 production due to its nutritional value as well as buffering capacity. Within an appropriate range, increasing phosphate concentration could increase the ability of hydrogen-producing bacteria to produce H_2 during fermentative H_2 production. But decrease in H_2 yield was observed at higher levels (Lay et al., 2005; Bisaillon et al., 2006). Thus an appropriate C/N and C/P ratio is essential for better fermentative H_2 production. The optimal C/N and C/P for fermentative H_2 production reported by Argun et al. (2008) were 200 and 1000, respectively. On the other hand, O-Thong et al. (2008a) reported the values to be 74 and 559, respectively. The possible reason for this disagreement was the difference among these studies in terms of the substrate, C/N range, and C/P range studied. The results suggest that the C/N and C/P ratios have a significant effect on fermentative H_2 production.

9.4.8 Trace Metal Elements

Biohydrogen production requires certain essential trace metal elements (micronutrients) for bacterial metabolism and growth. Many different micronutrient formulations have been used in studies on biohydrogen, and they exhibited variations in H_2 production effectiveness. Fe^{2+} was the most widely investigated metal ion for fermentative H_2 production, as iron is a cofactor of hydrogenase, which catalyzes the reaction to generate H_2. Limitation in iron in the culture medium lowers hydrogenase activity (Wang and Wan, 2008). Lee et al. (2001) reported that low iron concentrations favored ethanol and butanol production from batch studies with mixed cultures on sucrose, whilst maximum H_2 yields were observed when 800 mg $FeCl_2$/L was added to the growth medium. Lin and Lay (2005) explored the effect of nutrient formulation for biological H_2 production by anaerobic microflora of sewage sludge in a batch experiment using Taguchi orthogonal arrays. Experimental results

indicated that the sewage sludge enriched with the proposed nutrients had a H_2 productivity of 3.43 mol H_2/mol sucrose, which was about 30% higher than those of a control and an acidogenic nutrient formulation. Magnesium, sodium, zinc, and iron were found to be important trace metals affecting H_2 production, with magnesium being the most significant. Zhang et al. (2005) investigated the effect of iron concentration (0–5000 mg $FeSO_4$/L) on H_2 yield in batch tests by heat-shocked mixed cultures growing on a sucrose mineral medium at 35°C. The maximum H_2 production (2.73 mol of H_2/mol sucrose) was obtained at an iron concentration of 1600 mg $FeSO_4$/L. The H_2 production yield and the butyric acid and acetic acid ratio followed a similar trend, suggesting that the formation of butyrate favors H_2 production. Yang and Shen (2006) investigated the role of ferrous ion concentration ($FeSO_4$) on anaerobic mixed bacteria for conversion of soluble starch to H_2 in both batch experiments at initial pH 7.0 and 8.0, respectively. At initial pH = 8.0, the H_2 yield significantly increased from 106.4 to 274.0 mL/g starch with increasing iron concentration from 0 to 200 mg $FeSO_4$/L. When iron concentration continued to increase from 200 to 4000 mg $FeSO_4$/L, iron inhibition did not happen. Furthermore, Zhang and Shen (2006) explored the effects of temperature and iron concentration on H_2 production from sucrose with mixed bacteria dominated by *Clostridium pasteurianum* in batch experiments. Experimental results showed that the optimum iron concentrations for H_2 production decreased with increasing culture temperature. For 25°C, 35°C, and 40°C, the maximum H_2 yield was obtained at iron concentrations of 800, 200, and 25 mg $FeSO_4$/L, respectively. In addition, several studies were also conducted to investigate the toxicity of heavy metals to fermentative H_2 production.

Recently, Li and Fang (2007b) reported that the relative toxicity of six heavy metals to fermentative H_2 production was in the following order: Cu > Ni–Zn > Cr > Cd > Pb. In contrast, Lin and Shei (2008) reported that the relative toxicity of three heavy metals to fermentative H_2 production was in the following order: Zn > Cu > Cr. Moreover, Zheng and Yu (2004) investigated the influence of copper and zinc on H_2 production from glucose by enriched anaerobic culture in batch experiments. Results showed that the specific H_2 production rate was enhanced by the dosage of Cu at 50–100 mg/L or the dosage of Zn at 100–250 mg/L, but was inhibited by Cu over 200 mg/L or Zn at 500 mg/L. The H_2 production yield was enhanced by 5–400 mg/L of Cu or 5–500 mg/L of Zn. In terms of the $C_{I,50}$ values, Cu was observed to be more toxic than Zn. Thus at a higher concentration, metal ions may inhibit the activity of hydrogen-producing bacteria, and a trace level of metal ion might be required for fermentative H_2 production (Li and Fang, 2007b). Table 9.8 summarizes several studies investigating the effect of metal ion concentration on fermentative H_2 production.

9.4.9 Hydrogen Partial Pressure (P_{H_2})

Generally, in biological production of H_2, all of the observed H_2 can be attributed to electrons derived from a single reaction: oxidative decarboxylation of pyruvate by pyruvate:ferredoxin oxidoreductase (Figure 9.3). Hexoses can be metabolized to pyruvate through several pathways, often involving the Embden–Meyerhof–Parnas (i.e., glycoly- sis) or the Entner–Doudoroff pathways. Both of these pathways produce 2 mol of pyru- vate and 2 mol of NADH for every mole of hexose that is transformed. Therefore, hexose metabolism by bacteria that contain pyruvate:ferredoxin oxidoreductase can result in the formation of 2 mol of H_2 per mole of hexose. If the H_2 partial pressure is sufficiently low (<60 Pa), the NADH produced may also be used to generate H_2 (at best, an additional 2 mol

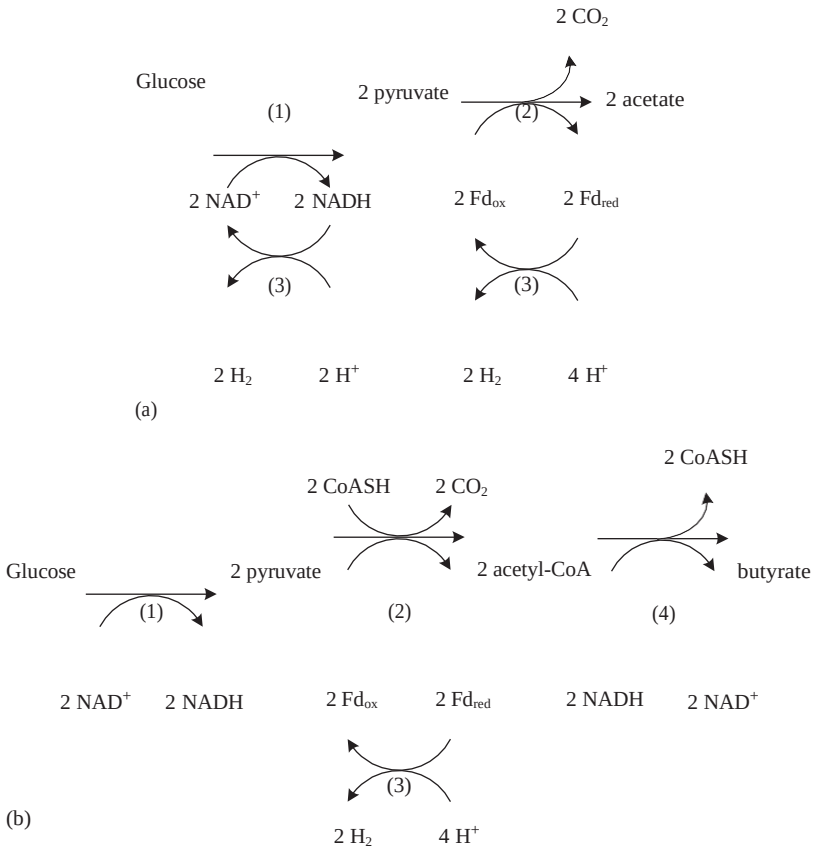


FIGURE 9.3

Effect of H_2 partial pressure on biological production of hydrogen: (a) Oxidation of NADH by produc- tion of H_2 is thermodynamically favorable only when the H_2 partial pressure is less than 60 Pa, other- wise, (b) other fermentation products must be formed. Reactions [(a) P_{H_2} < 60 Pa and (b) P_{H_2} > 60 Pa]: 1, glucose metabolism through glycolysis or the Entner–Doudoroff pathway; 2, oxidative decarboxylation of pyruvate by pyruvate:ferredoxin oxidoreductase; 3, formation of H_2 by hydrogenase; and 4, butyrate fermentation.

of H_2 mol of glucose). However, most of the NADH is probably oxidized through other fermentation pathways, such as butyrate fermentation (Figure 9.3, step 4). Some fermentation products (e.g., ethanol and lactate) represent the operation of alternative pathways for pyruvate metabolism that compete with pyruvate:ferredoxin oxidoreductase. As such, they are usually associated with systems that produce less than 2 mol of H_2 mol of glucose (Angenent et al., 2004).

The partial pressure of H_2 (P_{H_2}) is an extremely important factor for continuous H_2 generation. The increase in the partial pressure of H_2 (P_{H_2}) to a certain level in the reactor headspace might cause a diversion of metabolic shift toward alcohol production and thus lead to less H_2 production. H_2 synthesis pathways are sensitive to H_2 concentrations and subject to end-product inhibition. As H_2 concentration increases, H_2 synthesis decreases and metabolic pathways shift to production of more reduced substrates such as lactate, ethanol, acetone, butanol, or alanine (Levin et al., 2004). As the temperature increases, H_2 concentration affects H_2 synthesis more significantly. For continuous H_2 synthesis, P_{H_2} of <50 kPa at 60°C (Lee and Zinder, 1988), <20 kPa at 70°C (van Niel et al., 2002b), and <2 kPa

at 98°C (Adams, 1990) were reported.

Several strategies—mainly sparging with inert gas and using a silicone rubber membrane to avoid the negative effect of the accumulation of H_2 in the gaseous space—have been developed. Mizuno et al. (2000) have demonstrated that lowering H_2 partial pressure by sparging with N_2 gave a 68% increase in H_2 yield from a CSTR reactor containing an enriched mixed microflora with 10 g/L glucose at pH 6.0 and HRT 5 h. Liang et al. (2002) used a silicone rubber membrane to separate biogas from the liquid medium

in the H_2 fermentation reactor. Their results showed that the silicone rubber effectively reduced the biogas partial pressure in the H_2 fermentation reactor and improved the H_2 evolution rate by 10% and the H_2 yield by 15%. Hussy et al. (2005) investigated the effect of sparging on continuous H_2 production from sucrose and sugarbeet juice using mixed microflora. With N_2 sparging, H_2 yields were 1.9 and 1.7 mol H_2/mol hexose for sucrose and sugarbeet juice, respectively, at 14–15 h HRT, which was about 90% higher than those without sparging.

9.5 Bioreactor Configuration

Many studies were conducted in batch mode to examine the characteristics of H_2-producing bacteria and to optimize culture-operating conditions. The worse microbial cultures led to lower H_2 production rates. Enhancing H_2 production efficiency, stability, and sustainability is thus a major challenge in batch H_2 systems. Recently, Valdez-Vazquez et al. (2005a) examined H_2 production from municipal solid wastes in another semicontinuous pattern. Reactors that were fed with substrate twice a week in a fill-and-draw mode in an anaerobic chamber and operated continuously at 35°C and 55°C for 40 days demonstrated steady H_2 production. The high-rate biodegradation processes are based on the concept of retain- ing high-concentration viable biomass by some mode of bacterial sludge immobilization. These are achieved by one of the following methods (Hulshoff and Lettinga et al., 1981; Rajeshwari et al., 2000):

1. Entrapment of sludge aggregates between packing materials supplied to the reac- tor, for example, anaerobic filter (packed bed).
2. Bacterial attachment to high-density particulate carrier materials, for example, fluidized bed reactors and anaerobic expanded bed reactors.
3. Formation of highly settleable sludge aggregates combined with gas separation and sludge settling, for example, upflow anaerobic sludge blanket reactor and anaerobic baffled reactor.

9.5.1 Continuous-Flow Stirred-Tank Reactor

The literature survey suggests that most of the studies on fermentative H_2 production were conducted in batch mode because of its simplicity and easy operation and control. However, for large-scale H_2 production, continuous processes are required because of practical engineering reasons. Table 9.4 summarizes a number of studies using continuous reactors for fermentative H_2 production. Continuous-flow stirred-tank reactors (CSTRs) are the most frequently used reactors for continuous production of H_2 from organic matter (Das and Veziroglu, 2001; Hawkes et al., 2002; Chen and Lin, 2003; Levin et al., 2004; Gavala et al., 2006; Zhang et al., 2006, 2007; Lee et al., 2007; Chen et al., 2008b; Wu et al., 2008b; Wang and Wan, 2009). As shown in Table 9.4, glucose and sucrose were the most widely used substrates for continuous H_2 production under CSTR operation. The average yield obtained was between 1.5 and 2.3 mol H_2/mol glucose. A pilot-scale CSTR (with an avail- able volume of 1.48 m^3) for biohydrogen production was operated for over 200 days by Ren

et al. (2006). The system was operated under the organic loading rate (OLR) of 3.11–85.57 kg COD/m³/day with molasses as the substrate. A maximum H_2 production rate of 5.57 L/L/ day was obtained at an OLR of 68.21 kg COD/m³/day (HRT = 3.9 h).

In CSTR operation, the biomass is well suspended in the mixed liquor, which has the same composition as the effluent. It was observed that the biomass has the same retention time as the HRT and that washout of biomass may occur at shorter HRT. Recently, the effect of organic loading rate on H_2 production from glucose in chemostat reactors using a heat-shocked agricultural soil as inoculum was studied. In this study, at influent glucose concentrations of 5–10 g COD/L, substantial flocculation was observed particularly as the feeding rate increased due to a reduction in the HRT from 10 to 2.5 h. At an HRT of 2.5 h, the biomass concentration reached values as high as 25 g/L. The flocculant nature of the biomass allowed reactor operation at low HRTs with steady H_2 production and >90% glu- cose removal. However, when the HRT was reduced to 1 h at a glucose feed concentration of 2.5 g COD/L, there was little flocculation evident resulting in washout of the culture (van Ginkel and Logan, 2005). It has been demonstrated that in an appropriate range, increasing HRT could increase the ability of hydrogen-producing bacteria to produce H_2 during fermentative H_2 production. But marginal reduction in yield was observed at a much higher HRT level (Chen et al., 2008b). Furthermore, there exists certain disagree- ment on the optimal HRT for chemostat reactors, even for the same type of reactor. The optimal HRT for a CSTR was 96 h as reported by Cheng et al. (2002) and 12 h as reported by Arooj et al. (2008), whereas the optimal HRT for a CSTR was 0.5 h as reported by Zhang et al. (2007) (Table 9.4). The possible reason for the variation in optimal HRT might be due to the difference in terms of inoculum, substrate, and HRT range studied. Fang et al. (2002) demonstrated that hydrogen-producing acidogenic sludge agglutinated into granules in a well-mixed reactor treating a synthetic sucrose-containing wastewater at HRT = 6 h. They obtained a H_2 production rate of 13.0 L/L/day and a yield of 0.28 L/g sucrose (3.91 mol H_2/mol sucrose). However, CSTRs do have certain limitations. First, the CSTR system is very sensitive to environmental conditions such as changes in pH and HRT. Additionally, operation at a high dilution rate (or short residence time) can lead to washout of biomass, limiting its hydrogen-producing rate (Show et al., 2008). Therefore, several researchers attempt to retain high biomass by various bioreactor designs and/or operation strategies.

9.5.2 Anaerobic Sequencing Batch Reactor

A high-rate anaerobic sequencing batch reactor (ASBR) has been used to evaluate H_2 production from sucrose with acclimated sewage sludge by Lin and Jo (2003). Results show that the H_2 production depended on hydraulic retention time (HRT) and reaction/settling period (R/S) ratio. A short equivalent HRT, even up to 4 h, resulted in good H_2 productivity and high H_2 production rate (HPR). For each equivalent HRT, R/S ratio control also increased the H_2 productivity and HPR (Table 9.4). Reactor operation at an intimate control of HRT and R/S ratio was preferable for H_2 production. At an HRT of 8 h, an R/S ratio of 5.6, and an organic loading rate of 0.23 mol sucrose/L/day, the H_2 yield of the mesophilic hydrogenic reactor was 2.6 mol H_2/mol sucrose and the specific H_2 production rate was
0.069 mol H_2/day/g biomass. H_2 productivity by using an acid-enriched sewage sludge with sucrose (20 g COD/L) at 35°C was studied recently by using ASBR. The HRT was initially maintained at 12–120 h and thereafter at 4–12 h, with the R/S ratio maintained at 1.7. Hydrogenic activity of sludge microflora was found to be HRT-dependent, and proper pH control was necessary for a stable operation of the bioreactor. Higher H_2 production

was noted at an HRT of 8 h and an OLR of 80 kg COD/m^3/day, giving the highest yield of 2.8 mol H_2/mol sucrose and a specific production rate of 39 mmo H_2/g biomass/day. Extremely low HRT might deteriorate H_2 productivity. Concentration ratios of acidogenic and other soluble microbial products can be used as monitoring indicators for a hydrogenic bioreactor (Lin and Chou, 2004).

9.5.3 Membrane Bioreactor

Membrane bioreactors (MBRs) have recently emerged as an effective means for increasing biomass retention in wastewater treatment (Wen et al., 1999). Although MBRs allow high biomass concentration in the reactor without suffering mass transfer limitations, there is little information regarding the use of MBRs for fermentative H_2 production. Kim et al. (2005) used an MBR system with glucose as a substrate, which gave a yield of 1.1 mol H_2/mol glucose with a maximum VHPR of about 71.4 mmol/L/h. Liang et al. (2003) used a microfiltration membrane to recover hydrogen-producing bacteria, allowing accumulation of biomass from 500 mg/L to 5200 mg VSS/L. The fermentor employed mixed-culture consortia to ferment multiple substrates including peptone and glucose at 55°C. The maximum H_2-producing rate was 28 mmol H_2/L h and the maximum specific H_2-producing rate was 4.6 mmol H_2/g VSS/h when the fermentor was operated at more than 80 g COD/L day. The H_2 yield was 8.41 mmol H_2/g COD. Oh et al. (2004) reported that the H_2 production rate from glucose with mixed culture was enhanced 27% with MBR at a short HRT of 3.3 h, while the biomass concentration increased 164%. This demonstrates the possibility of using MBR to improve the performance of biohydrogen production (Table 9.4).

Lee et al. (2007) used an MBR system fabricated by connecting a hollow-fiber microfiltra- tion membrane module with a CSTR to enhance H_2 production through high–dilution rate operations. They demonstrated that the MBR system was effective in retaining biomass within the reactor as the system can be stably operated at a low HRT of 1 h with an opti- mal steady-state HPR of 1.48, 2.07, and 2.75 L/h/L, respectively, with glucose, sucrose, and fructose as the sole carbon source (Table 9.4). Nevertheless, the use of MBR systems has been limited to the laboratory scale. This may be due to the high operating cost as well as membrane caking and fouling problems. However, it has been shown that using MBRs in wastewater treatment could be more cost-effective when compared to conventional wastewater treatment plants with secondary clarification (Gander et al., 2000). Moreover, revolutionary advances in membrane technology have reduced the cost of membranes and also created methods to solve the problem of membrane fouling, such as the addition of coagulants, crossflushing, imposing a pulsed electric field, backwashing, and rapid back- pulsing (Ma et al., 2000). Therefore, the MBR is still a promising process for H_2 production from organic substrates.

9.5.4 Packed-Bed Reactor

Fixed- or packed-bed reactors offer the advantages of simplicity of construction, elimination of mechanical mixing, better stability at higher loading rates, and the capability to withstand large toxic shock loads and organic shock loads. The reactors can recover very quickly after a period of starvation. In stationary packed-bed (fixed-bed) reactors, the reactor has a biofilm support structure (media) such as activated carbon, PVC (polyvinyl chloride) supports, hard rock particles, or ceramic rings for biomass immobilization. The substrate (wastewater) is evenly distributed from above or below the media. The main limitation of this design is that the reactor volume is relatively high compared to other

high-rate processes due to the volume occupied by the media. Another constraint is clogging of the reactor due to the increase in biofilm thickness and/or high suspended solids concentration in the wastewater (Kennedy and Droste, 1985; Van den Berg et al., 1985; Rajeshwari et al., 2000) (Table 9.4).

Most of the studies on H_2 fermentation by employing packed-bed processes focused on pure cultures (Yokoi et al., 1997; Rachman et al., 1998; Palazzi et al., 2000; Kumar and Das, 2001). Support materials also have important effects on biomass retention and consequently H_2 production in fixed-bed reactors. Chang et al. (2002) conducted biohydrogen production by mixed culture with packed-bed bioreactors in batch and continuous modes. Three porous materials, namely, loofah sponge (LS), expanded clay (EC), and activated carbon (AC), were assessed because of their effectiveness in biofilm formation. It was found that LS was inefficient for biomass retention, while EC and AC exhibited better biomass yields. The packed-bed reactors with EC or AC were thus used for continuous H_2 fermentation at an HRT of 0.5–5 h. PBR with cylindrical activated carbon exhibited a better H_2 production rate of 1.32 L/L/h at an HRT of 1 h. However, the packed-bed reactor was of limited use in reducing the effective volume in the reactor due to the presence of solid supports, which occupied a significant portion of the working volume. Thus, the effect of the void fraction of the bed (ε_b, 70–90%) on H_2 fermentation in packed-bed systems was examined (Lee et al., 2003). The results showed that higher ε_b favored H_2 production, and the optimal H_2 production rate (7.35 L/L/h) was obtained with ε_b = 90% at HRT = 0.5 h with 20 g COD/L of sucrose in the feed. During the investigation of void fraction effect, flocculation of cells to form granular sludge was accidentally observed, which was more abundant when the void space increased.

Kumar and Das (2001) observed that both H_2 production and substrate conversion rate of a packed-bed reactor increased with recycling ratio and the maximum H_2 production rate (1.69 L/L/h) was observed at a recirculation ratio of 6.4. Moreover, Rachman et al. (1998) observed that high H_2 molar yield could not be maintained consistently in a packed-bed reactor, although the pH in the effluent was controlled at >6.0. This is because pH gradient dis- tribution along the reactor column resulted in a heterogeneous distribution of microbial activ- ity. In order to overcome the mass transfer resistance and pH heterogeneous distribution, a fluidized-bed or an expanded-bed reactor system with recirculation flow was recommended to be more appropriate in further enhancing the H_2 production rate and yield. Increasing slurry recycle ratio can thus alleviate mass transfer resistance in a packed-bed reactor.

9.5.5 Fluidized-Bed Reactor

Cell immobilization techniques have been applied to improve cell retention and were shown to be suitable for continuous H_2 production (Wu et al., 2003). Most H_2 fermentation associated with immobilized cells was conducted in packed-bed reactors (Yokoi et al., 1997; Rachman et al., 1998; Palazzi et al., 2000; Kumar and Das, 2001), which often suffer from inefficient mass transfer even though they are relatively inexpensive and easy to operate. However, for immobilized cells created by entrapment methods, mass transfer efficiency is often a limiting factor. In addition, when using immobilized systems, it is important to consider that the excessive amount of gases (H_2 and CO_2) in the reactor could lead to inhibition of hydrogen-producing microorganisms. This may be due to changes in pH (Table 9.4).

Generation of gaseous products from H_2 fermentation further highlights the importance of mass transfer efficiency for the immobilized-cell system. As a result,

fluidized-bed reactors may be preferable to the packed-bed reactors in biohydrogen production. However, reports regarding the use of fluidized beds for H_2 fermentation have been quite rare. Wu et al. (2003) used three-phase fluidized beds to produce H_2 from sucrose with immobilized hydrogen-producing sludge. The fluidized bed can be stably carried out at a high loading rate (HRT as low as 2 h), and the maximal H_2 production rate and yield were 0.93 L/L/h and 2.67 mol H_2/mol sucrose, respectively. Recently, fluidized-bed reactor (FBR) and draft tube fluidized-bed reactor (DTFBR) sys- tems with immobilized cells were studied for the production of H_2 using sucrose (Wu et al., 2006). The results showed that the VHPR obtained with DTFBR (95.23 mmol/L/h) was higher than that obtained with FBR (50.27 mmol/L/h) (Table 9.4).

9.5.6 Granular Sludge Reactors

Upflow anaerobic sludge blanket (UASB) technology is being used extensively for effluents from different sources such as distilleries, food processing units, tanneries, and municipal wastewater. The active biomass in the form of sludge granules is retained in the reactor by direct settling for achieving high cell retention time, thereby achiev- ing highly cost-effective designs. A major advantage of this technology is the compara- tively less investment costs when compared to a packed-bed or a fluidized-bed system. Moreover, a UASB reactor essentially consists of a gas–solid separator (to retain the anaerobic sludge within the reactor), an influent distribution system, and effluent draw- off facilities. Effluent recycling (to fluidize the sludge bed) is not necessary as sufficient contact between wastewater and sludge is guaranteed even at low organic loads with the influent distribution system (Rajeshwari et al., 2000). However, a long start-up period and the requirement for a sufficient amount of granular seed sludge for faster start-up are among notable disadvantages.

Vijayaraghavan et al. (2006) demonstrated H_2 production from solid waste consisting of jackfruit peel with microflora isolated from cow dung in an upflow anaerobic contact filter packed rigid with circular porous plastic balls of 40 mm diameter. The effect of HRT on the destruction efficiency of volatile solids was investigated for an influent volatile solids content of 33 g/L at an HRT of 7 and 12 days. The results showed a volatile solids destruction efficiency of 22% and 50%, respectively. In this study H_2 production rate and H_2 yield were 23.6 mL/L/h and 16.2 mmol/g VS destroyed, respectively, at an HRT of 12 days (Table 9.4).

Liu et al. (2003) reviewed the existing mechanisms and models for anaerobic granulation in the UASB reactor, and proposed a general three-step model for anaerobic granulation as follows:

Step 1: Physical movement to initiate bacterium-to-bacterium contact or bacterial attachment onto nuclei. The forces involved in this step are hydrodynamic force, diffusion force, gravity force, thermodynamic forces like Brownian movement, and cell mobility.

Step 2: Initial attractive forces to keep stable multicellular contacts. Those attractive forces are physical, chemical, and biochemical forces:

Physical forces: Van der Waals forces, opposite charge attraction, thermodynamic forces including free energy of surface; surface tension, hydrophobicity, and filamentous bacteria that can serve as bridges to link or grasp individual cells together.

Chemical forces: H_2 liaison, formation of ionic pairs and triplets, and interparticulate bridge.

Biochemical forces: Cellular surface dehydration, cellular membrane fusion, signaling, and collective action in bacterial community.

Step 3: Microbial forces making cell aggregation mature. The process is as follows: Extracellular polymers such as exopolysaccharides are produced by bacteria. Then growth of cellular clusters is observed, and finally metabolic change and genetic competence are induced by the environment, which facilitate cell–cell interaction and result in a highly organized microbial structure. In the last stage, the steady-state three-dimensional structure of microbial aggregates is shaped by hydrodynamic shear forces. The microbial aggregates are finally shaped by hydrodynamic shear force to form a certain structured community. The outer shape and size of microbial aggregates are determined by the interactive pattern between aggregates and by the hydrodynamic shear force, microbial species, and substrate loading rate.

Yu et al. (2002) investigated continuous H_2 production from a high-strength rice winery wastewater by a mixed bacterial flora, using an upflow reactor. The H_2 yield was in the range of 1.37–2.14 mol/mol hexose. Chang and Lin (2004) examined the H_2 production from sucrose with a UASB reactor and demonstrated the feasibility of using the UASB system for H_2 production. Gavala et al. (2006) examined and compared the biological H_2 production from glucose in a CSTR and a UASB at various HRTs (2–12 h) under mesophilic conditions. The results showed that the H_2 production rate in the UASB reactor was significantly higher than that of the CSTR at low retention times (19.05 and 8.42 mmol H_2/h/L, respectively, at 2 h HRT), while H_2 yield was higher in the CSTR reactor at all HRTs tested due to low glucose utilization. Yu and Mu (2006) evaluated the performance of a UASB for H_2 production from sucrose-rich synthetic wastewater at various substrate concentrations (5.33–28.07 g COD/L) and HRTs (3–30 h) for over 3 years. Experimental results showed that the H_2 production rate increased with both increasing substrate con- centration and decreasing HRT. The H_2 yield was in the range of 0.49–1.44 mol H_2/mol glucose. The physicochemical characteristics of the granules were also evaluated (Mu and Yu, 2006). The mature granules had a diameter ranging from 1.0 to 3.5 mm and an average density of 1.036 g/mL, having good settling ability and a high settling velocity of 32–75 m/h (Table 9.4). The low ratio of proteins/carbohydrates of the extracellular poly- meric substances (EPS) in the granules suggests that carbohydrates rather than proteins might play an important role in the formation of H_2-producing granules. The contact angle of the mature granules was larger than that of the seeding sludge, indicating that the microbial cells in the H_2-producing granules had higher hydrophobicity. Results also suggested that molecular diffusion plays an important role in mass transfer through the H_2-producing granules.

It was reported that the presence of nuclei or biocarriers for microbial attachment is one of the contributing factors to the development of granules from suspended sludge (Imai et al., 1997; Teo et al., 2000). The attachment of cells to these particles has been proposed as the initiating step for granulation. The second step was the formation of a dense and thick biofilm on the cluster of inert carriers and could be considered as biofilm forma- tion. In other words, once the initial aggregates are formed, subsequent granulation could be regarded as an increase in biofilm thickness. Hence, the sludge granulation process in UASB reactors with added inert particles might be interpreted as a biofilm-forming phenomenon (Yu et al., 1999). Lettinga et al. (1981) claim that clay and other inorganic

particles are harmful for the formation of granular sludge. Several investigators have studied the effect of inert particles on granulation. According to Morgan et al. (1991), the addition of supplements to a nongranular inoculum during the start-up of UASB reac- tors is beneficial. A granular activated carbon (GAC) supplement offers two advantages: (1) sheltered ecological niches that enhance biological attachment and thus initiate gran- ule formation and, possibly, (2) a capacity for the adsorption of pollutants, which can then be degraded in the immobilized state. The activated carbon particles also enhance the development of an attached biofilm and thus act as a nucleus for granule formation. Yu et al. (1999) studied the effects of powdered activated carbon (PAC) and GAC on sludge granulation during the start-up of UASB reactors. Results showed that the addition of PAC or GAC clearly enhanced the sludge granulation process and accelerated the start- up process. Sludge granulation, defined as the time by which 10% of the granules are larger than 2.0 mm, took approximately 95 days to achieve in the reactor without addi- tion of inert materials, while the time required for sludge granulation reduced by 25 and 35 days in the PAC-and GAC-added reactors, respectively. Besides, the addition of GAC and PAC provoked higher biomass concentrations throughout the experiment and earlier observation of visible granules. It also improved the volumetric COD removal capacity. Moreover, the addition of GAC showed slightly more beneficial effects during the start- up of UASB reactors than PAC. The enhanced granulation by the addition of PAC or GAC was attributed to a better attachment of the filamentous bacteria on the activated carbon. Imai et al. (1997) studied the effects of adding water-absorbing polymer (WAP) particles into the inoculated sludge. WAP is a resin that is mainly composed of acrylic compounds and shows a complex network structure with a high specific surface for microbial attach- ment. Moreover, WAP shows a low density (wet density of 1.0 g/mL), which means that the contact between the particles and biomass is improved when compared to sand and other materials. Although the average granule size was not affected, the addition of WAP clearly enhanced the granulation in the lab-scale and pilot-scale UASB reactors using glu- cose or VFA as substrate by serving as a biocarrier to allow more biomass attachment. Yu et al. (1999) proposed the following guidelines for the choice of inert materials to enhance sludge granulation:

- High specific surface area
- Specific gravity similar to anaerobic sludge
- Good hydrophobicity
- Spherical shape

Since bacteria have negatively charged surfaces under normal pH conditions, a basic idea to expedite anaerobic granulation processes is to reduce electrostatic repulsion between negatively charged bacteria by introducing multivalence positive ions, such as calcium, ferric, aluminum, or magnesium ions, into the seeding sludge (Figure 9.4). Reduced electrostatic repulsion between bacterial particles could promote anaerobic sludge granulation (Liu et al., 2003). Kim et al. (2005) employed two immobilization methods, biofilm forma- tion on polyvinyl alcohol (PVA) and granulation of the sludge with cationic and anionic polymers, to immobilize sewage digester sludge and conducted continuous H_2 production tests in a stirred reactor simultaneously. The result showed that the granular sludge system produced much more H_2 gas than the biofilm system (ca. 120 mL/L/h vs. 20 mL/L/h at 20 h HRT). The reason was that granular sludge harbored more microorganisms (approximately

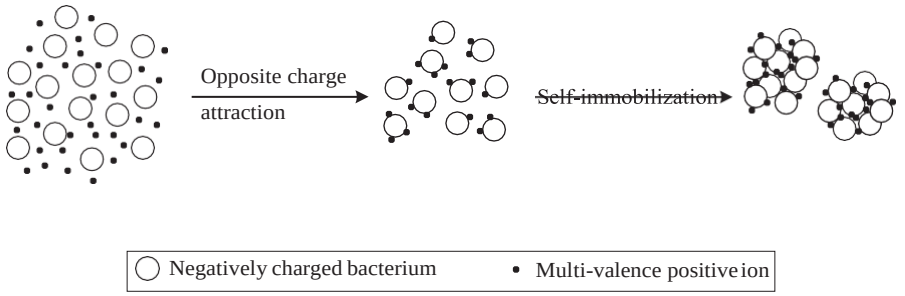


FIGURE 9.4

Schematic representation of the multivalence positive ion-bonding model. (From Liu, Y. et al., *Water Res*., 37, 661, 2003.)

7 g/L vs. 4 g/L) and its density was higher than that of the biofilm on a PVA medium. Therefore, granulation was considered to be a better method for continuous H_2 production. Lee et al. (2004a) used the inert carriers with biofilm to induce sludge granulation for enhancing H_2 production, and thereby a novel carrier-induced granular sludge bed (CIGSB) bioreactor was developed (Figure 9.5). A variety of carrier matrices were exam- ined for their effectiveness in stimulating sludge granulation. Among the carriers exam- ined, spherical activated carbon (SAC) and cylindrical activated carbon (CAC) were the more effective inducers for granular sludge formation. The SAC–CIGSB bioreactor achieved an optimal volumetric H_2 production rate of 7.33 L/L/h and a maximal H_2 yield of 3.03 mol H_2/mol sucrose when operated at an HRT of 0.5 h with an influent sucrose concentration of 20 g COD/L. In their next study, Lee et al. (2004b) stated that supplemen- tation of calcium ion enhanced the mechanical strength of the granular sludge. Addition of 5.4–27.2 mg/L of Ca^{2+} led to an over threefold increase in biomass concentration and a nearly fivefold increase in the H_2 production rate when the CIGSB bioreactor caused washout of biomass at an HRT of 0.5 h. Lee et al. (2004b) utilized two reflux strategies, both liquid and gas reflux, to enhance the mass transfer efficiency when the dead zones were found in the CIGSB due to poor mixing efficiency of the reactor. The liquid reflux (LR) strategy enhanced the H_2 production rate 2.2-fold at an optimal liquid upflow velocity of 1.09 m/h, which also gave a maximal biomass concentration of ca. 22 g VSS/L. A similar optimal H_2 production rate of 1.0–1.49 m/h was also obtained with the gas reflux (GR) strategy, whereas the biomass concentration decreased to 2–7 g VSS/L, and thereby the specific H_2 production rate was higher than that with LR. Lee et al. (2006a) also designed

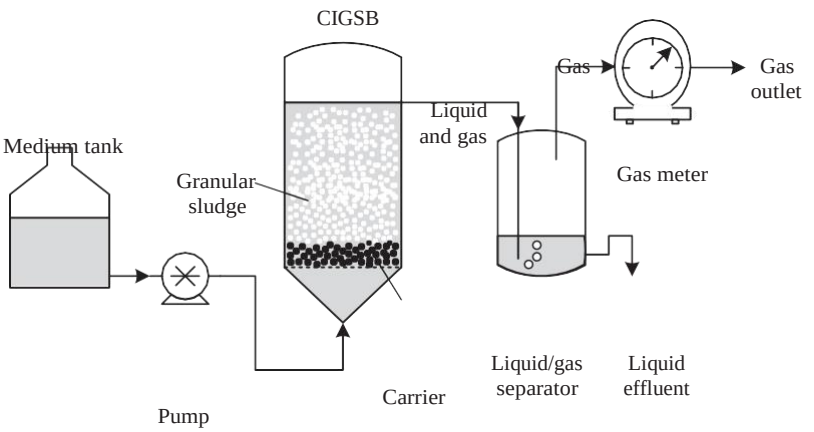


FIGURE 9.5

Schematic description of carrier-induced granular sludge bed (CIGSB) reactor.

experiments to adjust the height-to-diameter (H/D) ratios of the CIGSB bioreactor to improve the mixing efficiency for better biomass–substrate contact. The results show that the liquid upflow velocity (v_{up}) is a key factor to influence the H_2 production efficiency with a different H/D ratio. Increasing the H/D ratio gives higher v_{up}, allowing better hydraulic mixing to enhance the biomass–substrate contact, but an excessively large H/D ratio may also cause sludge floatation to diminish the sludge retention. Supply of additional mechanical agitation for the CIGSB reactor (H/D = 12) alleviated the phenomenon of sludge piston floatation, leading to further increases in the H_2 production rate and H_2 yield to 9.31 L/L/h and 4.02 mol H_2/mol sucrose, respectively.

In a traditional UASB reactor, channeling of the wastewater through the bed is frequently encountered, resulting in poor substrate–biomass contact (Jeison and Chamy, 1999). In light of this, the expanded granular sludge bed (EGSB) reactor was designed to cope with the aforementioned drawbacks of the UASB reactors. The EGSB reactors are operated at high liquid upflow velocities by increasing the height/diameter (H/D) ratio and by recirculation of effluent liquid, thereby providing better mixing of the reactor contents and allowing more efficient contact between substrate and biomass (Hwu et al., 1998). Francese et al. (1998) also showed that upflow velocity affects physical characteristics and the specific activity of granules.

Culture temperature is often an important environmental factor for the performance of a bioreactor, because it may strongly affect the growth rate and metabolic activity of bacteria in the reactor. In addition, Schmidt and Ahring (1996) observed that the concentration of extracellular polymeric substance (EPS), which plays a crucial role in cell adhesion, was lower in granules at high temperatures. Lee et al. (2006b) explored the temperature effects on biohydrogen production in the CIGSB system. This implies that the culture temperature may also affect the efficiency of sludge granulation.

Recently, Wu et al. (2006) developed a novel continuously stirred anaerobic bioreactor (CSABR) seeded with silicone-immobilized sludge for high-rate fermentative H_2 production. The CSABR system was operated at an HRT of 0.5–6 h and an influent sucrose concentration of 10–40 g COD/L. Formation of self-flocculated granular sludge occurred during operation at a short HRT. A high biomass concentration of up to 35.4 g VSS/L was achieved even though the reactor was operated at an extremely low HRT (i.e., 0.5 h). With a high feeding sucrose concentration (i.e., 30–40 g COD/L) and a short HRT (0.5 h), the CSABR reactor produced H_2 more efficiently with the highest volumetric rate of 15 L/L/h and an optimal yield of ca. 3.5 mol H_2/mol sucrose. By or after comparing the different configurations of reactors to draw a conclusion with regard to what configuration is better even under specific set conditions since many factors in particular H_2 yield and H_2 production rate depends significantly upon experimental conditions such as temperature, pH, substrate concentration, type of substrate, metal ion and HRT as well as long-term stability of the reactor and scale-up performance which directly influence on the economics of fermentative H_2 production.

9.6 Molecular Techniques for Microbial Community Characterization

For years, typically, microbial species were isolated and subsequently characterized based on their physiological and biochemical properties and culture-based studies to main- tain and evaluate process conditions. However, these methods are limited by the lack of knowledge on preparation of suitable cultivation media. Most microorganisms, presumably more than 99% of naturally occurring microbes in a particular environment, cannot

be readily isolated or cultured in laboratories with conventional enrichment techniques (Amann et al., 1995). This lack of ability in isolating unculturable microbes from a particular environment has been an obstacle in microbial community analyses. In addition, these cultivation methods are time-consuming, labor-intensive, and susceptible to bias toward nonpredominant culturable microorganisms (Vazquez and Poggi-Varaldo, 2009). As such, modern molecular techniques have revolutionized and expanded the scope of microbial systematics and physiology. The development and application of molecular techniques for microbial diversity analysis has proven superior to cultivation methods since the culture-independent molecular phylotype approaches, based on comparative analysis of gene sequences within the genome, can also infer evolutionary relationships among organisms studied (Hugenholtz and Pace, 1996). Because of its highly conserved nature, the bacterial 16S rRNA gene has emerged as one of the premier phylogenetic mark- ers, allowing for bacterial diversity studies of isolated strains and uncultured populations present in complex microbial communities. In addition, further characterization was carried out using indirect methods (metabolite distribution, enrichment methods and microscopic examination, etc.) and some advanced molecular biological techniques (DGGE, DNA cloning analysis, dot-blot hybridization, terminal restriction fragment length polymorphism) in order to determine microbial composition in hydrogenogenic processes. The strategies and some of the methods/tools used for characterizing microbial communities of environmental samples without cultivation are outlined in Figure 9.6, and the detailed discussion can be found in Hugenholtz and Pace (1996).

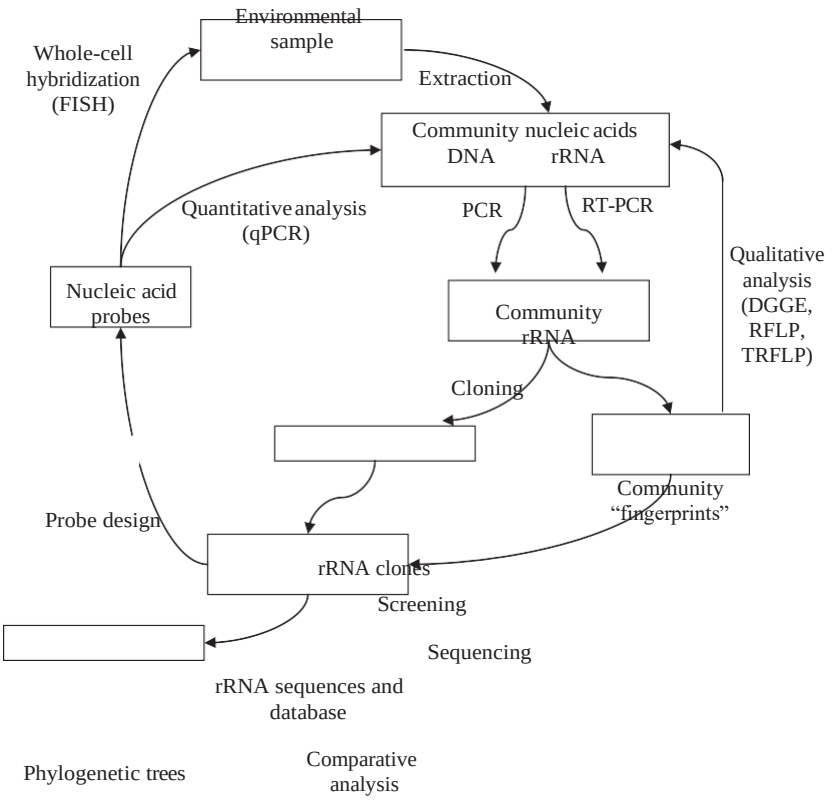


FIGURE 9.6

Strategies for characterizing microbial communities of environmental samples without cultivation. Abbreviations: DGGE, denaturing gradient gel electrophoresis; PCR, polymerase chain reaction; RFLP, restriction fragment length polymorphism; rRNA, ribosomal RNA; RT–PCR, reverse transcription PCR, qPCR, quantitative PCR, FISH, fluorescent in situ hybridization. (Modified from Hugenholtz, P. and Pace, N.R., *Trends Biotechnol*., 14, 190, 1996.)

9.6.1 Phylogenetic Analysis of Microbial Community in Biohydrogen Reactors

Researchers have attempted, using culture-independent molecular phylotype methods, to characterize the complex microbial community present in bioreactors producing H_2 from pure substrates such as glucose, sucrose, and cellulose as well as organic waste. It was observed that H_2 production using anaerobic consortia has many advantages, the main one being that organic waste or wastewater can be used without sterilization, which makes the process economically beneficial. H_2 production using microbial consortia have some major factors that need to be taken into account: a developed microbial consortium is likely to be quite complex, with not every organism present directly producing H_2, and the species composition of the consortium might vary with substrate, but this has not been examined in a systematic way. To enhance the process performance and maintain attrac- tive H_2 production, it is prudent to gain insight on the community structure using tech- niques such as DGGE and phylogenetic assignments made through analysis of 16S RNA. In addition, one way to determine which organisms that are present could potentially be responsible for the observed H_2 production is by probing the population for metabolism- specific genes.

Ueno et al. (2001), using 16S rDNA phylogenetic analyses, studied the microbial com- munity of hydrogen-producing thermophilic anaerobic microflora enriched from sludge compost treating cellulose with or without peptone addition. In the chemostat reac- tor with peptone addition, most of the dominant isolates belonged to the cluster of the *Clostridium/Bacillus/Thermoanaerobacterium* subphylum of low G+C Gram-positive bac- teria, including *Clostridium thermocellum*, *Clostridium cellulosi*, *Clostridium* sp., *Bacillus sporothermodurans*, and *Thermoanaerobacterium thermosaccharolyticum*. Without peptone addition, *Thermoanaerobacterium thermosaccharolyticum* and *Thermobacteroides acetoethylicus* were dominant but with a 50% reduced H_2 yield performance. Also, under thermophilic conditions but using a trickling biofilter fed with glucose, Ahn et al. (2005), based on 16S rDNA phylogenetic analyses, showed that *Thermoanaerobacterium thermosaccharolyti- cum* and *Mitsuokella jalaludinii* were the predominant microbes with a H_2 yield of 1.1 mol of H_2/mol glucose. For mesophilic conditions, Fang et al. (2002a) analyzed the microbial diversity of a mesophilic hydrogen-producing sludge with glucose as the substrate, using 16S rDNA–based techniques involving PCR amplification followed by DGGE screening, cloning, and sequencing. Phylogenetic analysis indicated that 64.6% of the major clones were closely related to *Clostridium* species including *C. cellulosi*, *C. acetobutylicum*, and

C. tyrobutyricum, and 19% were closely related to *Citrobacter* spp. A subsequent micro- bial community characterization of hydrogen-producing granular sludge treating syn- thetic sucrose-containing wastewater detected 69% of cloned 16S rDNA sequences closely related to *Clostridium* species including *C. pasterurianum*, *C. tyrobutyricum*, and *C. acidisoli*, and 14% closely related to the *Bacillus and Staphylococcus* group including *Sporolactobacillus racemicus* (Fang et al., 2002b). Iyer et al. (2004) operated a CSTR, inoculated with heat- treated soil, to evaluate hydrogen-producing bacterial communities at different tem- peratures and hydraulic retention times (HRTs). Using PCR-based detection of bacterial populations by ribosomal intergenic spacer analysis (RISA), *Bacillus myxolacticus*, *Bacillus racemilacticus*, *Clostridium acidisoli*, and *Klebsiella ornithinolytica* were found to be dominant at an HRT of 30 h with a H_2 yield of 0.9 mol of H_2/mol glucose, while *Clostridium* sp., *C. acidisoli*, *C. acetobutylicum*, *Citrobacter braakii*, and *Enterobacter cloacae*, but mostly *Clostridium* species, were dominant at an HRT of 10 h with a yield of 1.8 mol H_2/mol glucose. Also, with a mesophilic CSTR inoculated with heat-treated sludge but fed with dual substrates,

that is, glucose and peptone, Wang et al. (2003b), using 16S rDNA phylogenetic analyses for microbial diversity, found that 62% of total obtained clones were affiliated with the genus *Clostridium*, including *C. sporogenes*, *C. celerecrescens*, *C. butyricum*, *C. sartagoforme*, and *C. chauvoei*, 6% were affiliated with *Dendrosporobacter quercicolus* (formally *Clostridium quercicolum*), 3% were affiliated with the genus *Enterobacter*, and 2% were affiliated with the genus *Klebsiella*. Among the cloned *Clostridium* species, *C. sporogenes*, *C. celerecrescens*, and *C. butyricum*, representing 52% of relative abundance, were capable of producing H_2 from glucose fermentation (Hippe et al., 1992). Furthermore, *C. sporogenes* was revealed to metabolize various amino acids through the Stickland reaction (Stickland, 1934, 1935), and

C. celerecrescens was able to hydrolyze certain proteins such as gelatin (Hippe et al., 1992), presumably because they were the predominant hydrogen-producing bacteria (HPB) in the CSTR fed with glucose and peptone.

In addition to pure substrates, several studies have investigated microbial communities of hydrogen-producing reactors that were capable of converting organic wastes to H_2. In a thermophilic hydrogen-producing CSTR fed with food waste (Shin and Youn, 2005), *Thermoanaerobacterium thermosaccharolyticum*, based on 16S rDNA phylogenetic analyses, was found to be the ubiquitously predominant HPB with a H_2 yield of 1–2.2 mol/mol hexose at different pH (5, 5.5, 6) studied. Chin et al. (2003) conducted an investigation on microbial diversity of HPB, using both culture-dependent and culture-independent approaches, and obtained 174 isolates from composts and hydro- gen-producing reactors fed with different substrates including glucose, sucrose, cel- lulose, rice husk, wheat husk, and wasted yeast powder. Among these isolates, seven possessed superior hydrogen-producing ability, and, therefore, were further identi- fied based on 16S rDNA phylogenetic analyses. Four out of seven superior hydrogen- producing isolates were confirmed as members of clostridial clusters I and II (Collins et al., 1994) including *C. tyrobutyricum*, *C. butyricum*, *C. pasteurinasum*, and *C. tertium*, two were closely related to *Klebsiella pneumoniae*, and the remaining one was closely related to *Megasphaera elsdenii*.

9.6.2 Fingerprint Methods

The microbial community characterization studies mentioned earlier, based on phylogenetic analyses, mostly relied on a one-time sampling during reactor operation. Since microbial populations change over time, monitoring temporal changes is critical to understand the performance of a reactor. In most studies, reactor operating parameters are varied to increase H_2 production. It is vital to identify the shift in microbial populations due to changes in operating conditions in order to fully understand a reactor system and to optimize reactor performance.

The accumulation of genetic information and the development of polymerization chain reaction (PCR)-based techniques allow us to obtain phylotypes from the environmental sample without cultivation or isolation and make it possible to better understand the microbial ecology of that specific sample. The separation or detection of subtle differences in PCR-amplified specific sequences may provide important information about the microbial community structure. Several different polymorphism-based procedures have been developed as DNA fingerprint procedures and applied to study microbial ecology systems (Rosenbaum and Riesner, 1987; Hayashi, 1992; Muyzer et al., 1993; Hallenbeck, 2009). With the development of DNA fingerprinting techniques, the analysis of complex microbial communities has advanced rapidly during recent years. Among them, denaturing gradient gel electrophoresis (DGGE) and terminal restriction fragment length

polymorphism (T-RFLP) are some DNA fingerprinting techniques that have found popularity in the analysis of microbial diversity in anaerobic hydrogen-producing reactors (Lo et al., 2008b).

9.6.2.1 Denaturing Gradient Gel Electrophoresis

DGGE is one of the commonly used techniques to address questions related to diversity and dynamics of microbial communities. In this method, PCR-amplified 16S rRNA gene fragments from a bacterial community can be separated into discrete bands during electrophoresis in a polyacrylamide gel containing a linearly increasing gradient of DNA denaturant (mixture of urea and formamide) (Muyzer et al., 1993). The separation is based on the decreasing electrophoretic mobility of unwinding double-stranded DNA molecules, partially denatured according to their sequence (Figure 9.6). Partial denaturation causes unique bands to form in the gel. The attachment of a GC-rich sequence (GC clamp) to DNA fragments optimizes the detection of sequence variants, by generating only a single band for each denaturing fragment. The diversity of a microbial community can be visualized in terms of banding patterns in the electrophoresis gel. These individual bands can be excised, reamplified, and sequenced or hybridized with oligonucleotide probes to determine the composition of the bacterial community. Many researchers have applied the PCR–DGGE fingerprinting approach to study microbial communities in various environments such as ocean mats (Muyzer et al., 1993), activated sludge (Nielsen et al., 1999), and biofilms (Zhang and Fang, 2000). Recently, this technique was applied to characterize the microbial communities in hydrogen-producing reactors (Ueno et al., 2001; Fang et al., 2002a; Shin and Youn, 2004; Ahn et al., 2006; Wu et al., 2006). Based on PCR–DGGE analysis, Ueno et al. (2001) observed different predominant HPB communities present in hydrogen-producing reactors with and without peptone addition, before performing nucleotide sequences and phylogenetic analyses. By applying the PCR–DGGE fingerprinting approach to the samples obtained from thermophilic hydrogen-producing reactors fed with food wastes at different pH conditions, Shin and Youn (2005) demonstrated that the ubiquitously predominant HPB, *Thermoanaerobacterium thermosaccharolyticum*, was present at all tested pHs, but different *T. thermosaccharolyticum* strains were sensitive to the tested pHs (Figure 9.7). Ahn et al. (2006) performed the PCR–DGGE technique for the HPB samples collected from different heights of a thermophilic trickling biofilter, and the results suggested similar microbial populations present at these levels. In a high-rate hydrogen-producing bioreactor seeded with silicone-immobilized sludge and operated at different HRTs (0.5–6 h), Wu et al. (2006) observed a significant increase in H_2 production when the HRT was reduced to 0.5 h, presumably due to a corresponding HPB community shift, which was revealed with the PCR–DGGE procedure.

9.6.2.2 Terminal Restriction Fragment Length Polymorphism

The analysis of terminal restriction fragment length polymorphism (T-RFLP) is another more recently developed fingerprinting technique to assess the diversity of complex microbial communities. It allows rapid comparisons of community structure and diversity of different ecosystems (Liu et al., 1997). In this method, PCR is used to amplify a selected region of the 16S rRNA gene. One or both of the PCR primers are labeled with a fluorochrome. The resulting fluorescently labeled PCR products are digested with restriction enzymes, and an automated DNA sequencer determines the length and intensity of

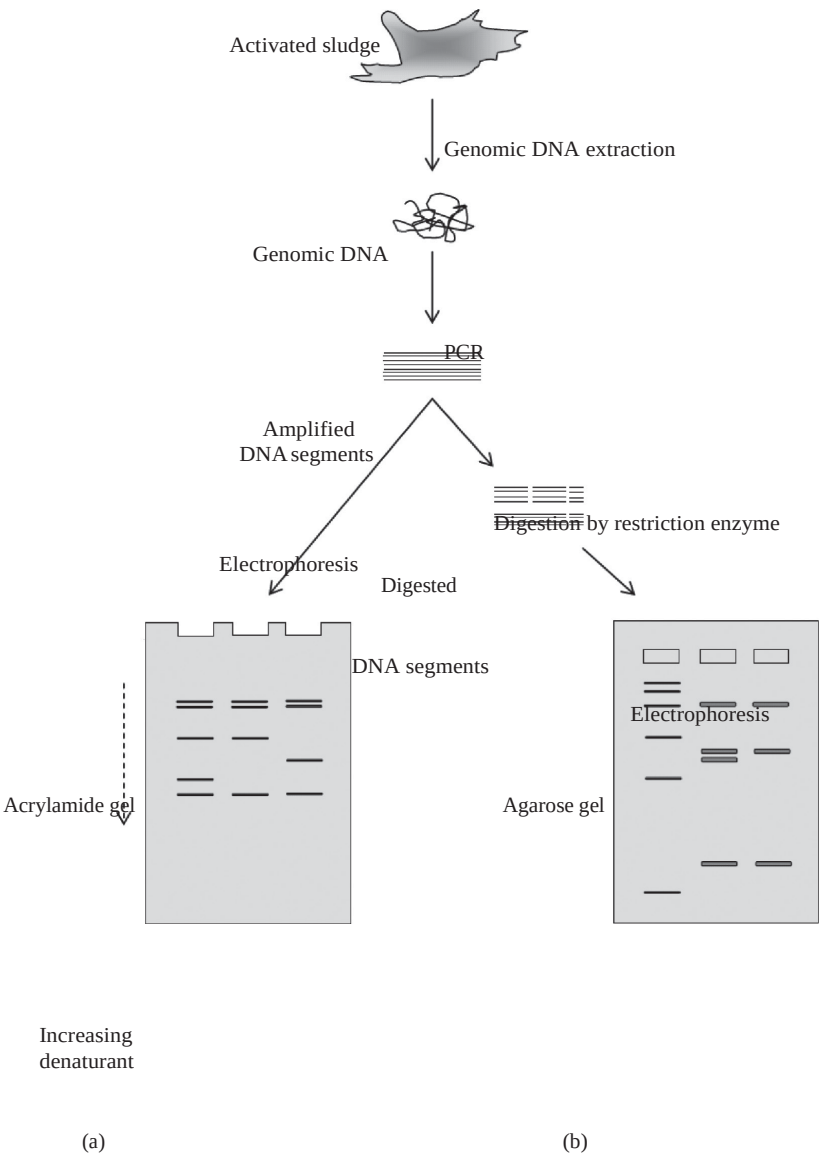


FIGURE 9.7

Schematic description of (a) DGGE and (b) RFLP analyses.

the resulting fluorescently labeled terminal fragments (Figure 9.7). Direct reference can be made to sequence databases to determine the composition of the microbial community (Marsh et al., 2000). The T-RFLP technique is gaining usage in microbial community characterization because of its rapidity and high resolving power. However, it has all the pitfalls associated with other molecular techniques in that it depends on efficient extraction of community DNA and on unbiased PCR amplifications (Figures 9.7 and 9.8). Raghavendra and Padmasree (2003) presented a T-RFLP fingerprinting methodology based on the clostridial 16S rDNA cluster classification defined by Collins et al. (1994) and Mitchell (1998) to monitor the dynamics and abundance of *Clostridium* species in hydrogen-producing

reactors. By using the T-RFLP methodology to investigate microbial population dynamics of a continuous flow reactor, Duangmanee et al. (2003) found that *Clostridium* cluster I and II organisms were abundant in the reactor when the H_2 production was at its maximum and confirmed that *Clostridium* clusters I and II contained hydrogen-producing microorganisms capable of elevated levels of H_2 production. Moreover, a decrease in the levels of *Clostridium* clusters I and II coincided with an increase in the levels of *Clostridium* clusters III and XI, corresponding to a decrease in H_2 production. Recently, Sung et al. (2002) used

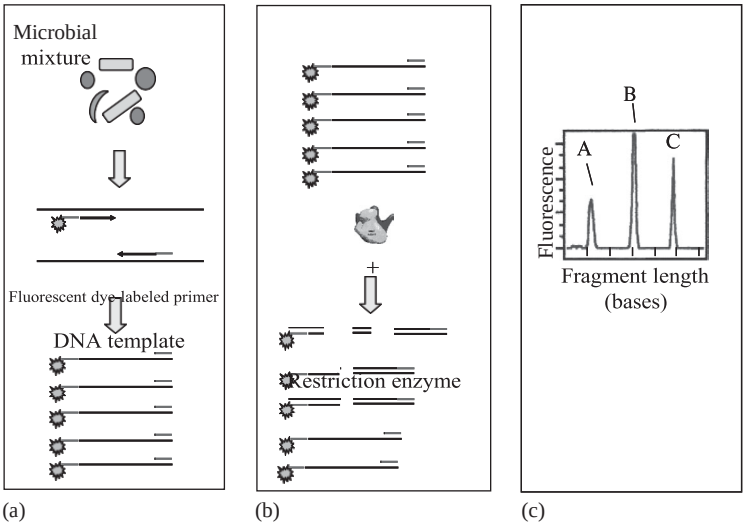


FIGURE 9.8

Schematic description of T-RFLP analyses: (a) PCR amplify and label target gene(s), (b) digest labeled PCR products, and (c) detect labeled terminal fragments.

terminal restriction fragment length polymorphism (T-RFLP) to identify mixed communities of H_2 producers in mesophilic continuous flow reactors using sucrose and heat-treated inocula. The reactor was equipped with an activation chamber that exposed a fraction of the settled sludge to a temperature of 90°C for 20 min. Their results indicated that two major groups of *Clostridium* species were dominant during the first 15 days of operation. The first dominant *Clostridium* group was composed of the following species: *C. beijerinckii*, *C. botulinum*, *C. putrificum*, and *C. sporogenes*. The second dominant population was identified to be *C. butyricum*. The authors found that a decrease in H_2 production was accompanied with a decrease in the total of *Clostridium* species and vice versa in the first 15 days of operation. However, after day 18, the two *Clostridium* species groups ceased to grow and the *Bacillus* species became dominant after day 22. They concluded that it was necessary to apply repeated heat treatments to maintain H_2 production in a continuous flow reactor.

9.7 Conclusions

The world population and consequently the energy demands are growing at an exponential rate; however, the impending shortage of energy resources and the negative impact on the environment due to the unsustainable use of fossil fuels are leading many scientists to search for alternative energy sources that are imperative and more advan- tageous. Among these energy resources, biohydrogen seems promising. Biohydrogen production has been established as a prospective alternative and an integral part of green sustainable energy. Biological systems have significant potential as an environ- mentally friendly means of producing H_2, a widely touted possible fuel of the future. However, a number of obstacles must be overcome if this potential is to be realized on a

practical scale. One attractive route that was discussed in detail in this chapter is the use of dark fermentation. Several factors influencing dark fermentative H_2 production were summarized and analyzed in this review, and the effect of each factor on fermentative H_2 production and the advances in research on better fermentative H_2 production were briefly introduced and discussed. We have also reviewed various approaches to this problem using either pure cultures or microbial consortia in a variety of reactor configu- rations with different substrates and the tools of molecular biotechnology. Optimization of the bioreactor design and operation can be useful in maintaining H_2 production at a high and stable level. It was assumed that biohydrogen is the key to accelerate the coming of the *H_2 economy* and solve the problem of *global warming* and *shortage of fossil fuel*. Pure cultures and defined substrates have proven useful for probing limiting fac- tors presented by different microbial physiologies whereas more engineering-type *black box* studies can highlight areas that need to be targeted in bioprocess development. In addition, it was observed that during dark H_2 fermentation, anaerobic bacteria could produce H_2 while converting organic substrates into volatile fatty acids and alcohols. To achieve better energy yield and lower chemical oxygen demand (COD) level in the effluent, these soluble metabolites (organic acids and alcohols) can be further utilized via photofermentation using photosynthetic bacteria, such as purple nonsulfur bacteria, resulting in more H_2 production as well as higher COD removal. Thus, an integration process combining dark and photo H_2 fermentation could be an effective and efficient energy process to increase H_2 production capacity, and enhancing energy recovery is thus a future prospective.

References

Adams MWW. 1990. The metabolism of hydrogen by extremely thermophilic sulphur-dependent bacteria. *FEMS Microbiol Rev* 75:219–238.

Ahn JM, Kim BC, Gu MB. 2006. Characterization of gltA: LuxCDABE fusion in *Escherichia coli* as a toxicity biosensor. *Biotechnol Bioprocess Eng* 11:513–521.

Akkerman I, Janssen M, Rocha J, Wijffels RH. 2002. Photobiological hydrogen production: Photochemical efficiency and bioreactor design. *Int J Hydrogen Energy* 27:1195–1208.

Amann RI, Ludwig W, Schleifer KH. 1995. Phylogenetic identification and in situ detection of indi- vidual microbial cells without cultivation. *Microbiol Rev* 59:143–169.

Angenent LT, Karim K, Al-Dahhan MH, Wrenn BA, Domíguez-Espinosa R. 2004. Production of bioenergy and biochemicals from industrial and agricultural wastewater. *Trends Biotechnol* 22:477–485.

Argun H, Kargi F, Kapdan IK, Oztekin R. 2008. Biohydrogen production by dark fermentation of wheat powder solution: Effects of C/N and C/P ratio on hydrogen yield and formation rate. *Int J Hydrogen Energy* 33:1813–1819.

Armor JN. 1999. The multiple roles for catalysis in the production of H_2. *Appl Catal A Gen* 176:159–176.

Arooj MF, Han SK, Kim SH, Kim DH, Shin HS. 2008. Continuous biohydrogen production in a CSTR using starch as a substrate. *Int J Hydrogen Energy* 33:3289–3294.

Asada Y, Miyake J. 1999. Photobiological hydrogen production. *J Biosci Biotechnol* 88:1–6.

Atif AAY, Fakhru'l-Razi A, Ngan MA, Morimoto M, Iyuke SE, Veziroglu NT. 2005. Fed batch produc- tion of hydrogen from palm oil mill effluent using anaerobic microflora. *Int J Hydrogen Energy* 30(13–14):1393–1397.

Bai MD, Cheng SS, Tseng IC. 2001. Biohydrogen produced due to peptone degradation by pre- treated seed sludge. *The IWA Asia-Pacific Regional Conference (WaterQual 2001)*, Fukuoka, Japan, pp. 315–320.

Bailey JE, Ollis DF. 1986. *Biochemical Engineering Fundamentals*, 2nd edn. McGraw-Hill, New York.
Benemann J. 1996. Hydrogen biotechnology: Progress and prospects. *Nat Biotechnol* 14:1101–1103.

Bisaillon A, Turcot J, Hallenbeck PC. 2006. The effect of nutrient limitation on hydrogen production by batch cultures of *Escherichia coli*. *Int J Hydrogen Energy* 31:1504–1508.

Brock TD, Madigan MT, Martinko JM, Parker J. 1994. *Biology of Microorganisms*, 7th edn. Prentice- Hall, Englewood Cliffs, NJ.

Bockris J. 2002. The origin of ideas on a hydrogen economy and its solution to the decay of the envi- ronment. *Int J Hydrogen Energy* 27:731–740.

Bossel U. 2003. Well-to-wheel studies, heating values, and the energy conservation principle.

European Fuel Cell Forum, Oberrohrdorf, Switzerland.

Cai ML, Liu JX, Wei YS. 2004. Enhanced biohydrogen production from sewage sludge with alkaline pretreatment. *Environ Sci Technol* 38:3195–3202.

Calli B, Boënne W, Vanbroekhoven K. 2006. Bio-hydrogen potential of easily biodegradable substrate through dark fermentation. In: *Proceedings of the 16th World Hydrogen Energy Conference*, Lyon, France, pp. 215–216.

Camilli M, Pedroni PM. 2005. Comparison of the performance of three different reactors for biohy- drogen production via dark anaerobic fermentations. In: *Proceedings of the International Hydrogen Energy Congress and Exhibition*, BHP 250, CD-ROM, Istanbul, Turkey.

Chang FY, Lin CY. 2004. Biohydrogen production using an up-flow anaerobic sludge blanket reactor.

Int J Hydrogen Energy 29:33–39.

Chang JS, Lee KS, Lin PJ. 2002. Biohydrogen production with fixed-bed bioreactors. *Int J Hydrogen Energy* 27:1167–1174.

Chang JS, Yang SM. 2006. Application of artificial neural networks coupled with sequential pseudo- uniform design to optimization of membrane reactors for hydrogen production. *J Chin Inst Chem Eng* 37:395–400.

Chen CC, Chen HP, Wu JH, Lin CY. 2008a. Fermentative hydrogen production at high sulfate concen- tration. *Int J Hydrogen Energy* 33:573–1578.

Chen CC, Lin CY. 2003. Using sucrose as a substrate in an anaerobic hydrogen producing reactor. *Adv Environ Res* 7:695–699.

Chen CC, Lin CY, Chang JS. 2001. Kinetics of hydrogen production with continuous anaerobic cul- tures utilizing sucrose as the limiting substrate. *Appl Microbiol Biotechnol* 57:56–64.

Chen CC, Lin CY, Lin MC. 2002. Acid-base enrichment enhances anaerobic hydrogen production process. *Appl Microbiol Biotechnol* 58:224–228.

Chen SD, Lee KS, Lo YC, Chen WM, Wu JF, Lin CY, Chang JS. 2008b. Batch and continuous bio- hydrogen production from starch hydrolysate by *Clostridium* species. *Int J Hydrogen Energy* 33(7):1803–1812.

Chen WH, Chen SY, Khanal SK, Sung S. 2006. Kinetic study of biological hydrogen production by anaerobic fermentation. *Int J Hydrogen Energy* 31(15):2170–2178.

Chen WM, Tseng ZJ, Lee KS, Chang JS. 2005. Fermentative hydrogen production with *Clostridium butyricum* CGS5 isolated from anaerobic sewage sludge. *Int J Hydrogen Energy* 30:1063–1070.

Cheng SS, Chang SM, Chen ST. 2002. Effects of volatile fatty acids to a thermophilic anaerobic hydro- gen fermentation process degrading peptone. *Water Sci Technol* 46:209–214.

Cheong DY, Hansen CL. 2006. Acidogenesis characteristics of natural, mixed anaerobes converting carbohydrate-rich synthetic wastewater to hydrogen. *Process Biochem* 41(8):1736–1745.

Chin HL, Chen ZS, Chou CP. 2003. Fedbatch operation using *Clostridium acetobutylicum* suspension culture as biocatalyst for enhancing hydrogen production. *Biotechnol Prog* 19:383–388.

Cohen A, van Gemert JM, Zoetemeyer RJ, Breure AM. 1984. Main characteristics and stoichiomet- ric aspects of acidogenesis of soluble carbohydrate containing wastewaters. *Proc Biochem* 19:228–232.

Collet C, Adler N, Schwitzguebel JP, Peringer P. 2004. Hydrogen production by *Clostridium thermo- lacticum* during continuous fermentation of lactose. *Int J Hydrogen Energy* 29(14):1479–1485.

Collins MD, Lawson PA, Willems A, Cordoba JJ, Fernandez-Garayzabal J, Garcia P, Cai J, Hippe H, Farrow JAE. 1994. The phylogeny of the genus *Clostridium*: Proposal of five new genera and eleven new species combinations. *Int J Syst Bacteriol* 44:812–826.

Dabrock B, Bahl H, Gottschalk G. 1992. Parameters affecting solvent production by *Clostridium pas- teurium. Appl Environ Microbiol* 58:1233–1239.

Das D, Veziroglu TN. 2001. Hydrogen production by biological processes: A survey of literature.

Int J Hydrogen Energy 26:13–28.

Das D, Veziroglu TN. 2008. Advances in biological hydrogen production processes. *Int J Hydrogen Energy* 33:6046–6057.

Das D. 2009. Advances in biohydrogen production processes: An approach towards commercializa- tion. *Int J Hydrogen Energy* 34:7349–7357.

Datar R, Huang J, Maness PC, Mohagheghi A, Czernik S, Chornet E. 2007. Hydrogen production from the fermentation of corn stover biomass pretreated with a steam-explosion process. *Int J Hydrogen Energy* 32:932–939.

Demirbas A. 2007. Progress and recent trends in biofuels. *Prog Energy Combust Sci* 33:1–18.

DeVrije T, deHaas GG, Tan GB, Keijsers ERP, Claassen PAM. 2002. Pretreatment of *Miscanthus* for hydrogen production by *Thermotoga elfii. Int J Hydrogen Energy* 27:1381–1390.

Duangmanee T, Padmasiri S, Simmons JJ, Raskin L, Sung S. 2002. Hydrogen production by anaerobic microbial communities exposed to repeated heat treatment. In: *WEFTEC 75th Annual Conference and Exhibition of the Water Environment Federation,* Chicago, IL*; Water Environment Federation,* Alexandria, VA.

Dunn S. 2002. Perspectives towards a hydrogen future. *Cogen On Site Power Product* 3:55–60.

Elam CC, Gregoire Padro CE, Sandrock G, Luzzi A, Lindblad P, Hagen EF. 2003. Realizing the hydro- gen future: The international energy agency's efforts to advance hydrogen energy technologies. *Int J Hydrogen Energy* 28:601–607.

Evvyernie D, Morimoto K, Karita S, Kimura T, Sakka K, Ohmiya K. 2001. Conversion of chitinous waste to hydrogen gas by *Clostridium paraputrificum* M-21. *J Biosci Bioeng* 91:339–343.

Fabiano B, Perego P. 2002. Thermodynamic study and optimization of hydrogen production by

Enterobacter aerogenes. Int J Hydrogen Energy 27:149–156.

Fan KS, Kan NR, Lay JJ. 2006a. Effect of hydraulic retention time on anaerobic hydrogenesis in CSTR.

Bioresour Technol 97(1):84–89.

Fan YT, Zhang YH, Zhang SF, Hou HW, Ren BZ. 2006b. Efficient conversion of wheat straw wastes into biohydrogen gas by cow dung compost. *Bioresour Technol* 97(3):500–505.

Fang HHP, Li CL, Zhang T. 2006. Acidophilic biohydrogen production from rice slurry. *Int J Hydrogen Energy* 31:683–692.

Fang HHP, Liu H. 2002. Effect of pH on hydrogen production from glucose by a mixed culture.

Bioresour Technol 82(2):87–93.

Fang HHP, Liu H, Zhang T. 2002. Characterization of a hydrogen producing granular sludge.

Biotechnol Bioeng 78(1):44–52.

Fang HHP, Liu H, Zhang T. 2002a. Characterization of a hydrogen-producing granular sludge. *Biotechnol Bioeng* 78:44–52.

Fang HHP, Zhang T, Liu H. 2002. Microbial diversity of mesophilic hydrogen producing sludge. *Appl Microbiol Biotechnol* 58:112–118.

Fardeau ML, Faudon C, Cayol JL, Magot M, Patel BKC, Ollivier B. 1996. Effect of thiosulphate as electron acceptor on glucose and xylose oxidation by *Thermoanaerobacterfinnii* and a *Thermoanaerobacter* sp. isolated from oil field water, *Res Microbiol* 147(3):159–165.

Ferchichi M, Crabbe E, Gil GH, Hintz W, Almadidy A. 2005. Influence of initial pH on hydrogen production from cheese whey. *J Biotechnol* 120(4):402–409.

Field CB, Campbell JE, Lobell DB. 2008. Biomass energy: The scale of the potential resource. *Trends Ecol Evol* 23:65–72.

Francese A, Cordoba P, Duran J, Sineriz F. 1998. High upflow velocity and organic loading rate improves granulation in upflow anaerobic sludge blanket reactors. *World J Microbiol Biotechnol* 14(3):337–341.

Gander M, Jefferson B, Judd S. 2000. Aerobic, MBRs for domestic wastewater treatment: A review with cost considerations. *Sep Purif Technol* 18:119–130.

Gavala HN, Skiadas IV, Ahring BK. 2006. Biological hydrogen production in suspended and attached growth anaerobic reactor systems. *Int J Hydrogen Energy* 31:1164–1175.

Gatze L, de Zeeuw W, Ouborg E. 1981. Anaerobic treatment of wastes containing methanol and higher alcohols. *Water Res* 15:171–182.

Ghirardi ML, Zhang L, Lee JW, Flynn T, Seibert M, Greenbaum E, Melis. 2000. Microalgae: A green source of renewable H_2. *Trend Biotechnol* 18:506–511.

Giallo J, Gaudin C, Belaich JP. 1985. Metabolism and solubilization of cellulose by *Clostridium cellulo- lyticum* H10. *Appl Environ Microbiol* 49:1216–1221.

Goldemberg J. 2007. Ethanol for a sustainable energy future. *Science* 315:808–810.

Goldemberg J, Johansson TB. 2004. World energy assessment overview: 2004 update. United Nations Development Programme, New York, http://www.undp.org/energy/weaover2004.htm.

Gong CS, Cao NU, Du J, Tsao GT. 1999. Ethanol production by renewable sources. *Adv Biochem Eng Biotechnol* 65:207–241.

Guo L, Li XM, Bo X, Yang Q, Zeng GM, Liao DX, Liu JJ. 2008. Impacts of sterilization, microwave and ultrasonication pretreatment on hydrogen producing using waste sludge. *Bioresour Technol* 99:3651–3658.

Gustavo DV, Sonia A, Felipe AM, Antonio de LR, Luis MRC, Elías RF. 2009. Fermentative bio- hydrogen production: Trends and perspectives. *Rev Environ Sci BioTechnol* (doi 10.1007/ s11157-007-9122-7).

Hallenbeck PC. 2005. Fundamentals of the fermentative production of hydrogen. *Water Sci Technol*

52:21–29.

Hallenbeck PC. 2009. Fermentative hydrogen production: Principles, progress, and prognosis. *Int J Hydrogen Energy* 34:7379–7389.

Hallenbeck PC, Benemann JR. 2002. Biological hydrogen production; fundamentals and limiting pro- cesses. *Int J Hydrogen Energy* 27:1185–1193.

Hallenbeck, PC, Ghosh D, Skonieczny MT, Yargeau V. 2009. Microbiological and engineering aspects of biohydrogen production. *Indian J Microbiol* 49:48–59.

Hawkes FR, Dinsdale R, Hawkes DL, Hussy I. 2002. Sustainable fermentative hydrogen production: Challenges for process optimization. *Int J Hydrogen Energy* 27:1339–1347.

Hawkes FR, Hussy I, Kyazze G, Dinsdale R, Hawkes DL. 2007. Continuous dark fermentative hydrogen production by mesophilic microflora: Principles and progress. *Int J Hydrogen Energy* 32:172–184.

Hayashi K. 1992. Genetic analysis: Review PCR-SSCP: A method for detection of mutations. *Biomol Eng* 9(3):73–79.

Hippe H, Andreesen JR, Gottschalk G. 1992. The genus *Clostridium*—Nonmedical. In *The Prokaryotes*, 2nd edn., A. Balows, H. C. Trüper, M. Dworkin, W. Harder, and K.-H. Schleifer, eds. Springer, New York.

Horiuchi J, Shimizu T, Kanno T, Kobayashi M. 1999. Dynamic behavior in response to pH shift dur- ing anaerobic acidogenesis with a chemstat culture. *Biotechnol Tech* 13:155–157.

Horiuchi JI, Shimizu T, Tada K, Kanno T, Kobayashi M. 2002. Selective production of organic acids in anaerobic acid reactor by pH control. *Bioresour Technol* 82:209–213.

Hugenholtz P, Pace NR. 1996. Identifying microbial diversity in the natural environment: A molecu- lar phylogenetic approach. *Trends Biotechnol* 14:190–197.

Hulshoff Pol LW, Lettinga G. 1986. New technologies for anaerobic wastewater treatment. *Water Sci Technol* 18(12):41–53.

Hussy I, Hawkes FR, Dinsdale R, Hawkes DL. 2003. Continuous fermentative hydrogen production from a wheat starch co-product by mixed microflora. *Biotechnol Bioeng* 84(6):619–626.

Hussy I, Hawkes FR, Dinsdale R, Hawkes DL. 2005. Continuous fermentative hydrogen production from sucrose and sugarbeet. *Int J Hydrogen Energy* 30(5):471–483.

Hwu CS, van Lier JB, Lettinga G. 1998. Physicochemical and biological performance of expanded granular sludge bed reactors treating long-chain fatty acids. *Process Biochem* 33(1):75–81.

Imai T, Ukita M, Liu J, Sekine M, Nakanishi H, Fukagawa M. 1997. Advanced start up of UASBreac- tors by adding of water absorbing polymer. *Water Sci Technol* 36:399–406.

Iyer P, Bruns MA, Zhang H, van Ginkel S, Logan BE. 2004. H_2 producing microbial communities from a heat treated soil inoculum. *Appl Microbiol Biotechnol* 66:166–173.

James WE, Jha S, Sumulong L, Son HH, Hasan R, Khan ME, Sugiyarto G, Zhai F. 2008. *Food Prices and Inflation in Developing Asia: Is Poverty Reduction Coming to an End?* Asian Development Bank, Manila, Philippines. http://www.adb.org/reports/food-prices-inflation/food-prices-inflation.pdf.

Jeison D, Chamy R. 1999. Comparison of the behaviour of expanded granular sludge bed (EGSB) and upflow anaerobic sludge blanket (UASB) reactors in dilute and concentrated wastewater treatment. *Water Sci Technol* 40:91–97.

Jo JH, Lee DS, Park D, Choe WS, Park JM., 2008. Optimization of key process variables for enhanced hydrogen production by *Enterobacter aerogenes* using statistical methods. *Bioresour Technol* 99:2061–2066.

Kadar Z, Vrije TD, van Noorden GE, Budde MAW, Szengyel Z, Reczey K, Claassen PAM. 2004. Yields from glucose, xylose, and paper sludge hydrolysate during hydrogen produc- tion by the extreme thermophile *Caldicellulosiruptor saccharolyticus. Appl Biochem Biotechnol* 113–116(12):497–508.

Kanai T, Imanaka H, Nakajima A, Uwamori K, Omori Y, Fukui T. Atomi H, Imanaka T. 2005. Continuous hydrogen production by the hyperthermophilic archaeon, *Thermococcus kodak- araensis* KOD1. *J Biotechnol* 116:271–282.

Kapdan IK, Kargi F. 2006. Biohydrogen production from waste materials. *Enzyme Microbial Technol*

38:569–582.

Kawagoshi Y, Hino N, Fujimoto A, Nakao M, Fujita Y, Sugimura S, Furukawa K. 2005. Effect of inocu- lum conditioning on hydrogen fermentation and pH effect on bacterial community relevant to hydrogen production. *J Biosci Bioeng* 100:524–530.

Keeney R, Hertel TW. 2008. *The Indirect Land Use Impacts of US Biofuel Policies: The Importance of Acreage, Yield, and Bilateral Trade Responses*. Center for Global Trade Analysis, Purdue University, West Lafayette, IN. http://www.gtap.agecon.purdue.edu/resources/download/3904.pdf.

Kennedy JL, Droste RL. 1985. Startup of anaerobic downflow stationary fixed film (DSFF) reactors.

Biotechnol Bioeng 27:1152–1165.

Khanal SK, Chen WH, Li L, Sung S. 2004. Biological hydrogen production: Effects of pH and inter- mediate products. *Int J Hydrogen Energy* 29(11):1123–1131.

Kim JO, Kim YH, Ryu JY, Song BK, Kim IH, Yeom SH. 2005. Immobilization methods forcontinuous hydrogen gas production biofilm formation versus granulation. *Process Biochem* 40:1331–1337.

Kim MS, Oh YK, Yun YS, Lee DY. 2006. Fermentative hydrogen production from anaerobic bacteria using a membrane bioreactor. In: *Proceedings of the 16th World Hydrogen Energy Conference*. Lyon, France, p. 50.

Koh LP, Ghazoul J. 2008. Biofuels, biodiversity, and people: Understanding the conflicts and finding opportunities. *Biolog Conserv* 141:2450–2460.

Koku H, Eroğlu İ, Gündüz U, Yücel M, Türker L. 2002. Aspects of the metabolism of hydrogen pro- duction by *Rhodobacter sphaeroides. Int J Hydrogen Energy* 27:1315–1329.

Kotay SM, Das D. 2006. Feasibility of biohydrogen production from sewage sludge using defined microbial consortium. In: *Proceedings of the 16th World Hydrogen Energy Conference*. Lyon, France, pp. 209–210.

Kotay SM, Das D. 2008. Biohydrogen as a renewable energy resource—Prospects and potentials. *Int J Hydrogen Energy* 33:258–263.

Kotsopoulos TA, Zeng RJ, Angelidaki I. 2006. Biohydrogen production in granular up-flow anaerobic sludge blanket (UASB) reactors with mixed cultures under hyper-thermophilic temperature (70°C). *Biotechnol Bioeng* 94(2):296–302.

Kraemer JT, Bagley DM. 2008. Optimisation and design of nitrogen-sparged fermentative hydrogen production bioreactors. *Int J Hydrogen Energy* 33:6558–6565.

Kumar N, Das D. 2000. Enhancement of hydrogen production by *Enterobacter cloacae* IIT-BT 08.

Process Biochem 35:589–593.

Kumar N, Das D. 2001. Continuous hydrogen production by immobilized *Enterobacter cloacae* IIT-BT 08 using lignocellulosic materials as solid matrices. *Enzyme Microb Technol* 29:280–287.

Kyazze G, Dinsdale R, Hawkes FR, Guwy AJ, Premier GC, Donnison IS. 2008. Direct fermentation of fodder maize, chicory fructans and perennial ryegrass to hydrogen using mixed microflora. *Bioresour Technol* 99(18):8833–8839.

Lay JJ. 2000. Modeling and optimization of anaerobic digested sludge converting starch to hydrogen.

Biotechnol Bioeng 68:269–278.

Lay JJ. 2001. Biohydrogen generation by mesophilic anaerobic fermentation of microcrystalline cel- lulose. *Biotechnol Bioeng* 74:280–287.

Lay JJ, Fan KS, Hwang J, Chang JI, Hsu PC. 2005. Factors affecting hydrogen production from food wastes by *Clostridium*-rich composts. *J Environ Eng* 131:595–602.

Lay JJ, Lee YJ, Noike T. 1999. Feasibility of biological hydrogen production from organic fraction of municipal solid waste. *Water Res* 33(11):2579–2586.

Lee KS, Hsu YF, Lo YC, Lin PJ, Lin CY, Chang JS. 2008. Exploring optimal environmental factors for fermentative hydrogen production from starch using mixed anaerobic microflora. *Int J Hydrogen Energy* 33:1565–1572.

Lee KS, Lin PJ, Chang JS. 2006b. Temperature effects on biohydrogen production in a granular sludge bed induced by activated carbon carriers. *Int J Hydrogen Energy* 31(4):465–472.

Lee KS, Lin PJ, Fang K, Chang JS. 2007. Continuous hydrogen production by anaerobic mixed microflora using a hollow-fiber microfiltration membrane bioreactor. *Int J Hydrogen Energy* 32:950–957.

Lee KS, Lo YC, Lin PJ, Chang JS. 2006a. Improving biohydrogen production in a carrier-induced granular sludge bed by altering physical configuration and agitation pattern of the bioreactor. *Int J Hydrogen Energy* 31(12):1648–1657.

Lee KS, Lo YS, Lo YC, Lin PJ, Chang JS. 2003. H_2 production with anaerobic sludge using activated- carbon supported packed-bed bioreactors. *Biotechnol Lett* 25:133–138.

Lee KS, Lo YS, Lo YC, Lin PJ, Chang JS. 2004b. Operation strategies for biohydrogen produc- tion with a high-rate anaerobic granular sludge bed bioreactor. *Enzyme Microb Technol* 35(6–7):605–612.

Lee KS, Wu JF, Lo YS, Lo YC, Lin PJ, Chang JS. 2004a. Anaerobic hydrogen production with an effi- cient carrier-induced granular sludge bed bioreactor. *Biotechnol Bioeng* 87(5):648–657.

Lee MJ, Zinder SH. 1988. Hydrogen partial pressures in a thermophilic acetate-oxidizing methano- genic co-culture. *Appl Environ Microbiol* 54:1457–1461.

Lee YJ, Miyahara T, Noike T. 2001. Effect of iron concentration on hydrogen fermentation. *Bioresour Technol* 80:227–231.

Lee YJ, Miyahara T, Noike T. 2002. Effect of pH on microbial hydrogen fermentation. *J Chem Technol Biotechnol* 77:694–698.

Levin DB, Pitt L, Love M. 2004. Biohydrogen production: Prospects and limitations to practical appli- cation. *Int J Hydrogen Energy* 29:173–185.

Li CL, Fang HHP. 2007a. Fermentative hydrogen production from wastewater and solid wastes by mixed cultures. *Crit Rev Env Sci Technol* 37:1–39.

Li CL, Fang HHP. 2007b. Inhibition of heavy metals on fermentative hydrogen production by granu- lar sludge. *Chemosphere* 67:668–673.

Liang TM. 2003. Application of membrane separation on anaerobic hydrogen-producing processes.

Doctor dissertation. National Cheng Kung University, ROC.

Liang TM, Cheng SS, Wu KL. 2002. Behavioral study on hydrogen fermentation reactor installed with silicone rubber membrane. *Int J Hydrogen Energy* 27:1157–1165.

Liang TM, Wu KL, Cheng SS. 2001. Hydrogen production of chloroform inhibited granular sludge.

The IWA Asia-Pacific Regional Conference (WaterQual 2001), Fukuoka, Japan, pp. 863–868.

Licht FO. 2008. World Ethanol & Biofuels Report. Agra Informa Ltd., Kent, U.K. http://www.agra-net.com/portal/puboptions.jsp?Option=menu&pubId=sag072.

Lin CY, Cheng CH. 2006. Fermentative hydrogen production from xylose using anaerobic mixed microflora. *Int J Hydrogen Energy* 31:832–840.

Lin CY, Chang CC, Hung CH. 2008a. Fermentative hydrogen production from starch using natural mixed cultures. *Int J Hydrogen Energy* 33(10):2445–2453.

Lin CY, Chang RC. 1999. Hydrogen production during the anaerobic acidogenic conversion of glu- cose. *J Chem Technol Biotechnol* 74(6):498–500.

Lin CY, Chang RC. 2004. Fermentative hydrogen production at ambient temperature. *Int J Hydrogen Energy* 29(7):715–720.

Lin CY, Cheng CH. 2006. Fermentative hydrogen production from xylose using anaerobic mixed microflora. *Int J Hydrogen Energy* 31(7):832–840.

Lin CY, Chou CH. 2004. Anaerobic hydrogen production from sucrose using an acid-enriched sew- age sludge microflora. *Eng Life Sci* 4:66–70.

Lin CY, Hung WC. 2008. Enhancement of fermentative hydrogen/ethanol production from cellulose using mixed anaerobic cultures. *Int J Hydrogen Energy* 33(14):3660–3667.

Lin CY, Jo CH. 2003. Hydrogen production from sucrose using an anaerobic sequencing batch reactor process. *J Chem Technol Biotechnol* 78:678–684.

Lin CY, Lay CH. 2004a. Carbon/nitrogen-ratio effect on fermentative hydrogen production by mixed microflora. *Int J Hydrogen Energy* 29:41–45.

Lin CY, Lay CH. 2004b. Effects of carbonate and phosphate concentrations on hydrogen production using anaerobic sewage sludge microflora. *Int J Hydrogen Energy* 29:275–281.

Lin CY, Lay CH. 2005. A nutrient formulation for fermentative hydrogen production using anaerobic sewage sludge microflora. *Int J Hydrog Energy* 30(3):285–292.

Lin CY, Lee CY, Tseng IC, Shiao IZ. 2006. Biohydrogen production from sucrose using base-enriched anaerobic mixed microflora. *Process Biochem* 41(4):915–919.

Lin CY, Shei SH. 2008. Heavy metal effects on fermentative hydrogen production using natural mixed microflora. *Int J Hydrogen Energy* 33:587–593.

Lin CY, Wu CC, Hung CH. 2008b. Temperature effects on fermentative hydrogen production from xylose using mixed anaerobic cultures. *Int J Hydrogen Energy* 33:43–50.

Liu GZ, Shen JQ. 2004. Effects of culture and medium conditions on hydrogen production from starch using anaerobic bacteria. *J Biosci Bioeng* 98:251–256.

Liu H, Fang HHP. 2002. Hydrogen production from wastewater by acidogenic granular sludge.

Water Sci Technol 47:153–158.

Liu J, Chen JM, Cihlar J, Park WM. 1997. A process-based boreal ecosystem productivity simulator using remote sensing inputs. *Remote Sens Environ* 62(2):158–175.

Liu Y, Xu HL, Yang SF, Tay JH. 2003. Mechanisms and models for anaerobic granulation in upflow anaerobic sludge blanket reactor. *Water Res* 37:661–673.

Liu Y, Yu P, Song X, Qu Y. 2008. Hydrogen production from cellulose by co-culture of *Clostridium thermocellum* JN4 and *Thermoanaerobacterium thermosaccharolyticum* GD17. *Int J Hydrogen Energy* 33:2927–2933.

Lo YC, Bai MD, Chen WM, Chang JS. 2008a. Cellulosic hydrogen production with a sequencing bac- terial hydrolysis and dark fermentation strategy. *Bioresour Technol*. 99:8299–8303.

Lo YC, Chen WM, Hung CH, Chen SD, Chang JS. 2008b. Dark H_2 fermentation from sucrose and xylose using H_2-producing indigenous bacteria: Feasibility and kinetic studies. *Water Res* 42:827–842.

Lo YC, Saratale GD., Chen WM, Bai MD, Chang JS. 2009. Isolation of cellulose-hydrolytic bacteria and applications of the cellulolytic enzymes for cellulosic biohydrogen production. *Enzyme Microb Technol* 44(6–7):417–425.

Logan BE. 2004. Extracting hydrogen and electricity from renewable resources. *Environ Sci Technol*

38(9):160A–167A.

Logan BE, Oh SE, Kim IS, Van Ginkel S. 2002. Biological hydrogen production measured in batch anaerobic respirometers. *Environ Sci Technol* 36:2530–2535.

Ma H, Brwman CN, Davis RH. 2000. Membrane fouling reduction by backpulsing and surface modi- fication. *J Membr Sci* 173:191–200.

Maddy J, Cherryman S, Hawkes FR, Hawkes DL, Dinsdale RM, Guwy AJ, Premier GC, Cole S. 2003.

Hydrogen. University of Glamorgan, Pontypridd, U.K.

Malina JF, Pohland JFG. 1992. *Design of Anaerobic Processes for the Treatment of Industrial and Municipal Wastes*. Technomic Pub Co, Lancaster, PA.

Mallette MF, Reece P, Dawes EA. 1974. Culture of *Clostridium pasteurianum* in defined medium and growth as a function of sulfate concentration. *Appl Microbiol* 28:999–1003.

Marsh TL, Saxman P, Cole J, Tiedje J. 2000. Terminal restriction fragment length polymorphism analysis program, a web-based research tool for microbial community analysis. *Appl Environ Microbiol* 66:3616–3620.

Matthies C, Kuhner CH, Acker G, Drake HL. 2001. *Clostridium uliginosum* sp. nov., a novel acid-tolerant, anaerobic bacterium with connecting filaments. *Int J Syst Evol Microbiol* 51(3):1119–1125.

Minnan L, Jinli H, Xiaobin W, Huijuan X, Jinzao C, Chuannan L, Fengzhang Z, Liangshu X. 2005. Isolation and characterization of a high H_2-producing strain *Klebsialle oxytoca* HP1 from a hot spring. *Res Microbiol* 156:76–81.

Mitchell WJ. 1998. Physiology of carbohydrate to solvent conversion by clostridia. *Adv Microbial Physiol* 39:31–130.

Mizuno O, Dinsdale R, Hawkes FR, Kawkas DL, Noike T. 2000. Enhancement of hydrogen produc- tion from glucose by nitrogen gas sparging. *Biotechnol Bioeng* 73(1):59–65.

Mohan SV, Bhaskar YV, Sharma PN. 2007. Biohydrogen production from chemical wastewater treat- ment in biofilm configured reactor operated in periodic discontinuous batch mode by selec- tively enriched anaerobic mixed consortia. *Water Res* 41:2652–1664.

Momirlan M, Veziroglu T. 2002. Current status of hydrogen energy. *Renew Sustain Energy Rev*

6:141–179.

Morgan JW, Evison LM, Forster CF. 1991. Changes to the microbial ecology in anaerobic digesters treating ice cream wastewater during start-up. *Water Res* 25:639–653.

Morimoto M, Atsuko M, Atif AAY, Ngan MA, Fakhru'l-Razi A, Iyuke SE, Bakir AM. 2004. Biological production of hydrogen from glucose by natural anaerobic microflora. *Int J Hydrogen Energy* 29:709–713.

Mu Y, Wang G, Yu HQ. 2006a. Kinetic modeling of batch hydrogen production process by mixed anaerobic cultures. *Bioresour Technol* 97(11):1302–1307.

Mu Y, Wang G, Yu HQ. 2006b. Response surface methodological analysis on biohydrogen production by enriched anaerobic cultures. *Enzyme Microb Technol* 38(7):905–913.

Mu Y, Yu HQ. 2006. Biologicalhydrogenproductionina UASBreactorwithgranules. I: Physicochemical characteristics of hydrogen-producing granules. *Biotechnol Bioeng* 94(5):980–987.

Mu Y, Zheng XJ, Yu HQ, Zhu RF. 2006c. Biological hydrogen production by anaerobic sludge at vari- ous temperatures. *Int J Hydrogen Energy* 31(6):780–785.

Muyzer G, Waal CDE, Uitierlinden AG. 1993. Profiling of complex microbial populations by denatur- ing gradient gel electrophoresis analysis of polymerase chain reaction-amplified genes coding for 16S rRNA. *Appl Environ Micrbiol* 59:695–700.

Nandi R, Sengupta S. 1998. Microbial production of hydrogen: An overview. *Crit Rev Microbiol*

24:61–84.

Nath K, Das D. 2003. Hydrogen from biomass. *Curr Sci* 85:265–271.

Nath K, Das D. 2004. Improvement of fermentative hydrogen production—Various approach. *Appl Microbiol Biotechnol* 65:520–529.

Nishio N, Nakashimada Y. 2004. High rate production of hydrogen/methane from various sub- strates and wastes. *Adv Biochem Eng Biotechnol* 90:63–87.

Nguyen TAD, Kim JP, Kim MS, Oh YK, Sim SJ. 2008. Optimization of hydrogen production by hyper- thermophilic eubacteria, *Thermotoga maritima* and *Thermotoga neapolitana* in batch fermentation. *Int J Hydrogen Energy* 33(5):1483–1488.

UNDP. 2000. *Energy and the Challenge of Sustainability*, World Energy Assessment, United Nations Development Programme, New York.

Valdez-Vazquez I, Elvira RL, Esparza-García F, Cecchi F, Poggi-Varaldo HM. 2005. Semi-continuous solid substrate anaerobic reactors for H_2 production from organic waste: Mesophilic versus thermophilic regime. *Int J Hydrogen Energy* 30:1383–1391.

van Niel EWJ, Budde MAW, de Haas GG, van der Wal FJ, Claassen PAM, Stams AJM. 2002a. Distinctive properties of high hydrogen producing extreme thermophiles, *Caldicellulosiruptor saccharolyticus* and *Thermotoga elfiii. Int J Hydrog Energy* 27:1391–1398.

van Niel EWJ, Claassen PAM, Stams AJM. 2002b. Substrate and product inhibition of hydrogen production by the extreme thermophile *Caldicellulosiruptor saccharolyticus. Biotechnol Bioeng* 81:255–262.

Nielsen AT, Liu WT, Filipe C, Grady L Jr, Molin S, Stahl DA. 1999. Identification of a novel group of bacteria in sludge from a deteriorated biological phosphorus removal reactor. *Appl Environ Microbiol* 65:1251–1258.

Nowak J, Florek M, Kwiatek W, Lekki J, Chevallier P, Zieba E. 2005. Composite structure of wood cells in petrified wood. *Mater Sci Eng* 25:119–30.

Ntaikou I, Gavala HN, Kornaros M, Lyberatos G. 2008. Hydrogen production from sugars and sweet sorghum biomass using *Ruminococcus albus. Int J Hydrogen Energy* 33:1153–1163.

Oh SE, Iyer P, Bruns MA, Logan BE. 2004. Biological hydrogen production using a membrane biore- actor. *Biotechnol Bioeng* 87(1):119–127.

Oh YK, Park MS, Seol EH, Lee SJ, Park S. 2003. Isolation of hydrogen-producing bacteria from granu- lar sludge of an upflow anaerobic sludge blanket reactor. *Biotechnol Bioprocess Eng* 8:54–57.

O-Thong S, Prasertsan P, Intrasungkha N, Dhamwichukorn S, Birkeland NK. 2008a. Optimization of simultaneous thermophilic fermentative hydrogen production and COD reduction from palm oil mill effluent by *Thermoanaerobacterium*-rich sludge. *Int J Hydrogen Energy* 33(4):1221–1231.

O-Thong S, Prasertsan P, Karakashev D, Angelidaki I. 2008b. Thermophilic fermentative hydrogen production by the newly isolated *Thermoanaerobacterium thermosaccharolyticum* PSU-2. *Int J Hydrogen Energy* 33(4):1204–1214.

Palazzi E, Fabino B, Perego P. 2000. Process development of continuous hydrogen production by

Enterobacter aerogenes in a packed column reactor. *Bioprocess Eng* 22:205–213.

Pan CM, Fan YT, Xing Y, Hou HW, Zhang ML. 2008. Statistical optimization of process parameters on biohydrogen production from glucose by *Clostridium* sp. Fanp2. *Bioresour Technol* 99:3146–3154.

Park W, Hyun SH, Oh SE, Logan BE, Kim IS. 2005. Removal of headspace CO_2 increases biological hydrogen production. *Environ Sci Technol* 39(12):4416–4420.

Podestá JJ, Navarro AMG, Estrella CN, Esteso MA. 1997. Electrochemical measurements of trace concentrations of biological hydrogen produced by *Enterobacteriaceae. Inst Pasteur* 148:87–93.

Puppan D. 2002. Environmental evaluation of biofuels. *Period Polytech Ser Soc Man Sci* 10:95–116.

Rachman MA, Nakashimada Y, Kakizono T, Nishio N. 1998. Hydrogen production with high yield and high evolution rate by self-flocculated cells of *Enterobacter aerogenes* in a packed-bed reac- tor. *Appl Microbiol Biotechnol* 49:450–454.

Ragauskas AJ, Williams CK, Davison BH, Britovsek G, Cairney J, Eckert CA, Frederick WJJR, Hallett JP, Leak DJ, Liotta CL. 2006. The path forward for biofuels and biomaterials. *Science* 311:484–489. Raghavendra AS, Padmasree K. 2003. Beneficial interactions of mitochondrial metabolism with pho-

tosynthetic carbon assimilation. *Trend Plant Sci* 8:546–553.

Rajeshwari KV, Balakrishnan M, Kansal A, Lata K, Kishore VVN. 2000. State-of-the-art of anaerobic digestion technology for industrial wastewater treatment. *Renew Sust Energ Rev* 4(2):135–156.

Ren N, Li J, Li B, Wang Y, Liu S. 2006. Biohydrogen production from molasses by anaerobic fermenta- tion with a pilot-scale bioreactor system. *Int J Hydrogen Energy* 31(15):2147–2157.

Ren NQ, Chen XL, Zhao D. 2001. Control of fermentation types in continuous-flow acidogenic reac- tors: Effects of pH and redox potential. *J Harbin Inst Technol (New Ser)* 8(2):116–119.

Ren NQ, Wang BZ, Huang JC. 1997. Ethanol-type fermentation from carbohydrate in high rate acido- genic reactor. *Biotechnol Bioeng* 54(5):428–433.

Rosenbaum V, Riesner D. 1987. Temperature-gradient gel electrophoresis; thermodynamic analysis of nucleic acids and proteins in purified form and in cellular extracts. *Biophys Chem* 26:235–246. Salerno MB, Park W, Zuo Y, Logan BE. 2006. Inhibition of biohydrogen production by ammonia.

Water Res 40:1167–1172.

Saratale GD, Chen SD, Lo YC, Saratale RG, Chang JS. 2008. Outlook of biohydrogen production from lignocellulosic feedstock using dark fermentation—A review. *J Sci Ind Res* 67:962–979.

Sasikala K, Ramana CV, Rao PR, Kovacs KL. 1993. Anoxygenic phototrophic bacteria: Physiology and advances in hydrogen technology. *Adv Appl Microbiol* 38:211–295.

Schmidt JE, Ahring BK. 1996. Granular sludge formation in upflow anaerobic sludge blanket (UASB) reactors. *Biotechnol Bioeng* 49(3):229–246.

Schubert C. 2006. Can biofuels finally take center stage? *Nat Biotechnol* 24:777–784.

Shin HS, Youn JH. 2005. Conversion of food waste into hydrogen by thermophilic acidogenesis.

Biodegradation 16:33–44.

Shin HS, Youn JH, Kim SH. 2004. Hydrogen production from food waste in anaerobic mesophilic and thermophilic acidogenesis. *Int J Hydrogen Energy* 29:1355–1363.

Show KY, Zhang ZP, Lee DJ. 2008. Design of bioreactors for biohydrogen production. *J Sci Ind Res*

67:941–949.

Stickland LH. 1934. The chemical reactions by which *Cl. sporogenes* obtains its energy. *Biochem J*

28(5):1746–1759.

Stickland LH. 1935. Studies in the metabolism of the strict anaerobes (Genus: *Clostridium*): The oxi- dation of alanine by *Cl. sporogenes*. IV. The reduction of glycine by *Cl. sporogenes*. *Biochem J* 29(4):889–898.

Slade R, Bauen A, Shah N. 2009. The commercial performance of cellulosic ethanol supply-chains in Europe. *Biotechnol Biofuels* (doi:10.1186/1754–6834-2-3).

Sparling R, Risbey D, Poggi-Varaldo HM. 1997. Hydrogen production from inhibited anaerobic com- posters. *Int J Hydrogen Energy* 22:563–566.

Sung S, Raskin L, Duangmanee T, Padmasiri S, Simmons JJ. 2002. Hydrogen production by anaerobic microbial communities exposed to repeated heat treatment. *Proceedings of the 2002 U.S.* DOE Hydrogen Program Review NREL/CP-610-32405.

Taguchi F, Mizukami N, Yamada K, Hasegawa K, Saito TT. 1995. Direct conversion of cellulosic mate- rials to hydrogen by *Clostridium* sp. strain No. 2. *Enzyme Microbiol Technol* 17:147–150.

Taguchi F, Yamada K, Hasegawa K, Takisaito T, Hara K. 1996. Continuous hydrogen production by *Clostridium* sp. Strain No. 2 from cellulose hydrolysate in aqueous two phase system. *J Ferment Bioeng* 82:80–83.

Tanisho S, Ishiwata Y. 1994. Continuous hydrogen production from molasses by bacterium

Enterobacter aerogenes. Int J Hydrogen Energy 19:807–812.

Teo KC, Xu HL, Tay JH. 2000. Molecular mechanism of granulation. II: Proton translocating activity.

J Environ Eng 126:411–418.

Turner J, Sverdrup G, Mann MK, Maness PC, Kroposki B, Ghirardi M, Evans RJ, Blake D. 2008.

Renewable hydrogen production. *Int J Energy Res* 32:379–407.

Ueno Y, Haruta S, Ishii M, Igarashi Y. 2001a. Characterization of a microorganism isolated from the effluent of hydrogen fermentation by microflora. *J Biosci Bioeng* 92:397–400.

Ueno Y, Haruta S, Ishii M, Igarashi Y. 2001b. Microbial community in anaerobic hydrogen-producing microflora enriched from sludge compost. *Appl Microbiol Biotechnol* 57(11):555–562.

Ueno Y, Kawai T, Sato S, Otsuka S, Morimoto M. 1995. Biological production of hydrogen from cel- lulose by natural anaerobic microflora. *J Fermen Bioeng* 79:395–397.

Ueno Y, Otsuka S, Morimoto M. 1996. Hydrogen production from industrial wastewater by anaero- bic microflora in chemostate culture. *J Ferment Bioeng* 82(2):194–197.

Valdez-Vazquez I, Poggi-Varaldo HM. 2009. Hydrogen production by fermentative consortia. *Renew Sustain Energy Rev* 13:1000–1013.

Valdez-Vazquez I, Rios-Leal E, Carmona-Martinez A, Munoz-Paez KM, Poggi-Varaldo HM. 2006. Improvement of biohydrogen production from solid wastes by intermittent venting and gas flushing of batch reactors headspace. *Environ Sci Technol* 40(10):3409–3415.

Valdez-Vazquez I, Rios-Leal E, Esparza-Garcia F, Cecchi F, Poggi-Varaldo HA. 2005a. Semi-continuous solid substrate anaerobic reactors for H_2 production from organic waste: Mesophilic versus thermophilic regime. *Int J Hydrogen Energy* 30:1383–1391.

Van den Berg L, Kennedy KJ, Samson R. 1985. Anaerobic downflow stationary fixed film reactor: Performance under steady-state and non-steady conditions. *Water Sci Technol* 17(1):89–102.

Van Ginkel S, Sung S, Lay JJ. 2001. Biohydrogen production as a function of pH and substrate con- centration. *Environ Sci Technol* 35:4726–4730.

Van Ginkel SW, Logan B. 2005. Increased biological hydrogen production with reduced organic loading. *Water Res* 39:3819–3826.

Vazquez IV, Sparling R, Risbey D, Rinderknecht SN, Poggi-Varaldo HM. 2005. Hydrogen generation via anaerobic fermentation of paper mill wastes. *Bioresour Technol* 96:1907–1913.

Vijayaraghavan K, Ahmad D. 2006. Biohydrogen generation from palm oil mill effluent using anaer- obic contact filter. *Int J Hydrogen Energy* 31(10):1284–1291.

Vijayaraghavan K, Ahmad D, Ibrahim MKB. 2006. Biohydrogen generation from jackfruit peel using anaerobic contact filter. *Int J Hydrogen Energy* 31(5):569–579.

Vijayaraghavan K, Ahmad D, Soning C. 2007. Bio-hydrogen generation from mixed fruit peelwaste using anaerobic contact filter. *Int J Hydrogen Energy* 32(18):4754–4760.

Vijayaraghavan K, Soom MAM. 2007. Trends in biological hydrogen production—A review. *Int J Hydrogen Energy*.

Wang A, Ren N, Shi Y, Lee DJ. 2008. Bioaugmented hydrogen production from microcrystalline cel- lulose using co-culture-*Clostridium acetobutylicum* X9 and *Ethanoigenens harbinense* B49. *Int J Hydrogen Energy* 33(2):912–917.

Wang CC, Chang CW, Chu CP, Lee DJ, Chang BV, Liao CS. 2003b. Producing hydrogen from waste- water sludge by *Clostridum bifermentans. J Biotechnol* 102:83–92.

Wang CC, Chang CW, Chu CP, Lee DJ, Chang BV, Liao CS, Tay JH. 2003a. Using filtrate of waste biosolids to effectively produce bio-hydrogen by anaerobic fermentation. *Water Res* 37(11):2789–2793.

Wang JL, Wan W. 2008. Effect of Fe^{2+} concentrations on fermentative hydrogen production by mixed cultures. *Int J Hydrogen Energy* 33:1215–1220.

Wang JL, Wan W. 2009. Factors influencing fermentative hydrogen production: A review. *Int J Hydrogen Energy* 34:799–811.

Wang L, Zhou Q, Li FT. 2006. Avoiding propionic acid accumulation in the anaerobic process for biohydrogen production. *Biomass Bioenergy* 30(2):177–182.

Wang XJ, Ren NQ, Xiang WS, Guo WQ. 2007. Influence of gaseous end-products inhibition and nutri- ent limitations on the growth and hydrogen production by hydrogen-producing fermentative bacterial B49. *Int J Hydrogen Energy* 32:748–754.

Wen C, Huang X, Qian Y. 1999. Domestic wastewater treatment using an anaerobic bioreactor cou- pled with membrane filtration. *Process Biochem* 35:335–340.

Woodward J, Orr M, Cordray K, Greenbaum E. 2000. Enzymatic production of biohydrogen. *Nature*

405:1014–1015.

Wu JH, Lin CY. 2004. Biohydrogen production by mesophilic fermentation of food wastewater. *Water Sci Technol* 49:223–228.

Wu KJ, Saratale GD, Lo YC, Chen SD, Chen WM, Tseng ZJ, Chang JS. 2008a. Fermentative produc- tion of 2,3 butanediol, ethanol and hydrogen with *Klebsiella* sp. isolated from sewage sludge. *Bioresour Technol* 99:7966–7970.

Wu SY, Hung CH, Lin CN, Chen HW, Lee AS, Chang JS. 2006. Fermentative hydrogen production and bacterial community structure in high-rate anaerobic bioreactors containing silicone- immobilized and self-flocculated sludge. *Biotechnol Bioeng* 93(5):934–946.

Wu SY, Hung CH, Lin CY, Lin PJ, Lee KS, Lin CN, Chang FY, Chang JS. 2008b. HRT-dependent hydrogen production and bacterial community structure of mixed anaerobic microflora in sus- pended, granular and immobilized sludge systems using glucose as the carbon substrate. *Int J Hydrogen Energy* 33:1542–1549.

Wu SY, Lin CN, Chang JS. 2003. Hydrogen production with immobilized sewage sludge in three- phase fluidized-bed bioreactors. *Biotechnol Prog* 19:828–832.

Wu SY, Lin CN, Chang JS, Chang JS. 2005. Biohydrogen production with anaerobic sludge immobi- lized by ethylene-vinyl acetate copolymer. *Int J Hydrogen Energy* 30(13–14):1375–1381.

Wu SY, Lin CN, Chang JS, Lee KS, Lin PJ. 2002. Microbial hydrogen production with immobilized sewage sludge. *Biotechnol Prog* 18:921–926.

Wu SY, Lin CY, Lee KS, Hung CH, Chang JS, Lin PJ, Chang FY. 2008c. Dark fermentative hydrogen produc- tion from xylose in different bioreactors using sewage sludge microflora. *Energy Fuels* 22:113–119.

Xing DF, Ren NQ, Wang AJ, Li QB, Feng YJ, Ma F. 2008. Continuous hydrogen production of auto- aggregative *Ethanoligenens harbinense* YUAN-3 under non-sterile condition. *Int J Hydrogen Energy* 33:1489–1495.

Yang H, Shao P, Lu T, Shen J, Wang D, Xu Z, Yuan X. 2006. Continuous bio-hydrogen produc- tion from citric acid wastewater via facultative anaerobic bacteria. *Int J Hydrogen Energy* 31(10):1306–1313.

Yang H, Shen J. 2006. Effect of ferrous iron concentration on anaerobic bio-hydrogen production from soluble starch. *Int J Hydrogen Energy* 31:2137–2146.

Yeonghee A, Park E-J, Oh Y-K, Park S, Webster G, Weightman AJ. 2005. Biofilm microbial commu- nity of a thermophilic trickling biofilter used for continuous biohydrogen production. *FEMS Microbiol Lett* 249:31–38.

Yoda M, Kitagawa M, Miyaji Y. 1989. Granular sludge formation in the anaerobic expanded micro carrier process. *Water Sci Technol* 21:109–122.

Yokoi H, Maki R, Hirose J, Hayashi S. 2002. Microbial production of hydrogen from starch-manufac- turing wastes. *Biomass Bioenerg* 22:389–395.

Yokoi H, Ohkawara T, Hirose J, Hayashi S, Takasaki Y. 1995. Characteristics of hydrogen production by aciduric *Enterobacter aerogenes* strain HO-39. *J Ferment Bioeng* 80:571–574.

Yokoi H, Saitsu AS, Uchida H, Hirose J, Hayashi S, Takasaki Y. 2001. Microbial hydrogen production from sweet potato starch residue. *J Biosci Bioeng* 91:58–63.

Yokoi H, Tokushige T, Hirose J, Hayashi S, Takasaki Y. 1997. Hydrogen production by immobilized cells of aciduric *Enterobacter aerogenes* strain HO-39. *J Ferment Bioeng* 83:481–484.

Yokoyama H, Waki M, Moriya N, Yasuda T, Tanaka Y, Haga K. 2007b. Effect of fermentation tempera- ture on hydrogen production from cow waste slurry by using anaerobic microflora within the slurry. *Appl Microbiol Biotechnol* 74:474–483.

Yokoyama H, Waki M, Ogino A, Ohmori H, Tanaka Y. 2007a. Hydrogen fermentation properties of undiluted cow dung. *J Biosci Bioeng* 104:82–85.

Yu HQ, Mu Y. 2006. Biological hydrogen production in a UASB reactor with granules. II: Reactor performance in 3-year operation. *Biotechnol Bioeng* 94(5):988–995.

Yu HQ, Tay JH, Fang HHP. 1999. Effects of added powdered and granular activated carbons on start- up performance of UASB reactors. *Environ Technol* 20:1095–1101.

Yu HQ, Zhu ZH, Hu WR, Zhang HS. 2002. Hydrogen production from rice winery wastewater in an upflow anaerobic reactor by using mixed anaerobic cultures. *Int J Hydrogen Energy* 27:1359–1365.

Zhang T, Fang HHP. 2000. Digitization of DGGE (denaturing gradient gel electrophoresis) profile and cluster analysis of microbial communities. *Biotechnol Lett* 22:399–405.

Zhang T, Liu H, Fang HHP. 2003. Biohydrogen production from starch in wastewater under thermo- philic condition. *J Environ Manage* 69:149–156.

Zhang Y, Liu G, Shen J. 2005. Hydrogen production in batch culture of mixed bacteria with sucrose under different iron concentrations. *Int J Hydrogen Energy* 30:855–860.

Zhang Y, Shen J. 2006. Effect of temperature and iron concentration on the growth and hydrogen production of mixed bacteria. *Int J Hydrogen Energy* 31(4):441–446.

Zhang ZP, Show KY, Tay JH, Liang DT, Lee DJ. 2008. Biohydrogen production with anaerobic fluid- ized bed reactors—A comparison of biofilm-based and granule-based systems. *Int J Hydrogen Energy* 33:1559–1564.

Zhang ZP, Show KY, Tay JH, Liang DT, Lee DJ, Jiang WJ. 2006. Effect of hydraulic retention time on biohydrogen production and anaerobic microbial community. *Process Biochem* 41:2118–2123.

Zhang ZP, Show KY, Tay JH, Liang DT, Lee DJ, Jiang WJ. 2007. Rapid formation of hydrogen-pro- ducing granules in an anaerobic continuous stirred tank reactor induced by acid incubation. *Biotechnol Bioeng* 96:1040–1050.

Zheng XJ, Yu HQ. 2004. Biological hydrogen production by enriched anaerobic cultures in the pres- ence of copper and zinc. *J Environ Sci Health Part A Toxic/Hazard Subst Environ Eng* 39(1):89–101.

Zheng XJ, Yu HQ. 2005. Inhibitory effects of butyrate on biological hydrogen production with mixed anaerobic cultures. *J Environ Manage* 74(1):65–70.

Zhu Y, Yang ST. 2004. Effect of pH on metabolic pathway shift in fermentation of xylose by *Clostridium tyrobutyricum*. *J Biotechnol* 110(2):143–157.

Zoetemeyer RJ, Arnoldy P, Cohen A, Boelhouwer C. 1982a. Infuence of temperature on the anaerobic acidification of glucose in a mixed culture forming part of a two-stage digestion process. *Water Res* 16(3):313–321.

Zoetemeyer RJ, Van den Heuvel JC, Cohen A. 1982b. pH influence on acidogenic dissimilation of glucose in an anaerobic digester. *Water Res* 16:303–311.

anaerobic digester. *Water Res* 16:303–311.

10

Biological Hydrogen Production:
Light-Driven Processes

Hisham Hafez
University of Western Ontario
Greenfield Specialty Alcohols
George Nakhla
University of Western Ontario
Hesham El Naggar
University of Western Ontario
Gamal Ibrahim
University of Menoufia
Said S.E.H. Elnashaie
University of British Columbia
New Mexico Technical University

CONTENTS

10.1 Introduction 322
10.2 Biological Hydrogen Production 322
10.2.1 Light-Driven Processes 323
10.2.1.1 General Considerations 323
10.2.1.2 Direct Biophotolysis 325
10.2.1.3 Indirect Biophotolysis 328
10.2.1.4 Photofermentation 330
10.2.2 Anaerobic (Dark) Fermentation 332
10.2.3 Hybrid Systems 332
10.2.3.1 Second Stage: Methane Fermentation 332
10.2.3.2 Second Stage: Photofermentation 333
10.2.3.3 Second Stage: Electrohydrogenesis 333
10.2.4 Summary and Conclusion 334
10.3 Photobioreactors 334
10.3.1 Open Ponds 336
10.3.2 Flat-Plate Photobioreactors 337
10.3.3 Tubular Photobioreactors 337
10.3.4 Vertical-Column Photobioreactors 338
10.3.5 Internally Illuminated Photobioreactors 338
10.3.6 Hydrodynamics and Mass Transfer Characteristics of Photobioreactors 339

10.3.7 Mass Cultivation of Algae 342
10.3.8 Conclusion and Perspectives of Photobioreactors 343
10.4 Hydrogen from Lignocellulosic Biomass 343
10.4.1 Pretreatment and Hydrolysis of Lignocellulosic Biomass 346
10.4.1.1 Prehydrolysis (Lignocelluloses Fractionation) 346
10.4.1.2 Cellulose Hydrolysis 347
10.4.2 Bioconversion of Lignocellulosic Hydrolysate to Hydrogen 347
10.4.2.1 Functional Microorganisms 347
10.4.2.2 Key Factors Affecting Bioconversion of Prehydrolysates/ Hydrolysates to H_2 350
10.4.2.3 Fermentation Tactics for Lignocellulosic Prehydrolysates to Hydrogen 351
10.4.3 Direct Microbial Conversion of Cellulose to Hydrogen 351
10.4.3.1 Microorganisms Involved in Converting Cellulose to Hydrogen 351
10.4.3.2 Bioaugmentation for Cellulose Degradation to Hydrogen 352
10.4.3.3 Key Factors Affecting Cellulose Degradation and Hydrogen Production 353
10.4.3.4 Integrated Process System for Multi-Output Solutions 354
10.4.3.5 Coupling Process of Hydrogen–Methane Fermentation 355
10.4.3.6 Integrated Process System for Multioutput Solutions 355
References 355

10.1 Introduction

The conventional hydrogen production methods involve fossil fuel reforming. This process usually generates large amounts of CO_2. Alternative methods of hydrogen generation include electrolysis of water, biophotolysis, and biological production from organic waste materials. In biological hydrogen production, bacteria or microalgae are used to process the organic material through metabolic action and produce hydrogen. Biological hydrogen production has two main advantages over the conventional methods: it generates less greenhouse gases and treats wastes rich in organics (e.g., biomass residues and domestic or food industry wastewaters), thus reducing their negative impact on the environment.

Although some observations of hydrogen production by microalgae and bacteria extend back over 100 years, basic research in this field started only in the late 1920s with bacterial H_2 production and in the 1940s with microalgal hydrogen production. Applied research and development (R&D) started only in the early 1970s. Most applied R&D has empha- sized photosynthetic processes. Over the past quarter century, numerous studies have been focused on microbial H_2 production, but advances toward practical applications have been minimal. This chapter reviews the various types of biohydrogen processes and dis- cusses some of their potential practical limitations.

10.2 Biological Hydrogen Production

Biological hydrogen production from renewable sources (biomass, water, and organic wastes) has the potential to meet the growing demand for energy. It offers a feasible means for sustainable supply of H_2 with low pollution and high efficiency, thereby considered a promising

ecofriendly energy source. Biological hydrogen production can be achieved by anaerobic and photosynthetic microorganisms using carbohydrate-rich and nontoxic raw materials. Under anaerobic conditions, hydrogen is produced as a by-product during conversion of organic wastes into organic acids, which can subsequently be used for methane generation. The acidogenic phase of anaerobic digestion of wastes can be manipulated to improve hydrogen production.

The main processes for biohydrogen production include the following:

1. Light-driven processes
2. Dark fermentation
3. Hybrid (two-stage integrated) systems

Anaerobic (or dark) fermentation and photosynthetic degradation are the two most widely studied biohydrogen production techniques. Anaerobic fermentation is advantageous due to its rapid hydrogen evolution rate, while in the photosynthetic process, complete conver- sion of organic matter is theoretically possible. Either process, however, suffers from rela- tively low yields when used independently. For biohydrogen production to be economically feasible, hydrogen yields on dissolved organic material should be approximately 60%–80%. Combining the two methods, either directly or in a two-stage series-type configuration, has then the potential to increase the hydrogen yield to achieve this conversion target. The rest of this chapter is focused on light-driven processes and hybrid processes.

10.2.1 Light-Driven Processes

10.2.1.1 General Considerations

Biological hydrogen production using light-driven processes can be classified into four different groups (Levin et al. 2004):

1. Direct biophotolysis
2. Indirect biophotolysis
3. Photofermentation

It is clear that the first two bioprocesses are non-biowaste-based processes, where the direct photolysis depends on the splitting of water molecules to hydrogen and oxygen and the indirect photolysis includes two main steps: the first step is utilizing CO_2 to build up biomolecules like glucose and the second step is the decomposing of these molecules to hydrogen. The third bioprocess is a biowaste-based process.

In light-driven biological hydrogen production, microorganisms are utilized to convert solar energy to hydrogen. The diffuse nature of solar energy and the consequent low energy density places severe economic restrictions on the efficiency of this process. Hallenbeck and Benemann (2002) estimated that \$10 worth of H_2/m^2/year would utilize an average solar radiation of 5 kWh/m^2/day, which corresponds to 6.6 GJ/year and represents a conversion efficiency of 10%. Even with this overly optimistic estimate, the US Department of Energy (US DOE) puts the price for H_2 at \$15/GJ. This renders the light-driven process uneconomical in view of the required expenditures for infrastructure (construction of facilities) and operation (considering energy input for mixing, gas exchange and compression, and cooling, etc.). Obviously, lower efficiencies translate to increased bioreactor surface areas and consequently cost for the production per unit output of hydrogen fuel. In spite of the importance of economic feasibility, only relatively few studies on photobiological hydrogen production reported conversion efficiencies, which typically fall well below 1% (i.e., <\$1 H_2/m^2/year).

In theory, photosynthesis in general and microalgal cultures in particular could achieve as much as a 10% total light energy conversion into a primary product, such as CO_2 fixed into biomass or even H_2. However, such expectations are based on data obtained under low-light conditions and do not account for the rather low efficiencies typically observed at the full sunlight intensity to which algal cultures would be exposed to in practice. Note that the dark reactions are the rate-limiting factor (i.e., the rate of transfer of electrons between the two photosystems [photosystem I, PSI, and photosystem II, PSII]), which is roughly 10 times lower than the rate of light captured by photosynthetic pigments (e.g., chlorophyll). This results in up to 90% of the photons captured by the photosynthetic apparatus under full sunlight not being used in photosynthesis but rather dissipated as heat or fluorescence. Similar considerations apply to photosynthetic bacteria whose pigment antenna systems absorb light at high rates for high light intensities, which cannot be productively used due to slow dark reactions. This energy waste is only somewhat ameliorated in dense cultures where most cells are not close to the culture surface and thus are not subjected to maximum solar intensity. This so-called light saturation effect is a major reason that algal productivity is not nearly as high as those projected from extrapolations of laboratory data at low light intensity.

The light saturation effect can be addressed by employing different techniques such as rapid mixing, dilution of light incident on the surface of the algal cultures, and using algal mutants with reduced chlorophyll contents that would absorb fewer photons. Rapid mixing may create a *flashing light effect* in eddies of turbulence surrounding the algal cells, wherein millisecond flashes of high-intensity light, followed by an approximately five- to tenfold longer dark period, maximize overall photon use efficiency. This is explained as follows.

During a brief light flash, each photosynthetic unit (containing several hundred chlorophyll molecules) captures only one photon. The subsequent longer dark phase allows for a slower transfer of electrons between photosystems. Achieving this flashing light effect with algal mass cultures, however, requires very high mixing power inputs, rendering the process impractical. Nonetheless, some mixing is required in algal mass cultures to sup- ply nutrients (in particular, CO_2) in order to prevent settling and to maintain uniformity of the culture. From a practical perspective, mixing velocities of 25–35 cm/s should not be exceeded, in particular for fuel production processes, as the power inputs required for mixing increase as a cubic function of velocity. The effect of such gentler mixing regimes on algal productivity is somewhat controversial. Weissman (1988) observed no enhancement of productivity over a wide range of mixing velocities (5–60 cm/s), while controlling other potentially confounding factors (pH, O_2 concentrations). However, other researchers noted that mixing (and the associated periodic light regime experienced by individual algal cells in mass cultures) has a profound effect on productivity.

Another approach to overcome the light saturation effect is using light attenuation devices to transfer sunlight into the depths of a dense algal culture. The simplest approach is to arrange photobioreactors in vertical arrays to reduce direct sunlight. However, this configuration increases the area of required photobioreactors proportionally, which is the limiting economic factor in any photobiological fuel production process. Another alternative is the use of optical fiber photobioreactors that collect light energy by employing large concentrating mirrors and piping light energy into small photobioreactors through optical fibers. More recently, this concept became the centerpiece of significant R&D efforts carried out in Japan on microalgae biofixation of CO_2 and greenhouse gas mitigation, including H_2 production, notwithstanding its technical and economic challenges.

Using mutants of algal cells with reduced pigment content (smaller amounts of *antenna* chlorophyll or other *light-harvesting* pigments such as phycobili proteins in cyanobacteria)

offers a practical alternative to rapid mixing. A photosynthetic apparatus with less light-harvesting chlorophyll absorbs fewer photons at high light intensity, and thus wastes fewer photons, suggesting that such algal strains do not readily exist in nature, as they are intermittently exposed to both high light intensity (at or near the surface) and low light intensity (deeper in the culture). This results in an evolutionary selection for strains with more light-harvesting pigments per photosynthetic reaction center. Generally, these cell types can capture more photons per cell than strains with a reduced ratio of antenna chlorophyll per reaction center. However, such cells waste most of the captured photons near the cul- ture surface, thus decreasing the overall culture productivity compared to cultures of cells containing a reduced antenna to reaction center pigment ratio. Even though similar observations were made over 50 years ago, the concept of increasing productivity by reducing antenna size has remained rather dormant.

This approach has recently been revived in Japan and the United States. In the Japanese project, laboratory experiments on cultures operating at high light intensity showed that microalgal mutants with reduced antenna sizes exhibited a 50% increase in pro- ductivity, compared to the wild type. This increase demonstrated the potential of this approach. Another study adopted a physiological approach using cultures of the green alga *Dunaliella salina*. Under stress conditions, these algae exhibited both damaged PSII centers and reduced antenna size. However, PSII centers were repaired before their antenna size increased when the stress was relieved. This allowed for a brief period of relatively high rates of photosynthesis under high light intensity. More recently, antenna mutants have been isolated and studied in the United States, with limited success in enhancing efficiency at high light intensity. The use of algal mutants believed to be deficient in the PSI complex but reportedly still able to produce H_2 and fix CO_2 is an alternative approach. This suggested the possibility of a *PSII-only* photosynthesis, which could double the overall solar conversion efficiency by requiring only one photon per electron transported from water to CO_2 or H_2. However, that work proved to be irreproducible.

Currently, photosynthetic efficiency (PE) of about 3% of solar energy converted into algal biomass can be achieved considering microalgae biomass production in outdoor cultures. The ultimate goal of photosynthetic H_2 production is therefore to increase solar conversion efficiency by at least threefold. This goal is crucial to the realization of practical microalgae processes for H_2 production.

10.2.1.2 *Direct Biophotolysis*

The potential use of microorganisms for biological production of hydrogen as an energy resource places hydrogen metabolism at the forefront of research on biological hydrogen production. The concept of *direct biophotolysis* encompasses light-driven simultaneous O_2 evolution on the oxidizing side of PSII and H_2 production on the reducing side of PSI, with a maximum H_2–O_2 (mol–mol) ratio of 2:1. Such a reaction with green algae could serve to provide a clean, renewable, and economically viable H_2 fuel. This process of photosynthetic hydrogen production does not entail CO_2 fixation or energy storage into cellular metabolites. Hydrogenase is the name given to the family of enzymes that catalyze the reversible oxida- tion of hydrogen into its elementary particle constituents, two protons (H^+) and two electrons. These enzymes are divided into three classes depending on the metal content at the active site: Fe hydrogenase, NiFe hydrogenase, and nitrogenase. Fe hydrogenase enzyme is used in the biophotolysis processes whereas photofermentation processes utilize nitrogenase. The Fe hydrogenases are enzymes that exhibit high sensitivity to O_2 and light. This may pose an additional problem for their biotechnological use in photosynthetic organisms such as algae.

Biological hydrogen can be generated from plants by biophotolysis of water using microalgae (green algae and cyanobacteria), fermentation of organic compounds, and photodecomposition of organic compounds by photosynthetic bacteria. Photosynthetic production of hydrogen from water is a biological process that can convert sunlight into useful, stored chemical energy by the following general reaction (Equation 10.1):

$$2H_2O \rightarrow 2H_2 + O_2 \tag{10.1}$$

This is an attractive process since solar energy is used to convert a readily available substrate, water, to oxygen and hydrogen. This reaction was first demonstrated with a cell-free chloroplast–ferredoxin (Fd)–hydrogenase system, but the existence of such a reaction in green algae had been suggested earlier. Indeed, due to the inherent liability of the various components in a cell-free oxic environment, more reliable systems using whole cells have been studied since then by many researchers. The hydrogen is generated in the case of the unicellular algae via the hydrogenase enzyme. In the case of cyanobacteria, on the other hand, the water-splitting process involves two enzymes, hydrogenase and nitrogenase, both of which catalyze the hydrogen generation process. The light energy is absorbed by the pigments at PSI, PSII, or both, which raises the energy level of electrons from water oxidation when they are transferred from PSI via PSII to Fd. The hydrogenase accepts the electrons from Fd to produce hydrogen as shown in Figure 10.1. Since hydrogenase is sensitive to oxygen, it is necessary to maintain the oxygen content at a level lower than 0.1% so that hydrogen production can be sustained. This condition can be achieved by utilizing green algae *Chlamydomonas reinhardtii* that can deplete oxygen during oxidative respiration.

In fact, photon energy conversion efficiency of some 22% of visible light energy into H_2 by direct biophotolysis corresponds to solar conversion efficiency of some 10%. This was demonstrated in vivo with the green microalga *C. reinhardtii* in laboratory experiments under low light intensities and very low partial pressures of O_2. This avoided the limitation of the light saturation effect and inhibition by photosynthetically produced O_2. In addition, when the culture of green microalga *C. reinhardtii* is deprived of inorganic S, the rates of O_2 synthesis and CO_2 fixation decline significantly within 24 h (in the light). The reason for this loss of activity is due to the need for frequent replacement of the H_2O-oxidizing protein D1 in the PSII reaction center.

The essential anaerobiosis in cells under light is achieved by depriving sulfur from the medium (<0.45 mM) to reduce the oxygenic PSII activity. Also, it is equally important to remove the generated oxygen by keeping the cell's respiration rate on exogenous acetate and/or endogenous carbohydrates. Acetate is a good carbon substrate for *C. reinhardtii* cells

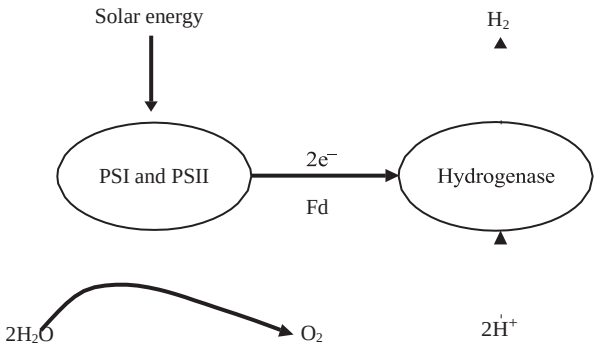


FIGURE 10.1

Schematic diagram for direct biophotolysis.

to maintain a high respiration rate. The primary processes of photosynthesis (i.e., light-triggered charge separation) occur with an unsurpassed efficiency of >95% but all subsequent processes up to the fixation of CO_2 in the so-called dark reactions dissipate a consider- able amount of energy. Although the conversion efficiency under ideal conditions (low irradiation, red light) is about 27% (21% for photosynthetic active radiation), the typical conversion efficiency to biomass is about 5% or can be even lower. Photosynthetic microorganisms, such as green algae and cyanobacteria (blue-green algae), have the potential to store efficiently the energy of incident sunlight as high-energy H_2 molecules, with a maximum theoretical efficiency of approximately 13%.

Simultaneous hydrogen and oxygen production with this system has only been demonstrated under very high inert gas sparging leading to very low concentrations of hydro- gen and oxygen. It is necessary to use special conditions since Fe hydrogenase activity is extremely oxygen sensitive. Although not specifically studied, it appears that in order for simultaneous production of H_2 and O_2 to occur, the O_2 partial pressures must be below 0.001 atm. It would not be possible to maintain such low partial pressure in any practical direct biophotolysis process due to the large amount of diluent gas and power input required for gas transfer. A direct biophotolysis process must therefore operate at a partial pressure of near one atmosphere of O_2, which is a thousand times the maximum likely to be tolerated. Thus, the O_2 sensitivity of the hydrogenase enzyme reaction and the supporting reductant-generating pathway remains the key problem, as it has been for the past 30 years. The O_2 absorbers can be used to overcome the O_2 sensitivity. The O_2 absorbers are of two types: irreversible, such as glucose/glucose oxidase and dithionite, and reversible such as hemoglobin. However, using irreversible or regeneration of reversible O_2 absorbers would not be practical in any scaled-up process as they reduce its net efficiency. Endogenous respiration by microalgae can reduce O_2 levels, as observed in a recent study. It should be noted that the results of this study were mistakenly attributed to an indirect biophotolysis process. However, respiratory O_2 uptake decreases by half the potential H_2 evolution, since for each H_2 mole produced, an equivalent amount of substrate is respired. This is an unacceptable loss of efficiency. Uptake hydrogenases have been made more O_2 tolerant through protein engineering, but these enzymes operate at a much higher redox potential than reversible (H_2 evolving) hydrogenases. In an attempt to achieve oxygen-tolerant hydrogenase activity through classical mutagenesis Ghirardi (1997) developed an experimental technique for the selection of O_2-tolerant, H_2-producing variants of *C. reinhardtii* based on the ability of wild-type cells to survive a short (20 min) exposure to metronidazole in the presence of controlled concentrations of O_2. In this approach, the number of survivors depends on the metroni- dazole concentration, light intensity, preinduction of the hydrogenase, and the presence or absence of O_2. The authors demonstrated that some of the selected survivors in fact exhibit H_2 production capacity that is less sensitive to O_2 than the original wild-type population. One approach that can resolve this problem is the use of heterocystous cyanobacteria. The heterocyst is the site of nitrogen fixation, with the vegetative cells carrying out nor- mal photosynthesis (e.g., CO_2 fixation and O_2 evolution) and providing the heterocyst with reduced carbohydrates. A heavy cell wall that reduces diffusion of gases in combination with high respiration rates allows the heterocysts to maintain an essentially anaerobic inter- nal environment. Under an inert gas, such as argon, such cyanobacteria simultaneously evolve H_2 and O_2. Subsequent work demonstrated the long-term sustainability of such a reaction, even in an outdoor demonstration of H_2 production using solar energy. However, the efficiencies of light energy conversion into H_2 were disappointing, at most 1%–2% in laboratory experiments at low light intensities and less than 0.3% outdoors with sunlight. Extensive work from many laboratories has expanded on this research without resolving

the fundamental problem of such systems: the very low efficiency of solar energy conversion into H_2. Although in part this also reflects limitations of photosynthesis, discussed in the succeeding text, the main reason for the low efficiencies was the very high metabolic cost of nitrogenase-based, and in particular heterocyst-based, H_2 production. Heterocysts biosynthesis and maintenance account for about half of the energy metabolism of these cyanobacteria, without even considering the actual nitrogenase reaction, which requires at least 4 ATP per H_2 evolved. This metabolic energy must be provided by light through PSI-mediated cyclic phosphorylation or by respiration, in either case reducing H_2 production and achievable solar conversion efficiencies to well below half those expected from simpler, hydrogenase-based, indirect biophotolysis processes. Furthermore, the simultaneous pro- duction of H_2 and O_2 by heterocystous cyanobacteria requires gas separation, at a signifi- cant economic cost, as would also be the case for direct biophotolysis processes. For all these reasons, heterocystous cyanobacteria specifically, and nitrogen-fixing cyanobacteria in gen- eral, can no longer be recommended as subjects for applied microalgal H_2 production R&D. Practical direct biophotolysis processes must be highly resistant to O_2 inhibition, but such a process is still lacking. Other challenges facing direct biophotolysis processes include the requirement of large photobioreactors and the need for separation of H_2 and O_2, both of which make such a process impractical. Direct biophotolysis requires that the entire production area be enclosed in photobioreactors in order to produce and capture H_2 and O_2. Few cost estimates are available for large-scale closed photobioreactors. One con- ceptual study of photobiological H_2 production using an inclined tubular photobioreactor with internal gas exchange arrived at an optimistic capital cost of only \$50/m^2. The study also assumed minimal operating costs, considering extrapolation of as little as \$15/GJ H_2 produced for a direct (or other single-stage) biophotolysis process operating at 10% solar conversion efficiency. The cost analysis, however, did not include costs associated with contingencies, engineering, gas separation, and handling. A more realistic cost for such photobioreactors would be in the range of \$100/m^2, without gas separation or even contingencies and engineering costs. This cost would render any single-stage process (e.g., direct biophotolysis or heterocystous cyanobacterial processes) uneconomical. Indeed, any handling of H_2/O_2 mixtures in large volumes and over larger areas would likely be impractical.

In conclusion, the solar conversion efficiency of a direct biophotolysis process is approximately 10% requiring a large bioreactor surface area and thus high capital costs. Furthermore, the overall rate of hydrogen evolution is slow as the algal hydrogenase is inhibited by oxygen that is generated during the process. Efforts have been made to genetically modify the microorganisms to obtain a system that is less sensitive to oxygen, but to date, there are no known significant successes in this field. Therefore, direct biophotolytic processes, though fundamentally attractive from an environmental point of view, are economically unfeasible due to the insurmountable barriers of oxygen sensitivity, intrinsic limitations of poor light conversion efficiencies, problems with gas capture and separation, and slow hydrogen production rate.

10.2.1.3 Indirect Biophotolysis

Reversible hydrogenase-based indirect biophotolysis processes have, at least conceptually, major advantages over the nitrogenase-based systems: The specific H_2 evolution activities of reversible hydrogenases are almost a thousandfold higher than those of nitrogenase and, most importantly, require no ATP. On the other hand, there are also some draw- backs. Reversible hydrogenases in microalgae are generally expressed at relatively low activities, resulting in H_2 production rates typically much lower than those observed with nitrogenase-based processes. Also, H_2 production by reversible hydrogenases is typically

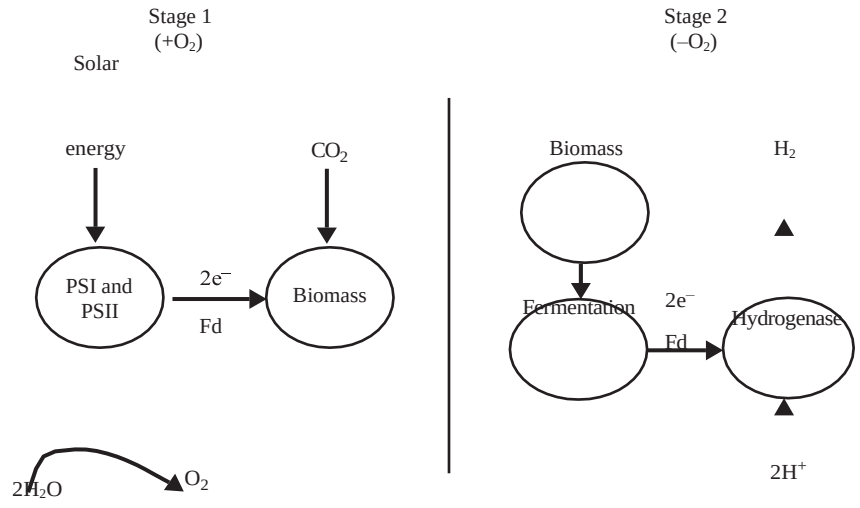


FIGURE 10.2

Schematic diagram for indirect biophotolysis.

inhibited by relatively low (<10%) partial pressures of H_2. Moreover, problems of sensitivity of the hydrogen evolution process are potentially circumvented by separating temporally and/or spatially oxygen evolution and hydrogen evolution. Thus, indirect biophotolysis processes involve separation of the H_2 and O_2 evolution reactions into separate stages, coupled through CO_2 fixation/evolution (see Figure 10.2).

One elaboration of this concept involved four distinct steps:

1. Production in open ponds at 10% solar efficiency of biomass high in storage carbohydrates. After carbohydrate accumulation, the cells would be removed from the growth pond or photobioreactor.
2. Concentrated if required.
3. Through respiratory O_2 uptake, allowed to become anaerobic and activate or induce the hydrogenase enzyme. H_2 evolution would then commence, first in the dark through endogenous fermentations.
4. In a light-driven (PSI-mediated) electron transport to convert remaining stored carbohydrates and fermentation products (e.g., acetate) to H_2. The depleted cells would be reused for additional cycles of CO_2 fixation–H_2 production.

Much information is available on each of these steps, but significant gaps remain. At pres- ent, the light-driven step of H_2 production has been demonstrated only in green algae. For unknown reasons, cyanobacteria that have reversible hydrogenases only seem to produce H_2 fermentatively in the dark, not in a light-driven or stimulated reaction. For green algae, hydrogenase levels are often not the limiting factor and it is possible to obtain high initial rates for short periods (seconds to minutes). However, sustained high rates have not been achieved, possibly due to competition with other reactions. Progress in the genetics of the hydrogenases, both reversible and uptake, in cyanobacteria and green algae has been rapid in recent years. Cyanobacteria have the unique characteristics of using CO_2 in the air as a carbon source and solar energy as an energy source (Equation 10.2). The cells take up CO_2 first to produce cellular substances, which are subsequently used for hydrogen production (Equation 10.3):

$$12H_2O + 6CO_2 \rightarrow C_6H_{12}O_6 + 6O_2$$

$$C_6H_{12}O_6 + 12H_2O \rightarrow$$

$$12H_2 + 6CO_2 \quad (10.3)$$

A cost estimate of $7/m^2 was developed for the highly conceptual process of indirect biophotolysis based on prior work on the economics of large-scale microalgae mass cultures in open ponds. The photobioreactors, requiring only one-tenth the area of the ponds, were not further specified and merely assumed to cost $100/m^2, which with contingencies, engineering, and other overheads gave a total capital cost of $135/m^2. With these assumptions, overall operational costs of such a process were estimated at about $10/GJ of H_2 (the cost of the photobioreactors was over half of the total costs). This was based on the assumption that less than one photon per H_2 evolved would be sufficient to drive H_2 evolution from the acetate. This assumption may not be correct with some experts believing that a minimum of two photons per H_2 is more realistic. Accordingly, the photobioreactor area required in such a process would increase from 10% to over 25% of the area of the pond cultures, that is, more than doubling the overall cost of H_2 produced by such a process. Another key issue is design, performance, and cost of the photobioreactors. Subsequently, Tredici (1998) devised that a simple, slightly inclined internal gas exchange tubular photobioreactor, consisting of forty 50 m long, 4.2 cm diameter tubes (glass or Teflon®), ganged together with a bottom manifold and top degasser, positioned on a slightly inclined (about 10% slope) earthen platform, and mixed by airlift. Despite simplicity, the Tredici-type reactor, suggested for biological H_2 production, was deemed to be too costly for such applications. In conclusion, indirect biophotolysis processes are still at the conceptual stage. More research has to be done, and its economical feasibility needs to be more qualified.

10.2.1.4 Photofermentation

Photosynthetic bacteria have long been studied for their capacity to produce hydrogen through the action of their nitrogenase system (Figure 10.3). Calculations of the efficiency of conversion of light energy into hydrogen often show values approaching 10%, but these estimates generally ignore the energy content of the organic substrate. True PE is much lower (less than 3%) under ideal (low) light conditions. Although little data are available, PE must be even lower under high-light (full sunlight) conditions since the

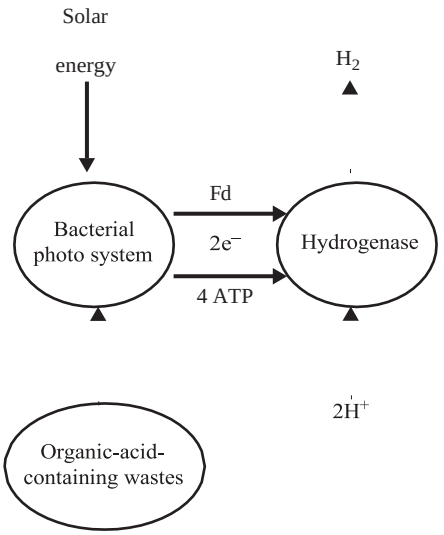


FIGURE 10.3

Hydrogen production via the action of the nitrogenase system using photosynthetic bacteria.

photosystem of the photosynthetic bacteria is, like that of microalgae and cyanobacteria (discussed earlier), optimized for low-light conditions.

Photosynthetic bacteria evolve molecular hydrogen catalyzed by nitrogenase under nitrogen-deficient conditions using light energy and reduced compounds.

Photoheterotrophs utilize dissolved organic compounds, as well as sunlight, and produce hydrogen under anaerobic/anoxic conditions. Many studies have demonstrated that photofermentation by photosynthetic bacteria can convert low–molecular weight fatty acids into H_2 and CO_2 with high efficiency.

Much work has been devoted to the development of systems that utilize photoheterotrophic bacteria for simultaneous hydrogen generation and waste disposal. Photosynthetic bacteria, such as *Rhodobacter sphaeroides*, generate hydrogen mainly through the action of the nitrogenase enzyme. This activity is inhibited by the presence of oxygen and high nitrogen/carbon ratios >1.4 N/C. In fact, high nitrogen concentrations have been linked to a metabolic shift where organic substrate is utilized mainly for biomass generation instead of hydrogen production. High biomass concentration is not desirable due to the reduction of light diffusion into the bioreactor. As with all biological systems, careful consideration must be given to operating conditions in order to maximize the desired parameters, in this case, hydrogen yield and rate of production. Depending on the temperature, pH, bacterial strain, irradiation, and substrate used, *R. sphaeroides* has exhibited variable results. The optimum temperature and pH were in the range of 30°C–35°C and 7.0–8.0, respectively, and irradiation was approximately 200 W/m^2. Though hydrogen production has been achieved with *R. sphaeroides* growing on various substrates, the bacteria seem to prefer organic acids such as acetic, butyric, malic, and lactic acid.

The utilization of simple sugars such as glucose and sucrose for hydrogen production is possible but usually results in lower substrate conversion and rate of H_2 evolution and is secondary if an organic acid cosubstrate is present. Some success in using industrial wastewater such as sugar refinery and tofu has been shown, but due to either the toxic nature of the effluent or color/opaqueness, pretreatment is needed prior to photosynthetic biohydrogen gas production.

Despite the success of hydrogen generation via photosynthetic degradation of organic compounds, much work is still needed to create a large-scale, economically attractive process. Even though the conversion of substrate is generally high, H_2 production rate is slow and the yield of hydrogen is far from the theoretical maximum. There are several other drawbacks to this process: (1) the use of the nitrogenase enzyme with its inherent high energy demand; (2) the low solar energy conversion efficiencies; and (3), as noted earlier, the requirement for elaborate anaerobic photobioreactors covering large areas. As with other light-based H_2 production processes, light diffusion and intensity play a key role in maximizing hydrogen yield. Increasing light intensity from 50 to 1000 W/m^{2}decreased the light conversion efficiency from approximately 8% to around 2%. Expensive equipment and the need for a large reactor surface area remain a drawback. Albeit cyclic light pro- cess operation (i.e., light/dark cycles) has been shown to increase the amount of hydrogen evolved when compared to continuous illumination, many questions remain unanswered regarding stability of overall light conversion efficiency to warrant large-scale systems. It is apparent that photosynthetic hydrogen production might have to be coupled with another process in order to make it an economically viable option of biogas production.

It is interesting to note that after extensive R&D on this system in Japan under the Research on Innovative Technologies for the Earth (RITE) program, it was dropped from further study. In conclusion, the rate and efficiency of hydrogen production by systems directly involving photosynthesis H_2 production (photobiological hydrogen production)

fall far short of economic feasibility. Since organic substrates are the ultimate source of hydrogen in photofermentations or indirect biophotolysis processes, it can be argued that it should be simpler and more efficient to extract the hydrogen from such substrates using a dark fermentation process. This approach is discussed thoroughly in the following.

10.2.2 Anaerobic (Dark) Fermentation

Anaerobic fermentation is similar to the photosynthetic process in that it makes use of microorganisms to produce hydrogen from organic matter. Anaerobic systems have an advantage over their photosynthetic counterparts in that they are simpler and less expensive and produce hydrogen at a much faster rate. The drawback, however, is that anaerobes are unable to utilize light energy and thus lack the ability to overcome the inherited thermodynamic energy barrier to fully decompose a substrate. Anaerobic fermentation presents an interesting yet largely unexplored avenue for the biological production of hydrogen. Much is presently known about the molecular biology and biochemistry of the hydrogen-producing enzymes, reductant-generating systems, and physiology of many hydrogen-producing fermentative microorganisms. Very little is presently known about the currently attainable yields or the possibilities for improving these yields in the future.

10.2.3 Hybrid Systems

Since hydrogen production from waste can only achieve partial conversion efficiency, as low as 33%, this means that the majority of the COD of waste streams remains untreated. A second-stage process downstream of the hydrogen reactor is a promising approach that renders the overall process more effective and economic. A variety of methods have been tested as a second stage in hydrogen production systems.

10.2.3.1 Second Stage: Methane Fermentation

Organic pollutants are anaerobically converted to methane in two distinct stages: acidification and methanogenesis. Acidification produces hydrogen as a by-product, which in turn is used as an electron donor by many methanogens at the second stage of the process. Separation of the two stages is feasible for hydrogen collection from the first stage. The second stage is further used for the treatment of the remaining acidification products, mainly volatile fatty acids (VFAs).

A number of recent studies have reported a successful operation of such two-stage systems. The disadvantage here is that two different gas streams are created and in reality, since the majority of the substrate is converted to methane, this is a methane fermenta- tion in which one is pulling off a little hydrogen. However, at least with some substrates (organic solid wastes), there may be advantages over a traditional methane fermentation, since the first stage acts effectively in solubilization. In addition, combining the two gas streams would create a hydrogen–methane mixture (20%–30% H_2 [after removal of CO_2], 80%–70% CH_4) shown to burn cleaner than methane alone.

Ueno (2007) using artificial organic solid waste (COD = 37,100 mg/L, VSS = 23,700 mg/L) in laboratory scale, showed that not only relatively high hydrogen yields coupled with methane yields twofold higher than a comparable single-stage process could be sustained but also overall chemical oxygen demand (COD) removal efficiency and volatile suspended solids (VSSs) decomposition were 80% and 96%, respectively. Recently, Hafez et al. (2009) used a hybrid system that comprised both a novel biohydrogen reactor with a

gravity settler followed by a second-stage conventional anaerobic digester for the production of methane gas. The authors tested their system with a synthetic wastewater/leachate solution and was operated at 37°C for 45 days. The maximum hydrogen yield was 400 mL H_2/g glucose with an average of 345 mL H_2/g glucose, and the methane yield for the second stage approached a maximum value of 426 mL CH_4/gCOD removed, with an overall COD removal efficiency of 94%.

10.2.3.2 Second Stage: Photofermentation

In another proposed process to recover additional hydrogen from the products of a dark hydrogen-generating fermentation, nonsulfur purple photosynthetic bacteria can be used to capture light and quantitatively convert organic acids to hydrogen in a reaction that has been known for nearly 60 years and has been named photofermentation. A great deal of research has gone into this area, which has been recently reviewed. In photofermentation, hydrogen evolution is driven by nitrogenase, and since this enzyme is ATP dependent (the requisite ATP is formed via the photosynthetic capture of light energy), hydrogen evolu- tion is essentially irreversible. Thus, in principle, photofermentation is capable of complete conversion of organic acids to hydrogen.

There have been a few studies where this capacity has been used to demonstrate the conversion of organic acids, principally acetate, produced during a first stage dark fermentation of sugars (glucose, sucrose) to hydrogen, thus increasing the overall hydrogen yield. The most severe constraint, as discussed previously, is the fact that photosynthetic efficiencies, with either solar radiation or tungsten lamps, are very low. At even moderate light intensities, the majority (>80%) of captured light is dissipated as heat. Obviously, this increases greatly the surface area required for the production of a given quantity of hydrogen. This, combined with the potentially high cost of transparent, hydrogen-impermeable photobioreactors, presents very significant hurdles for the development of a practical process based on photofermentation.

10.2.3.3 Second Stage: Electrohydrogenesis

In this recent (2005) approach, an electrical input provided to a modified microbial fuel cell (MFC) provides the energy necessary to convert organic acids, such as acetate, to hydrogen. In fact, these types of cells are rather versatile and have been shown to be able to generate hydrogen from a variety of substrates, including some wastewaters. Moreover, it is not necessary to start with a pure, defined bacterial culture with the desired characteristics, since the appropriate bacteria can be selected during operation. As originally constituted, these bioelectrochemical cells consisted of an anode chamber where, like in MFCs, electrogenic bacteria catabolize substrate using the electrode as an electron acceptor for their metabolism, thereby generating an electrical potential. Both the anode and cathode were operated anaerobically and connected by a proton (cation) exchange membrane. The potential generated from a substrate such as acetate (300 mV) isn't sufficient to drive hydrogen evolution at the cathode, so supplementary voltage input is required, around 110 mV in theory, but because of electrode resistance, this is actually >200 mV.

Although admittedly elegant in its demonstration of the thermodynamic principles of the manipulation of microbial metabolism for use in the biotechnological production of fuels, hydrogen evolution rates and efficiencies remain quite low. A number of prob- lems can be pointed out, and some of these have been at least partially dealt with in more recent publications. First, as is the case with MFCs, current densities obtained at the anode

(graphite) are quite low. Some improvement has been attained by ammonia treatment of carbon cloth anodes, but further gains are desirable. Secondly, the membrane separating the two chambers allows passage of cations, Na^+ and K^+, which are present at much higher concentrations than protons at the near-neutral pHs required. The resulting pH rise at the cathode limits hydrogen production, while acidification at the anode inhibits microbial activity. Thus, replacement with an anion-selective membrane (protons are transferred via negatively charged phosphate ions) leads to some improvement, and in fact, it has been demonstrated that it may be possible to do away with the membrane altogether.

A further obstacle is that the employed cathodes usually contain platinum, too expensive for the obtained current densities. In a novel approach to overcoming this problem, it has been proposed to replace the usual cathode with a biocathode where bacteria attached to an appropriate graphite surface catalyze hydrogen evolution. However, it is not clear that a sufficiently high catalytic density can be achieved using this approach. Thus, electrohydrogenesis is a novel approach, but it remains to be seen if sufficiently high volumetric rates can be achieved with nominal electrical inputs. Currently, high volumetric rates (around 3 m^3 H_2/m^3 reactor/day), which are however still almost two orders of magnitude lower than those seen with dark fermentations, are only observed at high (around 800 mV) applied voltages.

10.2.4 Summary and Conclusion

Photosynthetic hydrogen production is a theoretically perfect process for transformation of the *free* solar energy into hydrogen by photosynthetic bacteria; practical applications are cost prohibitive due to the low utilization efficiency of light, large footprint, low volumetric hydrogen production rate, and difficulties in designing the reactors for hydrogen production. On the other hand, comparison of the rates of H_2 production by various biohydrogen systems coupled with the associated complexity level of operation suggests that dark fermentation systems offer an excellent potential for practical application. Although fermentative biohydrogen technologies are still in their infancy, developing more efficient technologies offer potential for practical application. Therefore, fermentative hydrogen production has been receiving increasing attention in recent years.

10.3 Photobioreactors

A reactor for photobiological hydrogen production has to meet several conditions. Since the hydrogen gas has to be collected, a prerequisite of the batch photobioreactor is for it to be an enclosed system. It has to be possible to maintain a monoculture for an extended time (it must be practical to sterilize the reactor). Preferably, sunlight is the energy source. The productivity of photobioreactors is light limited, and a high surface-to-volume ratio is a prerequisite for a photobioreactor. The photochemical efficiencies are low (theoretically a maximum of 10% and in laboratory experiments ranges from 3% to 10% [Miron et al. 2000]) and tend to decrease at higher light intensities (the effect of light saturation; photons cannot all be used for reaction energy but are dissipated as heat energy). This means that in order to create an efficient biological process, it is important to either dilute the light or distribute it as much as possible over the reactor volume and/or mix the culture at a high rate, so that cells are light exposed only for a short period.

Janssen (2002) reviewed three types of photobioreactors: the vertical-column reactors (airlift loop reactor and bubble column), a panel reactor, and tubular reactors. He looked

at the light gradients and the mixing-induced light/dark cycles PE and scalability. Depending on the reactor type and the way it is operated, cells are exposed for a certain period of time at the irradiated surface or in a dark part of the reactor. The (mixing-induced) light/dark cycles, when they are in the range of micro- or milliseconds, can enhance PE, approaching the theoretical PEs at low light intensities. When the cycles are from several seconds to tens of seconds, there is no improvement and even a decrease in PE has been reported. The depth (and volume) of the photic zone depends on the dimensions and operations of the reactor, the algal concentration, and the specific absorption coefficient of the algae (and the wavelength of the incoming light). On the basis of model calculations and/or empirical data, several reactor types were compared. The results (for biomass production of photoautotrophs) are shown in Table 10.1. Flat panel reactors show a high photochemical efficiency or biomass yield on light energy, while biomass density is also high. Tubular reactors in theory should show better efficiencies because of the shorter average light/dark cycles.

The analysis of typical examples of microalgal cultivations in enclosed (outdoor) photobioreactors showed that the PE and productivity are determined by the light regime inside the reactors. In addition, only oxygen accumulation and shear stress limit productivity in certain designs.

TABLE 10.1

Enclosed Photobioreactors, Photosynthetic Efficiency (PE), and Biomass Yield on Light Energy

Photobioreactor Type	PE or Ydw; E a;b (% or g dw/mol)	Reference (Microorganism)
Bubble-column and airlift-column reactors	0:84 (Ydw;E)[c]	Camacho et al. (1999) (*Phaeodactylum tricornutum*)
Internal draught tube Split cylinder		
Airlift column	0:82 (Ydw;E)	Hu and Richmond (1996) (*Phaeodactylum tricornutum*)
Flat panel		
(a) Vertical	(a) 1:48 (Ydw;E) ≈ 16 (PE)	(a) Hu et al. (1998)
(b) Tilted	(b) 10–20 (PE)	(b) Torzillo et al. (1996) (*Spirulina platensis*)
Tubular reactor	0:60 (Ydw;E); 6.5 (PE)[d]	Thimijan and Heins (1983) (*Spirulina platensis*)
Tubular reactor		
Diameter 2:5 cm	(a) 0.480–0:63 (Ydw;E)[e]	Fontoynont et al. (1998)
Diameter 5:3 cm	(b) 0.680–0:95 (Ydw;E)[e]	(*Phaeodactylum tricornutum*)

Source: Janssen, M., Cultivation of microalgae: Effect of light/dark cycles on biomass yield. Thesis, Wageningen University, Wageningen, the Netherlands, 2002.

Ydw;E, the biomass yield in dry weight basses.

[a] Daily irradiance values in MJ/m^2/day were divided by 12 × 3600 s, assuming a day length of 12 h; multi- plied with 0.429, the fraction PAR in the solar spectrum [193]; and multiplied with 4.57, mol photons/MJ (Thimijan and Heins 1983).

[b] Monthly averages of daily solar irradiance on a vertical cylindrical surface in the same period of the year were obtained from the European Database of Daylight and Solar Radiation, www.satel-light.com (Fontoynont et al. 1998).

[c] Based on a linear growth phase with a productivity of about 0:49 g/L/day observed in an outdoor batch culture in three different reactor types.

[d] Before calculating PE and Ydw;E, irradiance data were corrected for transmittivity tubes (Thimijan and Heins 1983).

[e] Calculated by Janssen (2002).

The comparison of the bioreactors described earlier referred to processes with microalgae, diatoms, or cyanobacteria. Though photoheterotrophic bacteria differ, for instance, in photochemical efficiency, absorption coefficient, and size, the relative difference in performance of the reactor types might be extrapolated to the case of photoheterotrophics. The light regime, including mixing-induced light/dark cycles, is assumed to be much more determining than biological factors.

Considering the findings that panel reactors and tubular reactors (at least in theory) show highest efficiencies, it is worthwhile to look further into all types of reactors and their possibilities to be scaled up for practical purposes.

Ugwu et al. (2008) developed a recent review of the photobioreactors for mass cultivation of algae; this critical review includes some aspects of hydrodynamics and mass transfer characteristics of these photobioreactors. Algal culture systems can be illuminated by artificial light, solar light, or by both. Naturally illuminated algal culture sys- tems with large illumination surface areas include open ponds (Hase et al. 2000), flat-plate (Hu 1996), horizontal/serpentine tubular airlift (Rubio et al. 1999), and inclined tubular photobioreactors (Ugwu et al. 2002). Generally, laboratory-scale photobioreactors are artificially illuminated (either internally or externally) using fluorescent lamps or other light distributors. Some of these photobioreactors include bubble-column (Degen et al. 2001), airlift-column (Kaewpintong et al. 2007), stirred-tank (Ogbonna et al. 1999), helical tubular, conical (Watanabe and Saiki 1997), torus (Pruvost et al. 2006), and seaweed-type photobioreactors (Hallenback and Benemann 2002). Furthermore, some photobioreactors can be easily tempered. Tempering could simply be achieved by placing a photobioreactor in a constant temperature room. This approach is limited to compact photobioreactors. Large-scale outdoor systems such as tubular photobioreactors cannot be easily tempered with- out high technical efforts. However, several commercially available photobioreactors, for example, BIOSTAT photobioreactors (developed by Sartorius BBI Systems Inc.) (Pohl et al. 1988) can be readily tempered. Also, some efforts were undertaken to design temperature- controlled photobioreactors, such as double-walled internally illuminated photobioreac- tors with a heating and cooling water circuit (Pohl et al. 1988).

10.3.1 Open Ponds

Cultivation of algae in open ponds has been extensively studied in the past few years (Boussiba et al. 1988; Tredici and Materassi 1992; Uguwu 2002). Open ponds can be categorized into natural waters (lakes, lagoons, ponds) and artificial ponds or containers. The most commonly used systems include shallow big ponds, tanks, circular ponds, and raceway ponds. One of the major advantages of open ponds is that they are easier to construct and operate than most closed systems. However, major limitations in open ponds include poor light utilization by the cells, evaporative losses, diffusion of CO_2 to the atmosphere, and requirement of large areas of land. Furthermore, contamination by predators and other fast-growing heterotrophs have restricted the commercial pro- duction of algae in open-culture systems to only those organisms that can grow under extreme conditions. Also, due to inefficient stirring mechanisms in open cultivation systems, their mass transfer rates are very poor, resulting in low biomass productivity (Tredici and Materassi 1992).

In order to overcome the problems with open ponds, much attention is now focused on the development of suitable closed systems such as flat-plate, tubular, vertical-column, and internally illuminated photobioreactors.

10.3.2 Flat-Plate Photobioreactors

Flat-plate photobioreactors have received much attention for cultivation of photosynthetic microorganisms due to their large illumination surface area. The work presented by Milner (1953) paved way to the use of flat culture vessels for cultivation of algae. Following this work, Samson and Leduy (1985) developed a flat reactor equipped with fluorescence lamps. A year later, Ramos de Ortega and Roux (1986) developed an outdoor flat panel reactor by using thick transparent PVC materials. As time went on, extensive works on various designs of vertical alveolar panels and flat-plate reactors for mass cultivation of dif- ferent algae were reported (Tredici and Materassi 1992; Hu and Richmond, 1996; Hoekema et al. 2002; Zhang et al. 2002). Generally, flat-plate photobioreactors are made of transparent materials for maximum utilization of solar light energy. Accumulation of *d*issolved *o*xygen (*DO*) concentrations in flat-plate photobioreactors is relatively low compared to horizontal tubular photobioreactors. It has been reported that with flat-plate photobioreactors, high photosynthetic efficiencies can be achieved (Hu and Richmond 1996; Richmond 2000). Flat-plate photobioreactors are very suitable for mass cultures of algae. However, they also have some limitations as indicated in Table 10.2.

10.3.3 Tubular Photobioreactors

Among the proposed photobioreactors, tubular photobioreactor is one of the most suit- able types for outdoor mass cultures. Most outdoor tubular photobioreactors are usually constructed with either glass or plastic tube, and their cultures are recirculated either with pump or preferably with airlift system. They can be in the form of horizontal/serpentine (Chaumont et al. 1988; Molina et al. 2001), vertical (Pirt et al. 1983), near horizontal

TABLE 10.2

Prospects and Limitations of Various Culture Systems for Algae

Culture Systems	Prospects	Limitations
Open ponds	Relatively economical, easy to clean up after cultivation, good for mass cultivation of algae	Little control of culture conditions, difficulty in growing algal cultures for long periods, poor productivity, are easily contaminated, occupy small illumination surface area, their construction require sophisticated materials, shear stress to algal cultures, decrease of illumination surface area upon scale-up
Vertical-column photobioreactors	High mass transfer, good mixing with low shear stress, low energy consumption, high potentials for scalability, easy to sterilize, readily tempered, good for immobilization of algae, reduced photoinhibition and photooxidation	Require sophisticated materials, shear stress to algal cultures, decrease of illumination surface area upon scale-up
Flat-plate photobioreactors	Large illumination surface area, suitable for outdoor cultures, good for immobilization of algae, good light path, good biomass productivities, relatively cheap, easy to clean up, readily tempered, low oxygen buildup	Scale-up require many compartments and support materials, difficulty in controlling culture temperature, some degree of wall growth, possibility of hydrodynamic stress to some algal strains
Tubular photobioreactors	Large illumination surface area, suitable for outdoor cultures, fairly good biomass productivities, relatively cheap	Gradients of pH, dissolved oxygen and CO_2 along the tubes, fouling some degree of wall growth, requires large land space

(Tredici et al. 1998), conical (Watanabe and Saiki 1997), or inclined (Lee and Low 1991; Ugwu et al. 2002) photobioreactor. Aeration and mixing of the cultures in tubular photobioreactors are usually done by air-pump or airlift systems. Advantages and limitations of tubular photobioreactors are shown in Table 10.2. Table 10.2 summarizes the advantages and limitations of open ponds.

Tubular photobioreactor are very suitable for outdoor mass cultures of algae since they have large illumination surface area. On the other hand, one of the major limitations of tubular photobioreactor is poor mass transfer. It should be noted that mass transfer (oxygen buildup) becomes a problem when tubular photobioreactors are scaled up. For instance, some studies have shown that very high *DO* levels are easily reached in tubular photobioreactors (Torzillo et al. 1986; Richmond et al. 1993; Molina et al. 2001). Also, photoinhibition is very common in outdoor tubular photobioreactors (Vonshak and Torzillo 2004). When a tubular photobioreactor is scaled up by increasing the diameter of tubes, the illumination surface-to-volume ratio would decrease. On the other hand, the length of the tube can be kept as short as possible while a tubular photobioreactor is scaled up by increasing the diameter of the tubes. In this case, the cells at the lower part of the tube will not receive enough light for cell growth (due to light shading effect) unless there is a good mixing system. In any case, efficient light distribution to the cells can be achieved by improving the mixing system in the tubes (Ugwu et al. 2003, 2005a). Also, it is difficult to control culture temperatures in most tubular photobioreactors. Although they can be equipped with thermostat to maintain the desired culture temperature, this could be very expensive and difficult to implement. It should also be noted that adherence of the cells of the walls of the tubes is common in tubular photobioreactors.

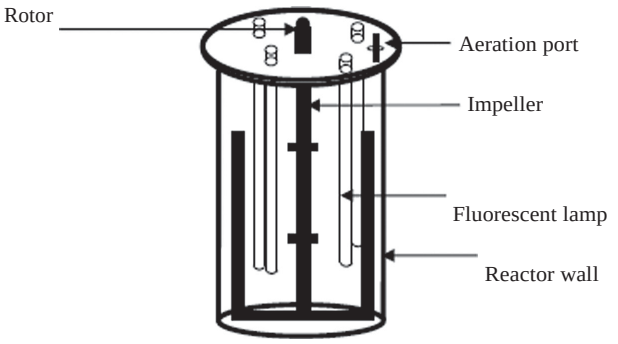
Furthermore, long tubular photobioreactors are characterized by gradients of oxygen and CO_2 transfer along the tubes (Camacho et al. 1999; Ugwu et al. 2003). The increase in pH of the cultures would also lead to frequent recarbonation of the cultures, which would consequently increase the cost of algal production.

10.3.4 Vertical-Column Photobioreactors

Various designs and scales of vertical-column photobioreactors have been tested for cultivation of algae (Choi et al. 2003; Lopez et al. 2006; Kaewpintong et al. 2007). Vertical-column photobioreactors are compact, low cost, and easy to operate monoseptically (Miron et al. 2002). Furthermore, they are very promising for large-scale cultivation of algae. It was reported that bubble-column and airlift photobioreactors (up to 0.19 m in diameter) can attain a final biomass concentration and specific growth rate that are comparable to values typically reported for narrow tubular photobioreactors (Miron et al. 2002). Some bubble-column photobioreactors are equipped with either draft tubes or constructed as split cylinders. In the case of draft tube photobioreactors, intermixing occurs between the riser and the downcomer zones of the photobioreactor through the walls of the draft tube. A summary of the prospects and limitations of vertical-column photobioreactors is shown in Table 10.2.

10.3.5 Internally Illuminated Photobioreactors

As mentioned earlier, some photobioreactors can be internally illuminated with fluorescent lamps. Figure 10.4 shows a typical internally illuminated photobioreactor. This photobioreactor is equipped with impellers for agitation of the algal cultures. Air and CO_2 are supplied to the cultures through the spargers.



Internally illuminated photobioreactor

FIGURE 10.4

Schematic diagram of internally illuminated photobioreactor.

This type of photobioreactor can also be modified in such a way that it can utilize both solar and artificial light system (Ogbonna et al. 1999). In that case, the artificial light source is switched on whenever the solar light intensity decreases below a set value (during cloudy weather or at night). There are also some reports on the use of optical fibers to collect and distribute solar light in cylindrical photobioreactors (Mori 1985; Matsunaga et al. 1991). One of the major advantages of an internally illuminated photobioreactor is that it can be heat sterilized under pressure, and thus, contamination can be minimized. Furthermore, sup- ply of light to the photobioreactor can be maintained continuously (both day and night) by integrating artificial and solar light devices. However, outdoor mass cultivation of algae in this type of photobioreactor would require some technical efforts (Ugwu et al. 2008).

10.3.6 Hydrodynamics and Mass Transfer Characteristics of Photobioreactors

Although relationship between hydrodynamics and mass transfer has been extensively investigated and correlated in bioreactors for heterotrophic cultures, only a few studies are available in phototrophic cultures that are applicable in photobioreactors. This includes the overall mass transfer coefficient (k_{La}), mixing, liquid velocity, gas bubble velocity, and gas holdup. k_{La} is the most commonly used parameter for assessing the performance of photobioreactors. The following equation governs mass transfer from the gas phase to the liquid phase:

$$N = k_L a * (C^*_{,l} - C_{,l}) \quad (10.4)$$

where

N is the mass transfer rate

k_L is the mass transfer rate
coefficient a is the interface area
$C^*_{,l}$ is the equilibrium gas concentration at the interface of the gas and liquid
$C_{,l}$ is the gas concentration in the liquid
k_{La} is generally used to describe the overall volumetric mass transfer coefficient in photobioreactors

The volumetric mass transfer coefficient of photobioreactors is dependent on various factors such as agitation rate, the type of sparger, surfactants/antifoam agents, and temperature. Mixing time can be defined as the time taken to achieve a homogenous mixture

after injection of tracer solution (Ugwu et al. 2008). Lee and Bazin (1990) define mixing time as the time taken for a small volume of dye solution added to the liquid to transverse the reactor. Generally, mixing time is determined in photobioreactors using tracer substances such as dyes. However, mixing time can also be measured by signal–response method using tracer and pH electrode (Camacho et al. 1999; Ugwu et al. 2005a; Pruvost et al. 2006). Furthermore, *c*omputational *f* luid *d*ynamic (*CFD*) models were used to evaluate global mixing in torus photobioreactor (Pruvost et al. 2006; Sato et al. 2006). Mixing time is a very important parameter in designing photobioreactors for various biological processes. Good mixing would ensure high cell concentration, keep algal cells in suspension, eliminate thermal stratification, help nutrient distribution, improve gas exchange as well as reduce the degree of mutual shading, and lower the probability of photoinhibition (Janvanmardian and Palsson 1991). It was also reported that when the nutritional requirements are suf- ficient and the environmental conditions are optimized, mixing aimed at inducing tur- bulent flow would result in high yield of algal biomass (Hu and Richmond 1996). Bosca et al. (1991) demonstrated that the productivity of alga is higher in mixed culture than in an unmixed one under the same condition. Various mixing systems are currently used in algal cultures depending on the type of photobioreactors. In open-pond systems, paddle wheels were used to induce turbulent flow (Boussiba et al. 1988; Hase et al. 2000). In stirred- tank photobioreactors, impellers were used in mixing algal cultures (Ogbonna and Tanaka 2001; Mazzuca et al. 2006). In tubular photobioreactors, mixing can be done by bubbling air directly or indirectly via airlift systems (Tredici et al. 1998; Ogbonna et al. 1999) or by installing static mixers inside the tubes (Ugwu et al. 2002). Mixing systems that uti- lized baffles in bubble-column photobioreactors were also demonstrated in algal cultures (Merchuk et al. 2000; Degen et al. 2001). In bubble-column and large-diameter tubular photobioreactors, demarcation exists between the light-illuminated and dark surfaces. Thus, mixing strategies should be introduced in cultures to circulate algal cells between the light-illuminated and dark regions of the photobioreactors (Molina et al. 1999; Ugwu et al. 2005b; Mazzuca et al. 2006). Increase in aeration rate would improve mixing, liquid circu- lation, and mass transfer between gas and liquid phases in algal cultures. However, high aeration could cause shear stress to algal cells (Mazzuca et al. 2006; Kaewpintong et al. 2007). Gas bubble velocity is a measure of culture flow rates in tubular photobioreactors (plug flow regime) since algal cultures are circulated along with gas bubbles. When fine spargers are used to increase gas dispersion inside horizontal tubular photobioreactors, relatively large bubbles are produced. However, the bubbles coalesce during flow to form interface between the liquid broth, gas, and the walls of the tube. The contact area between the liquid and the gas is reduced, thereby, resulting in poor mass transfer rates. Gas bubble velocity and size of the bubbles are dependent on the liquid flow rate. By increasing the gas flow rate, the bubble diameter increases, which consequently, would increase the gas bub- ble velocity. The rate of gas circulation may be interrupted when baffles or static mixers are installed inside the reactors to increase gas dispersion. However, the mixer elements would help to break down the large bubbles into fine ones, thereby improving the mass transfer rates. Some studies have indicated that relationship exists between superficial gas veloc- ity, bubble velocity, and the overall mass transfer coefficient in bioreactors (Lu et al. 1995; Wongsuchoto et al. 2003; Couvert et al. 2004). In some photobioreactors, the relationship between superficial gas velocity and the overall mass transfer coefficient (k_{La}) studied in various algal cultures can be evaluated (Table 10.3).

In a concentric tube airlift photobioreactor (which was used for *Phaeodactylum tricornu- tum* cultures), it was reported that at a superficial gas velocity of 0.055 m/s, the k_{La} of about
0.02 s^{-1} was obtained (Contreras et al. 1998). This k_{La} value was about the same as the one

TABLE 10.3

Relationship between the Superficial Velocities and Overall Mass Transfer Coefficient (k_{La}) in Various Cultures Systems

Photobioreactor	Volume (L)	Superficial Velocity (m/s)	k_{La} (s^{-1})	Strain	References
Concentric tube airlift	12	0.055	0.020	*Phaeodactylum tricornutum*	Contreras et al. (1998)
Internally illuminated	3	0.009	0.020	*Chlorella pyrenoidosa*	Ogbonna et al. (1998)
Airlift tubular horizontal	200	0.160	0.014	*Porphyridium cruentum*	Camacho et al. (1999)
Bubble column	13	$5.4–82 \times 10^{-4}$	$1.7–4.7 \times 10^{-3}$	*Porphyridium* sp.	Merchuk et al. (2000)
External-loop airlift tubular	200	0.250	0.006	*Phaeodactylum tricornutum*	Fernandez et al. (2001)
Inclined tubular	6	0.020	0.003	*Chlorella sorokiniana*	Ugwu et al. (2002)
Flat-plate	3	0.009	0.002	*Synechocystis aquatilis*	Boussiba et al. (1988)
Split-cylinder internal-loop airlift	2	0.024	0.009	*Haematococcus pluvialis*	Estrada et al. (2005)

Source: Ugwu, C.U. et al., *Bioresour. Technol.*, 99, 4021, 2008.

reported by Ogbonna et al. (1998) (with 3 L internally illuminated photobioreactor) for *Chlorella pyrenoidosa* cultures at a superficial gas velocity of 0.009 m/s. In 6 L inclined tubu- lar, which was used for cultivation of *Chlorella sorokiniana*, k_{La} of about 0.003 s^{-1} (at a super- ficial gas velocity of 0.02 m/s) was obtained [198]. Merchuk et al. (2000) reported that by varying the superficial gas velocity ($5.4–82 \times 10^{-4}$) in 13 L bubble-column photobioreactor (which was tested for cultivation of *Porphyridium* sp.), the k_{La} obtained was in the range of
1.7 and 4.7×10^{-3} s^{-1}. With 3 L flat-plate photobioreactor (which was used for cultivation of *Synechocystis aquatilis* cultures), the k_{La} obtained was 0.002 s^{-1} at a superficial gas velocity of 0.009 m/s (Zhang et al. 2002). At a superficial gas velocity of 0.024 m/s, the k_{La} reported in 2 L split-cylinder internal-loop airlift photobioreactors (which was used for cultivation of *Haematococcus pluvialis* cultures) was 0.009 s^{-1} (Vega et al. 2005). By using 200 L airlift tubular horizontal photobioreactors (at a superficial gas velocity of 0.16 m/s), the k_{La} reported was about 0.014 s^{-1} (Camacho et al. 1999). In the case of 200 L external-loop airlift tubular, which was tested for outdoor cultures of *Phaeodactylum tricornutum*, k_{La} of 0.006 s^{-1} was obtained at a superficial gas velocity of 0.25 m/s (Fernandez et al. 2001). It should be noted that com- parison of the k_{La} based on only superficial gas velocity could be misleading, considering the differences in photobioreactor scales (volume), geometry, algal strains, and cultures as well as the methods used for such studies. Furthermore, liquid velocity is a measure of liquid flow and degree of turbulence in photobioreactors that is required to ensure that all the cells are frequently exposed to light (Carlozzi 2003; Provost et al. 2006). Also, solid velocity would give an indication of how algal cells can be uniformly transported along the tube length as the cultures are aerated. Solid velocity is also a very important parameter for the determination of hydrodynamics and mass transfer characteristics of bioreactors. Couvert et al. (2004) reported that the nature (i.e., shape, size, and porosity) and quantity of solids have an influence on the mass transfer in bioreactors. In intense algal cultures, cells can aggregate to form some clumps inside photobioreactors. In narrow-bore tubes, these clumps may settle such that they cannot be recirculated uniformly along the tubes.

Another important aspect of hydrodynamics that has been used in characterizing photobioreactor design is gas holdup. Gas holdup is described as the fraction of the reactor volume taken by the gas. This can be estimated as the volume of the liquid displaced by the gas (expansion of liquid volume) due to aeration. Gas holdup is very important in photobioreactor design as it determines the circulation rate, the gas residence time, as well as the overall mass transfer rate (k_{La}). Some studies have demonstrated that a relationship exists between gas holdup, bubble size, gas–liquid interfacial surface area, and the overall mass transfer coefficient, k_{La} (Chisti 1998; Vandu et al. 2005) as shown in Table 10.3.

10.3.7 Mass Cultivation of Algae

A good number of photobioreactors can be used in production of various algal products. Apparently, while many photobioreactors are easily operated at laboratory scale, only few of them can be successfully scaled up to pilot scale. Scale-up of photobioreactors can be done by increasing the length, diameter, height, or the number of compartments of the culture systems (depending on the type of photobioreactor). These scale-up strategies are very challenging, mainly due to difficulty in maintaining optimum light, temperature, mixing, and mass transfer in photobioreactors. Nevertheless, few large-scale photobioreactors with relatively good biomass productivities have been developed.

Table 10.4 shows the algal biomass productivities reported with different types and scales of outdoor photobioreactors. In 200 L airlift tubular photobioreactor (which was used for outdoor cultivation of *Phaeodactylum tricornutum*), biomass productivity of 1.20–
1.50 g/L/day was obtained (Camacho et al. 1999; Fernandez et al. 2001).

Furthermore, with 200 L airlift-driven-tubular photobioreactor tested for outdoor cultivation of *Phaeodactylum tricornutum*, biomass productivity of 1.90 g/L/day was attained (Molina et al. 2001). In 11 L undular row tubular photobioreactor (for *Arthrospira platensis*), the productivity reported was about 2.7 g/L/day (Carlozzi 2003). Furthermore, about
0.27 g/L/day was obtained in 440 L outdoor flat-plate photobioreactor, which was used for cultivation of *Nannochloropsis* (Wu et al. 2001). In 55 L bubble-column photobioreactor (for out- door cultivation of *H. pluvialis*), the biomass productivity obtained was 0.06 g/L/day (Lopez et al. 2006). Also, in 25,000 L outdoor photobioreactor (developed for commercial production of astaxanthin from *H. pluvialis*), about 0.05 g/L/day was obtained (Olaizola 2000). It should be noted that aside from volumetric productivity (productivity per unit of reactor volume per unit of time), algal biomass productivity can be evaluated in photobioreactors based on areal productivity (productivity per unit of occupied-land area per unit of time), PE, or biomass yield (g-biomass per unit of solar radiation) (Ugwu et al. 2008).

TABLE 10.4

Productivity of Algal Strains Reported in Some Outdoor Photobioreactors

Photobioreactors	Volume (L)	Photosynthetic Strain	Productivity (g/L/day)	References
Airlift tubular	200	*Porphyridium cruentum*	1.50	Camacho et al. (1999)
Airlift tubular	200	*Phaeodactylum tricornutum*	1.20	Fernandez et al. (2001)
Airlift tubular	200	*Phaeodactylum tricornutum*	1.90	Molina et al. (2001)
Inclined tubular	6.0	*Chlorella sorokiniana*	1.47	Ugwu et al. (2002)
Undular row tubular	11	*Arthrospira platensis*	2.70	Carlozzi (2003)
Parallel tubular (AGM)	25,000	*Haematococcus pluvialis*	0.05	Lopez et al. (2006)
Flat-plate	440	*Nannochloropsis* sp.	0.27	Wu et al. (2001)

Source: Ugwu, C.U. et al., *Bioresour. Technol.*, 99, 4021, 2008.

10.3.8 Conclusion and Perspectives of Photobioreactors

Despite the fact that a great deal of work has been done to develop photobioreactors for algal cultures, more efforts are still required to improve photobioreactor technologies and know-how of algal cultures. Photobioreactor development is perhaps one of the major steps that should be undertaken for efficient mass cultivation of algae. The major issue in the design of efficient photobioreactors should be their capacity to maximize the out- door solar radiation. Large-scale outdoor photobioreactors should have large volume and occupy less land space. In addition, they should have transparent surfaces, high illumina- tion surfaces, and high mass transfer rates and should as well be able to give high biomass yields. Furthermore, design and construction of any photobioreactor should depend on the type of strain, the target product, geographical location, as well as the overall cost of production. It should be noted that for mass cultivation of algae, vast areas of land are required. This is actually a very serious setback of algal cultivation in many developed countries. Thus, the increasing population and, consequently, the exorbitant cost of land have attracted the attention of many scientists to look for alternative cultivation sites. In order to reduce the cost of producing algal biomass and products, intensive efforts should be made to increase the algal biomass productivity. Also, high-value metabolites should be produced to compromise the technical costs involved in algal production. Given that outdoor photobioreactors are usually naturally illuminated using solar light, biomass pro- ductivities (in such systems) would depend on the prevailing weather conditions in a par- ticular locality. Although commercial cultivation of algae is done in developed countries, there are seasonal variations in temperatures and solar light energy throughout the year in most of these regions. Due to these problems, it is difficult to carry out outdoor mass cultivation of algae all year round in such regions. However, in most tropical developing countries, outdoor cultures of algae can be maintained for relatively long periods of time in a year because there is neither winter nor cold seasons in those regions. Thus, tropical developing countries might be potential cultivation sites for commercial production of algal products (Ugwu et al. 2008).

10.4 Hydrogen from Lignocellulosic Biomass

This section is based on the review article "Bioconversion of lignocellulosic biomass to hydrogen: Potential and challenges" by Ren et al. (2009): Hydrogen is a promising alterna- tive to conventional fossil fuels since it does not have the same environmental impact asso- ciated with fossil fuels. A major doubt on hydrogen as a clean energy alternative is how it is produced. Hydrogen production by microbial biochemical reactions has attracted world- wide attention, due to its potential as an inexhaustible, low-cost, and renewable source of clean energy. Studies on biohydrogen production have been focused on biophotolysis of water using algae and cyanobacteria, photodecomposition of organic compounds by photosynthetic bacteria, and dark fermentation from organic compounds with anaerobes. Among these biological processes, anaerobic hydrogen fermentation seems to be favor- able, since hydrogen can be yielded at higher rates and at lower costs in degrading various organic wastes enriched with carbohydrates (Kumar and Das 2000; Chen et al. 2001; Ginkel et al. 2001; Fang et al. 2003; Xing et al. 2006; Lo et al. 2008a; Wang et al. 2008a). Lignocellulosic biomass in nature is by far the most abundant raw material from hardwood, softwood, grasses, and agricultural residues as well as municipal wastes (Table 10.5).

TABLE 10.5

Hydrogen Yields and Production Rates by Different Microorganisms

Microorganism	Conditions				Substrate	H_2 Yield mol/mol Monosaccharide	H_2 Production Rate (Maximal) mmol/h/L
	Culture	D (h^{-1})	pH	T (°C)			
Strict anaerobes							
Clostridia							
Clostridium sp. no 2	Batch		6.0	36	Glucose	2.0	23.9
	Batch		6.0	36	Xylose	2.1	21.7
C. paraputrificum M-21	Batch		Uncontrolled	37	GlcNAc[a]	2.5	31.0
C. butyricum LMG1213tl	Continuous	0.222	5.8	36	Glucose	1.5	21.7
Clostridium sp. no 2	Continuous	0.18	6.0	36	Glucose	2.4	7.1
	Continuous	1.16	6.0	36	Glucose	1.4	20.4
	Continuous	0.96	6.0	36	Xylose	1.7	21.0
Thermophiles							
Thermotoga maritime	Batch		Uncontrolled	80	Glucose	4.0	10
Thermotoga elfii	Batch		7.4	65	Glucose	3.3	2.7
Caldicellulosiruptor Saccharolyticus	Batch		7.0	70	Sucrose	3.3	8.4
Facultative anaerobes							
Enterobacter							
E. aerogenes E 82005	Batch		6.0	38	Glucose	1.0	21
E. cloacae IIT-BT 80 wt	Batch		Uncontrolled	36	Glucose	2.2	
	Batch		Uncontrolled	36	Sucrose	3.0	35
E. cloacae IIT-BT 08 m DM_{11}	Batch		Uncontrolled	36	Glucose	3.4	
E. aerogenes E 82005	Continuous	0.32	6.0	38	Molasses	0.7	20
E. aerogenes HU-101 wt	Continuous	0.67	Uncontrolled	37	Glucose	0.6	31

Coculture							
C. butyricum IFO13949+ *E. aerogenes* HO-39	Continuous	1.0	5.2	36	Starch	2.6	33
		HRT, h					
Mixed cultures from:							
Sludge compost	Continuous	12	6.8	60	Waste water Sugar factory	2.5	8.3
Sewage sludge	Continuous	6	5.7	35	Glucose	1.7	29.6
	Continuous	8	6.7	35	Sucrose	1.7	26.2
Fermented soybean meal	Continuous	8.5	6.0	35	Glucose	1.4	8

Source: Reith, J.H. et al., *Dutch Biol. Hydrogen Found.,* 2003.

[a] GlcNAc = *N*-Acetyl-d-glucosamine.

The annual yields of lignocellulosic biomass residues worldwide were estimated to exceed 220 billion tons, equivalent to 60–80 billion tons of crude oil. The lignocellulosic biomass hence presents an attractive, low-cost feedstock for hydrogen production. Its direct conversion to hydrogen needs pretreatment to hydrolyze the incorporated heterogeneous and crystalline structure. This section presents a critical review on the bioconversion of lignocellulosic biomass to hydrogen in terms of prehydrolysis and hydrolysis technology, bioconversion technology, and fermentation tactics for enhancing hydrogen production. Future perspectives of bioconversion of lignocellulosic biomass to hydrogen are discussed.

10.4.1 Pretreatment and Hydrolysis of Lignocellulosic Biomass

Lignocellulosic biomass is composed of carbohydrate polymers (cellulose and hemicellulose) and lignin. The agricultural residues, that is, wheat straw, corn stover, and rice straw, are comprised of 32%–47% cellulose, 19%–27% hemicellulose, and 5%–24% lignin. The composition of different softwoods varies widely. The cellulose and hemicellulose, which typically comprise two-thirds of the dry lignocellulosic materials, are polysaccharides. Both hemicellulose and lignin provide a protective sheath around the cellulose, which must be hydrolyzed prior to efficient utilization of the embedded polysaccharides. The hydrolysis generally includes prehydrolysis and cellulose hydrolysis: prehydrolysis of lignocellulosic materials is used to remove lignin and partly hydrolyze hemicellulose, while the cellulose hydrolysis is used to ferment reducing sugars. Figure 10.5 shows the general scheme for converting lignocellulose to biohydrogen.

10.4.1.1 Prehydrolysis (Lignocelluloses Fractionation)

Prehydrolysis, often referred to as pretreatment, is required to alter the structure of lignocellulosic biomass to make cellulose more accessible to the enzymes that convert the carbohydrate polymers to fermentable sugars (Wyman 1994). The prehydrolysis process can be performed by physical (mechanical comminution and hydrothermolysis), chemi- cal (ozonolysis, acid hydrolysis, alkaline hydrolysis, oxidative delignification, and organo- solv process), combined (acid-catalyzed steam explosion, ammonia fiber explosion, and CO_2 explosion), and biological (white or fungi) techniques (Fan et al. 1982; Wyman 1994; Fang et al. 1999; Ballesteros et al. 2002; Kim et al. 2002; Sun and Cheng 2002; Mosier et al. 2005; Pan et al. 2005; Yang and Wyman 2004; Yang and Wyman 2008). The selection of a pretreatment method affects the cost and performance in the subsequent hydrolysis and fermentation stages. An ideal prehydrolysis process should achieve high yields of fermentable reducing sugars, avoid degradation or loss of yielded sugars and the formation of inhibitors to the subsequent fermentation, and improve the later cellulose hydrolysis stage in terms of minimal energy, chemicals, and capital equipment use (Hamelinck et al. 2005).

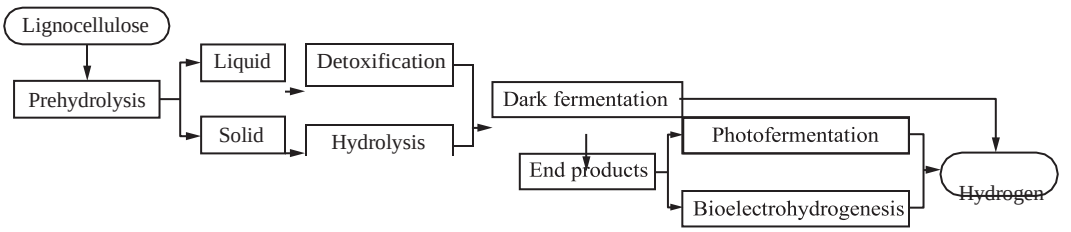


FIGURE 10.5

Flowchart of biohydrogen production from lignocellulosic biomass.

Of all pretreatments, the combined and the biological technologies are the most promising. The combined method, that is, sulfur-catalyzed steam explosion, is preferred for industrial applications, although it has some disadvantages such as destruction of a portion of the xylan fraction, removal/neutralization of the acid before fermentation, and generation of compounds that may be inhibitory to enzymes and microorganisms in the downstream processes (Nguyen et al. 1998; Larsson et al. 1999; Palmquist et al. 2000a,b). This pretreatment retains reasonably high sugar yields from hemicellulose and significantly increases the accessibility of enzymes to cellulose. Biological methods, although uncontrollable and insufficient, offer some unique advantages such as low energy requirement, low quantity of inhibitors produced, and operability at room temperature. White fungi, by secreting lignin-degrading enzymes including lignin peroxidases, manganese-dependent peroxidases, lignin peroxidases, and laccase during secondary metabolism (Sun and Cheng 2002), are widely adopted for lignin removal and lignocelluloses degradation although part of the cellulose would be consumed (Yang and Wyman 2008).

Through pretreatment, lignin and all or part of the hemicellulose is dissolved in the prehydrolysates. The free hemicellulose polymer is hydrolyzed to a mixture of monomeric and oligomeric sugars, including xylose, xylan, mannose, arabinose, galactose, and glucose that comes from cellulose hydrolysis. The residual cellulose and lignin can be filtered and washed. Following this way, cellulose could be collected in a separate process for hydrolysis—H_2 fermentation or direct H_2 fermentation (Hamelinck et al. 2005).

10.4.1.2 Cellulose Hydrolysis

The hydrolysis step is usually performed by enzymes or chemicals. The cellulose hydrolysates comprise of reduced saccharides with mainly glucose (Hamelinck et al. 2005). Although chemical processes are technically more mature, significant technical progress for enzymatic processes was made to make comparably low costs in terms of invest- ments and operations. Enzymatic hydrolysis has some important advantages such as high yield of reduced sugars acquired under mild process conditions and no corro- sion problems (Duff and Murray 1996; Hamelinck et al. 2005). Enzymatic hydrolysis of cellulose is carried out by cellulases that are from bacteria and fungi. These microor- ganisms could be aerobic or anaerobic, mesophilic or thermophilic. Among them, the Trichoderma is intensively studied for cellulase production (Sternberg 1976; Ghose and Bisaria 1979; Mononmani and Sreekantiah 1987; Beldman et al. 1988; Duff and Murray 1996). Simultaneous saccharification and fermentation (SSF) is adopted owing to reduced inhibition of end products from glucose and cellobiose. Using genetically engineered microorganisms harbored in the cellulase coding sequences provides new cellulase production system with improvement in enzyme production and activity (Sun and Cheng 2002; Hamelinck et al. 2005).

10.4.2 Bioconversion of Lignocellulosic Hydrolysate to Hydrogen

10.4.2.1 Functional Microorganisms

Functional microorganisms hydrolyzed the lignocellulosic biomass to fermentable reducing sugars, mainly composed of hexose and pentose (Sun and Cheng 2002; Mosier et al. 2005; Chen et al. 2008a,b). Identification of fermentative microorganisms that can effectively degrade hexose and/or pentose is essential to develop practical biohydrogen production process from lignocellulose.

10.4.2.1.1 Pentose Fermentation Microorganisms

The pentose fraction in hemicellulose consists mainly of xylose. Table 10.6 lists the functional microorganisms and mixed cultures reported for hydrogen production from xylose. Compared to hexose-fermenting microorganisms, only a few pentose-fermenting microorganisms have been identified. Among the known pentose-fermenting microorgan- isms, the mesophilic *Clostridium* sp. no. 2 (Taguchi et al. 1995) revealed the highest H_2 yield (2.36 mol H_2/mol xylose), even higher than the thermophiles of *Caldicellulosiruptor saccharolyticus* with a yield of 2.24 mol H_2/mol xylose (Kadar et al. 2004) and that of *Thermoanaerobacterium thermosaccharolyticum* W16 with a yield of 2.19 mol H_2/mol xylose (Ren et al. 2008a,b). Further isolation of the pentose-fermenting microorganisms is needed to explore the lignocellulosic hydrolysate utilization.

10.4.2.1.2 Simultaneous C5/C6 Fermentation Microorganisms

Lignocellulosic prehydrolysates contain a mixture of hexose and pentose. Typical hydrogen fermentation microorganisms, that is, *Ethanoligenens harbinense* B49 (Wang et al. 2007), could not metabolize pentoses. van Niel et al. (2003) and Kadar et al. (2004) demonstrated that their extreme thermophile *C. saccharolyticus* can produce H_2 from both mono- and disaccharides. Datar et al. (2007) reported that sewage sludge following heat pretreatment can simultaneously utilize mixed sugars to generate hydrogen from corn stover treated by a steam explosion process. The molar H_2 yields of 2.84 and 3.0 mol were obtained from the hydrolysates containing mixed sugars. Ren et al. (2008a,b) reported that a thermophilic strain of *T. thermosaccharolyticum* W16 could simultaneously ferment the mixture of glucose

TABLE 10.6

H2 Yields and Production Rates Reported in Xylose Fermentation Studies

Microorganism	Substrate	Conditions	*T* (°C)	pH	Q_{H_2} [a]	Y_{H_2} [b]
Pure cultures						
Clostridium sp. no. 2	Xylose	Continuous	25	6.0	21.0	2.36
Clostridium sp. HR-1	Xylose	Batch	35	6.5		2.14
C. tyrobutyricum ATCC 25755	Xylose	Batch	37	6.3	8.35	0.77
C. butyricum CGS5	Xylose	Batch	37	7.5	9.64	0.73
Enterobacter cloacae IIT-BT 08	Xylose	Batch	36	6.0	15.5	0.95
Caldicellulosiruptor saccharolyticus	Xylose	Batch	70	7.2	11.3	2.24
	Mix	Batch	70	7.2	9.2	2.32
	Glucose	Batch	70	7.2	10.7	2.5
T. thermosaccharolyticum W16	Xylose	Batch	60	6.5	10.7	2.19
	Mix	Batch	60	6.5	11.2–12.7	2.23–2.37
	Glucose	Batch	60	6.5	12.9	2.42
Mix cultures						
Sewage sludge	Xylose	Batch	35	6–7	5.94–8.93	1.92–2.25
	Xylose	Continuous	35	7.1	4.15	0.7
Sewage sludge	Xylose	Continuous	40	6.5	25.4	0.8
Microflora	Xylose	Batch	75	7.3	—	0.54
Sewage sludge	Xylose	Continuous	50	7.0	5.76	1.4
Compost	Xylose	Fed batch	55	5.0	0.27	1.7

Source: Ren, N. et al., *Biotechnol. Adv.*, 2009.

[a] Q_{H_2} is the maximal hydrogen production rate (mmol H_2/L/h).

[b] Y_{H_2} is the hydrogen yield (mol H_2/mol (substrate).

and xylose with a hydrogen yield of up to 2.37 mol H_2/mol substrate. Also, the W16 strain has a high tolerance to common prehydrolysate inhibitors, that is, acetate and furfural.

10.4.2.1.3 Microorganisms Involved in Cellulose Hydrolysates Fermentation

Hexose is the predominant component in the cellulose hydrolysates. Table 10.7 summarizes the reported microorganisms that can yield hydrogen from cellulose hydrolysate. The highest H_2 yield of approximately 83% of the theoretical value (theoretical is 4 mol/mol hexose) has been reported using thermophilic anaerobic bacteria (van Niel 2003).

The strict anaerobic *E. harbinense*, a new genus identified by Xing et al. (2006), also revealed high H_2 yield. The model strain, *E. harbinense* YUAN-3T, showed a special autoaggregation ability during shake cultivation. Hydrogen yield and hydrogen production rate of the strain *E. harbinense* YUAN-3T were 2.81 mol H_2/mol glucose and 27.6 mmol H_2/g dry cell/h, respectively. The autoaggregative property of the strain *E. harbinense* YUAN-3 renders this strain the potential to form cell granules for the development of compact hydrogen bioreactors for industrial use. The strict anaerobic Clostridia and facultative anaerobes produce hydrogen with comparable yields (approximately 2 mol H_2/mol glucose) (Heyndrickx et al. 1986; Tanisho et al. 1987; Taguchi et al. 1994; Kumar and Das 2000). The H_2 yield <2 mol H_2/mol glucose was reported for mixed cultures (Lin and Chang 1999; Chen et al. 2001). Wang et al. (2008) suggested that bioaugmentation with the addition of certain functional H_2-producing strains might be promising for further improving H_2 yield of mixed culture.

TABLE 10.7

Hydrogen Yields and Production Rates by Microorganisms as Reported in the Literature

Microorganism	Conditions	pH	*T* (°C)	Substrate	Y_{H_2} [a]	Q_{H_2} [b]
Strict anaerobes						
Clostridia						
C. sp. no 2	Batch	6.0	36	Glucose	2.0	23.9
C. butyricum LM G1213tl	Continuous	5.8	36	Glucose	1.5	21.7
C. beijerinckii AM21B	Batch	6.5	36	Glucose	2.0	
Thermophiles						
Thermotoga elfii	Batch	7.4	65	Glucose	3.3	2.7
Caldicellulosiruptor saccharolyticus	Batch	7.0	70	Sucrose	5.9	8.4
Ethanoligenens harbinense						
E. harbinense B49	Batch	3.9–4.2	35	Glucose	16–1.8	
E. harbinense Yuan-3	Batch		35	Glucose	2.81	
Facultative anaerobes						
Enterobacter						
E. aerogenes E.82005	Batch	6.0	38	Glucose	1.0	21
E. cloacae IIT-BT 08	Batch		36	Glucose	2.2	
E. aerogenes HO-39	Continuous	6–7	38	Glucose	1.0	
Mixed cultures						
Sludge compost	Continuous	6.8	60	Waste water		8.3
Sewage sludge	Continuous	5.7	35	Glucose	1.7	29.6
Sewage sludge	Continuous	6.7	35	Sucrose	1.7	26.2

Source: Ren, N. et al., *Biotechnol. Adv.*, 2009.

[a] Y_{H_2} is the hydrogen yield (mol H_2/mol) (substrate).

[b] Q_{H_2} is the maximal hydrogen production rate (mmol H_2/L/h).

10.4.2.2 Key Factors Affecting Bioconversion of Prehydrolysates/Hydrolysates to H_2

10.4.2.2.1 Inhibitors

Besides monomeric sugars, various toxic compounds were derived from lignocellulosic prehydrolysates such as fermentation inhibitors (Palmquist et al. 2000a,b; Mussatto et al. 2004). The fermentation inhibitors in the lignocellulosic prehydrolysates are composed of the following three groups:

1. The substances released during degradation of hemicellulose, including acetic acid and terpenes, alcohols, and aromatic compounds, whose toxicity was inter- preted as penetration of the undissociated acid into the cell and dissociation of acid at higher intracellular pH (Pampulha et al. 1989). The fermentability of ligno- cellulosic hydrolysate can hence be improved by raising the pH.
2. The second group includes furfural, 5-hydroxymethyl furfural, levulinic acid, formic acid, and humic substances, which are the by-products for sugar degrada- tion. Direct inhibition of both glycolytic (Banerjee et al. 1981) and nonglycolytic (Taherzadeh et al. 2000) enzymes has been suggested as a potential mechanism for furfural toxicity.
3. The third group of inhibitors is the lignin degradation products. This group of inhibitors includes a wide range of aromatic and polyaromatic compounds (Lo et al. 2008a; Wang et al. 2008).

10.4.2.2.2 pH and Temperature

These are two principal process factors that affect biohydrogen production performance. The reported optimal pH range for hydrogen production ranged 5.0–7.5 (Chen et al. 2001; Fang et al. 2002; Khanal et al. 2004; Calli et al. 2008). Ren et al. (1997) stated that the optimal pH for hydrogen production can be less than 5.0. Decline in pH value is noted in hydrogen production process owing to the production of organic acids that depletes the buffering capacity of the medium (Khanal et al. 2004). Since pH affects the activity of iron-containing hydrogenase enzyme, decreases in pH will inhibit hydrogen production (Dabrock et al. 1992).

Hydrogen production was tested under mesophilic conditions using glucose, sucrose, and wastewater as substrates (Mononmani et al. 1987; Ueno et al. 1996; Yokoi et al. 1998). Mesophilic biohydrogen production is preferred for preventing the need of external heating. However, hydrogen fermentation at high temperatures has high hydrogen yield, owing to the suppression of H_2-consuming bacteria and the capability to utilize numerous substrates (Talabardon et al. 2000; Fang et al. 2003). Lin et al. (2008) demonstrated a two-time hydrogen yield at thermophilic (50°C–55°C) compared with mesophilic (30°C–40°C) fermentation. Moreover, in terms of future application, it is possible to couple the H_2 fermentation with bioethanol production from lignocellulosic biomass under thermophilic condition.

10.4.2.2.3 Nutrient Supplementation

The medium components added to the hydrolysate affect the fermentation performance. Medium components should fulfill the carbon and nitrogen need of the involved microorganisms. Also, trace metals, growth factors, and vitamins are also essential for cell growth. Studies on hexose fermentation or lignocellulosic hydrolysates mainly conducted experiments using laboratory media with yeast extract and peptone. The strain *Thermotoga elfii*, which is capable of producing high yields of hydrogen from glucose, grows on a medium enriched with yeast extract (van Niel et al. 2002). The strain *T. thermosaccharolyticum* W16

can simultaneously intake glucose and xylose for hydrogen production without extract or tryptone. However, with these, the strain W16 can grow even better when extract and tryptone are present (Ren 2008a,b). The strain *Clostridium butyricum* AS1.209 exhibited a C/N-ratio-dependent growth characteristic, and a proper C/N ratio enhances biohydro- gen production in SSF from steam-exploded corn straw (Li and Chen 2007).

10.4.2.3 Fermentation Tactics for Lignocellulosic Prehydrolysates to Hydrogen

10.4.2.3.1 Detoxification

Removal of inhibitors from lignocellulosic hydrolysates enhances the fermentation efficiencies (de Vrije et al. 2002). Effects of adding activated charcoal, extracting with organic solvents, ion exchange, ion exclusion, or molecular sieves have been investigated (Palmquist et al. 2000a,b; Mussatto et al. 2004). Different detoxification methods removed partially on the hydrolysate toxicity in different magnitude. The choice of detoxification method depends on the hydrolysate origin and the involved fermentation microorganisms.

10.4.2.3.2 Bioaugmentation for Higher H_2 Production

Increasing cell density has been shown in several cases to be a suitable way of increasing the volumetric productivity of biohydrogen (Zhu et al. 1999; Jo et al. 2008). Moreover, high cell density is beneficial to overcome toxicity of lignocellulosic hydrolysate (Shreenath and Batch 1987). Cell recycling to reactor or cell immobilization enrich cell density. Cheap attachment material is developed (Kumar et al. 2001). Cells can be immobilized by adhesion to a surface (electrostatic or covalent), entrapment in polymeric matrices, or reten- tion by membranes for hydrogen production. The strain *Enterobacter cloacae* IIT-BT 08 was immobilized in an environmentally friendly solid matrix via adsorption technique. The maximum hydrogen production rate was 75.6 mmol/L/h at a dilution rate of 0.93 h^{-1}. The substrate conversion efficiency was increased by 15% at immobilized conditions (Kumar et al. 2001).

Single culture may not be capable of degrading a few monosaccharides in the lignocellulosic prehydrolysates. We believe that cocultured microorganisms should be a better configuration than single culture for most efficient hydrogen production from the lignocellulosic hydrolysates.

10.4.3 Direct Microbial Conversion of Cellulose to Hydrogen

10.4.3.1 Microorganisms Involved in Converting Cellulose to Hydrogen

10.4.3.1.1 Pure Culture

A few pure cultures can directly degrade cellulose to produce hydrogen. Wang et al. (2008) reported that *Clostridium acetobutylicum* X9 generated the maximum hydrogen production and cellulose hydrolysis rate of 6.4 mmol H_2/h/g dry cell and 68.3%, respectively, using microcrystalline cellulose as the substrate. These authors also showed that X9 can degrade pretreated acetic steam-explored corn stalks to hydrogen with specific hydrogen production rate of 3.4 mmol/g steam-exploded corn stalks. Levin et al. (2006) demonstrated that the hydrogen yield of strain *Clostridium thermocellum* 27405 could reach 1.6 mol H_2/mol glucose using *d*elignified *w*oods (*DLWs*).

The pure culture system is attractive and is preferred for mechanistic research and genetic reconstruction for improving cellulose hydrolysis rate and hydrogen yield. However, strain isolation technique is complicated and time-consuming. In addition, only a small fraction of microbes can be cultivated.

TABLE 10.8

Biohydrogen Production Performance from Cellulosic Biomass with Mixed Culture

Microorganism	Cellulosic Substrate	Experimental Conditions	Y_{H_2} [a]	Specific Q_{H_2} Rate
Heat-shock digested sludge	Microcrystalline cellulose	37°C, 12 days	2.18 mmol H_2/g Avice	18 mmol H_2/g VSS/day
Microflora	Cellulose	55°C, 200 h	4.55 mmol H_2/g cellulose	12.8 mmol H_2/g VSS/day
Pig-dung compost	Rice straw	37°C, 17 days	53.5 mL H_2/g TS	
Anaerobic digested sludge	Corn stover	36°C, 300 h	5.66 mmol H_2/gTVS	
	Beer lees		2.42 mmol H_2/gTVS	
	Wheat bran		4.55 mmol H_2/gTVS	
Cow-dung compost	Wheat straw	126.5 h	3.04 mmol H_2/g TVS	10.14 mL H_2/g TVS/h
Cow-dung microflora	α-Cellulose and saccharification products		2.8 mmol H_2/g cellulose	

Source: Ren, N. et al., *Biotechnol. Adv.*, 2009.

[a] The listed data were calculated based on the original data.

10.4.3.1.2 Mixed Cultures

Recently, the research on biological production of cellulose hydrogen has been focused on mixed-culture systems (Lay et al. 1999; Ginkel et al. 2001; Fang et al. 2002) for its greater cellulose conversion rates and broader carbon sources. In addition, the mixed culture, such as natural microflora, anaerobic digested sludge, or compost, contains large amounts of organisms that could serve as the ideal microorganism resources for cellulose hydrolysis. Table 10.8 lists the hydrogen yields from cellulosic materials with mixed cultures. Among them, the highest hydrogen yield reported to be 4.55 mmol H_2/g cellulose by microflora (Liu et al. 2003).

10.4.3.2 Bioaugmentation for Cellulose Degradation to Hydrogen

Bioaugmentation via coculture or community system to further enhance H_2 production was studied for a few years. Rarely, bioaugmentation is applicable to practical cellulose degradation to hydrogen process. Complementarily, functions between the augmented strains and the indigenous strains overcome the often encountered repression problem in cellulose hydrolysis process, such as the characteristic instability, structure, and mechanical pathway complication. Wang et al. (2008) reported dark fermentation of microcrystalline cellulose to produce biohydrogen using coculture of *C. acetobutylicum* X9 and *E. harbinense* B49. The maximum hydrogen yield in the bioaugmented cocultured system was 16.2 mg H_2/g cellulose. B49 can rapidly remove reduced sugar produced by X9 and hence improved cellulose hydrolysis and subsequent hydrogen production rates. *C. thermo- cellum* JN4 and its counterpart bacterium, a hydrogen-producing *T. thermosaccharolyticum* GD17, were investigated in terms of the mechanisms of interactive cooperation in cellulose degradation and hydrogen production. The data showed that when *C. thermocellum* JN4 was cocultured with *T. thermosaccharolyticum* GD17, hydrogen production increased about twofold and H_2 yield increased to a high level of 1.8 mol H_2/mol glucose (Liu et al. 2008a,b). Liu et al. (2008a) studied the cellulose hydrolysis activity of two mixed bacterial con- sortia (NS and QS). Using the cellulosic hydrolysate containing 0.8 g/L reducing sugar,

Clostridium pasteurianum CH_7 attained the best H_2 production and yield of approximately 23.8 mL/L and 1.21 mmol H_2/g reducing sugar, respectively.

Intensive research on microbial communities for cellulose degradation systems was conducted in terms of their stable functional characteristic, microbial community composition and structure, reaction pathways, and mechanism to tolerant harsh environments. Haruta et al. (2002) developed a microbial community capable of degrading N60% rice straw within 4 days at 50°C. The stability of the community was demonstrated using multiple subcultures for several times in medium with/without cellulosic material, being heated to 95°C and being frozen at −80°C. Ren et al. (2009) proposed a functional community (rumen cellulose degradation bacteria consortia) that could simultaneously degrade cellulose and produce hydrogen and establish the isolation strategy.

10.4.3.3 Key Factors Affecting Cellulose Degradation and Hydrogen Production

Factors affecting the cellulose degradation process mainly lie in environmental factors, such as initial and end fermentation pH, the addition quantity and type of nitrogen resource, feedback inhibition of cellulose hydrolysis products–soluble saccharide, as well as the inhibition of the end-products accumulation, such as acetate, lactate, and butyrate. In addition, substrate type and concentration also have strong effect on cellulose degrada- tion. *Bacteroides cellulosolvens* efficiently hydrolyzed a variety of cellulosic substrates. This strain can grow up to degradation of 20 g cellulose/L. Further, cellulose hydrolysis and sugar accumulation were accomplished by cellulose enzymes. This growth cessation was not due to low pH, to nutrient depletion, or to toxic accumulation of any of the major end products (CO_2, ethanol, acetic acid, lactic acid, cellobiose, glucose, or xylose) (Murray 1986; Narahiro and Sekiguchi 2007).

Initial pH may influence the lag phase in batch cellulose-to-hydrogen tests. Some studies reported that the low initial pH of 4.0–4.5 causes long lag periods of about 20 h (Khanal et al. 2004; Liu and Shen 2004). Alkaline pH decreases lag time; however, it may cause low yield of hydrogen (Zhang et al. 2003). Gradual decreases in pH during fermentation inhibit cellulose degradation since pH affects the activity of iron-containing cellulase enzyme (Dabrock et al. 1992). The pH could also affect the mechanisms of fermentation, the specific hydrogen production rate, and the hydrogen content in the gas phase. The optimal pH range for maximum hydrogen yield or specific hydrogen production rate is 5–6 (Lay 1999; Chen et al. 2001; Fang et al. 2003; Khanal et al. 2004), with some others declaring 6.8–8 (Lay 2001; Zhang et al. 2003; Collet et al. 2004; Kanai et al. 2005) or around 4.5 for the thermophilic culture (Shin et al. 2004).

Most studies revealed that the final pH in cellulose hydrolysis to hydrogen ranges 4.0–4.8 regardless of initial pH (Evvyernie et al. 2001; Lay 2001; Liu et al. 2003; Zhang et al. 2003; Liu and Shen 2004). The intense drop in pH level is due to the production of organic acids that weaken the buffering capacity of the medium (Khanal et al. 2004). The pH value should be properly controlled in biohydrogen production. The principal end products for anaerobic wastewater pretreatment from hard-to-decompose carbohydrates (cellulose) are propionate, acetate, CO_2, and butyrate (Karapinar and Fikret 2006). However, the production of propionate could have adverse effect on hydrogen production. Methane was not detected in most of the hydrogen production studies since heat treatment removes methane producers in sludge (Yu et al. 2002; Lin and Lay 2004; Liu and Shen 2004). Han and Shin (2004) probed methane by mesophilic cultures at long retention times of reactors.

Nitrogen is an essential nutrient for hydrogen production by dark fermentation under anaerobic conditions. Yokoi et al. (2002) reported that the highest level of hydrogen

(2.4 mol H_2/mol glucose) could be obtained from starch in the presence of 0.1% polypeptone. But no hydrogen production was observed when inorganic nitrogen salts were used as nitrogen source. Corn-steep liquor is a waste of corn starch manufacturing process that can be used as a nitrogen source (Yokoi et al. 2002). Lin and Lay (2004) reported that the C/N ratio affects hydrogen productivity more significantly than the specific hydrogen production rate.

The inhibition induced by accumulated saccharides can affect the performance of cellulose-to-hydrogen process. Ramos et al. (1986) observed lower hydrolysis rates at higher sugar concentrations. The removal of soluble sugars liberated during hydrolysis should enhance the efficiency of hydrolysis of the residual substrate. Levin et al. (2006) conducted batch tests with *C. thermocellum* 27,405 to produce biohydrogen from cornstalk wastes. Results showed that initial substrate type, substrate concentration, substrate moisture content, supplemental nutrient concentration, and duration of cultivation time could markedly affect the product quality. Zhang et al. (2007) converted cellulose in various wastewaters to H_2 by a mixed culture in batch tests at 55°C, pH 5.5–8.5, and cellulose concentrations of 10–40 g/L. The maximum cumulative H_2 yield of 149.69 mL H_2/g TVS was obtained at initial pH 7.0 and substrate concentration 15 g/L.

10.4.3.4 Integrated Process System for Multi-Output Solutions

Cellulose is the most abundant biopolymer in the world [384]. The 1.4 billion dry tons of lignocellulosic biomass produced annually in China can yield up to 100 billion kg H_2 (70% of the amount of total cellulose and hemicellulose was used for this preliminary calcula- tion). Here, producing 1.0 kg of H_2 (roughly equivalent to the energy content of a gallon of gasoline) would take 10.3 kg cellulose based on 73% of H_2 recovery reported by Cheng and Logan (2007a). This amount of H_2 is equivalent to 500 billion kg standard coal, which is around 22.4% of the total coal consumption (2.2 billion tons) amount in China in 2006. Hence, bioconversion of cellulose provides a viable approach to produce renewable hydro- gen from organic matter, provided a high efficient combinatory process system is adopted. The combined dark fermentation coupling with photofermentation or dark fermentation coupling with bioelectrohydrogenesis is a promising hydrogen production process from lignocellulosic biomass if the technological barriers can be overcome. First, the develop- ment of a well-integrated balanced system is the key. Because hydrogen production rates were much lower from cellulose (0.11 m^3/m^3/day) than from glucose (1.23 m^3/m^3/day), and the photofermentation rates were 100 times lower than the dark processes, the rates of hydrolysis and fermentation by electrohydrogenesis in microbial electrolysis cell (MEC) system or in photofermentation are different. The fermentation and electrohydrogenesis rates need to be regulated using feeding strategies or a two-stage process, using reactors especially designed to handle particulate substrates. Increasing the H_2 production effi- ciency by the functional microorganisms is another essential issue. Aiming at this, the metabolic modification at both molecular and physioecological levels is necessary. At the molecular level, as indicated in US DOE Genomics: GTL roadmap systems biology for energy and environment, studies are needed in modifying the key enzymes and func- tional pathways, controlling the organic matter transportation, and even regulating or reconstructing the entire metabolic network in order to increase the hydrogen yield and lignocelluloses degradation. At the microbial community level, establishing the linkage between process system function and microbial diversity is even more challenging. This problem is partially due to insufficient experimental information on community-wide spatial and temporal dynamics of microbial community structure, function, and activity

for rigorous examination. Overall, to develop a mature hydrogen production technology, bioconversion performance from lignocellulosic biomass will need to be further improved in production rates, cost-effectiveness, and system scale-up. Rapid advancements in the development of multiprocesses coupled with additional funding and mechanistic research into microbial processes should make rapid commercialization of this new biohydrogen technology possible (Ren et al. 2009).

10.4.3.5 Coupling Process of Hydrogen–Methane Fermentation

Biological hydrogen production process does not significantly reduce the organic content in terms of the COD of the feedstock. Usually, COD removal is below 20% during hydrogen production (Antonopoulou et al. 2008). The residual VFAs such as acetic acid exist in the fermenting waste liquor, which can be utilized if a methane fermentation stage is followed. The combined hydrogen fermentation and methane fermentation system will benefit the maximal energy recovery from feed biomass (Han and Shin 2004; Liu et al. 2006; Cooney et al. 2007; Ting and Lee 2007; Ueno et al. 2007; Zhu et al. 2008). For instance, Zhu et al. reported that, via coupling hydrogen and methane fermentation from potato waste, the total COD0 in the feedstock was removed by 64% and the hydrogen and methane yields were totally 30 L/kg TS (total solids) (with a maximum of 68 L/kg) or 183 L/kg TS (with a maximum of 225 L/kg). Cooney et al. reported that methane production in the two-phase anaerobic digestion process is more stable and effective than the one-phase process. The need for clean production of renewable energy from lignocellulosic biomass will thus hasten the development of combination of hydrogen and methane production (Ren et al. 2009).

10.4.3.6 Integrated Process System for Multioutput Solutions

Based on the aforementioned review, it is clear that the bioconversion of lignocelluloses to H_2 shows a very feasible solution to produce hydrogen via biotechnology. Concern remains on how to establish an applicable and affordable lignocellulose-to-H_2 process. A considerable pathway is to develop an integrated process for multioutputs from raw wastes including lignocellulosic H_2–CH_4, lignocellulosic ethanol, and for high- and low-value-added bioproducts (i.e., biobutanol, bioflocculants). Through this approach, a multichoice scheme might be performed according to the needs for the future bioenergy and bioproducts market. Aside from the scientific assessment, a careful and detailed economic programming is needed in order to boost this entire blueprint into practice.

References

Acién Fernández, F.G., Fernández Sevilla, J.M., Sánchez Peréz, J.A., Molina Grima, E., and Chisti, Y. Airlift-driven external loop tubular photobioreactors for outdoor production of microalgae: Assessment of design and performance. *Chem. Eng. Sci*. 56 (2001): 2721–2732.

Amos, W.A. Biological water-gas shift conversion of carbon monoxide to hydrogen: Milestone com- pletion report NREL/MP-560-35592 (January 2004).

Antonopoulou, G., Gavala, H.N., Skiadas, I.V., Angelopoulos, K., and Lyberatos, G. Biofuels genera- tion from sweet sorghum: Fermentative hydrogen production and anaerobic digestion of the remaining biomass. *Bioresour. Technol*. 99 (2008): 110–119.

Aoyama, K., Uemura, I., Miyake, J., and Asada, Y. Fermentative metabolism to produce hydrogen gas and organic compounds in a cyanobacterium *Spirulina Platensis. J. Ferment. Bioeng*. 83 (1997): 17–20. Artero, V. and Fontecave, M. Some general principles for designing electrocatalysts with hydrogenase activity. *Coor. Chem. Rev*. 249 (2005): 1518–1535.

Axelsson, R. and Lindblad, P. Transcriptional regulation of *Nostoc* hydrogenases: Effects of oxygen, hydrogen, and nickel. *Appl. Environ. Microbiol*. 68(1) (2002): 444–447.

Ballesteros, I., Oliva, J.M., Negro, M.J., Manzanares, P., and Ballesteros M. Enzymic hydrolysis of steam exploded herbaceous agricultural waste (*Brassica carinata*) at different particle sizes. *Process Biochem*. 38 (2002): 187–192.

Banerjee, N., Bhatnagar, R., and Viswanathan, L. Inhibition of glycolysis by furfural in *Saccharomyces cerevisiae. Eur. J. Appl. Microbiol. Biotechnol*. 11 (1981): 224–228.

Basak, N. and Das, D. The prospect of purple non-sulfur [Pns] photosynthetic bacteria for hydrogen production: The present state of the art. *World J. Microbiol. Biotechnol*. 23(1) (2007): 31–42.

Bauer, C.G. and Forest, T.W. Effect of hydrogen addition on the performance of methane-fueled vehicles. Part I. Effect on S.I. engine performance. *Int. J. Hydrogen Energy* 26 (2001): 55–70.

Beldman, G., Voragen, A.G.J., Rombouts, F.M., and Pilnik, W. Synergism in cellulose hydrolysis by endoglucanases and exoglucanases purified from *Trichoderma viride. Biotechnol. Bioeng*. 31 (1988): 173–178.

Benemann, J. Hydrogen biotechnology: Progress and prospects. *Nat. Biotechnol*. 14(9) (1996): 1101–1103.

Benemann, J.R. Hydrogen production by microalgae. *J. Appl. Phycol*. 12 (2000): 291–300.

Benemann, J.R., Berenson, J.A., Kaplan, N.O., and Kamen, M.D. Hydrogen evolution by chloroplast- ferredoxin-hydrogenase system. *Proc. Natl. Acad. Sci. USA* 70 (1973): 2317–2320.

Benemann, J.R. and Weare, N.M. Hydrogen evolution by nitrogen-fixing *Anabaena cylindrica* cultures. *Science* 184 (1974): 174–175.

Bisaillon, A., Turcot, J., and Hallenbeck, P.C. The effect of nutrient limitation on hydrogen production by batch cultures of *Escherichia coli. Int. J. Hydrogen Energy* 31 (2006): 1504–1508.

Bolton, J.R. Solar photoproduction of hydrogen, IEA Agreement on the Production and Utilization of Hydrogen. (1996).

Bosca, C., Dauta, A., and Marvalin, O. Intensive outdoor algal cultures. How mixing enhances the photosynthetic production rate. *Bioresour. Technol*. 38 (1991): 185–188.

Boussiba, S., Sandbank, E., Shelef, G., Cohen, Z., Vonshak, A., Ben-Amotz, A., Arad, S., and Richmond, A. Outdoor cultivation of the marine microalga *Isochrysis galbana* in open reactors. *Aquaculture* 72 (1988): 247–253.

Cai, M., Liu, J., and Wei, Y. Enhanced biohydrogen production from sewage sludge with alkaline pretreatment. *Environ. Sci. Technol*. 38(11) (2004): 3195–3202.

Call, D. and Logan, B.E. Hydrogen production in a single chamber microbial electrolysis cell lacking a membrane. *Environ. Sci. Technol*. 42(9) (2008): 3401–3406.

Calli, B., Schoenmaekers, K., Vanbroekhoven, K., and Diels, L. Dark fermentative H_2 production from xylose and lactose—Effects of on-line pH control. *Int. J. Hydrogen Energy* 33 (2008): 522–530.

Camacho, F.G., Gomez, A.C., Fernandez, F.G.A., Sevilla, J.M.F., and Grima, E.M. Use of concentric- tube airlift photobioreactors for microalgal outdoor mass cultures. *Enzyme Microb. Technol*. 24 (1999): 161–172.

Camacho Rubio, F., Acién Fernández, F.G., Sánchez Pérez, J.A., García Camacho, F., and Molina Grima, E. Prediction of dissolved oxygen and carbon dioxide concentration profiles in tubular photobioreactors for microalgal culture. *Biotechnol. Bioeng*. 62 (1999): 71–86.

Carlozzi, P. Dilution of solar radiation through culture lamination in photobioreactor rows facing south–north: A way to improve the efficiency of light utilization by cyanobacteria (*Arthrospira platensis*). *Biotechnol. Bioeng*. 81 (2003): 305–315.

Chaumont, D., Thepenier, C., and Gudin, C. Scaling up a tubular photobioreactor for continuous culture of *Porphyridium cruentum*—From laboratory to pilot plant. In: Stadler, T., Morillon, J., Verdus, M.S., Karamanos, W., Morvan, H., Christiaen, D. (Eds.), *Algal Biotechnology*. Elsevier Applied Science, London, U.K. (1988): pp. 199–208.

Chen, C.C., Lin, C.Y., and Chang, J.S. Kinetics of hydrogen production with continuous anaerobic cultures utilizing sucrose as the limiting substrate. *Appl. Microbiol. Biotechnol*. 57 (2001): 56–64. Chen, C.Y., Lu, W.B., Liu, C.H., and Chang, J.S. Improved phototrophic H_2 production with Rhodopseudomonas palustris WP3-5 using acetate and butyrate as dual carbon substrates.

Bioresour. Technol. 99 (2008a): 3609–3616.

Chen, C.Y., Lu, W.B., Wu, J.F., and Chang, J.S. Enhancing phototrophic hydrogen production of *Rhodopseudomonas palustris* via statistical experimental design. *Int. J. Hydrogen Energy* 32(8) (2007): 940–949.

Chen, C.Y., Yang, M.H., Yeh, K.L., Liu, C.H., and Chang, J.S. Biohydrogen production using sequential two-stage dark and photo fermentation processes. *Int. J. Hydrogen Energy* 33 (2008): 4755–4762. Chen, M., Zhao, J., and Xia, L.M. Enzymatic hydrolysis of maize straw polysaccharides for the pro-

duction of reducing sugars. *Carbohydr Polymers* 71 (2008b): 411–415.

Chen, S.D., Sheu, D.S., Chen, W.M., Lo, Y.C., Huang, T.I., Lin, C.Y. et al. Dark hydrogen fermentation from hydrolyzed starch treated with recombinant amylase originating from *Caldimonas taiwan- ensis* On1. *Biotechnol. Prog*. 23 (2007): 1312–1320.

Cheng, S. and Logan, B.E. Ammonia treatment of carbon cloth anodes to enhance power generation of microbial fuel cells. *Electrochem. Commun*. 9 (2007a): 492–496.

Cheng, S. and Logan, B.E. Sustainable and efficient biohydrogen production via electrohydrogenesis.

Proc. Natl. Acad. Sci. USA 104(47) (2007b): 18871–18873.

Cheng, S. and Logan, B.E. Sustainable and efficient biohydrogen production via electro-hydrogenesis.

PNAS 104 (2007c): 18871–18873.

Cheng-Wu, Z., Zmora, O., Kopel, R., and Richmond, A. An industrial size flat glass reactor for mass production of *Nannochloropsis* sp. (Eustigmatophyceae). *Aquaculture* 195 (2001): 35–49.

Cheong, D.Y. and Hansen, C.L. Bacterial stress enrichment enhances anaerobic hydrogen production in cattle manure sludge. *Appl. Microbiol. Biotechnol*. 72 (2006): 635–643.

Chin, H.L., Chen, Z.S., and Chou, C.P. Fedbatch operation using *Clostridium acetobutylicum* suspen- sion culture as biocatalyst for enhancing hydrogen production. *Biotechnol. Prog*. 19 (2003): 383–388.

Chisti, Y. Pneumatically agitated bioreactors in industrial and environmental bioprocessing: hydro- dynamics, hydraulic, and transport phenomena. *Appl. Mech. Rev*. 51 (1998): 33–112.

Choi, S.L., Suh, I.S., and Lee, C.G. Lumostatic operation of bubble column photobioreactors for *Haematococcus pluvialis* cultures using a specific light uptake rate as a control parameter. *Enzyme Microb. Technol*. 33 (2003): 403–409.

Collet, C., Adler, N., Schwitzguebel, J.P., and Peringer, P. Hydrogen production by clostridium thermolacticum during continuous fermentation of lactose. *Int. J. Hydrogen Energy*. 29 (2004): 1479–1485.

Contreras, A., García, F., Molina Grima, E., and Merchuk, J.C. Interaction between CO_2-mass transfer, light availability and hydrodynamic stress in the growth of *Phaeodactylum tricornutum* in a con- centric tube airlift photobioreactor. *Biotechnol. Bioeng*. 60 (1998): 318–325.

Cooney, M., Maynard, N., Cannizzaro, C., and Benemann, J. Two-phase anaerobic digestion for pro- duction of hydrogen–methane mixtures. *Bioresour. Technol*. 98 (2007): 2641–2651.

Couvert, A., Bastoul, D., Roustan, M., and Chatellier, P. Hydrodynamic and mass transfer study in a rectangular three-phase airlift loop reactor. *Chem. Eng. Proc*. 43 (2004): 1381–1387.

Dabrock, B., Bahl, H., and Gottschalk, G. Parameters affecting solvent production by *Clostridium pasteurium*. *Appl. Environ. Microbiol*. 58 (1992): 1233–1239.

Das, D., Dutta, T., Nath, K., Kotay, S.M., Das, A.K., and Veziroglu, T.N. Role of Fe-hydrogenase in biological hydrogen production. *Curr. Sci*. 90 (2006): 1627–1637.

Datar, R., Huang, J., Maness, P.C., Mohagheghi, A., Czernik, S., and Chornet, E. Hydrogen produc- tion from the fermentation of corn stover biomass pretreated with a steam-explosion process. *Int. J. Hydrogen Energy* 32 (2007): 932–939.

Degen, J., Uebele, A., Retze, A., Schmidt-Staigar, U., and Trosch, W.A. A novel airlift photobioreactor with baffles for improved light utilization through flashing light effect. *J. Biotechnol*. 92 (2001): 89–94.

Demirbas, A. Biodiesel: A realistic fuel alternative for diesel engines. *Chem. Mater. Sci*. (2008). Ditzig, J., Liu, H., and Logan, B.E. Production of hydrogen from domestic wastewater using a bio-

electrochemically assisted microbial reactor [BEAMR]. *Int. J. Hydrogen Energy* 32(13) (2007): 2296–2304.

Duff, S.J.B. and Murray, W.D. Bioconversion of forest products industry waste cellulosics to fuel ethanol: A review. *Bioresour. Technol*. 55 (1996): 1–33.

Ensign, S.A. and Ludden, P.W. Characterization of the CO oxidation/H_2 evolution system of Rhodospirillum rubrum. Role of a 22-kDa iron–sulfur protein in mediating electron trans- fer between carbon monoxide dehydrogenase and hydrogenase. *J. Biol. Chem*. 266 (1991): 18395–18403.

Eroglu, I., Aslan, K., Gunduz, U., Yucel, M., and Turker, L. Substrate consumption rates for hydrogen production by *Rhodobacter sphaeroides* in a column photobioreactor. *J. Biotechnol*. 70(1–3) (1999): 103–113.

Esper, B., Badura, A., and Rögner, M. Photosynthesis as a power supply for (bio-)hydrogen produc- tion. *Trends Plant Sci*. 11 (2006): 543–549.

Evyernie, D., Morimoto, K., Karita, S., Kimura, T., Sakka, K., and Ohmiya, K. Conversion of chitin- ous wastes to hydrogen gas by *Clostridium paraputrificum* M-21. *J. Biosci. Bioeng*. 91 (2001): 339–343.

Fabiano, B. and Perego, P. Thermodynamic study and optimization of hydrogen production by Enterobacter aerogenes. *Int. J. Hydrogen Energy* 27 (2002): 149–156.

Fan, L.T., Lee, Y.H., and Gharpuray, M.M. The nature of lignocellulosics and their pretreatments for enzymatic hydrolysis. *Adv. Biochem. Eng. Biotechnol*. 23(1982):158–187.

Fang, H.H.P., Li, C.L., and Zhang, T. Acidophilic biohydrogen production from rice slurry.

Int. J. Hydrogen Energy 31 (2006): 683–692.

Fang, H.H.P. and Liu, H. Effect of pH on hydrogen production from glucose by a mixed culture."

Bioresour. Technol. 82 (2002): 87–93.

Fang, H.H.P., Liu, H., and Zhang, T. Phototrophic hydrogen production from acetate and butyrate in wastewater. *Int. J. Hydrogen Energy* 30(7) (2005): 785–793.

Fang, H.H.P., Zhang, T., and Liu, H. Biohydrogen production from starch in wastewater under ther- mophilic condition. *J. Environ. Manag*. 69 (2003): 149–156.

Fang, H.H.P., Zhu, H., and Zhang, T. Phototrophic hydrogen production from glucose by pure and co-cultures of *Clostridium butyricum* and *Rhodobacter sphaeroides. Int. J. Hydrogen Energy* 31(15) (2006): 2223–2230.

Fang, J.M., Sun, R.C., Salisbury, D., Fowler, P., and Tomkinson, J. Comparative study of hemicel- luloses from wheat straw by alkali and hydrogen peroxide extractions. *Polym. Degrad. Stab.* 66 (1999): 423–432.

Fedorov, A.S., Tsygankov, A.A., Rao, K.K., and Hall, D.O. Hydrogen photoproduction by *Rhodobacter sphaeroides* immobilised on polyurethane foam. *Biotechnol. Lett*. 20 (1998): 1007–1009.

Fontoynont, M., Dumortier, D., Heinemann, D., Hammer, A., Olseth, J., Skarveit, A., Ineichen, P., Reise, Ch.P.J., Roche, L., Beyer, H.G., and Wald, L. Satellight: A www server which provides high quality daylight and solar radiation data for western and central Europe. *Proceedings of the Ninth Conference on Satellite Meteorology and Oceanography*, Paris, France (1998).

Gaffron, H. and Rubin, J. Fermentative and photochemical production of hydrogen in algae. *J. Gen.*

Physiol. (1942) 219–240.

García Malea López, M.C., Del Río Sánchez, E., Casas López, J.L., Acién Fernández, F.G., Fernández Sevilla, J.M., Rivas, J., Guerrero, M.G., and Molina Grima, E. Comparative analysis of the outdoor culture of

Haematococcus pluvialis in tubular and bubble column photobioreactors. *J. Biotechnol*. 123 (2006): 329–342.

Gest, H. and M.D. Kamen. Photoproduction of molecular hydrogen by *Rhodospirillum rubrum*. *Science* 109 (1949): 558–559.

Ghirardi, M.L., King, P.W., Posewitz, M.C., Maness, P.C., Fedorov, A., Kim, K., Cohen, J., Schulten, K., and Seibert, M. Approaches to developing biological H_2-photoproducing organisms and pro- cesses. *Biochem. Soc. Trans*. 33 (2005): 70–72.

Ghirardi, M.L., Togasaki, R.K., and Seibert, M. Oxygen sensitivity of algal H_2-production." *Appl. Biochem. Biotechnol*. 63 (1997): 141–151.

Ghose, T.K. and Bisaria, V.S. Studies on mechanism of enzymatic hydrolysis of cellulosic substances. *Biotechnol. Bioeng*. 21(1979): 131–146.

Ginkel, S.V., Sung, S.W., and Lay, J.J. Biohydrogen production as a function of pH and substrate con- centration. *Environ. Sci. Technol*. 35 (2001): 4726–4730.

Gonzalez, J.M. and Robb, F.T. Genetic analysis of *Caboxydothemus hydrogenoformans* carbon monoxide dehydrogenase genes *CooF* and *CooS*. *FEMS Microbiol. Lett*. 191 (2000): 243–247.

Greenbaum, E. Energetic efficiency of hydrogen photoevolution by algal water splitting. *Biophys. J*. 54 (1988): 365–368.

Guo, L., Li, X.M., Bo, X., Yang, Q., Zeng, G.M., Liao, D.X. et al. Impacts of sterilization, microwave and ultrasonication pretreatment on hydrogen producing using waste sludge. *Bioresour. Technol*. 99 (2008): 3651–3658.

Gyoo, Y.J., Jung, R.K., Ji-Young, P. and Sunghoon, P. Hydrogen production by a new chemoheterotro- phic bacterium *Citrobacter sp*. Y19. *Int. J. Hydrogen Energy* 27(6) (2002): 601–610.

Hafez, H., Nakhla, G., and El Naggar, H. An integrated system for hydrogen and methane pro- duction during landfill leachate treatment. *Int. J. Hydrogen Energy* in Press, Corrected Proof (2009).

Hallenbeck, P.C. Integration of hydrogen evolving systems with cellular metabolism: The molecular biology and biochemistry of electron transport factors and associated reductases. *Biohydrogen* II (2001): 171–184.

Hallenbeck, P.C. Fermentative hydrogen production: Principles, progress, and prognosis. *Int. J. Hydrogen Energy* 34 (2009): 7379–7389.

Hallenbeck, P.C. and Benemann, J.R. Biological hydrogen production; fundamentals and limiting processes. *Int. J. Hydrogen Energy* 27 (2002): 1185–1193.

Hallenbeck, P.C., Kochian, L.V., Weissman, J.C., and Benemann, J.R. Solar energy conversion with hydrogen producing cultures of the blue-green alga, *Anabaena cylindrica*. *Biotechnol. Bioeng. Symp*. 8 (1978): 283–297.

Hamelinck, C.N., van Hooijdonk, G., and Faaij, A.P.C. Ethanol from lignocellulosic biomass: Techno- economic performance in short-, middle- and long-term. *Biomass Bioenergy* 28 (2005): 384–410.

Han, S.K. and Shin, H.S. Performance of an innovative two-stage process converting food waste to hydrogen and methane. *J. Air. Waste Manag*. 54 (2004): 242–249.

Haruta, S., Cui, Z., Huang, Z., Li, M., Ishii, M., and Igarashi, Y. Construction of a stable microbial com- munity with high cellulose-degradation ability. *Appl. Microbiol. Biotechnol*. 59 (2002): 529–534.

Hase, R., Oikawa, H., Sasao, C., Morita, M., and Watanabe, Y. Photosynthetic production of microal- gal biomass in a raceway system under greenhouse conditions in Sendai City. *J. Biosci. Bioeng*. 89 (2000): 157–163.

Heyndrickx, M., Vansteenbeeck, A., Vos, P., and deLey, L. Hydrogen gas production from continuous fermentation of glucose in a minimal medium with *Clostridium butyricum* LMG 1213tl. *Syst. Appl. Microbiol*. 8 (1986): 239–244.

Hillmer, P. and Gest, H. H_2 metabolism in photosynthetic bacterium Rhodopseudomonas capsulata: H_2 production by growing cultures. *J. Bacteriol*. 129(2) (1977): 724–731.

Hoekema, S., Bijmans, M., Janssen, M., Tramper, J., and Wijffels, R.H. A pneumatically agitated flat- panel photobioreactor with gas recirculation: Anaerobic photoheterotrophic cultivation of a purple nonsulfur bacterium. *Int. J. Hydrogen Energy* 27(2002): 1331–1338.

Hoekema, S., Douma, R.D., Janssen, M., Tramper, J., and Wijffels, R.H. Controlling light-use by *Rhodobacter capsulatus* continuous cultures in a flat-panel photobioreactor. *Biotech. Bioeng*.95(4) (2006): 613–626.

Hu, Q., Faiman, D., and Richmond, A. Optimal tilt angles of enclosed reactors for growing photoau- totrophic microorganisms outdoors. *J. Ferment. Bioeng*. 8 (1998): 230–236.

Hu, Q. and Richmond, A. Productivity and photosynthetic efficiency of *Spirulina platensis* as a1ected by light intensity, algal density and rate of mixing in a flat plate photobioreactor. *J. Appl. Phycol*. 8 (1996): 139–145.

Hussy, I., Hawkes, F.R., Dinsdale, R., and Hawkes, D.L. Continuous fermentative hydrogen produc- tion from sucrose and sugarbeet. *Int. J. Hydrogen Energy* 30 (2005): 471–483.

Ishikawa, M., Yamamura, S., Takamura, Y., Sode, K., Tamiya, E., and Tomiyama, M. Development of a compact high-density microbial hydrogen reactor for portable bio-fuel cell system. *Int. J. Hydrogen Energy* 31 (2006): 1484–1489.

Jackson, D.D. and Ellms, J.W. On odors and tastes of surface waters with special reference to ana- baena, a microscopial organism found in certain water supplies of Massachusetts. *Rep. Mass. State Board Health* (1896): 410–420.

Janssen, M. Cultivation of microalgae: Effect of light/dark cycles on biomass yield. Thesis, Wageningen University, Wageningen, the Netherlands (2002).

Janvanmardian, M. and Palsson, B.O. High density photoautotrophic algal cultures: Design, construc- tion and operation of a novel photobioreactor system. *Biotechnol. Bioeng*. 38 (1991): 1182–1189.

Jo, J.H., Lee, D.S., Park, D., and, Park, J.M. Biological hydrogen production by immobilized cells of Clostridium tyrobutyricum JM1 isolated from a food waste treatment process. *Bioresour. Technol*. 99 (2008): 6666–6672.

Jung, G.Y., Kim, J.R., Park, J.Y., and Park, S. Hydrogen production by a new chemoheterotrophic bacterium *Citrobacter* sp. Y19. *Int. J. Hydrogen Energy* 27 (2002): 601.

Kadar, Z., Vrije, T.D., van Noorden, G.E., Budde, M.A.W., Szengyel, Z., Reczey, K. et al. Yields from glucose, xylose, and paper sludge hydrolysate during hydrogen production by the extreme ther- mophile *Caldicellulosiruptor saccharolyticus. Appl. Biochem. Biotechnol*. 113–116 (2004): 497–508.

Kaewpintong, K., Shotipruk, A., Powtongsook, S., and Pavasant, P. Photoautotrophic high-density cultivation of vegetative cells of *Haematococcus pluvialis* in airlift bioreactor. *Bioresour. Technol*. 98 (2007): 288–295.

Kanai, T., Imanaka, H., Nakajima, A., Uwamori, K., Omori, Y., Fukui, T. et al. Continuous 860 hydrogen production by the hyperthermophilic archaeon, *Thermococcus kodakaraensis* KOD1. *J. Biotechnol*. 116 (2005): 271–282.

Karapinar, K.I. and Fikret, K. Bio-hydrogen production from waste materials. *Enzyme Microb. Technol.*

38 (2006): 569–582.

Kellum, R. and Drake, H.L. Effects of cultivation gas phase on hydrogenase of the acetogen *Clostridium thermoaceticum. J. Bacteriol*. 160(1) (1984): 466–469.

Kerby, R.L. Hong, S.S., Ensign, S.A., Coppoc, L.J., Ludden, P.W., and Roberts, G.P. Genetic and physi- ological characterization of the *Rhodospirillum rubrum* carbon monoxide dehydrogenase sys- tem. *J. Bacteriol*. 174(16) (1992): 5284–5294.

Kerby, R.L., Ludden, P.W., and Roberts, G.P. Carbon monoxide-dependent growth of *Rhodospirillum rubrum. J. Bacteriol*. 177 (1995): 2241.

Khanal, S.K., Chen, W.H., Li, L., and Sung, S. Biological hydrogen production: Effects of pH and intermediate products. *Int. J. Hydrogen Energy* 29 (2004): 1123–1131.

Kim, B.S. and Lee, Y.Y. Diffusion of sulfuric acid within lignocellulosic biomass particles and its impact on dilute-acid pretreatment. *Bioresour. Technol*. 8 (2002): 165–171.

Kim, M.S. An integrated system for the biological hydrogen production from organic wastes and waste-waters. Paper presented at the *International Symposium on Hydrogen and Methane Fermentation of Organic Waste*, Tokyo, Japan (2002).

Kim, M.S., Baek, J.S., and Lee, J.K. Comparison of H_2 accumulation by *Rhodobacter sphaeroides* Kd131 and its uptake hydrogenase and Phb synthase deficient mutant. *Int. J. Hydrogen Energy* 31(1) (2006a): 121–127.

Kim, M.S., Baek, J.-S., Yun, Y.-S., Jun Sim, S. et al. Hydrogen production from *Chlamydomonas rein- hardtii* biomass using a two-step conversion process: Anaerobic conversion and photosynthetic fermentation. *Int. J. Hydrogen Energy* 31(6) (2006b): 812–816.

Klasson, K.T., Lundback, K.M.O., Clausen, E.C., and Gaddy, J.L. Kinetics of light limited growth and biological hydrogen production from carbon monoxide and water by *Rhodospirillum rubrum. J. Biotechnol*. 29 (1993): 177–188.

Kok, B. Algal culture: From laboratory to pilot plant. In: Burlew, J.S. (Ed.). Carnegie Institute of Washington, Washington, DC (1953): pp. 235–272.

Kok, B. Photosynthesis. *Proceedings of the Workshop on Bio Solar Hydrogen Conversion*, September 5–6 (1973).

Koku, H., Eroglu, I., Gunduz, U., Yucel, M., and Turker, L. Aspects of the metabolism of hydrogen production by *Rhodobacter sphaeroides*. *Int. J. Hydrogen Energy* 27 (2002): 1315–1329.

Koku, H., Eroglu, I., Gunduz, U., Yucel, M., and Turker, L. Kinetics of biological hydrogen production by the photosynthetic bacterium *Rhodobacter sphaeroides* O.U. 001. *Int. J. Hydrogen Energy* 28(4) (2003): 381–388.

Kraemer, J.T. and Bagley, D.M. Continuous fermentative hydrogen production using a two-phase reactor system with recycle. *Environ. Sci. Technol*. 39(10) (2005): 3819–3825.

Kumar, N. and Das, D. Enhancement of hydrogen production by *Enterobacter cloacae* IIT-BT 08. *Process Biochem*. 35 (2000): 589–593.

Kumar, N., Ghosh, A. and Das, D. Redirection of biochemical pathways for the enhancement of H_2 production by *Enterobacter cloacae*. *Biotechnol. Lett*. 23 (2001): 537–541.

Lambert, G.R. and Smith, G.D. The hydrogen metabolism of cyanobacteria (blue-green algae). *Biol.*

Rev. 56 (1981): 589–660.

Larsson, S., Palmqvist, E., Hahn-Hägerdal, B., Tengborg, C., Stenberg, K., Zacchi, G. et al. The gen- eration of fermentation inhibitors during dilute acid hydrolysis of softwood. *Enzyme Microb. Technol*. 24 (1999): 151–159.

Lay, J. Biohydrogen generation by mesophilic anaerobic fermentation of microcrystalline cellulose.

Biotechnol. Bioeng. 74 (2001): 280–287.

Lay, J.J., Lee, Y.J., and Noike, T. Feasibility of biological hydrogen production from organic fraction of municipal solid waste. *Water Res*. 33 (1999): 2579–2586.

Lee, E.T.Y. and Bazin, M.J. A laboratory scale airlift photobioreactor to increase biomass output rate of photosynthetic algal cultures. *New Phytol*. 116 (1990): 331–335.

Lee, J.Z., Klaus, D.M., Maness, P.C., and Spear, J.R. The effect of butyrate concentration on hydrogen production via photofermentation for use in a Martian habitat resource recovery process. *Int. J. Hydrogen Energy* 32 (2007): 3301–3307.

Lee, K.S., Hsu, Y.F., Lo, Y.C. Lin, P.J., Lin, C.Y., and Chang, J.S. Exploring optimal environmental fac- tors for fermentative hydrogen production from starch using mixed anaerobic microflora. *Int. J. Hydrogen Energy* 33 (2008): 1565–1572.

Lee, K.S., Lin, P.J., and Chang, J.S. Temperature effects on biohydrogen production in a granular sludge bed induced by activated carbon carriers. *Int. J. Hydrogen Energy* 31 (2006): 465–472.

Levin, D.B., Islam, R., Cicek, N., and Sparling, R. Hydrogen production by *Clostridium thermocellum*

27405 from cellulosic biomass substrates. *Int. J. Hydrogen Energy* 31 (2006): 1496–1503.

Levin, D.B., Pitt, L., and Love, M. Biohydrogen production: Prospects and limitations to practical application. *Int. J. Hydrogen Energy* 29 (2004): 173–185.

Li, D.M. and Chen, H.Z. Biological hydrogen production from steam-exploded straw by simultane- ous saccharification and fermentation. *Int. J. Hydrogen Energy* 32 (2007): 1742–1748.

Lin, C.-Y. and Chang, R.-C. Hydrogen production during the anaerobic acidogenic conversion of glucose. *J. Chem. Technol. Biotechnol*. 74 (1999): 498–500.

Lin, C.Y. and Lay, C.H. Carbon/nitrogen ratio effect on fermentative hydrogen production by mixed microflora. *Int. J. Hydrogen Energy* 29 (2004): 41–45.

Lin, C.Y., Wu, C.C., and Hung, C.H. Temperature effects on fermentative hydrogen production from xylose using mixed anaerobic cultures. *Int. J. Hydrogen Energy* 33 (2008): 43–50.

Liu, D.W., Liu, D.P., Zeng, R.J., and Angelidaki, I. Hydrogen and methane production from house- hold solid waste in the two-stage fermentation process. *Water Res.* 40 (2006): 2230–2236.

Liu, G. and Shen, J. Effects of culture medium and medium conditions on hydrogen production from starch using anaerobic bacteria. *J. Biosci. Bioeng*. 98 (2004): 251–256.

Liu, H., Grot, S., and Logan, B.E. Electrochemically assisted microbial production of hydrogen from acetate. *Environ. Sci. Technol*. 39 (2005): 4317–4320.

Liu, H., Zhang, T., and Fang, H.H.P. Thermophilic H_2 production from a cellulose-containing waste- water. *Biotechnol. Lett*. 25 (2003): 365–369.

Liu, W.Z., Wang, A.J., Ren, N.Q., Zhao, X.Y., Liu, L.H., Yu, Z.G. et al. Electrochemically assisted bio- hydrogen production from acetate. *Energy Fuels* 22 (2008a): 159–163.

Liu, Y., Yu, P., Song, X., and Qu, Y.B. Hydrogen production from cellulose by co-culture of Clostridium thermocellum JN4 and *Thermoanaerobacterium thermosaccharolyticum* GD17. *Int. J. Hydrogen Energy* 33 (2008b): 2927–2933.

Lo, Y.C., Bai, M.D., Chen, W.M., and Chang, J.S. Cellulosic hydrogen production with a sequencing bacterial hydrolysis and dark fermentation strategy. *Bioresour. Technol*. 99(17) (2008a): 8299–8303.

Lo, Y.C., Chen, W.M., Hung, C.H., Chen, S.D., and Chang, J.S. Dark H_2 fermentation from sucrose and xylose using H_2-producing indigenous bacteria: Feasibility and kinetic studies. *Water Res*. 42 (2008): 827–842.

Logan, B., Oh, S.E., Kim, I.K., and Van Ginkel, S.W. Biological hydrogen production measured in batch anaerobic respirometers. *Environ. Sci. Technol*. 36(11) (2002): 2530–2535.

Lu, W.J., Hwang, S.J., and Chang, C.M. Liquid velocity and gas hold up in three-phase internal loop airlift reactors with low density particles. *Chem. Eng. Sci*. 50 (1995): 1301–1310.

Manish, S. and Banerjee, R. Comparison of biohydrogen production processes. *Int. J. Hydrogen Energy*

33(1) (2008): 279–286.

Markov, S.A., Bazin, M., and Hall, D.O. The potential of using cyanobacteria in photobioreactors for hydrogen production. *Adv. Biochem. Eng*. (52) (1995): 59–86.

Matsunaga, T., Takeyama, H., Sudo, H., Oyama, N., Ariura, S., Takano, H., Hirano, M., Burgess, J.G., Sode, K., and Nakamura, N. Glutamate production from CO_2 by marine cyanobacterium *Synechococcus* sp. using a novel biosolar reactor employing light diffusing optical fibers. *Appl. Biochem. Biotechnol*. 28/29 (1991): 157–167.

Mazzuca Sobczuk, T., García Camacho, F., Molina Grima, E., and Chisti, Y. Effects of agitation on the microalgae *Phaeodactylum tricornutum* and *Porphyridium cruentum*. *Bioproc. Biosyt. Eng*. 28 (2006): 243–250.

McTavish, H., Sayavedra-Soto, L.A., and Arp, D.J. Substitution of *Azotobacter vinelandii* hydrogenase small subunit cysteines by serines can create insensitivity to inhibition by O_2 and preferentially damages H_2 oxidation over H_2 evolution. *J. Bacteriol*. 177(14) (1995): 3960–3964.

Melis, A. and Happe, T. Trails of green alga hydrogen research—From Hans Gaffron to new frontiers.

Photosyn. Res. 80 (2004): 401–409.

Melis, A., Neidhardt, J., and Benemann, J.R. *Dunaliella salina* (Chlorophyta) with small chlorophyll antenna sizes exhibit higher photosynthetic productivities and photon use efficiencies than normally pigmented cells. *J. Appl. Phycol*. 10 (1999): 515–525.

Melis, A., Zhang, L., Foestier, M., Ghirardi, M.L., and Seibert, M. Sustained photobiological hydro- gen gas production upon reversible inactivation of oxygen evolution in the green alga *Chlamydomonas reinhardtii*. *Plant Physiol*. 122 (2000): 127–136.

Merchuk, J.C., Gluz, M., and Mukmenev, I. Comparison of photobioreactors for cultivation of the microalga *Porphyridium* sp. *J. Chem. Technol. Biotechnol*. 75 (2000): 1119–1126.

Milner, H.W. Rocking tray. In: Burlew, J.S. (Ed.) *Algal Culture from Laboratory to Pilot Plant*. Carnegie Institution, Washington, DC, No. 600 (1953): p. 108.

Miron, A.S., Camacho, F.G., Gomez, A.C., Grima, E.M., and Chisti, M.Y. Bubble-column and airlift photobioreactors for algal culture. *AIChE J*. 46(9) (2000): 1872–1887.

Miyake, J. The science of biohydrogen. In: *BioHydrogen*. Plenum Press, New York, 1998.

Miyake, J., Mao, X.Y., and Kawamura, S. Efficiency of light energy conversion to hydrogen by the photosynthetic bacterium *Rhodobacter sphaeroides*. *Int. J. Hydrogen Energy* 12 (1987): 1147–1149.

Molina, E., Fernández, J., Acién, F.G., and Chisti, Y. Tubular photobioreactor design for algal cultures.

J. Biotechnol. 92 (2001): 113–131.

Molina Grima, E., Acién Fernández, F.G., García Camacho, F., and Chisti, Y. Photobioreactors: Light regime, mass transfer, and scale up. *J. Biotechnol*. 70 (1999): 231–247.

Mononmani, H.K. and Sreekantiah, K.R. Saccharification of sugarcane bagasse with enzymes from

Aspergillus ustus and *Trichoderma viride. Enzyme Microb. Technol*. 9 (1987): 484–488.

Mori, K. Photoautotrophic bioreactor using visible solar rays condensed by Fresnel lenses and trans- mitted through optical fibers. *Biotechnol. Bioeng. Symp*. 15 (1985): 331–345.

Mosier, N., Wyman, C., Dale, B., Elander, R., Lee, Y.Y., Holtzapple, M. et al. Features of promising technologies for pretreatment of lignocellulosic biomass. *Bioresour. Technol*. 96 (2005): 673–686.

Mu, Y., Wang, G., and Yu, H.Q. Response surface methodological analysis on biohydrogen produc- tion by enriched anaerobic cultures. *Enzyme Microb. Technol*. 38 (2006): 905–913.

Murray, W.D. Symbiotic relationship of *Bacteroides cellulosolvens* and *Clostridium saccharolyticum* in cellulose fermentation. *Appl. Environ. Microbiol*. 51 (1986): 710–714.

Mussatto, S.I. and Roberto, I.C. Alternatives for detoxification of diluted-acid lignocellulosic hydro- lyzates for use in fermentative processes: A review. *Bioresour. Technol*. 93 (2004): 1–10.

Myers, J. Algal culture. In: *Encyclopedia of Chemical Technology*. New York (1957): pp. 649–680. Najafpour, G., Younesi, H., and Mohamed, A.R. Effect of organic substrate on hydrogen produc-

tion from synthesis gas using *Rhodospirillum rubrum* in batch culture. *Biochem. Eng. J*. 21 (2004): 123–130.

Nakajima, Y., Tsuzuki, M., and Ueda, R. Improved productivity by reduction of the content of light harvesting pigment in *Chlamydomonas perigranulata. J. Appl. Phycol*. 13 (2001): 95–101.

Nakajima, Y. and Ueda, R. Improvement of microalgal photosynthetic productivity by reducing the content of light harvesting pigment. *J. Appl. Phycol*. 11 (1999): 195–201.

Nakajima, Y. and Ueda, R. The effect of reducing light-harvesting pigment on marine microalgal productivity. *J. Appl. Phycol*. 12 (2000): 285–290.

Nakashimada, Y., Rachman, M.A., Kakizono, T., and Nishio, N. Hydrogen production of *Enterobacter aerogenes* altered by extracellular and intracellular redox states. *Int. J. Hydrogen Energy* 27 (2002): 1399–1405.

Narihiro, T. and Sekiguchi, Y. Microbial communities in anaerobic digestion processes for waste and wastewater treatment: A microbiological update. *Curr. Opin Biotechnol*. 18 (2007): 273–278.

Nath, K., Kumar, A., and Das, D. Hydrogen production by *Rhodobacter sphaeroides* strain O.U.001 using spent media of Enterobacter cloacae strain Dm11. *Appl. Microbiol. Biotechnol*. 68 (2005): 533–541.

Neidhardt, J., Benemann, J.R., Baroli, I., and Melis, A. Maximizing photosynthetic productivity and light utilization in microalgae by minimizing the light-harvesting chlorophyll antenna size of the photosystems. *Photosyn. Res*. 56 (1998): 175–184.

Nguyen, Q., Tucker, M., Boynton, B., Keller, F., and Schell, D. Dilute acid pretreatment of softwoods.

Appl. Biochem. Biotechnol. (1998): 77–87.

van Niel, E.W.J., Budde, M.A.W., de Haas, G.G., van der Wal, F.J., Claassen, P.A.M., and Stams, A.J.M. Distinctive properties of high hydrogen producing extreme thermophiles, *Caldicellulosiruptor saccharolyticus* and *Thermotoga elfii. Int. J. Hydrogen Energy* 27 (2002): 1391–1398.

van Niel, E.W.J., Claassenb, P.A.M., and Stamsa, A.J.M. Substrate and product inhibition of hydrogen production by the extreme thermophile, *Caldicellulosiruptor saccharolyticus. Biotechnol. Bioeng*. 81 (2003): 255–262.

Noike, T. Biological hydrogen production of organic wastes-development of the two-phase hydrogen production process. Paper presented at the *International Symposium on Hydrogen and Methane Fermentation of Organic Waste*, Tokyo, Japan (March 2002).

Ntaikou, I., Gavala, H.N., Kornaros, M., and Lyberatos, G. Hydrogen production from sugars and sweet sorghum biomass using *Ruminococcus albus. Int. J. Hydrogen Energy* 33 (2008): 1153–1163. Ogbonna, J.C., Soejima, T., and Tanaka, H. Development of efficient large scale photobioreactors. In:

Zaborosky, O.R. (Ed.), *Biohydrogen*. Plenum Press, New York (1998): pp. 329–343.

Ogbonna, J.C., Soejima, T., and Tanaka, H. An integrated solar and artificial light system for internal illumination of photobioreactors. *J. Biotechnol*. 70 (1999): 289–297.

Ogbonna, J.C. and Tanaka, H. Photobioreactor design for photobiological production of hydro- gen. In: Miyake, J., Matsunaga, T., and San Pietro, A. (Eds.), *Biohygrogen II – An Approach to Environmentally Acceptable Technology*. Pergamon Press, London, U.K. (2001): pp. 245–261.

Oh, Y.K., Kim, H.J., Park, S., Kim, M.S., and Ryu, D.D.Y. Metabolic-flux analysis of hydrogen produc- tion pathway in *Citrobacter amalonaticus* Y19. *Int. J. Hydrogen Energy* 33 (2008): 1471–1482.

Olaizola, M. Commercial production of astaxanthin from *Haematococcus pluvialis* using 25,000-liter outdoor photobioreactors. *J. Appl. Phycol*. 12(2000): 499–506.

Palmqvist, E. and Hahn-Hägerdal, B. Fermentation of lignocellulosic hydrolysates. I: Inhibition and detoxification. *Bioresour. Technol*. 74 (2000a): 17–24.

Palmqvist, E. and Hahn-Hägerdal, B. Fermentation of lignocellulosic hydrolysates. II: Inhibitors and mechanisms of inhibition. *Bioresour. Technol*. 74 (2000b): 25–33.

Pampulha, M.E. and Lourero-Dias, M.C. Combined effect of acetic acid, pH, and ethanol on intracel- lular pH of fermenting yeast. *Appl. Microb. Biotechnol*. 31 (1989): 547–550.

Pan, X.J., Arato, C., Gilkes, N., Gregg, D., Mabee, W., Pye, K. et al. Biorefining of softwoods using ethanol organosolv pulping: Preliminary evaluation of process streams for manufacture of fuel- grade ethanol and co-products. *Biotechnol. Bioeng*. 90 (2005): 473–481.

Pezacha, E. and Wood, H.G. The synthesis of acetyl-coA by *Clostridium thermoaceticum* from carbon dioxide, hydrogen, coenzyme A, and methyltetrahydrofolate. *Arch. Microbiol*. 137 (1984): 63–69.

Philips, J.R., Clausen, E.C., and Gaddy, J.L. Synthesis gas as substrate for the biological production of fuels and chemicals. *Appl. Biochem. Biotechnol*. 45–46 (1994): 145–156.

Pin-Ching, M. and Weaver, P.F. Biological H_2 from fuel gasses and from H_2O. *Proceedings of the 2000 DOE Hydrogen Production Review*, NREL/CP-570-28890 (2000).

Pirt, S.J., Lee, Y.K., Walach, M.R., Pirt, M.W., Balyuzi, H.H.M., and Bazin, M.J. A tubular photobiore- actor for photosynthetic production of biomass from carbon dioxide: Design and performance.

J. Chem. Tech. Biotechnol. 33B (1983): 35–38.

Planchard, A., Mignot, L., Jouenne, T., and Junter, G.A. Photoproduction of molecular hydrogen by *Rhodospirillum rubrum* immobilized in composite agar layer/microporous membrane structure. *Appl. Microbiol. Biotechnol*. 31 (1989): 49–54.

Pohl, P., Kohlhase, M., and Martin, M. Photobioreactors for the axenic mass cultivation of microal- gae. In: Stadler, T., Mollion, J., Verdus, M.C., Karamanos, Y., Morvan, H., and Christiaen, D. (Eds.), *Algal Biotechnology*. Elsevier Applied Science, New York (1988): pp. 209–217.

Pruvost, J., Pottier, L., and Legrand, J. Numerical investigation of hydrodynamic and mixing condi- tions in a torus photobioreactor. *Chem. Eng. Sci*. 61 (2006): 4476–4489.

Ramos de Ortega, A. and Roux, J.C. Production of Chlorella biomass in different types of flat bioreac- tors in temperate zones. *Biomass* 10 (1986): 141–156.

Redding, K., Cournac, L., Vassiliev, I., Golbeck, J., Peltier, G., and Rochaix, J.D. Photosystem I is required for photoautotrophic growth, Co_2 fixation, and H_2 photoevolution in *Chlamydomonas reinhardtii. J. Biol. Chem*. 274(104) (1999): 66–73.

Reith, J.H., Wijffels, R.H., and Barten, H. Bio-methane & bio-hydrogen: Status and perspectives of biological methane and hydrogen production. *Dutch Biol. Hydrogen Found*. (2003): ISBN: 90-9017165-7.

Ren, N. et al. Bioconversion of lignocellulosic biomass to hydrogen: Potential and challenges.

Biotechnol. Adv. (2009): doi:10.1016/j.biotechadv.2009.05.007.

Ren, N.Q., Wang, B.Z., and Huang, J.C. Ethanol type fermentation from carbohydrate in high rate acidogenic reactor. *Biotechnol. Bioeng*. 54 (1997): 428–433.

Richmond, A. Efficient utilization of high irradiance for production of photoautotrophic cell mass: A survey. *J. Appl. Phycol*. 8 (1996): 381–387.

Richmond, A. Microalgal biotechnology at the turn of the millennium: A personal view. *J. Appl.*

Phycol. 12 (2000): 441–451.

Richmond, A., Boussiba, S., Vonshak, A., and Kopel, R. A new tubular reactor for mass production of microalgae outdoors. *J. Appl. Phycol*. 5 (1993): 327–332.

Rosenkranz, A. and Krasna, A.J. Stimulation of hydrogen photoproduction in algae by removal of oxygen by reagents that combine reversibly with oxygen. *Biotechnol. Bioeng*. 26(11) (1984): 1334–1342.

Rozendal, R.A., Hamelers, H.V.M., Euverink, G.J.W., Metz, S.J., and Buisman, C.J.N. Principle and perspectives of hydrogen production through biocatalyzed electrolysis. *Int. J. Hydrogen Energy* 31 (2006): 1632–1640.

Rozendal, R.A., Hamelersm, H.V.M., Molenkamp, R.J., and Buisman, C.J.N. Performance of single chamber biocatalyzed electrolysis with different types of ion exchange membranes. *Water Res*. 41 (2007): 1984–1994.

Rozendal, R.A., Jeremiasse, A.W., Hamelers, H.V.M., and Buisman, C.J.N. Hydrogen production with a microbial biocathode. *Environ. Sci. Technol*. 42(2) (2008): 629–634.

Samson, R. and Leduy, A. Multistage continuous cultivation of blue-green alga *Spirulina maxima* in the flat tank photobioreactors. *Can. J. Chem. Eng*. 63 (1985): 105–112.

Sánchez Miron, A., Cerón García, M.C., García Camacho, F., Molina Grima, E., and Chisti, Y. Growth and characterization of microalgal biomass produced in bubble column and airlift photobiore- actors: Studies in fed-batch culture. *Enzyme Microb. Technol*. 31 (2002): 1015–1023.

Sato, T., Usui, S., Tsuchiya, Y., and Kondo, Y. Invention of outdoor closed type photobioreactor for microalgae. *Energy Convers. Manage*. 47 (2006): 791–799.

Schulz, R. Hydrogenases and hydrogen production in eukaryotic organisms and cyanobacteria.

J. Mar. Biotechnol. 4 (1996): 15–22.

Shin, H.S., Youn, J.H., and Kim, S.H. Hydrogen production from food waste in anaerobic mesophilic and thermophilic acidogenesis. *Int. J. Hydrogen Energy* 29 (2004): 1355–1363.

Soboh, B., Linder, D., and Hedderich, R. Purification and catalytic properties of a CO-oxidizing: H_2-evolving enzyme complex from *Carboxydothermus hydrogenoformans. Eur. J. Biochem*. 269 (2002): 5712.

Spruit, C.J.P. Simultaneous photoproduction of hydrogen and oxygen by *Chlorella. Meded Landbouwhogesch Wageningen* 58 (1958): 1–17.

Sreenath, H.K. and Jeffries, T.W. Batch and membrane-assisted cell recycling in ethanol production by *Candida shehatae. Biotechnol. Lett*. 9 (1987): 293–298.

Sternberg, D. Production of cellulase by trichoderma. *Biotechnol. Bioeng. Symp*. (1976): 35–53. Strickland, L.H. The bacterial decomposition of formate. *Biochem. J*. 23 (1929): 1187.

Sun, Y. and Cheng, J. Hydrolysis of lignocellulosic materials for ethanol production: A review.

Bioresour. Technol. 83 (2002): 1–11.

Taguchi, F., Mizukami, N., Hasegawa, K, and Saito-Taki, T. Microbial conversion of arabinose and xylose to hydrogen by a newly isolated *Clostridium* sp. No. 2. *Can. J. Microbiol*. 40 (1994): 228–233.

Taguchi, F., Mizukami, N., Saito-Taki, T., and Hasegawa, K. Hydrogen production from continuous fermentation of xylose during growth of *Clostridium* sp. strain no. 2. *Can. J. Microbiol*. 41 (1995): 536–540.

Taguchi, F., Mizukami, N., and Yamada, K., Hasegawa, K., and Saito-Taki, T. Direct conversion of cel- lulosic materials to hydrogen by *Clostridium* sp. strain no. 2. *Enzyme Microb. Technol*. 17 (1993): 147–150.

Taguchi, F., Yamada, K., Hasegawa, K., Taki-Saito, T., and Hara, K. Continuous hydrogen production by *Clostridium* sp. Strain No. 2 from cellulose hydrolysate in an aqueous two-phase system. *J. Ferment. Bioeng*. 82 (1996): 80–83.

Taherzadeh, M.J., Gustafsson, L., Niklasson, C., and Lidén, G. Inhibition effects of furfural on aerobic batch cultivation of *Saccharomyces cerevisiae* growing on ethanol and/or acetic acid. *J. Biosci. Bioeng*. 90 (2000): 374–380.

Talabardon, M., Schwitzguebel, J.P., and Peringer, P. Anaerobic thermophilic fermentation for acetic acid production from milk permeate. *J. Biotechnol*. 76 (2000): 83–92.

Tanisho, S. and Ishiwata, Y. Continuous hydrogen production from molasses by fermentation using urethane foam as a support of flocks. *Int. J. Hydrogen Energy* 20 (1995): 541–545.

Tanisho, S., Kuromoto, M., and Kadokura, N. Effect of CO2 removal on hydrogen production by fermentation. *Int. J. Hydrogen Energy* 23(7) (1998): 559–563.

Tanisho, S., Suzuki, Y., and Wakao, N. Fermentative hydrogen evolution by *Enterobacter aerogenes*

strain E.82005. *Int. J. Hydrogen Energy* 12 (1987): 623–627.

Tao, Y., Chen, Y., Wu, Y., He, Y., and Zhou, Z. High hydrogen yield from a two-step process of dark- and photo-fermentation of sucrose. *Int. J. Hydrogen Energy* 32 (2007): 200–206.

Thimijan, R.W. and Heins, R.D. Photometric, radiometric and quantum light units of measure: A review of procedures for interconversion. *Hort. Sci*. 18(6) (1983): 818–822.

Ting, C.H. and Lee, D.J. Production of hydrogen and methane from wastewater sludge using anaero- bic fermentation. *Int. J. Hydrogen Energy* 32 (2007): 677–682.

Ting, C.H., Lin, K.R., Lee, D.J., and Tay, J.H. Production of hydrogen and methane from wastewater sludge using anaerobic fermentation. *Water Sci. Technol*. 50 (2004): 223–228.

Torzillo, G., Accolla, P., Pinzani, E., and Masojidek, J. In situ monitoring of chlorophyll fluorescence to assess the synergistic of low temperature and high irradiance stresses in Spirulina cultures grown outdoors in photobioreactors. *J. Appl. Phycol*. 8 (1996): 283–291.

Torzillo, G., Pushparaj, B., Bocci, F., Balloni, W., Materassi, R., and Florenzano, G. Production of Spirulina biomass in closed photobioreactors. *Biomass* 11 (1986): 61–74.

Tredici, M.R. and Chini Zittelli, G. Efficiency of sunlight utilization: Tubular versus flat photobioreac- tors. *Biotechnol. Bioeng*. 57 (1998): 187–197.

Tredici, M.R. and Materassi, R. From open ponds to vertical alveolar panels: The Italian experience in the development of reactors for the mass cultivation of photoautotrophic microorganisms. *J. Appl. Phycol*. 4 (1992): 221–231.

Tredici, M.R., Zittelli, G.C., and Benemann, J.R. A tubular internal gas exchange photobioreactor for biological hydrogen production. *BioHydrogen* (1998): 391–402.

Turcot, J., Bisaillon, A., and Hallenbeck, P.C. Hydrogen production by continuous cultures of

Escherichia coli under different nutrient regimes. *Int. J. Hydrogen Energy* 33 (2008): 1465–1470.

Turpin, D.H., Layzell, D.B., and Elrifi, I.R. Modeling the carbon economy of *Anabaena flos-aquae. Plant*

Physiol. 78(4) (1985): 746–752.

Ueno, Y., Fukui, H., and Goto, M. Operation of a two-stage fermentation process producing hydro- gen and methane from organic waste. *Environ. Sci. Technol*. 41(4) (2007): 1413–1419.

Ueno, Y., Morimoto, M., Otsuka, S., Kawai, T., and Sato, S. Process for the production of hydrogen by microorganisms. US Patent 5 (1995): 464–539.

Ueno, Y., Otsuka, S., and Morimoto, M. Hydrogen production from industrial wastewater by anaero- bic microflora in chemostat culture. *J. Ferment. Bioeng*. 82 (1996): 194–197.

Ueno, Y., Tatara, M., Fukui, H., Makiuchi, T., Goto, M., and Sode, K. Production of hydrogen and methane from organic solid wastes by phase-separation of anaerobic process. *Bioresour. Technol*. 98(9) (2007): 1861–1815.

Ugwu, C.U., Aoyagi, H., and Uchiyama, H. Review: Photobioreactors for mass cultivation of algae.

Bioresour. Technol. 99 (2008): 4021–4028.

Ugwu, C.U., Ogbonna, J.C., and Tanaka, H. Improvement of mass transfer characteristics and pro- ductivities of inclined tubular photobioreactors by installation of internal static mixers. *Appl. Microbiol. Biotechnol*. 58 (2002): 600–607.

Ugwu, C.U., Ogbonna, J.C., and Tanaka, H. Design of static mixers for inclined tubular photobioreac- tors. *J. Appl. Phycol*. 15 (2003): 217–223.

Ugwu, C.U., Ogbonna, J.C., and Tanaka, H. Light/dark cyclic movement of algal cells in inclined tubular photobioreactors with internal static mixers for efficient production of biomass. *Biotechnol. Lett*. 27 (2005a): 75–78.

Ugwu, C.U., Ogbonna, J.C., and Tanaka, H. Characterization of light utilization and biomass yields of *Chlorella sorokiniana* in inclined outdoor tubular photobioreactors equipped with static mixers. *Proc. Biochem*. 40 (2005b): 3406–3411.

Vandu, C.O., Liu, H., and Krishna, R. Mass transfer from Taylor bubbles rising in single capillaries.

Chem. Eng. Sci. 60 (1993): 6430–6437.

Van Ginkel, S.W., Oh, S.E., and Logan, B.E. Biohydrogen gas production from food processing and domestic wastewaters. *Int. J. Hydrogen Energy* 30(15) (2005): 1535–1542.

Vega Estrada, J., Montes Horcasitas, M.C., Dominígues Bocanegra, A.R., and Cañizares Villanueva, R.O. *Haematococcus pluvialis* cultivation in split-cylinder internal-loop airlift photobioreactor under aeration conditions avoiding cell damage. *Appl. Microbiol. Biotechnol*. 68 (2005): 31–35.

Vignais, P.M. and Colbeau, A. Molecular biology of microbial hydrogenases. *Curr. Issues Mol. Biol*.

6 (2004): 159–188.

Vonshak, A. and Torzillo, G. Environmental stress physiology. In Richmond, A. (Ed.), *Handbook of Microalgal Culture*. Blackwell Publishers, Oxford, U.K. (2004): pp. 57–82.

de Vrije, T., de Haas, G.G., Tan, G.B., Keijsers, E.R.P., and Claassen, P.A.M. Pretreatment of Miscanthus for hydrogen production by *Thermotoga elfii. Int. J. Hydrogen Energy* 27 (2002): 1381–1390.

Wakayama, T., Toriyama, A., Kawasugi, T., Arai, T., Asada, Y., and Miyake, J. Photohydrogen produc- tion using photosynthetic bacterium *Rhodobacter sphaeroides* Rv: Simulation of the light cycle of natural sunlight using an artificial source. *Biohydrogen* (1998).

Wang, A.J., Ren, N.Q., Shi, Y.J., and Lee, D.J. Bioaugmented hydrogen production from microcrystal- line cellulose using co-culture-*Clostridium acetobutylicum* X9 and *Ethanoigenens harbinense* B49. *Int. J. Hydrogen Energy* 33 (2008): 912–917.

Wang, C.C., Chang, C.W., Chu, C.P., Lee, D.J., Chang, B.V., and Liao, C.S. Producing hydrogen from wastewater sludge by *Clostridium bifermentans. J. Biotechnol*. 102 (2003a): 83–92.

Wang, C.C., Chang, C.W., Chu, C.P., Lee, D.J., Chang, B.V., Liao, C.S., and Tay, J.H. Using filtrate of waste biosolids to effectively produce bio-hydrogen by anaerobic fermentation. *Water Res*. 37(11) (2003b): 2789–2793.

Wang, G., Mu, Y., and Yu, H.Q. Response surface analysis to evaluate the influence of pH, tem- perature and substrate concentration on the acidogenesis of sucrose-rich wastewater. *Biochem. Eng. J*. 23 (2005): 175–184.

Wang, J.L. and Wan, W. Effect of temperature on fermentative hydrogen production by mixed cul- tures. *Int. J. Hydrogen Energy* 33 (2008): 5392–5397.

Wang, X.J., Ren, N.Q., Xiang, W.S., and Guo, W.Q. Influence of gaseous end-products inhibition and nutrient limitations on the growth and hydrogen production by hydrogen-producing fermen- tative bacterial B49. *Int. J. Hydrogen Energy* 32 (2007): 748–754.

Watanabe, Y. and Saiki, H. Development of photobioreactor incorporating *Chlorella* sp. for removal of CO_2 in stack gas. *Energy Convers. Manage*. 38 (1997): 499–503.

Weare, N.M. and Benemann, J.R. Nitrogen fixation by *Anabaena cylindrica*. I. Localization of nitrogen fixation in the heterocysts. *Arch. Mikrobiol*. 90 (1973): 323–332.

Weissman, J.C. and Benemann, J.R. Hydrogen production by nitrogen-fixing cultures of *Anabaena cylindrica. Appl. Environ. Microbiol*. 33 (1977): 123–131.

Weissman, J.C., Goebel, R.P., and Benemann, J.R. Photobioreactor design: Comparison of open ponds and tubular reactors. *Biotechnol. Bioeng*. 31 (1988): 336–344.

Wilde, E.W. and Benemann, J.R. Bioremoval of heavy metals by the use microalgae. *Biotechnol. Adv*.

11 (2005): 781–812.

Wolfrum, E.J. and Maness, P. Biological water gas shift. *U.S. DOE Hydrogen, Fuel Cell and Infrastructure Technologies Program Review;* May 19–22, 2003. Berkeley, CA (2003).

Wolfrum, E.J. and Watt, A.S. Bioreactor design studies for a novel hydrogen-producing bacterium. *Proceedings of the 2001 U.S. DOE Hydrogen Program Review. NREL/CP-570-30535*. National Renewable Energy Laboratory, Golden, CO (2001).

Wolfrum, E.J., Watt, A.S., and Huang, J. Bioreactor development for biological hydrogen produc- tion. *Proceedings of the 2002 U.S. DOE Hydrogen Program Review. NREL/CP-610-32405*. National Renewable Energy Laboratory, Golden, CO (2002).

Wongsuchoto, P., Charinpanitkul, T., and Pavasant, P. Bubble size distribution and gas–liquid mass transfer in airlift contactors. *Chem. Eng. J*. 92 (2003): 81–90.

Wu, K.J. and Chang, J.S. Batch and continuous fermentative production of hydrogen with anaerobic sludge entrapped in a composite polymeric matrix. *Proc. Biochem*. 42 (2007): 279–284.

Wyman, C.E. Ethanol from lignocellulosic biomass: Technology, economies, and opportunities.

Bioresour. Technol. 50 (1994): 3–15.

Xing, D.F., Ren, N.Q., Li, Q.B., Lin, M., and Wang, A. *Ethanoligenens harbinense* gen nov., sp. nov., isolated from molasses wastewater. *Int. J. Syst. Evol. Microbiol*. 56 (2006): 755–760.

Yang, B. and Wyman, C.E. Effect of xylan and lignin removal by batch and flow through pretreat- ment on the enzymatic digestibility of corn stover cellulose. *Biotechnol. Bioeng*. 86 (2004): 88–95. Yang, B. and Wyman, C.E. Pretreatment: The key to unlocking low-cost cellulosic ethanol. *Biofuels Bioprod. Biorefining* 2 (2008): 26–40.

Yetis, M., Gunduz, U., Eroglu, I., Yucel, M., and Turker, L. Photoproduction of hydrogen from sugar refinery wastewater by *Rhodobacter sphaeroides* O.U. 001. *Int. J. Hydrogen Energy* 25(11) (2000): 1035–1041.

Yokoi, H., Maki, R., Hirose, J., and Hayashi, S. Microbial production of hydrogen from starch manu- facturing wastes. *Biomass Bioenergy* 22 (2002): 389–395.

Yokoi, H., Ohkawara, T., Hirose, J., Hayashi, S., and Takasaki, Y. Characteristics of hydrogen produc- tion by aciduric *Enterobacter aerogenes* strain Ho-39. *J. Ferment. Bioeng*. 80 (1995): 571–574.

Yokoi, H., Tokushige, T., Hirose, J., Hayashi, S., and Takasaki, Y., H_2 production from starch by a mixed culture of *Clostridium butyricum* and *Enterobacter aerogenes. Biotechnol. Lett*. 20 (1998): 143–147.

Yokoyama, H., Waki, M., Moriya, N., Yasuda, T., Tanaka, Y. and Haga, K. Effect of fermentation tem- perature on hydrogen production from cow waste slurry by using anaerobic microflora within the slurry. *Appl. Microbiol. Biotechnol*. 74 (2007): 474–483.

Yu, H.Q., Zhu, Z.H., Hu, W.R., and Zhang, H.S. Hydrogen production from rice wastewater in an upflow anaerobic reactor by using mixed anaerobic cultures. *Int. J. Hydrogen Energy* 27 (2002): 1359–1365.

Yu, J. and Takahashi, P. Biophotolysis-based hydrogen production by cyanobacteria and green micro- algae. *Commun. Curr. Res. Educ. Top. Trends Appl. Microbiol*. (2007): 79–89.

Zhang, H., Bruns, M.A., and Logan, B.E. Biological hydrogen production by *Clostridium acetobutyli- cum* in an unsaturated flow reactor. *Water Res*. 40 (2006): 728–734.

Zhang, K., Kurano, N., and Miyachi, S. Optimized aeration by carbon dioxide gas for microalgal production and mass transfer characterization in a vertical flat-plate photobioreactor. *Bioproc. Biosys. Bioeng*. 25 (2002): 97–101.

Zhang, M.L., Fan, Y.T., Xing, Y., Pan, C.M., Zhang, G.S., and Lay, J.J. Enhanced biohydrogen pro- duction from cornstalk wastes with acidification pretreatment by mixed anaerobic cultures. *Biomass Bioenergy* 31 (2007): 250–254.

Zhang, T., Liu, H., and Fang, H.H.P. Biohydrogen production from starch in wastewater under ther- mophilic conditions. *J. Environ. Manag*. 69 (2003): 149–156.

Zhu, H., Ueda, S., Asada, Y., and Miyake, J. Hydrogen production as a novel process of wastewater treatment—Studies on Tofu wastewater with entrapped *R. sphaeroides* and mutagenesis. *Int. J. Hydrogen Energy* 27 (11–12) (2002): 1349–1157.

Zhu, H.G., Stadnyk, A., Béland, M., and Seto, P. Co-production of hydrogen and methane from potato waste using a two-stage anaerobic digestion process. *Bioresour. Technol*. 99 (2008): 5078–5084.

Zhu, H.G., Suzuki, T., Tsygankov, A.A., Asada, Y., and Miyake, J. Hydrogen production from tofu wastewater by *Rhodobacter sphaeroides* immobilized in agar gels. *Int. J. Hydrogen Energy* 24 (1999): 305.

11

Photobiological Hydrogen Production

Laurent Pilon
University of California, Los Angeles

Halil Berberoğlu
University of Texas at Austin

CONTENTS

11.1 Introduction 370
11.1.1 Motivation 370
11.1.2 Current Hydrogen Production and Usage 371
11.1.3 Sustainable Hydrogen Production Technologies 371
11.1.4 Solar Radiation 372
11.1.5 Scope of This Chapter 374
11.2 Photosynthesis 374
11.2.1 Photosynthetic Apparatus and Light-Harvesting Pigments 376
11.2.1.1 Chlorophylls and Bacteriochlorophylls 376
11.2.1.2 Carotenoids 377
11.2.1.3 Phycobiliproteins 377
11.2.2 Anoxygenic and Oxygenic Photosynthesis 378
11.2.2.1 Electron Transport in Anoxygenic Photosynthesis 378
11.2.2.2 Electron Transport in Oxygenic Photosynthesis 380
11.3 Microbiology of Photobiological Hydrogen Production 380
11.3.1 Hydrogen-Producing Microorganisms 380
11.3.1.1 Green Algae 382
11.3.1.2 Cyanobacteria 382
11.3.1.3 Purple Nonsulfur Bacteria 384
11.3.1.4 Dark Fermentative Bacteria 384
11.3.2 Enzymatic Pathways 385
11.3.2.1 Enzyme Systems 385
11.3.2.2 Pathways for Biological Hydrogen Production 387
11.3.3 Performance Assessment and Units 389
11.3.3.1 Microorganism Concentration 389
11.3.3.2 Hydrogen Production Rate 390
11.3.3.3 Illumination 390
11.3.3.4 Light-to-Hydrogen Energy Conversion Efficiency 391
11.4 Photobioreactor Systems 391
11.4.1 Photobioreactor Types 391
11.4.2 Closed Outdoor Photobioreactor Designs and Performances 393
11.4.3 Microorganism and Photobioreactor Performances 395

11.4.4 Simulating Photobioreactors 395
11.4.4.1 Simulating Light Transfer 395
11.4.4.2 Simulating Hydrodynamic Conditions 399
11.5 Technical Challenges and Limitations 401
11.5.1 Light Transfer 401
11.5.2 Mass Transfer and Hydrodynamics 402
11.5.3 Nutrient Composition 403
11.5.4 Thermal Management 403
11.5.5 Sterility and Monoculture 403
11.5.6 Freshwater Consumption 403
11.6 Prospects 404
11.6.1 Bioengineering of Microorganisms 404
11.6.1.1 Truncating the Light-Harvesting Antenna 404
11.6.1.2 Oxygen-Tolerant Enzymes 405
11.6.1.3 Eliminating the Expression of Uptake Hydrogenase 406
11.6.1.4 Inserting Proton Channels in Photosynthetic (Thylakoid) Membranes ... 407
11.6.2 Process Optimization 407
11.6.2.1 Symbiotic and Mixed Cultures 407
11.6.2.2 Advanced Light Delivery Systems 408
11.6.2.3 Immobilized Cell Photobioreactors 408
11.7 Economic and Environmental Considerations 409
11.7.1 Economic Analysis 409
11.7.2 Environmental Impacts 410
11.8 Conclusion 411
References 412

11.1 Introduction

11.1.1 Motivation

Industrial and developing nations are facing an unprecedented combination of economic, environmental, and political challenges. First, they face the formidable challenge to meet ever-expanding energy needs without further impacting the climate and the environment. Second, the continued population growth in developing countries and the emergence of a global economy are creating unprecedented stress on the resources of the Earth. Emerging countries are claiming access to the same standard of living as industrial nations, resulting in large needs for energy sources, fast and reliable transportation systems, and industrial equipment. From the standpoint of international security, energy issues include the potential for conflict over access to remaining supplies of inexpensive fossil fuels, which are often concentrated in politically unstable regions.

Currently, fossil fuels supply more than 81% of the world's energy needs estimated at about 137 PWh/year (1 PW = 1^{15} W) or 493 EJ/year (1 EJ = 10^{18} J) [1]. Oil meets more than 92% of the world transportation energy needs [1]. However, its production is expected to peak between 2000 and 2050 after which its production will enter a terminal decline [2–5]. Simultaneously, the world energy consumption is expected to grow by 50% between 2005 and 2030 [5]. Thus, the end of easily accessible and inexpensive oil is approaching.

Moreover, intensive use of fossil fuels increases concentrations of carbon dioxide (CO_2) in the atmosphere, and their contribution to world climate changes is a topic of worldwide concerns [6]. For example, 71.4% of the electricity consumed in the United States is generated from fossil fuel, especially coal [7], making the United States responsible for about 21% of the world CO_2 emission in 2005 [8]. It is predicted that atmospheric CO_2 levels above 450 ppm will have severe impacts on sea levels, global climate patterns, and survival of many species and organisms [6].

Consequently, the growing energy needs will necessitate much greater reliance on a combination of fossil fuel–free energy sources and on new technologies for capturing and converting CO_2. Hydrogen offers a valuable alternative as an energy carrier for stationary and mobile power generation. It has much larger gravimetric energy content than fossil fuels [9]. In addition, its combustion with oxygen does not produce CO_2 but simply water vapor.

11.1.2 Current Hydrogen Production and Usage

Hydrogen is not a fuel but an energy carrier; as such, it is as clean as the production method. Worldwide, 48% of hydrogen is currently produced by steam reforming, partial oxidation, or autothermal reforming of natural gas, 30% from petroleum refining, and 18% from coal gasification [10]. However, all these thermochemical processes require fossil fuel and produce CO_2. The remaining 4% of hydrogen is produced via water electrolysis [11]. This technology used to be the most common process for hydrogen production, but it now represents a small fraction of the world's production. It is used mainly for producing high-purity hydrogen. Thus, current H_2 production fails to address outstanding issues related to depleting oil reserves, energy security, and global warming.

In 2005, 45% of the US hydrogen production was used in oil refineries and 38% in the ammonia industry [10]. It is also used in rocket propulsion applications [12]. In the future, hydrogen could be used in different energy conversion systems such as (1) internal combustion engines for surface transportation [13], (2) high-pressure H_2/O_2 steam generators for power generation [14–16], and (3) proton exchange membrane (PEM) fuel cells [17]. The demand for hydrogen is expected to increase significantly in the next decades as these technologies become more affordable and reliable.

11.1.3 Sustainable Hydrogen Production Technologies

Several technologies offer the advantage of producing hydrogen in a sustainable manner without either relying on fossil fuels or producing carbon dioxide. They can be listed as follows:

1. *Water electrolysis* can be performed using electricity generated in a sustainable manner, by photovoltaic solar cells, for example. Both photovoltaics and electro- lyzers are very expensive and cost remains the major challenge of this technology. Typical efficiency of such a system is less than 8% [10]. Alternatively, wind electrol- ysis uses electricity generated from wind energy to carry out water electrolysis.
2. *Photoelectrochemical* hydrogen production uses catalysts that absorb solar radia- tion and generate large current densities on the order of 10–30 mA/cm^2 [18]. This enables the water-splitting reactions to take place at a significantly lower voltage than conventional electrolysis. Research results for the development of photoelec- trochemical water-splitting systems have shown a solar-to-hydrogen efficiency of 12.4% for the lower heating value (LHV) of hydrogen using concentrated sunlight [10]. Catalyst stability and large band gap are the current challenges to be overcome in this technology [10].

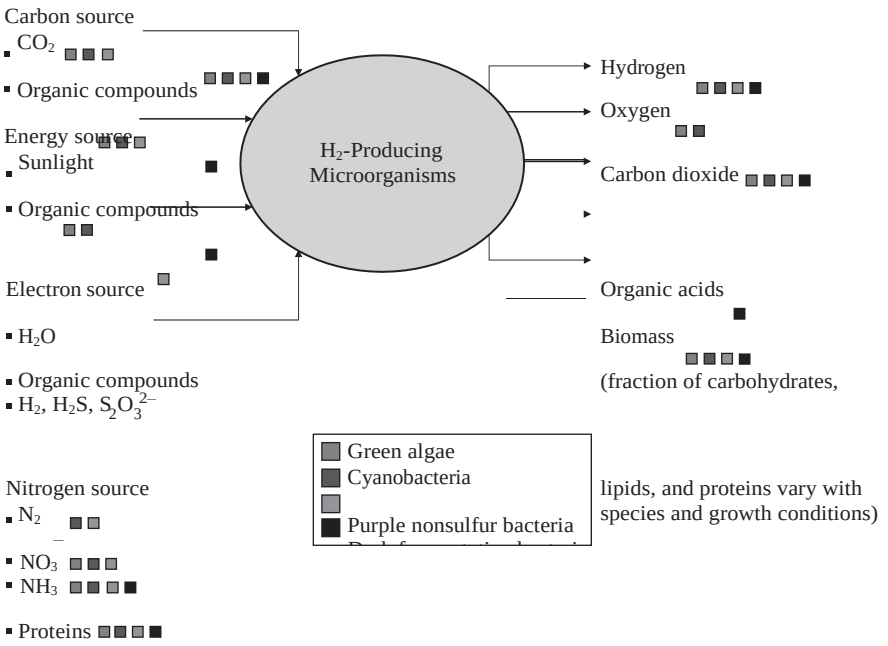


FIGURE 11.1

Schematic of the microalgae/cyanobacteria consuming CO_2 and producing H_2.

3. *Solar-driven thermochemical hydrogen production* uses solar collectors to concentrate thermal radiation from the sun to produce H_2 from various high-temperature thermochemical cycles. This process is an active area of research [19].
4. *Biological hydrogen production* by cultivation of microorganisms offers a clean and sustainable alternative to thermochemical or electrolytic hydrogen production technologies with the possible advantage of CO_2 capture. Under certain physiolog- ical conditions, some microorganisms can produce H_2. Biological hydrogen pro- duction offers several advantages over currently used technologies: (a) it occurs under mild temperatures and pressures; (b) the reaction specificity is typically higher than that of inorganic catalysts; (c) it is tolerant to sulfur gases, thus reduc- ing the cleanup cost of the gas prior to use; and (d) a diverse array of raw materials can serve as feedstock. The major drawbacks of this technology lie in its currently low efficiency and the fact that it requires large surface area and amounts of water.

Like all living organisms, algae or bacteria need (1) an electron source, (2) an energy source, (3) a carbon source, and (4) a nitrogen source to produce biomass. The latter can further be used as a value-added by-product or as animal feed, fertilizer, and raw material for biofuel production [20]. There are four different hydrogen-producing microorganisms, namely, (1) green algae, (2) cyanobacteria, (3) purple nonsulfur bacteria, and (4) dark fermentative bacteria. Figure 11.1 schematically shows these microorganisms as *black boxes* with the different combinations of input and output parameters. More details about photosynthesis and hydrogen production pathways are provided in the next sections.

11.1.4 Solar Radiation

Solar radiation is the most abundant and renewable energy source on Earth. Through

photosynthesis, it has provided human beings with food, fuel, heat, and even fossil fuels generated as a result of geologically deposited biomass chemical transformation of over billions of years under extreme pressures and temperatures [9].

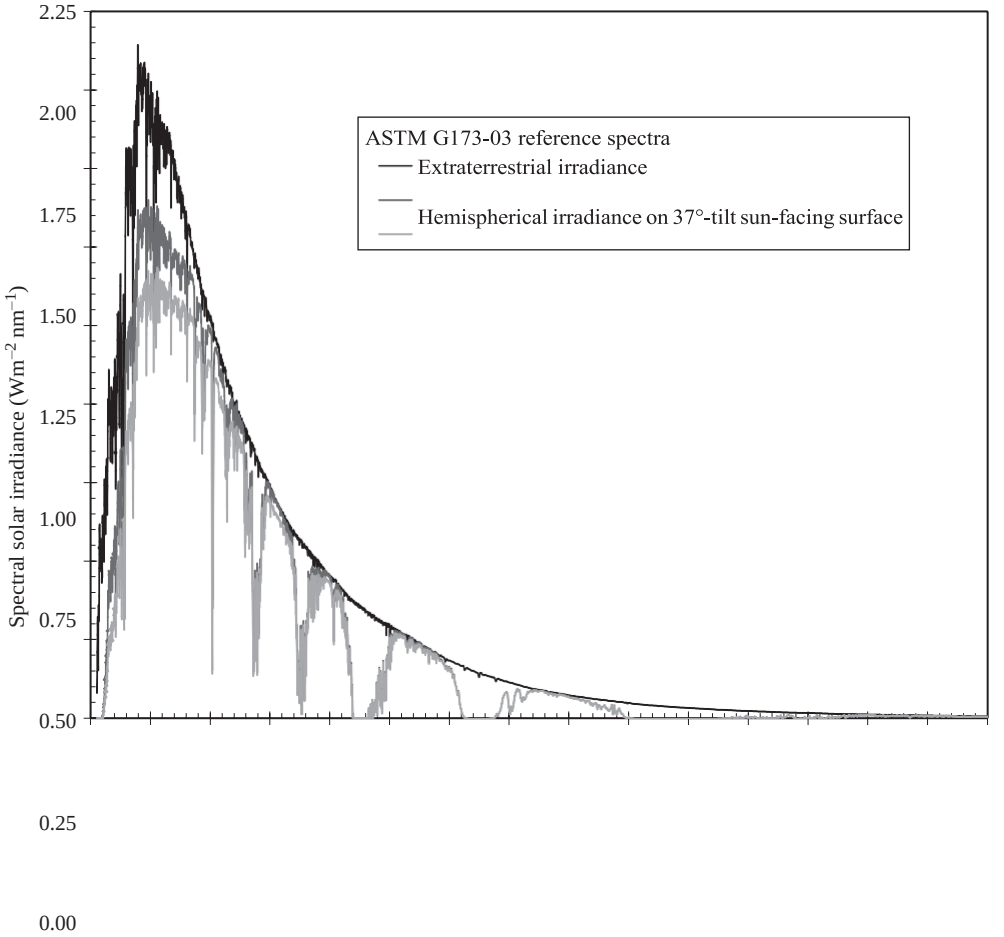
Seen from the Earth, the sun is approximately a disk of radius 6.96×10^{8} m at an average distance of 1.496×10^{11} m and viewed with a solid angle of 6.8×10^{-5} sr. The sun is often approximated as a blackbody at 5800 K emitting according to Planck's law [21].

The solar constant is defined as the total energy incident per unit surface area at the outer surface of Earth's atmosphere and oriented perpendicular to the sun's rays. It is estimated to be 1367 W/m^2 [21,22].

As the solar radiation travels through the Earth's atmosphere, it is (1) absorbed by atmospheric gases (e.g., CO_2, H_2O) and (2) scattered by gas molecules and larger aerosol particles, ice crystals, or water droplets. Once it reaches the Earth's surface, most of the ultraviolet (UV) component has been absorbed by oxygen and ozone molecules. Attenuation in the visible is mainly due to Rayleigh scattering by small gas molecules such as oxygen (O_2) and water vapor (H_2O). In the near-infrared (NIR) part of the spectrum, the main absorber is water vapor with contributions from carbon dioxide. Other minor absorbers include nitrous oxide (N_2O), carbon monoxide (CO), and methane (CH_4) [21].

The solar radiation reaching the Earth's atmosphere consists of 6.4% of UV radiation ($\lambda < 380$ nm), 48% of visible light ($380 \leq \lambda \leq 780$ nm), and 45.6% of infrared radiation ($\lambda > 780$ nm) [22]. Overall, the sun delivers 1.73×10^{17} W or 6.38×10^{19} Wh/year on the surface of the atmosphere [22]. This should be compared with the 2006 world energy consumption rate of 1.56×10^{13} W or an annual total energy of 1.37×10^{17} Wh/year [1].

The American Society for Testing and Materials (ASTM) G173-03 standard [23] provides ref- erence terrestrial solar spectral irradiance distributions for wavelength from 280 to 4000 nm averaged over 1 year and over the 48 contiguous states of the continental United States under atmospheric conditions corresponding to the US standard atmosphere [24]. Figure 11.2 shows



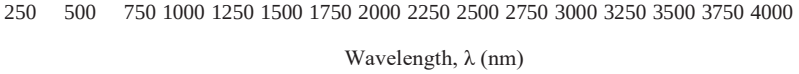


FIGURE 11.2

Averaged daily extraterrestrial solar irradiance and ASTM G173-03 (direct and hemispherical, 37° sun-facing tilted) sea level irradiance in W/m^2 nm. (From Gueymard, C. et al., *Sol. Energy*, 73(6), 443, 2002.)

(1) the extraterrestrial spectral irradiance [23], (2) the direct normal spectral irradiance at sea level with an air mass of 1.5, and (3) the hemispherical (or global) spectral irradiance on an inclined plane at sea level, tilted at 37° toward the equator and facing the sun. The data were produced using the Simple Model for Atmospheric Transmission of Sunshine (SMARTS2 version 2.9.2) [25]. Absorption due to atmospheric O_3, O_2, CO_2, and H_2O is apparent in the direct normal irradiance.

Moreover, Figure 11.3 shows the amount of daily solar irradiance in hours incident on an optimally tilted surface during the worst month of the year based on worldwide solar insolation data [26]. The most promising regions for harvesting solar energy are the southwest United States and northern Mexico, the Andes, northern and southern Africa and the Middle East, as well as Australia. Other regions with favorable conditions include southern Europe, southern China, Southeast Asia, Brazil, and most of Africa. Note that many of these regions have limited freshwater resources, and microorganisms should be selected accordingly. Selection criteria to minimize water use include tolerance to wastewater or seawater and to high microorganism concentrations.

11.1.5 Scope of This Chapter

This chapter focuses on photobiological hydrogen production by green algae, cyanobacteria, and purple nonsulfur bacteria. During photobiological hydrogen production, these microorganisms are cultivated in enclosures known as photobioreactors [27]. Due to the multidisciplinary nature of photobiological hydrogen production, this chapter provides the reader with the background on (1) the fundamentals of photosynthesis and photobio- logical hydrogen production, (2) photobioreactor technologies, and (3) the associated chal- lenges. Finally, economic and environmental considerations along with prospects for this technology are discussed.

11.2 Photosynthesis

Photosynthesis is a series of biochemical reactions converting sunlight into chemical energy [28]. Fixation of CO_2 into organic matter, such as carbohydrates, lipids, and proteins, through photosynthesis also provides food for all living creatures [28]. In other words, photosynthesis is the process to convert solar energy (energy source) and CO_2 (car- bon source) into organic material essential for life on Earth.

Photosynthesis involves two types of reactions, namely, (1) light and (2) dark reactions. During light reactions, photons are absorbed by the microorganisms and are used to produce (1) adenosine triphosphate (ATP), the principal energy-carrying molecule in cells, and (2) the electron carrier nicotinamide adenine dinucleotide phosphate (NADPH). These products of the light reaction are then used in the subsequent dark reactions such as CO_2 fixation [28] and H_2 production [29]. The electrons that drive these reactions usually come (1) from reduced sulfur sources such as hydrogen sulfide (H_2S), sulfur (S^0), or thiosulfate ($S_2O_3^{2-}$) in photosynthetic bacteria and (2) from water (H_2O) in plants, algae, and cyanobacteria [30]. When water is used as the electron source, O_2 is produced as a by-product. These processes are known as oxygenic photosynthesis. Those that do not produce O_2 are known as anoxygenic photosynthesis [30]. The reader is referred to Section 11.2.2 for detailed discussion of anoxygenic and oxygenic photosynthesis.

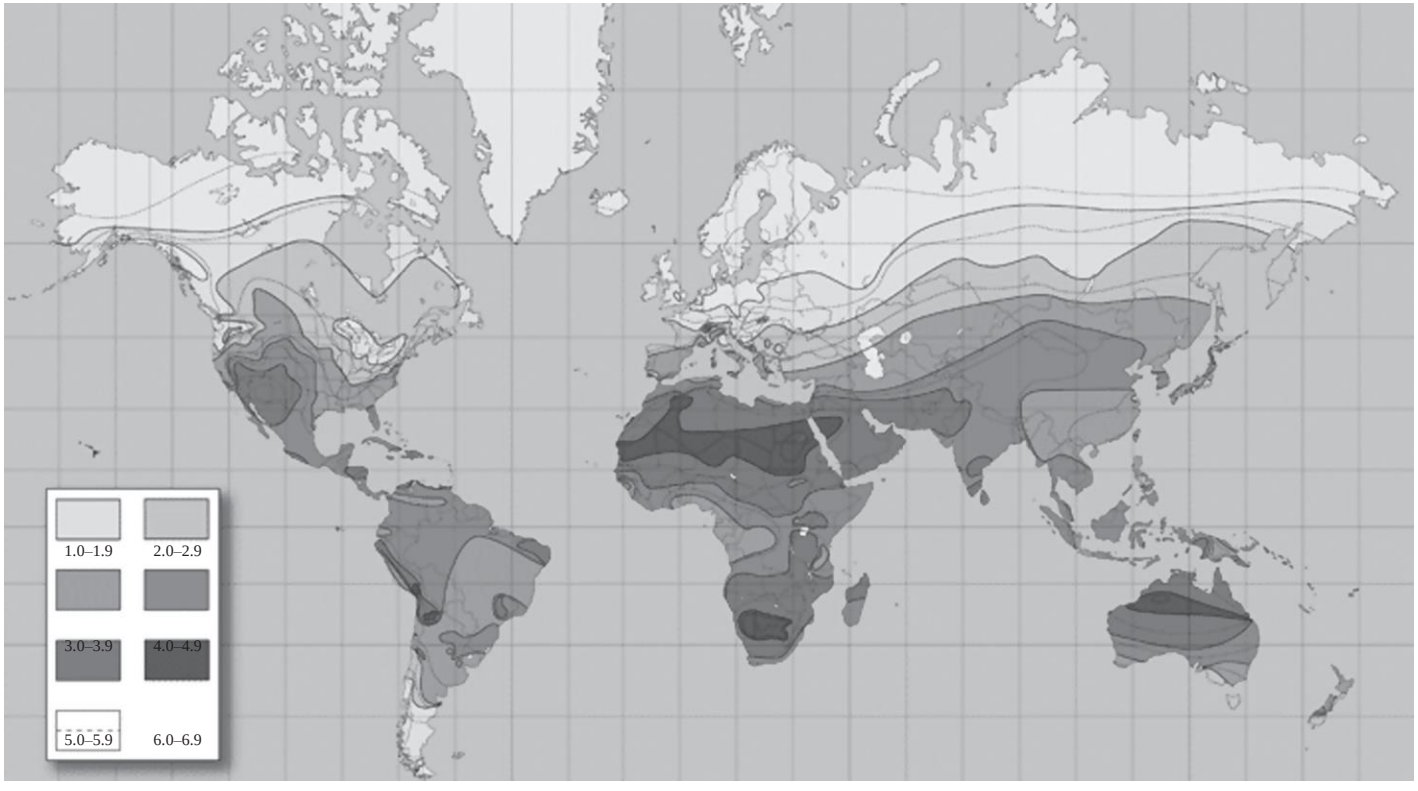


FIGURE 11.3

Average daily local solar irradiance on an optimally tilted surface during the worst month of the year (units are in kWh/m^2/day). (Courtesy of SunWize Technologies, Kingston, New York, World insolation map, http//www.sunwize.com/info_center/solar-insolation-map.php, 2008, Used by permission. All rights reserved. [copyright] 2009 SunWize Technologies.)

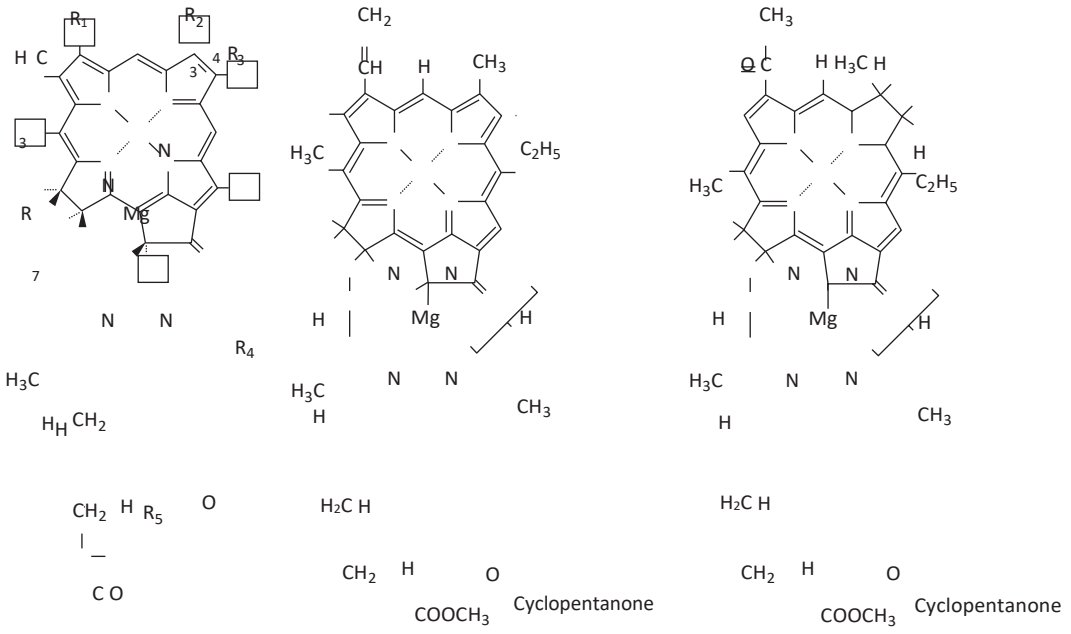
11.2.1 Photosynthetic Apparatus and Light-Harvesting Pigments

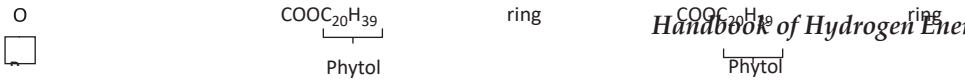
Photosynthesis begins with the absorption of photons by the photosynthetic appara- tus. The latter consists of three major parts: (1) the reaction center, (3) the core antenna, and (3) the peripheral antenna. Photochemical charge separation and electron transport take place in the reaction center [28]. The core antenna contains the minimum number of pigments, consisting only of chlorophylls or bacteriochlorophylls, which are necessary for photosynthesis. It is surrounded by the peripheral antenna, which is an assembly of chlorophylls, bacteriochlorophylls, and other accessory pigments such as carotenoids and phycobiliproteins. The peripheral antenna is particularly important in channeling additional photon energy to the reaction center at small light intensities. In algae and cyanobacteria, the photosynthetic apparatus is located on the photosynthetic membrane called thylakoid as shown in transmission electron microscope (TEM) micrographs in Figures 11.8 [31] and 11.9 [32]. In purple bacteria, it is located on vesicular photosynthetic membranes as shown in Figure 11.10 [30,33]. Each of the pigments used in the photosynthesis process is described in detail in the next sections.

11.2.1.1 Chlorophylls and Bacteriochlorophylls

The main pigments necessary for oxygenic photosynthesis are called chlorophylls and those responsible for anoxygenic photosynthesis are called bacteriochlorophylls [30]. Both are molecules containing a magnesium atom at their center. Figure 11.4a shows the structural formula of chlorophyll and bacteriochlorophyll molecules where R1 through R7 are organic chains [30]. The nature of the substituents present in the positions R1 through R7 defines different chlorophylls and bacteriochlorophylls. For example, Figure 11.4b and c shows the structure of chlorophyll *a* and bacteriochlorophyll *a*, respectively.

Moreover, the absorption peak wavelengths of common chlorophyll and bacteriochlorophyll pigments are summarized in Table 11.1. It shows that chlorophylls *a* and *b* have two absorption peaks, one in the blue and one in the red part of the visible spectrum [28]. Chlorophyll *a* absorbs around 430 and 680 nm, while chlorophyll *b* absorbs around 450 and 660 nm. Since they do not absorb green light ($\lambda \approx 520$–570 nm), they appear green to the human eye. These pigments are also responsible for the green color of plants. On the other





(a) (b) (c)

FIGURE 11.4

Structural formulae of (a) general chlorophyll molecule, (b) chlorophyll *a*, and (c) bacteriochlorophyll *a*. (From Madigan, M.T. and Martinko, J.M., *Biology of Microorganisms*, Pearson Prentice Hall, Upper Saddle River, NJ, 2006.)

TABLE 11.1

Common Photosynthetic Pigments in Photosynthetic Microorganisms

Pigment Group	Pigment Name	Absorption Maxima (nm)	Microorganism Type
Chlorophylls	Chl *a*	430, 680	Cyanobacteria, green algae
	Chl *b*	450, 660	Green algae
Bacteriochlorophylls	Bchl *a*	805, 830–890	Purple bacteria
	Bchl *b*	835–850, 1020–1040	Purple bacteria
	Bchl *c*	745–755	Green sulfur bacteria
	Bchl c_s	740	Green nonsulfur bacteria
	Bchl *d*	705–740	Green sulfur bacteria
	Bchl *e*	719–726	Green sulfur bacteria
	Bchl *g*	670–788	Heliobacteria
Carotenoids	*B*-carotene	425, 448, 475	All photosynthetic microbes
	Lutein	421, 445, 474	All photosynthetic microbes
	Violaxanthin	418, 442, 466	All photosynthetic microbes
	Neoxanthin	418, 442, 467	All photosynthetic microbes
	Spheroidene	429, 455, 486	All photosynthetic microbes
Phycobilins	Phycocyanin	620	Cyanobacteria
	Phycoerythrin	550	Cyanobacteria

Sources: Ke, B., *Photosynthesis, Photobiochemistry and Photobiophysics*, Kluwer Academic Publishers, Dordrecht, the Netherlands, 2001; Madigan, M.T. and Martinko, J.M., *Biology of Microorganisms*, Pearson Prentice Hall, Upper Saddle River, NJ, 2006.

hand, bacteriochlorophylls absorb light mainly in the far-infrared to NIR part of the electromagnetic spectrum ($700 \leq \lambda \leq 1000$ nm) [28].

11.2.1.2 Carotenoids

Carotenoids are accessory pigments found in all photosynthetic microorganisms. They absorb mainly the blue part of the spectrum ($400 \leq \lambda \leq 550$ nm) and are responsible for the yellow color of leaves in autumn and orange color of carrots [28]. Carotenoids serve two major functions: (1) shielding the photosynthetic apparatus from photooxidation under large light intensities and (2) increasing the solar light utilization efficiency by expand- ing the absorption spectrum of the microorganism. They are hydrophobic pigments com- posed of long hydrocarbon chains and are embedded in the photosynthetic membrane. There are numerous carotenoids [28]. The most common ones are listed in Table 11.1 along with their absorption peak wavelength.

11.2.1.3 Phycobiliproteins

Phycobiliproteins are also accessory pigments that play a role in light harvesting and transferring this energy to the reaction centers. They are found in cyanobacteria and red algae [30]. Two major ones are phycoerythrin absorbing mainly around 550 nm and phycocyanin absorbing strongly at 620 nm [30]. They are essential to the survival of these microorganisms at low light intensities.

Different pigment molecules absorb at different spectral bands of the solar spectrum enabling more efficient utilization of solar energy. They also allow for the coexistence of different photosynthetic microorganisms by sharing different bands of the solar spectrum. Figure 11.5 shows the absorption spectra of chlorophylls *a* and *b*, β-carotenoid,

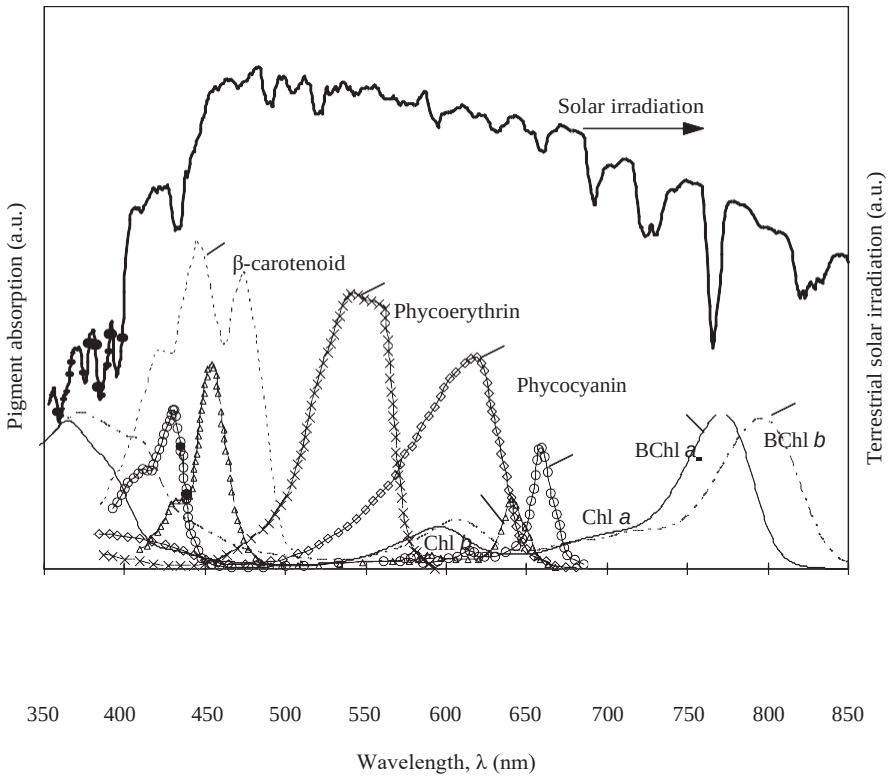


FIGURE 11.5

Absorption spectra of β-carotenoid, phycoerythrin, phycocyanin, chlorophyll *a* (Chl *a*), chlorophyll *b* (Chl *b*), bacteriochlorophyll *a* (BChl *a*), and bacteriochlorophyll *b* (BChl *b*) in relation to the terrestrial solar irradiation spectrum. The figure is in arbitrary units and the spectra of different molecules have been scaled arbitrarily for the sake of clarity. (From Ke, B., *Photosynthesis, Photobiochemistry and Photobiophysics*, Kluwer Academic Publishers, Dordrecht, the Netherlands, 2001.)

phycoerythrin, and phycocyanin over the spectral region from 400 to 700 nm, known as the photosynthetically active radiation (PAR) [28]. It also shows the profile of solar radiation spectrum (in arbitrary units) indicating that these pigments have evolved to absorb at wavelengths where the solar energy is most abundant.

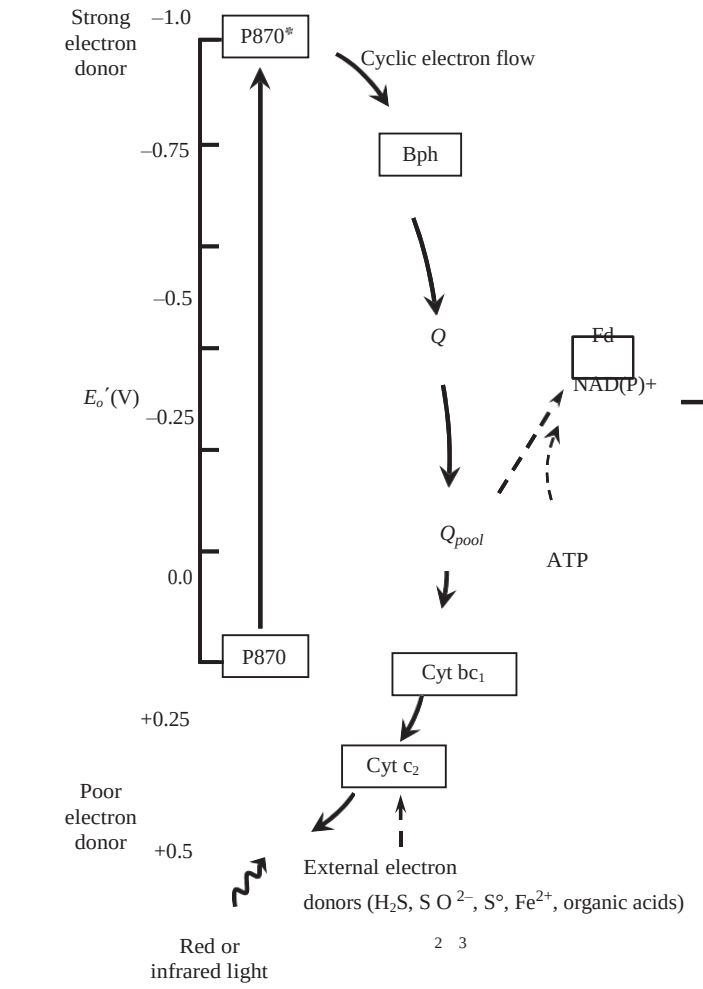
11.2.2 Anoxygenic and Oxygenic Photosynthesis

Two types of photosynthetic processes exist depending on whether molecular oxygen is evolved as a by-product [30]. Anoxygenic photosynthesis is mainly conducted by purple and green sulfur and nonsulfur bacteria, whereas oxygenic photosynthesis is conducted by green algae, cyanobacteria, and plants [28,30]. The source of electrons in anoxygenic photosynthesis can be molecular hydrogen, sulfide, or organic acids. However, in oxygenic photosynthesis, the source of electrons is always water [28]. Details of the electron transport in both types of photosynthesis are described in the following sections.

11.2.2.1 Electron Transport in Anoxygenic Photosynthesis

Figure 11.6 shows the electron flow in anoxygenic photosynthesis, conducted by purple bacteria, for example, with respect to the reduction potential E'_o of the molecules expressed in volts [30]. Anoxygenic photosynthesis begins when a photon with wavelength 870 nm is

absorbed by the antenna and transferred to the reaction center. The reaction center, known as P870, is a strong electron donor P870* with very low reduction potential. The electrons


Strong electron donor
–1.0
P870*
Cyclic electron flow
–0.75
Bph
–0.5
Q
Fd
NAD(P)+
NAD(P)H
E_o'(V)
–0.25
Q_{pool}
ATP
0.0
P870
Cyt bc_1
+0.25
Cyt c_2
Poor electron donor
+0.5
External electron donors (H_2S, S O_3^{2-}, S°, Fe^{2+}, organic acids)
Red or infrared light
(a)

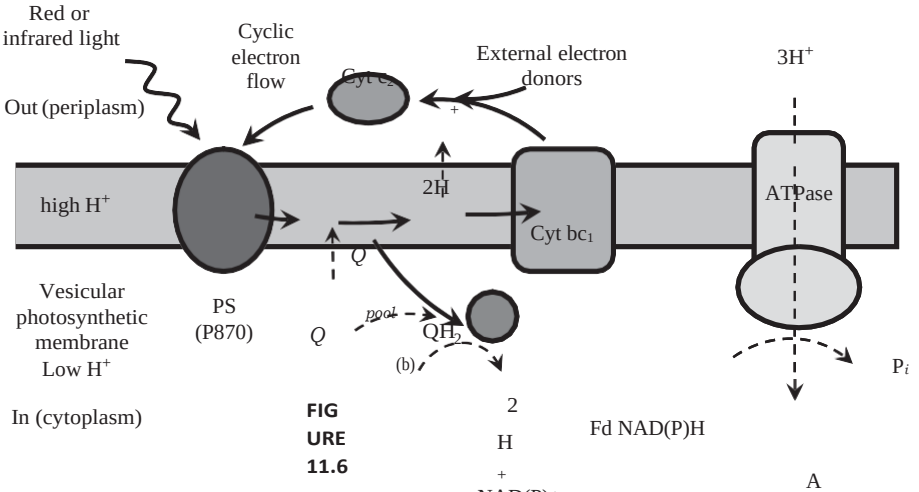

Red or infrared light
Cyclic electron flow
External electron donors
$3H^+$
Out (periplasm)
Cyt c_2
$2H^+$
high H^+
ATPase
Cyt bc_1
Q
Vesicular photosynthetic membrane
Low H^+
PS (P870)
Q
pool
QH_2
P_i
(b)
In (cytoplasm)
Fd NAD(P)H
$2H^+$
NAD(P)+
ATP
ADP+

FIGURE 11.6

ATP

$3H^+$

Electron flow in anoxygenic photosynthesis in purple bacteria illustrated as (a) redox potentials and (b) mem- brane schematic. (From Madigan, M.T. and Martinko, J.M., *Biology of Microorganisms*, Pearson Prentice Hall, Upper Saddle River, NJ, 2006.)

from P870* are donated very quickly to bacteriopheophytin *a* (Bph) within the reaction center to prevent electron recombination. These electrons are transported from the reaction center through a series of quinone molecules within the photosynthetic membrane denoted by *Q* (Figure 11.6). The electron flow in the photosynthetic membrane is also shown schematically in Figure 11.6b. The transport of electrons induces a proton gradient

across the membrane known as the proton motive force that drives the synthesis of ATP through a reaction known as phosphorylation [30]. With additional energy in the form of ATP, electrons are transferred from quinone pool of the photosynthetic membrane denoted by Q_{pool} either (1) to ferredoxin, which carries electrons to be used in nitrogen fixation and/or hydrogen production, or (2) to $NAD(P)^+$ to be converted to NAD(P)H, which carries electrons to biosynthetic reactions such as CO_2 fixation in the Calvin cycle [30,34]. Unused electrons return back to the reaction center via cytochromes Cyt bc_1 and Cyt c_2, thus forming an electron cycle [30]. The electrons lost during the electron cycle are replaced during photofermentation by the cytochrome Cyt c_2 that oxidizes organic acids such as acetate or reduced compounds such as H_2S [30,34].

11.2.2.2 Electron Transport in Oxygenic Photosynthesis

In contrast, during oxygenic photosynthesis conducted by algae and cyanobacteria, electron transport is not cyclic but follows the *Z-scheme* shown in Figure 11.7 [30].

In this scheme, two distinct but interconnected photochemical reactions known as photosystem I (PSI) and photosystem II (PSII) function cooperatively. Oxygenic photosynthesis begins when photons with wavelength around 680 nm are absorbed and transferred to the reaction center known as P680 located in PSII. This converts P680 to a strong reductant that can oxidize water to liberate electrons and protons and evolve molecular O_2 according to $2H_2O \rightarrow 4e^- + 4H^+ + O_2$. Electrons from the reduced P680* are quickly transferred to pheophytin (Ph) within the reaction center to prevent electron recombination. Subsequent electron transfer in the photosynthetic membrane from the reaction center drives the proton motive force responsible for the generation of ATP. The electrons reaching the cytochrome Cyt *bf* are transported to P700 of PSI with plastocyanin (PC). Absorbing light energy at about 700 nm, P700 is reduced to P700*, which has a very low reduction potential. The electrons are quickly donated to a special chlorophyll *a* molecule (Chl a_o) within the reaction center. These electrons are then donated to $NAD(P)^+$ to synthesize NAD(P) H through a cascade of quinone molecules (*Q*), nonheme iron–sulfur protein (FeS), ferredoxin (Fd), and flavoprotein (Fp) as shown in Figure 11.7. Since the electrons generated from water splitting are not returned back to P680, this form of ATP generation is known as noncyclic phosphorylation. However, if sufficient reducing power is present in the cells, a cyclic phosphorylation can also take place around PSI as shown in Figure 11.7 [35,36]. In both oxygenic and anoxygenic photosynthesis, ATP and NAD(P)H produced are used by the microorganisms as their energy and electron carriers in order to fix CO_2.

11.3 Microbiology of Photobiological Hydrogen Production

11.3.1 Hydrogen-Producing Microorganisms

There are various methods for biological hydrogen production depending on the type of microorganism used in the process. Thus, it is necessary to classify the different hydrogen-producing microorganisms and understand their metabolism. On the most basic premise, microorganisms can be divided into two major groups known as prokary- otes and eukaryotes. Unlike prokaryotes, eukaryotes have a nucleus where the genetic material is stored and other membrane-enclosed organelles [30]. Members of *bacteria* such

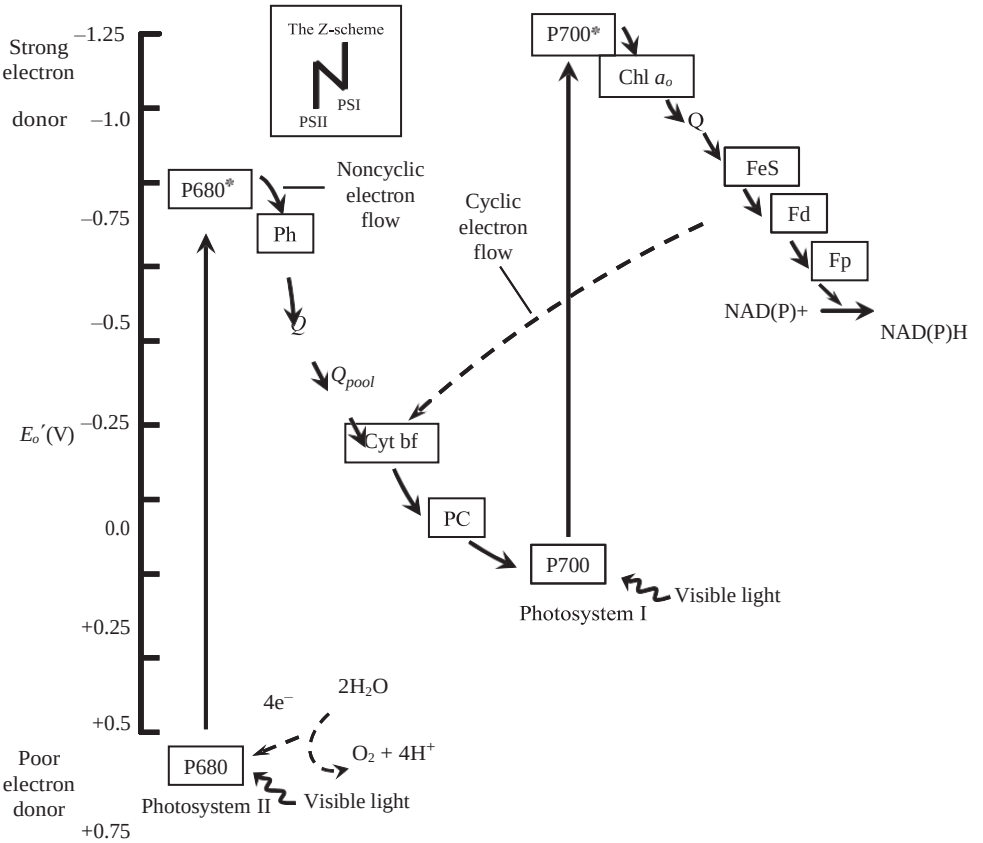

The Z-scheme
PSII
PSI
Strong electron donor
–1.25
–1.0
–0.75
–0.5
–0.25
0.0
+0.25
+0.5
+0.75
E_o'(V)
Poor electron donor
P680*
Ph
Noncyclic electron flow
Cyclic electron flow
Q
Q_{pool}
Cyt bf
PC
P680
P700*
Chl a_o
Q
FeS
Fd
Fp
NAD(P)+
NAD(P)H
P700
Visible light
Photosystem I
Photosystem II
$4e^-$
$2H_2O$
$O_2 + 4H^+$
(a)
Visible light
3H+
+1.0
2H O
Out (periplasm) high H+
Thylakoid
Ps II
Cyt bf
PC
Ps I
ATPase
photosynthetic membrane
(P680)
Q
QH2
(P700)
Low H+
In (cytoplasm)
2H+
Fd
Fp
ADP +Pi
ATP
NAD(P)+
NAD(P)H
(b)

FIGURE 11.7

Electron flow in oxygenic photosynthesis in cyanobacteria and green algae illustrated as (a) redox potentials and (b) membrane schematic. (From Madigan, M.T. and Martinko, J.M., *Biology of Microorganisms*, Pearson Prentice Hall, Upper Saddle River, NJ, 2006.)

as cyanobacteria, purple nonsulfur bacteria, and fermentative bacteria are prokaryotes. Algae, on the other hand, are eukaryotes.

Microorganisms that can use solar radiation as their energy source and CO_2 as their sole carbon source are known as photoautotrophs. Cyanobacteria, algae, and purple non- sulfur bacteria are capable of a photoautotrophic life style. Among these, cyanobacteria

and algae use water as their electron source and conduct oxygenic photosynthesis (see Section 11.2.2.2). Purple nonsulfur bacteria use molecular hydrogen, sulfide, or organic acids as their electron source and conduct anoxygenic photosynthesis (see Section 11.2.2.1). Some of these photoautotrophs can also live as photoheterotrophs, that is, they can utilize light as their energy source and organic compounds as both their carbon and electron sources. Organic compounds include (1) organic acids (e.g., acetic acid, amino acids, lactic acid, citric acid, butyric acids) and (2) carbohydrates (sugars) such as mono- saccharides (e.g., glucose, sucrose, fructose, $(CH_2O)_n$) and polysaccharides (e.g., starch, cellulose, $(C_6H_{10}O_5)_n$).

On the other hand, some microorganisms use chemical compounds as their energy source and are known as chemolithotrophs. Among these, those using organic com- pounds as their energy, carbon, and electron sources are known as chemoorganotrophs. This is the case of dark fermentative bacteria. Finally, prokaryotes, like most cyanobacteria and all purple nonsulfur bacteria, are capable of using molecular nitrogen as their nitro- gen source. They achieve this through nitrogen fixation that uses special enzymes called nitrogenase and requires energy in the form of ATP. On the other hand, eukaryotes cannot fix molecular nitrogen and require sources of nitrogen in the form of ammonia, nitrates, or proteins (e.g., albumin, glutamate, yeast extract) [30,37].

11.3.1.1 Green Algae

Green algae are eukaryotic organisms that contain chlorophylls and conduct oxygenic photosynthesis [38,39]. They live in freshwater and most of them have cellulose cell walls. They can produce hydrogen through direct and indirect biophotolysis as well as photofermentation (Section 11.3.2.2). All these processes require anaerobic conditions, that is, the absence of oxygen from the algae environment. Examples of green algae capable of photobiological hydrogen production include (1) freshwater species such as *Chlamydomonas reinhardtii* [40], *Chlamydomonas moewusii* [41], and *Scenedesmus obliquus*
[42] as well as (2) saltwater species such as *Chlorococcum littorale* [43], *Scenedesmus obliquus* [44], and *Chlorella fusca* [45]. Figure 11.8 depicts the TEM micrograph of the green algae *Chlamydomonas reinhardtii* [31]. It shows the location of the nucleus; the chlo- roplast, where photosynthetic pigments are located; and the pyrenoid, where CO_2 fixa- tion takes place.

11.3.1.2 Cyanobacteria

Cyanobacteria, also known as blue-green algae, are photoautotrophic prokaryotes that are capable of conducting oxygenic photosynthesis [30]. These microorganisms are the first organisms that could evolve oxygen and are responsible for converting Earth's atmosphere from anoxic (oxygen lacking) to oxic (oxygen containing) [28]. There exist unicellular and filamentous forms and their size can range from 0.5 to 40 μm in diameter depending on the strain [30]. Most species are capable of fixing atmospheric nitrogen using the nitrogenase enzyme and play an important role in the global nitrogen cycle [30]. Some filamentous forms have evolved to contain the nitrogenase enzyme in special cells called heterocysts. Heterocysts protect nitrogenase from oxygen inhibition.

Just like green algae, cyanobacteria can produce hydrogen through direct and indirect biophotolysis as well as photofermentation (Section 11.3.2.2). In addition to anaerobic conditions, nitrogen-fixing cyanobacteria also require the absence of nitrogen sources (N_2, NO_3^-, or NH_4) in order to produce H_2. Examples of cyanobacteria capable of photobiological

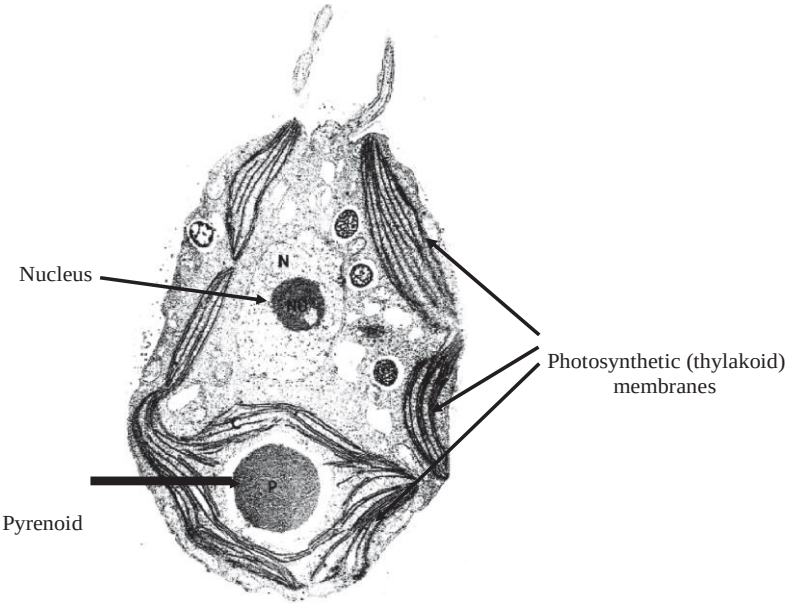


FIGURE 11.8

TEM micrograph of *Chlamydomonas reinhardtii*. A typical cell is ellipsoidal with major and minor diameters equal to about 9 and 8 μm, respectively. (From Harris, E.H., *The Chlamydomonas Sourcebook*, Vol. 1, Academic Press, San Diego, CA, 1989. With permission; Berberoğlu, H. et al., *Int. J. Hydrogen Energy*, 33, 6467, 2008. With permission.)

hydrogen production include (1) freshwater species such as *Anabaena variabilis* [46], *Anabaena azollae* [46], and *Nostoc punctiforme* [47] as well as (2) saltwater species such as *Oscillatoria* Miami BG7 [48] and *Cyanothece* 7822 [49]. Figure 11.9 presents the TEM micrograph of the filamentous cyanobacterium *Anabaena variabilis* ATCC 29413 [32]. It shows the location of the thylakoid membrane where the photosynthetic apparatus is located. Note the absence of nucleus and organelles.

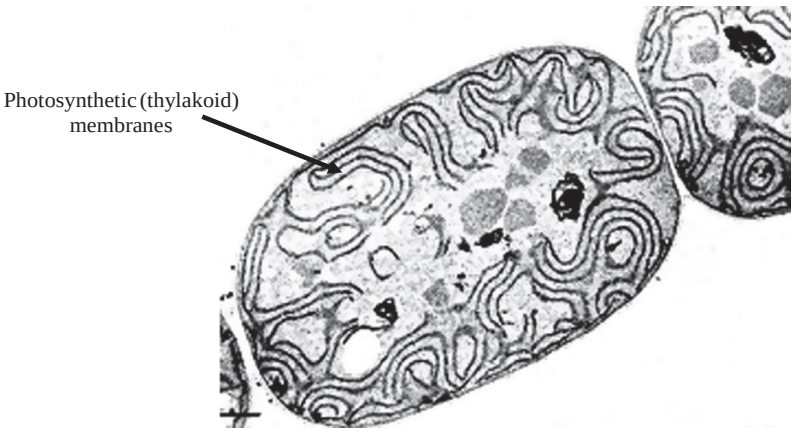


FIGURE 11.9

TEM micrograph of *Anabaena variabilis* ATCC 29413. Typical cell is 5 μm wide. (From Lang, N.J. et al., *J. Bacteriol*., 169(2), 920, 1987. With permission.)

11.3.1.3 Purple Nonsulfur Bacteria

Purple nonsulfur bacteria are prokaryotes that conduct anoxygenic photosynthesis, that is, they do not produce oxygen. In general, purple nonsulfur bacteria survive by photoheterotrophy using light as their energy source and organic compounds as their carbon source. Organic compounds include fatty, organic, or amino acids; sugars; alcohols; and aromatic compounds [30]. Purple nonsulfur bacteria contain bacteriochlorophylls and carotenoids and have a brown/dark red color, hence their name. The photosynthetic apparatus of purple nonsulfur bacteria is located on an intracytoplasmic photosynthetic membrane [30]. Some species can also grow in the dark conducting fermentation and anaerobic respiration, while others can grow photoautotrophically fixing CO_2 using H_2 or H_2S as their electron source [30]. All species have the nitrogenase enzyme and can fix molecular nitrogen. Purple nonsulfur bacteria produce hydrogen by photofermentation, which requires removal of both oxygen and nitrogen from the environment (Section 11.3.2.2). Examples of purple nonsulfur bacteria capable of producing hydrogen include *Rhodobacter sphaer- oides* [37,41] and *Rhodospirillum rubrum* [50]. Figure 11.10 illustrates the TEM micrograph of the purple nonsulfur bacterium *Rhodobacter sphaeroides* during cell division [33]. It shows the location of the intracytoplasmic membranes where the photosynthetic apparatus is located.

11.3.1.4 Dark Fermentative Bacteria

Dark fermentative bacteria are chemoorganotrophs deriving their energy, carbon, and electrons from the degradation of organic compounds including carbohydrates, amino acids, cellulose, purines, and alcohols [30]. Their size is typical of bacteria, that is, 0.5–1.5 μm. They live in soil and organic nutrient–rich waters. Some grow best at temperatures ranging from 25°C to 40°C and are known as mesophiles, and others grow best at even higher temperatures ranging from 40°C to 80°C and are known as thermophiles. Examples of hydrogen-producing mesophiles and thermophiles are *Enterobacter cloacae* IIT BT-08 [51] and *Clostridium butyricum* [52], respectively.

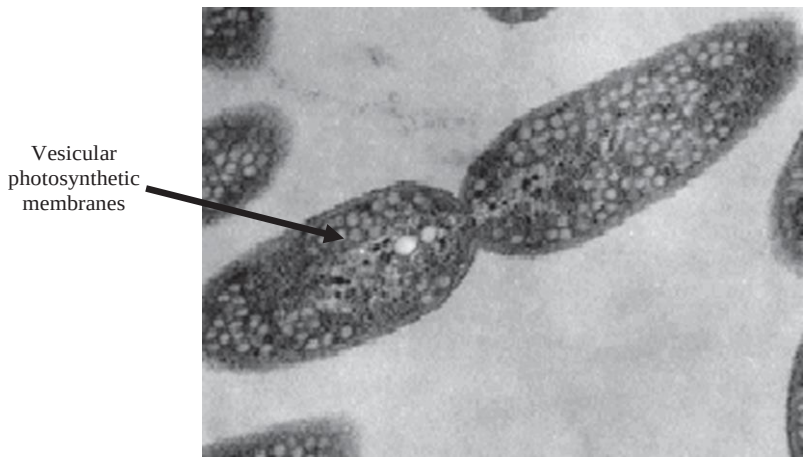


FIGURE 11.10

TEM micrograph of *Rhodobacter sphaeroides*. A typical cell is about 1.5 μm long. (From Department of Energy, *Rhodobacter sphaeroides*, Joint Genome Institute, Walnut Creek, CA, http://genome.jgi-psf.org/finished-microbes/rhosp/rhosp.home.html, accessed on April 19, 2008.)

TABLE 11.2

Energy, Carbon, Electron, and Nitrogen Sources of H_2-Producing Microorganisms

Microorganism	Green Algae	Cyanobacteria	Purple Nonsulfur Bacteria	Dark Fermentative Bacteria
Energy source	Light (oxygenic)	Light (oxygenic)	Light (anoxygenic)	Organic matter
Carbon source	CO_2 or organic matter	CO_2	Organic matter	Organic matter
Electron source	H_2O	H_2O	Organic matter	Organic matter
Nitrogen source	Ammonia or NO_3^-	NH_4, NO_3^-, N_2, or proteins	NH_4, NO_3^-, N_2, or proteins	NH_4, NO_3^-, or proteins
Photosynthetic pigments	Chl *a*, Chl *b*, carotenoids	Chl *a*, carotenoids, phycobilins	Bchl *a*, Bchl *b*, carotenoids	None
H_2-producing enzyme	[Fe-Fe]-hydrogenase	[NiFe]-hydrogenase and/or nitrogenase	Nitrogenase	[NiFe]-hydrogenase
Products	H_2, O_2, carbohydrates	H_2, O_2, CO_2, carbohydrates	H_2, organic acids	H_2, organic acids

Table 11.2 summarizes the energy, carbon, electron, and nitrogen sources for each of the microorganisms described earlier along with the enzymes responsible for H_2 production and the by-products of this process in these microorganisms. The table also lists the pigments present in these microorganisms that are responsible for absorbing and utilizing solar radiation. These enzymes and pigments are presented in detail in the next section.

11.3.2 Enzymatic Pathways

Photobiological hydrogen production takes place when the electrons generated during (1) the light reactions, (2) the degradation of carbohydrates, or (3) respiration are directed to specific enzymes. There are two types of enzymes that catalyze the production of hydro- gen in microorganisms, namely, nitrogenase and hydrogenase [53]. Table 11.3 summarizes the advantages and disadvantages of each enzyme group.

11.3.2.1 Enzyme Systems

11.3.2.1.1 Nitrogenase

Nitrogenase is found in prokaryotes such as most photosynthetic bacteria and some cyanobacteria [30]. It is not present in eukaryotes such as green algae [53]. The main role of nitrogenase is to reduce molecular nitrogen to ammonia during fixation of nitrogen dissolved

TABLE 11.3

Advantages and Disadvantages of Nitrogenase and Hydrogenase Enzymes in Producing Hydrogen

Enzyme	Microorganisms	Advantages	Disadvantages
Nitrogenase	Most photosynthetic bacteria and some cyanobacteria	Robust H_2 production Able to generate H_2 under large H_2 partial pressure	Low efficiency (16%) Small turnover rate Requires 2 ATP/electron Sensitive to O_2
Hydrogenase	Cyanobacteria, green algae, and purple nonsulfur bacteria	Does not require ATP High efficiency (41%) Large turnover rate (very active)	Unable to generate H_2 under large H_2 partial pressure Very sensitive to O_2

Source: Prince, R.C. and Kheshgi, H.S., *Crit. Rev. Microbiol*., 31(1), 19, 2005.

in the liquid phase [41] that provides the nitrogen source needed by the microorganism to produce biomass. This primary reaction catalyzed by nitrogenase is given by [53]

$$N_2 + 8e^- + 8H^+ \rightarrow 2NH_3 + H_2 \tag{11.1}$$

In this reaction, H_2 is produced at low rates as a by-product of nitrogen fixation. In the absence of N_2, nitrogenase catalyzes the irreversible production of H_2 provided that reductants, that is, electrons, and ATP are present via

$$2H^+ + 2e^- + 4ATP \rightarrow H_2 + 4ADP + 4P_i \tag{11.2}$$

where ADP and P_i are adenosine diphosphate and inorganic phosphate, respectively. Since the cell energy carrier ATP is used by nitrogenase, this hydrogen production route is energy intensive. The electrons for nitrogenase are donated either by ferredoxin (Fd) or by flavoprotein (Fp) flavodoxin from the photosynthetic electron flow shown in Figures 11.6 and 11.7 [53]. This enables nitrogenase to evolve H_2 even at a partial pressure of H_2 larger than 50 atm making the process robust [53]. However, nitrogenase-based H_2 production suffers from (1) a small turnover rate of less than 10 s^{-1}, that is, nitrogenase can catalyze less than 10 reactions per second, and (2) low quantum efficiency, defined as the ratio of the number of moles of H_2 produced to the number of photons absorbed by the photosystems. Thus, both the rate of H_2 production and the solar-to-H_2 energy conversion efficiency are low.

Nitrogenase enzymes have an organometallic reaction center. The efficiency of H_2 production by the nitrogenase enzyme varies depending on the type of transition metal located at the reaction center [53]. The most common type of nitrogenase enzyme uses molybdenum at its reaction center, but vanadium and iron can also be found [53].

11.3.2.1.2 Hydrogenase

There are two types of bidirectional (or reversible) hydrogenase enzymes, namely, (1) [Fe-Fe]-hydrogenase and (2) [FeNi]-hydrogenase, also called uptake hydrogenase. The iron [Fe-Fe]-hydrogenase is present in green algae [53]. It is a very active bidirectional enzyme with a large turnover rate of 10^6 s^{-1} [53]. It receives electrons from ferredoxin (Fd in Figures 11.6 and 11.7) and does not require energy (ATP) to produce H_2. Thus, [Fe-Fe]-hydrogenase has better quantum efficiency than nitrogenase. The bidirectional [Fe-Fe]-hydrogenase catalyzes both the production and consumption of hydrogen through the reaction

$$2H^+ + 2e^- = H_2 \tag{11.3}$$

The rate at which [Fe-Fe]-hydrogenase can catalyze the production of hydrogen decreases significantly with increasing partial pressure of H_2.

Finally, [NiFe]-hydrogenase is the commonly known uptake hydrogenase that is found in nitrogen-fixing microorganisms [54]. It is present only in nitrogen-fixing microorganisms such as cyanobacteria and purple nonsulfur bacteria [29]. It catalyzes both H_2 evolution and uptake. In purified form, it has been shown to evolve hydrogen at a low turnover rate of 98 s^{-1}. It also enables microorganisms to consume back H_2 produced as a by-product of nitrogen fixation (Equation 11.1) and, thus, recover some energy.

Both [Ni-Fe]- and [Fe-Fe]-hydrogenases are very sensitive to the presence of O_2. In particular, the [Fe-Fe]-hydrogenase is irreversibly inhibited by O_2, whereas the [NiFe]-hydrogenase is reversibly affected (see Section 11.6.1.2) [53].

11.3.2.2 Pathways for Biological Hydrogen Production

Biological processes resulting in hydrogen production can be grouped in four catego- ries, namely, (1) direct and (2) indirect biophotolysis, (3) photofermentation, and (4) dark fermentation.

11.3.2.2.1 Direct Biophotolysis

In this mechanism, H_2 is produced by diverting the electrons generated from water splitting from the Calvin cycle to the bidirectional hydrogenase enzyme according to Equation 11.3 [41]. The energy source is the sunlight in the spectral range from 400 to 700 nm. This mechanism is theoretically the most energy efficient for H_2 production with a theoretical maximum of 40.1% [53]. However, the oxygen produced during water splitting irreversibly inhibits the functioning of the [Fe-Fe]-hydrogenase and makes the process impractical for industrial applications [54]. Green algae such as *Chlamydomonas reinhardtii*, *Chlamydomonas moewusii*, *Scenedesmus obliquus*, and *Chlorococcum littorale* are capable of producing H_2 via direct biophotolysis [41].

11.3.2.2.2 Indirect Biophotolysis

The source of electrons in indirect biophotolysis is also water. However, in this mechanism, the electrons are first used to reduce CO_2 into organic compounds during photosynthe- sis where O_2 is generated. Then, the electrons are recovered from the degradation of the organic compounds and used in generating H_2 through the action of nitrogenase [54]. Thus, no O_2 is generated during H_2 production. The maximum possible light-to-H_2 energy conversion efficiency of indirect biophotolysis is only 16.3% [53] due to the facts that (1) multiple steps are involved in converting solar energy to H_2 and (2) the use of nitrogenase enzyme requires ATP. Cyanobacteria such as *Anabaena variabilis*, *Anabaena azollae*, *Nostoc muscorum* IAM M-14, and *Oscillatoria limosa* are capable of indirect biophotolysis [49]. The nitrogenase enzyme also gets inhibited by O_2; however, cyanobacteria have evolved in many ways to circumvent this problem [55]. For example, *A. variabilis* has evolved to contain the nitroge- nase enzyme in special O_2 protective cells called heterocysts as illustrated in Figure 11.11.

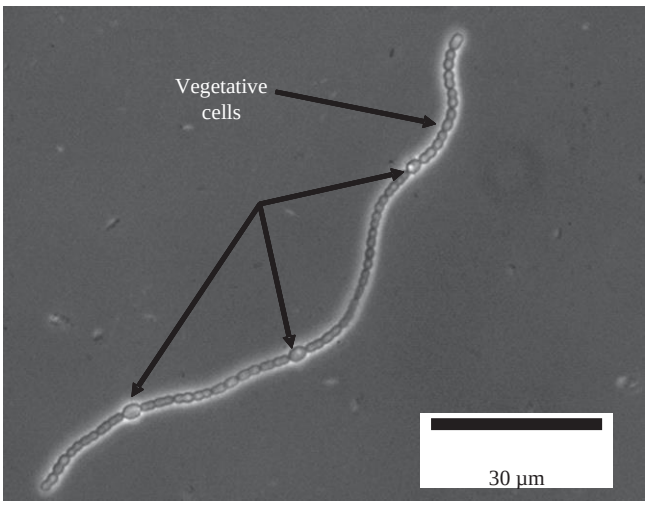


FIGURE 11.11

Micrograph of *Anabaena variabilis* ATCC 29413-U. (From Berberoğlu, H. and Pilon, L., *Int. J. Hydrogen Energy*, 32(18), 4772, 2007.)

11.3.2.2.3 Photofermentation

This mechanism is similar to indirect biophotolysis with the distinction that the organic compounds used are produced outside the cells via the photosynthesis of other organisms, for example, plants. These extracellular organic materials, such as organic acids, carbohydrates, starch, and cellulose [37], are used as the electron source, and sunlight is used as energy source to produce H_2 by nitrogenase enzyme [41]. Due to the fact that the cells do not need to carry out photosynthesis, no O_2 is generated and all the solar energy can be used to produce H_2. Thus, this mechanism is viewed as the most promising microbial system to produce H_2 [41]. The major advantages of this route are (1) the absence of O_2 evolution that inhibits the H_2-producing enzymes and (2) the ability to consume a wide variety of organic substrates found in wastewa- ters. Due to their ability to harvest a wider spectrum of light, from 300 to 1000 nm, purple nonsulfur bacteria such as *Rhodobacter sphaeroides*, pictured in Figure 11.12, *Rhodospirillum rubrum*, and *Rhodopseudomonas sphaeroides* hold promise as photofer- mentative H_2 producers.

11.3.2.2.4 Dark Fermentation

In dark fermentation, anaerobic bacteria use the organic substances (e.g., glucose, hexose monophosphate, and pyruvate [41]) as both their energy and electron sources. These bacteria mainly use the [NiFe]-hydrogenase enzyme to produce H_2. Due to the absence of O_2 in the environment and the use of hydrogenase, they can produce H_2 at a higher rate without inhibition. Moreover, H_2 production is continuous throughout the day and night because these microorganisms do not depend on sunlight as their energy source. The hydrogen production is accompanied by CO_2 production as well. Examples of fermentative hydrogen producers include *Enterobacter cloacae* IIT BT-08, *Enterobacter aerogenes*, *Clostridium butyri- cum*, and *Clostridium acetobutylicum* [41]. This process falls outside the scope of this chapter and will not be discussed further.

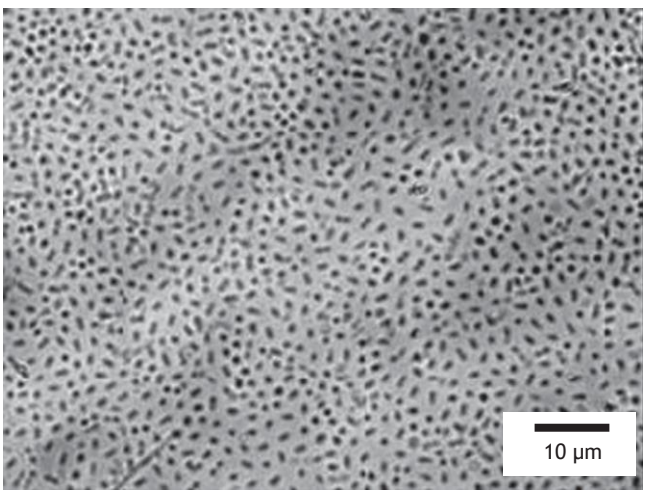


FIGURE 11.12

Micrograph of *Rhodobacter sphaeroides* ATCC 494119.

11.3.2.2.5 Quantum Efficiency of Different Photobiological H_2 Production Pathways

In order to compare the different photobiological pathways, Prince and Kheshgi [53] defined the maximum theoretical quantum efficiency of H_2 production based on monochromatic illumination at 680 nm as

$$\eta_{th} = \frac{n_{H_2}\Delta H_{H_2}}{n_{p,680}hc/\lambda} \tag{11.4}$$

where

n_{H_2} is the number of moles of produced H_2

ΔH_{H_2} is the enthalpy of formation of hydrogen equal to 285.83 kJ/mol at standard state (25°C and 0.1 MPa) [56]

Light input energy is computed as the product of the number of moles of photons needed at 680 nm denoted by $n_{p,680}$ and the energy of photons at 680 nm that is equal to hc/λ = 176 kJ/mol. In their definition, photons at 680 nm are used as this wavelength corresponds to the absorption peak of the reaction center in PSII. Note that the absorption peak of PSI is at 700 nm and that of purple bacteria is at 790 and 850 nm. The minimum number of photons needed is evaluated by considering the electron and ATP requirement of the reactions and assuming that two photons are needed per electron and two ATPs are needed per electron [53]. Finally, note that this definition of efficiency does not apply to process efficiency of a photobioreactor.

11.3.3 Performance Assessment and Units

Photobiological hydrogen production and/or carbon dioxide mitigation are very interdisciplinary topics involving researchers from many different disciplines including microbiologists and plant biologists as well as engineers. Owing to its diversity, it lacks standards in units to report experimental conditions and results and to enable direct comparisons between studies and microorganisms. This section aims to inform the reader on the different units found in the literature.

11.3.3.1 Microorganism Concentration

The microorganism concentration is usually reported in kilogram of dry cell per cubic meter of the liquid medium denoted by kg dry cell/m^3 or simply kg/m^3. This requires sampling a known volume of the cell suspension, drying it using an oven overnight, and weighing it using a high-precision analytical balance. Another method is to report the number of cells per cubic meter of liquid medium. This also requires sampling a known volume of cell suspension and counting the cells in that volume as observed under an optical microscope. This technique may be challenging if the microorganisms are (1) very small (<1 μm) such as purple nonsulfur bacteria, (2) in high concentration, and/or (3) having a morphology that is complex such as filamen- tous cyanobacteria (see Figure 11.11). Finally, some researchers perform chlorophyll *a* extraction and report the chlorophyll *a* concentration, denoted by mg Chl *a*/m^3, as a measure of the microorganism concentration. Chlorophyll *a* is chosen as it is present in all plants, algae, and cyanobacteria that photosynthesize. The results reported in mg Chl *a*/m^3 make comparisons difficult with other results as the chlorophyll *a* content

per microorganism depends on the species and growth conditions. Moreover, differ- ent microorganisms can have different pigment concentrations or different pigments altogether. Then, reporting the chlorophyll *a* concentration can make results difficult to compare.

Thus, it is recommended that the microorganism concentration be reported in kg dry cell/m^3 or in number density (#/m^3). Rapid measurements of microorganism concentra- tions can be performed by measuring the optical density (OD) of microorganism suspen- sion at one or more wavelengths using a UV–visible spectrophotometer. Then, convenient calibration curves can be developed to relate the OD to the dry cell weight or the number density.

11.3.3.2 Hydrogen Production Rate

The hydrogen production rate is reported either as the total mass or volume of hydrogen produced per unit time by the photobioreactor, expressed in kg/h, mmol/h, or m^3/h, or as the specific rate per kg dry cell or per milligram of Chl *a*, denoted by kg/kg dry cell/h or kg/mg Chl *a*/h. When reported in volumetric units, the pressure and temperature of the sample must be specified. Unfortunately, many volumetric production rates reported in the literature lack this detail making the results impossible to compare with other studies.

It is recommended that hydrogen production be reported in kg of H_2/h as this rate does not depend on the temperature and pressure of the measurement conditions. Similarly, the specific hydrogen production rates can be reported in kg of H_2/h per kg dry cell or in kg of H_2/h per unit volume of the photobioreactor.

11.3.3.3 Illumination

Light irradiance G_{in} is reported (1) in total luminous flux expressed in lux (1 lux = 1 cd· sr/m^2), (2) in photon flux expressed in $\mu mol/m^2/s$, or (3) in energy flux expressed in W/m^2. The total luminous flux, also known as illuminance, is a photometric unit that measures light account- ing for the human eye sensitivity. The energy emitted by the source is wavelength weighted by the luminosity function that describes the average sensitivity of the human eye to light at different wavelengths between 400 and 700 nm. Different light sources with different emis- sion spectra could have the same illuminance. Thus, illuminance is not recommended for reporting illumination.

On the other hand, photon flux refers to the number of moles of photons (6.02 × 10^{23} photons/mol) incident on a unit surface area per unit time in the PAR, that is, from 400 to 700 nm. This is a more appropriate unit for reporting the incident energy in photosynthetic systems. It is measured with a quantum sensor that is calibrated to mea- sure the photon flux in the PAR. However, both illuminance and photon flux are valid only in the spectral range from 400 to 700 nm and cannot be used to quantify energy in the NIR part of the spectrum. Thus, in experiments using microorganisms that absorb in NIR such as purple nonsulfur bacteria, illumination reported in illuminance or pho- ton flux cannot be used. Instead, the energy flux should be recorded with a pyranometer having the sensitivity from about 300 to 2800 nm and reported in W/m^2 μm. Moreover, it is recommended that the spectral sensitivity of the detector and the emission spectrum of the light source be also reported for clarity and reproducibility of the experiments. For benchtop experiments using artificial light, it is useful to report not only the total but also the spectral irradiance.

11.3.3.4 Light-to-Hydrogen Energy Conversion Efficiency

Light-to-hydrogen energy conversion efficiency of photobioreactors is defined as the ratio of (1) the energy that would be released from the reaction of the produced hydrogen with oxygen to produce water and (2) the energy input to the system as light, that is [57],

$$\eta_{H_2} = \frac{[\Delta G_o + RT \ln(P_{H_2}/P_o)]R_{H_2}}{G A_{in\,s}} \quad (11.5)$$

where

R_{H_2} is the rate of production of H_2 in mol/s
A_s is the illumination area in m^2
ΔG_o is the standard-state free energy of the formation of H_2 from the water-splitting reaction, equal to 236,337 J/mol at 303 K and 1 atm

The term $RT \ln(P_{H_2}/P_o)$ is the correction factor for ΔG_o when H_2 production takes place at H_2 partial pressure P_{H_2} instead of the standard pressure P_o of 1 atm. The term G_{in} is the power input to the system as light, that is, irradiance in W/m^2. In reporting the light energy conversion efficiency, it is important to report the spectral range over which G_{in} is measured. Indeed, the efficiency computed using G_{in} defined over the PAR is about 2.22 times larger than that obtained with G_{in} computed over the entire solar spectrum.

11.4 Photobioreactor Systems

Photobiological hydrogen production by direct and indirect biophotolysis and by photofermentation typically consists of a first stage when microorganisms are grown by photosynthesis in the presence of air and CO_2. It is followed by a second stage when hydrogen is produced at constant microorganism concentration in the absence of CO_2, O_2, and N_2. During the growth phase, cyanobacteria fix CO_2 and nitrogen from the atmosphere to grow and produce photosynthates. In the H_2 production phase, they utilize the photosyn- thates to produce H_2. Alternatively, green algae *C. reinhardtii* are grown in a medium con- taining acetate. Then, the microorganisms are transferred into a sulfur-deprived medium where anoxia is induced by algae respiration resulting in H_2 production under relative high light irradiance, as first proposed by Melis et al. [40].

For economic reasons, the growth phase should be performed in open ponds [58]. In the hydrogen production phase, open systems will not be appropriate as the method of collection of hydrogen will pose serious difficulties. Similarly, closed indoor systems are not economically feasible since using artificial lighting defeats the purpose of solar energy utilization. Figure 11.13 schematically illustrates the typical process flow envisioned for photobiological hydrogen production at industrial scale [59]. This section presents the different types of photobioreactors used for the hydrogen production phase with emphasis on closed outdoor photobioreactors. It also discusses performances and modeling of mass and light transfer in photobioreactors.

11.4.1 Photobioreactor Types

Photobioreactors have been used for a wide range of applications including the production of pharmaceutics, food additives for humans, feed for animals, and cosmetic chemicals

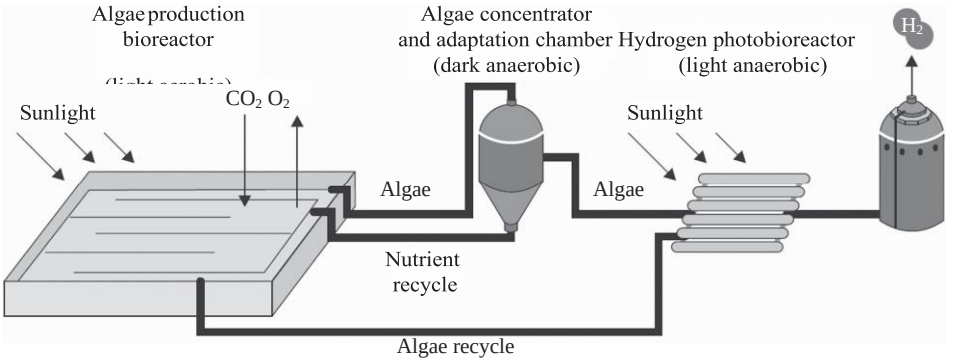


FIGURE 11.13

Typical process flow for industrial-scale photobiological hydrogen production. (From Riis, T. et al., Hydrogen production and storage—R&D priorities and gaps, International Energy Agency—Hydrogen Co-Ordination Group—Hydrogen Implementing Agreement, 2006, www.iea.org/Textbase/papers/2006/hydrogen.pdf; Courtesy of the International Energy Agency, Paris, France.)

using photosynthetic microorganisms [60]. They also found applications in environmental engineering such as wastewater treatment, heavy metal removal, and CO_2 mitigation [60]. More recently, they have been considered for hydrogen production [61–65].

On the most basic premises, photobioreactors can be grouped into three main catego- ries, namely, (1) open cultivation systems, (2) closed outdoor systems, and (3) closed indoor systems [66]. The open systems are constructed in natural or artificial ponds and utilize sunlight. Closed outdoor photobioreactors consist of specially designed light transparent containers usually in the form of tubes or flat plates and also utilize sunlight [66]. Closed indoor systems, on the other hand, use artificial lighting such as fluorescent lights and light-emitting diodes (LEDs). Their construction is usually a light transparent adaptation of the conventional fermenter systems including stirred-tank bioreactors and vertical cylindrical columns. The advantages and disadvantages of closed and open systems are summarized in Table 11.4.

TABLE 11.4

Comparison of Photobioreactors

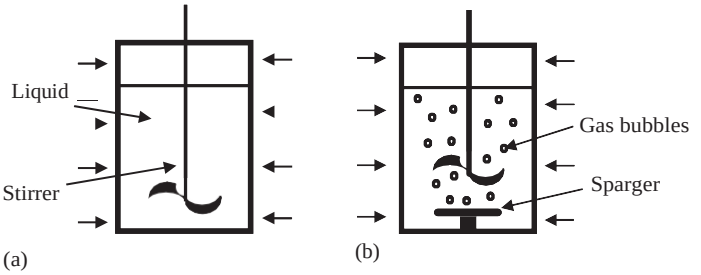
Type	Advantages	Disadvantages
Open Systems	Inexpensive to build and operate Uses sunlight	Small cell densities (0.1–0.2 g/L) Large space requirements Difficult to maintain monoculture Large water and CO_2 losses
Closed Outdoor	Improved control Limited water losses Uses sunlight Large cell densities (2–8 g/L) Easy to maintain monoculture	Relatively high installation costs Susceptible to ambient temperature variations Difficult to scale up Thermal management challenges Relatively high installation and operation costs
Closed Indoor	Large cell densities (2–8 g/L) Total control over physiological conditions	Inefficient

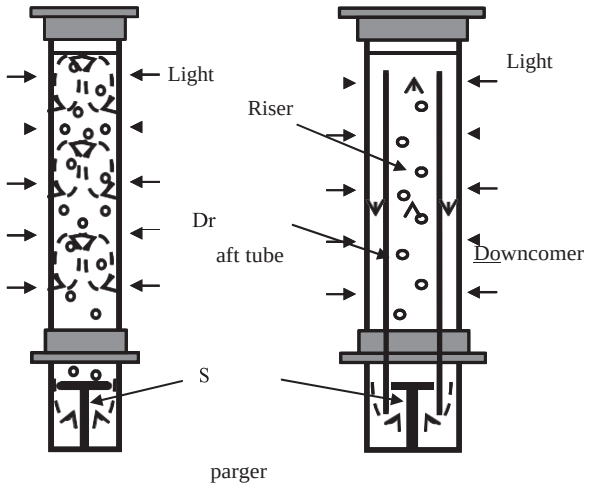
Sources: Pulz, O., *Appl. Microbiol. Biotechnol*., 57(3), 287, 2001; Suh, I.S. and Lee, C.G., *Biotechnol. Bioprocess Eng*., 8(6), 313, 2003.

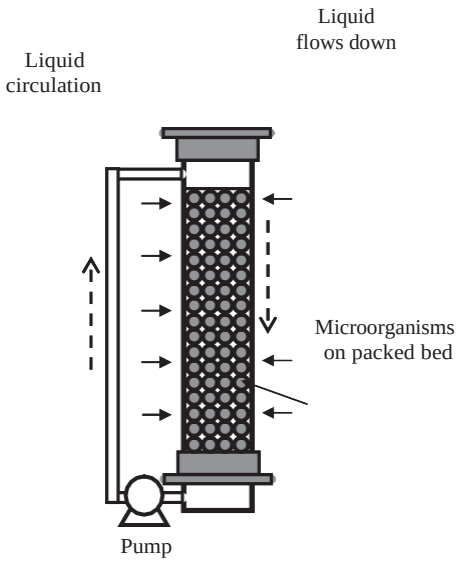
11.4.2 Closed Outdoor Photobioreactor Designs and Performances

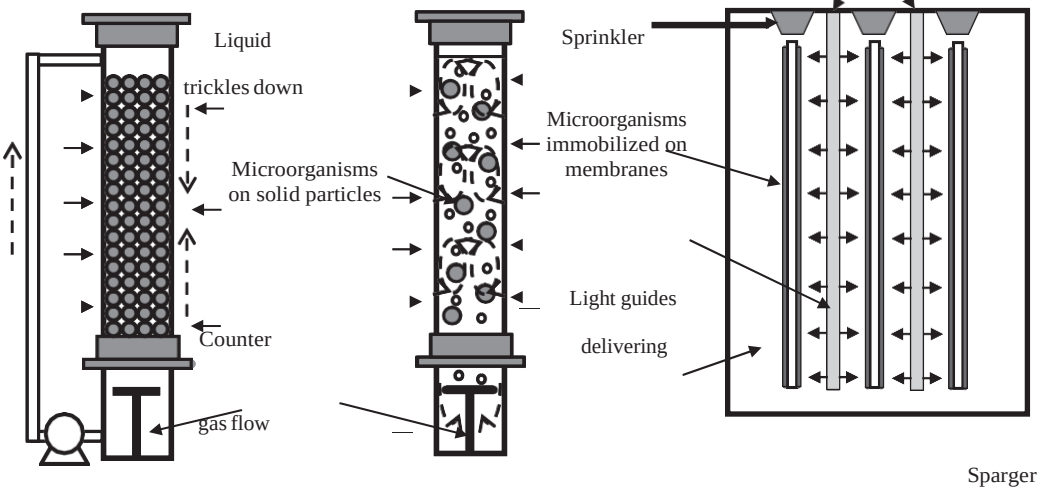
Most common types of closed photobioreactors are vertical or horizontal tubular, helical, and inclined or horizontal thin panel types [66]. Figure 11.14 shows some of these photobioreactor types that can be listed as follows:

- *Stirred-tank photobioreactors* are mechanically stirred photobioreactors to enhance mass transfer as shown in Figure 11.14a [67]. They are mostly suited for reac- tor volumes between 0.2 and 3 L. Examples include torus photobioreactors [68]. These reactors are often used for research purposes as they enable the control and uniformity of the growth conditions including hydrodynamics conditions, light exposure, concentrations, and pH. This permits full analysis of the system based on mass and energy conservation principles [69–71]. The drawback of these reactors is that very high stirring rates (>600 rpm) might be required to avoid the reactor to become mass transfer limited. Thus, continuously stirring the photobio- reactor increases the operating costs, makes scale-up difficult, and decreases the reliability of the system.
- *Sparged- and stirred-tank photobioreactors*. To effectively stir the photobioreactor, gas can be sparged into the photobioreactor as shown in Figure 11.14b [67]. Sparging consists of injecting gas into the liquid phase through a porous medium called sparger or diffuser. This creates bubbles that could be further broken up by mechanical stirring to increase the interfacial area between the liquid and gas and enhances mass transfer. These photobioreactors require lower stirring rates than nonsparged ones and can accommodate liquid volumes greater than 500,000 L [67].
- *Bubble-column photobioreactors* use only sparging for agitation and aeration pur- poses as shown in Figure 11.14c [67]. They have a high liquid height to base width ratio to increase the bubble residence time and consequently the interfacial area available for mass transfer. Compared with stirred-tank photobioreactors, bubble columns provide less shear on the microorganisms and thus are more suitable for cultivation of plant cells [67].
- *Airlift photobioreactors* are very similar to bubble-column reactors except that they house a draft tube to regulate the flow of bubbles in the reactor as shown in Figure 11.14d [67]. This draft tube provides better heat and mass transfer efficien- cies as well as more uniform shear levels. Excessive foaming and cell damage due to bubble bursting are among the drawbacks of airlift photobioreactors. Bubble- column and airlift designs include cylindrical or flat-plate types that can be ori- ented vertically upright or tilted at an angle [34,72].
- *Packed-bed photobioreactors*. The volume of the reactor is packed with small particles that provide a high surface area substrate on which microorganisms can grow as shown in Figure 11.14e [67]. The packed bed is completely filled with nutrient medium that is constantly circulated. Packed-bed photobioreactors suffer from clogging that inhibits effective mass transfer and limited light transfer to the microorganisms.
- *Trickle-bed photobioreactors* are very similar to packed-bed photobioreactors. However, the reactor liquid does not completely submerge the packing where the microorganisms are immobilized but, instead, trickles on the particles' surface as illustrated in Figure 11.14f [67]. This offers the advantage of minimizing water use. Usually, a gas flow counter to the liquid flow is also provided in trickle-bed photobioreactors for enhanced aeration. One drawback of these reactors is that


Liquid
Stirrer
(a)
Gas bubbles
Sparger
(b)


Light
Dr
aft tube
S
parger
(c)
Light
Riser
Downcomer
(d)


Liquid
flows down
Liquid
circulation
Microorganisms
on packed bed
Pump
(e)


Liquid
trickles down
Microorganisms
on solid particles
Counter
gas flow
Light
Sprinkler
Microorganisms
immobilized on
membranes
Light guides
delivering
Sparger

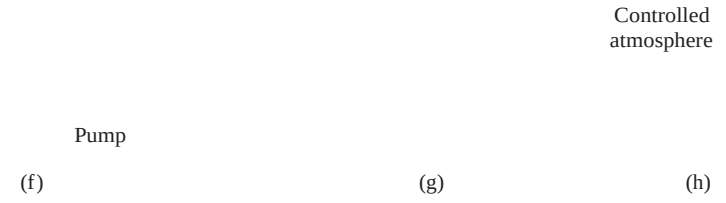


FIGURE 11.14

Typical photobioreactor designs: (a) stirred-tank, (b) sparged- and stirred-tank, (c) bubble-column, (d) airlift,

(e) packed-bed, (f) trickle-bed, (g) fluidized-bed, and (h) membrane photobioreactors. (After Bayless, D.J. et al., *J. Environ. Eng. Manage*., 16(4), 209, 2006.)

they have relatively low gas transfer per unit volume compared with sparged systems and have limited light transfer.

- *Fluidized-bed photobioreactors*. Microorganisms are immobilized within and/or on lightweight solid particles that are free to move with the fluid and are circulated within the photobioreactor as depicted in Figure 11.14g [67]. This can achieve large mass transfer rates at high cell concentrations.
- *Membrane photobioreactors*. Microorganisms are immobilized on membranes that are constantly being wet by a drip or a sprinkler system as shown in Figure 11.14h [73,74]. Light is collected by a heliostat unit and delivered to the microorganism via lightguides. These photobioreactors minimize the use of water, deliver controlled irradiance to the microorganisms, and can achieve large growth rates. However, they are expensive to build and operate.

Although most of these photobioreactor types were designed for fermenters, their adaptations to photobiological technologies have been discussed in the literature and need not be repeated here [66,75,76]. Despite recent advances, the performances of photobioreactors remain far from theoretical maxima even for benchtop systems [76].

11.4.3 Microorganism and Photobioreactor Performances

Table 11.5 provides a sample of selected studies conducted in laboratories reporting hydrogen production rates by a wide variety of microorganisms. The performance of various microorganisms and growth conditions and photobioreactors has been compared and discussed in Refs. [34,77,78].

Instead of providing an exhaustive review of past studies in this rapidly evolving field, the reader is referred to Ref. [79] for consulting and contributing to the latest experimental results. This wikipage makes use of the cyberinfrastructure to develop a virtual community focusing on photobiological CO_2 fixation and H_2 production. This resource should benefit this community in several ways. First, it provides a platform to share recent advances, experimental tips and data, database of bacterial properties, medium, as well as teaching material. Unlike textbooks, this resource can be regularly updated to reflect new advances so its content is less likely to become outdated. The content of the wiki is not dictated by a few experts but is entirely editable by the readers. Consequently, peer review is built into the publishing process and remains an active and continuous component throughout the life of the repository. Finally, it will bridge currently distinct communities in microbiology and plant biology on the one hand and engineering on the other.

11.4.4 Simulating Photobioreactors

In order to design, scale up, optimize, and compare the various photobioreactor designs, it is essential to develop experimentally validated simulation tools that account for light transfer, hydrodynamic conditions, and microorganism growth or H_2 production, along with mass conservation for nutrients and gas species. This section briefly reviews efforts in this area. For the sake of brevity, only selected studies are discussed.

11.4.4.1 Simulating Light Transfer

As light penetrates in the photobioreactor, it is absorbed by the microorganisms or by the medium and scattered by microorganisms and, possibly, by gas bubbles. These scat- terers are much larger than visible wavelengths and therefore scattering is strongly

TABLE 11.5

Maximum Reported Hydrogen Production Rates for Various Types of Microorganisms

	Strain Name	Maximum Reported H_2 Production Rate	References
Freshwater Green Algae	*Chlamydomonas moewusii*	460 mmol/g chl *a*/h	[136]
	Chlamydomonas reinhardtii	200 mmol/g chl *a*/h	[136]
	Lobochlamys segnis	96 mmol/g chl *a*/h	[136]
	Chlamydomonas noctigama	31 mmol/g chl *a*/h	[136]
Marine Green Algae	*Scenedesmus vacuolatus*	155 mmol/g chl *a*/h	[136]
	Scenedesmus obliquus	150 mmol/g chl *a*/h	[44]
	Chlorococcum littorale	52 mmol/g chl *a*/h	[43]
Freshwater Cyanobacteria	*Anabaena variabilis* PK 84	167.6 mmol/g chl *a*/h	[46]
	Anabaena variabilis PK 17R	59.18 mmol/g chl *a*/h	[46]
	Anabaena variabilis ATCC 29413	45.16 mmol/g chl *a*/h	[46]
	Anabaena azollae	38.5 mmol/g chl *a*/h	[46]
	Anabaena CA	2.14 mol/kg/h	[49]
	Gloeobacter PCC 7421	1.38 mmol/g chl *a*/h	[77]
	Anabaena cylindrica	1.3 mol/kg/h	[77]
	Nostoc muscorum IAM M-14	0.6 mmol/g chl *a*/h	[77]
	Synechococcus PCC 602	0.66 mmol/g chl *a*/h	[77]
Marine Cyanobacteria	*Cyanothece* 7822	0.92 mmol/g chl *a*/h	[137]
	Oscillatoria limosa	0.83 mmol/g chl *a*/h	[49]
	Oscillatoria Miami BG7	0.3 mol/kg/h	[49]
Purple Nonsulfur Bacteria	*Rhodopseudomonas sphaeroides*	133 mol/kg/h	[41]
	Rhodobacter sphaeroides	5.9 mol/kg/h	[138]
	Rhodospirillum rubrum	2.5 mol/kg/h	[139,140]
Dark Fermentative Bacteria	*Enterobacter cloacae* IIT BT-08	211.63 mol/kg/h	[51]
	Enterobacter aerogenes	17 mol/kg/h	[41]
	Citrobacter intermedius	11.5 mol/kg/h	[141]
	Clostridium butyricum	7.3 mol/kg/h	[142]

forward [80,81]. Light transfer through the photobioreactor is governed by the radiative transfer equation (RTE) that expresses an energy balance in a unit solid angle $d\Omega$, about the direction $\hat{s}$ at location $\hat{r}$. The steady-state RTE in a well-mixed photobioreactor containing microorganisms and bubbles is expressed as [82]

$$\hat{s}\cdot\nabla I_\lambda(\hat{r},\hat{s}) = -\kappa_{eff,\lambda} I_\lambda(\hat{r},\hat{s}) - \sigma_{eff,\lambda} I_\lambda(\hat{r},\hat{s}) + \frac{\sigma_{X,\lambda}}{4\pi}\int_{4\pi} I_\lambda(\hat{r},\hat{s}_i)\Phi_{X,\lambda}(\hat{s}_i,\hat{s})\,d\Omega_i + \frac{\sigma_{B,\lambda}}{4\pi}\int_{4\pi} I_\lambda(\hat{r},\hat{s}_i)\Phi_{B,\lambda}(\hat{s}_i,\hat{s})\,d\Omega_i \tag{11.6}$$

where

$I_\lambda(\hat{r},\hat{s})$ is the radiation intensity at wavelength λ in direction $\hat{s}$ at location $\hat{r}$
$\kappa_{eff,\lambda}$ and $\sigma_{eff,\lambda}$ are the effective spectral absorption and scattering coefficients, respectively

The coefficients $\sigma_{X,\lambda}$ and $\sigma_{B,\lambda}$ are the spectral scattering coefficients of the microorganisms and the bubbles, respectively

The scattering phase functions of microorganisms and bubbles are denoted by $\Phi_{X,\lambda}(\hat{s}_i, \hat{s})$ and $\Phi_{B,\lambda}(\hat{s}_i, \hat{s})$, respectively

They describe the probability that radiation traveling in the solid angle $d\Omega_i$ around the direction $\hat{s}_i$ will be scattered into the solid angle $d\Omega$ around the direction $\hat{s}$. They equal unity when scattering is isotropic. The effective absorption coefficient $\kappa_{eff,\lambda}$ accounts for the absorption by the liquid phase and by the microorganisms at wavelength λ. It can be written in terms of the bubble void fraction f_B and of the microorganism concentration X (in kg/m^3),

$$\kappa_{eff,\lambda} = \kappa_{L,\lambda}(1 - f_B - Xv_X) + A_{abs,\lambda}X \tag{11.7}$$

where v_X is the specific volume of microorganisms. The absorption coefficient of the liquid phase $\kappa_{L,\lambda}$ is expressed in m^{-1}, and the mass absorption cross section of microorganisms $A_{abs,\lambda}$ is expressed in m^2/kg. The term $\kappa_{X,\lambda} = A_{abs,\lambda}X$ corresponds to the absorption coefficient of microorganisms. Finally, the term Xv_X represents the volume fraction of the photobioreactor occupied by microorganisms. Assuming independent scattering, the effective scattering coefficient of the composite medium $\sigma_{eff,\lambda}$ can be expressed as the sum of the scattering coefficients of the microorganisms $\sigma_{X,\lambda}$ and of the bubbles $\sigma_{B,\lambda}$ as

$$\sigma_{eff,\lambda} = \sigma_{X,\lambda} + \sigma_{B,\lambda} = S_{sca,\lambda}X + \frac{A_i}{4}Q_{sca,B}(a, \lambda) \tag{11.8}$$

where

$S_{sca,\lambda}$ is the mass scattering cross section of microorganisms expressed in m^2/kg
$Q_{sca,B}(a,\lambda)$ is the scattering efficiency factor of monodisperse bubbles of radius a at wave- length λ obtained from the Mie theory [83]

The interfacial area concentration A_i is defined as the total surface area of bubbles per unit volume and expressed as $A_i = 3f_B/a$. Note that a similar approach can be used to model (1) mixed cultures, (2) scattering by beads in packed beds, and/or (3) polydispersed bubbles [84], for example.

Beer–Lambert's law provides the solution of the 1D steady-state RTE accounting for both absorption and out-scattering but ignoring in-scattering. It physically corresponds to cases when photons experience at most one scattering event as they travel through the reac- tor, that is, single scattering prevails. It gives the local spectral irradiance $G_\lambda(z)$ within the photobioreactor as

$$G_\lambda(z) = \int_0^{4\pi} I_\lambda(z, \hat{s})\, d\Omega = G_{\lambda,in}\exp(-\beta_{eff,\lambda} z) \tag{11.9}$$

where

$G_{\lambda,in}$ is the spectral irradiance incident on the photobioreactor
z is the distance from the front surface
$\beta_{eff,\lambda}$ is the effective extinction coefficient of the suspension at wavelength λ defined as $\beta_{eff,\lambda} = \kappa_{eff,\lambda} + \sigma_{eff,\lambda}$

Beer–Lambert's law has been used extensively to predict the local irradiance within pho-

tobioreactors [85,86].

Moreover, Cornet et al. [87–89] solved the RTE using the Schuster–Schwarzschild two-flux approximation to model light transfer in filamentous cyanobacterium *Spirulina platensis* cultures. This approach consists of solving a pair of coupled ordinary differential equations obtained by integrating the RTE over two complementary hemispheres. It can account for in-scattering terms as well as anisotropic scattering [84]. It can also provide an analytical solution for $G_\lambda(z)$ albeit more complex than Beer–Lambert's law [68,69,90]. Finally, most of the aforementioned studies did not account for the spectral dependency of the radiation characteristics and/or for the presence of bubbles. More recently, Berberoğlu and Pilon [82] simulated light transfer in a bubble sparged photobioreactor accounting for absorption and anisotropic scattering by bubbles and microorganisms. Spectral variations of radiation characteristics over the spectral range from 400 to 700 nm were accounted for using the box model [82]. Genetically engineered microorganisms with reduced pigment content were also considered. The authors established that (1) Beer–Lambert's law cannot be applied to predict the irradiance inside the photobioreactor, that is, multiple scattering must be accounted for, (2) isotropic scattering can be assumed for wild-strain microorganisms for all practical purposes in the absence of bubbles, (3) anisotropic scattering by the bubbles must be accounted for particularly as the interfacial area concentration increases, (4) for microorganisms with reduced pigment concentration, their anisotropic scattering should be considered.

In order to simulate light transfer in photobioreactors and use any of the aforementioned light transfer models, the spectral radiative characteristics, namely, κ_λ, σ_λ, and $\Phi_\lambda(\hat{s}_i, \hat{s})$ of the microorganisms and/or the bubbles are required. They can be determined either through experimental measurements [80,81] or theoretically by using the Mie theory [69]. Theoretical predictions often assume that the scatterers have relatively simple shapes (e.g., spherical) and ignore their heterogeneous nature by assuming that the complex index of refraction is uniform. Pottier et al. [69] acknowledged that for complex microorganism shapes (e.g., cylinders and spheroids), advanced numerical tools are required to predict radiative characteristics. Alternatively, experimental measurements account for the actual shape and morphology and size distribution of the microorganisms. A comprehensive review of the experimental techniques for measuring the radiation characteristics has been reported by Agrawal and Mengüç [91] and need not be repeated. Pilon and Berberoğlu [80,81] experimentally measured the radiation characteristics of H_2-producing microorganisms, namely, (1) purple nonsulfur bacteria *R. sphaeroides* [80], (2) cyanobacteria *A. variabilis* [80], and (3) green algae *Chlamydomonas reinhardtii* strain CC125 and its truncated chlorophyll antenna transformants *tla*1, *tlaX*, and *tla*1-CW$^+$ [81]. The absorption and scattering cross sec- tions of all strains studied were obtained over the spectral range from 300 to 1300 nm along with their scattering phase function at 632.8 nm. The latter can be assumed to be indepen- dent of wavelength in the PAR [92,93]. It was established that *R. sphaeroides* absorbs mainly in two distinct spectral regions from 300 to 600 nm and from 750 to 900 nm. The major absorption peaks can be observed around 370, 480, 790, and 850 nm and can be attributed to the presence of bacteriochlorophyll *b* and carotenoids in the antenna complexes B850 and the reaction center complex [30,94]. Moreover, *A. variabilis* and the wild strain *C. reinhardtii* CC125 absorb mainly in the spectral region from 300 to 700 nm with absorption peaks at 435 and 676 nm corresponding to in vivo absorption peaks of chlorophyll *a*. *A. variabilis* also absorbs at 621 nm corresponding to absorption by the pigment phycocyanin [30], while
C. reinhardtii has additional absorption peaks at 475 and 650 nm corresponding to absorption by chlorophyll *b*. The genetically engineered strains of *C. reinhardtii* were shown to have less chlorophyll pigments than the wild strain and thus smaller absorption cross sections as illustrated in Figure 11.15. In particular, the mutant *tlaX* features a significant reduction in chlorophyll *b* concentration. For all mutants, however, the reduction in the absorption

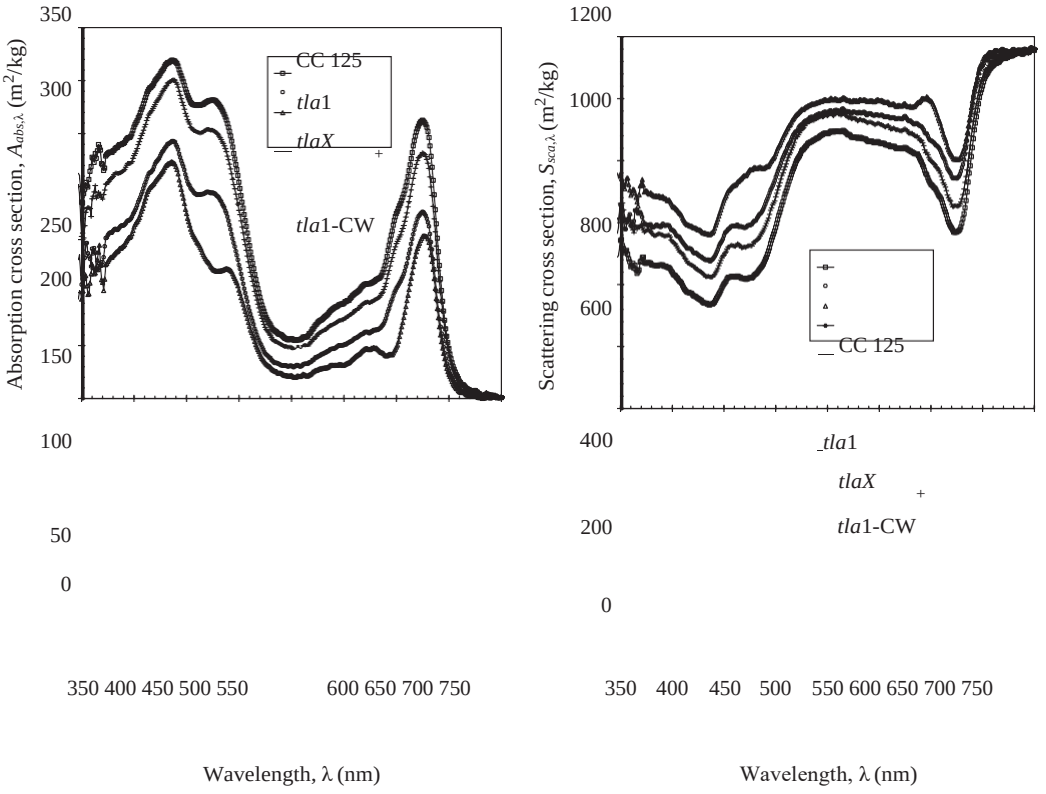


FIGURE 11.15

Absorption and scattering cross sections of the green algae *C. reinhardtii* CC 125 and its truncated chlorophyll antenna transformants *tla*1, *tlaX*, and *tla*1-CW$^+$. (From Berberoğlu, H. et al., *Int. J. Hydrogen Energy*, 33(22), 6467, 2008.)

cross section is accompanied by an increase in scattering cross section [81] (see Figure 11.15). Although scattering becomes the dominant phenomenon contributing to the overall extinction of light, it is mainly in the forward direction so light penetrates within the reactor.

11.4.4.2 Simulating Hydrodynamic Conditions

Hydrodynamic conditions in a photobioreactor affect the shear stress and the amount of light to which individual microorganisms are subjected. Both affect the system's productivity [90]. Simulations of hydrodynamic conditions consist of, first, solving mass and momentum (or Navier–Stokes) conservation equations for a specific reactor geometry to find the local fluid velocity within the photobioreactors. The Lagrangian approach is used to identify the trajectory of individual microorganisms as they are carried by the medium [85]. The instantaneous light flux received by a microorganism can, then, be determined as a function of time [85], and the frequency of light–dark cycles can be determined. These cycles are known to have a strong effect on the microorganism growth, and the cycle frequency should optimally range between 1 Hz and 1 kHz, which is difficult to achieve at industrial scale [76]. Finally, the average light energy received by a microorganism can be computed and used to estimate their growth or hydrogen production rate based on kinetic models.

11.4.4.2.1 Photosynthetic Growth Kinetics

During the growth phase, the time rate of change of microorganism concentration X can be modeled as [95]

$$\frac{dX}{d} = \mu X \tag{11.10}$$

where μ is the specific growth rate expressed in s^{-1} and function of the average available irradiance denoted by G_{av}. The specific growth rate has been modeled using the modified Monod model taking into account light saturation and inhibition as [67]

$$\mu = \mu_{max} \left(\frac{G_{av}}{K_{s,G} + G_{av} + (G_{av}^2 / K_{i,G})} \right) \tag{11.11}$$

where μ_{max} is the maximum specific growth rate while the coefficients $K_{s,G}$ and $K_{i,G}$ are the light half-saturation and inhibition constants, respectively. Similar models can be formulated to account for saturation and inhibition due to limited or excessive carbon dioxide concentrations or excessive microorganism concentrations, for example. The average available irradiance G_{av} can be estimated by averaging the local irradiance over the depth of the culture L as

$$G_{av} = \frac{1}{L}\int_0^L G(z)dz = \frac{1}{L}\int_0^\infty\int_0^\infty G_\lambda(z)d\lambda dz \tag{11.12}$$

where $G_\lambda(z)$ is estimated by (1) solving the RTE, (2) using approximate solutions such as Beer–Lambert's law (Equation 11.9), or (3) averaging the light energy received by microorganisms as predicted by hydrodynamics simulations. Fouchard et al. [71] identified μ_{max}, $K_{s,G}$, and $K_{i,G}$ for *C. reinhardtii* in TAP medium without acetate to be 0.2274 h^{-1}, 81.38 μmol photon/m^2/s, and 2500 μmol photon/m^2/s, respectively.

11.4.4.2.2 Photobiological H_2 Evolution Kinetics

Similarly, the specific production rate π_{H_2} has been modeled with a modified Michaelis–Menten-type equation given by [95]

$$\pi_{H_2}(z) = \pi_{H_2,max}\frac{G_{av}(z)}{K_{s,H_2} + G_{av}(z) + G_{av}^2(z)/K_{i,H_2}} \tag{11.13}$$

where $\pi_{H_2,max}$ is the maximum specific hydrogen production rate expressed in kg H_2/kg dry cell/h. The parameters K_{s,H_2} and K_{i,H_2} account for the saturation and the inhibition of hydrogen production due to excessive irradiation or limited light irradiance.

Nogi et al. [96] measured the specific hydrogen production rate π_{H_2} of the purple nonsulfur bacteria *Rhodopseudomonas rutila* as a function of incident irradiance. The authors reported the absorption spectrum, the hydrogen production rate as a function of spec- tral incident radiation, and the specific hydrogen production rate as a function of usable radiation. The parameters $\pi_{H_2,max}$, K_{s,H_2}, and K_{i,H_2} were estimated by least-squares fitting of the experimental data reported over the usable incident radiation range from 0 to 80 W/m^2[96]. The values of $\pi_{H_2,max}$, K_{s,H_2}, and K_{i,H_2} were found to be 1.3 × 10^{-3} kg H_2/kg dry cell/h, 25 W/m^2, and 120 W/m^2, respectively. Figure 11.16 compares the prediction of Equation 11.13 for π_{H_2} with data reported by Nogi et al. [96].

11.4.4.2.3 Mass Conservation Equations

Mass conservation principles should be satisfied by all gas and nutrient species such as dissolved oxygen, hydrogen, starch, and/or sulfur for green algae. For a well-mixed photobioreactor, the concentrations are assumed to be uniform throughout the reactor and their time rate of change is expressed as

$$\frac{dC_i}{dt} = r_i - k_La(C_i - C_{i,eq}) \tag{11.14}$$

where

r_i is the net production rate of species "i"
k_La is the specific gas–liquid mass transfer coefficient

$C_{i,eq}$ is the equilibrium concentration between the gas and the liquid phases.

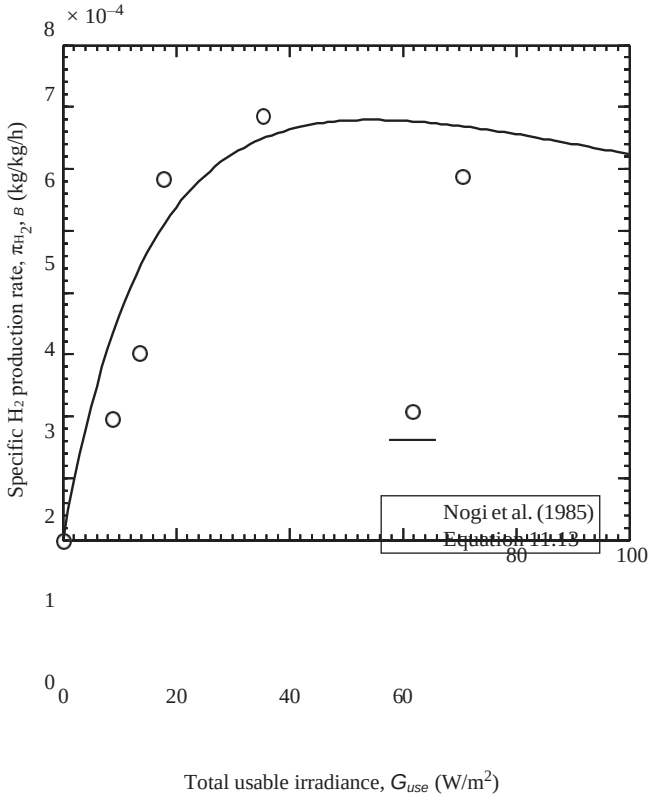


FIGURE 11.16

Experimental data and the modified Michaelis–Menten model (Equation 11.13) for the specific hydrogen produc- tion rate of *R. rutila* as a function of the usable incident radiation G_{use} with parameters $\pi_{H_2,max} = 1.3 \times 10^{-3}$ kg H_2/kg dry cell/h, K_G = 25 W/m², and K_I = 120 W/m². (From Nogi, Y. et al., *Agric. Biol. Chem*., 49, 3538, 1985.)

For oxygen, for example, r_{O_2} accounts for O_2 generated during photosynthesis and consumed by respiration. It is often assumed to be proportional to the microorganism growth rate, that is, $r_{O_2} = Y_{O_2}\mu X$, where Y_{O_2} is the yield coefficient of O_2 conversion. The reader is referred to Ref. [71] for an illustration of modeling of photobiological H_2 production by *C. reinhardtii* accounting for light transfer, algal growth, and extracellular and intracellular sulfur, starch, and oxygen consumption and/or production along with an estimate of the associated model parameters.

11.5 Technical Challenges and Limitations

Current photobiological hydrogen production suffers from low solar-to-hydrogen energy conversion efficiency that is typically less than 1% [97] under outdoor conditions. In addition, scale-up and economic viability remain major challenges mainly due to issues related to (1) light transfer limitation, (2) mass transfer and hydrodynamics limitations, (3) thermal management, (4) contamination and maintenance of monoculture, and (5) the photobioreactor cost.

11.5.1. Light Transfer

Light transfer in photobioreactors is one of the main barriers to the technology [98,99]. Indeed, photosynthetic microorganisms require an optimum irradiance to achieve the most efficient photosynthesis and H_2 production. This optimum depends on the particular

microorganism but, in general, is about 100 W/m^2 for naturally occurring strains [100]. Thus, photobioreactors can suffer from the following:

- *Light inhibition*. Excessive irradiance inhibits the microbial photosynthesis and H_2 production through a process called photooxidative damage [101,102]. In outdoor systems, where this technology is meant to be deployed, solar irradiance can reach as high as 1000 W/m^2 [103]. For more efficient use of sunlight, it has to be redistrib- uted uniformly throughout the photobioreactor.
- *Limited light penetration*. Due to light absorption by the microorganisms and the medium and scattering by both the microorganisms and gas bubbles, the local irradiance within the photobioreactor may decrease below the required levels for photosynthesis and/or H_2 production [87–89,97]. This, in turn, limits the produc- tivity and scale-up of the system.

Ways to address these light transfer challenges are discussed in Section 11.6.

11.5.2 Mass Transfer and Hydrodynamics

Hydrogen and possibly oxygen produced by the microorganisms have inhibitory effects on photobiological hydrogen production [55,103]. Therefore, these gas species must be efficiently removed from the photobioreactor for sustained H_2 production. The issues related to mass transfer and hydrodynamics are the following:

- *By-product buildup*. Algae and cyanobacteria produce O_2 as a by-product of photosynthesis. Excessive O_2 concentrations result in inhibition of nitrogenase and hydrogenase [97,101]. Similarly, excessive buildup of H_2 decreases the production rate in hydrogenase-based systems [101,104]. Methods such as applying partial vacuum [61] and sparging with an inert gas [105] have been suggested to remove H_2 and O_2. However, these techniques have been considered economically unfea- sible at industrial scale [106]. Currently, this challenge is being addressed by microbiologists where O_2-tolerant enzymes are being isolated/developed and expressed in selected microorganisms [106]. Alternatively, the inhibition of O_2 production by sulfur deprivation of green algae *C. reinhardtii* has been demon- strated [40].
- *Low interfacial area concentration*. Mass transfer from gas to liquid phase requires large gas–liquid interfacial area. As the reactor is scaled up, the surface area available for gas transfer per unit volume of the reactor decreases in nonsparged reactors. This makes CO_2 transfer a limiting factor, during the growth phase, for achieving large cell densities in scaled-up systems having volumes larger than 50 L [55,66]. It also limits the removal of O_2 and H_2 during the H_2 production phase and may result in by-product buildup and reduce the overall efficiency.
- *Sedimentation of microorganisms and nutrients*. This causes limitations on the availability of nutrients and light to the settled microorganisms [27,66]. The photo- bioreactor can be stirred or sparged with bubbles to keep microorganisms in suspension in addition to alleviating the mass transfer limitations. However, unfavorably high shear can be detrimental to microorganisms during liquid flow and/or bubble collapse [66,107]. In addition, stirring is prohibitively expensive for large-scale systems.

11.5.3 Nutrient Composition

The concentration of both macro- and micronutrients has significant effect on the CO_2 consumption and H_2 production by the microorganisms [55,101,105]. However, the effects of different nutrient concentrations and different media on photobiological hydrogen production and the associated pathways are not known precisely. The optimization of nutrient composition could contribute to increasing the efficiency of the photobiological system. For example, Berberoğlu et al. [108] reported a factor 5.5 increase in hydrogen production rate by *Anabaena variabilis* ATCC 29413 using Allen–Arnon medium compared with BG-11 and BG-11_o media under otherwise identical conditions (light, concentration, pH, tempera- ture). Moreover, the heterocyst frequency was 5%, 4%, and 9% for *A. variabilis* grown in BG-11, BG-11_o, and Allen–Arnon media, respectively. The authors also reported larger spe- cific hydrogen production rates, efficiencies, and cyanobacteria concentrations achieved using Allen–Arnon medium. This was attributed to higher concentrations of magnesium, calcium, sodium, and potassium in the medium. Finally, the presence of vanadium in Allen–Arnon medium could have induced the transcription of vanadium-based nitroge- nase that is capable of evolving more hydrogen than the molybdenum-based one. Further research is needed in this area.

11.5.4 Thermal Management

Economic and practical difficulties are faced in maintaining an optimum reactor temperature over night and day and over the season cycle [58,66]. Active temperature control has been considered in pilot systems but this adds cost and decreases the economic viability of the technology [58]. A practical solution for this problem can be the choice of favorable geographic locations or marine systems for which the ocean can act as a temperature bath whose temperature varies slightly over the course of the year. Alternatively, infrared solar radiation that would otherwise heat up the photobioreactor could be filtered before delivering only usable light to the photobioreactor.

11.5.5 Sterility and Monoculture

It is essential that the photobioreactors do not get contaminated by other microorganisms that could compete for light and nutrients, thus, adversely affecting the performance of the system [53]. This becomes a major challenge for large-scale systems. Alternatively, in order to overcome contamination, commercial algae growers have been using strains that survive in harsh environments such as high salinity and/or low pH media where most other microorganisms cannot live [58].

11.5.6 Freshwater Consumption

Many of the algal and cyanobacterial strains considered for CO_2 mitigation and H_2 production grow in freshwater. Once scaled up, such a system may require large quantities of freshwater competing with the resources used for domestic and agricultural needs. Several approaches for overcoming the need for large quantities of freshwater are (1) using trickle-bed, fluidized-bed, and membrane photobioreactors (Figure 11.14) minimizing the water usage [73,74], (2) using saltwater species where water from the oceans can be utilized [109], and (3) using wastewater where more value can also be added to the process through wastewater treatment [37].

11.6 Prospects

To date, the aforementioned limitations still remain challenges to the commercial realization of the technology. Several strategies are being pursued to increase the efficiency of photobiological hydrogen production. First, with the advent of genetic engineering, microorganisms can be engineered to have the desired pigment concentrations, optimum enzymatic pathways and electron transport, as well as reduced O_2 inhibitions. Second, processes and photobioreactors can be designed to increase efficiency by achieving optimum light delivery, maximizing sunlight utilization, and providing ideal conditions for growth and H_2 production. Third, the construction, operation, and maintenance costs of the photobioreactor systems should also be reduced.

11.6.1 Bioengineering of Microorganisms

As previously discussed, there are several intrinsic limitations to hydrogen production by the enzymes. These issues are being addressed by microbiologists and genetic engineers. Efforts include (1) truncating the light-harvesting antenna, (2) developing O_2-tolerant enzymes, (3) eliminating the expression of uptake hydrogenase, and (4) inserting proton channels in thylakoid membranes. Each of these approaches is briefly described in detail in the following sections.

11.6.1.1 Truncating the Light-Harvesting Antenna

Microorganisms that are found in nature are not always subjected to optimum illumination. Therefore, as a survival mechanism, they have adapted to produce relatively large amounts of pigments. This maximizes the probability of capturing and utilizing pho- tons at low light intensities. However, when these microorganisms are mass cultured in photobioreactors, they absorb more photons than they can utilize and waste the light energy as heat and fluorescence [102]. In addition, light does not penetrate deep into the photobioreactor. Thus, the quantum efficiency of photobiological hydrogen produc- tion decreases. Moreover, high intensities can catalyze the formation of harmful oxides that can damage the photosynthetic apparatus, a process known as photooxidation [28]. Therefore, it is desirable to decrease the chlorophyll antenna size down to the size of the core antenna [100].

Melis et al. [102,110] physiologically reduced the pigment content of the green algae *Dunaliella salina* from 1×10^9 chlorophyll molecules per cell (Chl/cell) to 0.15×10^9 Chl/cell. More recently, Polle et al. [100] genetically engineered the green algae *Chlamydomonas rein- hardtii* to have a truncated light-harvesting chlorophyll antenna size. The authors reported that the microorganisms with less pigments had higher quantum yield, photosynthesis rate, and light saturation irradiance [100].

Figure 11.17 shows the in vivo differential interference contrast (DIC) and chlorophyll fluorescence micrographs of green algae *C. reinhardtii* CC125 and its truncated chlorophyll antenna transformants *tla*1, *tlaX*, and *tla*1-CW$^+$ [81]. The images were obtained using a Zeiss 510 confocal scanning laser microscope in the transmission and epifluorescence mode simultaneously as reported by Chen and Melis [111]. The excitation was provided by a helium–neon laser at 543 nm, while the chlorophyll fluorescence emission was detected in the red region with a longpass filter with a cutoff wavelength of 560 nm placed in front of the detector. It illustrates the size and shape of each strain as well as the location of the

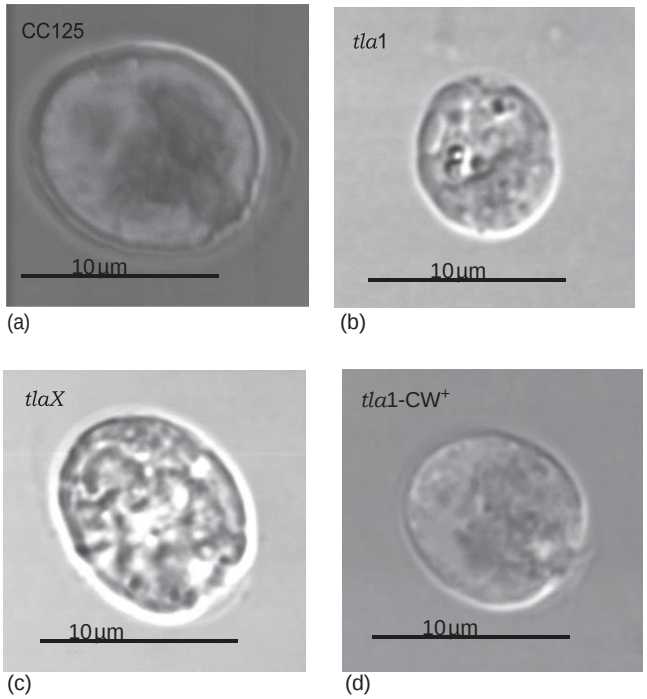


FIGURE 11.17

DIC and fluorescence micrographs of (a) CC125, (b) *tla*1, (c) *tlaX*, and (d) *tla*1-CW+. The scale bars correspond to 10 µm. (From Berberoğlu, H. et al., *Int. J. Hydrogen Energy*, 33(22), 6467, 2008.)

chlorophyll pigments that fluoresce in red [31]. The strong red fluorescence observed in the wild strain CC125 qualitatively shows that it has the largest concentration of chlorophyll while *tlaX* has the least.

11.6.1.2 Oxygen-Tolerant Enzymes

As previously discussed, there have been numerous approaches in overcoming the O_2 inhibition of hydrogen production such as applying partial vacuum [61], sparging with an inert gas [105], and sulfur deprivation [40]. Developing O_2-tolerant enzymes concerns mainly green algae and cyanobacteria as they produce O_2 as a result of oxidation of water during oxygenic photosynthesis. Moreover, it depends on the type of enzyme used by these microorganisms. Green algae use bidirectional [Fe-Fe]-hydrogenase, whereas cyanobacteria use either bidirectional [NiFe]-hydrogenase or nitrogenase.

[Fe-Fe]-hydrogenase in green algae: Hydrogen production by green algae is due to bidi- rectional [Fe-Fe]-hydrogenase [53]. However, the functioning of this enzyme is irreversibly inhibited by micromolar concentrations of O_2 [106]. Inhibition takes place when O_2 molecules bind to the catalytic site of the enzyme. Based on the structural modeling of the algal hydrogenase, Forestier et al. [112] suggested that inhibition takes place due to the presence of a large gas channel leading to the catalytic center. Figure 11.18 shows the structural model of the *C. reinhardtii* [Fe-Fe]-hydrogenase [112]. The channel enables the formed H_2 molecule to escape. However, due to its large size, it can also let O_2 diffuse to the catalytic center and

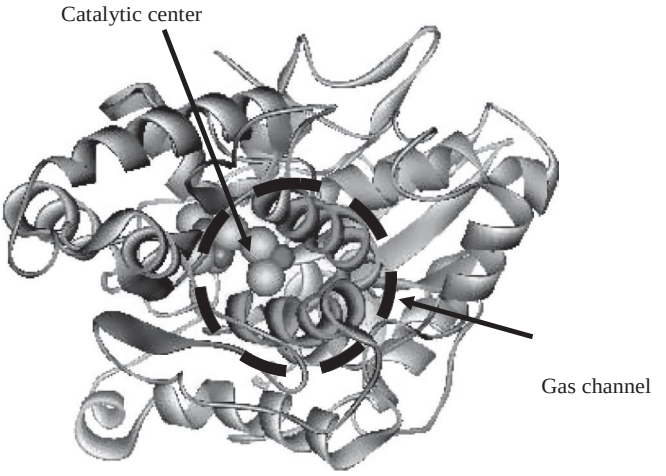


FIGURE 11.18

The structural model of the *C. reinhardtii*'s [Fe-Fe]-hydrogenase enzyme. (From Forestier, M. et al., *Eur. J. Biochem*., 270(13), 2750, 2003.)

inactivate the enzyme. Strategies to engineer a novel hydrogenase with a steric restriction to O_2 diffusion and express it in algae are being pursued [112]. This will allow the photobiological hydrogen production to take place in air making the process more efficient and less expensive.

[NiFe]-hydrogenase in Cyanobacteria: Another approach for overcoming O_2 inhibi- tion is to identify naturally occurring oxygen-tolerant [NiFe]-hydrogenases in photosynthetic bacteria (e.g., *Rubrivivax gelatinosus* and *Thiocapsa roseopersicinas*) and expressing them in selected cyanobacteria (e.g., *Synechocystis* sp. PCC6803) [113,114].

Nitrogenase in Cyanobacteria: The thermophilic filamentous actinobacteria *Streptomyces thermoautotrophicus* synthesize a unique nitrogenase that is both structurally and functionally different from the classic [Mo]-nitrogenase. This unusual nitrogenase is reported to be completely insensitive to O_2 and consumes half the amount of ATP consumed by the classic [Mo]-nitrogenase [30]. However, hydrogen produc- tion by this enzyme has not been demonstrated. The expression of such a nitroge- nase in cyanobacteria through genetic engineering can prove beneficial for more robust and cost-effective photobiological H_2 production.

11.6.1.3 Eliminating the Expression of Uptake Hydrogenase

Uptake hydrogenase is found in cyanobacteria that produce hydrogen using nitrogenase. It catalyzes the consumption of H_2 in the presence of O_2 to recover energy and produce water [53]. This decreases the net H_2 production rate by cyanobacteria. To address this issue, several researchers have proposed to improve the cyanobacterial H_2 production by eliminating the expression of uptake hydrogenase [46,115,116]. Sveshnikov et al. [46] reported that *Anabaena variabilis* mutant PK84 lacking the uptake hydrogenase had 3–4.3 times larger hydrogen production rates compared with the wild strain. In an independent study, Tsygankov et al. [117] reported that at a dissolved O_2 concentration of 315 μM in the medium, the net hydrogen production rate of the wild strain *A. variabilis* was only 7%

of the control experiment with no dissolved oxygen in the medium. On the other hand, under the same conditions, the mutant PK84 showed 75% of the hydrogen production rate of the same control experiment. Note that the equilibrium concentration of dissolved O_2 in water exposed to air at 1 atm and 25°C is about 250 μM.

11.6.1.4 Inserting Proton Channels in Photosynthetic (Thylakoid) Membranes

The rate of photobiological H_2 production from water is slowed down by inefficient electron coupling to ferredoxin due to the large proton gradient across the algal photosyn- thetic (thylakoid) membrane [113,118]. Lee [118] proposed that genetic insertion of proton channels in the photosynthetic membrane can decrease the proton gradient and overcome this limitation. Moreover, this will aid in preventing the electrons from participating in the Calvin cycle and in diverting the electron flow to hydrogenases, thus improving the rate of H_2 production.

11.6.2 Process Optimization

Several process optimizations have been considered to further develop photobiologi- cal hydrogen production technologies including (1) symbiotic or mixed cultures of dif- ferent types of microorganisms, (2) controlled and optimum light delivery, and (3) cell immobilization.

11.6.2.1 Symbiotic and Mixed Cultures

To date, the majority of research efforts have concentrated on cultivating single species of microorganisms for photobiological hydrogen production. Among these, cyanobacteria and green algae that utilize solar energy in the spectral range from 400 to 700 nm to produce hydrogen have been studied extensively [119]. On the other hand, purple nonsulfur bacteria have also been identified as potential hydrogen producers that mainly use solar energy in the NIR part of the spectrum from 700 to 900 nm [96]. Note that only about 45% of the total solar radiation is emitted between 400 and 700 nm and an additional 20% is emitted between 700 and 900 nm [50].

Thus, mixed cultivation of green algae and purple bacteria has the potential to achieve higher solar-to-hydrogen energy conversion efficiencies than single cultures by using solar radiation in the spectral range from 400 to 900 nm where 65% of the total solar radiation is concentrated. Such a mixed culture has been demonstrated by Melis and Melnicki [50] where the green algae *C. reinhardtii* were cocultured with the purple bacteria *Rhodospirillum rubrum*. The authors suggested that once the photosynthesis to respiration (P/R) ratio of the green algae is reduced to 1, such a coculture could be used for more efficient photobio- logical hydrogen production. Currently, the wild-strain algae have a P/R of about 4 [50]. Unfortunately, the purple bacteria also absorb light in the visible part of the spectrum due to the presence of bacteriochlorophyll *b* and carotenoids [80]. Consequently, the two spe- cies may compete for light during both the growth and the hydrogen production phases.

Recently, Berberoğlu and Pilon [120] reported a numerical study aiming to maximize the solar-to-hydrogen energy conversion efficiency of a mixed culture containing the green algae *Chlamydomonas reinhardtii* and the purple nonsulfur bacteria *Rhodobacter sphaeroides*. The authors used the radiation characteristics measured experimentally [80,81] as input parameters for calculating the local spectral incident radiation within a flat-panel photo- bioreactor. Their results show that for monocultures, the solar-to-H_2 energy conversion

efficiency depends only on the optical thickness of the system. The maximum solar energy conversion efficiency of monocultures of *C. reinhardtii* and *R. sphaeroides*, considering the entire solar spectrum, was found to be 0.061% and 0.054%, respectively, corresponding to optical thicknesses of 200 and 16, respectively. Using mixed cultures, a total conversion efficiency of about 0.075% could be achieved corresponding to an increase of about 23% with respect to that of a monoculture of *C. reinhardtii*. The choice of microorganism concentrations for maximum solar energy conversion efficiency in mixed cultures was nontrivial and requires careful radiation transfer analysis coupled with H_2 production kinetics.

Another strategy is to grow symbiotic cultures such as combining purple nonsulfur bacteria and anaerobic fermentative bacteria. For example, Miyake et al. [121] used symbiotic cultures of the anaerobic fermentative bacteria *Clostridium butyricum* and the purple nonsulfur bacteria *R. sphaeroides* to produce H_2. In this symbiotic culture, the anaerobic bacteria converted sugars to H_2 and organic acids, whereas the purple nonsulfur bacteria converted the organic acids to H_2. Overall, their symbiotic system produced 7 mol of H_2 per mole of glucose.

11.6.2.2 Advanced Light Delivery Systems

The saturation irradiance of a photosynthetic apparatus is on the order or 5000–6000 lux [108]. This corresponds to about one-tenth of the total solar irradiance where the rest of the energy is wasted as heat and fluorescence. Thus, light can be delivered to a 10 times larger surface area using solar collectors and lightguides to enhance the solar energy utilization efficiency. To do so, cost-effective light delivery technologies need to be developed and integrated into the design of future photobioreactors.

System engineers are designing novel photobioreactors that collect and deliver solar light in a controlled manner within the photobioreactor [34,73,109,122–124]. These systems usually involve a heliostat comprised of either Fresnel lenses [109] or reflective dishes [34,73] that concentrate the solar radiation to be distributed via fiber optics or lightguides. The lightguides are made of glass or acrylic and can deliver sunlight deep into the photobioreactors by total internal reflection. At desired locations, the lightguides have rough surfaces and light *leaks* out providing the desired irradiance. In some elaborate designs, LEDs are also incorporated into the lightguide delivery system to provide artificial light to the microorganisms at night [74]. Lightguides and fiber optics have been used to increase the light irradiance in the center of photobioreactors where it is typically the smallest [124]. However, this technology is judged too costly to be adopted at industrial scale [98].

Alternatively, Kondo et al. [98] proposed the simultaneous culture of the purple nonsulfur bacteria *Rhodobacter sphaeroides* RV and its reduced pigment mutant MTP4 in two separate but stacked plate-type photobioreactors. MTP4 produces H_2 more efficiently under large irradiance, while *R. sphaeroides* RV is more efficient under low irradiance. The authors showed that two stacked flat-plate photobioreactors with MTP4 in the front reactor facing the light source and *R. sphaeroides* RV in the rear reactor produced more H_2 than any other configuration. The front reactor acted as an absorption filter to the second.

11.6.2.3 Immobilized Cell Photobioreactors

In order to achieve high H_2 production rates, Markov et al. [61] immobilized *A. variabilis* on hollow fibers. They operated the photobioreactor in two stages alternating between (1) growth and (2) H_2 production phases. The authors reported a CO_2 consumption rate of 7000 mmol/kg dry cell/h and an H_2 production rate of 830 mmol H_2/kg dry cell/h.

Moreover, Bagai and Madamwar [125] immobilized a mixed culture of the nonheterocystous cyanobacteria *Phormidium valderianum*, the halophilic bacteria *Halobacterium halo- bium*, and the hydrogenase containing *Escherichia coli* in polyvinyl alcohol (PVA) alginate beads for prolonged production of H_2. The authors demonstrated H_2 production by the mixed culture for over 4 months.

More recently, Laurinavichene et al. [126] immobilized *C. reinhardtii* on glass mesh cloth in an enclosed photobioreactor of a total volume of 160 mL. The immobilized system enabled easy switch between sulfur-containing and sulfur-depleted media during growth and H_2 production stages, respectively. The authors reported a maximum hydrogen yield of 380 mL over 23 days with a maximum H_2 production rate of 45 mL/day. The immobilized cell system prolonged the H_2 production up to 4 weeks compared with suspended cell systems investigated by Kosourov et al. [127].

11.7 Economic and Environmental Considerations

Photobiological hydrogen production aims to produce hydrogen in an environmentally friendly and sustainable manner. Thus, its environmental impacts must be discussed in terms of toxicity, water usage, and lifecycle analysis. Economic considerations are also essential to assess the feasibility of the technology and ensure it provides a viable and competitive alternative to fossil fuel or other H_2 production technologies.

11.7.1 Economic Analysis

The US Department of Energy (DOE) set a hydrogen cost goal of \$2.00–\$3.00 (2005 US dollars) per kilogram of delivered and untaxed H_2 by 2015 [128]. For comparison with gasoline cost, note that the energy contained in 1 kg of H_2 is equivalent to that contained in 1 gal of gasoline. The average 2002 price for compressed hydrogen gas produced from fossil fuel and delivered in tube trailers was \$11.0/kg of H_2. The price of pipeline-delivered compressed-H_2 merchant hydrogen ranged from \$0.8 to \$3.4/kg of H_2 in 2003 [129]. Prices for commercial hydrogen have risen steadily in recent years primarily due to growing demand in the refinery sector and increase in oil and natural gas prices. Similarly, the price of gasoline has increased sig- nificantly and may make hydrogen more competitive if produced from renewable energy. For example, the cost of H_2 produced by wind electrolysis was \$5.90/kg of H_2 in 2006 [10].

Economic analysis of photobiological hydrogen production considers (1) the construction and maintenance costs of the photobioreactor; (2) the operating cost including labor, power, and water supplies for mixing, periodic cleaning, and powering compressors, for example; (3) the purification of hydrogen gas and its compression for transportation or storage; (4) land purchase; and (5) daily solar irradiance of the site. It was estimated that to achieve a 10% return on investment, the photobioreactor cost should be less than \$165/m^2 of footprint, for a system having 10% light-to-H_2 energy conversion [57]. Moreover, to be economically viable, the system should achieve conversion efficiencies larger than 10% [57]. Note that theoretically, H_2-producing microorganisms have a maximum light-to-H_2 efficiency ranging between 16% and 41% depending on the metabolic pathway used [53].

Photobioreactor cost is a major contributing factor to the cost of photobiologi- cal H_2 production and the most important parameter to the economic feasibility of the

technology [57,130]. For example, it was estimated that the price of a photobioreactor could be in excess of \$100/m^2 if glass or plexiglass were used as transparent windows. It could be reduced to about \$1/m^2 if low-density polyethylene (LDPE) films were used [130]. Amos [130] estimated the selling price of H_2 at \$ 2.04/kg for hydrogen delivered via a pipeline and produced by *C. reinhardtii* at a concentration of 0.2 g/L in a 10 cm deep photobioreactor and accounting for a 15% return on investment. However, the price can rise up to \$13.53/kg for purified and compressed H_2 at 2 MPa for a photobioreactor cost of \$10/m^2. In this case, the compression and storage cost alone contributed \$2.25/kg. The author acknowledged that the algal hydrogen production rate was the maximum rate biologically possible that is much larger than that achieved in practice even in benchtop photobioreactors. Finally, cost associated with energy consumption for mixing and gas injection was stated not to exceed 2 W/m^2 [76].

The annual average solar irradiance (over 24 h and over 365 days) at favorable locations such as the southwestern United States is about 210 W/m^2 [131]. In addition, fuel cells running on hydrogen have fuel efficiency of about 30%–50%, whereas internal combustion engines using gasoline are only about 30% efficient. Thus, a hydrogen refueling station providing similar service to public will have to supply about one-third the fuel supplied by a gasoline station. A light-to-hydrogen conversion efficiency of 10% would represent a production rate of 5.45 kg of H_2/m^2/year. To put this in perspective, it would require a surface area of 54,000 m^2 or 14 ac to supply the equivalent of 800,000 gal of gasoline sold every year by one of the 168,000 gasoline service stations in the United States [53]. Further improving the efficiency of this technology through photobioreactor design and genetic engineering would reduce the footprint requirement.

Moreover, to achieve sustainable energy production, the total energy used to build the system should be much lesser than that produced by the system during its entire lifetime. Thus, the service lifetime and the energy cost of materials used for building the photobioreactors should be considered in addition to their financial cost. Burgess and Fernandez-Velasco [132] defined the so-called net energy ratio (NER) as the ratio of the higher heating value of the produced hydrogen to the total primary energy input into the construction of the system. The authors reported that for tubular photobioreactors, LDPE film and glass have significantly higher NER than rigid polymers such as polymethyl methacrylate (acrylic) [132]. Similar lifecycle analysis should be performed for other novel photobioreactor designs to assess their sustainability.

In brief, photobiological hydrogen production is at a very early stage of development. It currently does not constitute an economically viable hydrogen production method and needs additional basic and applied research to approach practical efficiency and production rates. Thorough economic analysis has to be performed for various organisms and photobioreactor design in order to assess the viability in the short run and the sustainability in the long run of photobiological hydrogen production. More realistic economic analysis will require operation, maintenance, and field data from pilot photobioreactor systems taking into account the seasonal performance variations.

11.7.2 Environmental Impacts

Some strains of cyanobacteria are known to produce toxins that are harmful to human and animal health such as anatoxins, microcystins, or saxitoxins [133]. Most algae species are harmless to animals and humans. These toxins can cause acute or chronic illnesses such as gastroenteritis, adverse respiratory effects, skin irritations, allergic responses,

and liver damage [134]. In addition to producing toxins, freshwater cyanobacteria can cause nuisance effects such as excessive accumulations of foams and scums and discoloration of water [135].

Moreover, current photobiological hydrogen production would require large amounts of water if the benchtop processes were scaled up for industrial production. This would create large demand for freshwater that would compete with domestic and agriculture uses both of which are scarce in regions with high solar irradiance. One may argue, how- ever, that the system would be closed and water would simply need to be supplied to compensate for evaporation and separation needs. Thus, water consumption for H_2 pro- duction is likely to be much lesser than that of agricultural crops. In addition, photobiore- actors designed to be constructed on land are likely to compete with land use for humans, forests, or agricultural use.

Alternatively, wastewater or seawater in combination with cyanobacteria and marine algae could be used to reduce demand on freshwater and land space. Marine green algae *Chlorococcum littorale* and marine cyanobacteria *Oscillatoria* sp. as well as *Miami BG7*, *Anabaena cylindrical* B-629, and *Calothrix scopulorum* 1410/5 are known hydrogen producers [77]. Marine-based systems benefit from (1) thermal regulation of the ocean preventing the overheating of the photobioreactors under direct sunlight and (2) agitation of the reac- tor fluid that could be achieved by the ocean waves. Some of the major issues concerning the development of marine photobioreactors include (1) contingency engineering for pos- sible microorganism leakage into the ocean, (2) durability of the materials used in marine environment, and (3) contamination and damage to the photobioreactors by the marine animals and microorganisms. Thus, research should be directed to address these issues for developing cost-effective marine photobioreactors.

Finally, public perception and potential fear associated with the use and possible release of genetically modified microorganisms in the environment will need to be addressed. Public reaction is expected to vary from one region of the world to another. However, it may constitute a major obstacle in some countries. Past experiences with genetically modified crops (e.g., corn or soybean) can constitute a valuable reference and provide useful lessons.

11.8 Conclusion

This chapter presented the current state of knowledge in photobiological H_2 production as well as CO_2 fixation. It provided the reader with a basic background in the microbiol- ogy of photosynthesis and photobiological H_2 production. Then, photobioreactor designs, operations, performances, and simulation tools were reviewed. The challenges associated with the technology were discussed followed by strategies to overcome the biological barriers and to optimize the process. Finally, economic analysis and potential environmental impacts were presented. In brief, photobiological hydrogen production is at a very early stage of development and requires additional basic and applied research efforts. However, progresses from genetic engineering to innovative photobioreactor designs with advanced light delivery and reduced water consumption are promising. If successful, this technology can offer a long-term solution for sustainable hydrogen production. It can also alleviate concerns over energy security with the advantage of capturing CO_2.

References

1. International Energy Agency, Key world energy statistics 2013, http://www.iea.org/ publications/, accessed on December 6, 2013.
2. M.K. Hubbert, Nuclear energy and the fossil fuels, Presented before the *Spring Meeting of the Southern District*, American Petroleum Institute, San Antonio, TX, 1956.
3. B. Holmes and N. Jones, Brace yourself for the end of cheap oil, *New Scientist*, 179(2406), 9–11, 2003.
4. K.S. Deffyes, *Hubbert's Peak: The Impending World Oil Shortage*, Princeton University Press, Princeton, NJ, 2001.
5. Energy Information Administration, International energy outlook 2008—Highlights, Report DOE/EIA-0484, June 2008.
6. IPPC, Climate change 2007: Impacts, adaptation and vulnerability. Contribution of working group ii to the fourth assessment report of the intergovernmental panel on climate change, Cambridge, U.K., 2007, Cambridge University Press, Cambridge, U.K.
7. U.S. Central Intelligence Agency, *The World Factbook 2013*, https://www.cia.gov/cia/ publications/factbook/index.html, accessed on December 6, 2013.
8. Energy Information Administration, Emissions of greenhouse gases in the United States 2005, Report DOE/EIA-0573, 2005.
9. P. Kruger, *Alternative Energy Resources: The Quest for Sustainable Energy*, John Wiley & Sons, Hoboken, NJ, 2006.
10. U.S. DOE, Hydrogen, fuel cells, and infrastructure technologies program, http://www1.eere. energy.gov/hydrogenandfuelcells/, 2006, accessed on December 6, 2013.
11. U.S. Department of Energy, *Hydrogen Data Book*, Hydrogen Analysis Resource Center, Pacific Northwest National Laboratory, Richland, WA, http://hydrogen.pnl.gov/cocoon/morf/ hydrogen/article/103, 2008, accessed on December 6, 2013.
12. G.P. Sutton and O. Biblarz, *Rocket Propulsion Elements*, 7th edn., John Wiley & Sons, New York, 2000.
13. J.M. Norbeck, J.W. Heffel, T.D. Durbin, B. Tabbara, J.M. Bowden, and M.C. Montano, *Hydrogen Fuel for Surface Transportation*, SAE International, Warrendale, PA, 1996.
14. H.J. Sternfeld and P. Heinrich, A demonstration plant for the hydrogen/oxygen-spinning reserve, *International Journal of Hydrogen Energy*, 14(10), 703–716, 1989.
15. H.J. Sternfeld, Capacity control of power stations by O_2/H_2 rocket combustor technology, *Acta Astronautica*, 37, 11–19, 1995.
16. S.P. Malyshenko, A.N. Gryaznov, and N.I. Filatov, High-pressure H_2/O_2-steam generators and their possible applications, *International Journal of Hydrogen Energy*, 29(6), 589–596, 2004.
17. G. Hoogers, *Fuel Cell Technology Handbook*, CRC Press, Boca Raton, FL, 2002.
18. P.J. Sebastian, Photoelectrochemical water splitting for hydrogen generation, *International Journal of Hydrogen Energy*, 26(2), 115, 2001.
19. J.E. Funk, Thermochemical hydrogen production: Past and present, *International Journal of Hydrogen Energy*, 26(3), 185–190, 2001.
20. D.O. Hall, S.A. Markov, Y. Watanabe, and K.K. Rao, The potential applications of cyanobacte- rial photosynthesis for clean technologies, *Photosynthesis Research*, 46(1–2), 159–167, 1995.
21. K.N. Liou, *An Introduction to Atmospheric Radiation*, 2nd edn., Academic Press, San Diego, CA, 2002.
22. J.A. Duffie and W.A. Beckman, *Solar Engineering of Thermal Processes*, 3rd edn., John Wiley & Sons, Hoboken, NJ, 2006.
23. C. Gueymard, D. Myers, and K. Emery, Proposed reference irradiance spectra for solar energy systems testing, *Solar Energy*, 73(6), 443–467, 2002.
24. The National Oceanic and Atmospheric Administration (NOAA), U.S. standard atmosphere, 1976, in NOAA/NASA/USAF-NOAA-S/T76-1562. Washington, DC, 1976.
25. C. Gueymard, Smarts code, version 2.9.2 users direct beam spectral irradiance data for pho- tovoltaic cell manual, Solar Consulting Services, Golden, CO, http://www.nrel.gov/rredc/ smarts/, 2002, accessed on December 6, 2013.

26. SunWize Technologies, World insolation map, Kingston, New York, 2008.
27. O. Pulz, Photobioreactors: Production systems for phototrophic microorganisms, *Applied Microbiology and Biotechnology*, 57(3), 287–293, 2001.
28. B. Ke, *Photosynthesis, Photobiochemistry and Photobiophysics*, Kluwer Academic Publishers, Dordrecht, the Netherlands, 2001.
29. P.F. Weaver, S. Lien, and M. Seibert, Photobiological production of hydrogen, *Solar Energy*, 24(1), 3–45, 1980.
30. M.T. Madigan and J.M. Martinko, *Biology of Microorganisms*, Pearson Prentice Hall, Upper Saddle River, NJ, 2006.
31. E.H. Harris, *The Chlamydomonas Sourcebook*, Vol. 1, Academic Press, San Diego, CA, 1989.
32. N.J. Lang, J.M. Krupp, and A.L. Koller, Morphological and ultrastructural-changes in vegeta- tive and heterocysts of *Anabaena variabilis* grown with fructose, *Journal of Bacteriology*, 169(2), 920–923, 1987.
33. Department of Energy, *Rhodobacter sphaeroides*, Joint Genome Institute, Walnut Creek, CA. http://genome.jgi-psf.org/finished-microbes/rhosp/rhosp.home.html, accessed on April 19, 2008.
34. I. Akkerman, M. Jansen, J. Rocha, and R.H. Wijffels, Photobiological hydrogen production: Photochemical efficiency and bioreactor design, *International Journal of Hydrogen Energy*, 27, 1195–1208, 2002.
35. P. Joliot and A. Joliot, Cyclic electron transport in plant leaf, *Proceedings of the National Academy of Sciences USA*, 99(15), 10209–10214, 2002.
36. Y. Munekaga, M. Hashimoto, C. Miyake, K.I. Tomizawa, T. Endo, M. Tasaka, and T. Shikanai, Cyclic electron flow around photosystem I is essential for photosynthesis, *Nature*, 429(6991), 579–582, 2004.
37. I.K. Kapdan and F. Kargi, Bio-hydrogen production from waste materials, *Enzyme and Microbial Technology*, 38(5), 569–582, 2006.
38. A. Melis, Bioengineering of green algae to enhance photosynthesis and hydrogen produc- tion, in *Artificial Photosynthesis: From Basic Biology to Industrial Applications*, A.F. Collings and C. Critchley, eds., pp. 229–240. Wiley-VCH Verlag GmbH, Weinheim, Germany.
39. M.L. Ghirardi, A. Dubini, J. Yu, and P.-C. Maness, Photobiological hydrogen-producing sys- tems, *Chemical Society Review*, 38, 52–61, 2009.
40. A. Melis, L. Zhang, M. Forestier, M.L. Ghirardi, and M. Seibert, Sustained photobiological hydrogen gas production upon reversible inactivation of oxygen evolution in the green alga C*hlamydomonas reinhardtii*, *Plant Physiology*, 117(1), 129–139, 2000.
41. D. Das and T.N. Veziroğlu, Hydrogen production by biological processes: A survey of litera- ture, *International Journal of Hydrogen Energy*, 26(1), 13–28, 2001.
42. Y. Ueno, N. Kurano, and S. Miyachi, Purification and characterization of hydrogenase from the marine green alga *Chlorococcum littorale*, *FEBS Letters*, 443(2), 144–148, 1999.
43. L. Florin, A. Tsokoglou, and T. Happe, A novel type of iron hydrogenase in the green alga *Scenedesmus obliquus* is linked to the photosynthetic electron transport chain, *Journal of Biological Chemistry*, 276(9), 6125–6132, 2001.
44. M. Pavetic, H. Tausch, G. Stehlik, and M. Roehr, Influence of ruthenium, rhodium and vana- dium ions on photoproduction of hydrogen by *Chlorella fusca*, *Photochemistry and Photobiology*, 40(1), 15–21, 1984.
45. D.A. Sveshnikov, N.V. Sveshnikova, K.K. Rao, and D.O. Hall, Hydrogen metabolism of mutant forms of *Anabaena variabilis* in continuous cultures and under nutritional stress, *FEMS Microbiology Letters*, 147, 297–301, 1997.
46. P. Lindberg, K. Schutz, T. Happe, and P. Lindblad, A hydrogen-producing, hydrogenase- free mutant strain of *Nostoc punctiforme* ATCC29133, *International Journal of Hydrogen Energy*, 27(11–12), 1291–1296, 2002.
47. S. Kumazawa and A. Mitsui, Characterization and optimization of hydrogen photoproduction by a saltwater blue green alga, *Oscillatoria* sp. miami bg7. enhancement through limiting the supply of nitrogen nutrients, *International Journal of Hydrogen Energy*, 6(4), 339–348, 1981.

48. F.A.L. Pinto, O. Troshina, and P. Lindblad, A brief look at three decades of research on cya- nobacterial hydrogen evolution, *International Journal of Hydrogen Energy*, 27(11–12), 1209–1215, 2002.
49. A. Melis and M. Melnicki, Integrated biological hydrogen production, *International Journal of Hydrogen Energy*, 31(11), 1563–1573, 2006.
50. N. Kumar, P.S. Monga, A.K. Biswas, and D. Das, Modeling and simulation of clean fuel produc- tion by *Enterobacter cloacae* IIT-BT 08, *International Journal of Hydrogen Energy*, 25(10), 945–952, 2000.
51. H. Yokoi, Y. Maeda, J. Hirose, S. Hayashi, and Y. Takasaki, H_2 production by immobilized cells of *Clostridium butyricum* on porous glass beads, *Biotechnology Techniques*, 11(6), 431–433, 1997.
52. R.C. Prince and H.S. Kheshgi, The photobiological production of hydrogen: Potential efficiency and effectiveness as a renewable fuel, *Critical Reviews in Microbiology*, 31(1), 19–31, 2005.
53. P.C. Hallenbeck and J.R. Benemann, Biological hydrogen production: Fundamentals and limit- ing processes, *International Journal of Hydrogen Energy*, 27, 1185–1193, 2002.
54. D. Madamwar, N. Garg, and V. Shah, Cyanobacterial hydrogen production, *World Journal of Microbiology and Biotechnology*, 16(8–9), 757–767, 2000.
55. G.M. Bodner and H.L. Pardue, *Chemistry: An Experimental Science*, John Wiley & Sons, New York, 1995.
56. J.R. Bolton, Solar photoproduction of hydrogen, IEA Technical Report, International Energy Agency, Paris, France, IEA/H2/TR-96, 1996.
57. J. Sheehan, T. Dunahay, J. Benemann, and P. Roessler, A look back at the U.S. Department of Energy's aquatic species program—Biodiesel from algae, National Renewable Energy Laboratory, Golden, CO, 1998.
58. T. Riis, E.F. Hagen, P.J.S. Vie, and Ø. Ulleberg, Hydrogen production and storage—R&D priori- ties and gaps, International Energy Agency—Hydrogen Co-Ordination Group—Hydrogen Imple- menting Agreement, 2006, http://www.iea.org/publications/freepublications/publication/ hydrogen.pdf, accessed on December 6, 2013.
59. N.J. Kim, I.S. Suh, B.K. Hur, and C.G. Lee, Simple monodimensional model for linear growth rate of photosynthetic microorganisms in flat-plate photobioreactors, *Journal of Microbiology and Biotechnology*, 12(6), 962–971, 2002.
60. S.A. Markov, R. Lichtl, K.K. Rao, and D.O. Hall, A hollow fibre photobioreactor for continu- ous production of hydrogen by immobilized cyanobacteria under partial vacuum, *International Journal of Hydrogen Energy*, 18(11), 901–906, 1993.
61. S.A. Markov, M.J. Bazin, and D.O. Hall, Hydrogen photoproduction and carbon dioxide uptake by immobilized *Anabaena variabilis* in a hollow-fiber photobioreactor, *Enzyme and Microbial Technology*, 17(4), 306–310, 1995.
62. S.A. Markov, A.D. Thomas, M.J. Bazin, and D.O. Hall, Photoproduction of hydrogen by cyano- bacteria under partial vacuum in batch culture or in a photobioreactor, *International Journal of Hydrogen Energy*, 22, 521–524, 1997.
63. A.A. Tsygankov, A.S. Fedorov, S.N. Kosourov, and K.K. Rao, Hydrogen production by cyano- bacteria in an automated outdoor photobioreactor under aerobic conditions, *Biotechnology and Bioengineering*, 80(7), 777–783, 2002.
64. J.H. Yoon, J.H. Shin, M.S. Kim, S.J. Sim, and T.H. Park, Evaluation of conversion efficiency of light to hydrogen energy by *Anabaena variabilis*, *International Journal of Hydrogen Energy*, 31(6), 721–727, 2006.
65. I.S. Suh and C.G. Lee, Photobioreactor engineering: Design and performance, *Biotechnology and Bioprocess Engineering*, 8(6), 313–321, 2003.
66. J.A. Asenjo and J.C. Merchuk, *Bioreactor System Design*, Marcel Dekker, New York, 1995.
67. S. Fouchard, J. Pruvost, B. Degrenne, and J. Legrand, Investigation of H_2 production using the green microalga *Chlamydomonas reinhardtii* in a fully controlled photobioreactor fitted with on- line gas analysis, *International Journal of Hydrogen Energy*, 33(13), 3302–3310, 2008.

68. L. Pottier, J. Pruvost, J. Deremetz, J.F. Cornet, J. Legrand, and C.G. Dussap, A fully predictive model for one-dimensional light attenuation by C*hlamydomonas reinhardtii* in a torus photobio- reactor, *Biotechnology and Bioengineering*, 91(5), 569–582, 2005.
69. J. Pruvost, L. Pottier, and J. Legrand, Numerical investigation of hydrodynamic and mixing conditions in a torus photobioreactor, *Chemical Engineering Science*, 61(14), 4476–4489, 2006.
70. S. Fouchard, J. Pruvost, B. Degrenne, M. Titica, and J. Legrand, Kinetic modeling of light limita- tion and sulfur deprivation effects in the induction of hydrogen production with *Chlamydomonas reinhardtii*: Part I. Model development and parameter identification, *Biotechnology and Bioengineering*, 102(1), 232–245, 2009.
71. J.C. Merchuk, Y. Rosenblat, and I. Berzin, Fluid flow and mass transfer in a counter current gas liquid inclined tubes photo-bioreactor, *Chemical Engineering Science*, 62(24), 7414–7425, 2007.
72. D.J. Bayless, G. Kremer, M. Vis, B. Stuart, L. Shi, J. Cuello, and E. Ono, Photosynthetic CO_2 miti- gation using a novel membrane-based photobioreactor, *Journal of Environmental Engineering and Management*, 16(4), 209–215, 2006.
73. E. Ono and J.L. Cuello, Design parameters of solar concentrating systems for CO_2 mitigating algal photobioreactors, *Energy*, 29(9–10), 1651–1657, 2004.
74. E.J. Wolfrum, A.S. Watt, and J. Huang, Bioreactor development for biological hydrogen produc- tion, *Proceedings of the 2002 U.S. DOE Hydrogen Program Review (NERL CP-610-32405)*, Golden, CO, 6–10 May 2002, pp. 10–19; NREL Report No. CP-510-32407.
75. C. Posten, Design principles of photo-bioreactors for cultivation of microalgae, *Engineering in Life Sciences*, 9(3), 165–177, 2009.
76. D. Dutta, D. De, S. Chaudhari, and S.K. Bhattacharya, Hydrogen production by cyanobacteria, *Microbial Cell Factories*, 4(36), 1–11, 2005.
77. D. Das and T.N. Veziroğlu, Advances in biological hydrogen production processes, *International Journal of Hydrogen Energy*, 33, 6046–6057, 2008.
78. H. Berberoğlu and L. Pilon, Experimental measurement of the radiation characteristics of *Anabaena variabilis* ATCC 29413-U and *Rhodobacter sphaeroides* ATCC 49419, *International Journal of Hydrogen Energy*, 32(18), 4772–4785, 2007.
79. H. Berberoğlu, A. Melis, and L. Pilon, Radiation characteristics of *Chlamydomonas rein- hardtii* CC125 and its truncated chlorophyll antenna transformants *tla1*, *tlaX*, and *tla1*-CW$^+$, *International Journal of Hydrogen Energy*, 33(22), 6467–6483, 2008.
80. H. Berberoğlu, J. Yin, and L. Pilon, Simulating light transfer in a bubble sparged photobiore- actor for simultaneous hydrogen fuel production and CO_2 mitigation, *International Journal of Hydrogen Energy*, 32(13), 2273–2285, 2007.
81. G. Mie, Beiträge zur Optik trüber Medien, speziell kolloidaler Metallsungen, *Annalen der Physik*, 25(3), 377–445, 1908.
82. M.F. Modest, *Radiative Heat Transfer*, Academic Press, San Diego, CA, 2003.
83. J. Pruvost, J. Legrand, P. Legentilhomme, and A. Muller-Feuga, Simulation of microalgae growth in limiting light conditions: Flow effect, *AIChE Journal*, 48(5), 1109–1120, 2002.
84. F.G. Acién Fernández, F. García Camacho, J.A. Sánchez Pérez, J.M. Fernández Sevilla, and E. Molina Grima, A model for light distribution and average solar irradiance inside outdoor tubular photobioreactors for the microalgal mass culture, *Biotechnology and Bioengineering*, 55(5), 701–714, 1997.
85. J.F. Cornet, C.G. Dussap, and G. Dubertret, A structured model for simulation of cultures of the cyanobacterium spirulina platensis in photobioreactors: I. Coupling between light transfer and growth kinetics, *Biotechnology and Bioengineering*, 40(7), 817–825, 1992.
86. J.F. Cornet, C.G. Dussap, P. Cluzel, and G. Dubertret, A structured model for simulation of cultures of the cyanobacterium spirulina platensis in photobioreactors: II. Identification of kinetic param- eters under light and mineral limitations, *Biotechnology and Bioengineering*, 40(7), 826–834,1992.
87. J.F. Cornet, C.G. Dussap, J.B. Gross, C. Binois, and C. Lasseur, A simplified monodimensional approach for modeling coupling between radiant light transfer and growth kinetics in photo- bioreactors, *Chemical Engineering Science*, 50(9), 1489–1500, 1995.

88. J. Pruvost, J.-F. Cornet, and J. Legrand, Hydrodynamics influence on light conversion in photobio- reactors: An energetically consistent analysis, *Chemical Engineering Science*, 63(14), 3679–3694, 2008.
89. B.M. Agrawal and M.P. Mengüç, Forward and inverse analysis of single and multiple scatter- ing of collimated radiation in an axisymmetric system, *International Journal of Heat and Mass Transfer*, 34, 633–647, 1991.
90. M.N. Merzlyak and K.R. Naqvi, On recording the true absorption spectrum and scattering spectrum of a turbid sample: Application to cell suspensions of cyanobacterium *Anabaena varia- bilis*, *Journal of Photochemistry and Photobiology B*, 58, 123–129, 2000.
91. D. Stramski and C.D. Mobley, Effect of microbial particles on oceanic optics: A database of single-particle optical properties, *Limnology and Oceanography*, 42, 538–549, 1997.
92. R.M. Broglie, C.N. Hunter, P. Delepelaire, R.A. Niederman, N.H. Chua, and R.K. Clayton, Isolation and characterization of the pigment–protein complexes of *Rhodopseudomonas sphaer- oides* by lithium dodecylsulfate/polyacrylamide gel electrophoresis, *Proceedings of the National Academy of Sciences of the United States of America*, 77(1), 87–91, 1980.
93. I.J. Dunn, E. Heinzle, J. Ingham, and J.E. Prenosil, *Biological Reaction Engineering; Dynamic Modelling Fundamentals with Simulation Examples*, 2nd edn., Wiley-VCH Verlag GmbH, Weinheim, Germany, 2003.
94. Y. Nogi, T. Akiba, and K. Horikoshi, Wavelength dependence of photoproduction of hydrogen by *Rhodopseudomonas rutila*, *Agricultural and Biological Chemistry*, 49, 3538, 1985.
95. J.R. Benemann, Hydrogen production by microalgae, *Journal of Applied Phycology*, 12(3–5), 291–300, 2000.
96. T. Kondo, M. Arakawa, T. Wakayama, and J. Miyake, Hydrogen production by combining two types of photosynthetic bacteria with different characteristics, *International Journal of Hydrogen Energy*, 27(11–12), 1303–1308, 2002.
97. J.C. Ogbonna, T. Soejima, and H. Tanaka, An integrated solar and artificial light system for internal illumination of photobioreactors, *Journal of Biotechnology*, 70(1–3), 289–297, 1999.
98. J.E. Polle, S.D. Kanakagiri, and A. Melis, *tla1*, a DNA insertional transformant of the green alga *Chlamydomonas reinhardtii* with a truncated light-harvesting chlorophyll antenna size, *Planta*, 217(1), 49–59, 2003.
99. J.H. Yoon, S.J. Sim, M.S. Kim, and T.H. Park, High cell density culture of *Anabaena variabilis* using repeated injections of carbon dioxide for the production of hydrogen, *International Journal of Hydrogen Energy*, 27(11–12), 1265–1270, 2002.
100. A. Melis, J. Neidhardt, and J.R. Benemann, *Dunaliella salina (Chlorophyta)* with small chlorophyll antenna sizes exhibit higher photosynthetic productivities and photon use efficiencies than normally pigmented cells, *Journal of Applied Phycology*, 10(6), 515–525, 1999.
101. A. Melis, Green alga hydrogen production: Process, challenges and prospects, *International Journal of Hydrogen Energy*, 27(11–12), 1217–1228, 2002.
102. J.W. Van Groenestijn, J.H.O. Hazewinkel, M. Nienoord, and P.J.T. Bussmann, Energy aspects of biological hydrogen production in high rate bioreactors operated in the thermophilic tempera- ture range, *International Journal of Hydrogen Energy*, 27(11–12), 1141–1147, 2002.
103. V.B. Borodin, A.A. Tsygankov, K.K. Rao, and D.O. Hall, Hydrogen production by *Anabaena variabi- lis* PK84 under simulated outdoor conditions, *Biotechnology and Bioengineering*, 69(5), 478–485, 2000.
104. M.L. Girardi, P. King, S. Kosourov, M. Forestier, L. Zhang, and M. Seibert, Development of algal systems for hydrogen photoproduction: Addressing the hydrogenase oxygen sensitivity problem, in *Artificial Photosynthesis: From Basic Biology to Industrial Applications*, A.F. Collings and C. Critchley, eds., pp. 211–228. Wiley-VCH Verlag GmbH, Weinheim, Germany.
105. K. van't Riet and J. Tramper, *Basic Bioreactor Design*, Marcel Dekker, New York, 1991.
106. H. Berberoğlu, J. Jay, and L. Pilon, Effect of nutrient media on photobiological hydrogen pro- duction by *Anabaena variabilis* ATCC 29413, *International Journal of Hydrogen Energy*, 33(3), 1172– 1184, 2008.
107. S. Hirata, M. Hayashitani, M. Taya, and S. Tone, Carbon dioxide fixation in batch culture of *Chlorella* sp. using a photobioreactor with a sunlight-collection device, *Journal of Fermentation and Bioengineering*, 81(5), 470–472, 1996.

108. A. Melis and T. Happe, Trails of green alga hydrogen research—From Hans Gaffron to new frontiers, *Photosynthesis Research*, 80(1–3), 401–409, 2004.
109. H.C. Chen and A. Melis, Localization and function of SulP, a nuclear-encoded chloroplast sulfate permease in *Chlamydomonas reinhardtii*, *Planta*, 220, 198–210, 2004.
110. M. Forestier, P. King, L. Zhang, M. Posewitz, S. Schwarzer, T. Happe, M.L. Girardi, and M. Seibert, Expression of two Fe-hydrogenases in *Chlamydomonas reinhardtii* under anaerobic conditions, *European Journal of Biochemistry*, 270(13), 2750–2758, 2003.
111. U.S. Department of Energy, Prospectus on biological hydrogen production, hydrogen program, http://www1.eere.energy.gov/hydrogenandfuelcells/production/photobiological.html, 2008, accessed on December 6, 2013.
112. Q. Xu, P.C. Maness, and R. Gerald, Hydrogen from water in a novel recombinant oxygen- tolerant cyanobacterial system, U.S. Department of Energy, Hydrogen Program, 2007 Annual Progress Report, pp. 175–177, 2007.
113. T. Happe, K. Schutz, and H. Bohme, Transcriptional and mutational analysis of the uptake hydrogenase of the filamentous cyanobacterium *Anabaena variabilis* ATCC 29413, *Journal of Biotechnology*, 182(6), 1624–1631, 2000.
114. L.E. Mikheeva, O. Schmitz, and S. Shestakov, Mutants of the cyanobacterium *Anabaena varia- bilis* altered in hydrogenase activities, *Zeitschrift Fur Naturforschung C – A Journal of Biosciences*, 50(7–8), 505–510, 1995.
115. A.A. Tsygankov, L.T. Serebryakova, K.K. Rao, and D.O. Hall, Acetylene reduction and hydro- gen photoproduction by wild-type and mutant strains of *Anabaena* at different CO_2 and O_2 concentrations, *FEMS Microbiology Letters*, 167(1), 13–17, 1998.
116. J.W. Lee, Photobiological hydrogen production systems: Creation of designer alga for efficient and robust production of H_2 from water, U.S. Department of Energy, Hydrogen Program, 2006 Annual Progress Report, pp. 125–127, 2006.
117. A. Melis and T. Happe, Hydrogen production: Green algae as a source of energy, *Plant Physiology*, 127(3), 740–748, 2001.
118. H. Berberoğlu and L. Pilon, Maximizing solar to H_2 energy conversion efficiency of outdoor photobioreactors using mixed cultures, *International Journal of Hydrogen Energy*, 35, 500–510, 2010.
119. J. Miyake, X.Y. Mao, and S. Kawamura, Photoproduction of hydrogen from glucose by a co-culture of a photosynthetic bacterium and *Clostridium butyricum*, *Journal of Fermentation Technology*, 62(6), 531–535, 1984.
120. R.M.A. El-Shishtawy, S. Kawasaki, and M. Morimoto, Biological H_2 production using a novel light-induced and diffused photobioreactor, *Biotechnology Techniques*, 11(6), 403–407, 1997.
121. C. Stewart and M.A. Hessami, A study of methods of carbon dioxide capture and seques- tration—The sustainability of a photosynthetic bioreactor approach, *Energy Conversion and Management*, 46(3), 403–420, 2005.
122. C.Y. Chen, C.M. Lee, and J.S. Chang, Hydrogen production by indigenous photosynthetic bac- terium *Rhodopseudomonas palustris* WP3-5 using optical fiber-illuminating photobioreactors, *Biotechnology Engineering Journal*, 32(1), 33–42, 2006.
123. R. Bagai and D. Madamwar, Long-term photo-evolution of hydrogen in packed bed reactor containing a combination of *Phormidium valderianum, Halobacterium halobium,* and *Escherichia coli* immobilized in polyvinyl alcohol, *International Journal of Hydrogen Energy*, 24(4), 311–317, 1999.
124. T.V. Laurinavichene,A.S. Fedorov, M.L. Ghirardi, M. Seibert, andA.A. Tsygankov, Demonstration of sustained hydrogen production by immobilized, sulfur-deprived *Chlamydomonas reinhardtii* cells, *International Journal of Hydrogen Energy*, 31(5), 659–667, 2006.
125. S. Kosourov, M. Seibert, and M.L. Ghirardi, Effects of extracellular ph on the metabolic path- ways in sulfur-deprived H_2 producing *Chlamydomonas reinhardtii* cultures, *Plant Cell Physiology*, 44(2), 146–155, 2003.
126. U.S. Department of Energy Hydrogen, Targets for on-board hydrogen storage systems, http://www.eere.energy.gov/hydrogenandfuelcells/pdfs/freedomcar_targets_explanations.pdf, accessed on December 20, 2008.

127. M.K. Mann and J.S. Ivy, Renewable hydrogen: Can we afford it? *Solar Today*, May/June 2004, pp. 28–31; NREL Report No. JA-560-36056 (2004) http://www.americanhydrogenassociation. org/H2today23-1.pdf, 2004, accessed on December 6, 2013.
128. W.A. Amos, Updated cost analysis of photobiological hydrogen production from *Chlamydomonas reinhardtii* green algae, Milestone Completion Report, National Renewable Energy Laboratory, Golden, CO, NREL/MP-560-35593, January 2004.
129. B.G. Liepert, Observed reductions of surface solar radiation at sites in the United States and worldwide from 1961 to 1990, *Geophysical Research Letters*, 29(10), 1421–1426, 2002.
130. G. Burgess and J.G. Fernandez-Velasco, Materials, operational energy inputs, and net energy ratio for photobiological hydrogen production, *International Journal of Hydrogen Energy*, 32(9), 1225–1234, 2007.
131. Purdue University, A webserver for cyanobacterial research, http://www-cyanosite.bio. purdue.edu, 2004, accessed on December 6, 2013.
132. Department of Health and Human Services, Harmful algal blooms, Center for Disease Control and Prevention, http://www.cdc.gov/nceh/hsb/hab/default.html, 2008, accessed on December 6, 2013.
133. D. Westwood, *The Microbiology of Drinking Water – Part 1 – Water Quality and Public Health*. U.K. Environmental Agency, Bristol, U.K., 2002.
134. M. Winkler, A. Hemschemeier, C. Gotor, A. Melis, and T. Happe, [Fe]-hydrogenases in green algae: Photo-fermentation and hydrogen evolution under sulfur deprivation, *International Journal of Hydrogen Energy*, 27(11–12), 1431–1439, 2002.
135. J. Van der Oost, B.A. Bulthuis, S. Feitz, K. Krab, and R. Kraayenhof, Fermentation metabo- lism of the unicellular cyanobacterium *Cyanothece* PCC-7822, *Archives of Microbiology*, 152(5), 415–419, 1989.
136. K. Sasikala, C.V. Ramana, and P.R. Rao, Environmental regulation for optimal biomass yield and photoproduction of hydrogen by *Rhodobacter sphaeroides* O.U. 001, *International Journal of Hydrogen Energy*, 16(9), 597–601, 1991.
137. H. Zürrer and R. Bachofen, Hydrogen production by the photosynthetic bacterium *Rhodospirillum rubrum*, *Applied and Environmental Microbiology*, 37, 789–793, 1979.
138. H. Zürrer and R. Bachofen, Aspects of growth and hydrogen production of the photosynthetic bacterium *Rhodospirillum rubrum* in continuous culture, *Biomass*, 2(3), 165–174, 1982.
139. J.D. Brosseau and J.E. Zajic, Continual microbial production of hydrogen gas, *International Journal of Hydrogen Energy*, 7(8), 623–628, 1982.
140. I. Karube, T. Matsunaga, S. Tsuru, and S. Suzuki, Continuous hydrogen production by immo- bilized whole cells of *Clostridium butyricum*, *Biochimica et Biophysica Acta*, 444(2), 338–343, 1976.

3.Hydrogen Generation and Explosion Safety

1 Introduction

High priority research directions for the hydrogen economy include safety as a technological, a psychological and sociological issue (US Department of Energy, 2004). This book provides the state-of-the-art in hydrogen safety as a technological issue and introduces a reader to the subject of hydrogen safety engineering. Hydrogen safety engineering is defined as application of scientific and engineering principles to the protection of life, property and environment from adverse effects of incidents/accidents involving hydrogen. The use of hydrogen as an energy carrier presents several unusual hazards. The best investment in hydrogen safety is educated and trained personnel, informed public. This book is a

contribution to hydrogen safety knowledge transfer and education of all stakeholders including technology developers and safety engineers, consultants and users, policy makers and investors, etc. It can be used as a textbook for higher education programmes in hydrogen safety, e.g. MSc in Hydrogen Safety Engineering course at the University of Ulster.

1.1. Why hydrogen?

The scarcity of fossil fuel reserves, geopolitical fears associated with fossil fuel depletion, and issues of environment pollution and climate change as well as the need to ensure independence of energy supply make the low-carbon economy with an essential hydrogen vector inevitable in the coming decades. Today first series of hydrogen-fuelled buses and cars are already on the road and refuelling stations are operating in different countries around the world. How safe are hydrogen technologies and fuel cell products? This book will help to understand the state-of-the-art in hydrogen safety engineering and assist to make this fast emerging market inherently safer. Global fuel cell demand will reach $8.5 billion in 2016 (PennWell Corporation, 2007).

1.2. Public perception of hydrogen technologies

Public perception of hydrogen technologies is still affected by the 1937 *Hindenburg* disaster. The catastrophe is often associated with hydrogen as a reason even there is an opinion that the difference in electrical potential between the zeppelin "landing" rope and the ground during descending had generated electrical current that ignited the dirigible canopy made of extremely combustible material. This was followed by diffusive combustion of hydrogen in air without generation of a significant blast wave able to injure people. Figure 1–1 shows a photo of burning *Hindenburg* dirigible fire demonstrating that there was no "explosion" (Environmental graffiti alpha, 2010).



Figure 1–1. Photo of the *Hindenburg* dirigible fire demonstrating that there was no "explosion" (Environmental graffiti alpha, 2010).

Contrary to popular misunderstanding hydrogen helped to save 62 lives in the *Hindenburg* disaster. The NASA research has demonstrated (Bain and Van Vorst, 1999) that the disaster would have been essentially unchanged even if the airship were lifted not by hydrogen but by non-combustible helium, and that probably nobody aboard was killed by a hydrogen fire. The 35% who died were killed by jumping out, or by the burning diesel oil, canopy, and debris (the cloth canopy was coated with what nowadays would be called rocket fuel). The other 65% survived, riding the flaming dirigible to earth as the clear hydrogen flames swirled harmlessly above them.

1.3. The importance of hydrogen safety

There is a clear understanding by all stakeholders of the role of hydrogen safety for emerging hydrogen and fuel cell technologies, systems and infrastructure. This is supported by investment to safety of about 5–10% of the total funding of hydrogen and fuel cell programmes both in USA and in Europe. Hydrogen safety studies were initiated decades ago as a result of accidents in the process industries, and were supported by safety research for nuclear power plants and aerospace sector. For example, a study of the Three Mile Island nuclear plant (USA) accident in 1979 (Henrie and Postma, 1983) demonstrated that almost homogeneous 8% by volume of hydrogen in air mixture deflagrated. Fortunately, the deflagration pressure increases to about 190 kPa only that was considerably below the strength of the large concrete containment building.

Recentdisasters involving hydrogen, i.e. the Challenger Space Shuttle explosion(1986) and the Fukushima nuclear tragedy (2011), demonstrated that our knowledge and engineering skills to deal safely with hydrogen even within these industries require more investment, from both intellectual and financial perspective.

Nowadays dealing with hydrogen is getting out of hands of highly trained professionals in industry and become everyday activity for public. This implies a need in establishment of a new safety culture in society, development of innovative safety strategies and breakthrough engineering solutions. It is expected that the level of safety and risk at the consumer interface with hydrogen must be similar or exceeds that present with fossil fuel usage. Thus, safety parameters of hydrogen and fuel cell products will directly define their competitiveness on the market.

Hydrogen safety engineers, technology developers and infrastructure designers, scientists using research facilities, technical staff at maintenance workshops and refuelling stations, first responders should be professionally educated to deal with hydrogen systems at pressures up to 100 MPa and temperatures down to -253°C (liquefied hydrogen) in open and confined spaces. Regulators and public officials should be provided with the state-of-the-art knowledge and a guidance to professionally support the safe introduction of hydrogen and fuel cell systems to everyday life of public. Engineers, including those who have handled hydrogen in different industries for several decades, need to undergo periodic retraining through continuous professional development courses to acquire the latest knowledge and skills for using hydrogen in the public domain. Indeed, emerging hydrogen systems and infrastructure *will create in a close future entirely new environment of hydrogen usage, which is not covered by industrial experience or through existing codes and recommended practice* (Ricci et al., 2006).

Hydrogen-powered vehicles are one of the main applications of hydrogen and fuel cell technologies. Hazards and associated risks for hydrogen-fuelled cars should be understood and interpreted in a professional way with full comprehension of consequences by all stakeholders starting from system designers through regulators to users. Probably the first comparison of the "severity" of a hydrogen and gasoline fuel leak and ignition was performed by Swain (2001). Figure 1–2 shows snapshots of hydrogen jet fire and gasoline fire at 3 s (left) and 60 s (right) after car fire initiation.



Figure 1–2. Hydrogen jet fire and gasoline fire: 3 (left) and 60 (right) seconds after car fire initiation (Swain, 2001).

The scenario with hydrogen-fuelled car presented in Fig. 1–2 is rare, e.g. it can be realised at a false self-initiation of a pressure relief device (PRD). Indeed, a release of hydrogen through the PRD from the onboard storage would be in majority of cases initiated by an external fire. A scenario with the external fire drastically changes hazards and associated risks compared to the situation shown in Fig. 1–2.

Figures 1–3 and 1–4 demonstrate results of a study on hydrogen-powered cars fire performed in Japan (Tamura et al., 2011). The hydrogen fuel cell vehicle (HFCV) was equipped with a thermal pressure relief device (TPRD) with vent pipe internal diameter of 4.2 mm. In a test shown in Fig. 1–3 the compressed hydrogen gas tank was installed exactly at the position of the removed gasoline tank. By this reason, there was no chance to install a larger storage vessel and a small tank of 36 litres volume at pressure 70 MPa was used.

The fire spread from a gasoline vehicle to HFCV was investigated to address scenarios when different types of vehicles are catching fire in car collision or natural disaster like earthquake. The experiment revealed that when the TPRD of HFCV is activated by gasoline fire a fireball of more than 10 m diameter is formed (Fig. 1–3, right).



Figure 1–3. A HFCV gasoline pool fire test: (left) – gasoline fire just before initiation of TPRD, (right) – 1 second after TPRD initiation (Tamura et al., 2011).

In another test of Tamura et al. (2011) two vehicles were parked approximately 0.85 m apart and the spread of fire from HFCV to the gasoline vehicle was investigated. Figure 1–4 shows two vehicles after the TPRD initiation in the HFCV. It can be concluded that self-evacuation from the car or safeguarding by first responders with such design of hydrogen release system is impossible and car manufacturers yet have to address this customer safety issue.



Figure 1–4. The HFCV with initiated TPRD (left) and the gasoline car (right) (Tamura et al., 2011).

In test conditions (Tamura et al., 2011) the cause of fire spread from the HFCV to the adjacent gasoline vehicle, in authors' opinion, is the flame spreading from the interior and exterior fittings of the HFCV but not the hydrogen flame from the TPRD (it is worth noting that the small storage tank of only 36 litres with a shorter hydrogen release time was used in the study by Tamura et al. (2011) instead of a larger tank that is needed to provide competitive driving range). Authors concluded that in car carrier ships and other similar situations with closely parked HFCVs, the test results point to the possibilities of a fire in an HFCV to activate its TPRD and thereby to generate hydrogen flames which in turn may cause the under floor TPRD activation in adjoining HFCV.

To minimize damage by HFCV fire, therefore, authors suggested that it is important to early detect and extinguish fire before the TPRD activation. It is known that hydrogen fire is difficult if not possible to extinguish in many practical situations. Hopefully, car manufacturers will develop appropriate safety engineering solutions, including reduction of flame length from hydrogen-powered vehicle in a mishap, thus excluding the "domino" effect in accident development and assisting first responders to control such fires and successfully perform rescue operations. Experiments by Tamura et al. (2011) have clearly demonstrated that hydrogen-powered vehicle fire consequences can be very "challenging" both from life safety and property loss points of view.

Hydrogen is not more dangerous nor safer compared to other fuels (Ricci et al., 2006). Safety of hydrogen and fuel cell systems and infrastructure fully depends on how professionally it is handled at the design stage and afterwards. The safe and successful use of hydrogen starts with knowing of and adhering to the state-of-the-art knowledge in hydrogen safety engineering, appropriate regulation for the design of the systems and facilities. Safety shall be considered at all stages of a hydrogen system of infrastructure life cycle, beginning with its initial design and continuing through its manufacturing, construction, operation, maintenance, and ending with its decommissioning.

1.4. Hazards, risk, safety

Hazard can be defined as a chemical or physical condition that has the potential for causing damage to people, property and the environment. Hydrogen accident could have different hazards, e.g. asphyxiation due to release in closed space, frostbite by liquefied hydrogen, thermal hazards from jet fire, pressure effects from deflagrations and detonations, etc. Hazard could lead to no damage, if the proper safety measures are applied, or could lead to costly consequences up to fatalities if the system or infrastructure has been designed and used without professional knowledge in hydrogen safety.

The modern definition of risk is provided by ISO/IEC Guide 73:2002 (2002) stating that it is the "*combination of the probability of an event and its consequence"* while safety is defined as the *"freedom from unacceptable risk"*. This means that safety is a societal category and cannot be numerically defined while risk is a technical measure that can be calculated (LaChance et al., 2009). Society, in consequence, establishes acceptable levels of risk or risk acceptance criteria.

The general requirement is that the risk associated with hydrogen-fuelled vehicles should be the same or below the risk for today's vehicles using fossil fuels. Currently this requirement is not yet achieved throughout the whole range of hydrogen and fuel cell systems. Indeed, consequences of hydrogen-powered car fire to life safety and property loss, e.g. in confined spaces such as garages and tunnels, are more "costly" compared to consequences of fossil fuel vehicle fire at a current level of fire resistance of hydrogen onboard storage and design of pressure relief devices. In fact, the probability of external to vehicle fire, e.g. at home garages and general vehicle parking garages will be the same independent of a vehicle type.

The garage fires statistics from National Fire Protection Association (NFPA) is as follows. During the four-year period of 2003–2006 an estimated average of 8,120 fires per year that started in the vehicle storage areas, garages, or carports of one or two-family homes (Ahrens, 2009). These fires caused an average of 35 civilian deaths, 367 civilian injuries, and $425 million in direct property damage. Further to this NFPA estimated (Ahrens, 2006) that during 1999–2002, an average of 660 structure fires and 1,100 vehicle fires in or at general vehicle parking garages were reported per year (include bus, fleet, or commercial parking structures). 60% of the vehicle fires and 29% of the structure fires in these properties resulted from failures of equipment or heat source. Vehicles were involved in the ignition of 13% of these structure fires. Exposure to another fire was a factor in roughly one-quarter of both structure and vehicle fires. The data does not distinguish between open and enclosed garages.

Please click the advert



This statistics makes it clear that safety strategies and solutions, including those developed by car manufacturers, yet have to be improved to rely on a firm engineering design rather than a general risk assessment of which uncertainties are impossible to define for emerging technologies.

The general approach to consideration of hazards and associated risks can be based on the former NASA (1997) guidelines. An analysis shall be conducted to identify all fire and explosion hazards and accomplish the following:

- Significant hazards shall be eliminated or reduced to acceptable risk levels;
- Where the hazard cannot be eliminated or reduced, the system components associated with the hazard shall be relocated to an area less threatening to people and property as directed by the Authority Having Jurisdiction (AHJ);
- Where the hazard cannot be eliminated, reduced, or removed, the system components associated with the hazard shall be isolated within the facility so as not to pose a danger to the remainder of the structure or its occupants;
- Where the hazard cannot be eliminated, reduced, relocated, or isolated, protection shall be provided to ensure adequate levels of human and structural safety. Should an incident/accident occur, the occupants of the facility shall be provided with protection to enable them to leave the area safely and the structure will be protected to ensure its continued integrity.

1.5. Hydrogen safety communication

The European network of excellence (NoE) HySafe "Safety of Hydrogen as an Energy Carrier" (2004–2009. www.hysafe.org) with €12M of the European Community funding paved the way to defragmentation of hydrogen safety research in Europe and beyond, and closing knowledge gaps in the field. Since 2009, when the HySafe project was formally finished, the coordination of international hydrogen safety activities is led by the International Association for Hydrogen Safety (http://www.hysafe.org/IAHySafe) that brings together experts in hydrogen safety science and engineering from industry, research organizations, and academia from all over the globe.

The International Energy Agency's Hydrogen Implementation Agreement Task 31 "Hydrogen Safety" is also contributing to the prioritization of problems to be solved, discussions of work-in-progress, and the cross-fertilization of safety strategies and engineering solutions developed in different countries around the globe.

The main sources of published knowledge in hydrogen safety include at the moment the Biennial Report on Hydrogen Safety (2008) initiated by NoE HySafe, Proceedings of the International Conference on Hydrogen Safety, and the International Journal of Hydrogen Energy.

The main educational/training activities in the area of hydrogen safety include the European Summer School on Hydrogen Safety and other technical and summer schools, the International Short Course and Advanced Research Workshop (ISCARW) series "Progress in Hydrogen Safety", and the World's first postgraduate course in hydrogen safety, i.e. MSc in Hydrogen Safety Engineering at the University of Ulster. However, the need in an increasing stream of highly qualified university graduates to underpin the emerging industry and early markets is obvious.

The Workgroup on Cross Cutting Issues of the European HFC Technology Platform (Wancura et al., 2006) indicated that educational and training efforts are key instrument in lifting barriers imposed by the safety of hydrogen. This Workgroup has estimated that during the FP7 period (2007–2013), the educated staff needed may amount to 500 new graduates from postgraduate studies on an annual basis in all of Europe. In a study of the European e-Academy of Hydrogen Safety performed within the NoE HySafe, it was estimated that the subset of these necessary graduates specialising in hydrogen safety would amount to 100 on an annual basis (Dahoe and Molkov, 2007).

Unfortunately, to describe all recent progress made in the field of hydrogen safety science and engineering by the international hydrogen safety community is a difficult if not impossible task. The materials presented here are mainly results of the Hydrogen Safety Engineering and Research (HySAFER, http://hysafer.ulster.ac.uk/) Centre at the University of Ulster studies performed as a seeding research and within projects funded by the European Commission and the Fuel Cell and Hydrogen Joint Undertaking.

1.6. The subject and scope of hydrogen safety engineering

The subject of hydrogen safety engineering (HSE) is defined as the application of scientific and engineering principles to the protection of life, property and environment from adverse effects of incidents/accidents involving hydrogen. The scope of hydrogen safety engineering is reflected in the updated HySafe activities matrix (Fig. 1–5) developed by the HySafe consortium (www.hysafe.org). "Vertical" activities are relevant to key phenomena, hazards and risks, including but not limited to releases and dispersion, spontaneous ignition and thermal effects from fires, pressure effects from deflagrations and detonations, mitigation technologies and safety devices, etc. "Horizontal" activities are relevant to safety of various applications and infrastructure, including hydrogen production and distribution, automotive and other transportation, storage, fuel cell components, portable and micropower applications, infrastructure such as refuelling stations, garages, tunnels , etc. The intersection of these vertical and horizontal activities defines the scope of hydrogen safety engineering. Both knowledge of phenomena and engineering safety solutions for hydrogen and fuel cell systems are expected to feed relevant regulations, codes and standards (RCS).

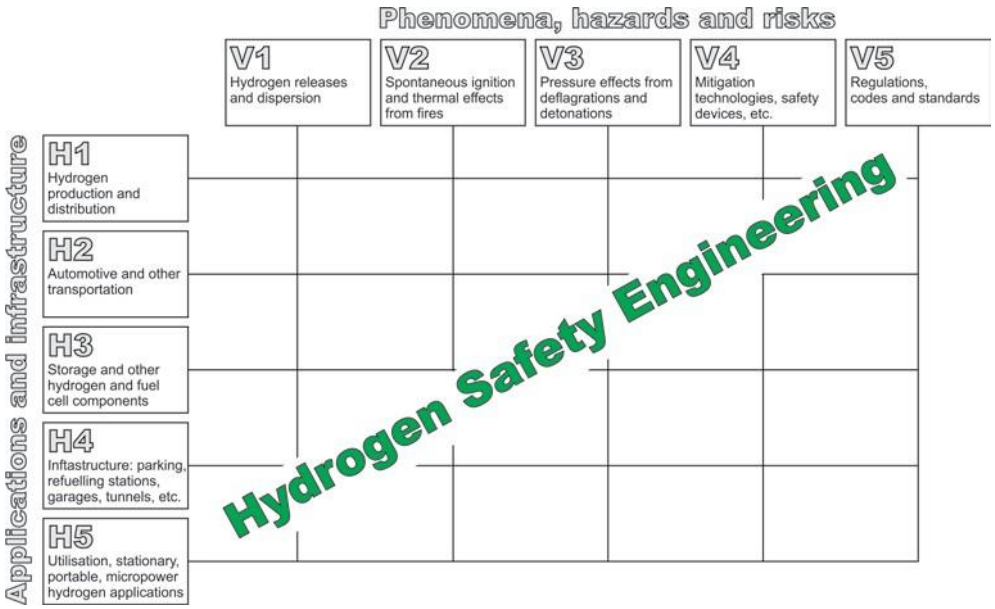


Figure 1–5. The HySafe activity matrix.

The HSE can be applied to existing and new hydrogen systems, including but not limited to stationary, e.g. combined heat and power systems, or portable, e.g. mobile phone and computers, applications for indoor and outdoor use, hydrogen transportation and refuelling infrastructure, power generation, hydrogen production and distribution units, storage, infrastructures such as garages, parking, tunnels, pipelines networks, etc. A hydrogen system could be defined as an equipment dealing with hydrogen e.g. storage, production, delivery, distribution, consumption, etc. Hydrogen should remain contained within hydrogen system from its production/delivery to its final use.

1.7. The emerging profession of hydrogen safety engineering

The higher education of researchers and engineers is a key to surmount challenges of hydrogen safety. The development of an International Curriculum on Hydrogen Safety Engineering (www.hysafe.org/Curriculum) was the first step in the establishment of the profession undertaken by the European e-Academy of Hydrogen Safety in collaboration with partners around the globe. About 70 renowned international experts contributed to the draft for development of the Curriculum. The Curriculum has been already implemented into the World's first postgraduate course in hydrogen safety, i.e. MSc in hydrogen safety engineering at the University of Ulster (http://www.ulster.ac.uk/elearning/programmes/view/course/10139), continuous professional development course at Warsaw University of Technology, hydrogen technology and safety course at the HECTOR School of the Karlsruhe Institute of Technology. The main contributor to the establishment of the profession through a closing of knowledge gaps and educational/training programmes is the international hydrogen safety community led by the International Association for Hydrogen Safety (IA HySafe).

The HSE discipline is developing on the experience and lessons learnt by fire safety engineering, which is today a well-established profession focused mainly on building fires. Unfortunately, graduates of fire safety engineering courses are not taught currently to tackle specific problems of hydrogen safety such as high pressure leaks and dispersion, spontaneous ignition and thermal effects of under-expanded jet fires, pressure loads of hydrogen-air deflagrations/detonations and blast waves, emergency services intervention at an accident scene with a hydrogen system, etc. However, there are common problems, knowledge and experience which HSE can utilise to some extent, such as fire resistance of structures and life safety.

Fire safety was originally regulated by prescriptive codes, aiming to protect societies from adverse effects of fires in traditional buildings with low hazard occupancies (Croce et al., 2008). However, for more complex buildings, the prescriptive approach didn't meet the needs of designers or approval bodies. Those prescriptive codes didn't offer flexibility for innovation, they didn't necessarily provide optimum solution for a particular project, they provided requirements without statement of objectives, they might lag many years behind modern design practice and their use unable to anticipate all eventualities (BSI, 2001; Hadjisophocleous and Benichou, 2002).

In the late 1980s, a project led by the Warren Centre in Australia made a significant contribution by proposing fundamental improvements to fire safety. The purpose was to define a basis for a new generation of RCS. Among the numerous recommendations of the Warren Centre Report (1989), some are directly applied to hydrogen safety systems:

Please click the advert



- design for safety should be treated as "*an engineering responsibility rather than as a matter for detailed regulatory control*";
- designers should develop a greater understanding of fire phenomena and human behaviour and adopt appropriate engineering techniques in their design of fire safety systems;
- fire engineering design courses and training strategies should be developed and implemented, up to and including postgraduate level, etc.

This report led to a worldwide attention towards fire safety engineering. The methodology highlighted by this approach was dedicated to measure design's performance using different tools, e.g. simple engineering calculations and contemporary computer-based models.

There was an intention to implement non-complex documents (Hadjisophocleous and Benichou, 2002) in performance-based fire safety regulations to provide greater flexibility when designing and evaluating a project, and to promote innovation in building design, materials, products, and fire protection systems (Croce et al., 2008). This approach nevertheless requires education of professionals and the validation of tools and methods used for quantification (Hadjisophocleous and Benichou, 2002).

The developments in hydrogen safety engineering are greatly inspired by and based on the developments of fire safety engineering, including performance-based RCS, educational programmes and freely available contemporary CFD (Computational Fluid Dynamics) tools like Fire Dynamics Simulator (http://fire.nist.gov/fds/).

The framework for fire safety engineering is described by Deakin and Cooke (1994). Some of their statements can be directly transferred to define the HSE framework:

- **Provide a systematic approach.** The process used to undertake HSE and evaluate the performance of a design, should be clearly defined and explained.
- **Define acceptance criteria.** The performance of a design is evaluated by comparison with deterministic, comparative or probabilistic criteria.
- **Simplify the problem.** The HSE process is separated into analysis of Technical Sub-Systems (TSS) that can be used individually to address specific issues or together to address all aspects.
- **Illustrate interactions.** The complexity of phenomena and interactions between elements of hydrogen system, people and the built environment in a case of incident/accident requires a simplified approach by underlining interactions between different TSS.
- **Ensure adequate consideration of all those factors relevant to any aspect of the design.** In order to identify all significant variables in a quantification process, it is essential to list relevant scenarios. Doing this, it is possible for each scenario to inventory critical factors from hydrogen system/infrastructure, e.g. parameters of accident scenario including occupancy, etc.

- **Insist on clear presentation and comment on calculation methods and data sources.** As the application of HSE might be subject to review and approval, it is essential that findings, calculations and assumptions, are presented in a report that can be clearly and readily understood.

1.8. Knowledge gaps and future progress

In Europe the priorities in hydrogen safety research are formulated by industry through calls of the Fuel Cell and Hydrogen Joint Undertaking (FCH JU, http://www.fch-ju.eu/) mainly as a part of cross- cutting issues. The international hydrogen safety community contributes to the prioritization of research through different activities of the International Association for Hydrogen Safety (www.hysafe.org). The International Energy Agency Hydrogen Implementation Agreement Task 31 "Hydrogen Safety" (http://www.ieah2safety.com/) is actively involved in the process too. A gap analysis of CFD modelling of accidental hydrogen release and combustion has been performed recently by an expert group led by JRC, Institute for Energy, The European Commission (Baraldi et al., 2010).

In spite of indubitable progress in hydrogen safety in the last decade, there are still numerous gaps of knowledge and a need in science-intensive tools, based on contemporary theories and thorough validation against a series of experiments carried out at different conditions. The non-exhaustive list of research topics has been prioritized by the hydrogen safety community, including but not limited to the following items grouped by phenomena or application. Based on the report by Baraldi et al. (2010) author updated the list of knowledge gaps in hydrogen safety as follows.

***Release and dispersion phenomena*:** hydrogen leak source characterization and modelling; shape of leak source effects; dispersion and accumulation in enclosed areas in presence of natural and mechanical ventilation; surface effects on jet release and separation distance; criteria for uniform or layered distribution of hydrogen in vented enclosure; liquid hydrogen release behaviour; behaviour of cold jets released in humid air; releases in complex geometries; effect of wind on indoor (natural ventilation) and outdoor releases in areas with complex surroundings; behaviour of expanded and under-expanded plane jets compared to round jets; interaction of multiple jets; transient effects in high momentum jets; transition from momentum- to buoyancy-controlled flow; flammable envelope for downward free and impinging jets; dynamics of unsteady releases (blow-downs and hydrogen puff, etc.); initial stage of release and dispersion in ventilated enclosure; applicability limits for pressure peaking phenomenon; etc.

***Ignition phenomena*:** mechanisms of hydrogen ignition during release; CFD modelling and validation of the membrane rupture and the associated transient processes; CFD modelling of transition from spontaneous ignition to jet fires and/or the quenching of the spontaneous ignition; development and validation of sub-grid scale models accounting for interaction of turbulence and chemistry; ignition in complex geometries like pressure relief devices; extinction of spontaneous ignition in piping; jet ignition delay time and position of ignition source for simulations of deflagration overpressure; effect of spontaneous ignition on deflagration overpressure as compared to spark ignition at different distances

from the release source; ignition in complex geometries like pressure relief devices; etc.

***Hydrogen fires*:** behaviour of free jet flames, e.g. thermal radiation in the presence of a crosswind and surface effects on flame jet propagation; development of models and validation of CFD tools for large-scale hydrogen jet fires, including under transient conditions of decreasing notional nozzle diameter and temperature during a blowdown; thermal and pressure effects of indoor hydrogen fires; understanding of under-ventilated fires, self-extinction and re-ignition phenomena; impinging jet fires and heat transfer to structural elements, storage vessels, etc.; predictive simulations of blow-off, lift-off, and blow-out phenomena; expanded and under-expanded plane jet flames; predictive simulations of micro-flame quenching and blow-off; effect of micro-flames on materials degradation; etc.

***Deflagrations and detonations*:** effect of hydrogen jet ignition delay time and position of ignition source on predictive simulation of deflagration overpressure; flammability and detonability limits of gaseous mixtures containing hydrogen; modelling of coherent deflagration during venting of deflagration in low-strength equipment accounting for Rayleigh-Taylor instability; effect of inertia of vent cover on deflagration dynamics, including DDT; partially premixed flames, in particular triple flames in hydrogen-air layers and their pressure effects in enclosed space; development of SGS models of DDT at large industrial scales accounting for Richtmyer-Meshkov instability; etc.

***Storage*:** fire resistance of onboard storage vessels and effect of PRD; metal hydride dust cloud deflagration hazard; engineering solutions to reduce heat transfer to storage tanks from external fire scenarios (localized and engulfing fires); etc.

***High pressure electrolysers*:** an explosion of a pressurized electrolyser at operational pressure 40 MPa happened on December 7, 2005 at a demonstration hydrogen stand at Kyushu University (http://www.kyushuu.ac.jp/news/hydrogen/hydrogensummary0330.pdf; http://www.nsc.go.jp/senmon/shidai/kasai/kasai004/ssiryo4-1.pdf). Possibly after the membrane leak an internal hydrogen-oxygen jet fire resulted in metal (titanium) fire and explosion or rupture of the electrolyzer shell. Internal fluid and combustion products were released into surrounding including parking area around the laboratory building. Several vehicle glass damages occurred due to the exposure to hydrogen fluoride which formed by the decomposition of polymer materials of the membrane. A French-Russian study (Millet et al., 2011) reports the analysis of the failure mechanisms of PEM water electrolysis cells which can ultimately lead to the destruction of the electrolyser. A two-step process involving firstly the local perforation of the solid polymer electrolyte followed secondly by the catalytic recombination of hydrogen and oxygen stored in the electrolysis compartments has been evidenced. Photographs of a stainless steel fitting and nut drilled by a hydrogen-oxygen flame formed inside the PEM stack are presented (Millet et al., 2011). Millet et al. (2011) concluded that the internal hydrogen-oxygen combustion prevails over "explosion".

***Hazard and risk identification and analysis for early markets*:** data collection from new hydrogen-based operating devices, systems and facilities; failure statistics of new hydrogen applications; systems safety analysis of hydrogen applications; engineering correlations, etc. Since new technologies are penetrating densely populated urban environment, special attention should be paid to hazards and risk mitigation technologies and methods such as sensors, barriers/walls and separation distances.

walls and separation distances.

2 Hydrogen properties and hazards

As a unique gas hydrogen was discovered by Henry Cavendish in 1766. It was given the name "water forming" by Antoine Lavoisier seven years later, who proved that water was composed of hydrogen and oxygen. The word "hydrogen"originates from the Greek words *hydōr* (water) and *gignomai* (forming). However, it has to be mentioned that hydrogen was observed and collected by Robert Boyle in 1671, who dissolved iron in diluted hydrochloric acid, i.e. long before it was recognized as a unique gas by Henry Cavendish.

Hydrogen is one of the main compounds of water and of all organic matter, and it's widely spread not only in The Earth but also in the entire Universe. It is the most abundant element in the Universe representing 75% by mass or 90% by volume of all matter (BRHS, 2009). Hydrogen forms 0.15% of The Earth crust.

This chapter presents selected properties of hydrogen that are relevant to safety provisions and associated hazards. Safety of hydrogen and fuel cell systems and infrastructure at the user interface will be provided when the technology developers, designers, regulators, operational personnel, first responders and finally public are aware through education and training of the specific hazards associated with the handling and use of hydrogen and understand how to prevent the incident/accident or mitigate/control it if happened.

Please click the advert

STUDY FOR YOUR MASTER'S DEGREE
IN THE CRADLE OF SWEDISH ENGINEERING

Chalmers University of Technology conducts research and education in engineering and natural sciences, architecture, technology-related mathematical sciences and nautical sciences. Behind all that Chalmers accomplishes, the aim persists for contributing to a sustainable future – both nationally and globally.

Visit us on Chalmers.se or Next Stop Chalmers on facebook.



2.1. Physical and chemical properties

2.1.1. Atomic and molecular hydrogen, ortho- and para-hydrogen

Atomic number of hydrogen (symbol H) in the periodic table is one, and atomic mass is 1.008 g/mol (approximated by four digits). The hydrogen atom is formed by a nucleus with one unit of positive charge (proton) and one electron. The electron carries a negative charge and is usually described as occupying a "probability cloud" surrounds the nucleus somewhat like a fuzzy, spherical shell. Charges of the proton and electron of each hydrogen atom cancel each other out, so that individual hydrogen atom is electrically neutral. The mass of a hydrogen atom is concentrated in its nucleus. Indeed, the proton is more than 1800 times more massive than the electron. Neutron can be present in the nucleus. Neutron has almost the same mass as proton and does not carry a charge. The radius of the electron's orbit, which defines the size of the atom, is approximately 100,000 times as large as the radius of the nucleus. Size of hydrogen atom in its ground state is 10^{-10} m (1 angstrom).

There are three hydrogen isotopes: protium (found in more than 99,985% of the natural element; only a proton in the nucleus), deuterium (found in nature in 0.015% approximately; a proton and a neutron in the nucleus), and tritium (appears in small quantities in nature, but can be artificially produced by various nuclear reactions; a proton and two neutrons in the nucleus) with atomic mass 1, 2 and 3 respectively (approximated by one digit). Tritium is unstable and radioactive (generates β rays – fast moving electrons as a result of neutron conversion into a proton, 12.3 years half-decay time).

In normal conditions hydrogen is a gas formed by diatomic molecules, H_2 (molecular mass 2.016), in which two hydrogen atoms have formed a covalent bond. This is because the atomic arrangement of a single electron orbiting a nucleus is highly reactive. For this reason, hydrogen atoms naturally combine into pairs. Hydrogen is colourless, odourless and insipid. That is why its leak is difficult to detect. Compounds such as mercaptans, which are used to scent natural gas, cannot be added to hydrogen for use in PEM (proton exchange membrane) fuel cells as they contain sulphur that would poison the fuel cells.

The hydrogen molecule exists in two forms, distinguished by the relative rotation of the nuclear spin of the individual atoms in the molecule. Molecules with spins in the same direction (parallel) are called ortho-hydrogen; and those with spins in the opposite direction (anti-parallel), para-hydrogen (NASA, 1997). These molecules have slightly different physical properties but are chemically equivalent. The chemistry of hydrogen, and in particular the combustion chemistry, is little altered by the different atomic and molecular forms.

The equilibrium mixture of ortho- and para-hydrogen at any temperature is referred to as equilibrium hydrogen. The equilibrium ortho-para-hydrogen mixture with a content of 75% ortho-hydrogen and 25% para-hydrogen at room temperature is called normal hydrogen. At lower temperatures, equilibrium favours the existence of the less energetic para-hydrogen (liquid hydrogen at 20 K is composed of 99,8% of para- hydrogen). The ortho-para-hydrogen conversion is accompanied by a release of heat, 703 kJ/kg at 20 K for ortho- to para-hydrogen conversion, or 527 kJ/kg for normal to para-hydrogen conversion (NASA, 1997).

This feature of hydrogen underpins inherently safer storage of hydrogen as cryo-compressed rather than liquefied fluid (fluids with temperatures below –73ºC are known as cryogenic fluids) in automotive applications due to essential reduction if not exclusion at all of the hydrogen boil-off phenomenon at day-to-day normal driving. In fact, due to conversion of para- to ortho-hydrogen during "consumption" of external heat the release of hydrogen from storage tank as a result of boil-off phenomenon is practically excluded for cryo-compressed storage with clear safety implications.

The process of hydrogen liquefaction includes the removal of the energy released by the ortho-para state conversion. The heat of conversion is 715.8 kJ/kg. This is 1.5 times of the heat of vaporization (ISO/TR 15916:2004). The liquefaction is a very slow exothermic process that can take several days to complete, unless it is accelerated with the use of a paramagnetic catalyst.

2.1.2. Gas, liquid, and solid phases

The phase diagram of hydrogen is presented schematically in Fig. 2–1. There are three curves. One curve shows change of boiling (condensation for the opposite phase transition) temperature with pressure, another gives change of melting (freezing) temperature with pressure, and the third indicates pressures and temperatures when *sublimation* is possible. The process of condensation is also known as liquefaction.

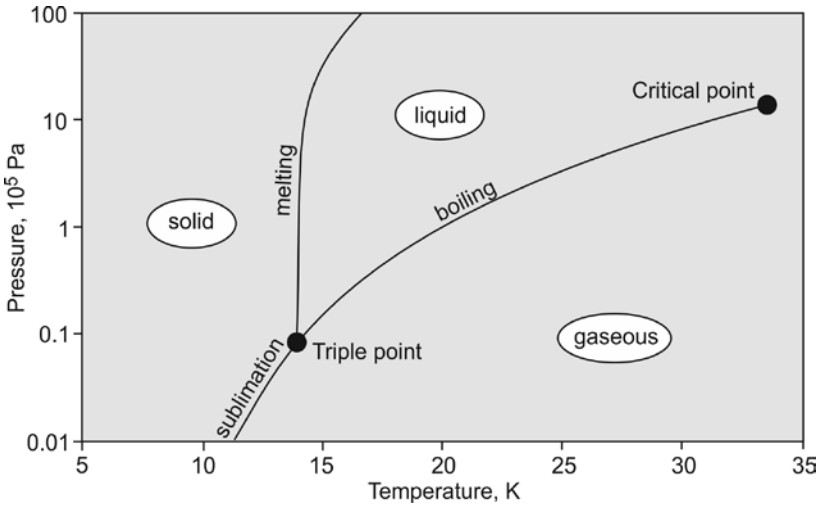


Figure 2–1. Phase diagram of hydrogen.

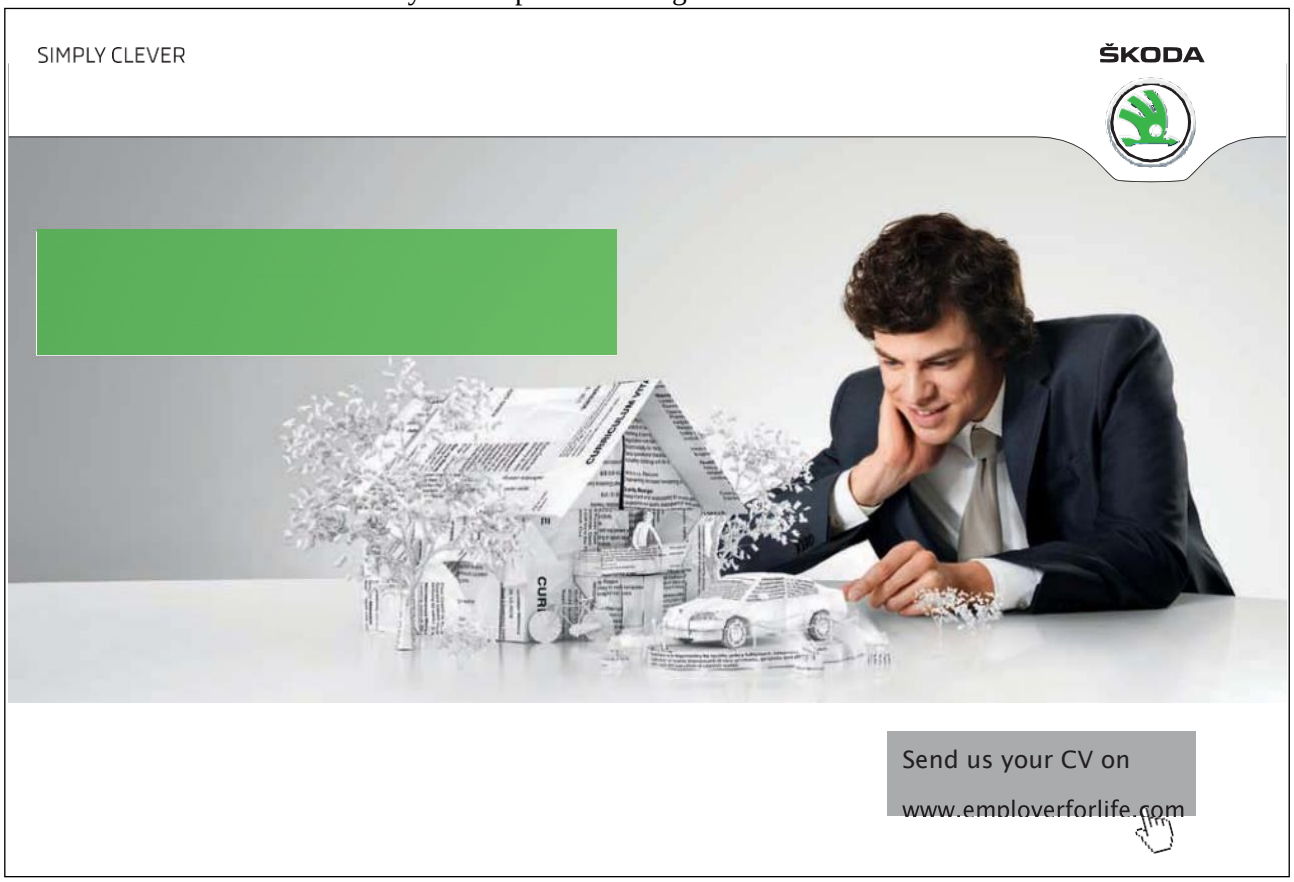
Hydrogen is used in gaseous, liquid, or slush forms. Liquid hydrogen is transparent with a light blue tint. Slush hydrogen is a mixture of solid and liquid hydrogen at the triple point temperature. The phase transition of hydrogen is dominated by the low temperatures at which transitions between gas, liquid, and solid phases occur. The *triple point* (see phase diagram), which is the condition under which all three phases can coexist, is temperature 13.8 K and pressure 7.2 kPa. The vapour pressure of slush hydrogen can be as low as 7.04 kPa (NASA, 1997) and safety measures must be taken during operations to prevent air leakage into the system that could create flammable mixture.

The highest temperature, at which a hydrogen vapour can be liquefied, is the critical temperature, which is 33.145 K (see "critical point" on the phase diagram). The corresponding critical pressure is 1.3 MPa (density at critical point is 31.263 kg/m^3). Above the critical temperature it is impossible to condense hydrogen into liquid just by increasing the pressure. All you get is cryo-compressed gas. The molecules have too much energy for the intermolecular forces to hold them together as a liquid.

The normal boiling point (NBP, boiling temperature at absolute pressure of 101,325 kPa) of hydrogen is 20.3 K. The normal melting point is 14.1 K (101,325 kPa). Hydrogen has the second lowest boiling and melting points of all substances (helium has lowest value of boiling temperature of 4.2 K and melting temperature of 0.95 K). All these temperatures are extremely low and below the freezing point of air. It is worth reminding that at absolute zero temperature of 0 K (–273.15 ºC), which is the lowest temperature in the universe, all molecular motion stops.

Liquid para-hydrogen (NBP) has a density of 70.78 kg/m^3. The corresponding *specific gravity* is 0.071 (the reference substance is water with specific gravity of 1). Thus, liquid hydrogen is approximately 14 times less dense than water. Ironically, every cubic meter of water (made up of hydrogen and oxygen) contains 111 kg of hydrogen whereas a cubic meter of liquid hydrogen contains only 70.78 kg of hydrogen (College of the Desert, 2001). Thus, water packs more mass of hydrogen per unit volume, because of its tight molecular structure, than hydrogen itself. This is true of most other liquid hydrogen-containing compounds such as hydrocarbons as well. The higher density of the saturated hydrogen vapour at low temperatures may cause the cloud to flow horizontally or downward immediately upon release if liquid hydrogen leak occurs. These facts have to be accounted for by first responders during intervention at an accident scene.

Please click the advert



An essential safety concern of liquid hydrogen's low temperature is that, with the exception of helium, all gases will be condensed and solidified should they be exposed to it. Leaks of air or other gases into direct exposure with liquid hydrogen can lead to several hazards (ISO/TR 15916:2004). The solidified gases can plug pipes and orifices and jam valves. In a process known as cryo-pumping the reduction in volume of the condensing gases may create a vacuum that can draw in yet more gas,
e.g. oxidiser like air. Large quantities of material can accumulate displacing the liquid hydrogen if the leak persists for long periods. At some point, should the system be warmed for maintenance, these frozen materials will re-gasify possibly resulting in high pressures or explosive mixtures. These other gases might also carry heat into the liquid hydrogen and cause enhanced evaporation losses or "unexpected" pressure rise.

Liquid hydrogen is usually transferred in vacuum insulated lines. However, cold hydrogen flowing through tubes which are not sufficiently thermally insulated can easily cool the system below 90 K so that condensed air with an oxygen content of up to 52 % is present (NBP of nitrogen is 77.36 K, NBP of oxygen is 90.15 K, NBP of carbon dioxide is 216.6 K). The liquid condensate flows and looks like liquid water. This oxygen-enriched condensate enhances the flammability of materials and makes materials combustible that normally are not. This includes for example bituminous road covers. This is of particular concern when transferring large quantities of hydrogen. If a piece of equipment cannot be insulated, the area underneath should be free of any organic material.

Oxygen enrichment can increase the flammability and even lead to the formation of shock-sensitive compounds. Oxygen particulate in cryogenic hydrogen gas may even detonate. Vessels with liquid hydrogen have to be periodically warmed and purged to keep the accumulated oxygen content in the vessel to less than 2% (ISO/TR 15916:2004). Caution should be exercised if carbon dioxide is used as a purge gas. It may be difficult to remove all carbon dioxide from the system low points where the gas can accumulate.

2.1.3. Heat of vaporization, melting, and sublimation

Heat of vaporization (condensation) at NBP is 445.6 kJ/kg. Heat of melting (fusion) at melting (freezing) point is 58.8 kJ/kg. Heat of *sublimation* is 379.6 kJ/kg.

2.1.4. Hydrogen expansion ratio

The volume of liquid hydrogen expands with the addition of heat significantly more than can be expected based on our experience with water. The coefficient of thermal expansion at NBP is 23 times that of water at ambient conditions (ISO/TR 15916:2004). The significance for safety arises when cryogenic storage vessels have insufficient ullage space to accommodate expansion of the liquid. This can lead to an over pressurisation of the vessel or penetration of the liquid hydrogen into transfer and vent lines.

A considerable increase in volume is associated with the phase change of liquid to gaseous hydrogen, and yet another volume increase occurs for gaseous hydrogen that is allowed to warm from the NBP to NTP. The ratio of the final volume to the initial volume for the phase change from liquid to gaseous hydrogen and expansion of heated gas is 847 (ISO/TR 15916:2004). This total volume increase can result in a final pressure of 177 MPa (starting with an initial pressure of 0.101 MPa) if the gaseous hydrogen is in a closed vessel. Pressure relief devices should be installed as a safety measure in any volume in which liquid hydrogen or cold gaseous hydrogen could be trapped, to prevent overpressure from expansion of the liquid hydrogen or cold gaseous hydrogen.

When hydrogen is stored as a high pressure gas at 25 MPa (gauge) and atmospheric temperature, its expansion ratio to atmospheric pressure is 1:240 (College of the Desert, 2001). While a higher storage pressure increases the expansion ratio somewhat, gaseous hydrogen under any conditions cannot approach the expansion ratio of liquid hydrogen.

2.1.5. Buoyancy as safety asset

The main hydrogen safety asset, i.e. its highest on The Earth buoyancy, confers the ability to rapidly flow out of an incident scene, and mix with the ambient air to a safe level below the lower flammability limit (LFL) of 4% by volume of hydrogen in air. Indeed, hydrogen has a density of 0.0838 kg/m^3 (NTP) which is far below than air density of 1.205 kg/m^3 at the same conditions. The unwanted consequences of hydrogen releases into the open atmosphere, and in partially confined geometries, where no conditions to allow hydrogen to accumulate exist, are drastically reduced by buoyancy.

Contrary, heavier hydrocarbons are able to form a huge combustible cloud, as in cases of disastrous Flixborough in 1974 (Health and Safety Executive, 1975) and Buncefield in 2005 (Buncefield Investigation, 2010) explosions. In many practical situations, hydrocarbons may pose stronger fire and explosion hazards than hydrogen. Hydrogen high buoyancy affects its dispersion considerably more than its high diffusivity.

Pure hydrogen is positively buoyant above a temperature of 22 K, i.e. over almost the whole temperature range of its gaseous state (BRHS, 2009). Buoyancy provides comparatively fast dilution of released hydrogen by surrounding air below the lower flammability level. In unconfined conditions only small fraction of released hydrogen would be able to deflagrate. Indeed, a hydrogen-air cloud evolving from the inadvertent release upon the failure of a storage tank or pipeline liberates only a small fraction of its thermal energy in case of a deflagration, which is in the range 0.1-10% and in most cases below 1% of the total energy of released hydrogen (Lind, 1975; BRHS, 2009). This makes safety considerations of hydrogen accident with large inventory at the open quite different from that of other flammable gases with often less or no harmful consequences at all.

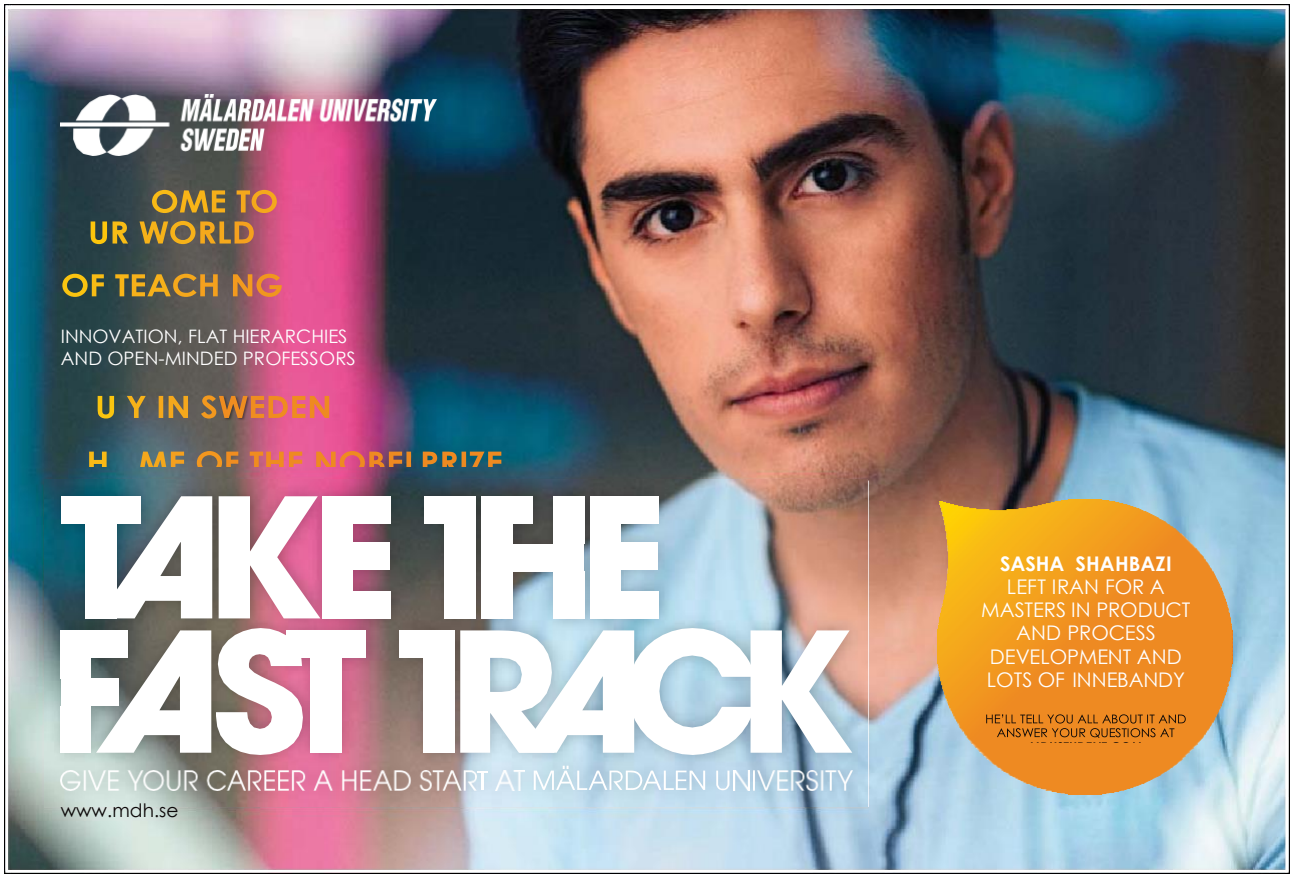
Caution should be taken in applying gaseous hydrogen buoyancy observations to releases of hydrogen vapours at cryogenic temperatures. Hydrogen vapours at low temperature can be denser than air at NTP. Usually the condensation of atmospheric humidity will also add water to the mixture cloud, firstly making it visible, and secondly increasing the molecular mass of the mixture even more.

2.1.6. Diffusivity and viscosity

Diffusivity of hydrogen is higher compared to other gases due to small size of the molecule. Data on the diffusion coefficient of hydrogen in air are ranging from 6.1E-05 m²/s (Alcock et al., 2001) to 6.8E-05 m²/s (Baratov et al., 1990).

Helium and hydrogen effective diffusion coefficients through gypsum panels were measured by Yang et al. (2011). The estimated average diffusion coefficients are found to be D_e=1.3-1.4E-05 m²/s for helium (3.3E-06 m²/s for painted gypsum panel), and D_e=1.4E-05 m²/s for hydrogen at room temperature 22 C. Authors underlined that since the interior of most garages in the U.S. have large surface areas covered with gypsum panels together with the fact that hydrogen can readily diffuse through gypsum panels, this diffusion process should not be overlooked in the hazard assessment of accidental release of hydrogen in garages or enclosures lined with gypsum panels. The quasi-steady diffusive molar flux (mol/m²/s) through the unit area of a panel of thickness δ (m) can be approximated by $D_e(C\text{-}C_S)/\delta$, where C (mol/m³) is the molar concentration of hydrogen in enclosure and C_S (mol/m³) is the concentration in the surrounding.

Please click the advert



The low viscosity of hydrogen and the small size of the molecule cause a comparatively high flow rate if the gas leaks through fittings, seals, porous materials, etc. This negative effect is to a certain extent offset by the low energy density (volumetric) of hydrogen in comparison with e.g. methane or other hydrocarbon gases. Viscosity of gaseous hydrogen (μPoise): 89.48 (NTP) and 11.28 (NBP). Viscosity of liquid hydrogen at NBP is 132.0 μPoise (BRHS, 2009).

2.1.7. Interaction with materials

Hydrogen can cause a significant deterioration in the mechanical properties of metals (NASA, 1997). This effect is referred to as hydrogen embrittlement. Hydrogen embrittlement involves a large number of variables such as the temperature and pressure of the environment; the purity, concentration, and exposure time of the hydrogen; and the stress state, physical and mechanical properties, microstructure, surface conditions, and nature of the crack front of the material. Many hydrogen material problems involve welds or the use of an improper material.

The selection of a structural material for use in liquid or slush service is based primarily on the mechanical properties of the material such as yield and tensile strength, ductility, impact strength, and notch insensitivity (NASA, 1997). The material must have certain minimum values of these properties over the entire temperature range of operation, with appropriate consideration for non-operational conditions such as a fire. The material must be metallurgically stable so phase changes in the crystalline structure do not occur with time or repeated thermal cycling.

Hydrogen is non-corrosive. Many metals absorb hydrogen, especially at high pressures. Hydrogen absorption by steel can result in embrittlement, which can lead to fails in the equipment. There is an atomic solution of hydrogen in metals. Permeated through a metal atomic hydrogen recombines to molecules on the external surface of storage to diffuse into surrounding gas afterwards. The choice of material for hydrogen system is an important part of hydrogen safety.

2.1.8. Specific heat and thermal conductivity

Non-nuclear energy applications typically use material data that applies to normal hydrogen, i.e. two protium atoms arranged in 75% as ortho-hydrogen and 25% as para-hydrogen molecules. The only exception occurs for cryogenic applications such as liquid and cryo-compressed hydrogen storage, in which heat is an important parameter. The larger property differences between ortho- and para-hydrogen occur in those properties for which heat is important, that is enthalpy, specific heat capacity and thermal conductivity, whereas other properties, such as density, vary little between ortho-hydrogen and para-hydrogen.

On a molar basis, the heat capacity of hydrogen is similar to that of other diatomic gases despite its low molecular mass (ISO/TR 15916:2004). Specific heat of gaseous hydrogen at constant pressure c_p (kJ/kg/K): 14.85 (NTP), 14.304 (STP), 12.15 (NBP). Specific heat of liquid hydrogen at boiling point is 9.66 kJ/kg/K (BRHS, 2009). The specific heat at constant pressure of liquid para-hydrogen is c_p=9.688 kJ/kg/K. This is more than double that of water and greater than 5 times that of liquid oxygen at its NBP. Gas constant of hydrogen is 4.1243 kJ/kg/K (this is the universal gas constant divided by the molecular mass). The specific heats ratio of hydrogen at NTP conditions (293.15 K and 101.325 kPa) is γ=1.39 and STP conditions (273.15 K and 101.325 kPa) is γ=1.405.

Thermal conductivity of hydrogen is significantly higher than that of other gases. Gaseous hydrogen (W/m/K): 0.187 (NTP), 0.01694 (NBP). Liquid hydrogen (W/m/K): 0.09892 (NBP).

2.1.9. The Joule-Thomson effect

In 1843 Joule investigated the dependence of energy of gases on pressure using the simple apparatus that included a copper bulb N1 filled with air under pressure, isolated from an evacuated similar bulb N2 by a valve. The bulbs were immersed in a well-stirred water bath equipped with a sensitive thermometer. After thermal equilibrium had been established, the valve was opened to allow the gas to expand into bulb N2. No change in temperature was detected and Joule concluded that "no change of temperature occurs when air is allowed to expand in such a manner as not to develop mechanical power", i.e. do no external work, $\Delta W = 0$. Since "no change of temperature" was observed, $\Delta Q = 0$, and therefore

$$\Delta W = \Delta Q = \Delta U = 0. \quad (2\text{–}1)$$

Thus, Joule concluded that the expansion of gas occurred at constant internal energy U.

Unfortunately, the system used by Joule for this experiment had a very large heat capacity compared with the heat capacity of air, and the small change of temperature that took place was not observed. In fact, the gas in bulb N1 warmed up slightly and the one which had expanded into bulb N2 was somewhat cooler and when thermal equilibrium was finally established the gas was at a slightly different temperature from that before the expansion.

Later Joule in association with Thomson, who devised a different experimental procedure, performed another study of the dependence of the energy and enthalpy of real gases during expansion. The gas in new experiment freely expanded from a pressure *P1* to pressure *P2* by the throttling action of the porous plug. The system was thermally insulated, thus the expansion occurred adiabatically. Gas was allowed to flow continuously through the porous plug, and when steady state conditions have been reached the temperatures of the gas before and after expansion, *T1* and *T2*, were measured by sensitive thermocouples.

It can be shown that throttling (the expansion of fixed mass flow rate of gas) occurs at constant enthalpy. Indeed, if two imaginary pistons introduced into the system with parameters *V1, P1, T1* upstream of the plug and *V2, P2, T2* downstream of the plug then the work done by the surroundings on the system downstream and upstream of the plug is respectively $+P1V1$ and $-P2V2$. Thus, the overall change in internal energy of the gas during the adiabatic expansion (ΔQ=0) following the second law of thermodynamics is $\Delta U = P1V1 - P2V2$. By definition $\Delta H = \Delta U + \Delta PV$ and thus this expansion is isenthalpic (ΔH=0)

$$H_2 = H_1 \tag{2–2}$$

It is worth noting that this is done in an assumption that the difference in the specific kinetic energy of gas before and after the plug can be neglected (Moran and Shapiro, 2006). However, this is not the case when there is a release from the storage with practically zero flow velocity through the small orifice where velocity can reach supersonic values.

The throttling experiment by Joule and Thomson measures directly the change in temperature of a gas with pressure at constant enthalpy which is called the Joule-Thomson coefficient

$$\mu_{JT} = \left(\frac{\partial T}{\partial P} \right)_H . \tag{2–3}$$

Please click the advert

STUDYINSWEDEN.SE

Question:
What do Skype and Spotify have in common with color screen graphics and the computer mouse?

–They are all Swedish inventions.



Be innovative. Study in Sweden

For expansion, the change of pressure is negative and therefore a positive value for Joule-Thomson coefficient corresponds to gas cooling on expansion and negative coefficient corresponds to gas heating.

For an ideal gas and isenthalpic process

$$\left(\frac{\partial H}{\partial P}\right)_T = \left(\frac{\partial H}{\partial T}\right)_P \left(\frac{\partial T}{\partial P}\right)_H = -c_P \cdot \mu_{JT} = 0. \qquad (2\text{–}4)$$

Because the heat capacity at constant pressure c_p is not zero, Joule-Thomson coefficient must be zero for an ideal gas.

For real gases, if Joule-Thomson experiments are performed with different conditions downstream of the porous plug, a curve with constant enthalpy can be drawn in coordinates temperature-pressure *T*-*P* (see Fig. 2–2). A series of curves could be generated by performing experiments at different conditions upstream of the plug. Figure 2–2 is typical of all real gases.

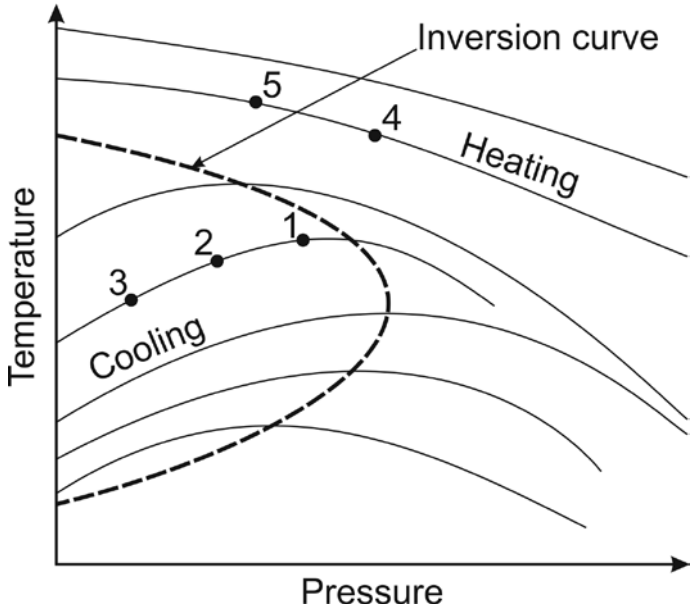


Figure 2–2. Isenthalpic curves (solid lines) and inversion curve (dash line).

If the temperature is quite low the curves pass through a maximum called the inversion point. The locus of the inversion points is called the inversion curve. The slope of an isenthalpic curve at any point is equal to Joule-Thomson coefficient and at the maximum of the curve, or the inversion point, it is equal to 0. It is evident that when the Joule-Thomson effect is to be used in the liquefaction of gases by expansion, the conditions must be chosen so that the temperature will decrease. For example, a drop in temperature would be produced by an expansion from point 1 to point 2 and then to point 3. However, a temperature rise would result in an expansion from point 4 to point 5.

At higher temperatures or lower temperatures coupled with high pressures expansion will heat the gas (see Fig. 2–2). In a Joule-Thomson process, starting at ambient temperature, the temperature of hydrogen will not drop but rise. Most gases at ambient temperatures cool when expanded across a porous plug. However, the temperature of hydrogen increases when the gas is expanded at a temperature above its inverse Joule-Thomson temperature 193 K. Yet, the inverse Joule-Thomson effect cannot be the primary cause of any ignition that occurs when hydrogen is vented from a high-pressure storage. The temperature increase from the Joule-Thomson effect is only a few degrees Kelvin at the most. It would not raise the gas temperature to its ignition value unless the gas was already near the ignition temperature after mixing with surrounding gas.

2.1.10. Ideal and real gas equations

The ideal gas equation that is applied to hydrogen at moderate pressures can be written in the form

$$p = \rho \,.\, R_{H2} \,.\, T, \tag{2–5}$$

where p is the pressure, Pa; ρ is the density, kg/m^3; T is the temperature, K; R_{H2} is the hydrogen gas constant (4124.24 J/kg/K) that is equal to the ratio of the universal gas constant R (8.3145 J/mol/K) to the molecular mass of hydrogen M=2.016 kg/kmol.

The ideal gas equation is not applicable to hydrogen storage pressures above 10–20 MPa when effects of non-ideal gas are essential. The Abel-Noble equation of state for real hydrogen gas is (Chenoweth, 1983)

$$p = Z \,.\, \rho \,.\, R_{H2} \,.\, T, \tag{2–6}$$

where the compressibility factor Z is

$$Z = \frac{1}{1 - b\rho}, \tag{2–7}$$

in which b=7.69E-03 m^3/kg is the co-volume constant for the Abel-Noble equation.

Use of the ideal gas law equation instead of the real gas equation has an important safety implications. The ideal gas law if applied for a release from high pressure storage would overestimate the mass flow rate of the leak and the total mass discharged. The compressibility factor Z gives a value of this overestimation. The compressibility factor for arbitrary storage pressure and temperature can be calculated by the following equation derived from the previous two

$$Z = 1 + \frac{b \cdot p}{R_{H2} \cdot T}. \tag{2–8}$$

For example, it is equal to Z=1.01 at 1.57 MPa, Z=1.1 at 15.7 MPa, and Z=1.5 at 78.6 MPa (temperature 293.15 K). This means that at storage pressure of 78.6 MPa the amount of released hydrogen would be overestimated by 50% if the ideal gas equation of state is applied for carrying out hydrogen safety engineering calculations.

2.1.11. Speed of sound in ideal gases

Speed of sound in ideal gases is

$$C = \sqrt{\gamma \frac{p}{\rho}}, \tag{2–9}$$

where p is the pressure, Pa; ρ is the density, kg/m^3; $\gamma = c_p / c_v$ is the ratio of specific heats at constant pressure c_p and constant volume c_v respectively (both in J/mol/K). Using the ideal gas law equation in the form

$$p = \rho \frac{R \cdot T}{M}, \tag{2–10}$$

where M is the molecular mass, kg/mol, and R is the universal gas constant, the speed of sound equation can be rewritten as

$$C = \sqrt{\gamma \frac{R \cdot T}{M}}. \tag{2–11}$$

Please click the advert



Speed of sound in gaseous hydrogen is 1294 m/s at NTP and 355 m/s at NBP (normal boiling point – boiling temperature of hydrogen 20.3 K at pressure 101,325 Pa). Speed of sound in liquid hydrogen is 1093 m/s (boiling point). Speed of sound in stoichiometric hydrogen-air mixture is 404 m/s (BRHS, 2009).

2.2. Combustion properties

At normal temperature hydrogen is a not very reactive substance, unless it has been activated somehow, e.g. by an appropriate catalyser. Hydrogen reacts with oxygen to form water at ambient temperature extraordinarily slow. However, if the reaction is accelerated by a catalyser or a spark, it proceeds with high rate and "explosive" violence. Molecular hydrogen dissociates into free atoms at high temperatures. Atomic hydrogen is a powerful reductive agent, even at ambient temperature e.g. when it diffuses from a high temperature zone of a flame front into its pre-heating low temperature zone. The heat released when the hydrogen atoms recombine to the hydrogen molecule is used for example to obtain high temperatures in the atomic hydrogen welding.

Hydrogen burns in a clean atmosphere with an invisible flame. It has a somewhat higher adiabatic premixed flame temperature for a stoichiometric mixture in air of 2403 K compared to other fuels (BRHS, 2009). This temperature can be a reason for serious injure at an accident scene, especially at clean laboratory environment where the hydrogen flame is practically invisible. However, hydrogen combustion and hot currents will cause changes in the surroundings that can be used to detect the flame. Although the non-luminous hydrogen flame makes visual detection difficult, there is a strong effect of heat and turbulence on the surrounding atmosphere and raising plume of hot combustion products. These changes are called the signature of the fire.

2.2.1. Stoichiometric mixture, equivalence ratio, and mixture fraction

Stoichiometric mixture is a mixture in which both fuel and oxidiser are fully consumed (complete combustion) to form combustion product(s). For example, the two diatomic gases, hydrogen (H_2) and oxygen (O_2), can combine to form water as the only product of an exothermic reaction between them, as described by the equation

$$2H_2 + O_2 = 2H_2O. \quad (2\text{–}12)$$

Thus, the stoichiometric hydrogen-oxygen mixture is composed of 66.66% by volume of hydrogen and 33.33% of oxygen. Let us calculate a stoichiometric concentration of hydrogen in mixture with air composed of 21% by volume of oxygen and 79% of nitrogen (actually ambient air is a mixture of nitrogen, at about 78%, oxygen, at about 21%, with the remaining 1% composed of carbon dioxide, methane, hydrogen, argon, and helium; there can be some water vapour present depending on the humidity)

$$2H_2 + (O_2 + 3.76N_2) = 2H_2O + 3.76N_2. \quad (2\text{–}13)$$

Thus, the stoichiometric concentration of hydrogen in air (assuming 21% of oxygen and 79% of nitrogen) is 29.59% by volume (2/(2+1+3.76)=0.2959) with air content of 70.41%.

The equivalence ratio is the ratio of the actual fuel-to-oxidizer ratio to the fuel-to-oxidiser ratio in the stoichiometric mixture

$$\exists = \frac{m_f / m_{ox}}{(m_f / m_{ox})_{st}} = \frac{n_f / n_{ox}}{(n_f / n_{ox})_{st}}, \quad (2\text{–}14)$$

where m is mass and n is number of moles, subscripts "f","ox", "st" denotes fuel, oxidiser, and stoichiometric mixture respectively. The equivalence ratio is 1.0 at stoichiometry, the ratios are less than 1.0 for lean by fuel mixtures, and are greater than 1.0 for rich mixtures.

There is essential advantage of using the equivalence ratio over a fuel–oxidiser ratio. The equivalence ratio does not have the dependence on the units being used, i.e. it is the same value either mass or number of moles are used. Contrary, the fuel–oxidiser ratio based on mass of fuel and oxidiser is not same as the fuel-oxidiser ratio based on number of moles. Let us consider for example a mixture of one mole of hydrogen (H_2) and one mole of oxygen (O_2). Indeed, two different fuel-oxidizer ratio (FOR), one based on mass and another on number of moles, are different

$$FOR_m = \frac{2}{32} = 0.0625 \quad \text{and} \quad FOR_n = \frac{1}{1} = 1. \quad (2\text{–}15)$$

At the same time the equivalence ratio calculated by mass is

$$\exists = \frac{m_f / m_{ox}}{(m_f / m_{ox})_{st}} = \frac{2/32}{(4/32)_{st}} = 0.5 \quad (2\text{–}16)$$

and by number of moles is

$$\exists = \frac{n_f / n_{ox}}{(n_f / n_{ox})_{st}} = \frac{1/1}{(2/1)_{st}} = 0.5 \quad (2\text{–}17)$$

i.e. exactly the same (0.5) for the mixture composed of 1 mole of hydrogen and 1 mole of oxygen.

The ratio of actual air-fuel ratio (AFR) to stoichiometric mixture ratio is denoted by lambda (λ). The relationship between λ and AFR is

$$Z = \frac{AFR}{(AFR)_{st}}$$

(2–18)

The equivalence ratio and lambda are relates as

$$\phi = \frac{1}{\lambda}. \tag{2–19}$$

Dealing with *FOR* or *AFR* is not always convenient especially for computer simulations as they have a value of infinity at either the pure air (oxidiser) or pure fuel side (computers get extremely upset when they try to tackle calculations with infinity), or they do not map the complete mixture spectrum (Wikipedia). Thus, for simulations in many cases a property is needed which is bounded. The mixture fraction, ξ, is usually taken as unity in the fuel stream and is nil in the oxidizer stream. It varies linearly between this two bounds such that at any point of a frozen flow the fuel mass fraction is $Y_F = \xi Y_{F0}$ and the oxidizer mass fraction is $Y_O = (1- \xi) Y_{O0}$, where Y_{F0} and Y_{O0} are the fuel and oxidizer mass fractions in the fuel and oxidizer streams, respectively.

All of the atoms present at the unburned mixture are present in the combustion products although they may be reorganized into different molecules. The mixture fraction that is independent of element *i* can be defined as

$$\xi = \frac{Z_i - Z_{i,O0}}{Z_{i,F0} - Z_{i,O0}}, \tag{2–20}$$

with an element mass fraction Z_i, i.e. the ratio of the mass of element *i* to the total mass, equal to

$$Z_i = \sum_{j=1}^{S} \mu_j w_j \text{ , } i=1...E \text{ , } \tag{2–21}$$

Please click the advert


Nido
Luxurious accommodation
Central zone 1 & 2 locations
Meet hundreds of international students
BOOK NOW and get a £100 voucher from voucherexpress
Nido Student Living - London
Visit www.NidoStudentLiving.com/Bookboon for more info.
+44 (0)20 3102 1060

where μ_{ij} is the mass fraction of the element i in the species j, w_j is the species mass fraction in the mixture, S is the number of different species, and E is the number of different elements in the mixture. It can be shown that the stoichiometric mixture fraction, that is where diffusion flame front is located, is equal to

$$\xi_{st} = \frac{1}{1+\phi} = \frac{\lambda}{1+\lambda} . \quad (2\text{–}22)$$

2.2.2. Heat of combustion

The lower heating value (heat of combustion) of hydrogen is 241.7 kJ/mol and the higher heating value is 286.1 kJ/mol (BRHS, 2009). The difference of about 16% is due to the heat of condensation of water vapour, and this value is larger compared to other gases.

2.2.3. Flammability limits

The flammability range of hydrogen is wider compared to most hydrocarbons, i.e. 4% to 75% by volume in air at NTP. The flammability range of hydrogen expands with temperature, e.g. the lower flammability limit drops from 4% at NTP to 3% at 100°C (for an upward propagating flame), and depends on pressure (see below). In addition to this, the flammability limits of hydrogen depend on a direction of flame propagation. Ranges of the flammability limits for different direction of flame propagation referenced in (Coward and Jones, 1952) are presented in Table 2–1. For example, in an initially quiescent mixture a conservative value of LFL changes from 3.9% by volume for upward propagation, through 6% for horizontally propagating flames, to 8.5% for downward propagating flames.

Upward propagation		Horizontal propagation		Downward propagation	
LFL	UFL	LFL	UFL	LFL	UFL
3.9–5.1%	67.9–75%	6.0–7.15%	65.7–71.4%	8.5–9.45%	68–74.5%

Table 2–1. Flammability limits of hydrogen-air for upward, horizontal, and downward (spherical) propagation in hydrogen concentration by volume (Coward and Jones, 1952).

The flammability limits depend on the apparatus applied to determine them. For example, the highest value of LFL (5.1% by volume) and the lowest value of UFL (67.9%) for upward propagating flame were observed in the narrowest throughout the entire spectrum of tube used of only 8 mm.

Coward and Jones (1952) describe an initial stage of flame propagation after ignition of 4% by volume hydrogen-air mixture as follows: a vortex ring of flame was seen just above the spark gap; it rose, expanded for about 40 cm, then broke and disappeared. Upward flame propagation at concentrations close to LFL of 4% is in a form of a collection of small balls of flame, which travel steadily to the top of the vessel. For hydrogen concentrations in the range 4.4–5.6%: similarly a vortex ring rose about 40 cm, then broke into segments each subdivided into balls of flame that travel to the top.
subdivided into balls of flame that travel to the top.

There is unburnt mixture in between of these small ball flames. An increasing fraction of the hydrogen present was burned as the amount of it was increased. The mixture with 5.6% of hydrogen showed about 50% combustion. This observation explains why burning of a quiescent hydrogen-air mixture near LFL of 4% by volume in a closed vessel can generate negligible in a practical sense overpressure. It is worth noting that a quiescent hydrogen-air mixture in the range of concentration 4–6% could burn practically without overpressure for a number of scenarios, e.g. if ignited at the top of an enclosure, as in such conditions it cannot propagate flame in any direction and thus no heat is released accompanied by pressure build up can be observed.

Table 2–2 shows the scattering of the flammability limits (measured in % by volume) determined by different standard apparatuses and procedures applied (Schröder and Holtappels, 2005).

Limit	DIN 51649	EN 1839 (T)	EN 1839 (B)	ASTM E 681
LFL	3.8%	3.6%	4.2%	3.75%
UFL	75.8%	76.6%	77.0%	75.1%

Table 2–2. The flammability limits of hydrogen-air mixture at NTP determined by different standards (Schröder and Holtappels, 2005).

The flammability range expands with increase of temperature. The lower flammability limit for upward flame propagation (% by volume) as a function of temperature (K) at ambient pressure can be calculated by the modified Burgess-Wheeler equation (Zabetakis, 1967; Verfondern, 2008)

$$LFL(T) = LFL(300\,K) + \frac{3.14}{OH_C}(T - 300) = 4.0 + 0.013 \bullet (T - 300), \quad (2\text{–}23)$$

where ΔH_C is the lower heat of combustion, 241.7 kJ/mol. For hydrogen at the boiling point LFL is 7.7% by volume (Verfondern, 2008). The upper flammability limit dependence on mixture temperature in the range of temperature 150-300 K can be represented by the following equation (Eichert, 1992)

$$UFL(T) = 74.0 + 0.026 \bullet (T - 300). \quad (2\text{–}24)$$

Figure 2–3 shows dependence of LFL and UFL on mixture temperature for upward flame propagation (Schröder and Holtappels, 2005) and downward flame propagation (Coward and Jones, 1952). The flammability range expands practically linearly with temperature. While LFL decreases by about 2.5% by volume (from 4% to 1.5% by volume) with increase of temperature from 20°C to 400°C, UFL increases more significantly – by about 12.5% by volume for the same change of mixture temperature.

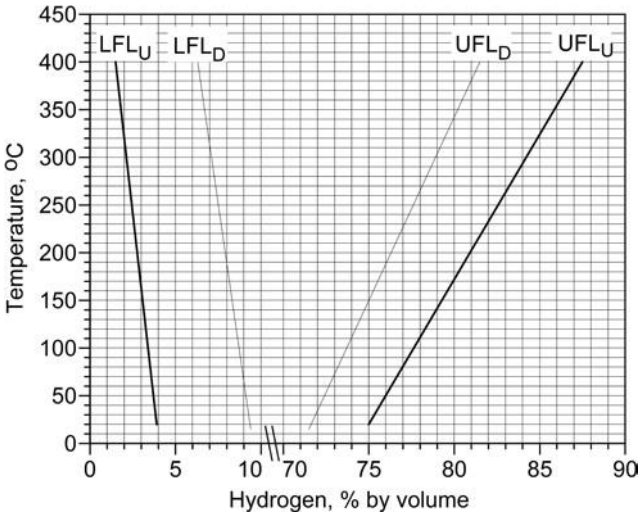


Figure 2–3. LFL and UFL of hydrogen-air mixture as a function of temperature: thick lines – upward flame propagation (Schröder and Holtappels, 2005); thin lines – downward flame propagation (Coward and Jones, 1952).

Dependences of LFL and UFL for upward flame propagation on pressure are shown in Fig. 2–4 (Schröder and Holtappels, 2005). LFL monotonically decreases in the range 0.1–5.0 MPa to 5.6% by volume and then is constant up to pressure of 15 MPa. UFL changes not monotonically: decreases from 76.6% to 71% with pressure growth from 0.1 to 2.0 MPa, then increases from 71% to 73.8% with pressure increase from 2.0 to 5.0 MPa, and again decreases insignificantly from 73.8% to 72.8% with pressure raise from 5.0 to 15.0 MPa.

Please click the advert

Destination MMU

Manchester Metropolitan University

MMU is proud to be one of the most popular universities in the UK. Some 34,000 students from all parts of the globe select from its curricula of over 1,000 courses and qualifications.

We are based in the dynamic yet conveniently compact city of Manchester, located at the heart of a sophisticated transport network including a major international airport on the outskirts. Parts of the campus are acclaimed for their architectural style and date back over 150 years, in direct contrast to our teaching style which is thoroughly modern, innovative and

forward-thinking.

MMU offers undergraduate and postgraduate courses in the following subject areas:

- Art, Design & Performance
- Computing, Engineering & Technology
- Business & Management
- Science, Environmental Studies & Geography

- Law, Education & Psychology
- Food, Hospitality, Tourism & Leisure Studies
- Humanities & Social Science

For more details or an application form please contact MMU International.
email: international@mmu.ac.uk
telephone: +44 (0)161 247 1022
www.mmu.ac.uk/international

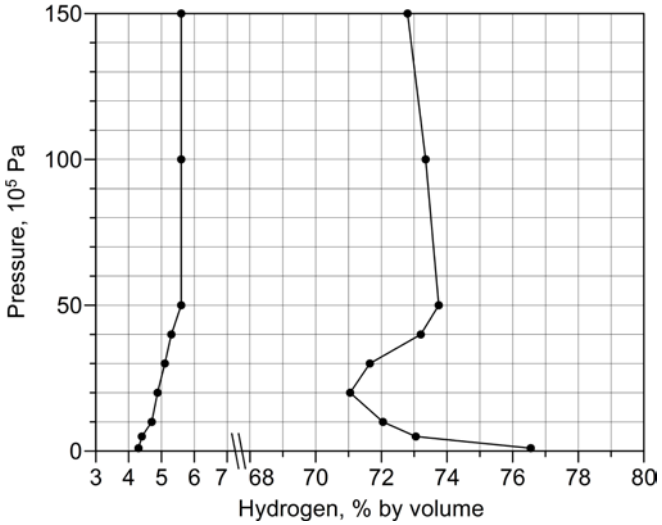


Figure 2–4. LFL and UFL of hydrogen-air mixture as a function of pressure (Schröder and Holtappels, 2005).

2.2.4. Limiting oxygen index

The limiting oxygen index is the minimum concentration of oxygen that will support flame propagation in a mixture of fuel, air, and nitrogen. No mixture of hydrogen, air, and nitrogen at NTP conditions will propagate flame if the mixture contains less than 5% by volume oxygen (NASA, 1997).

2.2.5. Ignition properties

Experience shows that escaped hydrogen is very easily ignited (NASA, 1997). Ignition sources include mechanical sparks from rapidly closing valves, electrostatic discharges in ungrounded particulate filters, sparks from electrical equipment, catalyst particles, heating equipment, lightning strikes near the vent stack, etc. Ignition sources must be eliminated or isolated in appropriate way and operations should be conducted as if unforeseen ignition sources could occur.

The ignition energy of hydrogen-air mixture varies with its composition, and becomes infinite at the flammability limits. Less energy is needed to ignite a mixture that is closer to its stoichiometric composition. Over the flammable range of hydrogen-air mixtures, the ignition energy varies by almost three orders of magnitude. The minimum ignition energy (MIE) is 0.017 mJ for the most ignitable mixture (Baratov et al., 1990). The ignition energy depends in addition to the mixture composition on other factors such as the initial pressure and temperature. Since most ignition sources generate more than 10 mJ, practically all common fuels would be ignited in mixture with air if their concentration exceeds the lower flammability limit. Ignition sources capable of forming shocks, for example high-energy spark discharges and high explosives, can directly initiate detonation.

The energy stored as static electricity on an object varies depending on the size of the object and its capacitance, the voltage to which it is charged, and the dielectric constant of the surrounding medium (Wikipedia). For modelling the effect of static discharge, a human being is represented as a capacitor of 100 picofarads, charged to a voltage of 4,000 to 35,000 volts. The total energy is of the order of millijoules. Larger objects will store more energy. This energy is typically discharged in less than a microsecond and sufficient to ignite not only near stoichiometric mixtures yet mixtures close to the flammability limits. Insulation materials such as wood, paper, and some fabrics will typically form a conductive layer that can prevent static build-up by absorbing water from the air in environments where the relative humidity is greater than 50% (ISO/TR 15916:2004).

Hydrogen is essentially an electrical insulator in both gaseous and liquid phases. The flow or agitation of hydrogen gas or liquid may generate charges of static electricity similar to all non-conductive liquids or gases (for this reason, all hydrogen conveying equipmentmustbe thoroughly grounded). Only above some critical "breakdown" voltage, where ionization occurs, does it become an electrical conductor (BRHS, 2009). When high velocity hydrogen flow accompanies high-pressure vessel blowdown this property can potentially be responsible for the generation of static electrical charge of present in piping particulates by triboelectricity, which is a type of contact electrification in which certain materials become electrically charged after they come into contact with another different material and are then separated (Wikipedia). The probability of hydrogen ignition by this mechanism increases with increase of the blowdown time (time to empty a storage tank) with the same other conditions.

The standard auto-ignition temperature of hydrogen in air is above 510°C (Baratov et al., 1990). It is relatively high compared to hydrocarbons having long molecules. However, it can be lowered by catalytic surfaces. Objects at temperatures from 500 to 580°C can ignite hydrogen-air or hydrogen-oxygen mixtures at atmospheric pressure. Substantially cooler objects of about 320°C can cause ignition under prolonged contact at less than atmospheric pressure (NASA, 1997). Hot air jet ignition temperature is 670°C (BRHS, 2009).

2.2.6. Laminar burning velocity and flame propagation speed

The laminar burning velocity S_u (stretched value, i.e. accounting for both spherical flame curvature and strain) of a stoichiometric hydrogen-air mixture can be calculated as an experimental propagation velocity S_v of spherical flame, e.g. observed by schlieren photography – a method to register the flow of fluids of varying density (see for instance Wikipedia), divided by the expansion coefficient of combustion products E_i

$$S_u = S_v / E_i, \tag{2–25}$$

where E_i is the expansion coefficient (ratio) equal to the ratio of the unburned mixture density to the density of combustion products at the same pressure.

The dependence of expansion coefficient E_i on hydrogen concentration in air is shown in Fig. 2–5 for the entire flammability range. The expansion coefficient E_i was calculated in the HySAFER Centre by using the software Cantera (GRI mechanism) for a composition of air 79% by volume of N_2 and 21% of O_2, and the combustion products comprising the following species: H_2, H, O, O_2, OH, H_2O, HO_2, H_2O_2, N, NH, NH_2, NH_3, NNH, NO, NO_2, N_2O, HNO and N_2.

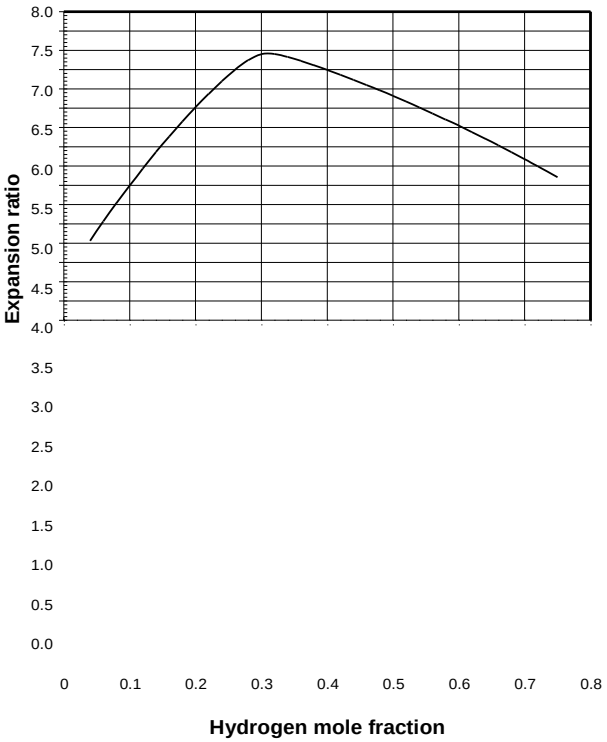
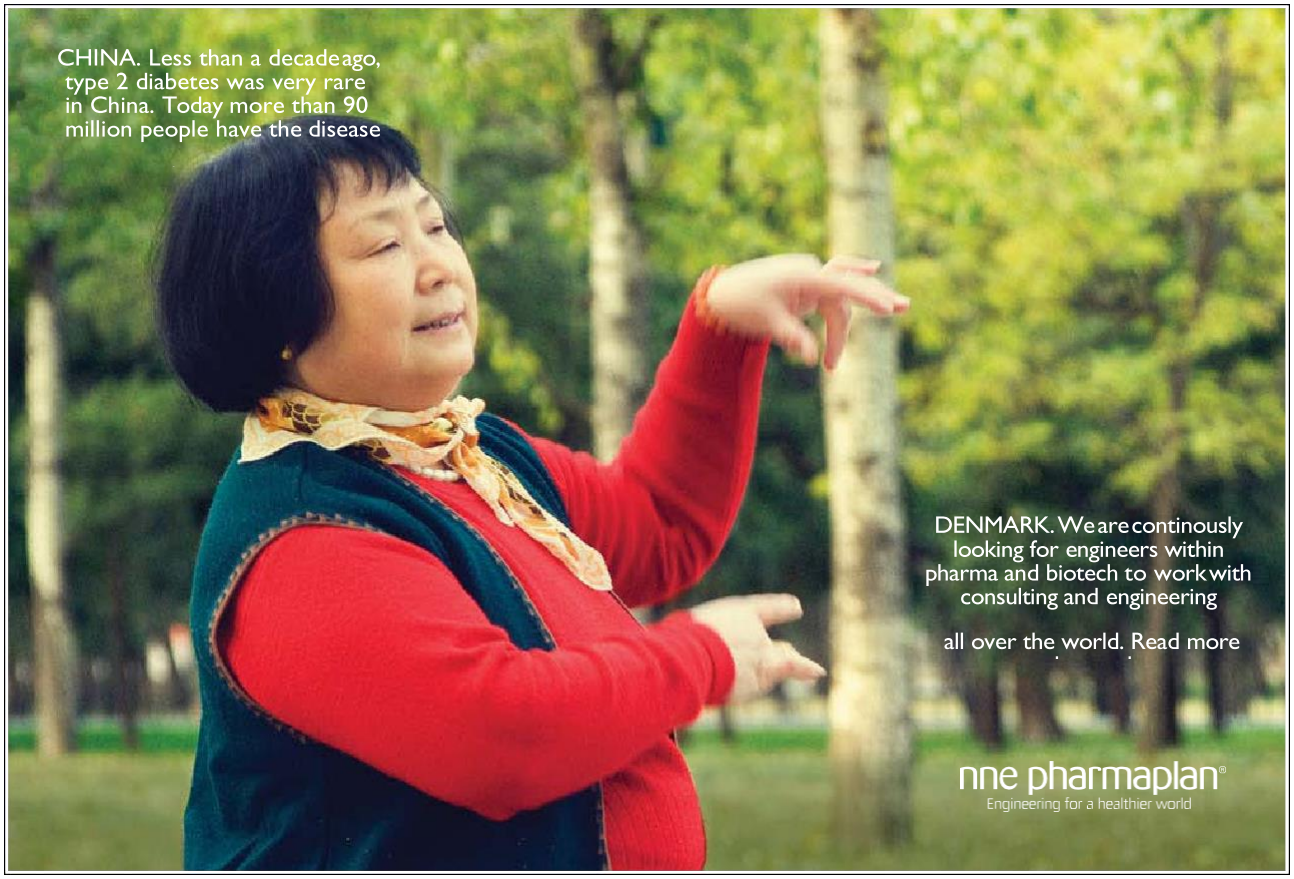


Figure 2–5. Expansion coefficient of combustion products E_i as a function of hydrogen mole fraction in air.

Please click the advert


CHINA. Less than a decadeago,
type 2 diabetes was very rare
in China. Today more than 90
million people have the disease
DENMARK. We are continously
looking for engineers within
pharma and biotech to work with
consulting and engineering
all over the world. Read more
nne pharmaplan®
Engineering for a healthier world

Values of stretched, i.e. actual strained and curved spherical flame, laminar burning velocities are accepted in the HySAFER Centre numerical studies following the experimental study by Lamoureux et al. (2003). It is worth noting that the maximum burning velocity for a hydrogen-air mixture is reached not at a near stoichiometric mixture of 29.5% (by volume) hydrogen but in a mixture with hydrogen concentration in air 40.1% (BRHS, 2009). It increases from about 2 m/s for 29.5% hydrogen-air mixture to about 2.45 m/s for 40.1% hydrogen-air mixture. This effect of shifting of the maximum laminar burning velocity is due to the high molecular diffusivity of hydrogen in air. Thus, the maximum burning velocity for a hydrogen-air premixed flame occurs at an equivalence ratio of 1.6 while for hydrocarbon-air flames it occurs at around 1.1.

The laminar burning velocity as a function of hydrogen concentration in air is presented in Fig. 2–6 for studies by Zimont and Lipatnikov (1995), based on experiments by Karpov and Severin, Tse et al. (2000), Lamoureux et al. (2003). Data by Lamoureux et al. (2003) for stretched flames were used to get values of the laminar burning velocity presented on the graph (application of stretched values in HySAFER simulations explains why these data a below of that by other researchers). Zero burning rates at flammability limits shown in Fig. 2–6 is an approximation. The near-limit "burning velocity" (quotes are used to indicate that flame propagation at the limit is not in the form of continuous flame rather as separate flame balls) for 5% by volume hydrogen-air flame measured in zero-gravity conditions can be estimated as 2.5–3.5 cm/s (Ronney, 1990).

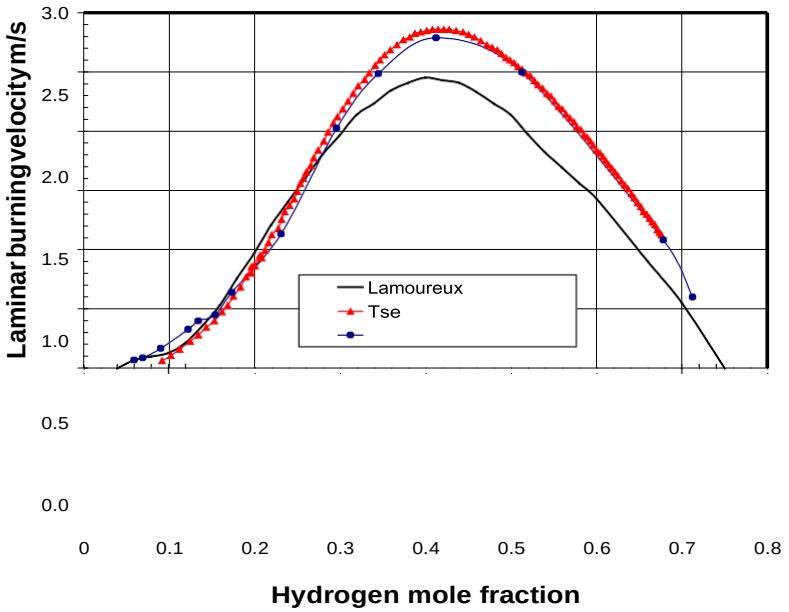


Figure 2–6. Laminar burning velocity of hydrogen-air mixture as a function of hydrogen mole fraction in air.

The maximum possible flame propagation speed, i.e. deflagration front velocity relative to a fixed observer, is given by the speed of sound in the combustion products, which is 975 m/s for a stoichiometric

hydrogen-air mixture (BRHS, 2009).

2.2.7. Quenching

Hydrogen flames are difficult to quench. For example, premixed hydrogen-air combustion can be aggravated by heavy sprays of water due to induced turbulence and ability of mixture to burn around the droplets. Hydrogen has the lowest quenching distance compared to other flammable gases. Quenching of any flame occurs when heat losses from flame are comparable with heat generation due to combustion, and then the chemical reactions cannot be sustained. Published data are quire scattered and terminology used can complicate the problem further.

Usually quenching distance is reported as the minimum pipe diameter through which a premixed flame can pass. For example, Kanury (1975) measured the quenching distance as 0.51 mm. Technical report of ISO (ISO/TR 15916:2004) states that the quenching gap in air (NTP) for hydrogen is 0.64 mm.

Hydrogen has the narrowest maximum experimental safe gap (MESG) of 0.08 mm (BRHS, 2009) to prevent premixed flame propagation out of a shell, composed of two hemispherical parts, through the gap between flanges of these hemispheres. It is worth noting that pressure within the shell during the test approaches the maximum explosion (deflagration) pressure in closed vessel. Because of difference in the experimental set up (high deflagration pressures between hemispheres in MESG testing), the MESG is always smaller than the quenching gap. The lowest reported quenching distance for hydrogen is 0.076 mm (Wionsky, 1972).

The quenching distance decreases with increase of pressure and temperature, depends of mixture composition, etc. This is probably the main reason of the published data scattering. Hydrogen-air mixture with higher burning rate generally has smaller quenching gap, and flame arresters for faster burning gases require smaller apertures. To author's knowledge there are flame arresters only for hydrogen-air not for hydrogen-oxygen mixtures at the moment.

There is another limit for "quenching" of hydrogen flames. This is the blow-off limit which occurs when the flow rate is reached beyond which the flame blows off the nozzle.

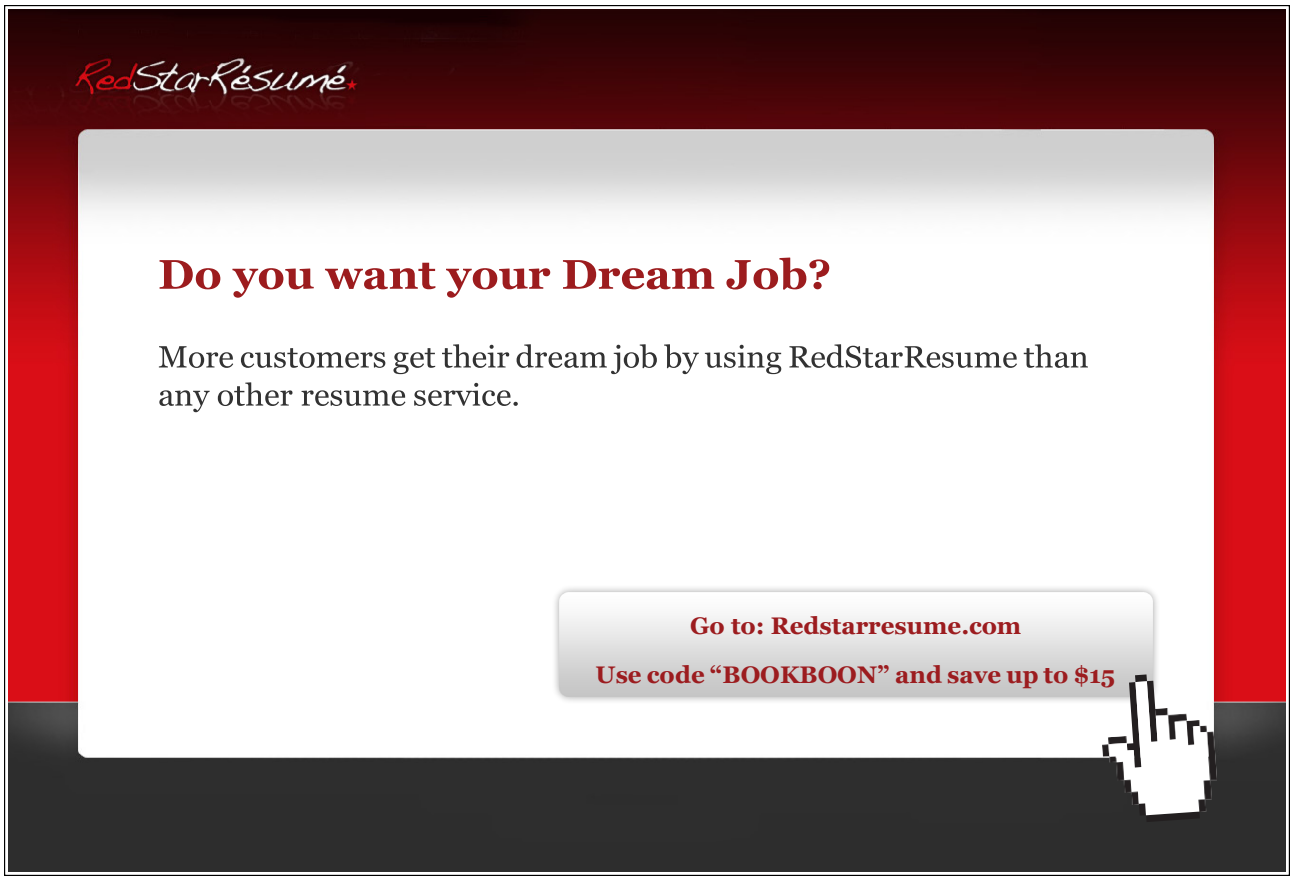
2.2.8. Detonability limits

Detonation is the worst case scenario for hydrogen accident (Zbikowski et al., 2008). The detonation wave is a complex of precursor shock and combustion wave propagates with a speed of von Neumann spike. Detonation front thickness is a distance from the precursor shock to the end of reaction zone where the Chapman-Jouguet condition (sonic plane) condition is reached.

The detonability range mentioned in technical report ISO/TR 15916:2004 is 18–59% by volume of hydrogen in air. The detonation range of 13–70% is reported for hydrogen-air in a 43 cm diameter tube (Tieszen et al., 1986). A lower detonability limit of 12.5% by volume was observed in the Russian detonation test facility RUT, the largest of its kind. The widest detonability range of hydrogen in air 11–59% by volume is recommended by Alcock et al. (2001).

A conservative generalisation of available data gives the detonability range of hydrogen in air 11–70% by volume. This is narrower and as expected within the flammability range of 4–75%. The detonability limits are not fundamental characteristics of the mixture as they strongly depend on the size of the experimental set up where they are measured. Indeed, a diameter of the tube, where detonation can propagate, should be of the order of a detonation cell size. A detonation cell size increases with approaching the detonability limits. Thus, the larger is the scale of an experimental apparatus the smaller is the lower detonability limit (the larger is the upper detonability limit). The detonability limits of hydrogen-air mixture of the same concentration expand with the scale of a flammable cloud. This explains the difference between the lower detonability limit of hydrogen 11% by volume reported by Alcock et al. (2001) and the underestimated value of 18% suggested by the international standard (ISO/TR 15916:2004). Experimental values of detonation cell size for a stoichiometric hydrogen-air mixture are 1.1–2.1 cm (Gavrikov et al., 2000).

Please click the advert



2.2.9. Run-up distance for deflagration-to-detonation transition (DDT)

The experimentally observed run-up distance for transition from deflagration to detonation (DDT) in stoichiometric hydrogen-air mixture in a tube has typical length to diameter ratio of approximately 100. The DDT phenomenon is still one of the challenging subjects for combustion research. Different mechanism are responsible for a flame front acceleration to a velocity close to the speed of sound in an unburned mixture, including but not limited to increase of laminar burning velocity with pressure in conditions of adiabatic compression, increase of burning rate due to preferential diffusion phenomenon, turbulence in an unburned mixture, turbulence generated by flame front itself, fractal type of flame front area growth with flame radius and decrease of inner cut-off, and various instabilities such as hydrodynamic, Rayleigh-Taylor, Richtmyer-Meshkov, Kelvin-Helmholtz, etc. Then, there is a jump from the maximum deflagrative flame propagation velocity, which is about the speed of sound in combustion products for near stoichiometric hydrogen-air mixture, to the detonation velocity that is about twice of the maximum deflagration velocity.

The presence of obstacles in a tube can essentially reduce run-up distance for DDT. This is thought to be due to significant contribution of the Richtmyer-Meshkov instability just before the DDT. Indeed, the Richtmyer-Meshkov instability increases a flame front area in both directions of a shock passage through the flame front. This is opposite to the Rayleigh-Taylor instability, where only one direction is unstable to the pressure gradient (acceleration of flow in the direction from lighter combustion products to heavier unburned mixture). The DDT is thought to happen in a so-called hot spot(s), which potentially could be located within the turbulent flame brush or ahead of it, e.g. in a focus of a strong shock reflection. The peculiarities of DDT mechanisms do not affect the steady-state detonation wave following DDT.

Safety measures to exclude the potential DDT are very important. Indeed, while the deflagration of quiescent stoichiometric hydrogen-air cloud in the open atmosphere generates pressure wave of only 0.01 MPa (below a level of eardrum injury), the detonation of the same mixture would be accompanied by a blast of more than two orders of magnitude higher pressure of about 1.5 MPa (far above the fatal pressure of about 0.08–0.10 MPa).

2.3. Comparison with other fuels

Hydrogen is an unusual fuel. Indeed, hydrogen leaks support combustion at flow rates much lower than leaks of other fuels (Butler et al., 2009), and hydrogen flames cause much faster corrosion than methane flames when the flames impinge on samples of aluminium, stainless steel, and silicon carbide fibres (Sunderland, 2010). Hydrogen flames are the dimmest of any fuel, and its mass flow rate blow-off limits are higher than similar limits for methane and propane. Volumetric flow rate of hydrogen through the same leak path at the same supply pressure were found to be significantly higher than for methane and propane (Swain and Swain, 1992). Hydrogen has smallest molecular mass, lowest density, and lowest viscosity. The thermal conductivity of hydrogen is significantly higher than that of other gases. The diffusion coefficient in air is highest among all gases.

2.3.1. Physical parameters

Parameters of hydrogen in comparison with other fuels, as well as with water and air are summarised in Tables 2–3 and 2–4.

Substance	MM, g/mol	Density, kg/m3	Viscosity, μPoise	Diffusivity in air*, cm^2/s	Thermal conductivity, mW/(m.K)
Hydrogen (H2)	2.016	70.78 (L, NBP) 1.312 (G, NBP) 0.0838 (G, NTP)	132.0 (L, NBP) 89.48 (G, NTP) 11.28 (G, NBP)	0.68	168.35 (G)
Methane (CH4)	16.043	422.62 (L, NBP) 1.819 (G, NBP) 0.668 (G, NTP)	200 (G, NTP) 102.7 (G, STP)	0.196	32.81 (STP)
Propane (C3H8)	44.096	582 (L, NBP) 2.423 (G, NBP) 1.882 (G, NTP)	1,100 (300 K)	0.0977	15.198 (STP)
Gasoline (C4-C12)	100–105	677–798*	~6,000** (L, NTP)	-	~130**
Diesel (C8-C25)	~200	788–920*	~25,000** (L, NTP)	-	-
Methanol (CH3OH)	32.04	786.9 (L, 25°C)*	5,900 (L, NTP)	0.162	250
Water (H2O)	18.016	1000 (NTP)	10,000 (L, NTP) 130 (G, NTP)	-	670
Air	28.9**	1.205 (NTP)	180 (G, NTP)		26

Note: MM – molecular mass; TC – thermal conductivity; L – liquid; G – gas or vapour; * – Baratov et al. (1990); ** – approximated.

Table 2–3. Properties of hydrogen compared to other substances (Part 1).

The dynamic viscosity of hydrogen, methane, and propane measured in [g/m/s] is $8.76x10^{-3}$, $1.09x10^{-2}$, and $7.95x10^{-3}$ respectively (Weast and Astle, 1979; Butler et al., 2009).

Substance	NBP, °C	Critical point	Critical density, kg/m^3	HV (SBP), kJ/kg	γ	SW, v/v
Hydrogen (H2)	-252.8	-240°C 1.3 MPa	31.263	451.9	1.384 (25°C)	0.0214 (Poor)
Methane (CH4)	-161.58	-82.7°C 4.596 MPa	162	760	1.305 (25°C)	0.054 (2°C)
Propane (C3H8)	-42.06	96.6°C 4.25 MPa	217	356	1.134 (25°C)	0.039 (NTP)
Gasoline (C4-C12*)	37-204	-	-	~349 (15.6°C)	-	Poor
Diesel (C12H23*)	180-340	-	-	~233 (15.6°C)	-	Poor
Methanol (CH3OH)	64.9	239.45°C 8.09 MPa	272	1004	1.2	Infinitely
Water (H2O)	100	373.946°C 22.064 MPa	322	2257 (NBP)	1.33 (steam)	-
Air	- (183–196)	-140.8°C 3.77 MPa	-	-	1.4	-

Note: NBP – boiling temperature (point) at normal pressure of 101,325 Pa; HV – latent heat of vaporisation; SBP – standard boiling point (at 0.1 MPa); SW – solubility in water; γ – specific heats ratio.

Table 2–4. Properties of hydrogen compared to other substances (Part 2).

Only helium has lower than hydrogen NBP. Hydrogen is slightly more soluble in organic solvents than in water.

2.3.2. Heating values

The higher and lower heating values of different fuels per gram of fuel are indicated in Table 2–5 (College of the Desert, 2001). Although the term heating value does not apply to batteries, the energy density of a lead acid battery is significantly lower – approximately 0.108 kJ/g. The water that results from both combustionof hydrogen in air and the electrochemical reactionwithin a fuel cell occurs as steam, therefore the lower heating value represents the amount of energy available to do external work. Hydrogen has the highest heating value per unit of mass and lowest per unit volume. To provide competitive driving range hydrogen has to be stored as gas under pressure or liquid. This has obvious safety implications.

Fuel	Higher Heating Value (25 °C, 0.101 MPa)	Lower Heating Value (25 °C, 0.101 MPa)	Lower Heating Value (volumetric) (15 °C)
Hydrogen	141.86 kJ/g	119.93 kJ/g	10,050 kJ/m3 (gas, 0.101 MPa) 1,825,000 kJ/m3 (gas, 20.2 MPa) 4,500,000 kJ/m3 (gas, 69.7 MPa) 8,491,000 kJ/m3 (liquid)
Methane	55.53 kJ/g	50.02 kJ/g	32,560 kJ/m3 (gas, 0.101 MPa) 6,860,300 kJ/m3 (gas, 20.2 MPa) 20,920,400 kJ/m3 (liquid)
Propane	50.36 kJ/g	45.6 kJ/g	86,670 kJ/m3 (gas, 0.101 MPa) 23,488,800 kJ/m3 (liquid)
Gasoline	47.5 kJ/g	44.5 kJ/g	31,150,000 kJ/m3 (liquid)
Diesel	44.8 kJ/g	42.5 kJ/g	31,435,800 kJ/m3 minimum (liquid)
Methanol	19.96 kJ/g	18.05 kJ/g	15,800,100 kJ/m3 (liquid)

Table 2–5. Heating values of different fuels (College of the Desert, 2001).

2.3.3. Fire and explosion indices

Comparison of key fire and explosion indices for hydrogen and other fuels is presented in Table 2–6 based on the selection of conservative values from Baratov et al. (1990), College of the Desert (2001).

Fuel	Flashpoint, °C	AIT, °C	Flammability range, % vol.	P_{max}*, kPa	MIE*, mJ	MESG, mm
Hydrogen	< -253	510*	4-75	730	0.017	0.08
Methane	-188	537*	5.28*-15	706	0.28	-
Propane	-96*	470*	2.2-9.6	843	0.25	0.92*
Gasoline	-(11-45)*	230-480	0.79-8.1*	-	0.23-0.46	0.96-1.02
Diesel	37-110*	210-370*	0.6-6.5	-	-	-
Methanol	6*	385	6-36.5	620	0.14	-

Note: AIT – auto-ignition temperature; * - Baratov et al. (1990); P_{max} – maximum pressure of deflagration in closed vessel; MIE – mimimum ignition energy; MESG – maximum experimental safe gap.

Table 2–6. Fire and explosion indices of different fuels.

Thelowerflammabilitylimitofhydrogenishighcomparedtomosthydrocarbons. Thenear-stoichiometric concentration of hydrogen is air (29.5% by volume) is very much higher than that of hydrocarbons (only a few percent). At the lower flammability limit the ignition energy requirement of hydrogen is similar to that of methane, and weak ignition sources such as electrical equipment sparks, electrostatic sparks or sparks from striking objects typically involve more energy than is required to ignite these flammable

mixtures (Dryer et al., 2007).

This laminar burning velocity of stoichiometric hydrogen-air mixture of about 2 m/s is far greater compared to most of hydrocarbons when velocities are in the range 0.30–0.45 m/s. Hydrogen is more prone to deflagration-to-detonation transition (DDT) compared to most other flammable gases.

Compared to other fuels hydrogen is the most prone to spontaneous ignition during sudden releases to air by the so-called diffusion mechanism, when high temperature air, heated by a shock, mixes with cold hydrogen at the contact surface between these two gases and chemical reactions can be initiated, when critical conditions are reached. Indeed, sudden hydrogen releases into piping filled with air, after a safety burst disk ruptures, can be spontaneously ignited at pressures as low as about 2 MPa (Dryer et al., 2007).

On the other hand, the standard auto-ignition temperature of hydrogen in air is above 520°C which is higher than for hydrocarbons. Another swing - the hot air jet ignition temperature is lowest for hydrogen compared to all hydrocarbons decreasing further with increasing jet diameter.

The performance of octane (hydrocarbon) is used as a standard to measure resistance to knock in internal combustion engines, and is assigned a relative octane rating of 100. Fuels with an octane number over 100 have more resistance to auto-ignition than octane itself. Hydrogen has a very high research octane number and is therefore resistant to knock (combustion under lean conditions), i.e. 130+ (lean combustion) compared to other fuels: methane (125), propane (105), gasoline (87), diesel (30). The octane number has no relevance for use of hydrogen with fuel cells.

The quenching distance (the minimum pipe diameter through which a premixed flame can propagate) for hydrogen, methane, and propane are 0.51 mm, 2.3 mm, and 1.78 mm respectively (Kanury, 1975). Thus, hydrogen has the lowest quenching distance.

2.3.4. Extinction of diffusion flames

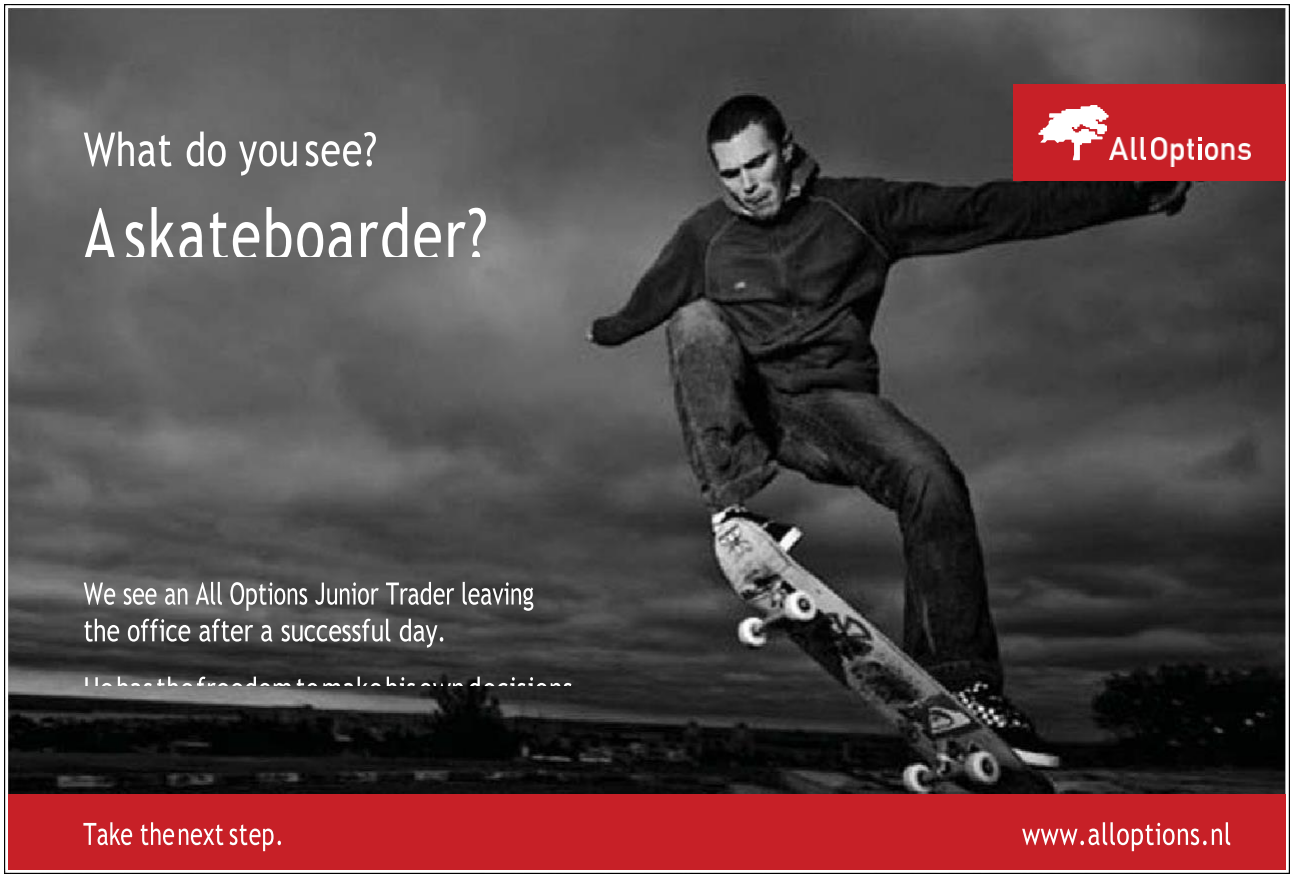
Hydrogen fires normally are not extinguished until the supply of hydrogen has been shut off because of the danger of re-ignition and “explosion”.

Creitz (1961) published results on extinction of diffusion flames on a burner placed in a Pyrex jacket for six fuels. The difference in extinguishing effectiveness of an inhibitor introduced on the two sides of the reaction zone of diffusion flames has been measured as a function of oxygen concentration in the O_2-N_2 mixture supplied to the flames. Comparison of extinguishment characteristics of nitrogen (N_2), methyl bromide (CH_3Br), trifluoromethyl bromide (CF_3Br) for various fuels burning in air is shown in Table 2–7 in percentage by volume.

Fuel	Percentage of inhibitor in air or fuel at extinction						Efficiency relative to nitrogen			
	When added to air			When added to fuel			Added to air		Added to fuel	
	N_2	CH_3Br	CF_3Br	N_2	CH_3Br	CF_3Br	CH_3Br	CF_3Br	CH_3Br	CF_3Br
H2	94.1	11.7	17.7	52.4	58.1	52.6	8.0	5.3	0.9	1.0
CH4	83.1	2.5	1.5	51.0	28.1	22.9	33.2	55.4	1.8	2.2
C2H6	85.6	4.0	3.0	57.3	36.6	35.1	21.4	28.5	1.6	1.6
C3H8	83.7	3.1	2.7	58.3	34.0	37.6	27.0	31.0	1.7	1.6
C4H10	83.7	2.8	2.4	56.8	40.0	37.9	29.9	34.9	1.4	1.5
CO	90.0	7.2	0.8	42.8	19.9	-	12.5	112	2.2	-

Table 2–7. Comparison of extinguishment characteristics of nitrogen, N_2, methyl bromide, CH_3Br, and trifluoromethyl bromide, CF_3Br (Creitz, 1961).

Please click the advert


What do you see?
A skateboarder?
All Options
We see an All Options Junior Trader leaving
the office after a successful day.
Take the next step.
www.alloptions.nl

It was found that when the inhibitor was added to the fuel, the volume percentage required for extinguishment was much greater than when added to the oxygen side of the reaction zone, with the single exception of CO flames inhibited by trifluoromethyl bromide. Author assumes that this result of Craitz (1961) can be explained by the entrainment law stating that a mass flow rate of entrained into plume surrounding gas grows with distance from the source of fuel and with momentum flux of the plume. It is well known from fire safety science that the amount of air entrained into fire at flame height is about two orders of magnitude greater than amount of released fuel.

Above oxygen concentrations on the order of 25% by volume, methyl bromide was completely ineffective when added to the oxygen side of the reaction zone, and above about 32% oxygen it was ineffective when added to the fuel, since at this oxygen concentration it burns without additional fuel.

Extinction of a diffusion flame may be affected by a number of factors, among them being the rate at which the fuel is supplied to the burner and the velocity of the secondary air past the flame (Craitz, 1961). The latter effect was found to be important at rather low or very high flow rates. When the rate of fuel supply was too low, for a given burner size, the flame would not burn, and conversely, when the rate was too high, lifting occurred and the flame tended to float off and be extinguished . In author's opinion the latter observation of Craitz (1961) could be due to shielding effect of Pyrex jacket that limits oxidiser entrainment to the flame. This particular test condition limits the importance of conclusions of such experiments.

In test by Craitz (1961) conditions the extinction of hydrogen is the most difficult among fuels tested and requires more inhibitor. Methyl bromide is more efficient to extinguish hydrogen diffusion flame in air compared to trifluoromethyl bromide. Work of Craitz (1961) can be considered as a comparative study of extinction efficiency of selected inhibitors for different fuels rather than quantitative recommendation on inhibitor concentrations for extinction of real flames, especially non-premixed turbulent flames which are characteristic for hydrogen technologies.

2.4. Health hazards

Hydrogen is not expected to cause mutagenicity, teratogenicity, embryotoxicity or reproductive toxicity. There is no evidence of adverse effects if skin or eyes are exposed to hydrogen, it cannot be ingested (unlikely route). However, inhaled hydrogen can result in a flammable mixture within the body.

Hydrogen is classified as a simple asphyxiant, has no threshold limit value (TLV), and it is not a carcinogen (NASA, 1997). High concentrations of hydrogen in air can cause an oxygen-deficient environment. Individuals breathing such an atmosphere may experience symptoms which include headaches, dizziness, drowsiness, unconsciousness, nausea, vomiting, depression of all the senses, etc. A victim may have a blue colour skin, and under some circumstances, death may occur. If hydrogen is inhaled and above symptoms observed then remove a person to fresh air, give oxygen if breathing is difficult, or apply artificial respiration if not breathing.

The system design shall prevent any possibility of asphyxiation of personnel in adjacent areas (NASA, 1997). The system design shall provide for prevention of personnel entering the enclosure unless confined space entry procedures are strictly followed. It is recommended to check oxygen content before entering an incident/accident area (no odour warning available if dangerous concentrations are present). Hydrogen concentrations have to be measured with a suitable detector.

Oxygen concentration levels below 19.5% by volume are biologically inactive for humans, and no effects of oxygen deficiency are usually observed. At concentrations below 12%, immediate unconsciousness may occur with no prior warning symptoms. Stages of asphyxiation have been noted based on the oxygen concentration (NASA, 1997):

- 15–19% by volume – decreased ability to perform tasks; may induce early symptoms in persons with heart, lung, or circulatory problems;
- 12–15% – deeper respiration, faster pulse, poor coordination;
- 10–12% – giddiness, poor judgment, slightly blue lips;
- 8–10% – nausea, vomiting, unconsciousness, ashen face, fainting, mental failure;
- 6–8% – death in 8 min (50% death and 50% recovery with treatment in 6 min, 100% recovery with treatment in 4 to 5 min);
- 4% – coma in 40 s, convulsions, respiration ceases, death.

Please click the advert



Contact with liquid hydrogen or its splashes on the skin or in the eyes can cause serious burns by frostbite or hypothermia. Inhaling vapour or cold hydrogen produces respiratory discomfort and can result in asphyxiation. Direct physical contact with liquid hydrogen, cold vapour, or cold equipment can cause serious tissue damage. Momentary contact with a small amount of the liquid may not pose as great a danger of a burn because a protective film may form (NASA, 1997). Danger of freezing occurs when large amounts are spilled and exposure is extensive. Cardiac malfunctions are likely when the internal body temperature drops to 27°C, and death may result when the internal body temperature drops to 15°C. It is safest in the field to do nothing other than to protect the involved area with a loose cover.

2.5. Concluding remark

It can be concluded that hydrogen is not more dangerous or safer compared to other fuels. Hydrogen is different and has to be professionally handled with knowledge of underpinning science and engineering to provide public safety and competitiveness of hydrogen and fuel cell products and infrastructure.

3 Regulations, codes and standards and hydrogen safety engineering

The quality of hydrogen safety provisions directly depends on availability of an overall performance-based hydrogen safety engineering (HSE) methodology rather than a group of codes and standards, which are often prescriptive in nature and out of date. The HSE methodology must be in compliance with current regulations as well as with standards and codes which are explicitly mentioned in the regulations. Besides regulations, codes and standards (RCS) the HSE needs a highly educated workforce and contemporary engineering tools, including freely available to hydrogen safety engineers Computational Fluid Dynamics (CFD) software.

There is an overestimation to some extent of expectations from the role of RCS in safety design of hydrogen and fuel cell (HFC) systems and infrastructure from the author's point of view. Indeed, standards are at least three years old compares to the current level of knowledge in the field due to the procedure of their development and approval. They can be quite narrowed by a particular topic or include only general statements without concrete information for safety engineering. Standards cannot account for all possible situations to be resolved in real life, especially for new and developing technologies. Safety information in standards relevant to hydrogen and fuel cell systems is "naturally" fragmented throughout a constantly growing number of standards in the area.

Standards are written from the perspective of the industry and reflect mainly the interests of the industry rather than all stakeholders, including public. Some statements of standards are at least questionable if not leading to potentially catastrophic consequences. For example, all three parts of the draft standard ISO 11119 "Gas cylinders of composite construction – Specification and test methods" contain the following criteria for fire resistance test: "The cylinder shall not burst during a period of two minutes from the start of the fire test. It may vent through the pressure relief device or leak through the cylinder wall or other surfaces". There are clear safety concerns for public if such criteria are applied to products on the market. The requirement of "no burst" in two minutes implies fast blowdown of hydrogen from the storage vessel through PRD with comparatively large aperture area. This in turn would create large separation distances due to long jet flame (flame length is proportional to the PRD diameter as will be shown later) and thus prevent first responders from intervention at the accident scene. Besides, in a case of accident initiation in an enclosure like garage the typical structure will be destroyed in seconds by so called pressure peaking effect explained later.

Some standards can include information derived from risk assessment methods. Risk-informed methodology and quantitative risk assessment require statistical data. In the author's opinion they can compliment but not substitute innovative safety engineering design of hydrogen and fuel cell systems. Indeed, emerging technologies can hardly be characterized by availability of statistical data. This, at the moment, makes the use of probabilistic methods in hydrogen safety less valuable. The public is keen to know that everything possible has been done by engineers to make hydrogen-powered systems safe, rather than be satisfied by information that a probability of personal fatality is 10^{-4} or 10^{-6} or 10^{-8}. The same is valid for court proceedings as presented at the 2003 AIChE Loss Prevention Symposium in New Orleans (USA).

There is another implication that risk assessment methods "oversell", i.e. resources are diverted away from a creative engineering, including hydrogen safety engineering, and practical problem solving to everlasting discussions on acceptable risk level of which uncertainty is often unacceptably high and questionable. In spite of knowledge about uncertainties, often only "averaged" value goes to industry to open the market for their products. Unfortunately, the Fukushima disaster (Shepherd, 2011) proved these author's doubts once again and stressed the need in an overarching safety-oriented standard for hydrogen safety engineering, which gives a methodology to carry out HSE, and that systemizes and maintains the knowledge in this field.

A list of *international Regulations*, which are international laws to be complied with, relevant to hydrogen safety is presented in Table 3–1. Currently hydrogen is not yet considered as a fuel but still as one of "dangerous goods" and it will take time to update regulations for the emerging hydrogen and fuel cell systems and infrastructure.

Commission Regulation (EU) No 406/2010 of 26 April 2010 implementing Regulation (EC) No 79/2009 of the European Parliament and of the Council on type-approval of hydrogen-powered motorvehicles:

http://eur-lex.europa.eu/JOHtml.do?uri=OJ:L:2010:122:SOM:EN:HTML

IMO International Code for the Construction and Equipment of Ships Carrying Liquefied Gases in Bulk (IGC Code): http://www.imo.org/environment/mainframe.asp?topic_id=995

ADR UN ECE Agreement concerning the International Carriage of Dangerous Goods by Road: http://www.unece.org/trans/danger/publi/adr/adr_e.html

---

RID is the European Agreement on the International Carriage of Dangerous Goods by Rail. The regulations appear as Appendix C to the Convention concerning International Carriage by Rail (COTIF) concluded at Vilnius on 3 June 1999: http://www.otif.org/en/law.html

---

ADN is the European Agreement concerning the International Carriage of Dangerous Goods by Inland Waterways concluded at Geneva on 26 May 2000:

http://www.unece.org/trans/danger/publi/adn/adn_e.html

The rules related to transport of dangerous goods, regulated in Europe by the international agreements, mentioned in the three items above, that is, the ADR, RID, and ADN, have also been extended to national transport in the EU under the Inland transport of dangerous goods Directive 2008/68/EC: http://europa.eu/legislation_summaries/transport/rail_transport/tr0006_en.htm

---

The International Maritime Dangerous Goods (IMDG) Code covers the transport of dangerous goods by sea:
http://www.imo.org/safety/mainframe.asp?topic_id=158

UN Recommendations on the Transport of Dangerous Goods, Model Regulations. These are updated every two years. Recommendations relevant to hydrogen are UN 1049 (Hydrogen, Compressed), UN 1066 (Hydrogen, refrigerated liquid) and UN 3468 (hydrogen in a metal hydride storage system):
http://www.unece.org/trans/danger/publi/unrec/12_e.html

Dangerous Substances Directive: 67/548/EEC:
http://ec.europa.eu/environment/chemicals/dansub/home_en.htm
http://eur-lex.europa.eu/JOHtml.do?uri=OJ:L:2009:011:SOM:EN:HTML

Low Voltage Directive (LVD) 2006/95/EC:
http://ec.europa.eu/enterprise/sectors/electrical/lvd/
http://ec.europa.eu/enterprise/sectors/electrical/files/lvdgen_en.pdf

Electromagnetic Compatibility Directive (EMC) 2004/108/EC:
http://ec.europa.eu/enterprise/sectors/electrical/emc/
http://ec.europa.eu/enterprise/sectors/electrical/files/emc_guide updated_20100208_v3_en.pdf

Pressure Equipment Directive (PED) 97/23/EC:
http://ec.europa.eu/enterprise/sectors/pressure-and-gas/documents/ped/index_en.htm

http://www.bsigroup.com/en/ProductServices/About-CE-Marking/EU-directives/Pressure-Equipment-Directive-PED/

Simple Pressure Vessels Directive (SPVD) 2009/105/EC :
http://ec.europa.eu/enterprise/sectors/pressure-and-gas/documents/spvd/index_en.htm

Transportable Pressure Equipment Directive (TPED) 1999/36/EC:
http://ec.europa.eu/transport/tpe/index_en.html

Gas Appliances Directive 2009/142/EC Includes fuel cells (where the primary function is heating):
http://ec.europa.eu/enterprise/sectors/pressure-and-gas/gas_appliances/index_en.htm

Equipment and protective systems for potentially explosive atmosphere Directive (ATEX 95) 94/9/EC:
http://ec.europa.eu/enterprise/sectors/mechanical/atex/index_en.htm

Directive on minimum requirements for improving the safety and health protection of workers potentially at risk from explosive atmospheres (ATEX 137) 99/92/EC:

http://eur-lex.europa.eu/LexUriServ/LexUriServ.do?uri=CELEX:31999L0092:en:NOT

Machinery Directive (MD) 2006/42/EC:
http://ec.europa.eu/enterprise/sectors/mechanical/files/machinery/guide_application_directie_2006-42-ec-2nd_edit_6-2010_en.pdf

http://ec.europa.eu/enterprise/sectors/mechanical/machinery/

Seveso II Directive: http://ec.europa.eu/environment/seveso/index.htm

The integrated pollution prevention and control Directive (IPPC) 2008/1/EC:
http://ec.europa.eu/environment/air/pollutants/stationary/ippc/summary.htm

Measures to encourage improvements in the safety and health of workers 89/391/EEC:
http://europa.eu/legislation_summaries/employment_and_social_policy/health_hygiene_safety_at_work/c11113_en.htm

Personal protective equipment Directive 89/686/EEC:
http://ec.europa.eu/enterprise/sectors/mechanical/documents/legislation/personalprotectiveequipment/

Note: Japan has a national regulation in force covering fuel cell passenger cars with compressed hydrogen storage. An unofficial English version is available (http://www.unece.org/trans/main/wp29/wp29wgs/wp29grsp/sgs_legislation.html). The International Fire Code (IFC) and the International Building Code (IBC), both produced by the International Code Council (ICC) in the USA, are likely to be used in other countries.

Table 3–1. International regulations relevant to hydrogen safety.

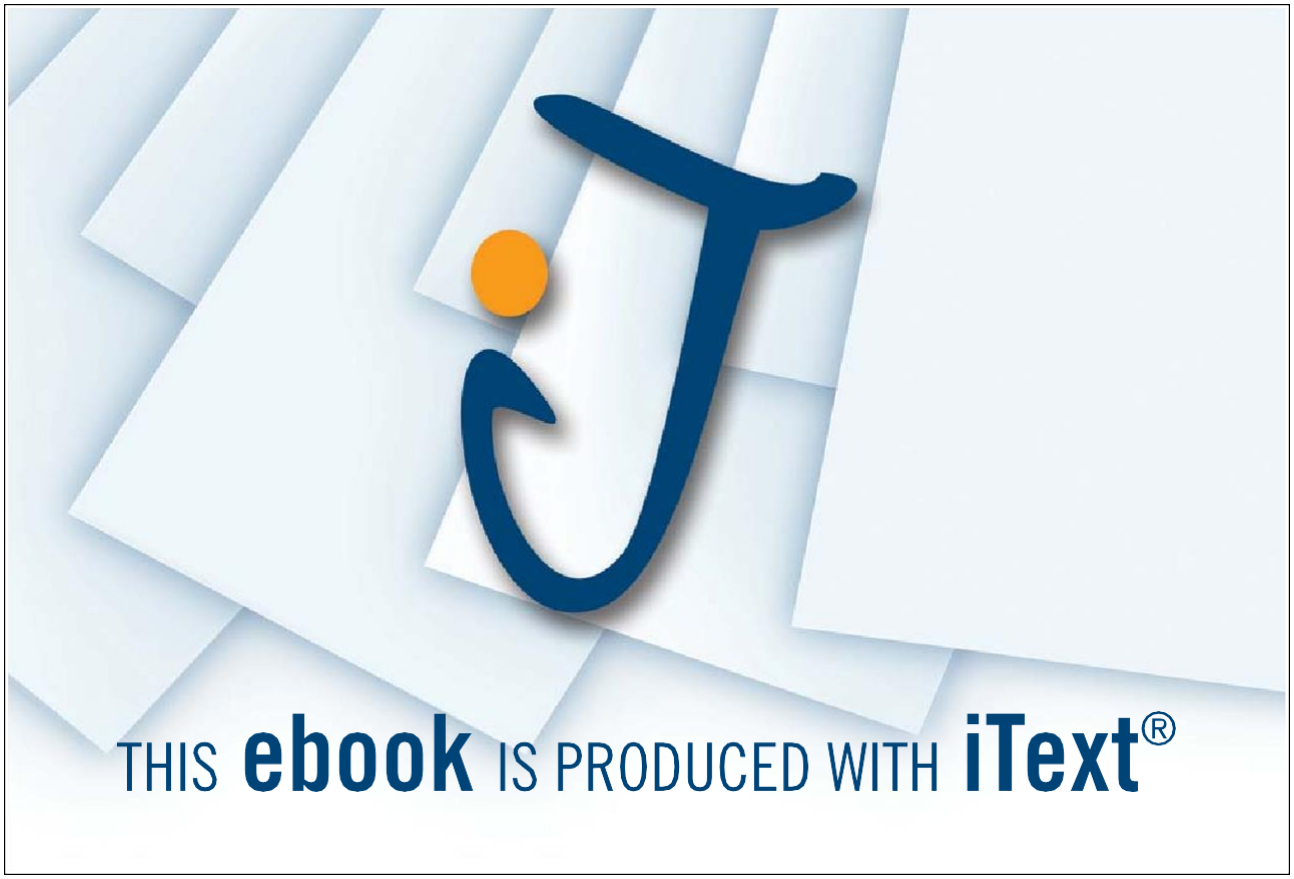
Four technical committees (TC) of the International Organization for Standardization (ISO) produce standards relevant to hydrogen and fuel cell technologies, systems, and infrastructure. Technical Committee 197 "Hydrogen Technologies" published a number of documents including:

- ISO/TR 15916:2004 Basic considerations for the safety of hydrogen systems;
- ISO 14687 Hydrogen fuel - Product specification;
- ISO 16110-1:2007 Hydrogen generators using fuel processing technologies – Part 1: Safety;
- ISO/TS 20100:2008 Gaseous hydrogen - Fuelling stations;
- ISO 17268:2006 Compressed hydrogen surface vehicle refuelling connection devices;
- ISO 22734-1:2008 Hydrogen generators using water electrolysis process – Part 1: Industrial and commercial applications;
- ISO 26142:2010 Hydrogen detection apparatus – Stationary applications.

Technical Committee 22, sub-committee (SC) 21, on electric road vehicles issued standards with safety specifications:

- ISO 23273-2:2006 Fuel cell road vehicles – Safety specifications – Part 2: Protection against hydrogen hazards for vehicles fuelled with compressed hydrogen;
- ISO 23273-3:2006 Fuel cell road vehicles – Safety specifications – Part 3: Protection of persons against electric shock, etc.

Please click the advert


THIS ebook IS PRODUCED WITH iText®

Technical Committee 58 on gas cylinders published several parts of standard ISO 11114 Transportable gas cylinders – Compatibility of cylinder and valve materials with gas contents, etc. Technical Committee 220 on cryogenic vessels published a number of standards related to large transportable vacuum-insulated vessels, gas/materials compatibility, and valves for cryogenic service, etc.

The International Electrotechnical Commission (IEC) publishes standards relevant to fuel cell technologies. These include:

- IEC 62282-2 (2007-03) Fuel Cell Modules;
- IEC 62282-3-1 (2007-04) Stationary Fuel Cell Power Systems – Safety;
- IEC 62282-3-200 (2011-10) Stationary Fuel Cell Power Systems – Performance Test Methods;
- IEC 62282-3-3 (2007-11) Stationary Fuel Cell Power Systems – Installation;
- IEC 62282-5-1 (2007-02) Portable Fuel Cell Appliances – Safety;
- IEC 62282-6-100 (2010-03) Micro Fuel Cell Power Systems – Safety.

Working Group #8 / IEC/PAS 62282-6-150 Micro Fuel Cells – Safety – Water reactive (UN Division 4.3) compounds in indirect PEM fuel cells

Working Group #9 / IEC 62282-6-200 (2007-11) Micro Fuel Cell Power Systems – Performance

Working Group #10 / IEC 62282-6-300 (2009-06) Micro Fuel Cell Power Systems – Fuel Cartridge Interchangeability

Working Group #11 / IEC 62282-7-1 Single Cell Test Method for Polymer Electrolyte Fuel Cells

The USA National Fire Protection Association (NFPA) has a number of relevant standards:

- NFPA 2 Hydrogen Technologies Code; NFPA 52 Vehicular Gaseous Fuel Systems Code;
- NFPA 55 Compressed Gases and Cryogenic Fluids Code; NFPA 50A Standard for Gaseous Hydrogen Systems at Consumer Sites;
- NFPA 50B Standard for Liquefied Hydrogen Systems at Consumer Sites;
- NFPA 221 Standard for High Challenge Fire Walls, Fire Walls, and Fire Barrier Walls;
- NFPA 853 Standard for the Installation of Stationary Fuel Cell Power Systems.

The USA Society of Automotive Engineers (SAE) relevant standards include:

- J2578 Recommended Practice for General Fuel Cell Vehicle Safety;
- J2601 Fuelling Protocols for Light Duty Gaseous Hydrogen Surface Vehicles;
- J2719 Information Report on the Development of a Hydrogen Quality Guideline for Fuel Cell Vehicles;
- J2799 70 MPa Compressed Hydrogen Surface Vehicle Fuelling Connection Device and Optional Vehicle to Station Communications, etc.

The European Industrial Gas Association (EIGA) produced the following documents among others:

- IGC Document 122/04 Environmental impacts of hydrogen plants;
- IGC Document 15/06 Gaseous hydrogen stations;
- IGC Document 121/04 Hydrogen transportation pipelines;
- IGC Document 6/02 Safety in storage, handling and distribution of liquid hydrogen;
- IGC Document 23/00 Safety training of employees;
- IGC Document 75/07 Determination of Safety Distances;
- IGC Document 134/05 Potentially explosive atmosphere – EU Directive 1999/92/EC, etc.

The Compressed Gas Association (CGA) documents include:

- G-5.3 Commodity Specification for Hydrogen;
- G-5.4 Standard for Hydrogen Piping Systems at User Locations;
- G-5.5 Hydrogen Vent Systems;
- G-5.8 High Pressure Hydrogen Piping Systems at Consumer Locations;
- C-6.4 Methods for External Visual Inspection of Natural Gas Vehicle (NGV) and Hydrogen Vehicle (HV) Fuel Containers and Their Installations, etc.

The American Society of Mechanical Engineers (ASME) standards include:

- ASME B31.12: Hydrogen piping and pipelines;
- ASME PTC 50: Performance Test Code for Fuel Cell Power Systems Performance;
- ASME BPVC Boiler and Pressure Vessel Code, etc.

The Canadian Standards Association (CSA) published standards: Stationary Fuel Cell Power Requirements:

- ANSI/CSA AMERICA FC 1-2004 – Stationary Fuel Cell Power Systems;
- ANSI/CSA AMERICA FC 3-2004 – Portable Fuel Cell Power Systems;
- CSA America HPRD1, Standards for Basic Requirements for Pressure Relief Devices for Compressed Hydrogen Vehicle Fuel Containers, etc.

The website http://www.fuelcellstandards.com/ tracks the world-wide development of over 300 hydrogen and fuel cell standards, and its matrix can be searched by the following applications or geographic areas: Stationary Fuel Cells, International, Hydrogen & Fuel Cell Vehicles, The Americas, Portable & Micro Fuel Cells, Europe, Hydrogen Infrastructure, Pacific Rim.

There are a number of useful guidelines in the field that are compiled in Table 3–2.

Installation Permitting guidance for small stationary hydrogen and fuel cell systems (HYPER) interactive handbook and PDF document: http://www.hyperproject.eu/
US installation guidelines for refuelling stations and stationary applications: http://www.pnl.gov/fuelcells/permit_guide.stm
HyApproval handbook: European handbook for the approval of hydrogen refuelling stations: http://www.hyapproval.org/
NASA: Safety standard for hydrogen and hydrogen systems: Guidelines for Hydrogen System Design, Materials Selection, Operations, Storage, and Transportation: http://www.hq.nasa.gov/office/codeq/doctree/canceled/871916.pdf (cancelled on 25.07.2005)
NASA/TM—2003–212059 Guide for Hydrogen Hazards Analysis on Components and Systems: http://ston.jsc.nasa.gov/collections/TRS/_techrep/TM-2003-212059.pdf
American Institute of Aeronautics and Astronautics (AIAA) guide to Safety of Hydrogen and Hydrogen Systems (G-095-2004e): http://www.AIAA.org

Table 3–2. Guidelines relevant to hydrogen safety.

Please click the advert

FOSS

Dedicated Analytical Solutions

Sharp Minds - Bright Ideas!

Employees at FOSS Analytical A/S are living proof of the company value - First - using new inventions to make dedicated solutions for our customers. With sharp minds and cross functional teamwork, we constantly strive to develop new unique products - Would you like to join our team?

FOSS works diligently with innovation and development as basis for its growth. It is reflected in the fact that more than 200 of the 1200 employees in FOSS work with Research & Development in Scandinavia and USA. Engineers at FOSS work in production, development and marketing, within a wide range of different fields, i.e. Chemistry, Electronics, Mechanics, Software, Optics, Microbiology, Chemometrics.

We offer

A challenging job in an international and innovative company that is leading in its field. You will get the opportunity to work with the most advanced technology together with highly skilled colleagues.



The Family owned FOSS group is the world leader as supplier of dedicated, high-tech analytical solutions which measure and control the quality and produc- tion of agricultural, food, phar- maceutical and chemical produ- cts. Main activities are initiated from Denmark, Sweden and USA with headquarters domiciled in Hillerød, DK. The products are marketed globally by 23 sales companies and an extensive net of distributors. In line with the corevalue to be 'First', the company intends to expand

its market position.

4 Hydrogen safety engineering: framework and technical subsystems

4.1. Framework

Hydrogen safety engineering (HSE) is defined as an application of scientific and engineering principles to the protection of life, property and environment from adverse effects of incidents/accidents involving hydrogen (Molkov and Saffers, 2012). Despite the progress in hydrogen safety science and engineering during the last decade, especially through the HySafe partnership (BRHS, 2009), an overarching performance-based methodology to carry out HSE is still formally absent.

HSE comprises a design framework and technical sub-systems. A design framework for HSE, developed at the University of Ulster, is similar to British standard BS7974 for application of fire safety engineering to the design of buildings (BSI, 2001) and is expanded to reflect specific hydrogen safety related phenomena, including but not limited to high pressure under-expanded leaks and dispersion, spontaneous ignition of sudden hydrogen releases to air, high momentum jet fires, deflagrations and detonations, mitigation techniques, e.g. venting of deflagration and natural/forced ventilation, etc.

The HSE process includes three main steps (see Fig. 4–1). *Firstly*, a qualitative design review (QDR) is undertaken by a team that can include owner, hydrogen safety engineer, architect, representative of authorities having jurisdiction, e.g. emergency services, and other stakeholders. The team defines accident scenarios, suggests trial safety designs, and formulates acceptance criteria. *Secondly*, a quantitative safety analysis of selected scenarios and trial designs is carried out by qualified hydrogen safety engineer(s) using the state-of-the-art knowledge in hydrogen safety science and engineering and validated models and tools. *Thirdly*, the performance of a hydrogen and/or fuel cell system under the trial safety designs is assessed against predefined acceptance criteria.

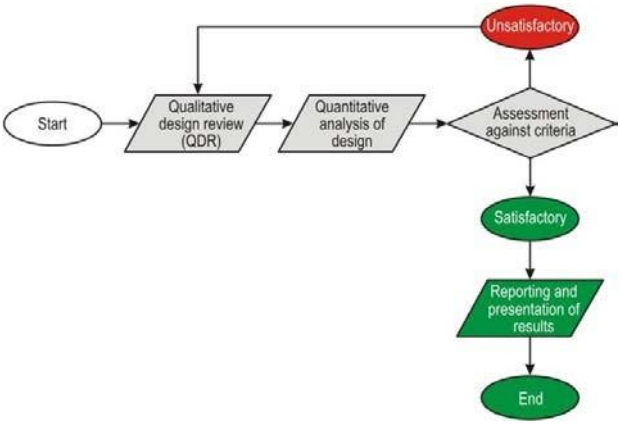


Figure 4–1. Hydrogen safety engineering process (Molkov and Saffers, 2012).

The QDR is a qualitative process based on the team's experience and knowledge. It allows its members to establish a range of *safety strategies*. Ideally, QDR has to be carried out early in the design process and in a systematic way, so that any substantial findings and relevant items can be incorporated into the design of HFC application or infrastructure before the working drawings are developed. In practice however, the QDR process is likely to involve some iterations as the design process moves from a broad concept to greater detail.

Safety objectives should be defined during the QDR. They should be appropriate to the particular aspects of the system design, as HSE may be used either to develop a complete hydrogen safety strategy or to consider only one aspect of the design. *The main hydrogen safety objectives* are safety of life, loss control and environmental protection. The QDR team should establish one or more *trial safety designs* taking into consideration *selected accident scenario(s)*. The different designs could satisfy the same safety objectives and should be compared with each other in terms of cost-effectiveness and practicability. At first glance, it is essential that trial designs should limit hazards by implementing prevention measures and ensuring the reduction of severity and frequency of consequences. Although HSE provides a degree of freedom, it is mandatory to fully respect relevant regulations when defining trial designs.

The QDR team has to establish the *acceptance criteria* against which the performance of a design can be judged. Three main methods can be used: *deterministic, comparative, and probabilistic*. The QDR team can, depending on trial designs, define acceptance criteria following all three methods. The QDR team should provide a set of qualitative outputs to be used in the quantitative analysis: results of the architectural review; hydrogen safety objectives; significant hazards and associated phenomena; specifications of the scenarios for analysis; one or more trial designs; acceptance criteria and suggested methods of analysis. Following QDR the team should decide which trial design(s) is likely to be optimum. The team should then decide whether quantitative analysis is necessary to demonstrate that the design meets the hydrogen safety objective(s).

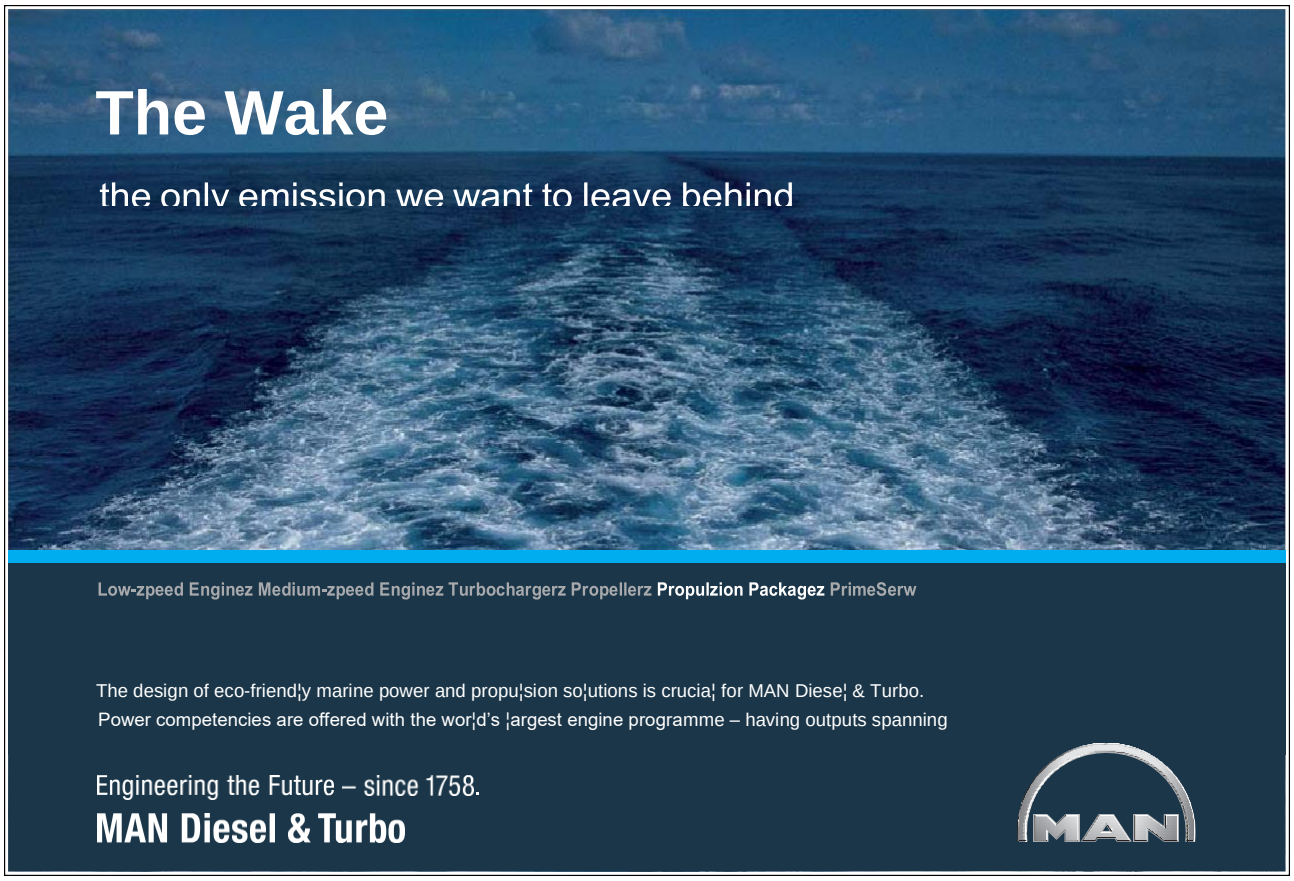
Following the QDR a *quantitative analysis* may be carried out using Technical Sub-Systems (TSS) where various aspects of the analysis can be quantified by a deterministic study or a probabilistic study. The quantification process is preceded by the QDR procedure for two main reasons: to ensure that the problem is fully understood and that the analysis addresses the relevant aspects of the hydrogen safety system; and to simplify the problem and minimise the calculation effort required. In addition, the QDR team should identify appropriate methods of analysis among: simple engineering calculations; CFD simulations; simple probabilistic study; full probabilistic study, etc. A deterministic study using comparative criteria will generally require fewer data and resources than a probabilistic approach and is likely to be the simplest method of achieving an acceptable design. A full probabilistic study is only likely to be justified when a substantially new approach to hydrogen system design or hydrogen safety practice is being adopted. The analysis may be a combination of some deterministic and some probabilistic elements.

Following the quantitative analysis, the results should be compared with the *acceptance criteria* identified during the QDR exercise. Three basic types of approach can be considered to access the performance of safety system against criteria:

- Deterministic approach shows that on the basis of the initial assumptions a defined set of conditions will not occur;
- Comparative approach shows that the design provides a level of safety equivalent to that in similar systems and/or conforms to prescriptive codes (as an alternative to performance-based HSE);
- Probabilistic approach shows that the risk of a given event occurring is acceptably low, e.g. equal or below the established risk for similar existing systems.

If none of the trial designs developed by the QDR team satisfies the specified acceptance criteria, QDR and quantification process should be repeated until a hydrogen safety strategy satisfies acceptance criteria and other design requirements. Several options can be considered when re-conducting QDR following recommendations (BSI, 2001): development of additional trial designs; adoption of more discriminating design approach, e.g. using deterministic techniques instead of a comparative study; re-evaluation of design objectives, e.g. if the cost of hydrogen safety measures for property loss prevention outweighs the potential benefits. When a satisfactory solution has been identified, the resulting HSE strategy should be fully documented.

Please click the advert


The Wake
the only emission we want to leave behind
Low-zpeed Enginez Medium-zpeed Enginez Turbochargerz Propellerz Propulzion Packagez PrimeSerw
The design of eco-friend¦y marine power and propu¦sion so¦utions is crucia¦ for MAN Diese¦ & Turbo.
Power competencies are offered with the wor¦d's ¦argest engine programme – having outputs spanning
Engineering the Future – since 1758.
MAN Diesel & Turbo
MAN

Depending on particularities and scope of the HSE study, the reporting of the results and findings could contain the following information (BSI, 2001):

- Objectives of the study;
- Full description of the HFC system/infrastructure;
- Results of the QDR;
- Quantitative analysis (assumptions; engineering judgments; calculation procedures; validation of methodologies; sensitivity analysis);
- Assessment of analysis results against criteria;
- Conclusions (hydrogen safety strategy; management requirements; any limitations on use);
- References (e.g. drawings, design documentation, technical literature, etc.).

4.2. Technical sub-systems

To simplify the evaluationof a HSE design, the quantificationprocess is broken downinto several technical sub-systems (TSSs). The following requirements should be accounted for development of individual TSS:

- TSS should together, as reasonably as possible, cover all possible aspects of hydrogen safety engineering;
- TSS should be balanced between their uniqueness or capacity to be used individually, and their complementarities and synergies with other TSSs;
- TSS should be a selection of the state-of-the-art in the particular field of hydrogen safety, validated engineering tools, including empirical and semi-empirical correlations and contemporary tools such as CFD models and codes;
- TSS should be flexible to allow update of existing or use of new appropriate and validated methods, reflecting recent progress in hydrogen safety science and engineering.

The following TSSs are currently suggested and under development for HSE (Molkov and Saffers, 2012):

- TSS1: Initiation of release and dispersion;
- TSS2: Ignitions;
- TSS3: Deflagrations and detonations;
- TSS4: Fires;
- TSS5: Impact on people, structures, and environment;
- TSS6: Mitigation techniques;
- TSS7: Emergency services intervention.

Hydrogen safety engineering is a key to the success of the hydrogen economy. It is the powerful tool for provision of hydrogen safety by qualified specialists in the growing market of HFC systems and infrastructure. Last not least the HSE can secure high level of competitiveness for hydrogen and fuel

cell products.

5 Unignited releases

5.1. Expanded and under-expanded jets

Hydrogen-powered vehicles have onboard storage at pressures up to 70 MPa, and refuelling infrastructure operates at pressures up to 100 MPa. Unscheduled release at such pressures creates a highly under-expanded (pressure at the nozzle exit is above atmospheric pressure) turbulent jet that behaves differently from expanded jets (pressure at the nozzle exit is equal to atmospheric pressure) extensively studied previously. The majority of leaks from hydrogen storage and equipment will be in a form of an under-expanded jet at least at the beginning.

In an under-expanded a pressure at the nozzle exit has not fully dropped to the atmospheric. At high pressures a velocity at the exit from the nozzle remains locally sonic, but the exit pressure rises above ambient. As the result the expansion down to ambient conditions takes place outside the nozzle. The critical pressure ratio for sonic (choked) flow of compressible gas is about 1.9 at STP (γ=1.405) and 1.89 at NTP (γ=1.39) according to the theoretical equation for choked flow conditions

$$\frac{P_R}{P_N} = \left(\frac{\gamma+1}{2}\right)^{\gamma/(\gamma-1)}, \qquad (5\text{–}1)$$

where P_R and P_N are pressure in the reservoir and the nozzle exit respectively, and γ is the ratio of specific heats. This equation can be applied to estimate the pressure at the leak (nozzle) exit by the storage pressure at the reservoir.

Ishii et al. (1999) reported that jets of diatomic gas (γ=7/5) exhausted from the open end of their test tube tend to be subsonic matched jets for ratios of pressures in the high-pressure and the low-pressure chambers (the only parameter controlling the jet strength) between 1 and 4.1, sonic under-expanded jets for pressure ratios in the range from 4.1 to 41.2, and supersonic under-expanded jets for pressure ratios above 41.2. Pressure ratio 4.1 is above the critical ratio 1.9 for sonic (choked) flow. However, there is no contradiction. Indeed, each of two pressure ratios (high-pressure chamber to tube exit, and tube exit to low-pressure chamber) can be p_R/p_N=2.05 that is close to the theoretical critical pressure ratio of 1.9 for sonic flow. The difference could be attributed to losses between high-pressure and low-pressure chambers.

For under-expanded jet the flow expansion occurs near the nozzle exit and is characterised by the complex shock structure, which is well documented and published elsewhere (Dulov and Luk'yanov, 1984). The schematic presentation of an under-expanded shock structure is given in Fig. 5–1 (left) (Dulov and Luk'yanov, 1984), and distribution of the Mach number (dimensionless number equal to ratio of a local flow velocity to the local speed of sound) in a numerically simulated under-expanded jet (initial stage of release) for pressure ratio in a storage tank and the atmosphere 160 is shown in Fig. 5–1 (right).

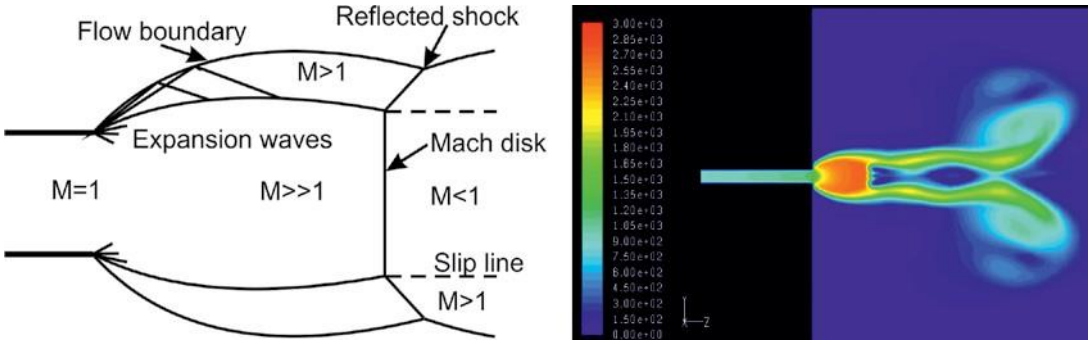


Figure 5–1. The schematic presentation of an under-expanded jet structure (left) (Dulov and Luk'yanov, 1984), and an initial stage of under-expanded jet release at 16.1 MPa through a channel of 0.25 mm (mass flow rate 0.46 g/s).

Figure 5–1 shows that local sonic velocity is established at the nozzle exit with Mach number M=1. Then, out flowing gas undergoes rapid expansion and quickly accelerates to high Mach numbers (up to M=8 for 70 MPa storage pressure) with decrease in pressure and density. A series of expansion waves are formed at the nozzle exit edge. These expansion waves are reflected as compression waves from the free surface at the jet flow boundary, coalesce and form a barrel shock and a Mach disk. As gas with very high Mach number crosses the Mach disk, it undergoes an abrupt decrease in velocity to subsonic speeds and increases in pressure (to the atmospheric) and density. The resulting flow structure after the Mach disk comprises of subsonic core (M<1) surrounded by supersonic shell (M>1) with a turbulent eddy producing shear layer called slip line dividing these two regions.

Please click the advert



ELECTRONICS
AUTOMATION &
PROCESS CONTROL
MECHANICAL
ENGINEERING
INDUSTRIAL
DATA COMMS
ELECTRICAL
POWER

For high ratios of nozzle exit to atmospheric pressure above 40 the barrel shock culminates with a strong Mach disk without a diamond structure, and below this critical pressure ratio of 40 – with the diamond structure. This estimate of the critical pressure ratio is based on simulations of hydrogen under-expanded jets carried out at the HySAFER Centre. The ratio of a storage pressure in a vessel to a nozzle pressure can be roughly estimated as 2 for cases without losses (short nozzles). This means that no diamond structure can be expected for under-expanded hydrogen jets to the atmosphere at storage pressures below about 8 MPa. This preliminary conclusion yet has to be confirmed by experiments.

Hydrogen under-expanded jet exit shock structure was qualitatively imaged using schlieren photography by Ruggles and Ekoto (2011). Figure 5–2 shows a mean image of the Mach disk structure (left), and a mean image of Mach disk and diamond shock structure (right). Nominal pressure ratio was 10:1 and nozzle diameter was 0.75 mm.

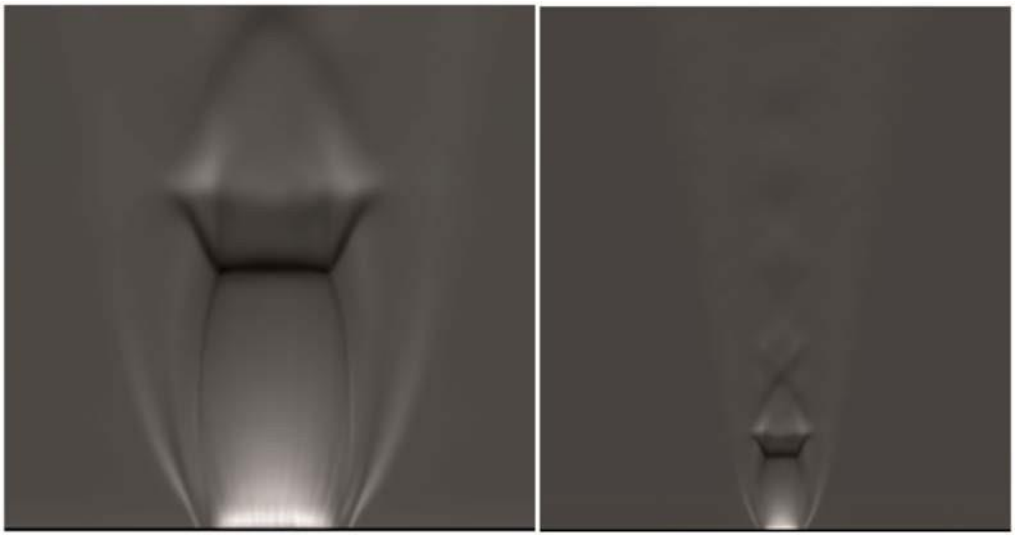


Figure 5–2. Images of the Mach disk structure (left), and Mach disk and diamond shock structure (right) (Ruggles and Ekoto, 2011).

Ruggles and Ekoto (2011) used corrected instantaneous images of flow to create a root-mean-square (r.m.s.) image of the flow fluctuations, which is shown in Fig. 5–3 and illustrates the downstream mixing layers. They noted that the schlieren image results should be interpreted with caution. Their measurements were a path averaged integration of the refractive index gradient, which may have been caused by differences in mixture fraction due to scalar mixing, but also may have been the result of changes in pressure and temperature. In the region surrounding the barrel shock structure, however, it is feasible that refractive index gradients were the result of the air entrainment ahead of the Mach disk. This would then require the inclusion of an entrainment correction in the current notional nozzle models (Ruggles and Ekoto, 2011).

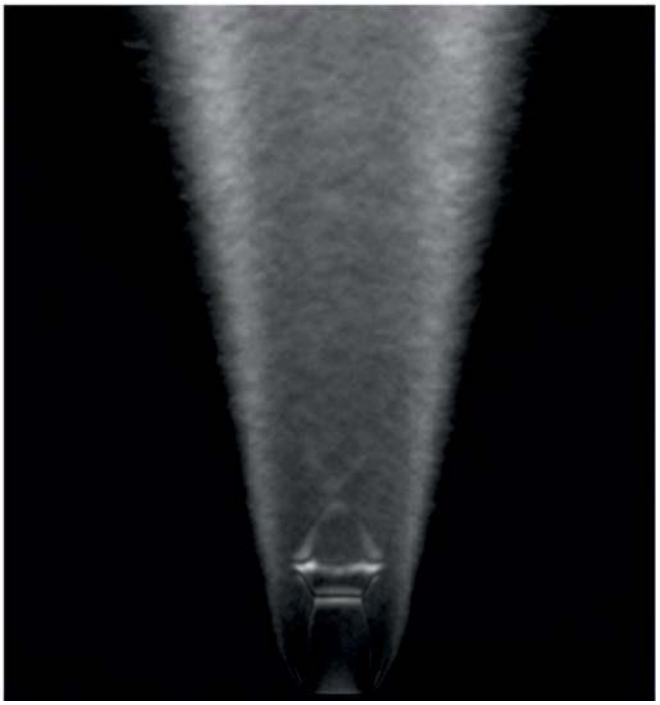


Figure 5–3. R.m.s. image of the Mach disk and diamond structure (Ruggles and Ekoto, 2011).

5.2. Under-expanded jet theories

It is convenient for some engineering calculations to substitute an under-expanded jet from actual nozzle by an expanded jet from so-called effective or notional nozzle. There are a number of notional nozzle theories. One of the most cited is the model by Birch et al. (1984). However, these former models are built on the ideal gas equation of state and thus not applicable to gas storage pressures above 10-20 MPa when effects of gas non-ideality must be accounted for. Indeed, the Abel-Noble equation of state $p=Z\rho R_{H2}T$, where $Z=1/(1-b\rho)$ is the compressibility factor, has $Z=1.01$ at 1.57 MPa, $Z=1.1$ at 15.7 MPa, and $Z=1.5$ at 78.6 MPa (at temperature 293.15 K).

The first theory of under-expanded jet that accounts for non-ideal behaviour of highly compressed hydrogen has been published by Schefer et al. (2007). The notional nozzle diameter calculations by Schefer et al. (2007) are similar to Birch et al. (1984) yet the Abel-Noble equation is applied and the assumption by Birch et al. about the speed of sound at the notional nozzle is relaxed. As a result the theory of Schefer et al. (2007) predicts uniform super-sonic velocities at the notional nozzle exit at high storage pressures.

In 2009 author and colleagues developed the alternative to Schefer et al. (2007) under-expanded theory that is presented here. This theory (Molkov et al., 2009) is based on mass and energy conservation equations rather than mass and momentum (Schefer et al., 2007). Similar to Birch et al. (1984) the developed model (Molkov et al., 2009) is based on the assumption of uniform sonic flow through the

notional nozzle. The under-expanded jet scheme is shown in Fig. 5–4.

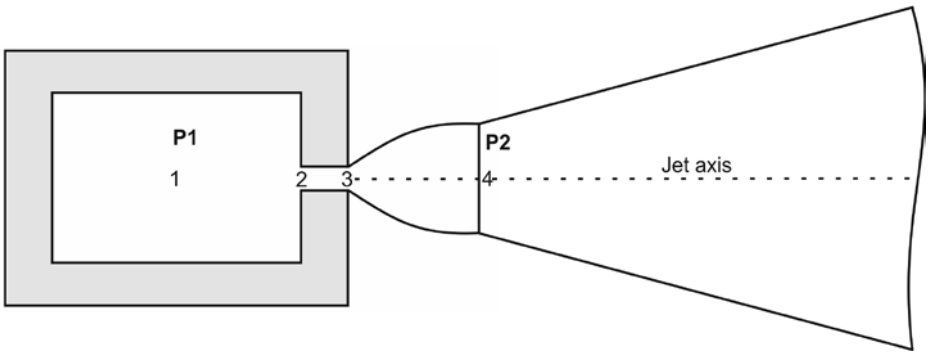


Figure 5–4. The under-expanded jet scheme: 1 – storage vessel, 2 – nozzle entrance, 3 – nozzle exit, 4 – notional nozzle exit.

It is assumed that flow velocity in the storage reservoir, 1, is zero. The flow parameters at the entrance to the leak channel are referred to by subscript 2, and at the actual nozzle exit by subscript 3. For sonic and super-sonic flows the parameters at the nozzle exit, 3, are those for choked flow and therefore the nozzle exit velocity is equal to the local speed of sound (Mach number M=1). The notional nozzle is between the actual nozzle exit, 3, and the notional nozzle exit, 4. The notional nozzle exit, 4, parameters correspond to fully expanded jet with the pressure equal to ambient and uniform flow velocity equal to local speed of sound. In some cases there can be essential minor and friction losses in the flow pathway 2–3 that cannot be neglected, e.g. the case of very narrow crack.

Please click the advert

International
free wor


I joined MITAS because
I wanted real responsibilifi
fle Graduate Programme
for Engineers and Geoscientists
Maersk.com/Mitas
Month16
I was a construction
supervisor in
the North Sea
advising and
he ping foremen
Real work
Internation l opportunities
ree w rk placements
MAERSK

In this section two under-expanded jet theories will be presented – first without and then with losses. Both exploit the Abel-Noble equation of state for real hydrogen gas is applied (Chenoweth, 1983) described in Chapter 2

$$p = Z \,.\, \rho \,.\, R_{H2} \,.\, T\,, \tag{5–2}$$

where the compressibility factor is $Z = 1/\,(\,1 - b\rho)$.

5.2.1. Theory without losses

It is assumed that the expansion of the Abel-Noble gas from the reservoir, 1, to the nozzle exit, 3, is isentropic, without losses in the flow between nozzle entrance, 2, and nozzle exit, 3. It is assumed that there is no air entrainment to an expanding jet between the actual nozzle exit, 3, and the notional nozzle exit, 4. The system of nine equations with nine unknown parameters ($\rho_1, \rho_3, u_3, T_3, p_3, \rho_4, u_4, T_4, A_4$) is as follows (known parameters are: p_1, T_1, A_3, p_4 and constants c_p, R_{H2}, b, γ). Here ρ is the density (kg/m^3), u is the gas velocity (m/s), A is the cross-section area (m^2), c_p is the specific heat capacity at constant pressure (J/kg/K). Subscripts "1" through to "4" denote gas parameters at locations "1" to "4" shown in Fig. 5–4.

Three equations of state for gas parameters at the reservoir, 1, the real nozzle exit, 3, and the notional nozzle exit, 4, are

$$\theta_1 = \frac{p_1}{1 - b\rho_1 R_{H2} T_1}, \quad \theta_3 = \frac{p_3}{1 - b\rho_3 R_{H2} T_3}, \quad \theta_4 = \frac{p_4}{R_{H2} T_4}\,. \tag{5–3}$$

Two equations of energy conservation, one between the reservoir, 1, and the actual nozzle exit, 3, and another between the actual nozzle exit, 3, and the notional nozzle exit, 4, are

$$c_p T_1 = c_p T_3 + \frac{u_3^2}{2}, \quad c_p T_3 + \frac{u_3^2}{2} = c_p T_4 + \frac{u_4^2}{2}\,. \tag{5–4}$$

Two equations for the speed of sound, one for choked flow in the nozzle exit, 3, and another for the assumption of the speed of sound at the notional nozzle exit, 4, are

$$u_3^2 = a_3^2 = \left(\frac{\gamma p_3}{\rho_3}\right), \quad u_4 = a_4 = \sqrt{\frac{\gamma p_3}{1 - b\rho_3}}\,. \tag{5–5}$$

The mass conservation equation between entrance to the notional nozzle, 3, and exit from the notional nozzle, 4, is

$$\rho_3 u_3 A_3 = \rho_4 u_4 A_3. \tag{5–6}$$

The isentropic expansion equation between the reservoir, 1, and the actual nozzle exit, 3, is

$$\left(\frac{1}{\quad}\right)^{\gamma} \qquad \left(\frac{1}{\quad}\right)^{\gamma}$$

$$p_1\left(\frac{1}{\rho_1}-b\right)=p_3\left(\frac{1}{\rho_3}-b\right). \quad (5\text{–}7)$$

Let us rewrite the equation (5-4) for energy conservation between the reservoir, 1, and the actual nozzle exit, 3, in the form

$$\frac{T_1}{T_3}=1+\frac{u_3^2}{2c_pT_3}, \quad (5\text{–}8)$$

and multiply numerator and denominator in the second term of the right-hand side by square of the speed of sound that is for Abel-Noble gas is

$$a^2 = \frac{\gamma P}{\rho(1-b\rho)} \tag{5–9}$$

to obtain the equation

$$\frac{T_1}{T_3} = 1 + \frac{\rho_3\left(\frac{\gamma P_3}{\rho_3}\right)}{2c_p R_{H2} T_3}\left(\frac{R_{H2} M_3^2}{1-b\rho_3}\right) \tag{5–10}$$

in which $M = u / a$ is Mach number of the flow in state 3. Taking into account that $\frac{R_{H2}}{c_p} = \frac{\gamma - 1}{\gamma}$

$$\frac{T_1}{T_3} = 1 + \frac{\rho_3\left(\frac{\gamma P_3}{\rho_3}\right)}{2R_{H2}T_3}\left(\frac{\gamma - 1}{1-b\rho_3}\right)M_3^2 = 1 + \frac{(\gamma-1)M^2\left[\frac{P_3}{\rho_3 R_{H2} T_3}\right]}{2(1-b\rho_3)}. \tag{5–11}$$

By substitution $P_3 = \frac{1}{1-b\rho_3}$ and accounting for chocked flow in the actual nozzle exit 3 (M_3=1) the following equation is derived

$$\frac{T_1}{T_3} = 1 + \frac{\gamma - 1}{2(1-b\rho_3)^2} M_3^2 = 1 + \frac{\gamma - 1}{2(1-b\rho_3)^2}. \tag{5–12}$$

Let us rewrite (5–7) with use of the Abel-Noble equation of state as

$$\frac{\theta_1}{(1-b\theta_1)} = \frac{\theta_3}{(1-b\theta_3)}\left(\frac{1}{1-b\theta_1}\right)\theta_3 RT_3 \tag{5–13}$$

By uniting the density terms in (5-13) and substituting for the temperature ratio from (5-12) we obtain

$$\left(\frac{\rho_1}{1-b\rho_1}\right)^{\gamma-1} = \left(\frac{\rho_3}{1-b\rho_3}\right)^{\gamma-1}\left(1 + \frac{\gamma-1}{2(1-b\rho_3)^2}\right). \tag{5–14}$$

The procedure for the notional nozzle diameter (d_3=d_e) calculation is as follows (Molkov et al., 2009). Calculate hydrogen density in the reservoir from the Abel-Nobel equation. $\theta_1 = P_1 / ZR_{H2}T_1$. Solve a transcendental equation of isentropic expansion to find density at the actual nozzle exit (5–14). Find temperature T_3 at the actual nozzle exit from the equation(5–12) and then pressure P_3 from the Abel-Noble equation (5–2). At the actual nozzle exit, 3, the flow is chocked and hydrogen velocity can be calculated using the equation for the speed of sound (5–9). From the energy conservation equation between the actual nozzle exit and the notional nozzle exit (5–4) written per unit mass, and with the assumption that at the notional nozzle exit hydrogen velocity is equal to the local speed of sound $a_4^2 = \gamma R_{H2} T_4$, it is easy to derive that the temperature at the notional nozzle exit is

$$T_4 = \frac{2T_3}{(\gamma+1)} + \frac{(\gamma-1)}{(\gamma+1)} \frac{P_3}{\rho_3 (1-b\rho_3) R_{H2}}. \qquad (5\text{–}15)$$

Then, hydrogen density at the notional nozzle can be calculated with P_4 equal to the ambient pressure as well as the velocity of gas $u_4=a_4$. Finally, from the continuity equation it follows that the notional nozzle exit diameter is

$$d_4 = d_3 \sqrt{\frac{\rho_3 u_3}{\rho_4 u_4}}. \qquad (5–16)$$

The under-expanded jet theory (Molkov et al., 2009) was used to build and validate described further in this manuscript the universal similarity law that is valid for both expanded and under-expanded jets in the momentum-controlled regime, the novel correlation for hydrogen jet flame length, blow down time of hydrogen release from the storage vessel, etc. The theory is an essential tool to carry out hydrogen safety engineering.

5.2.2. Theory with losses

Minor losses in gas flow represent entrance to the channel, abrupt reduction or increase in channel cross-section area, presence of valves, elbows, etc. They are described in this theory through the minor losses factor K. Frictional losses are considered to be due to friction on walls. They are described through equation $F=fL/d$, where f is the friction factor, L is the channel/nozzle length, and d is channel diameter. The system of 12 equations describing this process is given in Table 5–1 following paper (Molkov and Bragin, 2009).

Please click the advert


www.job.oticon.dk
oticon
PEOPLE FIRST

$P_2 - P_1 + \rho_2 u_2^2 (K/4+1) = 0$	$\rho_2 u_2 = \rho_3 u_3$
$c_P T_1 = c_P T_2 + (K+1)\cdot u_2^2/2$	$u_3 = \sqrt{\gamma R_{H2} T_3/(1-b\rho_3)}$
$\theta_2 = P_2/(bP_2 + R_{H2}T_2)$ or $P_2 = \theta_2 R_{H2} T_2/(1-b\theta_2)$	$u_4 = a_4 = \sqrt{\gamma R_{H2} T_4}$
$P_3 - P_2 + \rho_2 u_2^2 (F/4-1) + \rho_3 u_3^2 (F/4+1) = 0$	$\rho_4 = P_4/(R_{H2}T_4)$
$c_p T_2 + u_2^2/2 = c_p T_3 + (F/4+1)\cdot u_3^2/2$	$c_p T_3 + u_3^2/2 = c_p T_4 + u_4^2/2$
$\theta_3 = P_3/(bP_3 + R_{H2}T_3)$	$\rho_3 u_3 A_3 = \rho_4 u_4 A_4$

Table 5–1. The system of equations for the model of under-expanded jet with losses (Molkov and Bragin, 2009).

The system of equations in Table 5–1 can be reduced to the following two equations with two unknown parameters, i.e. u_3 and T_3,

$$u_3\left(\frac{\sqrt{\psi R_{H2}T_3}}{1-b\rho_3}+\sqrt{\frac{R_{H2}T_3}{\theta_3}}\right)+\sqrt{\frac{2}{K}\left(c_P T_1 - c_P T_3 - \frac{u_3^2}{2}\frac{F}{4}\right)}\left(\frac{F}{4}+1\right)+u_3\left(\frac{F}{4}+1\right)-P_1=0; \quad (5\text{-}17)$$

After u_3 and T_3 are found by solving the system of two equations (5–17), the rest of parameters in the under-expanded jet can be easily calculated.

Both under-expanded jet theory without losses (Molkov et al., 2009) and under-expanded jet theory with losses (Molkov and Bragin, 2009) are applied to calculate parameters of under-expanded hydrogen jet exiting from a narrow channel of 0.75 mm diameter and 15 mm length at pressures up to 40 MPa (see Table 5–2). The results of predictions by the under-expanded jet theories are compared against numerical simulations (LES model). The ambient temperature is assumed 287.65 K. The correlation by Nikuradse for friction factor $(1/\sqrt{f} = 0.869 \bullet ln\left(Re\sqrt{f}\right) - 0.8)$ is applied. The Reynolds number in this formula is taken as an average of values at flow states 2 and 3. Predictions by the theory with losses are found to closely reproduce the numerical simulations whereas the theory without losses essentially over predicts the mass flow rate. The last has direct economical implication due to unjustifiably increased separation distance.

Method of calculation	0.53 MPa	10.5 MPa	40 MPa
Under-expanded theory without losses	1.44	2.80	9.56
Under-expanded theory with losses	1.05	2.08	7.76
Large Eddy Simulation	1.05	2.10	8.10

Table 5–2. Mass flow rates (g/s) through 15 mm length and 0.75 mm diameter channel at different storage pressures (Molkov and Bragin, 2009).

There is somewhat over prediction by LES of mass flow rate at high pressures (see Table 5–2). It is thought due to the fact that LES results obtained in simulations with the ideal gas equation of state that is known to over predict mass flow rate compared to the Abel-Noble equation of state.

5.3. The similarity law for concentration decay in momentum-dominated jets

Unscheduled hydrogen releases from high pressure equipment and infrastructure will create highly under-expanded jets. This could lead to formation of a large flammable hydrogen-air envelope. The size of the flammable envelope is the deterministic separation distance from the release source. Indeed, if the flammable envelope (hydrogen concentration in air equal to the lower flammability limit of 4% by volume) reaches a location of air intake into high-rise buildings, then consequences for occupants and building structure can be catastrophic.

Presence of ignition source within the envelope could initiate severe jet fires, deflagration, and potentially deflagration-to-detonation transition. It has to be noted that thermal effects of jet fires and pressure effects of deflagration or detonation could override the separation distance determined by the size of flammable envelope. Thus, knowledge of laws describing hydrogen dispersion and flammable cloud formation, including axial concentration decay, for arbitrary jets with various parameters is essential for reliable hydrogen safety engineering.

In this section an overview of previous studies on non-reacting hydrogen jets emerging into the still atmosphere is given. The similarity law for prediction of axial concentration decay of a leaking gas for sub-sonic, sonic, and super-sonic jets is presented. The similarity law is shown to be valid in a wide range of conditions from expanded to highly under-expanded jets. It can be applied for calculation of deterministic separation distances informed by the size of the flammable envelope. The non-ideal behaviour of hydrogen at high pressures and the under-expansion of flow in a nozzle exit are taken into account.

5.3.1. Expanded jets

Ricou and Spalding (1961) demonstrated by using the dimensional analysis that when the fluid density is uniform, the Reynolds number is high, and the distance x from the nozzle along the jet axis is much larger the diameter of the orifice D, then the total mass flow rate $m(x)$, including entrained surrounding gas, through a cross-section at right angle to the jet axis, is proportional to x

$$m(x) = K_1 M_{0s}^{1/2} \rho^{1/2} x, \tag{5–18}$$

where the momentum flux of the jet at orifice is $M_0 = \rho_N U^2 \pi D^2 / 4$, ρ_N and ρ_S are the densities of the nozzle and the surrounding gas respectively, U is the velocity in the nozzle.

It was found experimentally (Ricou and Spalding, 1961): the equation for mass flow rate holds for non-uniform density without modification provided that buoyancy effects are negligible; a numerical constant K_1 has the value 0.282 irrespective of the density ratio; and the presence of combustion reduces K_1. The experimental data for isothermal injection of different gases (hydrogen, air, propane, carbon dioxide) into stagnant air can be held to obey the following simple relation that can be derived from (5–18)

$$\frac{m(x)}{m_N} = 0.32 \frac{x}{D} \sqrt{\frac{\theta_S}{\rho}}, \tag{5–19}$$

where m_N is the mass flow rate of the gas in the nozzle.

A mass fraction of fuel averaged through the jet cross-section area can be calculated as a reciprocal to the left-hand side of equation (5–19)

$$C_{av} = 3.1 \sqrt{\frac{\theta_N}{\rho}} \frac{D}{x}. \tag{5–20}$$

Please click the advert



GCHQ

TOP 100

INVESTORS IN PEOPLE

it's an interesting world

Get under the skin of it.

Graduate opportunities
Cheltenham | £24,945 + benefits

One of the UK's intelligence services, GCHQ's role is two-fold: to gather and analyse intelligence which helps shape Britain's response to global events, and, to provide technical advice for the protection of Government communication and information systems. In doing so, our specialists – in IT, internet, engineering, languages, information assurance, mathematics and intelligence – get well

TOP GOVERNMENT EMPLOYER

A mean mass fraction fuel on a jet axis is higher compared to the fuel mass fraction averaged through the jet cross-section. The axial concentration can be calculated by similarity laws (Chen and Rodi, 1980) for round and plane jets respectively

$$\frac{C_{ax}}{C_N} = 5.4\sqrt{\frac{\theta_N}{\rho}}\frac{D}{x} \quad \textit{(round jet)}, \tag{5–21}$$

$$\frac{C_{ax}}{C_N} = 2.13\sqrt{\frac{\theta_N}{\rho}}\sqrt{\frac{D}{x}} \quad \textit{(plane jet)}, \tag{5–22}$$

where C_N is the mass fraction of hydrogen in the nozzle (C_N=1 for pure hydrogen release).

Two important conclusions can be drawn from the similarity laws (5–21) and (5-22). The first conclusion is that for hydrogen jets to stagnant air the ratio of a distance, x=L, to a fixed concentration expressed in percents by mass, C_{ax}, to the nozzle diameter is a constant, i.e. L/D=const. This means, for example, that the distance to the lower flammability limit (separation distance) is proportional to the leak diameter. Thus, the design of hydrogen and fuel cell systems has to be carried out bearing in mind the requirement to minimise the internal diameter of piping to satisfy technological requirements to mass flow rate. The second conclusion is that a plane jet decays slower ($\propto \sqrt{D}$) compared to a round jet of the same size ($\propto D$). It is worth noting that this conclusion is valid for "infinite" plane jets. Plane jets with limited length to width ratio do not follow the similarity law (5-22) as has been demonstrated in recent research at the HySAFER Centre, at least at a far field where they are decaying similar to round jets (Molkov et al., 2010).

The mass fraction, C_M, can be calculated by the volumetric (mole) fraction, C_V, by equation

$$\frac{1}{C_M} = 1 + \left(\frac{1}{C_V} - 1\right)\frac{M_S}{M_N} \tag{5–23}$$

where M_S and M_N are molecular masses of surrounding gas (28.84 g/mol is accepted for air in calculations) and nozzle gas respectively. For example, mass fraction 0.0282 corresponds to volumetric fraction 0.295 (29.5% by volume of hydrogen in air – stoichiometric mixture), mass fraction 0.0.044365 corresponds to volumetric fraction 0.401 (40.1% – mixture with maximum burning velocity), 0.013037 – 0.16 (16%), 0.008498–0.11(11%), 0.005994–0.08(8%), 0.00288–0.04(4%), 0.00141–0.02(2%), 0.0007–0.01(1%).

For expanded jets the similarity laws (5–21) and (5–22) give for round (plane) jet the following ratios of a distance to particular axial hydrogen concentration (in percents by volume), L, to the characteristic nozzle size, D (with density ratio ρ_S/ρ_N=14.45): $(L/D)_{30\%}$=49.3 (379); $(L/D)_{8.5\%}$=222 (7689); $(L/D)_{4\%}$=493

(37854); $(L/D)_{2\%}$=1008 (157926); $(L/D)_{1\%}$=2029 (640760). For example, the distance to the lower flammability limit of hydrogen in air (4% by volume) in momentum-controlled expanded jets is equal to 493 nozzle diameters.

It is worth noting that the correlations (5–21) and (5–22) by Chen and Rodi (1980) were validated by concentration measurements in vertical jets up to value L/D=50 only. Their applicability above this range should be confirmed.

Shevyakov et al. (1980) published theoretical and experimental study on hydrogen concentration decay in unignited hydrogen jets into stagnant air. It was shown, in particular, that for momentum-controlled jets (at high nozzle Froude numbers $Fr=U^2/gD>10^5$) the dimensionless distance to 30% by volume of hydrogen $(L/D)_{30\%}$ is a constant 47.9. This is an excellent agreement with published independently at the same year 1980 work by Chen and Rodi (1980) that gives value 49.3. The theoretical formula derived by Shevyakov et al. (1980) gives an estimate for the flammable envelope length $(L/D)_{4\%}$=410, which is close to the Chen and Rodi's value of $(L/D)_{4\%}$=493.

5.3.2. Previous studies of under-expanded jets

Thring and Newby (1953) were probably the first to introduce the pseudo-diameter (or notional source/ nozzle diameter). They suggested that the pseudo-diameter is equal to $D_{eff} = D \sqrt{\rho / \rho_{eff}}$, where D_{eff} is the aperture of a jet through which the same mass flow rate of nozzle fluid would have emerged with the same jet momentum but with density ρ_{eff} instead of ρ. However, this relationship is valid only if flow velocity at the real and the notional nozzles are equal, which is not an obvious assumption.

Birch et al. (1984) assumed that the similarity law by Chen and Rodi (1980) could work not only for expanded but also for under-expanded jets. The behaviour of under-expanded jets was expected to be similar to classical free jets provided that an appropriate scaling factor is employed to describe the effective size of the jet source.

Authors stated that the resultant concentration field behaves as if it was produced by a larger source than the actual nozzle. Birch et al. (1984) demonstrated that for a 2.7 mm diameter round nozzle and pressures from 0.35 to 7.1 MPa the data for mean concentration of natural gas decay along the centreline, when plotted against the non-dimensional coordinate $x/(D\sqrt{p_R/p_S})$, where p_R is the pressure in storage tank, collapse onto a single curve.

The range of validation was L/D=30-170 (Birch et al., 1984). It was underlined that the notional nozzle does not necessarily exist in the physical sense – it is merely postulated to agree with chosen definition. The model by Birch et al. is built on the ideal gas law, the equation for conservation of mass between choked flow through an actual nozzle exit and a sonic flow through a notional nozzle exit. Other assumptions applied are: uniform sonic velocity after jet expansion to ambient pressure, and expanded flow temperature equal to initial temperature in the reservoir. Three years later Birch et al. (1987) published another paper that contributed to conclusions of the previous study.

Unfortunately, an incorrect form of the similarity law was reproduced by Birch et al. (1984, 1987). This error regrettably generated a number of misinterpretations of the similarity law in the hydrogen safety community. The incorrect equation (Birch et al., 1984, 1987) casts as

$$C_{ax}^{V} = 5.4 \quad . \qquad (5–24)$$

Downloadfreebooksatbookboon.com

There are three essential differences with the Chen and Rodi correlation for expanded jets (5–21) and equation (5–24) suggested by Birch et al. (1984, 1987) for under-expanded jets. Firstly, the volumetric fraction, C^V, was used instead of original mass fraction, C_{ax}, as in the original correlation (Chen and Rodi, 1980; Wang et al., 2008). Secondly, the density ratio applied by Birch et al. is reciprocal to the original. Thirdly, the notional nozzle exit diameter or effective diameter (D_{eff}) is applied instead of the actual nozzle diameter (D). These three critical differences with the original similarity law have generated inconsistencies in a number of following publications by different researchers trying to use the correlation in the form suggested by Birch et al., e.g. (BRHS, 2009; Houf and Schefer, 2008).

Birch and colleagues didn't validate the form of the correlation they publish. Instead, only the correlation between the inverse concentration (in volume fraction) and the axial displacement, x/D_{eff}, was presented in their paper (Birch et al., 1987). However, mass and volumetric fractions are changing practically linearly at values of natural gas concentrations at which measurements were carried out (6–50% by volume). This linearity provides a "good" looking correlation even without a right coefficient of proportionality.

There is another reason why Birch et al. (1984, 1987) and similar approaches cannot be applied to calculate concentration decay in jets from high pressures hydrogen equipment and storage, i.e. due to limitations for application of the ideal gas law at high pressures above 10 MPa. This is an essential problem with clear safety implications. Indeed, the ideal gas law overestimates the hydrogen mass flow rate from a 70 MPa storage by about 45% as can be estimated by the Abel-Noble equation.

Please click the advert

UNIVERSITY OF COPENHAGEN

The difference is your ambition!

Copenhagen Master of Excellence

are two-year master degrees taught in English at one of Europe's leading

Come to Copenhagen - *and aspire!*

Apply now at www.come.ku.dk

PHARMACEUTICAL SCIENCES
LIFE SCIENCES
COPENHAGEN
RELIGIOUS STUDIES
LAW
SOCIAL SCIENCES
HUMANITIES

Download free ebooks at bookboon.com

Thus, the guess by Birch and colleagues about the universal character of the similarity law (Chen and Rodi, 1980) yet has to be confirmed. The procedure of the similarity law application to under-expanded jets has to be developed and validated.

5.3.3. The similarity law for expanded and under-expanded jets

If the similarity law (Chen and Rodi, 1980) is applicable in its original form (5–21) for both expanded and under-expanded jets, then the calculation of deterministic separation distances for unignited hydrogen round jets would be straight forward by equation (5–21). However, for under-expanded jets there will be one unknown parameter, i.e. a density of gas in the actual nozzle exit, ρ_N. This density can be calculated by one of justified under-expanded theories, e.g. without losses (Molkov et al., 2009) or with losses (Molkov and Bragin, 2009). For expanded hydrogen jets the application of the similarity law (5–21) is straight forward with hydrogen density at the nozzle exit ρ_N=0.0838 kg/m^3 (NTP).

The similarity law for concentration decay along the axis of the momentum-controlled jets is shown in Fig. 5–5 along with experimental data for hydrogen under-expanded releases. It is based on the hypothesis of using the original form of the similarity law by Chen and Rodi (1980) with the only unknown parameter being the density of hydrogen at the nozzle exit (Molkov, 2009a). Only 60 of total 302 experimental points in the momentum-controlled regime are presented in Fig. 5–5 to avoid overlapping of data on the graph (Molkov et al., 2010). These 60 points are the maximum and minimum values of each experiment and in some cases an additional intermediate value. The validation of the similarity law with use of the under-expanded theory for calculation of hydrogen density in the actual nozzle exit was carried out against experimental data described in details below.

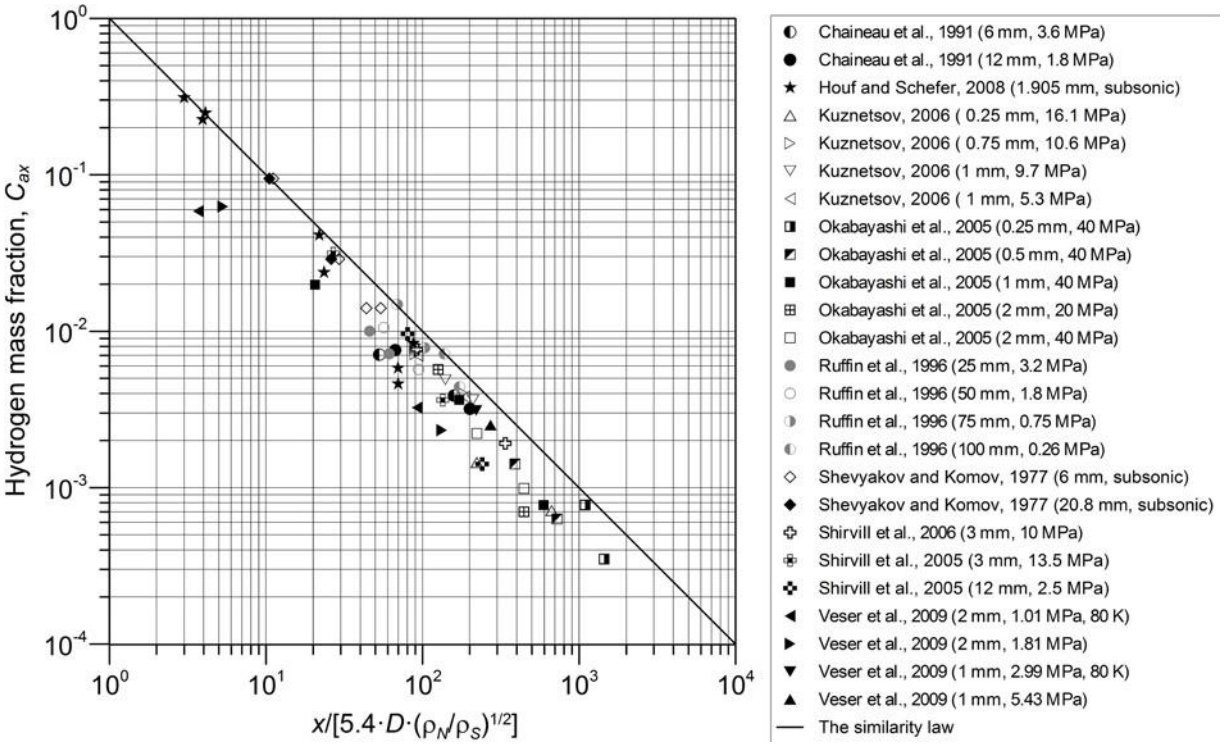


Figure 5–5. The similarity law (solid line) and experimental data on axial concentration decay in momentum-controlled expanded and under-expanded hydrogen jets.

Download free ebooks at bookboon.com

Shevyakov et al. (1977) conducted a series of subsonic releases from nozzle diameter from 6 mm to 96 mm and hydrogen velocity in the nozzle ranging from 2.52 m/s to 861.21 m/s. The regime of each release (buoyancy- or momentum-dominated) was determined by a value of Froude number. $Fr = U^2/(g \bullet D)$. Only momentum-controlled jets were selected here for the validation of the similarity law. Data for 4 releases with nozzle diameter of 6 mm and 2 releases with nozzle diameter of 20.8 mm are given in Table 3–5.

Test	T_R	D	p_t	ρ_N	x	$C_{ax\text{-}v}^{\ a}$	$C_{ax\text{-}m}^{\ b}$	
	K	mm	MPa	kg·m^{-3}	m	Volume fraction	Mass fraction	$\frac{x}{5.4 \cdot D \cdot \sqrt{\frac{\rho_N}{\rho_S}}}$
Chaineaux et al. (1991)	207	6	3.6**	2.58	7.50	0.053	0.0039	158.7
Chaineaux et al. (1991)	207	6	3.6**	2.58	2.50	0.093	0.0071	52.9
Chaineaux et al. (1991)	174	12	1.8***	1.56	15	0.044	0.0032	200.6
Chaineaux et al. (1991)	174	12	1.8***	1.56	5	0.099	0.0076	66.9
Houf and Schefer (2008)	298*	1.905	-	0.08	0.24	0.108	0.0084	87.3
Houf and Schefer (2008)	298*	1.905	-	0.08	0.01	0.866	0.3108	3.0
Houf and Schefer (2008)	298*	1.905	-	0.08	0.19	0.078	0.0058	69.7
Houf and Schefer (2008)	298*	1.905	-	0.08	0.06	0.382	0.0412	21.9
Houf and Schefer (2008)	298*	1.905	-	0.08	0.01	0.826	0.2484	4.1
Houf and Schefer (2008)	298*	1.905	-	0.08	0.19	0.062	0.0046	69.8
Houf and Schefer (2008)	298*	1.905	-	0.08	0.06	0.259	0.0238	23.5
Houf and Schefer (2008)	298*	1.905	-	0.08	0.01	0.807	0.2257	3.9
Kuznetsov (2006)	287	0.25	16.1	7.68	2.25	0.010	0.0007	666.6
Kuznetsov (2006)	287	0.25	16.1	7.68	0.75	0.020	0.0015	222.2
Kuznetsov (2006)	287	0.75	10.6	5.25	1.50	0.055	0.0040	179.2
Kuznetsov (2006)	287	0.75	10.6	5.25	0.75	0.094	0.0072	89.6
Kuznetsov (2006)	287	1	9.7	4.84	2.25	0.050	0.0036	210.1
Kuznetsov (2006)	287	1	9.7	4.84	1.50	0.066	0.0049	140.0
Kuznetsov (2006)	287	1	5.3	2.73	1.50	0.052	0.0038	186.5
Kuznetsov (2006)	287	1	5.3	2.73	0.75	0.092	0.0070	93.3
Okabayashi et al. (2005)	288	2	20	9.29	13.22	0.010	0.0007	444.4
Okabayashi et al. (2005)	288	2	20	9.29	3.74	0.076	0.0057	125.9
Okabayashi et al. (2005)	288	0.25	40	16.45	7.15	0.005	0.0003	1444.4
Okabayashi et al. (2005)	288	0.25	40	16.45	5.41	0.011	0.0008	1092.6
Okabayashi et al. (2005)	288	0.5	40	16.45	7.15	0.009	0.0006	722.2
Okabayashi et al. (2005)	288	0.5	40	16.45	3.85	0.020	0.0014	388.9

Table 5–3 (Part I). Data on concentration decay in hydrogen under-expanded jets.

Download free ebooks at bookboon.com

Test	T_R	D	p_t	ρ_N	x	$C_{ax\text{-}v}^{a}$	$C_{ax\text{-}m}^{b}$	$\frac{x}{5.4 \cdot D \cdot \sqrt{\frac{\rho_N}{\rho_S}}}$
	K	mm	MPa	kg·m^{-3}	m	Volume fraction	Mass fraction	
Okabayashi et al. (2005)	288	1	40	16.45	11.73	0.011	0.0008	592.6
Okabayashi et al. (2005)	288	1	40	16.45	3.39	0.050	0.0036	171.3
Okabayashi et al. (2005)	288	1	40	16.45	0.41	0.225	0.0198	20.6
Okabayashi et al. (2005)	288	2	40	16.45	17.59	0.014	0.0010	444.4
Okabayashi et al. (2005)	288	2	40	16.45	8.79	0.031	0.0022	222.2
Okabayashi et al. (2005)	288	2	40	16.45	3.52	0.101	0.0078	88.9
Ruffin et al. (1996)	288	25	3.24#	1.79	10.00	0.094	0.0072	61.2
Ruffin et al. (1996)	288	25	3.24#	1.79	7.50	0.127	0.0100	45.9
Ruffin et al. (1996)	288	50	1.8#	1.18	25	0.076	0.0057	94.2
Ruffin et al. (1996)	288	50	1.8#	1.18	15	0.133	0.0106	56.5
Ruffin et al. (1996)	288	75	0.75#	0.63	30	0.102	0.0078	103.3
Ruffin et al. (1996)	288	75	0.75#	0.63	20	0.178	0.0149	68.9
Ruffin et al. (1996)	288	100	0.26#	0.35	50	0.060	0.0044	172.2
Ruffin et al. (1996)	288	100	0.26#	0.35	40	0.094	0.0072	137.8
Shevyakov et al., (1977)	288	6	-	0.08	0.37	0.170	0.0141	43.8
Shevyakov et al., (1977)	288	6	-	0.08	0.46	0.170	0.0141	54.0
Shevyakov et al., (1977)	288	6	-	0.08	0.10	0.600	0.0945	11.1

Table 5–3 (Part II). Data on concentration decay in hydrogen under-expanded jets.

Please click the advert



Download free ebooks at bookboon.com

Test	T_R	D	p_t	ρ_N	x	$C_{ax\text{-}v_a}$	$C_{ax\text{-}m_b}$	$\frac{x}{5.4 \cdot D \cdot \sqrt{\frac{\rho_N}{\rho_S}}}$
	K	mm	MPa	kg·m^{-3}	m	Volume fraction	Mass fraction	
Shevyakov et al., (1977)	288	6	-	0.08	0.25	0.300	0.0290	29.3
Shevyakov et al., (1977)	288	20.8	-	0.08	0.77	0.300	0.0290	26.1
Shevyakov et al., (1977)	288	20.8	-	0.08	0.31	0.600	0.0945	10.5
Shirvill et al. (2006)	287	3	10	4.98	11.00	0.027	0.0019	337.2
Shirvill et al. (2006)	287	3	10	4.98	3.00	0.100	0.0076	92.0
Shirvill et al. (2005)	287	3	13.5	6.57	9.00	0.020	0.0014	240.4
Shirvill et al. (2005)	287	3	13.5	6.57	3.00	0.122	0.0096	80.1
Shirvill et al. (2005)	287	12	2.5	1.32	9.00	0.050	0.0036	134.3
Shirvill et al. (2005)	287	12	2.5	1.32	1.80	0.318	0.0315	26.9
Veser et al. (2009)	298	1	5.43	2.70	2.20	0.035	0.0025	271.8
Veser et al. (2009)	298	1	5.43	2.70	0.19	0.272	0.0253	23.5
Veser et al. (2009)	80	1	2.99	5.32	2.50	0.043	0.0031	219.9
Veser et al. (2009)	80	1	2.99	5.32	0.19	0.368	0.0389	16.7
Veser et al. (2009)	298	2	1.01	1.88	0.05	0.472	0.0585	3.70
Veser et al. (2009)	298	2	1.01	1.88	1.25	0.045	0.0032	92.44
Veser et al. (2009)	80	2	1.81	0.92	0.05	0.490	0.0627	5.29
Veser et al. (2009)	80	2	1.81	0.92	1.25	0.032	0.0023	132.19

Notes. T_R – temperature measured in the storage reservoir or nozzle (* - assumed); p_t – discharge pressure at sampling time; ** – pressure given 5 s after discharge initiation; *** - pressure given 2 s after discharge initiation; # – pressure calculated 2 s after discharge initiation using the under-expanded jets theory and blowdown model (Molkov et al., 2009); [a] – experimental data (axial volumetric fraction of hydrogen); [b] – mass fraction calculated from volumetric fraction.

Table 5–3 (Part III). Data on concentration decay in hydrogen under-expanded jets.

Chaineaux et al. (1991) conducted experiments to measure the axial concentration decay along the axis of horizontal jets of hydrogen and methane in air. They used a cylindrical vessel 0.12 m^3 (55 cm diameter and 55 cm height) pressurized to 10 MPa and placed by its rear side against a wall, with vessel axis 2.2 m above the ground. An outlet tube of 50 mm diameter was attached to the vessel. A steel plate with a hole was at the end of the tube at some distance from the pyrotechnic valve. The jet exit orifice diameters for hydrogen experiments were set at 5 mm (tests 1 and 2), 12 mm (tests 3 and 4) and 24 mm (tests 5, 6 and 7). The measurements of hydrogen concentration along jet axis were done by sampling the mixture at defined locations and times using stainless steel sampling bulbs of volume 150 cm^3 attached to vertical masts disposed along jet axis. Authors assumed the jet is "stabilized" (quasi-steady state) when the flammable cloud reaches its maximum volume. At the moment of stabilisation of the jet the pressure in the vessel has decreased from its initial value to lower pressure. For each experiment, Chaineaux and colleagues gave hydrogen concentration (% by vol.) at various locations, initial temperature in the vessel before gas venting, the minimum temperature in the vessel and the time at which this temperature was reached, as well as the residual pressure in the tank at each sampling time. For example, in test 2 the minimum temperature in the tank reached -104°C at 19 seconds after the start of release.

Download free ebooks at bookboon.com

Among 7 tests carried out with hydrogen only 2 were considered as valid by Chaineaux et al. (tests 2 and 3). Test 1 was used for calibration, test 4 resulted in spontaneous ignition, test 5 was not valid due to displacement of a mast supporting sampling bulbs, and tests 6 and 7 were, according to authors, not "stabilized" due to large orifice diameter of 24 mm. The maximum and minimum values of measured concentrations for the tests 2 and 3 (Chaineaux et al., 1991) are presented in Table 5–3.

Ruffin et al. (1996) measured the axial concentration decay in the sub-sonic region of hydrogen and methane jets in air, where the Mach number $M<0.3$. They exploited a 5 m^3 volume tank at initial pressure and temperature prior to venting 4 MPa and 288 K respectively. The tank was vented through a horizontal pipe fitted with an orifice at its outer end. To ensure the ground had no effect on the development of the jet, the experimental rig was placed on the edge of a cliff 5 m above the ground with 100 m free space along the axis.

Four experiments with hydrogen release were carried out with different orifice diameter of 25, 50, 75 and 100 mm (Ruffin et al., 1996). Three concentration sensors used in this study, i.e. pellistors placed on a tube equipped with a vacuum pump, were located in the sub-sonic part of the jet and continuously drew the mixture at various distances from the nozzle depending on the nozzle diameter. Sensors with response time less than 1 s were mounted on thin cables positioned perpendicularly to the flow. The change in hydrogen concentration measured by different sensors as a function of time during tank's blow down was analysed. Authors suggested that it is only after the sensors have detected the maximum concentration and before the gas flow from the tank has fallen too low that a quasi-steady state can be assumed. For that reason they consider only results obtained within about 2 seconds after the onset of venting.

Unfortunately, there is no data on transient pressure within the vessel for experiments (Ruffin et al., 1996). Therefore, the under-expanded jet theory and blow-down model (Molkov et al., 2009) was applied to calculate the 2 first seconds of the blow-down of the tank for 4 experiments with different orifice diameter of 25, 50, 75 and 100 mm respectively. These calculations showed that for diameters 50, 75 and 100 mm the pressure felt after 2 seconds of release to pressures 1.79, 0.746 and 0.257 MPa respectively. The maximum and minimum values for each of the 4 experiments are given in Table 5–3, thus representing eight points. The experimental data of Ruffin et al. (1996) are partially processed using the under-expanded theory and therefore, are represented in grey in Fig. 5–5.

Okabayashi et al. (2005) investigated realistic accidental release scenarios for hydrogen refuelling stations. The experiments were performed to assess the safety of flammable gas dispersion from high pressure vessel, firstly for a steady pinhole leakage from a micro crack and secondly unsteady large-scale leakage. Five cylinders of 50 litres capacity each at pressure of 65 MPa were used, while tests were performed at lower release pressure. No data on the cylinders temperature was given in the paper. High pressure hydrogen storage of 65 MPa allowed to provide pressure 40 MPa just before the nozzle to the atmosphere.

Download free ebooks at bookboon.com

There was a 25 mm diameter piping system between vessels and the nozzle. A valve was controlling the gas release immediately upstream of the nozzle. Four tests were performed with release pressure 40 MPa, measured just upstream of the nozzle, with different nozzle diameters: 0.25 mm (5 measurement points in different locations), 0.5 mm (3 points), 1.0 mm (21 points) and 2.0 mm (6 points), and one test at release pressure of 20 MPa with nozzle diameter 2.0 mm (5 points).

The releases (Okabayashi et al., 2005) were carried out from the nozzles located 1 m above the ground at low wind velocities less than 1 m/s. Eight sensors were located at distance 4, 6, 8, 11, 15, 20, 30 and 50 m from the nozzle and mounted on vertical poles. Authors plotted the time averaged volumetric concentrations of hydrogen along the jet axis against a non-dimensional distance from the nozzle, x/θ, where $\theta = D \cdot \sqrt{\rho_N / \rho_S}$. Unfortunately, it is not clear from the paper where density ρ_N was calculated – at

actual or notional nozzle exit. In assumption that ρ_N was calculated at the actual nozzle exit, the similarity law for axial hydrogen concentration decay (5–21) can be rewritten in the form $C_{ax-m} = 5.4 \bullet \theta / x$. The

maximum and minimum values for each of 5 experiments (Okabayashi et al., 2005) are plotted in Fig. 5–5. In addition, an intermediate point for 2 experiments with release diameter 1 mm and 2 mm (both at 40 MPa) are included to validate the similarity law.

In 2005–2006 a series of experiments was performed by Shell Global Solutions (UK) and Health and Safety Laboratory (UK) to characterize the hazards arising from reacting and non-reacting hydrogen release from pressurized vessels (Shirvill et al., 2005, 2006). Some experiments were carried out to investigate

Please click the advert

Download free ebooks at bookboon.com

Question:
What do Skype and Spotify have in common with color screen graphics and the computer mouse?

–They are all Swedish inventions.

STUDYINSWEDEN.SE



Be innovative. Study in Sweden

Download free ebooks at bookboon.com

the size of the flammable envelope for unignited free jets at low and high pressures. The low pressure system was composed of four multi-cylinder packs of 17 cylinders each with an initial pressure of 17.3 MPa, capable of maintaining a constant discharge pressure of 2.6 MPa for 2 minutes. The authors used two discharge orifice diameters of 6 mm and 12 mm and three discharge pressures of 0.6 MPa, 1.6 MPa and 2.6 MPa.

The high pressure system (Shirvill et al., 2005, 2006) was composed of eight multi-cylinder packs of 17 cylinders each with the same initial pressure of 17.3 MPa, capable to maintain a constant discharge pressure for a few seconds with the largest discharge orifice diameter of 12 mm. Orifice diameter of 1, 3, 4, 6 or 12 mm and discharge pressures in a range 1.1–15.1 MPa were applied in experiments. All releases were horizontal, 1.5 m above the ground. The hydrogen jet was initiated by a release valve. The pressure was recorded in the pipe on both side of the release valve and the hydrogen temperature was recorded close to the nozzle, downstream of the release valve.

The hydrogen concentration was derived (Shirvill et al., 2005, 2006) from continuous measurements of the oxygen concentration within the jet using sensors, assuming any decrease of oxygen concentration was caused by displacement by hydrogen. Oxygen concentration was measured using self-powered electrochemical oxygen sensors located 1.0, 1.5 and 2.0 m above the ground and orientated with opening perpendicular to the gas flow direction. Authors reported hydrogen concentration (% by vol.) as a function of time at each sensor location. The jet was assumed stabilized when the maximum concentration at each sensor was reached and remained steady for several seconds. The results of two experiments (2.5 MPa and 13.5 MPa) are available in (Shirvill et al., 2005) and of one experiment (10 MPa) in (Shirvill et al., 2006). The maximum and minimum values for each of the three selected experiments are shown in Table 5–3.

Kuznetsov (2006) conducted experiments to analyse hydrogen distribution in horizontal free turbulent jet in a compartment with an internal volume of 160 m^3. Experimental facility included a high pressure gas system with bundles at 30 MPa to provide hydrogen release at quasi-steady pressures in the range 2–26 MPa through a nozzle of diameter from 0.16 mm to 1 mm. The high pressure gas system with pressure and flow rate control used high speed valves and Prandtl type Pitot tubes. Hydrogen concentration profile and flow velocity were simultaneously measured at distances 0.75, 1.5, and 2.25 m from the nozzle using ultrasonic hydrogen sensor with accuracy of ±0.1%. A total of 8 experimental points from (Kuznetsov, 2006) are shown in Table 5–3 (maximum and minimum values of 4 experiments).

Veser et al. (2009) performed experiments to investigate the hydrogen distribution in a horizontal jet. The pressure, temperature and mass flow rate were regulated by using a bypass configuration. The gas was released into an attached 60 mm long pipe with inner diameter 10 mm. Pressure and temperature in the pipe were measured. The pipe fed an orifice of diameter 1, 2 or 4 mm at pressures 0.5–6.0 MPa. The exiting gas was released at temperature 35 K, 65 K, 80 K or 298 K. Orifices were positioned 0.9 m above

Download free ebooks at bookboon.com

the ground and the jet, horizontally orientated and adjusted by laser, was released into a 5.5×8.5×3.4 m test chamber with air at ambient temperature. The temperature was measured using type K thermocouples with uncertainty ±2K and the maximum error of pressure sensors was ±0.5%. Hydrogen concentrations were measured using spherical gas probes of volume 0.3 dm^3 disposed at different locations along the jet axis. The probes content was analysed after experiments with uncertainty ±0.1%.

Houf and Schefer (2008) measured hydrogen concentration decay in small subsonic hydrogen jets. The hydrogen concentration was determined using planar laser-Rayleigh scattering. The laser sheets were imaged on a CCD camera, where concentration contours can be determined. They plot the axial time averaged hydrogen concentration along jet axis for vertical jets. The sub-sonic releases were all performed using a 1.905 mm diameter orifice and hydrogen density at the nozzle exit was 0.0838 kg/m^3. The results of 3 different experiments were published with flow velocity at the nozzle exit ranging from 49 m/s to 133 m/s. For each of 3 tests, three points (the maximum and minimum values plus one intermediate point) are presented in Table 5–3 and in Fig. 5–5.

To perform analysis of data (Veser et al., 2009) presented in the form of the reciprocal of hydrogen concentration in air by volume versus normalized distance from the nozzle, additional information on pressure in the nozzle was acquired (Kuznetsov M, 2010). Four experiments were analysed: 2 experiments with hydrogen stored at ambient temperature and released through 1 mm diameter nozzle at 5.43 MPa and through 2 mm diameter nozzle at 1.01 MPa; and 2 experiments with hydrogen stored at very low temperature of 80 K and released through 1 mm diameter nozzle at 2.99 MPa and through 2 mm diameter nozzle at 1.81 MPa.

The similarity law in its original form (Chen and Rodi, 1980) is validated here against 60 representative experimental points on axial concentration decay of pure hydrogen momentum-controlled subsonic, sonic and supersonic jets, released from vessels of different volume pressurized up to 40 MPa, and through nozzles with diameter from 0.25 mm to 100 mm. Hydrogen concentration in air was measured in the range from 1% to 86.6% by volume. The similarity law is validated for the ratio of distance from a nozzle to the nozzle diameter in the range x/D=4-28580, which is essentially beyond the maximum ratio in previous studies, e.g. expanded jets up to x/D=50 (Chen and Rodi, 1980), and under-expanded jets x/D=30-170 (Birch et al., 1984).

Laminar and turbulent, expanded and under-expanded momentum-controlled jets were used to validate the universal character of the similarity law in the original form suggested by Chen and Rodi (1980). The transition from laminar to turbulent flows for hydrogen is at Re=2000–2300 as reported by (Hawthorne et al., 1949) and (Shevyakov and Komov, 1977) respectively. Reynolds number changes in used

Download free ebooks at bookboon.com

experimental data from laminar Re=927 to highly turbulent Re=9.44×10^6.

It is worth noting that cold jets with initial storage gas temperature down to 80 K (Veser et al., 2009) obey the similarity law also. It was suggested in one of previous studies (Sunavala et al., 1957) to introduce a square root of ratio of surrounding temperature to gas temperature in the nozzle into the similarity law. This ratio does not appear to be necessary.

Figure 5–5 shows that all the experimental points are on or below the similarity law line. This is thought due to friction and minor losses in experimental equipment, which were not accounted for when the under-expanded jet theory without losses (Molkov et al., 2009) was applied. Indeed, from the similarity law equation it follows that if losses decrease pressure at the nozzle exit, and then they reduce hydrogen density and therefore the concentration in the jet for a fixed distance from the nozzle. This is equivalent to shifting experimental points down on the graph. If the spouting pressure (actual nozzle exit pressure) is applied instead of the pressure in a storage tank the difference between the similarity law curve and experimental data would reduce to zero in the limit. The universal character of the similarity law for both expanded and under-expanded jets makes it an efficient tool for hydrogen safety engineering.

5.3.4. The nomogram for concentration decay calculation in unignited jets

The nomogram for graphical calculation of hydrogen concentration decay by the similarity law and the under-expanded jet theory without losses is shown in Fig. 5–6. The nomogram includes four core graphs

Please click the advert

STUDY FOR YOUR MASTER'S DEGREE IN THE CRADLE OF SWEDISH ENGINEERING

Chalmers University of Technology conducts research and education in engineering and natural sciences, architecture, technology-related mathematical sciences and nautical sciences. Behind all that Chalmers accomplishes, the aim persists for contributing to a sustainable future – both nationally and globally.

Visit us on Chalmers.se or Next Stop Chalmers on facebook.



Download free ebooks at bookboon.com

("Volumetric to mass fraction", "The similarity law", "Choose leak diameter", and "Choose density in the nozzle exit") and one additional graph "Calculate density in the nozzle exit by storage tank pressure and temperature" (based on calculations by the under-expanded jet theory without losses). Let us demonstrate how to use the nomogram to calculate the distance from the nozzle of 1 mm diameter to concentrations of hydrogen in air 4% (dash line, corresponds to the lower flammability limit of hydrogen in air) and 11% (solid line, corresponds to the average location of jet flames tip, see section "Jet fires") by volume along the axis of a release from a storage tank at pressure 70 MPa and temperature 300 K.

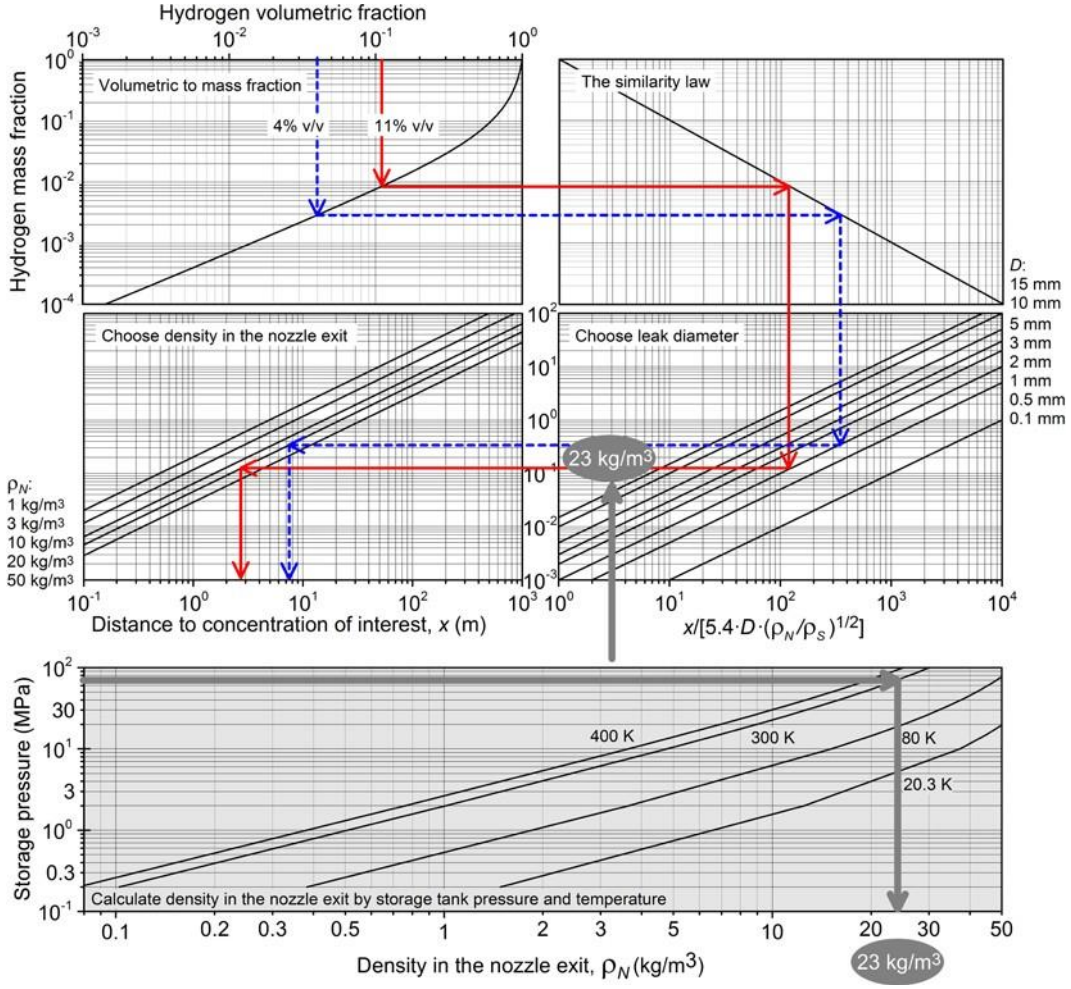


Figure 5–6. The nomogram for concentration decay calculation in unignited jets.

Firstly, the line from the axis "Hydrogen volumetric fraction" is drawn downward from the chosen concentration of interest (4% and 11% by volume in our example) until the intersection with the line of the graph "Volumetric to mass fraction". Secondly, the horizontal line from this intersection point is drawn to the intersection with the similarity law line at the right top graph "The similarity law". Thirdly, the vertical line is drawn downward until intersection with line "1 mm" at the graph "Choose leak diameter". There are eight lines on "Choose leak diameter" graph which correspond to the following leak diameters (from top to bottom): 15 mm, 10 mm, 5 mm, 3 mm, 2 mm, 1 mm, 0.5 mm, 0.1 mm).

Download free ebooks at bookboon.com

The legend is shown at the right side of the graph.

The fourth stage is to calculate the density using the additional graph "Calculate density in the nozzle exit by storage tank pressure and temperature" at the bottom of the nomogram using given pressure (70 MPa) on the ordinate axis and a line corresponding the chosen temperature (300 K). This is shown by two thick grey lines on the "Calculate density in the nozzle exit by storage tank pressure and temperature" graph. Calculated graphically density at the nozzle exit for 70 MPa and 300 K is about 23 kg/m^3.

The calculated value of density of 23 kg/m^3 is applied at the fifth stage of calculations to draw the horizontal line from the intersection with "1 mm" line at the "Choose leak diameter" graph to the left until the intersection with an imaginary line corresponding to 23 kg/m^3 at the "Choose density in the nozzle exit" graph (between two shown on the graph lines 20 kg/m^3 and 50 kg/m^3). There are five lines at the graph corresponding to densities 1 kg/m^3, 3 kg/m^3, 10 kg/m^3, 20 kg/m^3, and 50 kg/m^3 from top to bottom respectively. The legend is shown at the left side of the graph.

The final stage is to draw the vertical line downward from the intersection with the line 23 kg/m^3 to the intersection with abscissa axis of the "Choose density in the nozzle exit" graph. Thus, the calculated graphically distance from the nozzle exit to hydrogen concentration of 4% by volume is about 7.7 m, and to concentration of 11% by volume is about 2.7 m. The calculation by the equation for similarity law (5–21) with the accurate value of the density at the nozzle calculated by the under-expanded jet theory (23.95 kg/m^3) and air density of 1.205 kg/m^3 (NTP) is 8.36 m for 4% and 2.83 m for 11%. The error of graphical calculations is at the acceptable level of below 10%.

The similarity law forunder-expanded jets and the nomogram are performance-based tools forcalculation of deterministic separation distances for unignited releases as the alternative to prescriptive codes. For instance, the International Fire Code (2006) presents a table of prescribed separation distances between a hydrogen system and various potential targets, including air intake to building. However, this code does not provide or require any information either on the hydrogen storage parameters (pressure and temperature) and leak size from the system. This code is an example of archaic prescriptive approach that contradicts to modern requirements to codes and standards to be performance-based.

The standard NFPA 55 (2010) made one step further compared to the prescriptive International Fire Code (2010), by presenting a set of 4 equations to calculate separation distances to the axial concentration of 4% by volume of hydrogen in air. Unfortunately, there are two weak points in NFPA 55 (2010) from author's point of view. To "simplify" the use of the methodology by practitioners each of 4 equations is assigned to a quite wide range of pressures. This is resulted in "programmed" over-prediction and under-prediction of separation distance depending on the storage pressure. However, the most serious disadvantage in calculation of separation distance by NFPA 55 (2010) is the use of a leak size of only 3% of the flow area of the pipe (this choice is based on leak frequencies of other gases available to gas industry).

Indeed, the similarity law states that for the same density of hydrogen in the nozzle exit ρ_N, i.e. for the same storage pressure, the separation distance is directly proportional to leak diameter. If, the questionable

Powered by free books at bookboon.com

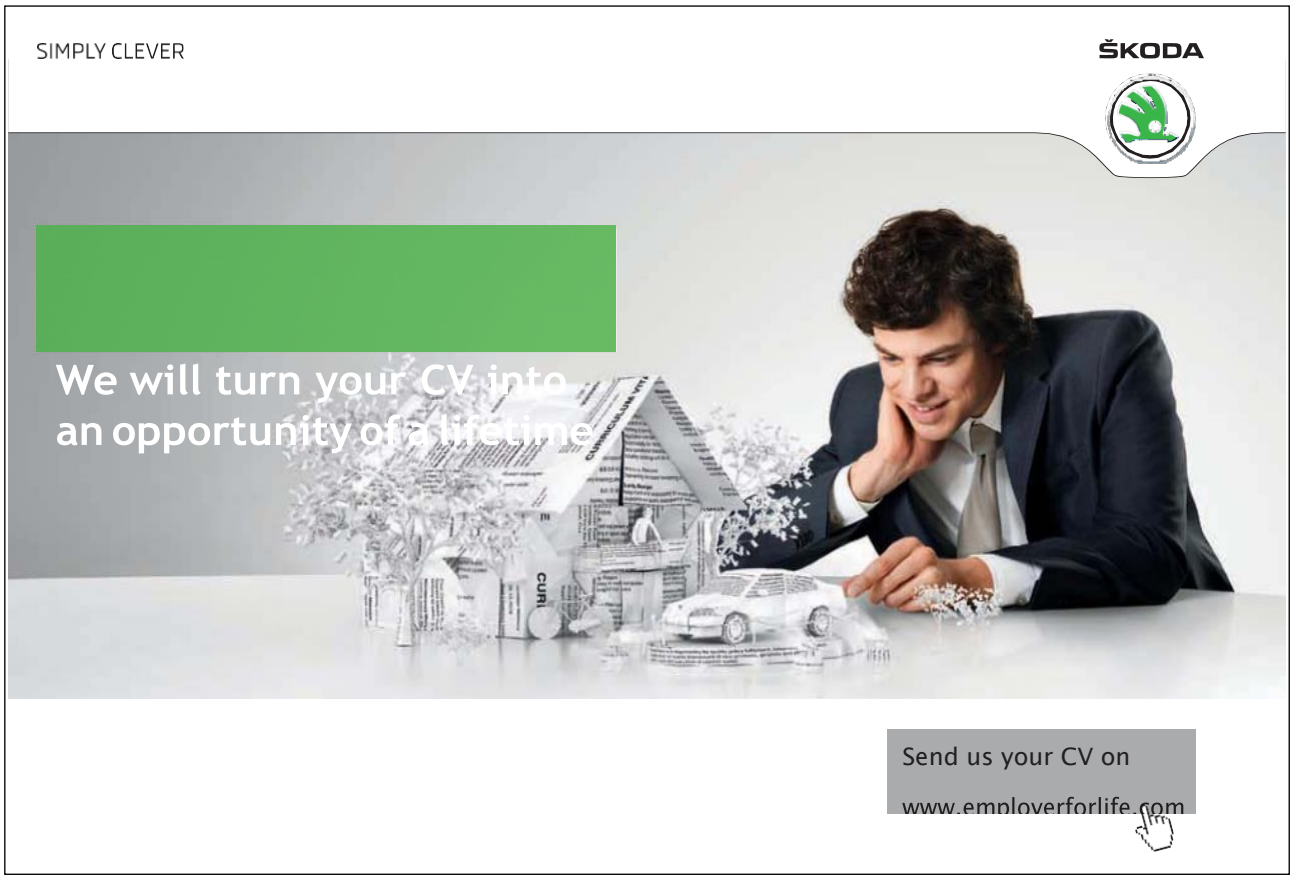
by author choice of a leak size as 3% of cross-section area of the pipe in NFPA 55 (2010) results in the "prescribed" decrease of separation distance by reciprocal to square root from 0.03, i.e. by 5.77 times. It is clear that in case of full bore rupture of the hydrogen pipe consequences could be catastrophic if this "3%" approach is widely applied and enforced by regulators. The risk-informed approaches cannot compromise the science-informed engineering design. The alternatives to this "forced" decrease of separation distance is safety engineering design of hydrogen systems, e.g. reduction of pressure in the pipe when possible and the pipe diameter to the minimum size required by the technological reasons and/or substitution of one large pipe by a number of smaller pipes, use of PRD with enhanced safety characteristics, etc.

The conclusion can be drawn that the similarity law calculates separation distance more accurately compared to currently available standards and codes. This methodology is scientifically underpinned and can account for friction and minor losses in a leak pathway when necessary. Last but not least the hydrogen safety engineering guarantees the freedom to consider worst-credible scenario of full bore rupture rather than the questionable 3% of cross section area of pipe approach as suggested by some codes and standards.

5.4. Concentration decay in transitional and buoyancy-controlled jets

All jets can be divided into three types based on the effect of buoyancy. These jet types are shown schematically in Fig. 5–7 for a horizontal jet. Fully momentum-controlled jets are not affected by buoyancy. Fully buoyancy-controlled jets are quickly diverted from the horizontal to vertical flow

Please click the advert



direction. Third type of jets that can be called transitional have momentum-dominated part closer to the nozzle and buoyancy-controlled flow further downstream when jet velocity drops and jet diameter increases. For hydrogen safety engineering it is important to know when this transition takes place. This has direct implication on the separation distance and thus safety and costs of hydrogen system or infrastructure.

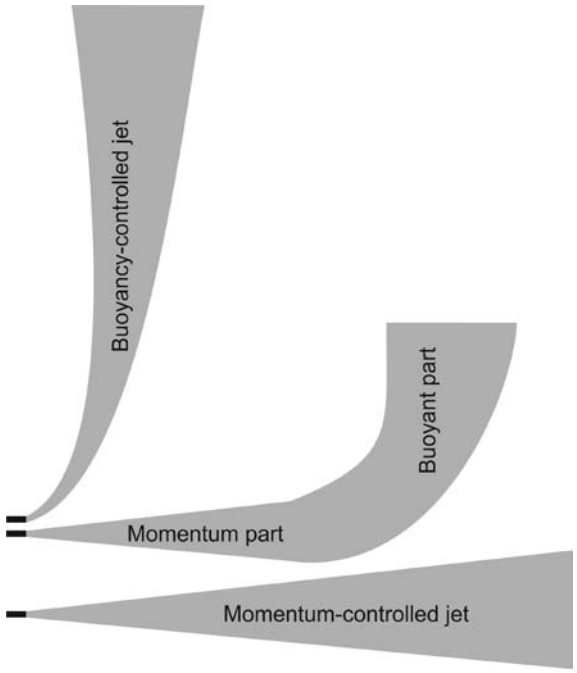


Figure 5–7. Fully momentum-controlled jet (bottom), transitional jet (middle), and fully buoyancy-controlled jet.

The engineering technique presented here to qualify a hydrogen jet (both expanded and under-expanded) or its part as momentum-controlled, and the rest of the jet downstream as buoyancy-controlled, is based on the work by Shevyakov et al. (1980, 2004) that was carried out with expanded jets only. Figure 5–8 shows in logarithmic coordinates the dependence of the distance to nozzle diameter ratio x/D (ordinate) for particular concentration of hydrogen in air on the Froude number (abscissa) in its classical form

$$Fr = \frac{U^2}{gD}, \tag{5–25}$$

where U is the velocity at the nozzle exit (notional nozzle exit for under-expanded jets) in m/s, g is the gravitational acceleration (standard acceleration of gravity on Earth is 9.80665 m/s^2), and D is the nozzle diameter (notional nozzle exit diameter for under-expanded jet) in meters. For under-expanded jets in Fig. 5–8 the notional nozzle exit diameter and velocity at the notional nozzle exit were calculated by the under-expanded jet theory (Molkov et al., 2009). Both expanded and under-expanded jets obey the same functional dependence with accuracy 20% acceptable for engineering applications.

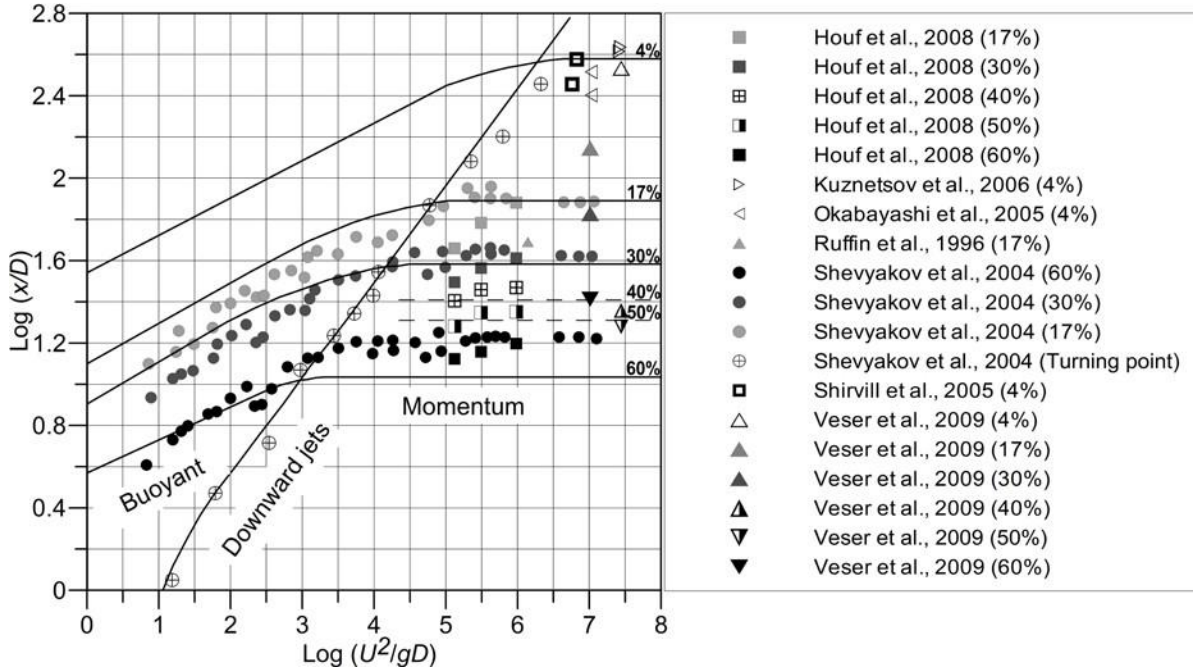


Figure 5–8. The dependence of the distance to nozzle diameter ratio for particular concentration of hydrogen in air on the Froude number.

Five theoretical curves (solid lines) by Shevyakov et al. (1980, 2004), experimental data for expanded jets (Shevyakov et al., 1980, 2004), and data of other researchers for under-expanded jets are shown in Fig. 5–8. Practically all under-expanded jets in hydrogen incidents/accidents will be in the momentum-controlled regime as follows from available tests applied to validate the correlation in Fig. 5–8. Four of five theoretical curves in the graph are related to hydrogen concentrations of 4%, 17%, 30%, and 60% by volume respectively. Each of these four curves has an ascending buoyant part and a momentum "plateau" part.

It is important to stress that the Froude number at transition from the buoyant part of the curve to the momentum part depends on the concentration of hydrogen under consideration. For example, at axial concentration of hydrogen 60% by volume the jet stays in momentum-controlled regime until *Log* (*Fr*)>3.5, while for the jet to be in the momentum-controlled regime at axial location where hydrogen concentration drops to 4% by volume (LFL) the nozzle exit Froude number has to be much higher, i.e. *Log* (*Fr*)>6.5 (three orders of magnitude higher).

The fifth curve in Fig. 5–8 "Downward jets" is of special interest for hydrogen safety engineering. It gives for a jet directed vertically downward a dimensionless distance from the nozzle to the turning point, where the jet changes direction of flow from downward to upward. To calculate the distance to turning point only knowledge of the Froude number at the nozzle (notional nozzle) is required. The fifth curve intersects each of the four other curves in Fig. 5–8 in the region of transition from momentum-dominated to buoyancy-controlled flow as expected.

The following sequence is applied in use of the correlation in Fig. 5–8. Firstly, the nozzle exit Froude number is calculated and its logarithm. The under-expanded theory is applied to calculate the notional nozzle exit diameter and the velocity in the notional nozzle exit when applicable. Then, a vertical line is drawn upward from a point on the abscissa axis equal to the calculated Froude number logarithm. The intersection of this vertical line with the line marked "Downward jets" on the graph indicates the concentration above which the jet is momentum-dominated and below which the jet is buoyancy-controlled.

For example, if a jet exit Froude number is *Log* (*Fr*)=4.25 (intersection of the vertical line with line "Downward jets" is at location of the theoretical curve corresponding to 30% by volume of hydrogen) then the jet is in momentum-dominated regime while the concentration in the jet is above 30% by volume and it becomes buoyant when the concentration on the jet axis is below 30% (further downstream of the axial concentration of 30% by volume).

This technique is quite simple to apply and at the same time can be very useful to develop cost-effective hydrogen safety solutions. For instance, the separation distance for a horizontal jet release can be essentially reduced as only a length of the momentum-dominated part of the jet can be taken as an indication of the separation distance rather than aggregated (both momentum- and buoyancy-controlled parts of the jet) distance to 4% by volume (LFL).

3. Hydrogen Explosion safety

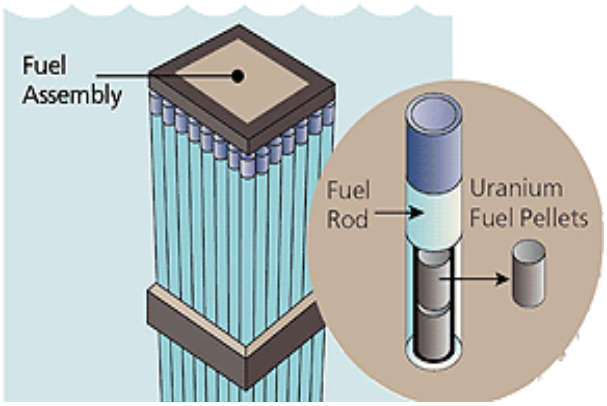
i.eXecUTiVe SUMMARY

As demonstrated during the March 2011 severe nuclear accident in Fukushima, Japan, accumulation and subsequent detonation of hydrogen gas produced by an overheated nuclear core reacting with steam can breach a reactor's containment structures and result in widespread radioactive contamination.[1] The gas is initially generated by the rapid oxidation of the zirconium alloy tubes ("fuel cladding") that surround the low-enriched uranium fuel pellets in commercial power reactors (Figure 1).

When the fuel cladding enters a certain temperature range well above its typical operating temperature, the zirconium-steam reaction becomes "autocatalytic," meaning that it propagates via self-heating from the chemical reaction itself. This produces large quantities of hydrogen in a brief period. This intense reaction also causes the fuel cladding to erode and breach, which releases harmful levels of radionuclides into the reactor vessel. The fuel cladding is the first line of defense among multiple barriers—the reactor vessel, a steel and/or reinforced concrete "containment," and a further, secondary containment in some designs[2]—that are intended to prevent release to the environment of the biologically hazardous

radionuclides produced by nuclear fission (see Figure 2). In some accident scenarios, over-pressurization of the reactor vessel can be exacerbated by the buildup of hydrogen from the zirconium-steam reaction, causing seals at the multiple penetrations of the vessel required for reactor monitoring and control to leak hydrogen into the containment.

Figure 1: Structure of a Uranium Fuel Assembly



Source: NrC

To protect the integrity of the reactor's cooling system, pressure relief valves are designed to open automatically, resulting in discharge of radioactively contaminated steam and hydrogen gas into the containment. In older boiling water reactor (BWR) designs, this discharge is initially into the "pressure suppression pool" or "wetwell" portion of the primary containment.[3]

In the March 2011 Fukushima Daiichi accident—in which the cores of three GE-designed boiling water reactors lost all cooling and melted down—hydrogen leaked from the primary containments into the reactor buildings. The hydrogen accumulated in the reactor buildings and detonated, causing large releases of harmful radionuclides that contaminated a wide area and prompted the evacuation of some 90,000 people. A smaller hydrogen explosion also occurred in the March 1979 Three Mile Island Unit 2 (TMI-2) accident—a partial core meltdown of a pressurized water reactor (PWR)—that did not breach the containment.

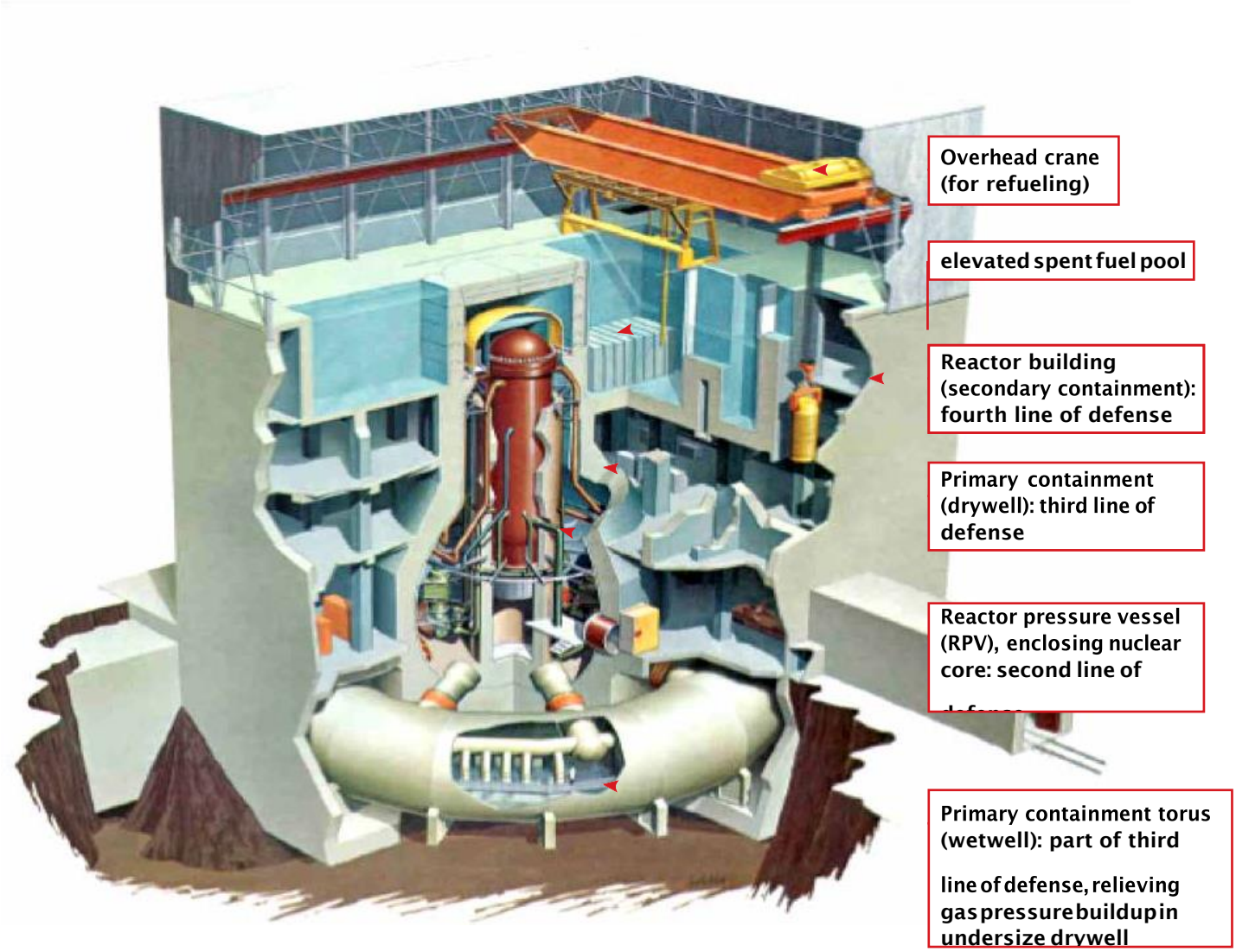
The U.S. Nuclear Regulatory Commission (NRC) has a checkered history when it comes to requiring measures that would effectively reduce the risk of hydrogen explosions in the event of a severe accident at a U.S. nuclear power plant. This regulatory lapse is rooted in the history of the development of commercial nuclear power in the United States, when the NRC's predecessor agency, the Atomic Energy Commission (AEC), had a dual mandate: both to *promote* and to *regulate* commercial nuclear power.

As a consequence of this internal conflict of interest, rather than consult independent scientific and technical institutions, the AEC entrusted two companies that designed nuclear reactors—Westinghouse and General Electric (GE)—with the mission of demonstrating that in a large-pipe-break loss-of-coolant accident (LOCA), the emergency core-cooling systems for their respective reactor designs would in fact prevent overheating of the core, and hence prevent the generation of large quantities of explosive hydrogen gas.

In response to the TMI-2 partial meltdown in 1979, the NRC revised its regulations regarding the control of hydrogen in an effort to help prevent hydrogen explosions in severe nuclear accidents. In 1981, the NRC issued a requirement that GE-BWRs with the small-volume Mark I and somewhat larger Mark II containments operate with their atmospheres inerted with nitrogen, to minimize the risk of hydrogen combustion. In 1985, the NRC required installation of hydrogen igniters—systems to burn off leaked hydrogen before it accumulates

Figure 2: cutaway View of a ge Mark i boiling Water Reactor (bWR)

this is the design that exploded at Fukushima Daiichi, Japan, in March 2011. twenty-two units of this design are still operational in the U.S.



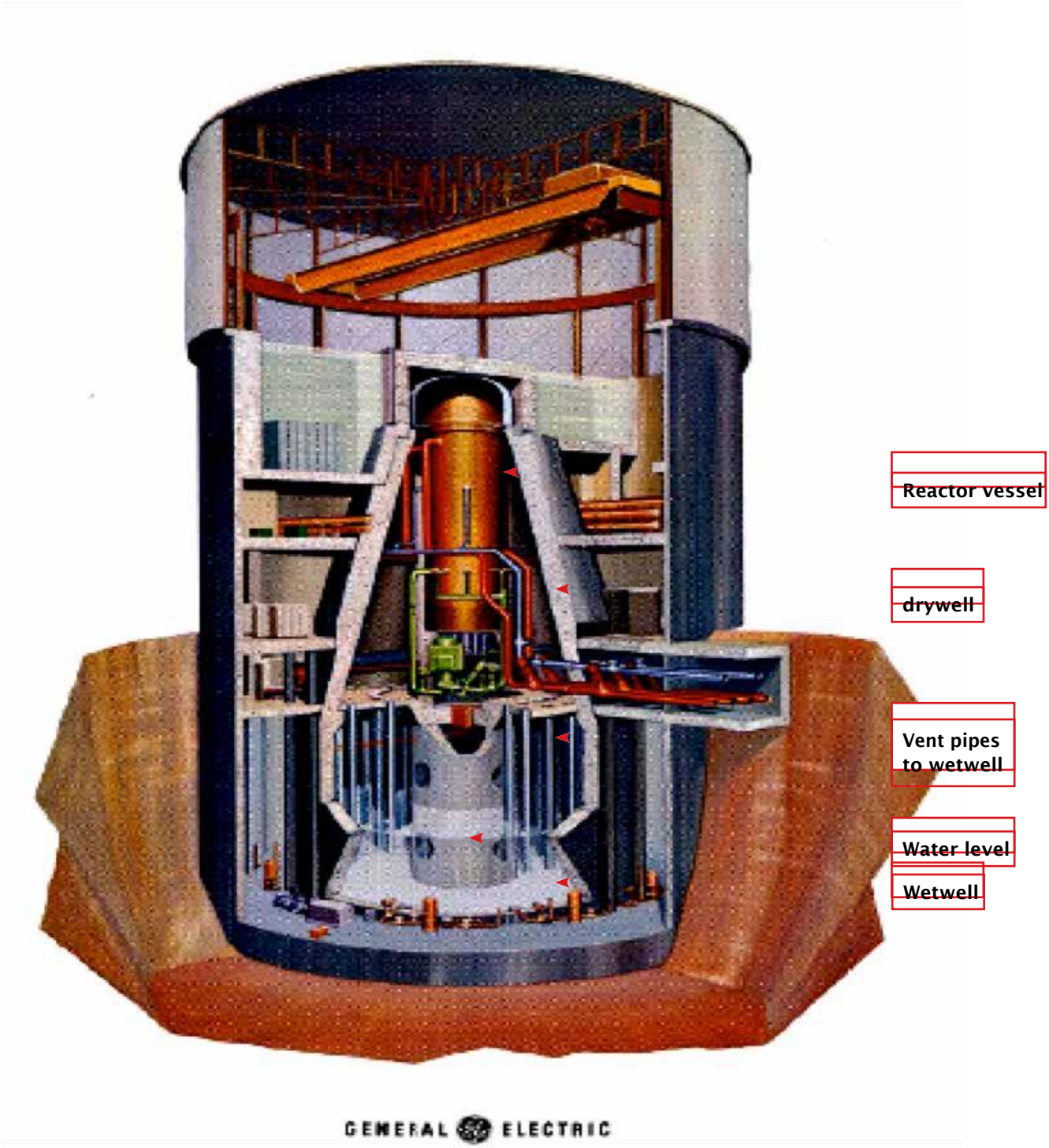
Source: NrC reactor Concepts Manual, rev. 0200

to explosive concentrations—in pressurized water reactor (PWR) "ice condenser" containments and GE-BWR Mark III containments.

By contrast, after Fukushima Daiichi's three devastating hydrogen explosions, the NRC decided to relegate investigating severe accident hydrogen safety issues to the *lowest-priority* and least proactive stage (Tier 3) of its post–Fukushima Daiichi accident response. Hence, beyond ensuring reliable containment pressure relief vents are added to obsolescent Fukushima-type reactors, it could take many years, or even decades, before the U.S. nuclear industry implements further hydrogen control measures.

Multiple technical pathways exist for minimizing the risk of hydrogen explosions in severe nuclear accidents. However, in the aftermath of the Fukushima Daiichi accident, the NRC has merely declared that severe nuclear accidents are vanishingly rare events that can be either prevented or sharply limited in scope, thereby avoiding any significant buildup of hydrogen and attendant explosion risk. The reality, however, is that merely waving a rhetorical magic wand over

this design is deployed at Limerick Units 1 and 2, Susquehanna 1 and 2, and Nine Mile point 2. the primary containment volume is only slightly larger than that of the Mark I.



Source: Containment Integrity Research at Sandia National Laboratories - An Overview, NUreG/Cr-6906

the problem of hydrogen explosion risk flies in the face of a number of unresolved safety issues, including:

- experimental evidence that current reactor computer safety models do not accurately predict the onset of rapid hydrogen generation in severe nuclear accidents, and that they under-predict the rates of hydrogen generation that occur in such accidents;
- an aging fleet of U.S. reactors that will increasingly operate beyond the 40-year term of their initial licenses while facing severe competitive pressures from other electricity generation technologies, creating a perilous tradeoff between economic viability and public safety;
- the compromised ability of 40-year old containments to prevent hydrogen leakage (for example, at the seals of pipe and cable penetrations) under the elevated-pressure conditions that are expected to occur in severe accidents;
- the apparent willingness of the NRC to accede to licensee requests to relax and defer requirements for periodic containment pressurization and leak rate testing; and
- the lack of technical readiness of U.S. power reactor owners to detect and control dangerous concentrations of hydrogen in all the places where it could migrate and explode in a nuclear power plant.

We conclude that the NRC is failing to meet the statutory standard of "adequate protection" of the public against the hazard of hydrogen explosions in a severe reactor accident. Our reasons are summarized below and set forth in more detail in the body of this report.

1. nRc computer safety models underpredict the rates of hydrogen generation that have occurred in experiments simulating severe nuclear accidents.

Reports from the Oak Ridge National Laboratory (1997), the OECD Nuclear Energy Agency (2001), and the International Atomic Energy Agency (IAEA) (2011) support the conclusion that current computer safety models underpredict the rates of hydrogen generation that may occur in severe accidents when zirconium fuel cladding and other core components react with steam, especially during a re-flooding of an overheated reactor core. Unfortunately, the NRC's 2011 *Recommendations for Enhancing Reactor Safety in the 21st Century: Near-Term Task Force Review of Insights from the Fukushima Daiichi Accident* and subsequent Fukushima safety review documents do not discuss the fact that the NRC's computer safety models—such as the widely used MELCOR code developed by Sandia National Laboratories— underpredict the hydrogen generation rates that occur in severe accidents. By overlooking the deficiencies of computer safety models, the NRC undermines its own philosophy
of defense-in-depth, which requires the application of conservative models. When hydrogen generation rates are underpredicted, hydrogen mitigation systems are not likely to be designed so that they can handle the hydrogen gas generation rates that would occur in actual severe accidents.

2. bWR Mark i and Mark ii primary containments are especially vulnerable to overpressurization and hydrogen leaks.

In 1972, the chief nuclear safety analyst for the AEC recommended discouraging further use of the type of primary containments used in the GE-BWR Mark I and Mark II designs, claiming they were susceptible to overpressurization. One reason these containments are vulnerable is that their volumes are relatively small: typically about one-ninth and one-sixth the volume, respectively, of PWR large dry containments. In September 1989, the NRC publicly acknowledged that BWR Mark I primary containments might not be able to withstand the internal gas pressures that would build up in severe accidents. However, at the time, the NRC merely issued guidance that was not legally binding, recommending that owners of BWR Mark I designs "on their own initiative" install a "hardened vent" to the external environment for each reactor unit's doughnut-shaped wetwell—to reduce the internal gas pressure and remove decay heat in the event of a severe accident.

In the United States, the vents currently installed in each BWR Mark I wetwell (see Figure 1) do not have a standardized design, are not outfitted with high-capacity filters to prevent the release of harmful radionuclides in accidents, are not subject to NRC inspection for proper maintenance and continuing operability, and do not have an independent train of backup power sources to help ensure remote operation during a station blackout (i.e., a total loss of both grid- connected and backup alternating current power at a nuclear power plant).

As overall leak-rate tests demonstrate, GE-BWR Mark I and Mark II primary containments are not designed to prevent hydrogen leakage in accidents. These tests are legally required at U.S. nuclear power plants for determining how much radiation would be released from the containment in a "design-basis accident" (i.e., an anticipated accident in which, by design, a core melt would be prevented). In overall leak rate tests—conducted below their nominal design pressures—BWR Mark I and Mark II primary containments have been shown to leak hundreds of pounds of air per day. For example, in 1999, tests conducted at Nine Mile Point Unit 1 (a BWR Mark I) and at Limerick Unit 2 (a BWR Mark II) found that overall leakage rates at both units exceeded 350 pounds of air per day, an amount that is less than the maximum allowed leak rates. This means that in a severe accident, even if there were no damage to a primary containment, hydrogen would leak into the secondary containment (reactor building). Leak rates would increase as the internal pressure increased, and they would become even greater if the seals at the various piping and cable penetrations were damaged. (Typical BWR containments have 175 penetrations, almost twice as many as typical PWR containments.)

Figure 4: internet images of the Fukushima daiichi nuclear Power Station from the Ocean Side before and After the March 2011 Tsunami and Hydrogen explosions destroyed (from Right) Units 1, 3, and 4

A plume is visible coming from a blown-out shield building panel in the side of the Unit 2 reactor, which, while still intact, also experienced a core melt.

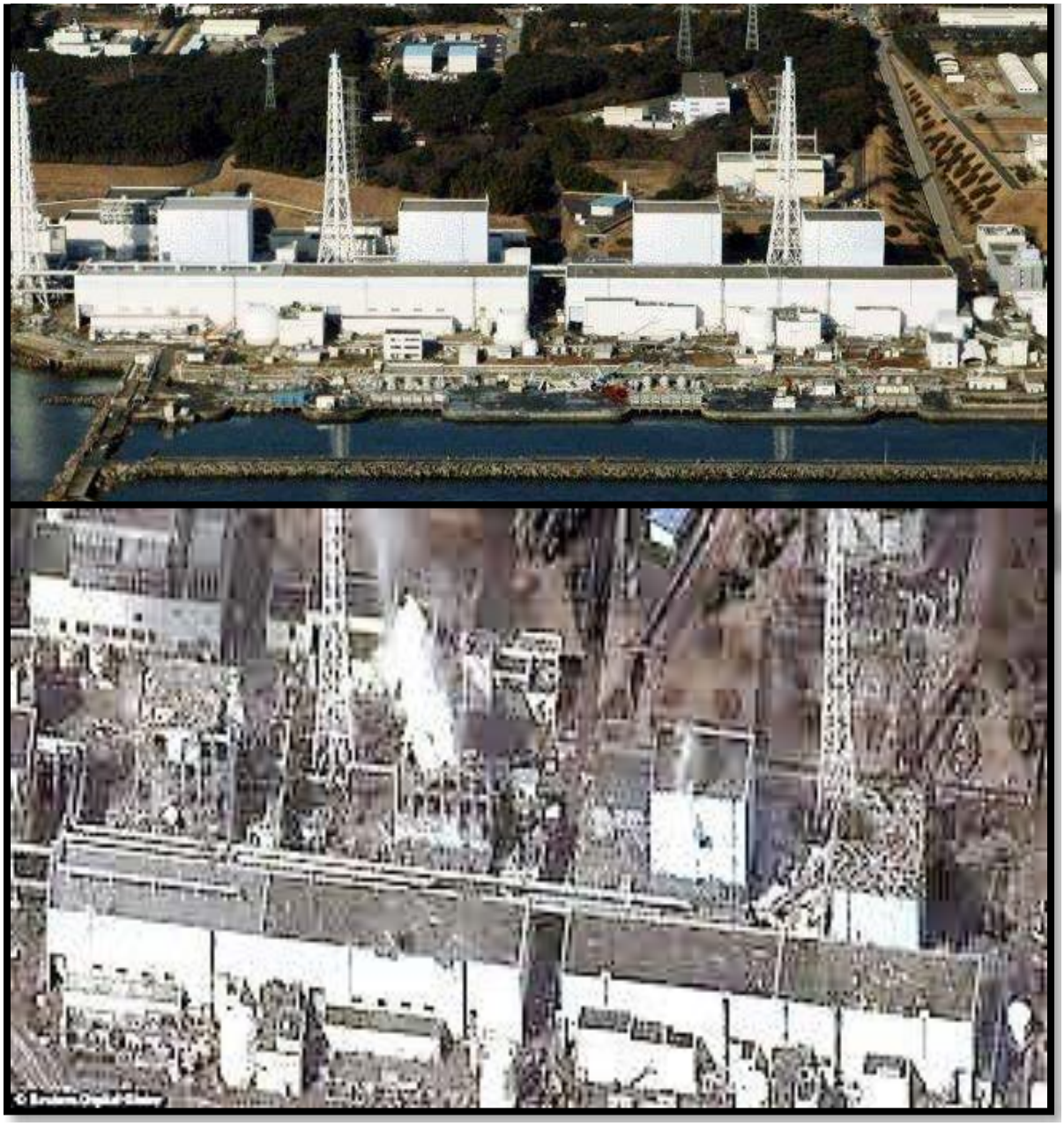


Photo credits: top, unknown; bottom, Digital Globe

3. ge-bWR Mark i and ii containments perform poorly in leak rate tests, yet the nRc is planning to further relax requirements for leak rate testing.

BWR Mark I primary containments have failed a number of overall leak rate tests; for example, Oyster Creek—the oldest operating commercial reactor in the United States, which is considered to be quite similar to Fukushima Daiichi Unit 1—has failed at least five tests. In one test, Oyster Creek's primary containment leaked at a rate 18 times greater than its design leak rate; if this test was conducted at the same pressure as subsequent Oyster Creek tests, which seems likely, the primary containment leaked more than 6800 pounds of air per day. Such results raise the questions: What were the observed pre-accident leak rates—*below design pressure*—of the three primary containments that leaked hydrogen at Fukushima Daiichi? Could there have been excessive hydrogen leakage at one or more of the primary containments, without it becoming overpressurized?

Since the Fukushima Daiichi accident, the problem of hydrogen leakage from primary containments has still not been adequately addressed. Mark II primary containments must also be assessed as likely to incur hydrogen leaks in severe accidents. Nevertheless, the NRC is currently preparing to extend the intervals at which overall and local leak rate tests must be conducted to once every 15 years (from the current 10 years) and once every 75 months (from the current five years), respectively. This will only further decrease the safety margin of BWR Mark I and Mark II designs. In its safety analyses to assess extending the test intervals, the NRC overlooked the fact that BWR Mark I and Mark II primary containments are particularly vulnerable to hydrogen leakage.

In a severe accident, BWR Mark I primary containments that leak excessively in tests *conducted below their design pressure* would leak dangerous quantities of explosive hydrogen gas into secondary containments; however, the NRC does not seem concerned about these excessive leakage rates. A 1995 NRC report, NUREG-1493, concluded that "increasing allowable leakage rates by 10 to 100 times results in a *marginal risk increase*, while reducing costs by about 10 percent" [emphasis added]. And a 1990 NRC report, NUREG-1150, concluded that even if there is leakage equivalent to 100 percent of the contained gas volume per day, "the calculated individual latent cancer fatality risk is below the NRC's safety goal." But this safety goal clearly would not be achieved if leaking hydrogen were to detonate in the reactor buildings, as it did at Fukushima Daiichi.

In March 2013, the NRC asserted that "[s]ensitivity analyses in NUREG-1493 and other studies show that *light water reactor accident risk is relatively insensitive to the containment leakage rate* because the risk is dominated by accident sequences that result in failure or bypass of containment" [emphasis added]. In reality, the progression of the Fukushima Daiichi accident was indeed affected by the leakage of hydrogen gas. The evidence suggests that Unit 3's primary containment *did not fail* before hydrogen leaked into the Unit 3 reactor building and detonated. The internal pressure of Unit 3's primary containment actually *increased* after the hydrogen explosion occurred.

In a nuclear power plant accident, a mixture of hydrogen, nitrogen, and steam could leak from the primary containment; as internal pressures increase and the accident progresses, the concentration of hydrogen in the leaking mixture would increase. If there were *no damage* to the primary containment, the quantity of hydrogen that leaked (by weight) would be relatively small, because hydrogen is about one-fourteenth as dense as air. However, a secondary containment could be breached if, for example, only 20 to 40 pounds of hydrogen were to leak into it, accumulate locally, and explode.

4. Large-volume PWR dry containments, made of reinforced concrete with a steel liner, are a prominent safety feature of many U.S. nuclear power plants; however, they are not necessarily invulnerable to the effects of hydrogen explosions.

The NRC mistakenly claims that the large containment volumes of most PWRs—a reactor design found in about two-thirds of the U.S. nuclear fleet—would keep the pressure spikes from potential hydrogen explosions within their design pressures. But this claim is predicated on an uncertain and therefore misplaced assumption that hydrogen combustion would occur in the form of a "deflagration," a combustion wave traveling at a subsonic speed relative to the unburned gas.

However, when local hydrogen concentrations are greater than about 10 percent by volume, it is possible for a deflagration to transition into a "detonation," a combustion wave traveling at a supersonic speed relative to the unburned gas. Unfortunately, in a severe accident, a hydrogen detonation could occur within a PWR large dry containment if there were elevated local hydrogen concentrations, especially in the presence of carbon monoxide and high temperatures; this could cause internal pressure spikes to exceed twice the containment's design pressure.

Furthermore, a local hydrogen explosion occurring inside the containment could propel debris, such as concrete blocks from internal walls, into the containment structure at high velocities. The impact of such internally generated missiles could damage essential safety systems and severely crack a PWR's containment.

According to a 2011 IAEA report on the mitigation of hydrogen hazards in severe nuclear accidents, "no analysis ever has been made on the damage potential of flying objects generated in an explosion" of hydrogen. Yet we know from the Fukushima Daiichi accident that debris propelled from hydrogen detonations caused extensive damage to backup emergency power supplies and hoses that were intended to inject seawater into overheated reactors. Some of the debris dispersed around the site by explosions was highly radioactive, exposing personnel to higher dose rates and setting back their efforts to control the accident.

As nuclear safety expert David Lochbaum has noted, "During design basis accidents, the response of operators and workers is primarily passive—verifying that automatic equipment actions have occurred. In essence, workers are observers during design basis accidents. During severe accidents, workers get off the bench and into the game.

The keystone of [the U.S. nuclear] industry's response to Fukushima is "FLEX," an array of portable components moved into place by workers. Inadequate hydrogen control during a severe accident would seem to render FLEX virtually useless."[4]

5. in the presence of the quantities of hydrogen generated in severe accidents, untimely ignitions from currently installed devices for controlling the buildup of hydrogen inside some U.S. nuclear reactor containments could cause hydrogen detonations.

Hydrogen "recombiners" are devices that eliminate hydrogen by combining it with oxygen, a reaction that produces steam and heat. There are two types of hydrogen recombiners: passive autocatalytic recombiners (PARs), which operate without electric power, utilizing catalytic surfaces to facilitate the combining of hydrogen and oxygen molecules; and thermal recombiners, which are electrically powered.

In September 2003, the NRC rescinded its requirement that most types of PWRs operate with hydrogen recombiners installed in their containments, because it decided that the quantity of hydrogen that would be released in design-basis accidents is not risk-significant. Indian Point on the Hudson River near New York City is the only nuclear power plant in the United States that currently operates with PARs. The new Westinghouse AP1000 design, under construction in Georgia, South Carolina, and China, is intended to operate with only two PARs installed in its containment. The hydrogen removal capacity of a single recombiner unit is only several grams per second whereas hydrogen generation in a severe accident could range from 100 to 5,000 grams per second.

If a PWR still operates with hydrogen recombiners, there are typically only two units installed in its containment, their mission being to reduce the quantity of hydrogen generated in a design basis accident. By contrast, European PWR containments typically have 30 to 60 such devices installed, with the mission of reducing the quantity of hydrogen generated in a severe accident.

Clearly, just two recombiners would not be capable of eliminating, in timely fashion, the quantity of hydrogen generated in a severe accident. But this is not their only limitation. When hydrogen recombiners are exposed to the elevated hydrogen concentrations that occur in severe accidents, they have a tendency to malfunction and incur ignitions, which could cause a hydrogen detonation that compromised the containment. Hence, it seems that maintaining the token capacity of two recombiners actually presents a *net safety hazard*. This is especially a problem with PARs, which operators would not be able to deactivate; at least electrically powered thermal recombiners could be switched off when a hydrogen concentration reached a level at which the recombiner could incur ignitions.

The NRC requires that hydrogen igniters be installed in reactor containments that are neither inerted nor designed to withstand high internal pressures—PWR ice condenser and BWR Mark III containments. Igniters are intended to burn off

hydrogen as it is generated in an accident, before it can reach concentrations at which combustion would threaten the integrity of the less sturdy containment. In a severe accident, to safely actuate hydrogen igniters, operators would need to know the local concentration of hydrogen in the vicinity of each igniter; if igniters were actuated too late—after local detonable concentrations of hydrogen built up—they could actually cause a hydrogen detonation that breached the containment.

6. **The nRc has insufficient requirements for monitoring the quantities of hydrogen generated in severe accidents.** NRC rules state that in nuclear accidents, hydrogen monitors must begin to function within 90 minutes of the emergency injection of coolant water into the reactor vessel. Ninety minutes could be too late in a fast-moving accident scenario. In 2003, the NRC took the odd step of reclassifying both hydrogen and oxygen monitors (required for BWR primary containments that operate with nitrogen-inerted atmospheres) as non-safety-related equipment, meaning that the equipment does not need to have redundancy, seismic resistance, or an independent train of onsite standby power.

Furthermore, GE-BWR Mark I and Mark II designs operate with hydrogen monitors installed only in their inerted primary containments, not in their reactor buildings. In the Fukushima Daiichi accident, hydrogen from three nuclear units leaked into these buildings and exploded.

7. **Operators of PWRs lack a sufficient capability to monitor the onset and progression of core degradation in the event of an accident.** This insufficient capability limits operator knowledge of when to transition from emergency operating procedures (EOPs)—intended to *prevent* core damage—to severe accident management guidelines (SAMGs)—intended to stabilize a damaged reactor core with auxiliary ad-hoc cooling measures while preventing significant off-site releases of radionuclide contamination. The operating measures appropriate to preventing core damage early in an accident are obviously not the same as those intended to contain the consequences of core damage that has already occurred while forestalling further compounding events, such as hydrogen explosions, that could result in a significant loss of containment. Not knowing which regime one is operating in could have severe consequences.

In PWRs, core-exit thermocouples—temperature measuring devices—are the primary equipment that would be used to detect inadequate core-cooling and to signal the point at which operators should transition from EOPs to SAMGs. However, data from experiments demonstrate that core-exit temperature measurements are neither an accurate nor a timely indicator of *maximum fuel-cladding temperatures* in the core, and hence an unreliable indicator of the likelihood of significant hydrogen production. In the most realistic severe accident experiment ever conducted— in which an actual reactor core was heated with decay heat

before melting down—core-exit temperatures were measured at approximately 800°F when maximum in-core fuel-cladding temperatures exceeded 3300°F.

In a severe accident, plant operators are supposed to implement SAMGs before the onset of the rapid zirconium-steam reaction, which leads to thermal runaway in the reactor core. Clearly, using core-exit thermocouple measurements in order to detect inadequate core cooling or uncovering of the core is neither reliable nor safe. For example, PWR operators could end up re-flooding an overheated core simply because they do not know the actual condition of the core. Unintentionally re-flooding an overheated core could generate hydrogen, at a rate as high as 5,000 grams per second, and the containment could be compromised if large quantities of that hydrogen were to detonate, as occurred at Fukushima.

nRdc'S RecOMMendATiOnS FOR RedUcing THe RiSK OF HYdROgen eXPLOSiOnS in SeVeRe nUcLeAR AccidenTS

A. The nRc should develop and experimentally validate computer safety models that can conservatively predict rates of hydrogen generation in severe accidents.

The NRC needs to acknowledge that its existing computer safety models underpredict the rates of hydrogen generation that occur in severe accidents. The NRC should conduct a series of experiments with multi-rod bundles of zirconium alloy fuel rod simulators and/or actual fuel rods as well as study the full set of existing experimental data. The NRC's objective in this effort should be to develop models capable of predicting with greater accuracy the rates of hydrogen generation that occur in severe accidents.

b. The safety of existing hydrogen recombiners should be assessed, with the use of PARs potentially discontinued until technical improvements are developed and certified.

Experimentation and research should be conducted in order to improve the performance of PARs so that they will not malfunction and incur ignitions in the elevated hydrogen concentrations that occur in severe accidents. The NRC and European regulators should perform safety analyses to determine if existing PARs should be removed from plant containments—and, if so, whether they should be replaced with electrically powered thermal hydrogen recombiners that have their own independent train of emergency power. The latter course would require operators to have instrumentation capable of providing timely information on the local hydrogen concentrations throughout the containment, so they could deactivate the thermal recombiners when hydrogen concentrations reached the levels at which the recombiners malfunction and incur ignitions.

c. existing oxygen and hydrogen monitoring instrumentation should be significantly improved.

In line with the conclusions of the NRC's own Advisory Committee on Reactor Safeguards (ACRS), the NRC should reclassify oxygen and hydrogen monitors as safety-related equipment that must undergo full qualification (including seismic qualification), have redundancy, and have has its own independent train of emergency electrical power.

The current NRC requirement that hydrogen monitors be functional within 90 minutes of emergency cooling water injection into the reactor vessel is clearly inadequate for protecting public and plant worker safety. Following onset of an accident, NRC regulations should require that hydrogen monitors be functional within a timeframe that enables immediate detection of quantities of hydrogen indicative of core damage and a potential threat to containment integrity.

The NRC should also require hydrogen monitoring instrumentation to be installed in:

1. BWR Mark I and Mark II secondary containments;
2. fuel-handling buildings of PWRs and BWR Mark IIIs; and
3. any plant structure where it would be possible for hydrogen to enter.[5]

d. current core diagnostic capabilities require upgrading to provide plant operators a better signal for when to transition from emergency operating procedures to severe accident management guidelines.

The NRC should require plants to use thermocouples placed at different elevations and radial positions throughout the reactor core to enable plant operators to accurately measure a wide range of temperatures inside the core under both typical and accident conditions. In the event of a severe accident, in-core thermocouples would provide plant operators with crucial information to help them track the progression of core damage and manage the accident, indicating, in particular, the correct time to transition from EOPs to implementing SAMGs.

e. The nRc should require all nuclear power plants to control the total quantity of hydrogen that could be generated in a severe accident.

The NRC should require all nuclear power plants to operate with systems for combustible gas control that would effectively and safely control the total quantity of hydrogen that could potentially be generated in different severe accident scenarios; and to have strategies for venting gas from the inerted primary BWR Mark I and Mark II containments without causing significant radiological releases. The NRC should also require nuclear power plants to operate with systems for combustible gas control that are capable of preventing local concentrations of hydrogen in the containment from reaching concentrations that could support explosions powerful enough to breach the containment, or damage other essential accident-mitigating

features. Hydrogen explosions are not expected to occur inside the primary BWR Mark I and Mark II containments, which operate with inerted atmospheres, unless somehow oxygen is present.

The NRC should require licensees who operate nuclear power plants with hydrogen igniter systems to perform analyses demonstrating that these systems would effectively and safely mitigate hydrogen in different severe accident scenarios. Licensees unable to do so would be ordered to upgrade their systems to adequate levels of performance.

F. The nRc should require that data from leak rate tests be used to help predict the hydrogen leak rates of the primary containment of each bWR Mark i and Mark ii licensed by the nRc in different severe accident scenarios. The NRC should require that data from overall leak rate tests and local leak rate tests—already required by Appendix J to Part 50 for determining how much radiation would be released from the containment in a design basis accident—also be used to help predict hydrogen leak rates for a range of severe accident scenarios involving the primary containments of each GE-BWR Mark I and Mark II licensed by the NRC. If data from an individual leak rate test were to indicate that dangerous quantities of explosive hydrogen gas would leak from a primary containment in a severe accident, the plant owner should be required to repair the containment.

The rationale for this requirement is obvious: Hydrogen explosions, or hydrogen concentrations in the reactor building that pose a detonation risk, can severely inhibit emergency response actions essential to containing the accident. Or even worse, emergency response actions themselves, such as hooking up portable power equipment, could actually provide the spark for hydrogen explosions in critical areas of the plant.

The NRC should also end its practice of allowing repairs to be made immediately before leak rate tests are conducted to evaluate potential leakage paths, such as containment welds, valves, fittings, and other components that penetrate containment. This "repair before test" practice obviously defeats the nuclear safety objective of providing an accurate statistical sample of actual pre-existing containment leak rates.

Finally, the NRC should reconsider its plan to extend the intervals of overall and local leak rate tests to once every 15 years and 75 months, respectively. The NRC needs to conduct safety analyses that consider BWR Mark I and Mark II primary containments are vulnerable to hydrogen leakage. It also seems probable that as old reactors are kept in service beyond their original licensed lifetimes, the intervals between leak rate tests should be shortened rather than extended.

ii. HYdROgen geneRATiOn in nUcLeAR POWeR PLAnT AccidenTS

A. TecHnicAL bAcKgROUnd: deSign bASiS AccidenTS And THe ZiRcOniUM- STeAM ReAcTiOn

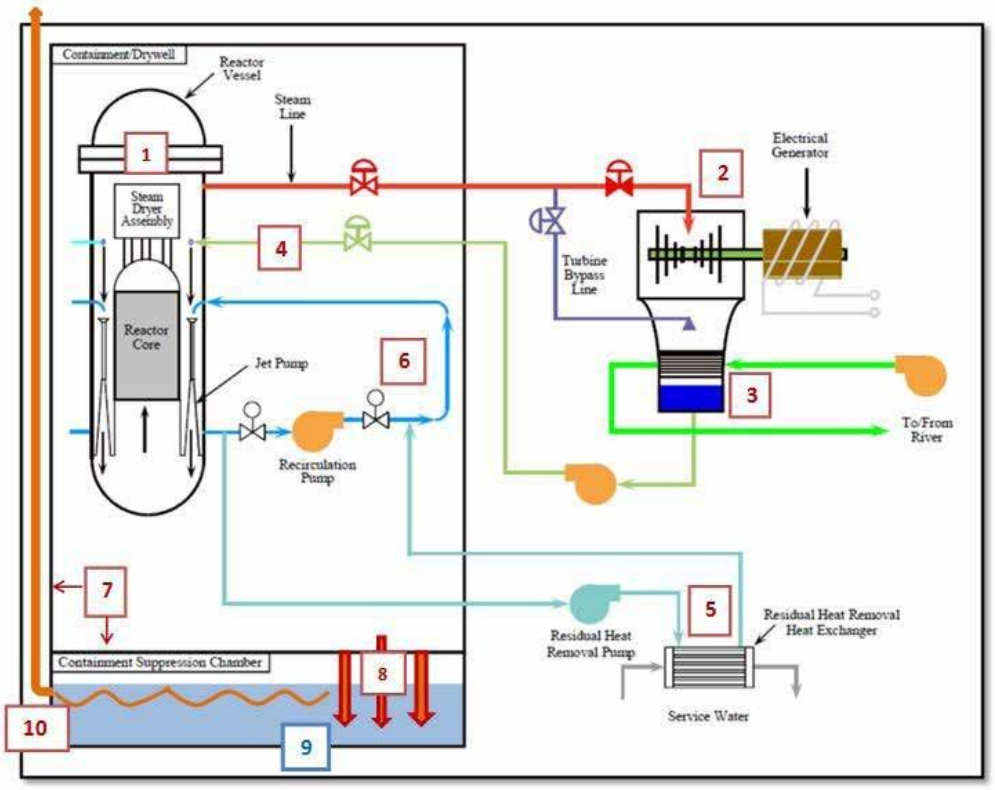
In typical operating conditions at a nuclear power plant, highly pressurized coolant[6] water is pumped through the reactor coolant system[7] piping into the reactor pressure vessel where it flows between the fuel rods, carrying away heat produced by the fission (splitting) of uranium (^{235}U) atoms in the fuel. The coolant water's temperature exceeds 500°F; nonetheless, it still provides cooling for the fuel rods located in the reactor core as long as a sufficient flow of coolant is maintained.[8]

U.S. nuclear power plants are referred to as light water reactors because they use ordinary water (H_2O), as opposed to heavy water (^2H_2O or D_2O), as a coolant. In a boiling water reactor like those that suffered hydrogen explosions at Fukushima, the coolant exits the reactor core as a steam- water mixture. Water droplets are removed in a steam dryer located above the core, and then the steam passes through the steam line to the main turbine, which powers an electric generator, and is condensed back into water before reentering the core (see Figure 5).

Figure 5: Schematic diagram of Heat Removal from a boiling Water Reactor (bWR)

Heat is removed during normal operation by generating steam, which rises to the top of the reactor vessel **(1)**, and is then used directly **(red line)** to drive a turbine **(2)** that spins an electrical generator. When a reactor shuts down, however, the core continues to produce heat from radioactive decay. this decay heat is removed initially by bypassing the turbine and delivering the steam directly to the condenser **(3)**, which is cooled by water pumped from lakes, rivers, or ocean **(green)**, with the condensed steam **(blue)** returning to the reactor as coolant **(4)**. When steam pressure drops to approximately 50 pounds per square inch, the residual heat removal (**rHr**) system **(5)** is used to complete the cool-down process. Water in the normal coolant recirculation loop **(6)** is diverted from the recirculation pump to the **rHr** pump which sends it through a supplementary heat exchanger and back to the reactor.

Multiple electrically controlled pumps and valves are dependent on external sources of electricity for safe operation in the critical period following reactor shutdown. In a severe accident, "drywell" containment **(7)** is designed to vent **(8)** excess radioactive steam pressure into a "wetwell" suppression chamber **(9)** half filled with water, which operators, in turn, can vent to the atmosphere through "reliable Hardened Vents" **(10)** to relieve excess pressure. Currently, such vents do not filter radioactive aerosols and gases.



Source: N**r**C **r**eactor Concepts Manual, **r**ev. 0200, pages 3-7, with additional explanatory features by ND**r**C

In a pressurized water reactor the coolant typically circulates to and from the reactor in two to four closed "primary loops," where it is maintained at a pressure high enough to prevent the water from boiling. Each primary loop has a steam generator (heat exchanger) where the coolant heats and boils water circulating through a secondary loop—maintained at a lower pressure than the primary loop—producing pressurized steam to spin the main turbine and generate electricity (see Figures 6 and 7).

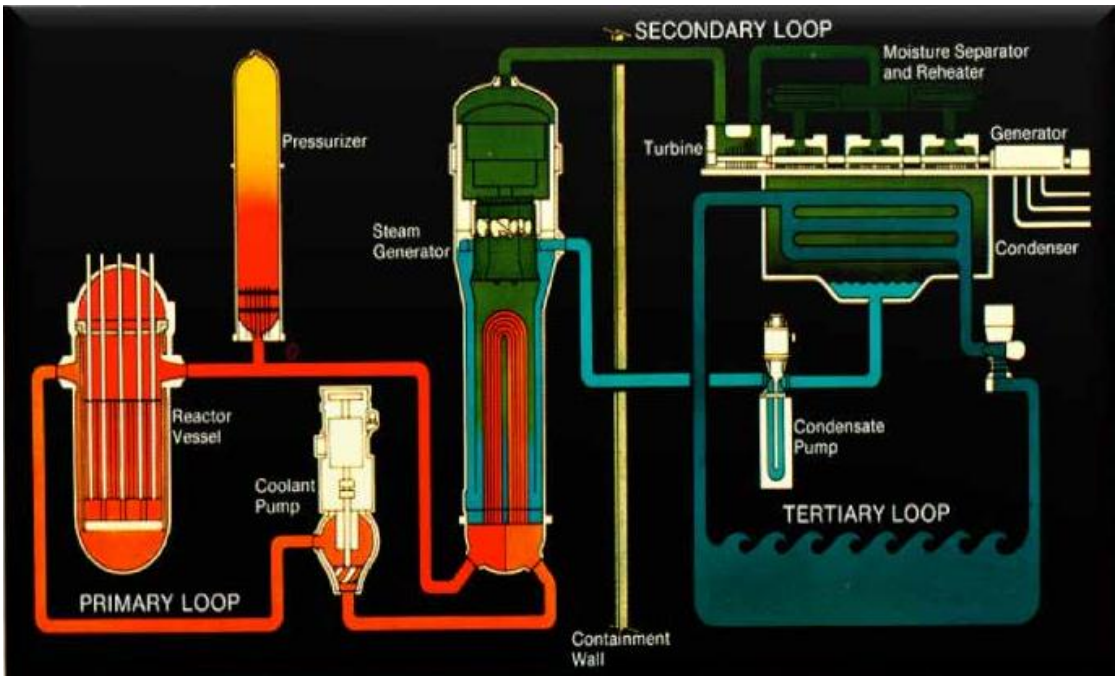
Both reactor types have main condensers to condense the steam back into water after it exits the turbines; this water is pumped back to the reactor pressure vessel (in a BWR) or steam generator (in a PWR). The main condensers of both BWRs and PWRs rely on vast amounts of water, drawn from a local water body such as a lake, river, or ocean. This water may be returned directly to the local water body at elevated temperatures, sometimes damaging the local ecology; alternately, cooling towers may be deployed to remove heat from this water. Roughly two-thirds of the thermal energy produced by a nuclear reactor is not converted into electricity but rather is discharged to the environment as waste heat.

Reactor cores have tens of thousands of uranium fuel rods, bundled together into "fuel assemblies." For example, each reactor at Indian Point Energy Center near New York City has 87 metric tons of fuel contained in 193 fuel assemblies (each with 204 fuel rods), or almost 40,000 fuel rods. The cladding of the fuel rods is made of zirconium alloy.[9] The fuel cladding is a thin tube, typically with a diameter of less than half an inch, sheathing small cylindrical uranium-dioxide fuel pellets stacked one on top of the other. The active fuel region of the fuel rods (the length of the cladding containing the fuel pellets) is approximately 12 feet long.

In sum, a reactor core contains large amounts of zirconium metal that can react with steam at high temperatures to produce vast quantities of hydrogen gas. In the event of a design basis accident,[10] BWR and PWR emergency core cooling systems are designed to inject and circulate water through the reactor core to prevent the fuel rods from overheating when the normal reactor cooling system ceases to function. The respective emergency core cooling systems are required to mitigate a number of postulated design-basis accidents, including the worst-case scenario envisioned

Figure 6: Simplified Schematic diagram of a Westinghouse Pressurized Water Reactor (PWR) with Three intersecting Heat Transfer Heat Loops

pWr designs typically have two to four primary loops and a corresponding number of steam generators and main coolant pumps. Water in the primary loop is maintained by the pressurizer at around 2250 pounds per square inch, about twice the pressure of a BWr. Weak points in this system from a radiation containment perspective are the numerous valves and penetrations of the reactor vessel required to control and cool the reactor; the seals of the main coolant pumps, which must be actively cooled and are prone to leakage; and the thousands of small-diameter, thin-walled primary loop "steam tubes" in the steam generators, which are prone to erosion and leakage into the secondary loop. the tertiary loop can be "open," returning heated water from the turbine condenser directly to a local river, lake, or bay; or "closed," utilizing one or more "wet" (evaporative) or "dry" (fan-driven air) cooling towers



(not shown) to recycle the tertiary coolant in a "semiclosed" loop (makeup water must be added to the system due to evaporative losses).

Source: The Westinghouse Pressurized Water Reactor Nuclear Power Plant, page 4

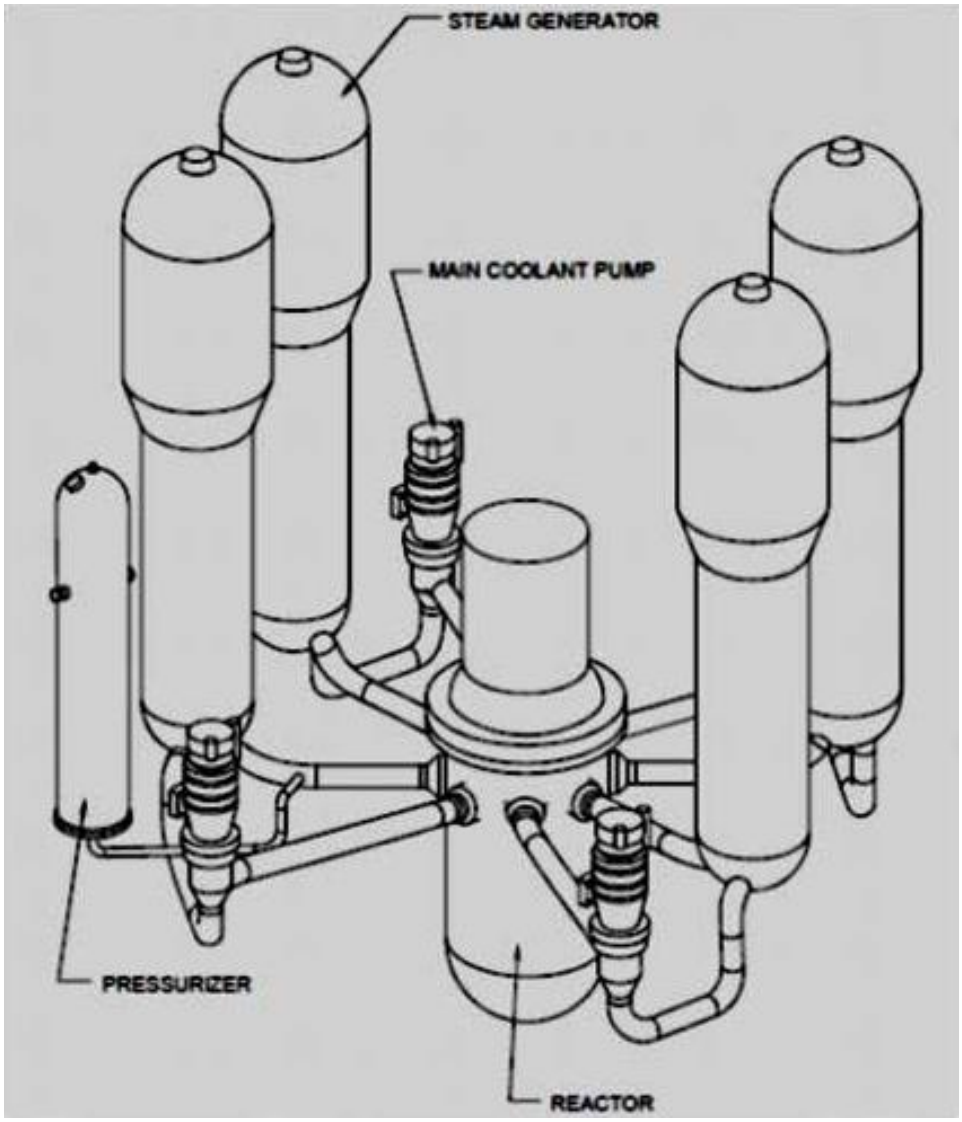
by regulators: a large-pipe-break loss-of-coolant accident (LOCA). Note that the March 2011 Fukushima Daiichi accident in Japan is considered a "beyond design basis" accident[11] or a "severe" accident that exceeded the design parameters of the plant.

In a hypothetical large-pipe-break LOCA at a PWR, the largest pipe in the reactor coolant system would break, causing a rapid discharge of coolant; the core would be either partly or completely emptied of water. The reactor's power would shut down within seconds, because the absence of the coolant, which is also a neutron moderator,[12] and the rapid insertion of control rods would stop the fission chain reaction. A control rod is a rod, plate, or tube containing a neutron-absorbing material used to control the power of a nuclear reactor by preventing further fissions. However, the maximum local temperature of the fuel cladding would increase—from approximately 600°F to more than 1000°F within 60 seconds[13] due to the absence of coolant. The fuel cladding would be heated by the residual heat in the fuel and by decay heating (the radioactive decay of fission products), which at the beginning of an accident would generate about 7 percent of the thermal power produced during normal operation. The decay heat decreases as the accident progresses yet remains a significant heat source for the duration of the accident.

If local fuel-cladding temperatures were to approach 1800°F, the cladding would incur additional heating from the exothermic (heat-generating) reaction of its zirconium content with the steam present in the reactor core. This chemical reaction is variously referred to as a "metal-water reaction," "zirconium-steam reaction," or "zirconium oxidation." The latter term is used because the zirconium-steam reaction produces zirconium dioxide (ZrO_2), in addition to hydrogen and heat.[14]

Figure 7: Layout of a Westinghouse Four-Loop Pressurized Water Reactor (PWR)

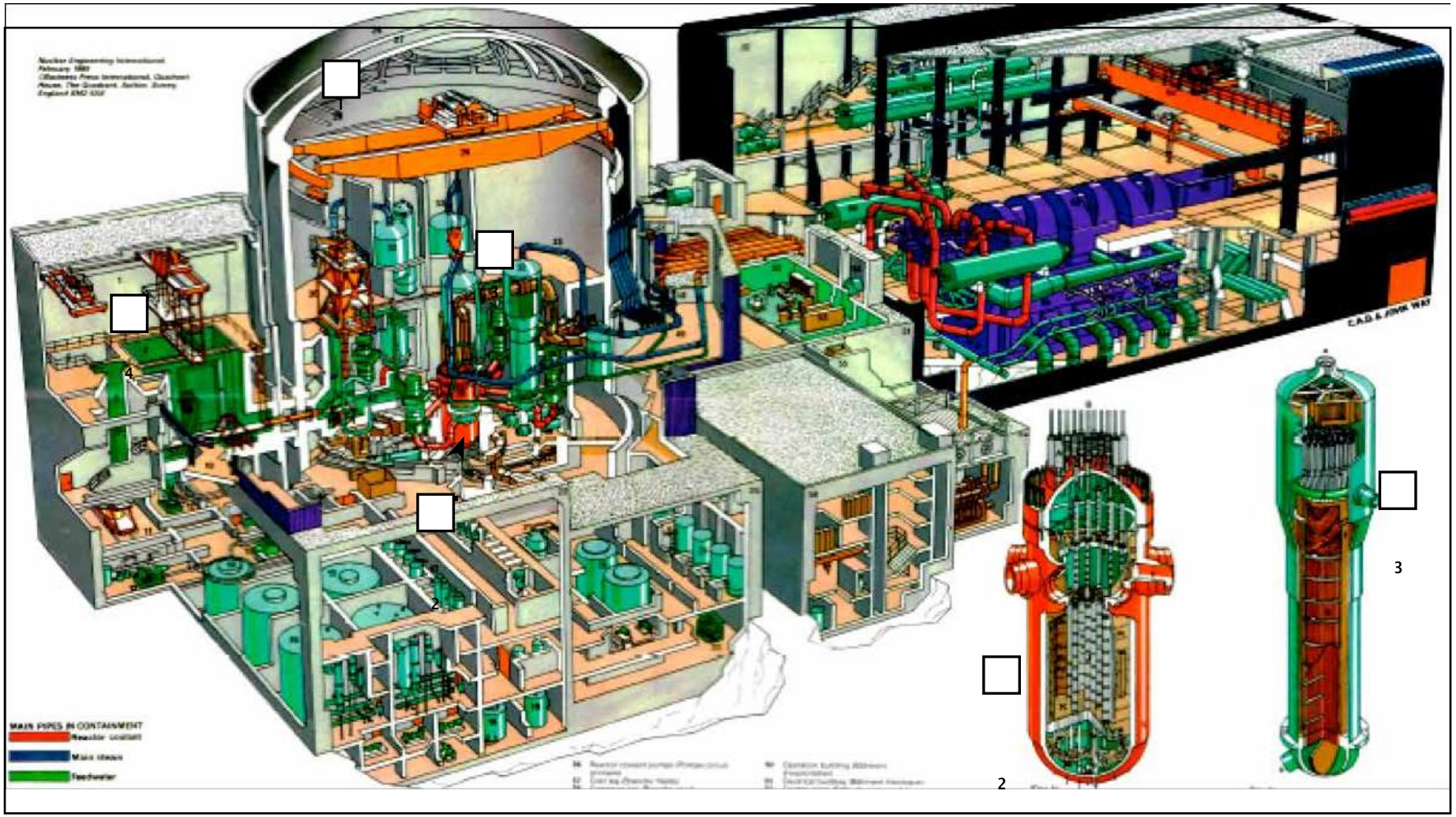
the reactor has four steam generators and four main coolant pumps (the fourth pump is hidden by the perspective of the drawing). All these components are massive. to set the scale, the interior of the reactor vessel is about 15 feet wide by 40 feet high. U.S. examples include Indian point Units 2 and 3 (New York), Vogtle Units 1 and 2 (Georgia), Comanche peak Units 1 and 2 (texas) and Diablo Canyon Units 1 and 2 (California).



Source: NRC Reactor Concepts Training Manual, Pressurized Water Reactor Systems, Section 4-1

Figure 8: cutaway View of French n4 Standardized PWR design, based on Westinghouse Technology but with a double-Walled Primary containment Structure (1)

reactor pressure vessel **(2)** and primary coolant loop piping are shown in **red**; main steam lines (in **blue**) are shown coming from the top of the steam generators **(3)**, shown in **light green**. these are supplied by the feedwater system (**dark green** piping), which also cools the spent fuel pool (4) and main coolant pump seals (dark green). the turbine building (5) encloses a steam-driven turbine generator unit (in **purple**) with a rated output of 1500 MWe. the tertiary cooling loop for the turbine steam condenser is not shown.



Source: University of New Mexico Libraries exhibition Nuclear engineering Wall Charts

the NrC's 2011 Near-term task Force review of Insights from the Fukushima Daiichi Accident states that an important aspect of the NrC's approach to safety through defense-

in-depth is the mitigation of the consequences of severe accidents, including the mitigation of the hydrogen that would be generated in such an accident. However, the Near-term task Force report discusses neither the rates of hydrogen generation that could occur nor the total quantity of hydrogen that could be generated in severe accidents. Given that in the Fukushima Daiichi accident, hydrogen explosions caused large radiological releases, this must be considered a major weakness in the NrC's report and its continuing regulatory response to the lessons learned from the Fukushima accident.

If the emergency core cooling system is to prevent the fuel cladding from overheating in a large-break LOCA, it must overcome the heat from three primary sources: 1) the residual heat stored in the fuel, 2) the heat from radioactive decay, and 3) the heat generated by the zirconium-steam reaction.

b. SeVeRe AccidenTS And THe HeAT PROdUced bY THe ZiRcOniUM-STeAM ReAcTiOn

Practically speaking… [zirconium] oxidation runaway comes in…due to the heat of the oxidation reaction increasing generally faster than heat losses from other mechanisms.… [I]f peak [fuel-cladding] temperatures remain below 1000°C [1832°F], you will probably escape the runaway [oxidation], but if you get to 1200°C [2192°F], you will probably see the oxidation "light up" like a 4th of July sparkler (literally that's what it looks like) as it looks like) as it goes into the "rapid oxidation" regime.[15]

—Randall O. Gauntt, Sandia National Laboratories

The Three Mile Island Unit 2 (TMI-2) accident, which occurred in March 1979, was a small-break LOCA[16] that transitioned into a severe accident—a partial meltdown—because there was inadequate cooling of the core. Decay heating caused local fuel-cladding temperatures to increase up to the point at which the cladding began to rapidly react with the steam present in the reactor core, which in turn produced more heat.

Robert E. Henry—an Argonne National Laboratory nuclear safety expert,[17] suggested that in the TMI-2 accident, when local fuel-cladding temperatures reached about 1832°F (1000°C), the heat produced by the zirconium-steam reaction was approximately equal to the heat produced by radioactive decay,[18] and that "from [that] point on, the core was in a thermal runaway state."[19,20] Henry stated that "[t]he [zirconium] oxidation rate increase[d] with increasing temperature, which [led] to an escalating core heatup rate. Therefore, *the core damage was generally caused by the [zirconium] cladding oxidation*" [emphasis added].[21]

Unignited releases

Once thermal runaway (runaway zirconium oxidation)

commences in a severe accident, maximum local fuel-cladding temperatures increase rapidly—tens of degrees Fahrenheit per second. Thermal runaway is what leads to a partial or complete meltdown. After thermal runaway commenced in the TMI-2 accident (plausibly at about 1832°F [1000°C]), within a few minutes, maximum local fuel- cladding temperatures would have reached the melting point of zirconium, which exceeds 3300°F.[22]

In the March 2011 Fukushima Daiichi accident, the respective reactor cooling systems of Units 1, 2, and 3 reportedly survived the earthquake more or less intact. However, the plant incurred a loss-of-offsite power, then flooding from the tsunami caused its backup diesel generators to fail, and backup batteries were depleted within about eight hours. The latter were insufficient in any case to power emergency core-cooling pumps once the steam-driven backup pumps became inoperative. Hence, the three units lost the ability to remove their reactors' decay heat. This caused the coolant water to boil away and uncover the fuel rods in the cores of the three units, exposing them to steam. Once the fuel rods were uncovered, decay heating caused cladding temperatures to increase to the point at which their zirconium content rapidly reacted with the steam and generated large quantities of hydrogen gas.

The NRC needs to consider that not all severe accidents would be relatively slow-moving "station-blackout" accidents caused by natural disasters, like the Fukushima Daiichi accident. Fast-moving accidents could also occur; for example, a large-pipe-break LOCA could rapidly transition into a severe accident, because of thermal runaway. A meltdown could commence within 10 minutes of the onset of such an accident.[23]

c. HYdROgen geneRATiOn in AccidenTS: RATeS And QUAnTiTieS

It should be noted that in an unmitigated BWR severe accident the entire Zircaloy inventory of the reactor would eventually oxidize (either in the reactor vessel or on the drywell floor), generating as much as 6000 [pounds] (2722 kg) of hydrogen (plant specific value).[24]

—Sherrell R. Greene of Oak Ridge National Laboratory

In a reactor accident, fuel-cladding temperatures, plant operator actions, and other factors would affect hydrogen generation rates and the total quantity generated.

In a PWR accident in which the maximum fuel-cladding temperature at any point in the core does not exceed 2200°F (the regulatory fuel-cladding temperature limit for design basis accidents[25]), hydrogen generation is predicted to occur at rates from 1 to 50 grams per second;[26] similar rates would occur in a BWR design basis accident. A safety analysis conducted for Indian Point Unit 3 (a large PWR) found, reassuringly, that after a design basis LOCA, it would take a total of 23 days for the hydrogen concentration in the containment to reach 4 percent of the containment's volume (the lower flammability limit).[27]

However, in a severe PWR accident, the picture changes dramatically: hydrogen generation could occur at rates from 100 to 5,000 grams per second[28] (two orders of magnitude greater than in a design basis accident), and similar rates would occur in a severe BWR accident. An OECD Nuclear Energy Agency report states, a "rapid initial [hydrogen]-source occurs in practically all severe accident scenarios because the large chemical heat release of the [zirconium]-steam reaction causes a fast self-accelerating temperature excursion during which initially large surfaces and masses of reaction partners are available."[29]

If an overheated reactor core were re-flooded with water, up to 300,000 grams of hydrogen could be generated in 60 seconds.[30] In this scenario, according to one report, between 5,000 and 10,000 grams of hydrogen could be generated per second.[31] (In the TMI-2 accident, re-flooding of the uncovered reactor core by the emergency core cooling system caused a spike in the hydrogen generation rates; it has been estimated that approximately 33 percent of all the hydrogen produced occurred during re-flooding.[32])

The total quantity of hydrogen that could be generated in a severe accident is different for PWRs and BWRs. Considering hydrogen generated only from the oxidation of zirconium: if the total amount of the zirconium in a typical PWR core, approximately 26,000 kilograms (kg), were to chemically react with steam, this would generate approximately 1150 kg of hydrogen; if the total amount of zirconium in a typical BWR's core, approximately 76,000 kg, were to chemically react with steam, this would produce about 3360 kg of hydrogen.[33]

Large BWR cores typically have about a 58-percent greater initial uranium mass than large PWR cores,[34] and this larger mass is divided into approximately 45 percent more fuel rods than in a PWR. However, these differences alone do not account for the fact that BWR cores have almost three times the mass of zirconium in their cores than PWRs.[35,36] BWR cores have significantly more zirconium mainly because, unlike PWRs, BWR fuel assemblies have "channel boxes" surrounding the fuel rods. The mass of each BWR assembly channel box is greater than 100 kg.[37] Thus a BWR core with 800 fuel assemblies would actually have more than the 76,000 kg of zirconium cited by the IAEA as typically present in a BWR core.)

The total quantity of hydrogen generated in a severe accident can vary widely: The Fukushima Daiichi accident, which resulted in three meltdowns, most likely generated more than 3,000 kg of hydrogen per affected unit; the amount produced in the TMI-2 accident is estimated at about 500 kg.[38] In a severe accident, hydrogen would also be generated within the reactor vessel from the oxidation of non-zirconium materials: metallic structures and boron carbide (in BWR cores).[39] In the TMI-2 accident, the oxidation of steel accounted for approximately 10 percent to 15 percent of the total hydrogen generation.[40] In a case in which the molten core penetrated the reactor vessel, hydrogen would be generated from the oxidation of metallic material (chromium, iron, and any remaining zirconium) during direct containment heating and also from interaction of the

molten core with concrete (out of which containment floors are made).[41] A safety study for the PWRs at Indian Point discusses a case in which interaction of a molten core with a concrete containment floor would generate more than 2721.5 kg of hydrogen.[42]

If a molten core interacted with concrete, carbon monoxide (which, like hydrogen, is a combustible gas) would also be generated. Depending on different accident scenarios, concrete types, and geometrical factors affecting the molten core-concrete interaction, the quantities of carbon monoxide generated could vary greatly; concentrations could differ by up to several volume percent in the containment.[43,44]

d. nRc MOdeLS UndeRPRedicT SeVeRe AccidenT HYdROgen geneRATiOn RATeS

A 2001 OECD Nuclear Energy Agency report advises that high hydrogen generation rates "must be taken into account in risk analysis and in the design of hydrogen mitigation systems." However, the same report notes that computer safety models used by regulators underpredicted the actual rates of hydrogen generation that occurred in two sets of experiments simulating severe accidents: the CORA tests and LOFT LP-FP-2.[45] (The CORA and LOFT LP-FP-2 experiments were conducted to investigate accidents that lead to a meltdown of the reactor core. LOFT LP-FP-2 was conducted with an actual nuclear reactor, 1/50th the volume of a full- size PWR, "designed to represent the major component and system response of a commercial PWR." LOFT LP-FP-2 was an actual core meltdown—the most realistic severe accident experiment conducted to date; it combined decay heating, severe fuel damage, and the quenching of zirconium fuel cladding with water.[46]) Computer safety models also failed to predict hydrogen generation in the initial QUENCH facility experiments.[47] This indicates that computer safety models also underpredict the hydrogen generation rates that would occur in severe accidents.[48]

A 1997 Oak Ridge National Laboratory (ORNL) report states that hydrogen generation in severe accidents can be divided into two separate phases: 1) a phase that runs from when the fuel cladding is still intact through the initial melting of the fuel cladding, which accounts for about 25 percent of the total hydrogen produced; and 2) a phase after the initial melting of the fuel cladding, in which there is additional melting, relocation, and the formation of uranium-zirconium-oxygen blockages, which accounts for about 75 percent of the total hydrogen generated (as indicated in analyses of the BWR CORA-28 and -33 tests).[49]

According to the 1997 ORNL report, computer safety models predict hydrogen generation rates "reasonably well" for the first phase, in which the fuel cladding remains intact, but predict hydrogen generation rates for the second phase "much less robustly." The 1997 ORNL report stresses that it is obvious that computer safety models need to accurately predict hydrogen generation rates when the fuel cladding is no longer intact, especially because most of the hydrogen

generation occurs in that phase.[50]

A 2011 International Atomic Energy Agency (IAEA) report states that computer safety models underpredict the rates of hydrogen generation that would occur during a re-flooding of an overheated reactor core.[51] The report cautions that, in different scenarios, re-flooding could cause hydrogen generation rates to vary to a large degree and that predictions need to consider the possible range of outcomes in order to help prepare for severe accident hydrogen risk. In the BWR CORA-17 test, which simulated the re-flooding and quenching of an overheated core, approximately 90 percent of the hydrogen generation occurred during re-flooding.[52]

Unfortunately, recent reports do not explicitly state the extent that computer safety models under-predict hydrogen generation rates during the re-flooding and quenching of an overheated core—i.e., a percentage value of the under-prediction has not been provided. However, presentation slides from a 2008 European meeting state that the "total amount of hydrogen under reflooding remains *highly underestimated* in [the] CORA-13 and LOFT LP-FP-2 experiments" [emphasis added]. In fact, regarding recent computer simulations of LOFT LP-FP-2, the same presentation slides state: "High temperature excursions with extended core degradation and enhanced hydrogen release observed in the test during reflood was not reproduced *due to the lack of adequate modeling*"[53] [emphasis added].

Despite these reports dating back to 1997, the NRC's 2011 Near-Term Task Force report on insights from the Fukushima Daiichi accident failed to mention, much less discuss, the fact that the NRC's computer safety models—such as the widely used MELCOR code developed by Sandia National Laboratories—underpredict the hydrogen generation rates that occur in severe accidents. By overlooking the deficiencies of computer safety models, the NRC undermines its own philosophy of defense-in-depth, which requires the application of conservative models.[54] When hydrogen generation rates are underpredicted, hydrogen mitigation systems are not likely to be designed so that they could handle the generation rates that would occur in actual severe accidents.

e. An ATTeMPT TO eLiMinATe HYdROgen RiSK: deVeLOPing nOn-ZiRcOniUM FUeL cLAdding

Perhaps the most effective way to help prevent hydrogen explosions in severe accidents would be to develop fuel cladding that does not generate large quantities of hydrogen when the core overheats in such accidents. Zirconium alloy cladding could possibly be replaced with silicon carbide, molybdenum alloys, molybdenum-zirconium alloys, or iron-chromium-aluminum alloys.[55] Silicon carbide is perhaps the most promising alternate; in the design basis accident temperature range—below 2200°F—silicon carbide is far less reactive than zirconium with steam,[56] generating much less hydrogen.

In 2010, according to an article in *Nuclear Engineering International*, a type of silicon carbide fuel cladding with a triplex design[57] was "still in the early stages of development and testing" the article opines that developing such cladding is "a high-risk, but potentially high-payoff"[58] venture. It remains to be seen if triplex silicon carbide would be a suitable replacement for zirconium alloy as a fuel-cladding material; there are a number of problems with silicon carbide cladding that still need to be resolved.

One problem is that during typical reactor operation the fuel pellets in silicon carbide cladding would have higher temperatures than they do when sheathed in zirconium. This would occur for two reasons: First, after extended irradiation, silicon carbide has a lower thermal conductivity than zirconium alloy,[59] meaning less of the fuel's heat would pass through the cladding and into the coolant. Second, the thin gap between the fuel pellets and the cladding would not be closed early in the first fuel cycle as occurs when zirconium cladding is used.[60] Both of these phenomena would prevent the pressurized water from cooling the fuel pellets in silicon carbide cladding as effectively as it does when the fuel pellets are sheathed in zirconium cladding.

A second problem is that an effective means of hermetically sealing the ends of silicon carbide fuel-cladding rods has not yet been developed.[61] If the fuel-cladding rods were not hermetically sealed during reactor operation, fission products would escape from the fuel rods and enter the coolant water.

A June 2012 Nuclear Energy Advisory Committee report lists additional problems with silicon carbide fuel cladding, such as a lack of ductility (the ability to bend, expand or contract without breaking) compared with currently used cladding types. The report also speculates that within four years further research and experimentation should confirm whether or not such problems can be resolved. If the problems are resolved, in-reactor testing of silicon carbide fuel cladding could take an additional 10 to 20 years.[62] Hence, even if all were to go well, it could take more than two decades before silicon carbide fuel cladding is ready for commercial use. There is certainly no reason to expect that zirconium alloy fuel cladding will ever be widely replaced in the aging U.S. fleet of nuclear power plants, which are facing obsolescence in the 2025-2050 timeframe.

iii. Severe Accident Hydrogen Explosions: An Unresolved Safety Issue

In the Fukushima Daiichi accident, hydrogen detonated in— and seriously damaged—the reactor buildings housing Units 1, 3, and 4, causing large radiological releases. The hydrogen explosion that occurred in the Unit 1 reactor building also "caused a blowout panel in the Unit 2 reactor building to open, which resulted in a loss of secondary containment integrity."[63] Actually, from a strict technical perspective, "secondary containment integrity" was lost the moment the flooded emergency diesel generators failed to supply backup power. Maintaining secondary containment integrity requires (a) an intact reactor building structure, and (b) a standby gas treatment system to filter releases from the intact structure to the atmosphere and maintain the structure at a lower pressure than ambient pressure (thus ensuring, in the case of small leaks, that outside air leaks *in* rather than inside air leaking *out*). Flooding of the emergency diesel generators by the tsunami took away (b) hours before the explosion took away (a).[64]

As discussed in the preceding sections, the zirconium-steam reaction will generate large quantities of hydrogen in severe accidents. When it reaches a sufficient local concentration inside the containment, this hydrogen will explode if exposed to an ignition source, of which there are many, given the amount of electrical equipment and wiring located inside the containment. In the TMI-2 accident, a hydrogen explosion—probably initiated by an electric spark[65]—occurred in the containment (a PWR large dry containment). The TMI-2 accident explosion did not breach the containment; however, the integrity of either a PWR ice condenser containment or a BWR Mark III containment could be compromised by an explosion of the quantity of hydrogen generated in the TMI-2 accident, because such containments have substantially smaller volumes and lower design pressures than PWR large dry containments.[66,67]

The fact that a hydrogen explosion did not breach TMI-2's containment does not preclude the possibility that if a meltdown were to occur at another PWR with a large dry containment, a hydrogen explosion could breach the containment, exposing the public to a large radiological release. Nonetheless, the NRC 2011 Near-Term Task Force report on insights from the Fukushima Daiichi accident claims that the pressure spike of potential hydrogen explosions would remain within the design pressure of PWR large dry containments.[68] However, according to NRC safety analyses,[69] conducted a decade ago, hydrogen explosions inside PWR large dry containments—of the quantity of hydrogen generated from zirconium-steam reactions of 100 percent of the active fuel-cladding length—could cause pressure spikes as high as 114 pounds per square inch (psi)[70] to 135 psi[71]—over twice the design pressure of a typical PWR large dry containment.

Such extreme pressure spikes could cause a PWR large dry containment to fail. There are also other safety analyses with worrisome results. For example, analyses conducted for Indian Point Units 2 and 3 about three decades ago found that peak pressures caused by hydrogen explosions could exceed the estimated failure pressure of Indian Point's containments—approximately 126 pounds per square inch gauge[72] (psig) or 141 pounds per square inch absolute[73] (psia).[74] For certain severe accident scenarios, peak pressure spikes were predicted to be 160 psia, 169 psia, about 157 psia, and 180 psia or greater.[75] (Some nuclear safety experts believe the accuracy of containment failure pressure estimates is questionable; according to one, "Experimental data on the ultimate potential strength of containment buildings and their failure modes are lacking."[76])

A. THe POTenTiAL dAMAge OF MiSSiLeS PROPeLLed bY HYdROgen eXPLOSiOnS

In a severe accident, a local hydrogen explosion within the containment could propel debris, such as concrete blocks from disintegrated compartment walls, at extremely high speeds. The impact of such debris ("internally-generated missiles") could compromise essential safety systems and even breach the containment, especially if it were made of steel.[77] If a PWR large dry containment made of reinforced concrete with a steel liner[78] were struck by a missile propelled by a hydrogen explosion, the containment would be more likely to incur cracks than to experience gross failure. Yet this is mere speculation: According to a 2011 IAEA report, "no analysis ever has been made on the damage potential of flying objects, generated in [a hydrogen]-explosion."[79]

An Institute of Nuclear Power Operations (INPO) report, published in November 2011 thoroughly documents how in the Fukushima Daiichi accident, internally generated missiles and missiles from secondary containments, propelled by hydrogen explosions, caused a considerable amount of damage and set back efforts to control the accident.[80] The report states:

> [D]ebris from the explosion struck and damaged the cables and mobile generator that had been installed to provide power to the standby liquid control pumps. The debris also damaged the hoses that had been staged to inject seawater into Unit 1 and Unit 2. ..... Some of the debris
> was also highly contaminated, resulting in elevated dose rates and contamination levels around the site. As a result, workers were now required to wear additional protective clothing, and stay times in the field were limited. The explosion significantly altered the response to the event and contributed to complications in stabilizing the units.[81]

b. HYdROgen eXPLOSiOnS: deFLAgRATiOnS And deTOnATiOnS

In a severe accident, water pumped into the reactor core to cool the fuel rods would heat up and produce thousands of kilograms of steam, which would enter the containment through pressure relief valves or a break in the cooling system circuit. At different points in an accident the presence of large quantities of steam in the containment would have an inerting effect, either helping to prevent or completely preventing hydrogen combustion if the steam concentration were 55 volume percent[82] or greater. (If hydrogen combustion were to occur, the presence of steam would help reduce its intensity.[83]) However, after enough steam condensed and this would be inevitable at some point in an accident, either naturally or by the use of containment spray systems[84]—either local or global hydrogen combustion could occur.

In a dry atmosphere of hydrogen and air, the lower flammability limit of hydrogen is a concentration of 4.1 volume percent.[85] If hydrogen concentrations were from 4.1 to about 8.0 volume percent, hydrogen combustion would be in the form of a deflagration with a relatively slow flame speed.[86] A deflagration is a combustion wave traveling at a subsonic speed relative to the unburned gas. (In the TMI-2 accident, a hydrogen deflagration occurred when the hydrogen concentration was 8.1 volume percent[87] causing a rapid pressure increase of approximately 28 psi in the containment.[88]) A famous instance of a hydrogen deflagration occurred on May 6, 1937, when the hydrogen-filled dirigible Hindenburg ignited while landing at Lakehurst, NJ and collapsed into a smoldering mass of twisted wreckage on the ground within a matter of seconds.

In a severe reactor accident, hydrogen could randomly deflagrate when its concentrations were at 8.0 volume percent or lower, because only a small quantity of energy is required for igniting hydrogen; sources of random ignition include electric sparks from equipment and static electric charges.[89] It has been postulated that in the TMI-2 accident, the hydrogen deflagration was initiated by a ringing telephone[90] and in the case of the Hindenburg, by the buildup of a static electric charge on its specially-coated outer skin.

In one sense, random or in some instances deliberate ignition of hydrogen at relatively low concentrations is beneficial, in that it can prevent the hydrogen from building up to more dangerous detonable concentrations. Unfortunately, in a severe accident, the average hydrogen concentration in the containment could reach 7.0 to 16.0 volume percent, or higher; local concentrations could be much higher. In a dry atmosphere of hydrogen and air, with hydrogen concentrations above about 10.0 volume percent,

Table 1: calculated Hydrogen (H2) production due to 75% Zirconium-Water Reaction

Note that all the predicted containment hydrogen concentrations (far right-hand column) are above the combustion threshold of 4.1 volume percent, and most are above temperature-dependent detonation thresholds of 11.6 and 9.4 volume percent hydrogen, at 68°F and 212°F, respectively.

Plant Name	Fuel Design ID	75% Wt. of Zr (lb)	Vol. of H_2 STP (ft^3)*	Containment Vol. (ft^3)	H_2 Conc. in Dry Air (%)
Arkansas-1	B&W B-2,3,4	31382	268432	1.78×10^6	13.10
Bellefonte 1,2	B&W Mark C	35793	306159	3.00×10^6	9.26
Millstone-2	CE 14x14	31111	266109	1.90×10^6	12.29
Palisades	CE 15x15	35415	302928	1.64×10^6	15.59
Arkansas-2	CE 16x16	30958	264807	1.78×10^6	12.95
Point Beach 1,2	W 14x14	16686	142728	1.00×10^6	12.49
Turkey Pt. 3,4	W 15x15	24674	211057	1.55×10^6	11.98
Zion 1,2	W 15x15	30332	259452	2.60×10^6	9.07
Trojan	W 17x17	32124	274775	2.00×10^6	12.08
Fort Calhoun	Exxon CE-14	22460	192116	1.10×10^6	14.87
Palisades	Exxon CE-14	34450	294674	1.64×10^6	15.23
Maine Yankee	Exxon CE-14	36645	313452	1.80×10^6	14.83
Fort Calhoun	Exxon CE-15	22713	194283	1.10×10^6	15.01
Palisades	Exxon CE-15	34839	297998	1.64×10^6	15.38
Maine Yankee	Exxon CE-15	37059	316988	1.80×10^6	14.97
Ginna	Exxon W-15	23259	198948	0.997×10^6	16.64
Robinson-2	Exxon W-15	30179	258139	2.10×10^6	10.95
Ginna	Exxon W-17	21327	182424	0.997×10^6	15.47
Robinson-2	Exxon W-17	27672	236699	2.10×10^6	10.13

*1 lbm of Zr will generate 0.044 lbm of H_2 and density of H_2 at STP = 5.144×10^{-3} lbm/ft^3

Source: D. W. Stamps et al., Sandia National Laboratories, *Hydrogen-Air-Diluent Detonation Study for Nuclear Reactor Safety Analyses*, NUreG/Cr-5525, January 1991, available at: www.nrc.gov, NrC Library, ADAMS Documents, Accession Number: ML071700388)

flames can accelerate up to and beyond the speed of sound: this phenomenon is termed "deflagration-to-detonation transition."[91] A "detonation" is a combustion wave traveling at a supersonic speed (greater than the speed of sound) relative to the unburned gas. Hydrogen combustion in the form of detonations occurred in the Fukushima Daiichi accident.

Higher temperatures and/or the presence of carbon monoxide could increase the likelihood of a deflagration-to-detonation transition. In a dry hydrogen-air mixture, the lower concentration limits at which deflagration-to-detonation transition can occur is 11.6 volume percent at temperature of 68°F; at 212°F, the lower concentration limit falls to 9.4 volume percent.[92] And in the presence of 5.0 volume percent of carbon monoxide (generated if a molten core interacts with a containment's concrete floor), 10.0 volume percent of hydrogen can detonate at approximately 68°F.[93]

One safety expert has concluded that within the large geometries of PWR-containments a slow laminar deflagration would be very unlikely. In most cases, highly efficient combustion modes must be expected."[94] In a small-break LOCA, large quantities of steam could enter the containment well before hundreds of kilograms of hydrogen were released into the containment. In such a scenario, thermal stratification could prevent the hydrogen from mixing with the steam.[95] In scenarios in which large quantities of steam were present in the containment, the hydrogen could reach high concentrations because the inerting effect of the steam could prevent the hydrogen from igniting at lower concentrations. After the steam condensed, a deflagration could transition into a etonation.

Table 2: Release Paths in LWR containments

Rupture of Containment wall or shell
Leakage past Sealing Surfaces (Operable Penetrations) ○ Pressure Seating Equipment Hatches ○ Pressure Unseating Hatches (Drywell Heads, Equipment Hatches) ○ Personnel Air Locks
Leakage past Purge and Vent Valves
Leakage from Electrical Penetration Assemblies
Leakage due to Failure of a Bellows (Expansion Joint)

Source: Containment Integrity Research at Sandia National Laboratories: An Overview, Sandia National Laboratories, NUreG/Cr-6906/ SAND2006-2274p, July 2006

c. LiMiTATiOnS OF cOMPUTeRSAFeTY MOdeLS TO PRediCT HYdROgen diSTRibUTiOn in THe cOnTAinMenT And HYdROgen deFLAgRATiOn-TO-deTOnATiOn TRAnSiTiOn

In a September 2011 meeting of the Advisory Committee on Reactor Safeguards (ACRS), Dana Powers, senior scientist at Sandia National Laboratories, expressed concern over the fact that hydrogen detonations occurred in the Fukushima Daiichi accident and stated that in experiments, "detonations are…extraordinarily hard to get."[96,97,98] Consequently, computer safety models (codes) derived from these experiments have limitations in predicting the hydrogen distribution and steam condensation that would occur in the containment in different severe accident scenarios.

A 2007 OECD Nuclear Energy Agency report states, "Further work in code development…and code user training, supported by suitable complex experiments, is necessary to achieve more accurate predictive capabilities for containment thermal hydraulics and atmospheric gas/ steam distribution. As a result of the code assessment, the modeling of the following three phenomena appeared to be the major issues: *condensation, gas density stratification, and jet injection*" [emphasis added].[99]

Computer safety models also have limitations in predicting the phenomenon of hydrogen deflagrations transitioning into detonations; as well as the maximum pressure loads the containment would incur from detonations, in different scenarios. Westinghouse's probabilistic risk assessment for its new and supposedly "passively safe" AP1000 reactor design, under construction in Georgia and South Carolina, observes that the phenomenon of hydrogen "deflagration-to-detonation transition is complex and not completely understood" and that the maximum pressure loads from detonations are difficult to calculate."[100]

The Fukushima Daiichi accident demonstrated that the NRC needs to conduct more realistic hydrogen combustion experiments—perhaps in facilities on the same scale as actual reactor containments, at elevated temperatures and with the large quantities of hydrogen that are produced in severe accidents.

iV. SeVeRe AccidenT HYdROgen MiTigATiOn

A. HYdROgen-MiTigATiOn STRATegieS FOR diFFeRenT cOnTAinMenT deSignS

Over the course of six decades, the NRC and its predecessor agency, the Atomic Energy Commission, have licensed six basic types of reactor containments (see Table 3), but within each type there are numerous design and construction differences (see Table 4) that translate into a wide and highly uncertain range of capacities to contain a severe reactor accident.

PWRs with Large dry containments and PWRs with Subatmospheric containents

The NRC does not require the owners of PWRs with large dry containments (52 out of 53 such units are currently operational in the U.S.), or the owners of PWRs with sub-atmospheric containments, maintained at an internal pressure below atmospheric pressure (five out of seven such units are currently operational in the U.S.) to mitigate the hydrogen that would be generated in severe accidents. The agency assumes that the large containment volumes of such PWRs are sufficient to keep the pressure spikes of potential hydrogen deflagrations within the design pressures of the structures.[101]

One hydrogen mitigation strategy for these types of containments would be to mix the hydrogen entering the containment using its fan coolers; this would reduce local hydrogen concentrations and mix the hydrogen with steam, which has an inerting effect.[102] A second hydrogen mitigation strategy for such PWRs would be to use hydrogen recombiners, safety devices that eliminate hydrogen in an accident by recombining hydrogen with oxygen—a reaction that produces steam and heat. There are two types of recombiners: passive autocatalytic recombiners (PAR), which operate without electric power, and electrically powered thermal recombiners. The hydrogen removal capacity for one hydrogen recombiner unit is only several grams per second.[103]

Table 3: U.S. Power Reactor containment Structures, by Type

Containment Type	Number
PWR Large Dry	53
PWR Subatmospheric	7
PWR Ice Condenser	9
Total PWRs	69
BWR Mark I	22
BWR Mark II	8
BWR Mark III	4
Total BWRs	34
US Total	103

Source: NUreG/Cr-6906/SAND2006-2274p, July 2006

In September 2003, the NRC likewise rescinded its requirement that PWRs with large dry containments and PWRs with sub-atmospheric containments operate with hydrogen recombiners installed in their containments. It decided that the quantity of hydrogen produced in design-basis accidents would not be risk-significant and that hydrogen recombiners would be ineffective at mitigating the quantity of hydrogen produced in severe accidents[104] when hydrogen generation could occur at rates as high as 5.0 kg per second.[105]

In the United States, if such PWRs still have hydrogen recombiners, there are typically two of them in each containment, to mitigate the quantity of hydrogen produced in a design basis accident. For example, Indian Point's containments each have two hydrogen recombiner units.[106] To help mitigate hydrogen in a wide range of severe accident scenarios, a group of European nuclear safety experts have recommended that such PWRs have from 30 to 60 hydrogen recombiner units distributed in their containments.[107] However, even 60 hydrogen recombiner units would not be capable of eliminating all of the hydrogen generated in some severe accident scenarios within the timeframe required to prevent a hydrogen explosion.

Table 4: U.S. PWRs classified by containment construction Type

Large Dry Primary Containment	Steel Cylinder	Steel Cylinder with Reinforced Concrete Shield Building	Kewaunee Prarie Island 1 Prarie Island 2 Davis-Besse St. Lucie 1 St. Lucie 2 Waterford 3	Arkansas 1 Arkansas 2 Oconee 1 Oconee 2 Oconee 3 Crystal River 3 Three Mile Island 1 Calvert Cliffs 1 Calvert Cliffs 2 Palisades Palo Verde 1 Palo Verde 2 Palo Verde 3 San Onofre 2 San Onofre 3 Braidwood 1 Braidwood 2 Byron 1 Byron 2 Callaway Farley 1 Farley 2 Point Beach 1 Point Beach 2 South Texas 1 South Texas 2 Summer Turkey Point 3 Turkey Point 4 Vogtle 1 Vogtle 2 Wolf Creek
	Reinforced Concrete Cylinder with Steel Liner	Reinforced Concrete Cylinder with Steel Liner	Comanche Peak 1 Comanche Peak 2 Diablo Canyon 1 Diablo Canyon 2 Indian Point 2 Indian Point 3 Salem 1 Salem 2 Shearon Harris 1	
		Reinforced Concrete Cylinder with Steel Liner and Secondary Containment	Seabrook 1	
	Posttensioned Concrete Cylinder with Steel Liner	1-D Vertical Posttensioned Concrete Cylinder with Steel Liner	Ginna HB Robinson	
		Diagonal Posttensioned Concrete Cylinder with Steel Liner	Fort Calhoun	
		3-D Posttensioned Concrete Cylinder with Steel Liner		
		3-D Posttensioned Concrete Cylinder with Steel Liner and Secondary Containment	Millstone 2	
Subatmospheric Primary Containment		Reinforced Concrete Cylinder with Steel Liner	Beaver Valley 1 Beaver Valley 2 North Anna 1 North Anna 2 Surry 1 Surry 2	
		Reinforced Concrete Cylinder with Steel Liner	Millstone 3	
Ice Condenser Primary Containment		Steel Cylinder with Reinforced Concrete Shield Building	Sequoyah 1 Sequoyah 2 Watts Bar 1 Catawba 1 Catawba 2 McGuire 1 McGuire 2	
		Reinforced Concrete Cylinder with Steel Liner	DC Cook 1 DC Cook 2	

Source: NUREG/CR-6906/SAND2006-2274p, July 2006

Left: Large dry steel primary containment with reinforced-concrete shield. right: Containment constructed with post-tensioned concrete with steel liner (e.g., palisades).

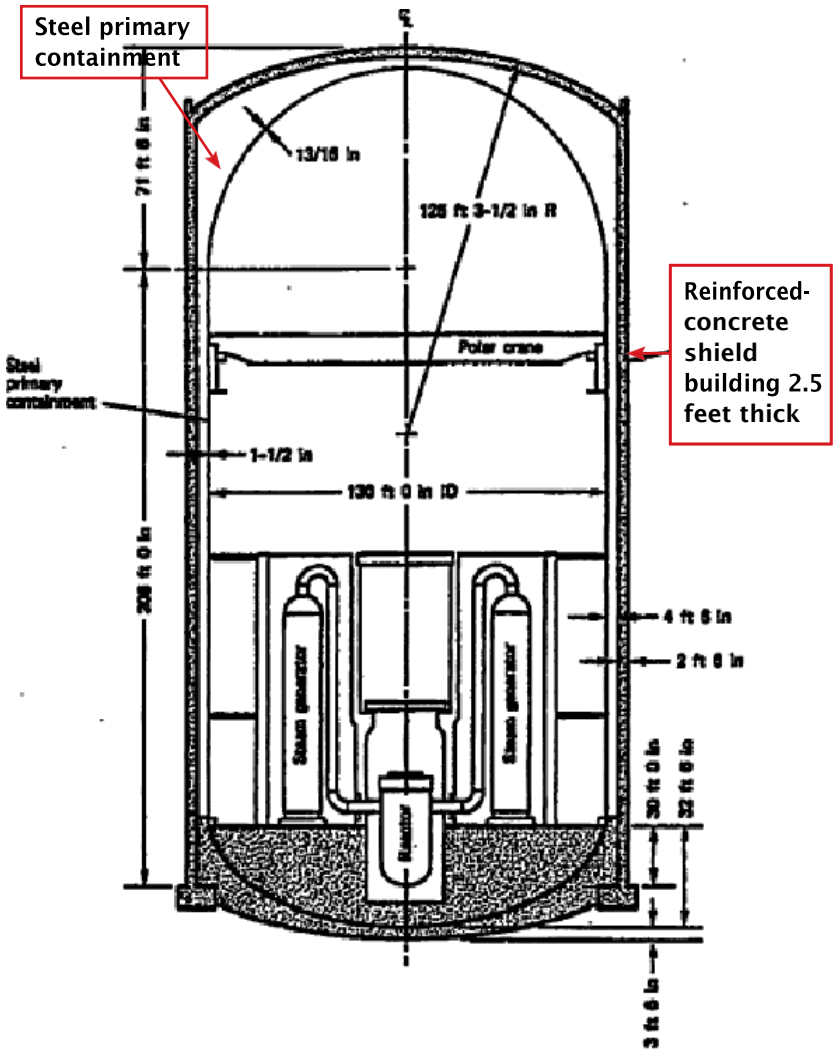


Figure 2 Large Dry Steel Containment with Reinforced Concrete Shield Buildir (e.g. Davis-Besse)

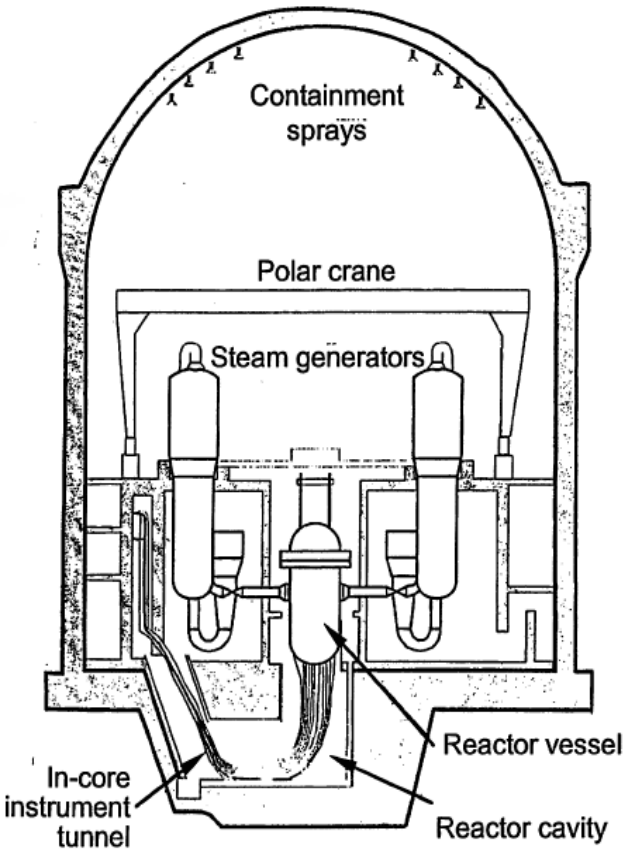


Figure 1 Typical PWR Large Dry Containment with Prestressed Containment (e.g. Palisades)

PWRs with ice condenser containments and bWR Mark iii The NRC requires that PWRs with ice condenser containments (nine such units are currently operational in the U.S.) and BWR Mark IIIs (four are currently operational in the United States) operate with hydrogen igniters installed in their containments in order to mitigate the hydrogen that would be generated in the event of a severe accident.[108] Hydrogen igniters are intended to burn off hydrogen as it is generated in an accident, before it reaches concentrations at which combustion would threaten the integrity of the containment. Hydrogen mitigation is essential for PWRs with ice condenser containments and BWR Mark IIIs *because their containments have relatively low design pressures,*[109] *which makes them more vulnerable to hydrogen exlosions.*

Such containments could be compromised by an explosion of the quantity of hydrogen that was generated in the TMI-2 accident.[110] Hydrogen igniters are intended to manage the quantity of hydrogen that would be generated by a zirconium-steam reaction of 75 percent of the fuel-cladding's active length,[111] which is considerably less than the quantity of hydrogen generated at each melted-down unit at Fukushima-Daiichi.

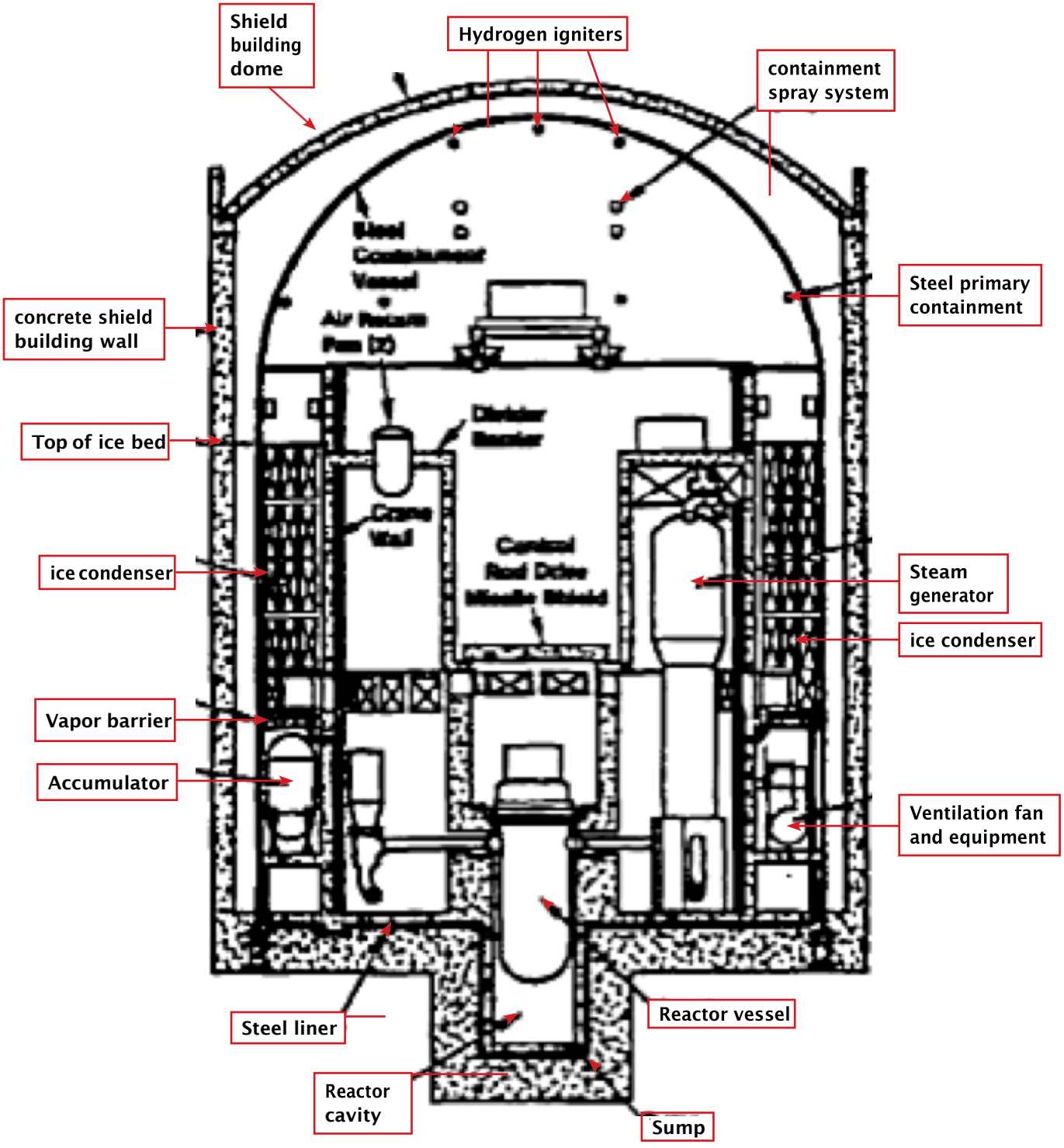
Table 5: U.S. bWRs by containment construction Type

A Mark I plant, Vermont Yankee, is missing from the NrC's compilation.

Free Standing Steel Primary Containment	Mark I Steel Drywell & Wetwell	Nine Mile Point 1 Oyster Creek Dresden 2 Dresden 3 Monticello Pilgrim 1 Quad Cities 1 Quad Cities 2 Browns Ferry 1 Browns Ferry 2 Browns Ferry 3 Cooper Duane Arnold Fermi 2 Fitzpatrick Hatch 1 Hatch 2 Hope Creek 1 Peach Bottom 2 Peach Bottom 3
	Mark II Steel Drywell & Wetwell	Columbia
	Mark III Reinforced Concrete Drywell Steel Wetwell	Perry 1 Riverbend 1
Reinforced Concrete Primary Containment with Steel Liner	Mark I Reinforced Concrete Drywell & Wetwell	Brunswick 1 Brunswick 2
	Mark II Reinforced Concrete Drywell & Wetwell	Limerick 1 Limerick 2 Susquehanna 1 Susquehanna 2 Nine Mile Point 2
	Mark III Reinforced Concrete Drywell & Wetwell	Clinton 1 Grand Gulf 1
Post-tensioned Concrete Primary Containment with Steel Liner	Mark II Reinforced Concrete Drywell Posttensioned Wetwell	LaSalle 1 LaSalle 2

Source: NNUreG/Cr-6906/ SAND2006-2274p, July 2006

Figure 10: Typical PWR ice condenser Steel containment with concrete Shield building (e.g., Sequoyah)



Source: NUREG/CR-6906/SAND2006-2274p, July 2006

bWR Mark i and bWR Mark ii

The NRC requires that BWR Mark Is (23 such units are currently operational in the U.S.) and BWR Mark IIs (eight such units are currently operational in the U.S.) operate with primary containments that have an inerted atmosphere[112]— to help prevent hydrogen combustion. An inerted containment atmosphere is defined as having less than 4.0 percent oxygen by volume.[113]

Nitrogen is used to inert BWR Mark I and Mark II primary containments because nitrogen is inexpensive and nontoxic. Such containments are relatively small, so deinerting and inerting for outages between fuel cycles can be achieved within hours; these processes are also inexpensive.[114]

If BWR Mark I and Mark II primary containments were not inerted, they would be extremely vulnerable to hydrogen explosions in severe accidents, because of their relatively small volumes.[115]

Such containments, if not inerted, could easily be compromised by an explosion of the quantity of hydrogen generated in the TMI 2 accident. A year after the Fukushima accident, in March 2012, the NRC ordered the installation of reliable hardened vents in BWR Mark I and Mark II containments by December 31, 2016.[116] A hardened vent could help control hydrogen in a severe accident but its primary purposes are to remove heat from and depressurize BWR Mark I and Mark II containments, which due to their small volumes are more susceptible than other containment designs to failure from overpressurization in an acident.

In September 1989, the NRC issued non-legally binding guidance to all owners of BWR Mark I facilities, recommending[117] that hardened vents be installed.[118] The NRC does not require that hydrogen be mitigated in the secondary containments of BWR Mark I and Mark II units.

Figure 11: cross-section View of a Typical bWR Mark iii containment (e.g., Perry, Riverbend)

Freestanding steel primary containment **(red)** with lower suppression pool **(blue)** and concrete shield building) has a low design pressure rating (15 psig), requiring that credit be given to the use of hydrogen igniters and containment sprays to meet containment requirements.

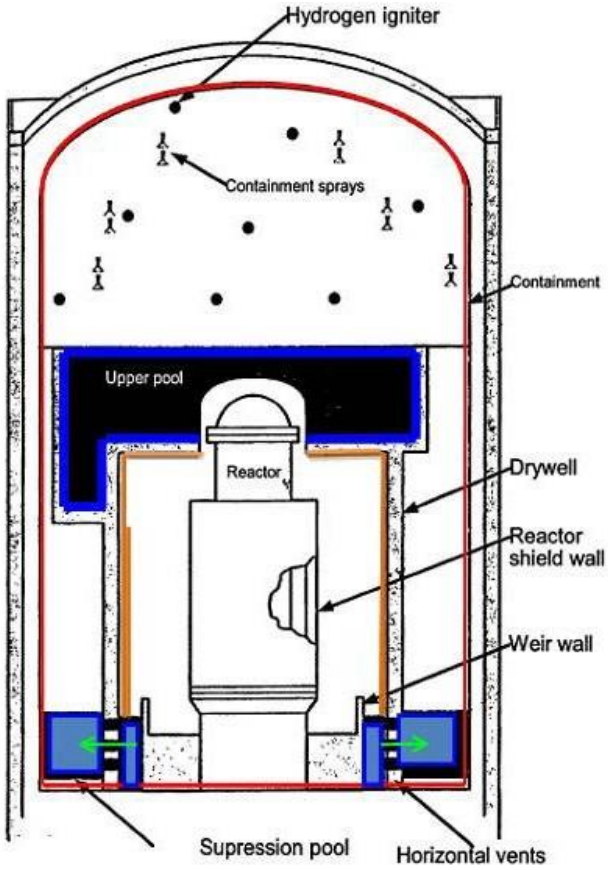


Figure 12: bWR Mark ii Reinforced concrete containment (Limerick Units 1 and 2)

Source: NNUreG/Cr-6906/SAND2006-2274p, July 2006

Drywell inerted with nitrogen **(orange)** is connected by pressure relief pipes **(red)** to wetwell **(green)**. Waterline is in **blue**.

Source: NNUreG/Cr-6906/SAND2006-2274p, July 2006

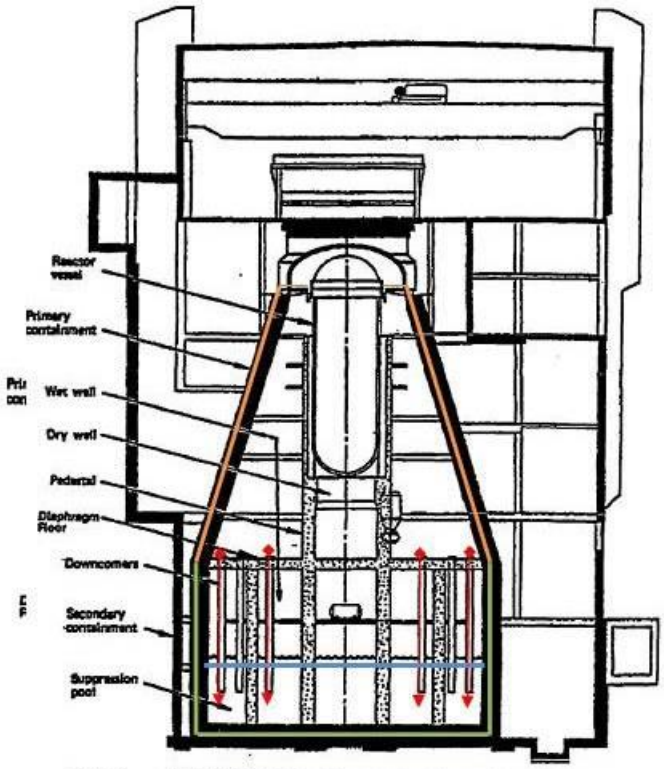


Figure 9 BWR Mark II Reinforced Concrete Containment (Limerick 1 & 2)

cASe STUdY: Hydrogen Risks in Westinghouse's Probabilistic Risk Assessment for the AP1000 and Plans for Managing an AP1000 Severe Accident

Currently four toshiba-Westinghouse Ap1000 units are under construction in South Carolina and Georgia. the NrC purports to have more stringent safety requirements for the Ap1000, that "reflect the Commission's expectation that future designs will achieve a higher standard of severe accident performance" than currently operating light water reactors.[119] And Westinghouse has touted the Ap1000 as having, in the event of a severe accident, a far lower probability of breaching its containment than currently operating nuclear power plants. However, Westinghouse's probabilistic risk assessment (prA) for the Ap1000 erroneously claims that it would not be possible for a hydrogen detonation to occur in the Ap1000's containment if the hydrogen concentration were less than 10.0 volume percent. A hydrogen detonation could compromise the containment and thus cause a large radioactive release. In fact, Westinghouse's prA assumes that the containment would fail "in all cases," in which hydrogen deflagrations transitioned into detonations.[120]

Westinghouse's prA for the Ap1000 states that "[s]ince the lowest hydrogen concentration for which deflagration-to- detonation transition has been observed in the intermediate-scale FLAMe facility at Sandia [National Laboratories] is 15 percent,[121] and [NrC regulation] 10 CFr 50.44 limits hydrogen concentration to less than 10 percent, the likelihood of deflagration-to-detonation transition is assumed to be zero if the hydrogen concentration is less than 10 percent."[122]

Westinghouse does not consider that the lower concentration limits at which deflagration-to-detonation transition can occur, at temperatures of 68°F and 212°F, are 11.6 and 9.4 volume percent of hydrogen, respectively.[123] According to a 1998 Brookhaven National Laboratory report: "Most postulated severe accident scenarios are characterized by containment atmospheres of about 373K [212°F]… However, calculations have shown that under certain accident scenarios local compartment temperatures in excess of 373K [212°F] are predicted."[124]

It is perplexing that Westinghouse's prA for the Ap1000 as well as the NrC's regulations for "future water-cooled reactors" rely on *outdated* assumptions that the phenomenon of hydrogen deflagration-to-detonation transition cannot occur below hydrogen concentrations of 10.0 volume percent: in 1991, Sandia National Laboratories reported that, in an experiment, deflagration-to-detonation transition occurred at 9.4 volume percent of hydrogen.[125] the previous year, the same information was reported at the NrC's eighteenth Water reactor Safety Information Meeting.[126]

In a September 2011 Advisory Committee on reactor Safeguards meeting, Dana powers, a senior scientist at Sandia National Laboratories, expressed concern over the fact that hydrogen detonations occurred in the Fukushima Daiichi accident and stated that in experiments, "detonations are…extraordinarily hard to get."[127] However, neglecting to reassess hydrogen-combustion safety issues for the Ap1000 after Fukushima, the NrC went ahead and issued licenses for two Ap1000s in February 2012.

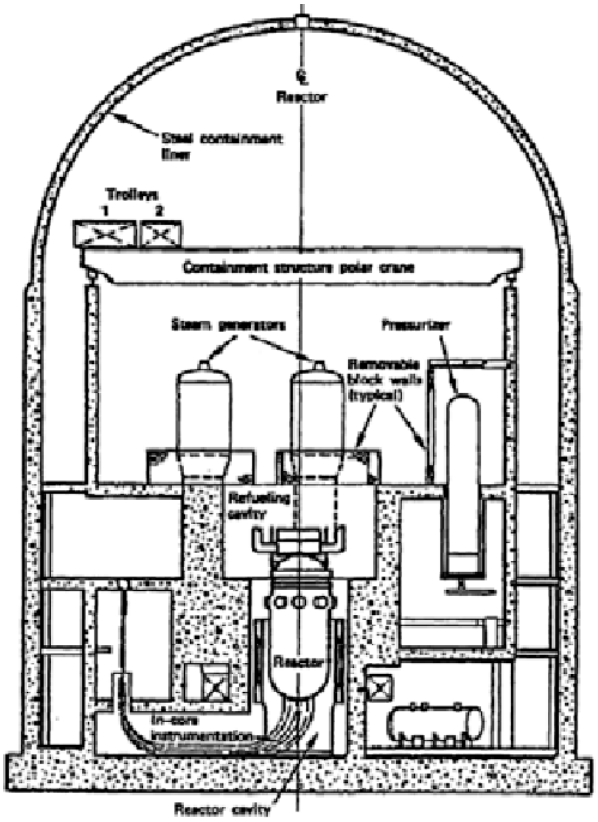
paradoxically, two of the Ap1000 containment's safety devices—hydrogen igniters, and passive autocatalytic hydrogen recombiner (pArs) units when they malfunction and behave like igniters—provide ignition sources that are capable of causing hydrogen detonations. In a severe accident, hydrogen igniters must be actuated at the correct time, because, as peter Hoffman wrote in the *Journal on Nuclear Materials*: "[t]he concentration of hydrogen in the containment may be combustible for only a short time before detonation limits are reached."[128]

If Ap1000 operators were to actuate the hydrogen igniters in an untimely fashion—after a local detonable concentration of hydrogen developed in the containment—it could cause a detonation. this especially could occur because Westinghouse's emergency response guidelines for the Ap1000 are flawed: operators are instructed to actuate hydrogen igniters when the core-exit gas temperature exceeds 1200°F. Westinghouse maintains that the core-exit temperature would reach 1200°F before the onset of the rapid zirconium-steam reaction of the fuel cladding,[129] which leads to thermal runaway in the reactor core; however, experimental data demonstrates that this would not necessarily be the case.

Westinghouse and the NrC, which approved the Ap1000 design, both overlooked data—available for more than a quarter century—from the most realistic severe accident experiment conducted to date (LoFt Lp-Fp-2), in which core-exit temperatures were measured at approximately 800°F when maximum in-core fuel-cladding temperatures exceeded 3300°F. In LoFt Lp-Fp-2, when core-exit temperatures were 800°F, the rapid zirconium-steam reaction of the fuel cladding had already occurred and the reactor core had started melting down. Hence, relying on core-exit temperature measurements in an Ap1000 severe accident could be unsafe: In a scenario in which operators re-flooded an overheated core simply because they did not know the actual condition of the core, hydrogen could be generated at rates as high as 5.0 kg per second. If operators were to actuate hydrogen igniters in such a scenario, it could cause a hydrogen detonation.

Westinghouse's general description of the Ap1000 states that "[pArs] control hydrogen concentration following design basis events."[130] However, in the elevated hydrogen concentrations that occur in severe accidents, pArs are prone to malfunctioning and behaving like hydrogen igniters. this is a problem: Ap1000 operators would not be able to switch off pArs, because they operate without electrical power. If the Ap1000 containment's pAr units malfunctioned and incurred ignitions after a detonable concentration of hydrogen developed in the containment, it could cause a detonation.[131] this could occur in a number of severe accident scenarios, especially those in which the Ap1000 containment's hydrogen igniter system was not operational,[132] enabling local detonable concentrations of hydrogen to develop in the containment.

Figure 13: Typical PWR Subatmospheric Reinforced concrete containment with Steel Liner (e.g., diablo canyon, north Anna, Surrey, beaver Valley)



Source: NUreG/Cr-6906/SAND2006-2274p, July 2006

The Uncertain Performance of different containment designs in a Severe Accident is Likely to Vary Widely

Figure 14 compares the calculated design pressure (in pounds per square inch above sea level atmospheric pressure, or "psig") of the six main types of U.S. commercial reactor containments with their net free volume in millions

of cubic feet. BWr Mark I and II have a nominally strong pressure rating, due to their use of pressure-suppression pools, but very low free volume. the BWr Mark III and pWr ice condenser designs have the lowest design pressures of the group as well as moderate volumes, while the two other pWr containment designs have the largest volumes along with comparatively high design pressures.

the actual safety situation is more complex than reflected in this figure. In reality, no two reactor containments, even at the same facility, are exactly alike, and units of the

same type can vary widely in their design and construction details. predictions of local failure mechanisms, which could lead to significant leakage in an accident even before overall design pressures are exceeded, depend on the availability of accurate as- built information (geometry

and material properties) at structural discontinuities (e.g., near containment doors or pipe and cable penetrations). "even if this information is available (not typical for actual containments), the prediction, a priori, of local failures

is at best an uncertain proposition.... Any evaluation of

b. PRObLeMS WiTH cURRenT HYdROgen-MiTigATiOn STRATegieS FOR ReSPecTiVe ReAcTOR deSignS

PWRs with Large dry containments and PWRs with Subatmospheric containments

As noted above, the NRC does not require owners of PWRs with large dry containments and PWRs with sub-atmospheric containments to mitigate the hydrogen that would be generated in severe accidents; however, in severe accidents, it would be possible for the pressure spikes of hydrogen explosions to exceed the design pressures of such containments. The NRC has reported that hydrogen detonations could occur in PWRs with large dry containments and PWRs with sub-atmospheric containments. For example, a 1990 NRC letter to plant owners states that in severe accidents, local and global hydrogen detonations could occur in PWRs with large dry or sub-atmospheric containments.[133]

Furthermore, a 1991 report by Sandia National Laboratories cautions that in severe accidents, in which 75 percent of the fuel-cladding active length oxidized, detonable concentrations of hydrogen could develop in dry hydrogen-air mixtures in such containments. The report

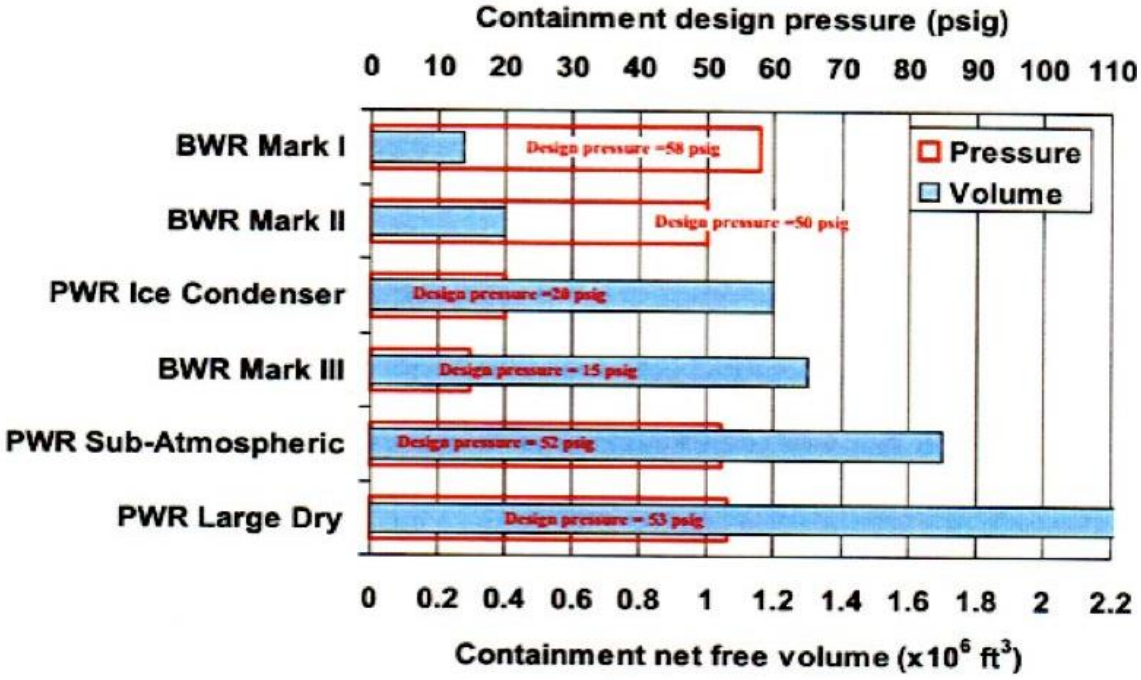
states that in a severe accident, steam typically would be present in the containment, yet the quantity of steam would be unpredictable because of condensation, which would be facilitated by containment spray systems. Detonations would most likely be initiated through deflagration-to-detonation transition, yet direct detonations could perhaps be possible at higher temperatures.[134]

Hydrogen recombiners would be prone to malfunctioning by incurring ignitions in the elevated concentrations that occur in severe accidents. This would be a serious problem: A recombiner's unintended ignition could cause a detonation.[135]

PARs could be advantageous in station-blackout accidents—a complete loss of grid-supplied and backup on-site alternating current power—because they operate without either external power or plant operator actuation; however, there is no way to prevent such recombiners from self-actuating or to shut them off in elevated hydrogen concentrations. Plant operators would be able to control the operation of electrically powered thermal hydrogen recombiners; yet operators should be cautious about actuating thermal recombiners in an accident. Plant operators should actuate thermal recombiners only if hydrogen concentrations are low and should deactivate them

Figure 14: Typical containment Volume and design Pressure for U.S. nuclear Plants

As a general rule, low volumes make it more likely that design basis pressures will be exceeded in a severe accident.



Source: NUreG/Cr-6906/SAND2006-2274p, July 2006

if hydrogen concentrations increase to dangerous levels. Of course, to soundly make such decisions, operators would need to ascertain local hydrogen concentrations throughout the containment, which would be especially difficult in the course of a fast-moving and/or chaotic accident scenario.

Among the PWRs in the United States that still have hydrogen recombiners installed, only one has PARs (Indian Point Unit 2); the others have thermal recombiners—typically two units in each containment. In Europe, some PWRs have from 30 to 60 PARs installed and distributed in their containments to help mitigate hydrogen in the event of a severe accident.[136] This is puzzling, given that such recombiners would be prone to behaving like igniters—malfunctioning by incurring ignitions—in elevated hydrogen concentrations.[137]

After intensive deliberation, European regulators decided not to require igniters in PWRs (those without ice condenser containments) because "[u]ncertainties were identified with respect to, among other aspects, hydrogen distribution and combustion behavior."[138] In line with the reasoning behind this decision, it seems that European regulators should also be hesitant about allowing PWRs to operate with PARs installed in their containments, because unintended ignitions from such recombiners would be neither predictable nor preventable in a severe accident.

Another problem with hydrogen recombiners is that in a severe accident, cesium iodide particles transported through them could be converted into volatile iodine, producing an additional source term of radiation exposure.[139]

PWRs with ice condenser containments and bWR Mark iii containments

The NRC requires that PWRs with ice condenser containments and BWR Mark IIIs operate with hydrogen igniters installed in their containments in order to mitigate the hydrogen that would be generated in the event of a severe accident.[140] However, hydrogen igniters should be used only in cases where the effects of their use are entirely predictable, and predictions must indicate that the containment would not be threatened by any potential deflagrations arising from the deliberate ignition of hydrogen.[141]

Safety experts have questioned the safety of using igniters to mitigate hydrogen at certain times in some severe accident scenarios. For example, an OECD Nuclear Energy Agency report published in August 2000 states, "The main question in the application of the igniter concept is its safety orientation. The use of igniters should reduce the overall risk to the containment and should not create new additional hazards such as a local detonation."[142]

Another paper, published in 2006, states that "[w]ith early ignition, the hydrogen will be eliminated by slow combustion without high thermal and temperature loads, but with late ignition, hydrogen detonation transition will quickly occur with high local thermal and pressure loads which will threaten the integrity of the containment."[143]

A 1990 NRC letter to plant owners cautions that hydrogen igniters would be prevented from operating in station blackouts at PWRs with ice condenser containments and

Figure 15: Prestressed concrete containment vessel (PccV) at the Ohi Unit 3 reactor in Japan

A 1:4 scale model of a prestressed concrete containment vessel (pCCV) at the ohi Unit 3 reactor in Japan, undergoes a massive rupture in a 2001 Sandia Laboratory test at 3.63 times its design pressure (pd), or 206.4 psig. the pressurized model had experienced leak rates in earlier tests, indicating functional failure at 2.4 times pd.



Source: NNUREG/CR-6906/SAND2006-2274p, July 2006

BWR Mark IIIs. If hydrogen were not burned off, it could reach detonable concentrations; if power were then restored, the igniters could cause a hydrogen detonation.[144]

bWR Mark i and bWR Mark ii containments

Hydrogen generation is a serious problem for the small-volume, inerted BWR Mark I primary containment, because hydrogen is non-condensable at the temperatures expected in a nuclear power plant.[145] In a BWR severe accident, hundreds of kilograms of non-condensable hydrogen gas would be generated (potentially exceeding 3,000 kg[146]) at rates as high as 5,000 to 10,000 grams per second if there were a re-flooding of an overheated reactor core.[147] This would increase the internal pressure of the primary containment. If enough hydrogen were generated, the containment would likely first leak excessively before failing catastrophically from overpressurization.

A BWR Mark I primary containment is made up of a drywell shaped like an inverted lightbulb, which contains the reactor vessel, and a steel wetwell (also called a torus) shaped like a doughnut, which surrounds the base of the drywell. The drywell and wetwell are connected by large pipes. The wetwell is half filled with water (typically about 790,000 gallons[148])—and is sometimes referred to as a suppression pool. A BWR Mark II primary containment also has a drywell and wetwell (concrete), but these are shaped and oriented from their BWR Mark I counterparts.

Unignited releases

In a severe accident, water already present or pumped into the reactor core to cool the fuel rods would heat up and produce thousands of kilograms of steam, which would enter the drywell of the primary containment. The water in the wetwell's suppression pool is intended to condense the steam and help absorb the heat released by the accident to reduce the pressure in the primary containment; as the steam pressure builds up in the drywell, steam vents downward into the wetwell through pipes, which terminate underwater in the suppression pool. (Without the condensation of the steam in the suppression pool, the relatively small primary containments of BWR Mark Is and Mark II units (often termed pressure suppression containments) would quickly fail from overpressurization.

However, the generation of sufficiently large quantities of non-condensable hydrogen gas in a severe accident could overwhelm the capacity of the primary containment. For example, there could be a severe accident scenario at a BWR Mark I in which there is a rapid accumulation of steam in the drywell and non-condensable gas (nitrogen[149] and hydrogen) in the wetwell; in such a scenario, the primary containment's pressure could rapidly increase "up to the venting and failure levels."[150]

early bWRs Perform Poorly in containment Leak-Rate Tests, even When Liberal Test Protocols Allow Pretest Repairs to Supposedly "As Found" condition of Seals and Valves

BWR Mark I and Mark II primary containments are designed to limit—not prevent—hydrogen leakage in accidents. In overall leak rate tests[151]—conducted below design pressure—such containments leak hundreds of pounds of air per day. For example, in 1999, tests conducted at Nine Mile Point Unit 1, a BWR Mark I, and Limerick Unit 2, a BWR Mark II, found that overall leakage rates at both units were in excess of 350 pounds of air per day,[152,153] which is actually less than the maximum *allowed* leak rates.

This means that in a severe accident even if there were *no damage* to a primary containment, hydrogen would leak into the secondary containment (the reactor building); leak rates would increase as the internal pressure increased and would become even greater if the seals at the various piping and cable penetrations were damaged. (Typical BWR containments have 175 penetrations, almost twice as many as typical PWR containments.)[154]

Regarding reactor containments and hydrogen leakage, a 2011 IAEA report states:

> [N]o containment is fully leak tight, [hydrogen] will leak to the surrounding areas, which often have the function of secondary containment. . . . Hence, there is a certain risk that combustion may occur outside the primary containment. This may lead to combustion loads exerted on the containment from outside. Usually, containments have considerable margin against loads from inside, as they are in principle designed to carry the pressure loads from a large break LOCA. The pressure bearing capability for loads from outside can be substantially less…"[155]

In an accident, a mixture of hydrogen, nitrogen, and steam would leak from a BWR primary containment; as internal pressures increased and the accident progressed, the concentration of hydrogen in the leaking mixture would increase. If there were no damage to the primary containment, the quantity of hydrogen that leaked (by weight) would be relatively small, because hydrogen is about 14 times less dense than air.[156] However, a BWR secondary containment—which has a design pressure of approximately 3.0 psig[157]—could be breached if, for example, between 20 to 40 pounds of hydrogen were to leak into it, accumulate locally, and explode.

In a severe accident, it is highly probable that the seals at the penetrations of BWR Mark I and Mark II primary containments would become degraded (of course, some penetration-seals could already be degraded by material aging before the accident occurred.) A 1984 report from Brookhaven National Laboratory advises that severe accident risk estimates should consider "[t]he potential for containment leakage through penetrations prior to reaching" estimated containment failure pressures. The report further notes it is highly probable that the leakage of BWR Mark I and Mark II primary containments would "prevent overpressurization," and that "[f]ailure of non-metallic seals for containment penetrations (primarily equipment hatches, drywell heads, and purge valves) are the most significant sources of containment leakage."[158] BWR drywell heads, which have diameters between 30 to 40 feet, would most likely incur the highest leak rates in the containment as internal pressures increased.[159]

Containments have had leaks, exceeding allowable leakage rates, that lasted for many months—"primarily from large penetrations, such as the purge and vent valves, [main steam isolation valves, for BWRs only], and valves inadvertently left open."[160] In fact, BWR Mark I primary containments have failed a number of overall leak rate tests; for example, Oyster Creek—the oldest operating commercial reactor in the U.S., which is considered to be quite similar to Fukushima Daiichi Unit 1—has failed at least five tests.[161]

In one test, Oyster Creek's primary containment leaked at a rate that was 18 times greater than its design leak rate;[162] if this test was conducted at 35 psig, the same pressure as subsequent Oyster Creek tests,[163] which seems likely, the primary containment leaked at a rate in excess of 6800 pounds of air per day.[164] Such results beg the question: what were the pre-accident leak rates—*below design pressure*—of the three primary containments that leaked hydrogen at Fukushima Daiichi?

Since the Fukushima Daiichi accident, the problem of hydrogen leakage from primary containments has not been adequately addressed. (Mark II primary containments would also incur hydrogen leaks in severe accidents.) In fact, the NRC is currently preparing to reduce the frequency of both local and overall leak rate testing from once every five and once every 10 years, respectively, to once every 75 months and 15 years, respectively.

Remarkably, the current 10-year requirement already represents a loosening of the original leak-test intervals, which stood at 2.0 to 3.3 years prior to 1995, depending on the particular nature of the test.[165] In its safety analyses to assess extending the test intervals, the NRC has simply overlooked the fact that BWR Mark I and Mark II primary containments are vulnerable to hydrogen leakage. Moreover, as reactors approach and exceed their originally-licensed lifetimes of 40 years, one might intuitively conclude that the need for containment leak rate testing is actually increasing, not diminishing, in order to gauge the impact of aging penetration seals and isolation valves on containment integrity under a range of accident scenarios, including severe accidents.

Local leak rate tests of containment penetrations are *supposed* to be conducted as "as-found tests," meaning that the penetrations are not supposed to be repaired immediately before testing; however, NUREG/ CR-4220 reports that all of the "NRC Senior Inspectors for containment systems [who] were contacted and asked to relate their experience with containment isolation system performance."[166] They stated that:

> [R]eported leakage rates often do not represent true leakage rates. Utilities are generally allowed to perform some minor repair on a valve prior to recording its "as-found" condition for a leakage test. Similarly, major repair (such as completely rebuilding a valve) is permitted prior to recording a valve's "as-left" condition at the end of its leakage test.[167]

Hence, around 1985 when NUREG/CR-4220 was published, it was a *common practice* for utilities to make minor repairs on valves immediately before recording their "as-found" leak rates. The local leak rate tests that are intended to measure leakage rates at containment isolation valves are termed "Type C tests." In September 1995, the NRC extended Type C test intervals from two years to five years. Interestingly, the failure rates of Type C "as-found" tests have decreased by about *one order of magnitude* since the test intervals for such tests were increased in 1995.[168] Such significant improvements beg the question: since 1995, to what degree have valves been repaired immediately before recording their "as-found" leak rates?

NUREG/CR-4220 states that one of the NRC Senior Inspectors "indicated that Types B and C tests [local leak rate tests] are performed before Type A [overall leak rate test], enabling repairs to be made so that the Type A test can be passed easily."[169]

In a March 2013 ACRS meeting, an ACRS member similarly observed that "[i]f they did all their preparations perfectly, they would never fail."[170] It is clear that overall leak rate tests and local leak rate tests would provide a far more accurate assessment of pre-existing containment leak rates if repairs were not allowed to be made immediately before testing.

A report from the Electric Power Research Institute's (EPRI), "Risk Impact Assessment of Extended Integrated

Table 6: Historical Reactor containment integrated Leak Rate Test (iLRT) Failures even with Test Protocol Allowing Pre-Test Repairs (circa 1985)

Reactor Name	Type	Test No.	Reactor Name	Type	Test No.
Beaver Valley-1	PWR	1	Oconee-1	PWR	1
Beaver Valley-1	PWR	2	Oconee-2	PWR	2
Big Rock Point	BWR	7	Oconee-3	PWR	1
Browns Ferry-1	BWR	1	Oyster Creek	BWR	1
Browns Ferry-2	BWR	2	Oyster Creek	BWR	3
Brunswick-2	BWR	1	Oyster Creek	BWR	4
Brunswick-2	BWR	2	Oyster Creek	BWR	5
Cal.Cliffs-1	PWR	1	Oyster Creek	BWR	6
Cook-1	PWR	2	Palisades	PWR	1
Dresden-1	BWR	1	Palisades	PWR	2
Dresden-1	BWR	6	Peach Bottom-2	BWR	1
Dresden-1	BWR	7	Peach Bottom-3	BWR	1
Dresden-3	BWR	2	Peach Bottom-3	BWR	2
Duane Arnold	BWR	1	Pilgrim-1	BWR	3
Fitzpatrick	BWR	1	Pilgrim-1	BWR	4
Fort Calhoun	PWR	2	Quad Cities-1	BWR	2
Ginna	PWR	2	Rancho Seco	PWR	1
Hatch-1	BWR	1	Robinson-2	PWR	2
Indian Point-1*	PWR	1	San Onofre-1	PWR	1
Indian Point-3	PWR	1	San Onofre-1	PWR	4
LaCrosse	BWR	1	Surry-2	PWR	1
LaCrosse	BWR	2	Surry-2	PWR	2
LaCrosse	BWR	6	Surry-2	PWR	3
LaCrosse	BWR	7	Three Mile Island-1	PWR	1
Millstone-1	BWR	2	Three Mile Island-1	PWR	2
Millstone-1	BWR	3	Turkey Point-4	PWR	1
Monticello	BWR	2	Turkey Point-4	PWR	2
Monticello	BWR	3	Vermont Yankee	BWR	1
Nine Mile Point-1	BWR	3	Vermont Yankee	BWR	2
Nine Mile Point-1	BWR	4			

* Note two failed ILRTs reported so count twice

Source: p.J. pelto et al., *Reliability Analysis of Containment Isolation Systems*, pacific Northwest Laboratory, NUreG/Cr 4220, June 1985, available at: NrC's ADAMS Documents, Accession Number: ML103050471

Leak Rate Testing Intervals,"[171] has been used by the NRC to help justify the extension of testing intervals.[172] However, this report overlooked the fact that in severe accidents, BWR Mark I and Mark II primary containments leak explosive hydrogen gas into secondary containments. A second major problem with EPRI's report is that its list of overall leak rate test failures does not include the majority of test failures reported in NUREG/CR-4220. NUREG/CR-4220 lists a total of 60 overall (integrated) leak rate tests that failed before March 1985;[173] in fact, NUREG/CR-4220 also reports that when considering the results of local leak rate tests that failed with excessive leakage rates, the number of overall leak rate tests that failed is a total of 109.[174]

By contrast, EPRI's report lists *a total of nine* "containment leakage or degradation events" that occurred before March 1985.[175] Regarding its methodology for assessing the risk impact of extended test intervals, EPRI's report states "The first step is to obtain current containment leak rate testing performance information. … *This information is used to develop the probability of a pre-existing leak in the containment* using the Jeffreys Non-Informative Prior statistical method" [emphasis added].[176] Clearly, the NRC needs to review a large portion of the existing data that EPRI overlooked and reassess the risk impact of extended test intervals.

In a severe accident, any primary containment in a condition that would cause it to fail a leak-rate test would leak dangerous quantities of explosive hydrogen gas into a reactor building, *even at below design pressure*; however, the NRC does not seem concerned about excessive leakage rates. A 1995 NRC report[177] "concluded that…increasing allowable leakage rates by 10 to 100 times results in a *marginal risk increase*, while reducing costs by about 10 percent"[178] [emphasis added]. And a 1989/1990 NRC report[179] concluded that even if there is a containment leakage of 100 percent per day, "the calculated individual latent cancer fatality risk is below the NRC's safety goal."[180] Clearly, this safety goal would not be achieved if leaking hydrogen were to detonate in secondary containments, as it did at Fukushima Daiichi.

In March 2013, the NRC stated that "[s]ensitivity analyses in NUREG-1493 and other studies show that *light water reactor accident risk is relatively insensitive to the containment leakage rate* because the risk is dominated by accident sequences that result in failure or bypass of containment"[181] [emphasis added]. The progression of the Fukushima Daiichi accident was certainly affected by the leakage of hydrogen gas. In fact, it is possible that Unit 3's primary containment *did not fail* before hydrogen leaked into the Unit 3 secondary containment and detonated.

The internal pressure of Unit 3's primary containment actually *increased* after the hydrogen explosion occurred. The explosion occurred on March 14 at 11:01 am, then at 12:00 pm the primary containment's pressure started increasing from 52.2 psia to 53.7 psia, at 4:40 pm the pressure started decreasing from 69.6 psia, and at 8:30 pm the pressure started increasing from 52.2 psia.[182] In the Fukushima Daiichi accident, the BWR Mark I primary containments of Units 1, 2, and 3 incurred internal pressures that exceeded the loads they were designed to sustain. According to an INPO report published in November 2011, the highest recorded internal pressures in the primary containments of Units 1, 2, and 3 were approximately 1.7, 1.7, and 1.4 times greater than their design pressures, respectively.[183] (In the accident, hydrogen leaked from the primary containments—according to INPO: "most probably" at the penetrations[184]—of Units 1, 2, and 3 and detonated in the secondary containments of Units 1, 3, and 4.) The NRC has stated that in the circumstances of the Fukushima Daiichi accident, it is reasonable to conclude that BWR Mark IIs would also incur devastating consequences, "because Mark II containment designs are only slightly larger in volume than Mark I containment designs[185] and also use wetwell pressure suppression."[186]

Reliable Hardened Vents

In an attempt to resolve the problems of BWR Mark I and Mark II primary containment overpressurization and decay heat removal, in March 2012, the NRC ordered that reliable hardened vents be installed in BWR Mark Is and Mark IIs by December 31, 2016.[187] (As stated above, in September 1989, the NRC had tried to solve the same problems by issuing non-legally binding guidance to all the owners of BWR Mark Is, *recommending*[188] that hardened vents be installed in Mark Is.[189]) The NRC's order stipulates a number of performance objectives and features that a new design of a hardened vent must have; for example, "shall include a means to prevent inadvertent actuation."[190]

It could be difficult to design a hardened vent that would perform well in scenarios in which there were rapid containment-pressure increases. A 1988 report by the Committee on the Safety of Nuclear Installations report states that "[f]iltered venting is less feasible for those sequences resulting in early over-temperature or overpressure conditions. This is because the relatively early rapid increase in containment pressure requires large containment penetrations for successful venting."[191] This indicates that a reliable hardened vent's piping will likely need a diameter and thickness greater than what has been voluntarily installed at BWR Mark I containments in the United States.[192]

If a hardened vent were designed for passive operation by means of a rupture disk, in place of a remotely or manually actuated valve, venting would occur if a predetermined threshold pressure were reached. A reliable passive venting capability could be beneficial in severe accident scenarios that have rapid containment pressure increases. However, a 1983 Sandia National Laboratories manual cautions that "it may be difficult to design vents that can handle the rapid transients involved" in a severe accident.[193]

It is important to consider that in the Fukushima Daiichi accident, the particular design of the installed vents may have caused the accident to be worse than it would have been without their use: The INPO report of November 2011 states that "it is postulated that the hydrogen explosion in the Unit 4 reactor building was caused by hydrogen from Unit 3."[194] Unit 3 and Unit 4's containment vent exhaust piping was interconnected, so hydrogen may have been vented from Unit 3 to Unit 4's secondary containment,[195] where it detonated.

In severe accidents, spent fuel pools are vulnerable to the hydrogen explosions that can occur in BWR Mark I and Mark II secondary containments. Spent fuel pools, which store fuel assemblies after they are discharged from the reactor core, are located in the secondary containment of these designs, elevated about 70 to 80 feet above ground level. If a spent fuel pool were compromised by a hydrogen explosion, it could cause large radiological releases.

Some thought initially that the explosion that occurred in Fukushima Daiichi Unit 4 at 6:00 am on March 15, 2011—3.63 days after the March 11, 2011 earthquake—could have been caused by the detonation of hydrogen gas generated by the reaction of steam with the zirconium cladding of fuel rods stored in the spent fuel pool. Subsequent investigations indicated that this was not the case.

However, according to a 2012 ORNL paper, the hydrogen that detonated *could* have come from the Unit 4 pool's fuel assemblies reacting with steam: If there were a loss of spent fuel pool cooling, the water in the pool would be heated by the fuel rods' decay heat until it reached the boiling point; then the water would boil away, uncovering the fuel rods. ORNL computer analyses found that in this scenario, a total of 1,800 kg to 2,050 kg of hydrogen could have been
generated. The analyses also found that 150 kg of hydrogen—an amount that could have caused the Unit 4 explosion—would have been generated 3.63 days after the accident commenced if the initial water level in the pool were 4.02 meters (at the top of the active length of the fuel rods).[196]

The NRC does not require that hydrogen be mitigated in the secondary containments of BWR Mark I and Mark II sites in severe accidents. This is a problem, because hydrogen could leak into secondary containments and explode, as occurred in the Fukushima Daiichi accident. The Fukushima Daiichi accident demonstrated that BWR Mark I secondary containments—essentially ordinary industrial buildings with design pressures of approximately 3.0 psig[197]—cannot withstand hydrogen explosions. (BWR Mark II secondary containments also have low design pressures.) In line with the NRC's approach to safety through defense-in-depth,[198] the Fukushima Daiichi accident scenario of hydrogen leaking from overpressurized primary containments and/or hardened vent systems should be considered as likely to occur again, in the event of a severe accident at either a BWR Mark I or BWR Mark II.

c. MOniTORing cORe degRAdATiOn And HYdROgen geneRATiOn in SeVeRe AccidenTS

In a severe accident, plant operators would need equipment that effectively monitored evolving conditions; information, such as temperatures in the reactor core and hydrogen concentrations in the containment, would help them manage an accident and implement hydrogen mitigation. Without accurate and prompt core and containment diagnostics, plant operators would not be able to properly manage an accident. Unfortunately, some of the current methods of monitoring core and containment diagnostics are inadequate.

Monitoring core degradation

In a severe accident involving a PWR, the primary tool used to detect inadequate core cooling and uncovering of the core would be coolant temperature measurements taken with core-exit thermocouples (temperature measuring devices) at a point above the active length of the fuel rods. In many cases, a predetermined core-exit thermocouple measurement would be used to signal the time for PWR operators to transition from emergency operating procedures (EOP) to severe accident management guidelines (SAMG). The NRC's Near-Term Task Force report states that "EOPs typically cover accidents to the point of loss of core cooling and initiation of inadequate core cooling (*e.g.*, core exit temperatures in PWRs greater than 649 degrees Celsius [1,200 degrees Fahrenheit])."[199]

Experimental data indicates that core-exit thermocouple measurements would not be an adequate indicator for when to safely transition from EOPs to SAMGs.[200] Two of the main conclusions from experiments are: 1) that core-exit temperature measurements display *in all cases* a significant delay (up to several hundred seconds) and: 2) that core-exit temperature measurements are *always* significantly lower (up to several hundred degrees Celsius) than the actual maximum cladding temperature.[201] In an experiment simulating a severe accident—LOFT LP-FP-2—core-exit temperatures were measured at approximately 800°F when in-core fuel-cladding temeratures exceeded 3300°F.[202]

In a severe accident, plant operators are supposed to implement SAMGs before the onset of the rapid zirconium-steam reaction, which leads to thermal runaway in the reactor core. Clearly, using core-exit thermocouple measurements in order to detect inadequate core cooling or uncovering of the core would be neither reliable nor safe. For example, PWR operators could end up re-flooding an overheated core simply because they did not know the actual condition of the core. Unintentionally re-flooding an overheated core could generate hydrogen, at rates as high as

effectiveness."[203]

Core-exit thermocouples are not installed in BWRs. In a severe accident involving this type of reactor, plant operators are supposed to detect inadequate core cooling or uncovering of the core by measuring the water level in the reactor core. However, after the onset of core damage BWR reactor water level measurements are unreliable; and can read erroneously

high in low-pressure accidents, like large-break LOCAs, and when there are high drywell temperatures.[204]

In the Fukushima Daiichi accident, plant operators did not know the actual condition of the reactor cores of Units 1, 2, and 3. In a December 2011 article, Saloman Levy—a former GE engineer-manager for BWRs[205]—stated his judgment that in the Fukushima Daiichi accident, plant operators should have recognized that water level measurements were unreliable and that reactor and containment pressures as well as the wetwell water temperature would be superior indicators of the state of the core. According to Levy, "The reactor and the containment pressures will rise faster when hydrogen is produced. Increased reactor and containment pressure rates and wetwell [water] temperature rises confirm accelerated core melt."[206] Yet what Levy recommends is not a solution to the problem of identifying the correct time to transition to SAMGs in a BWR severe accident, because *the rapid zirconium-steam reaction would have already commenced by the time operators confirmed an accelerated core melt.*

MOniTORing FOR THe PReSence OF OXYgen And HYdROgen

The NRC requires that BWR Mark I and Mark II units operate with oxygen monitors installed in their primary containments in order to confirm that the containment remains inerted during operation. In a severe accident, if a primary containment were to become de-inerted, "severe accident management strategies, such as purging and venting, would need to be considered."[207]

The NRC also requires that all licensed plants operate with the ability to monitor hydrogen concentrations in their containments. However, in 2003, the NRC reclassified hydrogen monitors (and oxygen monitors) as "non-safety-related" equipment,[208,209] meaning that this equipment does not have to undergo full qualification (including seismic qualification), does not have redundancy, and does not require onsite (standby) power.

In severe accidents, hydrogen monitors would be used to help assess the degree of core damage that had occurred and to help with accident management. For example, BWR Mark III's use hydrogen monitors to help guide emergency operating procedures: Hydrogen igniters would not be used In scenarios in which hydrogen reached concentrations that would threaten containment integrity if the hydrogen were to combust.

BWR Mark I and Mark IIs operate with hydrogen monitors installed in their inerted primary containments yet do not have such monitors in their secondary containments. David Lochbaum of the Union of Concerned Scientists has cautioned that "[t]he inability to monitor hydrogen concentrations could cause [plant] operators to not vent [BWR Mark I and Mark II] reactor buildings, thus leading to ignitions resulting in loss of secondary containment integrity." He states further that without the ability to monitor hydrogen, operators could "preemptively vent the reactor buildings when it was not necessary to do so," which would also cause radioactive releases.[210]

In 1983, the NRC issued an order requiring that in a severe accident, hydrogen monitors function within 30 minutes after coolant water is injected into the reactor vessel; in 1998, the NRC "determined that the 30-minute requirement can be overly burdensome" and imposed a 90-minute requirement, instead.[211] The NRC seems to believe that all severe accidents would be slow-moving station-blackout accidents—a complete loss of grid-supplied and backup onsite alternating current power—like the Fukushima Daiichi accident; it does not consider that fast-moving accidents are also possible.

Despite Fukushima Daiichi's three devastating hydrogen explosions, the NRC has relegated severe-accident hydrogen safety issues to the *least proactive* stage of its post-Fukushima regulatory responses to the accident (termed "Tier 3"). NRDC believes that the NRC should reconsider its approach and promptly address severe accident safety issues involving hydrogen. In this section we outline a number of safety initiatives that the NRC should pursue to reduce the risk of hydrogen explosions in severe accidents.

Figure 16: cutaway View of PWR Pressure Vessel and core of Korean Standard nuclear Power Plant Plus (KSnP+)

Deployed at Shin-Kori 1 and 2; Shin-Wolsong 1 and 2, South Korea.

Two-Loop PWR design based on U.S. Combustion Engineering System 80+.

To control the reactor, dozens of control rod extensions (2) must penetrate the vessel closure head (3) via nozzles (1) so that control rods can be withdrawn or inserted to control the fission reaction in nuclear fuel assemblies (8).

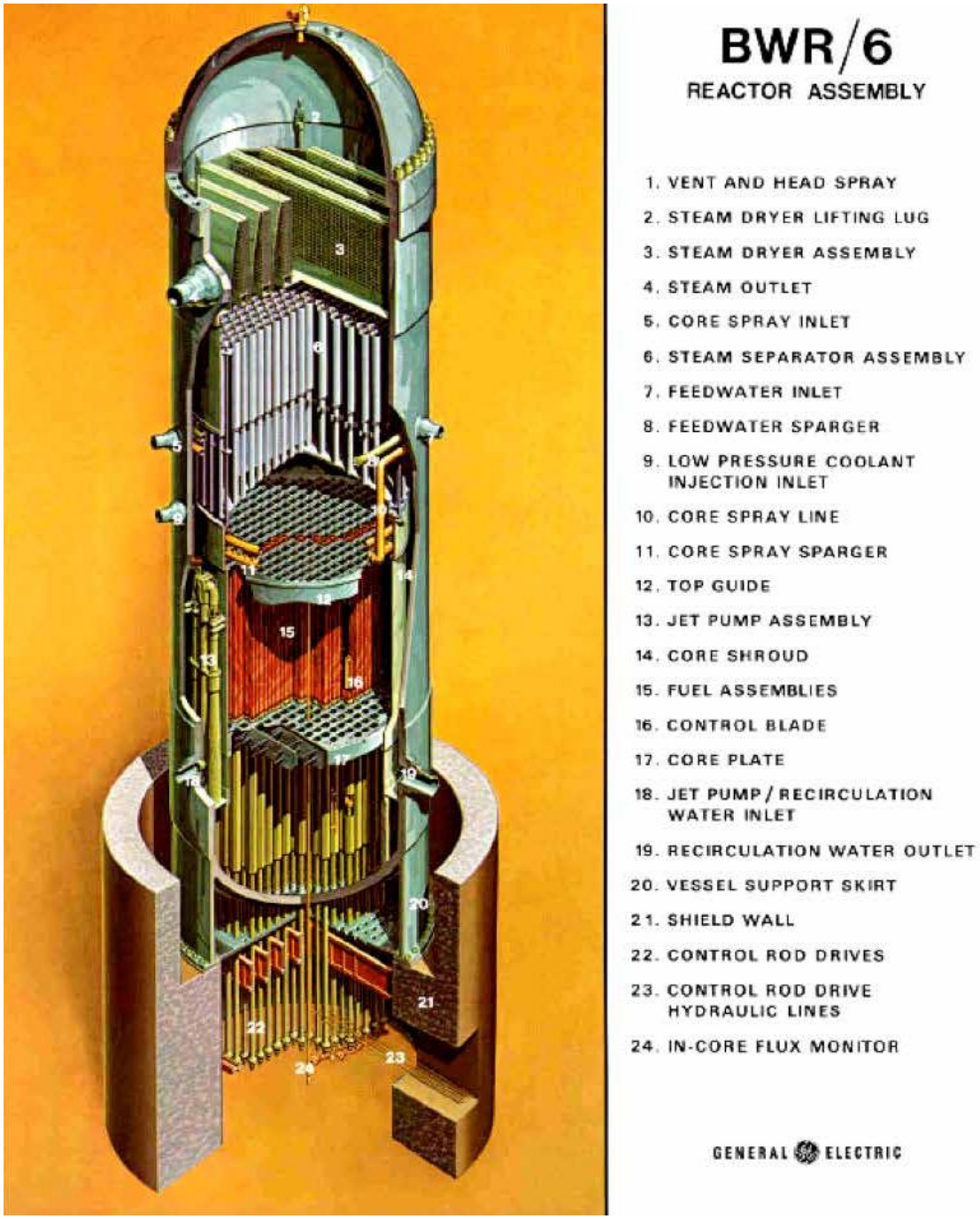
Highly pressurized water in the primary cooling loop enters the reactor vessel at (7) and exits at (5), the site of coolant temperature measurements that are supposed to guide operator actions in an accident



Source: econtent.unm.edu/cdm/search/collection/nuceng

Figure 17: GE Boiling Water Reactor (BWR) Model 6 Reactor Vessel

Note that control rod blades on the bottom must be hydraulically driven upward into the core, rather than dropping from above as they do in a PWR.



Source: USNR Technical Training Center Reactor Concepts Manual: Boiling Water Reactor (BWR) Systems, www.nrc.gov/reading-rm/basic-ref/teachers/03.pdf



Source: Reactor Concepts Manual, Boiling Water reactor Systems, USNrC, technical training Center, www.nrc.gov/reading-rm/basic-ref/teachers/03.pdf

V. nRdc'S RecOMMendATiOnS FOR RedUcing THe RiSK OF HYdROgen eXPLOSiOnS in SeVeRe nUcLeAR AccidenTS

A. deVeLOP And eXPeRiMenTALLY VALidATe cOMPUTeR SAFeTY MOdeLS THAT WOULd be cAPAbLe OF cOnSeRVATiVeLY PRedicTing RATeS OF HYdROgen geneRATiOn in SeVeRe AccidenTS

The NRC needs to acknowledge that its existing computer safety models underpredict the rates of hydrogen generation that occur in severe accidents. The NRC should conduct a series of experiments with multi-rod bundles of zirconium alloy fuel rods simulators and/or (actual) fuel rods as well as study the full set of existing experimental data. The NRC's objective in this effort should be to develop models capable of predicting with greater accuracy the rates of hydrogen generation that occur in severe accidents.

b. ASSeSS THe SAFeTY OF eXiSTing HYdROgen RecOMbineRS, And POTenTiALLY diScOnTinUe THe USe OF PARS UnTiL TecHnicAL iMPROVeMenTS ARe deVeLOPed And ceRTiFied

Experimentation and research should be conducted in order to improve the performance of PARs so that they would not malfunction and incur ignitions in the elevated hydrogen concentrations that occur in severe accidents. Some experimentation and research has already been conducted; however, the problem of PARs incurring ignitions in elevated hydrogen concentrations remains unresolved.

The NRC and European regulators should also perform safety analyses to determine if existing PARs should be removed from plant containments. It is possible such analyses would find that removing PARs would help improve safety in the event of a severe accident. Until PARs are developed that do not pose a risk of ignitions in elevated hydrogen concentrations, the NRC and European regulators should also review whether to replace PARs with electrically powered thermal hydrogen recombiners. However, this could prove costly, and thermal hydrogen recombiners would not function in a station-blackout accident unless provided with their own independent train of emergency power.

In a severe accident, plant operators would be able to turn off thermal recombiners in order to prevent them from operating in elevated hydrogen concentrations. However, to safely operate thermal recombiners, operators would be required to have instrumentation providing timely information on the local hydrogen concentrations throughout the containment.

c. SigniFicAnTLY iMPROVe eXiSTing OXYgen And HYdROgen MOniTORing inSTRUMenTATiOn

The NRC should reclassify oxygen and hydrogen monitors as safety-related equipment that has undergone full qualification (including seismic qualification), has redundancy, and has its own independent train of emergency electrical power. These recommendations are in accordance with the conclusions of the NRC's Advisory Committee on Reactor Safeguards (ACRS), which stated that "[t]he experience at Fukushima showed that essential reactor and containment instrumentation should be enhanced to better withstand beyond-design basis accident conditions" and that "[r]obust and diverse instrumentation that can better withstand severe accident conditions is needed to diagnose, select, and implement accident mitigation strategies and monitor their effectiveness."[212]

The NRC should require that, after the onset of a severe accident, hydrogen monitors be functional within a time frame that enables timely detection of quantities of hydrogen indicative of core damage and a potential threat to containment integrity. The current requirement that hydrogen monitors be functional within 90 minutes of the injection of coolant water into the reactor vessel is clearly inadequate for protecting public and plant worker safety.

NRDC supports the Union of Concerned Scientists' request to the NRC regarding hydrogen-monitoring instrumentation. The NRC should require that hydrogen monitoring instrumentation be installed in 1) BWR Mark I and Mark II secondary containments, 2) the fuel handling buildings of PWRs and BWR Mark IIIs, and 3) any other plant structure where it would be possible for hydrogen to enter.

d. UPgRAde cURRenT cORe diAgnOSTic cAPAbiLiTieS in ORdeR TO beTTeRSignAL TO PLAnT OPeRATORS THe cORRecT TiMe TO TRAnSiTiOn FROM eMeRgencY OPeRATing PROcedUReS TO SeVeRe AccidenT MAnAgeMenT gUideLineS

The NRC should require plants to operate with thermocouples placed at different elevations and radial positions throughout the reactor core to enable plant operators to accurately measure a wide range of temperatures inside the core under both typical and accident conditions. In the event of a severe accident, in-core thermocouples would provide plant operators with crucial information to help them track the progression of core damage and manage the accident—for example, indicating the correct time to transition from EOPs to SAMGs.

e. ReQUiRe ALL nUcLeAR POWeR PLAnTS TO cOnTROL THe TOTAL QUAnTiTY OF HYdROgen THAT cOULd be geneRATed in A SeVeRe AccidenT

The NRC should require all PWRs (with large dry containments, subatmospheric containments, and ice condenser containments) and BWR Mark IIIs to operate with systems for combustible gas control that would effectively and safely control the total quantity of hydrogen that could potentially be generated in different severe accident scenarios (this value is different for PWRs and BWRs). The NRC should also require the same for BWR Mark I and Mark II unless it is demonstrated that venting (without causing significant radiological releases) their inerted containments would effectively and safely control the hydrogen generated in severe accidents. Systems for combustible gas control also need to effectively and safely control the total quantity of hydrogen that could potentially be generated at all times throughout different severe accident scenarios, taking into account the potential rates of hydrogen generation.

Additionally, the NRC should require all PWRs and BWR IIIs to operate with systems for combustible gas control that would be capable of preventing local concentrations of hydrogen in the containment or other structures from reaching levels that would support combustions, deflagrations, or detonations that could cause a loss of containment integrity and/or necessary accident mitigating features.

Furthermore, the NRC should require licensees of PWRs with ice condenser containments and BWR Mark IIIs (and any other nuclear power plants that would operate with hydrogen igniter systems) to perform analyses demonstrating that their hydrogen igniter systems would effectively and safely mitigate hydrogen in different severe accident scenarios. Licensees unable to do so should be ordered to upgrade their systems to adequate levels of performance.

F. ReQUiRe THAT dATA FROM LeAK RATe TeSTS be USed TO HeLP PRedicT THe HYdROgen LeAK RATeS OF THe PRiMARY cOnTAinMenT OF eAcH bWR MARK i And MARK ii LicenSed bY THe nRc in diFFeRenT SeVeRe AccidenT ScenARiOS

The NRC should require that data from overall leak rate tests and local leak rate tests—already required by Appendix J to Part 50 for determining how much radiation would be released from the containment in a design basis accident— be used to help predict hydrogen leak rates from the primary containment of each BWR Mark I and Mark II licensed by the NRC under different severe accident scenarios. If data from an individual leak rate test indicates that dangerous quantities of explosive hydrogen gas would leak from a primary containment in a severe accident, the plant owner would be required to repair the containment.

NRDC also recommends that the NRC require that overall leak rate tests and local leak rate tests be conducted without allowing repairs to be made immediately before the testing of potential leakage paths, such as containment welds, valves, fittings, and components which penetrate containment.[213]

Additionally, NRDC recommends that the NRC reevaluate its plan to extend the intervals of overall and local leak rate tests to once every 15 years and 75 months, respectively.[214] (There are two types of local leak rate tests; Type B is required at least once every 10 years.) The NRC needs to conduct safety analyses that take into account the relatively greater vulnerability of BWR Mark I and Mark II primary containments to hydrogen leakage. It is probable that the intervals between leak rate tests would need to be shortened rather than extended.

The NRC also needs to consider that in the past it was a common practice to make repairs to valves immediately before conducting "as found" local leak rate tests. Clearly, such tests do not provide accurate assessments of preexisting containment leak rates. The NRC needs to investigate whether repairs have been recently made immediately before conducting "as found" tests. More important, the NRC needs to fully integrate into its regulatory role the fact that in the Fukushima Daiichi accident, hydrogen leaked from the primary containments of Units 1, 2, and 3 and detonated in the secondary containments of Units 1, 3, and 4, causing large radiological releases.

1 In this report we frequently refer to "severe" nuclear accidents: i.e., accidents in which there is severe damage to the reactor core—for example, a partial core meltdown. A severe nuclear accident could be caused by a natural disaster, mechanical failure, or plant operator errors. the accidents at three Mile Island Unit 2, Chernobyl Unit 4, and Fukushima Daiichi Unit 1, 2, and 3 were all severe accidents.

2 As nuclear safety expert David Lochbaum has noted, "Secondary containment is designed to have limited leakage…into the reactor building. the secondary containment leak test entails starting the standby gas treatment system. this system features fans, ductwork, dampers, and filter trains that draw air from the reactor building and refueling floors. this filtered air is discharged via an elevated release point. the filter trains are tested periodically to see if they remove over 99% of the radioactive particles from the discharge stream." Note to author from David L. Lochbaum, nuclear safety expert with the Union of Concerned Scientists, 01-06-2014.

3 Since hydrogen is a noncondensable gas, it will accumulate in the air space above the water surface of the suppression pool. When the differential pressure between the drywell and wetwell gets too great, vacuum breakers open automatically to transport hydrogen gas from the wetwell into the drywell, where it can accumulate or leak out into the surrounding reactor building.

4 Note to author from David L. Lochbaum, nuclear safety expert with the Union of Concerned Scientists, January 6, 2014.

5 this request to the NrC was first made by the Union of Concerned Scientists.

6 typical operating BWr and pWr coolant pressures are approximately 1000–1050 pounds per square inch (psi) and approximately 2250 psi, respectively. See International Atomic energy Agency (IAeA), "Assessment and Management of Ageing of Major Nuclear power plant Components Important to Safety: BWr pressure Vessels," IAeA-teCDoC-1470, october 2005, p. 7; and IAeA, "Assessment and Management of Ageing of Major Nuclear power plant Components Important to Safety: pWr pressure Vessels," IAeA-teCDoC-1120, october 1999, p. 5.

7 the NrC's definition of the reactor coolant system: the system used to remove energy from the reactor core and transfer that energy either directly or indirectly to the steam turbine. See www.nrc.gov/reading-rm/ basic-ref/glossary/reactor-coolant-system.html.

8 typical operating BWr and pWr coolant temperatures are 540°–550°F and 540°–620°F, respectively. See IAeA, "Assessment and Management of Ageing of Major Nuclear power plant Components Important to Safety: BWr pressure Vessels," IAeA-teCDoC-1470, october 2005, p. 7; and IAeA, "Assessment and Management of Ageing of Major Nuclear power plant Components Important to Safety: pWr pressure Vessels," IAeA- teCDoC-1120, october 1999, p. 5.

9 For consistency, this report will use the term *zirconium* to refer to all the various types of zirconium alloys that make up fuel cladding. Zircaloy, Zl**r**Lo, and M5 are particular types of zirconium alloy fuel cladding. In a LoCA environment, the oxidation behavior of the different fuel cladding materials, with various zirconium alloys, would be similar because of their shared zirconium content.

10 the NrC's definition of a design basis accident: A postulated accident that a nuclear facility must be designed and built to withstand without loss to the systems, structures, and components necessary to ensure public health and safety. See www.nrc.gov/reading-rm/basic-ref/glossary/design basis-accident.html.

11 the NrC states that "beyond design basis accident" is a term "used as a technical way to discuss accident sequences that are possible but were not fully considered in the design process because they were judged to be too unlikely. (In that sense, they are considered beyond the scope of design basis accidents that a nuclear facility must be designed and built to withstand.)" See www.nrc.gov/reading-rm/basic-ref/glossary/ beyond-design basis-accidents.html.

12 the coolant water slows down or "moderates" the kinetic energy of the neutrons produced by fission, enabling a self-sustaining fission reaction in the uranium isotope 235U, which makes up about 4 percent of the uranium in the fuel.

13 In a pWr, fuel rod temperatures could exceed 1830°F within 60 seconds; at a BWr, fuel rod temperatures could exceed 1830°F within three minutes.

14 the equation for the reaction is written as $Zr + 2H_2o \rightarrow Zro_2 + 2H_2 +$ energy. the energy (heat) generated by the reaction is about 6.5 megajoules per kilogram (kg) of Zr reacted.

15 randall o. Gauntt, Sandia National Laboratories, email to Jason Schaperow of NrC, "re: Cladding Behavior Under Steam and Air Conditions," January 31, 2000, available at: www.nrc.gov, electronic reading room, ADAMS Documents, Accession Number: ML010680338.

16 In the tMI-2 accident, cooling water was discharged from the pilot-operated relief valve, which was stuckopen.

17 robert e. Henry held research positions at Argonne National Laboratory during the decade leading up to the tMI-2 accident and was associate director of the reactor Analysis and Safety Division at Argonne when he became involved in the evaluation of the tMI-2 accident, as part of a group formed by the electric power research Institute's Nuclear Safety Analysis Center (NSAC).

18 robert e. Henry, presentation slides from "tMI-2: A textbook in Severe Accident Management," 2007 ANS/eNS International Meeting, November 11, 2007; seven of these presentation slides are in Attachment 2 of the transcript from "10 C.F.r. 2.206 petition review Board re: Vermont Yankee Nuclear power Station," July 26, 2010, available at: ADAMS Documents, Accession Number: ML102140405, Attachment 2.

19 robert e. Henry, presentation slides from "tMI-2: A textbook in Severe Accident Management."

20 It is acknowledged that runaway oxidation occurred in the tMI-2 accident; however, the temperature at which it commenced is unknown, because there is no thermocouple data from the hot spots of the fuel assemblies. NrDC does not intend to present robert e. Henry's postulation that runaway oxidation of zirconium cladding by steam commenced at 1832°F in the tMI-2 accident as evidence that a runaway reaction did in fact commence at 1832°F.

21 robert e. Henry, presentation slides from "tMI-2: A textbook in Severe Accident Management."

22 NrC, "Feasibility Study of a risk-Informed Alternative to 10 CFr 50.46, Appendix K, and GDC 35," June 2001, available at: ADAMS Documents, Accession Number: ML011800519, p. 3-1.

23 peter Hofmann, "Current Knowledge on Core Degradation phenomena, a review," *Journal of Nuclear Materials* 270, Nos. 1–2 (April 1, 1999), p. 205.

24 Sherrell r. Greene, oak ridge National Laboratory, "the role of BWr Secondary Containments in Severe Accident Mitigation: Issues and Insights from recent Analyses," 1988.

25 the regulation 10 C.F.r. § 50.46(b)(i) stipulates that in a postulated design basis accident, "[t]he calculated maximum fuel element cladding temperature shall not exceed 2200°F."

26 e. Bachellerie et al., "Generic Approach for Designing and Implementing a passive Autocatalytic recombiner pAr-System in Nuclear power plant Containments," *Nuclear Engineering and Design* 221, Nos. 1–3 (April 2003), p. 158 (hereinafter "Designing and Implementing a pAr-System in NppContainments").

27 Atomic energy Commission, "Safety evaluation report for Indian point Nuclear Generating Unit No. 3," Docket No. 50-286, September 21, 1973, available at: www.nrc.gov, electronic reading room, ADAMS Documents, Accession Number: ML072260465, p. 6-10.

28 e. Bachellerie et al., "Designing and Implementing a pAr-System in Npp Containments," p. 158.

29 oeCD Nuclear energy Agency, "State-of-the-Art report on Flame Acceleration and Deflagration-to-Detonation transition in Nuclear Safety," NeA/CSNI/r(2000)7, August 2000, available at: www.nrc.gov, NrC Library, ADAMS Documents, Accession Number: ML031340619, p. 6.38 (hereinafter "report on FA and DDt").

30 e. Bachellerie et al., "Designing and Implementing a pAr-System in Npp Containments," p. 158.

31 J. Starflinger, "Assessment of In-Vessel Hydrogen Sources," in *Projekt Nukleare Sicherheitsforschung: Jahresbericht 1999* (Karlsruhe: Forschungszentrum Karlsruhe, FZKA-6480, 2000).

32 oeCD Nuclear energy Agency, "In-Vessel Core Degradation Code Validation Matrix: Update 1996-1999," report by an oeCD NeA Group of experts, october 2000, p.13.

33 IAeA, "Mitigation of Hydrogen Hazards in Severe Accidents in Nuclear power plants," IAeA-teCDoC-1661, July 2011," p. 10 (hereinafter "Mitigation of Hydrogen Hazards in SA").

34 this estimate is based on that fact that large BWr cores and large pWr cores have up to approximately 800 and 200 fuel assemblies, respectively (see NrC, "Boiling Water reactors" (located at: http://www.nrc.gov/reactors/bwrs.html) and NrC, "pressurized Water reactors" (located at: http://www.nrc.gov/reactors/pwrs.html)); and recent designs of BWr and pWr fuel assemblies have up to approximately 190 kg and 480 kg of initial uranium mass per assembly, respectively (see NrC, "Certificate of Compliance No. 1014," Appendix B, "Approved Contents and Design Features for the Hi-Storm 100 Cask System," (available at ADAMS No: ML13351A189), pp. 2.39, 2.44). Hence, large BWr cores and large pWr cores are estimated to have a total of approximately 152,000 kg and 96,000 kg of initial uranium mass, respectively.

35 BWrs and pWrs have up to approximately 800 and 200 fuel assemblies in their cores, respectively. NrC, "Boiling Water reactors" (located at: http://www.nrc.gov/reactors/bwrs.html) and NrC, "pressurized Water reactors" (located at: http://www.nrc.gov/reactors/ pwrs.html).

36 recent designs of BWr and pWr fuel assemblies have on the order of 96 and 264 fuel rods per assembly, respectively. Hence BWr and pWr cores can have up to approximately 76,800 and 52,800 fuel rods per core, respectively; so BWrs cores can have approximately 45 percent more fuel rods. NrC, "Certificate of Compliance No. 1014," Appendix B, "Approved Contents and Design Features for the Hi-Storm 100 Cask System," (available at ADAMS No: ML13351A189), pp. 2.39, 2.44.

37 Yasuo Hirose et al., "An Alternative process to Immobilize Intermediate Wastes from LWr Fuel reprocessing," WM'99 Conference, February 28-March 4, 1999.

38 Jae Sik Yoo and Kune Yull Suh, "Analysis of tMI-2 Benchmark problem Using MAAp4.03 Code," *Nuclear Engineering and Technology* 41, No. 7 (September 2009), p.949.

39 IAeA, "Mitigation of Hydrogen Hazards in SA," p. 6.

40 report by Nuclear energy Agency Groups of experts, oeCD Nuclear energy Agency, "In-Vessel and ex-Vessel Hydrogen Sources," NeA/CSNI/r(2001)15, october 1, 2001, part I: B. Clément (IpSN), K. trambauer (GrS), and W. Scholtyssek (FZK), Working Group on the Analysis and Management of Accidents, "GAMA perspective Statement on In-Vessel Hydrogen Sources," p. 15 (hereinafter: "In-Vessel and ex-Vessel Hydrogen Sources," part I).

41 IAeA, "Mitigation of Hydrogen Hazards in SA," p. 6.

42 power Authority of the State of New York, Consolidated edison Company of New York, "Indian point probabilistic Safety Study," Vol. 8, 1982, available at: ADAMS Documents, Accession Number: ML102520201, p. 4.3-10.

43 the volume percent of the carbon monoxide in the containment is the volume of the carbon monoxide in the containment divided by the volume of the containment multiplied by 100.

44 IAeA, "Mitigation of Hydrogen Hazards in SA," p. 47.

45 report by Nuclear energy Agency Groups of experts, oeCD Nuclear energy Agency, "In-Vessel and ex-Vessel Hydrogen Sources," part I, p. 9.

46 t.J. Haste et al., organisation for economic Co-operation and Development, "Degraded Core Quench: A Status report," August 1996, p. 13.

47 L.J. ott, oak ridge National Laboratory, "Advanced BWr Core Component Designs and the Implications for SFD Analysis," 1997, p. 4.

48 LoFtLp-Fp-2 was conducted in the Loss-of-Fluid test Facility at Idaho National engineering Laboratory in July 1985. the CorA and QUeNCH tests were conducted at Karlsruhe Institute of technology in Germany in the 1980s and 1990s.

49 L. J. ott, "Advanced BWr Core Component Designs and the Implications for SFD Analysis," p. 4.

50 L. J. ott, "Advanced BWr Core Component Designs and the Implications for SFD Analysis," p. 4.

51 IAeA, "Mitigation of Hydrogen Hazards in SA," p. 14.

52 oeCD Nuclear energy Agency, "In-Vessel Core Degradation Code Validation Matrix: Update 1996-1999," report by an oeCD NeA Group of experts, october 2000, p.210.

53 G. Bandini et al., presentation Slides, "progress of ASteC Validation on Circuit thermal-Hydraulics and Core Degradation," 3rd european review Meeting on Severe Accident research September 23-25, 2008, pp. 24, 28 (located at: http://www.sar-net.org/upload/4-5_bandini_ ermsar2008_1.pdf).

54 Charles Miller et al., NrC, "recommendations for enhancing reactor Safety in the 21st Century: the Near-term task Force review of Insights from the Fukushima Daiichi Accident," SeCY-11-0093, July 12, 2011, available at: www.nrc.gov, NrC Library, ADAMS Documents, Accession Number: ML111861807, p. 3.

55 Burton richter et al., "report of the Fuel Cycle research and Development Subcommittee of the Nuclear energy Advisory Committee," June 2012, p. 5.

56 A.p. ramsey, t. McKrell, and M.S. Kazimi, "Silicon Carbide oxidation in High temperature Steam," Advanced Nuclear power program, MIt-ANp-tr-139, 2011, abstract.

57 A triplex cladding design consists of three layers of material surrounding the nuclear fuel: an inner layer of dense silicon carbide for fission gas retention, a central composite layer of wound silicon carbide fibers to enhance mechanical performance, and an outer environmental barrier coating to enhance corrosion resistance. See Ken Yueh, David Carpenter, and Herbert Feinroth, "Clad in Clay," Nuclear engineering International (January 2010), p.14-15.

58 Ken Yueh, David Carpenter, and Herbert Feinroth, "Clad inClay," *Nuclear Engineering International* (January 2010), p. 14.

59 A 2011 Idaho National Laboratory report states that the thermal conductivity of silicon carbide "can exceed the value of zirconium before irradiation. extended irradiation tends to lower the [thermal] conductivity to a value half to one-third that of zirconium." See George Griffith, Idaho National Laboratory, "U.S. Department of energy Accident resistant SiC Clad Nuclear Fuel Development," INL/CoN-11-23186, october 2011.

60 David M. Carpenter, Gordon e. Kohse, and Mujid S. Kazimi, "An Assessment of Silicon Carbide as a Cladding Material for Light Water reactors," Advanced Nuclear power program, MIt-ANp-tr-132, November 2010, abstract.

61 electric power research Institute, "Silicon Carbide provides opportunity to enhance Nuclear Fuel Safety," eprI progress report, September 2011, mydocs.epri.com/docs/CorporateDocuments/Newsletters/NUC/2011-09/09d.html.

62 Burton richter et al., "report of the Fuel Cycle research and Development Subcommittee of the Nuclear energy Advisory Committee," June 2012, p. 6.

63 INpo, "report on the Fukushima Dai-ichi Accident," p. 24.

64 the author is indebted to David Lochbaum of the Union of Concerned Scientists for raising this point.

65 e. Studer et al., Kurchatov Institute, "Assessment of Hydrogen risk in pWr," [undated], p. 1.

66 Allen L. Camp et al., Sandia National Laboratories, "Light Water reactor Hydrogen Manual," NUreG/Cr-2726, August 1983, p. 4-107.

67 pWr ice condenser and BWr Mark III containments have volumes of approximately 1.2 x 106 cubic feet and 1.3 x 106 cubic feet, respectively; pWr large dry containments have a volume of approximately 2.2 x 106 cubic feet. pWrs with ice condenser containments and BWr Mark IIIs have containment design pressures of approximately 20 psig and 15 psig, respectively; pWr large dry containments have a design pressure of approximately 53 psig. See M.F. Hessheimer et al., "Containment Integrity research at SNL," NUreG/Cr-6906, p. 24.

68 Charles Miller et al., "recommendations for enhancing reactor Safety in the 21st Century: the Near-term task Force review of Insights from the Fukushima Daiichi Accident," p. 42.

69 these analyses were conducted for different pWrs, which have containments with different free volumes and different quantities of fuel cladding (active length) in their cores; the containments of these pWrs also have different design pressures and estimated failure pressures. therefore, the results of these analyses do not directly apply to all pWrs. However, they do provide a general idea of the magnitude of the pressure spikes that a pWr containment might be expected to incur if an explosion—of the quantity of hydrogen generated from a zirconium-steam reaction of 100 percent of the active fuel cladding length—were to occur in the event of a severe accident.

70 t.G. Colburn, NrC, letter regarding three Mile Island Unit 1, license amendment from hydrogen control requirements, February 8, 2002, Attachment 2, "Safety evaluation by the office of Nuclear reactor regulation, related to Amendment No. 240 to Facility operating License No. Dpr-50, three Mile Island Unit 1," available at: www.nrc.gov, NrC Library, ADAMS Documents, Accession Number: ML020100578, p. 5.

71 Kahtan N. Jabbour, NrC, letter regarding turkey point Units 3 and 4, exemption from hydrogen control requirements, December 12, 2001, Attachment 2, "Safety evaluation by the office of Nuclear reactor regulation, turkey point Units 3 and 4," available at: www.nrc.gov, NrC Library, ADAMS Documents, Accession Number: ML013390647, p. 3.

72 "pounds per square inch gauge" is the value of a given pressure relative to the atmospheric pressure at sea level (14.7 pounds per square inch).

73 "pounds per square inch absolute" is the value of a given pressure relative to a vacuum (0.0 pounds per square inch).

74 power Authority of the State of New York, Consolidated edison Company of New York, "Indian point probabilistic Safety Study," Vol. 8, 1982, available at: www.nrc.gov, NrC Library, ADAMS Documents, Accession Number: ML102520201, p. 4.2-1 and Appendix 4.4.1, p. 14.

75 power Authority of the State of New York, Consolidated edison Company of New York, "Indian point probabilistic Safety Study," Vol. 8, 1982, available at: www.nrc.gov, NrC Library, ADAMS Documents, Accession Number: ML102520201, p. 4.3-22, 4.3-23.

76 M.F. Hessheimer et al., "Containment Integrity research at SNL," NUreG/Cr-6906, p. 28; the source of this quote is NrC, "Severe Accident risks: An Assessment or Five U.S. Nuclear power plants," NUreG-1150, Vol. 3, January 1991, Appendix D, "responses to Comments on First Draft of NUreG-1150," p. D-22.

77 IAeA, "Mitigation of Hydrogen Hazards in SA," p. 61-62.

78 M. F. Hessheimer et al., "Containment Integrity research at SNL," NUreG/Cr-6906, p. 8.

79 IAeA, "Mitigation of Hydrogen Hazards in SA," p. 62.

80 Institute of Nuclear power operations (INpo), "Special report on the Nuclear Accident at the Fukushima Daiichi Nuclear power Station," INpo 11-005, November 2011, p. 9, 12, 21, 24, 25, 32, 37, 79, 85, 86, 96.

81 Institute of Nuclear power operations (INpo), "Special report on the Nuclear Accident at the Fukushima Daiichi Nuclear power Station," INpo 11-005, November 2011, p. 9.

82 the volume percent of the hydrogen in the containment is the volume of the hydrogen in the containment divided by the volume of the containment multiplied by 100.

83 IAeA, "Mitigation of Hydrogen Hazards in SA," p. 35.

84 IAeA, "Mitigation of Hydrogen Hazards in SA," p. 63. Containment spray systems are typically located inside the roof dome of pWr containments and are designed to spray cool water to condense the steam and reduce internal gas pressure within the containment. See Figure 8.

85 IAeA, "Mitigation of Hydrogen Hazards in SA," p. 34.

86 IAeA, "Mitigation of Hydrogen Hazards in SA," p. 33.

87 Kahtan N. Jabbour, NrC, letter regarding turkey point Units 3 and 4, exemption from hydrogen control requirements, December 12, 2001, Attachment 2, "Safety evaluation by the office of Nuclear reactor regulation, turkey point Units 3 and 4," available at: www.nrc.gov, NrC Library, ADAMS Documents, Accession Number: ML013390647, p. 4.

88 W. e. Lowry et al., Lawrence Livermore National Laboratory, "Final results of the Hydrogen Igniter experimental program," NUreG/Cr-2486, February 1982, p. 4.

89 IAeA, "Mitigation of Hydrogen Hazards in SA," p. 35.

90 oeCD Nuclear energy Agency, "report on FA and DDt," p. 1.2.

91 IAeA, "Mitigation of Hydrogen Hazards in SA," p. 33.

92 D.W. Stamps et al., Sandia National Laboratories, "Hydrogen-Air-Diluent Detonation Study for Nuclear reactor Safety Analyses," NUreG/ Cr-5525, January 1991, available at: www.nrc.gov, NrC Library, ADAMS Documents, Accession Number: ML071700388, p. 43.

93 oeCD Nuclear energy Agency, "Carbon Monoxide-Hydrogen Combustion Characteristics in Severe Accident Containment Conditions: Final report," NeA/CSNI/r(2000)10, 2000, p. 18.

94 Helmut Karwat, "Igniters to Mitigate the risk of Hydrogen explosions—A Critical review," *Nuclear Engineering and Design* 118, 1990, p. 267.

95 IAeA, "Mitigation of Hydrogen Hazards in SA," p. 113.

96 Advisory Committee on reactor Safeguards, 586th Meeting, September 8, 2011, available at: ADAMS Documents, Accession Number: ML11256A117, p. 95.

97 A number of hydrogen combustion experiments have been conducted at Sandia National Laboratories; for example, such experiments were conducted in the 1980s at the FLAMe facility—a rectangular channel 100 feet long, 8 feet high, and 6 feet wide. M.p. Sherman et al., Sandia National Laboratories, "FLAMe Facility: the effect of obstacles and transverse Venting on Flame Acceleration and transition to Detonation for Hydrogen-Air Mixtures at Large Scale," NUreG/Cr-5275, available at: ADAMS Documents, Accession Number: ML071700076, abstract.

98 Most experiments investigating the lower hydrogen concentration limits at which deflagration-to-detonation transition occurs have been conducted in detonation tubes; such tubes have been 39 to 70 feet long and about 11 to 17 inches in diameter. oeCD Nuclear energy Agency, "report on FA and DDt," p. 3.5.

99 oeCD Nuclear energy Agency, "International Standard problem ISp-47 on Containment thermal Hydraulics: Final report," NeA/CSNI/r(2007)10, September 2007, p. 7.

100 Westinghouse, "Ap1000 Design Control Document," rev. 19, tier 2 Material, Chapter 19, "probabilistic risk Assessment," Sections 19.41 to 19.54, June 13, 2011, available at: www.nrc.gov, NrC Library, ADAMS Documents, Accession Number: ML11171A409, p. 19.41-2.

101 Charles Miller et al., "recommendations for enhancing reactor Safety," SeCY-11-0093, p. 42.

102 oeCD Nuclear energy Agency, "SoAr on Containment thermal Hydraulics and Hydrogen Distribution," 1999, p. 18.

103 oeCD Nuclear energy Agency, "report on FA and DDt," p. 1.6.

104 NrC, "Notice regarding eliminating the Hydrogen recombiner requirement," *Federal Register* 68, No. 186 (September 25, 2003), p. 55419.

105 e. Bachellerie et al., "Designing and Implementing a pAr-System in Npp Containments," p. 158.

106 Indian point energy Center, License renewal Application, technical Information, 2.0, "Scoping and Screening Methodology for Identifying Structures and Components Subject to Aging Management review and Implementation results," p. 2.3-61.

107 e. Bachellerie et al., "Designing and Implementing a pAr-System in Npp Containments," p. 159.

108 In January 1985, the NrC began requiring plant owners to install hydrogen control systems in the containments of such designs. See NrC policy Statement, "Combustible Gas Control in Containment," Federal register, Vol. 68, No. 179, September 16, 2003, p. 54124.

109 pWrs with ice condenser containments and BWr Mark IIIs have containment design pressures of approximately 20 psig and 15 psig, respectively. See M.F. Hessheimer et al., "Containment Integrity research at SNL," NUreG/Cr-6906, p. 24.

110 Allen L. Camp et al., Sandia National Laboratories, "Light Water reactor Hydrogen Manual," NUreG/Cr-2726, August 1983, p. 4-107.

111 NrC policy Statement, "Combustible Gas Control in Containment," *Federal Register* 68, No. 179 (September 16, 2003), p. 54124.

112 In December 1981, the NrC began requiring plant owners to operate BWr Mark Is and Mark IIs with inerted primary containments. See NrC policy Statement, "Combustible Gas Control in Containment," Federal register, Vol. 68, No. 179, September 16, 2003, p. 54123.

113 *Federal Register* 68, No. 179 (September 16, 2003), p. 54141.

114 IAeA, "Mitigation of Hydrogen Hazards in SA," p. 74.

115 BWr Mark I and Mark II primary containments have volumes of approximately 0.28 x 106 cubic feet and 0.4 x 106 cubic feet, respectively; these are about one-eighth and one-sixth the volumes, respectively, of typical pWr large dry containments. See M.F. Hessheimer et al., "Containment Integrity research at SNL," NUreG/Cr-6906, p. 24.

116 NrC, "order Modifying Licenses with regard to reliable Hardened Containment Vents," eA-12-050, March 12, 2012, available at: www.nrc.gov, NrC Library, ADAMS Documents, Accession Number: ML12054A694.

117 See NrC, "Installation of a Hardened Wetwell Vent," Generic Letter 89-16, September 1, 1989, p. 1. Generic Letter 89-16 states that "the Commission has directed the [NrC] staff to approve installation of a hardened vent under the provisions of 10 CFr 50.59 ["Changes, tests, and experiments"] for licensees, who on their own initiative, elect to incorporate this plant improvement."

118 NrC, "Installation of a Hardened Wetwell Vent," Generic Letter 89- 16, September 1, 1989, p. 1.

119 NrC policy Statement, "Combustible Gas Control in Containment," *Federal Register* 68, No. 179 (September 16, 2003), p. 54128; and see NrC policy Statement "Severe reactor Accidents regarding Future Designs and existing plants," *Federal Register* 50, No. 153 (August 8, 1985), p. 32138-32150.

120 Westinghouse, "Ap1000 Design Control Document," rev. 19, tier 2 Material, Chapter 19, "probabilistic risk Assessment," Sections 19.34 to 19.35, June 13, 2011, available at: www.nrc.gov, NrC Library, ADAMS Documents, Accession Number: ML11171A405, p. 19.34-4.

121 M.p. Sherman et al., Sandia National Laboratories, "FLAMe Facility: the effect of obstacles and transverse Venting on Flame Acceleration and transition to Detonation for Hydrogen-Air Mixtures at Large Scale," NUreG/Cr-5275, April 1989, available at: ADAMS Documents, Accession Number: ML071700076, p. 2.

122 Westinghouse, "Ap1000 Design Control Document," rev. 19, tier 2 Material, Chapter 19, "probabilistic risk Assessment," Sections 19.41 to 19.54, June 13, 2011, available at: www.nrc.gov, NrC Library, ADAMS Documents, Accession Number: ML11171A409, p. 19.41-4.

123 D.W. Stamps et al., Sandia National Laboratories, "Hydrogen-Air- Diluent Detonation Study for Nuclear reactor Safety Analyses," NUreG/ Cr-5525, January 1991, available at: www.nrc.gov, NrC Library, ADAMS Documents, Accession Number: ML071700388, p. 43.

124 G. Ciccarelli et al., Brookhaven National Laboratory, "the effect of Initial temperature on Flame Acceleration and Deflagration-to-Detonation transition phenomenon," NUreG/Cr-6509, May 1998, available at: www.nrc.gov, NrC Library, ADAMS Documents, Accession Number: ML071650380, p. 1.

125 D.W. Stamps et al., Sandia National Laboratories, "Hydrogen-Air- Diluent Detonation Study for Nuclear reactor Safety Analyses," NUreG/ Cr-5525, January 1991, available at: www.nrc.gov, NrC Library, ADAMS Documents, Accession Number: ML071700388, p. 43.

126 NrC, "proceedings of the U.S. Nuclear regulatory Commission eighteenth Water reactor Safety Information Meeting," NUreG/Cp-0114, Vol. 2, April 1991. S.B. Dorofeev et al., "evaluation of the Hydrogen explosion Hazard," available at: www.nrc.gov, NrC Library, ADAMS Documents, Accession Number: ML042250131, p. 328.

127 Advisory Committee on reactor Safeguards, 586th Meeting, September 8, 2011, available at: ADAMS Documents, Accession Number: ML11256A117, p. 95.

128 peter Hofmann, "Current Knowledge on Core Degradation phenomena, a review," *Journal of Nuclear Materials* 270, Nos. 1-2 (April 1, 1999), p. 208.

129 Westinghouse, "Ap1000 Design Control Document," rev. 19, tier 2 Material, Chapter 19, "probabilistic risk Assessment," Appendix 19D, "equipment Survivability Assessment," June 13, 2011, available at: www.nrc.gov, NrC Library, ADAMS Documents, Accession Number: ML11171A416, p. 19D-3.

130 Westinghouse, "Ap1000 Design Control Document," rev. 19, tier 2 Material, Chapter 1, "Introduction and General Description of plant," Section 1.9, June 13, 2011, available at: www.nrc.gov, NrC Library, ADAMS Documents, Accession Number: ML11171A337, p. 1.9-80.

131 K. Fischer, et al., "Hydrogen removal from LWr Containments by Catalytic-Coated thermal Insulation elements (tHINCAt)," *Nuclear Engineering and Design* 221 (January 2003), p. 146.

132 Westinghouse qualifies that the Ap1000 containment's hydrogen igniter system, "*if operational* during a severe accident, will burn hydrogen as soon as the lean upward flammability limits are met" [emphasis added]. See Westinghouse, "Ap1000 Design Control Document," rev. 19, tier 2 Material, Chapter 19, "probabilistic risk Assessment," Sections 19.41 to 19.54, p.19.41-4.

133 NrC, letter to all licensees holding operating licenses and construction permits for nuclear power plants, except licensees of BWr Mark I plants, "Completion of Containment performance Improvement program, etc.," July 6, 1990, available at: www.nrc.gov, NrC Library, ADAMS Documents, Accession Number: ML031210418, p. 1.

134 D.W. Stamps et al., Sandia National Laboratories, "Hydrogen-Air-Diluent Detonation Study for Nuclear reactor Safety Analyses," NUreG/Cr-5525, January 1991, available at: www.nrc.gov, NrC Library, ADAMS Documents, Accession Number: ML071700388, p. 53-p. 54.

135 K. Fischer et al., "Hydrogen removal from LWr Containments by Catalytic-Coated thermal Insulation elements (tHINCAt)," *Nuclear Engineering and Design* 221 (January 2003), p. 146.

136 e. Bachellerie *et al.*, "Designing and Implementing a pAr-System in Npp Containments," p. 159.

137 oeCD Nuclear energy Agency, "report on FA and DDt," p. 1.6. IAeA, "Mitigation of Hydrogen Hazards in SA," p. 66.

138 eckardt, Bernd A., Michael Blase, and Norbert Losch, "Containment hydrogen control and filtered venting design and implementation," *Framatome ANP*, *Offenbach*, *Germany* (2002), p. 3-4.

139 Sonnenkalb, Martin, and Gerhard poss, "the international test programme in the tHAI Facility and its use for code validation," *EUROSAFE Forum*, *Brussels*, *Belgium* (2009), pp. 16-17.

140 In January 1985, the NrC began requiring plant owners to install hydrogen control systems in the containments of such designs. See NrC policy Statement, "Combustible Gas Control in Containment," Federal register, Vol. 68, No. 179, September 16, 2003, p. 54124.

141 Helmut Karwat, "Igniters to Mitigate the risk of Hydrogen explosions—A Critical review," *Nuclear Engineering and Design* 118, 1990, p. 268.

142 oeCD Nuclear energy Agency, "report on FA and DDt," p. 1.10.

143 Xiao Jianjun, Zhou Zhiwei, and Jing Xingqing, "Safety Implementation of Hydrogen Igniters and recombiners for Nuclear power plant Severe Accident Management," *Tsinghua Science and Technology* 11, No. 5 (october 2006), p.557.

144 NrC, letter to all licensees holding operating licenses and construction permits for nuclear power plants, except licensees of BWr Mark I plants, "Completion of Containment performance Improvement program, etc.," July 6, 1990, p.1.

145 Hydrogen gas condenses to a liquid at approximately –423°F at the atmospheric pressure at sea level (14.7psia).

146 IAeA, "Mitigation of Hydrogen Hazards in SA," p. 10.

147 J. Starflinger, "Assessment of In-Vessel Hydrogen Sources," in *Projekt Nukleare Sicherheitsforschung: Jahresbericht 1999* (Karlsruhe: Forschungszentrum Karlsruhe, FZKA-6480, 2000).

148 NrC, "NrC Information Notice 2006-01: torus Cracking in a BWr Mark I Containment," January 12, 2006, available at: www.nrc.gov, NrC Library, ADAMS Documents, Accession Number: ML053060311, Attachment 1, p. 1.

149 Nitrogen is used to inert BWr Mark I and Mark II primary containments.

150 t. okkonen, oeCD Nuclear energy Agency, "Non-Condensable Gases in Boiling Water reactors," NeA/CSNI/r(94)7, May 1993, p. 4-5. For a 3300-megawatt thermal BWr Mark I, in scenarios in which hydrogen would be produced from a zirconium-steam reaction of 40 percent, 70 percent, and 100 percent of all the zirconium in the reactor core (equivalent to the quantity of hydrogen that would be produced from a zirconium-steam reaction of 72 percent, 126 percent, and 180 percent, respectively, of the active fuel cladding length), if the total quantity of noncondensable gases (including nitrogen) were to accumulate in the wetwell, the primary containment's pressure would increase up to 107 psi, 161 psi, and 215 psi, respectively. See t. okkonen, "Non-Condensable Gases in Boiling Water reactors," p. 6.

151 Appendix J to part 50, "primary reactor Containment Leakage testing for Water-Cooled power reactors," requires preoperational and periodic leak rate tests for BWr Mark I and BWr Mark II primary containments. Leak rate tests are required for determining how much radiation would be released from the containment in a design basis accident: an accident in which a meltdown would be prevented.

152 the following calculation is done by assigning the net free air volume of oyster Creek's Mark I primary containment—301,300 cubic feet—to NMp-1. (At oyster Creek, the minimum wetwell net water volume is 82,000 cubic feet.) See GpU Nuclear Corporation and pLG, Inc., "oyster Creek probabilistic risk Assessment: Level 2," Volume 1, June 1992, available at: NrC Library, ADAMS Documents, Accession Number: ML060550287, p. 3.5. the typical design pressure of a BWr Mark I primary containment is 58.0 pounds per square inch gauge (psig); see M.F. Hessheimer et al., "Containment Integrity research at SNL," NUreG/Cr-6906, July 2006, p. 24. the Nine Mile point Unit 1 test was conducted at 35.0 psig; it is assumed that the test was conducted at 70°F. the density of air at 70°F and 1 atmosphere pressure(atm)—14.696 pounds per square inch absolute (psia)—is 0.07495 pound percubic foot. At 1 atm, there would be 22,582 pounds of air in the primary containment; at 35.0 psig (3.38 atm), there would be 76,329 pounds of air in the primary containment. the overall leakage rate is 0.5045 percent of the containment air's weight (385 pounds) per day. For information on the 1999 Nine Mile point Unit 1 test, see NrC, "Nine Mile point Nuclear Station Unit No. 1—Issuance of Amendment re: one-time extension of primary Containment Integrated Leakage rate test Interval," Attachment 2, "Safety evaluation," March 2009, available at: NrC Library, ADAMS Documents, Accession Number: ML090430367, p. 4, 14.

153 the net free air volume of Limerick Unit 2's Mark II primary containment is 379,071 cubic feet. (At Limerick Unit 2, the minimum wetwell net water volume is 118,655 cubic feet.) See NrC, "Limerick Generating Station Units 1 and 2—Issuance of Amendments re: Application of Alternative Source term Methodology," Attachment 3, "Safety evaluation," August 2006, available at: NrC Library, ADAMS Documents, Accession Number: ML062210214, p. 32. the design pressure of Limerick Unit 2's primary containment is 55.0 psig; see exelon, "Limerick Generating Station Units 1 and 2: technical Specifications Change request—type A test extensions," Attachment 1, "evaluation of proposed Change," February 2007, available at: NrC Library, ADAMS Documents, Accession Number: ML070530296, p. 4.

the Limerick Unit 2 test was conducted at 44.0 psig; it is assumed that the test was conducted at 70°F, the density of air at 70°F and 1 atm is 0.07495 pound per cubic foot. At 1 atm, there would be 28,411 pounds of air in the primary containment; at 44.0 psig (3.99 atm), there would be 113,475 pounds of air in the primary containment. the overall leakage rate is 0.3272 percent of the containment air's weight (371 pounds)

per day. For information on the 1999 Limerick Unit 2 test, see exelon, "Limerick Generating Station Units 1 and 2: technical Specifications Change request—type A test extensions," Attachment 1, "evaluation of proposed Change," p. 3.

154 NrC, "regulatory effectiveness Assessment of option B of Appendix J: Final report," November 2002, available at: NrC's ADAMS Documents, Accession Number: ML023100201, p. 2.

155 IAeA, "Mitigation of Hydrogen Hazards in Severe Accidents in Nuclear power plants," IAeA-teCDoC-1661, July 2011, p. 61.

156 the density of hydrogen at 68°F and 1 atm is 0.005229 pound per cubic foot; the density of air at 70°F and 1 atm is 0.07495 pound per cubic foot.

157 Sherrell r. Greene, oak ridge National Laboratory, "the role of BWr Mark I Secondary Containments in Severe Accident Mitigation," proceedings of the 14th Water reactor Safety Information Meeting at the National Bureau of Standards, Gaithersburg, Maryland, october 27–31, 1986, exhibit 6.

158 G.H. Hofmayer et al., "Containment Leakage During Severe Accident Conditions," BNL-NUreG-35286, CoNF-8406124-13, 1984, p. 6, 7, 8.

159 G.H. Hofmayer et al., "Containment Leakage During Severe Accident Conditions," BNL-NUreG-35286, CoNF-8406124-13, 1984, p. 4.

160 A.K.Agraualetal.,"AnestimationofpreexistingLWrContainment Leakage Areas for Severe Accident Conditions," BNL-NUreG-34212, CoNF-840614-35, 1984, p.3.

161 p.J. pelto et al., "reliability Analysis of Containment Isolation Systems," pacific Northwest Laboratory, NUreG/Cr-4220, June 1985, available at: NrC Library, ADAMS Documents, Accession Number: ML103050471, p. 8.3.

162 oyster Creek's design leak rate is 0.5 percent of the primary containment air's weight per day; in one overall leak rate test, oyster Creek's primary containment leaked at a rate of 9.0 percent of its air's weight per day. See p.J. pelto et al., "reliability Analysis of Containment Isolation Systems," NUreG/Cr-4220, p. 8.5. See also NrC, "oyster Creek: Issuance of Amendment to Facility operating License," September 1996, available at: NrC Library, ADAMS Documents, Accession Number: ML011300129, enclosure 1, Amendment No. 186, p. 4.5-10.

163 NrC, "oyster Creek: Issuance of Amendment to Facility operating License," September 1996, available at: NrC Library, ADAMS Documents, Accession Number: ML011300129, enclosure 1, Amendment No. 186, p. 1.0-5.

164 the net free air volume of oyster Creek's Mark I primary containment is 301,300 cubic feet. (At oyster Creek, the minimum wetwell net water volume is 82,000 cubic feet.) See GpU Nuclear Corporation and pLG, Inc., "oyster Creek probabilistic risk Assessment: Level 2," Volume 1, June 1992, available at: NrC Library, ADAMS Documents, Accession Number: ML060550287, p. 3.5. the typical design pressure of a BWr Mark I primary containment is 58.0 psig. See M.F. Hessheimer et al., "Containment Integrity research at SNL," NUreG/Cr-6906, July 2006, p. 24. the test was conducted before March 1985 (when NUreG-/Cr-4220 was completed). NUreG-/Cr-4220 does not state what pressure the test was conducted at; however, it is highly probable that the test was conducted at 35.0 psig, the pressure—associated with a design basis loss-of-coolant accident—used for subsequent oyster Creek tests. It is assumed that the tests were conducted at 70°F. the density of air at 70°F and 1 atm is 0.07495 pound per cubic foot. At 1 atm, there would be 22,582 pounds of air in the primary containment; at 35.0 psig (3.38 atm), there would be 76,329 pounds of air in the primary containment. the overall leakage rate is 9.0 percent of the containment air's weight (6870 pounds) per day. For information on the oyster Creek test, see p.J. pelto et al., "reliability Analysis of Containment Isolation Systems," NUreG/ Cr-4220, p. 8.5.

Unignited releases

165 In September 1995, the NrC revised its regulations to extend the overall (type A) leak rate test interval from about 3 3 years to 10 years; to extend the interval for type B local leak rate tests, intended to measure leakage at penetrations (except for airlocks), from 2 years to a maximum of 10 years; and to extend the interval for type C local leak rate tests, intended to measure leakage at isolation valves, from 2 years to 5 years. After 1995, plant owners requested and received approval for one-time
5-year extensions to the 10-year interval requirement of the type A test for about 94 reactors. In recent years, the NrC has been preparing to extend type A test intervals to once every 15 years and extend type

C test intervals to once every 75 months. In the proposed revisions, a preoperational type A test would be required for new reactors, and a second test would be required within 4 years. If the first two tests were successful, one test would be required every 15 years. extensions of type B and type C test intervals would be permitted if two consecutive tests were successful. See NrC, Letter regarding regulatory Guide 1.163, "performance-Based Containment Leak-test program," March 20, 2013, available at: NrC Library, ADAMS Documents, Accession Number: ML13067A219, p. 2. See also Advisory Committee on reactor Safeguards (ACrS) 602nd Meeting transcript, March 7, 2013, p. 10, 31-32.

166 p.J. pelto et al., "reliability Analysis of Containment Isolation Systems," NUreG/Cr-4220, p. 4.6.

167 p.J. pelto et al., "reliability Analysis of Containment Isolation Systems," NUreG/Cr-4220, p. 4.7.

168 ACrS 602nd Meeting transcript, March 7, 2013, p. 32-33.

169 p.J. pelto et al., "reliability Analysis of Containment Isolation Systems," NUreG/Cr-4220, p. 4.7.

170 ACrS 602nd Meeting transcript, March 7, 2013, p. 16.

171 eprI, "risk Impact Assessment of extended Integrated Leak rate testing Intervals," 1009325, revision 2-A, october 2008.

172 ACrS 602nd Meeting transcript, March 7, 2013, p. 37-39.

173 p.J. pelto et al., "reliability Analysis of Containment Isolation Systems," NUreG/Cr-4220, p. 8.3. the manuscript of NUreG/Cr-4220 was completed in March 1985.

174 Local leak rate tests (type B and C tests) are typically performed before an overall leak rate test. "this implies that the leak rates noted in an [overall leak rate test] are smaller than the actual case. An additional review of 'as found' leakages from type B and type C tests was performed…A total of 49 [overall leak rate test] reports were identified for which the type A [overall leak rate] test did not fail but with the consideration of type B and C 'as found' leakage would be classified as a failure. …to simplify the analysis these 49 failures are added directly to the results presented above. thus a total of 109 [overall leak rate test] failures are identified. of these failures, 55 were for BWrs and 54 were for pWrs." See p.J. pelto *et al.*, "reliability Analysis of Containment Isolation Systems," NUreG/Cr-4220, p. 8.6.

175 eprI, "risk Impact Assessment of extended Integrated Leak rate testing Intervals," 1009325, revision 2-A, october 2008, p. A-3.

176 eprI, "risk Impact Assessment of extended Integrated Leak rate testing Intervals," 1009325, revision 2-A, october 2008, p.v.

177 NrC, "performance-Based Containment Leak-test program," NUreG-1493, September 1995.

178 NrC, "regulatory effectiveness Assessment of option B of Appendix J: Final report," November 2002, available at: NrC Library, ADAMS Documents, Accession Number: ML023100201, p. 3.

179 NrC, "Severe Accident risks: An Assessment for Five U.S. Nuclear power plants, Final Summary report," NUreG-1150, Vols. 1 and 2, June 1989 and December 1990.

180 NrC, "regulatory effectiveness Assessment of option B of Appendix J: Final report," November 2002, available at: NrC Library, ADAMS Documents, Accession Number: ML023100201, p. 6.

181 NrC, Letter regarding regulatory Guide 1.163, "performance-Based Containment Leak-test program," March 20, 2013, available at: NrC Library, ADAMS Documents, Accession Number: ML13067A219, p. 1.

182 Institute of Nuclear power operations (INpo), "Special report on the Nuclear Accident at the Fukushima Daiichi Nuclear power Station," INpo 11-005, November 2011, p.96.

183 Institute of Nuclear power operations (INpo), "Special report on the Nuclear Accident at the Fukushima Daiichi Nuclear power Station," INpo 11-005, November 2011, p. 11, 17, 24, 27, 29, 31.

184 Institute of Nuclear power operations (INpo), "Special report on the Nuclear Accident at the Fukushima Daiichi Nuclear power Station," INpo 11-005, November 2011, p.20.

185 BWr Mark I and Mark II primary containments have volumes of approximately 0.28 x 106 cubic feet and 0.4 x 106 cubic feet, respectively. See M.F. Hessheimer et al., "Containment Integrity research at SNL," NUreG/Cr-6906, p. 24.

186 NrC, "order Modifying Licenses with regard to reliable Hardened Containment Vents," eA-12-050, March 12, 2012, available at: www.nrc.gov, NrC Library, ADAMS Documents, Accession Number: ML12054A694, p. 3.

187 NrC, "order Modifying Licenses with regard to reliable Hardened Containment Vents," eA-12-050, March 12, 2012, available at: www.nrc.gov, NrC Library, ADAMS Documents, Accession Number: ML12054A694.

188 NrC, "Installation of a Hardened Wetwell Vent," Generic Letter 89-16, September 1, 1989, p. 1. Generic Letter 89-16 states that "the Commission has directed the [NrC] staff to approve installation of a hardened vent under the provisions of 10CFr50.59 ["Changes, tests, and experiments"] for licensees, who on their own initiative, elect to incorporate this plant improvement."

189 NrC, "Installation of a Hardened Wetwell Vent," Generic Letter 89- 16, September 1, 1989, p. 1.

190 NrC, "order Modifying Licenses with regard to reliable Hardened Containment Vents," eA-12-050, March 12, 2012, available at: www.nrc.gov, NrC Library, ADAMS Documents, Accession Number: ML12054A694, Attachment 2, p. 1.

191 r. Jack Dallman et al., "Filtered Venting Considerations in the United States," Committee on the Safety of Nuclear Installations (CSNI) Specialists Meeting on Filtered Vented Containment Systems, May 17– 18, 1988, paris, p. 3.

192 the piping of hardened vents currently installed at U.S. BWr Mark I plants is typically 8 inches in diameter.

193 Allen L. Camp et al., "Light Water reactor Hydrogen Manual," NUreG/Cr-2726, p. 2-66.

194 INpo, "report on the Fukushima Daiichi Accident," p. 34.

195 INpo, "report on the Fukushima Daiichi Accident," p. 33-34.

196 Juan J. Carbajo, oak ridge National Laboratory, "MeLCor Model of the Spent Fuel pool of Fukushima Daiichi Unit 4," 2012, p. 1-2.

197 Sherrell r. Greene, oak ridge National Laboratory, "the role of BWr Mark I Secondary Containments in Severe Accident Mitigation," proceedings of the 14th Water reactor Safety Information Meeting at the National Bureau of Standards, october 27–31, 1986, Gaithersburg, Maryland, exhibit 6.

198 the NrC's definition of defense-in-depth: An approach to designing and operating nuclear facilities that prevents and mitigates accidents that release radiation or hazardous materials. the key is creating multiple
independent and redundant layers of defense to compensate for potential human and mechanical failures so that no single layer, no matter how robust, is exclusively relied upon. Defense-in-depth includes the use

of access controls, physical barriers, redundant and diverse key safety functions, and emergency response measures. See www.nrc.gov/reading-rm/basic-ref/glossary/defense-in-depth.html.

199 Charles Miller, et al., "recommendations for enhancing reactor Safety in the 21st Century: the Near-term task Force review of Insights from the Fukushima Dai-ichi Accident," ML111861807 (2011), p. 47.

200 robert prior et al., oeCD Nuclear energy Agency, Committee on the Safety of Nuclear Installations, "Core exit temperature (Cet) effectiveness in Accident Management of Nuclear power reactor," NeA/ CSNI/r(2010)9, November 26 2010, p. 128-129.

201 robert prior et al., "Core exit temperature (Cet) effectiveness in Accident Management of Nuclear power reactor," p. 128.

202 robert prior et al., "Core exit temperature (Cet) effectiveness in Accident Management of Nuclear power reactor," p. 49-50.

203 ACrS, "review and evaluation of the Nuclear regulatory Commission Safety research program: A report to the U.S. Nuclear regulatory Commission," NUreG-1635, Vol. 10, April 2012, p. 11.

204 IAeA, "Generic Assessment procedures for Determining protective Actions During a reactor Accident," IAeA-teCDoC-955, August 1997, p. 25, 26.

205 See Salomon Levy, "How Would U.S. Units Fare?" *Nuclear Engineering International* (December 7, 2011). the journal's "Author Info" states that "Dr. Levy was the manager responsible for General electric (Ge) BWr heat transfer and fluid flow and the analyses and tests to support [Ge's] nuclear fuel cooling during normal, transient, and accident analyses from 1959 to 1977."

206 Salomon Levy, "How Would U.S. Units Fare?" *Nuclear Engineering International* (December 7, 2011). Levy makes a point of saying that his observations are not intended to be criticisms of the actions of the Fukushima Daiichi plant operators.

207 NrCpolicyStatement, "CombustibleGasControlinContainment," *Federal Register* 68, No. 179 (September 16, 2003), p. 54126.

208 NrCpolicyStatement, "CombustibleGasControlinContainment," *Federal Register* 68, No. 179 (September 16, 2003), p. 54126-54127.

209 In 2003, oxygen monitors were reclassified from Category 1 to Category 2, and hydrogen monitors were reclassified from Category 1 to Category 3. the NrC states, "In general, Category 1 provides for full qualification, redundancy, and continuous real-time display and requires on-site (standby) power. Category 2 provides for qualification but is less stringent in that it does not (of itself) include seismic qualification, redundancy, or continuous display and requires only a high-reliability power source (not necessarily standby power). Category 3 is the least stringent. It provides for high-quality commercial-grade equipment
that requires only offsite power." See NrC, regulatory Guide 1.97, "Instrumentation for Light-Water-Cooled Nuclear power plants to Assess plant and environs Conditions During and Following an Accident," revision 3, May 1983, available at: www.nrc.gov, NrC Library, ADAMS Documents, Accession Number: ML003740282, p. 1.97-4.

210 David Lochbaum, UCS, letter regarding installing hydrogen monitoring instrumentation in BWr Mark I and Mark II secondary containments as well as in the fuel handling buildings of BWr Mark IIIs and pWrs, to David L. Skeen, NrC, Deputy Director, Division of
engineering, office of Nuclear reactor regulation, January 20, 2012, p. 2.

211 NrC policy Statement, "Confirmatory order Modifying post- tMI requirements pertaining to Containment Hydrogen Monitors for Arkansas Nuclear one, Units 1 and 2," *Federal Register* 63, No. 192
(october 5, 1998), p. 53466-53467. NrC, regulatory Guide 1.7, "Control of Combustible Gas Concentrations in Containment," revision 3, March 2007, available at: www.nrc.gov, NrC Library, ADAMS Documents, Accession Number: ML070290080, p. 6.

212 ACrS, "review and evaluation of the Nuclear regulatory Commission Safety research program: A report to the U.S. Nuclear regulatory Commission," NUreG-1635, Vol. 10, April 2012, p. 11.

213 Appendix J to part 50, "primary reactor Containment Leakage testing for Water-Cooled power reactors."

NrC, Letter regarding regulatory Guide 1.163, "performance-Based Containment Leak-test program," March 20, 2013, available at: NrC's ADAMS Documents, Accession Number: ML13067A219, p.

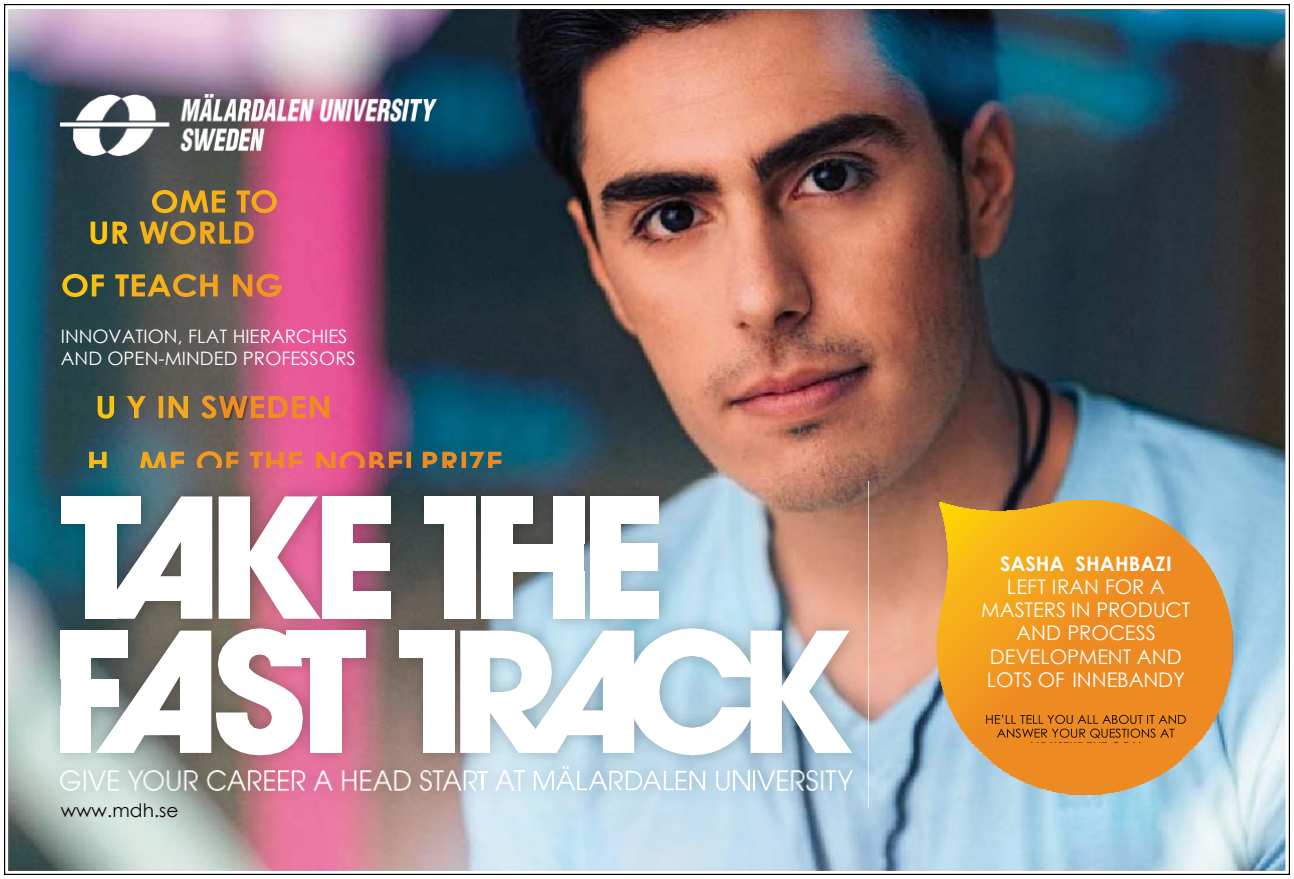
4. Research Overview

6 Dispersion of hydrogen in confined space

Please click the advert

The formation of a flammable mixture is a major safety concern for indoor use of hydrogen and fuel cell systems. One of relevant questions is how safe is permeation of hydrogen from an on-board storage and its dispersion in a garage. Is natural ventilation sufficient to eliminate potential hazard of flammable hydrogen-air mixture formation? Distribution of permeated hydrogen within an enclosure, when LFL of hydrogen in air (4% by volume) is reached, is important to define maximum allowable permeation rate for hydrogen fuel cell vehicles with compressed hydrogen tanks onboard.

A unique feature of hydrogen is the pressure peaking phenomenon. It is described in detail in this chapter. Another issue considered in this chapter is a limit of hydrogen mass flow rate in an enclosure with known natural ventilation, i.e. sizes and location of vents, that will definitely followed with time by 100% by volume of hydrogen atmosphere in the enclosure.


MÄLARDALEN UNIVERSITY
SWEDEN
OME TO
UR WORLD
OF TEACH NG
INNOVATION, FLAT HIERARCHIES
AND OPEN-MINDED PROFESSORS
U Y IN SWEDEN
TAKE THE
FAST TRACK
GIVE YOUR CAREER A HEAD START AT MÄLARDALEN UNIVERSITY
www.mdh.se
SASHA SHAHBAZI
LEFT IRAN FOR A
MASTERS IN PRODUCT
AND PROCESS
DEVELOPMENT AND
LOTS OF INNEBANDY
HE'LL TELL YOU ALL ABOUT IT AND
ANSWER YOUR QUESTIONS AT

6.1. Dispersion of permeated hydrogen in a garage

Definition of permeation could be found elsewhere (SAE J2578, 2009): *diffusion through the walls or interstices of a container vessel, piping or interface material*. It is especially pronounced for hydrogen as it is the smallest element with a highest diffusivity. It is worth noting that hydrogen permeation is atomic through metals and molecular through polymers (Schultheiß, 2007).

Compressed gaseous hydrogen (CGH_2) containers are categorised into the following four types (Commission Regulation, 2009): Type 1 – seamless metallic container, Type 2 – hoop wrapped container with a seamless metallic liner, Type 3 – fully wrapped container with a seamless or welded metallic liner, and Type 4 – fully wrapped container with a non-metallic liner. In Type 3 and 4 containers, the main purpose of the liner is containment of the hydrogen gas, while the overwrapping provides the structural strength of the container (Adams et al., 2011). Current Type 4 containers use a polymer as the liner, e.g. high-density polyethylene, typically overwrapped with carbon fibres set in a resin matrix. Other fibres such as glass or aramid may also be used, but most automotive systems use carbon fibre. The overwrap varies in thickness around the container depending on the stress distribution, as does the fibre direction. Type 3 or Type 4 containers are used for most automotive applications.

Permeation in the context of CGH_2 systems is diffusion through the walls or interstices of a container vessel, piping or interface material. Permeation may be categorised as a long term slow hydrogen release from a CGH_2 system. Controlling permeation has long been recognised as a key enabler in the development of hydrogen storage technologies (Mitlitsky et al., 2000). For metallic containers or containers with metallic liners, i.e. Types 1, 2 or 3, the permeation rate is considered to be negligible. However, hydrogen permeation is an issue for containers with non-metallic (polymer) liners, i.e. Type 4 containers.

In this section the dispersion of permeated hydrogen from a storage tank in a typical garage with adiabatic walls and still air is studied analytically and numerically. Numerical simulations are performed based on an original approach of a hydrogen mass source term introduction in the hydrogen conservation equation in control volumes around the tank surface. It is shown that the maximum hydrogen concentration in an enclosure is always on the top surface of the tank and it never reaches 100% by volume. Both the analytical analysis and numerical simulations have demonstrated that diffusion and buoyancy contributions to the hydrogen transport from the tank surface are balanced within 1 minute from the beginning of the process. The quasi-steady state conditions within the enclosure with approximately linear distribution of hydrogen from the top to the bottom are established in about 1 hour for considered permeation rates.

6.1.1. Permeation rate

The economical and technological viability of on-board hydrogen tanks depends amongst other things on their gravimetric and volumetric capacity. The gravimetric capacity is currently improved with thin walls made of light, non-metallic materials in types 4 tanks. However, they are characterized by a strong permeability. For example, at 293 K, aluminium has a low permeability 2.84×10^{-27} mol/s/m/$MPa^{1/2}$ (Korinko et al., 2001),while a polymer like Noryl has a permeability of 5.55×10^{-15} mol/s/m/$MPa^{1/2}$ (Stodilka et al., 2000), i.e. 12 orders of magnitude bigger.

The improvement of the volumetric capacity can be achieved by pressure increase from 35 MPa to 70 MPa for vehicles. However, this will increase the permeation rate. The permeation from onboard hydrogen tanks is a safety issue for enclosures where the hydrogen can accumulate over time to create a flammable mixture with air. In sealed enclosures without ventilation the lower flammability limit (LFL) of 4% by volume of hydrogen in air can be reached as a result of permeation after quite a long time. To estimate the time for reaching LFL locally, e.g. under the garage ceiling, or homogeneously throughout the garage it is important to know how hydrogen will be distributed in the enclosure.

The permeability of hydrogen for a particular material can be calculated as (Schefer et al., 2006a)

$$P = P_0 \exp(-E_0 / RT), \tag{6–1}$$

where the pre-exponential factor P_0 (mol/s/m/MPa$^{1/2}$) and the activation energy E_0 (J/mol) are material dependent, and T is temperature, K. The permeation rate through a single material's membrane is calculated using the equation (Schefer et al., 2006a)

$$J = P \frac{\sqrt{p_r}}{l}, \tag{6–2}$$

where p_r is the reservoir pressure, MPa; and l is the reservoir wall thickness, m. The permeation rate increases with an increase of storage pressure p_r and a decrease of membrane thickness l. Equations (6–1) and (6–2) are valid for metallic and non-metallic materials (Schultheiß, 2007) and applicable to a single membrane's wall but under limited range of pressure and temperature from 10 Pa to 50 MPa and ambient temperature less than 1273 K respectively (San Marchi et al., 2007).

For serial membranes of different materials like in type 4 tanks the total permeability for z layers can be calculated using correlations found elsewhere (Crank, 1975)

$$\frac{l}{P} = \sum_{i=1}^{z} \frac{l_i}{P_i}. \tag{6–3}$$

6.1.2. Diffusion and buoyancy transport of permeated hydrogen

It is important to understand: what is the maximum concentration of permeated hydrogen at a tank surface. Let us estimate permeated hydrogen concentration in the beginning of a process when pressurised storage tank is just placed into an enclosure with still air. Molecules of hydrogen permeated from the tank are subject to Brownian motion that is a random movement of molecules suspended in a liquid or a gas. The chaotic movement is influenced by collisions between molecules of hydrogen and other molecules in the air. Following the Einstein's law (1905), which is valid for Brownian motion, the displacement in direction of the x-axis that a particle experiences on the average, or, to be more precise, the root-mean-square displacement is

$$\lambda_x = \sqrt{\overline{\Delta x^2}} = \sqrt{2 \cdot D \cdot t}\ , \tag{6–4}$$

where D is the diffusion of hydrogen in air (at 25°C it can be accepted as 7.79 ×10^{-5} m^2/s), and t is the time, s. As the displacement of molecules during time t is $\sqrt{2 \cdot D \cdot t}$, a volume comprising all permeated hydrogen molecules around the tank surface of area A_r is $V_{mix} = A_r \sqrt{2 \cdot D \cdot t}$. The number of moles of permeated hydrogen in this volume is $n = J \cdot t \cdot A_r$. Assuming uniform distribution of hydrogen molecules in the volume V_{mix}, the volumetric concentration of hydrogen on the tank's surface at time t is the ratio of the volume of hydrogen to the total volume V_x can be calculated as

$$[H_2]_t = 100 \frac{n \bullet V_{m25}}{V_{mix}}, \tag{6–5}$$

where V_{m25} is the molar volume of ideal gas at 25°C (0.0244 m^3/mol). The equation can be rewritten as

$$[H_2]_t = 100 \frac{J \bullet t \bullet A_r \bullet V_{m25}}{\sqrt{2 \bullet D \bullet t} \bullet A_r} = 100 \frac{J \bullet V_{m25}}{\sqrt{2 \bullet D}} \times \sqrt{t}. \tag{6–6}$$

It is obvious that the buoyancy effect increases with the increase of hydrogen concentration in air. Thus, the hydrogen concentration on the tank surface increases with time as $[H_2]_t \propto \sqrt{t}$ until the buoyancy will overcome diffusion transport of hydrogen. A quasi-steady state will be established when diffusion and buoyancy will balance each other.

Please click the advert

STUDYINSWEDEN.SE

Question:
What do Skype and Spotify have in common with color screen graphics and the computer mouse?

–They are all Swedish inventions.



Be innovative. Study in Sweden

The second Newton's Law for buoyant motion of hydrogen-air mixture of density ρ_{mix} in air of density ρ_{air} can be written as $F = m_{mix} \cdot a = (\rho_{air} - \rho_{mix}) V_{mix} \cdot g$. From mechanics a distance passed by a body moving with acceleration a is $L_x = a \cdot t^2 / 2$, and therefore

$$\rho_{mix} \cdot a = \rho_{mix} \cdot \frac{2 \cdot L_x}{t^2} = (\rho_{air} - \rho_{mix}) g , \tag{6–7}$$

Thus, the displacement of mixture by buoyancy with time is

$$L_x = \left(\frac{\rho_{air}}{\rho_{mix}} - 1 \right) \cdot \frac{g \cdot t^2}{2} , \tag{6–8}$$

where the density of mixture is by definition

$$\rho_{mix} = \frac{[H_2]_t}{100} \cdot (\rho_{H_2} - \rho_{air}) + \rho_{air} . \tag{6–9}$$

The displacement of hydrogen by buoyancy becomes of the same order as the displacement of hydrogen by diffusion, $\lambda_x = L_x$, and process reaches the quasi-steady state when

$$\sqrt{2 \cdot D \cdot t} = \left| \frac{\theta_{air}}{\frac{J \cdot t \cdot V_{m25}}{\sqrt{2 \cdot D \cdot t}} (\theta_{H2} - \theta_{air}) + \theta_{air}} - 1 \right| \cdot \frac{g \cdot t^2}{2} . \tag{6–10}$$

This equation yields time 37 s for the permeation rate J=1 Ncm^3/hr/L (normal cubic centimetres of hydrogen per hour per litre of container internal volume) of tank capacity (scenario 1), and 16 s for the permeation rate J=45 Ncm^3/hr/L (scenario 2) as per SAE J2578 (2009) for a tank and a garage described in the next section.

Within the assumptions of this section, the hydrogen concentration on the tank's surface at these characteristic times can be calculated using Eq. (6–6) as 2.4×10^{-4} % by volume and 1×10^{-2} % by volume respectively. Both values of hydrogen concentrations at the tank surface are far below LFL of hydrogen in air of 4% by volume.

6.1.3. Uniformity of permeated hydrogen concentration distribution

In this section the question about an extent of uniformity of permeated hydrogen distribution within a

garage-like enclosure for different permeation rates is addressed. Numerical simulations of permeated hydrogen dispersion in an enclosure were performed for the two scenarios that differ by permeation rate only. A compressed hydrogen storage tank of 0.672 m long and of 0.505 m diameter with a hemispherical ends of 0.505 m diameter with surface area of A_r=1.87 m^2 and volume of about V_r=0.2 m^3 is located in the centre of an enclosure with sizes of typical garage $L \times W \times H$=5×3×2.2 m and volume of V_g=33 m^3 with clearance between the tank and the garage floor of 0.5 m. The ambient temperature is 298 K.

In scenario 1 the permeation rate is J=1 Ncm^3/hr/L, i.e. below the allowable by the European Law (Commission Regulation, 2010) permeation rate limit of 6 Ncm^3/hr/L (at 20^{o}C). In scenario 2 the permeation rate is J=45 Ncm^3/hr/L, i.e. above the European Law limit, and is equivalent to the maximum "*normal hydrogen discharges"* (including permeation leaks) of 150 Ncm^3/min per car at normal temperature and pressure recommended by SAE J2578 (2009).

If the enclosure would be perfectly sealed then the time t_c necessary for hydrogen to reach the homogenous LFL concentration of c=4% by volume is

$$t_c = \frac{V_g \bullet c}{V_{m25} \bullet J \bullet A_r}. \qquad (6–11)$$

This yields about 275 days for scenario 1 and 6 days for scenario 2. The time to create flammable mixture at LFL level would reduce if assumption about the uniformity of hydrogen distribution is not valid and permeated hydrogen would gather in a layer.

The CFD model applied to simulate permeated hydrogen dispersion and numerical details are described by Saffers et al. (2011). To decrease a simulation time the incompressible model was applied. To make the assumption of incompressibility consistent, a square vent of 0.2x0.2 m located on the floor of the garage with outflow boundary conditions was modelled. The presence of the vent creates in simulations artificial downward velocity of hydrogen-air mixture within the enclosure. This velocity is assessed using volumetric flow rate of permeated hydrogen and enclosure geometry and is about 3.62×10^{-9} m/s for scenario 1 and 1.63×10^{-7} m/s for scenario 2. For comparison the characteristic "diffusion" velocity of the order of D/H=3.54×10^{-5} m/s is much higher.

Dispersion of permeated hydrogen is a physical phenomenon essentially different from classical leaks, i.e. plumes and jets. Permeated hydrogen "leaks" in very small amounts uniformly along the surface of storage tank. Then hydrogen is driven out of the surface by diffusion and buoyancy. The source of permeated hydrogen was modelled using volumetric source of hydrogen in a thin layer of control volumes of 1 mm thickness around the tank surface. This is different modelling approach compared to artificial plumes/jets with 100% hydrogen concentration and non-physical momentum in the source.

Indeed, as demonstrate below, the permeation rate used in this study does not release enough hydrogen to cover the whole surface of the tank to form a single layer of pure hydrogen (100% by volume) as the diffusion process displaces quickly the hydrogen molecules away from the tank's surface.

One mole of ideal gas occupies 24.4 L at 25ºC, i.e. there are about 41 moles of ideal gas in 1 m^3. Let us estimate a number of hydrogen moles released from the tank surface of 1.87 m^2 in a unit of time. At the permeation rate of 45 $Ncm^3/hr/L$ (scenario 2) and V_r=200 L a volume of permeated hydrogen is 25×10^{-7} m^3 in a unit of time (1 s), i.e. 1.02×10^{-4} moles are permeated in 1 s. This number of moles will occupy a volume equal to the product of the tank surface area multiplied by a characteristic distance of hydrogen transport by diffusion from the surface that can be estimated as $D^{1/2}$ in a unit of time, i.e. 8.8×10^{-3} m. This volume is 0.0165 m^3. Thus, the number of moles of permeated hydrogen per unit volume close to the surface is 0.0062 mol/m^3.

This means that the mole fraction of hydrogen is $0.0062/41=1.5\times10^{-4}$ or 0.0015% by volume. This simplified estimate is consistent with results of numerical simulations (see results for rake 01) both providing a proof that there is no 100% by volume of hydrogen concentration at the tank surface during the permeation, and it is far below LFL even for scenario 2.

The calculation domain represented a quarter of the garage (see Fig. 6–1). Profiles of the hydrogen concentration distribution across the garage height are reported below at locations of three vertical rakes: in the centre of the garage (rake 01), in the middle between the tank and the wall (rake 02) and along the wall at distance 0.1 m from the wall (rake 03).

Please click the advert



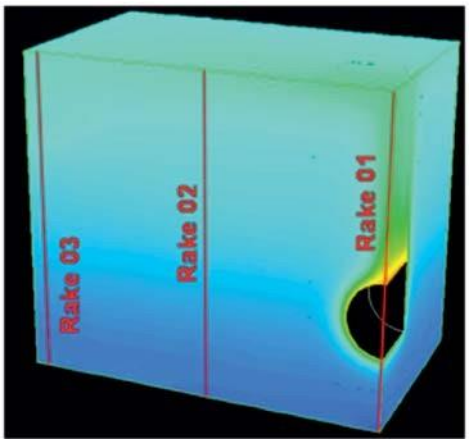


Figure 6–1. Calculation domain (garage quarter) and location of rakes.

To match the specified permeation rates, the hydrogen mass volumetric source term was equal to S_{H2}=2.43×10^{-6} kg/m^3/s for scenario 1 and to S_{H2}=1.09×10^{-4} kg/m^3/s for scenario 2. The minimum control volume (CV) size was on tank's surface and equal to Δx=0.5 mm, so the hydrogen was released in a layer of two CV thickness along the surface. The total number of CVs in the calculation domain was 194,464. SIMPLE algorithm was used for pressure-velocity coupling with 3rd order MUSCL discretisation scheme for convective terms, central difference for diffusion terms, and 2nd order implicit time stepping. It is a common practice to use implicit SIMPLE-similar procedure for incompressible flows. Hydrogen mass balance was monitored as a main indicator of acceptable numerical convergence.

The maximum hydrogen concentration in simulations is on the top of the tank as expected. The difference of 10% in thickness of hydrogen layer at the top and at the bottom of the tank surface is reached in simulations at 60 s and 12 s after the start of the process for scenarios 1 and 2 respectively. This is in an agreement with similar values obtained during the simplified analysis of the problem, i.e. 37 s and 16 s, characterising the time to the balance between contribution of diffusion and buoyancy to the hydrogen transport away from the tank surface.

The profiles of hydrogen concentration at location of rakes 01, 02 and 03 for both scenarios are shown in Fig. 6–2. The maximum concentration of hydrogen is always at the top of the tank. It reaches a negligible value of 6.24×10^{-3} % by volume for scenario 1 and 1.82×10^{-1} % by volume for scenario 2 after 133 min.

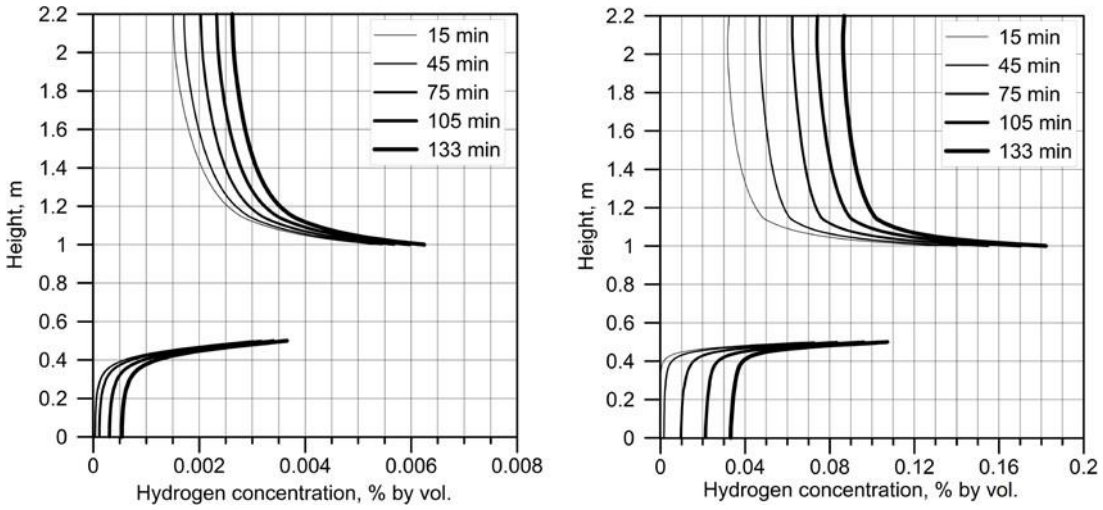


Figure 6–2. Hydrogen concentration profile across the garage height at location of rake 01 with time: left - scenario 1; right - scenario 2.

Profiles of hydrogen concentration across the garage height at rake 02 position are shown in Fig. 6–3. After about 60 minutes from the beginning of the process, a quasi-steady gradient of hydrogen concentration with height is reached. Starting from this moment the hydrogen concentration increases in time with the same increments both at the top and at the bottom of the garage thus preserving hydrogen concentration gradient. The established difference in concentration throughout the garage height obtained by numerical simulations is negligible in practical sense, i.e. 2×10^{-3} % by volume for scenario 1 and 5×10^{-2} % by volume for scenario 2. Both are essentially below the LFL of 4% by volume.

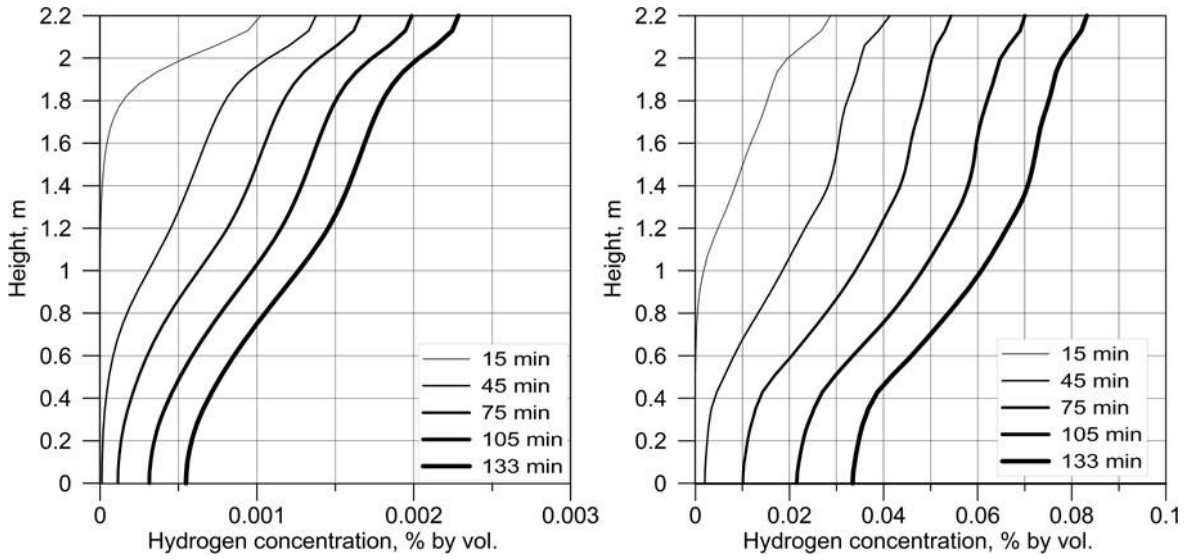


Figure 6–3. Hydrogen concentration profile across the garage height at location of rake 02 with time: left – scenario 1; right – scenario 2.

Profiles of hydrogen concentration across the garage height at rake 03 position are shown in Fig. 6–4. At 15 minutes after the start of permeation, the gradient of concentration is not linear due to the presence of the wall. The wall effect nevertheless disappears with time and the gradient linearity is established at about 60 minutes after the beginning of the process similar to rake 02.

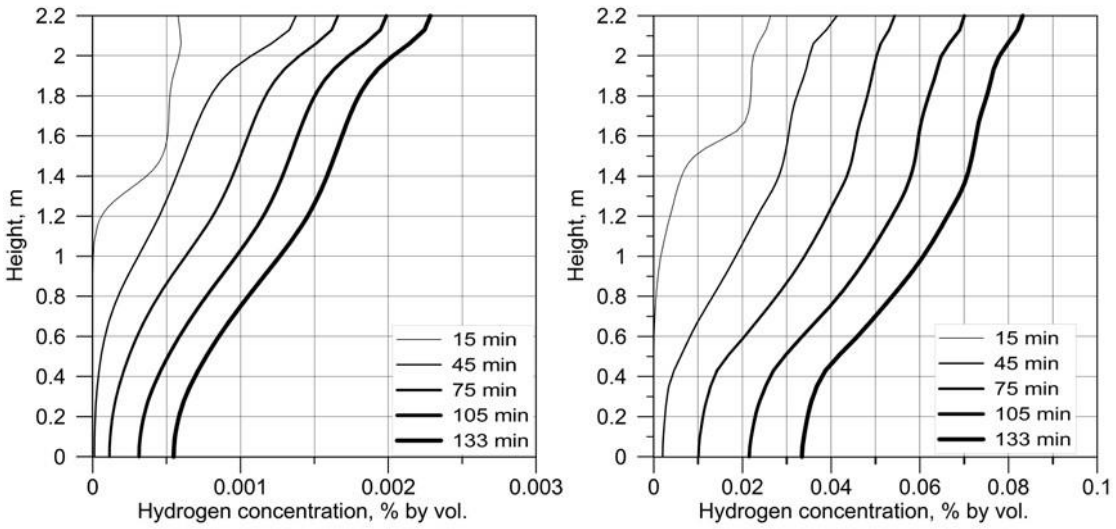


Figure 6–4. Hydrogen concentration profile across the garage height at location of rake 03 with time: left – scenario 1; right – scenario 2.

Please click the advert



The change of the ratio of hydrogen concentration at the bottom to concentration at the top of the garage is shown in Fig. 6–5. The difference in concentration diminishes with time and the ratio tends to be 1. This proves that there is no stratification of permeated hydrogen in the garage in a practical sense. Presence of non-adiabatic walls and air movement would facilitate a perfect mixing of permeated hydrogen with air within the enclosure. The larger the permeation rate the faster the uniformity will be achieved. For example, concentration at the bottom reaches 0.1 of concentration at the top at about 80 minutes for scenario 1 and at about 55 minutes for scenario 2.

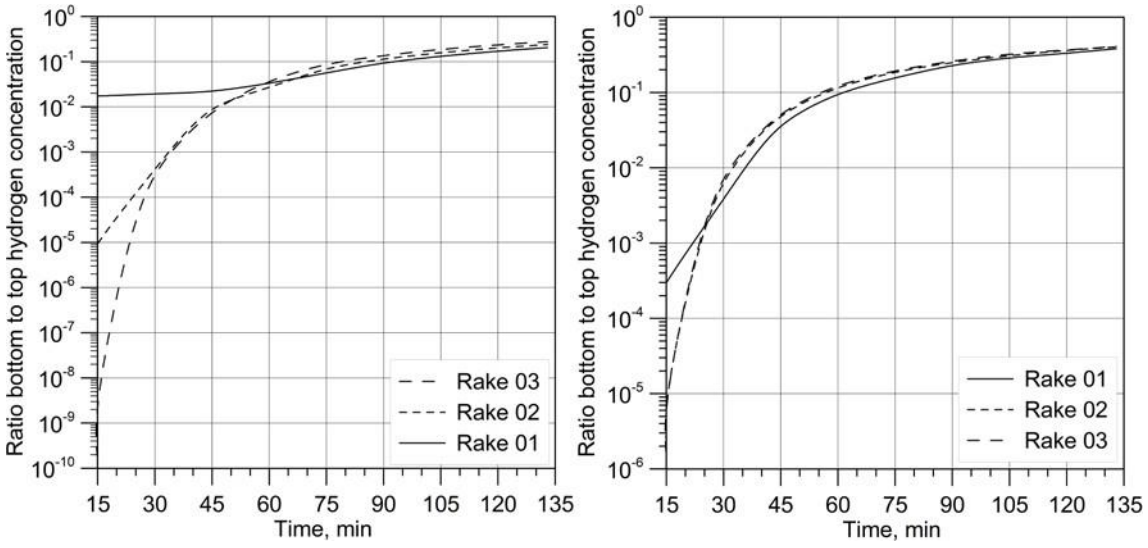


Figure 6–5. Change of the ratio of the bottom to top hydrogen concentration at the three rakes: left – scenario 1; right – scenario 2.

The following conclusions can be drawn for this section. The concentration of hydrogen on the tank's surface grows as square root of time at the initial stage of permeation. The maximum concentration of hydrogen is always on the top of the tank. However, it will never reach 100% of hydrogen by volume for any realistic enclosure (not perfectly sealed to continue accumulation). The buoyancy and the diffusion are in balance at about 37 seconds after the start of the process for 1 $Ncm^3/hr/L$ permeation rate and after 16 seconds for 45 $Ncm^3/hr/L$ rate according to the analytical estimate. This is confirmed by numerical simulations. Indeed, the 10% distortion by buoyancy of the cylindrical symmetry of hydrogen transport by diffusion is simulated at time 60 s and 12 s respectively. Numerical simulations, based on the original modelling approach of permeated hydrogen dispersion (source term of hydrogen in species equation at the tank surface rather than a plume of 100% of hydrogen with mass flow rate equal to permeation rate integrated throughout the tank surface), confirmed analytical estimate that hydrogen concentration on the surface is far below even the LFL of 4% by volume. Simulations have shown as well that distribution of hydrogen is uniform throughout the garage in the practical sense. The ratio of the bottom to the top hydrogen concentration tends to 1 with time. The uniformity of hydrogen-air mixture formed in enclosure as a result of permeation allows application of the perfect mixing equation (Marshall, 1983) to derive requirements to permeation rates (Adams et al., 2011) for the Commission Regulation (EU) No. 406/2010 of 26 April 2010.

6.1.4. Allowable permeation rate from hydrogen-powered vehicles

A long term slow hydrogen release such as that due to permeation from a vehicle into an inadequately ventilatedenclosedstructureisapotentialhazardandassociatedriskofhydrogeninautomotiveapplications. Due to its small size hydrogen permeates through the containment materials found in compressed gaseous hydrogen storage systems and is an issue that requires consideration for containers with non-metallic (polymer) liners (Adams et al., 2011). This section focuses on the development of a methodology to estimate an allowable upper limit for hydrogen permeation in automotive applications. Worst credible scenarios are identified and a maximum hydrogen permeation rate from road vehicles into enclosed garage structures is estimated. One of the key challenges in estimating an allowable hydrogen permeation rate is the very wide variation in the design, construction and ventilation requirements for enclosed structures.

Hydrogen is typically considered for use in city buses and cars with fuel cell based drivetrains and to a lesser extent internal combustion engines. Typical full size, single deck, non-articulated city bus dimensions are length 12 m, width 2.55 m, height 3 m, with a reasonable maximum hydrogen storage quantity of 50 kg according to the HyFLEET project. For a passenger car the maximum quantity of hydrogen required is in the order of 3–10 kg depending on the size and characteristics of the car, and stored at pressure 35 MPa or 70 MPa. Bus storage systems are usually roof mounted, with the fuel cells either mounted on the roof or at the back of the vehicle. For passenger cars, high pressure hydrogen storage systems are usually mounted near the rear axle as this position offers the best protection in the event of a traffic accident.

Typical enclosed structures used by road vehicles include domestic single or multi-vehicle garages, partially enclosed public parking like multi-storey parking with semi-open sides, fully enclosed public parking like underground parking, city bus garages, maintenance facilities, showrooms, covered bus stations, covered loading bays, containers for shipping vehicles, ferries, tunnels or wide over bridges, rail transport, e.g. Channel Tunnel vehicle shuttles, etc.

The methodology for estimating an allowable hydrogen permeation rate is based on the assumption that permeated hydrogen disperses homogeneously in enclosure, as shown in previous section, allowing the prefect mixing equation to be used to estimate the allowable rate. Specific focus is placed on assessing the maximum prolonged material temperature and worst credible enclosure ventilation.

With respect to hydrogen permeation, the critical cases were considered to be domestic garages for passenger cars and city bus maintenance facilities as being representative for commercial vehicles. For example, the proposed scenario for a single bus is based on the minimum maintenance volume (Adams et al., 2011). Typical working space requirements for a city bus maintenance facility are approximately 2 m to each side of the bus including the front and rear. Above the bus, 2 m is necessary to be able to lift the bus to work beneath it and a further 1.5 m is necessary for lighting and other services, giving a distance between the floor and roof of approximately 6.5 m.

6.1.4.1. Effect of temperature

One of the key parameters affecting the actual permeation rate of hydrogen through the walls of a hydrogen container is the temperature of the container materials (Mitlitsky et al., 2000). The temperature of a container wall material is influenced by thermodynamic processes inside the container, e.g. during refilling, and by the ambient temperature. All current RCS specify a maximum material temperature of 85^{0}C for container materials (Adams et al., 2011). In terms of normal usage of the system, the only time that a temperature of 85^{0}C would be experienced inside the container is immediately after fast refilling. Tests have repeatedly shown that the temperature falls rapidly after the refilling is complete so that the material temperature should drop below 50^{0}C in a few minutes (Jeary, 2001).

The hottest recorded ambient air temperature anywhere in the world is 57.8^{0}C recorded in El Azizia in Libya in 1922, while in Europe it is 48.0^{0}C recorded in Athens in 1977, lasting for 1–2 hours at most following references in (Adams et al., 2011). With respect to long term average temperatures, which are of more relevance to the permeation phenomenon, the maximum figures are somewhat lower. The average monthly maximum and minimum temperatures over a 38 year period between 1913 and 1951 for El Azizia in Libya show that for the hottest month, July, the average maximum and minimum temperatures were 37^{0}C and 20^{0}C respec- tively [21]. A statistical analysis of temperature loads for the StorHy project showed that in an example city (Athens) over a 30 year period average temperatures exceeded 35^{0}C for 5% of the year (Mair et al., 2007). The air temperature inside buildings will vary from the ambient outside temperature. Although no research was found on this subject the prolonged temperatures will be significantly lower than peak temperatures which will be of relatively very short duration in the context of the permeation issue (Adams et al., 2011).

Please click the advert

Destination MMU

Manchester Metropolitan University

MMU is proud to be one of the most popular universities in the UK. Some 34,000 students from all parts of the globe select from its curricula of over 1,000 courses and qualifications.

We are based in the dynamic yet conveniently compact city of Manchester, located at the heart of a sophisticated transport network including a major international airport on the outskirts. Parts of the campus are acclaimed for their architectural style and date back over 150 years, in direct contrast to our teaching style which is thoroughly modern, innovative and

forward-thinking.



MMU offers undergraduate and postgraduate courses in the following subject areas:

- Art, Design & Performance
- Computing, Engineering & Technology
- Business & Management
- Science, Environmental Studies & Geography
- Law, Education & Psychology
- Food, Hospitality, Tourism & Leisure Studies
- Humanities & Social Science

For more details or an application form please contact MMU International. email: international@mmu.ac.uk telephone: +44 (0)161 247 1022 www.mmu.ac.uk/international

It was concluded (Adams et al., 2011), a prolonged material temperature of 85^{0}C in an enclosed facility or beneath a vehicle is extreme and would only be experienced for short periods in comparison to the time necessary for permeation to produce hazardous concentrations of hydrogen which is in the order of weeks for a perfectly sealed enclosure. In addition, the permeation barrier, i.e. the liner, would be insulated by thick carbon fibre wrapping. Based on the above and allowing for the effect of some additional warming inside an enclosed structure, a reasonable and conservative maximum prolonged material temperature is accepted as 55^{0}C, which harmonises with (SAE J2579, 2009).

6.1.4.2. Worst-credible scenario

One of the key issues in determining an acceptable permeation rate is the worst-credible natural ventilation rate of enclosed structures such as garages. Life safety should be assured independent of the combination of vehicle and structure. A review of ventilation requirements undertaken within the HySafe consortium indicated that in some European countries there are no minimum requirements for natural garage ventilation (Miles, 2007). Although natural ventilation rates in many types of homes and other buildings are well studied, those for residential garages are not (Adams et al., 2011). Parameters of typical garages considered for the purpose of this section are given in (Adams et al., 2011).

Six references were identified providing detailed sets of real world natural garage ventilation measurements including two studies by the Canada Mortgage and Housing Association (2001, 2004), two studies by the Electric Power Research Institute in the USA (1991, 1996), and a study by TIAX (2001), (Waterland, 2005) in the USA. The lowest measurement identified in real world conditions was 0.03 ACH (air change per hour) from the TIAX (2001) study. It is worth noting that experiments in a well sealed experimental garage at CEA with all vents closed and doors sealed, gave a natural helium leak rate of 6 NL/min, which is equivalent to 0.01 ACH assuming that the helium leak rate corresponds to the natural ventilation rate (Cariteau et al., 2011).

The available real world measurements are shown in Fig. 6–6, excluding the data ranging from 17-47ACH from the Canadian studies which were considered to be unreasonably high for a reasonably weather proofed garage (Adams et al., 2011).

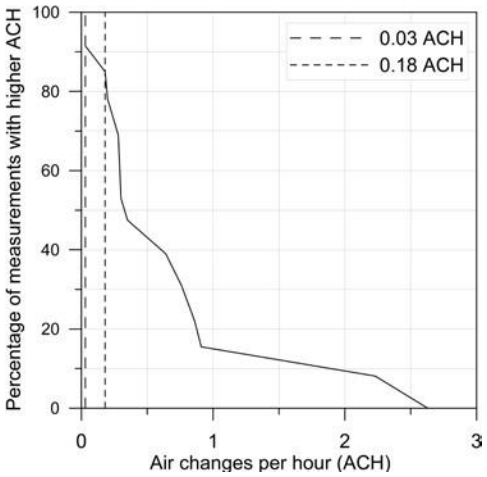


Figure 6–6. Available real world garage ventilation measurements (excluding Canadian studies): Electric Power Research Institute (1991, 1996), TIAX (2001), Waterland (2005).

Prior to this study the minimum natural ventilation rate used in other permeation studies was 0.18 ACH. However, based on research conducted for this report, the worst credible natural garage ventilation rate has now been agreed with the SAE as 0.03 ACH.

It is proposed that a worst-credible garage natural ventilation rate is 0.03 ACH (Adams et al., 2011). The value lies at a level reasonably above the lowest measured value of 0.01 ACH for the sealed CEA experimental facility and is equal to the lowest measured value for real world garages of 0.03 ACH (Waterland, 2005). This ventilation rate is also harmonised with the SAE Fuel Cell Safety Work Group.

6.1.4.3. Testing conditions

The conditions under which the test is performed represent the worst case for permeation from the container following the approach adopted in SAE J2579 (2009). If the test conditions are not representative of the worst case conditions the allowable rate must reflect the difference between the test conditions and the worst case conditions. Factors to be considered include (Adams et al., 2011): test pressure and temperature, new container or simulated end of life container. Testing should be undertaken at the nominal working pressure.

With respect to increasing material temperature, hydrogen permeation through polymer materials has been found to increase by an order of magnitude between approximately 24^{0}C and 82^{0}C (Mitlitsky et al., 1999). Material temperature/permeation characteristics are a key factor in determining the allowable permeation rate at a specified test temperature different to the maximum prolonged material temperature (Adams et al., 2011). Rothe (2009) published temperature/permeation rate data for three different materials (see Fig. 6–7). If the testing is undertaken at ambient temperature, the allowable permeation rate should be set such that the equivalent permeation at the maximum prolonged material temperature, previously proposed as 55^{0}C, results in a safe condition (Adams et al., 2011). The factor depends on the actual specified testing temperature and material behaviour. From Fig. 6–7, the following factor was estimated from the increase in permeation between the test temperature and maximum prolonged material temperature for the worst case material: for a test conducted at a temperature of 20^{0}C, a factor of 3.5 has to be used to convert from the maximum prolonged material temperature to the test temperature, and factor 4.7 if testing is at a temperature of 15^{0}C (conservative case of JARI Material 1).

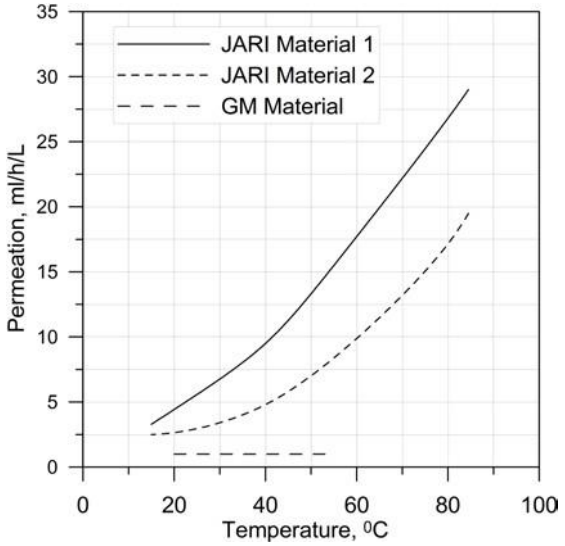


Figure 6–7. Permeation rate as a function of temperature for three materials (Rothe, 2009).

Testing is usually carried out on a new container. However, the container is a subject of aiging and permeation rate from a simulated end of life container is of interest for hydrogen safety engineering. It has been reported that the carbon fibre overwrap on new containers can significantly restrict the permeation rate (Mitlitsky, 2000). In a container that is reaching the end of its service life the carbon fibre/resin matrix will be affected by a significant amount of micro-cracking that will not affect the structural integrity, however, it could allow an increase in hydrogen permeation.

The increase in permeation for a container at end of life has been suggested to be twice that of a new container (Adams et al., 2011). Further investigations revealed conflicting opinions based on testing experience. One test centre has found that permeation does not increase significantly towards the end of life based on their test results (Webster, 2009). Other organisations suggest that increasing permeation has been observed (Novak, 2009) and also that a factor of 2 may not be adequate (Barthélémy, 2009). The investigations suggest that the effects of aging are not adequately understood and further research should be carried out, e.g. similar to the ENDEMAT project (2008). It is considered necessary to retain a factor of two reduction between end of life and new containers which would allow for unknown aging effects, use of new materials and statistical variation around limited existing data (Adams et al., 2011).

6.1.4.4. Calculation of allowable permeation rate

The following assumptions have been made (Adams et al., 2011):

- The allowable permeation rate will be specified in NmL/hr/L water capacity.
- Permeated hydrogen can be considered to disperse homogeneously.
- Worst-credible natural ventilation rate for a domestic garage is 0.03 ACH.
- Maximum permitted hydrogen concentration is 1% by volume, i.e. 25% LFL.

- Maximum long term material temperature is 55^{0}C.
- New container, with a factor of 2 to convert from the worst case end of life condition.
- For a test conducted at a temperature of 20^{0}C, a factor of 3.5 is used to convert from the maximum prolonged material temperature to the test temperature (factor 4.7 at temperature 15^{0}C).

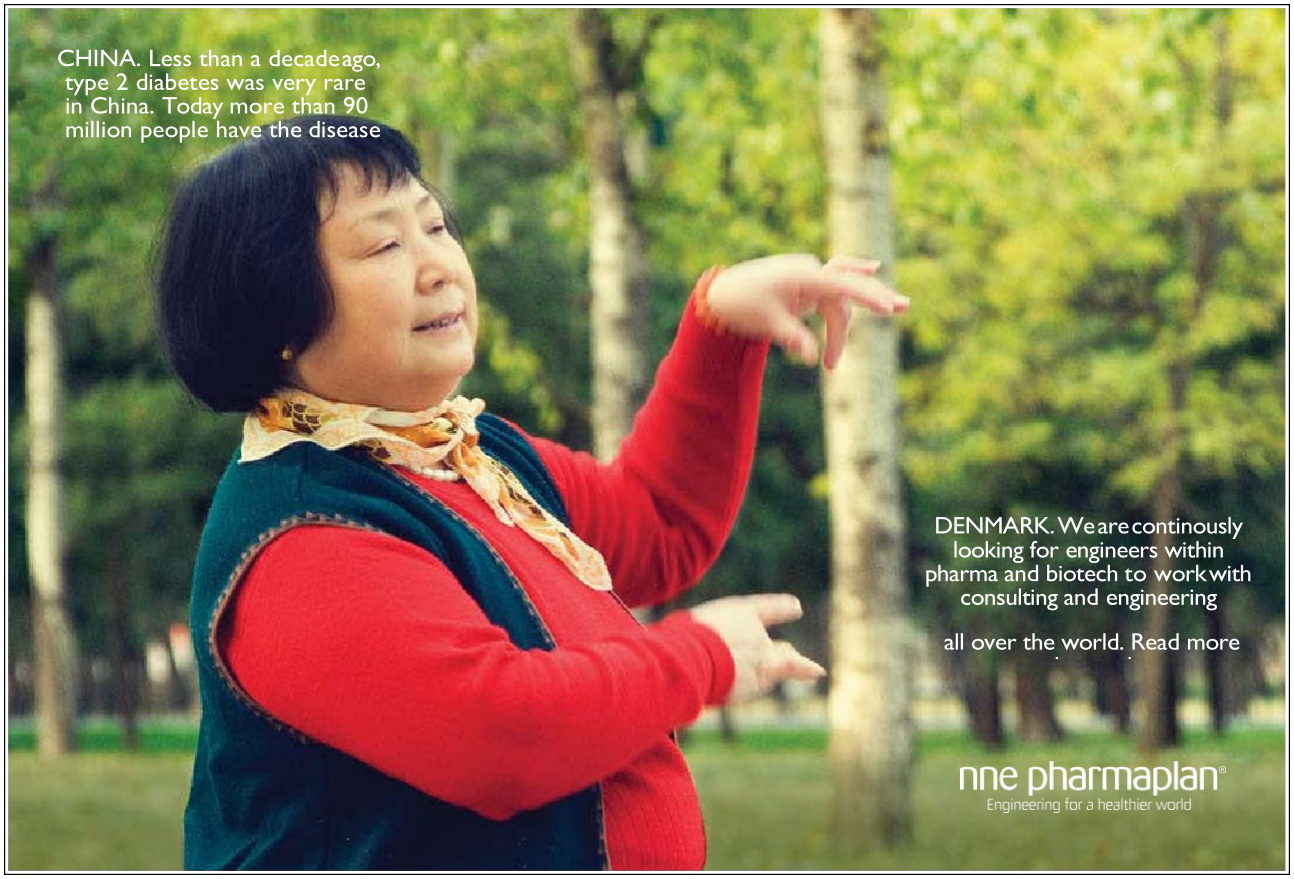
It should not be implied that these are considered to be the best test conditions. The aim is to identify an allowable permeation rate rather than test conditions. The basic method requires the calculation of the "safe" permeation rate at the end of life condition for the container combined with the maximum prolonged material temperature, and then the value is reduced to that for a new container at the nominal test temperature, e.g. 20^{0}C. A value was also derived for an alternative test temperature of 15^{0}C.

The perfect mixing equation can be used to calculate the hydrogen release rate required to give a steady state hydrogen concentration (Marshall, 1983)

$$C_{\%} = \frac{100 \cdot Q_g}{Q_a + Q_g}, \qquad (6\text{–}12)$$

where $C_{\%}$ is the steady state gas concentration, % by volume; Q_a is the air flow rate, m^3/min; and Q_g is the gas leakage rate, m^3/min.

Please click the advert



The maximum allowable hydrogen permeation rate is then

$$Qp_x = \frac{Q_a \bullet C_{\%}}{100 - C_{\%}} \cdot \frac{60 \cdot 10^6}{V \bullet f_a \cdot f_t}, \quad (6\text{–}13)$$

where Qp_x is the allowable permeation rate at a test temperature of x^0C, mL/hr/L water capacity; V is the water capacity of hydrogen storage, L; f_a is the aging factor, taken to be 2; and f_t is the test temperature factor of 3.5 at a test temperature of 20^{0}C or 4.7 at a test temperature of 15^{0}C.

Based on the above assumptions, scenarios and methodology, the theoretical allowable permeation rates to give a hydrogen concentration less than 1% are given in Table 6-1 (Adams et al., 2011). It is proposed that the passenger car rates can be accepted for the city bus scenarios, as the worst case bus scenario is the "minimum" garage with failed forced ventilation and even in this situation the passenger car rates would still give a hydrogen concentration significantly lower than 4% by volume.

Minimum Testing Temperature (^{0}C)	Maximum allowable permeation rate (mL/hr/L)	
	Passenger Car	City Bus
15	6.0	3.7
20	8.0	5.0

Table 6-1. Theoretical allowable permeation rates (Adams et al., 2011).

It is worth noting that an alternative value of maximum allowable permeation rate based on similar methodology at the SAE J2579 (2009) test conditions (55+ ^{o}C, simulated end of life) is 90 mL/min/std passenger vehicle. The HySafe proposals for allowable hydrogen permeation rates (Adams et al., 2011) are intended only for use in appropriate vehicle regulations and standards. The proposals are based on a range of garage scenarios that are considered to be representative of real world situations allowing the safe use of vehicles in typical enclosed structures such as domestic garages or maintenance facilities. The rates should not be applied to other situations or applications without further consideration. The proposed allowable hydrogen permeation rates are not applicable to hydrogen permeation into vehicle compartments. For hydrogen permeation into vehicle compartments the adoption of appropriate performance based requirements, or other requirements and engineering solutions as appropriate, in the relevant vehicle regulations or standards are necessary to avoid the potential development of flammable hydrogen-air mixtures and associated hazards.

In determining allowable hydrogen release rates from a vehicle, it is necessary to consider the different regulatory regimes that govern vehicles and buildings (Adams et al., 2011). The automotive industry increasingly has regulations harmonised at a global or regional level, however, vehicle regulations do not regulate the design of structures associated with vehicle use. In contrast, buildings and infrastructure are regulated at a national or local level by different authorities to those developing vehicle regulations. To achieve the safe introduction of hydrogen vehicles without unnecessary restrictions, it is necessary to ensure that vehicle and building/ infrastructure regulations are compatible. Any vehicle could be driven into a wide range of garages during its life, and the discharges should be safe for all reasonable conditions. Conversely a garage can contain different

vehicles. However, the structure needs to be safe regardless of the vehicle put inside. Vehicle regulations only control the approval of a vehicle and additional regulations control roadworthiness inspections.

6.2. The pressure peaking phenomenon

6.2.1. Hydrogen-powered car in a garage scenario

In vehicles hydrogen is most commonly stored today as a compressed gas in tanks which are required by the Commission Regulation (EU) No 406/2010 to be equipped with pressure relief devices (PRDs). The PRD is fitted to the fuel tank and starts to release hydrogen when high temperature of about 110°C is reached, e.g. in fire conditions. The PRD can provide rapid release of the hydrogen, if large orifice diameter is used, thus minimising the possibility of tank explosion during too long exposure to fire. High mass flow rates from PRDs are probably "acceptable" outdoors. However, the hazards resulting from a rapid release indoors are different.

Let us consider a hypothetical scenario involving a release from a typical onboard hydrogen storage tank at 35 MPa, through a 5.08 mm diameter orifice, representing a "typical" PRD (Brennan et al., 2010). The release is assumed to occur vertically upward in the centre, 0.5 m above the floor, of a small garage of size LxWxH=4.5x2.6x2.6 m (SAE J2579, 2009) and volume of 30.4 m^3 with a single vent equivalent in area to a typical brick LxH=25x5 cm located flash with the ceiling. A conservative approach is taken, i.e. a constant mass flow rate of 0.39 kg/s is applied (ignoring a pressure drop in the storage tank) after the PRD opening.

6.2.2. Phenomenological model

Let us assume that hydrogen fully occupies an enclosure to which it is released, and the steady state conditions are reached, when hydrogen mass flow rate from the enclosure through a vent is equal to mass flow rate from the nozzle of PRD to the enclosure, i.e. $\dot{m}_{vent} = \dot{m}_{nozz}$. Simple models such as the orifice equation for a subsonic regime are published elsewhere (Molkov, 1995)

$$\dot{m}_{vent} = CA\left\{\frac{\gamma}{\gamma-1} P_S \theta_{encl} \left[\frac{P_S}{P_{encl}}^{\frac{2}{\gamma}} - \frac{P_S}{P_{encl}}^{\frac{\gamma+1}{\gamma}}\right]^{\frac{1}{2}}\right\} \quad (6\text{–}14)$$

and the Bernoulli's equation in the assumption of zero flow velocity in the enclosure

$$P_{encl} - P_S = \frac{1}{2\rho_{H2}}\left(\frac{\dot{m}_{nozz}}{A}\right)^2 \quad (6\text{–}15)$$

can be used to estimate the steady state overpressure within the enclosure. In this equations C is the discharge coefficient; A is the vent area, m^2; γ is the ratio of specific heats; P_S is the surrounding pressure, Pa; P_{encl} is the pressure in the enclosure, Pa; ρ_{H2S} is the density of hydrogen at the surrounding conditions,

kg/m^3.

Equations (6–14) and (6–15) predict an overpressure in the enclosure of 17.9 and 15 kPa respectively for the scenario selected with C =0.6 (Emmons, 1995) and γ=1.4. It is worth noting that this is obtained in assumption of pure hydrogen within the enclosure. However, neither of two equations accounts for the injection of a lighter gas into a heavier gas and the subsequent overpressure in the garage to "push" the heavier gas air out of the garage.

The following simple system of equations is used to predict the overpressure dynamics within the enclosure with an assumption that each portion of released hydrogen is perfectly mixed with the uniform gas currently occupying the enclosure (Brennan et al., 2010)

$$m^{t+\Delta t} = m^{t} + \left(\dot{m}^{t}_{nozz} - \dot{m}^{t}_{vent}\right)\Delta t, \tag{6–16}$$

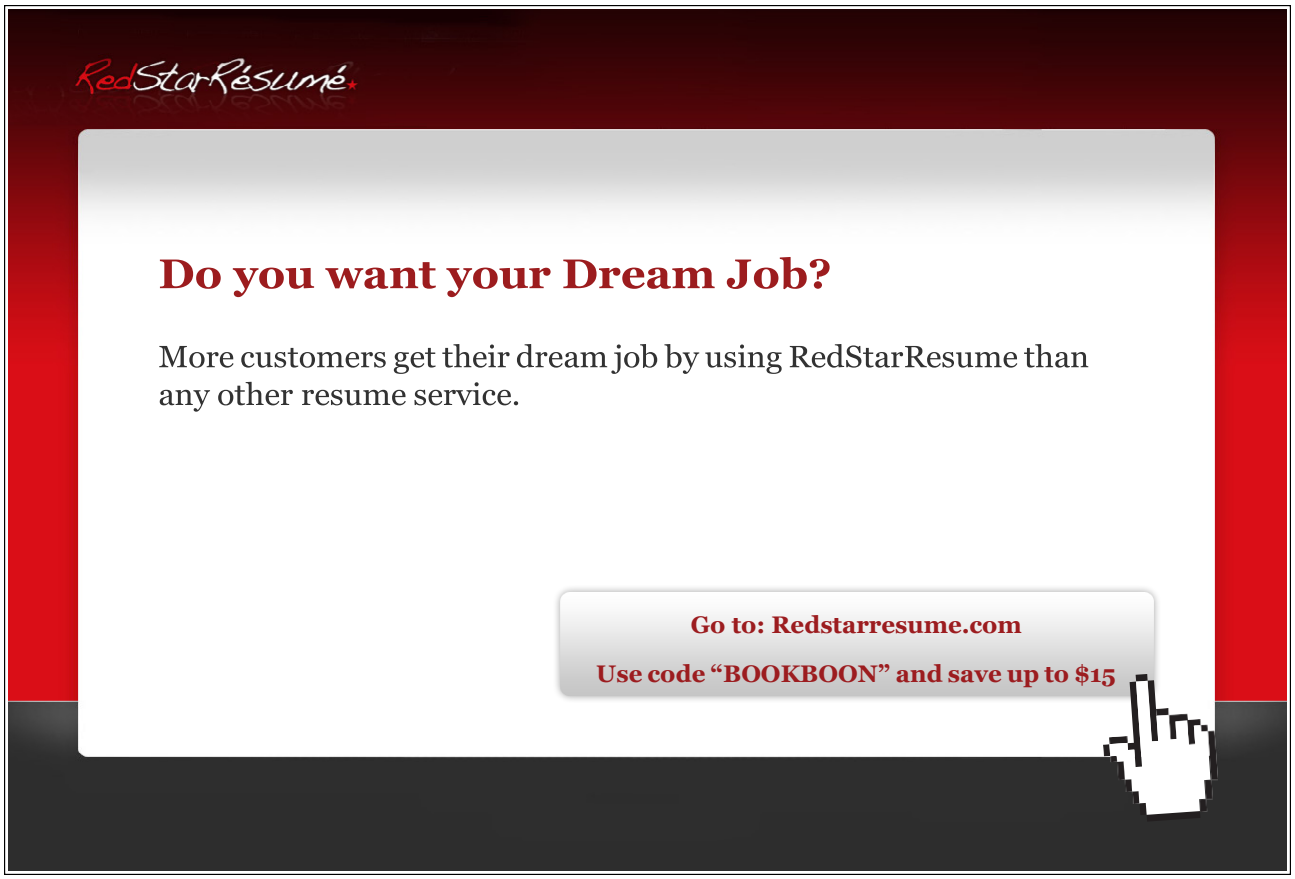
$$n^{t+\Delta t}_{encl} = n^{t}_{encl} + \left(\frac{\dot{m}^{t}_{nozz}}{M_{H_2}} - \frac{\dot{m}^{t}_{vent}\, n^{t}_{encl}}{m^{t}_{encl}}\right)\Delta t, \tag{6–17}$$

$$P^{t+\Delta t}_{encl} = \frac{n^{t+\Delta t}_{encl} RT}{V}, \tag{6–18}$$

$$\dot{m}^{t+\Delta t}_{vent} = C \cdot \left|\frac{\rho^{t+\Delta t}_{encl}}{V}\right| \cdot \left|\frac{\rho^{t+\Delta t}_{encl}}{m^{t+\Delta t}_{encl}}\right| \cdot A \cdot \sqrt{2\left(P^{t+\Delta t} - P\right)V}^{1/2}, \tag{6–19}$$

where superscripts "t" and "$t+\Delta t$" denotes previous and next time steps respectively; m is the mass of gas, kg; $\dot{m}$ is the mass flow rate, kg/s; n in the number of moles; Δt is the time step, s; V is the enclosure volume, m^3; P is the pressure, Pa.

Please click the advert



6.2.3. Pressure load of the unignited hydrogen release (constant mass flow rate)

The transient pressure load in the vented enclosure according to the selected scenario predicted by the system of equations (6–16)–(6–19) for constant mass flow rate is given in Fig. 6–8.

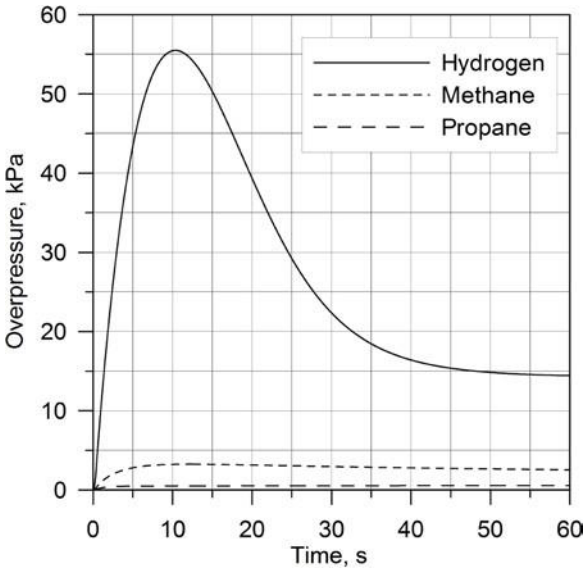


Figure 6–8. Pressure peaking phenomenon for release of hydrogen with mass flow rate 0.39 kg/s into the enclosure of 30.4 m3 with a vent of typical brick size 25x5 cm compared with pressure dynamics for releases of methane and propane at the same conditions.

The performed CFD simulation (Brennan et al., 2010) was run until just beyond the pressure maximum, after which point it was deemed unnecessary to continue the simulation. The predictions by the CFD and phenomenological models are within approximately 10%. A value of C=0.55 was found to perfectly match the CFD results.

The CFD study provided as well the dynamics of flammable hydrogen-air mixture development in the garage. It was found that almost 50% of the enclosure was engulfed by a flammable atmosphere in less than 1 s. Even after a release for 10 s the presence of the vent means that a mixture with potential to deflagrate exists in the majority of the enclosure, with the exception of a small rich region. The CFD results were shown to predict the formation of a flammable zone and mixing within the garage. This could not be shown using simple phenomenological models.

Figure 6–8 illustrates how the overpressure within the enclosure resulting from the injection of hydrogen reaches a level above 10 kPa capable of rupturing the garage (Baker et al., 1983) within only 1 s. Evacuation of people in this time is impossible and this life safety issue has to be yet addressed by car manufacturers. There is only one engineering solution that is the reduction of mass flow rate. This is turn will require higher fire resistance level of onboard storage tanks compared to current 3.5–6.5 minutes for type 4 vessels (Stephenson, 2005).

If the garage does not rupture first the pressure within the garage, for this particular scenario, reaches a maximum level in excess of 50 kPa. This maximum pressure then drops off and tends towards a steady state value, considerably lower, and equal to that predicted by the simple steady state estimations. It should be noted that this represents a worst case scenario with constant mass flow rate. Therefore, continuation of a constant mass flow rate release for 60 s is included in Fig. 6–8 purely to illustrate the time frame before a steady state conditions are reached when the garage is occupied by 100% of hydrogen.

The maximum pressure is reached in less than 10 s. Within this time the entire garage would be destroyed with missiles flying around and creating more damage. These are consequences of pressure build up without even considering the ignition of released hydrogen. Pressure peaking effect of unignited hydrogen release in vented enclosure is a new aspect of customers' safety that hydrogen safety engineers and manufacturers of hydrogen and fuel cell systems have to address.

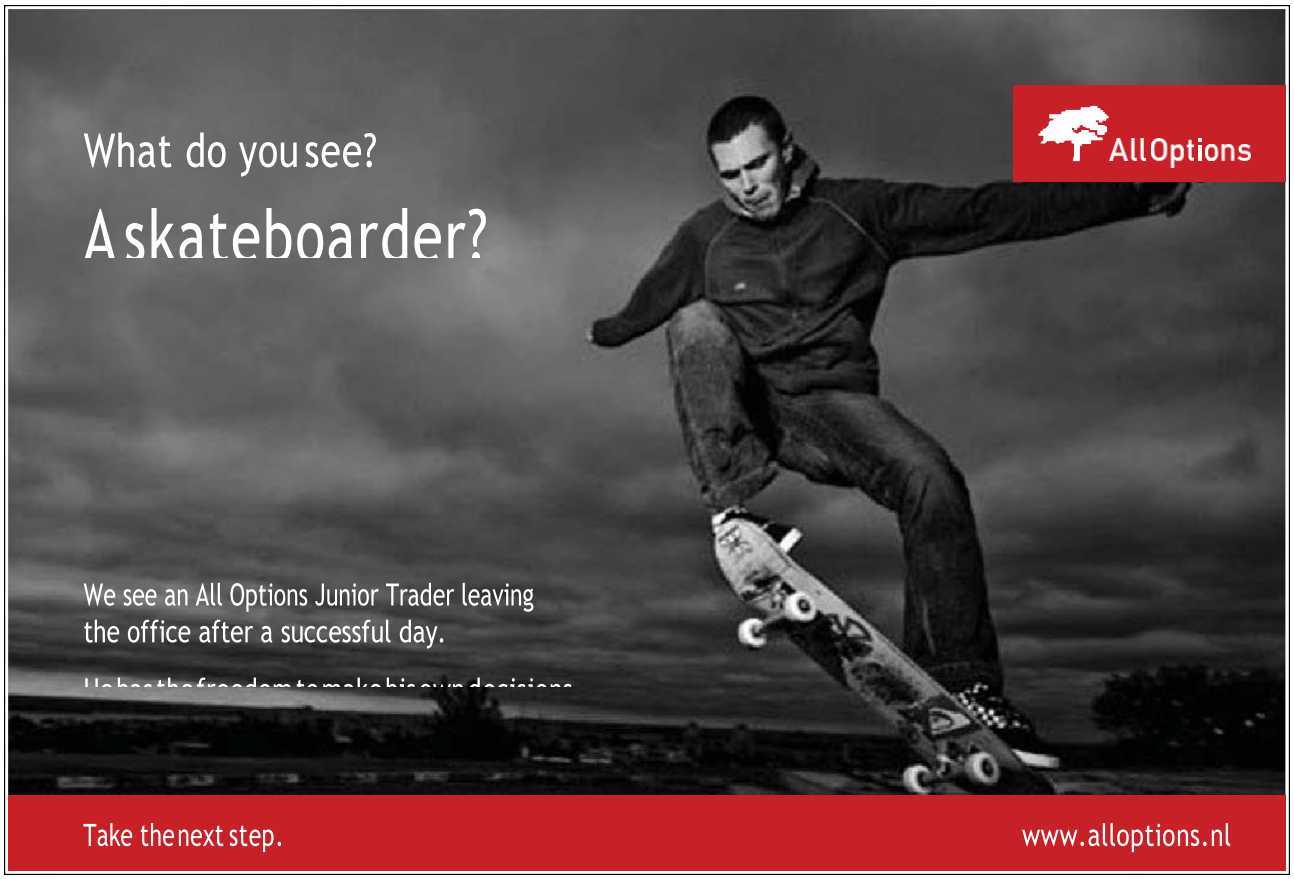
Figure 6–8 illustrates as well the predicted overpressure values versus time for a range of fuels with different molecular mass and the same mass flow rate of 0.39 kg/s at the same garage (with discharge coefficient C=0.6): hydrogen, methane, propane with the molecular masses of 0.002, 0.016 and 0.044 kg/kmol respectively. It is clearly seen how the maximum overpressure drops with increasing molecular mass. There is a small pressure peak for methane release as its molecular mass is below that of air. The pressure peaking phenomenon is absent for propane as its molecular mass is higher than air. Instead, the pressure generated by release of hydrogen into the vented enclosure is growing monotonically to reach a steady state value. This should be taken into account when designing PRDs for use with different gases for indoor systems. Indeed, the same PRD technology used for CNG or LPG should not be assumed to behave in the same way for hydrogen. They practically have no pressure peaking (methane) or cannot have at all (propane).

The pressure peaking phenomenon for a release of gas lighter than air into vented enclosure can be explained by analysing equation (6–16)–(6–19). Indeed, from the equations it follows that volumetric mass flow rate out of the enclosure is inversely proportional to the square root from the density of gas escaping the enclosure. Thus, in the beginning of the process when the density of hydrogen-air mixture is comparatively high and close to air density the constant volumetric inflow of pure hydrogen is essentially above the volumetric outflow of heavier hydrogen-air mixture out of the enclosure. The pressure within the enclosure grows to allow mass flow rate of outgoing gas, which is a function of pressure, to match constant (for this scenario) mass flow rate entering the enclosure from the leak. Then, the molecular mass of hydrogen-air mixture decreases with time as there is no air entering the enclosure for such high mass flow rates from PRD. This implies the volumetric flow rate increase. Thus, the pressure in the enclosure can drop to match the constant volumetric flow rate from PRD.

Thus, the simple engineering methods to calculate the overpressure in an enclosure with a vent at moderate releases of hydrogen (flow is only out of the enclosure) are under predicting the steady state overpressure. This is due to existence of the pressure peaking phenomenon for releases of gases lighter than air like hydrogen and helium. Indeed, straight forward approaches like the Bernoulli's equation predict a steady state overpressure in the garage in the region of 15 kPa. However, the pressure peaking phenomenon gives far higher maximum pressures in excess of 55 kPa, which is reached within the first 10 s in the considered scenario. The phenomenological model indicates that the over pressure level predicted by the simple steady state equations would not be achieved for approximately 40–60 s at which point the building would most likely have been long destroyed. Pressure peaking reaches a maximum level in excess of 100 kPa for pressure in storage tank of 70 MPa (Brennan and Molkov, 2011).

The pressure peaking phenomenon, i.e. existence of maximum pressure peak that is above the steady state value, during a release of lighter than air gas into vented enclosure, should be accounted for when performing safety engineering for indoor use of hydrogen systems. Overall the conclusion is drawn that PRDs currently available for hydrogen-powered vehicles should be redesigned, along with the increase of fire resistance rating of onboard hydrogen storage tanks, and RCS updated if the vehicle is intended for garage parking.

Please click the advert



6.2.4. "Safe" PRD diameter for unignited blow-down of hydrogen in a garage

This section discusses "safe" PRD diameters for enclosures of different volume with different natural ventilation level (Brennan and Molkov, 2011). The under-expanded jet theory and a blow-down model (Molkov et al., 2009) were utilised to analyse the pressure dynamics within garage-like enclosures. This model can be used to calculate decay of pressure and change of mass flow rate during a release from a storage tank of known volume through orifice of known diameter. The heat transfer during blow-down was not accounted for, and an isothermal approach which assumed a temperature of 288 K was used based on available experimental data for blow-downs at such pressures through orifices of similar size. For a given diameter, storage pressure, and hydrogen inventory, the output of the blow-down model (mass flow rate) was applied as an input to the phenomenological model to predict overpressure in a garage with a known volume and air changes per air (ACH).

A range of scenarios have been investigated whereby an unignited hydrogen release, from a PRD, is considered in a garage type enclosure with limited ventilation (Brennan and Molkov, 2011). The hypothetical events involve releases from typical onboard hydrogen storage tanks at pressures of 35 and 70 MPa. Inventory of 5 kg of hydrogen at each storage pressure is considered here. The release is assumed to occur in a garage with a vent. The volume of the garage and the size of the vent are varied. Free garage volumes of 18, 25, 30 and 46 m^3 were chosen to be representative of small, medium and large residential garages (InsHyde, 2009). A range of vent sizes were considered for each volume. The vent sizes were calculated to correspond to ACH below value of 1: 0.18, 0.3, 0.54 characteristic of residential garages (InsHyde, 2009; TIAX, 2004), and a value of 0.03 that is extremely conservative (it is the lowest measured value and representative of a worst case scenario (InsHyde, 2009)).

6.2.4.1. Air changes per hour and natural ventilation vent sizing

Let us relate garage volume and vent areas to ACH. Whilst values of ACH characteristic of residential garages can be found in the literature there was some uncertainty as to how ACH could be translated to vent area for a specific volume. By definition ACH is the ratio of volumetric air flow rate through an enclosure per hour, Q_{hr} (m^3/hr), to the enclosure volume, V (m^3),

$$\text{ACH} = Q_{hr}/V. \tag{6–20}$$

Bernoulli's equation can be used to calculate volumetric flow rate per second Q_s as a function of vent area, A (m^2), density of air, ρ (kg/m^2), discharge coefficient C, and pressure differential between the enclosure and the atmosphere, ΔP (Pa), i.e.

$$Q_s = CA\sqrt{2OP/\theta} \tag{6–21}$$

The pressure differential assumed between the interior and exterior of the enclosure will obviously have an influence on the vent area calculated for a given ACH. The larger the "standard" ΔP, the smaller the corresponding vent area for a given volume and given ACH. A value of 50 Pa was accepted for ΔP in the majority of this work. This was chosen as "n50" is a standard measurement to determine the air leakage rate in a residential buildings, which is calculated based on a pressure difference of 50 Pa (The Air Tightness Testing & Measurement Association, 2010). However, a pressure difference of 5 Pa, which is close to value used by some researchers, was also used for comparison in the case of 5 kg of hydrogen at 35 MPa. This was done to demonstrate the sensitivity of the calculations to the method chosen for calculating ACH. The discharge coefficient was taken as the commonly recommended C=0.6 (Emmons, 1995).

6.2.4.2. Methodology and nomograms

The phenomenological model described in section 6.2.2 has been used in combination with models for an under-expanded jet and blow-down to examine the pressure dynamics for a range of release scenarios in a garage. For each combination of storage pressure, storage inventory, ACH and garage volume, a "safe" diameter was determined which ensures the pressure in the garage during a release does not exceed 20 kPa (and no less than 15 kPa). The mass flow rate decay data is used as an input to the phenomenological model to predict overpressure in the garage based on the garage volume and vent area, where vent area is calculated from ACH.

To provide life safety objective it is undesirable for the tank to fail, e.g. in a fire, while the pressure inside is still high. If the PRD diameter is reduced to keep pressure peak in a garage below 20 kPa the tank will take longer to blow-down, and hence the storage pressure remains higher for longer. Thus, the blow-down times through the "safe" diameters could be used to give an indication of "ideal" fire resistance rating of the hydrogen storage tanks.

Figure 6–9 gives the pressure dynamics for a release of 5 kg of hydrogen at initial storage pressure of 35 MPa, in a garage of free volume 30 m^3 with an ACH=0.18 (the minimum natural ventilation rate used in permeation studies before study of Adams et al., 2011). The figure shows the pressure dynamics for a currently typical PRD diameter of 5 mm compared with the dynamics for the "safe" diameter, found to be 0.55 mm in this case. For this specific case the PRD diameter should be reduced by an order of magnitude compared with a "typical" PRD diameter. If the storage pressure is increased, the ACH is reduced, the volume of the garage is reduced then this diameter would need to be decreased even further. This indicates the need in innovative engineering solutions for a system storage tank-PRD (the decrease of a PRD diameter means the increase of blow-down time and thus the increase of fire resistance rating of the onboard storage).

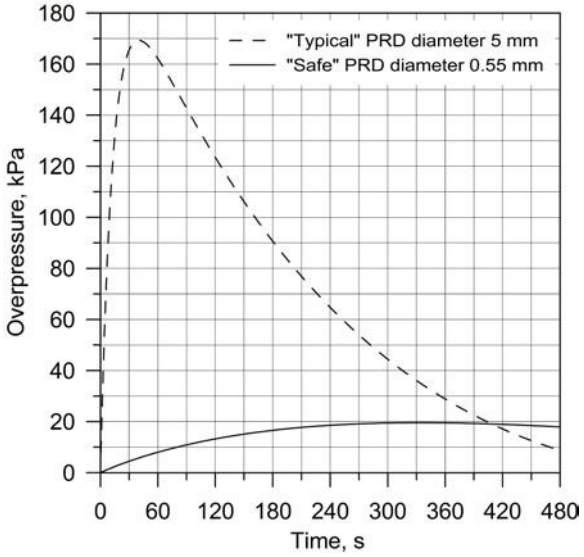
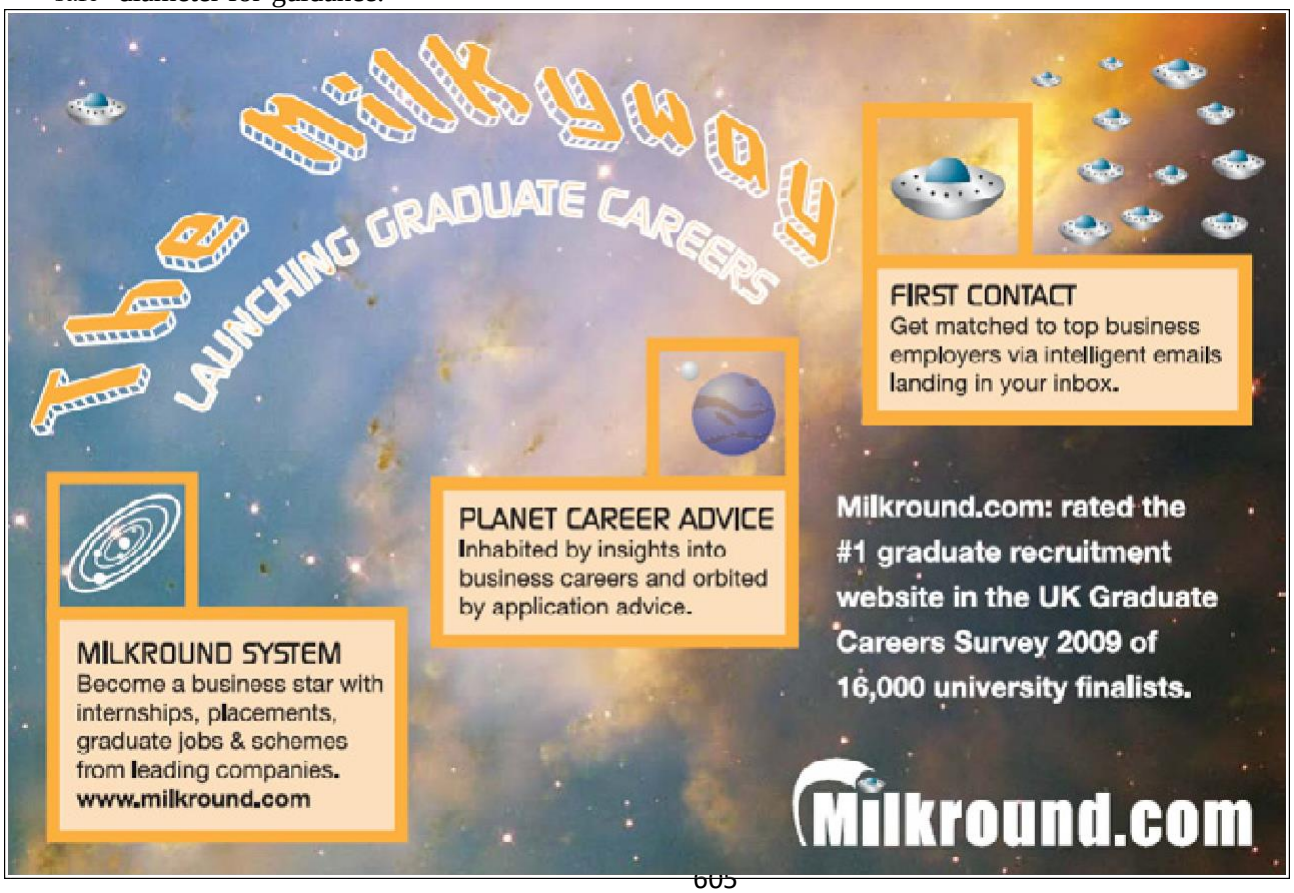


Figure 6–9. Pressure dynamics of unignited release in a 30 m³ garage, ACH=0.18, 5 kg of hydrogen at 35 MPa, diameters of 5 mm and 0.55 mm (Brennan and Molkov, 2011).

Figure 6–10 shows a nomogram for release of 5 kg of hydrogen at initial pressures of 35 MPa in garages of different free volume and different natural ventilation. The nomogram has two graphs which have the same x axis (Diameter, mm). The blow-down time from initial storage pressure down to values of 10 MPa, 5 MPa, 2 MPa, 1 MPa, 0.1 MPa and 0.01 MPa storage overpressure were determined for each "safe" diameter for guidance.

Please click the advert


The "safe" diameter can be estimated from the lower graph of the nomogram by reading horizontally across from the chosen volume until intersecting with the chosen ACH value, then read vertically up from this point of intersection to the x axis (values are shown for convenience at the top of the upper graph). The point of intersectionwiththe x axisisthe"safe" diameterforthechosen ACH, volume, inventoryofhydrogenandstorage pressure. Reading vertically up through/to the x axis to the point of intersection with the pressure curves on the upper graph can be used as a means to estimate blow-down time to that pressure for the "safe" diameter.

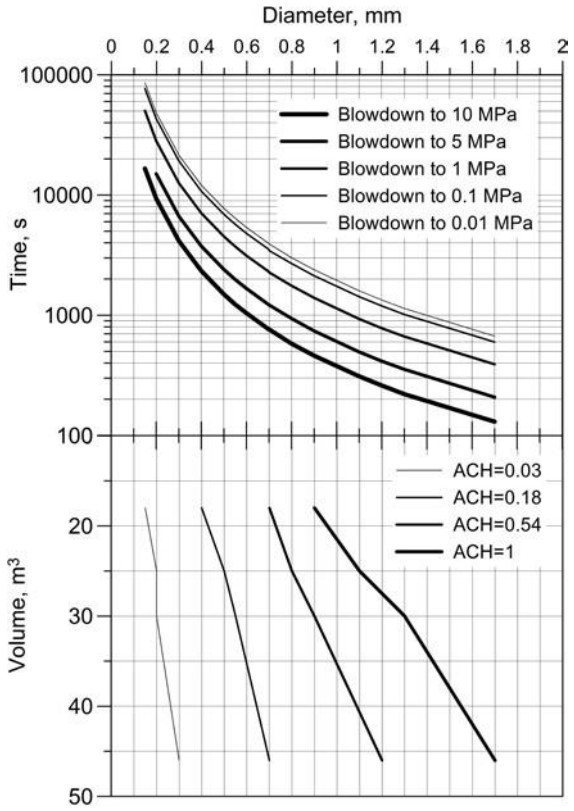


Figure 6–10. Nomogram for blow-down time of unignited release of 5 kg hydrogen in enclosures of different volume and ACH from initial pressure 35 MPa down to different residual overpressures through "safe" diameter PRD that mitigates the pressure peaking phenomenon to 15–20 kPa.

Figure 6–10 clearly demonstrates that "safe" diameter is essentially smaller than "typical" PRD diameters currently used. For lower ACH values the blow-down time through a "safe" diameter is increasing to several hours. This is an unrealistic currently requirement for fire resistance rating of type 3 and 4 tanks. More research is needed to generate innovative approaches for design of PRD and onboard storage.

Figure 6–11 represents a nomogram for calculating the "safe" diameter for 1 kg of hydrogen released at initial pressure 35 MPa or 70 MPa. The upper graph of the nomogram allows the blow-down time to an overpressure of 0.1 MPa within the tank to be calculated for each of two initial storage pressure. It is clear from comparison of Figs. 6–10 and 6–11 that storage tanks with inventories of 1kg does not present the same hazards as larger inventory of 5 kg. Thus smaller vehicles, with 1 kg tanks using "typical" PRD diameters should not cause significant problems in larger garages. As expected the "safe" diameter decreases and hence blow-down time increases with increasing hydrogen inventories and increasing storage pressure.

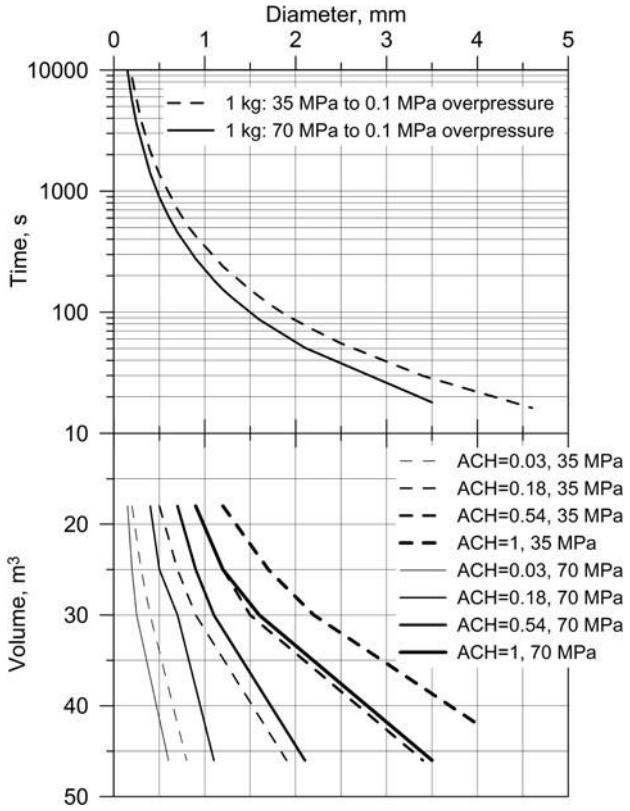


Figure 6–11. Nomogram for blow-down time of unignited release of 1 kg hydrogen in enclosures of different volume and ACH from initial pressures 35 MPa and 70 MPa down to overpressure of 0.1 MPa through

"safe" diameter PRD that mitigates the pressure peaking phenomenon to 15–20 kPa.

As described previously, the relationship between vent area and ACH is dependent on the value taken for the pressure difference between the interior and exterior of the enclosure, ΔP. Figure 6–12 takes the example of 5 kg of hydrogen at 35 MPa, "safe" diameters and corresponding blow-down time to an overpressure of 0.1 MPa in the tank are compared for the cases of vent area calculated based on ΔP = 50 Pa and ΔP = 5 Pa. It can be seen that how ACH is defined has a significant impact on calculation of "safe" diameter. This would indicate that a clear consensus should be reached for similar applications and validation experiments performed. It is unclear yet which value of ΔP should be taken to calculate ACH for hydrogen applications.

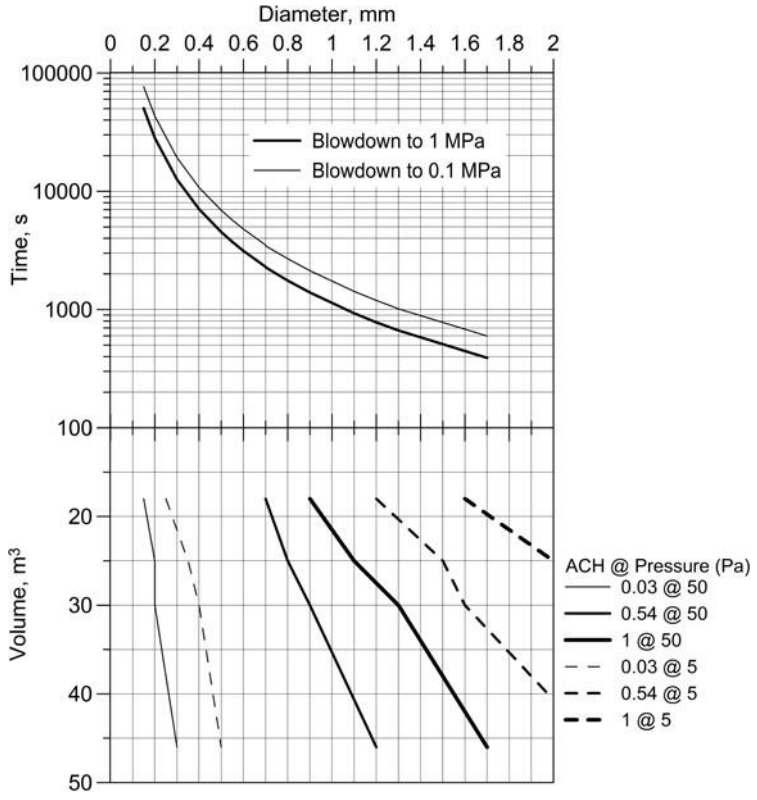


Figure 6–12. Nomogram for blow-down time of unignited release of 5 kg hydrogen in enclosures of different volume and three different ACH from initial 35 MPa down to overpressure 0.1 MPa and 1 MPa that mitigates the pressure peaking phenomenon to 15–20 kPa for ΔP = 50 Pa and ΔP = 5 Pa.

6.2.4.3. Concluding remarks

The pressure peaking is a unique phenomenon characteristic only for gases lighter than air when they are released into a ventilated enclosure. The phenomenon is the most pronounced for hydrogen which has the lightest molecule on the Earth. In practical situations it can be observed for helium and to very small extent for methane. It must be accounted for when performing hydrogen safety engineering for indoor use of hydrogen and fuel cell systems and has to be reflected in RCS.

Current approaches to fire resistance of onboard storage and parameters of PRD have a number of deficiencies. On the one hand, it is clear that existing arrangements are lacking sufficient fire resistance rating of onboard storage, and generate unacceptable safety performance of systems in enclosures if "typical" PRD of a few millimetres is activated even without combustion of release. On the other hand, simplified "redesign" of the onboard tank-PRD system to protect the garage structure from collapse puts extremely difficult to realise requirements to fire resistance of high pressure storage. Further research is needed to develop innovative safety strategies and engineering solutions to tackle the problem of fire resistance of onboard storage tanks and requirements to PRD performance, e.g. reduced flame length. Fire resistance rating of onboard storage equipment has to be provided by car manufacturers and/or other representatives of hydrogen industry as a part of permitting and certification procedures.

5. Methodology

7 Ignition of hydrogen mixtures

7.1. Overview of hydrogen ignition mechanisms

Astbury and Hawksworth (2007) have performed an analysis of hydrogen ignition mechanisms, and stated that over the last century, there have been reports of high pressure hydrogen leaks igniting for no apparent reason, and several ignition mechanisms have been proposed. They underlined that although many leaks have ignited, there are also reported leaks where no ignition has occurred. Investigations of ignitions where no apparent ignition source was present have often been superficial, with a mechanism postulated which, whilst appearing to satisfy the conditions prevailing at the time of the release, simply does not stand up to rigorous scientific analysis. Clearly there are gaps in the knowledge of the exact ignition mechanism for releases of hydrogen. Mechanisms which have been considered by Astbury and Hawksworth (2007) are: the reverse Joule–Thomson effect, electrostatic charge generation, diffusion ignition, sudden adiabatic compression, and hot surface ignition.

The search using the Major Hazard Incident Database Service of the Health and Safety Executive (UK) Astbury and Hawksworth (2007) revealed 81 incidents involving releases of hydrogen. Of those, a delay between release and ignition was reported for only 4 releases. Authors assumed that the others ignited immediately. In 11 cases, the source of ignition was identified, but in the remainder, i.e. 86.3% of incidents, the source was not identified. This contrasts with data on the non-hydrogen releases, where 1.5% did not ignite, and only 65.5% of ignition sources were not identified. This does prove the suggestion that there is a difference in propensity for ignition between hydrogen and non-hydrogen gases when released. It is worth noting that since this is a Major Hazard Incident Database, releases of hydrogen which simply dispersed and did not involve fire, explosion, or other major hazard are not recorded, so the non-ignition being reported as zero is not necessarily an indication that all hydrogen releases ignited.

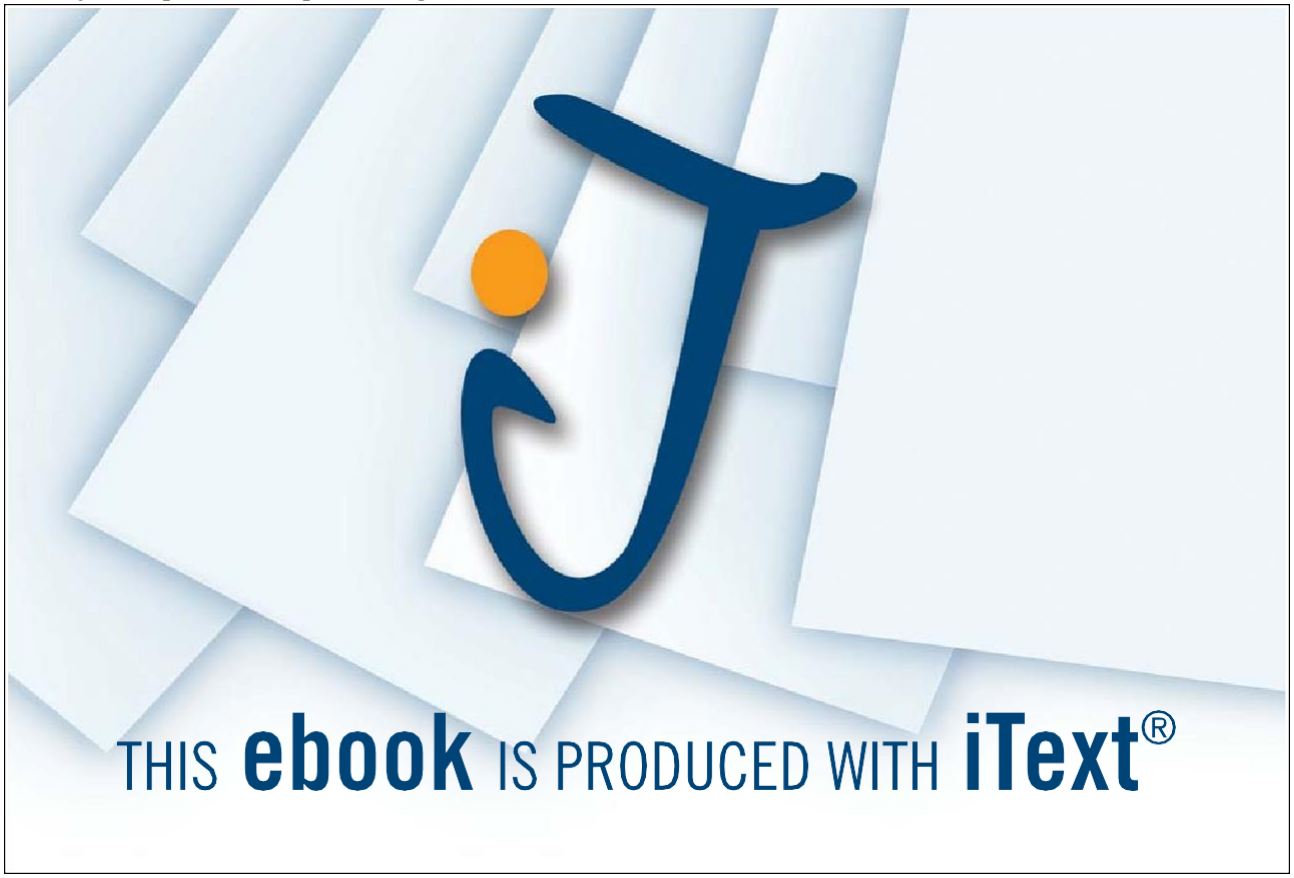
The following accidents have been described by Astbury and Hawksworth (2007) among others. From work undertaken by Nusselt in Germany several spontaneous ignitions of of hydrogen at 2.1MPa being discharged to atmosphere had been reported. Cylinders had been noted for having quantities of iron oxide (rust) in them even though they were apparently dry, and it was thought first that there was potential for electrostatic charging to occur. However, experiments on discharging hydrogen into an open funnel fitted with a long pipe showed no ignitions, except when the funnel was obstructed by an iron cap. The mechanism was not understood, so further trials were undertaken. Only when the trials were undertaken in the dark was a corona discharge observed. When the hydrogen leaked out of a flange – the corona discharge was visible, which increased when the pipe was tapped to stir up dust. An ignition followed after the tapping. Further work showed that when sharpened copper wires were used to promote corona

discharges, ignition occurred when the point was bent away from the gas direction, whereas no ignition occurred when the wire was pointing in the direction of flow.

Another incident reported by Astbury and Hawksworth (2007) refers to a cylinder of hydrogen being connected to a piece of laboratory apparatus. The laboratory technician cracked the valve open to clear any dirt out of the connection, and when he did so, the escaping gas ignited immediately. Bond (1991) attributes this ignition to the phenomenon of diffusion ignition. Whilst no pressure of gas is quoted in this second incident, it can be assumed that the pressure would have been the typical full cylinder pressure of 23 MPa.

Reider et al. (1965), released a large quantity of hydrogen to determine the sound pressure levels. The hydrogen was released at an initial pressure of 23.6 MPa and an initial rate of 54.4 kg/s, for a period of 10 s. The gas was transferred through a 200 mm nominal bore pipe and a 150 mm bore ball valve to a cylindrical vessel fitted with a convergent–divergent nozzle venting to atmosphere. In the run where the gas was not deliberately ignited, after 10 s, the 150 mm diameter valve was being closed, and 3 s after starting to close the valve, ignition occurred. The three potential ignition mechanisms examined were: electrification of the gas, electrification of particles in the gas, and metal particles abrading a metal bar welded across the mouth of the nozzle. Of these, the first was discounted as pure gases are known to have negligible electrostatic charging. The second mechanism was considered, but as the system had been thoroughly cleaned out and blown down prior to the test. Yet, the velocity of the gas being discharged, at 1216 m/s, was far higher during the run than had been used before, so this potential mechanism could not be discounted. The third mechanism was considered as a possibility as the discharge velocity was high thus possibly dislodging particles and impacting them on the bar. This mechanism too could not be discounted. However, after the ignition it was found that the bar had been torn loose at one end, and this may have presented a possible ignition source which had not been foreseen.

Please click the advert



"Unexpected" spontaneous ignition of hydrogen release in large-scale experiments was reported as well by Chaineaux et al. (1991), Groethe et al. (2005).

7.1.1. Ignition and reverse Joule–Thomson effect

Astbury and Hawksworth (2007) have disregarded the Joule-Thomson effect as potential mechanism of ignition in considered experiments. They made this conclusion using data by Michels et al. (1963) that the Joule–Thomson coefficient for hydrogen, estimated at pressures up to 250 MPa and 150°C, does not exceed 0.53K MPa at 100 MPa and temperatures up to 150°C. So, ignition by this mechanism is unlikely at the pressures in most of the incidents quoted above.

7.1.2. Electrostatic ignition

7.1.2.1. Sparks from isolated conductors

It has been mentioned that a stoichiometric mixture of hydrogen with air has a very low minimum ignition energy of 0.017 mJ (Baratov et al., 1990). There are three main types of electrostatic discharge: spark, brush, and corona discharges (Astbury and Hawksworth, 2007). The energy of a spark discharge (single plasma channel between the high potential conductor and an earthed conductor) from an isolated conductor is calculated as $E=CV^2/2$, where C is the capacitance of the item, and V is the potential (voltage).

For example, a person has a capacitance of about 100 pF, depending on body size, the area of their feet, and the construction and thickness of the soles of their footwear (Astbury and Hawksworth, 2007). Taking a typical MIE of 0.29 mJ for a hydrocarbon-air mixtures, say propane, then the voltage required to produce a spark of sufficient energy to ignite the atmosphere is given as $V=(2E/C)^{1/2}$. Substituting gives 2408 V. For air, the dielectric strength is about 30 kV/cm. So, the gap required between the charged conductor and the earthed point for breakdown to occur would be about 2400/30=0.08 cm or 800 micrometers.

People typically cannot feel an electrostatic shock of less than about 1 mJ, so would be unaware of the potential to ignite a hydrocarbon-air mixture (Astbury and Hawksworth, 2007). The gap over which the spark passes from a person to earth is rarely of a form which has pointed electrodes. Typically a finger has a tip radius of about 6 mm. So, a finger-tip approaching a flat earthed metal surface, though having a gap of 800 micrometers, would actually present a large almost flat area around the point at which the spark passes. This would tend to quench any ignition. This phenomenon of a spark not igniting a flammable mixture between two parallel plates is discussed by Metzler (1952) with relation to the prediction of MIE. The quenching of flames by parallel surfaces in close proximity has also been investigated by Potter (1960), who found that hydrocarbons have quenching distances of 2–3 mm.

Thus, theoretically, any ignition would not propagate from the plasma channel of the spark at such a "low" voltage of 2400 V. With a breakdown strength of 30 kV/cm, and a gap of 2 mm which would just allow the flame to propagate in hydrocarbon-air mixture, a potential of 6 kV would be required for a spark to occur (Astbury and Hawksworth, 2007).

If hydrogen is now considered, the corresponding voltages and gaps are much reduced (Astbury and Hawksworth, 2007). The dielectric strength of hydrogen atmospheres is only 17.5 kV/cm (Cassutt et al., 1962). Its quenching gap is only 0.64 mm (ISO/TR 15916:2004). The variation of dielectric strength with concentration of hydrogen in air mixtures is unknown, but as a simple case, it could be assumed to be linear within a specified narrow concentration range, so the theoretical dielectric strength of an about stoichiometric mixture of 30% of hydrogen in air would be (0.3x17.5 + 0.7x30) = 26.25 kV. With a quenching distance of 0.64 mm and a dielectric strength of 26.25 kV/cm the breakdown potential would correspond to a voltage of 26.25x0.064=1.68 kV, which corresponds to a stored energy of $0.5x[100x10^{-12}]x[1.68x10^{3}]^{2} = 1.41x10^{-4}$ J, i.e. 0.141 mJ. This is more than sufficient to ignite the stoichiometric hydrogen–air mixture that requires only 0.017 mJ.

Thus, whilst electrostatic charging of people refuelling vehicles with petrol rarely gives rise to ignitions, it is significant that the voltage required for hydrogen to be ignited is below 2 kV. This voltage can be generated easily, without their being aware of it, on people standing on an insulating surface so there is a potential for personnel to ignite hydrogen leaks very easily, without any apparent ignition source being present (Astbury and Hawksworth, 2007).

7.1.2.2. Brush discharges

These are typified by a discharge between a charged insulator and a conducting earthed point (Astbury and Hawksworth, 2007). They are characterised by many separate plasma channels, combining at the conductor. As the charged surface is a non-conductor, a capacitance and hence energy cannot be determined. Work by Gibson and Harper (1988) introduced the term of incendivity or equivalent energy which is where the brush discharge has the ability to ignite an atmosphere, with the same minimum ignition energy as a spark which will just ignite the flammable atmosphere. Typical equivalent energies were found to be about 4mJ for brush discharges from flat polyethylene sheets. However, Ackroyd and Newton (2003) found that certain more modern plastics, and thin plastic coatings on earthed metal, had higher equivalent energies.

7.1.2.3. Corona discharges

Corona discharges are silent, usually continuous discharges which are characterised by a current but no plasma channel. A corona discharge is able to ignite a hydrogen-air mixture without there being a discrete spark or single discharge event (Astbury and Hawksworth, 2007). Cross and Jean (1987) give an equation to determine the voltage required for a corona to start from a point given its tip-radius. The prevention of ignition of hydrogen deliberately vented to atmosphere has been applied before by using a polished toroidal ring at the end of the vent to ensure that the effective tip radius is large. In practice, corrosion and dirt deposits are effectively small radius protrusions, so anything which affects the polished finish could create small radius protrusions which would still have an effect (Astbury and Hawksworth, 2007). Studies undertaken many years ago on hydrogen vents showed that ignition was rare during fine weather, but was more frequent during thunderstorms, sleet, falling snow, and on cold frosty nights (Astbury and Hawksworth, 2007).

7.1.3. Diffusion ignition

This mechanism will be discussed in more detail further in this chapter. This section is based on the mechanism analysis presented by Astbury and Hawksworth (2007). The phenomenonof diffusion ignition has been postulated by Wolanski and Wojcicki (1972), who demonstrated that ignition occurred when high pressure hydrogen was admitted to a shock tube filled with air or oxygen. They found that ignition could be achieved even if the temperature was below the autoignition temperature of the hydrogen.

Wolanski and Wojcicki calculated that gas, composed of a 3:1 mixture of hydrogen and nitrogen, would ignite in air if the shock wave exceeded a Mach number of 2.8 at a temperature of 575 K. A shock wave of this Mach number would be produced by an upstream pressure of 3.9 MPa. They also calculated that ignition would occur at a lower Mach number of only 1.7, corresponding to an upstream pressure of 1.3 MPa, when the shock wave was reflected by an obstacle.

There is no indication whether the autoignition temperature was measured in (Wolanski and Wojcicki, 1972) at the expected final pressure in the shock tube, or at atmospheric pressure. Although their shock tube experiments produced ignition, their initial temperature was rather high at 575 K (302°C), requiring an increase of only 110 K to reach their autoignition temperature of hydrogen. This clearly implies more research on this mechanism. In t addition, it worthy to note that there is no experimental work undertaken with releases to an unconfined atmosphere, such as would be the case for a leak from high pressure hydrogen storage direct to atmosphere.

Please click the advert

FOSS

Sharp Minds - Bright Ideas!

Employees at FOSS Analytical A/S are living proof of the company value - First - using new inventions to make dedicated solutions for our customers. With sharp minds and cross functional teamwork, we constantly strive to develop new unique products - Would you like to join our team?

FOSS works diligently with innovation and development as basis for its growth. It is reflected in the fact that more than 200 of the 1200 employees in FOSS work with Research & Development in Scandinavia and USA. Engineers at FOSS work in production, development and marketing, within a wide range of different fields, i.e. Chemistry, Electronics, Mechanics, Software, Optics, Microbiology, Chemometrics.

We offer

A challenging job in an international and innovative company that is leading in its field. You will get the opportunity to work with the most advanced technology together with highly skilled colleagues.



Dedicated Analytical Solutions

FOSS

The Family owned FOSS group is the world leader as supplier of dedicated, high-tech analytical solutions which measure and control the quality and produc- tion of agricultural, food, phar- maceutical and chemical produ- cts. Main activities are initiated from Denmark, Sweden and USA with headquarters domiciled in Hillerød, DK. The products are marketed globally by 23 sales companies and an extensive net of distributors. In line with the corevalue to be 'First', the company intends to expand

its market position.

7.1.4. Adiabatic compression ignition

The ideal gas laws, then compressing it at constant entropy, would increase the pressure due to the compression in accordance with the relationship $PV^{\gamma}=const$. It can be shown with use of the equation of state for the ideal gas that as well $TV^{\gamma-1}=const$. For example, for compression ratio $V_1/V_2=28$ at initial NTP ($\gamma=1.39$) the initial temperature of 293.15 K would increase to $T_2=T_1(V_1/V_2)^{\gamma-1}=1075.2$ K, i.e. the temperature rise is 782 K. In experiments conducted by Pan et al. (1995), the actual measured temperature realised by a compression ratio of 28 times was only 149 K. Based on this, Astbury and Hawksworth (2007) concluded that isentropic compression is unlikely to occur in practice.

However, work by Cain (1997) indicates that compression ignition of hydrogen–oxygen–helium mixtures occurs at a relatively constant temperature of 1050 K, at pressure rise ratios of 35–70 starting at 300K at atmospheric pressure. Reverse calculation indicates that a temperature rise from 300 to 1050K would require a pressure rise ratio of $P_2/P_1=(T_1/T_2)^{\gamma/(\gamma-1)}$ = $(1050/300)^{1.39/0.39}=86.9$. Thus, adiabatic compression mechanism requires pressure rise ratio greater than that measured by Cain (1997), suggesting that there is another ignition mechanism present (Astbury and Hawksworth, 2007).

7.1.5. Ignition by hot surface

This is a phenomenon shared by most flammable gas or vapour air mixtures, in that providing the surroundings are at a high enough temperature, the rate of oxidation generates more heat than is being lost to the surroundings, so allowing the oxidation chain-reaction to progress (Astbury and Hawksworth, 2007). This is the usual method of determining autoignition temperatures, and the value obtained is very dependent on the apparatus used. It is known that the higher the temperature the shorter is ignition delay time. The lowest temperatures for ignition being associated with large volumes and surface areas (Snee and Griffiths, 1989).

Bulewicz et al. (1977) showed that the position and mode of heating a hot plate had an effect. They used a slow-heating method where free-convection was important, and a time delay between exposure and ignition was apparent, depending on the rate of temperature rise. The orientation of the heating surface also affected the delay, with a longer delay with the heated surface pointing down than when the heated surface was pointing up. Ungut and James (2001) reported as well that surfaces at the top of the enclosure having longer induction times.

7.1.6. Concluding remarks

From their analysis Astbury and Hawksworth (2007) concluded that no one considered mechanism is able to explain all of the recorded incidents. There is the potential for two or more potential mechanisms to work together. It is known that the minimum ignition energy of gases and vapours decreases with increases in temperature (Moorehouse et al., 1974), so expanding hydrogen would increase in temperature due to the reverse Joule–Thomson effect, and hence its ignition energy would reduce. Similarly, if particles were to be abraded from the walls of any flow path, the required energy for ignition from a corona discharge would be lower, so it is likely that less corona charging current would be required to ignite the hydrogen.

In several incidents, there is a suggestion in the reports that electrostatic effects may have been responsible. In particular, one of incidents involved only a fine stream of mercury, with no other potential ignition sources inside the closed system. The potential for drops and bursting bubbles to generate electrostatic charges has been proposed by Blanchard (1963), and the ability of such charges to ignite sensitive atmospheres has been illustrated by Pratt (1993).

It is generally recognised that pure gases do not become electrostatically charged under normal conditions (IEC, 2002), but this refers generally to low velocities and pressures. Where gases are released at very high pressures, the flow becomes sonic and the propensity of electrostatic charging occurring is not known. It is known that pure gases tend not to charge, but particles within the gas stream are known to become electrostatically charged.

The discharge path in many practical cases would probably be convoluted and not in a straight line. This would require the hydrogen to discharge through bends, which would potentially allow materials on the surface of the discharge path, e.g. piping, to be eroded and form particles which could become electrostatically charged.

In 2007 Astbury and Hawksworth suggested that the diffusion ignition mechanism to be likely only when the initial temperature is high. However, they continued that where valves on cylinders are briefly opened direct to atmosphere, presumably to clear any debris from the cylinder, ignition has occurred. The diffusion ignition effect appears to be reproducible in a shock tubes or similar closed equipment. Wolanski and Wojcicki (1972) appear to have only carried out work using a hydrogen-nitrogen mixture (Astbury and Hawksworth, 2007). Since 2007 more work both experimental and numerical has been performed on the diffusion mechanism. This is reported partially in the next section.

7.2. Spontaneous ignition of sudden releases

Many attempts have been made to explain this phenomenon over the last decades starting from pioneering study of Wolanski and Wojcicki (1972) of the so-called “diffusion ignition mechanism”. Experimental data give critical conditions of the phenomenon. Unfortunately, they cannot provide a detailed insight into the dynamics of the process. For example, exact location of initial ignition spots and progression of chemical reaction within tubing downstream the rupture disk or valve can hardly be identified by experimental means at high pressures.

It is an agreed opinion that the probability of hydrogen spontaneous ignition at a sudden release from high-pressure equipment is high if mitigation measures are not undertaken. However, no references to spontaneous ignition problem or engineering design to avoid or promote it can be found in codes and standards for piping, storage and use of high-pressure systems handling compressed hydrogen.

Control of spontaneous ignition of high-pressure hydrogen release is one of the challenging problems of hydrogen safety, for which a little fundamental explanation exists.

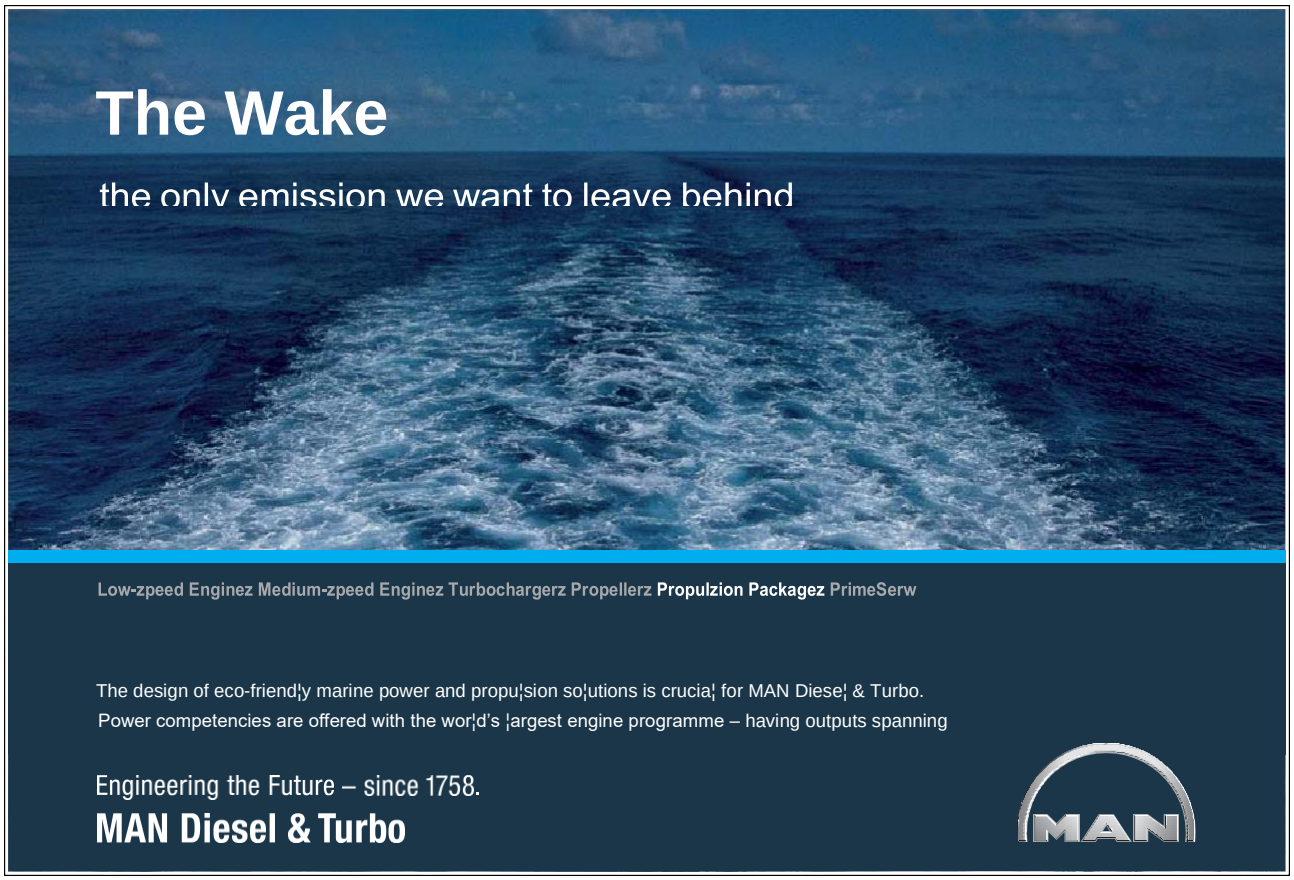
Earlier numerical studies by Liu et al. (2005), Bazhenova et al. (2006), and Xu et al. (2008, 2009) were focused on unconfined release from high-pressure storage directly into the atmosphere. While spontaneous ignition was demonstrated by numerical simulations (Liu et al., 2005; Bazhenova et al., 2006), no experimental proof exists up to date.

7.2.1. Overview of experimental and numerical studies

7.2.1.1. Experimental observations

Experimental confirmation of spontaneous ignition by diffusion mechanism for releases from high pressureequipmenttotheatmospherethroughatubewasobtainedin“controlledlaboratoryenvironment” by Dryer et al. (2007), Golub et al. (2007, 2008), Pinto et al. (2007), and Mogi et al. (2008). To facilitate spontaneous ignition various extension tubes and attachments were positioned downstream of a burst disk. Figure 7–1 combines critical conditions for experimentally registered spontaneous ignition obtained by different research groups.

Please click the advert



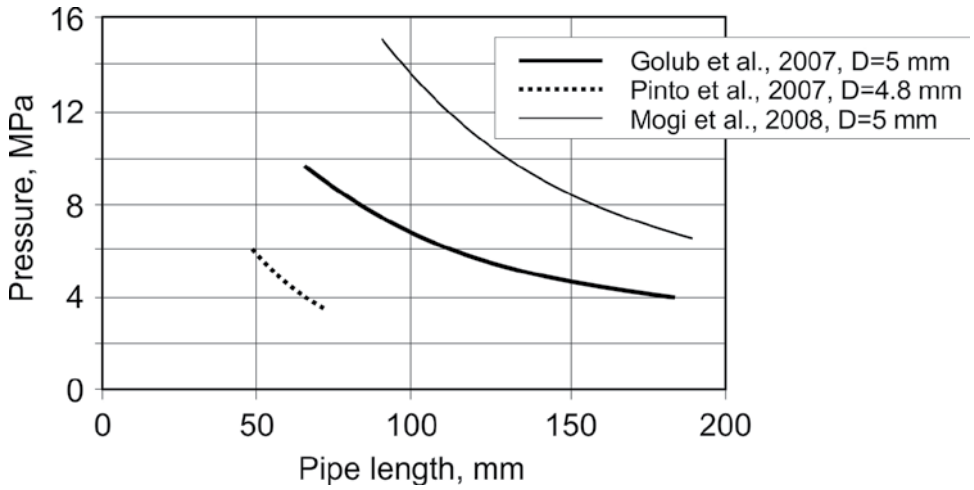


Figure 7–1. Experimental data on pressure limit of spontaneous ignition of hydrogen release into air in pipes of different length.

The data by Dryer et al. (2007) are not shown in Fig. 7–1, because of complicated internal geometry of fittings and rupture disk used which lowers the minimum pressure sufficient for spontaneous ignition down to 2.04 MPa. Although the data on spontaneous ignition of releases through practical fittings is very useful for hydrogen safety engineering, internal configurations of the fittings leaves a number of uncertainties in formulation of numerical experiments and prevents direct comparison with experimental results of other groups.

Experimental results agree in a general trend of the decrease of the critical (limit) pressure with the increase of a pipe length. However, the critical conditions of spontaneous ignition vary substantially due to difference in test arrangements. Sensitivity of spontaneous ignition to different not yet fully understood factors poses a number of issues to be studied.

Figure 7–1 shows an essential difference in critical conditions for spontaneous ignition obtained in different studies. It can be seen, for example, that for hydrogen storage pressure of 6 MPa in experiments by Pinto et al. (2007) the 50 mm pipe length is sufficient to provide spontaneous ignition. However, at the same storage pressure and practically the same internal diameter the channel length sufficient to provide spontaneous ignition in Golub et al. experiments (2007, 2008) is 110 mm, and in Mogi et al. (2008) tests the minimum length increases by four times to 200 mm. How these differences can be explained?

First of all, Golub et al. (2007, 2008) registered the onset of spontaneous ignition by monitoring the shock propagation and location of radiation from chemical reaction inside the pipe. Hence, critical conditions for spontaneous ignition in their experiments (see Fig. 7–1) represent the distance from the rupture disk to the location where ignition was captured by a radiation gauge.

Mogi et al. (2008) judged the occurrence of spontaneous ignition by optical observation of the area near the pipe exit to atmosphere. They showed that in some experiments spontaneous ignition did occur, but combustion was blown out by the flow. Unfortunately, no critical conditions for such releases were reported. Nevertheless, this fact confirms that not all spontaneously ignited releases transit into sustained jet fires. This is one likely reason for the shift of the critical curve in Mogi et al. (2008) experiments compared to Golub et al. (2007, 2008). However, the most probable reason explaining the shift of Mogi et al. (2008) data to higher pressures for the same pipe length was suggested in (Molkov, 2008). Indeed, in experiments by Mogi et al. (2008) the internal surface of the pipe between the diaphragm (rupture disk) and the exit to atmosphere was washed away by the aqueous Na_2CO_3 solution (1%) in order to allow visualization of the flame via the flame reaction of sodium. This solution could have interfered with boundary layer flow and chemistry of hydrogen combustion and draw away some heat from the process. Thus, the process happened later along the tube for the same initial pressure.

The experimental procedure applied by Pinto et al. (2007) was different as hydrogen was compressed just before the burst disk rupture using a piston combined with the shock tube. Nitrogen gas was injected into the high pressure section of the shock tube upstream of the piston to push it towards hydrogen gas in order to generate high pressure of hydrogen to burst the disk. This compression obviously caused heating of hydrogen in high-pressure chamber and the release was not at the ambient temperature, but somewhat higher. But since, neither the temperature measurements in high-pressure chamber, nor information of the time during which hydrogen was compressed are available, it is difficult to estimate accurately the initial hydrogen temperature.

The results of the Pinto et al. (2007) experiments are in full compliance with Bazhenova et al. (2006) who stated that the increase of initial hydrogen temperature stimulates spontaneous ignition to occur earlier and under lower initial pressures. Higher initial temperature of hydrogen is the most likely reason for shorter tube required for spontaneous ignition in experiments by Pinto et al. (2007) for the chosen pressure compared to experiments by Golub et al. (2007, 2008) and Mogi et al. (2008).

The way how the burst disk ruptures is probably the most important factor for spontaneous ignition as it affects the hydrogen-air mixing (Dryer et al., 2007). In experiments by Golub et al. (2007, 2008) burst disks were incised in the form of the cross to facilitate sharp “petal” opening at predetermined pressure, whereas in experiments by others a wider stochastic burst disk rupture pressure distribution was observed. Stochastic nature of an in-house made burst disk rupture produces variations in a structure and strength of the shock wave generated, even at constant burst pressure, and obviously can affect the repeatability of experimental data. Very good repeatability of experiments is stated by Golub et al. (2007, 2008) both in the measured pressure behind the generated shock wave, and the minimum initial pressure, which would provide spontaneous ignition at fixed tube length.

Pinto et al. (2007) compared results for smooth and screwed tubes. They found that the same initial pressure causing spontaneous ignition in smooth tube fails to cause ignition in case of screwed tube.

This observation, however, conflicts with the point of view of Dryer et al. (2007), who found that experiments with several tubes mated together produced ignition, where single tube (no mating unions) did not for the same initial pressure, the internal diameter and the overall tube length. These observations underline that the interaction of developing boundary layer with roughness of walls in the tube section downstream of the burst disk can promote as well as delay spontaneous ignition.

Dryer et al. (2007) reported that spontaneous ignition events are statistically distributed in a narrow pressure range of 2.04–2.21 MPa, with zero probability for membrane failure pressures less than 2.04 MPa and certain inflammation for failure pressures above 2.21 MPa, at their experimental set up. In addition to identifying a minimum pressure below which no spontaneous ignition can be observed, it is found that reducing the length of the 1.27 cm (½″) NPT pipe nipple to 3.81 cm (1.5″) led to no spontaneous ignition at all failure pressures even up to 5.66 MPa.

Experimental study by Golub et al. (2010a, 2010b) argues on a potential of spontaneous ignition in a T-shaped channel for initial hydrogen pressure in the range of pressure 1.2–2.9 MPa. However, there is some ambiguity in the interpretation of results of this study with statements of spontaneous ignition at 2.9 MPa in one communication and 2.43 MPa in another.

Please click the advert



ELECTRONICS
AUTOMATION &
PROCESS CONTROL
MECHANICAL
ENGINEERING
INDUSTRIAL
DATA COMMS
ELECTRICAL
POWER

Dryer et al. (2007) speculate on the importance of the initial stage of a membrane rupture on the mixing and subsequent spontaneous ignition process. They concluded that at low pressures, the chemical ignition time becomes the limiting factor, while at high pressures the mixing time to achieve significant flammable mixture volume limits the process. There is a need to have a "look inside" of the pipes to clarify physics of the spontaneous ignition in order to control it.

7.2.1.2. Numerical studies

The 2Danalysisofpressure-boundaryrupturerateonhydrogenspontaneousignitionduringreleasethrough a 3 mm hole in a wall of 0.1 mm thickness directly to atmosphere was carried out by Xu et al. (2009). Characteristic cell sizes used were 15–30 μm across the contact surface. Xu et al. (2009) found that if the rupture rate is below a certain threshold value, there would be no spontaneous ignition in the atmosphere. As the rupture rate increases, the temperature of the shock heated region grows more quickly owing to earlier flow expansion and once the rupture rate is sufficiently high, spontaneous ignition can occur. This simulation corresponds to a scenario of unconfined release for which no experimental evidence exists.

Hydrogen releases through a length of a tube 30–60 mm long and 3–6 mm internal diameter for storage pressures in a range 5–15 MPa were simulated by Wen et al. (2009). It was demonstrated that spontaneous ignition is governed by focusing of reflected from the tube wall shocks. Numerical studies by Xu et al. (2009) and Wen et al. (2009) confirmed the significance of a membrane opening time on the spontaneous ignition process.

Lee and Jeung (2009) investigated the effect of a burst disk shape on the ignition process at pressure of a burst disk rupture of 8.6 MPa and release into a pipe. Cartesian grid with a cell size of 19 μm was applied. The burst disk had a semi-spherical shape. However, an instant opening of the disk was applied in simulations. The spontaneous ignition first occurred in a boundary layer and consequently spread throughout a cross-section of the tube, i.e. through the contact surface between air and hydrogen where mixing takes place, similar to our previous 3D study with an instant opening of a flat membrane (Bragin and Molkov, 2009).

Simulations of hydrogen spontaneous ignition in air using the model accounting for viscous gas transport, multi-component diffusion, heat transfer, and incorporating a kinetic scheme of hydrogen oxidation with 9 equations were performed by Golub et al. (2008). The authors studied experimentally and numerically in 2D axisymmetric formulation the self-ignition in cylindrical and rectangular ducts and concluded that the governing mechanism for hydrogen spontaneous ignition is diffusion ignition on the contact surface assisted by the boundary layer effects. Combustion starts as kinetic one and then acquires diffusion character. Heat release and flame turbulence intensify mixing of reagents and such burning cloud may propagate along the tube far enough. Simulation with and without the boundary layer were also carried out and a conclusion is drawn that when boundary layer is not taken into account, ignition occurs at the duct axis, whereas it occurs near the wall if boundary layer is taken into account.

2D numerical simulations of the phenomenon were carried out by Pinto et al. (2007). Axisymmetric Euler equations and detailed chemical reactions mechanism were employed to simulate the behaviour of the hydrogen jet discharged from a storage vessel at pressures 10-70 MPa and temperature 300 K at an early stage of the leakage. The reduced kinetic mechanism by Petersen et al. (1999) with 9 species (H2, O2, O, H, OH, HO2, H2O2, H2O, and N2) and 18 elementary reactions was applied. Chemical reactions were treated by a point implicit way to avoid stiffness. Uniform grid with a cell size of 20x20 μm was used to carry out simulations. Dependencies of the length, where the spontaneous ignition occurs on the pressure in high-pressure chamber were obtained experimentally not only for smooth, but also for screwed tubes. It was found that screwed tubes produce some difficulty for spontaneous ignition affecting the boundary layer. Numerical simulations were reported only for one case of 10 mm diameter tube with 50 mm length and 3.8 MPa initial hydrogen pressure, but no comparison to experimental data has been presented.

In the study by Yamada et al. (2009) the model by Pinto et al. (2007) had been improved by adding viscosity effects. The governing equations used were the compressible 2D axisymmetric Navier-Stokes equations, the conservation of mass, total energy, chemical species, and the equation of state. The same reduced kinetic mechanism by Petersen et al. (1999) was applied. The governing equations were discretized in a finite difference formulation. The convective terms are evaluated using the second-order explicit Harten-Yee non-MUSCL modified-flux type TVD scheme, considering the properties of the hyperbolic equations. The viscous terms are evaluatedwiththe standardsecond-ordercentral difference formulae. The time integration method is the second-order Strang-type fractional step method. A grid with cell sizes of 20–45 μm was used to carry out simulations. Three inlet pressures were studied i.e. 3.6, 5.3 and 21.1 MPa, estimated from choked conditions at the exit resulting from initial pressure in the large hydrogen tank of 6.8, 10 and 40 MPa. The pipe had a 4.8 mm diameter and a length of 71 mm. It was found that a high-temperature area appears near the exit of the pipe. The vortex generated near the edge of the exit was observed similarly to experimental results by Mogi et al. (2008) and our numerical simulations (Bragin and Molkov, 2009). The vortex plays an important role in mixing the hydrogen provided from the pipe with surrounding air. It was shown that for a pressure of 3.6 MPa the spontaneous ignition does not occur in the vortex region; for a pressure of 5.3 MPa the shock wave retains a high temperature for spontaneous ignition, but chemical reactions do not continue long around the exit of the pipe; and only for the pressure of 21.1 MPa combusting area remains. The authors also compared release from the pipe and a hole for the same diameter. It was concluded that in the case of release from the hole, the confinement prevents the development of vortices and mixing of hydrogen with surrounding air in the recirculation zone (Yamada et al., 2009).

All described above simulations of hydrogen spontaneous ignition by the diffusion mechanism were carried out in 2D formulations, including axisymmetric, due to an understandable wish of researchers to have as fine mesh as possible to directly resolve the phenomenon. The large eddy simulation (LES) model developed and described in the next section employs “coarser” 3D grids. This “forced” increase in the mesh size is “compensated” by an advanced sub-grid scale (SGS) modelling of the combustion by the eddy dissipation concept (EDC) with a detailed chemistry and the SGS turbulence modelling by the renormalization group (RNG) theory. The aim of the LES model development at the HySAFER Centre is reproduction of experimental results obtained in complex realistic geometries, where 2D simulations cannot be applied without losing of predictive accuracy.

7.2.2. The large eddy simulation model of spontaneous ignition

The LES technique is recognised as the most promising computational fluid dynamics (CFD) approach to solve scientific and engineering problems. LES models have been successfully applied in the HySAFER Centre to model hydrogen-air deflagrations (Molkov et al., 2006a), detonations (Zbikowski et al., 2008), non-reacting under-expanded jets (Molkov et al., 2009), and jet fires (Brennan et al., 2009). The set of main governing equations can be found elsewhere (Molkov et al., 2006a). The RNG model has been employed for sub-grid scale (SGS) modelling of turbulence (Yakhot and Orszag, 1986). The reaction rate that appears in species transport equation was modelled using the eddy-dissipation-concept (EDC) model of turbulent combustion by Magnussen (1981). It incorporates detailed Arrhenius chemical kinetics. In this model the detailed 21-step chemical reaction mechanism of hydrogen combustion in air employing 37 elementary reactions by Gutheil et al. (1993) is applied. The FLUENT software has been used as the computational engine.

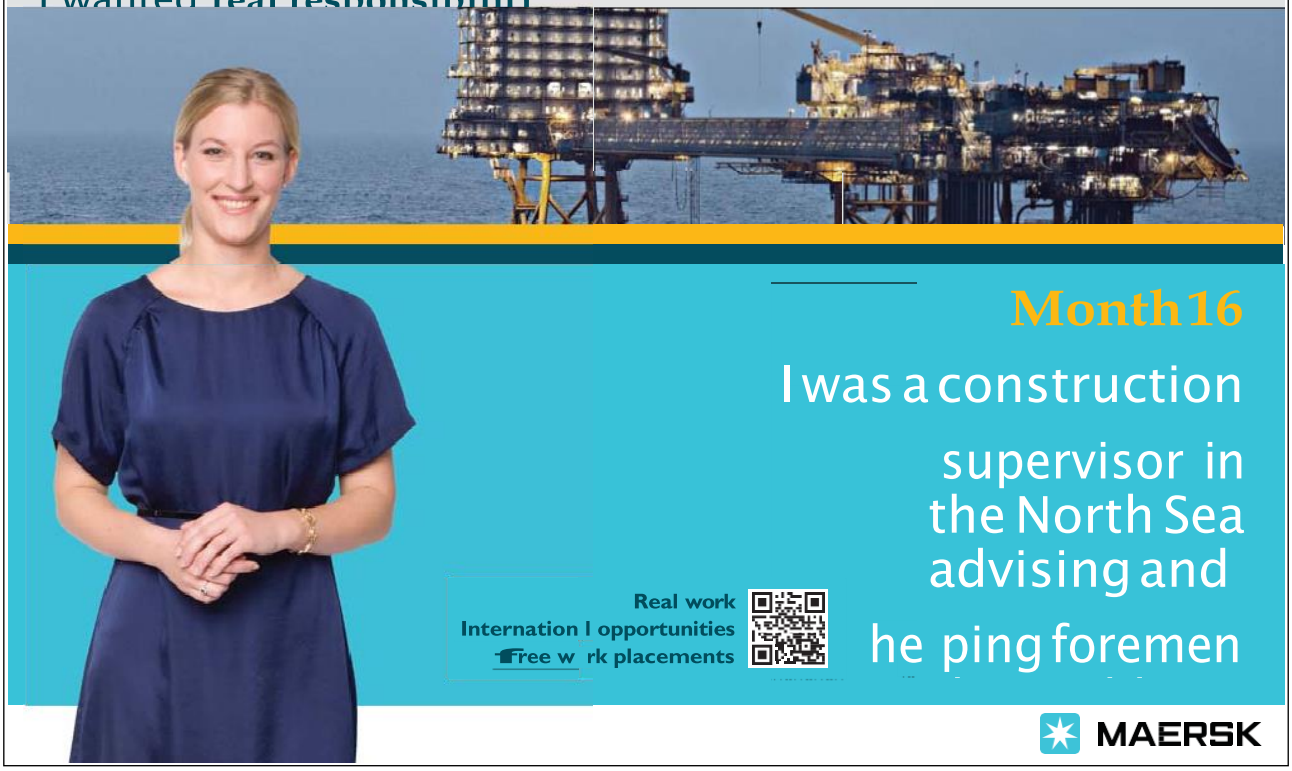
7.2.2.1. The governing equations

Thegoverningequationsarefilteredoverthecontrolvolumethree-dimensionalinstantaneousconservation equations for mass, momentum (Navier-Stokes), energy, and species for compressible Newtonian fluid

$$\frac{\partial \bar{\rho}}{\partial t} + \frac{\partial}{\partial x_j}\left(\rho \tilde{u}_j\right) = 0, \tag{7–1}$$

Please click the advert

International
free wor

I joined MITAS because
I wanted real responsibilifi
fle Graduate Programme
for Engineers and Geoscientists
Maersk.com/Mitas

Month16
I was a construction
supervisor in
the North Sea
advising and
he ping foremen
Real work
Internation I opportunities
free w rk placements
MAERSK

$$\frac{\partial \bar{\rho}\tilde{u}_i}{\partial t} + \frac{\partial}{\partial x_j}\left(\bar{\rho}\tilde{u}_i\tilde{u}_j\right) = -\frac{\partial \bar{p}}{\partial x_i} + \frac{\partial}{\partial x_j}\left[\left(\mu_{eff}\left(\frac{\partial \tilde{u}_i}{\partial x_j} + \frac{\partial \tilde{u}_j}{\partial x_i} - \frac{2}{3}\delta_{ij}\frac{\partial \tilde{u}_k}{\partial x_k}\right)\right)\right] + \bar{\rho}g_i, \quad (7\text{–}2)$$

$$\frac{\partial \bar{E}}{\partial t} + \frac{\partial}{\partial x_j}\left(\tilde{u}_j\left(\bar{\rho}\tilde{E} + \bar{p}\right)\right) = \frac{\partial}{\partial x_j}\left[\left(\frac{\mu_{eff}}{Pr_{eff}}\frac{\partial \tilde{h}}{\partial x_j} + \sum_m \left(\frac{\mu_{eff}}{Sc_{eff}}\frac{\partial \tilde{Y}_m}{\partial x_j}\right)h_{i,eff} + \tilde{u}_i\left(\tau_{ij} - \frac{2}{3}\delta_{ij}\frac{\partial \tilde{u}_k}{\partial x_k}\right)\right)\right] + \sum_m c_{p_m} + R_H, \quad (7\text{–}3)$$

$$\frac{\partial}{\partial t}\left(\bar{\rho}\tilde{Y}_m\right) + \frac{\partial}{\partial x_j}\left(\tilde{u}_j\tilde{Y}_m\right) = \frac{\partial}{\partial x_j}\left[\left(\frac{\mu_{eff}}{Sc_{eff}}\frac{\partial \tilde{Y}_m}{\partial x_j}\right)\right] + R_m. \quad (7\text{–}4)$$

where bars denote: – LES filtered quantity, ~ LES mass-weighted filtered quantity; E is the total energy, J/kg, $E = h - p/\rho + u^2/2$; h is the enthalpy, J/kg, $h = \int_{298.15}^{T} c_p dT$; c_p is the specific heat capacity of mixture at constant pressure, $c_p = \sum_m c_{p_m} Y_m$ (m is the m-th component of gas mixture); Y is the mass fraction; T is the temperature, K; p is the pressure, Pa; ρ is the density, kg/m^3, $\theta = pM/RT$; $u_{i,j,k}$ are velocity components, m/s, ($_{i,j,k}$ are spatial coordinate indexes); $x_{i,j,k}$ are spatial coordinates, m; t is time, s; g is the gravitational acceleration, m/s^2; H_c is the heat of combustion, J/kg.

The effective viscosity μ_{eff} is calculated using the RNG theory by Yakhot and Orszag (1986). The RNG model is capable to reproduce not only turbulent, but also transitional and laminar flows. At low Reynolds numbers the effective viscosity becomes equal to molecular viscosity. This allows the model to perform better in the vicinity of walls (Shah et al., 2001). The effective viscosity is calculated in RNG model as

$$\mu_{eff} = \mu\left[1 + H\left(\mu_s^2/\mu_{eff}/\mu^3 - 100\right)\right]^{1/3}, \quad (7\text{–}5)$$

where $\mu = \theta\left(C_{RNG}\right)_{V_{CV}}^{1/3} \sqrt{2\tilde{S}_{ij}\tilde{S}_{ij}}; \; H(x)$ is Heaviside function; C_{RNG} is the RNG LES constant, $C_{RNG} =$ 0.157 ; V_{CV} is the volume of a control volume, m^3; $\tilde{S}_{ij}$ is the rate of strain tensor, s^{-1}. In highly turbulent regions of the flow $\mu_{eff} \approx \mu_s$ and the RNG model reduces to the Smagorinsky model (1963). In laminar flow regions the argument of Heaviside function becomes negative and the model recovers molecular viscosity, $\mu_{eff} = \mu$. The effective Prandtl and Schmidt numbers are calculated following the RNG theory by entirely theoretical equations (Yakhot and Orszag, 1986)

$$\left|\frac{1.3929 - 1}{N_{eff} - 1}\right|^{0.6321} \left|\frac{2.3929 + 1}{N_{eff} + 1}\right|^{0.3679} = \frac{\mu}{\mu_{eff}}, \qquad (7\text{–}6)$$

where N stands for laminar Prandtl or Schmidt numbers. Laminar Prandtl and Schmidt numbers are calculated according to kinetic theory.

7.2.2.2. The EDC combustion model with full chemistry

The Eddy Dissipation Concept (EDC) model (Magnussen, 1981) with the updates that incorporates detailed Arrhenius chemical kinetics in turbulent flames was applied as the combustion sub-model (Bragin et al., 2011). EDC gives an expression for a combustion rate based on an assumption that chemical reactions occur in so-called fine structures of Kolmogorov's scale where the dissipation of turbulence energy takes place. In a flow of moderate to intense turbulence these fine structures are concentrated in isolated areas occupying only a small fraction of the flow. The characteristic size of the fine structures is much smaller than a LES filter width, i.e. a cell size in our case of "numerical LES" following the terminology by Pope (2004), and it needs to be computed as a function of flow parameters and a cell size. The EDC model adopted in FLUENT models a source term in the species transport equation as

$$R_m = \frac{\rho(\xi^*)^2}{\tau^*\left[1-(\xi^*)^3\right]}\left(Y_m^* - Y_m\right), \tag{7–7}$$

where R_m is the net rate of production of specie m by chemical reactions; ξ^* is the length fraction of the fine scale turbulent structures where the reaction occurs (* denotes fine scale quantities); Y^*_m is a fine scale species mass fraction (specie m) after reacting over the time τ^*, Y_m is a species mass fraction for specie m in the surrounding fine scales state. The multiplier in above equation with a square of the length fraction of fine scales represents the mass exchange between the surrounding and fine structure regions. The length fraction of fine structures is evaluated in this LES model similar to EDC RANS model as

$$\xi^* = C_\xi u_\eta / u_{SGS}, \tag{7–8}$$

where the volume fraction constant is taken as $C\xi = 2.1377$ similar to RANS. The upper limit $\xi^* = 1$ is applied when the fine scales velocity is larger than residual SGS velocity. The scale of a LES residual velocity at the sub-grid scale (SGS) level is

$$u_{SGS} = \mu_t/(\theta \bullet L_{SGS}) \tag{7–9}$$

where μ_t is the turbulent (effective) viscosity, and the SGS length scale is determined as

$$L_{SGS} = C_{RNG} V_{CV}^{1/3}. \tag{7–10}$$

The Kolmogorov's velocity u_η is

$$u_\eta = \left(\mu \cdot u^3_{SGS}\right)^{1/4}$$

$$\cdot L_{SGS}) \overline{\rho}, \tag{7–11}$$

where μ is the laminar viscosity.

Characteristic sub-grid eddy and Kolmogorov's timescales are respectively

$$\tau_{SGS} = L_{SGS} / u_{SGS}, \text{ and} \tag{7–12}$$

$$\tau_{\eta} = \left(\frac{\mu \cdot L}{\rho \cdot u^3} \right)_{SGS}^{1/2}. \tag{7–13}$$

The volume fraction of the fine scales is calculated as ξ^{*3} and species are assumed to react in the fine structures over a time scale

$$\tau^* = C_{\tau} \tau_{\eta}, \tag{7–14}$$

where a time scale constant is taken equal to C_{τ} = 0.4082 similar to applied in the EDC RANS model. Magnussen (1981) assumes that all the fine scales in the cell are perfectly stirred reactors with a residence time τ^*. Combustion at the fine scales is assumed in this model to take place as a constant-pressure reactor. The reactor type is determined by the choice of a mixing rate $1/\tau^*$ and a time-step Δt. In FLUENT initial conditions at the constantpressure reactorare takenas the currentspecies and temperature in the cell. Arrhenius reactions governed by equation (7-15) proceed over the time scale τ^*. The *in situ* adaptive tabulation ISAT algorithm (Pope, 1997), offering substantial reduction in run-time by up to three orders of magnitude, is applied.

Please click the advert


www.job.oticon.dk
oticon
PEOPLE FIRST

All of the reactions considered in the chemical mechanism involved are elementary (reversible). For reversible reaction the molar rate of creation or destruction of species i in reaction r is given by equation

$$\hat{R}_{m,R} = \Gamma \cdot \left(\nu''_{m,r} - \nu'_{m,r}\right) \cdot \left[k_{f,r} \prod_{n=1}^{N} C_{n,r}^{\nu'_{m,r}} - k_{b,r} \prod_{n=1}^{N} C_{n,r}^{\nu''_{m,r}} \right], \quad (7\text{–}15)$$

where N is the number of chemical species in the system; $\nu'_{m,r}$ is the stoichiometric coefficient for reactant m in reaction r; $\nu''_{m,r}$ is the stoichiometric coefficient for product m in reaction r; $k_{f,r}$ is the forward rate constant for reaction r; $k_{b,r}$ is the backward rate constant for reaction r; $C_{n,r}$ is the molar concentration of species n in reaction r. Γ represents the net effect of third bodies on the reaction rate and is given by

$$\Gamma = \sum_{n=1}^{N} \gamma_{n,r} C_n , \quad (7\text{–}16)$$

where $\gamma_{m,r}$ is the third-body efficiency of n-th species in the r-th reaction. The forward rate constant for reaction r without pressure dependency is computed in conventional form of Arrhenius equation

$$k_{f,r} = A_r T^{\beta_r} \exp\left(-E_r / RT\right), \quad (7\text{–}17)$$

where A_r is the pre-exponential factor for r-th reaction; β_r is the temperature exponent; E_r is the activation energy for the reaction, J/kmol; R is the universal gas constant, 8314.4 J/K/kmol. All reactions are reversible, the backward rate constant for reaction r is calculated from the forward rate (7–17) and the equilibrium constant K_r using the equation

$$k_{b,r} = k_{f,r} / K_r . \quad (7\text{–}18)$$

The equilibrium constant K_r computed as

$$K_r = \exp\left(\frac{\Delta S_r^0}{R} - \frac{\Delta H_r^0}{RT}\right) \left(\frac{P_{atm}}{RT}\right)^{\sum_{i=1}^{N} \left(\nu''_{m,r} - \nu'_{m,r}\right)}, \quad (7\text{–}19)$$

where P_{atm} denotes normal atmospheric pressure (101,325 Pa). The term within the exponential function represents the change in Gibbs free energy and its components are computed as

$$\frac{\Delta S^0}{R} = \sum_{i=1}^{N} \left(\nu''_{m,r} - \nu'_{m,r}\right) \frac{S^0_m}{R}, \tag{7–20}$$

$$\frac{OH^0}{RT} = \sum_{i=1}^{N} \left(\varpi''_{m,r} - \varpi'_{m,r}\right) \frac{h^0_m}{RT}, \tag{7–21}$$

where S^0_m and h^0_m are entropy and enthalpy respectively of the m-th species respectively evaluated at temperature T and atmospheric pressure. Specific heats of mixtures were approximated as piecewise-polynomial functions of temperature with polynomial coefficients calculated according to mass-weighted mixing law.

The detailed 21-step chemical reaction mechanism of hydrogen combustion in air by Gutheil et al. (1993) employing 37 elementary reactions is applied. The effect of nitrogen chemistry is taken into account by considering detailed mechanism of NO formation. The specific reaction rate constants are given in Table 7–1. The forward reaction rate constants are presented in the table, and backward rates for reversible reactions are calculated through the equilibrium constants (7-18).

No.	Reactions	*A, KJ/mol*	β_r	E_r, mol/m³
1	H+O2=OH+O	2.00E+14	0.00	70.30
2	H2+O=OH+H	1.80E+10	1.00	36.93
3	H2O+O=OH+OH	5.90E+09	1.30	71.25
4	H2+OH=H2O+H	1.17E+09	1.30	15.17
5	H+O2+M=HO2+M	2.30E+18	-0.8	0.00
	Third-body chaperon efficiencies H2/1./ H2O/6.5/ O2/0.4/ N2/0.4/			
6	H+HO2=OH+OH	1.50E+14	0.00	4.20
7	H+HO2=H2+O2	2.50E+13	0.00	2.93
8	OH+HO2=H2O+O2	2.00E+13	0.00	4.18
9	H+H+M=H2+M	1.80E+18	-1.00	0.00
	Third-body chaperon efficiencies H2/1./ H2O/6.5/ O2/0.4/ N2/0.4/			
10	H+OH+M=H2O+M	2.20E+22	-2.00	0.00
	Third-body chaperon efficiencies H2/1./ H2O/6.5/ O2/0.4/ N2/0.4/			
11	HO2+HO2=H2O2+O2	2.00E+12	0.00	0.00
12	H2O2+M=OH+OH+M	1.30E+17	0.00	190.38
13	H2O2+OH=H2O+HO2	1.E+13	0.00	7.53
14	O+HO2=OH+O2	2.E+13	0.00	0.00
15	H+HO2=O+H2O	5.E+12	0.00	5.90
16	H+O+M=OH+M	6.2E+16	-0.60	0.00
	Third-body chaperon efficiencies H2O:5, others 1			
17	O+O+M=O2+M	6.17E+15	-0.50	0.00
18	H2O2+H=H2O+OH	1.E+13	0.00	15.02
19	H2O2+H=HO2+H2	4.79E+13	0.00	33.26
20	O+OH+M=HO2+M	1.E+16	0.00	0.00
21	H2+O2=OH+OH	1.7E+13	0.00	200.0

	Nitrogen Chemistry			
22	O+N2=N+NO	1.82E+14	0.00	319.02
23	O+NO=N+O2	3.8E+09	1.00	173.11
24	H+NO=N+OH	2.63E+14	0.00	210.94
25	NO+M=N+O+M	3.98E+20	-1.50	627.65
26	N2+M=N+N+M	3.72E+21	-1.60	941.19
27	N2O+O=NO+NO	6.92E+13	0.00	111.41
28	N2O+O=N2+O2	1.E+14	0.00	117.23
29	N2O+N=N2+NO	1.E+13	0.00	83.14
30	N+HO2=NO+OH	1.E+13	0.00	8.31
31	N2O+H=N2+OH	7.6E+13	0.00	63.19
32	HNO+O=NO+OH	5.01E+11	0.50	8.31
33	HNO+OH=NO+H2O	1.26E+12	0.50	8.31
34	NO+HO2=HNO+O2	2.E+11	0.00	8.31
35	HNO+HO2=NO+H2O2	3.16E+11	0.50	8.31
36	HNO+H=NO+H2	1.26E+13	0.00	16.63
37	HNO+M=H+NO+M	1.78E+16	0.00	203.7

Table 7–2. Specific reaction rate constants (Gutheil et al., 1993).

Please click the advert



7.2.3. Non-inertial rupture disk case simulations

Considering the significant scattering of available experimental data and a number of mentioned uncertainties involved, e.g. internal geometry (Dryer et al., 2007), initial hydrogen temperature (Pinto et al., 2007), presence of wetting substance (Mogi et al., 2007), it was decided to compare simulations by the LES model of spontaneous ignition against experimental data by Golub et al. (2007, 2008).

The experimental setup includes a high-pressure chamber filled with hydrogen to required pressure, and a low-pressure chamber with air at atmospheric conditions connected by a pipe of 5 mm internal diameter and variable length Golub et al. (2007, 2008). The high pressure hydrogen and air at atmospheric pressure were separated by a copper rupture disk of 0.1–0.2 mm thickness, depending on designed rupture pressure, installed at entrance from the high-pressure chamber to the pipe. When the pressure in the high-pressure chamber exceeds the critical value, the burst disk ruptures and shock wave propagates through the low-pressure pipe with air into the low-pressure chamber. Critical pressure of hydrogen in high-pressure chamber varied in the range 2.0–13.2 MPa, while a length of the tube varied between 65 mm and 185 mm. In each experiment the rupture disk completely opens in a controlled manner with its petals fully pressed to tube walls. A pair of a pressure transducer and a light sensor was installed at different distance from the rupture disk to detect shock wave propagation and radiation from the spontaneous ignition. It should be noted that in each of the experiments only one pair of sensors was present. The distance from the rupture disk to sensors pair was changed from one test to another at the same conditions to identify the location of spontaneous ignition.

From a series of experiments the test with initial hydrogen pressure of 9.73 MPa and 65 mm extension pipe was chosen in order to keep simulation time to minimum. From the experimental data it is known the spontaneous ignition occurred at distance less than 33 mm from the rupture disk. Experimentally observed pressure behind the shock wave was in the range 2.69–3.40 MPa, and the delay between the shock wave front and the chemical reaction front (spontaneous ignition) at 33 mm from the burst disk was in the range 18–24 μs.

The simulated high-pressure chamber was 140 mm long and 20 mm diameter cylinder, the simulated low-pressure chamber was 145 mm long and 5 mm diameter cylinder (Bragin and Molkov, 2009). The grid was created using GAMBIT. In order to exclude the effect of mesh irregularities on combustion in reacting flow, the low-pressure chamber was meshed with an unstructured hexahedral grid with uniform CV size of about 200 μm both along the tube and a similar characteristic CV size in the cross-section. The high-pressure chamber was meshed with the smallest CV size of about 250 μm clustered near the entrance to the pipe and rapidly increasing away from it reaching the maximum cell width of 10 mm in a far field from the rupture disk. The total number of control volumes was equal to 430,976. Non-slip impermeable adiabatic boundary conditions were used on all of the walls. The shock tube was modelled as "closed" to exclude potential effects of numerical boundary conditions on the process. This assumption is applicable as the low-pressure chamber is long enough to simulate the process of ignition without getting the reflection of the shock wave from the closed end.

Initial conditions at the high-pressure chamber were pressure 9.6 MPa, temperature 300 K, and the mole fractionof hydrogen 1. The low-pressure chamber was filled with air (0.23 mass fractionof oxygen and 0.77 of nitrogen) at atmospheric pressure and temperature of 300 K. Non-physical values were encountered in simulations due to numerical instabilities if the imaginary rupture disk, i.e. the boundary separating gases, was placed exactly at the border between the larger in diameter (20 mm) high-pressure chamber and the smaller in diameter (5 mm) low-pressure chamber. To avoid instabilities during simulation of strong discontinuity in pressure accompanied by strong discontinuity in area, the simulated "rupture disk" was moved one pipe diameter (5 mm) downstream, i.e. high-pressure hydrogen was also initially present in the first 5mm of the pipe. In simulations the maginary rupture disk was "removed instantly" and a shock wave was allowed to propagate.

The problem was simulated using FLUENT 6.3.26, which realises control-volume based finite-difference method. The solver used explicit linearization of the governing equations with explicit method for solution of linear equation set. The third order MUSCL scheme with AUSM flux splitting was applied for flow discretisation. The four step Runge-Kutta algorithm was employed for advancement of solution in time. The time step was determined from Courant-Friedrichs-Lewy condition, where the CFL number was equal to 0.5 to ensure stability.

Figure 7–2 shows the dynamics of temperature (left) and hydrogen mole fraction (right) during the first 56 μs after the rupture disk instant opening (non-inertial rupture disk). At the initial moment t=0 the "rupture disk" boundary separating high-pressure hydrogen and atmospheric air, located at x=0, is instantaneously removed and a shock wave propagates into air heating it up due to compression. The shock wave is followed by a contact surface separating cold hydrogen and heated air. It is seen that the thickness of the heated air layer between the shock front and the contact surface increases in time.

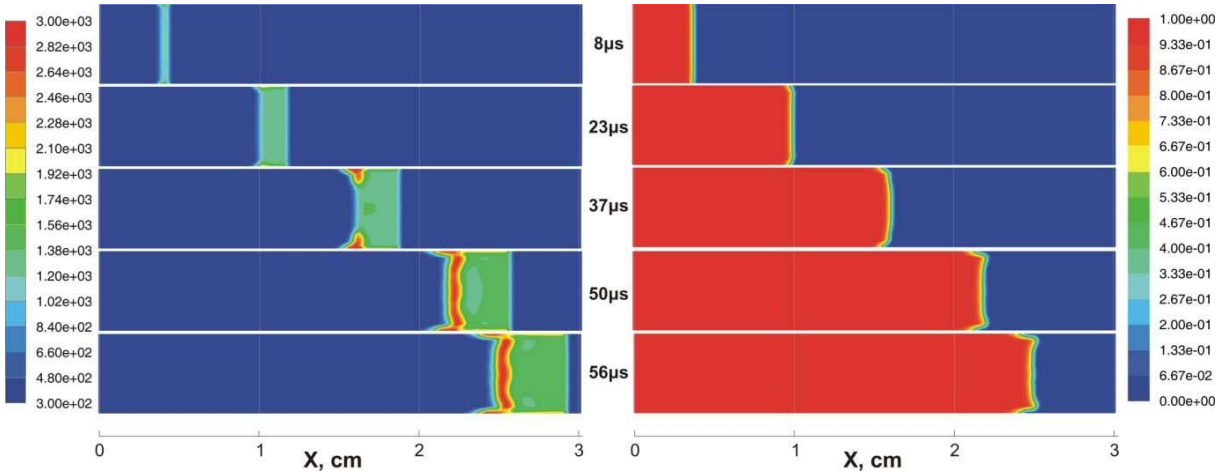


Figure 7–2. Dynamics of spontaneous ignition (Bragin and Molkov, 2009): temperature (left) and hydrogen mole fraction (right).

The shock wave propagates along the tube as a plane wave without any curvature outside the boundary layer. The shape of the contact surface changes from plane to slightly convex in the beginning due to non-slip conditions at the pipe walls. The highest temperature is observed in the boundary layer due to velocity decrease (stagnation conditions). Owing to counter diffusion of hydrogen and air the contact surface, and heat diffusion from hot air to cold hydrogen through the contact surface the spontaneous ignition occurs whencritical conditions forchemical reactionare reached. The chemical reactionpropagates in the direction from the wall to the tube axis as the contact surface propagates downstream. After 45 μs from the start of the process at distance 20 mm from the non-inertial "rupture disk" location the combustion occupies the whole cross-section area of the pipe. Initiation of the chemical reactions in the boundary layer accelerates propagation of the reaction front along the wall compared to the axial part leading to change of the convex shape of the contact surface in the most of the tube cross-section to a slightly concave form.

In numerical simulations the reaction front is established throughout the pipe cross-section at distance 20 mm from the burst disk at time 45 μs after the instant rupture. In the experiment by Golub et al. (2007, 2008) the light sensor was located 33 mm from the burst disk. Unfortunately, the time of the shock arrival at this location in experiment was not reported. In numerical simulations the shock reached the light sensor location of 33 mm at 58 μs, and the reaction front followed the shock with a delay of 7–10 μs. In the experiment the sensor started to register light 18–24 μs after the shock arrival. The deviation in delay of the flame front arrival after the shock could be explained by the inertial (not instant) opening of the real rupture disk, which was not accounted for in the simulations. Another factor, which could explain the deviation, could be the absence of heat transfer from the reaction zone to walls in the simulations.

Please click the advert

UNIVERSITY OF COPENHAGEN

The difference is your ambition!

Copenhagen Master of Excellence

are two-year master degrees taught in English at one of Europe's leading

Come to Copenhagen - *and aspire!*

Apply now at www.come.ku.dk

PHARMACEUTICAL SCIENCES
LIFE SCIENCES
COPENHAGEN
RELIGIOUS STUDIES
LAW
SOCIAL SCIENCES
HUMANITIES

7.2.4. Mechanism of flame separation by vortex

A sequence of photographs showing the flame exiting from a pipe, where spontaneous ignition has happened, was published by Mogi et al. (2008) using high-speed digital colour video camera. Initial pressure of hydrogen in chosen for numerical simulations experiment was 14.5 MPa and the pipe length was 185 mm. The pipe wall thickness was 4 mm. This sequence of snapshots shows combustion of spontaneously ignited hydrogen-air mixture emerging outside and stabilizing in the vicinity of the pipe exit. The authors observed that once the emerged from the pipe flame is stabilized near the nozzle, it acts as a pilot flame and ignites/sustains the jet fire afterwards. Therefore, the numerical observation of flame "stabilization" near the pipe exit may be taken as an indication of the transition from the spontaneous ignition to the sustained jet fire.

In this series of simulations (Bragin and Molkov, 2009) we have shifted the focus from the resolution of spontaneous ignition towards the transition from ignition within the pipe to combustion outside the pipe in the atmosphere. Therefore, it was decided to sacrifice resolution in the channel further in order to reduce CPU time to practically reasonable. The characteristic size of control volumes was twice larger than in simulations described in previous section and it was of the order of 400 μm. The larger cell size attached to the wall makes the boundary layer "wider" and thus, due to reducing the heat dissipation from the initial ignition spot, facilitates faster ignition.

The area in the immediate vicinity of the tube exit in the atmosphere was initially coarsely meshed with cells clustered around the anticipated under-expanded jet shock structure. Just before the initial shock wave and the spontaneously ignited mixture reached the end of the pipe, the grid outside the pipe was refined for the first time. As the process evolved and the jet flow increased in size, the second grid refinement was performed at 220 μs after the rupture disk opening. The number of control volumes increased due to the grid refinement from 261,640 to 478,528 during the simulation.

Since temperature of hydrogen and surrounding air were not reported in the experimental paper, they were accepted as 300 K in simulations. Atmospheric pressure of air (23% of oxygen and 77% nitrogen by volume) was taken as 101,325 Pa. At time t=0 the imaginary rupture disk was instantaneously removed to commence the discontinuity decay. Non-reflecting "far field" boundary conditions were set downstream and at radial boundaries of the calculations domain.

Figure 7–3 shows the dynamics of temperature, velocity, hydrogen and hydroxyl mole fractions. The field of view in all numerical snapshots is kept constant, where the channel length shown corresponds to 66.5 mm, and the external to the pipe area is 148 mm long and 130 mm wide. All snapshots represent 2D cross-section along the pipe axis. The maximum and minimum values in each series were fixed in order to lock the relation between colours and corresponding parameters in all frames. Minimum and maximum values in each set of frames were fixed to 0–2400 K for temperature, 0–3000 m/s for velocity, 0–1 for hydrogen mole fraction, and 0.001–0.01 for hydroxyl mole fraction. If values fall out of these limits, they are coloured according to the colour of limits – red for values above the upper limit and blue for values below the lower limit.

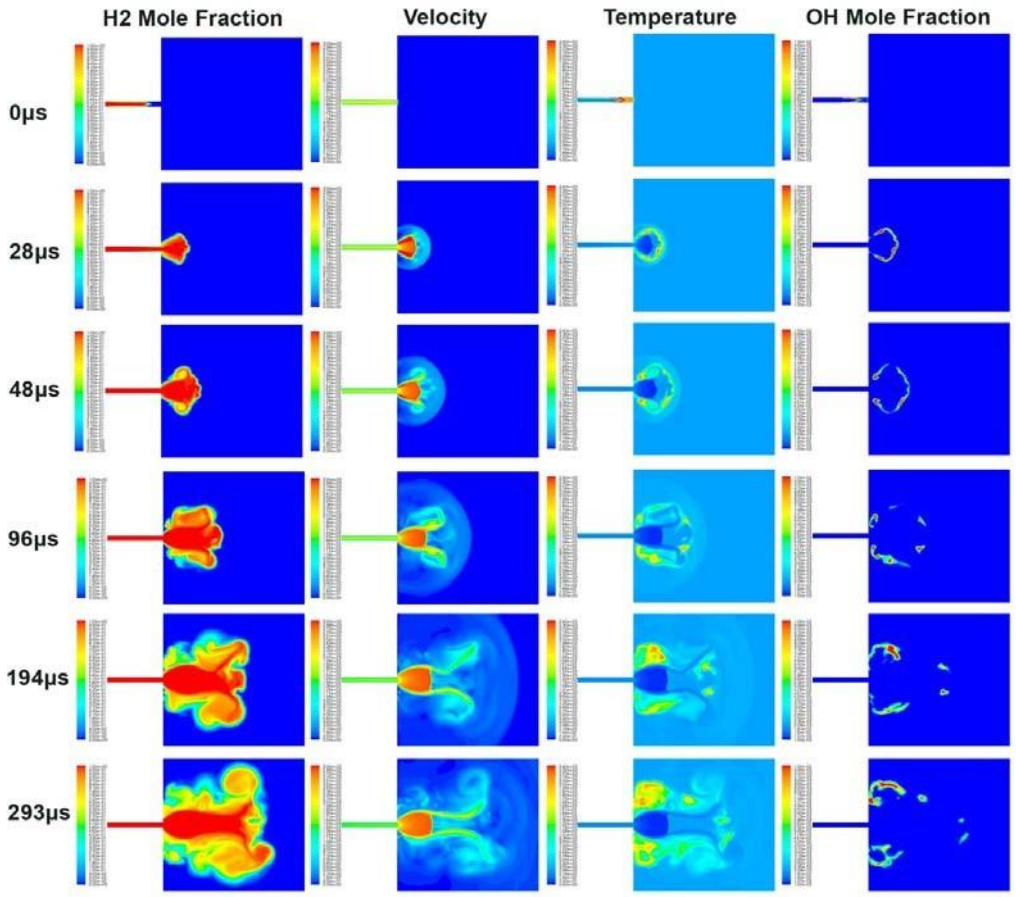


Figure 7–3. Dynamics of the velocity, temperature and mole fractions of hydrogen and hydroxyl in 2D slice along the pipe axis (Bragin and Molkov, 2009).

The dynamics of spontaneous ignition in the pipe was similar to the one described in previous section and is not shown here. The resulting flame front tip gets behind the shock wave by about 7 mm by the end of the pipe. The flame front width is about 3 mm near the pipe axis, while near the wall it extends as long as 35 mm. Combustion is more pronounced near walls, having wider regions with high temperature. The first frame in time series corresponds to the time 131.5 μs from the instant opening of the "rupture disk". For ease of interpretation of the transition process the reference time was set to 0 μs at this moment (see Fig. 7–3).

Figure 7–3 shows that as the shock wave emerges from the pipe exit it diffracts and transforms from a plane to a hemispherical form. The shock propagates outwards and quickly loses the strength. It is followed by the flame front pushed by the expanding hydrogen. Once hydrogen leaves the tube, hemispherical expansion starts and the flame front follows the expansion. The formation of Mach disk commences shortly after (see "28 μs" frame in Fig. 7–3) and the expansion of hydrogen is held back increasing the separation distance between the leading shock and the contact surface. Sudden deceleration of hydrogen stimulates turbulent mixing and the contact surface becomes turbulent.

In parallel to the Mach disk formation, the outer annular flow at the Mach disk's periphery forms. Owing to viscous forces this supersonic annular flow generates a large-scale vortex, which turns the flow back towards the pipe exit. The formation of vortex breaks the combusting gas (48 μs) into two parts – downstream and upstream parts (see comparison with experimental snapshots below).

Meanwhile, the shock barrel is not yet stabilized. Upstream combustion region is pushed back by the vortex tip (96 μs), while downstream combustion region in the vicinity of jet axis is forced out. As the vortex straightens, the supply of hydrogen to the recirculation area dies out and reduction of flow velocity allows necessary induction time for intensification of combustion. It can be seen that combustion affects the gas dynamic evolution of the jet and results in non-axis-symmetrical to some extent flow beyond the Mach disk (194 μs). Shock barrel is stabilized around 200 μs. The annular vortex increases in size widening distance from the axis where hydrogen is present. By the time of the last frame in Fig. 7–3 (293 μs) the downstream combustion is fully ceased, while the upstream combustion in the recirculation zone is sustained.

Unlike 2D CFD slices of reacting flow parameters, experimental snapshots give a side-view on the 3D combusting jet. Therefore, it is impossible to see the jet to the level of details the numerical experiments can produce, including profiles of all the parameters of interest. Experimental data on the flame size by Mogi et al. (2008) were critically analysed. The uncertainty in published snapshots lies in the scale of frames presented. The scale given should be reconsidered, since the inner diameter of the tube is known to be 5 mm, but according to the scale given on photographs (Mogi et al., 2008) an outer diameter of the tube is equal to 4.5 mm. From a private communication from Dr Mogi, it was clarified that the tube wall width was 4 mm. Thus, outer diameter of the tube shown in photographs was equal to 13 mm. Therefore, field of view in experimental photographs corresponds to 104 x 76.4 mm with pipe bulging out by 14.6 mm.

Please click the advert



Ø® ¢®®®Ø B®¢B Ø¢®B

In Paris or Online

International programs taught by professors and professionals from all over the world



BBA in Global Business

MBA in International Management / International Marketing
DBA in International Business / International Management
MA in International Education

Visit: www.HorizonsUniversity.org

Write: Admissions@horizonsuniversity.org

www.HorizonsUniversity.org

While some works base their estimation of the visible flame length on temperature, e.g. Brennan et al. (2009), in this study the flame is identified by the mole fraction of hydroxyl. Hydroxyl concentration coupled with high-temperature is widely acknowledged as an indication of combustion taking place. Here we identify visible flame by the hydroxyl mole fraction higher than 0.001. Figure 7–4 shows comparison between experimental and simulated snapshots. Numerical flame propagation can be referenced to experimental dimensions by vertical lines, which are positioned 10 mm apart.

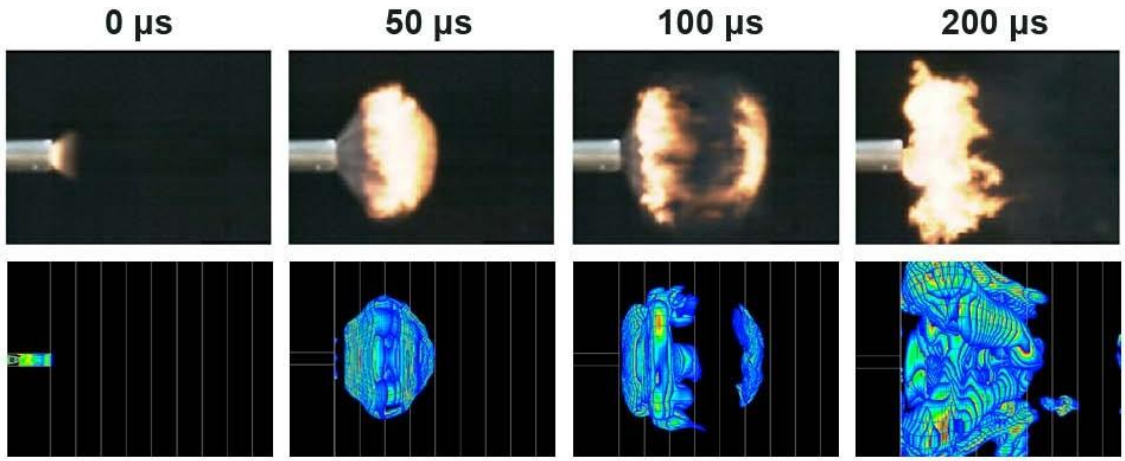


Figure 7–4. Comparison of high-speed video camera experimental photographs (Mogi et al., 2008) with numerical 3D snapshots (Bragin and Molkov, 2009).

The ignited within the pipe jet exits to atmosphere at 0 µs. It develops into a cocoon of combusting mixture (50 µs). Shortly after this the annular vortex, which cannot be seen here (see previous Fig. 7–3) causes the cocoon to break into upstream and downstream combusting regions (100 µs). As the downstream combustion region is blown away, the upstream region is stabilized near the tube exit (200 µs). The size of this region, however, is bigger in simulations. This can be explained by three potential reasons. Firstly, the chosen limit for the numerical visualisation of the flame front of 0.001 of OH (it is often is taken as 0.01 of OH). Secondly, there are difference conditions for air entrainment in the experiment and simulations. Indeed, simulations of hydrogen release were carried out not for the pipe with 5 mm internal diameter and 4 mm wall thickness, but for the channel of 5 mm in a wall with "infinite" dimension. Third reason for deviation in size of stabilised flame could be the wetting of the inside surface of the tube between the burst disk and the exit to the atmosphere by the aqueous Na_2CO_3 solution (1%) in order to allow visualization of the flame. This solution could have interfered with heat transfer and chemistry of hydrogen combustion and decreases the visible flame size.

The mechanism of transition from spontaneous ignition inside of the tube into sustained jet fire is described in this section within the computational limitations. It is assumed, following the experimental observations and numerical simulations, that the transition to the sustained jet flame is largely dependent on the initial jet formation stage, where developing annular vortex pushes combusting mixture upstream into the recirculation zone. Once the flame is stabilised near the pipe exit, it can act as a pilot flame to jet fire later on.

7.2.5. Lower pressure limit of spontaneous ignition in a T-shaped channel

7.2.5.1. Experimental set up

The geometry of the experimental set up, including a T-shaped channel mimicking PRD, is taken from Golub et al. (2010a) and is shown in Fig. 7–5. The high pressure system consists of a 210 mm long tube with 16 mm internal diameter (ID) followed by a 280 mm long tube with 10 mm ID at the end of which a flat rupture disk, made of copper or aluminium with cuts facilitating failure, is located followed by a mock-up PRD (T-shaped channel) open to the atmosphere.

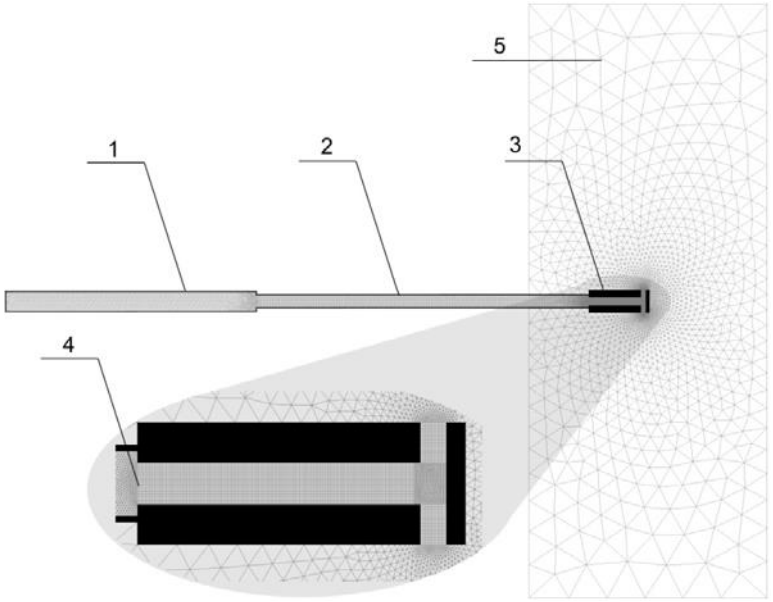


Figure 7–5. The geometry and computational domain: 1 and 2 – high pressure tubes, 3 – mock-up PRD (T-shaped channel), 4 – burst disk, 5 – external computational domain.

The PRD has a 48 mm long axial channel of 6.5 mm ID with a flat end, and two radial channels on opposite sides of the axial channel to vent hydrogen to atmosphere. Each radial channel has 6.25 mm length and 4 mm ID (distance from the end connected to the atmosphere of one radial channel to the end of another is 19 mm). Radial channels are flushed with the axial channel end wall and positioned so that the edge of each side channel touches tangentially the flat end wall of the axial channel. The rupture disk opening was estimated by Golub et al. (2010a) as about ten microseconds thus creating conditions for better mixing of hydrogen with air during the opening as compared to not realistic instant opening. To register spontaneous ignition a light sensor was installed along the axis of radial channels of the PRD. Temperature behind the shock wave reflected from the flat end wall was estimated by authors as more than twice higher than the temperature behind the incident shock wave. Golub et al. (2010a) stated that when the initial pressure in high pressure chamber did not exceed 1.2 MPa the light sensor did not record any signal, and when pressure was 2.9 MPa the ignition was registered. Unfortunately, there is no published experimental information on spontaneous ignition at storage pressures in between these two values. However, it has been stated by Golub (2010b) that light was registered at storage pressure 2.43 MPa as well.

7.2.5.2. Numerical details

The 3D grid was created using GAMBIT tool of FLUENT 6.3.26, which realises control-volume based finite-difference method (Bragin et al., 2011). The axial and radial channels of the PRD were meshed with a hexahedral grid with a uniform control volume (CV) size of about 400 μm both along the axial channel and in its cross-section, excluding the intersection zone. The intersection area of the axial and the radial channels was meshed with tetrahedral CVs with size of about 200 μm. This is the largest CV size used in numerical simulations of the spontaneous ignition phenomenon. This is due to the application of the LES technique requiring 3D domain and thus larger CV size to simulate a problem in reasonable computation time. The high-pressure chamber was meshed by tetrahedrons with the smallest CV size of about 250 μm clustered near the membrane of the PRD and rapidly increasing away from it reaching the maximum cell width of 10 mm at the far end. The total number of control volumes in the computational domain was equal to a moderate number of 417,685 cells.

Non-slip impermeable adiabatic boundary conditions were used on walls. Non-reflecting open "pressure-far-field" boundaries were used outside of the PRD. The high pressure system was modelled as closed to exclude potential effects of inlet boundary conditions on the process. This assumption is valid because the observation time in simulation is less than a time required for rarefaction wave to reach the far end of the high-pressure system. Four cases are presented below to illustrate changes in the process dynamics with initial hydrogen pressure in the high-pressure system of 1.35, 1.65, 2.43 and 2.90 MPa. Initial temperature of 300 K and the mole fraction of hydrogen equal to 1 were assumed in the high-pressure system before the start of inertial rupture disk opening in all four cases. Low pressure chamber was filled with air (0.23 mass fraction of oxygen and 0.77 of nitrogen) at pressure 0.101 MPa and temperature 300 K.

The solver used explicit linearisation of the governing equations with explicit method for solution of linear equation set. A second order upwind scheme with AUSM flux splitting was applied for flow discretisation. The four step Runge-Kutta algorithm was employed for advancement of simulations in time. The time step was determined from Courant-Friedrichs-Lewy condition, where the CFL number was equal to 0.2 to ensure stability.

7.2.5.3. Modelling of rupture disk opening

The rupture disk opening is expected to play an important role in the process of spontaneous ignition by diffusion mechanism due to its effect on the mixing between hydrogen and air. A modelling strategy is described below. The following formula is applied to calculate an opening time of a diaphragm (Spence and Woods, 1964)

$$t = k(\theta bd / p)^{1/2}, \quad (7\text{–}22)$$

where ρ is the density of the diaphragm material, b and d are thickness and diameter of the diaphragm respectively, and the values of k are found to be in a range 0.91–0.93 (Wen et al., 2009). Density of annealed copper is 8900 kg/m^3. For example, for 2.9 MPa case, the opening time can be calculated as

$$t = 0.92\left(8900 \cdot 5 \cdot 10^{-5} \cdot 6.5 \cdot 10^{-3} / 2.9 \cdot 10^{6}\right)^{1/2} = 29.1\ \mu s. \tag{7–23}$$

The opening of a membrane was approximated in simulations by 10 step-like process (see Fig. 7–6) with a time for each section given in Table 7–2 for four investigated cases.

Section	1	2	3	4	5	6	7	8	9	10
Opening time, μs [1.35 MPa case]	0	4.7	9.4	14.2	18.9	23.6	28.4	33.1	37.8	42.6
Opening time, μs [1.65 MPa case]	0	4.3	8.6	12.8	17.1	21.4	25.6	29.9	34.3	38.5
Opening time, μs [2.43 MPa case]	0	3.5	7.1	10.6	14.2	17.7	21.3	24.8	28.3	31.9
Opening time, μs [2.9 MPa case]	0	3.2	6.5	9.7	12.9	16.2	19.4	22.6	25.9	29.1

Table 7–2. Opening times of sections for simulated cases (Bragin et al., 2011).

Please click the advert



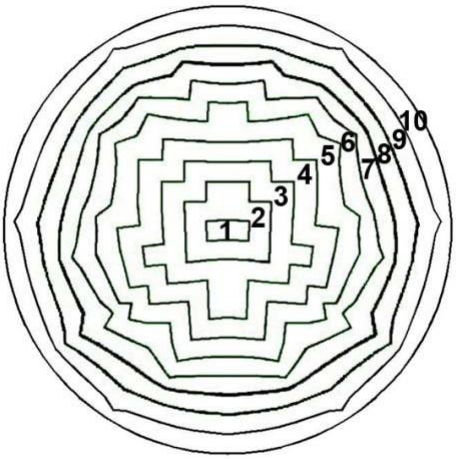


Figure 7–6. Step-like approximation of a burst disk rupture process: 1-10 are sections that open in series.

7.2.5.4. Initial stage following the membrane rupture

Figure 7–7 shows dynamics of temperature and hydrogen mole fraction at an initial stage of hydrogen release into air in the mock up PRD with instant opening (left) and inertial opening (right) of the rupture disk for initial pressure 1.35 MPa in the high-pressure chamber (Bragin et al., 2011). The inertial rupture disk opening is accompanied by formation of an under-expanded jet from increasing with time open area of the disk. A barrel-like structure can be seen for the case of inertial membrane opening (Fig. 7–7, right).

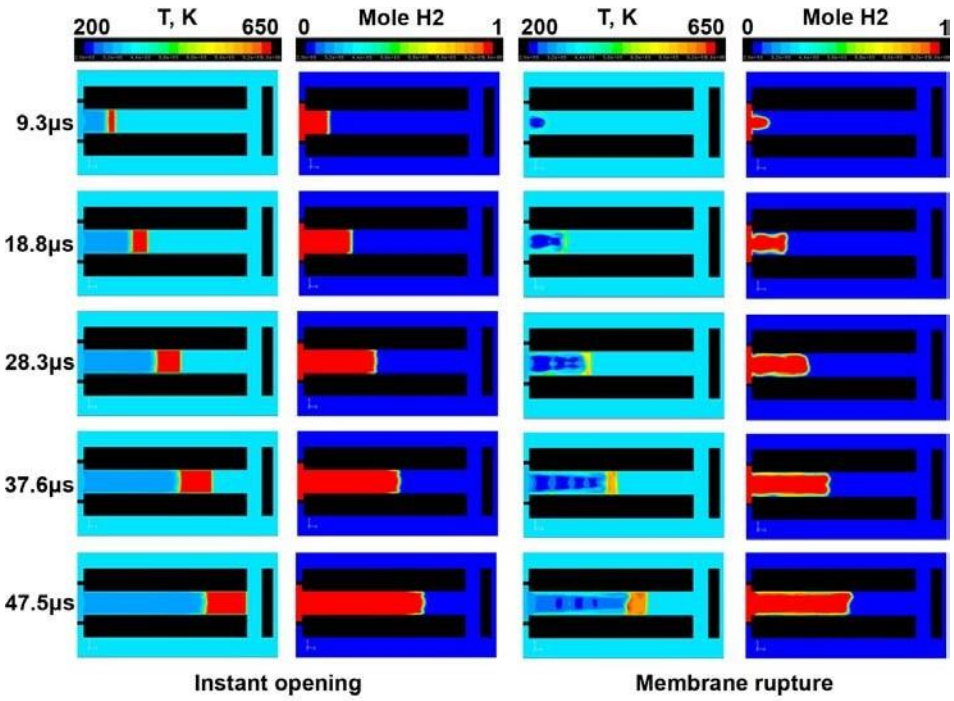


Figure 7–7. Dynamics of temperature and hydrogen mole fraction at the initial stage following an instant rupture disk opening (left) and inertial ten-step rupture disk opening (right) for the 1.35 MPa high-pressure chamber case.

The one by one opening of each of 10 sections of the rupture disk changes the barrel diameter to a larger one and the flow pattern looks similar to the multiple diamond-like pattern, which is characteristic for this range of pressures. For the case of instant opening of an imaginary non-inertial membrane the shock heated zone in air (red colour) is almost three times thicker compared to the inertial membrane rupture case at the same moment of time. It is obvious, that the inertial opening of the membrane generates more intense mixing of hydrogen and air, including in the boundary layer of the axial channel walls. Maximum temperature in the shock-heated air is 50 K lower for the inertial membrane opening case. Thus, modelling of the inertial rupture disk opening is an important part of predictive simulations of spontaneous ignition in complex geometries.

7.2.5.5. Shock reflection

Shock wave reflections can play an important role in the triggering of spontaneous ignition process. Reflected pressure at the flat end of the axial channel of the T-shaped PRD can be estimated using 1D gas dynamic equations that can be found elsewhere (Bragin et al., 2011). First, we estimate the Mach number M_S of the shock wave generated by the discontinuity

$$\frac{p_4}{p_1} = \left[1 + \frac{\gamma_1}{\gamma_1+1}\left(M_S - \frac{1}{M_S}\right)\right] \Big/ \left[1 - \frac{\gamma_4 - 1}{\gamma_1 + 1}\cdot\frac{a_1}{a_4}\cdot\frac{M_S^2-1}{M_S}\right]^{\frac{2\gamma_4}{\gamma_4-1}}, \tag{7–24}$$

where p_4/p_1 is initial hydrogen to atmospheric air pressure ratio when the membrane is removed, γ_1 and γ_4 are specific heat ratio for air and pushing gas respectively (for our case $\gamma_1 = \gamma_4 = 1.4$), a_1/a_4 – ratio of air to hydrogen speed of sound. Knowing M_S, pressure p_2 behind the leading shock wave (propagating in air) can be calculate

$$p_2 = p_1\left[\frac{2\gamma_1 M_S^2 - (\gamma_1 - 1)}{\gamma_1 + 1}\right]. \tag{7–25}$$

Finally, the pressure p_5 following normal reflection of leading shock wave can be calculated as

$$\frac{p_5}{p_2} = \frac{(3\gamma_1 - 1)p_2/p_1 - (\gamma_1 - 1)}{(\gamma_1 - 1)p_2/p_1 + (\gamma_1 + 1)}. \tag{7–26}$$

Table 7–3 gives results of calculations by 1D theory using Eqs. (7–24)–(7–26) and 3D numerical simulations (LES) for the reflected shock pressure. Results of LES simulations are close to the theoretical 1D prediction yet are by 8–10% above the theory. It is worth to note that, as numerical simulations have demonstrated,

spontaneous ignition at the flat end of the axial channel, where reflection takes place, is impossible as there is no hydrogen at this location for considerable time.

Initial hydrogen pressure, MPa	1.35	1.65	2.43	2.9
Mach number of leading shock wave Eq. (7–24)	2.47	2.64	2.98	3.15
Pressure behind leading shock wave Eq. (7–25), MPa	0.7	0.8	1.04	1.16
Calculated reflected pressure Eq. (7–26), MPa	2.96	3.61	5.15	6.0
Simulated reflected pressure (LES), MPa	3.25	3.9	5.56	6.6

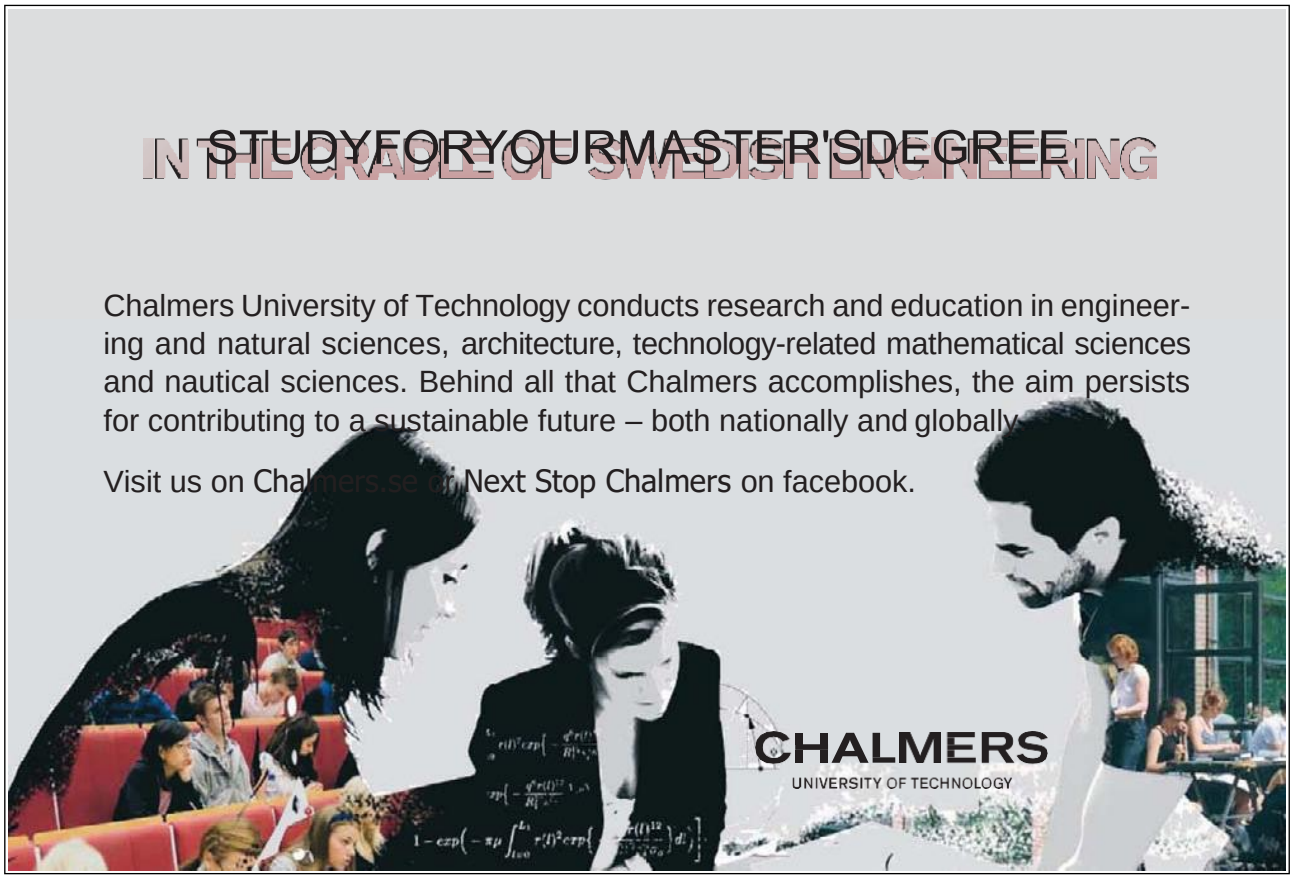
Table 7–3. Calculated parameters for normal shock wave reflection using Eqs. (7–24)–(7–26).

Applicability of 1D theories is limited to simple scenarios, e.g. propagation of a shock wave through uniform hydrogen-air pre-mixture and normal reflection from a flat surface. If the mixture is not uniform or the shock is oblique and surface is not flat then simple methods are hardly applied. The case of T-shaped channel is even more complicated due to absence of hydrogen-air mixture in an area of first reflection, i.e. at the flat end of the axial channel, and presence of multiple reflections from curved surfaces of the channels.

7.2.5.6. Effect of storage pressure on spontaneous ignition in a T-shaped channel

Temperature and hydroxyl mole fraction profiles in the axial cross-section for cases with initial pressure of 2.9 MPa and 2.43 MPa in the high-pressure chamber are presented in Figs. 7–8 and 7–9 respectively.

Please click the advert



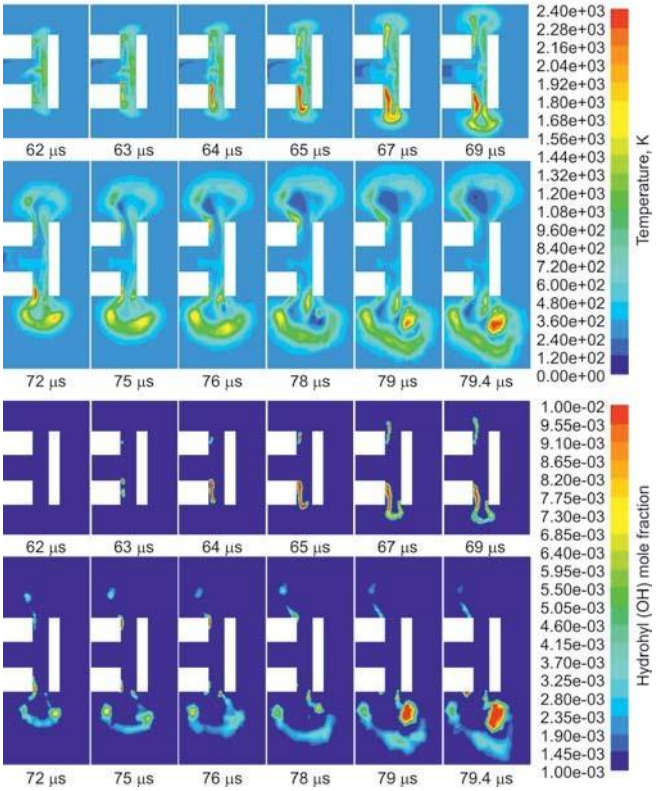


Figure 7–8. Temperature and hydroxyl mole fraction for 2.9 MPa storage pressure.

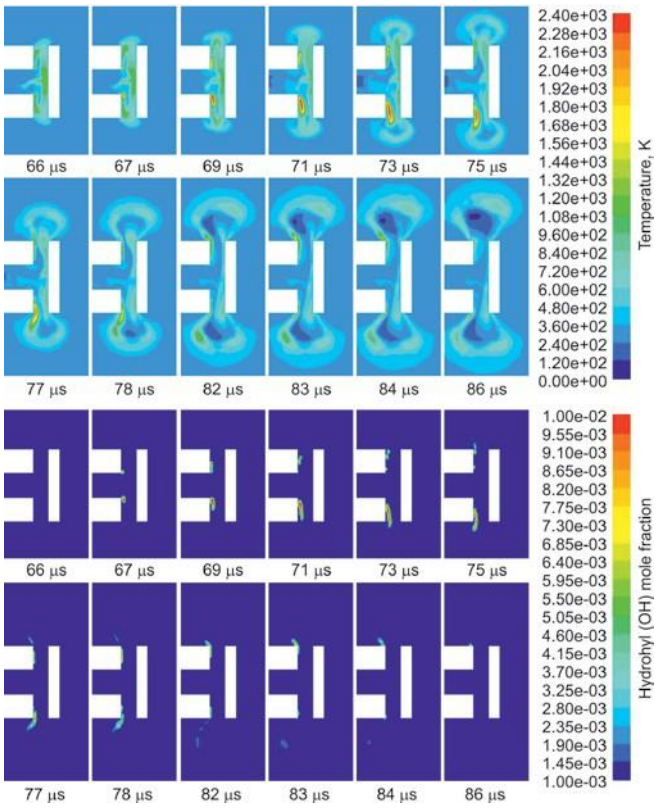


Figure 7–9. Temperature and hydroxyl mole fraction for 2.43 MPa storage pressure.

It is clear that ignition is not possible at location of the leading shock reflection on the flat end of the axial channel since hydrogen is not supplied to this area yet. Once the hydrogen flow diffracts around the edge from the axial into radial channels, it starts mixing with heated by shocks air. This provides the necessary conditions for ignition of the hydrogen-air mixture. It can be seen that for both initial pressures chemical reaction is initiated in the radial channel in a location close to the upstream wall.

Larger high temperature regions can be observed for storage pressure 2.9 MPa (Fig. 7–8) compared to pressure 2.43 MPa (Fig. 7–9). The difference becomes obvious when combusting mixture is pushed outside. At pressure 2.9 MPa a semi-spherical cocoon of a heated to critical conditions flammable hydrogen-air mixture is formed outside the PRD being followed by expanding hydrogen. Combustion is initiated in a number of spots within the cocoon (see snapshots of temperature and OH mole fraction at 79 μs). The concentration of hydrogen in these spots outside the PRD just before the ignition is in the range 29–36% by volume. Thus, a conclusion can be drawn that the ignition by the diffusion mechanism takes place in the most reacting hydrogen-air mixtures.

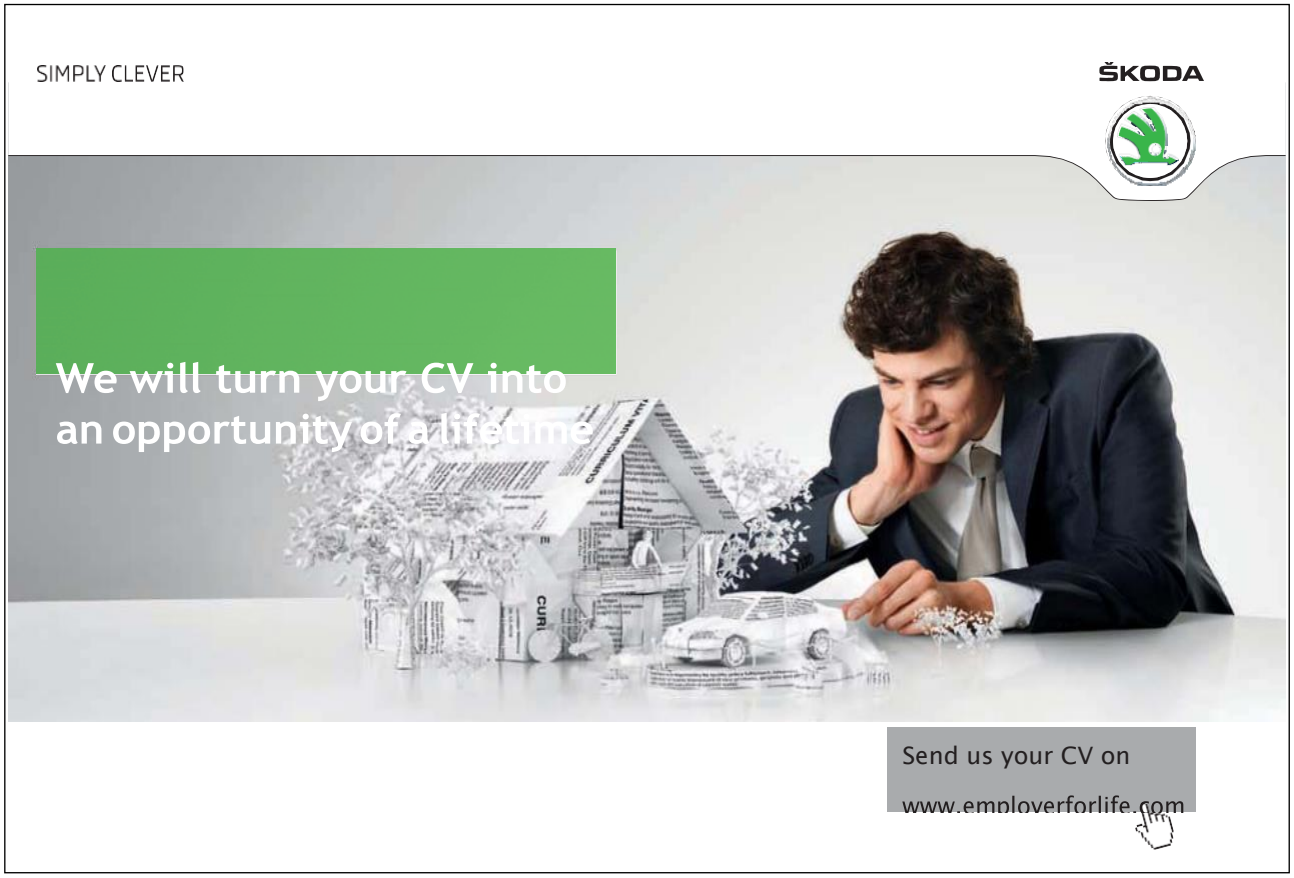
At storage pressure 2.43 MPa (Fig. 7–9) the combustion is rather weak, compared to the case of pressure 2.9 MPa, and the reacting mixture is dragged with the adjacent hydrogen flow, which leads to the elongation of combusting regions. Upon exit from the radial channels of the PRD, the flow undergoes an expansion and high-temperature regions disappear thus ceasing reaction and OH concentration, including the cooling role of expanding pure hydrogen jet on the flammable mixture.

The whole process from combustion initiation to self-extinction (disappearance of high temperature and OH mole fractions region, Fig. 7–9) takes a little more than 10 μs. This is sufficient to register the chemical reaction by a light sensor in the experiments. This explains the uncertainty in interpretation of experimental observations by Golub et al. (2010a, 2010b). Indeed, at pressure 2.9 MPa the combustion quite pronounced but at pressure 2.43 MPa the spot of spontaneous ignition is weak and disappears due to self-extinction. However, the light sensors still registered a signal during the spontaneous ignition. Thus, in full compliance with experimental observations the simulations confirmed the spontaneous ignition at storage pressure of 2.43 MPa.

Figures 7-8 and 7-9 demonstrate that the process is asymmetrical, i.e. the ignition in the upper radial channel is weaker than in the lower channel. At pressure 2.9 MPa the ignition survives the expansion from only the lower radial channel, while the upper part is extinguished. This is sought due to the asymmetrical opening of the rupture disk in simulations. This result demonstrates the sensitivity of spontaneous ignition to the membrane rupture process that should be investigated further along with effect of other factors such as air humidity, etc.

Figures 7–10 demonstrates temperature (left) and hydroxyl (OH) mole fraction (right) dynamics in 3D view for the case of storage pressure 1.65 MPa. This type of visualisation of simulation results is chosen because an ignition spot is located in this case not in the symmetry 2D plane. The ignition takes place on the wall within the axial channel when reflected from the flat end of the axial channel pressure wave enters the channel again. The combustion follows the flow behind the reflected pressure wave and propagates along the wall upstream of the release direction. When oxygen of air in the boundary layer is consumed the chemical reaction is self-extinguished. Thus, simulations can explain why the ignition was not reported in the experimental paper for the test at storage pressure of 1.65 MPa. Indeed, the light sensor can register only the ignition in the radial channels and cannot "see" the weak combustion process inside the axial channel unless special arrangements are done, e.g. the axial channel is made of transparent walls.

Please click the advert



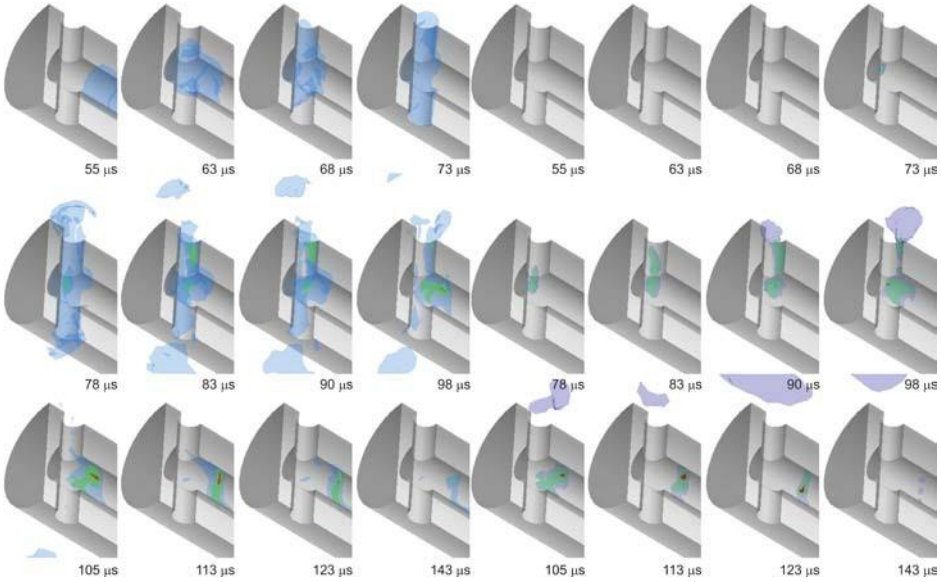


Figure 7–10. Temperature (left) and hydroxyl mole fraction (right) dynamics for 1.65 MPa storage pressure. Temperature colours: blue – 550 K, green – 1500 K, red – 2400 K. Hydroxyl mole fraction colours: blue – 0.0002, green – 0.002, red – 0.02.

Figure 7–11 shows temperature dynamics in T-shaped channel after inertial opening of the rupture disk at storage pressure of 1.35 MPa. The hydroxyl mole fraction dynamics is not presented as OH concentration is of the order of 10^{-9}–10^{-10} indicating that there is no combustion in the domain. Temperature scale is 0–1100 K in Fig. 7–11. This is different from the scale 0–2400 K applied in higher pressure when spontaneous ignition has been observed in simulations (1.65, 2.43, and 2.9 MPa) and experimentally (2.43, and 2.9 MPa).

Figure 7–11 is convenient to analyse the flow pattern and get insight into the process of the spontaneous ignition in T-shaped channel. Snapshot “60 μs” shows the contact surface between hydrogen at close to room temperature (in blue) and heated by pressure wave air (in green-yellow). The contact surface is inside the axial channel at this moment and it is disturbed by Rayleigh-Taylor instability. Close to the flat end of the axial channel there is a volume of air that is heated further by the reflected shock (in red). New areas of heated air (in red) in radial channels are seen in the next snapshot “63 μs” along with the increasing volume of hot air at the axial channel end. These new areas are probably due to the second reflection from a wall of the radial channel that is opposite to the flan end of the axial channel. At time 67 μs “cold” hydrogen starts to exit the axial channel and flows along one side of the radial channel. Hot air temperature in front of hydrogen reduces (snapshots from “67” to “77”). There is a drop in heated air temperature when hot air exits the radial channel to the atmosphere. Reflected shock is weak at storage pressure of 1.35 MPa and hot air in flow following the reflected pressure wave cannot enter the axial channel (only to small extent at the axial channel axis). At time 77 μs hydrogen starts exit to atmosphere and its temperature drops further down during this expansion.

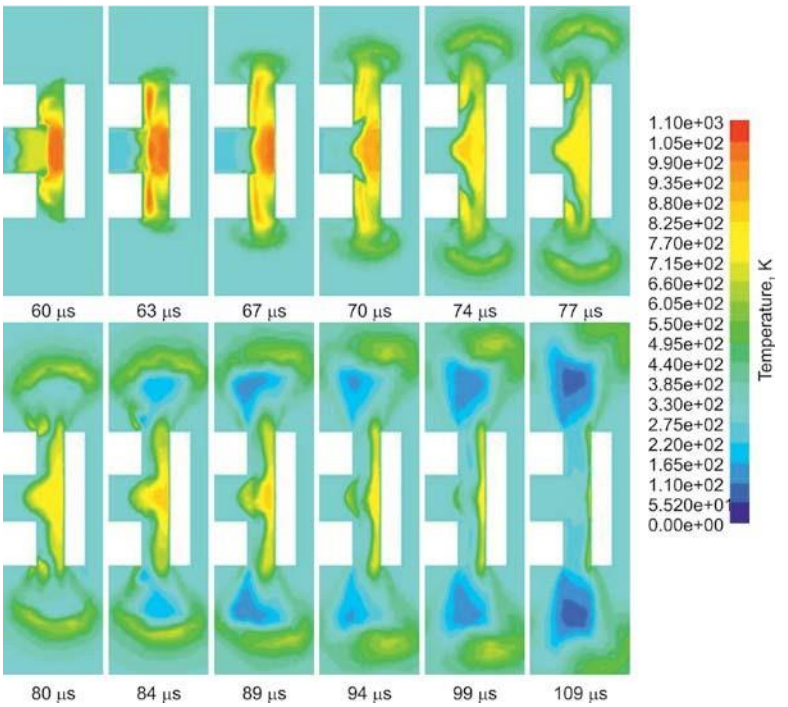


Figure 7–11. Temperature 2D profiles across the symmetry plane for storage pressure 1.35 MPa.

Thus, the conclusion can be drawn that the LES model based on the eddy dissipation concept (EDC) with detailed Arrhenius kinetics for the modelling of SGS combustion, and the renormalization group (RNG) theory for the modelling of SGS turbulence has been successfully applied to reproduce experimental data (Golub et al., 2010a, 2010b) and get an insight into the phenomenon of spontaneous ignition by diffusion mechanism in the T-shaped channel filled with air. It is confirmed that the modelling of a realistic inertial rupture disk opening is important to simulate properly the mixing process between heated by shock air and cold expanding hydrogen, and thus to find out the lower pressure limit of spontaneous ignition for particular geometry. The numerical efficiency of the EDC LES model as a tool for hydrogen safety engineering is confirmed at 3D grids with mesh size not less than 200 μk.

Numerical simulations have demonstrated that there is no ignition in T-shaped channel at storage pressure of 1.35 MPa. There is an ignition followed by a self-extinction of reaction at storage pressures
1.65 and 2.43 MPa. The minimum storage pressure at which the ignition has been observed numerically is 1.65 MPa. However, the initial spot of combustion is quickly self-extinguished in numerical test at storage pressure of 1.65 MPa. The

"sustainable" ignition, when chemical reaction is clearly seen outside the mock-up PRD, has been achieved at storage pressure of 2.9 MPa. Multiple spots of combustion are developing in the cocoon of the flammable mixture outside the PRD at this pressure.

The ignition by the diffusion mechanism is located in the most reacting hydrogen-air mixtures in the range of hydrogen concentrations 29–36% by volume. The pressure range 1.65–2.9 MPa can be considered as the lower pressure limit for spontaneous ignition of hydrogen in the studied T-shaped geometry. Only pressure at the upper part of this range is able support transition from spontaneous ignition to the sustained jet flame.

6. Related Work

8

Nuclear Hydrogen Production by ThermochemicalCycles

Greg F. Naterer
Memorial University of Newfoundland

Kamiel S. Gabriel
University of Ontario Institute of Technology

M. Lewis
Argonne National Laboratory

S. Suppiah
Atomic Energy of Canada Limited

CONTENTS

8.1 Introduction 216
8.1.1 Overview 216
8.1.2 Sulfur–Iodine (S–I) Cycle 216
8.1.3 Hybrid Sulfur Cycle (Also Known as Westinghouse, GA-22, or Ispra Mark) 217
8.1.4 University of Tokyo 3 Cycle 218
8.1.5 Ispra Mark 9 Cycle 218
8.1.6 Vanadium–Chlorine Cycle 218
8.1.7 Copper–Chlorine Cycle 219
8.2 Overview of the Thermochemical Cu–Cl Cycle 219
8.3 Thermochemical Reaction of Hydrogen Production 223
8.3.1 Proof-of-Principle Demonstrations 223
8.3.2 Design Issues of Hydrogen Reactor Scale-Up 225
8.4 Electrochemical Process of Copper or Hydrogen Production 225
8.4.1 Introduction 225
8.4.2 Proof-of-Principle Experiments 227
8.4.3 Predictive Formulation of Hydrogen Electrolysis 229
8.5 Drying of Aqueous Cupric Chloride 230
8.5.1 Introduction 230
8.5.2 Predictive Modeling and Scale-Up Design Issues 232
8.6 Hydrolysis Reaction for Copper Oxychloride Production 234
8.6.1 Introduction 234
8.6.2 Proof-of-Principle Experiments 235
8.6.3 Predictive Formulation of Hydrolysis Processes 236

8.7 Molten Salt Reactor for Oxygen Production 239
8.7.1 Introduction 239
8.7.2 Proof-of-Principle Experiments 241
8.7.3 Design Issues of Oxygen Reactor Scale-Up 242
Acknowledgments 244
References 244

8.1 Introduction

8.1.1 Overview

This chapter focuses on thermochemical cycles of hydrogen production, particularly the copper–chlorine cycle. Over 200 thermochemical cycles have been identified previously (McQuillan et al. 2002). Lewis and Taylor (2006) reported that a survey of the open literature between 2000 and 2005 did not reveal any other cycles. Very few have progressed beyond theoretical calculations to working experimental demonstrations that establish scientific and practical feasibility of the thermochemical processes. After considering factors of availability and abundance of materials, simplicity, chemical viability, thermodynamic feasibility, and safety issues, a number of cycles were identified in a nuclear hydrogen initiative (Lewis and Taylor 2002) as the most promising cycles.

Thermochemical hydrogen production is a method of splitting water by a series of chemical and physical processes. All chemical intermediates are recycled internally, without any emissions to the environment, so that water and heat are the only inputs, while hydrogen and oxygen gas are the only products. Hybrid thermochemical cycles require energy inputs in the form of both heat and electricity, although the predominant major- ity is typically in the form of heat input. The maximum temperature requirement of most thermochemical cycles is within the temperature range of 530°C–1100°C (Casper 1978). A comprehensive review of thermochemical cycles was presented by Goel et al. (2003) and Mirabel et al. (2004). Thermochemical cycles can be generally described based on the four following basic steps:

1. Water-splitting reaction
2. Hydrogen production
3. Oxygen production
4. Recycling and regeneration of intermediate compounds

This section will provide a brief overview of selected thermochemical cycles, with a sample including the sulfur–iodine (S–I) (Carty et al. 1981; Sakurai et al. 2000; Schultz 2003), hybrid sulfur, Cu–Cl (Sadhankar et al. 2005), University of Tokyo 3 (UT-3) (Sakurai et al., 1996; Lee et al. 2009), Ispra Mark 9, and vanadium–chlorine (V–Cl) (Knoche et al. 1984) cycles.

8.1.2 Sulfur-Iodine (S-I) Cycle

The S–I cycle is a leading example where equipment has been scaled up to a pilot plant level, with active development by General Atomics (United States), Sandia National Laboratory

(United States), Japan Atomic Energy Agency (JAEA), CEA (France), and others (Sakurai et al. 2000; Schultz 2003). JAEA has demonstrated a pilot facility up to 30 L/h of hydrogen with the S–I cycle. It aims to scale up the S–I cycle to much larger production capacities that could eventually support a significant volume of fuel cell vehicles.

The three reactions that produce hydrogen in the S–I cycle are shown as follows:

- $I_2 + SO_2 + 2H_2O \rightarrow 2HI + H_2SO_4$ (120°C)
- $2H_2SO_4 \rightarrow 2SO_2 + 2H_2O + O_2$ (830°C)
- $2HI \rightarrow I_2 + H_2$ (450°C)

In the first step, sometimes called the Bunsen reaction, HI is produced and then separated by distillation. Concentrated H_2SO_4 may react with HI, giving I_2, SO_2, and H_2O (back reaction). In the second step, the water, SO_2, and residual H_2SO_4 must be separated from the oxygen, typically by condensation. Iodine and any accompanying water or SO_2 are separated by condensation in the last step of the cycle, while hydrogen gas is produced as the main product.

The S–I cycle has been extensively developed, as it has a number of key advantages over other thermochemical cycles. For example, all of the working fluids exist in the liquid or gas phase; therefore, there is no solid handling, and the processes are well suited for continuous operation. The S–I cycle is more developed than other cycles. Another advantage is that hydrogen can be generated at high pressure (50 atmospheres), which eliminates the need for compressing the hydrogen for downstream utilization.

However, very high temperatures are required (at least 850°C). Corrosive reagents are used as intermediaries (iodine, sulfur dioxide, hydriodic acid, sulfuric acid); thus, advanced materials of construction are needed. Also, separation of the dense liquid phase from the acid-generating reaction into HI and I_2 is accomplished by extracting water into concentrated phosphoric acid, leading to a large recycle of phosphoric acid through a dehydration system that is capital intensive.

8.1.3 Hybrid Sulfur Cycle (Also Known as Westinghouse, GA-22, or Ispra Mark)

This variation of the S–I cycle reduces the number of steps by incorporating an electrolysis step:

- $H_2SO_4(g) \rightarrow SO_2(g) + H_2O(g) + 1/2O_2(g)$ (850°C)
- $SO_2(aq) + 2H_2O(l) \rightarrow H_2SO_4(aq) + H_2(g)$ (80°C electrolysis)

The cycle is still an all-fluid process, and it has the additional advantage of reducing the number of reactions and cycle complexity. The thermodynamic properties of the chemical compounds are well known, and side reactions are minimal. A demonstration pilot plant was developed and built by the Commission of the European Communities at the Ispra Research Establishment. The first step, called the sulfuric acid decomposition step, was demonstrated using concentrated solar energy from a solar power tower. However, there are some disadvantages, including an electrochemical process that has inherent scale-up problems and limitations due to the surface area of the electrodes. Scaling up beyond the maximum practical electrode area requires additional modules.

8.1.4 University of Tokyo 3 Cycle

This cycle consists of four chemical reaction steps as follows:

- $2Br_2(g) + 2CaO(s) \rightarrow 2CaBr_2(s) + 1/2O_2(g)$ (672°C)
- $3FeBr_2(s) + 4H_2O(g) \rightarrow Fe_3O_4(s) + 6HBr(g) + H_2(g)$ (560°C)
- $CaBr_2(s) + H_2O(g) \rightarrow CaO(s) + 2HBr(g)$ (760°C)
- $Fe_3O_4(s) + 8HBr(g) \rightarrow Br_2(g) + 3FeBr_2(s) + 4H_2O(g)$ (210°C)

This cycle is based on solids; however, the solid materials remain in fixed beds and only gaseous products are transported. The cycle has a reported efficiency of 40%. Disadvantages include an inability to operate in a steady-state mode unless there is movement of solids. The solid materials must be periodically changed from one temperature to another, which in addition occurs near the melting point of the bromides. If melting occurs due to temperature variations, the transport of molten bromides could lead to problematic blockage of the beds. A substantial amount of research has been done on this cycle since the initial invention and development at the University of Tokyo (Aihara et al. 1990; Sakurai et al. 1996). This cycle has been operated on a large pilot plant scale in Japan (Nakayama et al. 1984). The most recent theoretical and experimental work on this cycle has been done at the University of Florida and the University of South Florida by the Goswami Group (Lee et al. 2006, 2007, 2009). The group has developed an innovative method of immobilizing the solid reactants on woven alumina and yttria fabrics, which provides a much larger surface area for reactions than the porous pellets used by the University of Tokyo group and allows the gaseous reactants to pass through while reacting. This method also provides adequate volumetric space for the reactants as they expand and contract during the cyclic reactions. They evaluated the perfor- mance by cyclic bromination and hydrolysis reactions. Based on the experimental results in the cyclic reactions, the calcium oxide on the yttria fabric had continuous higher reactivity in the bromination reaction, and the rate of the hydrolysis reaction was comparable to or faster than that of the calcium oxide pellets in the previous studies (Lee et al. 2009).

8.1.5 Ispra Mark 9 Cycle

This cycle involves three chemical reactions, including processes that involve separation and movement of solids:

- $3FeCl_3(l) \rightarrow 3/2Cl_2(g) + 3FeCl_2(s)$ (420°C)
- $3/2Cl_2(g) + Fe_3O_4 + 6HCl \rightarrow 3FeCl_3 + 3H_2O + 1/2O_2(g)$ (150°C)
- $3FeCl_2(s) + 4H_2O(g) \rightarrow Fe_3O_4(s) + 6HCl(g) + H_2(g)$ (650°C)

It has been shown experimentally that $FeCl_3$ decomposition and hydrolysis of $FeCl_2$ to iron oxides were critical and difficult problems for which there has been no suitable solution found; thus, there has been no further development of this cycle.

8.1.6 Vanadium-Chlorine Cycle

The V–Cl cycle consists of four reaction steps as follows:

- $Cl_2(g) + H_2O(g) \rightarrow 2HCl(g) + 1/2O_2(g)$ (850°C)
- $2HCl(g) + 2VCl_2(s) \rightarrow 2VCl_3(s) + H_2(g)$ (25°C)

- $4VCl_3(s) \rightarrow 2VCl_4(g) + 2VCl_2(s)\,(700°C)$
- $2VCl_4(l) \rightarrow Cl_2(g) + 2VCl_3(s)\,(25°C)$

All of the process chemistry has been demonstrated by proof-of-principle experiments. One of the disadvantages is that the cycle involves processing and handling of solids. The HCl(g) and O_2(g) in the first step should be separated without the use of water. Any remaining water in the HCl would produce VOCl as a by-product of the second step. A variation of this V–Cl cycle was examined with flow sheets by the University of Aachen, with a calculated efficiency of 42.5%.

8.1.7 Copper-Chlorine Cycle

Most of the thermochemical cycles require process heat over 800°C. Due to lower temperature requirements of about 550°C and lower, the Cu–Cl cycle is a promising alternative that could be eventually linked with next-generation nuclear reactors, such as Canada's supercritical water reactor (SCWR). The Cu–Cl cycle has numerous advantages over the other existing cycles of hydrogen production. It has much lower operating temperatures than other thermochemical cycles, thereby potentially reducing material and maintenance costs. Also, it can effectively utilize low-grade waste heat, thereby improving cycle and power plant efficiencies. Other advantages include lower demands on materials of construction, common chemical agents, and reactions going to completion without side reactions. Disadvantages include solids handling and a high steam-to-copper ratio in the hydrolysis step, although ongoing advances are steadily decreasing this steam requirement.

The Cu–Cl cycle has been identified by Atomic Energy of Canada Limited (AECL) (Chalk River Laboratories [CRL]) as the most promising cycle for thermochemical hydrogen production with SCWR. Current collaboration between the University of Ontario Institute of Technology (UOIT), AECL, and the Argonne National Laboratory is focusing on enabling technologies for the Cu–Cl cycle, through the Generation IV International Forum (GIF). The remainder of this chapter presents the recent advances in the development of the copper–chlorine cycle for thermochemical water decomposition and hydrogen production.

8.2 Overview of the Thermochemical Cu–Cl Cycle

The Cu–Cl thermochemical cycle uses a series of reactions to achieve the overall splitting of water into hydrogen and oxygen as follows: $H_2O(g) \rightarrow H_2 + 1/2O_2$. The Cu–Cl cycle splits water into hydrogen and oxygen through intermediate copper and chlorine compounds. These chemical reactions form a closed internal loop that recycles all chemicals on a continuous basis, without emitting any greenhouse gases. Steps in the Cu–Cl cycle and a schematic realization of the cycle are shown in Table 8.1 and Figure 8.1, respectively. Table 8.2 shows the heat requirements of each individual step within the overall cycle.

Decomposing water into hydrogen and oxygen requires that sufficient energy be provided to break the chemical bond of hydrogen and oxygen atoms. From a thermodynamic perspective, the minimum enthalpy is equal to the formation enthalpy of water, that is, 286 kJ/mol (denoted as ΔH_f), if water, hydrogen, and oxygen are all contained at atmospheric pressure and 25°C. However, a series of intermediate processes is required to split water in the Cu–Cl cycle. As a consequence, the energy required to split water will also be a function of the processes, not solely the thermodynamic state alone. Table 8.2 summarizes the heat requirements for each individual step within the Cu–Cl cycle (Naterer et al. 2011a,b).

TABLE 8.1

Chemical Reaction Steps in the Cu–Cl Cycle

Step	Reaction	Temperature Range (°C)	Feed/Output[a]	
1	$2Cu(s) + 2HCl(g) \rightarrow 2CuCl(l) + H_2(g)$	430–475	Feed:	Electrolytic Cu + dry HCl + Q
			Output:	H_2 + CuCl(l) salt
2	$2CuCl(s) \rightarrow 2CuCl(aq) \rightarrow CuCl_2(aq) + Cu(s)$	Ambient (electrolysis)	Feed:	Powder/granular CuCl and HCl + V
			Output:	Electrolytic Cu and slurry containing HCl and $CuCl_2$
3	$CuCl_2(aq) \rightarrow CuCl_2(s)$	<100	Feed:	Slurry containing HCl and $CuCl_2$ + Q
			Output:	Granular $CuCl_2$ + H_2O/HCl vapors
4	$2CuCl_2(s) + H_2O(g) \rightarrow CuO*CuCl_2(s) + 2HCl(g)$	400	Feed:	Powder/granular $CuCl_2$ + $H_2O(g)$ + Q
			Output:	Powder/granular $CuO*CuCl_2$ + 2HCl(g)
5	$CuO*CuCl_2(s) \rightarrow 2CuCl(l) + 1/2O_2(g)$	500	Feed:	Powder/granular $CuO*CuCl_2(s)$ + Q
			Output:	Molten CuCl salt + oxygen

Note: Alternative 4-step cycle combines above steps 1 and 2 to produce hydrogen directly as follows: $2CuCl(aq) + 2HCl(aq) \rightarrow H_2(g) + 2CuCl_2(aq)$ (Figure 8.1 illustrates this 4-step version of Cu–Cl cycle).

[a] Q, thermal energy; V, electrical energy.

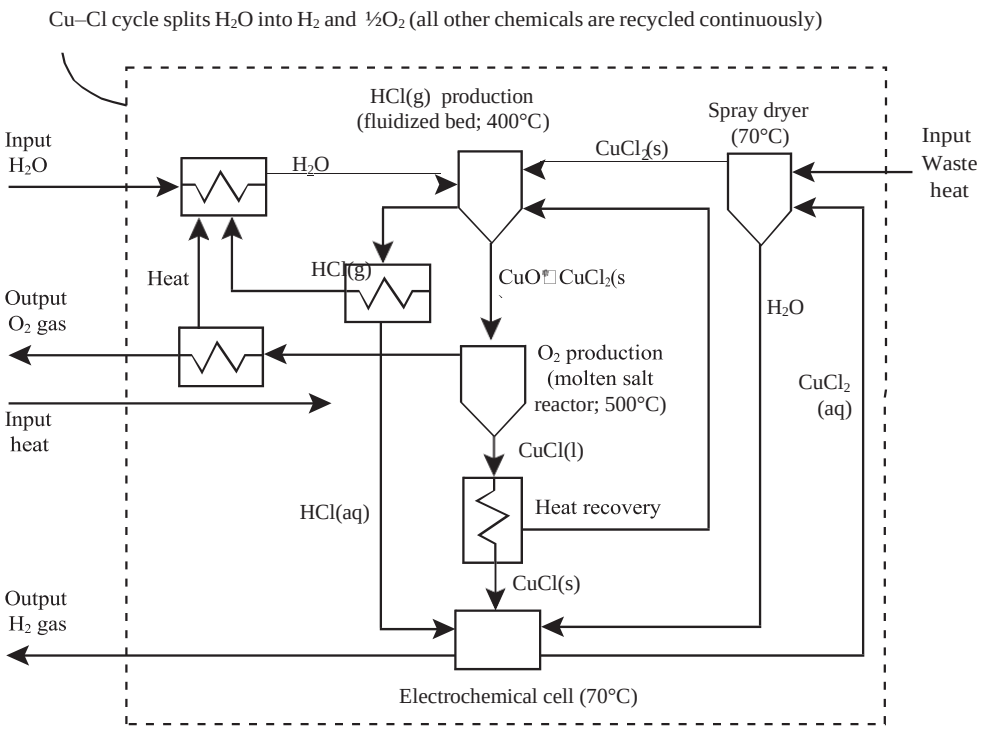


FIGURE 8.1

Schematic of the 4-step copper–chlorine cycle.

TABLE 8.2

Heat Requirements of Individual Steps and the Efficiency of Cu–Cl Cycle

Step	Processes in the Step	T °C	Heat in Case 3-A Drying: Total kJ/mol H_2	Heat in Case 3-A Drying: Low grade kJ/mol H_2	Heat in Case 3-B Drying: Total kJ/mol H_2	Heat in Case 3-B Drying: Low grade kJ/mol H_2	Heat Output kJ/mol H_2
1	$2Cu(s) + 2HCl = 2CuCl(l) + H_2(g)$						
	Hydrogen production step						
	Vaporizing moisture form Cu(s)	35 → 70	29.0	29.0	29.0	29.0	
	Heating Cu(s)	25 → 450	23.4	0.3	23.4	0.3	
	Heating HCl(g)	25 → 450	3.0	0.1	3.0	0.1	
	Heat of reaction	450					46.8
	Cooling and solidification of molten CuCl	450 → 25					80.8
	Cooling of $H_2(g)$ product	450 → 25					12.2
2	$4CuCl(aq) = 2CuCl_2(aq) + 2Cu(s)$	35–70	Electrical energy 62.6 kJ/mol H_2				
	Electrolysis step in HCl solution						
3	$2CuCl_2(aq) \rightarrow 2CuCl_2(s)$						
	Drying step						
3-A	Vaporizing water from $CuCl_2$ *precipitate*	35 → 70	122.0	122.0			
	$2.2H_2O(l) \rightarrow 2.2\ H_2O(g)$						
3-B	Vaporizing water from $CuCl_2$ *solution*	35 → 70			931	931	
	$16.7H_2O(l) \rightarrow 16.7\ H_2O(g)$						
4	$2CuCl_2(s) + H_2O(g) = CuOCuCl_2(s) +$ $2HCl(g)$						
	Hydrolysis step						
	Heating $CuCl_2(s)$	25 → 375	54.2	8.5	54.2	8.5	
	Heat of reaction	375	116.6		116.6		
	Steam production $H_2O(l) = H_2O(g)$	25 → 375	57.1	3.4	57.1	3.4	
5	$CuOCuCl_2(s) \rightarrow 2CuCl(l) + 1/2O_2(g)$						
	Oxygen production step						
	Heating $CuOCuCl_2(s)$	375 → 530	20.2		20.2		
	Heat of reaction	530	129.2		129.2		
	Cooling and solidification of molten CuCl	530 → 25					84.8
	Cooling of $O_2(g)$ product	530 → 25					7.4
	Sum	kJ/mol H_2	554.7	163.3	1363.7	972.3	232
		kJ/g H_2	277.4	81.7	681.9	486.2	116
	Percentage of low-grade heat			29.5%		71.3%	

Efficiency of Cu–Cl cycle										
Percentage of heat loss to environment (%)	0	0	20	20	20	20	20	20		
Percentage of recycled heat internally within the cycle (%)	0	100	0	30	50	70	90	100		
Practical efficiency of Cu–Cl cycle (%)	46	74	37	41	44	47	51	53		

Low-grade heat: The heat with a temperature that is lower than 70°C.

Thermochemical water decomposition with the Cu–Cl cycle is much more efficient than electrolysis via thermal power plants, because heat is used directly to produce hydrogen, rather than indirectly to first produce electricity, after which hydrogen is generated. A 42% efficiency (electricity) with Canada's next-generation reactor leads to about 30% net efficiency by electrolysis for hydrogen production. In contrast, a 54% heat-to-hydrogen efficiency has been demonstrated from Aspen Plus simulations for the Cu–Cl cycle (Lewis et al. 2005), although 43% is more realistic. This implies a sig- nificant margin of superior overall conversion efficiency, with more than one-third improvement over electrolysis, excluding even larger gains if *waste heat* is utilized in the thermochemical cycle.

A unique advantage of the Cu–Cl cycle is an ability to utilize low-grade *waste heat* from power plants or other sources to aid hydrogen production, rather than rejecting that heat to the environment (such as a nearby lake). This could significantly improve the econom- ics of hydrogen production, as well as potentially provide for the generation of electricity. For example, a nuclear plant's efficiency usually refers to electricity output alone, but the *efficiency* or output of an overall system to cogenerate electricity and hydrogen is higher than electricity generation alone, if waste heat contributes to the production of another valuable energy carrier, hydrogen, from the same nuclear heat source. The Cu–Cl cycle's efficiency implies that the heat supply comes at some *cost*. But if low-grade waste heat is utilized as a heat source at minimal or no cost, then the economics of hydrogen produc- tion is further improved and more attractive than other high-temperature thermochemical cycles that cannot use such low-grade heat.

Heat exchangers represent an important component within the Cu–Cl cycle. Between each step of the Cu–Cl plant, heat exchangers are needed for heat input/recovery and fluid transport between different steps of the thermochemical cycle. The oxygen produc- tion step has the highest temperature requirement (530°C) in the cycle. Since temperature drops are experienced across each heat exchanger, the inflow stream to the oxygen reactor must exceed 530°C. Furthermore, multiple heat exchangers are needed between the heat source and the oxygen reactor (step 5), through an intermediate loop. An intermediate loop with several heat exchangers in series is needed to give progressively higher tem- peratures. Ongoing research is underway to determine how flow rates, temperatures, and fluid streams should be most effectively partitioned for each step of the Cu–Cl cycle. Also, heat losses must be identified and evaluated throughout the piping network, with new methods developed for heat recovery.

Several types of fluid devices are used throughout the hydrogen plant, including chemi- cal reactors, electrochemical cells, heat exchangers, pumps, valves, pipes, and blowers (for gases). Certain components require substantial modifications of existing technologies with new materials to be economically viable in extreme operating conditions of high-tem- perature corrosive fluids. For example, common refractory materials for heat exchangers have poor thermal conductivity. Also, high-performance metal alloys cannot withstand corrosive fluids over a long duration. High-temperature alloys with coatings of silicone-based ceramics appear promising, but their thermal behavior and surface interactions in high-temperature multiphase conditions must be further developed. Further data are also needed to better understand the functionality of these materials with the working fluids in the Cu–Cl cycle. This includes thermal behavior, mechanical stresses, fracture tough- ness, strength, and corrosion resistance over time. Improvements to existing equipment can then be achieved through new materials developed specifically for operating condi- tions of the Cu–Cl cycle.

8.3 Thermochemical Reaction of Hydrogen Production

8.3.1 Proof-of-Principle Demonstrations

Two possible variations of the Cu–Cl cycle are depicted in Table 8.1: a 5-step and a 4-step (Figure 8.1) cycle. Step 1 in the 5-step Cu–Cl cycle is the H_2 production step, which occurs at 430°C–475°C, characterized by the reaction $2Cu(s) + 2HCl(g) \rightarrow H_2(g) + 2CuCl(l)$. Copper parti- cles enter the reactor vessel and react with HCl gas to generate H_2 gas and molten CuCl at the exit. Scientific practicality of this chemical reaction has been demonstrated experimentally by Serban et al. (2004). The experiments were conducted in a ½ in. by 14 in. quartz vertical reac- tor, as shown in Figure 8.2. All connecting lines and valves were made of Teflon. Anhydrous hydrochloric acid (99.99%), chlorine (99.99%), and argon (99.996%) were fed to the microreac- tors. The temperatures were controlled by Omega CN375–type temperature controllers con- nected to a Lindberg single-zone heated furnace, monitored with K-type thermocouples. The vertical reactor was connected online to a quadrupole mass spectrometer (QMS) 200 to con- tinuously monitor the hydrogen production. The mass spectrometer was calibrated for H_2, O_2, HCl, and Cl_2 using mixtures of pure gases with Ar over a wide range of compositions.

The reaction kinetics were investigated using only reagent-grade reactants of high purity. The experiments were conducted in beds of solid material with a continuous flow of excess gaseous reactants. Constant temperatures in any one experiment were assumed.

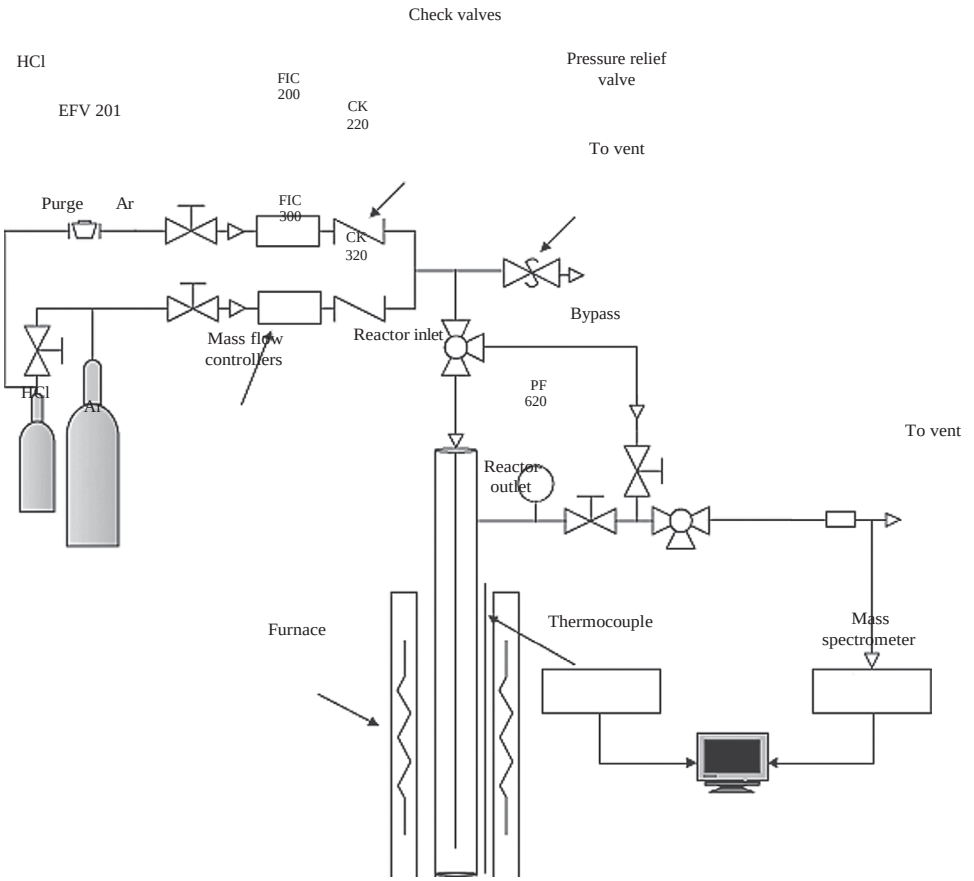


FIGURE 8.2

Lab-scale apparatus for the hydrogen and oxygen production reactions. (Adapted from Serban, M. et al. Kinetic study of the hydrogen and oxygen production reactions in the copper-chloride thermochemical cycle, in *AIChE 2004 Spring National Meeting*, New Orleans, LA, April 25–29, 2004.)

The kinetics analysis provided apparent activation energy values, where the internal mass diffusion limitations were not included (Serban et al. 2004). The reaction between HCl and Cu is a heterogeneous exothermic and reversible reaction. Experiments indicated that at low temperatures, the kinetics of the reaction were very slow. The kinetics of the reaction were accelerated at temperatures above the melting point of CuCl (423°C), facilitating the interaction between HCl and Cu. These results were surprising, since it was reported that the exothermic reaction between Cu and HCl should proceed rapidly at 230°C and 93% of HCl should be decomposed. However, no hydrogen was detected at this temperature, even though the Gibbs free energy change is −5.66 kcal at 230°C. In addition, it is believed that CuCl forms a passivating layer on the surface of the Cu particles. At 430°C–435°C, the CuCl starts to melt, facilitating the interaction between HCl and Cu. Similar experiments performed with Ag and HCl indicate the same behavior.

In an attempt to find the best experimental conditions for complete Cu conversion to CuCl and H_2, experiments were performed with varying sizes and shapes of Cu particles as well as varying HCl flow rates. The conversion of HCl to hydrogen was found to be a function of Cu particle size as shown in Figure 8.3 (Serban et al. 2004). The yields varied between 65% and 100%, with complete conversion in the case of 3 μm Cu particles. Yields were lower in the case of the larger 100 μm Cu particles, which were obtained in an electrolytic cell by dispropor- tionating CuCl to Cu and $CuCl_2$, a step that is an integral part of the overall thermochemical water-splitting cycle. The size and shape of the electrolytic copper particles varied with the operating parameters of the cell, which were not optimized for the subsequent experiments. All kinetic experiments were conducted using commercial dendritic 3 μm Cu particles. To directly measure the kinetics of the reaction between HCl and Cu, the reaction rates were measured at four different temperatures (400°C, 425°C, 450°C, and 475°C), and the molar ratio of HCl in Ar was varied between 0.33 and 0.67. A rate expression was obtained. The hydrogen yields were determined by comparing the measured amount of hydro- gen produced vs. the stoichiometric amount of hydrogen that would be formed if all of

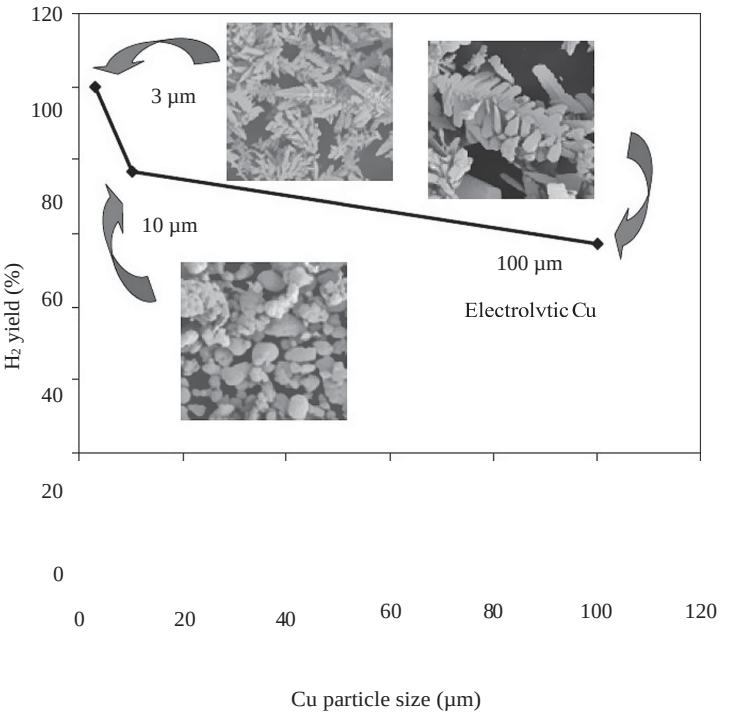


FIGURE 8.3

Hydrogen yields as a function of Cu particle size—fixed bed reactor, temperature = 450°C, HCl flow rate = 2.5 cm^3/min, 0.5 g of commercial (3 and 10 μm particle size), and electrolytic Cu (100 μm particle size). (Adapted from Serban, M. et al. Kinetic study of the hydrogen and oxygen production reactions in the copper- chloride thermochemical cycle, in *AIChE 2004 Spring National Meeting*, New Orleans, LA, April 25–29, 2004.)

the Cu were oxidized to CuCl (Serban et al. 2004). Hydrogen yields decreased with increasing Cu particle size, indicating that high surface areas of contact between HCl and Cu are necessary for high hydrogen yields (could be due to diffusion limitation). Figure 8.3 shows scanning electron microscope (SEM) images of the spheroidal and dendritic Cu particles used in the hydrogen generation reaction. No gaseous products other than hydrogen and HCl were observed in the effluent stream. X-ray diffraction (XRD) examination of the solid product resulting from the reaction showed patterns only for CuCl and Cu. Apparently, no secondary reactions are favored in the temperature range studied. Thermodynamic computations indicate that when CuCl(s) is heated to very high temperatures, CuCl(g) is formed, which would then spontaneously decompose to Cu and Cl_2. No Cl_2 was detected on the mass spectrometer at any time, suggesting that the extent of CuCl vaporization was negligible.

8.3.2 Design Issues of Hydrogen Reactor Scale-Up

If the net heat output from the exothermic reactor is only absorbed by hydrogen as the product of the reaction, then it can be shown that the temperature of hydrogen will reach about 1244°C. On the other hand, if the net heat is solely consumed by molten CuCl, then its temperature will rise by 180°C up to 639°C. If the net heat is consumed by both products, H_2 and molten CuCl, both temperatures will rise by 153°C up to a product temperature of 603°C. If this product temperature is higher than 550°C, then generation of CuCl vapor will become significant, thereby requiring separation of gaseous products from the exit stream. An operating temperature near 530°C is needed in the oxygen-producing process (step 5 of the Cu–Cl cycle; Table 8.1), where molten CuCl is also produced. As a result, heat generated from the exothermic hydrogen reactor can be supplied to the endothermic oxygen reactor, by controlling the heat output from the exothermic reactor. Assuming the highest temperature allowed in the hydrogen reactor is 530°C, it can be shown that the required heat to be removed from the exothermic reactor per kg of hydrogen is

$$\Delta H_{remove} = \left(c_P^{H_2} + 2 * c_P^{CuCl}\right) * (603 - 530) = 11.4 \text{ kJ} \tag{8.1}$$

where c_P refers to the specific heat. In practice, an excess quantity of HCl reactant gas is needed, which reduces the product temperature. Assuming a lower temperature of 450°C for the products (H_2 gas and molten CuCl), inlet temperature of Cu(s) of 80°C from the upstream cell, and 400°C inlet temperature of HCl gas, the net heat removed from the reactor per kg of hydrogen becomes

$$\Delta H_{remove} = \left(c_P^{H_2} + 2 * c_P^{CuCl}\right) * (603 - 450) = 23.9 \text{ kJ} \tag{8.2}$$

Effective recycling of heat released by the reactor to other steps within the Cu–Cl cycle is critical to improving the heat-to-hydrogen efficiency of the cycle. This thermochemical step provides a valuable high-temperature source of exothermic heat supply to other reactors.

8.4 Electrochemical Process of Copper or Hydrogen Production

8.4.1 Introduction

An electrochemical process is required, either separately from the hydrogen reaction (5-step Cu–Cl cycle) or combined together as $2CuCl + 2HCl \rightarrow 2CuCl_2 + H_2$ (4-step Cu–Cl cycle in Table 8.1 and Figure 8.1). This section investigates the latter process of cuprous

chloride/HCl electrolysis, whereby oxidation of cuprous chloride (CuCl) during an electrochemical reaction occurs in the presence of hydrochloric acid (HCl) to generate hydrogen. In the electrolysis process, the cuprous ion is oxidized to cupric chloride at the anode, and the hydrogen ion is reduced at the cathode. Electrolysis has similar characteristics as fuel cells but has the opposite objectives.

The two-phase flow in a direct methanol fuel cell (DFMC) is similar to flow that occurs in an electrolytic cell. Yan and Jen (2008) simulated the latter flow conditions and examined how the performance of the fuel cell was affected by temperature, pressure, and concentration of methanol. Naterer and Tokarz (2006) examined the entropy production in proton exchange membrane fuel cells (PEMFC). This section will present a similar study to characterize irreversible losses in an electrochemical cell of cuprous chloride electrolysis. Electrochemical mass transfer generates entropy, which increases the voltage losses. Mass transfer processes in rotating and large–Lewis number electrochemical cells have been examined by Weng et al. (1998) and Jiang et al. (1996), respectively. Voltage losses in electrochemical systems can be characterized effectively by entropy and the second law (Naterer and Camberos 2008).

Consider an electrochemical process involving electrolysis of cuprous chloride to produce hydrogen in Figure 8.4. The electrical circuit is completed by a resistor, ammeter, and dc voltage source connected by external wiring from one electrode to another. It is assumed that CuCl is supplied continuously to the anode, while HCl is supplied to the cathode. The working electrode is assumed to be platinum (Pt) on a gas diffusion layer (GDL). The electrolyte used on the anode side of the cell is a mixture of HCl and CuCl, while HCl is adopted on the cathode side. The operating parameters replicate conditions of experimental studies conducted by AECL (Stolberg et al. 2007).

Electrochemical reactions differ from chemical redox reactions in the way that reactions occur within the cell. Chemical redox reactions occur at the same location, while electrochemical reactions occur in two different sections of the cell, that is, anode and cathode, respectively. For this reason, the reactions in an electrolytic cell are split up into two half-cell reactions: anodic and cathodic reactions. The anodic half-cell reaction for the oxidation of copper (I) to copper (II) can be represented as

$$2CuCl + 2HCl \rightarrow 2CuCl_2 + 2H^+ + 2e^- \tag{8.3}$$

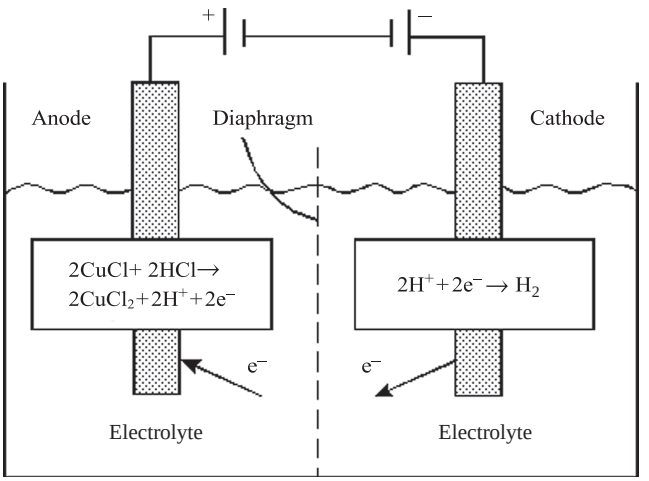


FIGURE 8.4

Schematic of the electrochemical cell.

When CuCl dissolves in 6 M HCl, anionic copper(I) chloride complexes such as $CuCl_2^-$ and $CuCl_3^{2-}$ are formed. Some possible oxidation reactions are given in the following:

$$CuCl_2^-(aq) \rightarrow Cu^{2+}(aq) + 2Cl^-(aq) + e^- \tag{8.4}$$

$$CuCl_2^-(aq) + Cl^-(aq) \rightarrow CuCl_3^-(aq) + e^- \tag{8.5}$$

$$CuCl_3^{2-}(aq) \rightarrow Cu^{2+}(aq) + 3Cl^-(aq) + e^- \tag{8.6}$$

The anodic reactions may involve a number of complexes, many of which have not yet been completely identified. The cathodic half-cell reaction for the reduction of hydrogen protons to hydrogen gas is represented as

$$2H^+ + 2e^- \rightarrow H_2 \tag{8.7}$$

Both the cathode and desired anode reactions can be combined as one reaction, based on the principles of conservation of charge and electron neutrality. As a result, the overall cell reaction can be written as

$$2CuCl + 2HCl \rightarrow 2CuCl_2 + H_2 \tag{8.8}$$

Introducing an electric field across the electrolyte generates a driving force for the ions dissolved in it. While electrons flow through the electrode, as a result of the applied current, ions in the electrolyte migrate as a result of diffusive and convective modes of transport.

8.4.2 Proof-of-Principle Experiments

Scientific viability of the process has been demonstrated experimentally by AECL (Stolberg et al. 2007). Important parameters studied include the chemical kinetics in the electrochemical cell, as a function of temperature, pressure, and compositions. A schematic of the experimental layout is illustrated in Figure 8.5. The copper(I) oxidation reaction is carried out using a 6 M HCl electrolyte. The anodic reaction has been found to require no noble metal catalyst and proceeds quite readily on graphite electrodes. However, the hydrogen production cathodic reaction requires a catalyst. Half-cell studies show that the rate of the CuCl/HCl electrolysis reaction should increase with temperature and CuCl concentration, when the reaction proceeds under mass transfer control. Also, it has been shown that copper crossover from the anolyte to the catholyte causes an increase in the cell voltage during constant current electrolysis experiments. Copper must, therefore, be removed from the catholyte.

In the benchtop experiments at AECL, a variety of electrode materials was tested, and hydrogen production was consistently observed at potentials as low as 0.5 V. However, typically around 0.65 V was required to achieve good current density. The results indi- cate that the reaction is feasible at reasonably low potentials and with inexpensive elec- trode materials. Current densities are low and fall from an initial value to a stable plateau. Sample results are shown in Figure 8.6. The current density can be improved considerably by changes to the cell's configuration and improvement of the electrodes.

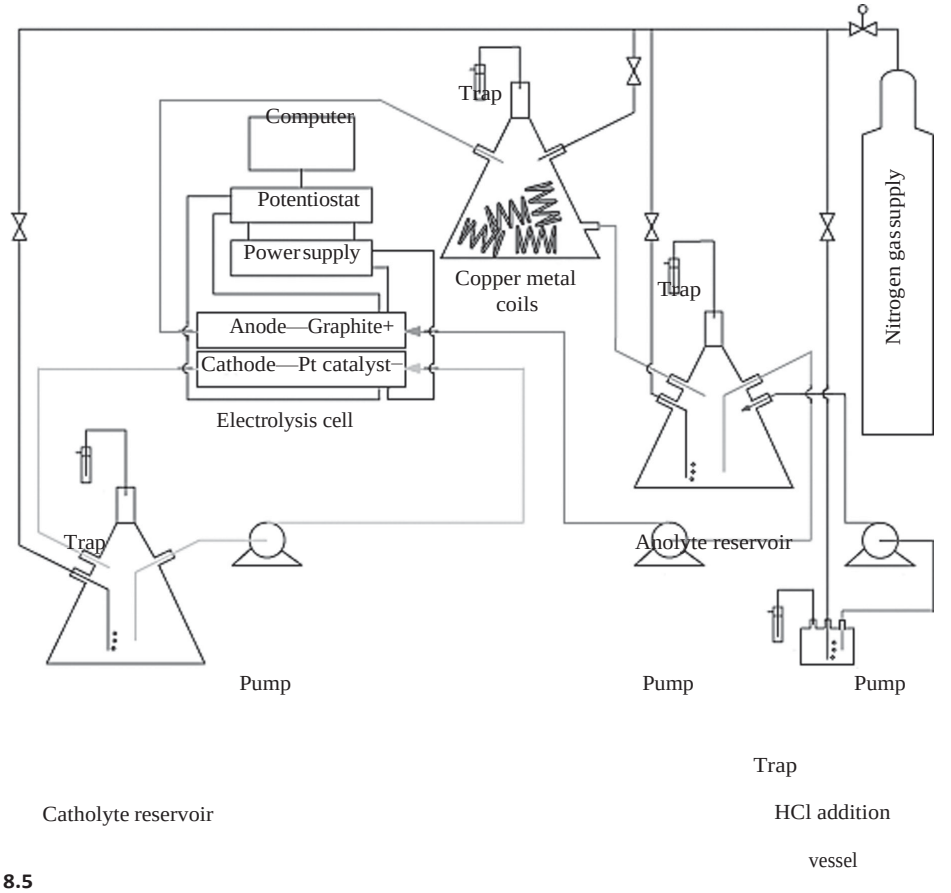


FIGURE 8.5

Experimental configuration of the electrochemical cell. (Adapted from Stolberg, L., et al. Recent advances at AECL in the Cu-Cl cycle for nuclear-produced hydrogen, in *ORF Workshops on Thermochemical Nuclear-Based Hydrogen Production*, Oshawa, ON, December 2007 and Chalk River, ON, October 2008.)

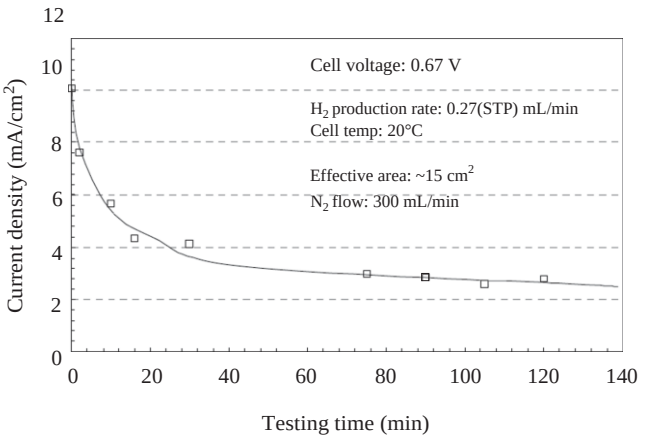


FIGURE 8.6

Typical current density for electrolysis of HCl/CuCl in a continuous system. (Adapted from Stolberg, L. et al., Recent advances at AECL in the Cu-Cl cycle for nuclear-produced hydrogen, in *ORF Workshops on Thermochemical Nuclear-Based Hydrogen Production*, Oshawa, ON, December 2007 and Chalk River, ON, October 2008.)

8.4.3 Predictive Formulation of Hydrogen Electrolysis

The voltage loss in the electrolysis cell includes the surface overpotential, ohmic overpotential, and the concentration overpotential. These losses are known to significantly affect the voltage losses across the cell, and hence they should be included in design considerations for the electrolytic cell. The activation losses can be interpreted as the voltage required in overcoming the open circuit voltage of the cell, when no load is connected in the circuit. Ohmic losses occur as a result of the internal resistance of the cell. Entropy generation in the electrolytic cell is a measure of these irreversibilities and voltage losses within the cell. The entropy generation associated with overpotentials discussed previously can be expressed as (Naterer et al. 2006)

$$\eta = \frac{TP_{act}}{2F} \tag{8.9}$$

where

P_{act} is the entropy generation

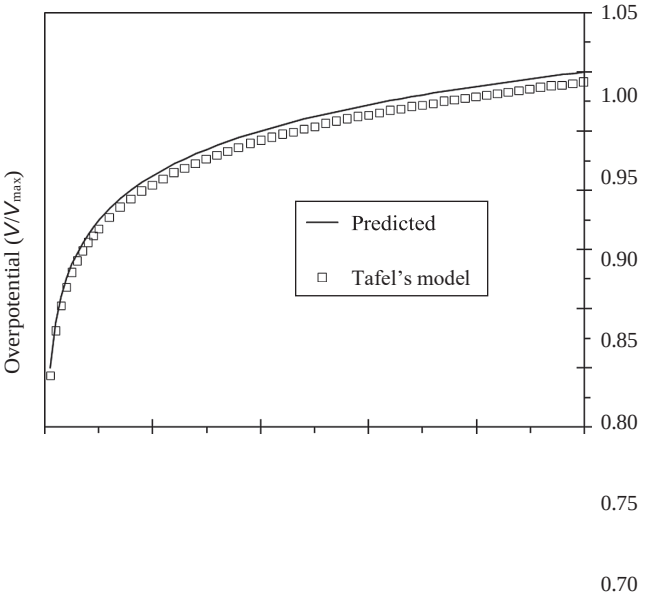
T is the operating temperature of the cell

It can be shown that

$$P_{act} = \frac{2F}{T}\left[\text{ROCV} - \left(ir + \frac{RT}{Z\alpha F}\ln\left(\frac{i}{i_o}\right)\right)\right] \tag{8.10}$$

From this equation, it can be observed that entropy production is dependent on temperature, current density, exchange current density, and charge transfer coefficient. In the previous equations, F is Faraday's constant (96,785 C/mol), η is overpotential (mV), Z is number of electrons, i is current density (mA/cm^2), i_o is exchange current density (A/cm^2), α is charge transfer coefficient, and r is electrical resistance (kΩ).

Comparisons between the predicted results and Tafel's model, as well as past experimental data (Stolberg et al. 2007), are shown in Figure 8.7 and Table 8.3, respectively. Close agreement between the results provides a useful validation of the predictive formulation.



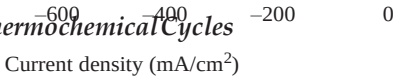


FIGURE 8.7

Comparison between predicted results and Tafel's model for CuCl electrolysis.

Free ebooks ==> www.Ebook777.com

TABLE 8.3

Comparison between Predicted and Measured Data

Operating Parameters	Measured	Predicted
Operating temperature of cell (T)	298.15 K	298 K
Activation potential (V_{act})	0.277 mV	0.261 mV
Current density (i)	250 mA/cm^2	250 mA/cm^2
ROCV	0.511 mV	0.515 mV

Source: Adapted from Naterer, G.F. et al. *International Journal of Hydrogen Energy* 36, 15472–15485, 2011a.

Table 8.3 shows that the magnitudes of the predicted overpotential in the formulation show close agreement with experimental half-cell data reported previously for cupric chloride electrolysis. The activation overpotential was measured experimentally (Stolberg et al. 2007) and compared against predicted results in Table 8.3, where it can be observed that the activation potential shows only about a 6% difference between the experimental activation potential and the predicted results. This relatively small difference may have occurred due to the measured uncertainty of reversible open circuit voltage (ROCV), as well as other forms of copper ions or impurities present in the cell.

8.5 Drying of Aqueous Cupric Chloride

8.5.1 Introduction

The drying step of the Cu–Cl cycle is given by $2CuCl_2(aq) \rightarrow 2CuCl_2(s)$. An aqueous $CuCl_2$ stream exiting from the electrochemical cell is supplied to a spray dryer to produce solid $CuCl_2(s)$, which is required for a subsequent hydrolysis step that produces copper oxychloride ($CuO*CuCl_2$) and HCl gas. The apparatus must add sufficient heat to evaporate and remove the water. The process is an energy-intensive step within the Cu–Cl cycle. Although the amount of heat required for the drying step is much higher than the other steps in the cycle, it is of lower temperature (lower quality) and therefore more readily available. Within the drying step, the energy requirement increases from 1 to 5 times for slurry feed to solution, depending on the $CuCl_2$ concentration. The overall cycle efficiency is higher with slurry feed in the drying step than drying aqueous solution. The heat required can be supplied from low-grade waste heat to improve the cycle efficiency. Commercial spray dryers are available for similar processes (used commercially for the production of powders, detergents, food products, and so forth). But further research is needed in the equipment for aqueous cupric chloride, particularly to determine whether aqueous or precipitate slurry from the electrochemical cell should be spray dried. Spray drying is an efficient method of water removal, due to the relatively large surface area available for heat and mass transfer, provided the liquid atomizes into sufficiently small droplets, on the order of several hundred microns.

Many past studies (Walton 2004; Ambike et al. 2005; Chen and Lin 2005) have examined the spray drying of solutions, emulsions, colloidal mixtures, temperature-sensitive materials, and spray conversions. Lin and Chen (2006) developed a droplet evaporation model based on a reaction engineering approach (REA), which uses a minimum energy barrier (called the activation energy) to activate the evaporation process. They used a characteristic drying rate curve (CDRC) approach, in addition to REA, and performed

www.Ebook777.com

an assessment of accuracy of the different methods. The CDRC approach considers constant and falling-rate periods of drying and relates the specific drying rate to the unhindered drying or constant drying period. The CDRC approach has been widely used in industry, due to its simplicity and ability to handle various chamber parameters.

Drying of aqueous cupric chloride occurs in multiple stages. There is heating of the droplet to the wet-bulb temperature of the surrounding hot air, then droplet evaporation and shrinkage at a constant temperature, after which the concentration of water reaches the critical point and solid crystals precipitate on the surface. Past studies have often assumed a receding interface with a dry core and a constant drying rate period, where fluid transport to the external surface occurs at a rate that matches evaporation. Then, in a falling-rate period, the fluid can no longer reach the surface at the same rate, so the rate of drying falls rapidly and continues until the moisture content falls down to the equilibrium value, then finally drying stops.

Consider a $CuCl_2$ solution with a concentration of 8.2 mol H_2O/mol $CuCl_2$ between 80°C and 100°C, to be dried at a minimum of 300 kPa absolute pressure to 2 mol H_2O/mol of $CuCl_2$ ($CuCl_2 \cdot 2H_2O$ solid). The solubility of $CuCl_2$ in water varies from 9.3 to 7.5 mol H_2O/mol $CuCl_2$ from 30°C to 80°C, and cooling the solution to 30°C leads to precipitate solids and a slurry and solution mixture, from which the solution is eventually recirculated within the Cu–Cl cycle. At these conditions, the slurry with 55% by volume solids contains 3.5 mol H_2O/mol $CuCl_2$. The spray drying occurs when the slurry contacts the drying medium (air) at 80°C. The drying of slurry instead of solution can drastically reduce the energy consump- tion. Under this approach, air heats the droplets until they reach the air wet-bulb tempera- ture. The water vapor concentration difference in air is a driving factor within the process. Analysis of the spray drying process often assumes that both external convection and internal conduction affect the drying process. Typically, hot air heats the droplets (see line J-A in Figure 8.8) until the liquid reaches the saturation point at atmospheric pressure. At this point, evaporation starts and continues (line A-E), as long as the heating temperature is higher than the saturation temperature of the liquid at atmospheric pressure, or the partial vapor pressure of the surrounding air is lower than that of the vapor on the droplet surface. The driving potential becomes a small vapor concentration differential between the droplet surface and surrounding air. This approach makes the drying rate substan- tially slower. Another drying alternative combines flashing and spraying into a chamber at atmospheric pressure, in contact with air preheated at a temperature above the solution temperature. A flashing effect evaporates a small portion of water, instantaneously out of the solution, into a cloud of droplets. The remaining droplets evaporate, subject to the temperature differential between droplets and air.

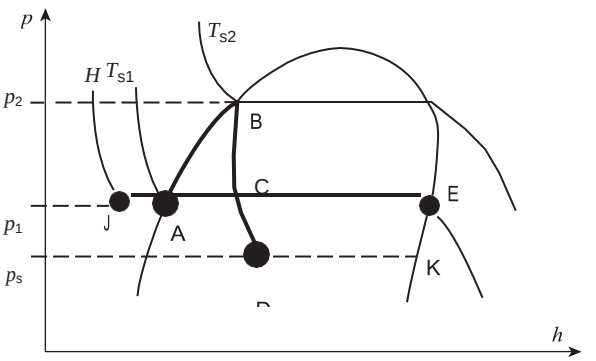


FIGURE 8.8

Pressure–enthalpy diagram for flashing (ABCD) and spraying (JACE) processes.

8.5.2 Predictive Modeling and Scale-Up Design Issues

This section presents a numerical formulation that predicts the spray drying of aqueous cupric chloride droplets. The analysis assumes that the mass and momentum changes of dispersed droplets do not contribute to corresponding changes of the drying medium (air). It also assumes that evaporation results in a continuous shrinkage of the droplet with no solid core formation but rather a continuous growth of $CuCl_2$ crystals, with the average thermal conductivity of the droplet remaining constant.

When the temperature differential between the droplet and air stream is significant, the heat transfer has the following influence on the droplet mass:

$$\frac{dm}{dt} = \frac{hA\left(T_g - T_d\right)}{\lambda} \tag{8.11}$$

where m, t, h, A, T_g, T_d, and λ refer to the droplet mass, time, heat transfer coefficient, droplet surface area, gas temperature, droplet temperature, and evaporation constant, respectively. The Nusselt number (Nu) is defined by the Ranz and Marshall correlation (1952) as follows:

$$\mathrm{Nu} = \frac{hD_d}{k_d} \tag{8.12}$$

$$\mathrm{Nu} = 2 + 0.6\,\mathrm{Re}^{1/2}\,\mathrm{Pr}^{1/3} \tag{8.13}$$

where k_d, D_d, Re, and Pr refer to the droplet conductivity, diameter, Reynolds number, and Prandtl number, respectively. Combining the previous equations and rewriting the result for droplet change in terms of the Spalding number, B, with the correction factor, $(1 + B)^{-0.7}$ (Levi-Hevroni et al. 1995) for the Nusselt and Sherwood numbers, with the Ranz–Marshall correlation, leads to

$$\frac{dD_d}{dt} = -\frac{2k_d\left(1+B\right)^{-0.7}}{\rho_{d,w}D_d\lambda}\left(2 + 0.6\,\mathrm{Re}^{1/2}\,\mathrm{Pr}^{1/3}\right)\left(T_g - T_d\right) \tag{8.14}$$

where the Reynolds number is

$$\mathrm{Re} = \frac{\rho_g\left(V_g - V_d\right)D_d}{\mu_g} \tag{8.15}$$

where V_g, V_d, ρ_g, and μ_g refer to the gas velocity, droplet velocity, density, and viscosity, respectively. The factor $(1 + B)^{-0.7}$ takes into consideration the flow in the boundary layer, and $B = C_{pv}(T_g - T_d)/\lambda$ is the Spalding number. In order to find the droplet shrinkage rate, it can be assumed that the droplet mass decrease is proportional to the droplet diameter shrinkage, thereby leading to the following mass transfer rate:

$$M_v = -0.5\pi\rho_d D^2 \frac{dD_d}{dt} \tag{8.16}$$

Numerical integration of these equations over time results in determination of the drying time of the particle under varying conditions of air humidity and temperature.

The following energy balance equation is used for calculating the droplet/particle temperature change with time:

$$mC_{p,d}\frac{dT_d}{dt} = hA\left(T_b - T_d\right) + \lambda\frac{dm}{dt} \tag{8.17}$$

During a spray drying operation, the selection of inlet and outlet air temperatures has a key influence on the drying characteristics. The diffusive concentration gradient between the wet surface of the droplet and unsaturated air leads to evaporative mass transfer. To minimize the moisture content of the final product, the inlet temperature of air must be as high as possible, and the temperature difference between inlet and outlet air must be as small as possible. Due to intense heat/mass transfer and loss of humidity, the droplet particle temperature rises to the exiting temperature of the air. The increase of air out- let temperature raises the droplet temperature and subsequently lowers the equilibrium moisture content in the droplet. Increasing the temperature difference between the inlet and outlet air, while holding the inlet air temperature constant, raises the moisture content in the final product. The outlet temperature depends on the mass flow rate of air, solid concentration of feed, and inlet air temperature.

Figure 8.9 illustrates the variation of drying time with air velocity, temperature, and operating pressure. It was observed that the drying time depends strongly on the inlet air humidity, temperature, particle size, and operating pressure. At a low humidity of 0.0025 kg water/kg dry air, the drying time is less than 6 s for droplet sizes less than 200 μm, at 35°C. At a humidity of 0.01 kg water/kg dry air, the drying time is less than 6 s for droplet sizes less than 100 μm, at 35°C, and droplet sizes less than 150 μm, at 70°C and 1 bar operating pressure. At low operating pressures of 0.5 bar, the drying time is less than 8 s for droplet sizes less than 200 μm, at 35°C. The results indicate that evaporative drying is possible down to low temperatures as low as 35°C, although such low-temperature dry- ing may limit the product quality and throughput.

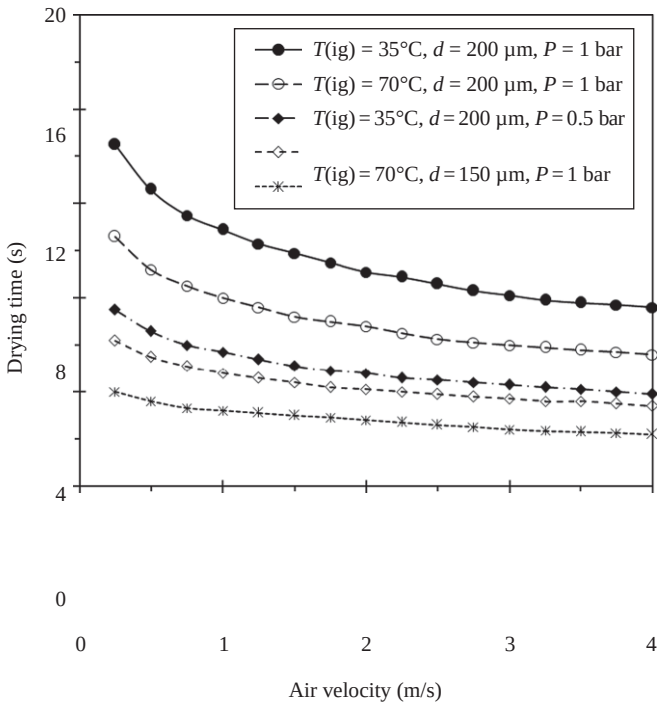


FIGURE 8.9

These results provide useful data for equipment selection of spray drying in the Cu–Cl cycle. Either an industrial drum dryer or spray dryer could be used to handle liquids or slurries. Drum dryers produce flakes, while spray dryers produce porous, small rounded particles that are often preferable to flakes. A particular advantage of spray dryers is their capability of large evaporation rates. Also, dust control is intrinsic to spray dryer construction, but not drum dryers. Drying proceeds until the moisture content of cupric chloride is reduced sufficiently, and the product is separated from air. Using the previous results such as the drying time data, the operating parameters can be established for the actual spray drying equipment, that is, atomizer design (type, rotational speed, nozzle diameter, and number of nozzles), feed (flow rate, temperature, and concentration), and air supply (flow rate, inlet temperature, outlet temperature, and humidity). Scale-up of the spray dry- ing equipment to larger flow capacities will require advances related to the atomizer, feed supply, air conditions, and flow rates to determine the residence time of droplets.

8.6 Hydrolysis Reaction for Copper Oxychloride Production

8.6.1 Introduction

The following hydrolysis reaction occurs within the Cu–Cl cycle (see Table 8.1): $H_2O(g) + 2CuCl_2(s) \rightarrow Cu_2OCl_2(s) + 2HCl(g)$. The reaction is an endothermic noncatalytic gas–solid reaction that operates between 350°C and 400°C. The solid feed to the hydrolysis reaction is cupric chloride, which comes from step 2 (electrolysis) in the form of an aqueous solution. The aqueous cupric chloride is dried to produce $CuCl_2$ solids, transported to the hydrolysis reactor, and then reacted with steam to produce copper oxychloride and hydrochloric gas. This section examines the transport phenomena of reactive spray drying (a combination of drying and hydrolysis), as well as a noncatalytic gas–solid reaction that separates drying and chemical reaction processes during hydrolysis.

Past experimental studies have examined various types of hydrolysis reactions. The reduction of metal oxides, followed by hydrolysis of the elementary metal with water, was proposed for conversion of solar energy to chemical energy, followed by hydrogen production (Berman and Epstein 2000). Wegner et al. (2006) reported the hydrolysis of zinc using Zn nanoparticles in the gas phase. The chemical conversion of Zn(g) was 83% after a single pass of H_2O with 0.85 s residence time. Hydrolysis is a complex multiphase process, involving transport phenomena of solid–gas interactions and heat transfer (Naterer 2002). This section examines spray flows with $CuCl_2$ during hydrolysis. Ortega-Lopez and Morales-Acevedo (1998) studied mixing and spraying of aqueous $CuCl_2$, in applications of pyrolysis to produce $CuInS_2$ for solar cells.

An alternative to reactive spray drying for the hydrolysis reaction is a conventional fluidized bed. Fluidized beds are widely used in chemical, pharmaceutical, and mineral industries for gas–solid systems. They are suitable for high-temperature gas–solid noncatalytic reactions. Cui et al. (2003) performed hydrodynamic measurements at temperatures up to 420°C in a fluidized bed reactor. Kocakusak et al. (1996) studied the production of anhydrous and crystalline boron oxide by dehydrating boric acid in a fluidized bed reactor with a gradual increase of bed temperature up to 250°C. Konttinen et al. (1997) examined sulfide zinc titanate regeneration in a fluidized bed reactor. Thurnhofer et al. (2005) reported the effects of iron ore reduction on the performance of a fluidized bed.

Depending on the output from an upstream reactor that produces solid $CuCl_2$ particles for hydrolysis in the Cu–Cl cycle, the type of solid feed may be spherical (single or mixed sizes) or flat particles (again single or mixed sizes). Possible reactor types for hydrolysis could be a nebulizer (reactive spray dryer), moving bed, moving feeder, rotary kiln, or a fluidized bed reactor. The three main factors that control the selection of the gas–solid reactor are (1) the reaction kinetics of particles, (2) the size distribution of the solids being handled, and (3) the flow pattern of solids and gas in the reactor. If solids and gas both enter the reactor in plug flow conditions, the composition and temperature change along the length of the reactor, thereby making the process nonisothernal. Examples are a countercurrent type of reactor (moving bed or rotary kiln), cross-flow type (moving belt feeder reactor), or cocurrent flow (rotary kilns). In fluidized beds, the solids move in mixed flow, and the gas flow pattern is more difficult to characterize. Both the solids and gas move in continuous flow, generally under near-isothermal conditions.

8.6.2 Proof-of-Principle Experiments

Ferrandon et al. (2008) have demonstrated experimentally the scientific feasibility of the hydrolysis reaction to produce HCl gas and solid copper oxychloride. Experimental studies were conducted in two types of reactors. The first used a microreactor system consisting of a 0.5 or 0.25 in. OD quartz tube heated by a split temperature-programmed furnace. The typical sample loading was 0.30 g of copper chloride dihydrate (as received $CuCl_2 \cdot 2H_2O$, 99.99%, Sigma Aldrich) packed between two layers of quartz wool. In order to vary the particle sizes, the material was first dried in a dessicator, crushed and sieved to the desired particles sizes, and then rehydrated. Ballmilled materials were obtained by placing dried $CuCl_2$ particles in a shaker with zirconia balls overnight and then rehydrating. The argon (99.999%) flowed between 50 and 250 mL/min through a humidifier with a set temperature varying between 30°C and 95°C. During the hydrolysis experiments, the sample was heated rapidly (within 10 min) in humidified Ar to reaction temperature, between 300°C and 400°C, and then held at the test temperature for a period, between 30 and 90 min. After the end of the experiment, the furnace was opened to allow the sample to cool rap- idly in humidified Ar down to 250°C. Dry Ar was then used to cool the sample down to ambient temperature. During the experiments, water and HCl in the gaseous product stream were condensed. Any remaining HCl was trapped using a NaOH solution and Cl_2 was trapped using Fe wool. The solid product samples were stored in closed vials in a des- sicator to prevent any air and moisture exposure. The results of these experiments showed relatively high conversion to the desired products when the molar steam to CuCl ratio was high (17:1) and the residence time of the $CuCl_2$ was short, which is desirable to prevent the formation of CuO and CuCl.

Experimental tests were performed at 375°C in the 0.5 in. OD quartz tube using $CuCl_2 \cdot 2H_2O$ as received. The test conditions and the product analyses are listed in Table 8.4. The first group of tests (Tests 1–3 in Table 8.4) was performed keeping the space velocity and steam-to-Cu molar ratio constant. The second group of tests (Tests 4–6 in Table 8.4) was performed keeping the space velocity and the H_2O vapor concentration constant. The test results were promising as they showed high yields of Cu_2OCl_2, up to 89 wt.%. The steam-to-copper molar ratio in these tests varied from 28 to 66, while the CuCl content in the product varied from 8% to 12%. The reason for the higher CuCl yield in the product for Test 1, compared to that in Test 5, cannot be easily determined. For Test 1 compared to Test 5, the steam-to-copper molar ratio is lower, but the test duration is longer. In addition, the small variation in CuCl concentration might be due to experimental error. While every

TABLE 8.4

Experimental Conditions and Elemental Analyses of the Products after the Hydrolysis of $CuCl_2 \cdot 2H_2O$ in a 0.5-in. OD Tube

Test #	Steam/Cu Molar Ratio	Ar (mL/min)	Time (min)	GHSV (h^{-1})	H_2O Vapor (%)	CuCl[a] (wt.%)	CuCl[b]	CuCl[c]
1	28.3	200	60	43,327	8	12.1	10.	86.9
2	27	195	43	43,313	10	15.5	1.3	83.2
3	27.1	185	28	43,079	14	14.8	5.2	80.0
4	38	160	20	43,135	26	16.4	10.8	72.8
5	52	160	30	43,135	26	8.0	3.2	88.8
6	66	160	40	43,135	26	11.1	1.5	87.4

[a] Error: ±0.3.

[b] Error: ±0.3–0.7.

[c] Error: ±0.5–0.7.

effort was made to obtain a representative sample, the small sample size precludes multiple analyses. The product in Test 4 had the shortest duration and yet the highest CuCl content. Thus, it was determined that a fixed-bed reactor and solids analysis does not provide sufficient information to determine reaction mechanisms and kinetics.

In order to minimize the decomposition reaction while keeping a low steam-to-Cu ratio, operating parameters, such as the test temperature, test duration, particle size of the starting $CuCl_2$ material, carrier gas flow rate, and steam concentration, were varied. In order to increase the gas velocity in the bed, the reactor tube diameter was reduced to 0.25 in. The amount of CuCl significantly decreased when the reaction temperature was decreased. At 340°C, the amount of CuCl in the sample was only 2.1 wt.%. However, as the tempera- ture was decreased, less Cu_2OCl_2 was produced and more $CuCl_2$ remained unreacted.

8.6.3 Predictive Formulation of Hydrolysis Processes

During the hydrolysis reaction, the particles may grow or shrink. The average conversion of solids depends on the rate of reaction and the residence time of a particle. A uniform-reaction model or shrinking-core model can be used to estimate the reaction rate of the gas–solid reaction. If the diffusion of a gaseous reactant, A, into a particle is much faster than the chemical reaction, the solid reactant B is consumed nearly uniformly throughout the particle (see Figure 8.10a). In this situation, a uniform-reaction model can be used. On the other hand, if the diffusion of a gaseous reactant, A, is much slower and it restricts the reaction zone to a thin layer that advances from the outer surface into the particle (Figure 8.10b), then the shrinking-core model can be adopted.

The rate of conversion of solid, X_B, for a uniform concentration of gas reactant, C_{Ag}, is

$$\frac{dX_B}{d} = k_r C_{Ag}\left(1 - X_B\right) \tag{8.18}$$

which can be integrated over time to yield

$$\left(1 - X_B\right) = \exp\left(-k_r C_{Ag} t\right) \tag{8.19}$$

where k_r is the reaction rate coefficient, based on a unit volume of solid.

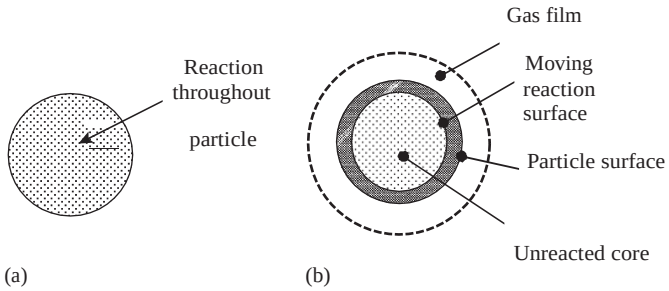


FIGURE 8.10

Schematic of (a) uniform conversion of the particle and (b) shrinking particle core with an ash surface layer and gas film.

In the shrinking-core model, it is assumed that the particles are spherical and the thickness of the reaction zone is smaller than the particle. During the reaction, the reaction zone advances from the outer surface into the particle, completely converting the reactant solid into product. The sequence of steps in the solid conversion process is listed as follows:

1. Diffusion of gaseous reactant, A, through a gas film surrounding the particle to the surface of the solid
2. Penetration and diffusion of A through a layer of ash to the surface of the unre- acted core
3. Reaction of gaseous A with solid at the reaction surface
4. Diffusion of gaseous products through the ash back to the exterior surface of the solid
5. Diffusion of gaseous products through the gas film back to the main body of the fluid

In certain conditions, some of these steps may not exist. The thermochemical resistance of each step varies, depending on the flow conditions, and the step of highest resistance will normally control the overall rate of particle conversion.

In the following analysis, the conversion equations will be analyzed for spherical particles, in which steps 1–3 are the rate-controlling steps. For step 1, with diffusion through the gas film, the kinetic equation based on the available surface, S_{ex}, can be written as

$$-\frac{1}{S_{ex}}\frac{dN_B}{dt} = -\frac{\rho}{bC}\frac{r^2\, dr_c}{R^2\, dt} = k_g\left(C_{Ag} - C_{As}\right) = k_g C_{Ag} \tag{8.20}$$

where N_B, ρ_B, r_C, R, k_g, C_{Ag}, and C_{As} refer to the molar density in the solid, density, radius of the unreacted core, radius of the solid particle, mass transfer coefficient, concentration of the gaseous reactant outside of the gas film, and concentration of the gaseous reactant at the particle surface.

The solution yields the following conversion of a single particle with time:

$$\frac{t}{\tau} = 1 - \frac{r_C}{R} = 1 - \left(1 - X_B\right)^{1/3} \tag{8.21}$$

where τ is the time of complete conversion of the solid:

$$\tau = t = \frac{\rho_B R}{bk'' C_{Ag}} \tag{8.22}$$

In this result, k'' is the first-order rate constant for the surface reaction. As soon as a product layer forms, the resistance for diffusion through the ash dominates the resistance through the gas film surrounding the particle, so the gas film resistance can be neglected. When the resistances of the chemical reaction and diffusion steps are comparable, the conversion of the particle in terms of the overall resistance is determined by

$$\frac{1}{S_p}\frac{dN_A}{dt} = k''C_A = \frac{C_A}{\left(d_p/(12D_e)\right)_{ash} + \left(1/k''\right)_{reaction}} \tag{8.23}$$

where S_p, d_p, and D_e refer to the surface area of the particle, particle diameter, and diffusion coefficient, respectively. The previous equations represent conversion of a single particle. In plug flow of solids, it is assumed that all solids stay in the reactors for the same length of time. The contact time, or reaction time needed for the solid conversion, can be calculated from the shrinking-core model, depending on the rate-controlling step.

For particles of a single unchanging size, in mixed flow of solids with a uniform gas composition in a fluidized bed, the conversion of reactant in a single particle depends on its length of time in the bed and the reaction-controlling step, or the main resistance mode (film, ash, or reaction). The length of time is not the same for different particles in the reactor. Hence, the conversion can be calculated through the exit age distribution of solids in the bed as follows:

$$\begin{pmatrix}\text{Mean value for}\\ \text{the fraction}\\ B \text{ unconverted}\end{pmatrix} = \sum_{particles}\begin{pmatrix}\text{Fraction of particles,}\\ \text{unconverted, between}\\ \text{time } t \text{ and } t+dt\end{pmatrix}\begin{pmatrix}\text{Fraction of exit stream}\\ \text{staying in the reactor}\\ \text{between } t \text{ and } t+dt\end{pmatrix} \tag{8.24}$$

$$1 - \overline{X_B} = \int_0^{\tau}(1 - X_B)E\,dt \tag{8.25}$$

where E is the exit age distribution of solids in the reactor.

The conversion of a mixture of particles in a mixed or plug flow has been predicted previously [35,36] for particles of spherical and nonspherical shapes. Ferrandon et al. (2008) presented data for measurements collected in a microreactor for the hydrolysis of $CuCl_2$ at 375°C, using sieved 150–250 μm particles. The solid conversion data were reported for different steam-to-$CuCl_2$ mole ratios and different time intervals. The vapor fraction for the corresponding steam-to-$CuCl_2$ ratio varied from 0.08 to 0.26 in the gas phase. The authors reported the influence of the reaction time, particle size, and inert gas flow on the thermal decomposition of $CuCl_2$ into CuCl. The following correlations have similar trends as the experimental data:

$$t = k_1\left[1 - 3\left(1 - X_B\right)^{2/3} + 2\left(1 - X_B\right)\right] \tag{8.26}$$

$$t = k_2\left[1 - \left(1 - X_B\right)^{1/3}\right] \tag{8.27}$$

where

$k_1 = 0.022\ \text{min}^{-1}$ is the diffusion time constant

$k_2 = 0.02\ \text{min}^{-1}$ is the reaction time constant

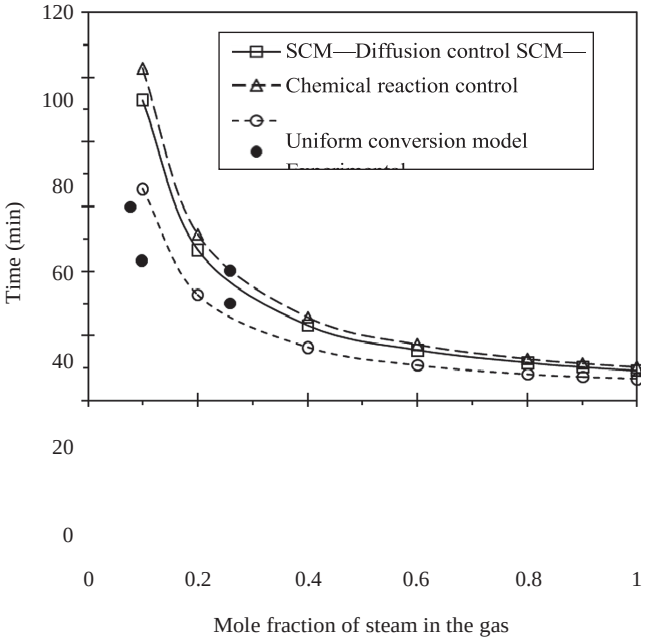


FIGURE 8.11

Comparison of solid conversion time with experimental data. (Adapted from Naterer, G.F. et al. *International Journal of Hydrogen Energy* 36, 15472–15485, 2011a.)

These k_1 and k_2 values will be used to evaluate the reaction rate constant, k'', and D_e, the effective diffusivity for an average steam concentration of $C_{Ag} = 3.8$ mol/m^3. The corresponding rate constants are $k'' = 0.00011$ m^3(STP)/m^2 solids and $D_e = 2.03 \times 10^{-9}$ m^2/s. The variation of solid conversion time with vapor fraction in the gas is illustrated in Figure 8.11. The experimental data of Ferrandon et al. (2008) are also used to predict the solid conversion for uniformly sized particles of 200 μm diameter in plug flow of solids. As the mole fraction of steam in the gas increases, the time of solid conversion decreases. The reaction rate constant for the uniform-reaction model is $k_r = 0.00063$ m^3(STP)/m^2 for solid conversion of $X_B = 0.99$. Also, at high conversions, all of the models predict essentially the same rate of conversion. The fraction of reacted core volume to the total particle volume increases over time, regardless of the resistance mode for mixed flow of solids.

8.7 Molten Salt Reactor for Oxygen Production

8.7.1 Introduction

The oxygen production step (see Table 8.1 and Figure 8.1) receives solid feed of $CuO*CuCl_2$ and produces O_2 gas and liquid cuprous chloride. The reaction is given by $CuOCuCl_2(s) = 2CuCl$ (molten) + $0.5O_2$ (gas) at 530°C. Gas species leaving the oxygen reactor include oxygen gas and potential impurities of products from side reactions, such as CuCl vapor, chlorine gas, HCl gas (trace amount), and H_2O vapor (trace amount). The substances exiting the reactor are molten CuCl, potentially solid $CuCl_2$ from the upstream reaction ($CuCl_2$ hydrolysis step), due to the incomplete decomposition of $CuCl_2$ at a temperature lower than 750°C, as well as reactant particles entrained by the flow of molten CuCl. In the oxy- gen reactor, copper oxychloride particles will decompose to molten salt and oxygen. The reactant particles absorb decomposition heat from the surrounding molten bath.

Within the reactor, heat is transferred from liquid (molten CuCl) to solid $CuO*CuCl_2$ (reactant) particles, and the molten bath can be sustained by the reaction product itself.

Free ebooks ==> www.Ebook777.com

The oxygen product will leave the reactant particles immediately, due to buoyancy of gas in the molten salt. This fast separation aids the minimization of heat transfer resistance to the reactant particles, which then helps make the overall reaction rate closer to the intrinsic reaction rate itself. The design of the reactor requires a high efficiency of heat exchange and separation of reactants from products, as well as product (oxygen) from product (molten salt).

A suitable method to heat the reactor is needed. A heated inert gas could be introduced, but there are two disadvantages with this approach: poor heat transfer and enhanced entrainment of undecomposed $CuO*CuCl_2$ (reactant) particles. To recycle these entrained $CuO*CuCl_2$ particles using sieves or cyclone/centrifugal separation would require significant power input. Also, the entrainment of fine particles would clog and corrode the equipment, especially components like flanges and screws. Another alternative is radiation, but again this is challenging because the process is more difficult to control, especially if the power input is high.

A more practical and efficient option is to heat the molten salt from the wall with a double-shell structure without using electricity. Flowing in the double shell, a secondary flow of molten salt provides heat to the reactor. The secondary flow of molten salt could be provided from a solar energy storage reservoir or nuclear heat exchanger, which uses molten salt as the heat storage and transferring medium. Since molten CuCl itself can be the heat storage medium used in the solar energy reservoir, the molten CuCl can also be pumped out of the oxygen production reactor to a solar energy reservoir and pumped back into the reactor. If necessary, agitation could be introduced into the bath. This approach would take advantage of both free and forced convection with heterogeneous mixing that facilitates both heat and mass transfer.

A difficulty is bubble spouting and separation of solid and molten salt. To address this issue, techniques used in iron-making or steel-making furnaces could be adopted, which commonly handle the removal of high-temperature molten iron, floating impurities/dross, slag, and the feeding of iron ore. The presence of bubbles in the molten bath has several advantages. For example, they enhance the local rates of heat transfer. The contact area between the $CuO*CuCl_2$ (reactant) particles and molten CuCl (product bath) increases when they are more heterogeneously mixed by ascending bubbles and descending particles. The aggregation of $CuO*CuCl_2$ (reactant) particles will reduce the contact area between particles and liquid, but fortunately the oxygen (product) bubbles can help to break these aggregations. Also, the upflow of oxygen (product) bubbles will resist the descent of solid particles, which will help to increase the residence time of $CuO*CuCl_2$ (reactant) particles in the molten salt; hence, they help decrease the reactor size. Due to the large density difference between oxygen and molten CuCl, the oxygen bubbles formed at the surface of the reactant particles will leave the surface immediately after the bubbles form, which ensures that the reaction is driven toward the direction of oxygen production.

The liquid level within the reactor may abruptly change with a sudden increase of bubbles due to flash decomposition, which may result in the entrainment of bubbles in the exit flow of molten CuCl, upon which the pipe could become choked by these bubbles. The liquid level may also change due to a sudden pressure fluctuation. If there is a sudden decrease of pressure, the bubbles may lift part of the liquid up to the top of the reactor, which could cause flooding or spouting of liquid. This problem can be addressed by a molten salt removal pipe of large diameter that is located on the reactor side, with fewer bubbles than the other side, so the liquid level is kept unchanged.

The reactant $CuO*CuCl_2$ does not melt in molten CuCl because it is first decomposed to oxygen and molten CuCl at 470°C. The reactor to produce oxygen is recommended to operate at about 530°C. In this temperature range, many metals would be oxidized by oxygen. The reactor and oxygen removal equipment must be corrosion resistant to oxygen, molten

www.Ebook777.com

CuCl, dry HCl (or even moist HCl), and possibly Cl_2 gas. If $CuCl_2$ is entrained in the reactor with CuO*$CuCl_2$ particles, then chlorine gas may appear and corrode the equipment material at a temperature of 530°C. Oxygen cooling in a heat exchanger downstream of the reactor requires a wall material that is also resistant to O_2 oxidization at 530°C, as well as dry HCl corrosion at such a high temperature.

8.7.2 Proof-of-Principle Experiments

Serban et al. (2004) have demonstrated experimentally the scientific feasibility of the oxygen production reaction. The reaction was conducted in a ½ in. by 14 in. quartz vertical reactor, as shown previously in Figure 8.1. The reaction was performed in a vertical reactor (Figure 8.1) connected to the mass spectrometer in order to monitor the oxygen evolution. Melanothallite was not commercially available. It was synthesized in the laboratory by heating stoichiometric amounts of $CuCl_2$ and CuO at temperatures between 370°C and 470°C. The resulting material was used in the kinetic study. The oxygen evolution was followed using a mass spectrometer, of Serban et al. (2004). The area under the peaks in the mass spectra was combined. Using separately obtained calibration data, it was determined that the oxygen yield at 500°C was 85% of the theoretical amount, and at 530°C, the yield was 100%. The XRD of the solid product indicates that the solid phase is pure CuCl. No chlorine was detected on the mass spectrometer, suggesting that no side reactions occurred. Thermodynamic data indicate that at 500°C, the equilibrium conversion is 60%. However, the reactions are always operated open to the atmosphere, and O_2 is continuously removed from the reaction zone. Under these conditions, complete conversions are possible because the equilibrium is shifted toward the right (Figure 8.12).

Mechanistic studies indicated that the overall oxygen generation reaction proceeds in two steps: (1) the decomposition of $CuCl_2$ to CuCl and Cl_2 and (2) the reaction of CuO

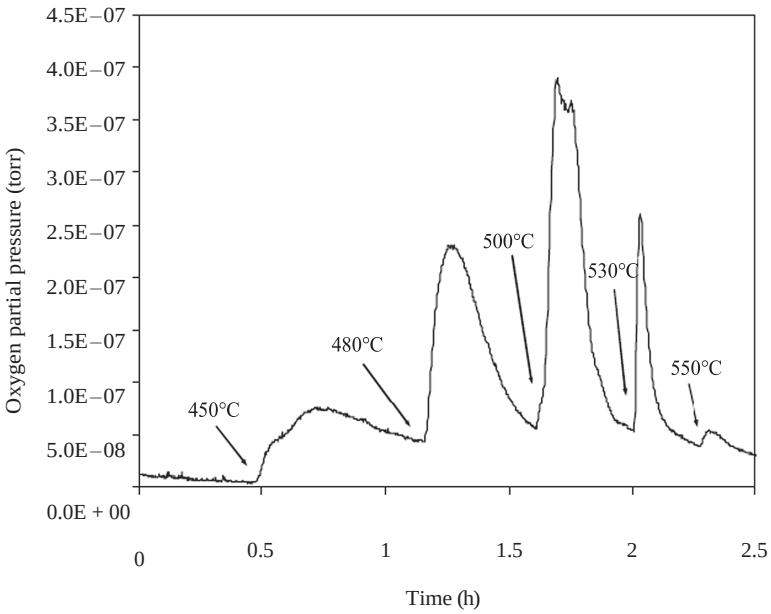


FIGURE 8.12

Oxygen evolution in time at different temperatures—fixed bed reactor, reactant = synthetic melanothallite made from an equimolar mixture of $CuCl_2$ and CuO, Ar flow rate = 30 cm^3/min. (Adapted from Serban, M. et al. Kinetic study of the hydrogen and oxygen production reactions in the copper-chloride thermochemical cycle, in *AIChE 2004 Spring National Meeting*, New Orleans, LA, April 25–29, 2004.)

with Cl_2. In the reaction between CuO and $CuCl_2$, oxygen started to evolve at 450°C, the temperature at which pure $CuCl_2$ starts to decompose and liberate Cl_2, which reacts with the CuO, producing CuCl and free oxygen. The overall oxygen generation reaction is limited by the decomposition of $CuCl_2$. Even though at 530°C only 55% of $CuCl_2$ is decomposed, the presence of CuO seems to facilitate its decomposition such that the products of reaction are O_2 and CuCl generated in stoichiometric amounts. Complete $CuCl_2$ decomposition is reported to be achieved at 630°C. Above 550°C, however, the CuCl vaporization becomes significant, and the experiment was stopped at this temperature.

The Cl_2 from the $CuCl_2$ decomposition is consumed completely in the reaction with CuO, since no Cl_2 was detected on the mass spectrometer. The kinetics of the reaction between CuO and $CuCl_2$ were analyzed in more detail by independently studying the $CuCl_2$ decomposition and the CuO and Cl_2 reactions in a thermal balance and a vertical reactor, respectively. A mixture of CuO and $CuCl_2$ generates O_2 at 500°C. In the experiment, 0.01 mol of CuO (0.8 g) and $CuCl_2$ (1.34 g) were used. Anhydrous $CuCl_2$ was obtained from dehydrated $CuCl_2$ by drying it in air at 175°C. The experiment was run in a flow-through-type quartz vertical microreactor using off-the-shelf reagents and an Ar flow rate of 15 cm^3/min. With the bulk density of 4.853 g/cm^3 for the mixture CuO and $CuCl_2$, the calculated space velocity is 2040 h^{-1}. The reaction was terminated after 45 min, and the oxygen yield was 85%. According to the thermodynamic equilibrium curves, at 500°C, the reaction is incomplete with only 0.3 mol of O_2 (72 cm^3 O_2 from 0.02 mol of solids) being generated. However, since the reaction was run under nonequilibrium conditions, that is, by continuously removing the O_2 from the reaction zone, the amount of oxygen generated surpassed the amount predicted by the equilibrium calculations. The only solid products of reaction were CuCl with traces of $CuCl_2$ as indicated by XRD examination.

8.7.3 Design Issues of Oxygen Reactor Scale-Up

For equipment scale-up beyond small test tubes and microreactors, several design issues must be addressed. This section discusses the broad implications of selected issues in this equipment scale-up. Solid feed of anhydrous solid CuO*$CuCl_2$ from the $CuCl_2$ hydrolysis reaction of the Cu–Cl cycle is provided to the oxygen production reactor. The bulk density of this material depends on the particle size and structure, which influence the volume of the reactor, feeder, and discharge vessels. The structure and shape of solid CuO*$CuCl_2$ are formed in the upstream $CuCl_2$ hydrolysis reactor. Aggregation into blocks of CuO*$CuCl_2$ particles may occur during the process of removing, conveying, and feeding of particles. The aggregation may choke or clog the feeder and cause sudden spouting of particles, so appropriate measures are needed to overcome these problems.

It is advantageous that the reactant CuO*$CuCl_2$ particles do not have a melting point below the decomposition temperature of 450°C. Unfortunately, there may exist embedded particles of $CuCl_2$ from the upstream hydrolysis reactor. The existence of $CuCl_2$ particles in CuO*$CuCl_2$ would lead to undesirable products and side reactions. For example, $CuCl_2$ may decompose to CuCl and Cl_2 gas. The existence of Cl_2 gas is highly corrosive. However, the existence of CuCl generated from $CuCl_2$ is not problematic, because molten CuCl is also a product generated from the decomposition of CuO*$CuCl_2$ particles. The most effective way to remove $CuCl_2$ particles from CuO*$CuCl_2$ is to ensure that the upstream $CuCl_2$ hydrolysis reaction to produce CuO*$CuCl_2$ is fully completed (conversion of $CuCl_2$ to CuO*$CuCl_2$ is 100%). The optimal conditions for full completion of the hydrolysis reaction are still under investigation.

In the oxygen reactor, the operation will be safer if the lowest feeding temperature is higher than the melting point of CuCl, that is, 430°C. If particles enter the reactor at a temperature lower than 430°C, a difficulty with the presence of bubbles in the molten salt may occur. Some CuCl vapor might condense, and molten CuCl might solidify around the $CuO*CuCl_2$ particles, thereby leading to blockage or confinement of bubbles. If an aggregation develops with particles, molten salt, and bubbles, the contact area between a reactant particle and heating medium (molten CuCl) will decrease, and the aggregations may float along the surface of the molten salt. This would deter the decomposition of reactant particles and potentially lead to choking of the reactor (a major safety concern). Fortunately, this issue can be avoided in several ways: hot feeding of the reactant particles, using an agitator, or protective mixing with hot oxygen (one of the decomposition products).

The decomposition temperature of $CuO*CuCl_2$ is higher than the melting point of CuCl. Therefore, the CuCl product will leave the reactor in molten form. The heat carried by molten CuCl is high-grade (high-temperature) heat that can be recovered to supply endothermic processes, such as evaporating water to superheated steam for use in the hydrolysis reaction in step 4 at a temperature of 375°C. Another option is to heat HCl gas from 375°C to 450°C for use in the hydrogen production reaction in step 1. The latter option is less preferable because the temperature difference between HCl gas and molten CuCl is much smaller than that between water and molten CuCl. In addition, the hydrogen generation reaction is exothermic, which implies that HCl gas could be self-heated. Also, to heat HCl gas using molten CuCl requires that the equipment material must be corrosion resistant to HCl gas at a high temperature of 450°C. For example, HCl gas may react with many common metals and their protective oxide film at a temperature of 400°C. In particular, if any moisture is present in the HCl gas, it will be more corrosive. However, this challenge is not as difficult with heating of H_2O.

To recover the heat carried by molten salt, the molten salt can be sprayed downward, while countercurrent motion of gas is flowing upward. For example, due to the very low solubility of CuCl in water (6.2×10^{-5} g/g water, 20°C), the molten salt can be first quenched in the quenching cell, and the vapor generated is then heated to a temperature of 375°C. The molten CuCl effluent from the oxygen production reactor might contain entrained particles of unreacted $CuO*CuCl_2$. In addition, fine oxygen bubbles may appear on the surface of the reactant particles when decomposing. If the bubbles detach slowly from the particles, $CuO*CuCl_2$ particles would not descend properly, thereby enhancing the likelihood of their entrainment in the molten CuCl. Some bubbles may be entrained by the molten CuCl, so the bubbles may plug the pipe where molten salt flows out of the reactor. The entrainment of reactant particles could also introduce safety issues involving the removal equipment. The particles may continue to decompose in the pipe after leaving the reactor, which would generate gas bubbles in the pipe and simultaneously decrease the temperature of molten salt. Since the decomposition requires heat input, this may result in solidification of molten salt. To prevent the entrainment problems, various potential methods are currently under investigation by the authors.

The Molten CuCl product is quenched to solid at a low temperature in the quenching unit. The solubility of CuCl in water is very low, and CuCl will solidify as the molten CuCl descends into liquid water. Simultaneously, part of the liquid water absorbs the heat released from molten CuCl, which then evaporates to steam. Rapid cooling and solidification of molten CuCl is desired in the quenching unit. The heat loss in the spray nozzle of molten CuCl must be small to avoid plugging of solid CuCl in the nozzle.

Another option to quench molten CuCl is that CuCl descends into an aqueous solution of HCl and possibly $CuCl_2$. An advantage of this method is to promote the direct dissolution

of CuCl. However, this will introduce other challenges. One challenge is that the mixture of HCl and steam at high temperatures will exist in the gas phase inside the equipment, due to the volatile nature of HCl gas. The mixture is strongly corrosive to many materials. As a result, the use of steam with HCl would be more problematic. Therefore, this quench- ing method is not recommended in the design.

The removal of oxygen must not be slower than the decomposition rate of the reactant, in order to prevent a sudden rise of the reactor pressure due to possible *flash decomposition* of the reactant particles in the molten salt. A sudden decrease of the reactor pressure could also lead to flooding or spouting of bubbles within the liquid. Prior to steady-state continuous operation, tests should be performed under batch operation of a continuous flow reactor, in order to assess the dependency of reaction kinetics on scale-up, that is, decomposition rate of reactant particles and the removal of oxygen and molten salt. In the processing of oxygen gas, trace amounts of CuCl vapor may be present in the oxygen gas after the oxygen bubbles ascend and leave the molten CuCl bath. Hot oxygen gas can be used to purge lower-temperature $CuO*CuCl_2$ particles. In this way, CuCl would condense and return back to the oxygen production reactor. Trace amounts of CuCl in the oxygen gas product are not problematic if passed through a cyclone first, as any CuCl will deposit on a cooler surface.

Acknowledgments

Support of this research from the following partners is gratefully acknowledged: AECL, Argonne National Laboratory (International Nuclear Energy Research Initiative; US Department of Energy), University Network of Excellence in Nuclear Engineering (notably Ontario Power Generation and Bruce Power), Ontario Research Excellence Fund, Natural Sciences and Engineering Research Council of Canada, and the Canada Research Chairs program.

References

Aihara, M., Umida, H., Tsutsumi, A., Yoshida, K. Kinetic study of UT-3 thermochemical hydrogen production process. *International Journal of Hydrogen Energy* 1990; 15(1): 7–11.

Ambike, A.A., Mahadik, K.R., Paradkar, A. Spray dried amorphous solid dispersions of simvastatin a low Tg drug: In vitro and in vivo evaluations. *Pharmaceutical Research* 2005; 22(6): 990–998.

Berman, A., Epstein, M. The kinetics of hydrogen production in the oxidation of liquid zinc with water vapor. *International Journal of Hydrogen Energy* 2000; 25: 957–967.

Carty, R.H., Mazumder, M., Schreider, J.D., Panborn, J.B. *Thermochemical Hydrogen Production*, vol. 1. Gas Research Institute for the Institute of Gas Technology, Chicago, IL, GRI Report 80-0023, 1981. Casper, M.S. *Hydrogen Manufacture by Electrolysis, Thermal Decomposition and Unusual Techniques*,

Noyes Data Corporation, Park Ridge, NJ, 1978.

Chen, X.D., Lin, S.X.Q. Air drying of milk droplet under constant and time dependent conditions.

AIChE Journal 2005; 51(6): 1790–1799.

Cui, H., Sauriol, P., Chaouki, J. High temperature fluidized bed reactor: Measurements, hydrody- namics and simulation. *Chemical Engineering Science* 2003; 58(3): 1071–1077.

Ferrandon, M.S., Lewis, M.A., Tatterson, D.F., Nankanic, R.V., Kumarc, M., Wedgewood, L.E., Nitsche, L.C. The hybrid Cu-Cl thermochemical cycle. I. Conceptual process design and H2A cost analysis. II. Limiting the formation of CuCl during hydrolysis, in *NHA Annual Hydrogen Conference*, Sacramento Convention Center, Sacramento, CA, March 30–April 3, 2008.

Goel, N., Mirabel, S.T., Ingley, H., Goswami, D.Y. Solar hydrogen production, SEECL Report 2003-01, Solar Energy & Energy Conversion Lab, University of Florida, Gainesville, FL—An Interim Report submitted to NASA Glenn Research Center, 2003.

Jiang, H.D., Ostrach, S., Kamotani, Y. Thermosolutal transport phenomena in large Lewis number electrochemical systems. *International Journal of Heat and Mass Transfer* 1996; 39: 841–850.

Knoche, K.F., Schuster, P., Ritterbex, T. Thermochemical production of hydrogen by a vanadium/ chlorine cycle. II: Experimental investigation of the individual reactions. *International Journal of Hydrogen Energy* 1984; 9: 473–482.

Kocakusak, S., Akcay, K., Ayok, T., Koroglu, H.J., Koral, M., Savasci, O.T., Tolun, R. Production of anhydrous, crystalline boron oxide in fluidized bed reactor. *Chemical Engineering Science* 1996; 35: 311–317.

Konttinen, J.T., Zevenhoven, C.A.P., Hupa, M.M. Modeling of sulfided zinc titanate regeneration in a fluidized bed reactor. 2. Scale-up of the solid conversion model. *Industrial Engineering Chemistry Research* 1997; 36: 5439–5446.

Kunii, D., Levenspiel, O. *Fluidization Engineering*, 2nd edn., Butterworth-Heinemann, Boston, MA, 1991.

Lee, M.S., Goswami, D.Y., Hettinger, B., Vijayaraghavan, S. Preparation and characteristics of calcium oxide pellets for UT-3 thermochemical cycle, in *the Proceedings of the 2006 ASME International Mechanical Engineering Congress and Exposition*, Chicago, IL, November 2006.

Lee, M.S., Goswami, D.Y., Kothurkar, N., Stefanakos, E.K. Fabrication of porous calcium oxide film for UT-3 thermochemical hydrogen production cycle, in *the Proceedings of the ASME Energy Sustainability 2007*, June 27–30, 2007, Long Beach, CA.

Lee, M.S., Goswami, D.Y., Stefanakos, E.K. Immobilization of calcium oxide solid reactant on an yttria fabric and thermodynamic analysis of UT-3 thermochemical hydrogen production cycle. *International Journal of Hydrogen Energy* 2009; 34: 745–752.

Levenspiel, O. *Chemical Reaction Engineering*, 3rd edn., John Wiley & Sons, New York, 1998.

Levi-Hevroni, D., Levy, A., Borde, I. Mathematical modeling of drying of liquid/slurries in a steady state one dimensional flow. *Drying Technology* 1995; 13: 1187–1201.

Lewis, M., Taylor, A. High temperature thermochemical processes, DOE Hydrogen Program, Annual Progress Report, Washington, DC, pp. 182–185, 2006.

Lewis, M.A., Masin, J.G., Vilim, R.B., Serban, M. Development of the low temperature Cu-Cl ther- mochemical cycle, in *International Congress on Advances in Nuclear Power Plants*, Seoul, Korea, May 15–19, 2005.

Lin, S.X.Q., Chen, X.D. Prediction of air-drying of milk droplet under relatively high humidity using the reaction engineering approach. *Drying Technology* 2005; 23: 1395–1406.

Lin, S.X.Q., Chen, X.D. A model for drying of an aqueous lactose droplet using the reaction engineer- ing approach. *Drying Technology* 2006; 24: 1329–1334.

McQuillan, B.W., Brown, L.C., Besenbruch, G.E., Tolman, R., Cramer, T., Russ, B.E., Vermillion, B.A. et al. High efficiency generation of hydrogen fuels using solar thermochemical splitting of water: Annual Report, GA-A24972, General Atomics, San Diego, CA, 2002.

Mirabel, S.T., Goel, N., Ingley, H.A., Goswami, D.Y. Utilization of domestic fuels for hydrogen pro- duction. *International Journal of Power and Energy Systems* 2004; 24(3): 239–245.

Nakayama, T., Yoshioka, H., Furutani, H., Kameyama, H., Yoshida, K. MASCOT—A bench-scale plant for producing hydrogen by the UT-3 thermochemical decomposition cycle. *International Journal of Hydrogen Energy* 1984; 9(3): 187–190.

Naterer, G.F. *Heat Transfer in Single and Multiphase Systems*, CRC Press, Boca Raton, FL, 2002. Naterer, G.F., Camberos, J.A. *Entropy Based Analysis and Design of Fluids Engineering Systems*, CRC Press, Boca Raton, FL, 2008.

Naterer, G.F., Suppiah, S., Stolberg, L., Lewis, M., Ferrandon, M., Wang, W., Dincer, I. et al., Clean hydrogen production with the Cu-Cl cycle—Progress of international consortium, I: Experimental unit operations. *International Journal of Hydrogen Energy*, 2011a; 36: 15472–15485.

Naterer, G.F., Suppiah, S., Stolberg, L., Lewis, M., Ferrandon, M., Wang, W., Dincer, I. et al. Clean hydrogen production with the Cu-Cl cycle—Progress of international consortium, II: Simulations, thermochemical data and materials. *International Journal of Hydrogen Energy*, 2011b; 36: 15486–15501.

Naterer, G.F., Tokarz, C.D., Avsec, J., Fuel cell entropy production with ohmic heating and diffusive polarization. *International Journal of Heat and Mass Transfer* 2006; 49: 2673–2683.

Ortega-Lopez, M., Morales-Acevedo, A. Characterization of CuInS2 thin films for solar cells prepared by spray pyrolysis. *Thin Solid Films* 1998; 330: 96–101.

Ranz, W.E., Marshall, W.R. Evaporation from droplets. *Chemical Engineering Progress* 1952; 48: 141–146. Sadhankar, R.R., Li, J., Li, H., Ryland, D., Suppiah, S. Hydrogen generation using high-temperature nuclear reactors, in *55th Canadian Chemical Engineering Conference*, Toronto, Ontario, Canada,

October 2005.

Sakurai, M., Bilgen, E., Tsutsumi, A., Yoshida, K. Adiabatic UT-3 thermochemical process for hydro- gen production. *International Journal of Hydrogen Energy* 1996; 21(10): 865–870.

Sakurai, M., Nakajima, H., Amir, R., Onuki, K., Shimizu, S. Experimental study on side-reaction occurrence condition in the iodine-sulfur thermochemical hydrogen production process. *International Journal of Hydrogen Energy* 2000; 23: 613–619.

Schultz, K. Thermochemical production of hydrogen from solar and nuclear energy, Technical Report for the Stanford Global Climate and Energy Project, General Atomics, San Diego, CA, 2003.

Serban, M., Lewis, M.A., Basco, J.K. Kinetic study of the hydrogen and oxygen production reac- tions in the copper-chloride thermochemical cycle, in *AIChE 2004 Spring National Meeting*, New Orleans, LA, April 25–29, 2004.

Stolberg, L., Boniface, H., Deschenes, L., York, S., McMahon, S., Suppiah, S. Recent advances at AECL in the Cu-Cl cycle for nuclear-produced hydrogen, in *ORF Workshops on Thermochemical Nuclear- Based Hydrogen Production*, Oshawa, ON, December 2007 and Chalk River, ON, October 2008.

Thurnhofer, A., Schachinger, M., Winter, F., Mali, H., Schenk, J.L. Iron ore reduction in a laboratory- scale fluidized bed reactor-effect of pre-reduction on final reduction degree. *ISIJ International* 2005; 45(2): 151–158.

Walton, D.E. The evaporation of water droplets: A single droplet drying experiment. *Drying Technology* 2004; 22(3): 431–456.

Wegner, K., Ly, H.C., Weiss, R.J., Pratsnis, S.E., Steinfeld, A. In situ formation and hydrolysis of Zn nanoparticles for H2 production by the 2-step ZnO/Zn water-splitting thermochemical cycle. *International Journal of Hydrogen Energy* 2006; 31: 55–61.

Weng, F.B., Kamotani, Y., Ostrach, S. Mass transfer rate study in rotating shallow electrochemical cells. *International Journal of Heat and Mass Transfer* 1998; 41: 2725–2733.

Yan, T.Z., Jen, T. Two-phase flow modeling of liquid-feed direct methanol fuel cell. *International Journal of Heat and Mass Transfer* 2008; 51: 1192–1204.

14

Life Cycle Analysis and Economic Assessment of Solar Hydrogen

Anton Meier
Paul Scherrer Institute

CONTENTS

14.1 Introduction 537
14.1.1 Objectives and Scope 538
14.1.2 System Boundary Definition 538
14.2 Methodology 539
14.2.1 Ecological Assessment 539
14.2.2 Economic Assessment 540
14.2.3 Eco-Efficiency 540
14.3 Fuels and Power Trains 540
14.3.1 Solar H_2 Pathways 540
14.3.2 Specifications and Assumptions 541
14.4 Production and Supply Chains 549
14.4.1 Emissions and Cumulated Energy Demand 549
14.4.1.1 GHG Emissions and CED of Solar H_2 Production 549
14.4.1.2 GHG Emissions and CED of Passenger Car Technologies 551
14.4.2 Life Cycle Impact Assessment 552
14.4.2.1 Eco-Indicator'99 Methodology 552
14.4.2.2 Eco-Scarcity'97 Methodology 553
14.4.2.3 Life Cycle Impact Assessment Example 553
14.5 Fuel and Vehicle Costs 554
14.5.1 Passenger Car Transportation Costs 556
14.5.2 Eco-Efficiency 558
14.6 Conclusions 558
Acknowledgments 559
References 559

14.1 Introduction

H_2 and electricity will likely become the main energy carriers in future low-carbon energy systems. Long-term energy scenarios such as the Energy Technology Perspectives of the International Energy Agency (IEA) [1] and the World Energy Technology Outlook 2050 (WETO-H_2) of the European Commission (EC) [2] predict considerable market penetration of emerging H_2 production and end use technologies [3]. H_2 is expected to be particularly

advantageous as transportation fuel due to its versatility, pollutant-free end use, and storage capability. H_2 produced from nonfossil fuels (e.g., renewable energy sources like solar energy) and used in fuel cells (FCs) can provide sustainable energy and thus reduce the adverse energy-related environmental effects on climate change, such as greenhouse gas (GHG) emissions. Of special interest are solar thermochemical H_2 production processes and their prospects in terms of technological and economic potential as well as their role in future H_2 supply [3].

14.1.1 Objectives and Scope

This chapter is based on a comprehensive well-to-wheel (WTW) analysis and an economic assessment for solar-produced H_2 and its utilization in fuel cell vehicles (FCVs) for passenger transportation [4]. Results from the life cycle analysis (LCA) include environmental impacts of GHG emissions and cumulative energy demand (CED), as well as damage caused to human health (HH), ecosystem quality (EQ), and natural resources [5]. The LCA encompasses all environmental interactions like extraction of resources, fuel processing steps, supply, use, and final disposal. The economic assessment provides H_2 production and supply costs for selected scenarios [6]. The eco-efficiency analysis method combines ecological and economic aspects in condensed form [6].

Conventional technologies used by industry to produce H_2 include steam reforming of natural gas (NG) (or steam methane reforming [SMR]), coal gasification (CGA), and water electrolysis (ELE). At the start of a growing hydrogen economy, it is anticipated that H_2 will be produced by advanced, process-optimized SMR [7] as well as CGA followed by CO_2 capture and sequestration [8]. In the long term, strong H_2 markets and a growing infrastructure will create opportunities for renewable H_2 production systems [7]. Of special interest are recent technological advances in the field of solar thermochemical production of H_2 using concentrated solar radiation as the energy source of high-temperature process heat [9]. Among the most promising H_2O-splitting thermochemical processes is the two-step Zn/ZnO cycle [10–12]. The intermediate energy carrier Zn is formed in an endothermic step either by solar thermal dissociation (STD) of ZnO at above 2000 K [13–15] or, alternatively, by solar carbothermic reduction (SCR) of ZnO at about 1500 K [16]. In both cases, H_2 is generated from H_2O in a nonsolar exothermic step by hydrolysis of Zn [17], the benchmark being solar H_2 production by state-of-the-art alkaline electrolysis of H_2O using electricity from solar thermal power plants (solar thermal electricity [STE]).

The WTW analysis includes solar H_2 production, transport, and usage in future passenger car transportation systems. The H_2 is assumed to be produced in a concentrating solar power (CSP) plant located in Southern Spain (ES) and transported to Central Europe exemplified by Switzerland (CH). Solar H_2 production methods (STD, SCR, and STE) are compared with selected conventional production technologies (SMR, CGA, ELE). Energy transport concepts include (1) Zn transport, (2) on-site Zn hydrolysis followed by H_2 pipeline transport, and (3) high-voltage direct current (HVDC) electricity transport from a solar thermal power plant. Utilization of H_2 in an FCV is compared with advanced power trains for the combustion of oil-based energy carriers [18].

14.1.2 System Boundary Definition

The system boundaries are determined by the complete process chain—from the exploitation of natural resources to the functional unit of one passenger kilometer (assuming average load of 1.59 passengers per car [19]). Each process step accounts for relevant energy and resource consumption, land use, and emissions. Data source for conventional

and ancillary processes is the Swiss LCA database *ecoinvent v1.2* [20] describing standard technology in Western Europe around the year 2000. This comprehensive dataset is a consistent background for all energy systems compared and is used here as an approximation for the reference year 2025, although alterations of involved processes may be expected. The average European electricity mix (UCTE'25) used for all background processes is predicted based on an EC business-as-usual scenario [21] that utilizes an increased share of NG in more efficient combined cycle plants. Uncertainties associated with the time frame of this study are being addressed with sensitivity calculations to further substantiate the results obtained.

14.2 Methodology

The LCA and WTW methodologies employed for the production of H_2 and its use in mobile applications show similarities but also differences [22]. WTW studies are specifi- cally aimed at transport applications focusing on the production and distribution of dif- ferent fuels and on the emissions of vehicles during use. They include GHG emissions (e.g., contributions from CO_2, N_2O, and CH_4) and an energy (efficiency) indicator. In con- trast, LCA is a general methodology that can be applied to any kind of system or product. LCA studies focus on full life cycles of products or product systems. Applied to transpor- tation, they typically include the three phases of a vehicle (production, use, and end of life) as well as the production and distribution processes of the fuels consumed. LCA studies usually include more impact categories than WTW studies, such as acidification, eutrophi- cation, ozone layer depletion, and carcinogens.

14.2.1 Ecological Assessment

LCA aims at quantifying cumulative environmental interactions in terms of resource consumption and emissions to air, water, and soil. Based on this life cycle inventory (LCI), a life cycle impact assessment (LCIA) can be conducted by rating these interactions using various methodologies. Their application follows a procedure described in ISO norms [23,24]. The basic idea is to use the cumulative inventories and multiply the resulting single elementary flows with substance-specific factors. The following methodologies are employed for the present assessment:

- *GHG* emissions are taken into account based on the GHG species' global warm- ing potential (GWP) using infrared forcing values relative to CO_2 according to the Intergovernmental Panel on Climate Change (IPCC) [25].
- *CED* describes primary energy resource consumption [26].
- The comprehensive *Eco-indicator '99 Hierarchist* (*EI'99-H*) method [27] provides quantification of aggregated environmental impacts of all emitted or used sub- stances in three damage categories: HH, EQ, and both fossil and mineral resources. The damage categories are normalized and weighted according to the *Hierarchist* perspective considered closest to the scientists' point of view.
- The *Eco-scarcity '97* (Umweltbelastungspunkt [*UBP*]) method [28] also yields an aggregated impact score. Conceptually, it is a distance-to-target model that

compares actual flows to the environment with critical flows derived from scientifically sound political targets such as emission limits. Multiplying each mass flow with its corresponding weighting factor yields a specific environmental impact value (so-called UBP). In contrast to *EI'99*, no damage categories are implemented in *Eco-scarcity*.

- *HH* and *EQ* both represent environmental damage categories described in the *Impact 2002+* methodology [29]. *HH* mainly considers respiratory damages and carcinogenic effects; *EQ* includes land use and ecotoxic emissions.

14.2.2 Economic Assessment

The economic competitiveness of the renewable processes considered in this study is judged according to different cost calculations:

- *Fuel and transportation costs* encompass fuel production costs per energy unit and passenger car transportation costs per passenger kilometer (pkm), respectively.
- *External costs* represent a measure of environmental damage normally not included in the direct costs of a technology. Internalization of external costs provides an economic indicator for cost-benefit analyses of alternative options.

14.2.3 Eco-Efficiency

The eco-efficiency methodology [30,31] links both ecological and economic aspects of a spe- cific technology under consideration. With this approach, an environmental indicator— such as GHG emissions—is combined with an economic indicator—such as production or service costs. Both indicators are normalized with a typical reference value, for example, the state-of-the-art technology, the specific technology to be substituted, or the average value of the technology alternatives. A weighting factor describes the importance of costs versus environmental impacts.

14.3 Fuels and Power Trains

14.3.1 Solar H_2 Pathways

H_2 from concentrated solar power (*CSP*). Figure 14.1 shows pathways for the provision of solar H_2 that encompass (1) the production of H_2 or an intermediate energy carrier (Zn or electricity) using concentrated solar energy; (2) the transport of H_2, Zn, or electricity from Southern Spain to Central Europe (Switzerland); and (3) further processing and, finally, use of H_2 in an FCV. The fuel production pathways and power trains considered are listed in Table 14.1.

Note that some important technologies have been excluded from the present study: compressed natural gas (CNG), although a viable option as transition fuel, does not fit into the long-term solar H_2 scenario; biofuels, represented by synthetic natural gas (SNG) from wood, are being addressed in a different work [4]; H_2-fueled internal combustion engines (ICEs) offer distinctly lower efficiencies than FCs [18]; and liquid H_2 is energetically inefficient compared to gaseous H_2 [32].

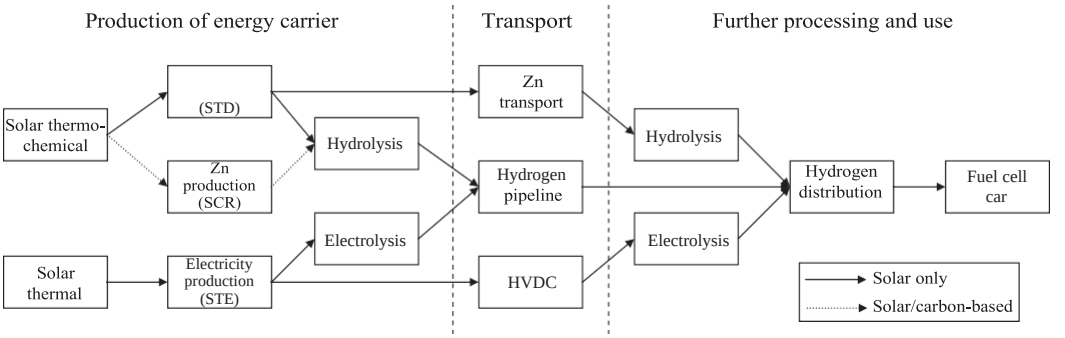


FIGURE 14.1

Pathways for (1) solar production of H_2 at a CSP plant located in Southern Spain; (2) transport of H_2 or an inter- mediate energy carrier such as Zn or electricity to Central Europe (Switzerland); (3) distribution and utilization of H_2 in an FCV. Acronyms are explained in Table 14.1. (From Felder, R. and Meier, A., *J. Sol. Energy Eng.*, 130(1), 011017-1/10, 2008.)

14.3.2 Specifications and Assumptions

For consistency, all solar technologies considered in this study use the same CSP tower configuration based on the PS10 plant near Seville, Spain [33,34], as specified in Table 14.2. A field of sun-tracking heliostats (624 glass–metal heliostats of 121 m^2 reflecting surface area each) concentrates direct solar radiation onto the top of a tower (100 m height). At the design point (insolation of 860 W/m^2 and optical efficiency of 77%), the reference CSP plant features 50 MW thermal power input into a receiver (for STE) [35] or a chemical reactor (for STD) mounted on top of the tower; for SCR, a tower reflector (TR) redirects the sunrays to a chemical reactor placed on the ground [36]. The average annual optical effi- ciency of the heliostat field (HF) is $\eta_1 = Q_{HF}/Q_{solar} = 64\%$. For typical sites in Southern Spain, the direct normal irradiance (DNI) is about 2000 $kWh/m^2/a$. A plant lifetime of 30 years is assumed [37]. Infrastructure data are taken from a detailed analysis of CSP tower plants generating STE [38].

It is conceivable that the HF will look different for the various solar applications compared: On one hand, a large receiver (for STE) operating at relatively low temperature and a TR (for SCR) both can accept sunlight from a wide angle; on the other hand, a chemical reactor (for STD) operating at high temperatures and solar concentrations near 5000 suns (1 sun = 1 kW/m^2) requires a compound parabolic concentrator (CPC) with a much smaller acceptance angle [39]. This leads to a different—usually elliptical—shape of the HF with a significant number of heliostats at larger distance from the tower, thus resulting in additional efficiency losses through atmospheric attenuation. It is anticipated that these losses may be compensated by advanced heliostat designs (e.g., with higher mirror quality), however, at the penalty of higher costs for STD. The validation of this assumption requires a detailed analysis of the various HF configurations, which lies outside the scope of this study.

STE. A benchmark for the thermochemical processes (STD, SCR) is STE generation followed by H_2 production via H_2O electrolysis (STE), as shown in Figure 14.2. Table 14.3 summarizes the assumptions for the STE scenario. The CSP tower plants currently in operation, under construction, or in planning use either the saturated steam receiver [34] or the molten salt receiver [40] concept. In both cases, the heat transfer medium absorbs concentrated solar energy and delivers heat via a heat exchanger to a steam turbine to drive an electric generator. Average thermal

TABLE 14.1

Summary of Fuel Production Pathways and Power Trains

Acronym	Fuel Production Pathways and Power Trains	Production Site	Transport
Compressed Gaseous Hydrogen			
Solar			
STD pipe	Solar thermal dissociation of ZnO + Zn hydrolysis	On-site ES	CG H_2 pipeline
STD zinc	Solar thermal dissociation of ZnO + Zn hydrolysis	CH	Zn, ship and rail
STE pipe	Solar thermal electricity + water electrolysis	On-site ES	CG H_2 pipeline
STE hvdc	Solar thermal electricity + water electrolysis	CH	HVDC
Fossil			
SMR	Steam methane reforming	Northern Europe	CG H_2 pipeline
CGA	Coal gasification (advanced)	NE Europe	CG H_2 pipeline
Electrolysis			
ELE CH mix	Electrolysis using predicted Swiss mix 2030	CH	—
ELE nuclear	Electrolysis using nuclear power	CH	—
ELE hydro	Electrolysis using hydro power	CH	—
ELE wind	Electrolysis using wind power	CH/Import	HVDC
ELE PV	Electrolysis using photovoltaics	CH	—
Power Train			
FCV	PEM fuel cell vehicle. 0.94 MJ_{LHV}/km		
Electricity			
Electricity Source			
STE hvdc	Solar thermal electricity	ES	HVDC
CH mix	Predicted Swiss consumer mix 2030	CH	—
Hydro	Hydropower	CH	—
Power Train			
BEV	Battery electric vehicle; 0.53 MJ/km		
CNG			
Wood			
SNG	Synthetic natural gas from wood gasification	CH	—
Fossil			
CNG	Compressed natural gas	EU	CNG pipeline
Power Train			
ICE CNG	Internal combustion engine; 1.93 MJ/km		
Liquid Hydrocarbons			
Fossil			
Gasoline	Gasoline	EU	Ship, truck
Diesel	Diesel	EU	Ship, truck
Power Trains			
ICE G	Internal combustion engine, gasoline; 1.90 MJ/km		
ICE D	Internal combustion engine, diesel; 1.80 MJ/km		

Indicated are acronyms, production sites of end energy carrier, and long-distance transport options for energy carriers.
Note: CH, Switzerland; ES, Spain; EU, European Union; CG, compressed gas; LHV, lower heating value.

TABLE 14.2

Solar Plant Specification (Baseline Case)

	Parameter	Unit	Value	Remarks
Baseline	Solar thermal power input	MW	50	Design point
CSP plant	Insolation	W/m²	860	Design point
	DNI	kWh/m²/a	2,000	Site dependent
	Optical efficiency:	—	0.77	PS10 [33]; design point
	$\eta_1 = Q_{HF}/Q_{solar}$		0.64	PS10 [33]; mean annual value
	Tower height	m	100	Derived from [33]
	Number of heliostats	—	624	Glass–metal [38]
	Single heliostat area	m²	121	PS10 [33]
	HF area	m²	75,504	
	Annual solar energy to receiver	GJ/a	347,922	Based on DNI
	Land use factor	—	0.2	[37]
	Land area	m²	377,520	Total plant area
	Plant lifetime	a	30	[37]

Source: Felder, R. and Meier, A., *J. Sol. Energy Eng.*, 130(1), 011017-1/10, 2008.

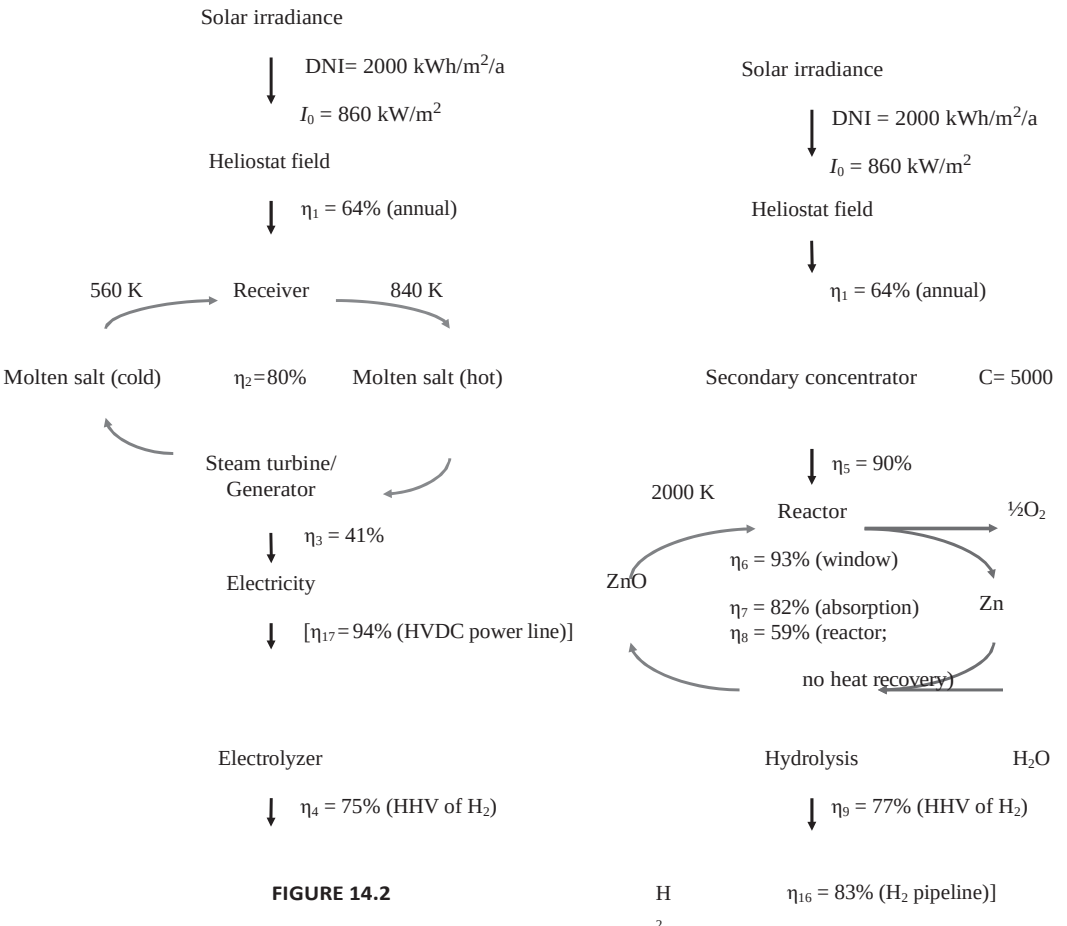


FIGURE 14.2

(a)

H_2 [η_{16} = 83% (H_2 pipeline)]
(b)

(a) Flow chart of H_2 production via STE generation followed by H_2O electrolysis. (b) Flow chart of H_2 produc- tion via solar thermal ZnO dissociation (STD) and Zn hydrolysis. For efficiencies, see Tables 14.3, 14.4, and 14.6, respectively. Higher heating value (HHV) of H_2 used.

energy conversion efficiencies $\eta_2 = Q_{receiver}/Q_{HF}$ of 80% for a molten salt receiver and $\eta_3 = Q_{el}/Q_{receiver}$ of 41% for the electricity generation cycle are taken from a CSP study [37]. H_2 is produced by H_2O electrolysis based on bipolar alkaline low-temperature technology with a thermal efficiency $\eta_4 = Q_{H_2}/Q_{el}$ of 75% (using HHV of H_2) [41].

STD of ZnO. Solar thermochemical cycles for fuel production offer the potential of high-energy conversion efficiencies [12]. Figure 14.3 presents the model flow diagram of the H_2O-splitting solar thermochemical Zn/ZnO cycle. Table 14.4

TABLE 14.3

STE Generation and H_2O Electrolysis

	Parameter	Unit	Value	Remarks
CSP plant (16 MW_{el})	Molten salt receiver efficiency: $\eta_2 = Q_{receiver}/Q_{HF}$	—	0.80	[37] (2020); adapted to actual plant size
	Power block efficiency: $\eta_3 = Q_{el}/Q_{receiver}$	—	0.41	[37] (2020); incl. parasitic losses
	Storage capacity (3h peak power)	MWh	180	Based on Solar Two Tower Plant [42]
H_2O electrolysis (12 $MW_{H_2,HHV}$)	Annual plant availability	—	0.94	CSP tower plant [37]
	H_2O + electricity ⟶ H_2 + ½O_2			Bipolar alkaline low-temperature technology
	H_2 production capacity at 30 bar	kg/h	290	Based on design point
	Electrolyzer efficiency (HHV): $\eta_4 = Q_{H_2}/Q_{el}$	—	0.75	[41]

Source: Felder, R. and Meier, A., *J. Sol. Energy Eng.*, 130(1), 011017-1/10, 2008.

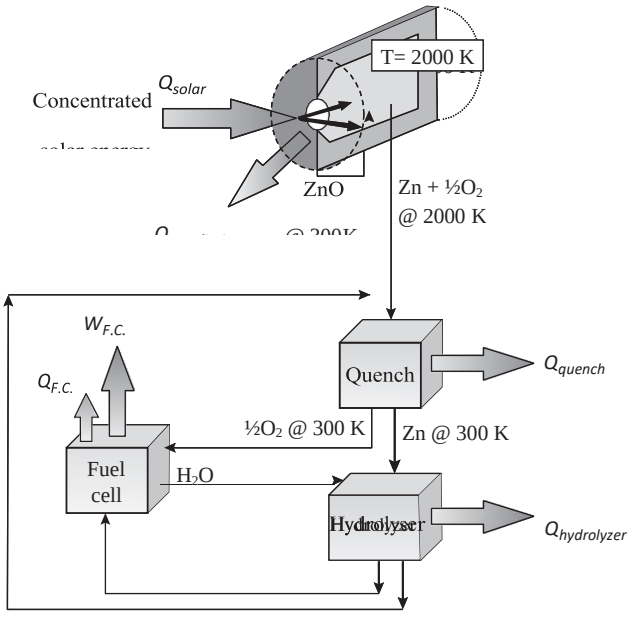


FIGURE 14.3

Model flow diagram of the H_2O-splitting solar thermochemical Zn/ZnO cycle. (Based on Steinfeld, A., *Int. J. Hydrogen Energy*, 27(6), 611, 2002.)

summarizes the assumptions used for the STD scenario. To achieve process

temperatures exceeding 2000 K, the solar radiation reflected from the HF has to be further concentrated using a nonimaging CPC. Thus, the optical efficiency $\eta_1 = Q_{HF}/Q_{solar}$ of 64% is decreased by absorption and spillage losses at the CPC (10%) and, in addition, by absorption and reflection losses at the quartz

TABLE 14.4

STD of ZnO and Zn Hydrolysis

	Parameter	Unit	Value	Remarks
CSP plant	Solar reactor:			
(20 MW_{Zn})	$ZnO + heat \rightarrow Zn + 0.5O_2$			
	Zn production capacity	kg/h	10,700	Design point (860 W/m^2)
	CPC: $\eta_5 = Q_{CPC}/Q_{HF}$	—	0.90	Own assumption
	Window: $\eta_6 = Q_{window}/Q_{CPC}$		0.93	Own assumption
	Absorption: $\eta_7 = Q_{reactor}/Q_{window/CPC}$		0.82	T = 2000 K; C = 5000 suns [44]
	Solar reactor: $\eta_8 = Q_{Zn}/Q_{reactor}$		0.59	Incl. thermal and quenching losses; min. insolation level
	Annual plant availability	—	0.94	CSP tower plant [37]
H_2 plant	Hydrolyzer:			
(16 $MW_{H_2,HHV}$)	$Zn + H_2O \rightarrow ZnO + H_2$			
Zn hydrolysis	H_2 production capacity at 1 bar	kg/h	300	Design point (860 W/m^2)
(16 $MW_{H_2,HHV}$)	Hydrolyzer efficiency (HHV):	—	0.77	95% molar conversion
	$\eta_9 = Q_{H_2,ES}/Q_{Zn}$			

Source: Felder, R. and Meier, A., *J. Sol. Energy Eng.*, 130(1), 011017-1/10, 2008.

window mounted in front of the solar chemical reactor (7%). Reradiation losses through the reactor aperture account for 18%, assuming a solar flux concentration of 5000 suns and a cavity temperature of 2000 K. Such high temperatures require a minimum insolation level for reactor operation [43], thus reducing the annual reactor efficiency $\eta_8 = Q_{Zn}/Q_{reactor}$, which is further decreased by convection and conduction heat losses from the well-insulated reactor (up to 10%) and losses by quenching the highly reactive gaseous mixture of Zn and O_2 to ambient temperature (up to 26% [12]). Quenching losses can somewhat be alleviated if the quench takes effect from 2000 to 700 K (instead of 298 K) and if part (up to 50%) of the sensible energy in the products can be recovered. Finally, H_2 production by Zn hydrolysis [17] is assumed proceeding at a thermal conversion efficiency $\eta_9 = Q_{H_2,ES}/Q_{Zn}$ of 77% (HHV of H_2) with 95% molar conversion.

SCR of ZnO. The technical feasibility of the SCR of ZnO has been successfully demonstrated in a 300 kW pilot plant implemented at a solar facility with beam-down optical configuration [45]. Table 14.5 summarizes the assumptions used for the SCR scenario. The optical efficiency η_1 of 64% is reduced by absorp- tion and spillage losses at the TR (10%) and the CPC (10%). Reradiation losses through the reactor aperture account for 19%, assuming solar a flux concentra- tion of 2000 suns and a cavity temperature of 1600 K. For large-scale industrial plants, maximum reactor efficiency $Q_{Zn}/Q_{reactor}$ of 69% is anticipated [46], result- ing in overall reactor efficiency $\eta_{13} = (Q_{Zn} + Q_{CO})/(Q_{reactor} + Q_C)$ of 64% if the energy contents of carbon (Q_C) and CO (Q_{CO}) are included [47] and 60% if, in addition, a minimum solar insolation level for operating the reactor is taken into account [43]. The source of carbon can be different kinds of coal powder. The so-called SOLZINC process made use of beech charcoal, which showed the best overall reaction properties [48], apart from being a renewable resource. However, for

TABLE 14.5

SCR of ZnO and Zn Hydrolysis

	Parameter	Unit	Value	Remarks
CSP plant	Solar reactor:			
(23 MW_{Zn} and 11 MW_{CO})	ZnO + C + heat ⟶ Zn +CO			
	Zn production capacity	kg/h	15,100	Design point (860 W/m^2)
	TR: $\eta_{10} = Q_{TR}/Q_{HF}$	—	0.90	Own assumption
	CPC: $\eta_{11} = Q_{CPC}/Q_{TR}$		0.90	Own assumption
	Absorption: $\eta_{12} = Q_{reactor}/Q_{CPC}$		0.81	T = 1600 K; C = 2000 suns
	Solar reactor:			
	$\eta_{13} = (Q_{Zn} + Q_{CO})/(Q_{reactor} + Q_C)$		0.60	Based on [46]; incl. thermal losses; min. insolation level
	Efficiency (total):			
	$\eta_{tot} = (Q_{Zn} + Q_{CO})/(Q_{solar} + Q_C)$		0.31	
	Annual plant availability	—	0.94	CSP tower plant [37]
H_2 plant	Hydrolyzer: Zn + H_2O ⟶ ZnO + H_2			
(27 $MW_{H_2,HHV}$)	CO shift: CO + H_2O ⟶ CO_2 + H_2			
Zn Hydrolysis	$\eta_9 = Q_{H_2,ES}/Q_{Zn}$ H_2 production capacity at 1 bar	kg/h	700	Design point (860 W/m^2)
(18 $MW_{H_2,HHV}$)				
+ CO–H_2O shift	Hydrolyzer efficiency (HHV):	—	0.77	95% molar conversion
(9 $MW_{H_2,HHV}$)	CO–H_2O shift efficiency (HHV):	—	1.00	Long term: 100%
	$\eta_{14} = Q_{H_2,ES}/Q_{CO}$			conversion [51]
	Combined efficiency (HHV):	—	0.84	Process efficiency
	$\eta_{15} = Q_{H_2,ES}/(Q_{Zn} + Q_{CO})$			considering Zn and CO mass flows

Source: Felder, R. and Meier, A., *J. Sol. Energy Eng.*, 130(1), 011017-1/10, 2008.

each solar plant, site-specific carbonaceous feedstock needs to be identified. Charcoal is produced using the Reichert procedure [49,50], an advanced technology including treatment and utilization of the wood gases in order to mini- mize external energy demand and emissions during production; in particular, release of CH_4 is eliminated. H_2 is produced by Zn hydrolysis [17] and also from CO via water–gas shift reaction [51] with a combined thermal efficiency η_{15} of 84% (HHV of H_2).

Transport options. H_2 can be produced at the CSP plant with subsequent pipeline delivery (STD pipe and STE pipe) over a distance of 1650 km assumed between Southern Spain (ES) and Central Europe, exemplified by Switzerland (CH); alternatively, H_2 can be produced at the consumer site after transport of either Zn powder (STD zinc) or electricity (STE hvdc). The assumptions for the transport options are summarized

in Table 14.6. H_2 produced on-site uses transport infrastructure based on today's CNG pipelines and storage tanks [52]. Losses for H_2 pipeline transport are quantified with 7.2% per 1000 km, plus additional loss of 5.1% for initial compression to pipeline pressure of 120 bar [52,53]. Electric transmission losses amount to 3.3% per 1000 km in 600 kV HVDC power lines [54] and to additional 1% in the Swiss medium-voltage alternating current (MVAC) grid [55]. For Zn transport by freight ship (1250 km) and rail (400 km), material losses are neglected, but energy consumption is taken into account.

TABLE 14.6

Summary of Transport Options

	Parameter	Unit	Value	Remarks
H_2 pipeline	Transport distance	km	1650	Southern Spain (ES) to Switzerland (CH)
	H_2 operating pressure	bar	120	In 2025 [54]
	Losses	%/1000 km	7.2	+5.1% losses for initial H_2 compression to 120 bar
	Efficiency: $\eta_{16} = Q_{H_2,CH}/Q_{H_2,ES}$	—	0.83	
Electricity transmission lines (HVDC and MVAC)	Transport distance (overland)	km	1650	Southern Spain (ES) to Switzerland (CH)
	Transmission loss (HVDC)	%/1000 km	3.3	600 kV [54]
	Transmission loss (MVAC)	%/100 km	1	20 kV [55]; CH grid
	Efficiency: $\eta_{17} = Q_{el,CH}/Q_{el,ES}$	—	0.94	
Zn/ZnO transport	Transport distance (freight ship)	km	1250	Southern Spain (ES) to Genoa, Italy
	Transport distance (rail)	km	400	Genoa, Italy to Switzerland (CH)
	Efficiency: $\eta_{18} = Q_{Zn,CH}/Q_{Zn,ES}$	—	1	Own assumption

Source: Felder, R. and Meier, A., *J. Sol. Energy Eng.*, 130(1), 011017-1/10, 2008.

Summary of solar H_2 production technologies. Table 14.7 summarizes energy conversion efficiencies for all considered solar H_2 pathways. The average annual solar-to-H_2 production efficiencies at the solar plant vary from 14.7% (STE) to 18.9% (STD) and 29.4% (SCR). If transport losses from Southern Spain to Switzerland are included, the annual solar-to-H_2 conversion efficiency ranges for STE from 12.2% (H_2 pipeline transport) to 13.8% (HVDC transport), for STD from 15.7% (H_2 pipeline transport) to 18.9% (Zn transport), while for SCR it is close to 25%.

Conventional H_2 production technologies and fuel options. The solar scenarios (STD, SCR, and STE) are compared with various pathways for alternative fuel production. Today's cheapest and most mature H_2 production technology is SMR (Table 14.8) with fuel conversion efficiency η_{19} of 89% (HHV of H_2) [41,56]. H_2 production from CGA (Table 14.9) based on autothermal gasification proceeds with thermal conver- sion efficiency η_{20} of 86% (HHV of H_2) [41,54,57]. H_2 can also be generated via H_2O electrolysis (ELE, Table 14.10) with an efficiency η_{21} of 75% (HHV of H_2) [41]. In this case, electricity is supplied either by the Swiss electricity mix (ELE, CH mix) [55] of locally produced CO_2-low hydro and nuclear power as predicted for 2030 [21] or—as a *worst-case scenario*—by the continental European electricity mix as fore- cast for the year 2025 (UCTE'25 [21]). Supply of nuclear, hydro, and wind power is documented in *ecoinvent* [58–60]. Photovoltaic (PV) data are taken from a Swiss study on renewable energies [61]. Vehicle data are based on a 55 kW Volkswagen Golf 4 [19]. H_2 powered FCV [62] is compared with advanced gasoline and diesel power trains [18,63]. LCI data for gasoline, diesel, and NG vehicles include car driving emissions [19,64,65] as well as construction, maintenance, and disposal of car and road infrastructure [19,66,67]. Vehicle efficiencies are taken from a study comparing future perspectives of different power trains (FCV, BEV, and ICE) [18].

TABLE 14.7

Average Annual Energy Conversion Efficiencies for Solar H_2 Pathways Depicted in Figure 14.1

Energy Conversion Efficiency (%)			STD pipe	STD zinc	SCR	STE pipe	STE hvdc
HF	Q_{HF}/Q_{solar}	η_1	64	64	64	64	64
TR	Q_{TR}/Q_{HF}	η_{10}	—	—	90	—	—
CPC	$Q_{CPC}/Q_{HF/TR}$	$\eta_{5,11}$	90	90	90	—	—
Window	Q_{window}/Q_{CPC}	η_6	93	93	—	—	—
Absorption	$Q_{reactor}/Q_{window/CPC}$	$\eta_{7,12}$	82	82	81	—	—
	STE: $Q_{receiver}/Q_{HF}$	η_2	—	—	—	80	80
Reactor	*STD:* $Q_{Zn}/Q_{reactor}$	η_8	59	59	—	—	—
	SCR: $(Q_{Zn} + Q_{CO})/(Q_{reactor} + Q_C)$	η_{13}	—	—	60[a]		
Electricity generation	$Q_{el}/Q_{receiver}$	η_3	—	—	—	41	41
Zn hydrolysis	*Zn:* $Q_{H_2,ES}/Q_{Zn}$	η_9	77	77	77	—	—
CO shift	CO: $Q_{H_2,ES}/Q_{CO}$	η_{14}	—	—	100		
	Zn + CO: $Q_{H_2,ES}/(Q_{Zn} + Q_{CO})$	η_{15}			84[a]		
Electrolysis	$Q_{H_2,ES}/Q_{el}$	η_4	—	—	—	75	75
Annual plant availability		η_{plant}	94	94	94	94	94
Annual solar-to-H_2 production efficiency	$Q_{H_2,ES}/(Q_{solar} + Q_C)$	η_{prod}	18.9	—	29.4	14.7	—
Transport	$Q_{H_2,CH}/Q_{H_2,ES}$	$\eta_{16–18}$	83	100	83	83	94
Total efficiency	$Q_{H_2,CH}/(Q_{solar} + Q_C)$	η_{tot}	15.7	18.9	24.4	12.2	13.8

Source: Felder, R. and Meier, A., *J. Sol. Energy Eng.*, 130(1), 011017-1/10, 2008. Higher heating value (HHV) of H_2 used; acronyms explained in Table 14.1.

[a] SCR also includes energy stored in carbon source (C) and product (CO).

TABLE 14.8

SMR

	Parameter	Unit	Value	Remarks
SMR plant ($155\ MW_{H_2,HHV}$)	Catalytic steam reforming of NG:			Low-temperature shift reactor
	$CH_4 + H_2O \rightarrow CO + 3H_2$			
	$CO + H_2O \rightarrow CO_2 + H_2$			
	H_2 production capacity at 30 bar	Nm^3/h	69,400	Based on [56]
	Fuel conversion efficiency (HHV):	—	0.89	[41]
	$\eta_{19} = Q_{H_2,CH}/(Q_{NG,feed} + Q_{NG,fuel})$			

Source: Felder, R. and Meier, A., *J. Sol. Energy Eng.*, 130(1), 011017-1/10, 2008.

TABLE 14.9

CGA

	Parameter	Unit	Value	Remarks
CGA plant	Autothermal gasification:			
(275 $MW_{H_2,HHV}$)	$C + H_2O \rightarrow CO + H_2$ $CO + H_2O \rightarrow CO_2 + H_2$			
	H_2 production capacity at 50 bar	Nm^3/h	100,000	Based on [54]
	Fuel conversion efficiency (HHV): $\eta_{20} = Q_{H_2,CH}/Q_{hardcoal}$	—	0.86	[41]

Source: Felder, R. and Meier, A., *J. Sol. Energy Eng.*, 130(1), 011017-1/10, 2008.

TABLE 14.10

ELE at Local Gas Station

	Parameter	Unit	Value	Remarks
ELE gas station	ELE:			Bipolar alkaline
(1.3 $MW_{H_2,HHV}$)	H_2O + electricity $\rightarrow$ H_2 + ½ O_2			low-temperature technology
	H_2 production capacity at 30 bar	kg/h	40	Based on [68]
	Efficiency (HHV): $\eta_{21} = Q_{H_2}/Q_{el}$	—	0.75	[41]
	Electricity demand	kWh/Nm^3	4.30	

Source: Felder, R. and Meier, A., *J. Sol. Energy Eng.*, 130(1), 011017-1/10, 2008 .

14.4 Production and Supply Chains

14.4.1 Emissions and Cumulated Energy Demand

14.4.1.1 GHG Emissions and CED of Solar H_2 Production

Figure 14.4 shows GHG emissions for the H_2 production and utilization pathways considered in this study. In general, GHG emissions are distinctly lower for the scenarios based on solar energy than for those relying on fossil resources; the best solar technologies emit GHG up to 6 times less than SMR and more than 10 times less than CGA. Solar thermochemical production of Zn with on-site hydrolysis and subsequent H_2 pipeline transport (STD pipe) performs best. In contrast, transporting Zn (STD zinc) almost doubles GHG emissions because of associated transport emissions. Solar carbothermic production of Zn with charcoal (SCR cc) involves only slightly higher GHG emissions, as long as CH_4-free charcoal production technologies are used. However, it is impor- tant to limit the wood/charcoal transport distance to the CSP plant, since total WTW- GHG emissions increase by about 10% (or 1 g CO_2-eq. per MJ H_2) for 1000 km of railway transport or 100 km of lorry transport. Solar carbothermic production of Zn with hard coal (SCR hc) leads to markedly higher GHG emissions, though lower than conventional CGA. Solar thermal electrolysis also emits low amounts of GHG, with an advantage for H_2 pipeline transport (STE pipe) compared to electricity transport (STE hvdc) because of N_2O emissions in the corona of HVDC transmission lines (GWP of N_2O is 296 times

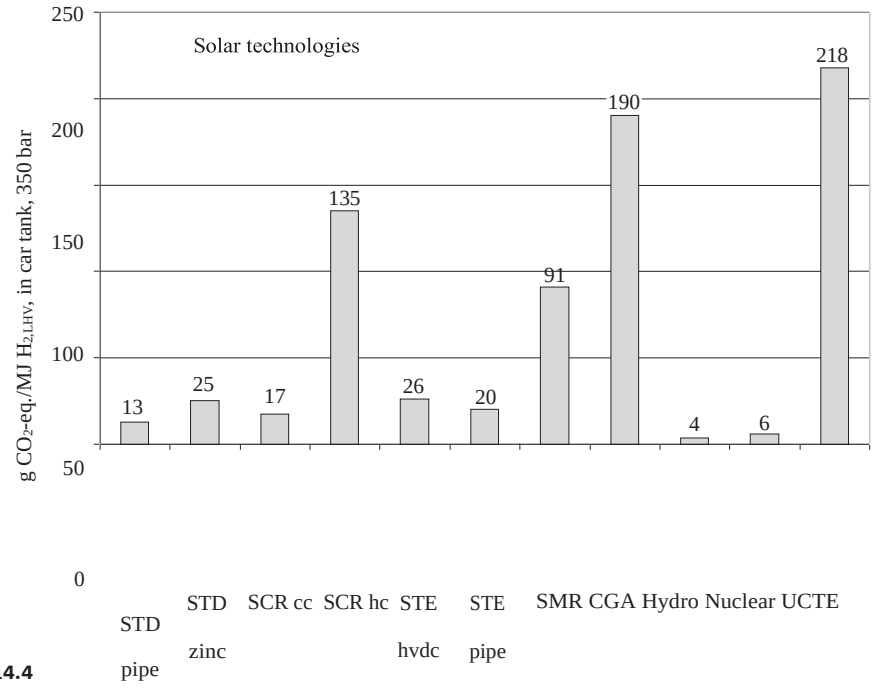
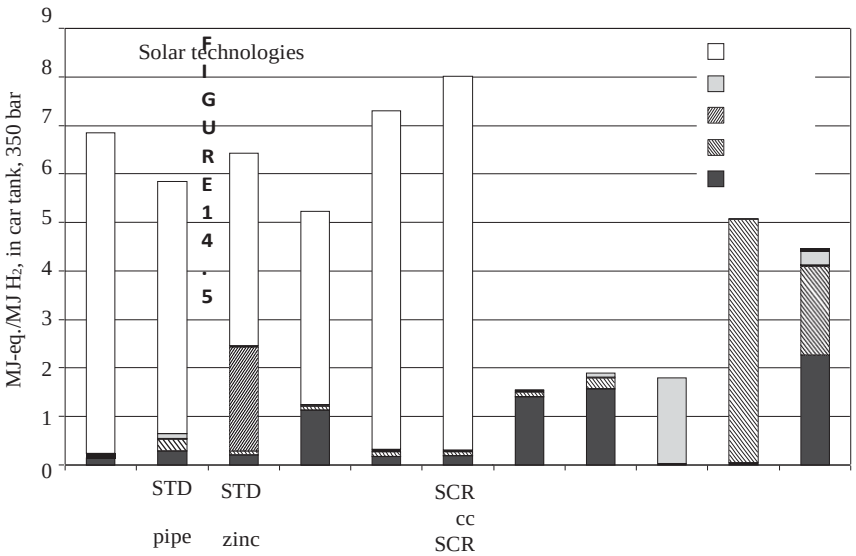


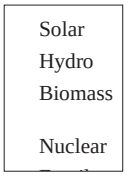
FIGURE 14.4

GHG emissions in g CO_2-eq. per MJ H_2 (LHV) in car tank at 350 bar. (From Felder, R. and Meier, A., *J. Sol. Energy Eng.*, 130(1), 011017-1/10, 2008.)

higher than that of CO_2 [25]). The life cycle GHG budget is lower for H_2O electrolysis using CO_2-low electricity from local Swiss nuclear power or hydropower, because the low GHG emissions at the CSP plant in Spain (7 g CO_2-eq. per MJ H_2) are increased by transport emissions and losses. However, producing H_2 from solar energy instead of using the future European electricity mix (UCTE'25) reduces GHG emissions by a factor of more than 10.

Figure 14.5 presents the CED for supplying H_2 to a car tank at 350 bar. The primary energy demand of solar-only pathways is very low apart from the considerable amount of solar energy needed due to low whole chain conversion efficiency. Fossil resource





STE
pipe
SM
R
CG
A
Hyd
ro
Nuc
lear
UC
TE

CED of primary energy sources, in MJ-eq. per MJ H_2 (LHV) in car tank at 350 bar. (From Felder, R. and Meier, A., *J. Sol. Energy Eng*., 130(1), 011017-1/10, 2008.)

consumption for the best solar option (STD pipe) is only slightly higher than for hydropower but distinctly lower than for all pathways directly using fossil energy. In conclusion, solar technologies offer sustainable H_2 production by saving fossil energy resources by a factor of about 10.

14.4.1.2 GHG Emissions and CED of Passenger Car Technologies

Figure 14.6 presents WTW-GHG emissions for all fuel/power train combinations assessed in this study. Contributions of life cycle stages include construction, maintenance, and disposal of car and road infrastructure as well as fuel chain and combustion emissions. Cars powered by renewable fuels emit about 44 ± 8 g CO_2-eq. per passenger kilometer (pkm). Assuming lifetime mileage of 150,000 km, up to 75% of the emissions are associated with material-intensive car construction. Compared to the gasoline/diesel car, GHG emissions from car infrastructure increase by 28% for the FCV with carbon-fiber aluminum pressurized gas tank and by 19% for the BEV. Differences in total GHG emission mainly result from fuel supply and use. In general, the BEV shows the lowest GHG emissions because of its higher energy conversion efficiency compared to the FCV. The best performer is the BEV using local Swiss hydro, nuclear, and wind power. Even with slightly higher fuel-associated GHG emissions, the ICE car using biofuel (SNG) is among the lowest- emitting options, profiting from simpler and less material-intensive car construction.

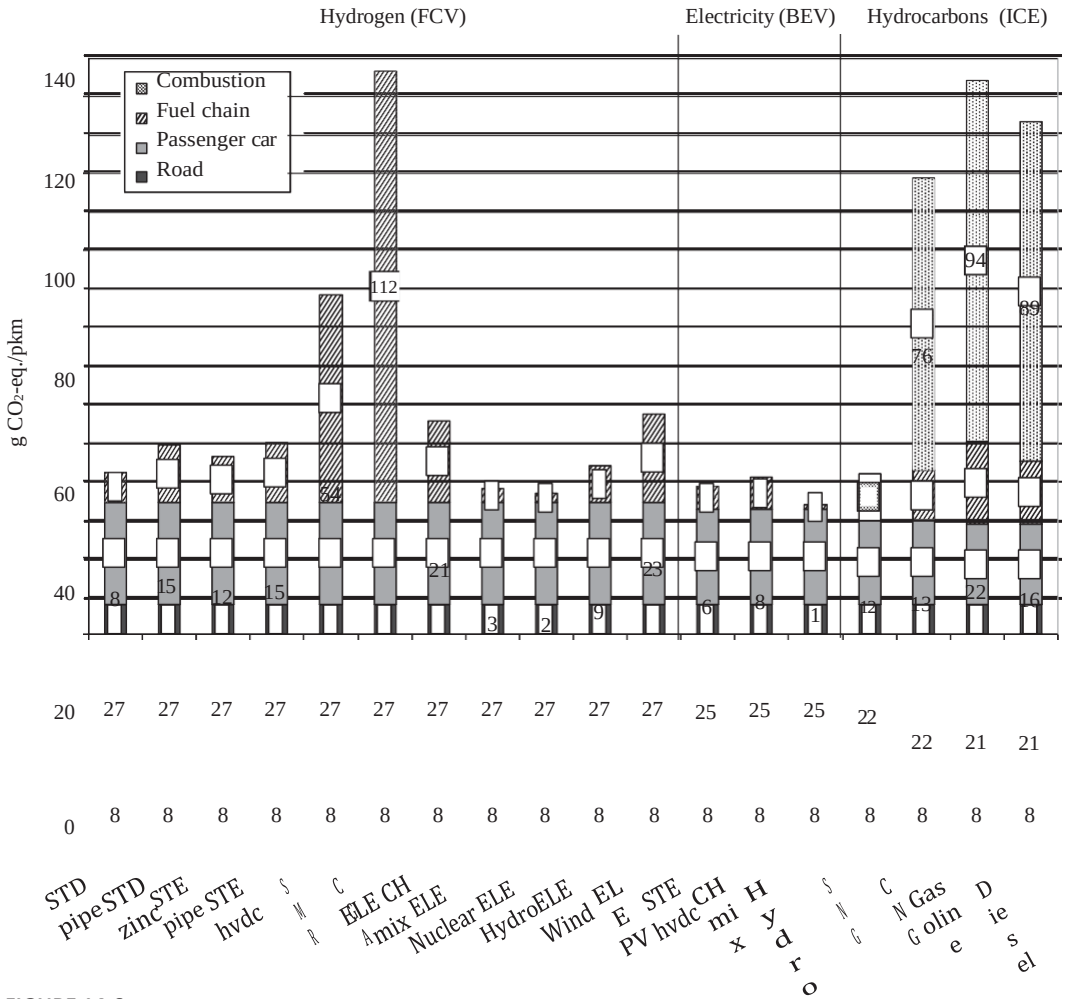


FIGURE 14.6

GHG emissions in g CO_2-eq. per pkm showing contributions of life cycle stages such as construction, mainte- nance, and disposal of passenger car and road infrastructure, fuel chain (production and supply); and direct combustion. Average load of 1.59 passengers per car is used [19]. For SNG, fuel chain and combustion emissions are summed up. For acronyms, see Table 14.1. (Details in Felder, R., Well-to-wheel analysis of renewable trans- port fuels: Synthetic natural gas from wood gasification and hydrogen from concentrated solar energy, PhD thesis, ETH No. 17437, ETH Zurich, Zurich, Switzerland, 2007.)

CSP technologies (STD, STE) reduce GHG emissions for the production of H_2 compared to conventional technologies by a factor of 7 (SMR) and 14 (CGA), which results in 50%–70% CO_2 savings in the FCV. CSP technologies also perform better than H_2O electrolysis using electricity from a future Swiss electricity mix (CH mix) or PV. However, compared to elec- trolysis using locally produced hydro, nuclear, or wind power, GHG emissions from CSP pathways are markedly higher due to steel-intensive infrastructure for the HF and energy transport losses from Southern Spain to Switzerland.

14.4.2 Life Cycle Impact Assessment

14.4.2.1 Eco-Indicator'99 Methodology

Figure 14.7 presents weighted LCIA results using the *Eco-indicator'99* (*EI'99*) methodology with the *Hierarchist* perspective. The dominant environmental impacts of solar H_2 production technologies are associated with the construction of the steel-intensive infrastructure for solar energy collection due to mineral and fossil resource consumption. In particular, today's steel production technology is responsible for GHG and other harmful emissions such as particulates causing respiratory damages. Land consumption and impacts on local flora and wildlife during the build-up of the CSP plant are often quoted as an issue [3]. However, *EI'99* possibly overrates the impact of land use, since CSP installations are preferably located at species-poor arid sites [5]. The damage category *other impacts* encompasses minor effects such as respiratory damages from organics, carcinogens, ecotoxicity, acidification, eutrophication, and ozone layer depletion. Operational impacts from CSP plants are negligible. Ancillary transports have only marginal effects except for Zn transport by freight ship and rail with associated fossil resource consumption and emission of CO_2, NO_x, SO_2, and particulates.

Environmental impacts from the carbothermic Zn/ZnO process (SCR) depend—apart from the construction of CSP plant infrastructure—on the reducing agent used: (1) For the production of charcoal, the main impact factors are land use for growing wood, pos- sible CH_4 release by conventional production procedures, and emission of particulates

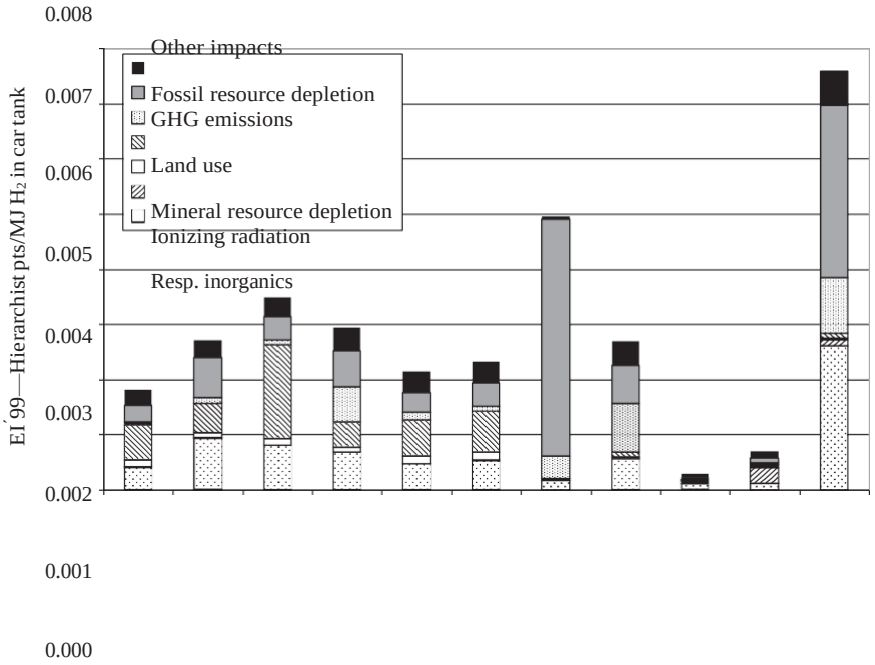


FIGURE 14.7 STD pipe

Eco-indicator'99 – Hierarchist impact values per MJ H_2 (LHV) in car tank at 350 bar, presented for the most important impact categories. For details, see text. (From Felder, R. and Meier, A., *J. Sol. Energy Eng.*, 130(1), 011017-1/10, 2008.)

during forestry; (2) using hard coal, negative impacts result from fossil resource consumption and GHG emissions. STE and STD of ZnO (STD pipe) show about the same LCIA impact scores because of the similar energy conversion efficiency. Overall, electricity transport via HVDC power lines is slightly advantageous compared to H_2 pipeline transport due to lower energy losses. Conventional H_2 production technologies are penalized by fossil resource consumption and net GHG emissions. Using local hydropower to produce electricity for H_2O electrolysis shows the lowest environmental impact. Aspects of nuclear power production (ionizing radiation) are rated low in *EI'99*.

14.4.2.2 Eco-Scarcity'97 Methodology

In contrast to *EI'99*, the *Eco-scarcity'97* (*UBP*) methodology strongly penalizes nuclear waste disposal (Figure 14.8). Emissions of GHG and other harmful gases and particu- lates as well as hazardous heavy metals receive a stronger weight since fossil and mineral resource depletion and land use are neglected. Compared to the best-rated hydropower pathway, the *UBP* score is elevated for all CSP technologies due to the accumulation of various environmental impacts associated with the construction of plant infrastructure, as discussed previously. In general, environmental impacts of the solar H_2 produc- tion pathways are similar as long as efficient energy transport systems (H_2 pipelines and HVDC transmission lines) and no continuous fossil resource input (hard coal) are used.

14.4.2.3 Life Cycle Impact Assessment Example

Figure 14.9 depicts LCIA results for the STD scenario with pipeline transport of H_2 and its use in an FCV. Compared to the reference case—advanced gasoline vehicle—GHG emissions can be reduced by 70% to 44 g CO_2-eq. per pkm. Due to the relatively low conversion efficiency of concentrated solar energy, total CED increases by a factor of about

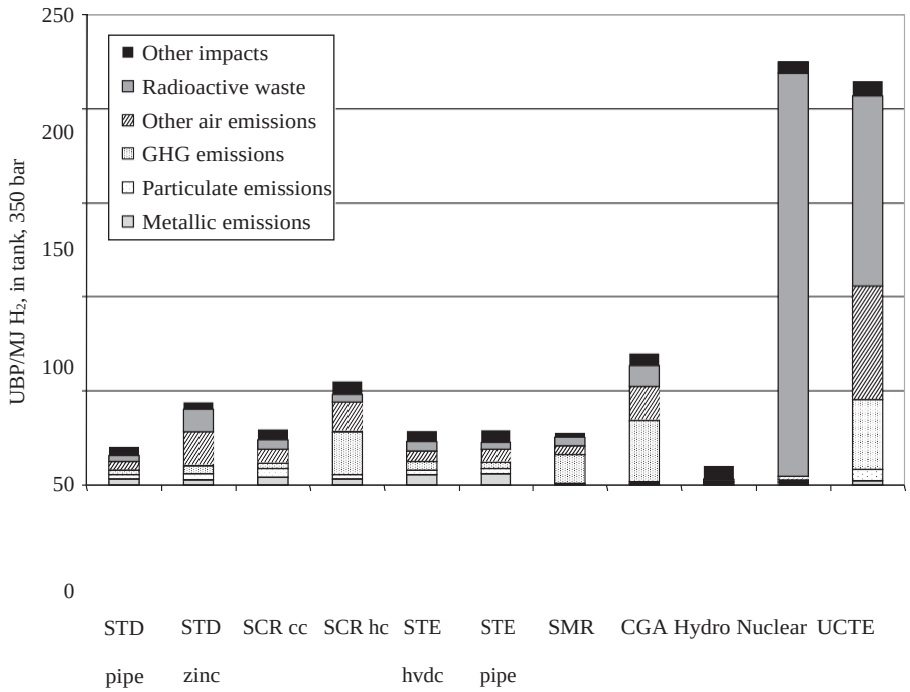


FIGURE 14.8

Eco-scarcity'97 impact values (UBP) per MJ H_2 (LHV) in car tank at 350 bar, presented for the most important impact categories. For details, see text. (From Felder, R. and Meier, A., *J. Sol. Energy Eng*., 130(1), 011017-1/10, 2008.)

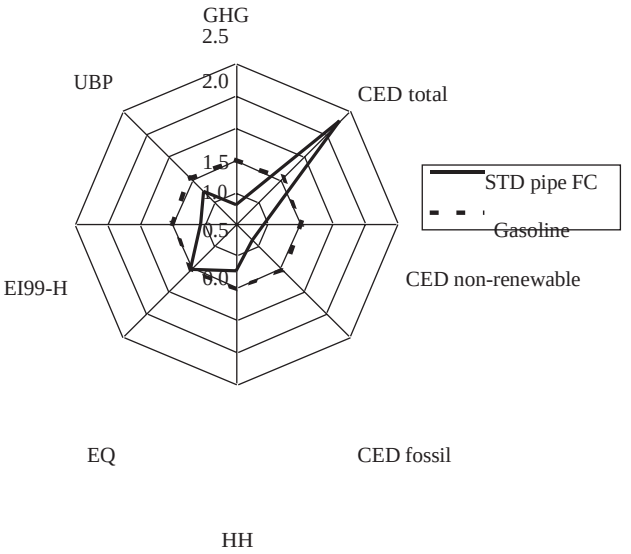


FIGURE 14.9

LCIA results for the STD scenario with pipeline transport of H_2 and its use in an FCV compared to an advanced gasoline vehicle. (For details, see text and Felder, R., Well-to-wheel analysis of renewable transport fuels: Synthetic natural gas from wood gasification and hydrogen from concentrated solar energy, PhD thesis, ETH No. 17437, ETH Zurich, Zurich, Switzerland, 2007.)

2.3 to about 7 MJ-eq./MJ H_2 (LHV) in the car tank at 350 bar. However, CED is reduced by 50% if only nonrenewable energy sources are considered (CED nonrenewable) and by 70% if only fossil energy sources are taken into account (CED fossil). *HH* impacts are reduced by 25%, mainly caused by the absence of emissions such as NO_x and SO_2 in the gasoline fuel chain, aromatic hydrocarbons at the gas station, and combustion. *EQ* does not improve, since dominant ecotoxic emissions from tire abrasion (Zn) are fuel-independent. The aggregated environmental impact is reduced by 50% when using the *EI'99-H* methodology—which strongly weights the consumption of fossil resources—and by 25% when using the *UBP* methodology. Here, the effect of lower GHG emissions and fossil resource consumption is partly counterbalanced by particulate emissions from steel production for the HF, land use, and consumption of mineral resources. The combined LCIA shows better overall environmental performance of the FCV with STD pipe scenario compared to an advanced gasoline vehicle.

14.5 Fuel and Vehicle Costs

Table 14.11 presents an overview of cost assumptions and results for solar H_2 produc- tion technologies (STD, STE) compared to conventional H_2 production (SMR, CGA) and H_2O electrolysis (ELE) based on electricity from different sources (CH mix, wind, PV). Cost of solar H_2 is calculated from various literature sources on CSP technologies [35] and H_2 production methods [41,69]. Passenger car transportation costs are taken from two comprehensive references [18,70]. Electricity costs used are 0.07 US$/kWh for conventional industrial plants [41], 0.09 US$/kWh for wind (average midterm scenario for 2020; exchange rate 1 USD = 1.2 CHF) [71], and 0.28 US$/kWh for PV (assumed for large Swiss plant in 2020; exchange rate 1 USD = 1.2 CHF) [71]. Costs for NG [69] of
0.22 US$/$Nm^3$ and for coal [41] of 30 US$/ton are anticipated for 2025. Assumptions

for vehicle transportation calculations encompass capital costs [72,73] and annual costs

TABLE 14.11

Cost Assumptions and Results for Solar H_2 Production (STD, STE) Compared to Conventional H_2 Production (SMR, CGA) and H_2O Electrolysis (ELE) Based on Electricity from Various Sources (CH Mix, Wind, and PV)

	Unit	STD pipe	STD zinc	STE pipe	STE hvdc	SMR	CGA	ELE CH mix	ELE wind	ELE PV
Solar plant (input into receiver)	MW_{th}	50	50	50	50					
H_2 production (LHV)[a]	MWh/a	24,138	28,398	18,951	18,951	1.6E06	1.6E06	4005	4005	4005
H_2 production (LHV)[a]	MW	13.3	15.7	10.4	10.4	177	177	0.55	0.55	0.55
Annual thermal eff. (LHV)	—	0.17	0.20	0.13	0.13	0.76	0.73	0.63	0.63	0.63
Capital cost	*mill. $*									
HF		10.6	10.6	10.6	10.6					
Tower		2.2	2.2	2.2	2.2					
CPC		0.9	0.9							
Receiver–reactor, quencher/periphery		8.2	8.2	8.2	8.2					
Hydrolyzer		2.5								
Molten salt storage system				2.0	2.0					
Power block				16.0	16.0					
Electrolyzer				12.2						
Compressor (1–30 bar)		5.5		4.7						
Zn			3.0							
Land costs		1.0	1.0	1.0	1.0					
Balance of plant,		6.0	6.0	6.0	6.0					
Indirect costs, contingency										
Total capital cost		37.3	31.9	62.8	46.0	79.1	258.5	4.15	4.15	4.15
Annual cost	*mill. $*									
Weighted lifetime	a	22.8	25.7	22.9	28.0	30	30	30	30	30
Capital charge rate	%	16.6	16.4	12.3	10.1	18.0	18.0	18.0	18.0	18.0
Capital costs		6.20	5.23	7.71	4.62	14.24	46.53	0.75	0.75	0.75
O&M		0.75	0.64	1.26	0.92	4.75	15.51	0.25	0.25	0.25
Compression (1–30 bar)		0.12		0.09						

(*continued*)

TABLE 14.11 (continued)

Cost Assumptions and Results for Solar H_2 Production (STD, STE) Compared to Conventional H_2 Production (SMR, CGA) and H_2O Electrolysis (ELE) Based on Electricity from Various Sources (CH Mix, Wind, and PV)

	Unit	STD pipe	STD zinc	STE pipe	STE hvdc	SMR	CGA	ELE CH mix	ELE wind	ELE PV
Fuel						84.37	10.20			
Electricity		0.07	0.05	0.00	0.00	5.21	18.15	0.46	0.61	1.83
Other inputs		0.12	0.19	0.06	0.06					
Total annual cost, at plant		7.26	6.11	9.12	5.60	108.56	90.39	1.46	1.61	2.83
Specific cost per unit										
Solar Zn, at plant	$/kg	0.25	0.25							
Electricity, at plant	$/kWh			0.19	0.19			0.07	0.09	0.28
H_2 30 bar, at plant (LHV)	$/kg	10.0		16.0		2.2	1.7	12.0	13.0	23.4
Zn transport	$/kg		0.01							
Solar Zn, at gas station	$/kg		0.26							
Electricity transport	$/kWh				0.01					
Solar electricity, at gas station	$/kWh				0.21					
H_2 pipeline transport (LHV)	$/kg	3.7		4.7		0.8	1.3			
H_2 30 bar, at gas station (LHV)	$/kg	13.7	10.0	20.7	20.0	3.0	3.0			
H_2 fueling 30–350 bar (LHV)	$/kg	1.0	0.3	1.0	0.3	1.0	1.0	0.3	0.3	0.3
H_2 350 bar, in car tank (LHV)	$/kg	14.7	10.3	21.7	20.3	4.0	4.0	12.3	13.3	23.7

[a]*Note:* Each scenario has different H_2 production capacities, which has an impact on H_2 costs.

(depreciation, taxes, O&M) [70] for a variety of vehicles with different fuels and power trains (FCV, BEV, CNG, gasoline, and diesel).

14.5.1 Passenger Car Transportation Costs

Figure 14.10 depicts passenger car transportation costs for selected scenarios show- ing contributions of road infrastructure, operation and maintenance (O&M), fuel production and supply, and external costs. Main cost component is O&M, comprising total annual costs for the consumer (consisting to a large extent of car depreciation)

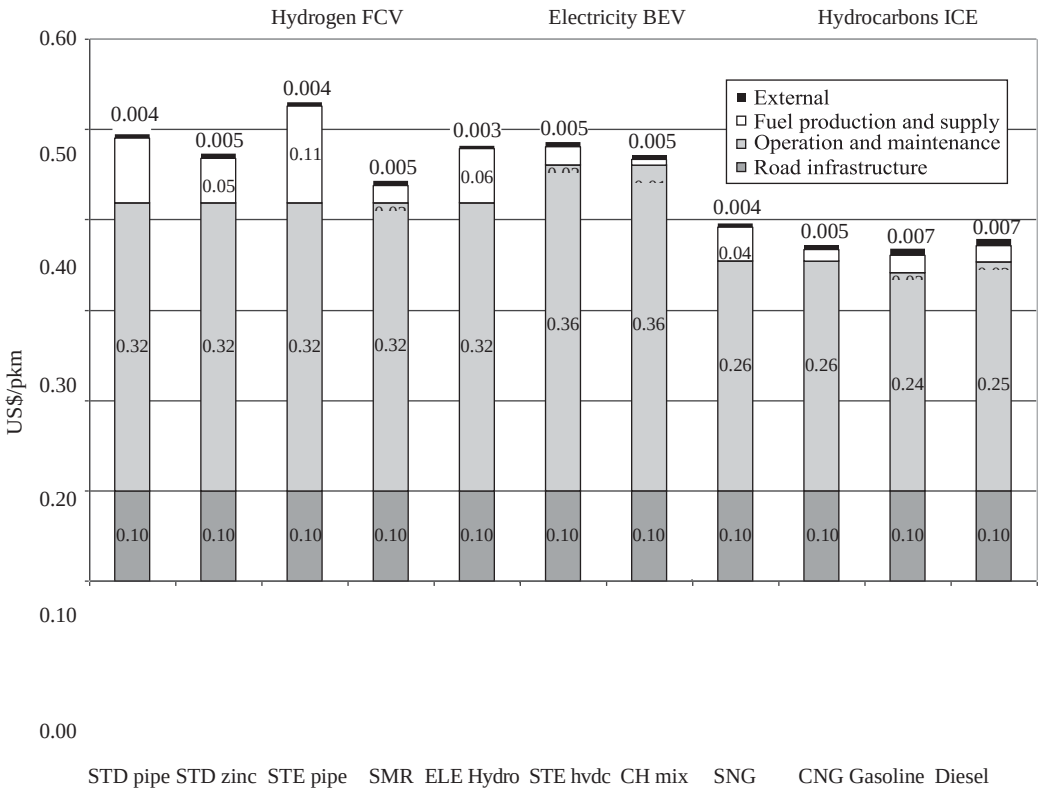


FIGURE 14.10

Transportation costs per pkm for selected scenarios with contribution of road infrastructure, O&M (total annual costs for consumer not including fuel), fuel production and supply, and external costs. Average load of

1.59 passengers per car is used [19]. For acronyms, see Table 14.1. (Details in Felder, R., Well-to-wheel analysis of renewable transport fuels: Synthetic natural gas from wood gasification and hydrogen from concentrated solar energy, PhD thesis, ETH No. 17437, ETH Zurich, Zurich, Switzerland, 2007.)

excluding fuel costs. Assuming equal maintenance and repair costs for all power trains, total costs are higher by about 0.07–0.15 US$/pkm for alternative vehicle con- cepts (FCV and BEV) compared to conventional hydrocarbon technologies. Among the ICE cars, SNG is relatively cost-competitive, with an increase of total costs by only 0.03 US$/pkm compared to gasoline. Although BEVs have rather low fuel costs, total costs are about 0.10 US$/pkm higher than for conventional vehicles due to their expen- sive car infrastructure. The most economic alternative option is the FCV using H_2 pro- duced by SMR, costing 0.07 US$/pkm more than a gasoline vehicle while fuel costs are similar (about 0.02 US$/pkm, corresponding to 4 US$/kg H_2 in car tank). Total trans- portation costs may increase by 0.12–0.16 US$/pkm or 0.20–0.25 US$/km for an FCV powered by solar H_2 compared to an ICE vehicle using gasoline, depending on fossil fuel price development.

H_2 production and supply costs for CSP scenarios are 2.5–5.5 times higher than for SMR (4 US$/kg H_2 in car tank), depending on the chosen scenario. STD with H_2 pipeline transport (STD pipe) costs about 0.07 US$/pkm, corresponding to 14.7 US$/kg H_2 in car tank and 10.1 US$/kg H_2 at plant. STE with H_2 pipeline transport (STE pipe) costs about 0.11 US$/pkm (21.9 US$/kg H_2 in car tank and 16.1 US$/kg H_2 at plant). For comparison, the most economic CSP option using Zn transport (STD zinc) costs around 0.05 US$/pkm or 10.2 US$/kg H_2 in car tank, less than H_2 fuel costs using hydro or wind electricity for H_2O electrolysis (about 0.06 US$/pkm). External costs have marginal impact on total costs. Only

for conventional low-cost fuels, external costs increase fuel costs by about 40%. For most of the alternative fuels, internalization of external costs virtually has no effect, since fuel costs are much higher.

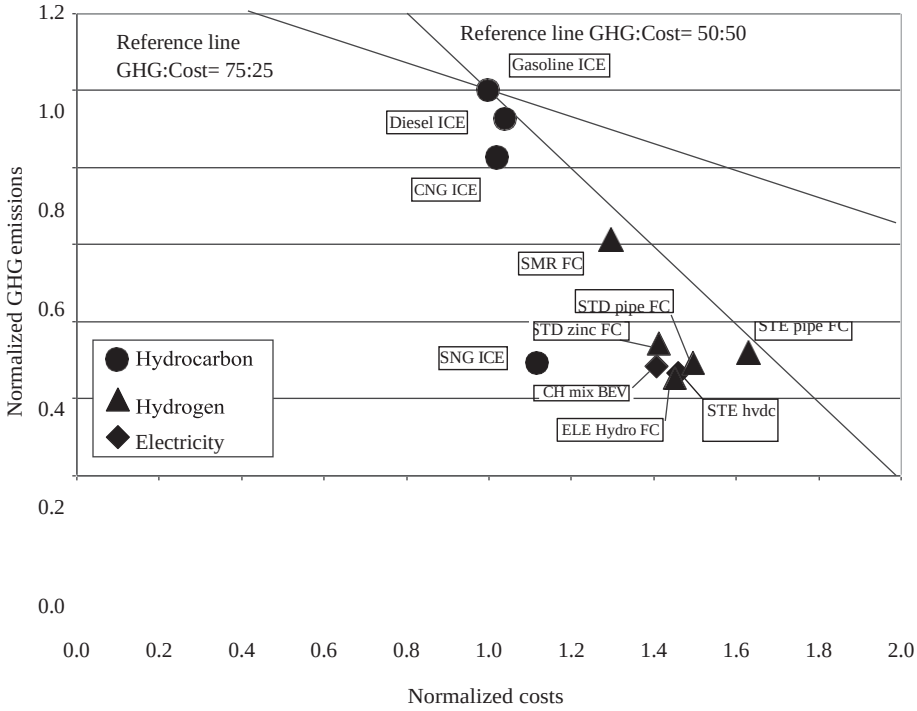


FIGURE 14.11

Eco-efficiency for selected fuel/power train combinations showing normalized GHG emissions versus cost per pkm; reference is the gasoline ICE vehicle. Two reference lines are shown: (1) weighting of 50:50 for GHG emissions versus costs (GHG emissions = 2 − costs) and (2) weighting of 75:25 for GHG emissions versus costs (GHG emissions = 4/3 − 1/3 * costs). For acronyms, see Table 14.1. (Details in Felder, R., Well-to-wheel analysis of renewable transport fuels: Synthetic natural gas from wood gasification and hydrogen from concentrated solar energy, PhD thesis, ETH No. 17437, ETH Zurich, Zurich, Switzerland, 2007.)

14.5.2 Eco-Efficiency

Figure 14.11 presents eco-efficiency results in terms of normalized GHG emissions versus normalized costs per pkm, referenced to the gasoline ICE vehicle. Data points below the reference line indicate higher eco-efficiency than the reference case; moreover, the larger their perpendicular distance to the reference line, the better their relative eco-efficiency performance. Assuming a weighting ratio of 50:50 for GHG emissions ver- sus cost, the SNG ICE vehicle shows highest eco-efficiency. The other technologies are at roughly the same level with slight advantage for FCV using ELE hydro and BEV using CH mix. All CSP pathways exhibit a better eco-efficiency than the gasoline ICE vehicle. Assuming a more environmentally oriented stakeholder perspective by setting a weighting ratio of 75:25 for GHG emissions versus costs favors renewable fuels over fossil-based fuels.

14.6 Conclusions

A WTW analysis and an economic assessment have been conducted for the production, transport, and usage of H_2 as future transportation fuel. Solar H_2, produced by the thermochemical Zn/ZnO cycle in Southern Spain and transported to Central Europe, was compared with SMR, advanced CGA, and ELE based on renewable electricity gen- erated in solar thermal, PV, wind, and hydropower plants. Usage of H_2 in an FCV was anticipated for 2025. It was found that cars powered by renewable fuels emit about

42 ± 8 g CO_2-eq. per passenger kilometer. In general, the battery electric vehicle (BEV) shows the lowest GHG emissions because of its higher energy conversion efficiency compared to the FCV. In the specific case of Switzerland, the best performers are BEVs using local hydro, nuclear, and wind power. CSP technologies reduce GHG emissions for the production and supply of H_2 by a factor of 7 (SMR) and 14 (CGA), resulting in 50%–70% CO_2 savings in an FCV. Total environmental impact of passenger car trans- portation can be reduced by replacing advanced gasoline vehicles with FCVs powered by H_2 from CSP.

High capital investments for HF infrastructure and long-distance transport result in 2.5–5.5 times higher H_2 production and supply costs for solar scenarios vis-à-vis conventional SMR (4 US$/kg H_2 in car tank). Total transportation costs may increase by 0.20–0.25 US$/km for an FCV powered by solar H_2 compared to an ICE vehicle using gasoline. Assuming long-term market acceptance associated with return on invest- ment being reduced from 15% for new technologies to 5% for established technologies, costs of the most economic CSP technology (STD with Zn transport) would decrease to 6 US$/kg H_2 and become competitive to costs of SMR and CGA, which are expected to rise due to fossil resource shortage. External costs have only marginal impact on total costs of alternative fuels, where fuel costs are dominant. Eco-efficiency is low for all solar H_2 production technologies, since their relatively high costs are not outweighed by their environmental benefit, unless ecological aspects are stronger weighted than economics.

Acknowledgments

The financial support by the Swiss Federal Office of Energy (SFOE) and the Baugarten Foundation is gratefully acknowledged. This work is based on the PhD thesis of R. Felder, who tragically passed away shortly after his doctoral exam. The author would like to thank A. Wokaun, A. Steinfeld, and C. Wieckert for fruitful discussions.

References

1. IEA, 2008, Energy technology perspectives 2008, International Energy Agency, Paris, France, 2008.
2. EC, 2006, World Energy Technology Outlook—2050 (WETO-H2), European Commission, Directorate-General for Research, Brussels, Belgium, 2006, ISBN 92-79-01636-9.
3. Pregger, T., Graf, D., Krewitt, W., Sattler, C., Roeb, M., Möller, S., 2009, Prospects of solar ther- mal hydrogen production processes, *Int. J. Hydrogen Energy*, **34**, 4256–4267.
4. Felder, R., 2007, Well-to-wheel analysis of renewable transport fuels: Synthetic natural gas from wood gasification and hydrogen from concentrated solar energy, PhD thesis, ETH No. 17437, ETH, Zurich, Switzerland.
5. Felder, R., Meier, A., 2008, Well-to-wheel analysis of solar hydrogen production and utilization for passenger car transportation, *J. Sol. Energy Eng*., **130**(1), 011017-1/10.

6. Felder, R., Meier, A., Wokaun, A., 2008, Solar hydrogen as future transportation fuel— Well-to-wheel analysis and economic assessment, *Proceedings of the 14th Biennial Concentrating Solar Power SolarPACES Symposium*, Las Vegas, NV, March 4–7, 2008.
7. Midilli, A., Ay, M., Dincer, I., Rosen, M.A., 2005, On hydrogen and hydrogen energy strategies: I: Current status and needs, *Renewable Sustainable Energy Rev*., **9**(3), 255–271.
8. Winter, C.-J., 2005, Into the hydrogen energy economy—Milestones, *Int. J. Hydrogen Energy*, **30**(7), 681–685.
9. Steinfeld, A., 2005, Solar thermochemical production of hydrogen—A review, *Sol. Energy*, **78**(5), 603–615.
10. Abanades, S., Charvin, P., Flamant, G., Neveu, P., 2006, Screening of water-splitting thermo- chemical cycles potentially attractive for hydrogen production by concentrated solar energy, *Energy*, **31**(14), 2805–2822.
11. Perkins, C., Weimer, A.W., 2004, Likely near-term solar-thermal water splitting technologies, *Int. J. Hydrogen Energy*, **29**(15), 1587–1599.
12. Steinfeld, A., 2002, Solar hydrogen production via a two-step water-splitting thermochemical cycle based on Zn/ZnO redox reactions, *Int. J. Hydrogen Energy*, **27**(6), 611–619.
13. Abanades, S., Charvin, P., Flamant, G., 2007, Design and simulation of a solar chemical reactor for the thermal reduction of metal oxides: Case study of zinc oxide dissociation, *Chem. Eng. Sci*., **62**, 6323–6333.
14. Schunk, L.O., Haeberling, P., Wepf, S., Wuillemin, D., Meier, A., Steinfeld A., 2008, A receiver- reactor for the solar thermal dissociation of zinc oxide, *J. Sol. Energy Eng*., **130**(2), 021009-1/6.
15. Schunk, L.O., Lipiński, W., Steinfeld A., 2009, Heat transfer analysis of a solar receiver-reactor for the thermal dissociation of ZnO—Experimental validation at 10 kW and scale-up to 1 MW, *Chem. Eng. J*., **150**, 502–508.
16. Wieckert, H.-C., 2005, Design studies for a solar reactor based on a simple radiative heat exchange model, *J. Sol. Energy Eng*., **127**(3), 425–429.
17. Ernst, F., Tricoli, A., Steinfeld, A., Pratsinis, S.E., 2006, Co-synthesis of H_2 and ZnO by in-situ Zn aerosol formation and hydrolysis, *AIChE J*., **52**, 3297–3303.
18. Edwards, R., Griesemann, J.-C., Larivé, J.-F., Mahieur, V., 2006, Well-to-wheels analysis of future automotive fuels and powertrains in the European context. Well-to-Wheels report. Version 2b, EUCAR, CONCAWE, JRC/IES.
19. Spielmann, M., Kägi, T., Stadler, P. et al., 2003, Life cycle inventories of transport services. Ecoinvent report No. 14, Swiss Centre for Life Cycle Inventories, Dübendorf, Switzerland.
20. Frischknecht, R., Jungbluth, N., Althaus, H.-J. et al., 2004, Overview and methodology. Ecoinvent report No. 1, Swiss Centre for Life Cycle Inventories, Dübendorf, Switzerland.
21. Bauer, C., Dones, R., 2006, Axpo-Stromperspektiven 2030. Ongoing projects from GaBe project at PSI, Villigen PSI, Switzerland, Personal Communication, 5.4.2006.
22. Geerken, T., Lassaux, S., Renzoni, R., Timmermans, V., 2004, Review of hydrogen LCA's for the Hysociety project, Final Report, EU FP5 Project, Contract No. 11673.
23. ISO, 1998, Environmental management—Life cycle assessment—Goal and scope definition and inventory analysis. International Organization for Standardization, ISO 14041.
24. ISO, 2000, Environmental management—Life cycle assessment—Life cycle impact assessment. International Organization for Standardization, ISO 14042.
25. IPCC, 2001, *Climate Change 2001: The Scientific Basis*. Contribution of Working Group I to the Third Assessment Report of the Intergovernmental Panel on Climate Change, J.T. Houghton, Y. Ding, D.J. Griggs, M. Noguer, P.J. van der Linden, X. Dai, K. Maskell, and C.A. Johnson, eds., Cambridge University Press, Cambridge, U.K.
26. Frischknecht, R., Jungbluth, N., Althaus, H.-J. et al., 2004, Implementation of life cycle impact assessment methods. Ecoinvent report No. 3, Swiss Centre for Life Cycle Inventories, Dübendorf, Switzerland.
27. Goedkoop, M., Effting, S., Collignon, M., 2001, The eco-indicator 99. A damage oriented method for Life Cycle Impact Assessment, PRé Consultants B.V., Amersfoort, the Netherlands.

28. Brand, G., Scheidegger, A., Schwank, O. et al., 1998, Weighting in ecobalances with the ecos- carcity method, Environment Series No. 297, Swiss Agency for the Environment, Forests and Landscape, Berne, Switzerland.
29. Jolliet, O., Margni, M., Charles, R. et al., 2003, Impact 2002+: A new life cycle impact assessment methodology, *Int. J. LCA*, **8**(6), 324–330.
30. Saling, P., Kicherer, A., Dittrich-Krämer, B. et al., 2002, Eco-efficiency analysis by BASF: The method, *Int. J. LCA*, **7**(4), 203–218.
31. Suh, S., Lee, K.M., Ha, S., 2005, Eco-efficiency for pollution prevention in small to medium- sized enterprises, *J. Ind. Ecol*., **9**(4), 223–240.
32. Colella, W.G., Jacobson, M.Z., Golden, D.M., 2005, Switching to a U.S. hydrogen fuel cell vehi- cle fleet: The resultant change in emissions, energy use, and greenhouse gases, *J. Power Sources*, **150**, 150–181.
33. Osuna, R., Fernandez, V., Romero, S., 2004, PS10: A 11.0-MWe solar tower power plant with saturated steam receiver [CD-ROM], *Proceedings of the 12th SolarPACES International Symposium*, Oaxaca, Mexico, ISBN 968-6114-18-1.
34. PS10, 2006, 10 MW solar thermal power plant for southern Spain, Final Technical Project Report, EU FP5 Contract No. NNE5-1999-356.
35. ECOSTAR, 2005, ECOSTAR—European Concentrated Solar Thermal Road-Mapping, Final Report, EU FP6 Contract No. SES6-CT-2003-502578, R. Pitz-Paal, J. Dersch, B. Milow, eds., DLR, Cologne, Germany.
36. Segal, A., Epstein, M., 1999, Comparative performances of tower-top and tower-reflector cen- tral solar receivers, *Sol. Energy*, **65**, 206–226.
37. Sargent & Lundy LLC Consulting Group, 2003, Assessment of parabolic trough and power tower solar technology cost and performance forecasts, NREL/SR-550-34440, Prepared for the US Department of Energy and National Renewable Energy Laboratory, Golden, CO.
38. Weinrebe, G., 2000, Technische, ökologische und ökonomische Analyse von solarthermischen Turmkraftwerken [Technical, ecological and economic analysis of solar thermal tower power plants], PhD thesis in Energietechnik, University of Stuttgart, Stuttgart, Germany.
39. Pitz-Paal, R., Merz, T., Bayer Botero, N., Steinfeld, A., 2009, Heliostat field layout optimiza- tion for high temperature solar thermochemical processing, *Proceedings of the 15th SolarPACES Conference*, Berlin, Germany, September 15–18, 2009.
40. Romero, M., Buck, R., Pacheco, J.E., 2002, An update on solar central receiver systems, projects, and technologies, *J. Sol. Energy Eng*., **124**(2), 98–108.
41. Simbeck, D., Chang, E., 2002, Hydrogen supply: Cost estimate for hydrogen path- ways—Scoping analysis, NREL/SR-540-32525, National Renewable Energy Laboratory, Golden, CO.
42. Reilly, H.E., Kolb, G.J., 2001, An evaluation of molten-salt power towers including results of the Solar Two Project, SAND 2001-3674, Sandia National Laboratories, Albuquerque, NM.
43. Meier, A., Gremaud, N., Steinfeld, A., 2005, Economic evaluation of the industrial solar produc- tion of lime, *Energy Convers. Manage*., **46**, 905–926.
44. Müller, R., Steinfeld, A., 2007, Band-approximated radiative heat transfer analysis of a solar chemical reactor for the thermal dissociation of zinc oxide, *Sol. Energy*, **81**(10), 1285–1294.
45. Wieckert, C., Frommherz, U., Kräupl, S., Guillot, E., Olalde, G., Epstein, M., Santen, S., Osinga, T., Steinfeld, A., 2007, A 300 kW solar chemical pilot plant for the carbothermic produc- tion of zinc, *J. Sol. Energy Eng*., **129**, 190–196.
46. Wieckert, H.-C., 2005, Solzinc reactor efficiency, Villigen PSI, Switzerland, Personal Communication, September 2005.
47. Epstein, M., Olalde, G., Santén, S., Steinfeld, A., Wieckert, C., 2008, Towards the industrial solar carbothermal production of zinc, *J. Sol. Energy Eng*., **130**, 014505-1/4.
48. Kräupl, S., Frommherz, U., Wieckert, H.-C., 2006, Solar carbothermic reduction of ZnO in a two-cavity reactor: Laboratory experiments for a reactor scale-up, *J. Sol. Energy Eng*., **128**(1), 8–15.

49. FAO, 1985, Industrial charcoal making. FAO Forestry Paper 63, Chapter 3.3, Food and Agriculture Organization of the United Nations (FAO), Rome, Italy, http://www.fao.org/docrep/X5555E/X5555E00.htm, accessed on 03.12.2013.
50. Winnacker, K., Küchler, L., 1971, Organische Technologie I [Organic technology I], in *Chemische Technologie* [*Chemical Technology*], 3rd edn., Carl Hanser Verlag, Munich, Germany.
51. Criscuoli, A., Basile, A., Drioli, E., 2000, An analysis of the performance of membrane reactors for the water-gas shift reaction using gas feed mixtures, *Catal. Today*, **56**(1–3), 53–64.
52. Faist Emmenegger, M., Jungbluth, N., Heck, T., 2003, Erdgas [Natural Gas]. Ecoinvent report No. 6-V, Swiss Centre for Life Cycle Inventories, Dübendorf, Switzerland.
53. Bossel, U., Eliasson, B., Taylor, G., 2005, The future of the hydrogen economy: Bright or bleak? in European Fuel Cell Forum, Lucerne, Switzerland.
54. Angloher, J., Dreier, T., 2000, Techniken und Systeme zur Wasserstoffbereitstellung. Perspektiven einer Wasserstoff-Energiewirtschaft (Teil 1). [Techniques and systems for hydrogen sup- ply. Perspectives of a hydrogen energy economy (Part 1)], in *Perspektiven einer Wasserstoff- Energiewirtschaft*, U. Wagner, ed., wiba—Koordinationsstelle der Wasserstoff-Initiative Bayern, Munich, Germany.
55. Frischknecht, R., Faist Emmenegger, M., 2003, Strommix und Stromnetz [Electricity mix and network]. Ecoinvent report No. 6, Swiss Centre for Life Cycle Inventories, Dübendorf, Switzerland.
56. Spath, P.L., Mann, M.K., 2001, Life cycle assessment of hydrogen production via natural gas steam reforming, NREL/TP-570-27637, National Renewable Energy Laboratory, Golden, CO.
57. Stiegel, G.J., Ramezan, M., 2006, Hydrogen from coal gasification: An economical pathway to a sustainable energy future, *Int. J. Coal Geol.*, **65**(3–4), 173–190.
58. Dones, R., 2003, Kernenergie [Nuclear energy]. Final report ecoinvent 2000 No. 6-VII, R. Dones, ed., Swiss Centre for Life Cycle Inventories, Dübendorf, Switzerland.
59. Bolliger, R., Bauer, C., 2004, Wasserkraft [Hydro power]. Final report ecoinvent 2000 No. 6-VIII, Swiss Centre for Life Cycle Inventories, Dübendorf, Switzerland.
60. Burger, B., Bauer, C., 2004, Windkraft [Wind power]. Final report ecoinvent 2000 No. 6-XIII, Swiss Centre for Life Cycle Inventories, Dübendorf, Switzerland.
61. Durisch, W., Bauer, C., 2005, Photovoltaik [Photovoltaics], in *Erneuerbare Energien und neue Nuklearanlagen* [*Renewable Energies and New Nuclear Power Plants*], Paul Scherrer Institute, Villigen, Switzerland, pp. 124–172.
62. Pehnt, M., 2003, Life-cycle analysis of fuel cell system components, in *Handbook of Fuel Cells – Fundamentals, Technology and Applications*, W. Vielstich, A. Lamm, and H.A. Gasteiger, eds., John Wiley & Sons, Ltd., Chichester, U.K., pp. 1293–1317.
63. Jungbluth, N., 2004, Erdöl [Crude Oil]. Final report ecoinvent 2000 No. 6-IV, in *Sachbilanzen von Energiesystemen: Grundlagen für den ökologischen Vergleich von Energiesystemen und den Einbezug von Energiesystemen in Ökobilanzen für die Schweiz*, R. Dones, ed., Swiss Centre for Life Cycle Inventories, Dübendorf, Switzerland.
64. Dones, R., Heck, T., Bauer, C. et al., 2005, New Energy Technologies—Final Report on Work Package 6—Release 2, July 2005. ExternE-Pol Project 'Externalities of Energy: Extension of Accounting Framework and Policy Applications', European Commission, Brussels, Belgium.
65. INFRAS, 1998, Ökoprofile von Treibstoffen [Ecological profiles of fuels], Umwelt-Materialien Nr. 104, Swiss Agency for the Environment, Forests and Landscape SAEFL, Berne, Switzerland.
66. Röder, A., 2001, Integration of life-cycle assessment and energy planning models for the evalu- ation of car powertrains and fuels, PhD Thesis, ETH, Nr. 14291, Zurich, Switzerland.
67. Rade, I., Andersson, B.A., 2001, Requirement for metals of electric vehicle batteries, *J. Power Sources*, **93**, 55–71.
68. Ivy, J., 2004, Summary of electrolytic hydrogen production. Milestone completion report, NREL/ MP-560-35948, National Renewable Energy Laboratory, Golden, CO.
69. Hydrogen Analysis Resource Center, US DOE, http://www.hydrogen.energy.gov/resource_ center.html, accessed on November 15, 2006.

70. Zwyssig, M., 2005, *Vergleich der Flottenkosten von Erdgas- und konventionell angetriebenen Fahrzeugen* [*Comparison of Fleet Costs of Natural Gas and Conventional Cars*], Departement Wirtschaft und Management, Zentrum für Accounting & Controlling, Winterthur, Switzerland.
71. Hirschberg, S., Bauer, C., Burgherr, P. et al., 2005, *Erneuerbare Energien und neue Nuklearanlagen: Potenziale und Kosten* [*Renewable Energies and New Nuclear Power Plants: Potential and Cost*], Paul Scherrer Institute, Villigen, Switzerland. ISSN 1019-0643.
72. Edwards, R., Griesemann, J-C., Larivé, J.-F. et al., 2006, Well-to-wheels analysis of future auto- motive fuels and powertrains in the European context. Tank-to-Wheels Report, Version 2b, Appendix 1. EUCAR, CONCAWE, JRC/IES.
73. Weiss, M.A., Heywood, J.B., Drake, E.M. et al., 2000, *On the Road in 2020: A Life-Cycle Analysis of New Automobile Technologies*, Energy Laboratory Report # MIT EL 00-003, Massachusetts Institute of Technology, Cambridge, MA.

Section VII

Hydrogen Storage, Transportation, Handling, and Distribution

15

Overview of Hydrogen Storage, Transportation, Handling, and Distribution

Ned T. Stetson
U.S. Department of Energy

Robert C. Bowman Jr.
Oak Ridge National Laboratory

Gregory L. Olson
HRL Laboratories, LLC

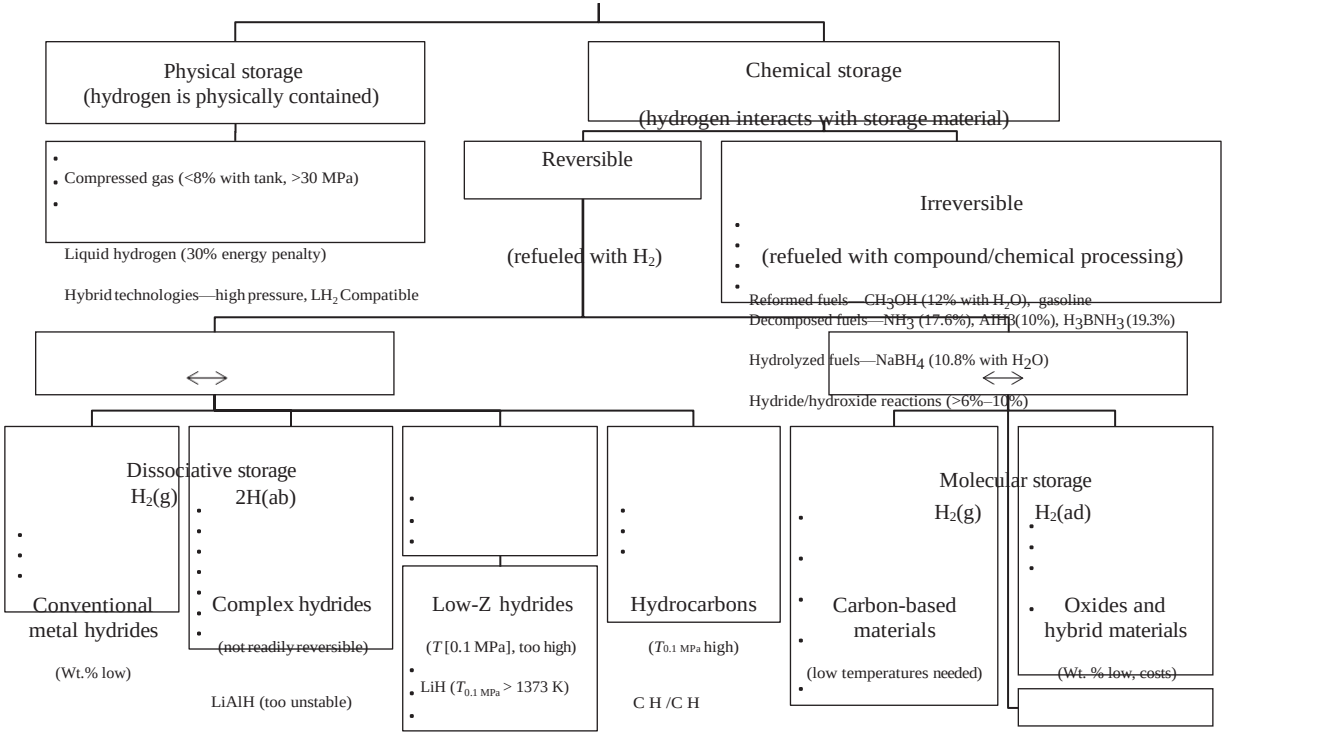
CONTENTS

15.1 Background 567
15.2 Physical Storage as Compressed Gas or Cryogenic Liquid 569
15.3 Transition Metal Hydrides 572
15.4 Complex Hydrides 575
15.4.1 Thermodynamics 576
15.4.2 Kinetics 578
15.4.3 Summary 580
15.5 Chemical Hydrogen Storage Materials 580
15.6 Hydrogen Sorbents 583
15.7 Engineering Aspects of Hydrogen Storage Systems 585
15.8 Summary 586
References 587

15.1 Background

As hydrogen finds increasing use in emerging applications, the need for improved storage methods is becoming more important. Hydrogen has a normal boiling temperature of about 20 K and a critical temperature of approximately 33 K, above which a liquid cannot be formed through the application of pressure. It is therefore a gas at essentially all normal use and storage temperatures. Hydrogen is the lightest of all elements, and since it behaves as an ideal gas close to ambient temperatures (~300 K) and pressure conditions, it has a very low normal density of 0.09 g/L (or 11 L/g) at 288 K and 0.1 MPa. To put this density in perspective, with a lower heating value of about 120 kJ/g, the normal energy density of hydrogen is 10 kJ/L. While gasoline has a specific energy of only about 42 kJ/g, its energy density is 32,000 kJ/L [1] and thus has an energy density about 3,200 times greater than normal hydrogen gas.

Hydrogen storage options and materials



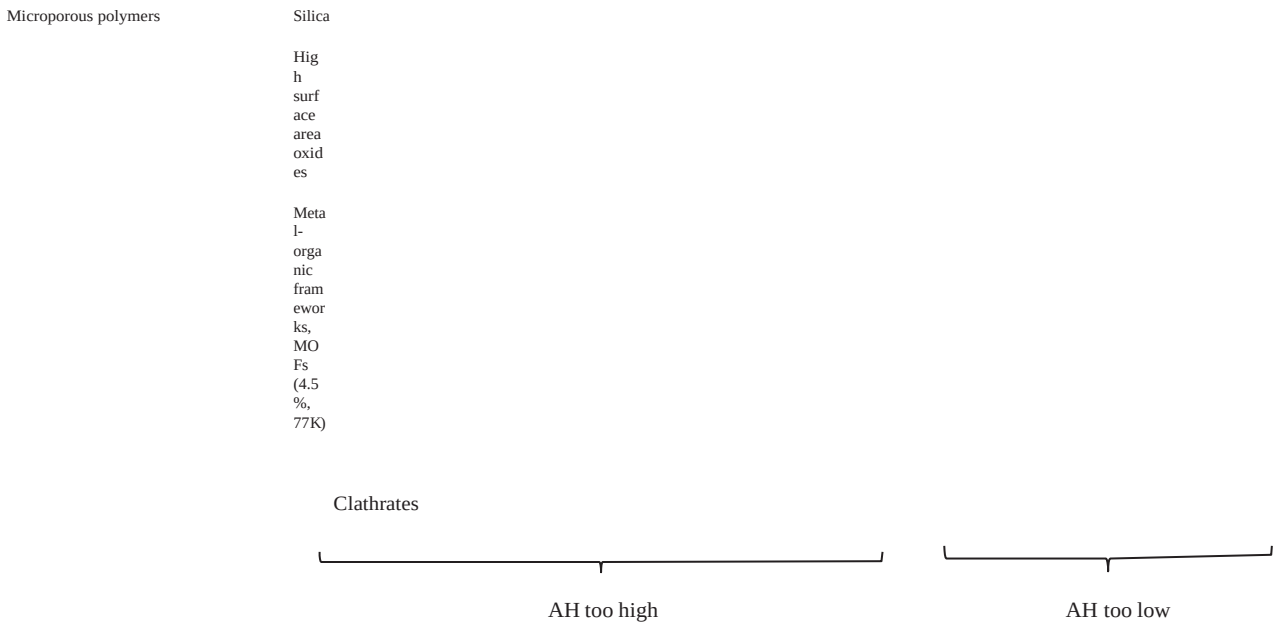


FIGURE 15.1

Various hydrogen storage technologies along with some of their advantages and disadvantages. (Courtesy of Dr. John Vajo.)

To overcome the low density of normal hydrogen gas, it has typically been either produced *over the fence* from the point of use (e.g., near petroleum refineries), liquefied at cryogenic temperatures (i.e., 20 K), or compressed to high pressures (typical merchant hydrogen is delivered at 15–25 MPa). For many new applications, such as a fuel for fuel cells in stationary, mobile, and portable applications, the traditional hydrogen storage options have issues with, for example, cost, weight, volume, dormancy, and/or overall practicality. For instance, in stationary applications for backup power, dormancy (i.e., the length of time the hydrogen can be stored without loss), fast start, ease of refill, and cost may be critical issues, while weight and volume may not, whereas for portable power, weight, volume, robustness, and safety may be vital, while cost and dormancy may be of less importance. Automotive applications, which are likely the most challenging, have very severe requirements with respect to weight, volume, speed of refill, transient operation, and cost. To meet the need of these demanding consumer applications, there have been increasing efforts at developing advanced storage options, such as the use of solid or liquid materials in which the hydrogen may be either weakly physisorbed as the dihydrogen molecule or more strongly chemically bound as monatomic hydrogen. Figure 15.1 shows a number of hydrogen storage options that have been proposed, along with some of their identified strengths and weaknesses. This overview gives a brief introduction to many of these options with more in-depth discussions in the following chapters. Two recent monographs [2,3] also provide comprehensive assessments of hydrogen storage systems and materials.

15.2 Physical Storage as Compressed Gas or Cryogenic Liquid

Hydrogen has been stored and transported as a compressed gas in metal cylinders since at least the 1880s when the British used wrought-iron metal cylinders for transporting hydrogen to inflate war balloons during expeditions across Asia and Africa [4]. While hydrogen behaves almost as an ideal gas with its density increasing linearly with pres- sure near ambient conditions, as shown in Figure 15.2, significant deviation from ideal behavior occurs at elevated pressure, and the gas density increases much more slowly than the pressure. Storing gas at high pressures requires robust pressure vessels that may incur significant weight and cost penalties. The design, manufacture, transport, and use of gas cylinders and pressure vessels, and their appurtenances, are typically regulated

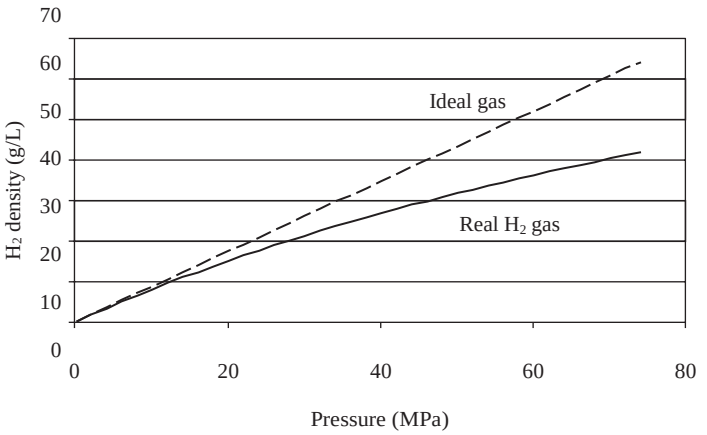


FIGURE 15.2

Comparison of real hydrogen gas density to ideal gas as a function of pressure.

by government agencies. The regulations often require compliance with specific design, manufacture, and/or use codes and standards developed by organizations such as the International Standards Organization (ISO), the Compressed Gas Association (CGA), and the American Society of Mechanical Engineers (ASME).

There are four standard types of cylinders used for the transport and storage of hydrogen: Type I, all metal cylinders; Type II, hoop-wrapped composite cylinders; Type III, fully wrapped composite cylinders with load-bearing metallic liners; and Type IV, fully wrapped composite cylinders with non-load-bearing nonmetallic liners. Type I steel or aluminum cylinders are the most common type found in use for merchant hydrogen delivery and storage. The cylinders are designed for a maximum working pressure, with the minimum wall thickness determined by a formula relating the pressure to the metals' yield and tensile strength. Figure 15.3 shows the minimum wall thickness for 6061-T6 aluminum* and 4140 steel† cylinders with nominal outer diameter of 300 mm calculated using Equation 15.1 in standards ISO 7866:1999(E) [5] and ISO 9806–1:1999(E) [6], respectively. Also shown in Figure
15.3 is the ratio of the internal volume to the total cylindrical volume (i.e., the internal vol- ume divided by the sum of internal plus wall volumes, neglecting the volume of the ends). This shows that at higher pressures, the useable volume, and thus the effective hydrogen density, decreases significantly, especially for lower-strength metals such as aluminum. Additionally, the mass of the metal is substantial such that the mass of hydrogen stored is typically only 1% or 2% of the cylinder mass, dropping to less than 1% at pressures of about 35 MPa and higher. For automotive applications, weight and volume constraints make Type I cylinders impractical; consequently, significant efforts have been devoted to developing Type III and IV cylinders. In these cylinders, a thin, lightweight metal or nonmetallic liner is wrapped by a fiber/epoxy matrix. The fiber wrapping supplies the strength to contain the high pressure, while the liner primarily acts as a gas permeation barrier. Fiberglass and carbon fiber are typical materials used to provide the strength, with high-tensile-strength carbon fiber being the material of choice for 35 and 70 MPa cylinders. Analyses indicate that hydrogen system capacities of 5.9% and 4.7% by weight can be obtained for 35 and 70 MPa

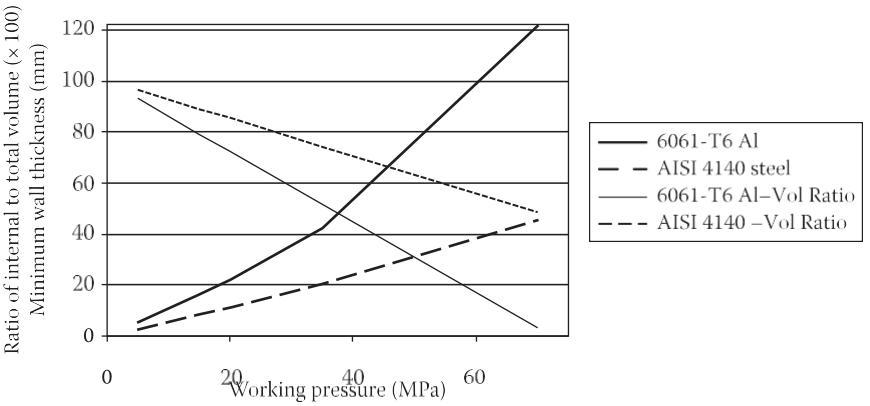


FIGURE 15.3

Minimum wall thickness and the ratio of internal volume to total volume as a function of working pressure for aluminum and steel cylinders.

* 6061-T6 aluminum properties used in calculations: Density = 2.6 g/cc; tensile strength = 290 MPa; yield strength = 241 MPa.

† 4140 steel properties used in calculations: Density = 7.8 g/cc; tensile strength = 655 MPa; yield strength = 417 MPa.

Type IV cylinders [7]. While the fiber wrapping can lower the weight of the cylinders dramatically, they add significant costs, currently projected to be close to three-quarters of the cylinder costs even with high volume manufacture [8].

Lower storage temperatures can also be used to increase hydrogen density. At its normal boiling point of 20 K, liquid hydrogen has a density of about 71 g/L, which is about 1.8 times the density of 70 MPa hydrogen at 288 K. A drawback with liquid hydrogen is that the liq- uefaction process is energy intensive, consuming an energy equivalence of 30% or more of the energy content of the stored hydrogen [9,10]. One factor that makes it so energy intensive is the need to convert the hydrogen molecules into the para state. The hydrogen molecule is composed of two hydrogen atoms, each with one proton and one electron. In the molecule, each atom can have a nuclear spin of either +½ or −½, leading to a total nuclear spin (l) for the molecule of either $l = 0$ (antiparallel spin or para state) or $l = 1$ (parallel spin or ortho state). The para state is lower in energy than the ortho state; however, normal hydrogen gas at ambient temperature is about 75% ortho and 25% para. At the normal boiling point, the equilibrium concentration of ortho-hydrogen to para-hydrogen is 0.2%, but the noncatalyzed conversion rate from ortho to para is very slow. Thus, if hydrogen is liquefied without forcing an ortho– para conversion, the ortho state will be much higher than its equilibrium concentration and it will slowly self-convert. At 20 K, the ortho–para conversion energy is 523 kJ/kg, which is greater than the latent heat of vaporization, 452 kJ/kg, and thus, the ortho–para self-conver- sion would cause significant evaporation [10]. Modern commercial hydrogen liquefaction processes therefore include catalytic processes to convert ortho-hydrogen to para-hydrogen. To store liquid hydrogen, it is critical to minimize heat leakage into the interior of the vessel to prevent boil-off. Boil-off occurs when heat transfer to the stored hydrogen causes sufficient evaporation that the pressure within the inner vessel builds to a critical point where the vessel vents hydrogen, typically at a pressure of 1 MPa or less. Cryogenic liquid hydrogen tanks are typically double-walled vessels with the annular space between the walls evacuated and containing multiple layers of thin metal foil separated by a thermal insulator such as glass wool (known as multilayer vacuum superinsulation [MLVSI]), to prevent both convective and radiative heat transfer. All connections between the outer and inner vessels are specially designed and constructed to minimize thermal conduc- tion to the inner tank. Even with the use of designs to minimize radiative, convective, and conductive thermal transport, some heat leakage to the inner vessel occurs, and even- tual boil-off can be expected. Linde has developed a novel approach for further delaying boil-off called *CooLH*$_2$ [11]. When cold liquid hydrogen is drawn off the tank, it is passed through a heat exchanger to liquefy dried air as the hydrogen is warmed. The liquefied air at 82 K is circulated through a cooling jacket around the inner vessel, further shielding it. The CooLH$_2$ system can reportedly extend the dormancy period to greater than 12 days versus 3 days or so for tanks without the CooLH$_2$ system [11].

Figure 15.4 is a plot that relates hydrogen density to temperature and pressure. At temperatures slightly above its critical temperature of 33 K [12], the gas density increases rapidly with application of pressure. The use of low, cryogenic temperatures in conjunction with pressure is therefore another potential method to increase the density of hydrogen. The temperature and pressure of the hydrogen fill and storage as well as the target dormancy period determine the type of cryogenic pressure vessel needed. For vessels designed for only moderately cold hydrogen (e.g., 233 K) and short dormancy periods, single-walled insulated cylinders may be sufficient. For applications such as onboard vehicles where it is desired to achieve significant increases in density with dor- mancy periods of days, lower temperatures, such as 77 K, have been proposed. At these temperatures, the storage vessel typically uses double-walled vessels with MLVSI

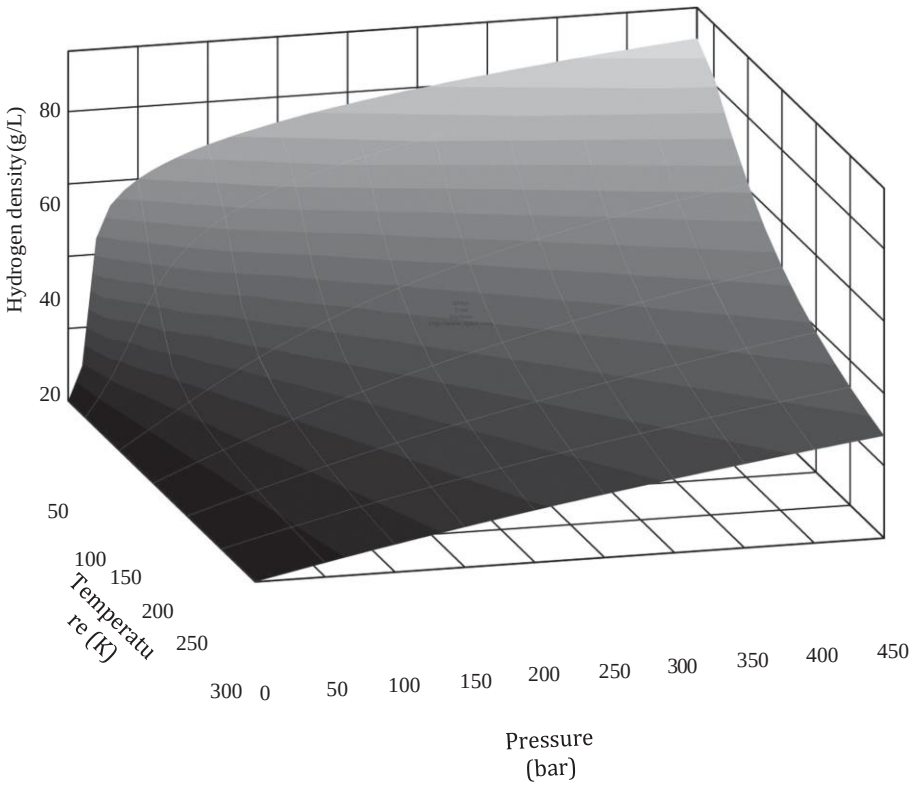


FIGURE 15.4

Plot of hydrogen density as a function of temperature and pressure.

similar to liquid hydrogen; however, the inner vessel is a Type I, II, or III pressure ves- sel. Prototype cryogenic-capable pressure vessels have demonstrated two to three times higher capacities than ambient pressure vessels and with low evaporative losses [13].

Summary: Hydrogen has typically been stored and transported as either a cryogenic liquid or a compressed gas. All Type I metal cylinders have very low gravimetric capacities at the high pressures required to increase the hydrogen density to meet the needs of the new emerging applications. Type III and IV tanks consisting of a lightweight liner overwrapped with a fiber/epoxy matrix have been developed to have higher gravimetric densities at significantly higher pressures (35–70 MPa) than typi- cally found for merchant hydrogen. Even greater densities are obtained at cryogenic temperatures with either liquid or cryo-compressed hydrogen. These low tempera- tures require specialty double-walled vessels with MLVSI to minimize heat leakage and extend dormancy times. Physical hydrogen storage technologies are discussed in more detail in Chapters 16 through 19, 25 and 26.

15.3 Transition Metal Hydrides

Metal hydrides (MH_x) are a broad class of materials formed by the usually reversible reac- tions of metals and alloys with hydrogen as represented by the generic reaction:

$$M + \left(\frac{x}{2}\right) H_2 = MH_x + Q \tag{15.1}$$

In Equation 15.1, ΔQ represents the heat either released (i.e., an exothermic reaction) or absorbed (i.e., endothermic reaction) during formation of the MH_x phase. Although some metals (e.g., Pt, Ni, Fe) with endothermic absorption of hydrogen show catalytic activity, only those metals that form hydrides via exothermic reactions are viable candidates for hydrogen storage. The book edited by Mueller et al. [14] is a comprehensive description of the synthesis, properties, and applications of hydrides as stud- ied through the middle of the 1960s and is still an excellent resource for the modern researcher. The book edited by Manchester is another comprehensive reference on the phase diagrams, crystal structures, thermodynamics, as well as other properties of the binary hydrides [15]. While a few binary hydrides (i.e., PdH_x, VH_2, UH_3) have been used for decades to store and purify hydrogen isotopes in laboratory research and niche applications, it was the series of discoveries of hydrogen reactions with interme- tallic compounds and alloys (starting during the late 1960s) that simulated extensive development of metal hydrides for various energy storage and conversion applications as described in numerous reviews [9,16–25]. The ideal reversible reaction of an intermetallic alloy A_nB_m where metal A forms stable binary hydride phases and metal B does not form a stable hydride is

$$A_nB_m + xH_2 = A_nB_mH_{x/2} + \Delta Q \qquad (15.2)$$

While literally hundreds of intermetallic alloys have been prepared and their hydrogenation potentials assessed [18,26], relatively few have the right combination of properties that permit their use for hydrogen storage or other applications [21,22]. The most viable candidates include alloys with the following compositions: A_2B (e.g., Mg_2Ni), AB (e.g., TiFe), AB_2 (e.g., $ZrMn_2$, $TiCr_{1.9}$), AB_5 (e.g., $LaNi_5$), and the body-centered-cubic (bcc) $A_{1-y}B_y$ alloys (e.g., $V_{0.85}Ti_{0.1}Fe_{0.05}$). A key advantage of many intermetallic alloys is the ability to alter their hydrogen sorption behavior by substitution for either or both the A and B metals that often improve their performance in various applications.

Based upon their crystal structures, the volumetric densities of most metal hydrides can be very high (i.e., >100 g H_2/L) that significantly exceed the density of cryogenic liquid hydrogen [26]. Unfortunately, hydrides are nearly always brittle materials that fracture into fine powders (the notable exception is Pd metal and many of its alloys) during hydrogen absorption and desorption cycling that decreases their filling capaci- ties in storage beds, which reduces effective packing densities by at least a factor of two. The poor thermal conductivity with powders usually requires internal components (i.e., foams, fins) within the hydride beds in order to manage [27] the heat associated with reactions (15.1) and (15.2). Hence, the volumetric capacities of practical hydride storage systems are further impacted.

Nearly all of the readily reversible hydrides are composed of transition or rare earth metals, which results in intrinsic gravimetric capacities of 1–4 wt.%. It is unusual that hydrides with gravimetric capacities below 1 wt.% are considered for any energy stor- age systems including stationary applications [20–22]. However, metal hydrides are suitable for numerous systems [21]. The greatest current limitation of metal hydrides is for onboard hydrogen storage in passenger vehicles where the system densities exceed- ing 6 wt.% are desired [25,27], which imposed requirements greater than ~9 wt.% on the hydride materials. None of the hydrides based on transition metals can meet these gravimetric densities.

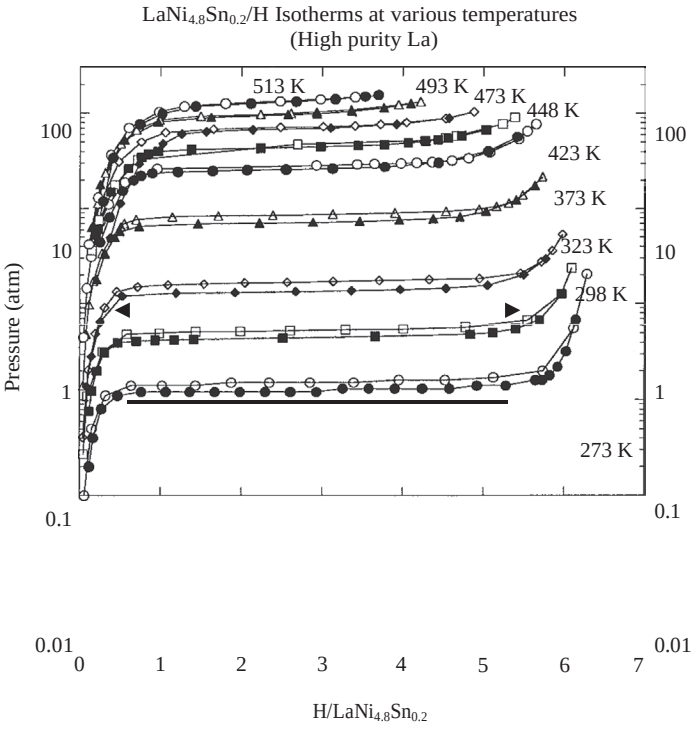


FIGURE 15.5

Hydrogen absorption and desorption isotherms experimentally determined on the alloy $LaNi_{4.8}Sn_{0.2}$. The arrow indicates the reversible storage capacity for this system.

The primary property for the selection of a hydrogen storage material is its ability to provide sufficient amounts of hydrogen gas at the appropriate pressures over the operating temperature of the planned application [9,17–27]. These character- istics of metal–hydrogen systems are usually established from their equilibrium pressure–composition–temperature (PCT) isotherms. Figure 15.5 illustrates the PCT iso- therms that had been determined for the $LaNi_{4.8}Sn_{0.2}$ alloy by Luo et al. [28]. As indicated in Figure 15.5, the reversible capacity of a metal hydride is usually defined by the plateau length in its PCT isotherms, which is always somewhat less than the total hydrogen content. For a $LaNi_{4.8}Sn_{0.2}H_x$ system, these values are 1.24 and 1.40 wt.%, respectively. This hydride also has relatively little hysteresis between the absorption and desorption isotherms, which is often an advantage in many applications such as heat pumps and compressors [21]. As described in previous reviews [17–20], the PCT plateau pressures provide fundamental thermodynamic parameters using the relationship

$$\ln P = \frac{\Delta S}{R} - \frac{\Delta H}{RT} \tag{15.3}$$

where

R is the universal gas constant

ΔS is the entropy

ΔH is the enthalpy for the reaction between hydrogen and the metal/alloy

The pressures shown in Figure 15.5 lead to $\Delta H = -32.8$ kJ/mol H_2 and $\Delta S = -105$ J/K-mol H_2 for the $LaNi_{4.8}Sn_{0.2}H_x$ system. The ideal range of enthalpies for storing hydrogen to use with proton exchange membrane (PEM) fuel cells is often suggested to be 20–50 kJ/mol-H_2 depending on entropy change [25].

While the gravimetric/volumetric capacities and thermodynamics are often the first considerations in choosing a storage candidate, numerous other properties must also be simultaneously satisfied by the hydride material for any given application [21]. Some examples include ease of activation or initial hydriding, sensitivity to air or impurities, volume expansion during hydrogen absorption, decrepitation into fine powder during cycling, pyrophoricity, toxicity, and costs of the raw materials and any processing necessary to produce the storage alloys. In many cases though, either the reaction kinetics or durability of the hydride phases to retain reversibility during extended cycling determines whether a candidate material can be used in a given application. The apparent rates for hydride reactions are sometimes limited by the intrinsic kinetics of the materials via either diffusion within the solids or the chemical reactions on particle surfaces; but in hydrides of the AB, AB_2, and AB_5 alloys, it is usually the heat transfer within the beds of hydride powders [19,21] that dominates. The selective oxidation and segregation of metal A on the surface of the particles leave the catalytic B metal to promote hydrogen molecules to adsorb and dissociate while forming the hydride phases. On the other hand, when A forms a very stable binary hydride phase AH_x, the $A_nB_mH_{x/2}$ phase is metastable and often disproportionates irreversibly into AH_x and B-enriched compounds or alloys [21,26]. This process can severely impact the ideal reversible reaction of Equation 15.2 and has often eliminated candidates from various storage applications.

Summary: The traditional metal hydrides have efficiently and successfully stored hydrogen in numerous laboratory and niche applications where their reversibility and rapid kinet- ics offset disadvantages from their lower range of gravimetric capacity. Various hydrides remain viable storage candidates for stationary power systems as well as specialty and utility vehicles (e.g., forklifts, carts) since their H_2 delivery pressures can be met using the waste heat from operating PEM fuel cells. Additional information on the properties and current R&D status of hydrides for storage can be found in Chapter 20.

15.4 Complex Hydrides

A particularly interesting class of compounds for hydrogen storage applications include group I or II metal cations (e.g., Li, Na, Mg, Ca) bonded to complex anions comprising light central atoms covalently bound to two or more hydrogen atoms (e.g., $[NH_2]^-$ (amides), $[BH_4]^-$ (borohydrides), and $[AlH_4]^-$ (alanates)). Some noteworthy examples include $LiNH_2$, $LiBH_4$, and $NaAlH_4$. These *complex hydrides* are especially compelling for vehicular hydro- gen storage due to their high gravimetric capacity for hydrogen arising from the low atomic weights of the alkali or alkaline earth cations and the central atom in the anion, as well as the existence of multiple hydrogen atoms in compound. For example, $LiBH_4$ has a total gravimetric capacity of approximately 18.5 wt.% hydrogen. For comparison, transi- tion metal hydrides have a capacity that is typically 1–4 wt.%. In addition, these materi- als have moderate densities that translate into high volumetric capacities for hydrogen, another important feature that makes them desirable for onboard transportation applica- tions. The structure, properties, and hydrogen storage characteristics of alanates, borohy- drides, and amides are described in comprehensive reviews [9,10,25,29–36]. In addition, recent research on binary and ternary metal–N–H systems and multinary systems involv- ing metal amides and other complex hydrides (e.g., $NaNH_2$–$LiAlH_4$) is reviewed by Chen et al. [37]. Complex hydrides are also discussed in considerable detail later in this chapter.

Although complex hydrides have hydrogen capacity characteristics that would seem to make them ideal candidates for onboard storage, problems with high thermodynamic stability and prohibitively slow hydrogen adsorption/desorption kinetics have limited their use as reversible hydrogen storage media. Research on these materials over the past 15 years has been devoted almost exclusively to overcoming those obstacles. The thermodynamics and kinetics issues and general approaches that have been used to address the issues are summarized in the following texts.

15.4.1 Thermodynamics

As discussed earlier, transition metal hydrides are characterized by metallic bonding that stabilizes the molecular structure at ambient temperatures and pressures. However, due to the comparatively weak delocalized bonding in the structure, the bonds can be broken and hydrogen released at modest temperatures ($\leq$350 K). In contrast, complex hydrides contain much stronger covalent and ionic/covalent bonds resulting in higher thermodynamic sta- bility and correspondingly lower equilibrium hydrogen pressures. Tables 3–4 in Ref. [29] summarize the hydrogen storage properties of alanates, amides, borohydrides, and related materials. The enthalpy for dehydrogenation is of particular importance for hydrogen storage applications because it provides a quantitative measure of the amount of heat that is required to release hydrogen from the compound. As a rule of thumb, to operate at temperatures consistent with PEM fuel cells, the reaction enthalpy should lie in the range of 20–50 kJ/mol. Of course, it is understood that even though an enthalpy value in this range is necessary for adequate system performance, it is *not sufficient* because, as discussed in the following, kinetics considerations can seriously impact complex hydride sorption behavior.

Two primary approaches for overcoming unfavorable thermodynamics have been explored. The first focuses on new single-phase materials whose thermodynamic properties are altered by atomic substitution or alloying [37–43]. In that approach, an intermetallic alloy with an enthalpy lower than the pure starting material is formed. Although that is usually accomplished using cation substitution, more complex combinations can also favorably alter the reaction enthalpy. For example, it is now well known that reac- tions between amides and hydrides can occur and that those reactions can facilitate the formation of new alloys with concomitant liberation of hydrogen at reduced temperatures (e.g., see Refs. [37,42]).

Although related, the second approach to relaxing thermodynamic constraints in metal hydrides employs additives that form new compounds or alloys *during dehydrogenation*. The proper selection of an additive can reduce the enthalpy for dehydrogenation, thereby increasing the equilibrium hydrogen pressure and effectively destabilizing the hydride(s) [44–46]. A schematic illustration of destabilization through alloy formation in the dehydrogenated state is shown in Figure 15.6. In the absence of the alloying agent, the hydride undergoes the dehydrogenation reaction with a rela- tively high enthalpy (ΔH). However, if the original hydride MH_x is combined with additive, X, then the alloy MX can form during hydrogen release. Since the formation of MX is exothermic, the enthalpy of the dehydrogenated state ($\Delta H'$) is reduced. When the additive is present, the system can now cycle between the hydride, MH_x, and the alloy, MX (instead of the nonalloyed material, M). By forcing a change in the reaction pathway through alloy formation in the dehydrogenated state, the hydride is thereby *destabilized*. We point out that the addition of the alloying species does reduce the net gravimetric capacity for hydrogen that is achieved in the reaction system. Therefore, it is desirable to select low-Z destabilization agents.

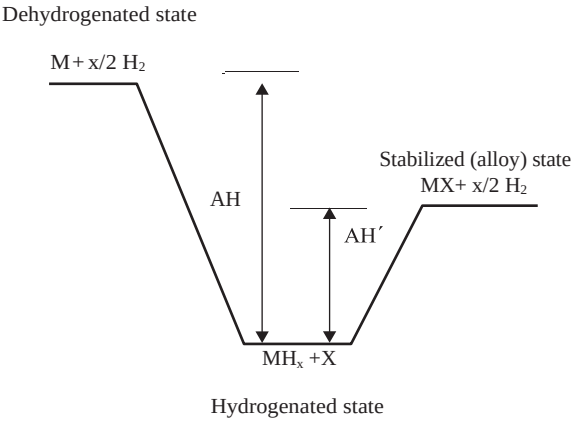


FIGURE 15.6

Generalized enthalpy diagram showing transition between hydrogenated and dehydrogenated states and how enthalpy change is reduced when system is destabilized by alloy formation upon dehydrogenation.

This hydride destabilization process was first introduced by Reilly and Wiswall over 40 years ago in studies of $Mg_2Cu + MgH_2$ [44]. It was found that the temperature to achieve an equilibrium pressure of 0.1 MPa was approximately 49 K lower in the mixed system than in pure MgH_2, suggesting that MgH_2 is destabilized by $MgCu_2$ ($MgCu_2$ forms upon dehydrogenation). This concept was recently extended to a wide range of low-Z binary and complex hydrides [45–48]. For example, upon heating, $LiBH_4$ dissociates by the following reaction:

$$2LiBH_4 \leftrightarrow 2LiH + B + 3H_2 \tag{15.4}$$

The enthalpy of the $LiBH_4$ dehydrogenation reaction is ~67 kJ/mol, resulting in a temperature of 683 K to achieve an equilibrium hydrogen pressure of 0.1 MPa. However, if the destabilizing agent MgH_2 is added, the dehydrogenation reaction proceeds as follows [46]:

$$2LiBH_4 + MgH_2 \leftrightarrow 2LiH + MgB_2 + 4H_2 \tag{15.5}$$

In this case, the formation of MgB_2 in the dehydrogenated state reduces the reaction enthalpy from ~67 to ~45 kJ/mol, which translates to a temperature of 441 K to achieve an equilibrium hydrogen pressure of 0.1 MPa—more than 240° lower than for the simple $LiBH_4$ dissociation reaction. Although the destabilization approach has been employed successfully to modify the thermodynamics in selected complex hydrides, serious kinetics challenges that limit the overall reaction rate remain to be solved. A review of recent work on destabilization of complex hydrides is given in Ref. [47]. Following the initial experimental studies on thermodynamic tuning by destabilization of complex hydrides, a wide range of new systems were explored in a comprehensive series of theory and simulation investigations [49–56]. Many of the new reaction systems discovered in that work are currently being tested experimentally.

Although the two approaches described previously for altering reaction thermodynamics have received the most research attention in recent years, a third approach, based upon thermodynamic changes that accompany reduction in reactant particle size, has also been considered. As will be discussed in the following, a reduction in particle size to nanoscale dimensions can have large effects on reaction kinetics (e.g., reduction in

diffusion distances results in a faster net reaction rate). However, it has been shown theoretically that thermodynamics can be affected as well. For example, using ab initio Hartree–Fock method and density functional theory (DFT), Wagemans et al. [57] calculated that when particles of MgH_2 are reduced to a grain size less than 1.3 nm, the hydrogen desorption temperature decreases significantly. For instance, they showed that the desorption temperature for 0.9 nm particles is approximately 100° less than desorption in the bulk material. On the other hand, a more recent theoretical study using a different approach showed a much more modest effect of particle size on desorption tempera- ture [58]. Although changes in thermodynamic properties with particle size are certainly intriguing from a theoretical standpoint, it remains a serious challenge to experimentally produce nanoscale reactants and then maintain the small reactant size during multiple hydrogen sorption cycles. Methods for encapsulation or confinement of the nanoscale particles seem to be the most viable way to maintain small particle sizes in multiple cycled reaction system (for instance, see Ref. [59]).

15.4.2 Kinetics

The approaches summarized earlier are being successfully employed to alter the thermodynamics of hydrogen sorption reactions in complex hydrides so that reversible dehydrogenation/hydrogenation reactions can be potentially achieved at temperatures compatible with PEM fuel cell operation. However, in most complex hydride systems, the hydrogen sorption reactions often proceed via multiple reaction steps, and in many cases, they can involve nucleation and growth of different material phases. The kinetic barriers that exist for these steps can greatly impede the overall reaction rate, thereby producing desorption behavior that is markedly different than what might be expected from thermodynamic considerations alone. The two main approaches for addressing these kinetics limitations generally involve the use of catalysts to enhance the reaction rate and the use of nanoengineering methods to reduce reactant particle size, thereby limiting diffusion distances and increasing the surface reaction area. There are several recent reviews of nanoengineering approaches that have been employed to favorably alter reaction kinetics [31,60–62].

Arguably, the most important development to date in the improvement of reaction kinetics in complex hydrides was made in 1997 by Bogdanović and Schwickardi [63] who demonstrated that $NaAlH_4$ could be induced to reversibly hydrogenate and dehydrogenate at modest temperatures and pressures by the addition of a titanium catalyst. Although the thermodynamic properties and gravimetric storage capacity of $NaAlH_4$ were recognized as being favorable for mobile hydrogen storage/fuel cell applications, it had previously been impossible to dehydrogenate and rehydrogenate the material under practical operat- ing conditions.

The dehydrogenation of $NaAlH_4$ occurs in two consecutive steps involving alanate phases with different crystal structures. Although the total hydrogen release is relatively high (5.6 wt.%), the elevated decomposition temperatures 493 and 523 K preclude the use of the undoped material for practical storage applications. However, Bogdanović and Schwickardi showed that the addition of a few mole percent titanium reduced the dehydrogenation temperatures to 373 and 458 K (equilibrium H_2 pressure ~1 MPa H_2), respectively. Those results were particularly noteworthy because they revealed for the first time that dramatic modifications of reaction kinetics could be achieved in an operationally practical complex hydride material and it stimulated a major resurgence of interest in complex hydrides for hydrogen storage. The precise role of the titanium and other transition metals

in catalyzing the sorption reaction(s) has been widely studied, and the reader is referred to several excellent reviews [9,10,25,29–36] for additional detail.

Catalysts are now routinely used to enhance the rate of hydrogen sorption reactions in complex hydrides. In addition to the catalytic behavior due to the presence of metal additives, a novel *self-catalyzing* set of reactions has also been reported [64]. In some systems (e.g., $NaAlH_4$), the catalytic effects are sufficient to promote reactions at temperatures and pressures compatible with PEM fuel cell operation. However, even though beneficial catalytic effects by dopants or other additives are observed in many other complex hydrides, the magnitude of the effects is generally insufficient to increase sorption rates to values needed for hydrogen delivery to PEM fuel cells under standard operating conditions. Consequently, other approaches for improving reaction kinetics are also being considered. The most widely studied approach involves *nanoengineering* to reduce the particle size of the reactants [31,60–62]. Reduction in reactant particle size to the nanoscale does not necessarily alter the intrinsic hydrogenation/dehydrogenation kinetics, but rather, sorption rates are improved simply because the diffusion distances become much shorter and the reactant surface area is increased in the nanoscale material.

Traditionally, energetic ball milling has been used to produce small reactant particles. Even though the particle size remains comparatively large (>1 μm), much smaller crystallite sizes within the ball-milled particle can promote enhanced mass transport and increased interface reaction rates compared to the bulk [62]. Although this approach is now widely used for solid-state reactant synthesis, it is often preferable to reduce the actual size of the particles themselves to <100 nm in order to overcome the notoriously slow kinetics in complex hydrides. This can lead to an increase in the rate of hydrogen diffusion across the particle by at least two orders of magnitude compared to the bulk. A wide variety of methods exist for producing nanoparticles of primary reactants and cata- lysts [31,60–62]. However, as pointed out earlier, in reversible hydrogen storage systems employing complex hydrides, multiple cycles of hydrogenation and dehydrogenation generally act to induce sintering or particle agglomeration, which produces unwanted particle growth and reduced reaction rates. It is therefore not particularly desirable to employ synthesis methods that produce a large number of free particles in contact with each other (e.g., *nanomarbles in a bowl*).

To overcome the problem of particle growth upon cycling, approaches based on particle confinement in nanoporous host materials are being explored. For example, compared to the bulk, greatly improved kinetics were observed when ammonia borane (a nonreversible chemical hydrogen storage material) was encapsulated in a mesoporous silica network [65]. That work was later extended to include $NaAlH_4$ [66] and $LiBH_4$ [67] reactants encapsulated in carbon aerogels. Carbon was selected for the latter work because of its comparatively lightweight, low reactivity, and ease of forming meso- and nanoporous scaffold frameworks. The aerogel serves both as a structure-directing agent to restrict reactant particle size and as a host to confine the reactant particle before and during the sorption reac- tion. When $LiBH_4$ was incorporated into a C-aerogel with pore sizes ranging from 10 to 30 nm, the dehydrogenation temperature was reduced by approximately 100° [67] and the desorption rate increased by up to 60 times [68] compared to the bulk material. This result, together with those published previously, suggests that the scaffold facilitates reduced diffusion distances and promotes an increase in the reactant surface area, which, in turn, improves the overall desorption kinetics.

There are clearly advantages to employing nanoscale reactants and catalysts to improve reaction kinetics in complex hydride materials. However, in nanoporous scaffold systems, the framework material imposes a gravimetric penalty that must be accounted for.

Free ebooks ==> www.Ebook777.com

Likewise, the nanoscale scaffold must be robust to multiple sorption cycles. Also, in nanoscale systems, there is a greater potential for the formation of unwanted (inert) phases that can impede sorption reactions or terminate them altogether. Those problems notwithstanding, it is likely that development of nanoscale engineering approaches will continue to be an active research topic as further attempts are made to improve the hydrogen sorption kinetics in complex hydride materials.

15.4.3 Summary

The high gravimetric and volumetric capacities for hydrogen in complex hydrides have made these materials attractive candidates for onboard hydrogen storage applications. Significant progress has been made by the international research community over the past 15 years to improve the thermal characteristics, sorption kinetics, and reversibility, obstacles that have historically limited the use of these materials in highly demanding transportation applications. Although they are emerging as potentially viable media for hydrogen storage and delivery to PEM cell systems, there is no single material that meets the stringent onboard storage requirements. Several candidate systems that meet the thermodynamic requirements have been identified, but kinetic barriers and, in most cases, cycling problems still limit their incorporation in practical fuel cell systems.

Current research is focused primarily on five areas: (1) elucidating the detailed reac- tion mechanisms and identifying the rate-limiting step(s) that reduce the sorption reaction rates, (2) developing a detailed understanding of how metal catalysts influence elemen- tary reaction steps, (3) exploring new ways to alter reaction pathways to eliminate product *sinks* that reduce the cycling efficiency, (4) discovering new nanoengineering approaches that create a reaction environment that improves diffusion rates and limits formation of unwanted material phases, and (5) exploring (theoretically and experimentally) entirely new material combinations that possess improved thermodynamic and kinetic properties. This is clearly a fertile area for research and development in materials science, and based upon the impressive advances that have been made thus far, it is anticipated that prog- ress will be made in future work to overcome the limitations of current complex hydride materials for practical hydrogen storage applications. The current status of R&D in complex hydrides and plans for addressing existing barriers and obstacles are described in greater detail in Chapter 21. In addition, the discovery and development of new materials, including complex hydrides, were conducted a focused, 5-year, technical effort in the US Department of Energy (DOE) Metal Hydride Center of Excellence (MHCoE), an applied R&D consortium comprising industry, university, and government laboratories. The reader is referred to final report from the MHCoE [69].

15.5 Chemical Hydrogen Storage Materials

Chemical hydrogen storage materials are a class of storage compounds containing large quantities of chemically bound hydrogen that can be released either by heating or by reactions with other materials (e.g., hydrolysis reactions). Unlike metal hydrides or physisorption materials that store and desorb hydrogen reversibly, the chemical hydrogen storage material must be regenerated using separate (off-board) processing steps following release of the hydrogen. Due to their high gravimetric storage capacities (>10 wt.% H_2) and fast

www.Ebook777.com

desorption kinetics at near ambient temperatures, these systems are ideal for *single-use* applications where disposal of the spent fuel is acceptable or in situations where efficient fuel regeneration schemes exist. A recent review [70] summarizes status and progress in the thermochemistry and engineering of chemical hydrogen storage systems; the topic is also discussed in greater detail later in Chapter 23.

Common chemical hydrogen storage materials can be either liquids or solids, and the thermodynamics and mechanisms of hydrogen release can vary markedly in specific systems. For example, some materials such as cyclohexane [71], decalin [72], and pi-conjugated materials [73] release hydrogen catalytically in endothermic reactions. On the other hand, hydrogen release can also occur exothermically from, for example, hydrolysis reactions involving hydrogen-rich materials such as sodium borohydride ($NaBH_4$) [74] or from catalytically activated release of hydrogen from ammonia borane [70,75].

Hydrolysis reactions have been actively investigated because they can potentially release large amounts of hydrogen in a process that can be readily integrated with PEM fuel cell systems. In the case of sodium borohydride, simple thermal decomposition of the compound occurs at ~400°C, a high temperature that is incompatible with fuel cell operation. However, a metal-catalyzed $NaBH_4$–H_2O hydrolysis reaction proceeds at ambient temperatures to produce hydrogen and sodium metaborate ($NaBO_2$) [74]:

$$NaBH_4 + 2H_2O \rightarrow 4H_2 + NaBO_2. \quad (15.6)$$

In this simplified view of the overall hydrolysis reaction, the participation of water in the reaction effectively doubles the amount of hydrogen that would be obtained by simple thermal decomposition. Unfortunately, $NaBO_2$ has only about half the solubility of $NaBH_4$ at 293 K. Consequently, the $NaBH_4$ concentration must be kept lower than the solubility of the $NaBO_2$ to preclude precipitation of the metaborate [76]. This greatly reduces the overall storage capacity of the system. For example, 20% $NaBH_4$ solution (with a 1% NaOH stabilization additive) was used in a commercial system (Millennium Cell). The low $NaBH_4$ concentration reduces the overall storage capacity to only 4% [9]. In addition to the reduced storage capacity in this system, regeneration of the hydride from the metaborate solution is energy intensive, making the system useful only for special storage applications.

Recent work has focused on hydrogen release from ammonia borane [70,77–80]. This compound has received considerable attention because of its high storage capacity for hydrogen (>19 wt.% H_2 and 150 g H_2/L) and the potential to controllably release hydrogen at temperatures <100°C in a metal-catalyzed reaction system [70]. Although some problems with hydrogen kinetics remain to be solved before ammonia borane can be utilized in a practical hydrogen storage application, they appear to be tractable. On the other hand, the development of an efficient and scalable regeneration method remains a serious chal- lenge. The reader is referred to several recent reviews [70,77–80] that summarize the status of ammonia borane as a practical hydrogen storage medium and address the problems that remain to be solved for applications that require efficient recycling of the starting material. Extensions to other novel amidoborane compounds are discussed in Ref. [81].

A major research and development effort was carried out within the US DOE Chemical Hydrogen Storage Center of Excellence (CHSCoE) to optimize hydrogen release characteristics of ammonia borane and to develop improved regeneration methods. In addition, investigators within the CHSCoE are exploring new systems that have even better performance. The reader is referred to annual progress reports given in Ref. [82] for information concerning the center activities and progress.

Aluminum hydride (AlH_3—alane) is another chemical hydrogen storage material that is attracting increasing attention in the hydrogen storage R&D community. Alane has

gravimetric and volumetric capacities of 10.1 wt.% H_2 and 148 g-H_2/L, respectively. These characteristics make alane attractive for onboard storage applications. Although all phases of the compound are thermodynamically unstable under ambient temperature, the existence of a passivating Al_2O_3 surface layer inhibits decomposition at room temperature. Graetz and Reilly [83] recently demonstrated that the α-, β-, and γ-phases of AlH_3 decompose readily at 373 K at rates commensurate with onboard fuel cell operation. Likewise, Sandrock et al. [84] showed that the hydrogen desorption kinetics could be improved at practical fuel cell tem- peratures using particle size control and doping with alkali metal hydrides. Although the dehydrogenation properties of alane make it a potentially promising candidate for onboard storage applications, direct hydrogenation of aluminum to AlH_3 requires an unacceptably high H_2 pressure (>10^4MPa at 300 K), which historically has rendered the alane system impractical as a hydrogen storage medium.

Recent work has shown that problems with hydriding of aluminum can be overcome using alternate approaches involving low-temperature and low-pressure organometallic reactions [85] and electrochemical regeneration [86]. In the former process, a slurry of titanium-doped aluminum powder and triethylenediamine (TEDA) in tetrahydrofuran in a H_2 gas atmosphere forms an AlH_3–TEDA adduct at room temperature and at pressures <3.5 MPa. The addition of the Ti catalyst allows the adduct formation reaction to proceed at pressures an order of magnitude lower than had been previously reported [87]. The adduct can be recovered by precipitation or recycled to generate H_2 gas, thereby providing a pathway to achieving effi- cient dissociation/regeneration cycle performance. A detailed analysis of an onboard storage hydrogen storage system that uses an alane slurry as the hydrogen carrier is given in Ref. [88].

The second method that has been studied recently for alane regeneration employs an electrochemical cycle to avoid high hydriding pressures and formation of unwanted stable by-products [86]. The cycle utilizes electrochemical potential to generate alane and alkali hydride from an ionic alanate salt. The feasibility of a recyclable process has been demon- strated, and work is in progress to improve the efficiency and scale up the reaction system. Both this method and the adduct formation process are producing encouraging results that should significantly impact the use of aluminum hydride in a wide range of hydrogen storage applications. These processes were investigated in the DOE MHCoE; additional information is provided in the MHCoE final reports [69].

The trade-offs between liquid and solid systems must also be carefully considered in the selection of optimum systems for chemical hydrogen storage. Powders and slurries have been investigated for both alane and ammonia borane systems. In general, liq- uids have advantages for distribution both within a fuel delivery network and within a vehicle. Crabtree has discussed these advantages, specifically with respect to use of liquid organic heterocycle compounds [89]. Likewise, the system implications of storage and delivery strategies in solid and liquid systems are discussed in detail by Aardahl and Rassat [70].

Summary: The high gravimetric and volumetric storage capacities for hydrogen together with favorable hydrogen release kinetics at operationally relevant temperatures and pressures make chemical hydrogen storage materials potentially important candidates for a range of storage applications. However, since these materials require off-board regeneration, the energy effi- ciency and scalability of the regeneration processes are critical to successful deployment of the materials in situations that require reuse of the materials. These issues are being addressed in laboratories worldwide and good progress is being made. The thermochemistry and kinetics of hydrogen release from chemical hydrogen storage materials as well as processes for efficient regeneration of spent fuel will be discussed in detail in Chapter 23.

15.6 Hydrogen Sorbents

Van der Waals interactions between a hydrogen molecule and the surface of a solid can result in adsorption of hydrogen on localized surface sites. Since these dispersive interactions result in weak bonding (1–10 kJ/mol), significant physisorption occurs only at low temperatures (generally much less than 273 K). Since molecular adsorption occurs predominantly in the first monolayer, the use of a high surface area material is desirable in order to achieve hydrogen capacities that are useful for practical hydrogen storage applications in instances where cooling of the adsorbent is acceptable. In this case, simple monolayer saturation of the adsorption sites can be described by a Langmuir isotherm [10]. A significant benefit of the physisorption mechanism is that the adsorption process is not activated, implying that the adsorption kinetics are fast. Moreover, the low binding energy trans- lates into a low barrier for desorption, leading to good reversibility in system applications. Hydrogen storage systems based upon molecular physisorption are being explored at R&D organizations worldwide, several excellent reviews are available [9,10,25,31,36,60,61,90–96], and the topic is discussed in detail later in this chapter.

As expected for coverage limited to a monolayer, the amount of adsorbed hydrogen is proportional to the specific surface area of the adsorbent, which leads to approximately 2.5 wt.% adsorbent per 1000 m^2 surface area at cryogenic temperatures [97]. This dependence of adsorption capacity on the surface area has motivated the search for new adsorbents with the highest possible number of adsorption sites, including metal oxide frameworks (MOFs) [98–103], covalent organic frameworks (COFs) [104–106], zeolites [107], and nanostructured carbon (e.g., nanotubes, templated carbons, fullerenes, aerogels, substituted polymers, and intercalated graphite) [31,60,61,91–96]. Due to their extremely high porosity, MOFs have become especially intriguing candidates for physisorption applications [98–103]. MOFs are highly porous, 3D polymeric structures comprising inorganic building units connected by organic linkers. In the case of MOF-177 (zinc acetate building units linked by 1,3,5-benzen- etribenzoate), the Langmuir surface area is extremely large (~4500 m^2/g), giving rise to a storage capacity of 7.5 wt.% at 7 MPa and 77 K [99,108].

The structure and properties of specific physisorption systems will not be discussed in this introduction. Although many systems have been explored, the hydrogen adsorption capacities at ambient temperatures and modest pressures (10 MPa) are less than 0.8 wt.% H_2; that is, as mentioned earlier, practical gravimetric storage capacities are only achievable at low temperatures (typically 77 K) in these materials. (The general trend of hydrogen uptake as a function of specific surface area at cryogenic temperatures is shown for a wide variety of porous adsorbents in Ref. [96].) Consequently, considerable research attention has been directed toward finding ways to modify the adsorbent surface to increase both the adsorption potential and the number of available sorption sites.

A particularly interesting approach that has been proposed to achieve enhanced storage capacity at ambient temperatures utilizes hydrogen *spillover* from substituted metal atoms on adsorbent surfaces [108]. In this process, the surface of the adsorbent is doped with a catalytic additive, typically a metal, which serves to promote dissociation of molecu- lar hydrogen and facilitate transport of atomic hydrogen to the adsorbent surface sites. The molecular dissociation is believed to occur rapidly, and the rate-determining step for adsorption involves diffusion of the hydrogen atoms to/on the receptor surface. Since binding energy for atomic hydrogen is greater than for H_2, the storage capacity is expected to be enhanced at elevated temperatures. For example, it has been reported that in IRMOF-8 (zinc acetate units with naphthalenedicarboxylate linkers), the heat of adsorption for

atomic hydrogen is ~20 kJ/mol [109] compared to ~6 kJ/mol for molecular adsorption [110]. Yang and coworkers reported that the H_2 uptake was increased from 0.5 wt.% in pure IRMOF-8 at 298 K and ~10 MPa to 4 wt.% on bridged IRMOF-8 (bridge building facilitates enhanced secondary spillover between two dissimilar materials) [109].

Hydrogen spillover in a large number of adsorbent systems, including carbon nanotubes, zeolites, MOFs, COFs, and other nanostructured materials, has been investigated, and significant enhancements in hydrogen uptake at room temperature have been reported [109]. However, diminished surface diffusion rates that may arise from site filling near the active metal center remain a serious concern. For example, recent DFT calculations have shown that diffusion of atomic hydrogen from the metal nanoparticle to a graphitic substrate is both kinetically and thermodynamically inefficient and limits the spillover rate [111]. Lack of reproducible adsorption capacity and slow diffusion kinetics in some spillover systems are outstanding issues that must be addressed before the process can be used in practical applications. The detailed aspects of the spillover mechanism and the limits of hydrogen storage capacity in different material systems remain topics of active research.

Another approach that is being explored to enhance adsorption energies employs the so-called Kubas interaction between hydrogen and a metal complex [112–114]. In this process, the hydrogen molecule bonds *side-on* to the metal through donation of its two σ orbitals to a vacant metal orbital, forming a two-electron, three-center bond [114]. Since a stable H_2–metal complex is created in this interaction, the binding energy is greater than what would be expected from weak van der Waals interactions between the H_2 and the adsorbent. The increase in the binding potential via Kubas interactions is being explored in a large number of nanostructured systems; a review of these interactions and some perspectives on utilizing them for enhanced hydrogen storage in different adsorbent systems is given in Refs. [113,114]. In addition to extensive experimental studies on hydrogen storage via physisorption in highly porous media, considerable theoretical work has been performed to explore new materials and surface modification approaches. The current state of the art in molecular and quantum mechanical modeling of physisorption and diffusive transport in MOFS is discussed in a recent review [115]. Also, simulations that predict enhanced hydrogen storage in 3D COFs are described in Ref. [106]. Hydrogen adsorption in doped fullerenes and related carbon nanostructures has also been studied theoretically. For example, first- principles DFT and quantum Monte Carlo calculations have suggested enhanced bind- ing of molecular hydrogen on substitutional B and Be sites in fullerenes [116]. Likewise, a first-principles study showed that a single titanium atom on a titanium-decorated single- walled carbon nanotube can bind up to four hydrogen molecules [117]. In most cases, the theoretical predictions have not been experimentally validated, largely because of the dif- ficulty in preparing the tailored adsorbent and competing reactions of the isolated metal atom or complex with foreign species. A broadly based theoretical effort on enhanced physisorption in highly porous systems was conducted within the US DOE Hydrogen Sorption Center of Excellence. The reader is referred to the final report of the DOE's Hydrogen Sorption Center of Excellence [118]. Additional information concerning theory and modeling of hydrogen adsorption on tailored surface sites is summarized in several review articles [9,10,25,31,36,60,61,90–96].

Summary: A large variety of materials with high surface area and enhanced surface adsorption capacities are being investigated for hydrogen storage applications. Modification of surface properties to increase the binding energy with hydrogen and thereby enhance the sorption capacity at elevated temperatures is an especially active area of study. Compared to other solid-state hydrogen storage approaches that involve the formation and rupture of strong

covalent or ionic bonds and complex phase changes during hydrogenation and dehydrogenation cycles, the physisorption process is more conceptually straightforward. However, the development of reproducible approaches for achieving adsorption at elevated temperatures in extremely porous materials remains a significant technical challenge. Likewise, as pointed out by Felderhoff et al. [9], physisorption of hydrogen under cryogenic conditions in a practi- cal engineering system requires a large amount of excess heat to be removed. This places seri- ous demands on the heat management system and can result in prohibitively large amounts of liquid nitrogen or other cryogens to be consumed during charging. The materials and engineering challenges that impact the implementation of the physisorption approach for hydrogen storage in a practical system are described in greater detail in Chapter 24.

15.7 Engineering Aspects of Hydrogen Storage Systems

While the attributes and limitations of each storage medium are the first considerations for any given application, numerous engineering factors impact the design and performance of the integrated hydrogen storage system. Reliable and safe containment of hydrogen is required over the entire range of pressure and temperature during the projected opera- tional lifetime with adequate margins of safety. Hence, the materials used to fabricate these vessels and all hydrogen-exposed components must have appropriate mechanical strengths and not be susceptible to hydrogen embrittlement or other detrimental chemi- cal reactions such as corrosion. Materials with these characteristics are often relatively expensive that contribute to making hydrogen storage systems much more costly when compared to other fuel storage options such as gasoline or natural gas.

Beyond the demands for mechanical integrity, significant heat transfer issues must also be addressed for all hydrogen storage methods [119]. The designs of vessels and refueling stations for H_2 gas compressed to high pressures (i.e., above ~10 MPa) should provide for accommodating heat generated during both compression and the inverse Joule–Thomson effect under ambient conditions in order to achieve efficient filling of the vessel. The cryogenic storage of hydrogen as either liquid or cryo-compressed gas [13] requires designs that provide efficient thermal insulation that can minimize loss of hydrogen by boil-off or excessive vaporization from extraneous heat leaks to extend the dormancy life described previously in this chapter. For hydrogen storage using adsorption on activated carbon or other high surface materials, the thermal con- ductivity within the sorbent bed also needs to be enhanced by additional components (e.g., metallic foams, fins, or mesh network) to manage the heat of reaction during adsorption or desorption. Ahluwalia and Peng [120] present an engineering analysis on the behavior of such a system based upon the activated carbon AX-21 for potential automotive storage. The much greater heats of reaction of ~20–100+ kJ/mol for hydro- gen absorption by the metal and complex hydrides significantly exacerbate the need for improved thermal conductivity within the storage beds [17,19,21,120]. Due to the added complexity of reactions associated with chemical hydrogen systems where both initial fuel material and the products formed during decomposition must be processed and/ or separated as hydrogen is released, extensive physical and thermal management engi- neering is needed for various components and auxiliary subsystems are necessary [70]. Because metal hydrides have been considered for numerous energy storage and conver- sion applications for over 30 years and these materials are commonly known to have very

poor thermal conductivities in powder form [17,19,21], extensive efforts have been made to develop hydride bed designs with various configurations that enhance the effective conductivity within the bed without seriously impacting filling capacity, bed mass, and internal gas flow. Most of these approaches included the use of foams and compacts as was reviewed by Zhang et al. [120]. Numerous analytical models have been developed by various workers that attempt to represent the complex relationship of heat exchange and thermal management during the absorption and desorption processes within hydride beds in order to either predict performance or compare with experimental testing of pro- totypes. A recent example of these analyses is the work by Hardy [121,122] who also cites a number of earlier studies conducted by others. The primary storage system considered by Hardy is based upon a prototype storage bed design using titanium-catalyzed $NaAlH_4$ as the storage media as described by Mosher et al. [123]. Ahluwalia has performed indepen- dent analyses of the kinetics and thermodynamics for $NaAlH_4$ in the same prototype that indicated these properties are insufficient to meet performance targets for storage onboard fuel cell–powered passenger cars [123].

Summary: In order to achieve the best performance from any hydrogen storage material in a given application, careful and thorough system engineering must be considered with respect to the vessel design as well as the chemical and physical properties of the media and the components that used to enhance heat and mass transfers during both the filling and discharge operations. As the performance targets with respect to operating conditions such as temperature and time become more demanding, increasing penalties are incurred with respect to mass, volume, and costs for the resulting storage system.

15.8 Summary

Traditional methods of hydrogen storage do not provide suitable performance for many emerging applications for hydrogen use as a fuel, especially with PEM fuel cells. Therefore, there are considerable efforts directed at developing advanced hydrogen storage methods. These efforts include lightweight Type III and IV high-pressure com- posite cylinders, cryogenic-capable high-pressure vessels, reversible metal and complex hydrides, and regenerable chemical hydrogen storage materials and hydrogen sorbents. While significant progress has been made in the development of these technologies, none currently meets all of the stringent performance requirements for the most demanding applications, such as onboard vehicle storage. The materials-based technologies require further development of materials with improved sorption kinetics, less extreme oper- ating temperature and pressures, and higher volumetric and gravimetric capacities. Additionally, there are remaining engineering challenges for the materials-based and physical storage methods, not the least of which is to reduce the costs. This chapter pro- vided a brief overview of these technologies and their current status. The following chap- ters provide a much more in-depth review of the various storage technologies. For physical storage methods, Chapter 16 discusses gaseous storage, Chapters 17 and liquid storage, Chapter 19 cryo-compressed storage, and Chapter 25 storage in hollow microspheres and Chapter 26 slush hydrogen storage. For materials-based storage, Chapter 20 covers metal hydrides, Chapter 21 complex hydrides, Chapter 22 nanomaterials, Chapter 23 chemical hydrogen storage, and Chapter 24 sorbents. Additionally, Chapter 29 hydrogen distribu- tion, and Chapters 30 and 31 safety, codes, and standard efforts.

References

1. Davis, S.C., S.W. Diegel, R.G. Boundy. 2009. *Transportation Energy Data Book*, 28th edn. Table B.4. Oak Ridge National Laboratory, Oak Ridge, TN. http://cta.ornl.gov/data/down- load28.shtml
2. Broom, D.P. 2011. *Hydrogen Storage Materials: The Characterization of the Storage Properties*. London: Springer.
3. Klebanoff, L. 2012. *Hydrogen Storage Technology: Materials and Applications*. Boca Raton, FL. CRC Press.
4. Irani, R.S. 2002. Hydrogen storage: High-pressure gas containment. *MRS Bull*. 27(9):680–682.
5. ISO 7866:1999(E), Gas cylinders—Refillable seamless aluminum alloy gas cylinders—Design, construction and testing, International Standards Organization, http://www.iso.org/iso/iso_catalogue/catalogue_tc/catalogue_detail.htm?csnumber=14795
6. ISO 9809-1:1999(E), Gas cylinders—Refillable seamless steel gas cylinders—Design, construc- tion and testing—Part 1: Quenched and tempered steel cylinders with tensile strength less than 1 100 MPa, International Standards Organization, http://www.iso.org/iso/iso_catalogue/catalogue_tc/catalogue_detail.htm?csnumber=17683
7. Ahluwalia, R.K., T.Q. Hua, J.-K. Peng, R. Kumar. 2009. *System Level Analysis of Hydrogen Storage Options*, DOE Hydrogen Program Review, Arlington, VA. http://www.hydrogen.energy.gov/pdfs/review09/st_13_ahluwalia.pdf
8. Hua, T.Q., R.K. Ahluwalia, J.-K Peng, M. Kromer, S. Lasher, K. McKenney, K. Law, J. Sinha. 2011. Technical assessment of compressed hydrogen storage tank systems for automotive applications. *Int. J. Hydrogen Energy* 36:3037–3049.
9. Felderhoff, M., C. Weidenthaler, R. von Helmolt, U. Eberle. 2007. Hydrogen storage: The remaining scientific and technological challenges. *Phys. Chem. Chem. Phys*. 9:2643–2653.
10. Züttel, A., M. Hirscher, K. Yvon et al. 2008. Hydrogen storage, chapter 6. In *Hydrogen as a Future Energy Carrier*, A. Züttel, A. Borgschulte, L. Schlapbach, eds., pp. 165–264. Weinheim, Germany: Wiley-VCH Verlag GmBH & Co.
11. Wolf, J. 2002. Liquid-hydrogen technology for vehicles. *MRS Bull*. 27(9):684–687.
12. The plotted temperature/pressure/density values were calculated using the National Institute of Standards and Technology's on-line Chemistry WebBook for the isothermal fluid properties for hydrogen. Lemmon, E.W., M.O. McLinden, D.G. Friend. Thermophysical properties of fluid systems. In *NIST Chemistry WebBook*, P.J. Linstrom, W.G. Mallard, eds., NIST Standard Reference Database Number 69. Gaithersburg, MD: National Institute of Standards and Technology. http://webbook.nist.gov (retrieved February 8, 2010).
13. Aceves, S.M., F. Espinosa-Loa, E. Ledesma-Orozco, T.O. Ross, A.H. Weisberg, T.C. Brunner, O. Kircher. 2010. High-density automotive hydrogen storage with cryogenic capable pressure vessels. *Int. J. Hydrogen Energy* 35(3):1219–1226. DOI: 10.1016/j.ijhydene.2009.11.069.
14. Mueller, W.M., J.P. Blackledge, G.G. Libowitz. 1968. *Metal Hydrides*. New York: Academic Press.
15. Manchester, F.E., ed. 2000. *Phase Diagrams of Binary Hydrogen Alloys*. Materials Park, OH: ASM International.
16. Reilly, J.J., G. Sandrock. 1980. Hydrogen storage in metal hydrides. *Sci. Am*. 242(2):118–129.
17. Sandrock, G., S. Suda, L. Schlapbach. 1992. Applications. In *Hydrogen in Intermetallic Compounds II*, L. Schlapbach, ed., Topics in Applied Physics, vol. 67, pp. 197–258. Berlin, Germany: Springer-Verlag.
18. Sandrock, G. 1995. Applications of hydrides. In *Hydrogen Energy System – 2 Production and Utilization of Hydrogen and Future Aspects*, Y. Yurum, ed., NATO ASI Series E 295, p. 253. Amsterdam, the Netherlands: Kluwer.
19. Dantzer, P. 1997. Metal-hydride technology: A critical review. In *Hydrogen in Metals III*, H. Wipf, ed., pp. 279–340. Berlin, Germany: Springer.
20. Sandrock, G. 2003. Hydride storage. In *Handbook of Fuel Cells – Fundamentals, Technology and Applications*, W. Vielstich, H.A. Gasteiger, A. Lamm, eds., vol. 3(2), pp. 101–112. Chichester, U.K.: Wiley.

21. Bowman, Jr. R.C., B. Fultz. 2002. Metal hydrides i: Hydrogen storage and other gas-phase appli- cations. *MRS Bull*. 27(9):688–693.
22. Sandrock, G., R.C. Bowman, Jr. 2003. Gas-based hydride applications: Recent progress and future needs. *J. Alloys Compd*. 356/357:794–799.
23. Sakintuna, B., F. Lamari-Darkrim, M. Hirscher. 2007. Metal hydride materials for solid hydro- gen storage: A review. *Int. J. Hydrogen Energy* 32:1121–1140.
24. Sandrock, G., G. Thomas. Metal hydride applications list, in the Hydride Information Center (Hydpark) section of the DOE on-line hydrogen storage materials database. http://hydrogenmaterialssearch.govtools.us/ (accessed February 8, 2010).
25. Yang, J., A. Sudik, C. Wolverton, D.J. Siegel. 2010. High capacity hydrogen storage materials: Attributes for automotive applications and techniques for materials discovery. *Chem. Soc. Rev*. 39:656–675. DOI: 10.1039/b802882f.
26. Sandrock, G. 1999. A panoramic overview of hydrogen storage alloys from a gas reaction point of view. *J. Alloys Compd*. 293–295:877–888.
27. Satyapal, S., J. Petrovic, C. Read, G. Thomas, G. Ordaz. 2007. The U.S. Department of Energy's National Hydrogen Storage Project: Progress towards meeting hydrogen-powered vehicle requirements. *Catal. Today* 120:246–256.
28. Luo, S., W. Luo, J.D. Clewley, T.B. Flanagan, R.C. Bowman, Jr. 1995. Thermodynamic and degra- dation studies of $LaNi_{4.8}Sn_{0.2}$-H using isotherms and calorimetry. *J. Alloys Compd*. 231:473–478.
29. Orimo, S.-I., Y. Nakamori, J.R. Eliseo, A. Züttel, C.M. Jensen. 2007. Complex hydrides for hydro- gen storage. *Chem. Rev*. 107:4111–4132.
30. Schüth, F., B. Bogdanović, M. Felderhoff. 2004. Light metal hydrides and complex hydrides for hydrogen storage. *Chem. Commun*. 2249–2258. DOI: 10.1039/b406522k.
31. Varin, R.A., T. Czujko, Z.S. Wronski. 2009. *Nanomaterials for Solid State Hydrogen Storage*. New York: Springer. ISBN 978-0-387-77711-5.
32. Bogdanović, B., U. Eberle, M. Felderhoff, F. Schüth. 2007. Complex aluminum hydrides. *Scr. Mater*. 56:813–816.
33. Züttel, A., A. Borgschulte, S.-I. Orimo. 2007. Tetrahydroborates as new hydrogen storage mate- rials. *Scr. Mater*. 56:823–828.
34. Hauback, B.C. 2008. Structures of aluminium-based light weight hydrides. *Z. Kristallogr*. 223:636–648.
35. Grochala, W., P.P. Edwards. 2004. Thermal decomposition of the non-interstitial hydrides for the storage and production of hydrogen. *Chem. Rev*. 104:1283–1315.
36. Ross, D.K. 2006. Hydrogen storage: The major technological barrier to the development of hydrogen fuel cell cars. *Vacuum* 80:1084–1089.
37. Chen, P., Z. Xiong, G. Wu, Y. Liu, J. Hua, W. Luoc. 2007. Metal–N–H systems for the hydrogen storage. *Scr. Mater*. 56:817–822.
38. Graetz, J., Y. Lee, J.J. Reilly, S. Park, T. Vogt. 2005. Structures and thermodynamics of the mixed alkali alanates. *Phys. Rev. B* 71:184115.
39. Rönnebro, E., E. Majzoub. 2006. Crystal structure, Raman spectroscopy and ab-initio calcula- tions of a new bialkali alanate K_2LiAlH_6. *J. Phys. Chem. B* 110:25686–25691.
40. Nakamoria, Y., G. Kitaharaa, K. Miwab et al. 2005. Hydrogen storage properties of Li–Mg–N–H systems. *J. Alloys Compd*. 404–406:396–398.
41. Nakamori, Y., S.I. Orimo. 2004. Destabilization of Li-based complex hydrides. *J. Alloys Compd*. 370:271–275.
42. Pinkerton, F.E., G.P. Meisner, M.S. Meyer, M.P. Balogh, M.D. Kundrat. 2005. Hydrogen desorp- tion exceeding ten weight percent from the new quaternary hydride $Li_3BN_2H_8$. *J. Phys. Chem. B* 109:6–8.
43. Nakamori, T., K. Miwa, A. Ninomiya et al. 2006. Correlation between thermodynamical sta- bilities of metal borohydrides and cation electronegativites: First-principles calculations and experiments. *Phys. Rev. B* 74:045126–045135.
44. Reilly, J.J., R.H. Wiswall. 1967. The reaction of hydrogen with alloys of magnesium and copper. *Inorg. Chem*. 6:2220–2223.

45. Vajo, J.J., F. Mertens, C.C. Ahn, R.C. Bowman, Jr., B. Fultz. 2004. Altering hydrogen storage properties by hydride destabilization through alloy formation: LiH and MgH_2 destabilized with Si. *J. Phys. Chem. B* 108:13977–13983.
46. Vajo, J.J., S.L. Skeith, F. Mertens. 2005. Reversible storage of hydrogen in destabilized $LiBH_4$. *J. Phys. Chem. B* 109:3719–3722.
47. Vajo, J.J., G.L. Olson. 2007. Hydrogen storage in destabilized chemical systems. *Scr. Mater*. 56:829–834.
48. Yang, J., A. Sudik, C. Wolverton. 2007. Destabilizing $LiBH_4$ with a metal (M = Mg, Al, Ti, V, Cr, or Sc) or metal hydride (MH_2 = MgH_2, TiH_2, or CaH_2). *J. Phys. Chem. C* 111:19134–19140.
49. Alapati, S.V., J.K. Johnson, D.S. Sholl. 2006. Identification of destabilized metal hydrides for hydrogen storage using first principles calculations. *J. Phys. Chem. B* 110:8769–8776.
50. Siegel, D., C. Wolverton, V. Ozolins. 2007. New hydrogen storage reactions based on destabi- lized $LiBH_4$. *Phys. Rev. B: Condens. Matter Mater. Phys*. 76:134102.
51. Alapati, S.V., J.K. Johnson, D.S. Sholl. 2007. Using first principles calculations to identify new destabilized metal hydride reactions for reversible hydrogen storage. *Phys. Chem. Chem. Phys.* 9:1438–1452.
52. Alapati, S.V., J.K. Johnson, D.S. Sholl. 2007. Stability analysis of doped materials for reversible hydrogen storage in destabilized metal hydrides. *Phys. Rev. B* 76:104108.
53. Alapati, S.V., J.K. Johnson, D.S. Sholl. 2007. Predicting reaction equilibria for destabilized metal hydride decomposition reactions for reversible hydrogen storage. *J. Phys. Chem. C* 111:1584–1591.
54. Alapati, S.V., J.K. Johnson, D.S. Sholl. 2008. Large-scale screening of metal hydride mix- tures for high-capacity hydrogen storage from first-principles calculations. *J. Phys. Chem. C* 112:5258–5262.
55. Ozolins, V., E.H. Majzoub, C. Wolverton. 2009. First-principles prediction of thermodynami- cally reversible hydrogen storage reactions in the Li-Mg-Ca-B-H system. *J. Am. Chem. Soc*. 131:230–237.
56. Ozolins, V., A.R. Akbarzadeh, H. Gunaydin, K. Michel, C. Wolverton, E.H. Majzoub. 2009. First-principles computational discovery of materials for hydrogen storage. *J. Phys.: Conf. Ser*. 180:012076.
57. Wagemans, R.W.P., J.H. van Lenthe, P.E. de Jongh, A. Jos van Dillen, K.P. de Jong. 2005. Hydrogen storage in magnesium clusters: Quantum chemical study. *J. Am. Chem. Soc*. 127(47):16675–16680.
58. Kim, K.C., B. Dai, J.K. Johnson, D.S. Sholl. 2009. Assessing nanoparticle size effects on metal hydride thermodynamics using the Wulff construction. *Nanotechnology* 20:204001.
59. Wu, H., W. Zhou, K. Wang et al. 2009. Size effects on the hydrogen storage properties on nanoscaffolded $Li_3BN_2H_8$. *Nanotechnology* 20:204002–204006.
60. For recent reviews of nanoengineered materials for hydrogen storage, see articles in: Viewpoint set no. 42—Fichtner, M., ed. 2007. Nanoscale materials for hydrogen storage. *Scr. Mater*. 56:801–858.
61. Thermodynamics, kinetics and structure of hydrogen storage materials at the nanoscale are given in: Vajo, J., Pinkerton, F., Stetson, N.T., eds. 2009. Special issue on nanoscale phenomena in hydrogen storage. *Nanotechnology* 20:200201–204030.
62. Zaluska, A., L. Zaluski, J.O. Ström-Olsen. 2001. Structure, catalysis and atomic reactions on the nano- scale: A systematic approach to metal hydrides for hydrogen storage. *Appl. Phys. A* 72:157–165.
63. Bogdanović, B., M. Schwickardi. 1997. Ti-doped alkali metal aluminum hydrides as potential novel reversible hydrogen storage materials. *J Alloys Compd*. 253/254:1–9.
64. Yang, J., A. Sudik, D.J. Siegel et al. 2007. Hydrogen storage properties of $2LiNH_2 + LiBH_4 + MgH_2$. *J. Alloys Compd*. 446/447:345–349.
65. Gutowska, A., L. Li, Y. Shin et al. 2005. Nanoscaffold mediates hydrogen release and the reac- tivity of ammonia borane. *Angew. Chem., Int. Ed*. 44:3578–3582.
66. Schüth, F., B. Bogdanović, A. Taguchi. Materials encapsulated in porous matrices for the revers- ible storage of hydrogen. Feb. 17, 2005. WIPO Patent WO 2005/014469 A1.

67. Gross, A.F., J.J. Vajo, S.L. Van Atta, G.L. Olson. 2008. Enhanced hydrogen storage kinetics of $LiBH_4$ in nanoporous carbon scaffolds. *J. Phys. Chem. C* 112:5651–5657.
68. Liu, P., J.J. Vajo. 2008. Thermodynamically tuned nanophase materials for reversible hydrogen storage. In the 2008 Annual Progress Report of the DOE Hydrogen Program. Report IV.A.1b. pp. 449–453. http://www.hydrogen.energy.gov/pdfs/progress08/iv_a_1b_liu.pdf
69. Klebanoff, L., J. Keller. 2012. Final report for the DOE Metal Hydride Center of Excellence. Sandia Report: SAND2012-0786. http://www1.eere.energy.gov/hydrogenandfuelcells/pdfs/metal_hydride_coe_final_report.pdf.
70. Aardahl, C.L., S.D. Rassat. 2009. Overview of systems considerations for on-board chemical hydrogen storage. *Int. J. Hydrogen Energy* 34:6676–6683.
71. Kariya, N.A., M. Ichikawa. 2002. Efficient evolution of hydrogen from liquid cycloalkanes over Pt-containing catalysts supported on active carbons under 'wet-dry multiphase conditions. *Appl. Catal., A* 233:91–102.
72. Hodoshima, S., H. Arai, Y. Saito. 2003. Liquid-film-type catalytic decalin dehydrogeno- aromatization for long-term storage and long-distance transportation of hydrogen. *Int. J. Hydrogen Energy* 28:197–204.
73. Pez, G.P., A.R. Scott, A.C. Cooper, H. Cheng. 2006. Hydrogen storage by reversible hydrogena- tion of pi-conjugated substrates. U.S. Patent No. 7101530.
74. Amendola, S.C., S.L. Sharp-Goldman, M.S. Janjua, N.C. Spencer, M.T. Kelly., P.J. Petillo, M. Binder. 2000. A safe, portable hydrogen gas generator using aqueous borohydride solution and Ru catalyst. *Int. J. Hydrogen Energy* 25:969–975.
75. Ramachandran, P.V., P.D. Gagare. 2007. Preparation of ammonia borane in high yield and purity, methanolysis, and regeneration. *Inorg. Chem*. 46:7810–7817.
76. Shang, Y., R. Chen. 2006. Hydrogen storage via the hydrolysis of $NaBH_4$ basic solution: Optimization of $NaBH_4$ concentration. *Energy Fuels* 20:2142–2148.
77. Hamilton, C.W., R.T. Baker, A. Staubitz, I. Manners. 2009. B–N compounds for chemical hydro- gen storage. *Chem. Soc. Rev*. 38:279–293.
78. Karkamkar, A., C. Aardahl, T. Autrey. 2007. Recent developments on hydrogen release from ammonia borane. *Mater. Matters* 2:6–9.
79. Marder, T.B. 2007. Will we soon be fueling our automobiles with ammonia–borane? *Angew. Chem. Int. Ed*. 46:8116–8118.
80. Stephens, F.H., V. Pons, R.T. Baker. 2007. Ammonia–borane: The hydrogen source par excel- lence? *Dalton Trans*. 25:2613–2626.
81. Xiong, Z., C.K. Yong, G. Wu. 2008. High-capacity hydrogen storage in lithium and sodium amidoboranes. *Nat. Mater*. 7:138–141.
82. Ott, K.C. 2012. Final report for the DOE Chemical Hydrogen Storage Center of Excellence. *Los Alamos Report: LA-UR-20074*. http://www1/.eere.energy.gov/hydrogenandfuelcells/pdfs/chemical_hydrogen_storage_coe_final_report.pdf
83. Graetz, J., J.J. Reilly. 2005. Decomposition kinetics of the AlH_3 polymorphs. *J. Phys. Chem. B* 109:22181.
84. Sandrock, G., J. Reilly, J. Graetz, W. Zhou, J. Johnson, J. Wegrzyn, 2004. Accelerated thermal decomposition of AlH_3 for hydrogen-fueled vehicles. *Appl. Phys. A* 80:687–690.
85. Graetz, J., S. Chaudhuri, J. Wegrzyn, Y. Celebi, J.R. Johnson, W. Zhou, J.J. Reilly. 2007. Direct and reversible synthesis of AlH_3 triethylenediamine from Al and H_2. *J. Phys. Chem. C* 111:19148–19152.
86. Zidan, R., B.L. Garcia-Diaz, C.S. Fewox, A.C. Stowe, J.R. Gray, A.G. Harter. 2009. Aluminium hydride: A reversible material for hydrogen storage. *Chem. Commun*. 25:3717–3719.
87. Ashby, E.C. 1964. The direct synthesis of amine alanes. *J. Am. Chem. Soc*. 86:882–883.
88. Ahluwalia, R.K., T.Q. Hua, J.K. Peng. 2009. Automotive storage of hydrogen in alane. *Int. J. Hydrogen Energy* 34:7731–7740.
89. Crabtree, R.H. 2008. Hydrogen storage in liquid organic heterocycles. *Energy Environ. Sci*. 1:134–138.
90. Züttel, A. 2004. Hydrogen storage methods. *Naturwissenschaften* 91:157–172.

91. Bénard, P., R. Chahine. 2007. Storage of hydrogen by physisorption on carbon and nanostruc- tured materials. *Scr. Mater*. 56:803–808.
92. Ströbel, R., J. Garche, P.T. Moseley, L. Jörissen, G. Wolf. 2006. Hydrogen storage by carbon mate- rials. *J. Power Sources* 159:781–801.
93. Nijkamp, M.G., J.E.M.J. Raaymakers, A.J. van Dillen, K.P. de Jong. 2001. Hydrogen storage using physisorption. *Appl. Phys. A* 72:619–623.
94. Hirscher, M., B. Panella. 2005. Nanostructures with high surface area for hydrogen storage. *J. Alloys Compd*. 404/406:399–401.
95. Shenderova, O.A., V.V. Ahimov, D.W. Brenner. 2004. Carbon nanostructures. *Crit. Rev. Solid State Mater. Sci*. 27:227–356.
96. Thomas, K.M. 2007. Hydrogen adsorption and storage on porous materials. *Catal. Today* 120:389–398.
97. Ansón, A., M. Benham, J. Jagiello et al. 2004. Hydrogen adsorption on a single-walled car- bon nanotube material: A comparative study of three different adsorption techniques. *Nanotechnology* 15:1503–1508.
98. Rosi, N.L., J. Eckert, M. Eddaoudi et al. 2003. Hydrogen storage in microporous metal-organic frameworks. *Science* 300:1127–1129.
99. Wong-Foy, A.G., A.J. Matzger, O.M. Yaghi. 2006. Exceptional H_2 saturation uptake in micropo- rous metal-organic frameworks. *J. Am. Chem. Soc*. 128:3494–3495.
100. Hirscher, M., B. Panella. 2007. Hydrogen storage in metal–organic frameworks. *Scr. Mater*. 56:809–812.
101. Collins, D.J., H.-C. Zhou. 2007. Hydrogen storage in metal–organic frameworks. *J. Mater. Chem*. 17:3154–3160.
102. Long, J.R., O.M. Yaghi. 2009. The pervasive chemistry of metal-organic frameworks. *Chem. Soc. Rev*. 38:1213–1214.
103. Thomas, K.M. 2009. Adsorption and desorption of hydrogen on metal–organic framework materials for storage applications: Comparison with other nanoporous materials. *Dalton Trans*. (9):1487–1505. DOI: 10.1039/b815583f.
104. Han, S.S., H. Furukawa, O.M. Yaghi, W.A. Goddard. 2008. Covalent organic frameworks as exceptional hydrogen storage materials. *J. Am. Chem. Soc*. 130:11580–11581.
105. Furukawa, H., O.M. Yaghi. 2009. Storage of hydrogen, methane, and carbon dioxide in highly porous covalent organic frameworks for clean energy applications. *J. Am. Chem. Soc*. 25:8876–8883.
106. Klontzas, E., E. Tylianakis, G.E. Froudakis. 2010. Designing 3D COFs with enhanced hydrogen storage capacity. *Nano Lett*. 10:452–454. DOI: 10.1021/nl903068a.
107. See, for example: Yang, Z., Y. Xia, R. Mokaya. 2007. Enhanced hydrogen storage capacity of high surface area zeolite-like carbon materials. *J. Am. Chem. Soc*. 129:1673–1679.
108. Furukawa, H., M.A. Miller, O.M. Yaghi. 2007. Independent verification of the saturation hydro- gen uptake in MOF-177 and establishment of a benchmark for hydrogen adsorption in metal– organic frameworks. *J. Mater. Chem*. 17:3197.
109. Wang, L., R.T. Yang. 2008. New sorbents for hydrogen storage by hydrogen spillover—A review. *Energy Environ. Sci*. 1:268–279 and references therein.
110. Dailly, A., J.J. Vajo, C.C. Ahn. 2006. Saturation of hydrogen sorption in Zn benzenedicarboxyl- ate and Zn naphthalenedicarboxylate. *J. Phys. Chem. B* 110:1099–1101.
111. Psofogiannakis, G.M., G.E. Froudakis. 2009. DFT study of enhanced hydrogen storage by spill- over on graphite with oxygen surface groups. *J. Phys. Chem. C* 113:14908–14915.
112. Kubas, G.J., R.R. Ryan, B.I. Swanson, P.J. Vergamini, H.J. Wasserman. 1984. Crystalline dihydro- gen complexes. Intramolecular and intermolecular interactions and dynamic behavior. *J. Am. Chem. Soc*. 106:451–452.
113. Hoang, T.K.A., D.M. Antonelli. 2009. Exploiting the Kubas interaction in the design of hydro- gen storage materials. *Adv. Mater*. 21:1787–1800.
114. Kubas, G.J. 2007. Dihydrogen complexes as prototypes for the coordination chemistry of satu- rated molecules. *Proc. Nat. Acad. Sci*. 104:6901–6907.

115. Keskin, S., J. Liu, R.B. Rankin, J.K. Johnson, D.S. Sholl. 2009. Progress, opportunities, and chal- lenges for applying atomically detailed modeling to molecular adsorption and transport in metal-organic framework materials. *Ind. Eng. Chem. Res*. 48:2355–2371.
116. Kim, Y.-H., Y. Zhao, A. Williamson, M.J. Heben, S.B. Zhang. 2006. Nondissociative adsorption of H_2 molecules in light-element-doped fullerenes. *Phys. Rev. Lett*. 96:016102–016105.
117. Yildirim, T., S. Ciraci. 2005. Titanium-decorated carbon nanotubes as a potential high-capacity hydrogen storage medium. *Phys. Rev. Lett*. 94:175501–175504.
118. Simpson, L. 2010. Hydrogen Sorption Center of Excellence (HSCoE) final report. http://www1.eere.energy.gov/hydrogenandfuelcells/pdfs/hydrogen_sorption_coe_final_report.pdf
119. Zhang, J., T.S. Fisher, P.V. Ramachandran, J.P. Gore, I. Mudawar. 2005. A review of heat transfer issues in hydrogen storage technologies. *J. Heat Transfer* 127:1391–1399.
120. Ahluwalia, R.K., J.K. Peng. 2009 Automotive hydrogen storage system using cryo-adsorption on activated carbon. *Int. J. Hydrogen Energy* 34:5476–5487.
121. Hardy, B.J. 2007. Geometry, heat removal and kinetics scoping models for hydrogen storage systems. Savannah River National Laboratory Report WSRC-TR-2007-00439. http://www1.eere.energy.gov/hydrogenandfuelcells/pdfs/bruce_hardy_srnl-2007–0043_part1.pdf
122. Hardy, B.J. 2007. Integrated Hydrogen Storage System. Savannah River National Laboratory Report WSRC-TR-2007-00440. http://www1.eere.energy.gov/hydrogenandfuelcells/pdfs/ bruce_hardy_srnl-2007–0043_part2.pdf
123. Mosher, D.A., S. Arsenault, X. Tang, D.L. Anton. 2007. Design, fabrication and testing of $NaAlH_4$ based hydrogen storage systems. *J. Alloys Compd*. 446–447:707–712.
124. Ahluwalia, R.K. 2007. Sodium alanate hydrogen storage system for automotive fuel cells. *Int. J. Hydrogen Energy* 32:1251–1261.
125. 1251–1261.

1. http://www.hydrogen.energy.gov/annual_review10_production.html#delivery.

19

Compact Hydrogen Storage in Cryogenic Pressure Vessels

Salvador M. Aceves
Lawrence Livermore National Laboratory

Francisco Espinosa-Loza
Lawrence Livermore National Laboratory

Elias Ledesma-Orozco
Universidad de Guanajuato

Guillaume Petitpas
Lawrence Livermore National Laboratory

CONTENTS

19.1 Introduction 651
19.2 Historical Perspective 652
19.3 Thermodynamics of Cryogenic Pressure Vessels 654
19.4 Potential Safety Advantages 658
19.5 Technology Validation 659
19.6 Increasing Packaging Efficiency with Dual-Volume Vessels 661
19.7 Conclusions 663
Acknowledgments 663
References 664

19.1 Introduction

As a universal transportation fuel that can be generated from water and any energy source, hydrogen is a leading candidate to supplant petroleum with the potential to ultimately eliminate petroleum dependence, associated air pollutants, and greenhouse gases [1]. The predominant technical barrier limiting widespread use of hydrogen automobiles is storing enough hydrogen fuel on board to achieve sufficient (500+ km) driving range in a compact, lightweight, rapidly refuelable, and cost-effective system.

There are three major conceptual approaches to storing hydrogen on board automobiles: (1) gas compressed to high pressures (e.g., 350–700 atm) [2,3], (2) lower pressure absorption of hydrogen within porous and/or reactive solids [4,5], or (3) cryogenic liquid (LH_2) at temperatures near its boiling point (20.3 K) [6]. Each approach faces fundamental limits. Hydrogen stored as a compressed gas occupies a relatively large volume at ambient temperature, while materials to absorb hydrogen add significant weight, cost, and thermal

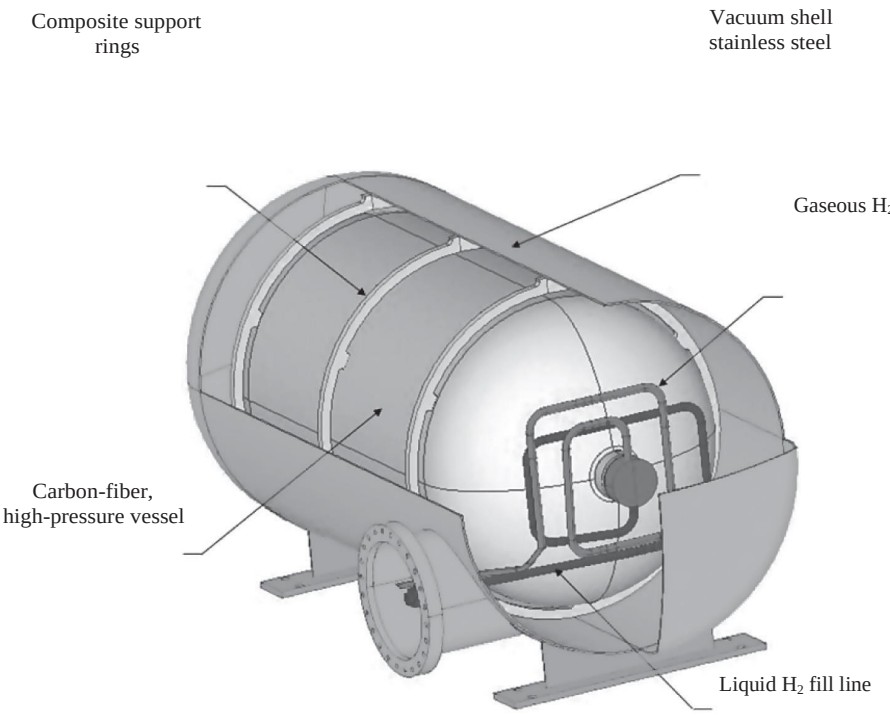


FIGURE 19.1

Cryogenic pressure vessel design. Inner vessel is an aluminum-lined, carbon fiber–wrapped pressure vessel typically used for storage of compressed gases. This vessel is surrounded by a vacuum space filled with numer- ous sheets of highly reflective metalized plastic (minimizing heat transfer into vessel) and an outer jacket of stainless steel.

complexity to onboard storage systems. Finally, liquid hydrogen (LH_2) evaporates very easily, pressurizing quickly as it absorbs heat from the environment (typically venting after 3 days of inactivity) or from distribution, transfer, and refueling operations.

A new approach has been developed over the last decade that combines existing storage technologies to capture the advantages of both: *cryogenic* pressure vessels [7–9]. Cryogenic vessels comprise a high-pressure vessel enclosed in high-performance vacuum multilayer thermal insulation (Figure 19.1), enabling hydrogen storage at cryogenic temperatures (as cold as 20 K) *and* high pressures (e.g., ~350 atm). For a pressure vessel of given size and cost, a cryogenic pressure vessel stores substantially more hydrogen than a vessel at ambient temperature without the additional weight and cost of hydrogen-absorbent materials but with far greater thermal endurance than conventional (i.e., low pressure) cryogenic LH_2 tanks. Cryogenic pressure vessels can essentially eliminate evaporative losses for practical automotive refueling and driving scenarios. High-density storage enables inexpensive, long-range hydrogen-fueled automobiles, and cryogenic operation reduces isentropic expansion energy, potentially improving safety of operation.

19.2 Historical Perspective

When initially proposed in the early 1970s, hydrogen-fueled vehicles demanded low-pressure LH_2 [10,11]. Pressurized hydrogen storage was not considered viable. Metallic tanks were extremely heavy and bulky, and composite materials were not available for automotive applications due to technical maturity and cost issues.

Progress in cryogenic technology (a factor of 1000 improvement on cryogenic insulation over 50 years [12]) made a compelling case for LH_2 vehicles. BMW, Linde, and Magna Steyr demonstrated LH_2 vessels with world-leading weight, volume, and cost performance [6,13]. However, while viable for large vehicles (>10 kg H_2), LH_2 tanks suffer from considerable evaporative losses when reduced in size due to lower thermal mass that magnifies the effect of environmental heat transfer.

The aerospace industry, more sensitive to weight and less sensitive to cost, did con- sider composite materials for multiple structural applications. In particular, storage of cryogenic propellants and oxidizers is a key application that was researched from the 1960s [14]. While light and efficient for space travel, cryogenic fluids suffer from evapo- rative losses during long missions, and minimizing these losses is critical for reducing launch weight. While most efforts have been dedicated to zero boil-off systems where high-performance thermal insulation is complemented by active cryocooling to elimi- nate evaporative losses [15,16], the concept of storing cryogens in a vessel rated for high pressure (34–120 atm) was also considered for this application [17]. The authors observed the thermodynamic potential for trading-off vessel strength (pressure rating) versus insulation performance: greater pressure rise allows more heat transfer and less insu- lation. Conversion between the two phases of hydrogen nuclear spin (para to ortho) is endothermic, and the authors also considered the use of catalysts to promote the reaction and further reduce evaporative losses. The results indicate an advantage for cryogenic pressure vessels versus low-pressure cryogenic vessels for Mars exploration due to lower evaporative losses.

Progress in composite pressure vessel technology enabled automotive application start- ing in the early 1990s and leading to the development of high-performance pressure vessels capable of storing hydrogen at large weight fraction (>10% H_2) [18]. However, volumetric performance—critical for efficient packaging within a vehicle—was still limited by the low density of compressed gas.

The first automotive cryogenic pressure vessels were developed at Concordia Univer- sity (Montreal, Canada) in the early 1990s [19,20]. The concept for these *thermocon- trolled* vessels consisted of filling insulated pressure vessels (rated for 300 atm) with LH_2, which was subsequently evaporated, initially from contact with the warm tank and finally by circulating warm gases (e.g., engine exhaust) through an in-tank heat exchanger. Aside from the capacity advantage of storing high-density LH_2, thermocon- trolled vessels provide a source of high-pressure hydrogen that can be used for direct injection into a hydrogen spark-ignited engine, eliminating power loss that would oth- erwise occur due to hydrogen displacing ambient air [21]. The potential for evaporative losses for infrequent drivers or during long periods of inactivity was not considered and may be an issue when the cryogenic vessel is pressurized through intentional heat transfer.

Detailed thermodynamic modeling of cryogenic pressure vessels was first conducted at Lawrence Livermore National Laboratory [8]. The analysis revealed the potential for high- capacity vessels that eliminate evaporative losses during regular use. The margin afforded by the high-pressure rating combined with the cooling that occurs as gaseous hydrogen is extracted reduces sensitivity to environmental heat transfer by an order of magnitude when compared to LH_2 vessels. It may also enable insulation simplifica- tion. While LH_2 tanks demand very-high-performance insulation (<3 W heat transfer), cryogenic pressure vessels can operate at higher heat transfer rates (possibly as much as 10 W), enabling thinner and/or simpler insulations that improve packaging efficiency and reduce system cost.

19.3 Thermodynamics of Cryogenic Pressure Vessels

Cryogenic pressure vessels address three key problems stemming from the high volatil- ity of LH_2: evaporative losses after a short period of inactivity (dormancy), cumulative evaporative losses for short daily driving distances, and risk of being stranded due to fuel evaporation after long-term parking.

The dormancy (period of inactivity before a vessel releases hydrogen to reduce pres- sure buildup) is an important parameter for LH_2 vehicle acceptability. Dormancy can be calculated from the first law of thermodynamics [22] and the properties of H_2 [23] and can be illustrated with a diagram of hydrogen thermodynamic properties (Figure 19.2) to simplify visualization and graphical calculation of dormancy for hydrogen vessels.

Figure 19.2 uses axes of internal energy and density instead of more traditional temperature and pressure. A dormancy calculation begins by identifying the initial thermodynamic state in Figure 19.2 (density and internal energy) of the hydrogen contained in the vessel. From this initial point (e.g., point A), the thermodynamic state of hydrogen fuel on board a parked vehicle moves horizontally to the right (warming at constant density) as

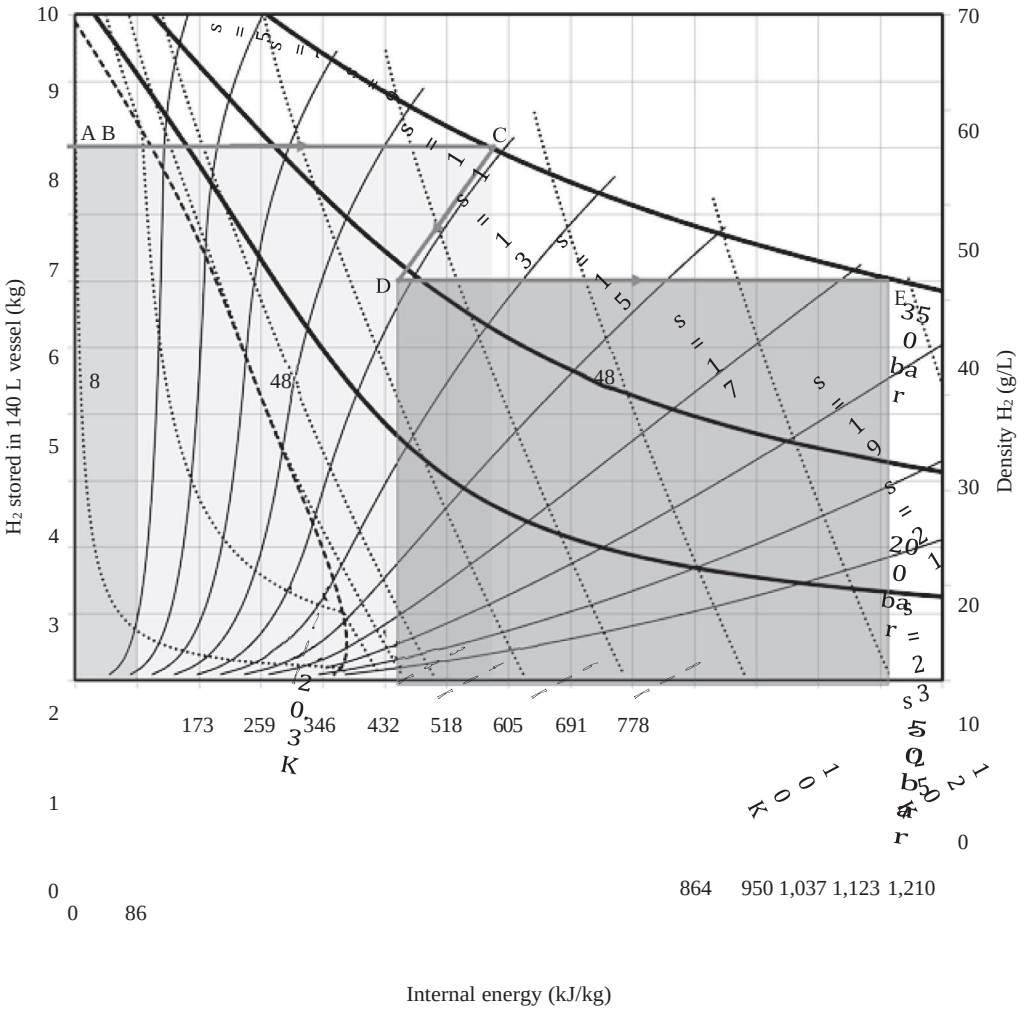


FIGURE 19.2

Phase diagram for hydrogen showing density (right vertical axis) and internal energy (horizontal axis), with lines for constant pressure (thick lines), temperature (dotted lines), and entropy (thin lines). The figure also shows a thick dashed saturation line that separates the supercritical phase (right) from the two-phase (liquid and vapor) region (left). A second vertical axis in the left shows the mass of hydrogen contained in a vessel with 140 L internal volume, which would store 10 kg of LH_2 at 20 K and 1 atm. The figure also shows letters and areas representing dormancy (in Watt days) of conventional LH_2 tanks (AB, medium-gray area) and cryogenic pres- sure vessels (B to E, medium + light + dark-gray areas).

heat enters from the environment, until the hydrogen pressure reaches the vessel maximum and some hydrogen needs to be used or vented. The cumulative thermal energy absorbed while a car is parked can be calculated by multiplying the amount of hydrogen in the vessel by the total change in its specific internal energy. This total thermal energy is shown as the *area* in Figure 19.2 under the horizontal line joining the initial and final points in the process (neglecting temperature stratification and vessel thermal capacity). Dormancy is then equal to the total heat absorbed (the area under the line) divided by the heat entry rate.

An appropriate choice of scales in Figure 19.2 radically simplifies dormancy calculations. The grid scale in the internal energy (horizontal) axis is set at 86.4 kJ/kg H_2, which converts to 1 W-day/kg H_2 (1 day = 86,400 s). The grid scale in the vertical axis represents 1 kg H_2. Therefore, the area of a grid square represents 1 W-day of heating. The total change in internal energy (in Watt-days) can be easily calculated by counting the squares under the horizontal line representing the parking process. Dormancy is calculated by dividing the internal energy change (in Watt-days) by the rate of heat transfer (in Watts).

As an illustration, consider a parked hydrogen automobile with a conventional LH_2 tank with 140 L internal volume and 6 atm maximum working pressure, which is 80% full with 8 kg LH_2 at 20 K and 1 atm (point A in Figure 19.2). Once the vehicle is parked, heat entry warms the hydrogen, increasing both its temperature and pressure. Dormancy ends in this case when the pressure reaches 6 atm (point B in Figure 19.2), when hydrogen venting becomes necessary to maintain pressure within the vessel's limits. Total heat absorbed during this process from point A to point B can be calculated by counting the number of squares (8 W-days) in the area marked in green. Dormancy can then be cal- culated by dividing 8 W-days by the heat transfer rate (e.g., 2 days for a vessel absorbing heat at a rate of 4 W).

Figure 19.2 illustrates the dramatic dormancy advantage of automobiles with cryogenic pressure vessels. An auto initially filled with 8 kg LH_2 at 1 atm and 20 K can remain parked until the pressure reaches 340 atm (point C in the figure) without venting any hydrogen. Counting squares under the line joining point A and point C, we obtain 8 + 48 = 56 W-days, *seven times* greater thermal endurance than a conventional LH_2 tank. Furthermore, unlike conventional LH_2 vessels, cryogenic pressure vessels dramatically extend dormancy as the vehicle is driven. For example, if the parked vehicle is driven when the hydrogen is at state C (Figure 19.2) consuming 2 kg of H_2 fuel, the remaining hydrogen in the vessel expands and cools following a constant entropy line from point C to point D, extending the thermal endurance of the vessel by an additional 48 W-days before any losses occur (at point E in Figure 19.2). Further driving substantially extends dormancy, essentially eliminating fuel evaporation for even very moderate driving patterns.

In principle, Figure 19.2 enables simple analyses of arbitrary cycles of driving and parking periods. Evaporative losses and dormancy are easily calculable, given a driving schedule, vessel volume, and thermal performance (i.e., heat transfer leak rate).

Figure 19.2 is somewhat conservative because it neglects secondary effects such as vessel heat capacity and heat potentially absorbed by conversion between the two states of nuclear spin arrangement (i.e., *para*-hydrogen conversion to *ortho*-hydrogen) of hydrogen molecules. Both of these effects tend to increase the dormancy of the vessels but are most significant only for warmer temperatures (T > 77 K) and partially full vessels where thermal endurance is a substantially easier challenge. Both effects are negligible at the very low (i.e., 20–30 K) temperatures where conventional LH_2 tanks operate.

From Figure 19.2, it is clear that insulation performance can be traded off versus ves- sel pressure rating: dormancy can be increased by either improving insulation or by

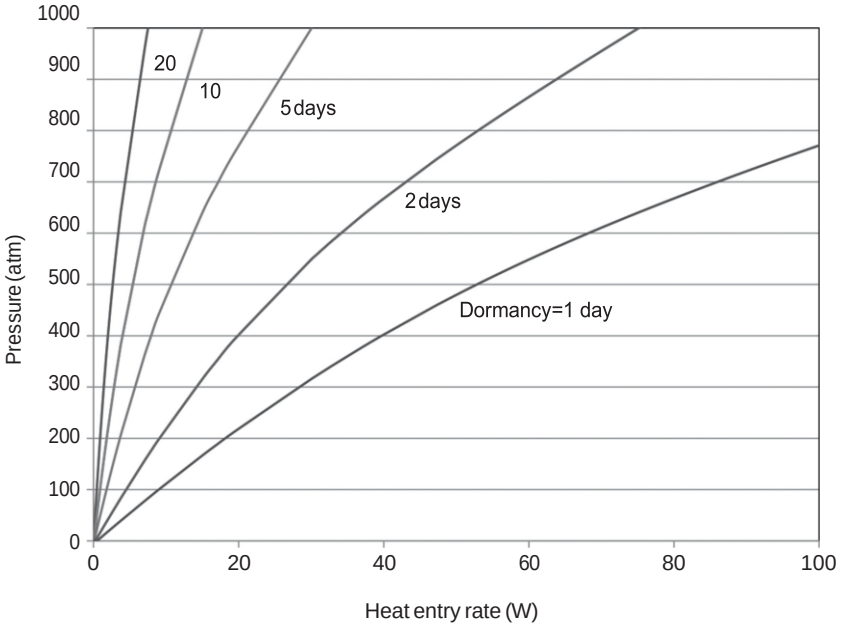


FIGURE 19.3

Contour lines of dormancy versus heat transfer rate (x-axis) and vessel rated pressure (y-axis) for an initially full vessel (140 L internal volume and 10 kg LH_2 at 1 atm).

strengthening the vessel. This trade-off is better illustrated in Figure 19.3, which shows contour lines of dormancy versus heat transfer rate (x-axis) and vessel rated pressure (y-axis) for an initially full vessel (140 L internal volume and 10 kg LH_2 at 1 atm). The figure shows that a pressure vessel may reach acceptable dormancy (5 days) through either (1) high-performance insulation (~3 W) at low rated pressure (~167 atm) or (2) high rated pressure (700 atm) at low-performance insulation (~17 W). Even larger heat transfer rates would be allowable in continuously driven vehicles (e.g., taxis, buses) since strong vessels (>500 atm rated pressure) deliver 1 day of dormancy at heat entry rates over 60 W. The optimum design point depends on the relative cost of fiber and insulation, as well as the particular mission requirements.

It should also be noted that Figure 19.3 assumes a completely full vessel—the best case for low-pressure vessels and the worst case for high-pressure vessels. Low-pressure vessels (<10 atm) have maximum dormancy when full because the thermal inertia of the evaporating LH_2 slows down pressure rise. On the other hand, cryogenic pressure vessels gain most of their dormancy from containing the hydrogen as they heat up and therefore have longest dormancy at low fill levels where the vessel can heat up more before reaching the rated pressure. Dormancy is infinite when ambient temperature hydrogen at rated pres- sure is denser than the cryogenic hydrogen stored in the vessel.

Considering that (1) vehicles are typically not filled to full capacity before extended parking and (2) even short distance driving plays a considerable role in cryogenic pres- sure vessel dormancy (Figure 19.2), it is important to consider all factors for enabling quick visualization of thermal performance and dormancy. Figures 19.4 (vessel rated for 135 atm) and 19.5 (vessel rated for 350 atm) assume a 140 L vessel (10 kg LH_2 when full) with 5 W heat transfer rate, installed on board an efficient vehicle (100 km/kg H_2). For any given vessel pressure (x-axis) and hydrogen mass (y-axis), the figures give (1) dormancy, (2) daily driving distance necessary to eliminate evaporative losses, (3) temperature, and (4) entropy.

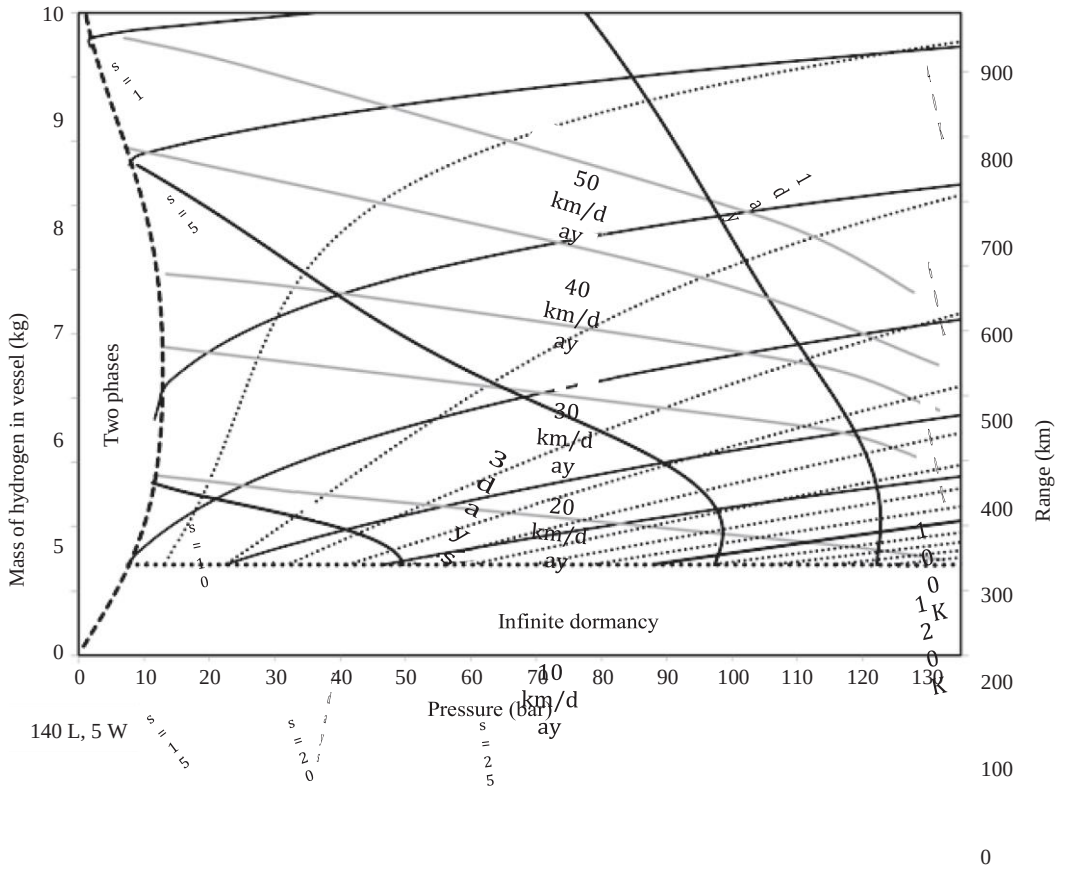


FIGURE 19.4

Contour lines of entropy (thin, continuous), temperature (dotted), dormancy (thick), and minimum daily driv- ing distance necessary for avoiding evaporative losses (gray), as a function of vessel rated pressure (x-axis) and hydrogen mass in vessel (y-axis). The figure assumes a 140 L vessel (10 kg LH_2 when full) with 5 W heat entry, installed on board an efficient vehicle (100 km/kg H_2), and 135 bar vessel rated pressure.

As an example of the application of these figures, assume that a vessel with a 140 L internal volume and 135 atm rated pressure contains 6 kg H_2 at a pressure of 105 atm. Finding the location of this point in Figure 19.4, we determine that the vessel contains hydrogen at ~60 K and will start venting in ~1 day if left unused and driving ~45 km/day will suffice for eliminating all evaporative losses.

A comparison between Figures 19.4 and 19.5 illustrates the thermal performance advantages of stronger vessels. The infinite dormancy region more than doubles in size as the pressure rating is increased to 350 atm (Figure 19.5) due to the higher ambient temperature storage capacity. Even in the regions where evaporative losses are possible, dormancy is considerably longer, and minimum daily driving distance is much shorter as the rated pressure is raised, eliminating evaporative loses under practical driving scenarios. These advantages of cryogenic pressure vessels must be balanced against the added cost and weight of structural materials and the cost of high-performance insulation.

It is worth noting that there is no risk of being stranded due to evaporative losses during cryogenic pressure vessel long-term parking. Even when thermal equilibrium with the

environment is reached (after months of parking), a substantial fraction of the original hydrogen remains (15% at 135 atm and 30% at 350 atm, infinite dormancy limit in Figures 19.4 and 19.5). This is sufficient for reaching a refueling station even in remote locations.

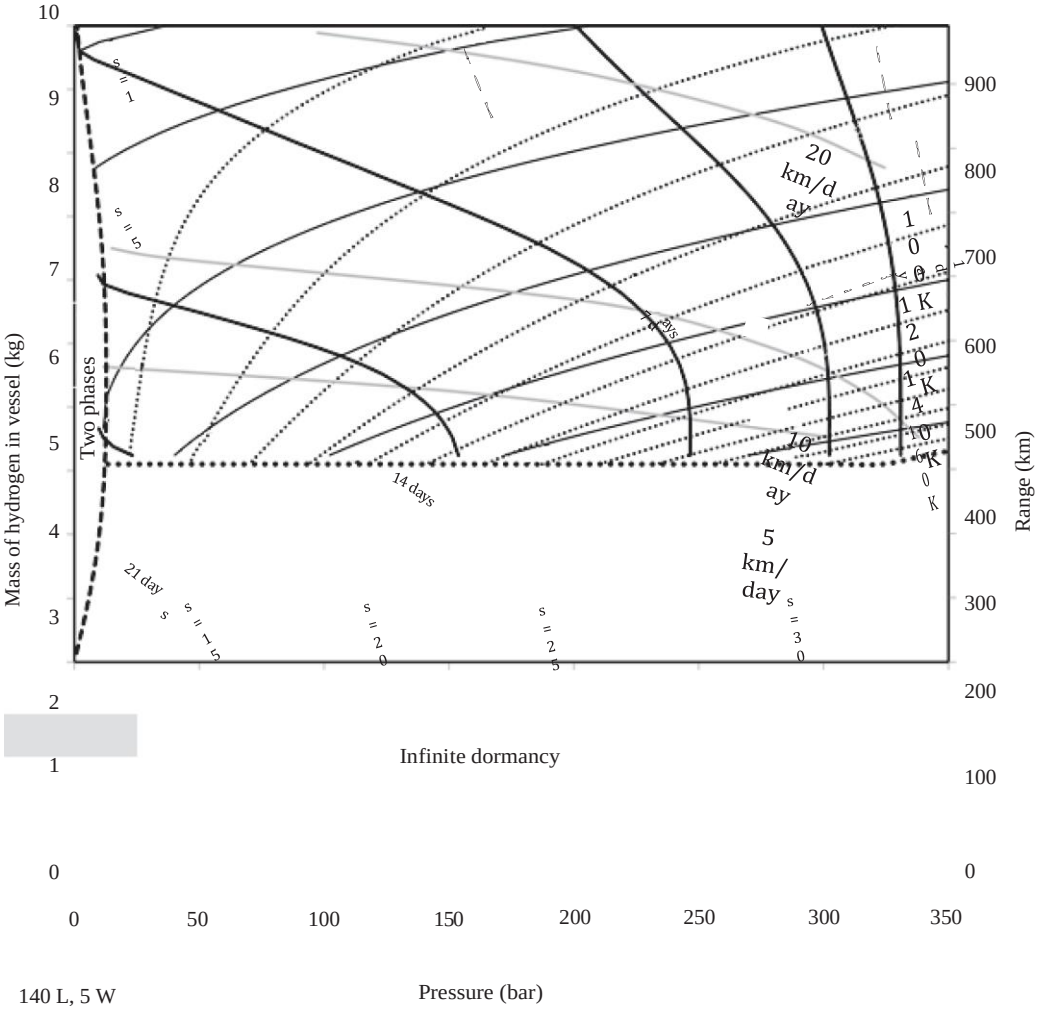


FIGURE 19.5

Contour lines of entropy (thin, continuous), temperature (dotted), dormancy (thick), and minimum daily driv- ing distance necessary for avoiding evaporative losses (gray), as a function of vessel rated pressure (x-axis) and hydrogen mass in vessel (y-axis). The figure assumes a 140 L vessel (10 kg LH_2 when full) with 5 W heat entry, installed on board an efficient vehicle (100 km/kg H_2), and 350 bar vessel rated pressure.

19.4 Potential Safety Advantages

Cryogenic pressure vessels offer a number of potential safety advantages. The most dramatic and perhaps counterintuitive is the radically lower theoretical burst energy of *low-temperature* H_2. Figure 19.6 shows the theoretical maximum mechanical energy released by a sudden adiabatic expansion to atmospheric pressure (e.g., in a vessel rupture) of high-pressure hydrogen gas from three temperatures (80, 150, and 300 K). H_2 stored at 70 atm and 300 K will release a maximum mechanical energy of 0.55 kWh/kg H_2 if suddenly (i.e., adiabatically) expanded to atmospheric pressure (cooling substantially in the process). Counterintuitively, this maximum energy release increases only slightly with *much* higher H_2 pressures. Raising vessel pressure to 1000 atm (1400% increase from 70

atm) increases maximum mechanical energy release by only 10% while shrink- ing vessel volume and strengthening (thickening) vessel walls many times over. The low burst energy and high hydrogen storage density of cryogenic temperatures com- bine synergistically, permitting smaller vessels that can be better packaged on board to withstand automobile collisions. The vacuum jacket surrounding a cryogenic pres- sure vessel (Figure 19.1) offers a second layer of protection, eliminating environmental impacts over the life of the pressure vessel. Vacuum jacketing also provides expansion

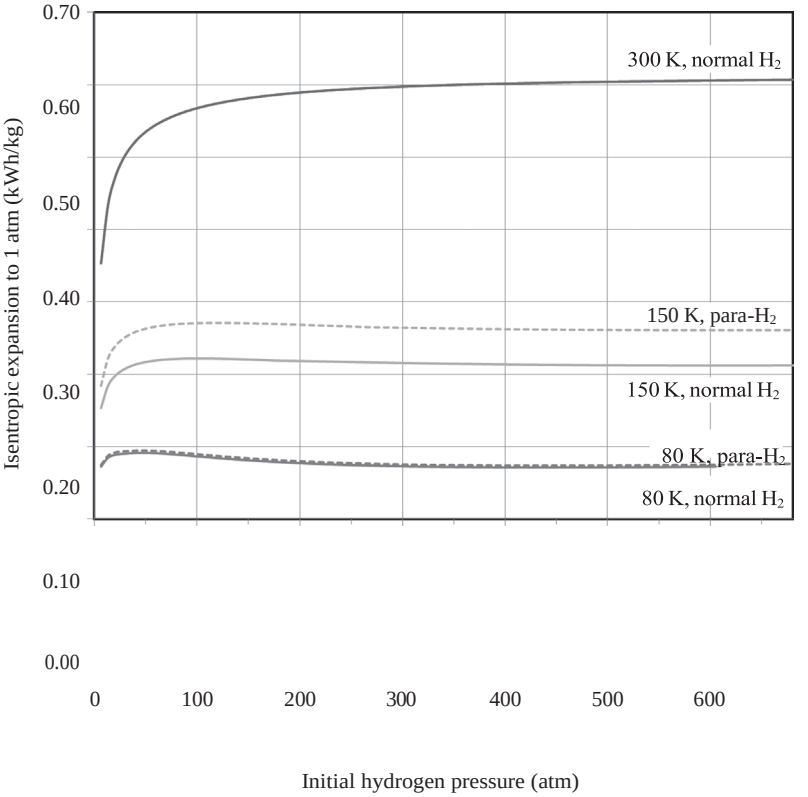


FIGURE 19.6

Maximum mechanical energy (per kilogram of hydrogen) released upon instantaneous expansion of H_2 gas (e.g., from a pressure vessel) as a function of initial storage pressure at 80, 150, and 300 K. For comparison, note that the chemical energy content of hydrogen is 33.3 kWh/kg. This mechanical energy is the theoretical maximum available work based on reversible adiabatic expansion from the pressure shown to 1 atm, calculated from internal energy differences of H_2 gas before and after isentropic expansion. The figure reports normal- hydrogen expansion energy at 300 K and para-hydrogen and normal-hydrogen expansion energy at 80 and 150 K. In the latter two cases, the real adiabatic expansion energies are slightly lower because the para content is less than 100% before expansion (between 99.8% para and equilibrium, depending on the previous use of the storage and the actual ortho-to-para transition rate).

volume to mitigate shocks from hydrogen release. Cryogenic vessels avoid the fast fill heating and overpressures (up to 25%) typical of ambient temperature vessels, consequently operating at higher safety factors, especially as driving the automobile cools the remaining hydrogen fuel and reduces average hydrogen pressures further over typical driving and refueling cycles. Finally, due to the high density of cryogenic hydrogen and the relatively low refueling pressure, the number and amplitude of pressure peaks in a cryogenic pressure vessel can be lower than in ambient high-pressure vessels.

19.5 Technology Validation

Three generations of cryogenic pressure vessels incorporating aluminum-lined, composite-wrapped vessels, an outer vacuum vessel, and multilayer vacuum insulation to minimize heat transfer have been designed, assembled, and demonstrated at LLNL (Figure 19.7). The designs also included instrumentation for pressure and temperature as well as safety

devices to prevent vessel failure. The figure shows specific weight and volume performance for the three vessels (weight fraction and grams of H_2 per liter), as well as the Department of Energy (DOE) 2010, 2015, and ultimate weight and volume targets [24].

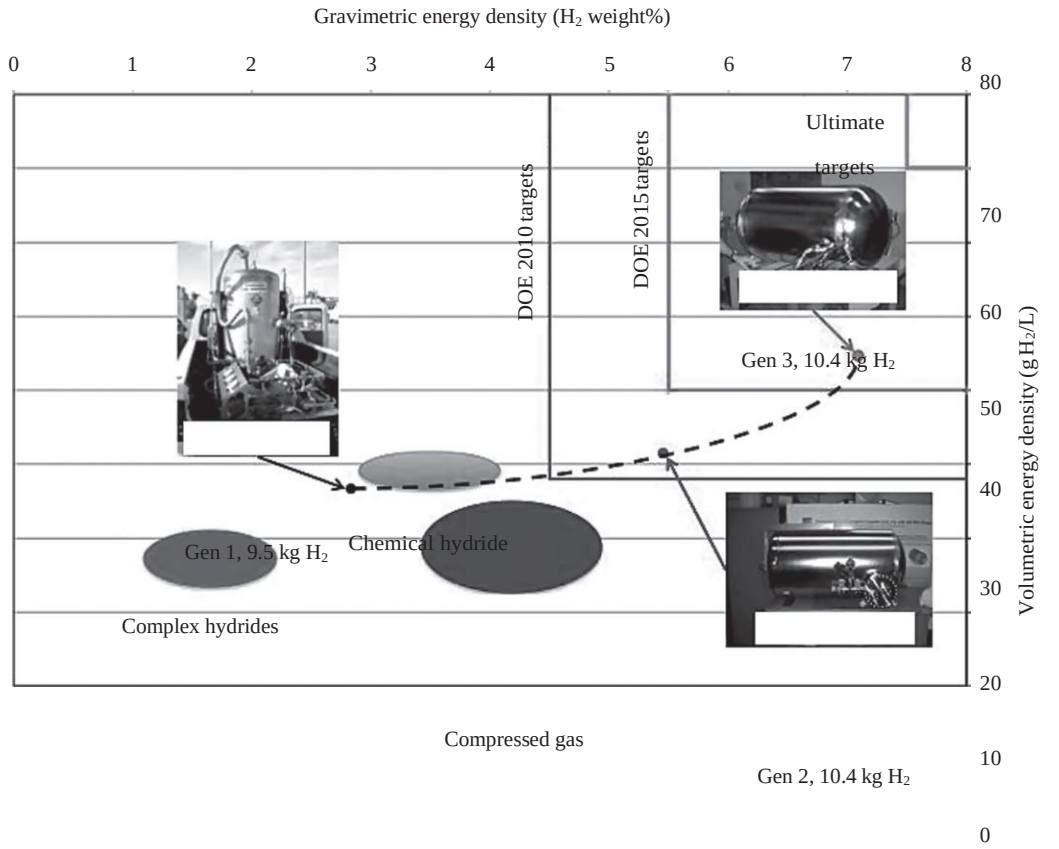


FIGURE 19.7

Weight and volume performance of three generations of cryogenic pressure vessel prototypes. The figure also shows weight and volume performances specified by the US DOE 2010 target (4.5% weight frac- tion and 30 g H_2/L), 2015 target (6% weight fraction and 40 g H_2/L), and ultimate target (7.5% weight fraction and 70 g H_2/L). (From Department of Energy, Office of Energy Efficiency and Renewable Energy Hydrogen, Fuel Cells & Infrastructure Technologies Program Multi-Year Research, Development and Demonstration Plan, http://www.eere.energy.gov/hydrogenandfuelcells/mypp.)

The latest prototype cryogenic pressure vessel (generation 3) takes advantage of the insensitivity to environmental heat transfer to considerably reduce insulation thickness (to ~1.5 cm vs. ~3 cm typical of LH_2 vessels), significantly reducing system volume. This more compact vessel is expected to still provide acceptable dormancy.

Table 19.1 lists detailed component weight and volume breakdown for the generation 3 cryogenic pressure vessel. Thin insulation produces a very compact and light design that meets the very challenging DOE 2015 weight and volume targets and is within 3 kg of meeting the DOE ultimate weight target. Further gains in packaging density may be obtained by pressurizing LH_2, theoretically increasing hydrogen storage capacity by ~20% for isothermal compression (84 kg/m^3 hydrogen density at 20 K and 250 atm), although 5%–10% density increase is more likely once pumping inefficiencies and compression heating are considered.

The US DOE has also established *cost* targets for hydrogen storage systems [24]. While cryogenic pressure vessels are projected to be cost competitive with respect to alterna- tives [25], they still cost three to four times more than the DOE 2010 target ($13.6/kWh vs. $4/kWh). Cost may therefore be the most challenging of DOE targets, even though future

improvements on vessel materials, manufacture, and insulation may reduce expense below projected values.

TABLE 19.1

Weight and Volume of the Main System Components for the Generation 3 Cryogenic Pressure Vessel and for the Dual-Volume System

	Generation 3		Dual Volume (Projected)	
Components	**Weight (kg)**	**Volume (L)**	**Weight (kg)**	**Volume (L)**
Hydrogen inside cylindrical vessel(s)	10.7	151	6.0	86.6
Hydrogen within low-pressure vessel	0	0	5.4	76.7
Total hydrogen stored	10.7	151	11.4	163.3
High-pressure vessel(s)	61	28	11.9	7.2
Low-pressure (interstitial) vessel	0	0	81.7	10.2
Insulation and vacuum shell	57	46	53.6	24.56
Total, vessel and vacuum shell	118	74	147.2	41.96
Total, vessel(s), vacuum shell, and hydrogen	129	225	158.6	205.26
Total for accessories	16	10	16	10
Total, storage system	145	235	174.6	215.26
H_2 weight fraction	7.38%		6.53%	
Volume performance, g/L		45.49		52.95

The generation 3 vessel was built and installed on board a Toyota Prius experimental vehicle. The dual-volume system has been designed and analyzed, but it has not been built. For compari- son, the DOE 2010 targets are 4.5% weight fraction and 30 g H_2/L; DOE 2015 targets are 6% weight fraction and 40 g H_2/L; ultimate DOE targets are 7.5% weight fraction and 70 g H_2/L [24]. Storage calculations assume 70.7 kg/m^3 hydrogen density (LH_2 at 20 K and 1 atm). The table assumes that all stored hydrogen is usable, although driving at high power for a long time may drop the vessel pressure below the necessary level to run the engine or fuel cell, reducing the net hydrogen storage density by a few percent [26].

19.6 Increasing Packaging Efficiency with Dual-Volume Vessels

Cryogenic pressure vessels store high-density LH_2 while avoiding evaporative losses with thin insulation resulting in high *system* storage density. However, even LH_2 is only a fourth as energetically dense as gasoline, and the generation 3 vessel is approximately six times larger than a gasoline tank with the same energy storage. While there is still potential for improving cryogenic pressure vessels through more compact construction, we also see the possibility of using *conformable* designs that may package better inside the vehicle than conventional cylindrical shapes.

Conformable vessels hold the promise of better filling *box*-shaped or even irregu- larly shaped spaces, improving packaging efficiency by 20%–40% over conventional cylindrical vessels. However, conformable vessels remain a structural challenge [27,28]. Noncylindrical, nonspherical shapes suffer from bending stresses that quickly exceed the strength of structural materials—even ultrastrong carbon fiber. Applicability of conform- able box-shaped vessels is therefore limited to low pressures (~6 atm), typically too low for compact hydrogen storage.

We can, however, take advantage of low-pressure conformable vessels through a new concept: *dual-volume containers*. The concept of a dual-volume container (Figure 19.8)

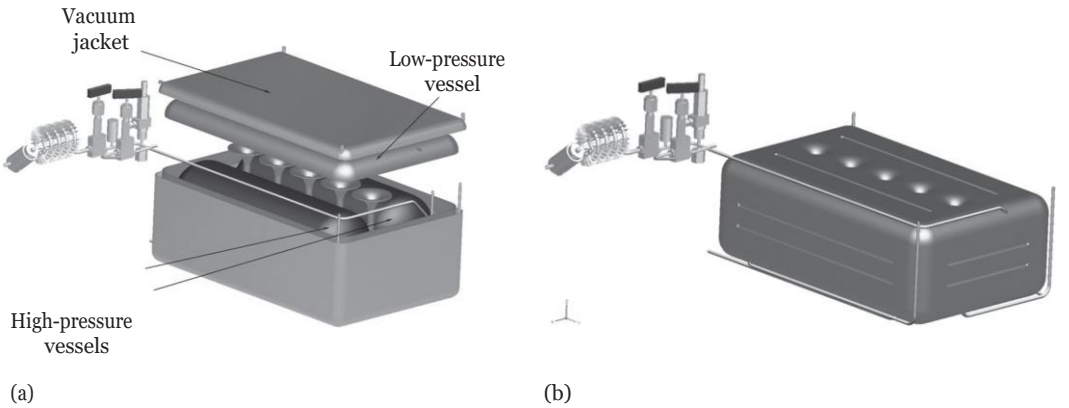


FIGURE 19.8

Geometry of dual-volume conformable pressure vessel comprising two cylindrical high-pressure (350 atm) vessels surrounded by a low-pressure (6 atm) interstitial box-shaped vessel. Finally, a vacuum vessel and mul- tilayer insulation surround the outer vacuum vessel. (a) Vessel with the upper vacuum and interstitial vessels removed for better visualization. (b) Fully assembled dual-volume vessel.

combines two high-pressure (~250 atm) cylindrical vessels enclosed within a low-pressure (~6 atm) box-shaped conformable container that can be filled with low-pressure LH_2, enabling utilization of interstitial spaces and corners that are normally wasted in cylindrical vessels. The low-pressure container is then surrounded with thin (6.5 mm) vacuum multilayer insulation for reducing heat transfer into the vessel.

The geometry of dual-volume vessels is synergistic with hydrogen properties because the interstitial space can store LH_2 at low pressure and high density. While the low-pressure container will have reduced thermal endurance (~2 days), it can be used for extending vehicle range when most needed—during long trips. Continuous driving quickly consumes hydrogen before any evaporative losses may occur. The driver may then fill only the cylindrical pressure vessels with LH_2 and leave the interstitial vessel empty when little driving is anticipated, avoiding evaporative losses while still maintain- ing a reasonable driving range.

The dual-volume design in Figure 19.8 has improved packaging efficiency due to interstice utilization. A system with 11.4 kg H_2 storage capacity would store 5.4 kg LH_2 in 76.7 L of interstitial space, often wasted in cylindrical vessels. Each of the inner high-pressure linerless vessels stores 3 kg LH_2 in 43.3 L of internal volume.

The dual-volume vessel in Figure 19.8 has been analyzed and designed by finite element. Table 19.1 lists the projected weight and volume of the vessel and accessories. The table shows that the dual-volume vessel has potential for producing very high weight and volume performance, and it is projected to meet or exceed the DOE 2015 targets.

Vessel volume listed in Table 19.1 is the total external volume (i.e., the *shrink-wrap* volume). However, considering that spaces in vehicles are typically box-shaped rather than cylin- drical, it may be appropriate to define vessel's *effective* volume performance not in terms of total external volume but rather in terms of the volume of a box that encloses the system. It would therefore make sense to define a conformability credit as the hydrogen volume stored in a conformable vessel that occupies a box-shaped space divided by the hydrogen volume in cylindrical vessels that can be packaged within the same box-shaped space. This criterion would give the dual-volume vessel a 22% conformability credit that would

increase the volumetric performance from 53 to 64 g H_2/L—over 90% of the density of pure LH_2 at ambient pressure (70.7 g/L).

It may be possible to reach the DOE ultimate volume target (70 g/L) by filling the cylindrical vessels with pressurized LH_2 and the interstitial vessel with low-pressure LH_2. At 84 g/L (LH_2 at 20 K and 250 atm), the total amount of hydrogen in the cylindrical vessels would grow to 7.3 kg, for a total of 12.7 kg once the interstitial vessel is considered. This would raise weight and volume performance metrics to 7.3% H_2 and 72 g H_2/L (assuming 22% conformability credit). If packaged into a vehicle, this dual-volume system would provide an unprecedented level of storage performance, potentially enabling practical range in most hydrogen vehicles.

19.7 Conclusions

Unlike other fuels, hydrogen can be produced and consumed without generating carbon dioxide. If generated using renewable energy, hydrogen becomes a versatile, storable, and universal carbonless energy carrier that does not pollute. The greatest engineering challenge associated with hydrogen fuel is storing enough hydrogen on board the vehicle for a reasonable range (500 km).

First developed for aerospace applications, cryogenic pressure vessels are now being researched for automotive use. Cryogenic pressure vessels can store high-density hydrogen, similar to LH_2 vessels, without the evaporative losses. They are more compact than compressed hydrogen, therefore reducing the need for expensive carbon fiber. They are light and offer potential safety advantages due to reduced isentropic expansion energy at low temperature.

The versatility and flexibility of cryogenic pressure vessels enable high hydrogen storage density while avoiding evaporative losses, maintaining reasonable cost, and allowing fast refueling. The recent generation 3 prototype is the first automotive hydrogen vessel to meet the DOE 2015 weight and volume targets.

Conformable dual-volume vessels store hydrogen in interstitial and corner spaces that typically go unused in cylindrical vessels, thereby improving packaging efficiency and providing even higher hydrogen storage performance, leading to unprecedented levels of volume storage capacity. Predicted storage packaging density would enable long-range hydrogen transportation in a broad line of today's vehicles. Ongoing and planned work is addressing the technical challenge of simultaneously improving insulation performance and packaging efficiency while maintaining low cost.

Acknowledgments

This project was funded by DOE's Fuel Cell Technologies Program, with Monterey Gardiner as the technology development manager. This work was performed under the auspices of the US DOE by Lawrence Livermore National Laboratory under contract DE-AC52-07NA27344.

References

1. Berry, G.D. and Aceves, S.M. The case for hydrogen in a carbon constrained world, *Journal of Energy Resources Technology*, 127, 89–94, 2005.
2. von Helmolt, R. and Eberle, U. Fuel cell vehicles: Status 2007, *Journal of Power Sources*, 165, 833–843, 2007.
3. Ciancia, A., Pede, G., Brighigna, M., and Perrone, V. Compressed hydrogen fuelled vehicles: Reasons of a choice and developments in ENEA, *International Journal of Hydrogen Energy*, 21, 397–406, 1996.
4. Ahluwalia, R.K. and Peng, J.K. Automotive hydrogen storage system using cryo-adsorption on activated carbon, *International Journal of Hydrogen Energy*, 34, 5476–5487, 2009.
5. Forde, T., Eriksen, J., Pettersen, A.G., Vie, P.J.S., and Ulleberg, O. Thermal integration of a metal hydride storage unit and a PEM fuel cell stack, *International Journal of Hydrogen Energy*, 34, 6730–6739, 2009.
6. Amaseder, F. and Krainz, G. Liquid Hydrogen Storage Systems developed and manufactured for the first time for Customer Cars, SAE Paper 2006-01-0432, SAE International, Warrendale, PA, 2006.
7. Aceves, S.M., Berry, G.D., and Rambach, G.D. Insulated pressure vessels for hydrogen storage on vehicles, *International Journal of Hydrogen Energy*, 23(7), 583–591, 1998.
8. Aceves, S.M. and Berry, G.D. Thermodynamics of insulated pressure vessels for vehicular hydrogen storage, *ASME Journal of Energy Resources Technology*, 120(2), 137–142, 1998.
9. Aceves, S.M., Berry, G.D., Martinez-Frias, J., and Espinosa-Loza, F. Vehicular storage of hydro- gen in insulated pressure vessels, *International Journal of Hydrogen Energy*, 31, 2274–2283, 2006.
10. Williams, L.O. Hydrogen powered automobiles must use liquid hydrogen, *Cryogenics*, 13, 693–698, 1973.
11. Gregory, D.P. The hydrogen economy, *Scientific American*, 228(1), 13–21, 1973.
12. Scurlock, R.G. Development of low-loss storage of cryogenic liquids over the past 50 years, in Timmerhaus, K.D. and Reed, R.P. (eds). *Cryogenic Engineering, Fifty Years of Progress*, Springer, New York, 2007.
13. Braess, H.H. and Strobl, W. Hydrogen as a fuel for road transport of the future: Possibilities and prerequisites, *Proceedings of the 11th World Hydrogen Energy Conference*, Stuttgart, Germany, 1996.
14. Hanson, M.P. Glass, boron and graphite filament-wound resin composites and liners for cryo- genic pressure vessels, *Journal of Macromolecular Science, Part B*, 1, 651–665, 1967.
15. Plachta, D. and Kittel, P. An updated zero boil-off cryogenic propellant storage analysis applied to upper stages or depots in an LEO environment, Paper AIAA-2002–3589, *Proceedings of the 38th Joint Propulsion Conference and Exhibit*, Indianapolis, IN, 2002.
16. Ho, S.H. and Rahman, M.M. Three-dimensional analysis for liquid hydrogen in a cryogenic storage tank with heat pipe-pump system, *Cryogenics*, 48, 31–41, 2008.
17. Mueller, P.J., Batty, J.C., and Zubrin, R.M. High-pressure cryogenic hydrogen storage system for a Mars sample return mission, *Cryogenics*, 36, 815–822, 1996.
18. Mitlitsky, F., Weisberg, A.H., and Myers, B. Vehicular hydrogen storage using lightweight tanks (regenerative fuel cell systems), *Proceedings of the U.S. DOE Hydrogen Program Annual Review Meeting*, Lakewood, CO, 1999.
19. Krepec, T., Miele, D., and Lisio, C. Improved concept of hydrogen on-board storage and supply for automotive applications, *International Journal of Hydrogen Energy*, 15, 27–32, 1990.
20. Tummala, M., Krepec, T., and Ahmed, A.K.W. Optimization of thermocontrolled tank for hydrogen storage in vehicles, *International Journal of Hydrogen Energy*, 22, 525–530, 1997.
21. White, C.M., Steeper, R.R., and Lutz, A.E. The hydrogen-fueled internal combustion engine: A technical review, *International Journal of Hydrogen Energy*, 31, 1292–1305, 2006.
22. Moran, M.J. *Availability Analysis: A Guide to Efficient Energy Use*, Prentice Hall, Inc., Englewood Cliffs, NJ, 1982.

23. McCarty, R.D. *Hydrogen: Its Technology and Implications, Hydrogen Properties, Volume III*, CRC Press, Cleveland, OH, 1975.
24. Department of Energy, Office of Energy Efficiency and Renewable Energy Hydrogen. Fuel Cells & Infrastructure Technologies Program Multi-Year Research, Development and Demonstration Plan, http://www.eere.energy.gov/hydrogenandfuelcells/mypp
25. Lasher, S., McKenney, K., Sinha, J., and Rosenfeld, J. Analyses of hydrogen storage mate- rials and on-board systems, *Proceedings of the DOE Hydrogen and Fuel Cell Annual Merit Review*, Crystal City, VA, 2008, http://www.hydrogen.energy. gov/pdfs/progress08/ iv_e_1_lasher.pdf
26. Ahluwalia, R.K. and Peng, J.K. Dynamics of cryogenic hydrogen storage in insulated pres- sure vessels for automotive applications, *International Journal of Hydrogen Energy*, 33, 4622–4633, 2008.
27. Haaland, A. High-pressure conformable hydrogen storage for fuel cell vehicles, *Proceedings of the US Department of Energy 2000 Hydrogen Program Review*, National Renewable Energy Laboratory Report NREL/CP-570-28890, Golden, CO, 2000. Available online at: http://www1. eere.energy.gov/hydrogenandfuelcells/pdfs/28890cc.pdf.
28. Aceves, S.M., Berry, G.D., Weisberg, A.H., Espinosa-Loza, F., and Perfect, S.A., Advanced con- cepts for vehicular containment of compressed and cryogenic hydrogen, *Proceedings of the 16th World Hydrogen Energy Conference*, Lyon, France, July 10–15, 2006.

20

Metal Hydrides

Sesha S. Srinivasan
Tuskegee University

Prakash C. Sharma
Tuskegee University

Elias K. Stefanakos
University of South Florida

D. Yogi Goswami
University of South Florida

CONTENTS

20.1 Metal Hydrides 667
20.1.1 Intermetallic Alloys 673
20.1.2 Solid Solutions 675
20.1.3 Composites 678
References 681

20.1 Metal Hydrides

Hydrogen storage by metal hydrides comprises an intermetallic alloy phase that has the capability to absorb and hold vast amounts of hydrogen by chemical bonding.[1] An appropriate hydrogen storage matrix should have the capacity to absorb and release hydrogen without compromising the matrix structure. Metal hydrides are prepared by reaction between a metallic phase and hydrogen. When exposed to hydrogen at certain pressures and temperatures, these phases absorb large quantities of hydrogen gas and form the corresponding metal hydrides. If this is the scenario, the hydrogen is distributed compactly throughout the intermetallic lattice. Metal hydrides represent an exciting process of hydrogen storage, which is inherently safer than the compressed gas or liquid hydrogen storage. Additionally, some intermetallics (including metals and alloys) store hydrogen at a higher volume density than liquid hydrogen.

The qualities required to make these intermetallics useful include the facility to absorb and release large amounts of hydrogen gas, many times without damaging the storage material and with good selectivity (only hydrogen absorption). Moreover, suitable metal hydrides absorb and release hydrogen at rates that can be controlled by adjusting temperature and/or pressure.

As mentioned in the preceding text, a typical relation of metal hydrides with hydrogen can be expressed as $M + x/2\ H_2 \leftrightarrow MHx + Heat$, where M represents the intermetallic matrix and H is hydrogen. The effect is reversible and the direction is determined by the pressure (and temperature) of the hydrogen gas. If the pressure is above a certain level (the equilibrium pressure), the effect proceeds to the right to form the hydride, whereas below the equilibrium pressure, hydrogen is liberated and the intermetallic matrix returns to its original state. The equilibrium pressure, itself, depends upon temperature. It increases due to expansion with an increment in temperature (and vice versa). The molecular hydrogen first dissociates into hydrogen atoms due to the available metal catalysts and interacts with the host metal lattice to form metal hydride as shown in the schematics of Figure 20.1a. Similarly, the reverse reaction yields hydrogen in gaseous form as represented in Figure 20.1b.

In general, hydrides are classified according to the nature of the bonding of hydrogen to the host lattice such as covalent, saline or ionic, and metallic, all of these classes bearing different bonding characteristics.[2] Such a classification doesn't always clarify the characteristic features of the compound in question. For example, lithium hydride is classified as a saline hydride, where in reality, it actually exhibits some covalent characteristics. The rare-earth hydrides are normally classified in the metallic hydride group, whereas they exhibit some characteristics similar to those of volatile and saline hydrides (e.g., high heat of formation). The ionic hydrides are usually crystalline and show high heats of formation and high melting points. The ionic alkali and alkaline-earth hydrides have a higher density than the pure alkali (45%–75%) and alkaline-earth metals (20%–25%).[3] Covalent hydrides are generally thermally unstable, and this instability goes up with

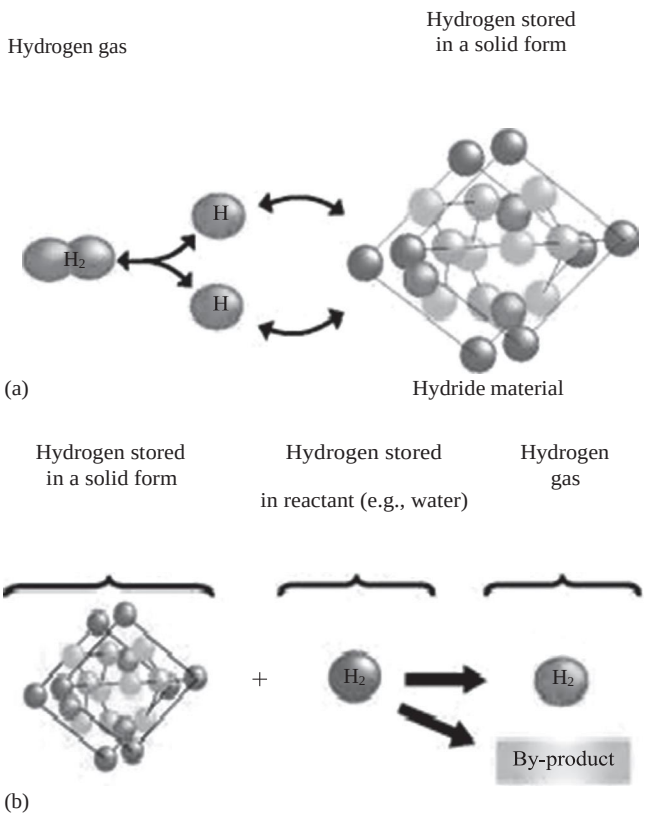


FIGURE 20.1

(a) Metal hydride formation during H_2 absorption in host metal lattice. (b) Hydrogen gas release during the dehydrogenation of metal hydride.

increasing atomic weight of the nonhydrogen element(s). Typical covalent hydrides are carbon hydrides, boron hydrides, germanium hydrides, etc. Covalent hydrides normally exhibit low symmetric structures. Metallic complex hydrides are normally formed by the transition metals, for example, ScH_2.[17] They generally exhibit metallic characteristic properties such as high thermal and electrical conductivity, hardness, luster, etc. Due to the wide homogeneity ranges adopted by metallic hydrides, they have occasionally been considered as solid solutions of hydrogen in the interstitials of metal, alloy, or intermetallic matrices. Yet another classification based on the carbon-based sorbents, for example, single-wall or multiwall carbon nanotubes, polymer nanostructures, zeo- lites, and metal organic frameworks, possesses weak van der Waals attraction toward hydrogen. The classification of hydrides on the basis of temperature of operation and thermodynamic values such as ΔH of reaction is schematically shown in Figure 20.2. It is clearly understood that the metal or complex hydrides operate in the region of moderate temperatures 0°C–100°C with appropriate ΔH of ~30–55 kJ/mol H_2. Whereas the ionic or covalent hydrides require high temperature, ΔH of ~70–80 kJ/mol H_2 and the carbon-based sorbent systems mandate cryogenic operating temperatures with ΔH <20 kJ/mol H_2.

Hydrogen can be packed and stored in a solid state by forming metal hydride.[4–12] During the formation of the metal hydride, hydrogen molecules are dissociated into hydrogen atoms, which insert themselves into interstitial spaces inside the lattice of intermetallic compounds and/or alloys (Figure 20.1).

At a large distance from the metal surface, the energy difference between a hydrogen molecule and two separate hydrogen atoms is the dissociation energy ($H_2 \rightarrow 2H$, E_D = 435.99 kJ/mol). The first attractive interaction of the hydrogen molecule approaching the

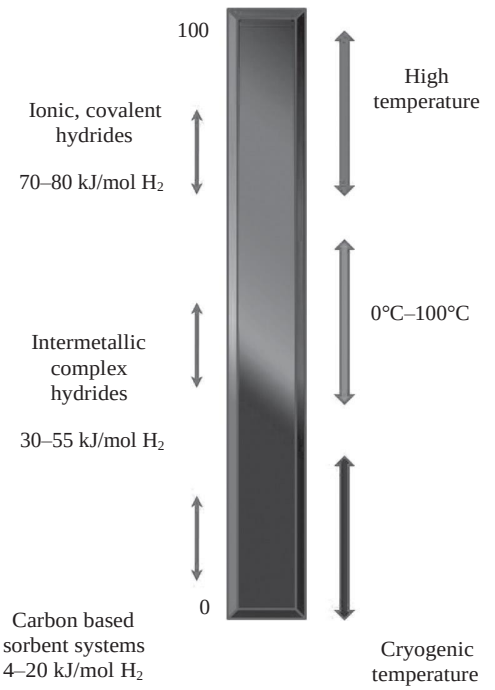


FIGURE 20.2

Classification of hydrogen storage systems on the basis of temperature of operation and the thermodynamic values such as heats of reaction.

metal surface is the van der Waals force leading to the physisorbed state ($E_{Phys} \approx 10$ kJ/mol) more or less one hydrogen molecule radius (≈0.2 nm) from the metal surface. Closer to the surface, the hydrogen has to overcome an activation barrier in order to dissociate and create the hydrogen metal bond. The height of the activation barrier depends on the surface elements involved. Hydrogen atoms sharing their electrons with the metal atoms at the surface are in the chemisorbed state ($E_{Chem} \approx 50$ kJ/mol · H_2). The chemisorbed hydrogen atoms may have a high surface mobility, interact with each other, and form surface phases at considerably high coverage. In the following step, the chemisorbed hydrogen atoms can jump into the subsurface layer and finally diffuse to interstitial sites through the host metal lattice as depicted in Figure 20.3. An interstitial hydrogen atom contributes its elec- tron to the band structure of the metal.

In the α-phase solid solution, the hydrogen to metal ratio is small (H/M < 0.1), and hydrogen is exothermically dissolved in the metal. The metal lattice expands relative to the hydrogen concentration by approximately 2–3 Å^3 per hydrogen atom.[13] At greater hydrogen concentrations in the host metal (H/M > 0.1), a strong H–H interaction due to the lattice expansion becomes significant, and the hydride phase (β-phase) nucleates and grows. The hydrogen concentration in the hydride phase is commonly found to be H/M = 1.

The volume expansion between the coexisting α- and the β-phase[14] corresponds in many cases 10%–20% of the metal lattice. Therefore, at the phase boundary, large stresses are created that frequently lead to a decrepitation of brittle host metals including intermetallic compounds resulting in a final hydride powder with a representative particle size of 10–100 μm.

An idealized representation of pressure–concentration–temperature (PCT) isotherms for the α-phase solid solution and β-phase hydride is shown in Figure 20.4. A plateau is observed on the pressure versus hydrogen/metal ratio for fixed temperature. When the reaction is complete, another sharp pressure rise is seen if more hydrogen is added.

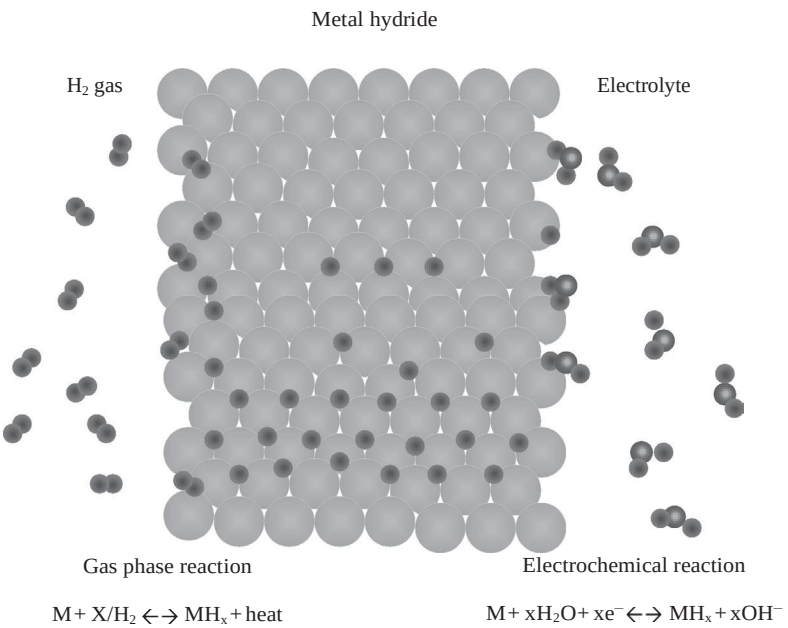


FIGURE 20.3

Schematic representation of the dissociation of hydrogen gas molecule.

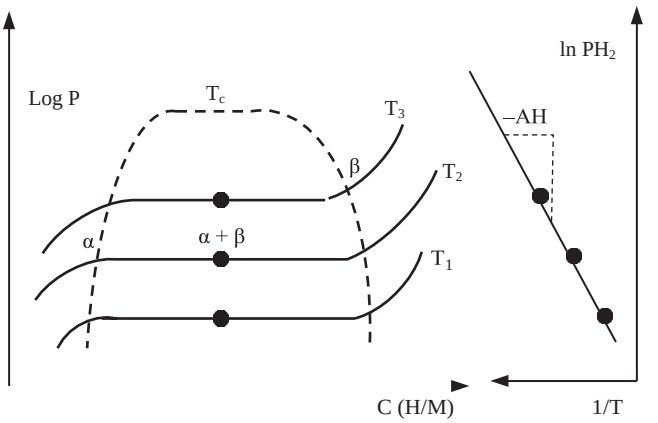


FIGURE 20.4

Effect of temperature on the general features of the PC isotherms.

At a certain temperature, the plateau pressure reflects one point on a pressure–temperature (van't Hoff) plot. The log of pressure versus reciprocal temperature is linear with a negative slope and is related to the heat of reaction (heat of hydriding); the plateau pressures must increase with temperature due to the linear relationship between pressure and temperature.

An increment in isothermal temperature causes the plateau pressure to increase and, at the same time, reduces the width of the plateau that represents the miscibility regime of the α- and β-phase. This narrowing process of the plateau with increasing of tempera- ture continues until, eventually, at a certain *critical temperature*, T_c, the plateau disappears totally, reducing the miscibility of the two phases to zero, and the α-phase converts continuously into the β-phase. The slope and length of the equilibrium plateau are of particular importance for hydrogen storage application; a flat plateau enables the reversible absorption and desorption of hydrogen from a metal simply by raising or lowering the surrounding hydrogen pressure above or below the plateau pressure.

The equilibrium pressure as a function of temperature is related to the changes of ΔH and ΔS, in that order, by the van't Hoff equation:[15–17]

$$\ln\left[\frac{p(H_2)}{p^\circ}\right] = \frac{\Delta H}{RT} - \frac{\Delta S}{R} \tag{20.1}$$

where

$p(H_2)$ is the hydrogen equilibrium pressure at α- to β-phase hydride conversion, determined from PCT isotherms
p° is the standard pressure
R is the gas constant
T is the temperature

The ΔH, of hydride formation is an important parameter characterizing the alloy as a proper hydrogen absorber for various applications. In general, the difference in stan- dard ΔS between a metal hydride alloy and its hydride is small and is on the order of

10 J/mol/K. The modification in ΔS with hydride formation is mainly provided by the loss of the standard ΔS of hydrogen gas (130.858 J/mol/K at 298 K), which means that ΔS can be assumed to be a constant and does not depend on the nature of the metal hydride alloy. The knowledge of ΔH particularly is significant to the heat management needed for practical engineering devices and is a fundamental measure of the M–H bond strength. The van't Hoff plot (lnP vs. 1/T) is a practical way to compare hydrides due to their thermal stabilities.

An overview of hydrogen storage alloys has been discussed from the solid–gas reaction point of view.[18] There are a number of important properties that must be considered in metal hydride storage. Some of the most important ones are (1) ease of activation, (2) heat transfer rate, (3) kinetics of hydriding and dehydriding, (4) resistance to gaseous impurities, (5) cyclic stability, (6) safety, (7) weight, and (8) cost. Although metal hydrides can theoretically store large amounts of hydrogen in a safe and compact way, the practical gravimetric hydrogen density is limited to <3 mass%. It is still a challenge to explore the properties of lightweight metal and complex hydrides.

Hydrogen is a highly reactive element and has been found to form hydrides and solid solutions with thousands of metals and alloys.[13] A hydride *family tree* of the elements, alloys, and complexes is shown in Figure 20.5.

The majority of the 91 natural elements below hydrogen in the periodic table will form hydrides under appropriate conditions such as VH_2, NaH, LaH_2, and ZrH_2. Unfortunately, the PCT properties are not very suitable for the 1–10 atm and 0°C–100°C range used for practical hydrogen storage. Only V is in the range, and there has been extensive study of solid solutions of V and other metals. Pd has been used for over 100 years for H storage,

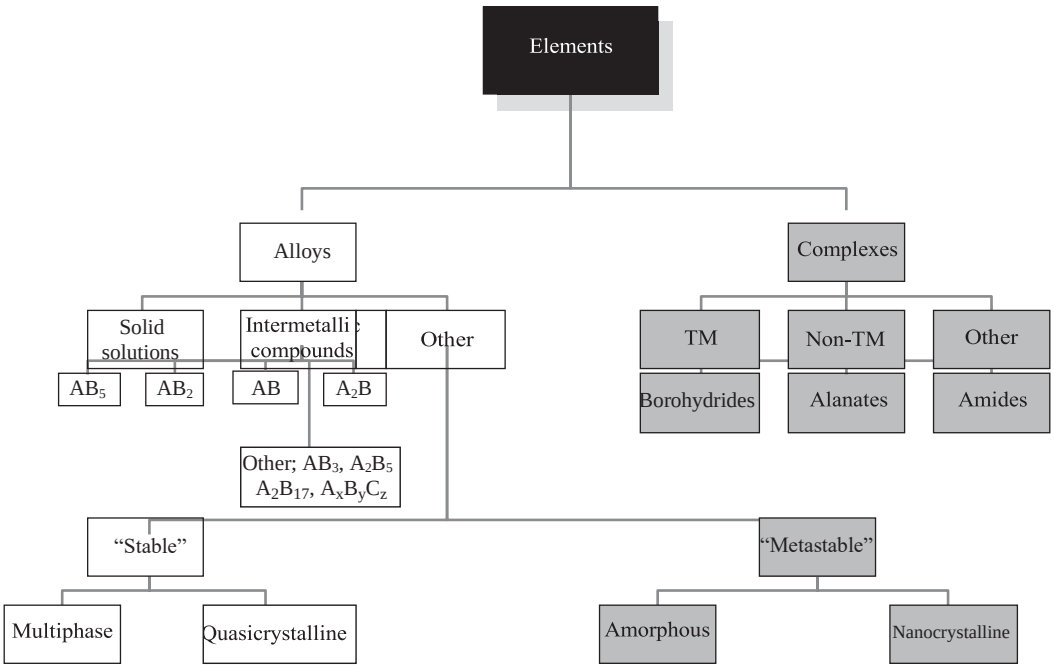


FIGURE 20.5

Family tree of the elements, alloys, and complexes.[13]

but it is very costly, it doesn't hold much hydrogen, and it requires heating temperatures above 100°C to release atomic hydrogen.

20.1.1 Intermetallic Alloys

To prepare useful reversible hydrides, strong hydride-forming (A) elements are combined with weak hydriding (B) elements to form alloys (especially intermetallic compounds) that have the desired intermediate thermodynamic affinities for hydrogen. A good example of this characteristic is the combination of La (forming LaH_2 with 25°C, $P_d = 3 \times 10^{-29}$ atm, and $\Delta H_f = -208$ kJ/mol H_2) and Ni (NiH with 25°C, $P_d = 3400$ atm, and $\Delta H_f = -8.8$ kJ/mol H_2) to form theintermetalliccompound $LaNi_5$ ($LaNi_5H_6$ with 25°C, $P_d = 1.6$ atm, and$\Delta H_f = -30.9$ kJ/mol H_2). This ability to *interpolate* between the extremes of elemental hydriding behavior opened the door to the modern world of reversible hydrides.

The AB_5 family has an exceptional versatility because many different elemental species can be substituted (at least partially) into the A and B lattice sites. The A elements tend to be one or more of the lanthanides (elements 57–71), Ca, or other elements such as Y and Zr. The B elements are based on Ni with many other possible substitutional elements such as Co, Al, Mn, Fe, Cu, Sn, Si, and Ti. Modern commercial AB_5 hydriding alloys are for the most part based on the use of the lanthanide mixture or mischmetal (Mm = Ce + La + Nd + Pr) for the A site and Ni + Al + Mn + Co + ... for the B site.

Hydrogen storage capacity is on the uncomfortably low side, not passing 1.3 wt.% on the plateau basis. Alloy raw material cost is high; at least by comparison to other systems (AB_2 and AB) that are discussed in the following, the AB_5 alloys are easy to activate, hardly requiring any heating. They decrepitate on the first H/D cycle to fine powder, which is mildly pyrophoric if suddenly exposed to air, a well-known property that must be included in safety considerations. Both easy activation and pyrophoricity indicate the AB_5 alloys do not form defensive oxide layers. Intrinsic kinetics of the AB_5 alloys is gen- erally very good. In an attempt to increase the kinetics and hydrogen storage capacity in AB_5-type alloys such as $MmNi_{4.6}Fe_{0.4}$, mechanochemical pulverization at room tem- perature was carried out.[19] Figure 20.6 represents the x-ray diffraction (XRD) profiles of $MmNi_{4.6}Fe_{0.4}$ prepared using radio-frequency induction melting followed by mechano- chemical pulverization.

The nanocrystallization of peaks was observed with broadening of full width at half max- imum (FWHM), thus enhancing the kinetics of hydrogen release as shown in Figure 20.7.

The scanning electron microscope (SEM) micrographs (see Figure 20.8) further justify the smaller and homogeneous crystallites with well-defined grains that enable for the higher hydrogen absorption and desorption cycling capacity with twofold increase of kinetics at room temperature.

Like the AB_5 compounds, the AB_2 intermetallics represent a large and versatile group of hydriding materials with good PCT properties at ambient temperature. The A elements are often from the IVA group (Ti, Zr, Hf) and/or rare-earth series (no. 57–71). The B ele- ments can be a variety of transition or nontransition metals with somewhat of a preference for atomic numbers 23–26 (V, Cr, Mn, Fe). A large variety of substitutions are possible for both A and B elements, thus providing a high degree of fine tuning of PCT properties.

The decisive advantages in regard to hydrogen storage and related thermal applications are high hydrogen capacity, ease of activation, very rapid rates of absorption and desorption, long cycling life, and low cost of materials. The main disadvantages for hydrogen storage are high ΔH values (moderate stabilities of hydrides). These properties make these com- pounds good for hydrogen compression applications. An excellent example is $ZrMn_2$ that

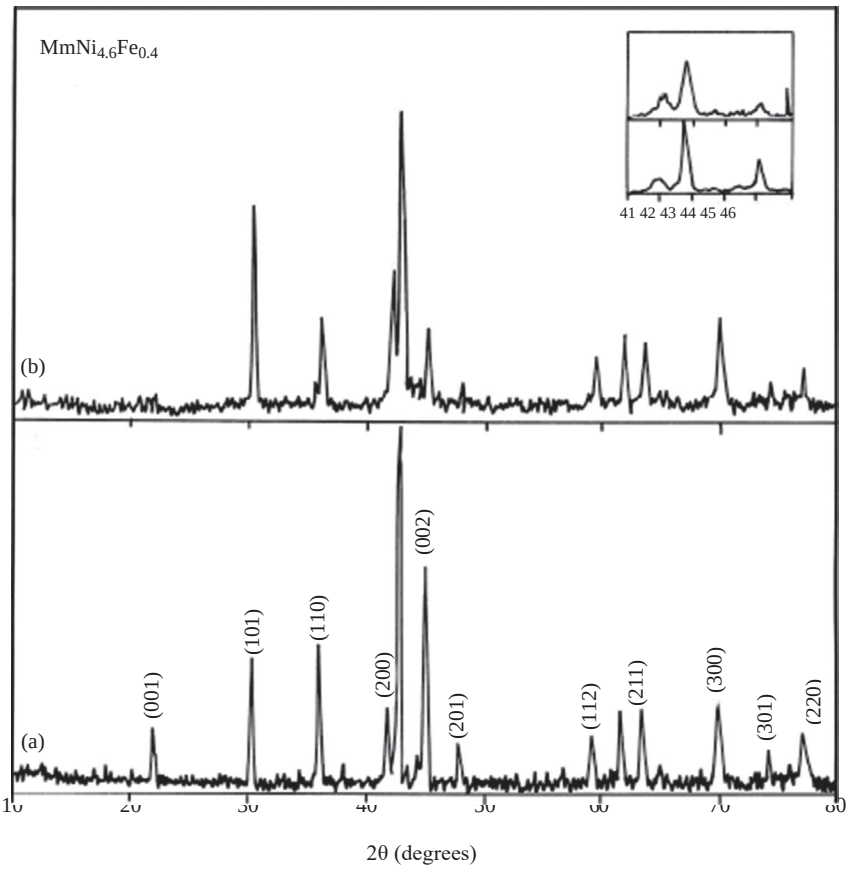


FIGURE 20.6

X-ray diffractograms of (a) as-synthesized $MmNi_{4.6}Fe_{0.4}$ using radio-frequency induction melting and (b) induc- tion melting followed by mechanical pulverization.

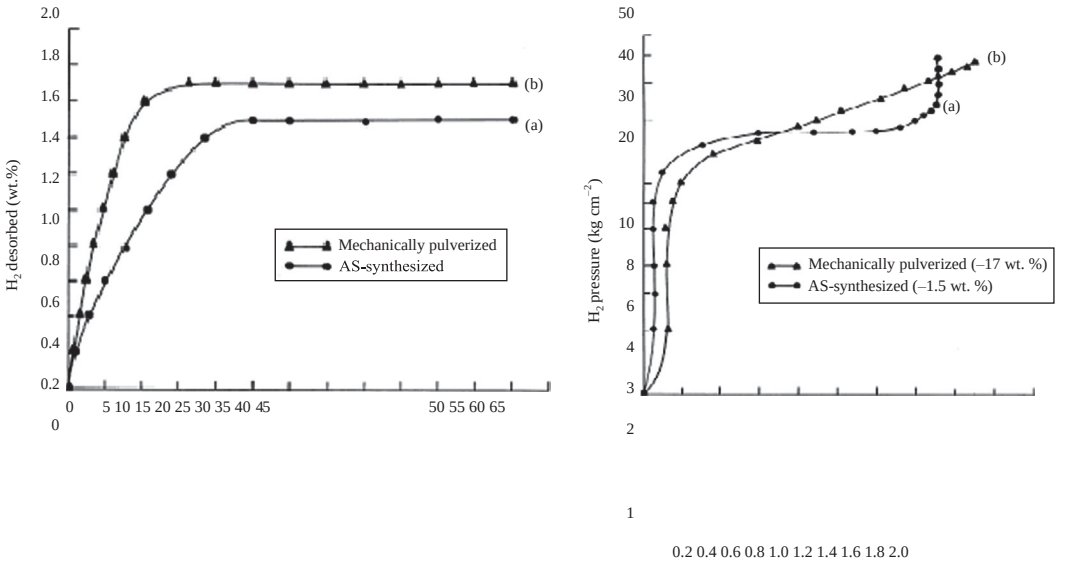
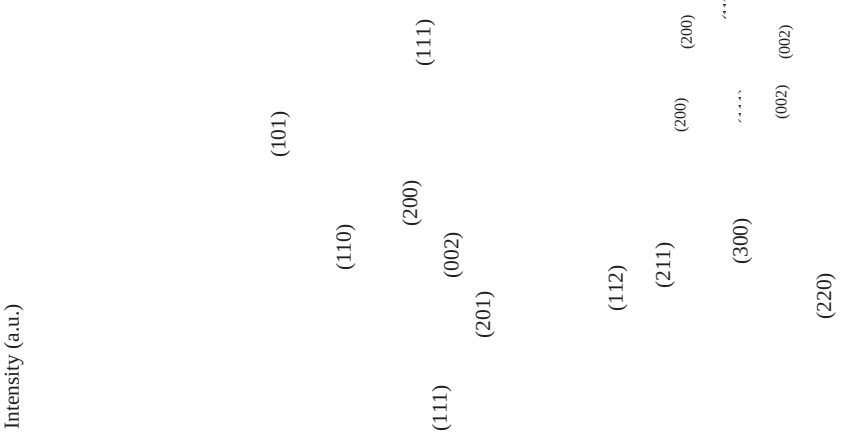


FIGURE 20.7

(a) Hydrogen desorption kinetic curves and (b) PCT of as-synthesized and mechanically pulverized $MmNi_{4.6}Fe_{0.4}$.



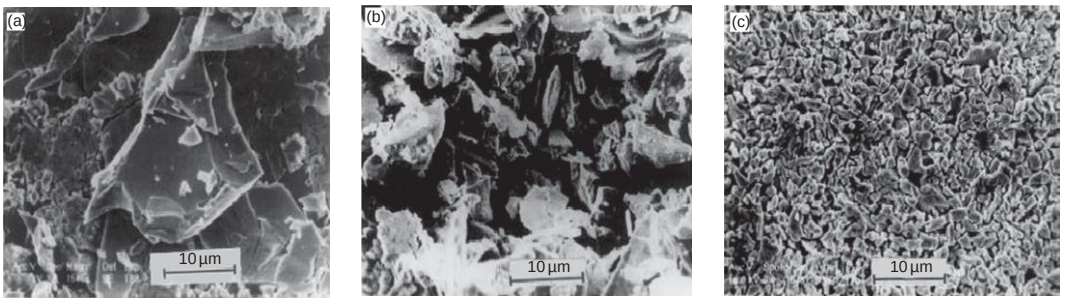


FIGURE 20.8

SEM micrographs of (a) as-synthesized (b) mechanically pulverized and (c) hydrogenated $MmNi_{4.6}Fe_{0.4}$ alloy.

contents 3.6 atoms of hydrogen and $\Delta H = -53.0$ kJ/mol H_2, showing a high hydrogen content and a high T_{dec}, related to the high ΔH.[20] The high T_{dec} and the high hydrogen content make this compound good for hydrogen compression.

Method of preparing an alloy of zirconium and manganese suitable for storing hydrogen consists in two steps[21]: make an intimate mixture of Zr and Mn in correct stoichiometric ratio and heat the sample between 900°C and 1150°C. The intimate mixture is done using a straightforward, repeatable, and inexpensive procedure, ball milling under a H_2 atmosphere. The annealing was applied for 10 h in a helium atmosphere at 1100°C.

A is typically of the group IVA elements Ti, Zr, or Hf, and B is a transition metal, typically Ni. Another family is based on Mg_2Ni.[22] Unfortunately, the A_2B's offer little in the 0°C–100°C and 1–10 atm range, at least with the present state of the art. They are definitely more stable. H storage capacity and cost properties of Mg_2Ni are attrac- tive, but desorption temperatures are too elevated for most applications. Mg_2Ni is not very amenable to modification of PCT properties by ternary and higher-order substi- tutions. Various attempts to lower desorption temperatures have not been especially successful.

20.1.2 Solid Solutions

The first example of a reversible intermetallic hydride was demonstrated with the AB compound, ZrNi, by Libowitz in 1957.[23] The hydride $ZrNiH_3$ has a 1 atm desorption temperature of about 300°C, too high for hydrogen storage applications but suitable for hydrogen compression.

These intermetallic alloys show good volumetric and gravimetric reversible H storage capacities, competitive with the best of the AB_5's and AB_2's. Activation is pretty slow and hard for the ZrNi-based alloys. In any event, it may take a day or so and high pressures (50+ atm) for total activation. The passive oxide films that can form on ZrNi (and its derivatives) don't result in a high degree of sensitivity to gaseous impurities in the H_2 used; hence, these alloys are resistant to impurities. Cyclic stability of the lower plateau is great, but the upper plateau tends to drift higher with H/D cycling. Although there is vast information available about ZrNi alloys, the intermediate compositional alloys ZrNi 70/30 and ZrNi 30/70 have been sparsely reported for hydrogen storage.[24,25] The XRD analysis of ZrNi70/30 before and after hydrogenation is shown in Figure 20.9. The XRD spectra show a significant change in the intensity of the peaks in ZrNi 70/30 hydride compared with the unhydrided sample (33.2°, 34.2°, 36.5°, and 43°) and the pres- ence of a new peak (36.7°) attributed to the ZrNi 70/30 hydride phase. The crystallite

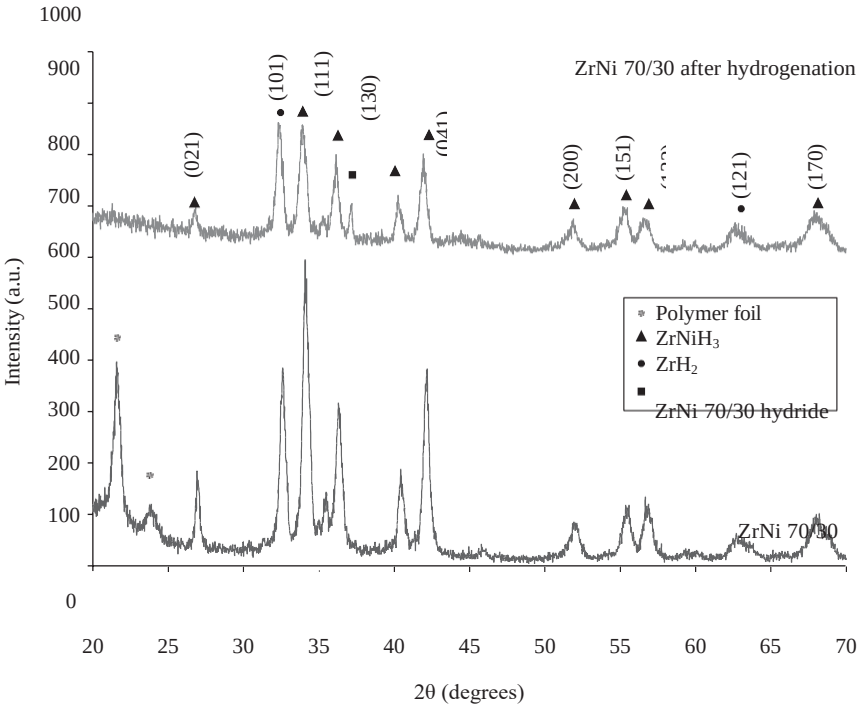


FIGURE 20.9

XRD spectra of ZrNi 70/30 before and after hydrogenation.

sizes of the $ZrNiH_3$ (~48 nm) and ZrH_2 (~39 nm) are calculated and compared with the unhydrided sample. The scanning micrographs of the ZrNi 70/30 after a number of hydrogenation cycles show the development of microcracks due to hydrogen interaction with the host lattice at high temperatures (Figure 20.10).

Figure 20.11 illustrates the absorption–desorption PCT for the ZrNi 70/30 alloy, giving evidence of a typical metal hydride behavior. The plateau region is the most important segment of a PCT plot, which represents the pressure of hydrogen in equilibrium with the metal–metal hydride ($\alpha + \beta$) phases, representing the dissociation pressure of the metal hydride at the desired temperature; the temperature indicates the thermal stability of the metal hydride. Moreover, when the temperature goes from 300°C, 325°C, 350°C, 375°C, and 390°C, it causes the plateau pressure to increase and, at the same time, reduces the width of the plateau that represents the miscibility regime of the α- and β-phase. As an example, at 375°C, hydrogen content of 1 wt.% is reached at 13 bars. According to the investigations, ZrNi 70/30 alloy presents a metal hydride behavior: low kinetics, moderate to high equilibrium pressures, and moderate to high hydrogen content, conditions that make this alloy the most convenient for hydrogen compression applications. From the PCT isotherms, the ΔH of reaction has been calculated to be ~39 kJ/mol H_2 for the ZrNi70/30.

In addition to the AB_5, AB_2, AB, and A_2B intermetallic compounds discussed previously, various other families of intermetallics have been shown capable of reversible hydriding/dehydriding reactions.[26,27] Examples include AB_3, A_2B_7, A_6B_{23}, A_2B_{17}, and A_3B. Most structures involve long-period AB_5 and AB_2 stacking sequences and are thus crystallographically related to these two classic families. Most have narrow pla- teaux with long sloping upper legs (e.g., $GdFe_3$) or multiple plateaux (e.g., $NdCo_3$ or Pr_2Ni_7).

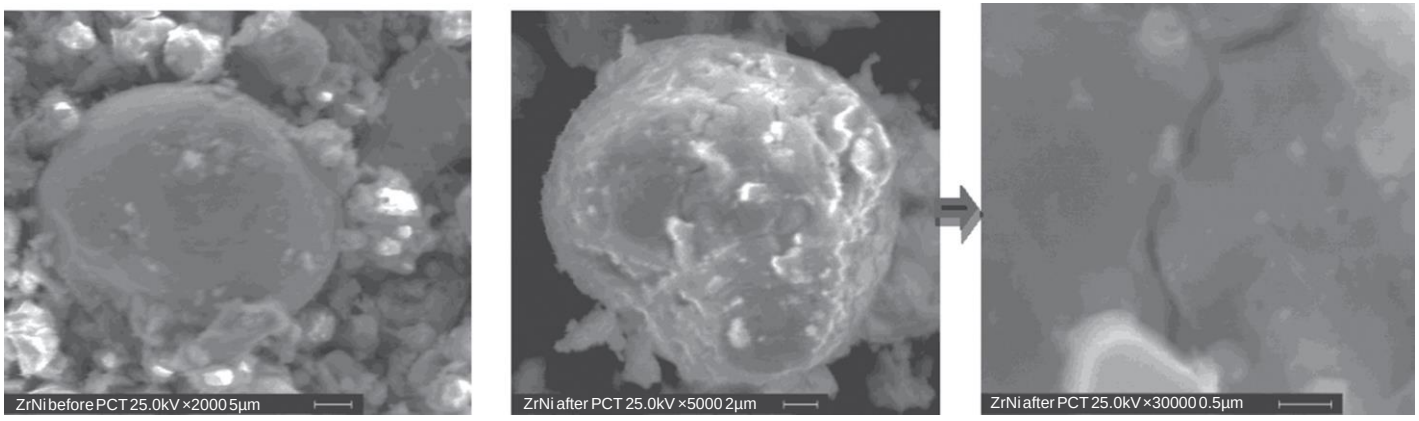


FIGURE 20.10

SEM micrographs of (a) pristine, (b) hydrogenated, and (c) hydrogenated in higher magnification showing microcracks of ZrNi 70/30 material.

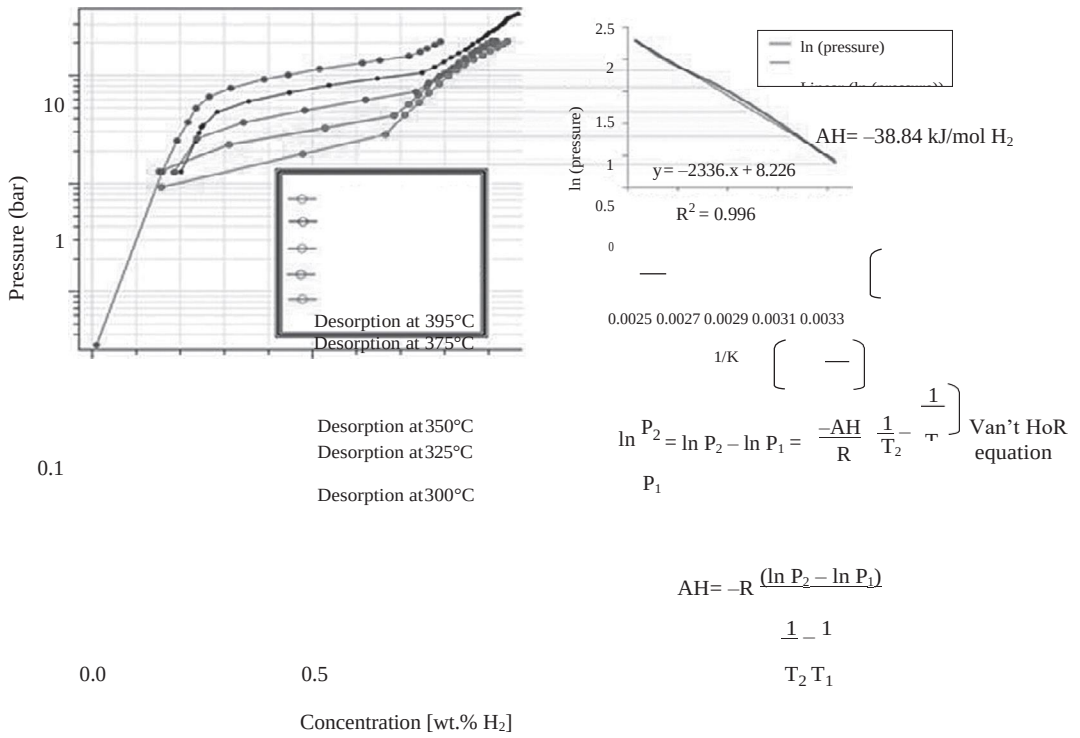


FIGURE 20.11

Absorption and desorption PCT of ZrNi70/30 at 300°C, 325°C, 350°C, 375°C, and 390°C.

TABLE 20.1

Theoretical Capacities of Hydriding Substances as Hydrogen Storage Media

Medium	Hydrogen Content (kg/kg)	Hydrogen Storage Capacity (kg/L of Vol.)	Energy Density (kJ/kg)	Energy Density (kJ/L of Vol.)
MgH_2	0.070	0.101	9,933	14,330
Mg_2NiH_4	0.0316	0.081	4,484	11,494
VH_2	0.0207		3,831	
$FeTiH_{1.95}$	0.0175	0.096	2,483	13,620
$TiFe_{0.7}Mn_{0.2}H_{1.9}$	0.0172	0.090	2,440	12,770
$LaNi_5H_{7.0}$	0.0137	0.089	1,944	12,630
$R.E.Ni_5H_{6.5}$	0.0135	0.090	1,915	12,770
Liquid H_2	1.00	0.071	141,900	10,075
Gaseous H_2 (100 bar)	1.00	0.0083	141,900	1,170
Gaseous H_2 (200 bar)	1.00	0.0166	141,900	2,340
Gasoline	—	—	47,300	35,500

When the mass of the metal or alloy is taken into account, the metal hydride grav- imetric storage density is comparable to storage of pressurized hydrogen. The best achievable gravimetric storage density is about 0.07 kg of H_2/kg of metal, for a high- temperature hydride such as MgH_2 as shown in Table 20.1, which gives a comparison of some hydriding substances with liquid hydrogen, gaseous hydrogen, and gasoline.[28,29] MgH_2 can effectively store hydrogen due to its thermodynamic stability; however, reaction kinetics are too slow and the decomposition temperature is high, at approxi- mately 330°C.[20] A possible way to achieve Mg-like storage capacity but with reversible

hydrogenation characteristics is to form composites with Mg as one of the components as discussed earlier. The other component may be one of the known hydrogen storage intermetallic alloys.[30]

Since the $MmNi_{4.6}Fe_{0.4}$ alloy discussed in Section 20.1.1 exhibited hydrogen storage capacity of less than 2.0 wt.%, a novel strategy of forming a composite phase Mg-Xwt.% $MmNi_{4.6}Fe_{0.4}$ was carried out.[31] This system has dual advantages in a sense that it reduces the weight penalty of the system for hydrogen storage applications and also enhances the hydrogen storage capacity >5 wt.% at moderate temperatures. The flowchart for the synthesis and characterization of Mg-Xwt.% $MmNi_{4.6}Fe_{0.4}$ (X = 10, 20, 30, 40, and 50) is shown
in Figure 20.12.

The dehydrogenation kinetic and PCT curves as demonstrated in Figure 20.13a and b reveal the high hydrogen storage capacity (~5 wt.%) at temperatures >300°C.

The XRD pattern of the composite material shows the presence of both Mg and $MmNi_{4.6}Fe_{0.4}$ phases; additional peak pertaining to MgH_2 was observed in the hydrogenated materials (see Figure 20.14). The effective hydrogenation and dehydrogenation in these composite materials have been confirmed through the hydrogen-induced microchannels as exhibited in SEM micrographs and are shown in Figure 20.15. The Mg in the host matrix of $MmNi_{4.6}Fe_{0.4}$ thus facilitates lower desorption temperatures due to the available catalytic nanoparticles of Ni and Fe, which surpassed the hydrogen storage characteristics of Mg_2Ni or other Mg-based intermetallic systems.

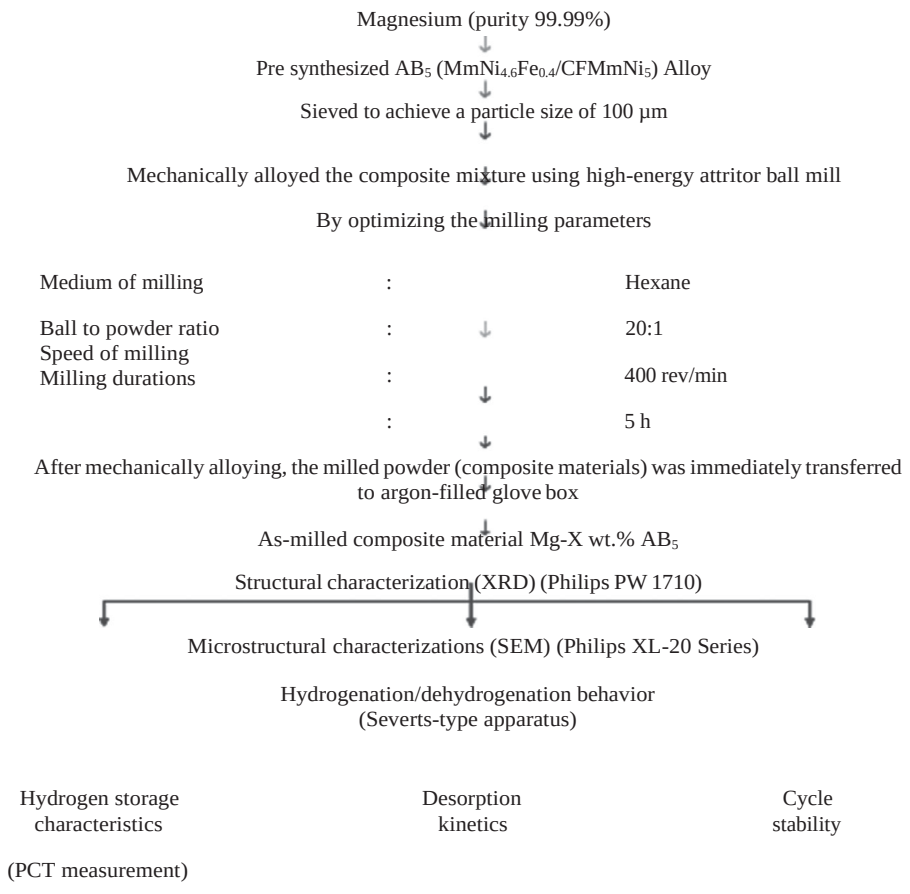


FIGURE 20.12
Flowchart diagram of synthesis and characterization of Mg-Xwt.% $MmNi_{4.6}Fe_{0.4}$ composite material.

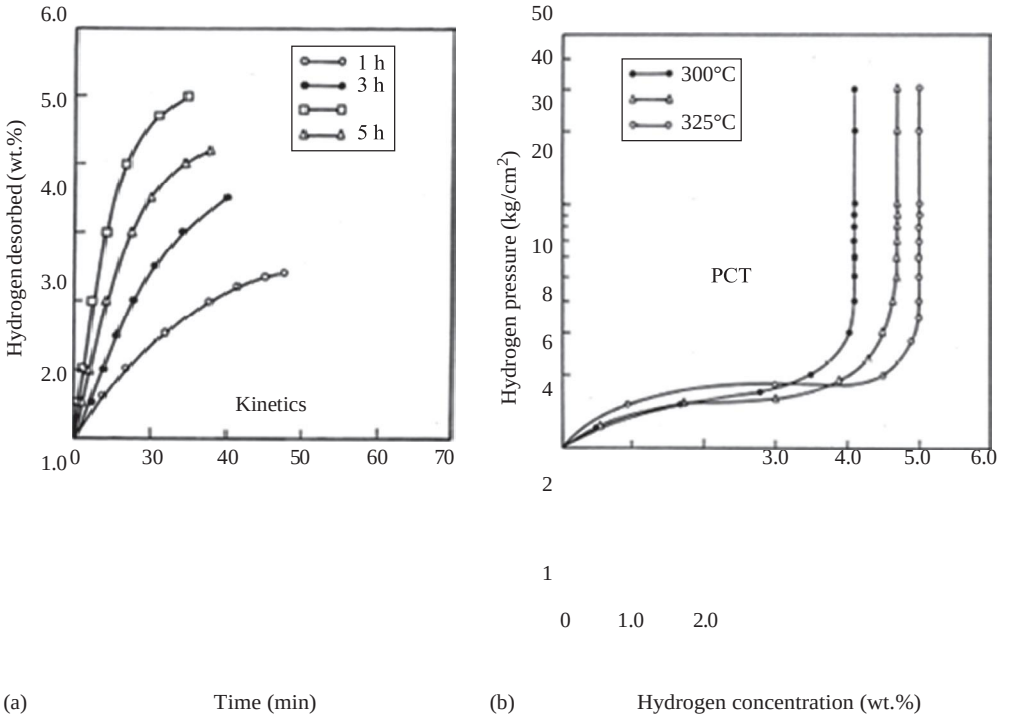
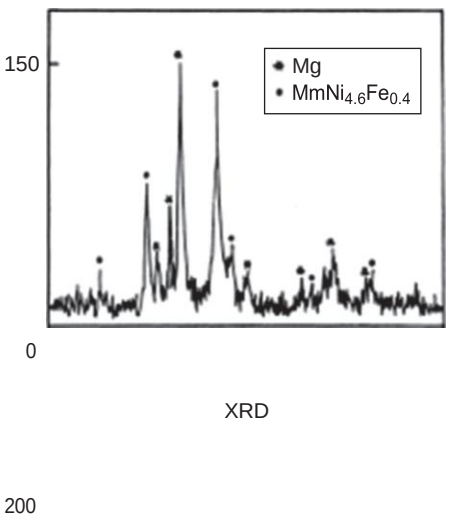


FIGURE 20.13

(a) Hydrogen desorption kinetics and (b) PCT characteristics of Mg-Xwt.% $MmNi_{4.6}Fe_{0.4}$ at moderate temperatures.



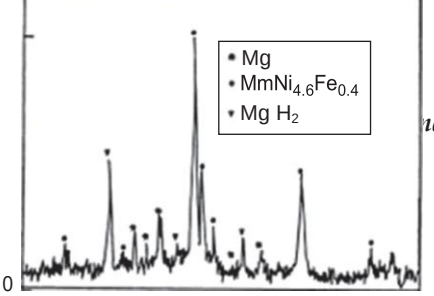


FIGURE 20.14

XRD pictures of Mg-Xwt.% $MmNi_{4.6}Fe_{0.4}$ before and after hydrogenation at moderate temperatures.

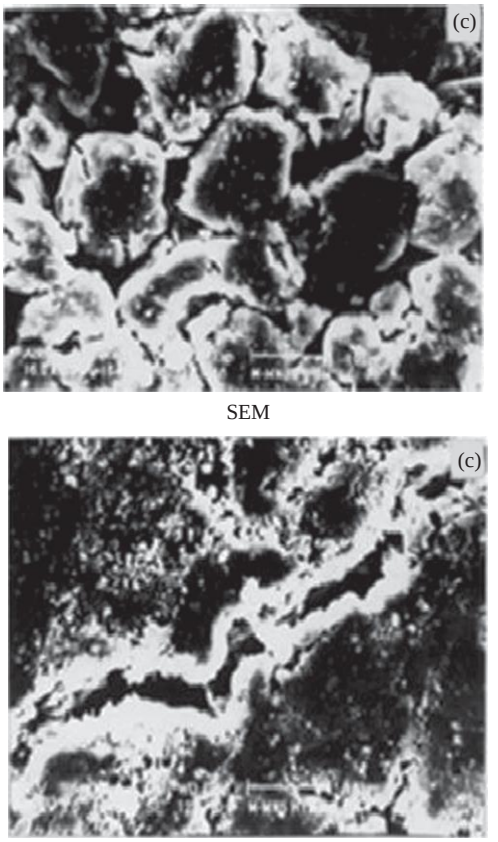


FIGURE 20.15

SEM pictures of Mg-Xwt.% $MmNi_{4.6}Fe_{0.4}$ before and after hydrogenation at moderate temperatures.

References

1. J.H.N. van Vucht, F.A. Kuipers, and H.C.A.M. Bruning (1970). Reversible room-temperature absorption of large quantities of hydrogen by intermetallic compounds, Phillips Research Reports. 25, 133–140.
2. Z.P. Li, B.H. Liu, K. Arai, N. Morigazaki, and S. Suda (2003). Protide compounds in hydrogen storage systems, *Journal of Alloys and Compounds*, 356–357, 469–474.
3. P. Vajeeston (2004). Theoretical modeling of hydrides, Dissertation presented for the degree of Doctor Scientiarum, University of Oslo, Oslo, Norway.
4. G.G. Libowitz and A.J. Maeland (1979). In *Handbook on the Physics and Chemistry of Rare Earths*, K.A.J. Gschneidner and L. Eyring, eds. North Holland Publishing, Amsterdam, the Netherlands.
5. Y. Fukai (1993). *The Metal-Hydrogen System, Basic Bulk Properties*, 1st edn., Springer-Verlag, Berlin, Germany
6. W.M. Muller, J.P. Blackledge, and G.G. Libowitz (1968). *Metal Hydrides*, Academic Press, New York.
7. B.L. Shaw (1967). *Inorganic Hydrides*, Pergamon Press, Oxford, U.K.
8. G.D. Sandrock (1978). In *Hydrides for Energy Storage, The Metallurgy and Production of Rechargeable Hydrides,* A.F. Anderson and A.J. Maeland, eds. Pergamon Press, Oxford, U.K., p. 353.

9. J.J. Reilly (1977). *Hydrogen: Its Technology and Implications*, 2, 13.
10. L. Schlapbach, A. Seiler, F. Stucki, and H.C. Siegman (1980). Surface effects and the formation of metal hydrides, *Journal of Less Common Metals*, T3, 145.
11. K.J. Gross (1998). Intermetallic materials for hydrogen storage, PhD thesis, University of Fribourg, Fribourg, Switzerland.
12. S.S. Sai Raman (2000). Hydrogen storage materials, PhD thesis, Banaras Hindu University, Varanasi, India.
13. G. Sandrock (1999). A panoramic overview of hydrogen storage alloys from a gas reaction point of view, *Journal of Alloys and Compounds*, 293–295, 877–888.
14. S. Bliznakov, E. Lefterova, L. Bozukov, A. Popov, and P. Andreev (2005). Techniques for char- acterization of hydrogen absorption/desorption in metal hydride alloys, *Proceedings of the International Workshop: Advanced Techniques for Energy Sources Investigation and Testing*, Sofia, Bulgaria.
15. L. Schlapbach, I. Anderson, J. Burger, and K.H.J. Buschov (1994). *Electronic and Magnetic Properties of Metals and Ceramics*, VCH, Weinheim, Germany, Part II, Vol. 331, p. 271.
16. M. Yamaguchi, E. Akiba, and K.H.J. Buschov (1994). *Electronic and Magnetic Properties of Metals and Ceramics*, VCH, Weinheim, Germany, Part II, p. 334.
17. J. Huot and C. Julien (2002). *Proceedings of New Trends in Intercalation Compounds for Energy Storage*, Kluwer Academic Publishers, Dordrecht, the Netherlands, Vol. 61, p. 109.
18. G. Sandrock (1999). A panoramic overview of hydrogen storage alloys from a gas reaction point of view, *Journal of Alloys and Compounds*, 293–295, 877–888.
19. V.V. Sarma, S.S. Sairaman, D.J. Davidson, and O.N. Srivastava (2001). On the mechanically pulverized $MmNi_{4.6}Fe_{0.4}$ as a viable hydrogen storage material, *International Journal of Hydrogen Energy*, 26, 231–236.
20. Hydrogen Storage Materials Database, US Department of Energy, http://www. hydrogenmaterialssearch.govtools.us/.
21. I.I. Bulyk, Yu.B. Basaraba, and A.M. Trostianchyn (2004). Features of the HDDR process in ZrT_2 (T = Cr, Mn, Fe, Co) compounds, *Journal of Alloys and Compounds*, 367, 283–288.
22. A. Maddalena, M. Petris, P. Palade, S. Sartori, G. Principi, E. Settimo, B. Molinas, and S.L. Russo (2006). Study of Mg-based materials to be used in a functional solid state hydrogen reservoir for vehicular applications, *International Journal of Hydrogen Energy*, 31(14), 2097–2103.
23. G.G. Libowitz, H.F. Hayes, and R. Thomas (1957). The system zirconium-nickel and hydrogen, *Journal Chemistry and Physics*, 27, 514.
24. L.E.A. Berlouis, N. Comisso, and G. Mengoli (2006). Changes in hydrogen storage properties of binary mixtures of intermetallic compounds submitted to mechanical milling, *Journal of Electroanalytical Chemistry*, 586, 105–111.
25. D. Escobar, S. Srinivasan, Y. Goswami, and E. Stefanakos (2008). Hydrogen storage behavior of ZrNi 70/30 and ZrNi 30/70 composites, *Journal of Alloys and Compounds*, 458(1–2), 223–230.
26. G. Sandrock (1997). State-of-the-art review of hydrogen storage in reversible metal hydrides for military fuel cell applications, Report Prepared for Department of the Navy, Office of Naval Research, Contract Number N00014-97-M-0001.
27. G. Sandrock (1995). *Hydrogen Energy System – Production and Utilization of Hydrogen and Future Aspects*, Kluwer Academic, Dordrecht, the Netherlands, p. 135.
28. T.N. Veziroglu (1987) Hydrogen technology for energy needs of human settlements, *International Journal of Hydrogen Energy*, 12(2), 99–129.
29. W. Grochala and P. Edwards (2004). Hydrides of the chemical elements for the storage and production of Hydrogen, *Chemical Review*, 104, 1283–1315.
30. S.S.S. Raman and O.N. Srivastava (1996). Hydrogenation behavior of the new composite stor- age materials, *Journal of Alloys and Compounds*, 241, 167–174.
31. D.J. Davidson, S.S. Sairaman, and O.N. Srivastava (1999). Investigation on the synthesis, char- acterization and hydrogenation behavior of new Mg-based composite materials Mg-Xwt.% $MmNi_{4.6}Fe_{0.4}$ prepared through mechanical alloying, *Journal of Alloys and Compounds*, 292, 194–201.

16

Gaseous Hydrogen Storage

S.A. Sherif
University of Florida

Frano Barbir
University of Split

CONTENTS

16.1 Large Underground Hydrogen Storage 593
16.2 Aboveground Pressurized Gas Storage Systems 594
16.3 Vehicular Pressurized Hydrogen Tanks 594
References 595

Depending on storage size and application, several types of hydrogen storage may be employed as follows:

1. *Stationary large storage systems*: These are typically storage devices at the produc- tion site or at the start or end of pipelines and other transportation pathways.
2. *Stationary small storage systems*: These are typically at the distribution or final user level, for example, a storage system to meet the demand of an industrial plant.
3. *Mobile storage systems for transport and distribution*: These include both large-capacity devices, such as a liquid hydrogen tanker–bulk carrier, and small systems, such as a gaseous or liquid hydrogen truck trailer.
4. *Vehicle tanks*: These are typically used to store hydrogen used as fuel for road vehicles.

Because of hydrogen's low density, its storage always requires relatively large volumes and is associated with either high pressures (thus requiring heavy vessels) or extremely low temperatures and/or a combination with other materials (much heavier than hydro- gen itself). Table 16.1 shows achievable storage densities with different types of hydrogen storage methods. Some novel hydrogen storage method may achieve even higher storage densities but have yet to be proven in terms of practicality, cost, and safety.

16.1 Large Underground Hydrogen Storage

Future hydrogen supply systems will have a structure similar to today's natural gas sup- ply systems. Underground storage of hydrogen in caverns, aquifers, depleted petroleum and natural gas fields, and man-made caverns resulting from mining and other activities is likely to be technologically and economically feasible [1–4]. Hydrogen storage systems

TABLE 16.1

Hydrogen Storage Types and Densities

	kg H_2/kg	kg H_2/m^3
Large volume storage (10^2–10^4 m^3 geometric volume)		
Underground storage		5–10
Pressurized gas storage (aboveground)	0.01–0.014	2–16
Metal hydride	0.013–0.015	50–55
Liquid hydrogen	~1	65–69
Stationary small storage (1–100 m^3 geometric volume)		
Pressurized gas cylinder	0.012	~15
Metal hydride	0.012–0.014	50–53
Liquid hydrogen tank	0.15–0.50	~65
Vehicle tanks (0.1–0.5 m^3 geometric volume)		
Pressurized gas cylinder	0.05	15
Metal hydride	0.02	55
Liquid hydrogen tank	0.09–0.13	50–60

of the same type and the same energy content will be more expensive (by approximately a factor of 3) than natural gas storage systems, due to hydrogen's lower volumetric heat- ing value. Technical problems, specifically for the underground storage of hydrogen other than expected losses of the working gas in the amount of 1%–3% per year, are not antici- pated. The city of Kiel's public utility has been storing town gas with a hydrogen content of 60%–65% in a gas cavern with a geometric volume of about 32,000 m^3 and a pressure of 80–160 bar at a depth of 1,330 m since 1971 [2–4]. Gaz de France (the French national gas company) has stored hydrogen-rich refinery by-product gases in an aquifer structure near Beynes, France. Imperial Chemical Industries of Great Britain stores hydrogen in the salt mine caverns near Teesside, United Kingdom [3,4].

16.2 Aboveground Pressurized Gas Storage Systems

Pressurized gas storage systems are used today in natural gas business in various sizes and pressure ranges from standard pressure cylinders (50 L, 200 bar) to stationary high-pressure containers (over 200 bar) or low-pressure spherical containers (>30,000 m^3, 12–16 bar). This application range will be similar for hydrogen storage.

16.3 Vehicular Pressurized Hydrogen Tanks

The development of ultralight but strong new composite materials has enabled storage of hydrogen in automobiles. Pressure vessels that allow hydrogen storage at pressures greater than 200 bar have been developed and used in automobiles (such as Daimler-Benz NECAR II). A storage density higher than 0.05 kg of hydrogen per 1 kg of total weight is easily achievable [4].

References

1. Taylor, J.B., Alderson, J.E.A., Kalyanam, K.M., Lyle, A.B., and Phillips, L.A., Technical and eco- nomic assessment of methods for the storage of large quantities of hydrogen, *Int. J. Hydrogen Energy*, 11(1), 5–22, 1986.
2. Carpetis, C., Storage, transport and distribution of hydrogen, in C.-J. Winter and J. Nitsch (eds.), *Hydrogen as an Energy Carrier*, Springer-Verlag, Berlin, Germany, pp. 249–289, 1988.
3. Pottier, J.D. and Blondin, E., Mass storage of hydrogen, in Y. Yurum (ed.), *Hydrogen Energy System: Production and Utilization of Hydrogen and Future Aspects*, NATO ASI Series E-295, Kluwer Academic Publishers, Dordrecht, the Netherlands, pp. 167–180, 1995.
4. Mitlitsky, F., Development of an advanced, composite, lightweight, high pressure storage tank for on-board storage of compressed hydrogen, *Proceedings of Fuel Cells for Transportation TOPTEC: Addressing the Fuel Infrastructure Issue*, Alexandria, VA. SAE, Warrendale, PA, 1996.

17

Cryogenic Refrigeration and Liquid Hydrogen Storage

Gary G. Ihas
University of Florida

CONTENTS

17.1 Introduction 597
17.2 Storage Vessels, Dewars, and Storage Techniques 598
17.2.1 Non-Vacuum-Insulated Containers 598
17.2.2 Dewars 599
17.2.3 Zero Boil-Off Storage 602
17.3 Small-Scale Refrigeration 603
17.3.1 ^{4}He Evaporation Refrigeration 603
17.3.2 ^{3}He Evaporation Refrigeration 604
17.3.3 ^{3}He–^{4}He Dilution Refrigeration 606
17.3.4 Refrigeration above 4.2 K 611
Acknowledgments 613
References 613

17.1 Introduction

The use of cryogenics and access to low temperatures, once confined to the laboratories searching for the liquefaction of the *permanent gases* [1], is now almost worldwide. All low-temperature apparatus must be contained in a *cryostat*, a word derived from Greek meaning literally *frost apparatus*. Cryogenic storage and refrigeration are becoming common in our everyday lives. Liquid nitrogen is used for food and living tissue preservation, liq- uid oxygen for medical patient respiration, and liquid hydrogen for power generation, transportation, and propulsion. Large superconducting magnets are used for magnetic resonance imaging (MRI). All these applications use either vacuum-insulated containers (dewars) or foam-insulated vessels to contain the cryogens. This is because direct exposure to environmental radiation supplies more than enough heat to evaporate the cryogen in a short time. In the future, the use of cryogenic equipment will rapidly increase with new demands, for example, in computers and communication systems (cold and superconducting electronics), medicine (surgery and diagnostics), materials fabrication, transportation (motor vehicles, ships, and magnetically levitated trains), and space travel (propulsion, cooling, and water generation), particularly in the hydrogen economy. This last item is important because large amounts of hydrogen will be used, stored, and transported. There is no better way to store or transport hydrogen than as a liquid cryogen, which is more

safe, less expensive, and at higher density than any other form. Scientifically, cryogenics are used in virtually every area of research, with the widest uses in propulsion (combustion and fuel cells), condensed matter and particle physics, physical chemistry, geology, biology, and medical sciences.

In this short chapter, we offer an overview of the state of the art of cryogenic storage and small-scale refrigeration, with references that provide more detailed information. This chapter is divided into two major parts: Section 17.2 covers dewars and storage techniques, and refrigeration apparatus and techniques are discussed in Section 17.3.

17.2 Storage Vessels, Dewars, and Storage Techniques

17.2.1 Non-Vacuum-Insulated Containers

Cryogens, defined as gases that liquefy below 123 K, including nitrogen, oxygen, neon, hydrogen, and helium, are stored, transported, and used in double-walled, vacuum-insulated dewars (large, improved versions of the thermos bottle) or foam-insulated containers. The purpose of this special container is to protect the cryogen from the heat of its surroundings, thus preserving the cold liquid and reducing evaporation (boil-off). This heat leak cannot be reduced to zero, regardless of cleverness of design, unless an active refrigerator, using external power, is employed (see Sections 17.2.3 and 17.3.4). The damaging heat leak to the interior of the vessel, as usual, may have three components: conduction, convection, and radiation.

Conduction heat is minimized by suspending the vessel inside an outer housing, which is otherwise filled with powder, foam, or other porous media to inhibit gas convection heat leaks. The inner vessel is suspended by relatively thin supports made of poorly con- ducting metal (stainless steel) or polymer. Because the cryogen-containing vessel may be quite massive, care must be taken to balance forces in the suspension, accounting for thermal contractions in the vessel and suspension. Often, the vessel is hung by a neck tube, through which the cryogen is introduced and removed (see Figure 17.1). For larger vessels, a centering snub at the bottom or snubbing pieces on the sides keep the vessel from swinging during motion. These do not make contact between the inner vessel and outer container during normal use.

The insulation between the inner vessel and outer container must be maintained as a poor thermal conductor. In humid environments, therefore, the space it occupies must be sealed, which is often difficult and/or expensive to accomplish. Because this insula- tion may require frequent replacement, inexpensive materials such as vermiculite, perlite, glass bubbles, Styrofoam, or polyurethane foam are usually used. All these materials have thermal conductances about four orders of magnitude less than bulk copper. Besides being poor bulk conductors, like cork, their insulating property is enhanced by another order of magnitude since they consist of poorly contacting, small particles.

Under certain circumstances, for example, to save cost or weight, the outer shell of these containers may be eliminated. The most famous example of this is the external tank on the US space shuttle vehicle, which contains two cryogens, liquid hydrogen and liquid oxygen, in two separate vessels, surrounded by ridged insulating foam. Since this container is used in a very humid environment (Florida), there is a large amount of ice buildup on this foam during use (just prior to launch). This contributes to the launch weight, but, more important, it produces extreme loads on the foam insulation during the acceleration

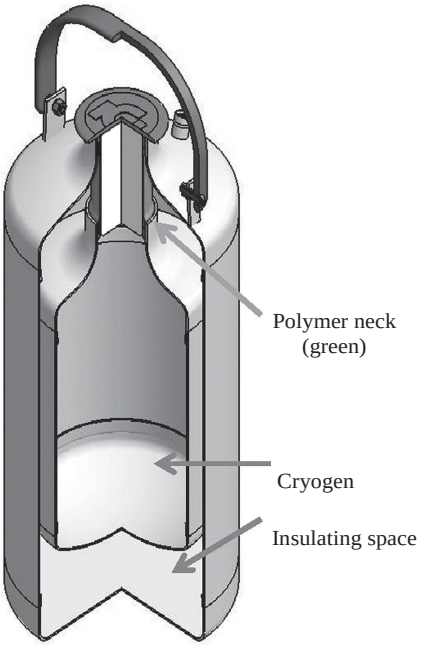


FIGURE 17.1

Basic cryogenic container. The inner vessel containing the cryogen is suspended by a polymer neck with poor thermal conductivity. The space between the inner vessel and outer container must be filled with a poorly conducting powder or foam to stop gas convection or be evacuated. (Courtesy of International Cryogenics, Inc., Indianapolis, IN.)

phase of achieving orbit. It is known that pieces of this foam have caused damage to the shuttle vehicle, particularly its wings and heat shield tiles. This caused the catastrophic SS Columbia accident.

17.2.2 Dewars

If the space between the inner vessel and outer container is evacuated, the whole apparatus is called a dewar, after Sir James Dewar (see next section), and was originally constructed of blown glass. The inner surfaces of the vacuum spaces in this construction are silvered. The vacuum space minimizes conduction heating, and the silvering minimizes radiant heating, but this vacuum is sometimes inconvenient or impossible, requiring stronger container walls, more safety apparatus, and construction of higher integrity.

Vacuum-insulated dewars are the preponderance of cryogenic storage and research containers. Although dewars used in research are physically quite different in appearance from storage and transport dewars, they have similar requirements to reduce heat leaks into the cryogen. Special features of storage and transport dewars necessary for these uses, such as more robust construction, are included in standard designs of manufacturers. Here, we will also discuss research dewars, likely to be of more concern to experimenters who may have to design or write specifications for a dewar.

In most research at low temperatures, liquid cryogen is transferred from a storage dewar (Figure 17.2) to a research dewar (Figure 17.3), designed for specific uses. The dewar in Figure 17.3, constructed of aluminum with a fiberglass neck, is designed for a large

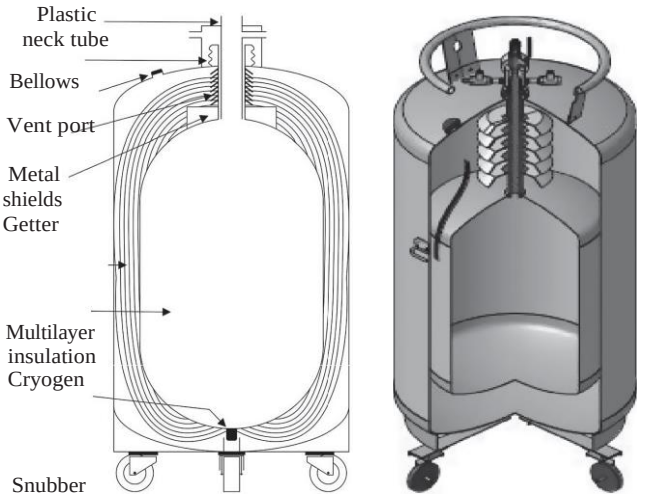


FIGURE 17.2

Cross-sectional view of standard transport (storage dewar), with cutaway drawing of the same. Cross-sectional view, courtesy of the author. (Courtesy of International Cryogenics, Inc., Indianapolis, IN.)



FIGURE 17.3

Research dewar with two inserts: Left is a 3 T magnet with a ^{4}He evaporative cooling stage. Right is a transport measuring probe on a continuous ^{3}He evaporative cooling stage. The dewar has an aluminum outer jacket and fiberglass G10 inner neck and aluminum bucket, with multilayer insulation in the vacuum space between. (Courtesy of Janis Research, Inc., Wilmington, MA.)

superconducting magnet. It has features to reduce helium consumption in common with most other dewars used in research and with storage and transport dewars.

Radiation from room temperature to the inner wall containing the cryogen is reduced dramatically by vapor-cooled heat shields and multilayer (super)insulation (usually aluminized Mylar film separated by thin, loose fiberglass layers) in the vacuum space. Heat transfer by conduction down the low-thermal-conductivity fiberglass neck is reduced further by these vapor-cooled shields attached to the neck at appropriate intervals, which are cooled by the enthalpy of the vapor boiling off the liquid cryogen. The large neck, necessary for inserting the superconducting magnet, also has baffles inside to reduce radiation from the top flange. A thin metal barrier is incorporated inside the fiberglass to prevent diffusion of helium and/or hydrogen into the vacuum space, which occurs if residual cryogen is left in the dewar on warming.

These features of the dewars shown in Figures 17.2 and 17.3 provide a quite low boil-off rate: about 1% of capacity for the storage dewar and less than 2 L/h for the research dewar, even in this relatively large dewar, which is about 3.7 m long with a neck diameter of 46 cm.

The absence of liquid-nitrogen shielding for these dewars has a number of advantages including simpler construction, lighter weight, with lower initial and operating costs, and also bothersome refilling of the nitrogen jacket is avoided. Furthermore, eliminating boiling nitrogen can reduce vibrations that may be critical in some uses.

Some small hand dewars and research dewars are constructed of Pyrex glass, in which case liquid-nitrogen shielding using a separate liquid-nitrogen dewar, surrounding the lower-temperature hydrogen or helium dewar, is common, since incorporation of superinsulation is impractical. In using Pyrex dewars, it is essential to avoid leaving helium and/or hydrogen gas in the dewar when it is warmed in order to prevent diffusion of gas into the vacuum space, which can create an insurmountable heat leak. The simplest way to achieve this is to terminate the vacuum space of the helium dewar with a single-wall neck at a point below the nitrogen level in the outer dewar. This construction also facilitates precooling of the lower dewar with liquid nitrogen.

Research dewars may also be of all-stainless-steel construction, with or without nitrogen shielding. Frequently, storage and transport dewars are also of all-stainless-steel construction in order to provide the necessary ruggedness. Additionally, the nonmagnetic stainless steel allows the dewar to be moved safely near a large magnet.

In cooling a dewar from room temperature, much less cryogen is used if the dewar is precooled with liquid nitrogen. In case a dewar has no nitrogen shielding, nitrogen is transferred directly into the cryogen space. After the equipment inside has been cooled to nitrogen temperature (and the shields, in the case of a vapor-shielded dewar), the nitrogen is back-transferred. This is accomplished by applying a small overpressure above the nitrogen surface to force it out through a tube extending through the top flange of the dewar to the inside bottom. Once liquid ceases to flow, the container space should be pumped, being careful to keep the pressure above the triple point of N_2, until there is very little flow of gas. This assures no liquid nitrogen remains in the dewar at the time cryogen is transferred (which would require a large quantity of cryogen to cool the nitrogen to the boiling point of the cryogen).

If a separate nitrogen dewar is used, then cooling from room temperature to liquid-nitrogen temperature can be accomplished simply by filling the nitrogen dewar and waiting for the inner dewar and the apparatus inside it to be cooled to near 77 K. In this case, it is essential that there be an exchange gas of air or N_2 at a pressure of a few mm Hg in the vacuum jacket of the inner dewar to provide heat transfer. Once the cryogen transfer begins, this exchange gas is frozen on the wall of the dewar, producing the high vacuum necessary for holding the cryogen.

The research dewar is usually closed at the top by a flange that constitutes the top of the cryostat insert used for the particular experiment. The insert has suitable tubulation

and electrical leads for the measurements to be made and for operation of the refrigera- tor. Cryogen is transferred from a storage dewar into the research dewar using a double- walled, vacuum-insulated transfer tube that extends to the bottom of the storage dewar. In the initial part of the transfer, it is important that the cryogen be introduced at the bottom of the research dewar in order to make full use of the enthalpy of the gas in cooling the dewar and equipment inside it. In subsequent topping-off of the cryogen, it is best that the liquid be introduced above the level of cryogen remaining in the dewar.

A port allows recovery of the cryogen's gas, or it is vented into the atmosphere if not recovered (not recommended for hydrogen). In a situation where large amounts of cryogen are transferred causing moisture condensation, it is useful for the port to be through a collar below the top flange, thus avoiding freezing of the top flange. Also, one or more relief ports may be needed to allow gas to escape quickly in cases of rapid boil-off such as when a superconducting magnet quenches. Relief valves are required on transport dewars for safety, but full dewars of liquid helium may be flown on commercial aircraft.

17.2.3 Zero Boil-Off Storage

In some situations, it is desired to have no loss of cryogen from the storage container. These applications include such common installations as MRI machines or special situations as onboard spacecraft or satellites. Since, as mentioned previously, it is impossible to completely avoid heat leaks to the cryogenic storage vessel, this heat leak must be intercepted by some refrigeration technique to achieve zero boil-off (ZBO).

Terrestrial applications, such as MRI machines in hospitals and clinics, research magnets, or particle accelerators, are straightforward to achieve ZBO. Electrical power is readily available, and gravity ensures that the cryogen is well behaved, that is, remains in the bottom of the dewar. Typically, a cryocooler, such as that described in Section 17.3.4, is employed. The cryocooler is mounted on top of the dewar, and a thermal connection, such as a heat pipe, draws in evaporated cryogen and recondenses it. Such a system is shown diagrammatically in Figure 17.4, which uses the latest innovation in cryocoolers, the pulse tube refrigerator.

Space applications, particularly to liquid hydrogen storage, are more challenging. A test of such a ZBO system for nonterrestrial use is described in Ref. [2].

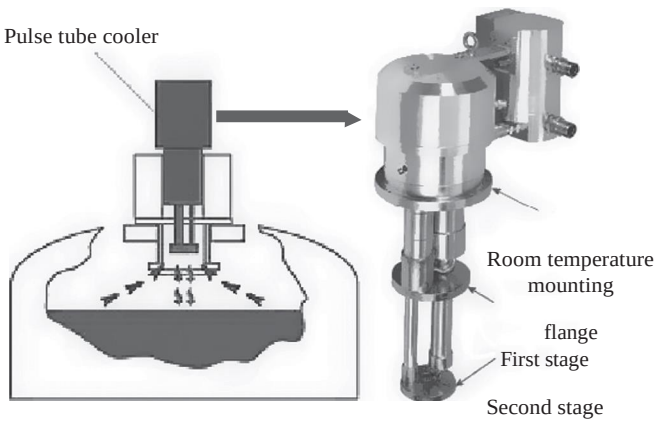


FIGURE 17.4

Dewar incorporating a pulse tube refrigerator (Courtesy of Janis Research, Inc., Wilmington, MA.), reducing the cryogen to ZBO. Detail of pulse tube refrigerator (Courtesy of CryoMech, Inc., New York.) shown to right.

17.3 Small-Scale Refrigeration

17.3.1 ^{4}He Evaporation Refrigeration

Temperatures from the normal boiling point of ^{4}He, 4.2 K, to as low as about 1.2 K (limited by the pumping speed of the system) can be achieved by pumping the vapor above liquid helium [2–4]. The simplest means of doing this, in terms of the equipment inside the dewar, is to pump the entire bath of helium. However, this method has several disadvantages. A large fraction of the helium is used in cooling the remaining helium to the minimum temperature of about 1.2 K. If the temperature is lowered below the lambda point, 2.18 K, a film of the superfluid helium creeps up the wall of the dewar, contributing significantly to the boil-off rate, resulting in higher consumption of helium [4].

The disadvantages just described can be overcome by keeping the main helium bath at 4.2 K and placing the experiment and a small pot of helium to be pumped to a lower temperature inside a vacuum space immersed in the helium bath, as shown in Figure 17.5. The pumped pot of helium can be refilled periodically from the bath using a valve at the top of the vacuum space, operated from outside the cryostat. Instead of filling periodically, a small needle valve may be used, which can be adjusted so that the flow of liquid into the pot is just adequate for the heat load. The arrangement shown requires no valve and allows continuous filling of the pot by using an impedance of appropriate size between the bath and the pot [5]. Even under varying heat loads, the temperature remains almost constant up to a critical power that equals the cooling by the incoming liquid. As shown, the inlet may be below the top of the vacuum space to give longer times between helium transfers into the dewar. The impedance must be in the vacuum space, and a filter is necessary to prevent clogging of the small line.

In experiments using a pumped pot of ^{4}He, care must be taken to ensure adequate thermal contact between the helium and the sample or equipment that must be cooled. This

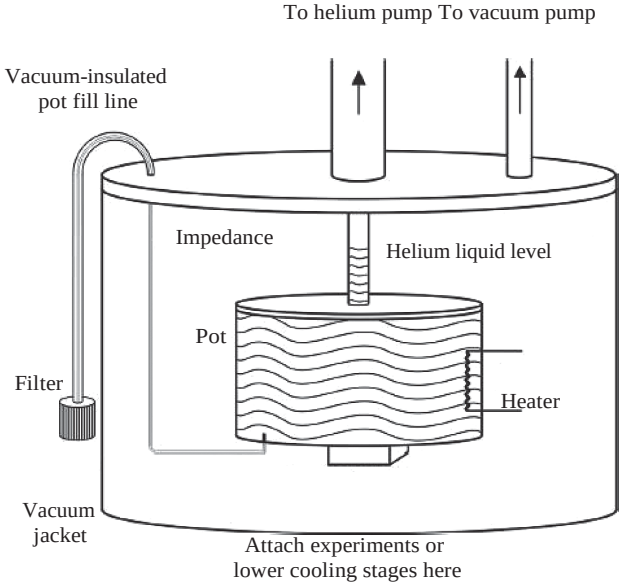


FIGURE 17.5

Schematic diagram of a continuously operating ^{4}He evaporation refrigerator. See Ref. 3 for details.

can be done by immersing the sample in the helium within the pot, with access from the top through the pumping line. Another approach is to mount the sample on the outside of the pot using a screw contact if the sample can be electrically grounded, or for a sample that must be insulated, contact may be made with varnish, epoxy, or grease. Care must be taken to thermally ground leads to the sample and thermometers, otherwise there may be a heat leak into the sample that will keep it at an elevated temperature. These precau- tions become ever more important as the temperature of the sample is lowered, such as by the techniques discussed in the following [3].

In cases where the experimental parts to be cooled can be made small, miniature cryo- stats with a pumped inner pot of helium have been constructed that may be inserted directly into a storage dewar with a wide neck (up to 60 mm diameter) [6]. These have the advantages that no transfer of helium is required, helium consumption is low, and the time required to reach the desired temperature is short.

Another arrangement used frequently to lower the temperature of superconducting magnets below 4.2 K is the "lambda-plate" refrigerator (see Figure 17.11 and Section 17.3.3). The lambda plate, situated in the lower portion of the dewar but above the magnet, has a needle valve for admission of liquid ^{4}He into a coil heat exchanger connected through a tube to the top of the cryostat where a pump is connected. The normal ^{4}He above the lambda plate is a very poor thermal conductor and remains at 4.2 K, while the helium in the lower portion of the dewar, where the magnet is located, is pumped to a reduced tem- perature, allowing the magnet to operate at a higher field.

17.3.2 ^{3}He Evaporation Refrigeration

The vapor pressure of ^{3}He is higher than that of ^{4}He at the same temperature, a conse- quence of the higher zero-point motion of the lighter isotope [2]. Furthermore, ^{3}He has no creeping film in the range of interest. Consequently, temperatures of 0.3 K or slightly lower can be obtained by pumping to lower the vapor pressure of ^{3}He.

Most ^{3}He is obtained from the decay of ^{3}H; therefore, it is quite expensive. Consequently, ^{3}He is used in relatively small quantities of a few liters of gas STP in a closed cycle, with sealed pumps (including the exhaust) to recover the helium. A ^{3}He refrigerator is usually run in a continuous mode, with the helium gas from the pump returned to the evaporator as a liquid, after it has been brought into thermal contact with a ^{4}He pot to remove the heat of vaporization. Also, the pressure of the returning ^{3}He gas must be brought above its saturated vapor pressure at the temperature of the ^{4}He pot by including sufficient impedance in the return line below the ^{4}He pot. A ^{3}He
refrigerator with gas-handling system is shown in Figure 17.6. A typical ^{3}He refrigera- tor, which may be directly inserted into a ^{4}He transport dewar, is shown in Figure 17.7. The advantage of this design is the avoidance of transferring the liquid ^{4}He for the bath, saving time and money.

Recently, heat exchangers have been developed for closed cycle refrigerators that allow operation of a ^{3}He refrigerator or a dilution refrigerator (see Section 17.3.3) without using pumped ^{4}He [7]. An example is shown in Figure 17.8.

One of the limiting factors in the temperature that may be reached, or the refrig- eration available by pumping ^{3}He, is the pumping speed of the system, including the pumping line and the external pumps. The pumping speed can be increased substan- tially by incorporating a small adsorption pump (usually with charcoal as the adsor- bate) within the vacuum container. Shown in Figure 17.9 is such an adsorption pump

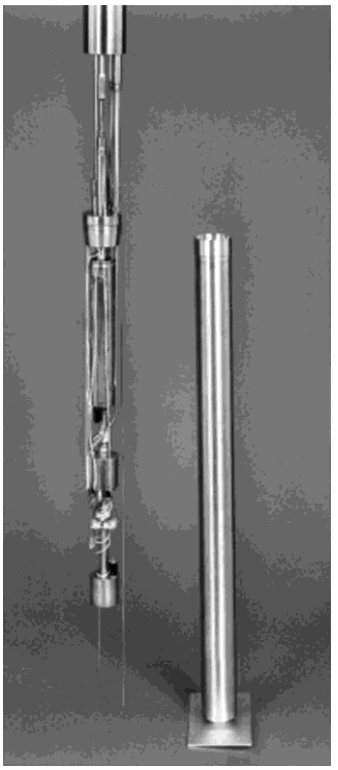


FIGURE 17.6

Continuously operating ^{3}He refrigerator with gas-handling system (^{4}He bath dewar not shown). (Courtesy of Janis Research Company LLC, Woburn, MA.)

in a miniature dilution refrigerator (see Section 17.3.3) designed for insertion into a storage dewar [8].

A feature of these miniature cryostats worth pointing out is the compact cone seal with vacuum grease that works well at helium temperatures (see Figure 17.8). Earlier, similar seals were made with Wood's metal, requiring undesirable heating to make the seal, or with bulkier bolted flanges using soft metal (e.g., indium or lead) O-rings.

Adsorption pumps may also be used to advantage in larger systems to increase the pumping speed and to reduce the expense, since large external pumps are not required. One disadvantage is that continuous operation would require a more complicated arrange- ment with two adsorbers and cold valves. However, this disadvantage can be partially overcome by including a larger quantity of ^{3}He in the system. A system capable of holding a few cm^3 of liquid ^{3}He can maintain the desired temperature for a few days if the heat input in the experiment is not great.

Because of the rapid increase of the thermal boundary resistance between materi- als as the temperature is decreased, the evaporator of a ^{3}He refrigerator should have several cm^2 of surface area in contact with the ^{3}He. This can easily be provided by some means such as milling slots in the body or by brazing a spiral sheet of copper to the bottom.



FIGURE 17.7

^{3}He refrigerator for insertion in storage dewar with vacuum jacket (on right). Vacuum jacket grease seal flange can be seen near top. By not requiring a separate research dewar, cooldown and turnaround time and liquid helium are saved at the expense of experimental volume. (Courtesy of Janis Research Company LLC, Woburn, MA.)

17.3.3 ^{3}He-^{4}He Dilution Refrigeration

Refrigeration by pumping ^{3}He is impractical below about 0.25 K because of the vanishingly small vapor pressure at lower temperatures. The most common means of reaching temperatures as low as a few millikelvin is by ^{3}He–^{4}He dilution refrigeration [3]. The physical process itself is quite easy to understand: cooling is provided by the heat of mixing when the two isotopes are mixed. This is possible at ultralow temperatures because the two isotopes remain liquids all the way to absolute zero and a finite amount, up to 6.5%, of ^{3}He will dissolve in ^{4}He at the lowest temperature [2,9].

A schematic drawing, depicting the essential components of a dilution refrigerator, is shown in Figure 17.10. This consists of a mixing chamber in which two separated phases exist, a concentrated phase of almost pure ^{3}He floating on top and a dilute phase of 6.5% ^{3}He in ^{4}He at the bottom; heat exchangers for transferring heat from the warm incoming stream of concentrated ^{3}He to the outgoing cold dilute phase; and a still for extracting the ^{3}He from the dilute phase, allowing the process to be continuous.

The refrigerator is immersed in a helium dewar to provide a 4.2 K environment. Typically, there is a heat shield (not shown) attached to the still to reduce the heat reaching the mixing chamber through 4.2 K radiation and thermal conduction through spacers. Also, a mixing-chamber heat shield may be used to reduce heat input to a sample or colder stage below the mixing chamber.

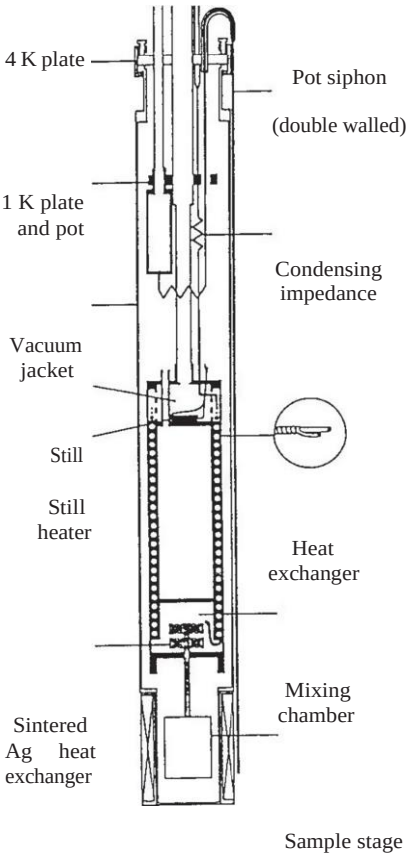


FIGURE 17.8

Completely self-contained cryogen-free ^{3}He refrigerator system. A pulse tube refrigerator, seen protruding from top, supplies the cooling to condense the circulating ^{3}He. Insert sample, plug into mains, and cool down. (Courtesy of Janis Research Company LLC, Woburn, MA.)

The very high vapor pressure of ^{3}He relative to ^{4}He provides a vapor phase in the still of almost pure ^{3}He above the liquid, which is less than 6.5% ^{3}He. Thus, almost pure ^{3}He is extracted from the still for recirculation, with most of the ^{4}He remaining in place to serve as a medium in which to dissolve the ^{3}He. Maintaining sufficiently high vapor pressure to allow the desired circulation rate requires that the still be kept at about 0.7 K by supplying the heat of vaporization with an electric heater.

The returning ^{3}He gas must be liquefied by removing the latent heat either with a pumped pot of ^{4}He as described in Section 17.3.1 or with a heat exchanger between the outgoing and incoming streams [3]. Just as with the ^{3}He refrigerator discussed in Section 17.3.2, the pressure of the incoming stream of gas must be brought above the saturated vapor pressure. Again, this requires a flow impedance below the ^{4}He pot or heat exchanger.

Perhaps the most critical parts of a dilution refrigerator are the heat exchangers that are necessary to cool the incoming stream from the still temperature of about 0.7 K to near that of the mixing chamber, which is much colder. With a simple counterflow capillary heat exchanger, minimum mixing-chamber temperatures of about 50 mK can be achieved.

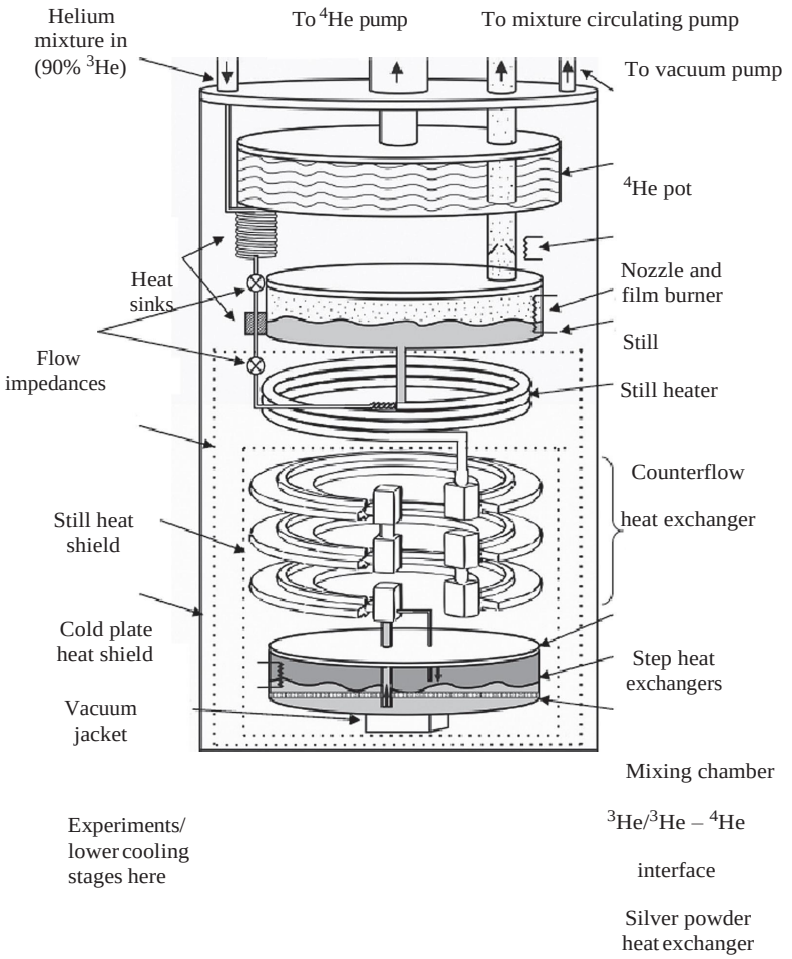


FIGURE 17.9

Schematic diagram of a miniature charcoal-pumped ^{3}He–^{4}He dilution refrigerator that may be used in a helium storage dewar. (Courtesy of Nanoway; From Uhlig, K., *Cryogenics*, 27, 454, 1987.)

Typically, a refrigerator designed to achieve the lowest temperatures has a counterflow exchanger followed by several *step exchangers*. These are also counterflow exchangers that have a large inside surface area of very fine sintered metal powder (silver is commonly used) for heat transfer between the two streams and are bulkier in construction than capillary exchangers [10].

One of the main requirements for the mixing chamber is that it has adequate surface area, usually provided with sintered metal powder, to minimize the temperature differ- ence between the chamber body and the cold dilute phase. Thermal contact to the material to be cooled can then be made using bolts screwed tightly to the mixing chamber. Another requirement is that the entrance tube for the dilute phase actually extends into this phase (see Figure 17.11).

An alternative to this "bottom-loading" refrigerator is to insert samples directly into the liquid in the mixing chamber, usually by loading them in through a vacuum port in the pumping line at the top of the cryostat. This "top-loading" refrigerator has the advantage that samples may be changed relatively quickly without warming the refrigerator to room

temperature. However, care must be taken to insert the sample slowly and to adequately heat-sink the sample, ensuring it does not remain at a significantly higher temperature than the liquid in the mixing chamber.

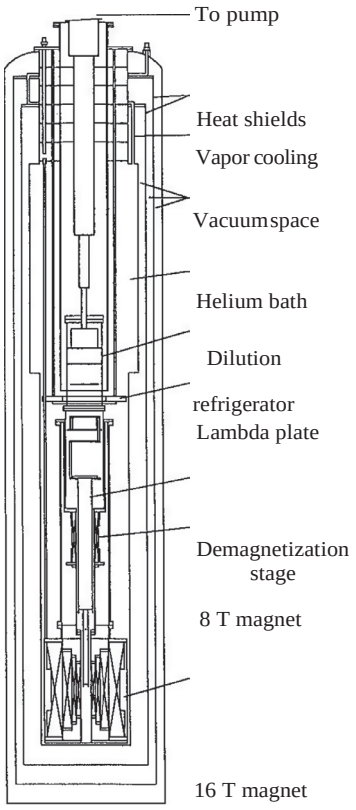


FIGURE 17.10

Block diagram of the essential components of a ^{3}He–^{4}He dilution refrigerator.

With a very-well-designed refrigerator, minimum temperatures of about 2.5 mK have been achieved, although commercial refrigerators have typical minimum temperatures of 5–10 mK. The maximum cooling power of a dilution refrigerator, $\dot{Q}(W)$, is given by

$$\dot{Q} = 84\dot{n}T_m^2 \tag{17.1}$$

where

$\dot{n}$ is the number of mol/s of ^{3}He being circulated

T_m is the mixing-chamber temperature (K)

The coefficient 84 is determined by the entropies of the dilute and concentrated phases [3,11]

Frequently, the cooling power of a dilution refrigerator is specified at 100 mK, which by Equation 17.1 is 840 μW/mmol/s of ^{3}He in circulation. Near the minimum temperature of the dilution refrigerator, the cooling power drops significantly below the value given by Equation 17.1 [11].

Two examples of commercially available dilution refrigeration units are shown in Figure

17.12. These may be purchased with varying cooling capacities up to 1 mW at



FIGURE 17.11

Schematic diagram of a $^{3}He–^{4}He$ dilution refrigerator in an aluminum and fiberglass research dewar (as in Figure 17.2b) containing a lambda-plate refrigerator and two high field magnets. The lambda plate allows the helium below it to be pumped to about 2.1 K, allowing the 16 T magnet to achieve full field. Pumps and external gas-handling system are not shown. (Courtesy of J.S. Xia, Microkelvin Research Laboratory, University of Florida, Gainesville, FL.)



FIGURE 17.12

Two examples of the business end of dilution refrigeration, with still at the top, mixing chamber at the bottom, and continuous and block heat exchangers in between. (Courtesy of Janis Research Company LLC, Woburn, MA.)

T = 0.1 K and then attached to the users' pumped ^{4}He cryostats. A sealed pumping system must be provided to continuously evaporate the ^{3}He from the still. Also, some care must be taken to isolate the cryostat from electrical oscillations (from low to very high frequency) and mechanical vibration, both of which will overwhelm the cooling power of the dilution unit if not eliminated.

Miniature dilution refrigerators employing adsorption pumping, similar in design to the ^{3}He refrigerator shown in Figure 17.8, for use in storage dewars, have been reported [8,12].

Dilution refrigerators provide the lowest temperature available for continuous cooling. The most common technique for achieving still lower temperatures is magnetic demagnetization using the nuclei of various metals such as copper. This technique, by which temperatures of nuclei of less than 1 nK have been reached, is quite specialized, and interested readers are referred to the literature [3].

17.3.4 Refrigeration above 4.2 K

There is more work done above the temperature of boiling liquid helium than below. Applications include almost anything also done at room temperature: light scatter- ing, microscopy, x-ray Raman scattering, Mossbauer and Hall effect, nuclear magnetic and electron spin resonance (NMR and ESR), magnetization and susceptibility, matrix isolation, resistivity, and radio astronomy, to name a few. Cold traps and cryopump- ing are also broadly applied. Systems that cool from room temperature down to 4.2 K fall into two classes: open and closed systems. Open systems use cryogenic fluids that eventually boil and are released into the environment. Closed systems use pressur- ized gases, such as helium, nitrogen, neon, or hydrogen, in some type of expansion process.

Most open systems use helium or nitrogen because of the explosive nature of hydrogen/air mixtures or the high cost of neon. This method of cooling simply transfers the cryogen from a storage dewar, through a triaxial (vacuum-insulated) transfer tube to a cold head. Here, the cryogen evaporates, cooling the apparatus, with the evolved gas returning through heat exchangers, heat shields, and the transfer tube middle-annular space, maxi- mizing efficient use of the cryogen. A heater at the cold head is used in an electric feedback circuit to hold the temperature at the desired value. If a Joule–Thomson expansion valve [13] is added to the cryogenic liquid exit port, temperatures as low as 2 K may be reached using helium.

Open systems are simple, have relatively high cooling capacity, and may be constructed to cool in confined spaces, such as in a magnet or with optical instrumentation. They may also be made quite vibration-free. Their obvious disadvantage is that cryogenic fluid must be continually supplied. Hence, expertise in handling the fluid and a source of the fluid must be maintained. In addition, as the system is adjusted to temperatures farther away from the boiling point, control becomes more and more difficult, with some intermediate temperatures becoming impossible to regulate. New types of microprocessor-based regulators (see Section 17.3.1) are reducing this problem.

Often, temperatures below 4 K and high cooling power are not necessary. In this case, closed cycle systems are often used. These systems require only electricity and a thermal bath (ambient air or cooling water) and run continuously for long periods of time. They may also be made very small and relatively vibration-free. There are three types of closed cycle refrigerators, all involving the expansion of a compressed gas: Joule–Thomson, Gifford–McMahon (GM) [14], pulse tube refrigerator [15], or a linear combination of these three types of expansion.

The Joule–Thomson expansion of a high-pressure gas extracts heat by doing work against the internal forces between the molecules of a nonideal gas. The expansion must begin in the region of the pressure–temperature plane where the isenthalps have positive slopes (the inversion region). For nitrogen, this includes room temperature, so that nitrogen expanded in this way from a gas cylinder can be made to reach 70 K with no moving parts (except the gas molecules). This process is used in *microminiature* refrigerators [16], which are centimeters in size, have essentially no electrical or mechanical vibrations, and require no maintenance. Larger versions can produce watts of cooling power below 100 K. The expanded cold gas must be used to precool the incoming pressurized gas for lowest temperatures to be achieved. As usual, efficient heat exchangers, often of counterflow construction, are necessary.

The GM process uses a displacer moving in a cylinder driven by pressurized gas. In addition, it uses a regenerator, which is essentially a single-chamber heat exchanger with the incoming and outgoing fluids sharing it at different times in the cycle. This regenerator must be extremely efficient (>98%). An advantage of the GM cycle is that stages may be easily put in series and driven on the same shaft to obtain lower temperatures and higher cooling capacities. Cooling powers of 2 W at 10 K and 100 W at 77 K have been achieved by commercial units [17]. A low temperature of less than 5 K may be reached if helium is the working medium.

Most units operate from a simple, small air-conditioning compressor using either helium or nitrogen gas. The compressor, ambient heat exchanger, and ancillary equipment are housed in a small (0.1 m^3) portable unit, connected to the cold head using standard flexible metal hoses. The cold head can be quite small and configured to meet almost any experimental need. It contains the moving displacer and valve disk/motor, which controls the gas cycle [18]. It may be operated in any orientation relative to gravity, or in zero gravity, since bulk cryogenic liquid is not part of the cycle. Experiments or samples may be ther- mally heat sunk to the cold head using mechanical or gas (heat pipe) contacts.

GM units are commonly used to cool the neck of a large cryostat, thus greatly reducing helium consumption. One dilution refrigerator (see Section 17.3.3) has been constructed using a GM machine to thermally shield the dilution unit and provide the cooling power to condense the circulating ^{3}He. No liquid cryogens are required, allowing operation anywhere that electrical power is available.

By using a GM machine to precool pressurized helium gas, the inversion region of helium may be reached (<45 K). This is also a closed system, as the helium gas is reused and pressurized in the same compressor that runs the GM cycle. This adds very little to the size of the cold head while achieving a low temperature of 3.6 K with a cooling power of 1 W at 4.2 K.

A pulse tube refrigerator is very similar to a GM refrigerator (also developed by Gifford) but has the advantage of no moving cold parts (except the gas working medium). It has the disadvantage of being gravitation field dependent. This is because there is no displacer per se, such as the piston in the GM machine, so the moving gas is susceptible to convection. Therefore, buoyancy effects are important. However, the pulse tube refrigerator can function in very low or zero gravity.

Recently, the performance of pulse tube refrigerators has been greatly improved. They can reach almost 1 K, have useful capacity, are compact and simple to operate, and produce relatively low vibration levels. The working medium, often helium gas, is self-contained and therefore does not require circulating, cleaning, or replenishing. This device has ushered in the age of the *cryogen-free* refrigerator that can reach temperatures as low as 6 mK and the *cryogen-free* superconducting magnets.

Acknowledgments

The author thanks Professor Dwight Adams for assisting in the assembling of the information presented here. Roman Ciapurin assisted in the preparation of several figures. Lydia Munday and Logan Bessll assisted in assembling references.

References

1. Mendelssohn, K., 1966. *The Quest for Absolute Zero*, McGraw-Hill, New York.
2. Hastings, L.J., Bryant, C.B., Flachbart, R.H., Holt, K.A., Johnson, E., Hedayat, A., Hipp, B., Plachta, D.W., 2010. Large-scale demonstration of liquid hydrogen storage with zero boiloff for in-space applications, NASA/TP-2010-216453, M-1302.
3. Wilks, J., 1967. *The Properties of Liquid and Solid Helium*, Clarendon Press, Oxford, U.K.
4. A full description of the cooling techniques described here can be found in: Lounasmaa, O.V., 1974. *Experimental Principles and Methods Below 1 K*, Academic Press, London, U.K.; Pobell, F., 1992. *Matter and Methods at Low Temperatures*, Springer-Verlag, Berlin, Germany.
5. For a description of general low-temperature techniques, see White, G.K., 1987. *Experimental Techniques in Low Temperature Physics*, Oxford University Press, Oxford, U.K.
6. De Long, L.E., Symco, O.G., and Wheatley, J.C., 1971. Continuously operating 4He evaporation refrigerator. *Rev. Sci. Instrum*. **42**, 147, http://dx.doi.sig/10.1063/1.1684846.
7. Engel, B.N., Ihas, G.G., Adams, E.D., and Fombarlet, C., 1984. Insert for rapidly producing temperatures between 300 and 1 K in a helium storage dewar. *Rev. Sci. Instrum*. **55**, 1489.
8. Uhlig, K., 1987. ^{3}He/^{4}He dilution refrigerator without a pumped ^{4}He stage. *Cryogenics*, **27**, 454.
9. Swartz, E.T., 1986. Efficient He-4 cryostats for storage dewars. *Rev. Sci. Instrum*. **57**, 2848 and references therein.
10. Edwards, D.O., Brewer, D.F., Seligman, P., Skertic, M., and Yaqub, M., 1965. Solubility of He^3 in liquid He^4 at 0°K. *Phys. Rev. Lett*. **15**, 773.
11. Frossati, G., 1978. Obtaining ultralow temperatures by dilution of ^{3}He into ^{4}He. *J. Phys*. **39**(C6), 1578.
12. Takano, Y., 1994. Cooling power of the dilution refrigerator with a perfect continuous counter- flow heat exchanger. *Rev. Sci. Instrum*. **65**, 1667.
13. Pobell, F., 1967. Chapters 3 and 4. In *The Properties of Liquid and Solid Helium*, Wilks, J., ed., Clarendon Press, Oxford, U.K.
14. Barron, R.F., 1985. *Cryogenic Systems*, 2nd edn., Oxford, New York, p. 64.
15. Barron, R.F., 1985. *Cryogenic Systems*, 2nd edn., Oxford, New York, p. 270.
16. Radebaugh, R., 2000. Development of the pulse tube refrigerator as an efficient and reliable cryocooler. *Proceedings of the Institute of Refrigeration of London*, London, U.K., vol. 96, pp. 11–29.
17. Little, W.A., 1984. Microminiature refrigeration. *Rev. Sci. Instrum*. **55**, 661.
18. CryoMech, Inc., New York; SHI-APD Cryogenics, Inc., Allentown, PA; and CTI-Cryogenics, Chelmsford, MA.

18

Magnetic Liquefaction of Hydrogen

Tom Burdyny
University of Victoria

Andrew Rowe
University of Victoria

CONTENTS

18.1 Introduction 616
18.1.1 Overview of Magnetic Refrigeration 616
18.1.2 History of Magnetic Liquefaction of Hydrogen 618
18.2 Thermodynamics 619
18.2.1 Magnetic Systems 619
18.2.1.1 Work 619
18.2.1.2 Entropy 620
18.2.2 Magnetic Refrigeration Cycles 622
18.2.2.1 Carnot Cycle 623
18.2.2.2 Brayton Cycle 624
18.2.2.3 Ericsson and Stirling Cycles 625
18.2.2.4 Active Magnetic Regenerator Cycle 626
18.2.3 Regenerator Design 628
18.3 Magnetocaloric Materials 629
18.3.1 Requirements for an Effective Refrigerant 630
18.3.1.1 Refrigerant Capacity 630
18.3.1.2 Tailoring Properties 631
18.3.2 AMR Performance 632
18.3.3 Refrigerant Selection 633
18.4 20–80 K Magnetic Refrigeration Devices 634
18.4.1 Design Considerations 634
18.4.1.1 Forces 634
18.4.1.2 Flow 635
18.4.1.3 Parasitic Magnet Load 636
18.4.2 Cryogenic AMR Devices 636
18.5 Magnetic Liquefier Concepts 639
18.5.1 Process Configurations 640
18.5.2 Liquefier Designs 642
18.6 Summary 646
References 647

18.1 Introduction

The ability to induce a reversible temperature change in a magnetic material by chang- ing the magnetization is called the magnetocaloric effect (MCE) and has been known for over 100 years. Magnetic cooling is a process that uses the MCE to reduce the temperature of another substance and was originally employed to produce temperatures lower than those possible with liquid helium (LHe). Since the early 1970s, advancements in materials (magnetic refrigerants, superconductors, permanent magnets) and our understanding of the thermodynamics of magnetic cycles have led to increased interest in using magnetic cycles for a variety of applications. One area of particular interest is the liquefaction of hydrogen. Although no commercial liquefiers using the MCE currently exist, the poten- tial for high efficiencies at smaller scales and lower cost than conventional gas expansion cycles is a driver of research and development activities. In addition, future energy sys- tems in which hydrogen is used as an energy carrier require logistical chains for transmis- sion, distribution, and storage. For this to happen, the need for hydrogen liquefaction will grow substantially from current levels.

This chapter describes some of the activities reported in the literature regarding mag- netic liquefaction of hydrogen. A brief history of magnetic refrigeration is provided and is followed by a summary of the basic thermodynamic relationships quantifying the performance of magnetocaloric materials and cycles. Following this, there is a review of proposed devices and their configurations. Some of the refrigerants that have been specifi- cally suggested for use in hydrogen liquefaction will be discussed, but, given the substan- tial research currently happening on material synthesis and characterization, no attempt will be made to cover this area rigorously. Instead, the reader will be directed to reviews where further information can be found. Likewise, much of the work on device devel- opment has been in national laboratories and companies through government contract research. Many of the details for these projects are not easily accessible; thus, this review will focus on information available in the open literature.

18.1.1 Overview of Magnetic Refrigeration

Magnetic refrigeration is based upon a phenomenon known as the MCE. The MCE is sometimes described as the isothermal entropy change due to a change in the applied magnetic field. In order to produce useful cooling or heat with a magnetic material, there must be a decrease or increase in temperature due to a change in the applied field—this is the adiabatic temperature change and is another way of reporting the MCE. Unlike eddy-current heating, the MCE is identified by the *reversible* change in temperature when adiabatically subjected to a magnetic field. For a given material, the magnitude of this temperature change is proportional to the strength of the applied magnetic field. Different materials also display this effect to varying degrees depending upon properties such as the Curie temperature, magnetic entropy, and lattice entropy.

Using the MCE, it is possible to form a cycle that parallels a vapor-compression pro- cess whereby a volume can be continuously refrigerated through a cyclical process. The compression and expansion stages of a gas-refrigeration system are replaced by magne- tizing and demagnetizing a magnetic material. Because the working substance is a solid with limited heat transfer capabilities, a heat transfer fluid is used to thermally couple the refrigerant to hot and cold heat sinks. An example of a particular process for a magnetic refrigeration cycle is summarized in the following paragraph with reference to Figure 18.1.

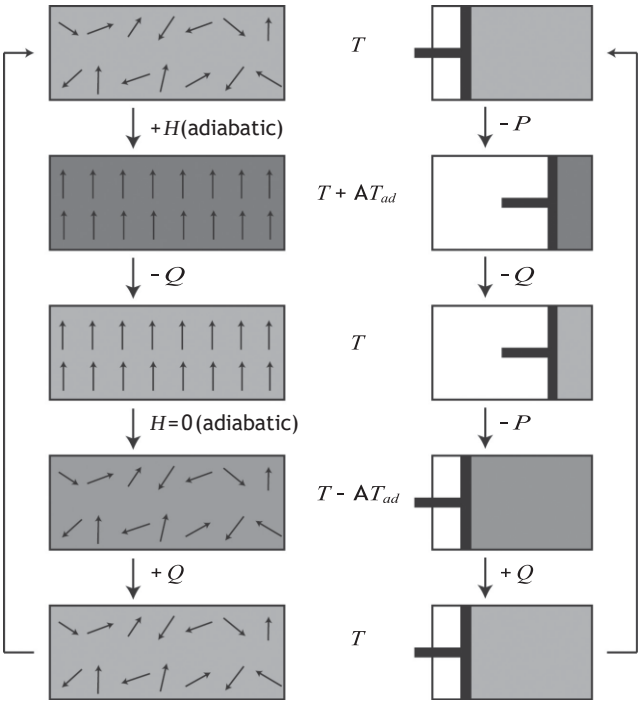


FIGURE 18.1

The general process of magnetic refrigeration as compared to gas systems.

When a conventional magnetocaloric material is reversibly subjected to a magnetic field change, the magnetic dipoles become more ordered. In practice, this can be observed by measuring the force on a substance in a nonuniform magnetic field. If the total entropy is to remain constant, adiabatic magnetization causes magnetic entropy to decrease, which results in an increase in temperature of the lattice. With the magnetic field still applied, the adiabatic condition is relaxed so that the material rejects heat and the temperature decreases. Next, an adiabatic condition is imposed, the magnetic field is then removed so that the magnetic order decreases, and the temperature decreases below its original value. Once again, the material is thermally coupled to absorb heat and the material returns to the original state, completing the cycle.

While all magnetic refrigeration cycles utilize the same basic steps, the actual cycle depends on the application (temperature span and cooling power) and available refrigerants. In addition, device geometries and heat transfer flow configurations can be quite different.

Although the MCE was hypothesized to exist by Kelvin [1] and measured by Weiss and Piccard [2] in 1918, magnetic cooling was not demonstrated until 1933 [3,4]. The idea of using the MCE for hydrogen liquefaction did not appear until the late 1970s.

The first applications of magnetic cooling were to produce sub-Kelvin temperatures with a *single-shot* process where the entire mass of refrigerant was brought to a uniform temperature and demagnetized. Larger amounts of material could cool more mass and maintain low temperatures for longer periods. For paramagnetic materials at low temperatures, the total entropy of the refrigerant is dominated by the magnetic entropy and, therefore, significant temperature changes are easy to produce. At higher temperatures,

the magnetic entropy change in a paramagnetic material becomes insignificant relative to the total entropy, making the temperature change small. The primary deterrent to high-temperature cooling was thought to be a lack of materials, which showed a signifi- cant temperature change when a moderate magnetic field (0–7 T) was applied.

In the mid-1970s, two important developments for magnetic refrigeration were reported by Brown: (1) a ferromagnetic material near its Curie temperature was used to produce a similar effect to that of the paramagnetic salts and (2) the limitations of the MCE were overcome using recuperation. Shortly after this work, the use of ferromagnetic materials for magnetic refrigeration in the range of 10 K to room temperature was described [5].

Brown demonstrated a magnetic refrigerator producing a temperature span of 47°C using gadolinium [6], and it was the first time that magnetic refrigeration was demonstrated at temperatures above 20 K. Brown's experimental testing was discussed by Steyert [7] who analyzed the reversibility of magnetic refrigeration. He concluded that continued prog- ress should allow for magnetic refrigeration to have higher efficiencies than existing gas-refrigeration technologies. Perhaps the most significant development for magnetic refrigeration at temperatures above 20 K was the idea of using the magnetocaloric material in the form of a regenerator. This idea was called an *active magnetic regenerator* (AMR) and was patented by Barclay and Steyert [8]. In addition to using regeneration, the AMR con- cept overcomes the limited range of a single magnetocaloric material by using a number of different materials in a layered structure. Similar to a passive regenerator, the solid matrix periodically exchanges heat with a fluid oscillating through the pores. Unlike a passive regenerator, however, the solid refrigerant is the working material that creates the tempera- ture distribution from the hot end to the cold end. Today, nearly all MR development above 20 K is making use of the AMR concept.

These initial papers subsequently led to several studies regarding magnetic materials, device design, and analytic studies of performance [9–12].

18.1.2 History of Magnetic Liquefaction of Hydrogen

The idea of using magnetic cycles for hydrogen liquefaction really started at the beginning of the 1980s. During 1982–1986, a number of related studies were performed by a group at Los Alamos National Laboratory [13]. The work was primarily funded by NASA and various offices in the US DOE. Hydrogen reliquefaction using a magnetic refrigerator was one application, and the development of a device operating between liquid nitrogen (LN_2) and liquid hydrogen was another. The latter was identified as having good commercialization potential due to the significant fraction of capital expenditures required for the 77–20 K range with conventional liquefiers [14]. A number of devices were designed, analyzed, and tested; details of those designed to work below LN_2 will be discussed later.

In 1991, Barclay summarized the status of magnetic refrigeration technology and discussed the future prospects for liquefaction of hydrogen [15]. This summary explained the technical aspects of magnetic refrigeration in addition to describing the thermody- namic advantages they have over conventional systems. The regenerator was identified as being the main design challenge to create a magnetic device spanning 300–20 K. This chapter concluded with a cost estimate of two different magnetic liquefiers operating from 77 to 20 K, indicating the potential for significantly lower cost than a gas-cycle device. In 1992, Janda et al. [16] reported the design of a 0.1 ton/day AMR refrigerator for liquefying hydrogen; this device was later analyzed by Zimm et al. [17] and Degregoria [18]. This study of this design was continued by Zhang et al. in 2000 in the form of an optimization study [19]. The most recent design and experimental unit was created by Kamiya et al. [20]

and Matsumoto et al. [21], which takes into account the actual condensation process of hydrogen using a Carnot magnetic refrigerator (CMR) stage.

The potential for magnetic refrigeration to be used in hydrogen liquefaction has made the 77–20 K range a focus for magnetic refrigeration. Multiple papers have now been dedicated to theoretical studies [22,23], numerical models [24–32], test devices [33–37], and review articles [38,39] in an effort to improve the process of hydrogen liquefaction and make magnetic liquefaction a competitive alternative to traditional gas expansion cycles.

The thermodynamics of the MCE is introduced in the following section and leads to a discussion of magnetic cycles.

18.2 Thermodynamics

This section discusses the fundamental theory and processes behind magnetic refrigeration. This includes the functional form for quantifying magnetic work, entropy, and specific heat. The basic cycles of magnetic refrigeration such as the Carnot, Stirling, Ericsson, and Brayton cycles are then reviewed. The AMR cycle is also described followed by a brief summary of some of the losses that limit magnetic cycle performance.

18.2.1 Magnetic Systems

The following sections review the fundamental thermodynamic quantities of a material with a reversible magnetic work mode. For simplicity, it is assumed that the material has no significant volume change, is homogenous and hysteresis-free, and has continuous spe- cific heat as a function of field and temperature. Materials that fit these assumptions well are some of the rare-earth elements and alloys and materials displaying a second-order magnetic phase change. A number of first-order materials have good potential as mag- netic refrigerants; however, their behavior tends to be more complicated than second-order materials. For those interested readers, more details on magnetocaloric materials can be found in the literature [40,41].

A challenge one encounters when dealing with magnetism, magnetic fields, and magnetocaloric materials is the wide range of units and potentials one can work with. Here we will work with the following symbols and magnetic quantities: B_0 is the flux density *applied* to a material and is considered to be due to the magnetic field, H_0, generated by a coil in free space. The magnetism of a material, M, is assumed to be a single-value function of temperature, T, and H. A significant amount of confusion (and error) can arise when discussing the magnetic field because the field *in* a body is generally not the same as the applied field and depends upon the shape of the material. The impact of shape on magnetization is often accounted for by a *demagnetizing* field, H_d. The local field determines the local magnetization, and the *local* internal field in a magnetic material is $H_i = H_0 + H_d$. Fields, fluxes, and magnetizations are vectors, but, for thermodynamic considerations, we will assume that all values are 1D.

18.2.1.1 Work

By strategically applying and removing a magnetic field to a magnetocaloric material, it is possible to develop a process that extracts heat from a cold environment and rejects it to a

hot environment. The act of magnetizing and demagnetizing a material parallels that of compressing and expanding a gas and, similarly, is achieved by a work interaction.

The first law of thermodynamics relates the energy change in a magnetic material to heat transfer and magnetic work:

$$du = dq + dw. \tag{18.1}$$

In the previous texts, the work and heat transfer are assumed to be *in* to the material system. A clear derivation of the appropriate generalized force and displacement for a magnetic system can be found in Appendix B of [42]. One can differentiate between work done by a power supply to generate a magnetic field and the work that changes the internal energy of the material. The latter is the magnetic work and the incremental value per unit volume of material is

$$dw = B_0 dM = \mu_0 H_0 dM, \tag{18.2}$$

where μ_0 is the permeability of free space. The applied field is analogous to the generalized force, and the magnetization (total magnetic moment per unit volume) is the generalized displacement. One can now see how the work done on magnetic material compares to that done in gas refrigeration by observing the fundamental relation of a simple compressible system:

$$du = dq - pdv. \tag{18.3}$$

Other potentials for magnetic systems can be derived using Maxwell's relationships [43,44].

18.2.1.2 Entropy

The entropy of a magnetic material can be introduced into Equation 18.1 by replacing the differential heat transfer with the entropy equivalent. The entropy of a simple magnetic material is a function of temperature and field strength, $s = s(T, H)$, and the differential change is

$$\underline{dq} = ds = \left(\frac{\partial s}{\partial T}\right)_H dT + \left(\frac{\partial s}{\partial H}\right)_T dH_0. \tag{18.4}$$
$$T$$

The first term in Equation 18.4 can be replaced using the definition of specific heat at constant field, c_H,

$$c_H \equiv \left(\frac{\partial s}{\partial T}\right)_H T. \tag{18.5}$$

The last term in Equation 18.4 can be written in terms of magnetization and temperature using Maxwell's relations,

$$\left(\frac{\partial M}{\partial T}\right) = \left(\frac{\partial s}{\partial \mu_0 \partial H}\right). \tag{18.6}$$

So, the variation in entropy due to temperature and field change is

$$ds = \frac{C_H}{T} dT + \left(\frac{\partial M}{\partial T} \right)_H \mu_0 dH_0. \tag{18.7}$$

Magnetization can be estimated by model calculations (i.e., molecular field theory) or by direct measurement.

The total entropy of the material can also be broken down into a summation of the lattice entropy (s_g), magnetic entropy (s_m), and entropy from conducting electrons (s_E):

$$s_{tot} = s_m + s_E + s_g. \tag{18.8}$$

Standard expressions can be used to quantify the lattice and electronic contributions to entropy (such as the Debye approximation for the lattice and quantum theory for a free-electron gas [45]). The isothermal change in magnetic entropy as a result of the applied magnetic field is determined by integrating Equation 18.7:

$$\Delta s_m(T,H) = \int_0^H \left(\frac{\partial M}{\partial T} \right)_H \mu_0 dH. \tag{18.9}$$

The isothermal magnetic entropy change is often called the MCE, but this is a derived quantity, whereas the adiabatic temperature change can be directly measured.

A reversible adiabatic process implies constant entropy; therefore, using Equation 18.7, the adiabatic temperature change can be calculated from specific heat and magnetization data as

$$\Delta T = -\int_0^H \frac{T}{C} \left| \frac{\partial M}{\partial T} \right|_H \mu_0 dH. \tag{18.10}$$

Thus, the dependence of adiabatic temperature change on magnetic entropy change is determined by the variation in specific heat with temperature.

The magnitude of the change in entropy, and the temperature change, is dependent upon the material and the operating temperature. At a certain point known as the Curie temperature, T_C, the MCE is a maximum. As a material is cooled below the Curie point, the material spontaneously magnetizes (orders) and displays properties similar to ferromagnetic materials. As the temperature rises above the Curie point, the dipoles become randomized again and the response to a magnetic field is more similar to a paramagnet. Every material has a distinct Curie temperature based upon its internal magnetic and crystal structure.

The relationship between adiabatic temperature change and isothermal magnetic entropy change for gadolinium is shown in Figure 18.2a. Gadolinium is a good prototype refrigerant ordering near room temperature. Figure 18.2b shows that the MCE decreases quickly as the temperature deviates from the Curie point. As will be discussed later, this

characteristic limits the use of magnetic cooling using traditional cycles.

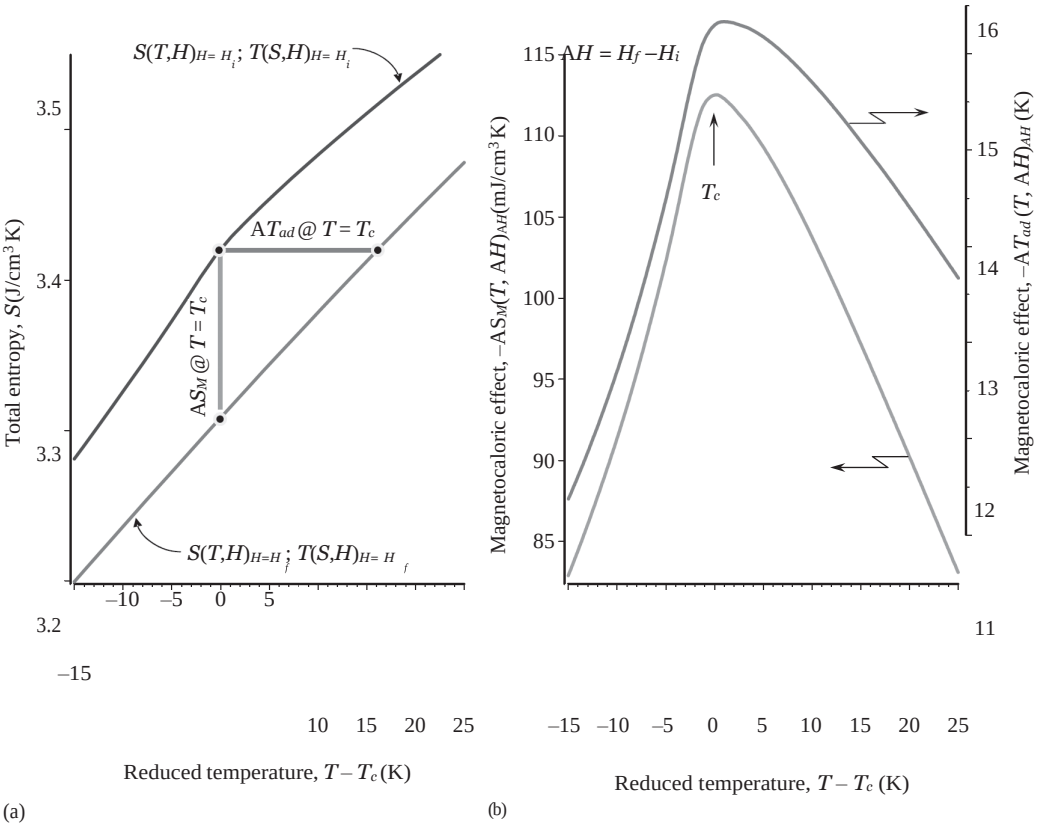


FIGURE 18.2

The total entropy for the initial and final magnetic fields (a) and the MCE (b) for gadolinium near the Curie temperature. (From Gschneidner, K.A., Jr., Pecharsky, V.K., and Tsokol, A.O., Recent developments in magneto- caloric materials, *Rep. Prog. Phys*., 68, 1479–1539, 2005. With permission from IOP Publishing Ltd.)

The impact of magnetization on specific heat can be shown using Equation 18.7. Noting that this is the total differential of entropy, the following result can be derived due to equivalence of the second partial derivatives [39]:

$$c_H(T, H) = c_0(T,0) + T\int_0^H \left(\frac{\partial^2 M}{\partial T^2}\right)\mu_0\, dH. \tag{18.11}$$

It can be seen that the heat capacity of the magnetic material is dependent upon the variation in magnetization with field and temperature. Near the Curie temperature, specific heat can be a strong function of field and temperature. This behavior complicates model- ing and optimal operating strategies.

An overview of magnetic cycles is presented in the following section. The cycle currently favored for magnetic refrigeration is an AMR. As no single material has the ideal properties for this type of process, there is a substantial research effort in the materials science community aimed at developing materials. Magnetic refrigerants for hydrogen liquefaction will be discussed following the overview of cycles.

18.2.2 Magnetic Refrigeration Cycles

Although all magnetic refrigeration processes make use of the same basic physical response, idealized processes can be defined depending upon how and when heat transfer

and field changes occur. This section will introduce the current cycles used in magnetic refrigeration processes and discuss the fundamental differences between them.

The primary cycles used with fluids are the classical thermodynamic cycles, that is, Brayton, Ericsson, and Stirling. Analogous cycles can be defined for magnetic solids where magnetization and field replace volume and pressure, respectively. The Carnot cycle quantifies the maximum performance of a cycle using isothermal heat rejection and absorption. An important consideration is that a Carnot cycle is not the most effi- cient process for gas liquefaction where sensible heat must be removed in addition to latent heat. This will become evident later when discussing proposed processes for hydrogen liquefaction.

18.2.2.1 Carnot Cycle

A magnetic Carnot cycle is composed of the four reversible processes shown in Figure 18.3:

1. (1–2): Adiabatic magnetization of the magnetic refrigerant
2. (2–3): Isothermal heat rejection
3. (3–4): Adiabatic demagnetization
4. (4–1): Isothermal heat addition

In adiabatic magnetization (1–2), the temperature of the material is increased isentropically due to an increase in the magnetic field. The magnetic field is then further increased while the magnetic refrigerant rejects heat to keep the material isothermal (2–3). In actuality, this continuous cooling effect would take a large heat exchanger and a large period of time, both of which are not ideal with respect to cost. With thermal isolation restored, the material is adiabatically cooled (3–4) by partially removing the magnetic field. The final step absorbs heat while simultaneously reducing the magnetic field (4–1).

In Figure 18.3, the net magnetic work, w, required in the cycle is equal to the area of the T-s diagram bounded by (1–2–3–4). Similarly, the cooling capacity, q_c, is the area underneath

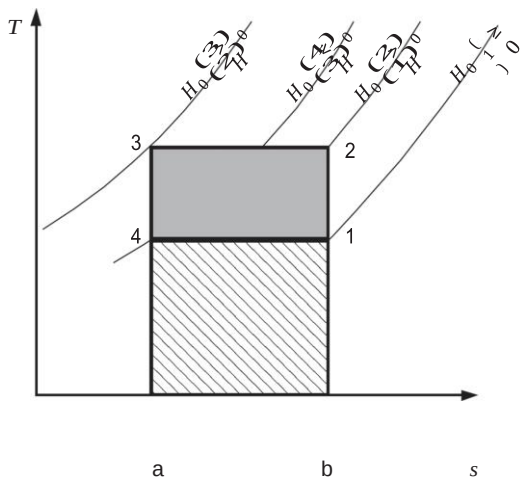


FIGURE 18.3

The Carnot cycle for a magnetic refrigeration application. (From Kitanovski, A. and Egolf, P.W., *Int. J. Refrig*., 29, 3, 2006. With permission.)

the Carnot cycle, which is (a–b–1–4). The coefficient of performance (COP) that describes the *efficiency* of a refrigerator can then be found:

$$\mathrm{COP}_R = \frac{q_c}{w} = \frac{T_1}{T_2 - T_1}. \tag{18.12}$$

This COP acts as an upper bound for the other refrigeration cycles as each of the four processes is reversible. Since isothermal processes are used, the cooling capacity per unit work is maximized. A disadvantage of the isothermal processes, however, is the reduced temperature spans available for a given magnetic field as compared to other cycles. This can be seen by considering Figure 18.2. The maximum span of a Carnot cycle is constrained by the total entropy curves at high field and low field. In the case of gadolinium using a high field, a Carnot cycle could only operate over spans on the order of 10 K.

18.2.2.2 Brayton Cycle

The Brayton cycle is a more practical cycle for substances not utilizing a first-order phase change as, in practice, it is easier to do. This cycle is composed of two adiabatic processes and two processes where heat is transferred under a constant magnetic field. This is summarized as follows:

(1–2): Adiabatic magnetization
(2–3): Heat rejection with a constant magnetic field, $H_0^{(2)}$
(3–4): Adiabatic demagnetization
(4–1): Heat addition with a constant magnetic field, $H_0^{(1)}$

A *T-s* diagram of the ideal magnetic Brayton cycle is provided in Figure 18.4. This ideal cycle ignores the irreversibilities associated with each process.

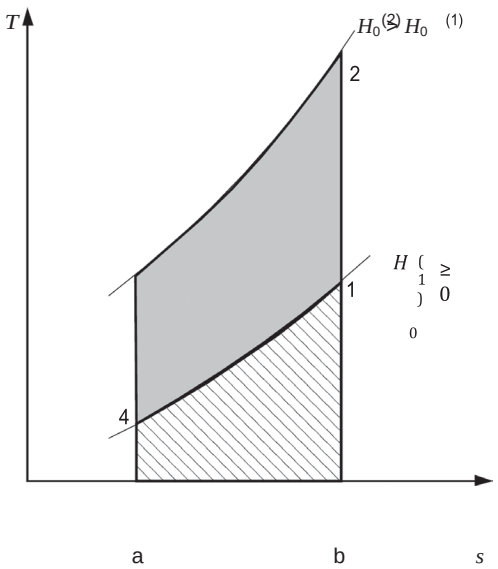


FIGURE 18.4

The Brayton cycle for a magnetic refrigeration process. (From Kitanovski, A. and Egolf, P.W., *Int. J. Refrig*., 29, 3, 2006. With permission.)

The work done by the magnetic material can be found by calculating the area defined by the process (1–2–3–4) while the heat removed from the working fluid is equal to the area under the cycle (a–b–1–4). In actual cycles, losses of efficiency will occur in the adiabatic magnetization (1–2) and demagnetization (3–4) processes due to an irreversible entropy change.

In theory, with an equivalent effective temperature span, the magnetic Brayton cycle sacrifices efficiency as compared to Carnot. Less heat is absorbed per cycle and more work is inputted; however, this neglects thermal resistances between the heat sinks in a Carnot cycle. For a material like gadolinium with a 10 T field change, the temperature span is about 15–20 K compared to the 5–10 K/10 T temperature change for the Carnot cycle [6]. This is because the heat transfer is done with a constant magnetic field instead of isothermally, resulting in a larger change in the magnetic field in the isentropic processes. A larger temperature range could be obtained by maintaining the isothermal processes of the Carnot cycle but regenerating heat under a constant magnetic field; this is the foundation for the Ericsson and Stirling cycles.

18.2.2.3 Ericsson and Stirling Cycles

The Ericsson and Stirling cycles are very similar to one another from an energy standpoint. These cycles both utilize the isothermal heat transfer of the Carnot cycle and both require heat regeneration to be considered ideal. The adiabatic magnetizing and demagnetizing of the material is however replaced by a constant magnetic field strength, H, in the Ericsson cycle and constant magnetization, M, in the Stirling cycle. The Ericsson cycle is summarized in the following and a T-s diagram of the ideal process with heat regeneration is in Figure 18.5:

(1–2): Heat addition with a constant magnetic field, $H_0^{(1)}$

(2–3): Isothermal heat rejection to working fluid

(3–4): Heat rejection with a constant magnetic field, $H_0^{(3)}$

(4–1): Isothermal heat addition from working fluid

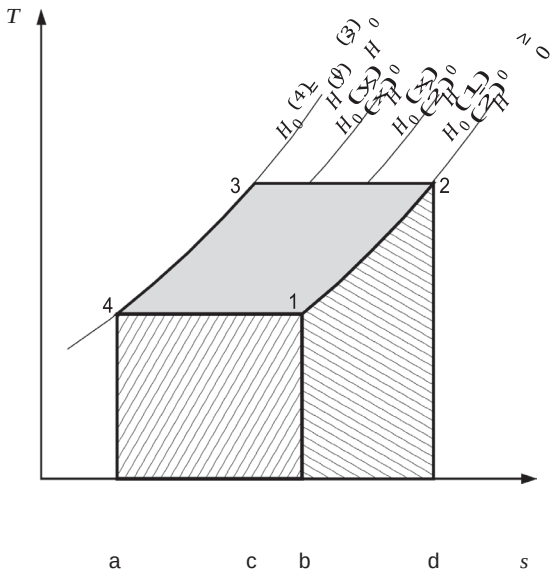


FIGURE 18.5

Magnetic Ericsson cycle for a magnetic refrigeration process. (From Kitanovski, A. and Egolf, P.W., *Int. J. Refrig.*, 29, 3, 2006. With permission.)

The magnetic work in the cycle is again equal to the confined area (1–2–3–4). The area (b–d–2–1) represents the regeneration heat that must be absorbed by the magnetocaloric material. In the ideal case, this area is equal to the heat rejected by the material (a–c–3–4). Since heat transfer is an irreversible process, however, this regeneration of the magnetic material reduces the overall efficiency of the cycles. The area (1–4–a–b) represents the cooling capacity of the Ericsson cycle.

The Ericsson and Stirling cycles are similar; the temperature span is greater than the Carnot cycle and, in the case of ideal regeneration, the Ericsson and Stirling cycles have a COP equivalent to that of the Carnot cycle. An important point to note for all of the cycles discussed so far is that all of the working material follows the same cycle. This is a subtle point but is important in understanding the AMR cycle that follows.

In theory, regeneration can provide high efficiencies and increased temperature spans; however, implementing this with magnetic refrigerants is not easy. Because the working substance is a solid, it is difficult to effectively couple the body to an external thermal storage medium that maintains a temperature distribution between the hot and cold reservoirs. Even if this can be solved, the refrigerants themselves have nonideal properties such that different amounts of heat need to be regenerated between the cooling and warming phases. These considerations were part of the reasoning that lead to the AMR cycle whereby the refrigerant itself is a regenerator linked to hot and cold reservoirs by a heat transfer fluid.

18.2.2.4 Active Magnetic Regenerator Cycle

The process currently employed in magnetic refrigeration cycles above 20 K is the AMR. The Brayton, Ericsson, and Stirling cycles all require high-quality regeneration to be efficient enough for magnetic refrigeration units to be competitive compared to vapor-compression units. The AMR cycle provides this by using the magnetic material itself as a regenerator that is in direct contact with the heat transfer fluid. Passive regenerators are used in various devices to increase the operating span. By using the working material itself as the thermal storage medium, the regenerator is said to be active [22]. A stepwise representation of the AMR process is shown in Figure 18.6. A schematic indicating the cycle-average temperature distri- bution and heat and work interactions at a location in the regenerator is shown in Figure 18.7. The cycle is assumed to be in periodic steady state so that the temperature distribution is a stationary periodic function in time. The refrigerant is made to be a porous solid with a large surface area per unit volume. A heat transfer fluid flows in the pores, oscillating between the cold and hot reservoirs in synchronization with the magnetic field waveform. The steps begin with the regenerator being magnetized so that the local temperature of the solid increases due to the local MCE. Fluid is then blown from the cold side to the hot side absorbing energy from the matrix and exiting at a temperature above that of the warm reservoir. As a result, heat is rejected in the warm heat exchanger. The fluid flow stops, the magnetic field is removed, and the temperature decreases at all points due to the MCE. The temperature of solid material at the cold end is now less than it was when the cycle began. Fluid now flows through the bed in the opposite direction, exiting at a lower temperature such that heat will be absorbed from the cold reservoir. The fluid flow stops, the bed is remagnetized, and the cycle begins again.

The solid refrigerant acts as a regenerator to the heat transfer fluid. At one point in the cycle, the regenerator removes heat from the fluid, while at a later point, this heat is returned and an additional amount of energy is added due to magnetic work. This increases the fluid temperature exiting the hot end of the regenerator so that heat

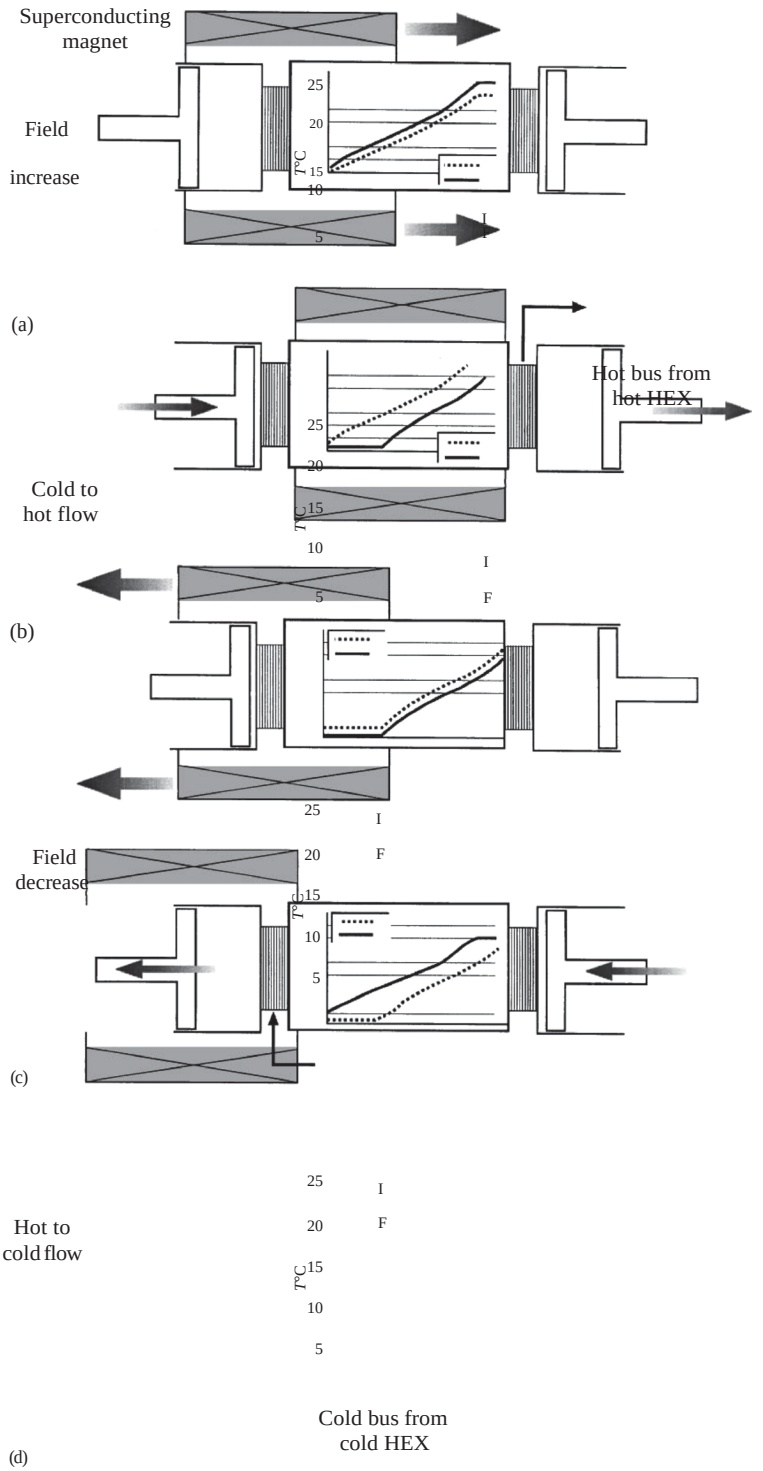


FIGURE 18.6

A stepwise representation of an AMR cycle. (a) Magnetization, (b) magnetized fluid flow from the cold side to the hot side, (c) demagnetization, and (d) fluid flow from the hot to cold side. (From Pecharsky, V.K. and Gschnieder, K.A., Jr., *J. Magn. Magn. Mater.*, 200, 44, 1999. With permission.)

can be rejected to the warm reservoir. The heat flux from the cold end to the warm end, Q, varies with position in the regenerator. Integrated over the entire bed, the total work input will balance the net heat transfer. An AMR can use a single material as the regen- erator or a combination of different materials. Using multiple materials complicates the regenerator design process but allows for a larger temperature span to be created between the hot and cold reservoirs.

Determining the optimal composition, structure, matrix geometry, and operating conditions of an AMR is an active area of research. The highly nonlinear properties of

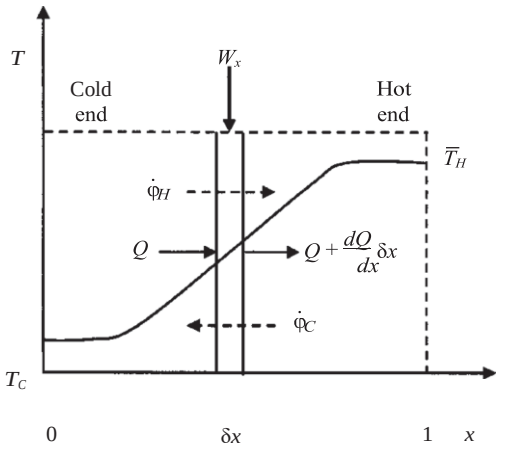


FIGURE 18.7

Temperature distribution in an AMR regenerator. (From Rowe, A.M. and Barclay, J.A., *J. Appl. Phys*., 93, 1672, 2003. With permission.)

both first- and second-order materials make this a complex problem. Simplified analyses provide some guidance regarding the ideal MCE and flow conditions that satisfy the macroscopic entropy balance on a regenerator [48,49]. When the field-dependent specific heat of a refrigerant is taken into consideration, the ideal MCE as a function of temperature, $\Delta T(T)_{ideal}$, is given by

$$\Delta T(T)_{ideal} = \left(\Delta T_{ref} + T_{ref}\right)\left|\frac{T}{T_{ref}}\right|^{\sigma} - T, \tag{18.13}$$

where σ is the ratio of specific heat at low field to that at high field and the subscript *ref* indicates the MCE at a reference temperature, T_{ref}. For this equation to be valid, the fluid thermal capacity ratio must also equal the specific heat ratio [48].

Although the temperature span is increased significantly with an AMR cycle and multiple refrigerants, a single AMR stage may not be enough to operate between 20 and 300 K. A number of AMR units can be arranged together to span large temperature differences, to increase cooling power, or to better match cooling to the enthalpy change of a fluid like hydrogen. In a series configuration, the cold reservoir of a warmer stage is also the hot reservoir of a lower-temperature stage. In a parallel configuration, one AMR stage precools hydrogen going to another stage with both stages rejecting heat to the same reservoir [50]. Because each stage in an overall liquefaction system may have different cooling loads and operating temperatures, an assortment of magnetocaloric materials are required. This adds a degree of complexity in the optimization of an entire liquefaction unit, in addition to added capital costs for building several AMRs. Irreversibilities resulting from various effects can also compound making minimization of entropy generation and losses in magnetic refrigeration an important exercise [23].

18.2.3 Regenerator Design

Magnetic liquefaction of hydrogen, like any process, contains irreversibilities. These irre-

versibilities reduce the efficiency of converting magnetic work into refrigeration, making

the overall process require more energy. Sources of inefficiency include nonideal materials, imperfect heat transfer, flow losses, eddy currents, and parasitic heat leaks in the device and from the environment.

Assuming suitable magnetic refrigerants are used, magnetic refrigerators using the AMR cycle require effective heat transfer. Regenerative heat transfer between the solid matrix and the fluid is done through direct contact, while transfer to the external res- ervoirs is through heat exchangers. If a single AMR stage is operating over a large tem- perature span, the impacts of imperfect convective heat transfer in the regenerator can be significant. In theory, because the cooling power of a device can be increased with the cycle frequency, there is a need for larger convective transfer rates. Optimizing regenerator structure and operating parameters using entropy generation minimization has also been performed on AMRs [51,52].

Regenerative heat transfer also requires careful design of the regenerator matrix so that the characteristic dimension of the structure is sufficiently small to ensure the material is being fully utilized [53]. Transfer of energy from the regenerators depends upon the solid thermal conductivity and specific heat. Higher conductivities allow for faster energy transfer to the working fluid, which reduces the time for parasitic heat leaks. Thermal diffusivity in the solid is linked to the operating frequency of an AMR through the Fourier number [54]. This plays an important role in optimized designs as the cooling capacity and losses of a system depend upon operating frequency. As discussed by Zhang et al., an optimum frequency exists, which minimizes the overall exergy destruction [23].

Other losses that contribute to decreased efficiency are flow losses and eddy currents. For a regenerator to have good thermal effectiveness, a large wetted area per unit volume is desired; however, this can lead to larger pumping powers needed to oscillate fluid through the structure. This problem becomes more significant as operating frequency increases. Eddy currents arise in conductors subjected to time-varying magnetic fields and are dissipated as heat due to resistance in the material. This problem scales with the square of the rate of field change [55]. Careful design choices and the use of materials with low electrical conductivity can minimize this problem. In the case of regenerators, spherical particle beds are common for the matrix, and, because of small size and point contacts between the particles, eddy-current losses can be small for typical operating frequencies [56].

18.3 Magnetocaloric Materials

Materials exhibit the MCE to varying degrees and single materials are only effective within a limited temperature range. This is one of the main challenges to developing commercial magnetic devices. A material with a wide operating range and a large MCE should reduce the required magnetic field strength while maintaining efficiency. This can benefit cost and relax some of the design constraints. For these reasons, devel- oping and characterizing magnetocaloric materials is an integral part of improving magnetic refrigeration and facilitating the use of magnetic cycles for hydrogen liq- uefaction [57]. This section briefly discusses refrigerants, desirable properties, and materials relevant to hydrogen liquefaction and their operating range. This overview will be brief as the subject of materials is vast; the reader is encouraged to explore the literature for more details.

18.3.1 Requirements for an Effective Refrigerant

The choice of materials to use within a given cycle is still open to debate. In recent years, first-order materials have received a significant amount of attention due to large mag- netic entropy changes using materials that are less expensive than rare-earth elements and intermetallic compounds on the basis of equivalent volume. Hysteresis tends to be significant in many of these materials and the width of the ordering transition in terms of temperature can be narrow.

18.3.1.1 Refrigerant Capacity

There are many properties that can be used to characterize refrigerants. Manufacturability, cost of materials and processing, toxicity, ductility, and a range of thermal properties can be considered. The most important are those that determine the ability to produce useful cooling efficiently; if this cannot be substantiated, the remaining properties are irrelevant. In terms of the AMR cycle, the ideal scaling of adiabatic temperature change with temperature has already been discussed. A general parameter used to characterize any refrigerant absorbing and rejecting heat isothermally is the refrigerant capacity (RC) as defined by Wood and Potter [57],

$$\mathrm{RC} \equiv \Delta S \Delta T_{sp},$$

where, in a reversible cycle, the isothermal entropy change, ΔS, is the same for hot and cold heat transfer processes and ΔT_{sp} is the temperature span. For a magnetic refrigerant, the magnetic entropy change as a function of temperature determines the maximum span and feasible operating points. For any magnetic refrigerant and applied field, a maximum value of RC can be determined. This parameter is useful in comparing magnetocaloric materials as it relates useful cooling to field strength on a volumetric basis. All other properties being the same, a material with a broad transition and large entropy change will have better potential as a refrigerant than one with a narrow transition and small entropy change.

A modified version of RC is used by Gschneidner and Pecharsky to compare materials [58]. They define a relative cooling power (RCP) in terms of the magnetic entropy change (RCP(S)) or the adiabatic temperature change (RCP(T)). The method is similar to [57]; however, to simplify things, they use the temperature span defined by the respective curve (entropy change or adiabatic temperature change) at half the maximum value, δT_{FWHM}. The RCP values are normalized by the applied field strength so that RCP(S) has units of energy per unit volume of refrigerant per unit field, that is, J/cm^3/T. A subset of materials for use in the 20–80 K range are listed in Table 18.1 [58].

One interesting fact to note in Table 18.1 is the magnitude of the adiabatic temperature change per unit field change. These values are on the order of 1 K/T and are the primary reason why a pure magnetic stage for hydrogen liquefaction requires superconducting magnets and highly effective regenerator designs.

The shapes of magnetic entropy curves as a function of temperature for various materials active below 100 K are shown in Figure 18.8. As can be seen, there tends to be a trade-off between the maximum entropy change and the width of the transition. While some materials have larger entropy spikes, they are only effective within a short temperature range. For example, $ErCo_2$ produces a large entropy spike around 35 K but becomes ineffective within 5 K in either direction, while $GdNi_2$ has a lower maximum entropy change but is effective

TABLE 18.1

Magnetocaloric Properties and Curie Temperatures for Materials with a Single Magnetic Transition

Material	T_C or T_{max}	$-\Delta S$ (mJ) ΔH (cm³KT)	$-\text{RCP}(S)$ (mJ) ΔH (cm³T)	ΔH(T)	ΔT_{ad} (K) ΔH (T)	RCP(T) (K²) ΔH (T)	$\sqrt{\Delta H}$(T)
$(Dy_{0.1}Er_{0.9})Al_2$	17.7	39.2	785	5	1.55	52.7	10
$DyNi_2$	20.5 ± 1.5	42.4	959	5	1.64	38.5	5
Gd_2PdSi_3	21	13.9	599	8	1.09	40.2	8
$(Gd_{0.14}Er_{0.86})Al_2$	24	—	—	—	1.27	53.4	7
$(Dy_{0.25}Er_{0.75})Al_2$	24.4	28.1	843	5	1.37	58.9	10
25–50 K							
$HoAl_2$	30 ± 3	39.0	1010	4	1.50	—	8
GdNiGa	30	24.0	839	9	1.17	50.4	9
$(Dy_{0.4}Er_{0.6})Al_2$	31.6	25.6	1070	5	1.25	68.8	10
$NdMn_2Si_2$	32	—	—	—	1.40	16.8	6
$(Dy_{0.5}Er_{0.5})Al_2$	38.2	25.2	909	5	1.26	68.0	10
GdPd	39 ± 1	—	—	—	1.36	32.6	5
$(Dy_{0.55}Er_{0.45})Al_2$	40.8	25.1	902	5	1.25	66.2	10
$ErCo_2$	44	45.0	770	7	1.69	21.1	7
$(Dy_{0.5}Ho_{0.5})Al_2$	46	26.6	839	—	—	—	—
$(Dy_{0.7}Er_{0.3})Al_2$	47.5	23.1	900	5	1.2	69.6	10
50–100 K							
$(Dy_{0.85}Er_{0.15})Al_2$	55.7	22.9	963	5	1.15	74.8	10
$DyAl_2$	63.9	22.0	951	5	1.10	73.7	10
GdNi	71	—	—	—	1.06	46.8	7
$GdNi_2$	72	19.6	861	7	0.83	40.1	7
$HoCo_2$	82	32.0	831	7	0.85	14.4	6
GdNiIn	94	13.9	1180	9	0.74	71.4	9

Source: Gschneidner, K.A., Jr. and Pecharsky, V.K., Magnetic refrigeration, Chapter 25 of *Intermetallic Compounds: Vol. 3, Principles and Practice*, John Wiley & Sons, New York, 2002.

over a wide temperature span. Based on the RCP(S) values listed in Table 18.1, $GdNi_2$ has a better potential as a refrigerant. The use of GdNi and $GdNi_2$ in the AMR cycle operating between 20 and 80 K for hydrogen liquefaction was discussed by Zimm et al. [17].

As discussed previously with the AMR concept, one way to utilize materials with larger spikes, but narrow transitions, is to use regenerators that contain multiple materials. This allows for the overall entropy change to remain relatively constant over a broad temperature span. However, regenerators composed of more than one material become difficult to model theoretically and numerically. With this in mind, several test devices and models have been developed with the intent of testing and understanding the properties of AMRs specifically in the 80–20 K range [22,24,26,27,31,33–36,60].

18.3.1.2 Tailoring Properties

Another useful property for a magnetic refrigerant is the ability for its Curie temperature to be shifted by altering its composition. This allows a material to be used in a specific

temperature range that may lack quality refrigerants or ones that are easy to work with. Furthermore, a less expensive material might be able to replace the operating region of a more expensive refrigerant.

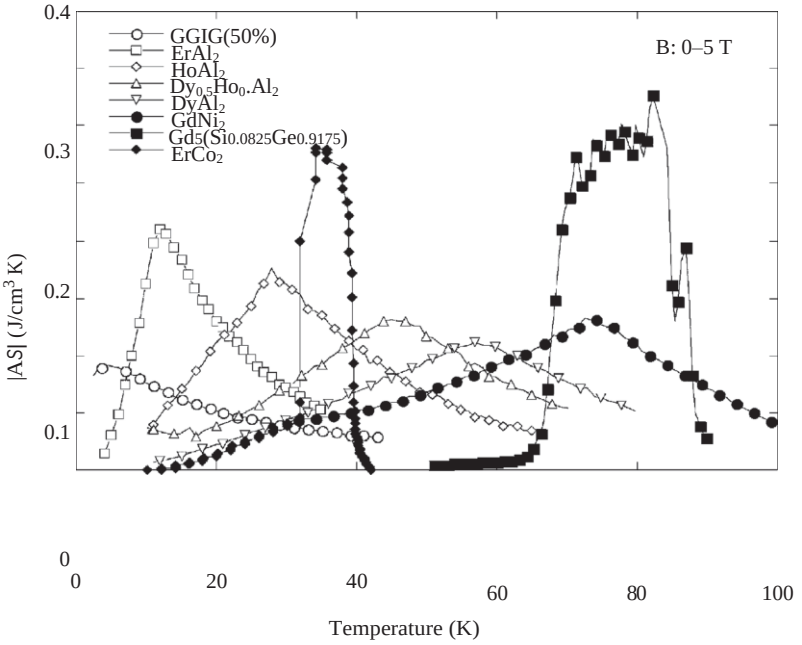


FIGURE 18.8

The entropy change of various materials over a range of temperatures. (From Sakata, K. et al., *J. Power Sources*, 159, 100, 2006. With permission.)

An example of a tunable alloy is $Gd_5(Si_xGe_{1-x})_4$—the ordering temperature increases with Si content. The $x = 0.0825$ composition is shown in Figure 18.8. (Note: the label in the legend is missing the subscript 4.) Matsumoto et al. characterized the magnetization and entropy change of this alloy with a range of compositions specifically for use in hydrogen liquefaction [61]. While large entropy changes were measured, they also noted hysteresis, which is an irreversibility that may have a significant impact on performance. Rare-earth alloys such as Gd_xEr_{1-x} are also tunable while maintaining good magnetocaloric properties.

One other avenue for creating a regenerator with desired properties is to produce a composite material that is a mixture of refrigerants [62–64]. This has been examined experimentally and theoretically for low- and high-temperature AMRs. One study of particular relevance for hydrogen liquefaction involved the creation of a composite material with a relatively uniform and broad magnetic entropy change below 80 K [63]. Creating a composite may create a better magnetic entropy curve; however, it will also create irreversibility due to heat transfer between particles.

18.3.2 AMR Performance

The consequences of material properties, regenerator composition, and operating parameters are discussed in a paper by Matsumoto et al. where an AMR hydrogen liquefaction unit operating from 77 to 20 K is analyzed numerically [26]. In the case of a single material AMR, the impacts of the working fluid's mass flow on the cooling capacity of the refrigerator are determined. It is found that both low and high mass flows reduce the cooling capacity while an intermediate value provides an optimum cooling capacity. The effect of using materials with different Curie temperatures is also assessed while maintaining the hot reservoir at 77 K and varying the overall temperature span of the bed. For materials with Curie tempera- tures of 60 K (Tc60), 70 K (Tc70), and 80 K (Tc80), each material appears beneficial in a differ-

ent aspect. The Tc80 material provides the highest COP value, the Tc70 material provides the highest cooling capacity, and the Tc60 material has the smallest COP and cooling capacity.

Evaluating the results for the high cooling capacity of Tc70 reveals that this material exhib- its the largest average entropy change within the 60–77 K region, which is similar to the oper- ating temperature region. From this, it is deduced that the highest cooling capacity comes when a material provides the largest average entropy change within the operating region of the AMR. Therefore, although the Tc60 had the largest peak entropy change, its entropy change throughout the entire operating temperature range of the material bed was poor compared to the Tc70 material. This is consistent with the RC method of ranking materials. These results also support the idea that using multiple materials for the regenerator in the AMR could be more beneficial than one material. Since the temperature of the refrig- erant bed is distributed as shown in Figure 18.7, using multiple materials allows for each material in the bed to operate closer to its Curie point and the maximum entropy change. Matsumoto et al. analyzed the effect of two-layered AMR beds with different quantities of the Tc60 and Tc80. It was found that the highest cooling capacity is obtained when the material bed is 30% Tc60. The COP however decreased with an increasing percentage of the lower Curie temperature material giving rise to the notion that the high-temperature side plays an important part in reducing the irreversibilities of the cycle [26].

18.3.3 Refrigerant Selection

A large number of materials have been discovered that are potentially useful as mag- netic refrigerants. Table 18.2 shows a list of some magnetic refrigerants and their Curie

TABLE 18.2

Curie Temperatures for a Variety of Magnetocaloric Materials

Material	T_C (K)	Reference	Material	T_C (K)	Reference
$GdMn_2$	300	[65]	$Gd_5(Si_{0.0825}Ge_{0.9175})$	75	[66]
Gd	293	[66]	GdN	65	[65]
$Gd_{0.9}Y_{0.1}$	281	[65]	$DyAl_2$	63	[66]
GdZn	268	[65]	$Gd_{025}Er_{0.75}$	60	[67]
$Gd_{0.73}Dy_{0.27}$	266	[66]	$Gd_{2.8}S_4$	58	[65]
$Gd_{0.8}Y_{0.2}$	254	[65]	$GdAg_{0.7}In_{0.3}$	57	[65]
$Gd_{0.36}Dy_{0.64}$	234	[66]	$Gd_{0.2}Er_{0.8}$	51	[67]
$GdZn_{0.85}In_{0.15}$	224	[65]	$Gd_{0.7}Th_{0.3}Al_2$	50	[65]
$Gd_{0.67}Y_{0.33}$	211	[65]	$Dy_{0.7}Er_{0.3}Al_2$	45	[66]
GdGa	200	[65]	$Gd_{2.76}S_4$	42	[65]
$Gd_{0.18}Dy_{0.82}$	195	[66]	$Gd_{0.139}Er_{0.861}Al_2$	40	[67]
$Gd_{0.7}La_{0.3}$	185	[65]	$GdNi_2$ (amorphous)	38	[65]
Dy	180	[66]	$Dy_{0.5}Er_{0.5}Al_2$	38	[66]
$GdAl_2$	153	[65]	$Gd_{0.1}Er_{0.9}Al_2$	33	[67]
$Gd_{0.8}Au_{0.2}$	150	[65]	$GdNi_5$	32	[65]
Gd_5	135	[66]	$Gd_{0.65}Th_{0.36}Al_2$	30	[65]
$Gd_{0.68}N_{0.32}$	125	[65]	$Gd_{2.73}S_4$	28	[65]
$Gd_5(Si_{0.225}Ge_{0.775})_4$	120	[66]	$GdAg_{0.8}In_{0.2}$	24	[65]
$GdAg_{0.5}In_{0.5}$	111	[65]	$Dy_{0.25}Er_{0.75}Al_2$	24	[66]
$Gd_{0.5}Ag_{0.5}$	100	[65]	$Gd_{2.71}S_4$	21	[65]
$Gd_{0.8}Th_{0.2}Al_2$	90	[65]	$Gd_{0.028}Er_{0.972}Al_2$	20	[67]
$Gd_5(Si_{0.15}Ge_{0.85})_4$	90	[66]	$ErAl_2$	12	[66]

$GdNi_2$ (crystalline)	81	[65]

temperatures. This list is not exhaustive but provides a good spread of materials from room temperature to the hydrogen boiling point.

Table 18.2 demonstrates the need for a wide range of refrigerants required to liquefy hydrogen from room temperature. Even if one material could be used for every 20 K temperature span, a minimum of 14 different materials would still be required. When considering the different combinations of materials that are possible, the design of a full magnetic liquefaction process from 300 K is complicated. Alternatively, hydrogen can be precooled by liquid natural gas (LNG) (112 K) or LN_2 (77 K) resulting in the use of fewer materials to reach liquid hydrogen. Given the challenge of a magnetic device operating between room temperature and liquid hydrogen, most designs have focused on a hybrid liquefier that used a conventional cycle to LN_2 and a magnetic stage(s) operating below 80 K. These low-temperature magnetic devices will be discussed in the following section.

18.4 20–80 K Magnetic Refrigeration Devices

A number of cryogenic devices have been developed to specifically test materials and operating parameters in the 80–20 K range. While not meant to be liquefiers, these devices were usually part of a liquefier development path, and results were used to assist in determining preferred configurations for magnetic stages operating below a LN_2 upper stage. Other devices have been developed to operate below 20 K using LH_2 as an upper heat sink or even below 4 K with LHe as the hot reservoir. Near-room-temperature MR is another active application area with device development activities. These devices will not be discussed further; instead, we will focus on those devices specifically relevant to LH_2 liquefaction. A discussion of some important design considerations for magnetic devices follows.

18.4.1 Design Considerations

Some unique considerations arise when building devices utilizing magnetic fields. To maximize cooling power, magnetic fields are as high as practically possible. Constraints on this arise due to magnetic forces which, in some cases, also restrict operating frequency. Another consideration is sealing and one must decide if the regenerators are to have static or dynamic seals. Because superconducting magnets can be expensive, simple designs are preferred. The desire to use solenoid coils instead of complex windings leads to device geometries built around the magnet field shape and ability to access the high field region.

18.4.1.1 Forces

Structural forces between current-carrying elements are present in systems using coil magnets (Lorentz forces); however, these are ignored as they typically concern the magnet design. The following discussion focuses on the forces related to magnetic work input.

A magnetic cycle requires cyclic application of a magnetic field waveform. This can be done in three ways: (1) fix a material and then charge and discharge a coil, (2) use a static field and move the AMR in or through the field, and (3) fix the AMR and move the field. The last two nearly are equivalent in theory, but differences arise due to the ability to create a semicontinuous regenerator structure and the appearance of a relatively con- stant permeability in the field region. Charging a coil is undesirable because of frequency

limitations and the additional power flows required due to the changing energy in the field. Some common configurations used are reciprocating AMRs and rotating structures housing regenerator beds. An analysis of force modeling for these two types of geometries was reported by Barclay et al. [68]. It was found that reciprocating geometries using single high field regions resulted in large unbalanced magnetic forces. This leads to an increase in structural and drive system ratings for these geometries. In the case of a rotating wheel regenerator structure, although there is good force balancing due to relatively constant permeability in the field region, there is however a radial force that must be designed for. An analysis of dynamic forces on a reciprocating AMR device is reported in [69]. Part of this work examined the use of a passive energy storage mechanism to reduce the size of a drive motor by damping out the reversing, unbalanced forces on the moving AMR structure. While reductions in torque were possible, the frequency of the torque waveform doubled and dynamic tuning would be needed.

A magnetic material in a field gradient will also have a net force. Magnetocaloric materials are subjected to magnetic forces when they are moved from regions of low field to high field, and the force depends upon the state of the material and the field variation in space. Forces on a refrigerant below the Curie temperature are higher than those above the Curie temperature. Regenerator matrix structures are often particle beds but can take various shapes. The matrix elements will be subjected to magnetic body forces that vary with location in the matrix and time. This can also create shear stresses and cyclic loading. Assuming the refrigerant is not too brittle, one of the main concerns with a particle bed is the movement and migration of particles. It is important that the solid matrix maintain its structure so that preferential flow paths do not arise and that the property distribution through the bed is as intended. Monolithic structures have advantages, but they can be difficult to make with large specific surface areas. One idea for creating a single structural element using particles is to bond them together [70]. This idea has been experimentally tested and does seem to work; however, because of the very small hydraulic diameters of the AMRs, creating the structure without affecting the homogenous nature of the void distribution is difficult. Another approach is to use sintered particle beds; however, maintaining material properties and eddy-current generation are concerns for this technique. Discrete microstructured elements can also be fabricated and used to create a larger regenerator and is a technique now being used.

18.4.1.2 Flow

The AMR concept requires effective regenerators in which the fluid–solid heat transfer occurs with small temperature differences. This must be balanced against pumping power requirements due to pressure drops through the regenerator and remaining fluid system. The regenerator is the element separating warm and cold temperature regions and must act as a thermal resistance between the reservoirs. These requirements come with trade- offs as good convective heat transfer often comes with small hydraulic diameters, which lead to higher pressure drops. No matter how oscillating flow is created and controlled, there will be a need for good sealing around the regenerator structure.

As with magnetic forces, the choices made in creating a magnetic field waveform for the refrigerant are linked to sealing requirements. Some designs can use static seals while others need dynamic seals. The latter are, of course, more challenging. Ideally, the void space in a regenerator is small and fluid flows uniformly through the matrix. Preferential channeling or leaks around the regenerator between the temperature reservoirs should be prevented. While rotating regenerator structures simplify the magnetic forces and

structural and drive system requirements, they usually have dynamic seals between the moving regenerators and the stationary housing. A good dynamic seal may impose additional losses due to friction. Dynamic seals must also be able to operate over long periods at cryogenic temperatures.

When using magnetic refrigeration stages for liquefaction, ideally, sensible heat is removed from hydrogen at a number of intermediate temperatures. However, sensible cooling can also occur using a portion of the cold AMR heat transfer fluid bypassing the regenerators and, instead, absorbing energy from the hydrogen stream through a heat exchanger [71]. Not only does this reduce entropy generation in cooling the hydrogen gas, it can also help to thermally balance the regenerator. This latter effect arises due to the difference in heat capacity of the refrigerant between high and low fields. As will be seen later, bypass flow configurations have been implemented in the design of staged magnetic liquefiers.

18.4.1.3 Parasitic Magnet Load

An unavoidable parasitic load for magnetic refrigeration systems using superconduct- ing magnets arises from the need to maintain the magnet at operating temperature. The needed cooling power can be relatively small as magnets can be operated in persistent mode, which means the power supply for the field is no longer needed. The parasitic load is then dominated by heat leaks to the magnet. The impacts of magnet cooling have been studied and results show that the impact on efficiency depends upon the operating tem- perature of the magnetic refrigerator and the cooling power of the device [72]. For low temperatures and high cooling powers relative to the magnet cooling requirement—as with hydrogen liquefaction applications—the impact of magnet cooling requirements can be very small. This study is now somewhat dated and had assumed a superconducting magnet operating at 4.2 K. Given recent progress using high-temperature superconduc- tors to build magnets, the impacts of magnet parasitic load may be even less of a concern, particularly for hydrogen liquefaction.

18.4.2 Cryogenic AMR Devices

Although designs for AMR devices for hydrogen liquefaction include reciprocating and rotary configurations, to date, all experimental devices operating between 80 and 20 K have been reciprocating. Experimental and theoretical results for some of these devices will be discussed.

The development of a test device designed to study magnetic refrigeration between 77 and 20 K using a lead recuperator was discussed by Matsumoto et al. [33]. This device did not use the refrigerant itself as a regenerator and, unlike the AMR cycle, the entire mass of refrigerant underwent the same cycle. This piston-type reciprocating device used sintered $DyAl_{2.2}$ as a refrigerant. In the design, the regenerator was moved by a piston throughout the cycle, transferring heat to and from the magnetic material. The refrigeration unit was found to produce a temperature span of between 50.3 and 58.7 K in the regenerator and 48.3 and 59.1 K in the magnetic refrigerant for a 5 T magnetic field and a cycle of 300 s. The primary source of losses noted in the experiment were due to poor heat transfer between the two solid materials of the regenerator and the magnetic refrigerant.

Degregoria et al. [34] describe an AMR refrigeration apparatus, seen in Figure 18.9, using an immersion-cooled superconducting magnet with fields up to 7 T. A novel feature of this design is that the magnet reciprocates while the regenerator beds are stationary. This allows for static sealing and simple flow system design.

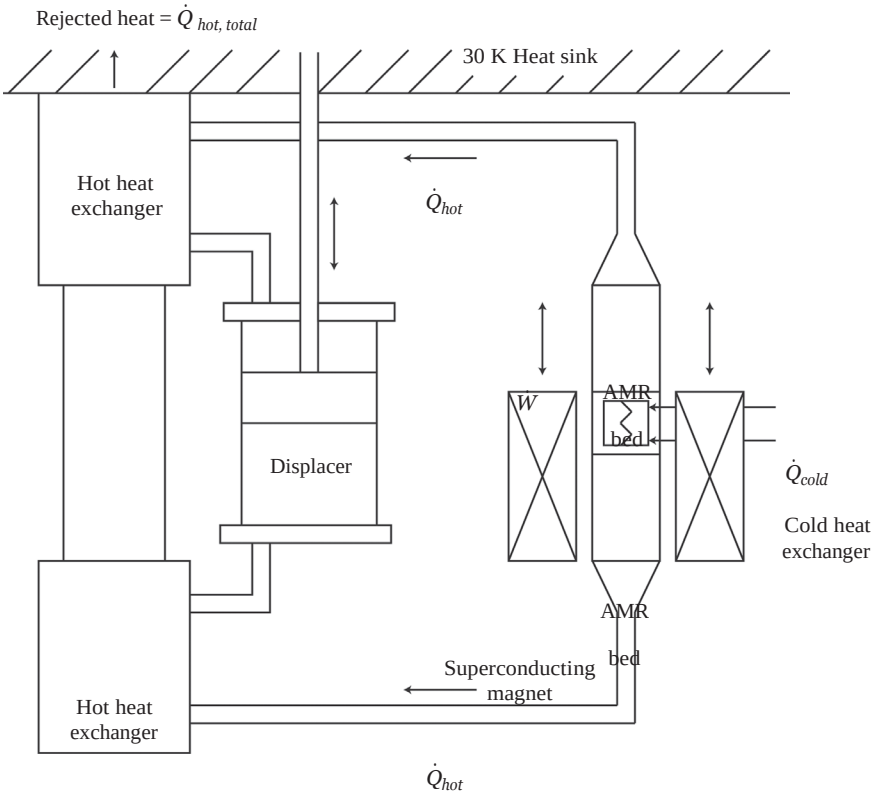


FIGURE 18.9

Component schematic for the Degregoria et al. AMR test apparatus. (From Degregoria, A.J. et al., *Adv. Cry. Eng.*, 37, 875, 1992.)

AMR performance was investigated in the range of 10–20 K using $Er_xGd_{1-x}Al_2$ and in $GdNi_2$ in the 40–80 K range. Tests were performed using fields of 5 and 7 T and results were compared to numerical predictions. The regenerator matrix was crushed irregular particles. Numerical results overestimated the actual test data; however, a zero-load tem- perature span of ~44 K was achieved at 5 T using $GdNi_2$. Errors in the model predictions were suggested to be a combination of poor correlations and uncertain material properties. Wang et al. [35] describe experimental results using an AMR test apparatus described in [34] but modified to use a LN_2 heat sink (seen in Figure 18.10) instead of a separate cryo- cooler. This modification allowed the heat rejection to be quantified by monitoring the boil-off rate. Heat loads could be set using a resistive heater in the cold section.

A large number of tests were performed using $GdNi_2$ with a focus on efficiency measures of the intrinsic AMR cycle, that is, using the magnetic work and pumping work across the regenerators. The sensitivity of efficiency to fluid displaced through the regenerator, temperature span, and cooling load was also measured. The intrinsic efficiency was found to be higher than 50% of Carnot over a range of operating conditions. This work suggests that with appropriate materials, the AMR cycle can produce high efficiency.

Zimm et al. [36] describe a reciprocating test apparatus using a stationary, 7 T super-

conducting magnet. One of the goals of this device shown in Figure 18.11 was to increase the amount of refrigerant significantly from previous tests and maximize the use of the high field volume. A total of four kilograms of $GdNi_2$ was used in the tests. The use of flex hoses to couple the reciprocating regenerator assembly to the heat exchangers resulted in a

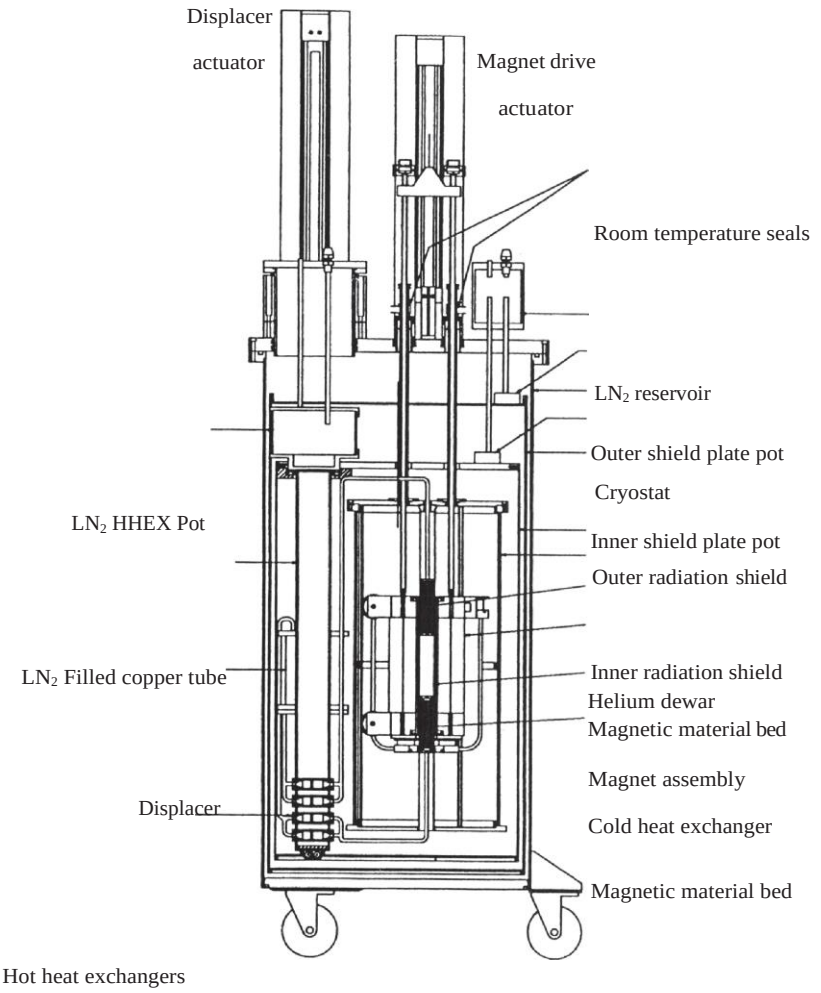


FIGURE 18.10

Cross-sectional view of the AMR test apparatus. (With kind permission from Springer Science+Business Media B.V.: *Cryocoolers*, Experimental results of an efficient active magnetic regenerator refrigerator, 8, 1995, 665–676, Wang, A.A., Johnson, J.W., Niemi, R.W., Sternberg, A.A., and Zimm, C.B.)

significant dead volume in the flow circuit. Numerical predictions suggested that a much larger cooling power could be obtained than was experimentally achieved and the flex hose volume was identified as a serious problem. Inserting Teflon liners to reduce the dead volume nearly doubled the cooling power.

Another reciprocating test apparatus was created by Rowe et al. with the intent of testing different regenerator materials and configurations with little turnover time [27]. This unit has the ability to test refrigerants over a wide range of temperatures to determine their effectiveness and temperature spans in relation to different magnetic fields. Various

refrigerant geometries can be used in single or multimaterial regenerator beds. The device uses small quantities of materials, which reduces material costs and design forces and can operate at frequencies as high as 1 Hz. Figure 18.12 shows a schematic of the apparatus configured for operation with LN_2.

Unlike the previous devices, this apparatus was designed to allow testing from room temperature down to 20 K. Most of the reported results using the device are for

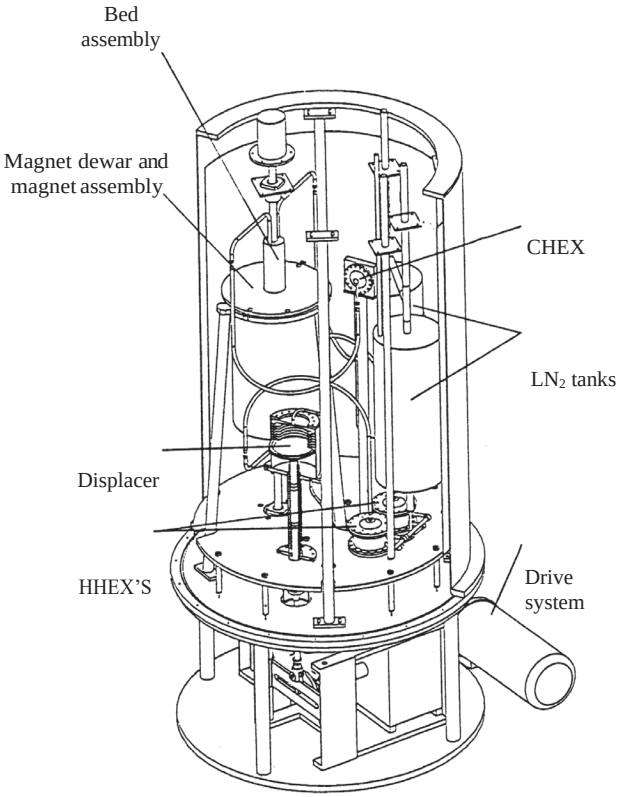


FIGURE 18.11

3D section view of the AMR device. (With kind permission from Springer Science+Business Media B.V.: *Adv. Cry. Eng.*, Test results on a 50 K magnetic refrigerator, 41, 1996, 1675–1681, Zimm, C.B., Johnson, J.W., and Murphy, R.W.)

near-room-temperature operation; however, tests have been carried out using $GdNi_2$, $DyAl_2$, and $Gd_5Si_{0.33}Ge_{3.67}$ alone and in layered structures. Results using $Gd_5Si_{0.33}Ge_{3.67}$ were reported in [23]. Due to an inability to maintain the hot heat sink much below 90 K, the maximum no-load span was 8 K at 5 T. Thus, the operating point was far above the temperature of the peak MCE (~75 K). Near-room-temperature tests using a three-material regenerator and 5 T produced a peak no-load temperature span of ~85 K.

Experience gained with test devices as well as model results has been used to guide the design of magnetic liquefiers of hydrogen. A limited amount of work on magnetic liquefaction is currently being performed in Japan, the United States, and Canada. Some liquefier concepts will be discussed in the following section.

18.5 Magnetic Liquefier Concepts

A wide variety of research has occurred in the field of magnetic refrigeration to deter- mine preferred system configurations for hydrogen liquefaction. Although the AMR cycle is at the heart of system designs, many process configurations are still being assessed.

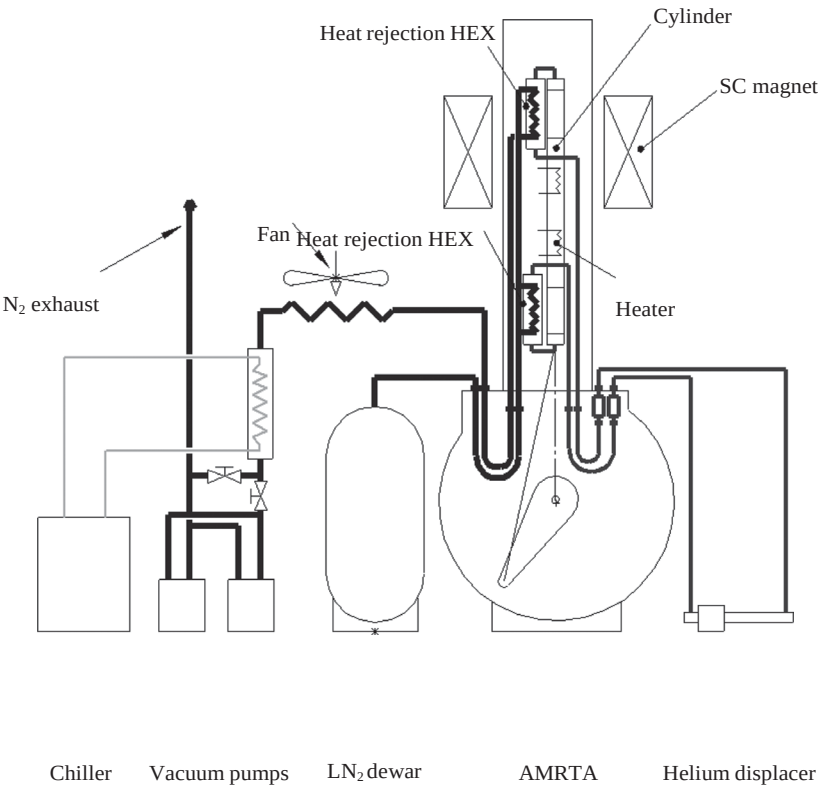


FIGURE 18.12

Picture and schematic for the AMRTA using LN_2 as the hot reservoir. (From Rowe, A. and Tura, A., *AIP Conf. Proc.*, 985, 1292, 2008. With permission.)

These include the number of AMR stages, how they are cascaded together, the type and number of materials to use, and the best operating parameters. Some processes utilize only magnetic cycles to span the 300–20 K temperature gap, while others use LN_2 or LNG to precool hydrogen before being liquefied magnetically. These are areas being investi- gated to improve the overall efficiency and cost-effectiveness of magnetic hydrogen lique- faction units.

18.5.1 Process Configurations

This section describes process flow configurations proposed for liquefying hydrogen with magnetic cycles. Recently, three different configurations have been analyzed by Utaki et al. [25] using the numerical model by Engelbrecht [73]. All three cases use series cascades of AMR systems with different precooling temperatures. Each configuration uses a magnetic Carnot stage (CMR) for the final removal of latent heat and liquefaction [20]. It is difficult to ascertain, but it appears that bypass flow is assumed in some stages. This study also looks at using hydrogen, propane, and glycol/water mixture as heat transfer fluids.

The starting temperatures for the three cases are 300, 77, and 120 K. Starting points of 77 and 120 K are established by precooling hydrogen with LN_2 and LNG, respectively. The model results for all cases assume a constant magnetic entropy change of 86.2 mJ/cm^3 K at 5 T independent of temperature. This assumes an ideal magnetocaloric material in an ideally layered regenerator. Making this assumption removes the dependency on available materials, allowing for a comparison between the fundamental configurations of each of

the three cases. The heat emitted by the conversion from ortho-hydrogen to para-hydrogen

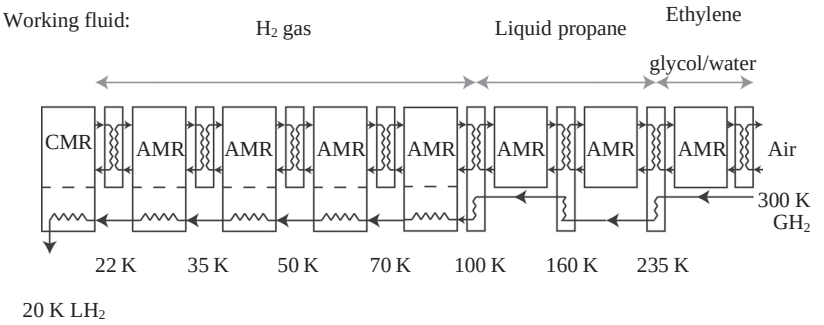


FIGURE 18.13

The aforementioned magnetic refrigerator is case 1, which uses 7 AMR stages and one CMR stage. (From Utaki, T. et al., *Cryocooler*, 14, 645, 2007.)

is also taken into account in the model and is included as a heat load during each of the liquefaction processes. To compare the work, COP, and liquefaction efficiencies, all cases produce the same amount of hydrogen and use optimized regenerator beds and mass flows for each stage.

The first case shown in Figure 18.13 utilizes seven AMR stages from room temperature to 22 K where a CMR stage is used to liquefy hydrogen from 22 to 20 K. The working fluids for the AMR stages are a 56% ethylene glycol/water mix from 300 to 235 K, liquid propane from 235 to 95 K, and gaseous hydrogen from 95 to 22 K. Ethylene glycol/water and liquid propane are used as these fluids were found to have a significantly higher COP per stage. The use of hydrogen as the heat transfer fluid in an AMR offers some potential advantages over helium; however, the ability of known refrigerants to operate in an H_2 environment is unknown.

The second case uses LN_2 to precool hydrogen to 77 K. From this point, hydrogen is cooled to 22 K through three AMR stages and then liquefied using a CMR. In the final case, gaseous hydrogen is first cooled to 120 K by LNG and then run through five AMR stages and a CMR liquefaction stage. Both cases 2 and 3 use hydrogen as the working fluid in the system. Process flow diagrams for cases 2 and 3 are provided in Figure 18.14.

Since the appeal of magnetic refrigeration is its theoretically low energy cost compared to gas systems, the most important results from the three separate cases are the work input and liquefaction efficiency. The work input is described as the work required to liquefy hydrogen from room temperature. In the case where precooling is performed with LN_2, additional energy is added to the AMR and CMR work totals to account for the work input to the nitrogen liquefier. The efficiency of each process is found by dividing the theoretical liquefaction energy by the actual energy required. For liquid hydrogen, which has been converted to ortho–para equilibrium, this theoretical work is 3.92 kWh/kg H_2 [39]. In the paper by Utaki et al., a 0.01 ton H_2/day unit is modeled so the minimum power required is then 1.63 kW. All three units are assumed to produce the same amount of product, making the CMR work identical in all cases. A Carnot efficiency of 50% is assumed based upon previous tests, making the power required for the CMR stage 1.30 kW [21]. Table 18.3 summarizes the work requirements for each part of the three cases in addition to the liquefaction efficiency of hydrogen.

From Table 18.3, case 2 shows the highest liquefaction efficiency at 46.5% followed closely by case 3 at 46.3%. Factors to take into account include the added capital cost for the addi- tional AMR units in the 5-stage process and increased irreversibilities that may occur in using a larger number of stages. Another result to note is the decreased amount of work in case 1 when the number of AMR stages is increased from seven to nine. The added stages allow for each AMR to cover smaller temperature spans resulting in an overall more efficient system.

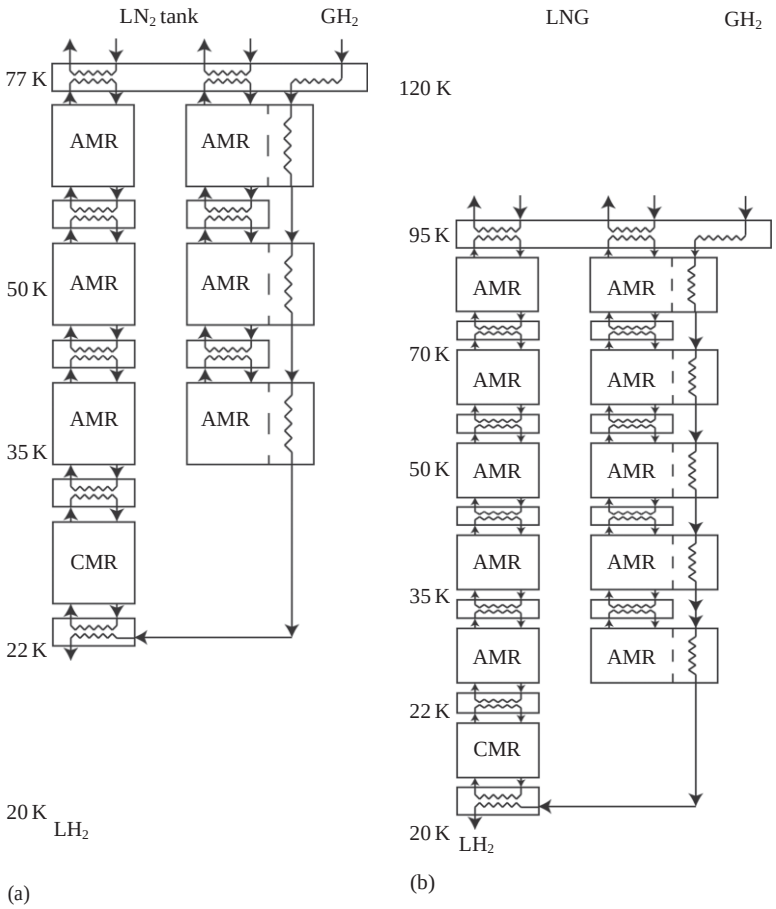


FIGURE 18.14

Case 2 (a) contains 3 AMR stages with a CMR stage and case 3 (b) contains 5 AMR stages with a CMR stage. (From Utaki, T. et al., *Cryocooler*, 14, 645, 2007.)

TABLE 18.3

Summary of the Input Work and Liquefaction Efficiency for Cases 1–3

	Case 1 (7 Stages)	Case 1 (8 Stages)	Case 1 (9 Stages)	Case 2	Case 3
Precooling work (kW)	0	0	0	1.49	2.23
AMR work (kW)	13.09	11.08	9.90	0.72	
CMR work (kW)	1.30	1.30	1.30	1.30	1.30
Total work (kW)	14.39	12.38	11.20	3.51	3.53
Liquefaction efficiency (%)	11.4	13.2	14.6	46.5	46.3

Source: Utaki, T. et al., *Cryocooler*, 14, 645, 2007.

Other process configurations using series and parallel AMR stages have been identified for efficient hydrogen liquefaction [50]. While multistaged processes can reduce operating costs by better matching the cooling requirements of hydrogen, capital costs may ultimately limit the number of stages. Some of the more detailed magnetic liquefier designs reported in the literature are discussed in the next section.

18.5.2 Liquefier Designs

To date, a small number of magnetic liquefier designs have been developed and analyzed in detail. These devices are summarized here and provide a background for the current development activities on magnetic liquefaction discussed in the final section.

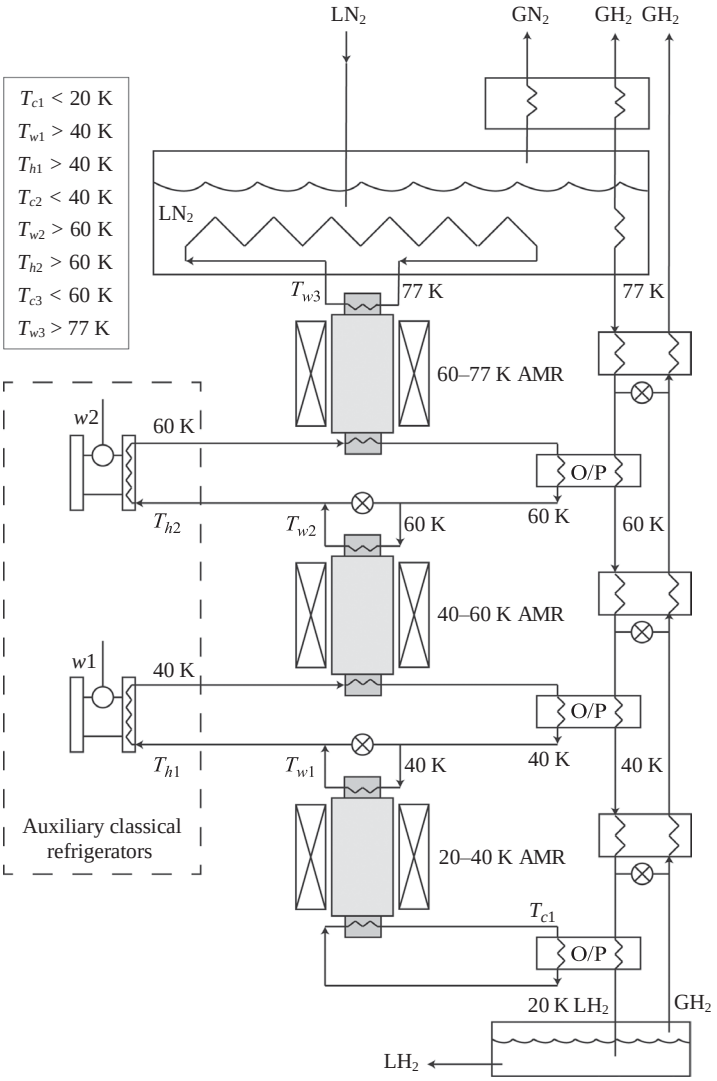


FIGURE 18.15

The aforementioned configuration represents the three-stage AMR liquefier used in the exergy analysis. (From Zhang, L. et al., *Cryogenics*, 33, 667, 1993.)

An early design operating with a LN_2 precooling system was analyzed by Zhang et al. [23,74]. The device depicted in Figure 18.15 uses three magnetic stages in series with ortho–para conversion assumed as a load for each stage. In the analysis, the cooling power and exergetic equivalent losses of the process are examined by altering various system parameters including material type, bed size, and temperature. Each regenerator stage in the design is also assumed to be made of a mixture of alloys from the family $Gd_{1-x}Er_xAl_2$, while the heat transfer fluid in the AMR system is helium at 10 atm. This fluid is then used to cool a 1 atm hydrogen stream through external heat exchangers. Entropy generation and exergy balances are used to determine the impacts of inefficiencies in the regenera- tors, auxiliary refrigeration units, and external heat exchangers.

Several design features were suggested from the study to improve the efficiency of liquid hydrogen production using this specific configuration and operating space. The first suggestion is to use a large magnetic material bed. A larger material bed reduces the exergy losses relative to the cooling capacity produced. The material bed should also be a shape that maximizes heat transfer to the working fluid. Increasing the mass flow of the helium was identified as a way of reducing losses by decreasing the temperature differ- ence between the working fluid and the stage temperature. This causes the cooling capac- ity to increase while the exergy destruction remains relatively constant. Alternately, the cycle's frequency can also be increased to achieve the same effect. A novel finding from this research is that using a high magnetic field may not always be advantageous to the overall system.

Following the test results for the AMR reported by Degregoria and described earlier [34], Janda et al. designed a process to liquefy hydrogen at a rate 0.01 ton H_2/day with the intention to eventually scale this up to 1 ton/day. The device uses two stages to span from 80 to 20 K and is shown in a simplified form in Figure 18.16. Helium is used as the working fluid in the AMRR while precooling is again performed using LN_2. The previously tested material $GdNi_2$ is hypothesized to span from 80 to 40 K under a 7 T magnetic field, while GdPd was to be used in the 40 to 20 K stage with a 5 T field. Although this specific unit was never built, it provided a foundation for a number of studies [18,19,23,74]. The most recent activity related to this device was an optimization study by Zhang et al. [19], which studied the impacts of particle size, material bed lengths, and the interstage temperature on the overall process efficiency.

A novel feature of the design is the use of unbalanced flow in the regenerators. This may actually benefit the AMR cycle efficiency due to the variation in specific heat of the magnetic material. If the materials are largely operating below their Curie temperatures,

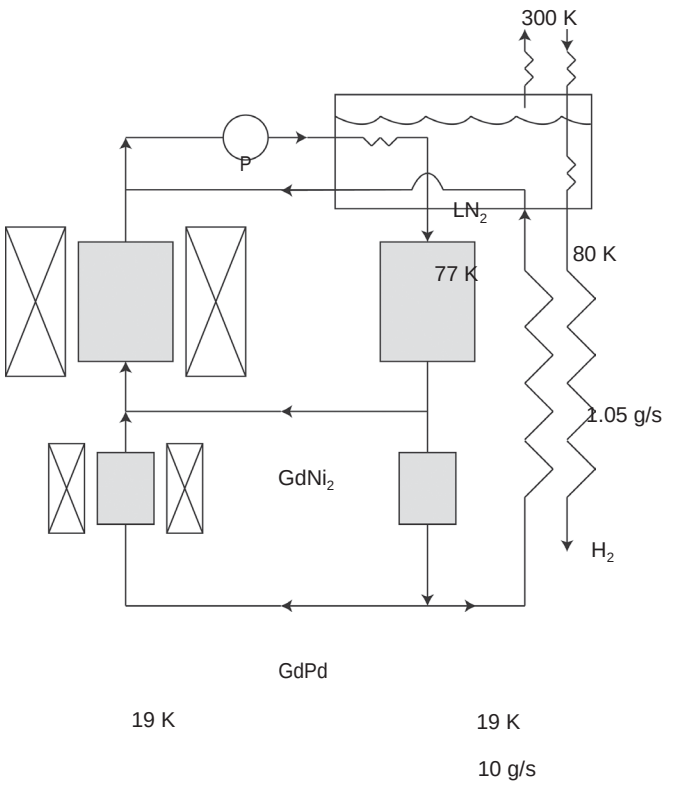


FIGURE 18.16

Simplified AMR schematic by Zhang et al. of Janda's two-stage hydrogen liquefier. (From Zhang, L. et al., *Cryogenics*, 40, 269, 2000.)

the specific heat in the demagnetized state is larger than when magnetized. For a local Brayton-type process to occur with this varying specific heat, the thermal mass of fluid should be different for high and low field blows. The optimized results indicated that the bypass ratio for the low-temperature stage was on the order of 12%, whereas for the high-temperature stage, it was ~2.5%. The optimal interstage temperature of the process was found to be 41 K, and the liquefaction efficiency was determined to be ~20%. This is a good number given the scale of the device.

As part of the Japanese World Energy Network project phase II, the potential of magnetic refrigeration for large-scale liquefaction at high efficiencies was investigated [66]. This study began by analyzing a 10 kg/day laboratory prototype. The schematic of the device is shown in Figure 18.17. One of the main design features is the use of a belt carrying discrete regenerator beds. The reason for this is so that an inexpensive solenoidal superconducting magnet could be used. The belt rotates the regenerators through the high and low field regions where manifolds are used to regenerate pressurized helium flowing through the heat exchange system. This type of design has the benefits of a rotary configuration in terms of force balancing; however, sealing and controlling flow is not a trivial problem. The design calculations assumed operation between room temperature and 20 K with six stages in parallel and the need for 14 different magnetocaloric materials. Overall, liquefaction efficiency was estimated to be ~50%.

Currently, research and development activities are occurring in Japan, Canada, and the United States. The US DOE is funding the development of a magnetic liquefier prototype by Heracles Energy [75]. In Canada, magnetic liquefaction is being studied by our group as part of a strategic research network on hydrogen (H2Can) funded by the Natural Sciences and Engineering Research Council of Canada (NSERC).

In Japan, recent work on hydrogen liquefaction was reported by Matsumoto et al. [21]. Their design is based upon the AMRR system of Utaki (discussed earlier) where hydrogen is precooled by LNG then run through three AMR stages and a final CMR liquefaction stage.

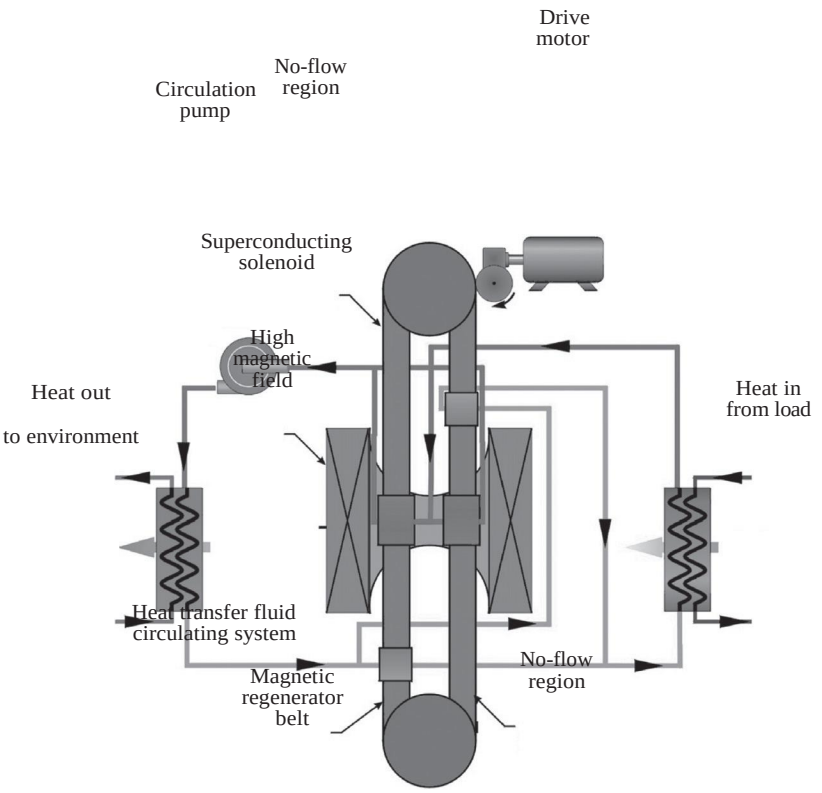


FIGURE 18.17

Schematic of an AMRR device using a belt of regenerators as the magnetocaloric material. (From Iwasaki, W., *J. Hydrogen Energy*, 28, 559, 2003. With permission.)

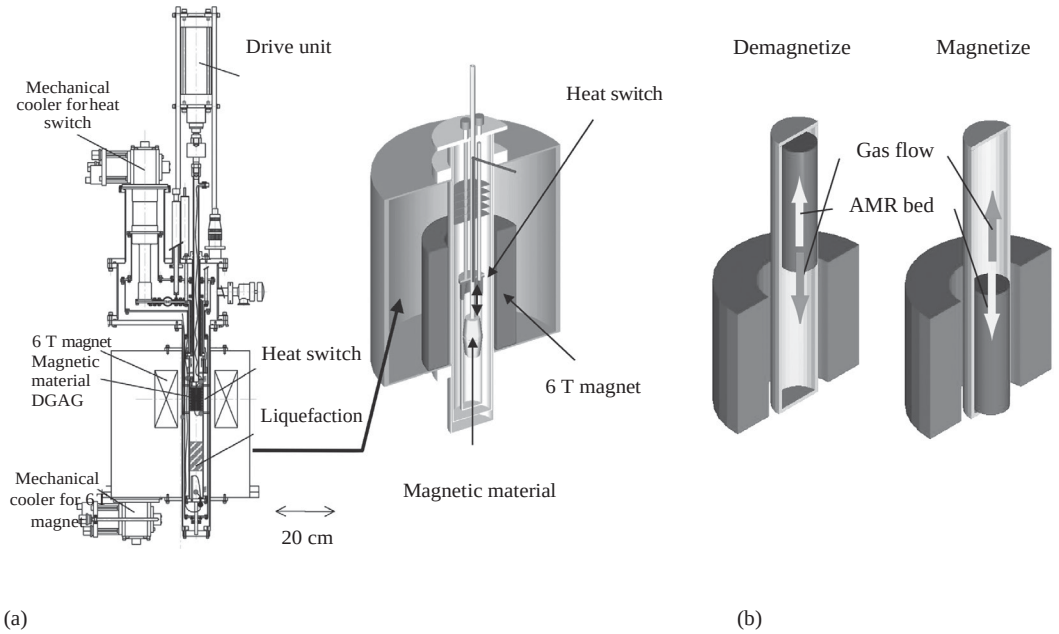


FIGURE 18.18

Cross-sectional view of the magnetic liquefaction test apparatus and CMR (a) and AMR (b) operation diagrams. (From Matsumoto, K., Kondo, T., Yoshioka, S., Kamiya, K., and Numazawa, T., Magnetic refrigerator for hydro- gen liquefaction, *J. Phys. Conf. Ser.*, 150, 012028, 2009. With permission from IOP Publishing Ltd.)

The starting point of 112 K was chosen due to the abundance of LNG plants in Japan. Because the AMR stages of this device have already been described, this final section will focus on the CMR stage.

The CMR converts gaseous hydrogen at 22 K to liquid hydrogen at 20 K. This is done through condensing hydrogen directly onto the refrigerant itself. Because most refrigerants are not hydrogen resistant, a ceramic material is used for this stage. This CMR refrigerant is $Dy_{2.4}Gd_{0.6}Al_5O_{12}$, or DGAG, and the thermal efficiency as compared to the ideal Carnot cycle is between 50% and 60% and the liquefaction efficiency is ~90% [21]. The active magnetic refrigerator stages have not yet been fixed in terms of the number of stages and materials used, but the entire process is to be examined in the near future from either a LN_2 or LNG starting point. A cross-sectional view of the test apparatus and CMR and AMR stages are seen in Figure 18.18.

18.7 Summary

When Brown used gadolinium as a magnetic refrigerant in 1976, the seed for magnetic liquefaction of hydrogen was planted. Thirty-five years later, a broad array of research has been performed, improving our understanding of magnetocaloric materials, regen- erator design, magnetic devices, and liquefaction processes. Studies addressing design principles, test devices, and magnetic refrigerants have proven that high efficiencies are possible; however, the development of commercial devices is still a challenge. The AMR cycle is the preferred method of generating cooling over significant temperature spans, but the thermodynamic implications of using multiple materials in a single AMR are still

being developed. Highly nonlinear material properties and a lack of analytic expressions describing AMR behavior make design a challenge. Devices operating with high magnetic fields must also accommodate for magnetic forces. Depending upon the chosen device geometry, these forces can be high and reversing and may lead to eddy-current heat- ing and other losses. While numerous magnetic refrigerants have been identified, there appears to be a trade-off between the maximum MCE and the width of the magnetic tran- sition. Layered AMR geometries may partially solve this problem, but there are limited experimental results to date.

With all of those mentioned earlier in mind, it should also be pointed out that the cumulative amount of work on magnetic liquefier development is relatively small compared to the effort that has gone into gas cycles. Gas compression and expansion technologies are mature with a diverse set of component manufacturers serving the market. As a result, we are likely to see only modest gains in conventional liquefier efficiency. The capital costs of large-scale conventional systems could easily decrease if repeated builds of standardized designs were to occur. Magnetic refrigeration provides an alternative process that may reduce the costs of liquid hydrogen at device scales that are uneconomical with conventional cycles. Higher efficiencies at smaller scales would allow liquefaction systems to be deployed in a more distributed manner instead of at large central facilities as we currently see. The preferred geometries and process configurations of magnetic liquefaction systems are still unknown, but with continued advances in high-temperature superconductors, materials, and our understanding of magnetic cycles, the prospects for commercialization of magnetic liquefiers are improving.

References

1. A. Smith, Who discovered the magnetocaloric effect? *Eur. Phys. J. H*., 2013;38(4);507–517.
2. P. Weiss, A. Piccard, Sur un nouveau phénomène magnétocalorique. *Compt. Rend. Ac. Sci*., 1918;166;352.
3. P. Debye, Einige Bemerkungen zur Magnetisierung bei tiefer Temperatur. *Ann. Phys*., 1926;81;1154–1160.
4. W.F. Giauque, A thermodynamic treatment of certain magnetic effects. A proposed method of producing temperatures considerably below 18 absolute. *J. Am. Chem. Soc*., 1927;49;1864–1870.
5. T. Hashimoto, T. Numasawa, M. Shino, T. Okada, Magnetic refrigeration in the tempera- ture range from 10 K to room temperature: The ferromagnetic refrigerants. *Cryogenics*, 1981;21;647–653.
6. G.V. Brown, Magnetic heat pumping near room temperature. *J. Appl. Phys*., 1976;47;3673.
7. W.A. Steyert, Magnetic refrigerators for use at room temperature and below. *J. de Physique Collogue*, 1978;39;1598.
8. J.A. Barclay, W.A. Steyert Jr., Active magnetic regenerator. United States Patent 4332135, 1982.
9. T. Hashimoto, T. Ikegami, T. Okada, Magnetic refrigeration in the temperature range from 10 K to room temperature: The ferromagnetic refrigerants. *Cryogenics*, 1981;21;647–653.
10. T. Hashimoto, New application of complex magnetic materials to the magnetic refrigerant in an Ericsson magnetic refrigerator. *J. Appl. Phys*., 1987;62;3873–3878.
11. T. Hashimoto, Recent investigations on refrigerants in magnetic refrigeration. *Adv. Cry. Eng*., 1986;32;261–270.
12. C.B. Zimm, W.F. Stewart, J.A. Barclay, C.K. Campenni, Measured properties if GdNi for mag- netic refrigeration. *Adv. Cry. Eng*., 1988;33;791–798.

13. J.A. Barclay, W.C. Overton Jr, W.F. Stewart, C.B. Zimm, Magnetic refrigeration for efficient cryo- gen liquefaction. Department of Energy, Division of Advanced Energy Projects, Final Report (1982–1986).
14. J.A. Waynert, A.J. Degregoria, R.W. Foster, J.A. Barclay, Evaluation of industrial magnetic heat pump/refrigerator concepts that utilize superconducting magnets, Argonne National Laboratory Report, ANL-89/23 June 1989.
15. J.A. Barclay, Prospects for magnetic liquefaction of hydrogen. *Proceedings of the XVIII International Congress of Refrigeration*, Montreal, Quebec, Canada, 1991, pp. 297–305.
16. D. Janda, A.J. Degregoria, J. Johnson, S. Kral, Design of an active magnetic regenerative hydro- gen liquefier. *Adv. Cry. Eng*., 1992;37;891–899.
17. C.B. Zimm, E.M. Ludeman, M.C. Severson, T.A. Henning, Materials for regenerative magnetic cooling. *Adv. Cry. Eng*., 1992;37;883–891.
18. A.J. Degregoria, Modeling the active magnetic refrigerator. *Adv. Cry. Eng*., 1992;37;867.
19. L. Zhang, S.A. Sherif, A.J. Degregoria, C.B. Zimm, T.N., Verziroglu, Design optimization of a 0.1 ton/day active magnetic regenerative H2 liquefier. *Cryogenics*, 2000;40;269–278.
20. K. Kamiya, H. Takahashi, T. Numazawa, H. Nozawa, T. Yanagitani, Hydrogen liquefaction by magnetic refrigeration. *Proceedings of the International Cryocooler Conference*, Boulder, CO, 2007.
21. K. Matsumoto, T. Kondo, S. Yoshioka, K. Kamiya, T. Numazawa, Magnetic refrigerator for hydrogen liquefaction. *J. Phys. Conf. Ser*., 2009;150;012028.
22. K. Matsumoto, T. Hashimoto, Thermodynamic analysis of magnetically active regenerator from 30 to 70 K with a Brayton-like cycle. *Cryogenics*, 1990;30;840–845.
23. L. Zhang, S.A. Sherif, T.N. Verziroglu, J.W. Sheffield, Second law analysis of active magnetic regenerative hydrogen liquefiers. *Cryogenics*, 1993;33;667–674.
24. J. Dikeos, A.M. Rowe, A. Tura, Numerical analysis of an active magnetic regenerator (AMR) refrigeration cycle. *Adv. Cry. Eng*., 2006;823;993–1000.
25. T. Utaki, K. Kamiya, T. Nakagawa, T.A. Tamamoto, T. Numazawa, Research on a magnetic refrigeration cycle for hydrogen liquefaction. *Cryocooler*, 2007;14;645.
26. K. Matsumoto, T. Kondo, T. Numazawa, Numerical analysis of active magnetic regen- erators for hydrogen magnetic refrigeration between 20 and 77 K. *Cryogenics*, 2010;doi: 10.1016/j.cryogenics.2010.06.003.
27. J.A. Barclay, The theory of an active magnetic regenerative refrigerator. NASA Report, NASA-CP-2287, 1983.
28. R.W. Murphy, F.C. Chen, V.C. Mei, G.L. Chen, Analysis of magnetic refrigeration cycles. *Proceedings of the 26th Intersociety Energy Conversion Conference*, Boston, MA, 1991, pp. 482–486.
29. C. Carpetis, Numerical study of magnetic refrigeration including consideration of magnetic nanocomposites. *Proceedings of the XVIII International Congress of Refrigeration*, Montreal, Quebec, Canada, 1991, pp. 331–337.
30. S. Schuricht, A.J. Degregoria, C.B. Zimm, The effects of a layered bed on active magnetic regen- erator performance. *Proceedings of the International Cryocooler Conference*, Santa Fe, NM, 1992.
31. L. Zhang, S.A. Sherif, T.N. Veziroglu, J.W. Sheffield, Performance analysis of reciprocating mag- netic liquefiers. *Int. J. Hydrogen Energy*, 1994;12;945–956.
32. C. Carpetis, An assessment of the efficiency and refrigeration power of magnetic refrigerators with ferromagnetic refrigerants. *Adv. Cry. Eng*., 1994;39;1407–1415.
33. K. Matsumoto, T. Ito, T. Hashimoto, An Ericsson magnetic refrigerator for low temperature. *Adv. Cry. Eng*., 1988;33;743–750.
34. A.J. Degregoria, L.J. Feuling, J.F. Laatsch, J.R. Rowe, J.R. Trueblood, Test results of an active magnetic regenerative refrigerator. *Adv. Cry. Eng*., 1992;37;875.
35. A.A. Wang, J.W. Johnson, R.W. Niemi, A.A. Sternberg, C.B. Zimm, Experimental results of an efficient active magnetic regenerator refrigerator, *Cryocoolers*, 1995;8;665–676.
36. C.B. Zimm, J.W. Johnson, R.W. Murphy, Test results on a 50 K magnetic refrigerator. *Adv. Cry. Eng*., 1996;41;1675–1681.
37. A. Rowe, A. Tura, Cryogenic testing of an active magnetic regenerative refrigerator. *AIP Conf. Proc*., 2008;985;1292–1298.

38. J.A. Barclay, Magnetic refrigeration: A review of a developing technology. *Adv. Cry. Eng*., 1988;33;719–731.
39. W. Peschka, *Liquid Hydrogen: Fuel of the Future,* Springer-Wein, New York, 1992.
40. V.K. Pecharsky, K.A. Gschnieder Jr., Y. Mudryyk, D. Paudyal, Making the most of the magnetic and lattice entropy changes. *J. Magn. Magn. Mater*., 2009;321;3541–3547.
41. K.A. Gschneidner Jr., V.K. Pecharsky, A.O. Tsokol, Recent developments in magnetocaloric materials. *Rep. Prog. Phys*., 2005;68;1479–1539.
42. H.B. Callen, *Thermodynamics and an Introduction to Thermostatistics*, 2nd edn., John Wiley & Sons, New York, 1985.
43. A. Kitanovski, P.W. Egolf, Thermodynamics of magnetic refrigeration. *Int. J. Refrig*. 2006;29;3–21.
44. G. Bisio, G. Rubatto, P. Schiapparelli, Magnetic systems depending on three or two variables; thermodynamic analysis and some existing and possible applications. *Energy Conv. Manage*., 1999;40;1267–1286.
45. T.H.K. Barron, Gruneisen parameters for the equation of state of solids. *Ann. Phys*., 1957;1;77–90.
46. V.K. Pecharsky, K.A. Gschnieder Jr., Magnetocaloric effect and magnetic refrigeration. *J. Magn. Magn. Mater*., 1999;200;44–56.
47. A.M. Rowe, J.A. Barclay, Ideal magnetocaloric effect for active magnetic regenerators. *J. Appl. Phys*., 2003;93;1672–1676.
48. C.R. Cross, J.A. Barclay, A.J. Degregoria, S.R. Jaeger, J.W. Johnson, Optimal temperature-entropy curves for magnetic refrigeration. *Adv. Cry. Eng*., 1988;33;767.
49. J.L. Hall, C.E. Reid, I.G. Spearing, J.A. Barclay, Thermodynamic considerations for the design of active magnetic regenerative refrigerators. *Adv. Cry. Eng*., 1996;41;1653.
50. J.A. Barclay et al. Apparatus and methods for cooling and liquefying a fluid using a magnetic refrigeration. United States Patent 6467274, 2002.
51. J.A. Barclay, S. Sarangi, Selection of regenerator geometry for magnetic refrigerator applications. In *Cryogenic Processes and Equipment*, P.J. Kerney (ed), The American Society of Mechanical Engineers, New York, 1984.
52. P. Li, M. Gong, J. Wu, Geometric optimization of an active magnetic regenerative refrigerator via second-law analysis. *J. Appl. Phys*., 2008;104;103536.
53. M. Ogawa, R. Li, T. Hashimoto, Thermal conductivities of magnetic intermetallic compounds for cryogenic regenerator. *Cryogenics*, 1991;41;405–410.
54. K. Engelbrecht et al., The effects of internal temperature gradients on regenerator performance. *Trans. ASME*, 2006;128;1060.
55. P. Kittel. Eddy current heating in magnetic refrigerators. *Adv. Cry. Eng*.,1990;35;1141–1148.
56. A. Tura, J. Roszmann, J. Dikeos, A. Rowe. Cryogenic active magnetic regenerator test appara- tus. *Adv. Cry. Eng*., 2006;51;985–992.
57. M.E. Wood, W.H. Potter, General analysis of magnetic refrigeration and its optimization using a new concept: Maximization of refrigerant capacity. *Cryogenics*, 1985;25;667–683.
58. K.A. Gschneidner Jr., V.K. Pecharsky. Magnetic refrigeration. Chapter 25 of *Intermetallic Compounds: Vol. 3, Principles and Practice*, J.H. Westbrook and R.L. Fleischer (eds), John Wiley & Sons, New York, 2002.
59. K. Sakata, E. Mizutani, K. Fukuda, A review of topics in hydrogen-related innovative materials in Japan. *J. Power Sources*, 2006;159;100–106.
60. J.A. Barclay, W.F. Stewart, W.C. Overton, R. Chesebrough, M. McCray, D. McMillan, An appa- ratus to determine the heat capacity and thermal conductivity of a material from 1 to 300 K in magnetic fields up to 9T. *Adv. Cry. Eng*., 1984;30;425–432.
61. K. Matsumoto, T. Okano, T. Kouen, T. Numazawa, K. Kamiya, S. Nimori, Magnetic entropy change of magnetic refrigerants with first order phase transition suitable for hydrogen refrig- eration. *IEEE Trans. Appl. Superconduct*., 2004;14;1738–1741.
62. C.E. Reid, J.A. Barclay, J.L. Hall, S. Sarangi, Selection of magnetic materials for an active mag- netic regenerative refrigerator. *J. Alloys Compounds*, 1994;207–208;366–371.
63. K.A. Gschneidner Jr., V.K. Pecharsky, S.K. Malik, The (Dy1-xErx)Al2 alloys as active magnetic regenerators for magnetic refrigeration. *Adv. Cry. Eng*., 1996;42;475–483.

64. A. Smaili, R. Chahine, Composite materials for Ericsson-like magnetic refrigeration cycles, *J. Appl. Phys*., 1997;81(2);824–829.

65. J.A. Barclay, Can magnetic refrigerators liquefy hydrogen at high efficiency. *ASME-Paper 81-HT-82, 20th Joint ASME/AICHE National Heat Transfer Conference*, Milwaukee, WI, August 2–5, 1981.
66. W. Iwasaki, Magnetic refrigeration technology for an international clean energy network using hydrogen energy (WE-NET). *J. Hydrogen Energy*, 2003;28;559–567.
67. L. Zhang, S.A. Sherif, T.N. Verziroglu, J.W. Sheffield, Performance analysis of reciprocating magnetic liquefiers. *J. Hydrogen Energy*, 1994;19;945–956.
68. J.A. Barclay et al., Design limitations on magnetic refrigerators imposed by magnetic forces. *Proceedings of the Fourth International Cryocooler Conference*, Easton, MD, September, 1986.

69. A. Rowe, J. Barclay, Static and dynamic force balancing in reciprocating active magnetic refrig- erators, *Adv. Cry. Eng*., 2002;47;1003–1010.
70. R.W. Merida, J.A. Barclay, Monolithic regenerator technology for low temperature (4 K) Gifford- McMahon cryocoolers. *Adv. Cry. Eng*., 1998;43;1597–1604.
71. A.J. Degregoria et al. Active magnetic regenerator method and apparatus United States Patent 5249424, 1993.
72. J.A. Barclay, W.F. Stewart, The effect of parasitic refrigeration on the efficiency of magnetic liq- uefiers. *Proceedings of the 17th Intersociety Energy Conversion Engineering Conference*, Los Angeles, CA, 1982, pp. 1166–1170.
73. K.L. Engelbrecht, A numerical model of an active magnetic regenerator refrigeration system. Master thesis, University of Wisconsin, Madison, WI, 2004.
74. L. Zhang, S.A. Sherif, T.N. Verziroglu, J.W. Sheffield, On exergy losses in AMR hydrogen liquefiers. *J. Hydrogen Energy*, 1994;19;447–452.
75. J. Barclay, Active magnetic regenerative liquefier. *2010 Annual Merit Review Proceedings*, 2010, Available at http://www.hydrogen.energy.gov/annual_review10_production.html#delivery.

7. Discussion

21

Complex Hydrides

Sesha S. Srinivasan
Tuskegee University

Prakash C. Sharma
Tuskegee University

Elias K. Stefanakos
University of South Florida

D. Yogi Goswami
University of South Florida

CONTENTS

21.1 Complex Hydrides 683
21.1.1 Alanates 684
21.1.2 Borohydrides 687
21.1.3 Amides 690
21.1.4 Quaternary Hydrides 690
References 693

21.1 Complex Hydrides

In a simple definition, complex metal hydrides are metallic elements (one or more metal elements) bonded with hydrogen. There are various types of complex metal hydrides that can be classified by the amount of different species present in the molecule: binary, ternary, and quaternary hydrides (see Table 21.1).

The general reactions for hydrogen desorption and absorption for binary metal hydrides are as follows:

$$MH_n \rightarrow M + \frac{n}{2} H_{2(g)} \tag{21.1}$$

$$M + \frac{n}{2} H_{2(g)} \rightarrow MH_n \tag{21.2}$$

Ternary and quaternary metal hydrides follow complex reactions path that are specific for each compound.

TABLE 21.1
Classification of Complex Hydrides

Classification	Example
Binary[3]	LiH, MgH_2, etc.
Ternary[3]	$LiBH_4$, $Zn(BH_4)_2$, etc.
Quaternary	$LaMg_2NiH_7$,[29] $LiMg_2RuH_7$,[30] etc.

The group one, two, and three light elements, for example, Li, Mg, B, Al, can form a large variety of metal–hydrogen complexes. They are very interesting due to their light weight and the number (often 2) of hydrogen atoms per metal atom. The principal distinction between the complex hydrides and the previously described metallic hydrides is the transition to an ionic or covalent compound of the metals upon hydrogen absorption. The hydrogen in the multifaceted hydrides is often located in the corners of a tetrahedron with boron or aluminum in the center. The negative charge of the anion, $[BH_4]^-$ and $[AlH_4]^-$, is compensated by a cation, for example, Li^+ or Na^+.[1]

There have been reports that there are about 70 known complex hydrides; some of those, such as $BaReH_9$ with 2.7 wt.% of hydrogen,[2] have been reported to dehydride below 100°C, but the low hydrogen content renders them ineffective as storage materials. The one family of complex hydrides that contains as much hydrogen as the aluminum hydrides is the borohydrides. The borohydrides vary greatly in hydrogen content, up to a maximum of 20.8 wt.% for $Be(BH_4)_2$. This compound is normally not considered because of the toxicity of beryllium; however, there are numerous other known borohydrides. These hydrides release hydrogen slowly. Unlike the metallic hydrides, hydrogen is released via cascade decompositions in complex hydrides, and the step reactions call for different circumstances. Therefore, there is a big difference between the theoretical and the practically attainable hydrogen capacities.

There are about 234 complex chemical hydrides that have been reported with theoretical hydrogen storage capacity.[3] A list of various complex chemical hydrides presently under investigation with their available capacities and operating temperature is given in Table 21.2.

21.1.1 Alanates

Complex hydrides, $MAlH_4$, MBH_4, and $N(AlH_4)_2$ (M = Na, Li, K; N = Mg), are emerging as promising hydrogen storage materials because of their high potential storage capacity.[3] However, they are generally characterized by irreversible dehydriding or extremely slow hydrogen cycling kinetics. The breakthrough discovery of doping with a few mole percent of Ti catalyst has enhanced the dehydrogenation kinetics of $NaAlH_4$ at low operating temperatures (<150°C) and was the starting point in reinvestigating these complex hydride systems for hydrogen storage.[4] However, reduced availability of reversible hydrogen (~4 to 5 wt.%), poor cyclic stability, and loss of the catalytic function of Ti species necessitate the search for new and efficient complex hydride systems. The hydride complexes such as $NaAlH_4$ and $NaBH_4$ are known to be stable and decompose only at elevated temperatures, often above the melting point of the complex. However, the addition of a few mole concentrations of titanium species to $NaAlH_4$ eases the release of hydrogen at moderate temperatures and ambient pressure.[4] The decomposition of Ti-doped $NaAlH_4$ proceeds in two

TABLE 21.2

Theoretical Hydrogen Storage Capacities of Complex Hydrides

No.	Complex Chemical Hydride	Theoretical Capacity (wt.%)	Reversible Capacity (wt.%)	Operating Temperature (°C)	Remarks
1	Ti-doped $NaAlH_4$	7.5	5.5	100–150	High rehydrogenation pressure, poor cycle life, loss of catalytic activity, less available capacity
2	Undoped and Ti-doped $LiAlH_4$	10.5	6.3	120–170	Problems with reversibility and reduced thermodynamic stability
3	Undoped and doped $LiBH_4$	18.2	9.0	200–400	High operating temperature, rehydrogenation problem, possible borane gas evolution
4	$Mg(AlH_4)_2$	9.3	6.6	200–250	High operating temperature, thermodynamic stability
5	$NaBH_4/H_2O$	10.5	9.2	Ambient	Hydrolysis reaction, irreversibility, one-time use
6	Li_3N ($LiNH_2$/LiH)	11.3	6.5–7.0	255–285	High operating temperature, possible ammonia evolution
7	B-H-Li-N	10.0		80–150	Rehydrogenation problem
8	AlH_3	10.5		150	Ball-milling-induced decomposition, irreversible
9	H_3BNH_3	18.3	12.6		Ammonia evolution possibility, irreversible

steps with the total released hydrogen of ~5.5 wt.% at 100°C–150°C as given in Equations 21.4 and 21.5:

$$3NaAlH_4 \rightarrow Na_3AlH_6 + 2Al + 3H_2 \,(3.72\ \text{wt.\%}\ H_2) \tag{21.3}$$

$$Na_3AlH_6 \rightarrow 3NaH + Al + \frac{3}{2}H_2\,(1.8\ \text{wt.\%}\ H_2) \tag{21.4}$$

Figure 21.1 represents the TGA profile of two-step hydrogen decomposition from $NaAlH_4$ with hydrogen release in weight percentage.[5] The differential seanning calorimetry (DSC) curves at different ramping rates such as 1°C–3°C/min also demonstrated two-step hydrogen decomposition by endothermic transitions as exhibited in Figure 21.1. It is also discernible that the heats of decomposition obtained from these endothermic profiles (ΔH = 30–40 kJ/mol H_2) are well matched with the theoretical limits.

Another advancement pertaining to the successful synthesis of $NaAlH_4$ from ball milling of NaH and Al in presence of Ti catalyst was reported.[6] Long-term hydrogenation and dehydrogenation cycling on this system reveals the complete reversibility of the Na_3AlH_6 phase; however, the partial regeneration of $NaAlH_4$ phase was obtained due to the lack of available aluminum and the catalytic activity of titanium in the host matrix (see Figure 21.2).

Following this breakthrough discovery, an effort was initiated in the US DOE hydrogen programtodevelop $NaAlH_4$ andrelatedalanates ashydrogenstoragematerials.[7,8] Another complex

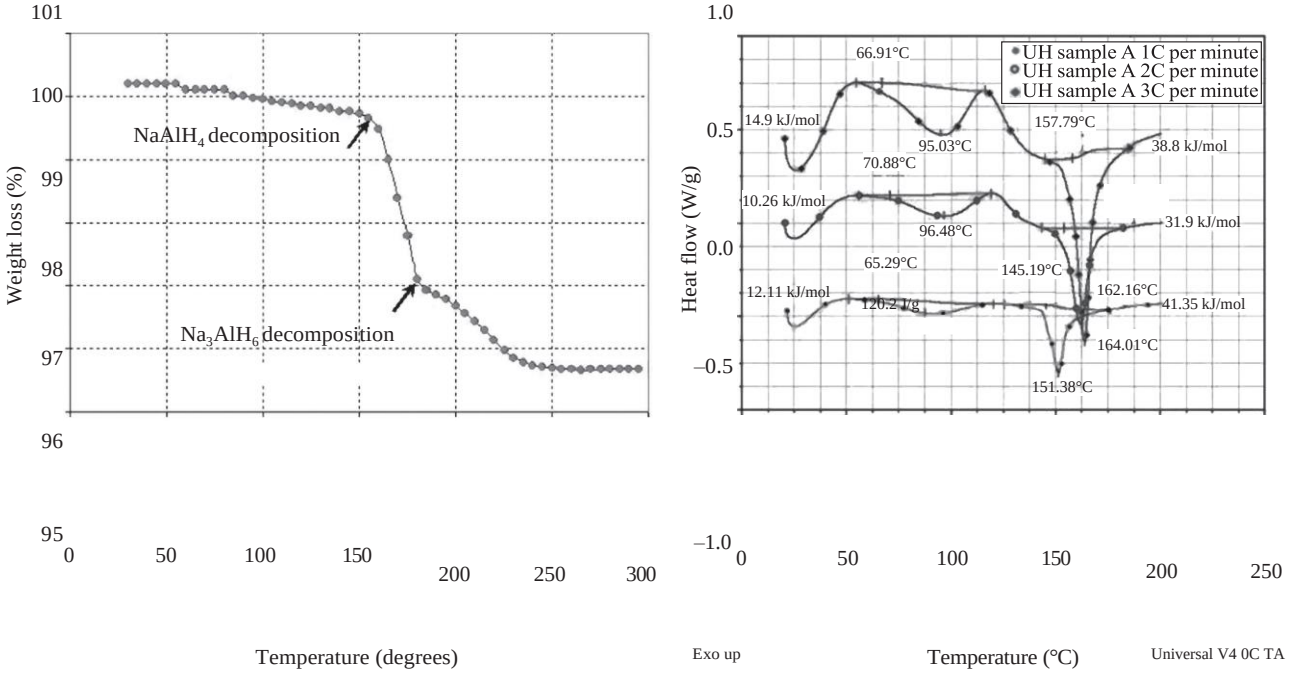


FIGURE 21.1

TGA and DSC profiles of $NaAlH_4$ with two steps of hydrogen decomposition.

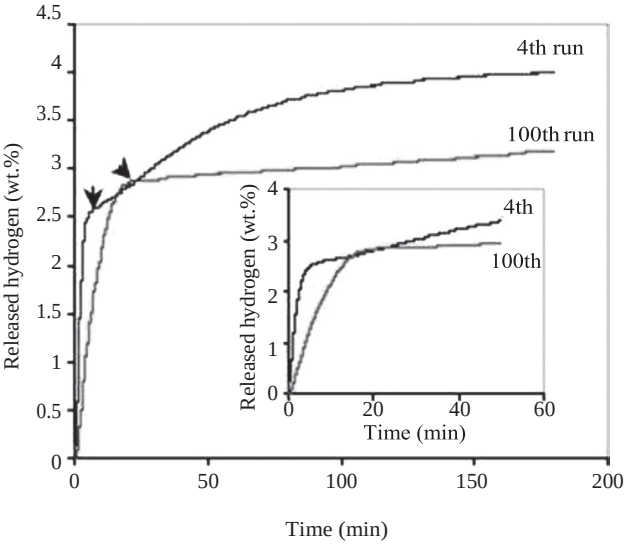


FIGURE 21.2

Hydrogen decomposition in $NaAlH_4$ during the 4th and 100th cycles.

TABLE 21.3

New Complex Hydrides and Their Hydrogen Storage Capacity

S. No.	Complex Hydride	Theoretical Capacity (wt.%)	Decomposition Temperature, T_{dec} (°C)
1	$LiAlH_2(BH_4)_2$	15.2	
2	$Mg(BH_4)_2$	14.8	260–280
3	$NH_4Cl + LiBH_4$	13.6	> ambient
4	$Ti(BH_4)_3$	12.9	ca. 25
5	$Fe(BH_4)_3$	11.9	−30 to −10
6	$Ti(AlH_4)_4$	9.3	−85
7	$Zr(BH_4)_3$	8.8	<250
8	$Zn(BH_4)_2$	8.4	85

hydride, $Mg(AlH_4)_2$, contains 9.6 wt.% of hydrogen that decomposes below 200°C.[9] Some of the new complex hydrides and their theoretical capacities are listed in Table 21.3.

21.1.2 Borohydrides

Borohydride complexes with suitable alkali or alkaline earth metals are a promising class of compounds for hydrogen storage. $LiBH_4$ is one of the lightweight and high hydrogen storage capacity materials. It has a theoretical gravimetric and volumetric hydrogen storage capacities of 18.5 wt.% and 121 kg H_2/m^3,[10] which surpasses the DOE and FreedomCAR targets. Initial investigations have demonstrated that the hydrolysis reaction (21.5)[11–13] of $LiBH_4$ at room temperatures effectively releases hydrogen exothermically; however, the process is irreversible with $LiBO_2$ as a by-product. Hydrolysis reaction proceeds as follows:

$$LiBH_4 + 2H_2O \rightarrow LiBO_2 + 4H_2 \quad (215)$$

TABLE 21.4

Thermal Analysis of $LiBH_4$

Temperature Range (°C)	Description
108–112	Endothermic peak. Structural transition.
268–286	Fusion process with a slight weight loss.
380	Main weight loss due to H_2 decomposition.
483–492	Authors are not certain; however, it coincides with a weight loss.

TABLE 21.5

Thermal Studies by Zuttel et al. on $LiBH_4$

Temperature Range (°C)	Description
100	Structural transition with a slight weight loss
270	Fusion phase
320	First significant weight loss
400–500	Second significant weight loss

TABLE 21.6

Thermal Studies by Orimo et al. on $LiBH_4$ [14]

Temperature Range (K)	Description
380 (~107°C)	Structural transition
550 (~277°C)	Melting phase
600 to 700 (~327°C to 427°C)	Dehydriding reaction

An alternate route that has been previously investigated is to thermally destabilize $LiBH_4$. $LiBH_4$ has a known melting point around 275°C.[18] For the thermal properties of $LiBH_4$, refer to Table 21.4.

Recent thermal studies by Zuttel et al.[18] and Orimo et al.[14] further expand the understanding regarding $LiBH_4$ behavior (see Tables 21.5 and 21.6).

As an additional note, the structural transition of $LiBH_4$ has been found to be from orthorhombic[15] to hexagonal structure.[16]

According to Stasinevich and Egorenko,[17] the decomposition of alkali metal tetrahydroborides can proceed as reactions:

$$MBH_4 \rightarrow M + B + 2H_2 \quad (21.6)$$

$$MBH_4 \rightarrow MH + B + \frac{3}{2}H_2 \quad (21.7)$$

For $LiBH_4$, the dehydriding reaction (21.8) and rehydriding reaction (21.9) can be generally described as

$$LiBH_4 \rightarrow LiH + B + \frac{3}{2}H_2 \quad (21.8)$$

$$LiH + B + \frac{3}{2}H_2 \rightarrow LiBH_4 \quad (21.9)$$

Theoretically, the reaction (21.8) releases around 13.8 wt.% of hydrogen. According to Orimo et al.,[14] the rehydrogenation of $LiBH_4$ was achieved; however, the energy lev- els consumed during this process, 35 Mpa of hydrogen and 873 K, might not make it cost-effective. Additional investigations performed with $LiBH_4$ included the doping with SiO_2 as a catalyst, thus enabling the decrease of $LiBH_4$ dehydriding temperature to 300°C.[18] A recent report indicates a dehydrogenation–rehydrogenation cycle improve- ment and reducing the reaction enthalpy of $LiBH_4$ by the addition of MgH_2 in a ratio of $2LiBH_4 + MgH_2$.[19] The addition of MgH_2 reversibly destabilizes $LiBH_4$, which in con- sequence increases the hydrogen equilibrium pressure as reaction (21.10) and also the scheme of Figure 21.3:

$$LiBH_4 + \frac{1}{2} MgH_2 \leftrightarrow LiH + \frac{1}{2} MgB_2 + 2H_2 \tag{21.10}$$

Zn(BH4)2 is a ternary complex metal borohydride with a decomposition temperature of around 85°C.[3] Its theoretical hydrogen capacity is about 8.5wt.%, and it can be synthesized by metathesis reaction of $NaBH_4$ and $ZnCl_2$ in diethyl ether.[20] A recent report from Eun Jeon et al.[21] indicates that zinc borohydride was successfully synthesized by ball milling $ZnCl_2$ and $NaBH_4$ without the use of a solvent; refer to the following reaction:

$$ZnCl_2 + 2NaBH_4 \rightarrow Zn(BH_4)_2 + 2NaCl \tag{21.11}$$

An example of the decomposition of a borohydride ($Zn(BH_4)_2$) is as follows:

$$Zn(BH_4)_2 \leftrightarrow Zn + 2B + 4H_2 \tag{21.12}$$

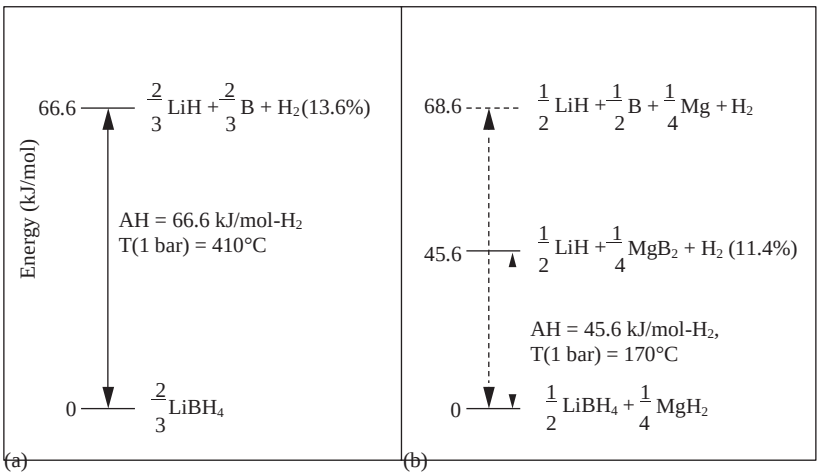


FIGURE 21.3

Dehydrogenation reaction mechanism with thermodynamic values for (a) pure $LiBH_4$ and (b) destabilized $LiBH_4$ with MgH_2.

which shows $Zn(BH_4)_2$ thermally decomposing into the constituent elements with release of hydrogen. The main reason that complex hydride compounds have not been considered for hydrogen storage before is their reported lack of reversibility.

21.1.3 Amides

Recently, a new hydrogen storage system, Li_3N, which absorbs 11.5 wt.% of hydrogen reversibly, has been reported.[22,23] The hydrogenation of Li_3N is a two-step reaction as shown in the schematics of Figure 21.4.

Li_3N absorbs 5.74 wt.% of hydrogen for the first step and 11.5 wt.% for second step. Since the hydrogen pressure for the reaction corresponding to the first step is very low (about 0.01 bar at 255°C), only the second step reaction of Li_2NH with H_2 leads to the reversible storage capacity. The plateau pressure for imides hydrogenation is 1 bar at a relatively high temperature of 285°C.[24] However, the lower temperature of reaction at 220°C and the increase of plateau pressure (27–32 bars) was achieved with MgH_2 addition as demonstrated in Figure 21.5.[25,26] Further research on this system may lead to additional improvements in operating conditions with improved capacity.

21.1.4 Quaternary Hydrides

There have been numerous works in finding complex hydrides for hydrogen storage, the most important and recent of which are summarized in Figure 21.6. While this figure certainly represents only a small portion of research performed on these systems, it nevertheless clearly illustrates that most materials either require temperatures that are too high for practical use or simply have a capacity that is too low. This figure summarizes mainly borohydride- and amide-based materials for hydrogen storage, as mentioned in the previous sections.

While it appears that there are several materials that would meet the DOE guidelines, the amidoborane samples,[27] such as $LiNH_2BH_3$ or $NaNH_2BH_3$, are nonreversible, thereby

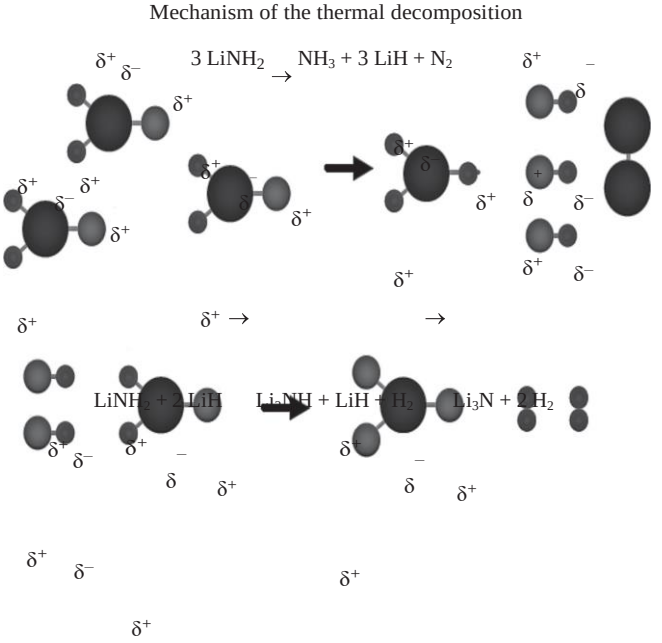


FIGURE 21.4

Schematics and the stepwise decomposition reaction of Li-amide system.[23]

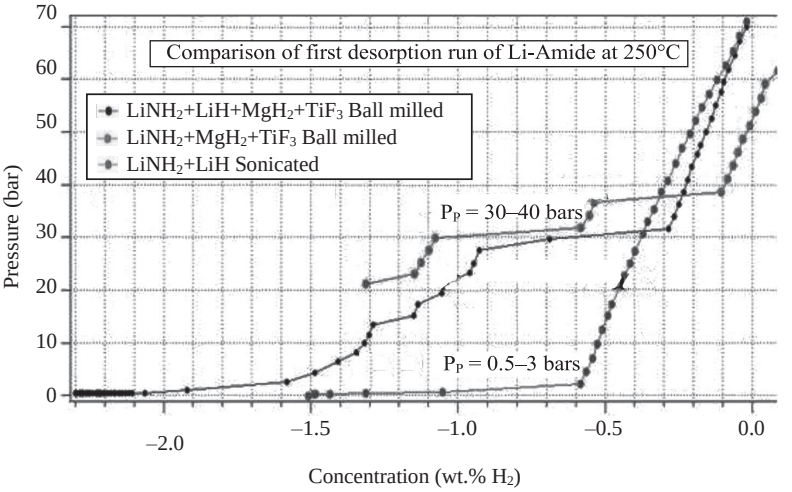


FIGURE 21.5

Pressure-composition isotherms of Li amide and Li amide/Mg hydride.

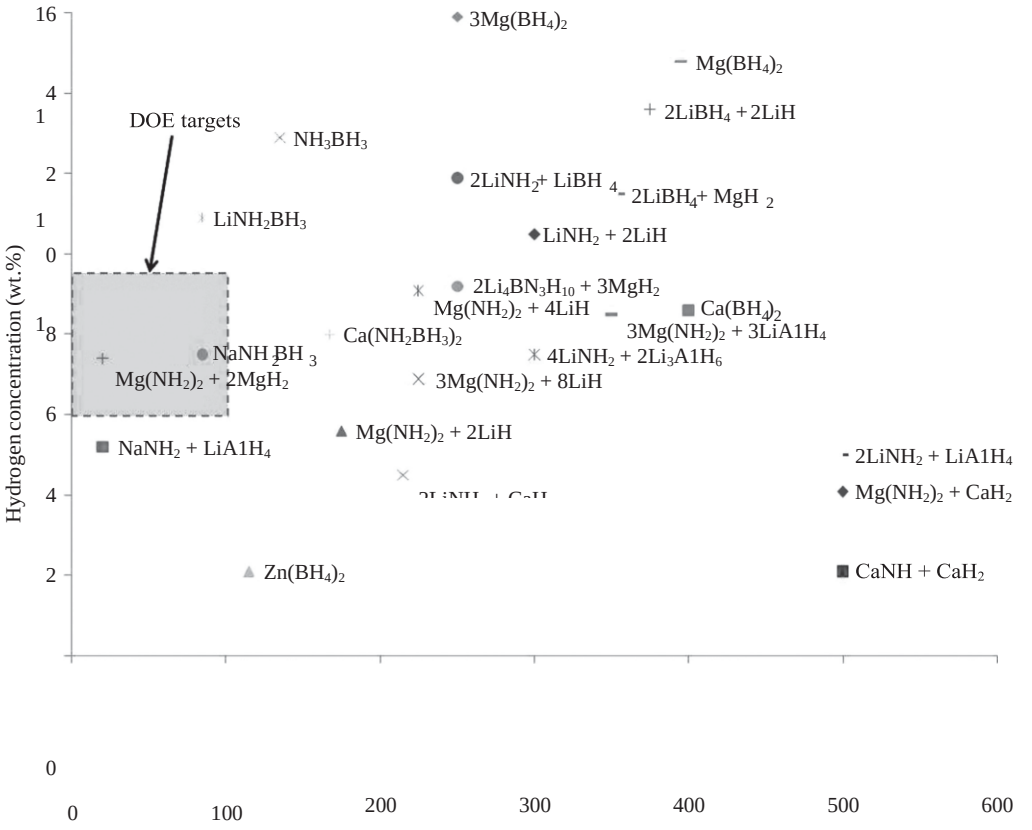


FIGURE 21.6

Hydrogen sorption capacity and temperature of selected complex hydrides and chemical hydrides with DOE target range highlighted.

making the systems impractical for mobile use, as required by the DOE. $Mg(NH_2)_2$ + $2MgH_2$ was found to release 7.6wt.% around room temperature during ball milling[28] but exhibited such a low enthalpy that a high pressure (much higher than that required by the DOE) would be required to rehydrogenate the material, thereby also making the material impractical for use as a reversible hydrogen storage system. A promising system for hydrogen storage has been magnesium amide ($Mg(NH_2)_2$) with a capacity of between 5.6 and 9.2 wt.%,[14,28,29] though all of these systems require temperatures of close to 200°C with a reduction in capacity directly proportional to the reduction in temperature.

By combining the advantages of some of these systems, namely, the borohydride family of materials with the magnesium amide systems, it is thought that a combinatorial effect can be achieved with a reduction in hydrogen sorption temperature, reversibility, as well as a high hydrogen capacity. The overall goal of the investigation of complex hydrides for hydrogen storage is to reduce the hydrogen release temperature, which can be accomplished either by reducing the particle size, as is the case for MgH_2, or by destabilizing the material through the addition of catalysts or other additives. Ball milling is the chosen processing technique, as this combines both chemical and mechanical synthesis of the material. By ball milling, a homogenous mixture with reduced particle size can be achieved, as schematically indicated by Figure 21.7. The parent compounds are combined in the ball mill container, and through milling at high speeds, the materials grind each other down to

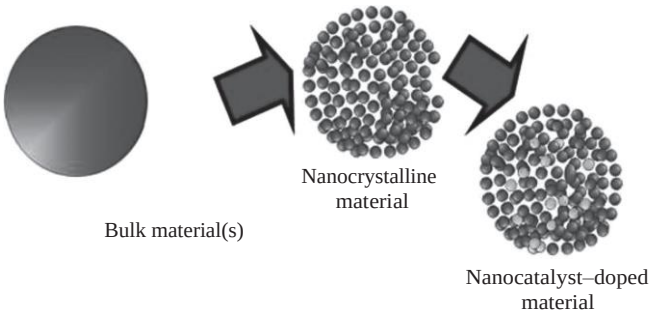


FIGURE 21.7

Schematic mechanochemical synthesis approach for complex hydrides to reduce particle size and achieve a homogenous mixture of parent compounds.

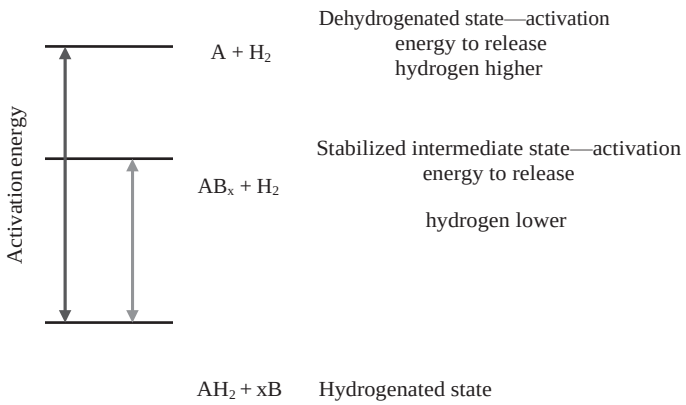


FIGURE 21.8

Destabilization of complex hydride through additives or catalysts.

a smaller particle size and produce a homogenous mixture, possibly with a new chemical composition.

Furthermore, by combining several materials, whether they are in small quantities, so as to count as a catalyst, or in larger quantities, to be considered destabilizers, the activation energy for hydrogen release or absorption can be altered and ideally brought to a point where a low temperature is enough to release the hydrogen. When a material is destabilized, it can react with the additive during dehydrogenation to form a new compound, one that requires a lower energy, as schematically shown in Figure 21.8. An additive, B, can allow the hydrogenated material, A, to form an intermediate compound, AB, while releasing hydrogen, thereby lowering the activation energy required for desorption. Various nano-additives are investigated for the complex hydride LiBNH as well as MgH_2, which is added in larger quantities. The details are described in the specific upcoming sections, as appropriate.

References

1. Z.P. Li, B.H. Liu, K. Arai, and S. Suda (2005). Development of the direct borohydride fuel cell, *Journal of Alloys and Compounds*, *404–406*, 648–652.
2. E. Orgaz and M. Gupta (1999). Electronic structure of BaReH9, *Journal of Alloys and Compounds*, *293–295*, 217–221.
3. Hydrogen Storage Materials Database, US Department of Energy, http://www.hydrogenmaterialssearch.govtools.us/
4. B. Bogdanovic and M. Schwickardi (1997). Ti-doped alkali metal aluminum hydrides as poten- tial novel reversible hydrogen storage materials, *Journal of Alloys and Compounds*, *253–254*, 1.
5. D. Sun, S.S. Srinivasan, T. Kiyobayashi, N. Kuriyama, and C.M. Jensen (2003). Rehydrogenation of dehydrogenation $NaAlH_4$ at low temperature and pressure, *Journal of Physical Chemistry B*, *107*(37), 10176–10179.
6. S.S. Srinivasan, H.W. Brinks, B.C. Hauback, C.M. Jensen, and D. Sun (2004). Long term cycling behavior of Titanium doped $NaAlH_4$ prepared through solvent mediated milling of Titanium ad-mixed NaH and Al, *Journal of Alloys and Compounds*, *377*, 283–289.
7. C.M. Jensen and R.A. Zidan (2002). Hydrogen storage materials and method of making by dry homogenation, US Patent, 6471935.
8. C.M. Jensen and K.J. Gross (2001). Development of catalytically enhanced sodium aluminum hydride as a hydrogen-storage material, *Applied Physics A*, *72*, 213.
9. M. Fichtner (2002). Synthesis and structure of magnesium alanates and two solvent adducts, *Journal Alloys and Compounds*, *345*(1–2), 286–296.
10. E.M. Fedneva, V.L. Alpatova, and V.I. Mikheeva (1964). $LiBH_4$ complex hydride materials, *Russian Journal of Inorganic Chemistry*, *9*, 826.
11. H.I. Schlesinger, H.C. Brown, A.E. Finholt, J.R. Gilbreath, H.R. Hoekstra, and E.K. Hyde (1953). Sodium borohydride, its hydrolysis and its use as a reducing agent and in the generation of hydrogen, *Journal of American Chemical Society*, *75*, 215–219.
12. V.C.Y. Kong, F.R. Foulkes, D.W. Kirk, and J.T. Hinatsu (1999). Development of hydrogen storage for fuel cellgenerators. i: Hydrogen generation using hydrolysishydrides, *International Journal of Hydrogen Energy*, *24*, 665–675.
13. Y. Kojima, Y. Kawai, M. Kimbara, H. Nakanishi, and S. Matsumoto (2004). Hydrogen genera- tion using sodium borohydride solution and metal catalyst coated on metal oxide, *International Journal of Hydrogen Energy*, *29*, 1213–1217.
14. S. Orimo, Y. Nakamori, G. Kitahara, K. Miwa, N. Ohba, S. Towata, and A. Zuttel (2005). Dehydriding and rehydriding reactions of $LiBH_4$, *Journal of Alloys and Compounds*, *404–406*, 427–430.

15. P.M. Harris and E.B. Meibohm (1947). Structure of lithium borohydride $LiBH_4$, *Journal of American Chemical Society*, *69*, 1231.
16. S. Gomes, H. Hagemann, and K. Yvon (2002). Lithium boro-hydride $LiBH_4$: II. Raman spectros- copy, *Journal of Alloys and Compounds*, *346*, 206.
17. D.S. Stasinevich and G.A. Egorenko (1968). Thermographic investigation of alkali metal and magnesium tetrahydroborates at pressure up to 10 atm, *Russian Journal of Inorganic Chemistry*, *13*, 341–343.
18. A. Zuttel, S. Rentsch, P. Fischer, P. Wenger, P. Sudan, Ph. Mauron, and Ch. Emmenegger (2003). Hydrogen storage properties of $LiBH_4$, *Journal of Alloys and Compounds*, *356–357*, 515–520.
19. J.J. Vajo, S.L. Skeith, and F. Mertens (2005). Reversible storage of hydrogen in destabilized $LiBH_4$, *Journal of Physical Chemistry B*, *109*, 3719–3722.
20. T.J. Marks and J.R. Kolb (1977). Covalent transition metal, lanthanide, and actinide tetrahy- droborate complexes, *Chemical Review*, *77*, 263.
21. E. Jeon and Y.W. Cho (2006). Mechanochemical synthesis and thermal decomposition of zinc borohydride, *Journal of Alloys and Compounds*, *422*, 273–275.
22. P. Chen, Z. Xiong, J. Luo, J. Lin, and K.L. Tan (2002). Interaction of hydrogen with metal nitrides and imides, *Nature*, *420*(2), 302.
23. P. Chen, Z. Xiong, J. Luo, J. Lin, and K.L. Tan (2003). Interaction between lithium amide and lithium hydride, *Journal of Physical Chemistry B*, *107*, 10967.
24. H.I. Schlesinger and H.C. Brown (1940). Metallo borohydrides. III. Lithium borohydride, *Journal of American Chemical Society*, *62*, 3429–3435.
25. W.F. Luo (2004). $LiNH_2$-MgH_2: A viable hydrogen storage system, *Journal of Alloys Compounds*, *381*, 284–287.
26. S.S. Srinivasan, E. Stefanakos, Y. Goswami, M. Jurcyzk, and M. Smith (2006). *16th World Hydrogen Energy Conference*, Leon, France, June'06, Transition metal assisted new complex hydrides for hydrogen storage, *WHEC Proceedings*.
27. Z. Xiong, C.K. Yong, G. Wu, P. Chen, W. Shaw, A. Karkamkar, T. Autrey, M.O. Jones, S.R. Johnson, P.P. Edwards, and W.I.F. David (2008). High-capacity hydrogen storage in lithium and sodium amidoboranes, *Nature Materials*, *7*, 138–141.
28. J. Hu, G. Wu, Y. Liu, Z. Xiong, P. Chen, K. Murata, K. Sakata, and G. Wolf (2006). Hydrogen release from $Mg(NH_2)_2$-MgH_2 through mechanochemical reaction, *Journal of Physical Chemistry B*, *110*, 14688–14692.
29. G. Renaudin, L. Guénée, and K. Yvon (2003). La_2MgNiH_7, a novel quaternary metal hydride containing tetrahedral $[NiH]^{4-}$ complexes and hydride anions, *Journal of Alloys and Compounds*, *350*, 145–150.
30. B. Huang, K. Yvon, and P. Fischer (1994). $LiMg_2RuH_7$, a new quaternary metal hydride contain- ing octahedral $[Ru(H)H_6]^{4-}$ complex anions, *Journal of Alloys and Compounds*, *210*, 243–246.

22

Nanomaterials for Hydrogen Storage

Sesha S. Srinivasan
Tuskegee University

Prakash C. Sharma
Tuskegee University

Elias K. Stefanakos
University of South Florida

D. Yogi Goswami
University of South Florida

CONTENTS

22.1 Nanomaterials for Hydrogen Storage 695
22.1.1 Nanoparticles/Nanocrystalline 695
22.1.2 Nanocatalytic Dopants 698
References 701

22.1 Nanomaterials for Hydrogen Storage

22.1.1 Nanoparticles/Nanocrystalline

It is generally known that pristine MgH_2 theoretically can release ~7.6 wt.% H_2 at decomposition temperatures >300°C at a H_2 pressure of ~1 bar.[1–3] However, so far, MgH_2 based materials have limited practical applications because both hydrogenation and dehydrogenation reactions are very slow, and hence, relatively high temperatures are required.[4] The phenomenon of mechanical milling helps to pulverize the particles of MgH_2 into micro- or nanocrystalline phases and thus leads to lowering the activation energy of desorption. Without using catalysts, the activation energy of absorption corresponds to the activation barrier for the dissociation of the H_2 molecule and the formation of hydro- gen atoms. The activation energies of the H_2 sorption for the bulk MgH_2, mechanically milled MgH_2, and nanocatalyst-doped MgH_2 are 162, 144, and 71 kJ/mol, respectively. It is undoubtedly seen that the activation barrier has been drastically lowered by nanocata- lyst doping. Figure 22.1 represents the thermogravimetric profiles of bulk MgH_2, which exhibits weight loss due to H_2 decomposition at 415°C.

However, mechanochemical milling of MgH_2 introduces defects and reduces the particle size. Thus, obtained micro-/nanocrystalline MgH_2 grains show endothermic H_2 decomposition (see Figure 22.2) at an earlier temperature of 340°C. In addition to nanoscale formation, doping by a nanocatalyst certainly decreases the onset transition temperature by as much as 100°C (Figures 22.1 and 22.2).

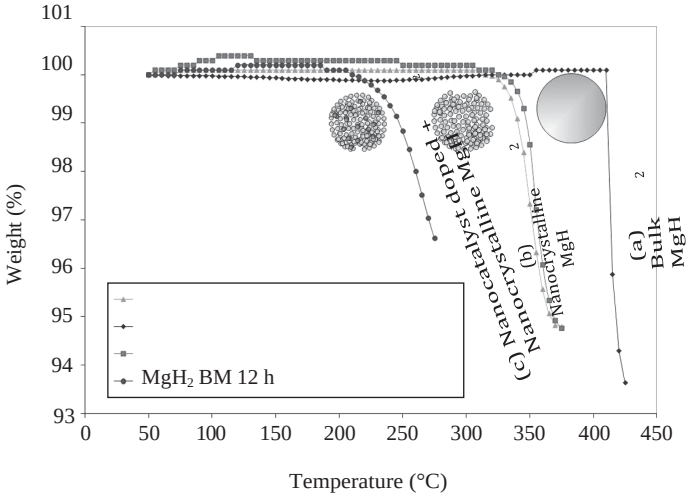


FIGURE 22.1

Thermogravimetric profiles of (a) bulk MgH_2, (b) nanocrystalline MgH_2, and (c) nanocatalyst-doped nanocrys- talline MgH_2.

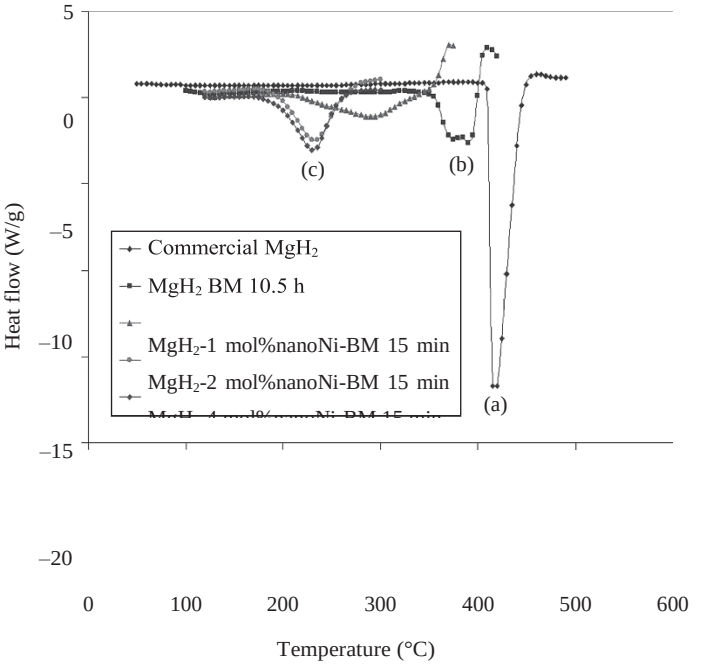


FIGURE 22.2

DSC profiles of (a) bulk MgH_2, (b) nanocrystalline MgH_2, and (c) nanocatalyst-doped nanocrystalline MgH_2.

Moreover, the enthalpy of decomposition, ΔH, obtained from these profiles is given in Table 22.1.

The structural characterization of the bulk, mechanochemically prepared, and nanocatalyst-doped MgH_2 has been carried out using XRD and is shown in Figure 22.3. The Bragg reflection of bulk MgH_2 shows sharp crystalline peaks. However, in the mechanochemically prepared MgH_2, the crystallite size is reduced to nanodimension (approximately five times

reduced intensity) with broadening of the FWHM. No additional peaks correspond to MgO or no other impurities were observed in the ball-milled samples. For the nanocatalyst-doped MgH_2, a small inflection peak at an angle of 45° represents the nano-Ni. A lattice strain was found in the mechanochemically milled samples in comparison to the bulk MgH_2.

TABLE 22.1

Enthalpy of H_2 Decomposition (ΔH_{dec})

Sample	T_{dec} (°C)	ΔH_{dec} (kJ/mol H_2)
Commercial MgH_2	415	55.98 ± 0.50
MgH_2(MC)	375	46.35 ± 0.50
MgH_2(MC)–nano-Ni	225	36.50 ± 0.50

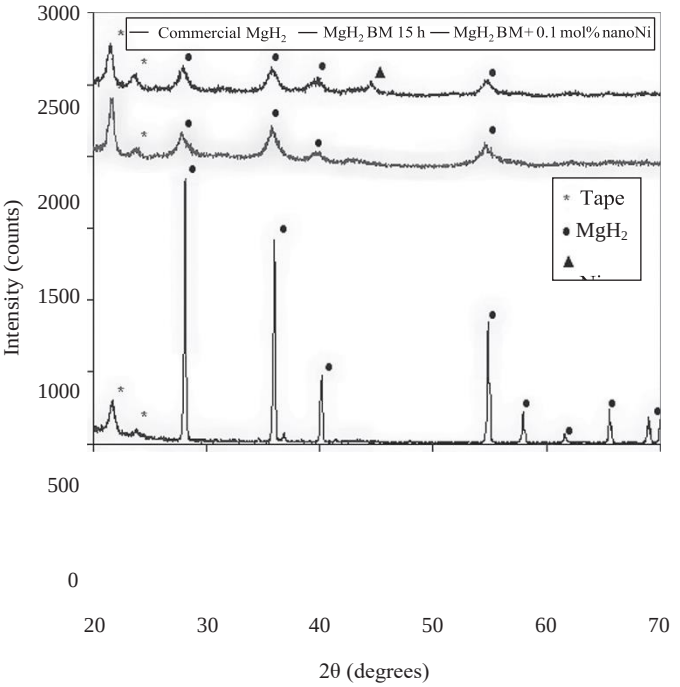
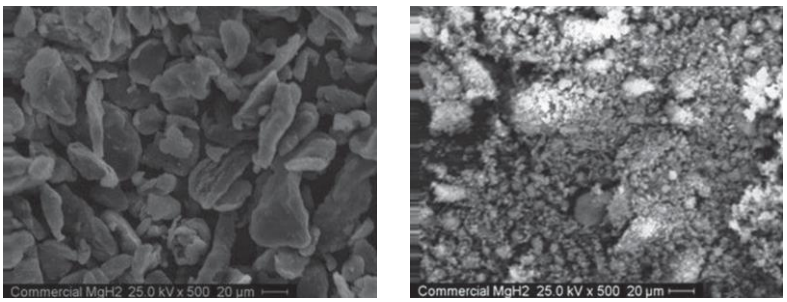


FIGURE 22.3

X-ray diffraction profiles of bulk, mechanochemically processed, and nanocatalyst-doped MgH_2 show the pres- ence of MgH_2 structural phase.



(a) (b)

FIGURE 22.4

SEM micrographs of (a) bulk and (b) nanocrystalline MgH_2.

Another significant improvement in the nanocrystalline MgH_2, over bulk samples, is the

reduced particle size as confirmed by SEM microstructural observations indicated in Figure 22.4. Bulk MgH_2 exhibits a larger crystallite size of 212 nm, whereas the nanocrystalline counterpart is shown to be about 27 nm, almost an order of magnitude less. The reduction in the particle size is thought to be the cause of the associated reduction of the decomposition temperature by at least 100°C (see Figures 22.1 and 22.2).

22.1.2 Nanocatalytic Dopants

Transition metal complexes, TMH_x (T = Mg; M = Fe, Co, Ni), have been identified as the potential candidates for H_2 storage. These hydrides, especially Mg_2FeH_6, have shown excellent cyclic capacities even without a catalyst.[5] However, at low temperatures, the cyclic nature of the hydride is limited. Also Mg_2FeH_6 shows the highest known volumetric H_2 density of 150 kg/m^3, which is more than double that of liquid H_2 as shown in Figure 22.5.[6] Its gravimetric H_2 density exceeds 5 wt.%, at ~400°C, and is only slightly lower than that of MgH_2 (~7.6 wt.%).

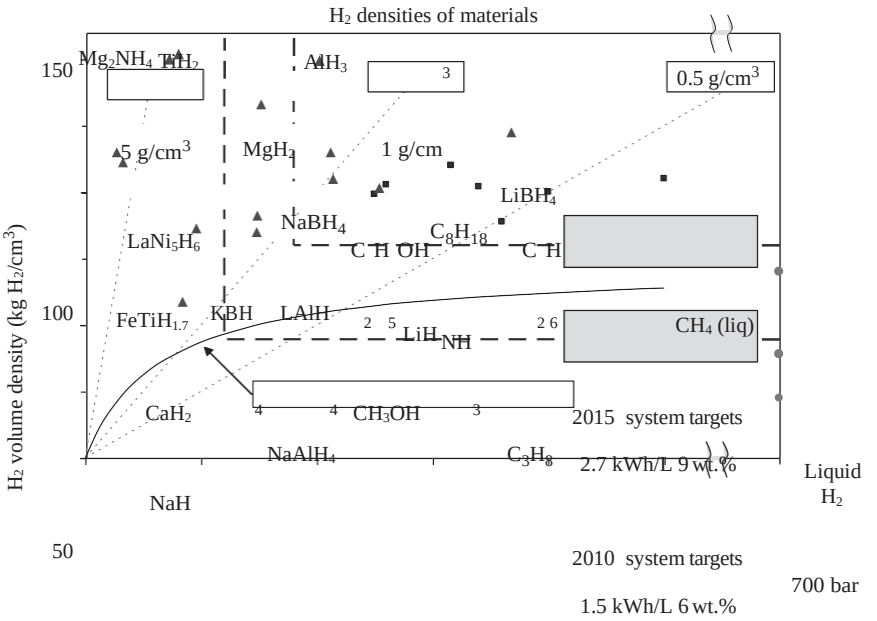
The Mg_2FeH_6 hydride belongs to the family of Mg-transition metal complex hydrides that have TMH_x complexes analogous to the $[AlH_4]^{1-}$ alanate complexes, for example, the $[FeH_6]^{4-}$ complex in Mg_2FeH_6 or $[NiH_4]^{4-}$ in Mg_2NiH_4.[7] MgH_2 forms ternary and quaternary hydride structures by reacting with various transition metals (Fe, Co, Ni, etc.) and thus leads to improved kinetics.[8] Moreover, the nanoscale version of these transition metal par- ticles offers an additional H_2 sorption mechanism via its active surface sites.[9] In a similar way, the synergistic approach of doping nanoparticles of Fe and Ti with a few mol% of car- bon nanotubes (CNTs) on the sorption behavior of MgH_2 has recently been investigated.[10] The addition of CNTs significantly promotes H_2 diffusion in the host metal lattice of MgH_2 due to the short pathway length and creation of fast diffusion channels.[11]

Fe does not form intermetallic compounds with Mg but instead readily combines with H_2 and Mg to form the ternary Mg_2FeH_6 hydride[5] according to the following reactions:

$$2Mg + Fe + 3H_2 \leftrightarrow Mg_2FeH_6 \quad (22.1)$$

$$2MgH_2 + Fe + H_2 \leftrightarrow Mg_2FeH_6 \quad (22.2)$$

The synthesis of nanostructured Mg_2FeH_6 has been carried out by an inexpensive mechanochemical process (Fritsch Pulverisette 6) under reactive gas (H_2) milling. The appropriate stoichiometries of elemental Mg (−325 mesh, 99.9% pure) and fine Fe powder



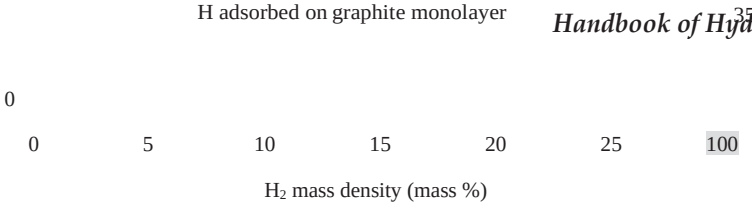


FIGURE 22.5

Volumetric and gravimetric H_2 densities of various hydrogen storage systems.

(−100 mesh, 99.8% pure) were taken in a 2:1 mole ratio and milled under continuous flow of H_2 (~2–3 atm). The milling parameters, such as speed (300 rpm), mode of rotations (forward and reverse motion), and time duration (5 h), were optimized to control the nanostructure grain size of the 2Mg + Fe mixture. After 5 h of milling, the sample was collected in a N_2-filled glove box for further characterization. X-ray diffraction profiles of bulk and nanocrystalline Mg_2FeH_6 are shown in Figure 22.6. It is clearly discernible from this figure that the crystallite size of the nanocrystalline sample is reduced by a factor of 3 when compared to the bulk counterparts. Powder x-ray diffraction of the mixture before and after mechanochemical processing under H_2 ambient shows the disappearance of sharp crystalline peaks corresponding to Mg and formation (FWHM calculations) of nanocrystalline reflections as exhibited in Figure 22.6.

Figure 22.7 represents the comparative differential scanning calorimetric (DSC) patterns of bulk and nanocrystalline Mg_2FeH_6. It is interesting to note that the endothermic peak

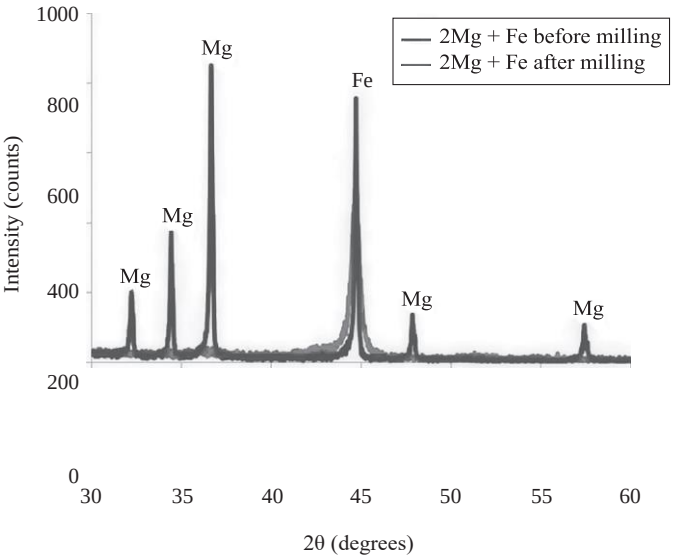


FIGURE 22.6

XRD profiles of bulk and nanocrystalline Mg_2FeH_6.

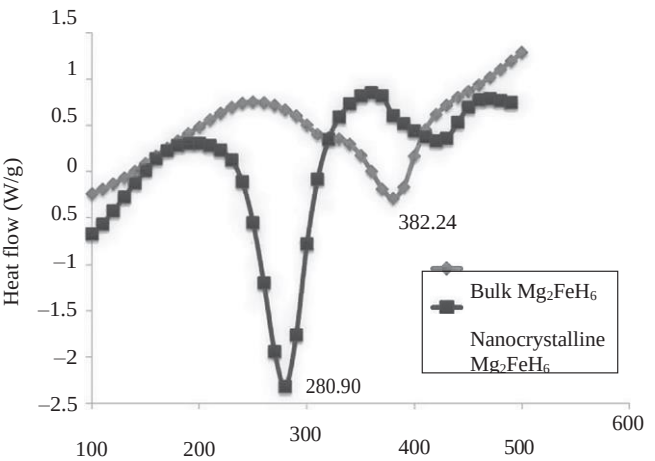


FIGURE 22.7

DSC curves of bulk and nanocrystalline Mg_2FeH_6.

due to H_2 desorption occurs at a lower temperature, 280°C, for the nanocrystalline structure, whereas the bulk sample exhibits an endothermic peak at 383°C. An early onset at around 250°C is observed for the nanocrystalline material (n-Mg_2FeH_6).

We have also presented in the present review that the kinetics of absorption and desorption increase upon nanocrystallization and Ti-catalyst doping into the host lattice structure of Mg_2FeH_6. Figure 22.8 clearly shows at least a threefold–fourfold improvement in the hydrogenation kinetics of Mg_2FeH_6 by the simultaneous nanocrystallization and nanocatalytic doping.

The absorption kinetics of Ti-doped nanocrystalline Mg_2FeH_6 increases with increas- ing cycle number as depicted in Figure 22.9. This is due to the fact that during each and

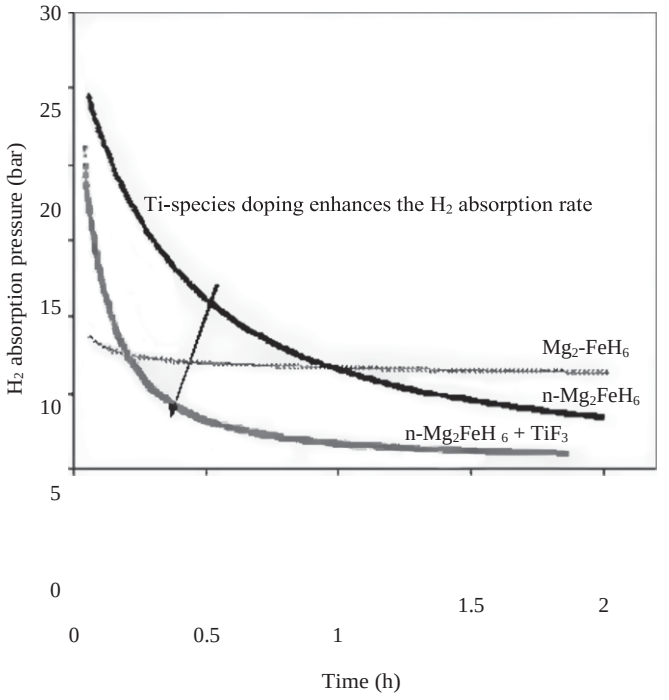
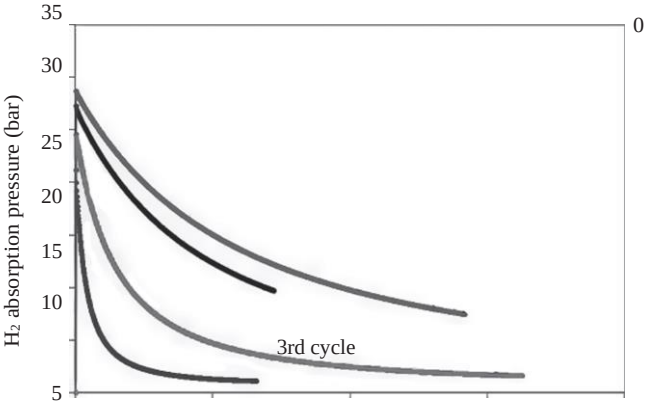


FIGURE 22.8

Absorption kinetics of bulk Mg_2FeH_6, nanocrystalline Mg_2FeH_6, and Ti-doped nanocrystalline Mg_2FeH_6 at 250°C.



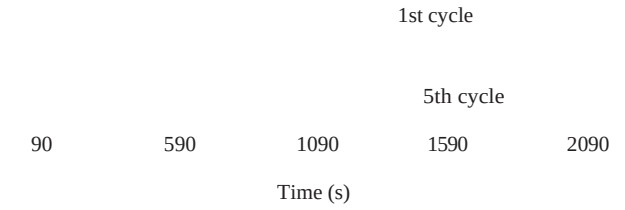


FIGURE 22.9

H_2 absorption kinetics of Ti-doped nanocrystalline Mg_2FeH_6; rate increases with cycling (sample mass of 1.5 g and temperature of desorption of 250°C).

every cycle, greater number of H atoms is being absorbed by the host lattice structure. Additionally, Ti addition only influences the sorption kinetics of nanocrystalline Mg_2FeH_6 and does not improve the overall H capacity.

References

1. Zaluska A, Zaluski L, Strom-Olsen JO. Structure, catalysis and atomic reactions on the nano- scale: A systematic approach to metal hydrides for hydrogen storage, *Appl. Phys. A* 2001;72:157.
2. Price TCE, Grant DM, Walker GS. Synergistic effect of $LiBH_4 + MgH_2$ as a potential reversible high capacity hydrogen storage material, *Ceram. Trans*. 2009;202:97.
3. Niemann MU, Srinivasan SS, McGrath K, Kumar A, Goswami DY, Stefanakos EK, Nanocrystalline effects on the reversible hydrogen storage characteristics of complex hydrides, *Ceram. Trans*. 2009;202:111.
4. Huot J, Liang G, Boily S, Van Neste A, Schulz R. Structural study and hydrogen sorption kinet- ics of ball-milled magnesium hydride, *J. Alloys Comp*. 1999;293/295:495.
5. Bogdanovic B, Schlichte K, Reiser A. Thermodynamic properties and cyclic-stability of the sys- tem Mg_2FeH_6. In: *Hydrogen Power: Theoretical and Engineering Solutions*, T.O. Saetre, ed., Kluwer Academic, Dordrecht, the Netherlands, 1991, p. 291.
6. Zuttel A, Wenger P, Rentsch S, Sudan S, Mauron P, Emmenegger C. $LiBH_4$ a new hydrogen stor- age material, *J. Power Sources* 2003;118:1.
7. Sandrock G. A panoramic overview of hydrogen storage alloys from a gas reaction point of view, *J. Alloys Comp*. 1999;293–295:877.
8. Yvon K, Bertheville B. Magnesium based ternary metal hydrides containing alkali and alkaline- earth elements, *J. Alloys Comp*. 2006;425:101.
9. Jeon K-J, Theodore A, Wu C-Y, Cai M. Hydrogen absorption/desorption kinetics of magnesium nano-nickel composites synthesized by dry particle coating technique, *Int. J. Hydrogen Energy* 2007;32(12):1860–1868.
10. Yao X, Wu CZ, Wang H, Cheng HM, Lu GQ. Effects of carbon nanotubes and metal catalysts on hydrogen storage in magnesium nanocomposites, *J. Nanosci. Nanotechnol*. 2006;6(2):494.
11. Wu CZ, Wang P, Yao X, Liu C, Chen CM, Lu GQ, Cheng HM. Hydrogen storage properties of MgH_2/SWNT composite prepared by ball milling, *J. Alloys Comp*. 2006;420:278.

23

Chemical Hydrogen Storage

Sesha S. Srinivasan
Tuskegee University

Prakash C. Sharma
Tuskegee University

Elias K. Stefanakos
University of South Florida

D. Yogi Goswami
University of South Florida

CONTENTS

23.1 Chemical Hydrogen Storage 703
References 705

23.1 Chemical Hydrogen Storage

The term *chemical hydrogen storage* is used to describe storage technologies in which hydrogen is generated through a chemical reaction. Common reactions involve chemical hydrides with water or alcohols. Typically, these reactions are not easily reversible on-board a vehicle. Hence, the *spent fuel* or by-products must be removed from the vehicle and regenerated off-board.

Hydrolysis reactions involve the oxidation reaction of chemical hydrides with water to produce hydrogen. The reaction of sodium borohydride has been the most studied to date.[1] This reaction is

$$NaBH_4 + 2H_2O \rightarrow NaBO_2 + 4H_2 \quad (23.1)$$

In the first embodiment, slurry of an inert stabilizing liquid protects the hydride from contact with moisture and makes the hydride pumpable. At the point of use, the slurry is mixed with water and the consequent reaction produces high-purity hydrogen. The reaction can be controlled in an aqueous medium via pH and the use

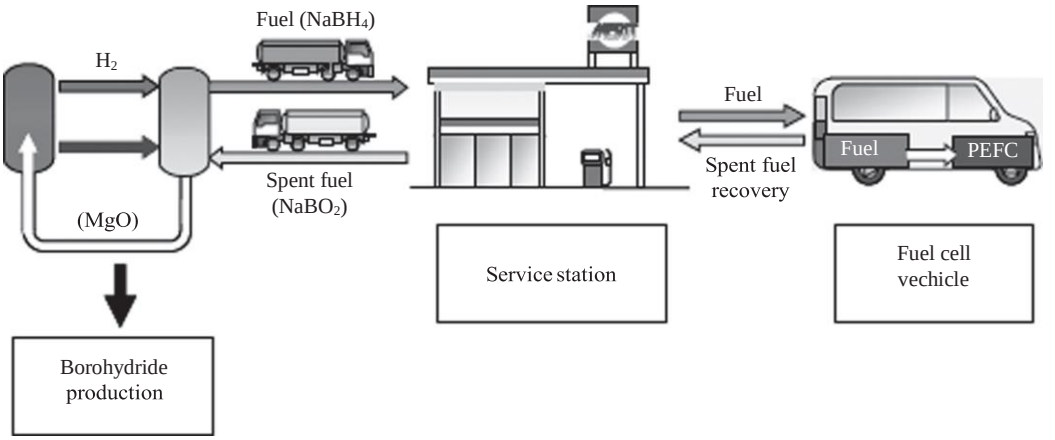


FIGURE 23.1

Hypothetical hydrogen economy using $NaBH_4$ as hydrogen storage.

of a catalyst. While the material hydrogen capacity can be high and the hydrogen release kinetics fast, the borohydride regeneration reaction must take place off-board. Regeneration energy requirements cost and life-cycle impacts are key issues currently being investigated.

Millennium Cell has reported that their $NaBH_4$-based Hydrogen on Demand™ sys- tem possesses a system gravimetric capacity of about 4 wt.%.[1] Similar to other mate- rial approaches, the issues include system volume, weight and complexity, and water availability.

Another hydrolysis reaction that is presently being investigated by Safe Hydrogen is the reaction of MgH_2 with water to form $Mg(OH)_2$ and H_2.[2] In this case, particles of MgH_2 are contained in nonaqueous slurry to inhibit premature water reactions when hydrogen generation is not required. Material-based capacities for the MgH_2 slurry reaction with water can be as high as 11 wt.%. However, similar to the $NaBH_4$ approach, water must also be carried on-board the vehicle in addition to the slurry, and the $Mg(OH)_2$ must be regenerated off-board.

An idea on how the complex metal hydrides would be processed during the hydrogen economy is depicted in Figure 23.1 using sodium borohydride ($NaBH_4$).

A new chemical approach may be hydrogen generation from ammonia borane materials by the following reactions:

$$NH_3BH_3 \rightleftharpoons NH_2BH_2 + H_2 \rightleftharpoons NHBH + H_2 \quad (23.2)$$

The first reaction, which occurs at less than 120°C, releases 6.1 wt.% hydrogen, while the second reaction, which occurs at approximately 160°C, releases 6.5 wt.% hydrogen.[3] Recent studies indicate that hydrogen release kinetics and selectivity are improved by incorporating ammonia borane nanosized particles in a mesoporous scaffold.

References

1. Wu C, Bai F, Yi Y, Zhang B. Cobalt boride catalysts for hydrogen generation from alkaline $NaBH_4$ solution. *Materials Letters* 2005;59:1748–1751.
2. Mcclaine AW, Tullmann S, Brown K. Chemical hydride slurry for hydrogen production and storage, *Proceedings of the US DOE Hydrogen Energy Program*, Progress Report, 2004:204–209.
3. Karkamkar A, Aardahl C, Autrey T. Recent developments on hydrogen release from ammonia borane, *Material Matter* 2007;2(2):6–9.

24

Hydrogen Adsorption and Storage on Porous Materials

K. Mark Thomas
Newcastle University

CONTENTS

24.1 Introduction 707
24.2 Experimental Methods for Hydrogen Adsorption 709
24.3 Activation of Porous Materials 710
24.4 Characterization of Porous Materials 711
24.5 Hydrogen Adsorption Measurements 712
24.6 MOF Series Based on Dicarboxylate and Tetracarboxylate Ligands 712
24.7 Hydrogen Adsorption Studies up to 1 Bar Pressure 719
24.8 Hydrogen Adsorption Capacity Studies at High Pressure 721
24.9 Temperature Dependence of Hydrogen Physisorption 734
24.10 Hydrogen–Surface Interactions in Pores 735
24.10.1 Isosteric Enthalpies of Hydrogen Adsorption 737
24.10.2 Diffraction Studies of Hydrogen in Pores 742
24.10.3 Spectroscopic Studies of Hydrogen–Surface Interactions 743
24.10.3.1 Framework Flexibility and Hysteretic Adsorption in MOFs 745
24.10.3.2 Kubas-Type Compounds Doped in Porous Materials 746
24.10.3.3 Hydrogen Spillover on Porous Materials 746
24.10.3.4 Comparison of H_2 and D_2 Adsorption 747
24.11 Applied Electric Field and Hydrogen Adsorption 748
24.12 Conclusions 748
Acknowledgments 750
Abbreviations 750
References 752

24.1 Introduction

The current interest in hydrogen as a sustainable fuel is related to strategic and environmental concerns. The former includes security of supply with the increasing worldwide demand for energy, concerns that world oil production is close to reaching a peak,[1] and the long-term availability of oil supplies. The latter is related to the need for more environmentally friendly alternative fuel due to pollution from fossil fuel combus- tion leading to poor air quality and global warming due to carbon dioxide emissions.

There are major scientific and engineering challenges, which need to be overcome before the development of a hydrogen-based economy and widespread use of hydrogen as an alternative fuel to oil can be achieved. The storage of hydrogen for use in vehicles is perhaps the most difficult problem to overcome. Handling and storage technologies for hydrogen in an industrial situation, where safety issues can be closely controlled, are well established. However, the use of hydrogen for onboard transport applications involving the general public is much more difficult because of safety, scientific, engi- neering, and economic constraints.

Hydrogen storage requirements for vehicles are extremely challenging because of safety issues and are determined by storage volume requirements that should not compromise interior space and performance requirements. The US DOE hydrogen on-board storage system targets[2] for vehicles include the weight of the storage tank and associated cooling, pressure, and delivery control equipment in the calculations for real vehicle applications. The target for 2015 is a hydrogen-powered average corporate vehi-cle with storage capacity of 5–13 kg of hydrogen giving a refueling range >300 miles (483 km) with a refueling time < 5 min. Smaller more fuel-efficient cars are likely to be used in the future leading to slightly less demanding hydrogen storage requirements.

When hydrogen is used as a fuel for transport applications, a much larger storage tank is required than used for current hydrocarbon-fuelled vehicles. The reason for this is that while hydrogen has a higher combustion enthalpy than hydrocarbon fuels on a weight basis, it has a much lower value on a volume basis. Safety issues and convenience are paramount for storage applications and there are severe practical limitations for tank size, refueling range, etc. The limitations on storage space for hydrogen in vehicles lead to the requirement for greater efficiency, and this could be provided by fuel-cell-powered vehicles, which have greater efficiency than internal combustion engines. However, larger storage volumes are still required compared with current vehicles. The durability of fuel cells and their current reliance on precious metal catalyst are issues. The devel- opment of a hydrogen economy has potential strategic and environmental benefits pro- vided that hydrogen can be produced in an environmentally sustainable manner leading to reduced reliance on imported oil, air pollution, and release of carbon dioxide.

The development of a suitable hydrogen storage method is the major scientific challenge to overcome, before the technology necessary for change from petroleum to sustainable hydrogen, as an energy carrier for transport applications can be implemented. The storage methods currently being considered include high-pressure gas, liquid hydrogen, adsorp-tion on porous materials at lower pressures, complex hydrides, and hydrogen intercala- tion in metals.[3] The main constraint for vehicles is the volume required to store sufficient hydrogen for acceptable refueling ranges. Although hydrogen storage tanks up to 70 MPa have been used, there is still a limitation on the amount of hydrogen that can be delivered from a given size of tank. The energy required to compress the gas is a consideration in relation to total energy use. Liquid hydrogen provides a higher hydrogen storage density ($\sim \times 2$) that of compressed hydrogen gas tank, but there are limitations due to the extremely low temperatures required (critical temperature 32.98 K),[4] and significant losses of hydro-gen may occur due to evaporation during storage. Liquefaction costs are also significant. Compressed gas and liquid hydrogen storage methods currently available do not fully satisfy the safety and refueling range criteria for hydrogen storage for vehicles. Therefore, novel hydrogen storage methods involving high-pressure vessel containing porous mate-rials, metal hydrides, or other materials are being considered. This approach combines the advantages of both compressed gas and solid state material storage to increase the total hydrogen storage capacity at lower pressures than compressed gas alone.

Porous materials have nanometer-sized pores that provide large internal surface areas and pore volumes. These materials are widely used for gas storage,[3,5] purification and separation,[6,7] removal of trace pollutant species,[8,9] and as catalysts and catalyst supports.[10,11] Hydrogen physisorption on range porous materials is one of the storage methods being investigated for use in transport applications.[12–22] A wide range of carbons, aluminosilicates, aluminophosphates, silicas, microporous polymers, covalent organic frameworks (COFs), and porous metal–organic framework (MOF) materials with a wide variety of porous structures, surface chemistry, and structural flexibility have been studied. Porous carbons have relatively rigid structures and the surface sites are limited to hydrophobic graphene layers and oxygen and nitrogen surface functional groups. The structures of MOF coordination polymers were reported[23,24] but the first gas adsorption studies were not published until 1997.[25] These materials may have diverse surface chemistry,[26] pore architectures,[27] framework flexibility,[12] and very large internal surface areas and pore volumes.[28] Porous coordination polymers may be prepared from a wide range of multidentate ligands and metals or metal clusters (secondary building units [SBUs]) to give materials with diverse surface chemistry and porous structure characteristics.[27,29,30] The pore structure and surface chemistry of MOFs may be tailored to specific applications and have the greatest range of surface chemistry for optimizing hydrogen interactions with surface sites varying from unsaturated metal centers to hydrophobic ligand surfaces. MOFs with zeolite-type structures have also been synthesized and these may also have applications for gas storage.[31,32]

Hydrogen adsorption characteristics have good correlations with a variety of pore structural characteristics determined by gas adsorption methods for a wide range of porous materials.[13,17,19] The current status of experimental studies of hydrogen physisorption and storage on porous materials is reviewed and future prospects are discussed.

24.2 Experimental Methods for Hydrogen Adsorption

Hydrogen adsorption measurements for porous materials require stringent experimental protocols and validation using extensive reproducibility studies in order to establish the accuracy.[13,29,33] These measurements can be obtained using either (a) direct gravimetric instruments of adsorption or (b) indirect volumetric (or manometric) measurements using a Sievert apparatus. Gravimetric measurements are usually used up to ~20 bar and volumetric measurements can be used up to 200 bar pressure although results have usually only been reported up to 100 bar. Volumetric instruments have a simpler design, which is cheaper to construct for high-pressure instruments. Adsorption/desorption in volumetric instruments is driven by pressure differences. Gravimetric measurements are carried out under isobaric conditions (constant chemical potential) and, hence, may provide accurate adsorption/desorption kinetics.[6,34] Both measurement techniques require ultraclean high-vacuum systems with all metal seals with diaphragm and turbo pumps, which can be evacuated to 10^{-10} bar to completely degas the material, and a gas purification system is needed to remove trace impurities from hydrogen. The buoyancy corrections for gravimetric measurements and the sample volume measurement for volumetric measurements are equivalent since helium is used to determine both corrections.[33] The equilibrium

degassed state for porous material is easily determined for gravimetric instruments, but establishing that the sample is completely degassed is more difficult in the case of volumetric measurements. In the latter, errors associated with introduction of doses of gas are cumulative for each isotherm pressure step and increase with increasing pressure.[33,35] Also, the importance of the amount remaining unadsorbed in the dead space increases with increasing pressure.[36] The relative magnitudes of the corrections and amounts adsorbed lead to a major source of uncertainty influencing the accuracy of high-pressure hydrogen adsorption measurements. Broom et al. have provided a detailed discussion of sources of errors for hydrogen adsorption measurements.[33,37] Reproducibility studies carried out by various laboratories have been reported[38–40] and reasonable agreement has been obtained.

Adsorption isotherms are presented on either surface excess or absolute basis in moles/g of outgassed adsorbent.[36,41] Sometimes, for gas storage applications, total wt% loading is quoted.[42–44] The adsorbed hydrogen phase is similar to an incompressible fluid, and the adsorbate densities for various hydrogen/adsorbent systems estimated from the maximum amount of hydrogen adsorbed with the total pore volumes obtained from gas adsorption studies or crystallographic pore volumes determined using the PLATON software package are typically in the range of 0.045–0.07 g cm^{-3}.[45–47] In comparison, the density values for liquid hydrogen are 0.0708 g cm^{-3} at 20.28 K and 0.077 g cm^{-3} at 13.8 K.[4] The density of liquid H_2 probably represents an upper limit for the density of hydrogen adsorbed in pores at 77 K and higher temperatures.

24.3 Activation of Porous Materials

The stability of porous materials and the conditions to obtain fully degassed porous structures for adsorption studies vary considerably. Porous carbons usually require heating to ~150°C under high vacuum to remove adsorbed material. However, in the case of MOFs, the activation procedure is often more complex. The stability,[43] purity,[48] and activation procedures[49] for MOFs are sometimes issues resulting in difficulties in obtaining repeatable adsorption results. Comparison of x-ray powder diffraction data with single-crystal data allows the purity of MOF samples prior to activation to be confirmed. The guests (templates, solvent, or coordinated solvent trapped inside MOFs) must be removed to form the porous structure and this may result in structural change that needs to be character- ized. Activation of MOFs to form porous structures can be achieved by heating in ultrahigh vacuum, exchanging with a more volatile solvent to facilitate removal and extraction with supercritical carbon dioxide. Comparison of the methods for four MOFs shows that supercritical carbon dioxide drying results in large increases in the surface area as determined by gas adsorption measurements.[50] It was proposed[50] that supercritical carbon dioxide extraction inhibits mesopore collapse leaving micropores accessible to gases. It is evident that supercritical carbon dioxide drying has advantages in activating the porous structures of some MOFs.

The removal of coordinated solvent may lead to the formation of unsaturated or *open* metal centers, which are high-energy sites for adsorption. Therefore, thermal and chemical stability and framework flexibility of desolvated MOF porous material structures and activation procedures are important considerations when comparing adsorption characteristics.

24.4 Characterization of Porous Materials

Pores are classified by the International Union of Pure and Applied Chemistry (IUPAC) on the basis of size as micropores (<2 nm), mesopores (2–50 nm), and macropores (>50 nm).[36] Adsorption of hydrogen in the narrowest pores (<0.5 nm), where hydrogen is similar in size to pore dimensions, has the complication of quantum molecular seiving effects, giving rise to slow rates of adsorption and desorption due to activated diffusion effects.[51,52] Rigorous distinction of adsorption characteristics based on the classes of microporosity is not possible because they depend on adsorbate and adsorbent interactions rather than dimensions.[53] The terms *nanopore and nanoporosity* are not defined in the IUPAC scheme but generally refers to nanometer-sized pores. Characterization of the porous structures of materials is difficult, for example, MOF materials are flexible and the structure may partially collapse on desolvation. A variety of isotherm equations and adsorptives have been used to characterize porous structures using gas adsorption techniques. Porous structures are characterized by surface areas (determined using Langmuir, Brunauer–Emmett–Teller [BET], Dubinin–Radushkevich [DR], etc., equations), pore volumes (total, micropore [DR], etc.), and pore size distributions. Pore volumes, surface areas, and pore size distributions are estimates for relative comparisons for characterization purposes.

BET surface areas obtained from nitrogen adsorption at 77 K are frequently used as a standard procedure for characterization of porous materials.[54] Studies suggested that BET surface area correlates with MOF surface areas determined from crystallographic data.[55] However, heterogeneous surfaces are found in MOFs and the BET surface area is best described as an *apparent* surface area. If a Type I isotherm has a plateau at high relative pressure, the pore volume is given by the amount adsorbed (converted to a liq- uid volume) since the mesopore volume and external surface are both relatively small. Porous structure characterization parameters (Langmuir and BET surface areas and pore volumes) obtained from gas adsorption studies of MOFs have interrelated correlations.[19] The surface excess obtained from the high-pressure adsorption isotherm is the amount present in the interfacial layer over the gas concentration present at the same equilibrium gas pressure, in which the gas-phase concentration is constant up to the Gibbs surface.[36] High-pressure adsorption studies usually report the surface excess, but in the case of gas storage, the total amount of gas that can be stored by a porous material is also relevant. Accurate measurements of the absolute amounts of adsorbed hydrogen are more difficult.[56] The total amount adsorbed is often estimated from the following equation[57]:

$$n_{tot} = n_e + p_v \times \rho_{gas}$$

where

n_{tot} is the total absolute uptake
n_e is the surface excess uptake
ρ_{gas} is the bulk density of gas (hydrogen)
p_v is the pore volume

The use of crystal density, which is mainly used for reporting hydrogen storage on MOFs may give unrealistically high volumetric storage values.[58] It was suggested that tap or packing densities were the most suitable. A comparison of two carbons and MOF-5 showed that the carbons gave the highest volumetric capacity.[58]

The amount adsorbed on a volumetric basis is the most appropriate for hydrogen storage for transport applications. The gas uptake on a volumetric basis for real systems is also subject to packing effects, which are determined by particle size and shape. Packing effects will reduce the uptake of real systems and further work is required to establish limitations associated with these effects.

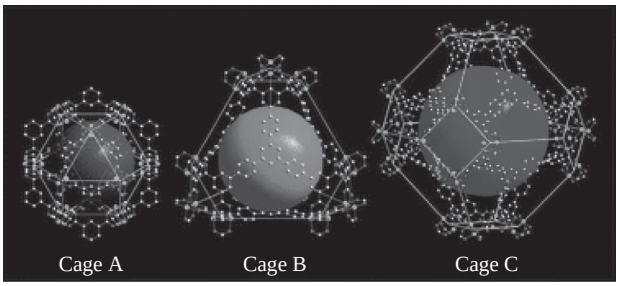
24.5 Hydrogen Adsorption Measurements

Hydrogen adsorption has been investigated for a wide range of porous materials ranging from amorphous materials (activated carbons [ACs], porous polymers, etc.) to crystalline materials (MOF materials, zeolites, etc.) and also, metal-doped materials. The hydro- gen adsorption isotherms for porous materials at 77 K have been studied extensively and are related to pore structure characterization parameters. Hydrogen adsorption at room temperature is much lower. Similarities are observed for the all types of porous materials.

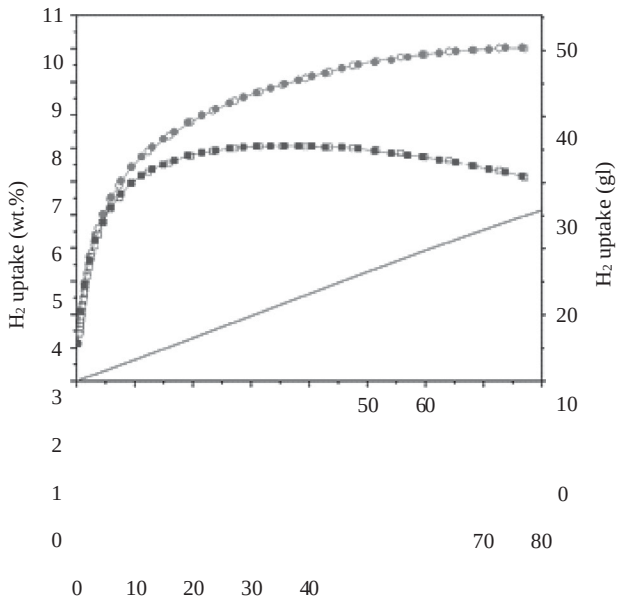
Hydrogen adsorption on MOFs has received much recent attention because of the wide range of surface chemistry and crystalline structures with some of the largest pore volumes and surface areas available. Figure 24.1 shows the structure of $[Cu_3(dcbpyb) \cdot (H_2O)_3] \cdot 8dmso \cdot 15dmf \cdot 3H_2O$ (NOTT-112) and hydrogen adsorption isotherms on a surface excess and total hydrogen basis over the pressure range of 0–77 bar at 77 K.[59] The maximum surface excess is 7.07 wt% at 35–45 bar while the total hydrogen adsorption was 10 wt% at 77 bar. The polyhedral framework material has one the highest total volumetric capacities (54 g L^{-1}) at 80 bar and 77 K.[57] The surface excess adsorption isotherm has a maximum, and this is the amount of hydrogen present in the interfacial layer over the gas concentration present at the same equilibrium gas pressure, in which the gas-phase concentration is constant up to the Gibbs surface.[36] The total amount present takes into account the high-pressure gas present in the pores at equilibrium. NOTT-112 has a structure containing three types of cages: (1) cage A (12 open copper sites and diameter 13 Å), (2) cage B (diameter 13.9 Å), and (3) cage C (diameter 20 Å). NOTT-112 has a substantial uptake of 2.3 wt% at 1 bar and this is attributed to open Cu(II) centers present in rela- tively small cage A (see Figure 24.1a).

24.6 MOF Series Based on Dicarboxylate and Tetracarboxylate Ligands

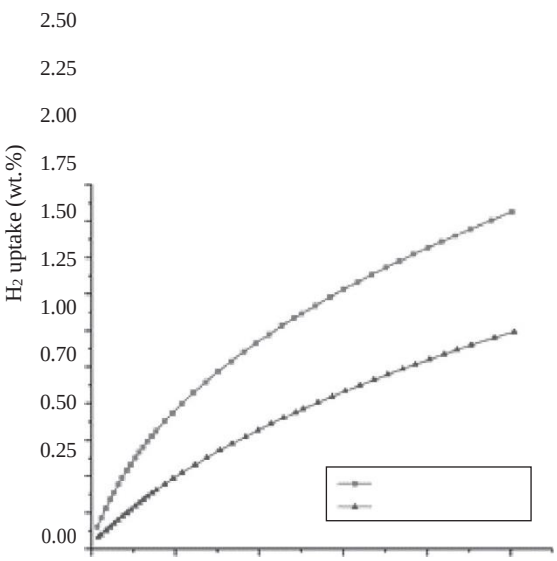
Hydrogen adsorption has been investigated for two series of MOFs where there is a systematic change in the length of the ligand framework linker to change the pore volume and surface area without changing the structural topology: (1) isoreticular metal–organic frameworks (IRMOFs) of Yaghi et al.[5,60–66] based on Zn_4OL_3 stoichiometry (L = various dicarboxylate linkers) (see Figure 24.2) and (2) the NOTT homologous series with stoichiometry Cu_2L' (L′ = various tetracarboxylate ligands) of Schroeder et al. (see Figure 24.3).[44,45] The IRMOF series of MOF materials were used in the identification of a correlation between H_2 saturation amount and Langmuir surface area determined from N_2 adsorption at 77 K.[65]


Cage A
Cage B
Cage C

(a)


H2 uptake (wt.%)
H2 uptake (gl)
Pressure (bar)

(b)


H2 uptake (wt.%)

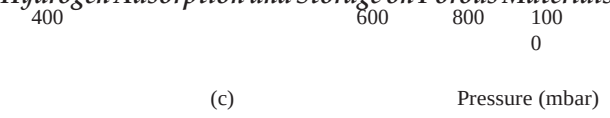


FIGURE 24.1

Structure and high-pressure hydrogen sorption excess adsorption isotherms for NOTT-112[59]. (a) Structure showing cages (b) surface excess (squares), total uptake (circles), and density of gas (line)—filled symbols (adsorption) and open symbols (desorption)—and (c) gravimetric total H_2 uptakes at 78 and 88 K up to 1 bar. (Yan, Y., Lin, X., Yang, S. H., Blake, A. J., Dailly, A., Champness, N. R., Hubberstey, P., Schroder, M., *Chem. Commun*., 1025–1027, 2009. Reproduced by permission of the Royal Society of Chemistry.)

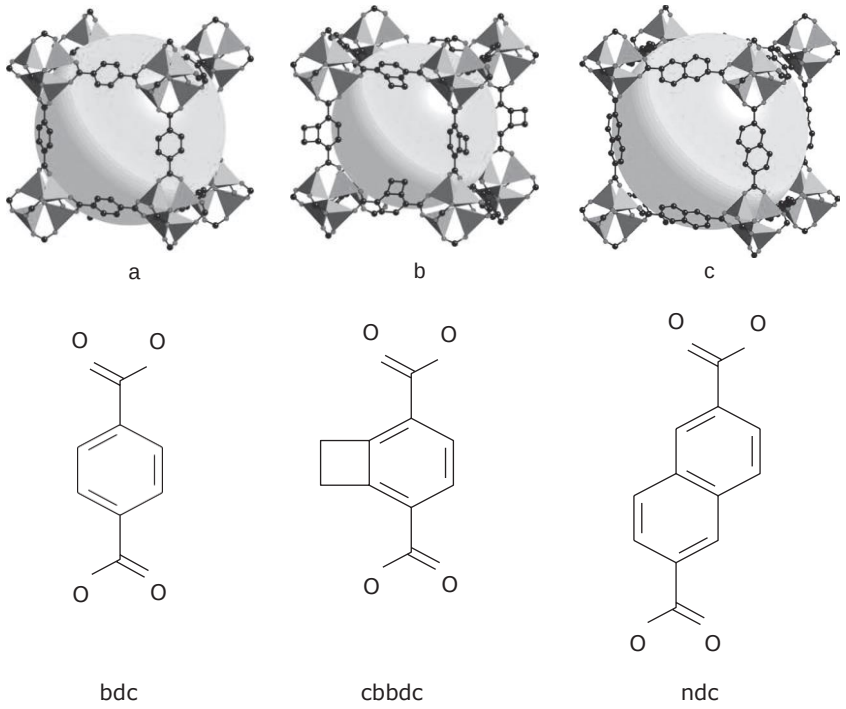
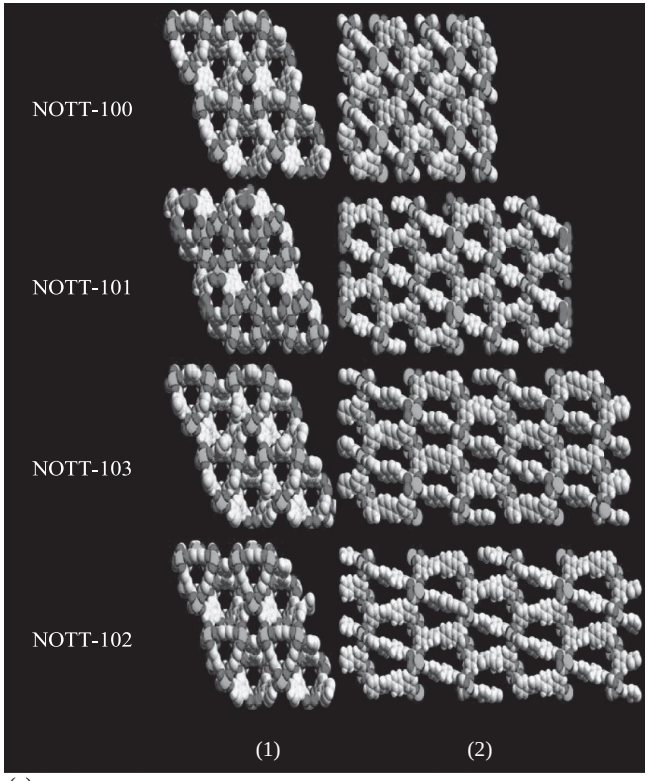


FIGURE 24.2

Structure of some of the IRMOF series of MOFs and the corresponding ligands: (a) IRMOF-1, (b) IRMOF-6, and (c) IRMOF-8. (Rosi, N. L., Eckert, J., Eddaoudi, M., Vodak, D. T., Kim, J., O'Keeffe, M., Yaghi, O. M., *Science*, 300, 1127–1129, 2003. Reproduced with permission from Science.)

Figure 24.4 shows a comparison of the amount of hydrogen adsorbed at 1 bar and at high pressure (at or close to saturation) with BET and Langmuir surface areas and pore volume for the IRMOF series. The results show that good correlations are observed for the hydrogen uptake at high pressure and pore characterization parameters. A correla- tion between hydrogen uptake at 1 bar and BET surface area and pore volume was not observed. Figure 24.5 shows the variation amount of hydrogen adsorbed at 1 bar and high pressure with BET and total pore volume for the NOTT tetracarboxylate series of MOFs. Good correlations were observed between the hydrogen uptake at high pressure on a weight basis and the pore characterization parameters. This series also does not show any correlations between the hydrogen uptakes on a weight basis at 1 bar pres- sure and pore structure characterization parameters. Both these series of MOF structures show progressive increases in hydrogen–surface excess adsorption at or close to satura- tion at high pressure with increasing pore size, pore volume, and surface area character- ization parameters. Similar correlations were not observed for hydrogen adsorption at 1 bar pressure.

Hydrogen adsorption isotherms vary subtly with pore size. Adsorption potential is higher in narrow pores because of overlap of potential energy fields from the pore walls and this increases adsorption at low pressure. Hydrogen interactions with sur- faces can also be enhanced by changing the surface chemistry. The inclusion of open or unsaturated metal centers is a possible method of enhancing hydrogen–surface interactions.[26,67,68] Henry's law constant (K_H) and isosteric enthalpies of adsorption



(a)

FIGURE 24.3

(a) Structures of some of the NOTT series of Cu_2L (L, tetracarboxylate ligand) MOFs: (1) view along the *c* axis and (2) view along the *a* axis. (Reproduced with permis- sion from Lin, X., Telepeni, I., Blake, A. J., Dailly, A., Brown, C. M., Simmons, J. M., Zoppi, M., Walker, G. S., Thomas, K. M., Mays, T. J., Hubberstey, P., Champness, N. R., Schroder, M., *J. Am. Chemi. Soc*., 131, 2159–2171. Copyright 2009, American Chemical Society; Lin, X., Jia, J., Zhao, X., Thomas, K. M., Blake, A. J., Walker, G. S., Champness, N. R., Hubberstey, P., Schroder, M., *Angew. Chem. Int. Ed*., 45, 7358–7364. Copyright 2006, American Chemical Society.)

(*continued*)

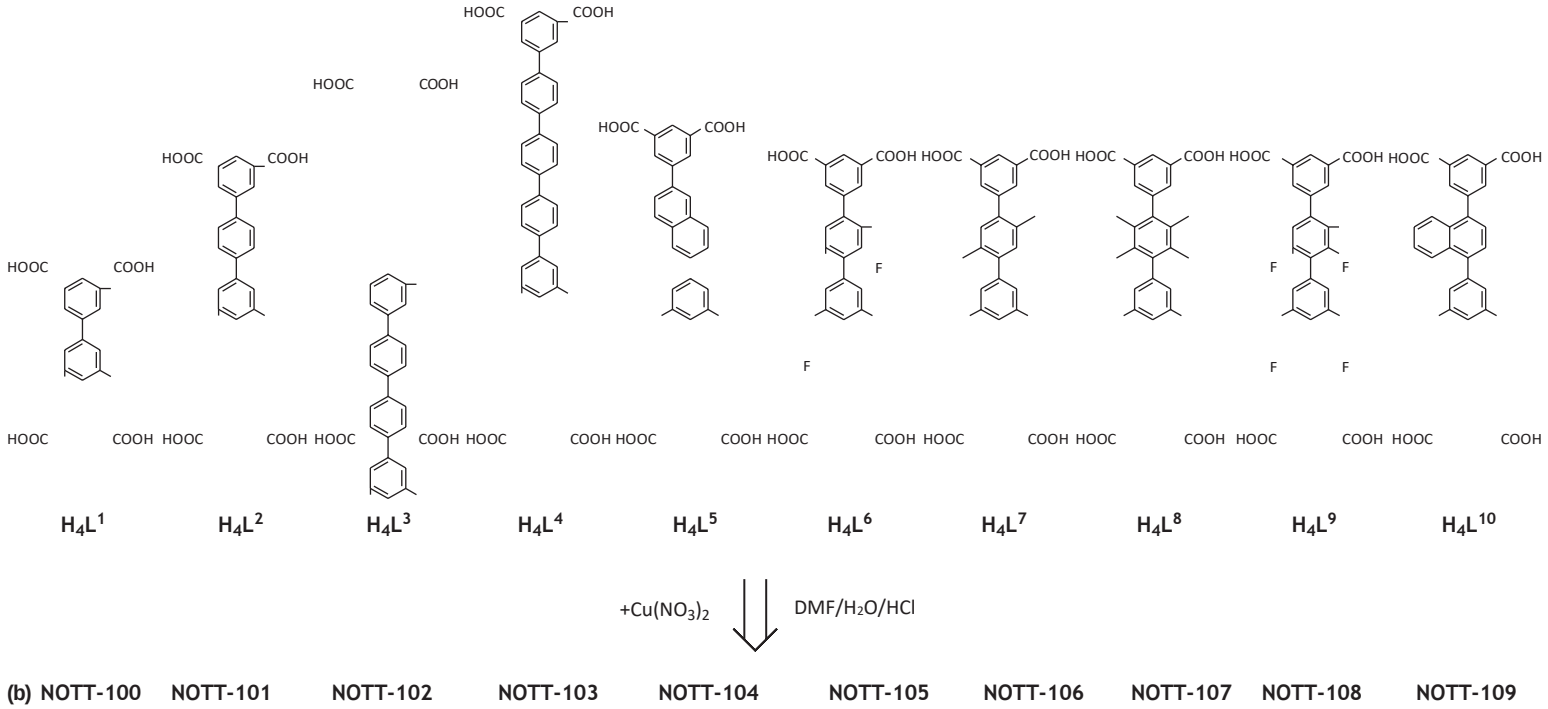
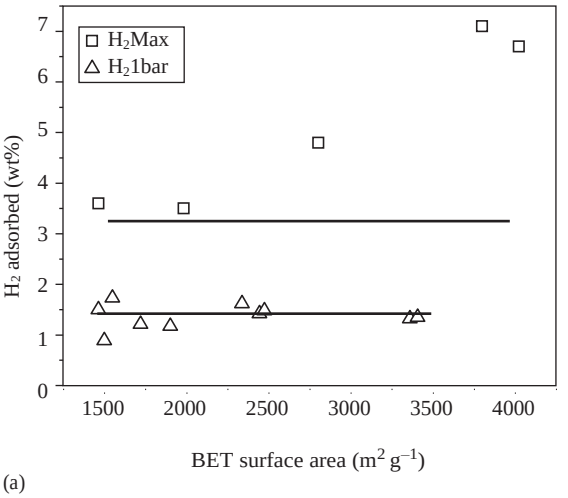
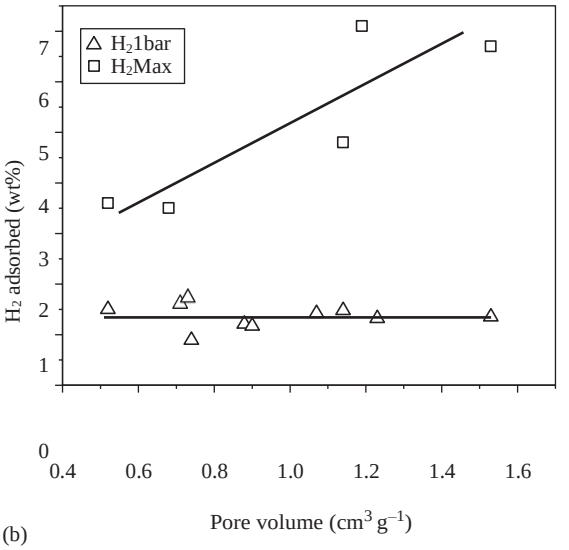


FIGURE 24.3 (continued)

(b) Structures of the series of tetracarboxylic acid ligands in the NOTT series of MOFs. (Reproduced with permission from Lin, X., Telepeni, I., Blake, A. J., Dailly, A., Brown, C. M., Simmons, J. M., Zoppi, M., Walker, G. S.,Thomas, K. M., Mays, T. J., Hubberstey, P., Champness, N. R., Schroder, M., *J. Am. Chemi. Soc.*, 131, 2159–2171. Copyright 2009, American Chemical Society.)



(a)



(b)

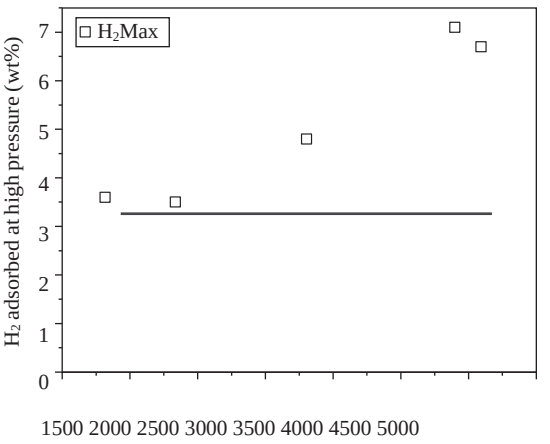
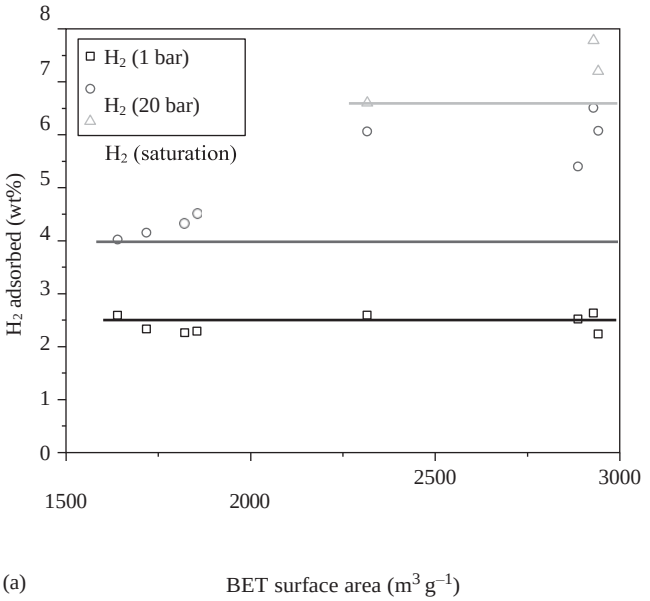


FIG URE 24.4

(c) Langmuir surface area ($m^2 g^{-1}$)

The variation of H_2 adsorbed at high pressure at 77 K with pore characterization parameters for the IRMOF series of MOFs.[20,43,62,65,69,191,193] (a) BET surface area, (b) pore volume, and (c) Langmuir surface area.



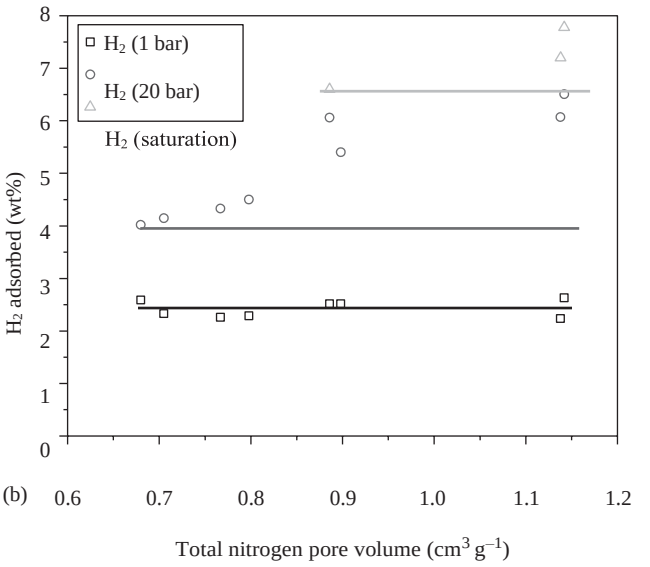


FIGURE 24.5

The variation of H_2 adsorbed at high pressure at 77 K with pore characterization parameters for the NOTT series of MOFs. (a) BET surface area and (b) total nitrogen pore volume. (Reproduced with permission from Lin, X., Telepeni, I., Blake, A. J., Dailly, A., Brown, C. M., Simmons, J. M., Zoppi, M., Walker, G. S.,Thomas,

K. M., Mays, T. J., Hubberstey, P., Champness, N. R., Schroder, M., *J. Am. Chemi. Soc.*, 131, 2159–2171. Copyright 2009, American Chemical Society; Lin, X., Jia, J., Zhao, X., Thomas, K. M., Blake, A. J., Walker, G. S., Champness,

N. R., Hubberstey, P., Schroder, M., *Angew. Chem. Int. Ed.*, 45, 7358–7364. Copyright 2006, American Chemical Society.)

at zero surface coverage are measures of H_2–surface interactions. Materials with larger pores and total pore volumes provide increased adsorption capacity at high pressures.[69] The influence of these factors can be seen in the crossover of isotherms observed with changing pore size for the NOTT copper tetracarboxylate series of MOFs (see Figure

24.6). Cu_2(bptc) has a higher affinity with H_2 than Cu_2(tptc) at low pressure

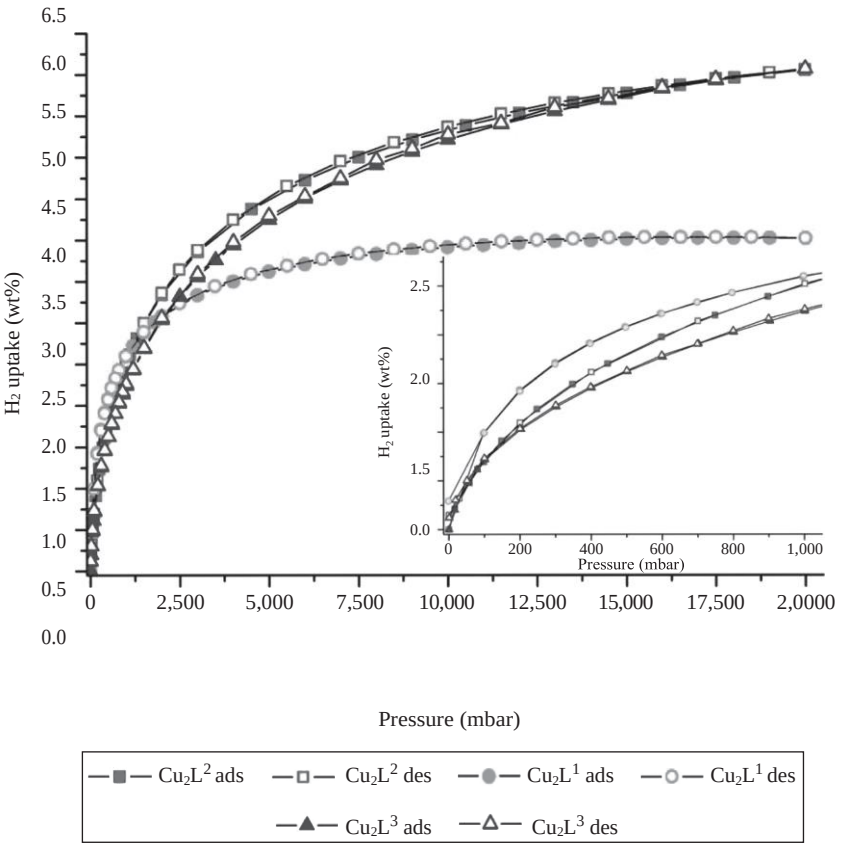


FIGURE 24.6

Adsorption isotherms for Cu_2L (L^1 = bptc, L^2 = tptc, and L^3 = qptc); filled symbols (adsorption) and open symbols (desorption). (Lin, X., Jia, J., Zhao, X., Thomas, K. M., Blake, A. J., Walker, G. S., Champness, N. R., Hubberstey, P., Schroder, M.: *Angew. Chem. Int. Ed*. 2006. 45, 7358–7364. Copyright Wiley-VCH Verlag GmbH & Co. KGaA. Reproduced with permission.)

but the lower pore volume limits the maximum H_2 adsorption to 4.02 wt% at 20 bar, while Cu_2(tptc) has higher hydrogen adsorption at >1.2 bar and 6.06 wt% at 20 bar.[44] At low pressure and surface coverage (or loadings), the enthalpy of hydrogen adsorp- tion is important, whereas at high pressure, the total pore volume provides a limit for hydrogen adsorption. It is evident that there is a compromise for the structure of porous materials for optimum hydrogen adsorption characteristics, between adsorp- tion saturation capacity at high pressure and increased adsorption at low pressure. The density of the porous material is also a factor since this defines the mass that can be put in a storage tank of a specific volume.

24.7 Hydrogen Adsorption Studies up to 1 Bar Pressure

Initially, most hydrogen adsorption studies for all porous materials were carried out at pressures up to 1 bar pressure because of the lack of availability of high-pressure instruments. These measurements provide data for determining the isosteric enthalpies of

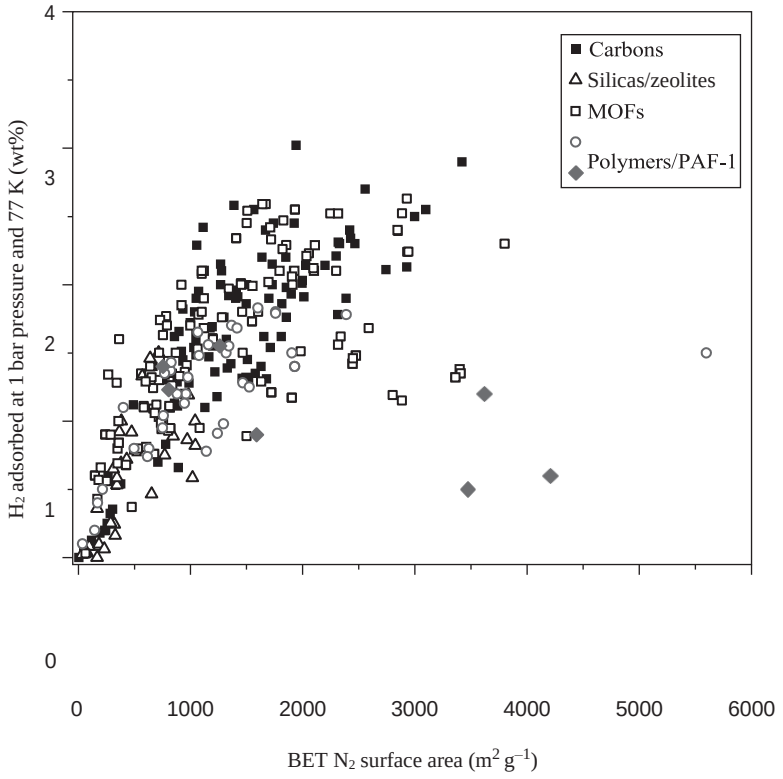


FIGURE 24.7

The variation of selected H_2 amounts adsorbed at 1 bar and 77 K with BET surface area for porous adsorbents: carbon materials,[46,51,70,72–77,80,82–84] silicas/zeolites,[72,86–88] polymers,[91–96] COFs,[98–102] and MOFs.[26,32,42,44,45,59,65–67,104–135,137,143–145]

adsorption at zero surface coverage, which is a fundamental measure of the hydrogen–surface interaction and a significant factor in determining the hydrogen desorption characteristics as a function of temperature. As discussed earlier, the uptakes at 1 bar pressure are not related to the maximum surface capacity at high pressure. The smallest micro- pores contribute more to the hydrogen adsorption uptake at 1 bar than larger pores.[46,70,71] Figure 24.7 shows the variation of H_2 uptakes at 1 bar and 77 K versus BET surface area for carbons,[46,51,70,72–84] silicas, aluminas, zeolites,[72,79,85–90] porous polymers,[91–97] COFs,[98–103] and MOFs.[26,32,42,44,45,59,62,65–67,96,104–145] It is evident that similarities exist for H_2 adsorption at 1 bar for all porous materials with surface areas below ~2000 $m^2 g^{-1}$. However, a distribution of results is observed and this is much wider for high (>2000 $m^2 g^{-1}$) surface area materials. It is apparent that measurement of hydrogen adsorption uptakes at 1 bar is not a guide to ultimate hydrogen capacity.

Pressure is a significant parameter for storage applications and high adsorption at low pressure is of interest in this respect. Recently, there has been a report of 6.1 wt% reversible hydrogen adsorption on lithium-doped conjugated microporous polymer (Li-CMP).[146] This is at least twice that of the highest amounts adsorbed at 1 bar observed for a wide variety of porous materials as shown in Figure 24.7. Lithium doping in the range up to 7 wt% was investigated with the maximum uptake being for 0.5 wt%. The isosteric enthalpy of adsorption at zero surface coverage was 8.1 kJ mol^{-1} and this decreased with increasing surface coverage. This enthalpy of adsorption is within the typical range of values obtained for nondoped materials. The hydrogen sorption of Li-CMP with optimal

Li content (0.5 wt%) at 273 K and 0.1 MPa was very low.

24.8 Hydrogen Adsorption Capacity Studies at High Pressure

Hydrogen adsorption has been studied for a wide range of porous materials including carbons,[46,51,70,72–84,147–173] carbon nanotubes,[174,175] silicas,[72,176] aluminas[72], zeolites,[85–88,177–179] porous polymers,[91–95,180–188] COFs,[98–103] PAFs,[97] and MOFs.[26,32,42,45,57,59,62,65–67,104–137,143,144,189–246] Selected hydrogen adsorption data at high pressure and 77/298 K and corresponding pore structural characterization data are given in Table 24.1.

Studies of adsorption of gases on porous materials for storage applications have been directed at the synthesis of materials with ultrahigh porosities. Investigation of hydrogen adsorption on MOFs allows comparison with crystallographic void volumes and pore volumes and surface areas determined from gas adsorption studies. However, the densities of materials with very high crystallographic void volumes are very low. Several measurements of hydrogen storage capacity are used to compare the relative merits of materials. These capacity measurements are the surface excess (mass%) and total adsorption (mass%) and the total volumetric capacity (g L^{-1}). The relative merits of a set of materials differ depending on the hydrogen capacity measurement used. The total uptake is more relevant for practical applications of H_2 as a fuel, but it cannot be measured easily by experimental methods and, therefore, is calculated using the pore volume and the gas density. The hydrogen isotherms for these MOFs reach saturation uptakes, and the saturation pressure increases with an increase in cavity size.

MOFs are the porous materials with the highest void volumes, intrinsic surface areas, and pore volumes that have been prepared to date. The materials with the lowest densities are MOF-200 ($Zn_4O(bbc)_2(H_2O)_3{\cdot}H_2O$) and MOF-210 ($Zn_4O(bte)_{4/3}(bpdc)$) and have void volumes (densities) determined from crystallographic analyses of 90% (0.22 g cm^{-3}) and 89% (0.25 g cm^{-3}), respectively. The ultrahigh BET surface areas (10,400 $m^2\ g^{-1}$) obtained for both MOF-200 and MOF-210 are close to the ultimate limit for solid materials. Comparison of hydrogen adsorption capacities gives the relative merits for the best performing materials. Hydrogen excess capacities on a mass% basis are

$$\text{MOF-210}\ (8.6) > \text{NOTT-112}(7.6) > \text{MOF-200}\ (7.4) > \text{MOF-177}\ (7.3)$$

$$> \text{MOF-205}\ (7\ ) > \text{UCMC-2}\ (6.9) > \text{PCN-14}\ (4.4)$$

A range of values (5.3%–7.6%) have been reported for MOF-5.[43,57]

Hydrogen total capacities on a mass% basis are

$$\text{MOF-210}\ (17.6) > \text{MOF-200}\ (16.3) > \text{UCMC-2}\ (12.4) > \text{MOF-205}\ (12)$$

$$> \text{MOF-177}\ (11.7\ ) > \text{NOTT-112}(10.7\ ) > \text{PCN-14}\ (6.7\ )$$

A range of values (8.2%–10.6%) have been reported for MOF-5. On the amount adsorbed per volume basis (g L^{-1}),

$$\text{PCN-14}\ (55) > \text{NOTT-112}(54) > \text{UCMC-2}(50) > \text{MOF-177}\ (50)$$

$$> \text{MOF-205}\ (46) > \text{MOF-210}\ (44) > \text{MOF-200}\ (36)$$

TABLE 24.1

Selected High-Pressure Hydrogen Adsorption and Porous Structure Characterization Data for Porous Materials

Porous Materials	Surface Area ($m^2 g^{-1}$)	Pore Volume ($cm^3 g^{-1}$)	Amount Adsorbed (77 K/wt%)	Amount Adsorbed Ambient Temperature (wt%)	References
MOFs					
$Zn_4O(bdc)_3$ (MOF-5, IRMOF-1)	4171[L]		5.2 (48 bar)		[65]
	3534[B]				[65]
		1.19			[69]
	3080[L]				[191]
	3362[L]		4.3 (30 bar)	0.45 (60 bar)	[62]
	2296[B]		5.1 (65 bar)	0.28 (65 bar)	[192]
	3840[L]			0.9 (60 bar/200 K)	[192]
	2295[B]				[193]
	2833[B]				[194]
	4400[L]		7.1 (40 bar)		[43]
	3800[B]				[43]
	2885[B]	1.18			[137]
			5.75 (35 bar)	0.3 (60 bar)	[210]
	2860[B]		5.3[E] (80 bar)		[57]
	3480[L]		8.2[Tot] (80 bar)		[57]
		1.22	7.6[E] (80 bar)		[43,57]
		1.55	10.6[Tot] (80 bar)		[43,57]
MOF-5	3917[L]	1.39	6.9[E] (100 bar)		[138]
	2449[B]		11.8[Tot] (120 bar)		[138]
$Zn_4O(cbbdc)_3$ (IRMOF-6)	3305[L]		4.8 (50 bar)		[65]
	2804[B]				[65]
	2516[B]				[194]
	3263[L]	1.14			[66]
	2476[B]				[66]
$Zn_4O(ndc)_3$ (IRMOF-8)	1818[L]		3.6 (10–15 bar)	0.4 (30 bar)	[62,191]
	1466[L]				[62,191]

	1215[B]	0.52	3.5 (~20 bar)		[69]
$Zn_4O(hpdc)_3$ (IRMOF-11)	2337[L]		3.5 (34 bar)		[65]
	1984[B]	0.68			[69]
	1911[L]				[62]
	2096[B]				[194]
$Zn_4O(ttdc)_3$ (IRMOF-20)	4593[L]		6.7 (70–80 bar)		[65]
	4024[B]				[65]
	4346[L]				[66]
	3409[B]	1.53			[69]
Zn_3O_3(dhbdc)(MOF-74)	1072[L]		2.3 (26 bar)		[65]
	950[B]				[65]
	816[B]				[194]
	1132[L]	0.39			[66]
	783[B]				[66]
	870[B]		2.8 (30 bar)		[208]
Zn_4O(btb) (MOF-177)	5640[L]		7.5 (70 bar)		[65]
	4746[B]				[39]
	4526[L]				[62]
	3100[B]	1.58		0.62 (100 bar, 298 K)	[196]
	4300[L]				[196]
	4508[B]				[194]
	4500[B]	1.89	7.3[E] (80 bar)		[39,57]
	5340[L]		11.6[Tot] (80 bar)		[39,57]
$Zn_4O(fma)_3$	1120[B]		5.2 (39 bar)	0.32 (40 bar)	[243]
	1618[L]				[243]
$Zn_4O(bdc)(btb)_{4/3}$	2932[B]	1.47	5.43[E] (20 bar)		[231]
	3950[L]		6.23[A] (20 bar)		[231]
$ZnO_4(L1)_3$	502[B]	0.2[DR]		1.12 (48 bar)	[197]
$ZnO_4(L2)_3$	396[B]	0.13[DR]		0.98 (48 bar)	[197]
$Cr_3OF(btc)_2$ (MIL-100(Cr))	2700[L]	1.0	3.28 (26.5 bar)	0.15 (73.3 bar)	[69]
MIL-101(Cr)TM	3197[B]	1.73	4.01 (10 bar)		[246]
	4546[L]				[246]

(*continued*)

TABLE 24.1 (continued)

Selected High-Pressure Hydrogen Adsorption and Porous Structure Characterization Data for Porous Materials

Porous Materials	Surface Area ($m^2 g^{-1}$)	Pore Volume ($cm^3 g^{-1}$)	Amount Adsorbed (77 K/wt%)	Amount Adsorbed Ambient Temperature (wt%)	References
$Cr_3OF(ntc)_{3/2}$ (MIL-102 (Cr))	42.1^{L}	0.12	1.0 (35 bar)	0.05 (35 bar)	[206]
$Al(OH)(bdc)_3$ (MIL-53(Al))	1100^{B}		3.8 (16 bar)		[125]
	1590^{L}	0.59			[69]
	1779^{L}		2.9 (~20 bar)		[193]
	933^{B}				[193]
$Cr(OH)(bdc)_3$, MIL-53(Cr)	1100^{B}		3.1 (16 bar)		[125]
	1500^{L}	0.56			[69]
$Cr_3OF(bdc)_3$ (MIL-101b(Cr))	5500	1.9	6.1 (60 bar)	0.43 (80 bar)	[69]
$Cu_3(btc)_2$ (HKUST-1)	2257^{L}		3.2 (~50 bar)		[65]
	1944^{B}				[65]
	1154^{B}		3.6 (~30 bar)	0.35 (65 bar)	[192]
	1958^{L}				[193]
	1781^{B}				[194]
	2175^{L}	0.75			[66]
	1507^{B}				[66]
		0.684^{N2}	3.6 (10 bar)		[47]
		0.703^{CO2}			[47]
		0.72^{X}			[47]
	1482^{B}	0.828	4.1 (26 bar)		[49]
	2302^{L}				[49]
$Cu_2(bptc)$ (NOTT-100, MOF-505)	1830^{L}	0.63^{DR}			[26]
	1547^{B}				[194]
	1670^{B}	0.680^{N2}	4.02 (20 bar)		[44,45]
		0.683^{X}	4.2^{e}		[44,45]
$Cu_2(tptc)$ (NOTT-101)	2247^{B}	0.886^{N2}	6.06 (20 bar)		[44,45]
	2316^{B}	1.083^{X}	6.7^{e}		[44,45]
			6.6^{Tot} (60 bar)		[44,45]

Cu_2(qptc) (NOTT-102)	2942[B]	1.138[N2]	6.07 (20 bar)		[44,45]
		1.284[X]	7.01[e]		[44,45]
			7.2[Tot] (60 bar)		[44,45]
$Cu_2(C_{26}O_8H_{12})$ (NOTT-103)	2929[B]	1.142[N2]	6.51[Tot] (20 bar)		[44]
			7.78[Tot] (60 bar)		[44]
$Cu_2(C_{22}O_8H_8F_2)$ (NOTT-105)	2387[B]	0.898[N2]	5.40[Tot] (20 bar)		[44]
$Cu_2(C_{24}H_{14}O_8)$ (NOTT-106)	1855[B]	0.798[N2]	4.50[Tot] (20 bar)		[44]
$Cu_2(C_{26}H_{20}O_8)$ (NOTT-107)	1822[B]	0.767[N2]	4.46[Tot] (20 bar)		[44]
$Cu_2(C_{26}O_8H_{12})$ (NOTT-109)	1718[B]	0.705[N2]	4.15[Tot] (20 bar)		[44]
Cu_2(pddip)$(H_2O)_2(DMF)_{7.5}$ $(H_2O)_5$ (NOTT-110)	2960[B]	1.22[N2]	5.43[E] (55 bar)		[244]
			7.62[Tot] (55 bar)		[244]
			8.5[Sat]		[244]
$[Cu_2$(dhpddip)$(H_2O)_2]$$(DMF)_{7.5}$ $(H_2O)_5$ (NOTT-111)	2930[B]	1.19[N2]	5.47[E] (48 bar)		[244]
			7.36[Tot] (48 bar)		[244]
Cu_3(dcbpyb) (NOTT-112)	3800[B]	1.62[N2]	7.07[E] (35–40 bar)		[59]
		1.69[Ar]	10.0[Tot] (77 bar)		[59]
			10.7[Tot] (80 bar)		[57]
Cu_2(bdi) (PCN-46)	2500[B]	1.012	7.16[Tot] (60 bar)		[237]
$Cu_3(tatb)_2$ catenated (PCN-6)	3800[L]		7.2[E] (50 bar)		[240]
			9.5[Tot] (50 bar)		[240]
$Cu_3(tatb)_2$ noncatenated (PCN-6′)	2700[L]		4.2[E] (50 bar)		[240]
			5.8[Tot] (50 bar)		[240]
Mn(btt)	2100[B]	0.795[X]	5.1 (40 bar)	0.95 (90 bar)	[42]
			6.9 (90 bar)		[42]
$Zn_7O_2(pda)_5$		0.17[H2O]		1.01 (71.43 bar)	[198]
		0.21[M]			[198]
$Zn(mim)_2$ (ZIF-8)	1810[L]	0.663[X]	3.1 (55 bar)		[32]
	1630[B]	0.636μp			[32]
	1400[L]				[31]
	1030[B]				[31]
			3.3 (30 bar)	0.13 (60 bar)	[210]
Zn(ndc)$(bpe)_{1/2}$	303[L]	0.2	2.0 (40 bar)	0.3 (65 bar)	[199]
Ni_2(dhtp)	1083[L]	0.41	1.8 (50 bar)	0.3 (65 bar)	[110]

(*continued*)

TABLE 24.1 (continued)

Selected High-Pressure Hydrogen Adsorption and Porous Structure Characterization Data for Porous Materials

Porous Materials	Surface Area ($m^2 g^{-1}$)	Pore Volume ($cm^3 g^{-1}$)	Amount Adsorbed (77 K/wt%)	Amount Adsorbed Ambient Temperature (wt%)	References
$Ni_3(btc)_2(3\text{-pic})_6(pd)_3$		0.63	2.6 (15 bar)	0.15 (15 bar)	[200]
$Cu_2(hfipbb)_2(H_2hfipbb)$				1.0 (48 bar)	[201]
$Fe_3(OH)(pbpc)_3$	1200[B]		3.05 (20 bar)		[143]
$Ni_3(OH)(pbpc)_3$	1553[B]		4.15 (20 bar)		[143]
$Cu_2(abtc)$ (SNU-5)	2850[L]	1.0	5.22[E] (50 bar)		[245]
			6.76[Tot] (50 bar)		[245]
$Zn_2(abtc)(dmf)_2$ (SNU-4)	1460[L]	0.53	3.70[E] (50 bar)		[245]
			4.49[Tot] (50 bar)		[245]
$Cu_2(abtc)(H_2O)_2(dmf)_2 \cdot H_2O$ (JUC-62)		0.888[X]	4.71 (40 bar)		[203]
$Cu_2(abtc)(H_2O)_2 \cdot 3dma$ (PCN-10)	1779[L]	0.67	4.33[E] (20 bar)	0.25 (45 bar)	[118]
	1407[B]				[118]
$Cu_2(sbtc)(H_2O)_2 \cdot 3dma$ (PCN-11)	2442[L]	0.91	5.05[E] (20 bar)	0.34 (45 bar)	[118]
	1931[B]				[118]
$Cu_2(adip)$ (PCN-14)	1753[B]	0.87	4.42[E] (45 bar)		[241]
	2176[L]		6.7 (80 bar)		[57,241]
$[Ni_3O(H_2O)_3(adc)_3] \cdot (dma)_2\}n$, (PCN-19)	723B	0.38	1.67 (48 bar)		[234]
	823L				[234]
$Cu_3(ttca)_2$(PCN-20)	3525[B]		6.2[E] (50 bar)		[242]
	4237[L]				[242]
$Zn(bdc)(ted)_{0.5}$	1794[B]	0.73	4.1 (20 bar)	0.2 (50 bar)	[128,204]
$Zn_3(bdc)_3Cu(pyen)$ (M′MOF1)		0.257[M]	1.25 (10 bar)		[52]
		0.29[X]	1.35[e]		[52]
$Co(bdc)(dabco)_{0.5}$	1595[B]		4.11 (40 bar)	<0.5 (100 bar)	[205]
	2120[L]				[205]
$Cu(bdc)(dabco)_{0.5}$	1300[B]		2.7 (40 bar)		[205]
	1703[L]				[205]
$Zn(bdc)(dabco)_{0.5}$	1165[B]		3.17 (40 bar)		[205]

$Mn_3[(Mn_4Cl)_3(tpt\text{-}3tz)_8(dmf)_{12}]_2$	1580[B]		3.7 (25 bar)	0.5 (68 bar)	[217]
	1700[L]				[217]
$Cu_3[(Cu_4Cl)_3(tpb\text{-}3tz)_8]_2 1{\cdot}1CuCl_2$	1120[B]		2.8 (30 bar)	0.5 (68 bar)	[217]
	1200[L]				[217]
$Fe_3[(Fe_4Cl)_3(btt)_8(MeOH)_4]_2$ (Fe-btt)	2010[B]			1.1 (100 bar, 298 K)	[273]
Co(bdp)	2670[L]	0.93	3.1 (30 bar)		[207]
$Cu(dccptp)(NO_3)$	268[B]	0.113	1.91 (20 bar)		[144]
$Cd_3(bpdc)_3$ (JUC-48)	880[L]	0.19	2.8 (40 bar)		[211]
$Ni_3(OH)(pbpc)_3$	1553[B]		4.15 (20 bar)		[143]
$Fe_3(OH)(pbpc)_3$	1200[B]		3.05 (20 bar)		[143]
$Zn_2(bpytc)$	312.7[B]	0.187[X]	1.08 (4 bar)	0.057 (4 bar)	[212]
	423.7[L]				[212]
$Cu_3(bhtc)_2$ (UMCM-150)	2300[B]		5.7 (45 bar)		[127]
	3100[L]				[127]
$Zn_4O(t^2dc)(btb)_{4/3}$(UCMC-2)	5200[B]	2.32	6.9[Ex] (46 bar),		[57,232]
	6060[L]		12.4[Tot] (80 bar)		[57,232]
	6060[L]				[57,232]
MOF-200, $Zn_4C_{90}H_{60}O_{16}$ Bbc	4530[B]	3.59	7.4[Ex], 16.3[Tot] (80 bar)		[57]
	10400[L]				[57]
MOF-205 $Zn_4C_{48}H_{26}O_{13}$ bttb, ndc	4460[B]	2.16	7.0[Ex], 12.0[Tot] (80 bar)		[57]
	6170[L]				[57]
MOF-210 $Zn_4C_{58}H_{28}O_{13}$ bte, bpdc	6240[B]	3.60	8.6[Ex], 17.6[Tot] (80 bar)		[57]
	10400[L]				[57]
$Cu_3(bipy)_{1.5}(ndc)_3$	113		1 (15 bar)		[233]
$[Cu(bpe)_{0.5}(ndc)]{\cdot}0.5H_2O$	337		1 (15 bar)		[233]
$Zn_9O_3(2,7\text{-}ndc)_{12}(dmf)_3$	901[B]	0.458	2.32 (20 bar)[E]		[135]
	1281[L]				[135]
$Cu_2(bpndc)_2(bpy)$ (SNU-6)	2590[B]	1.05	4.87[E] (70 bar)		[134]
	2910[L]		10.0[Tot] (70 bar)		[134]
$Zn_2(bpndc)_2(bpy)$ (SNU-9)	1034[L]	0.366	3.63[E] (90 bar)		[236]
	824[B]		6.23[Tot] (90 bar)		[134]
$Y(btc)(H_2O)$			2.1 (10 bar)		[202]

(*continued*)

TABLE 24.1 (continued)

Selected High-Pressure Hydrogen Adsorption and Porous Structure Characterization Data for Porous Materials

Porous Materials	Surface Area ($m^2 g^{-1}$)	Pore Volume ($cm^3 g^{-1}$)	Amount Adsorbed (77 K/wt%)	Amount Adsorbed Ambient Temperature (wt%)	References
$Ag_2[Ag_4(trz)_6]$ FMOF-1	810[B]	0.324	2.33 (77 bar)		[238]
			4.1[vol] (64 bar)		[238]
$[Sm_2(oxdaa)_6Zn_3(H_2O)_6]\cdot 1.5H_2O$	719[B]		1.19 (34 bar)	0.54 (35 bar, 298 K)	[239]
$(Me_2NH_2)[In(bptc)]$	820[B]	0.325	2.36 (20 bar)		[228]
$(Me_2NH_2)[In(bptc)]^-Li^+$	1024[B]	0.419	2.88 (20 bar)		[228]
Carbon materials					
Carbon nanotubes					
Multiwalled carbon nanotubes (MWNTs)	165–406[B]	0.588–1.063[TPV]		<0.78 (100 bar, 298 K)	[174]
		0.097–0.178μp			[174]
Nanotubes	800		1.7 (35 bar)	0	[175]
MWNTs	246–260	0.08–0.12		0.2–0.34 (90 bar, 298 K)	[82]
Activated MWNT	1220[B]	0.29μp	2[E] (40 bar)	0.16 (200 bar, 298 K)	[162]
Nanofibers					
Nanofibers and activated nanofibers	150–265[B]	0.03–0.1μp	0.8[E] (40 bar)	0.15–0.2 (200 bar, 298 K)	[162]
Activated (steam/KOH) rayon carbon fibers	3144[B]	0.744μp	7.01 (40 bar)	1.46 (40 bar, 298 K)	[170]
Carbon nanofibers (phenol formaldehyde resin/ KOH activated)	520–1765[B]	0.26–1.0[TPV]	1.65–3.45 (40 bar)		[172]
		0.26–0.48[μpCO2]			[172]
Graphene					
Graphene-like nanosheets	640		1.2 (10 bar)	0.1 (10 bar)	[250]
Porous Carbons					
CVD carbons from acetonitrile using zeolite β-template	2191–3150[B]	1.74–2.41[TPV]	3.9–6.9 (20 bar)		[161]
	1150–2397μp	0.56–1.13[μp]	4.67–8.33[e]		[161]
CVD carbons from acetonitrile using zeolite β-template	1721–2535[B]	1.09–1.56[TPV]	3.3–5.3 (20 bar)		[157]
CVD carbons from acetonitrile using Mg–Al (Mg/Al = 2) layered double hydroxides (LDH)	800–1268[B]	1.2–1.5[TPV]	1.8–2.8 (20 bar)		[158]

template

CVD carbons from acetonitrile or ethylene using	808–1918[B]	0.49–1.38[TPV]	2.0–4.5 (20 bar)		[159]
zeolite 13X or zeolite Y template	194–1077[μp]	0.1–0.5[μp]			[159]
Porous Carbons and carbon nanotubes	22–2564[B]	0.0065–0.75[dB]	0–4.4[I]	0–0.54[I]	[156]
Carbons from biomass	2000–3100[B]	1.11–1.68[TPV]	3.99–5.05 (10 bar)		[81]
ACs	890–3000	0.48–1.6[TPV]	1.9–4.5 (10 bar)		[75]
Ordered mesoporous carbon materials using silica	711–2390[B]	0.5–1.22[TPV]	1.4–3.5 (10 bar)		[80]
KOH superactivated carbon KAU5	3183[B]	0.72[μpCO2]		1.2 (200 bar)	[162]
ACs and superactivated carbons	1058–3808[B]	0.43–0.68[CO2μp]	2.2–5.6 (40 bar)	0.6–1.1 (200 bar)	[162]
AC and carbon cloths	1049–1730[B]	0.79–0.39[TPV]		0.24–0.56 (90 bar, 298 K)	[82,83]
		0.27–0.5[CO2μp]			[82,83]
Chemically activated phenolic resin carbons	1424–2811[B]		2.81–5.75[E] (40 bar)	0.5 (RT, 40 bar)	[166]
Carbon (wood derived + KOH activation)	2450[B]	1.19[TPV]		0.8 (298 K, 2 MPa)	[248]
		0.63[μPCO2]			[248]
		0.83[μPN2]			[248]
Carbide-derived carbons	1150–3038[B]	0.48–1.34	2.9–4.7[E] (60 bar)		[167]
B-doped carbon	780[B]		3.2 (40 bar)	0.4 (56 bar)	[247]
BC_{11}	780[B]		3 (80 bar)	0.37 (80 bar, ambient)	[256]
BC_6	609[B]		3.8 (80 bar)	0.54 (80 bar, ambient)	[256]
Polycarbonate char	320–2096[B]	0.13–0.87[TPV]	2.27–4.68 (26 bar)	0.17–0.29 (26 bar, 273 K)	[164]
	370–2456[N2DR]				[164]
	713–1400[CO2μp]				[164]
Nitrogen-containing carbons	1912–3698[B]	0.99–1.71[TPV]	3.4–5.3[E] (20 bar)		[163]
	1510–2838[μP]	0.65–1.24[μPV]	4.1–6.9[Tot] (20 bar)		[163]
Nanoporous carbon particles	2711[L]	0.87[TPV] 0.38[μP]	4.2 (50 bar)	0.25 (50 bar)	[160]
	1995[B]				[160]
Carbon monoliths	2147–2647[B]	0.894–1.512[TPV]		0.40–0.46 (50 bar)	[165]
		0.422–0.515[DRμPCO2]			[165]
Nitrogen-doped carbons, KOH activated	334–2745[B]	0.36–2.12[TPV]	1.27–6.84 (20 bar), 8.24[Le]		[168]
Carbon CO_2/KOH activated	2009–3190[B]	1.0–1.69[TPV]	5.63–7.08 (20 bar)		[169]

(*continued*)

TABLE 24.1 (continued)

Selected High-Pressure Hydrogen Adsorption and Porous Structure Characterization Data for Porous Materials

Porous Materials	Surface Area ($m^2 g^{-1}$)	Pore Volume ($cm^3 g^{-1}$)	Amount Adsorbed (77 K/wt%)	Amount Adsorbed Ambient Temperature (wt%)	References
Carbon KOH activated	1579[B]	0.9[TPV]	4.54 (20 bar)		[84]
	2930[B]	1.52[TPV]	6.24 (20 bar)		[84]
Carbon AX21	2780[B]	0.86[TPV]	5.2 (29 bar)		[171]
Carbide-derived carbons	1908–2301	0.6–1.06	4.61[E] (28 bar)	0.67–0.78[E] (100 bar)	[173]
			4.0[E] (25 bar)		[173]
MCM materials					
MCM-41	916–1060[B]		1.68–2.01[E] (30–45 bar)	0.1 (45 bar, 296 K)	[176]
Si, Zn–doped MCM-41	516–875[B]		1.07–1.83[E] (40 bar)		[176]
Porous Polymers					
Polyporphyrins	1522[B]	0.85[TPV]	5.0 (65 bar)		[186]
	2030[L]				[186]
Hyper-cross-linked polymer	2992[L]	0.633[μP]	3.68 (15 bar)		[184]
4,4′-bis(chloromethyl)-1,1′-biphenyl (BCMBP),					
	1904[B]	0.54[DFT]			[184]
Hyper-cross-linked polymer dichloroxylene	2096[L]	0.494[μP]	3.18 (15 bar)		[184]
(p-DCX)	1370[B]	0.46[DFT]			[184]
Hyper-cross-linked polyanilines	630[B]	0.94[TPV]	2.2 (30 bar)		[182]
Triptycene-based polymer (Trip-PIM)	1416[B]		2.71 (10 bar)		[94,95]
Hyper-cross-linked BCMBP	1366[B]		2.8 (15 bar)		[187]
	2096[L]	0.55[DFT]			[187]
PIMs PIM-1, HATN,CTC	760–830[B]		1.44–1.70 (10 bar)		[92]
Hyper-cross-linked polymer vinylbenzyl	1466[B]	0.48	3.04 (15 bar)		[91]
chloride					
Triptycene-based polymers (Me and iPr)	1760[B]		3.4 (18 bar)		[95]
	1601[B]		3.3 (18 bar)		[95]
Porph-PIM	960[B]		2.0 (18 bar)		[251]
CTC-PIM	770[B]		1.7 (10 bar)		[92]

PIM-1	750[B]		1.45 (18 bar)		[92]
Polyimide framework OFP3	1159[B]		3.94 (10 bar)		[252]
Polymer PS4AC2, PS4AC1, Pt4AC, PS4TH	762–1043[B]	0.425–0.757	2.2–3.7 (60 bar)	0.43–0.50 (298 K, 70 bar)	[253]
	1122–1412[L]				[253]
Polymers	1246[B]	0.729	3.0 (75 bar)		[188]
	1515[L]				[188]
Porous aromatic framework (PAF-1)	5600[B]	3.1	7.0[E] (48 bar)		[97]
	7100[L]				[97]
COFs					[98]
COF-1, C_3H_2BO	750[B]		1.48[Sat]		[103]
	970[L]				[103]
COF-5, $C_9H_4BO_2$	1670(2050)[B]		3.58[Sat]		[103]
	1990(3300)[L]				[103]
COF-6, $C_8H_3BO_2$	750[B]		2.26[Sat]		[103]
	980[L]				[103]
COF-8, $C_{14}H_7BO_2$	1350(1710)[B]		3.5[Sat]		[103]
	1400(2110)[L]				[103]
COF-10, $C_{12}H_6BO_2$	1760(1980)[B]		3.92[Sat]		[103]
	2080(4620)[L]				[103]
COF-102, $C_{25}H_{24}B_4O_8$	3620[B]		7.24[Sat]		[103]
	4650[L,]				[103]
COF-103, $C_{24}H_{24}B_4O_8Si$	3530[B]		7.05[Sat]		[103]
	4630[L,]				[103]
Zeolites					
Zeolites, Na-LEV, H-OFF, Na-MAZ, and Li-ABW			1.02–2.07 (16 bar)		[179]
Zeolites Na–A, Na–Li–A, Li–A, K–A				0.42–0.49 (60 bar, 293 K)	[178]
Ion-exchanged zeolites	384–725[B]		1.32–2.19 (15 bar)		[85]
Zeolites A, X, Y, and RHO	3–725[B]		0–1.81 (15 bar)		[86]
Low silica Type X zeolite	717[B]	0.568		0.6 (100 bar)	[87]

[B] determined using BET equation; [L] determined using Langmuir equation; [DR] determined using Dubinin–Radushkevich equation; [e] estimate of saturation; [E] surface excess; M determined from methanol adsorption; [X] determined from x-ray diffraction studies; [H_2O] determined from water vapor adsorption; [dB] determined an extension of de Boer's *t*-method for the micropore volume; [I] interpolated from graph in paper; [μp] micropore volume or surface area; DFT density functional theory calculation.

The different orders for hydrogen saturation amounts on the basis of weight and volume mainly arise because of the low density of some of the materials with the largest pore volumes. Examples of materials with low densities are MOF-177 (0.427 g cm^{-3}), MOF-200 (0.22 g cm^{-3}), MOF-205 (0.38 g cm^{-3}), and MOF-210 (0.25 g cm^{-3}). The best materials on a volumetric basis are PCN-14 (0.83 g cm^{-3}), NOTT-112 (0.48 g cm^{-3}), and UCMC-2 (0.40 g cm^{-3}). The results indicate that a highly porous material with an ultrahigh gravimetric storage capacity may not necessarily be an optimum volumetric H_2 storage material. Therefore, it is evident that comparisons of hydrogen storage capacity on a volumetric basis with porous structure char- acteristics are more complex. Hydrogen adsorption on amorphous porous materials such as ACs on a surface excess gives similar or slightly lower values. Comparisons of hydrogen volumetric storage capacities are needed on precisely the same basis.

The amounts of hydrogen adsorbed under high pressure at 77 and 298 K and corresponding surface areas and pore volumes have been investigated for MOFs,[32,44,59,62,65,66,69,125,137,143,144,179,191–208,210,211,212,228,238–244,246] carbons,[81,156,160–162,247–250] zeolites,[85–87,178,179] silicas,[176] polymers,[91,92,94,95,182,184,251–253] and COFs.[98,103] Correlations have been observed between the amount of hydrogen at saturation (or close to saturation capacity) on a wt% adsorbent basis at 77 K and Langmuir surface area, BET surface area, and total pore volumes, as shown in Figures 24.8 through 24.10 for all types of porous materials. A similar correlation is observed between the amount of hydrogen at saturation (or close to saturation capacity) and micropore volume obtained from carbon dioxide adsorption data for carbon materials.[13,19] Porous materials for storage applications have wider pores and the BET N_2 surface area, Langmuir surface area, and total pore volume have good correlations for all porous materials, as shown in Table 24.1. The correlation for hydrogen high-pressure uptake with BET surface area is observed for porous materials with Type I and II nitrogen adsorption isotherms, and therefore, the correlation is more general (see Figure 24.9). Figure 24.10 shows the

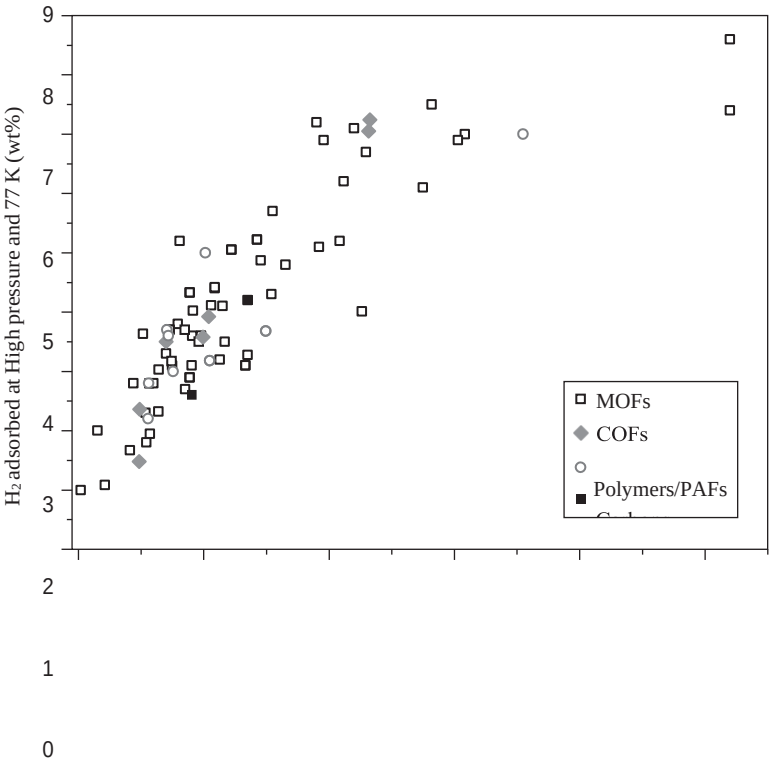
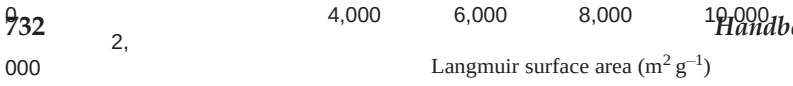


FIGURE 24.8



The variation of H_2 adsorbed (wt%) at saturation at 77 K with Langmuir surface area ($m^2\ g^{-1}$) for porous MOF materials,[26,32,39,43,45,49,57,62,65,66,69,110,118,125,127,134,135,138,191–193,196,199,205–208,210–212,217,231,232,234,236,240–242,245] polymers,[97,184,186,188,253] COFs,[103] and carbon materials.[160] (Data are taken from the references in Table 24.1.)

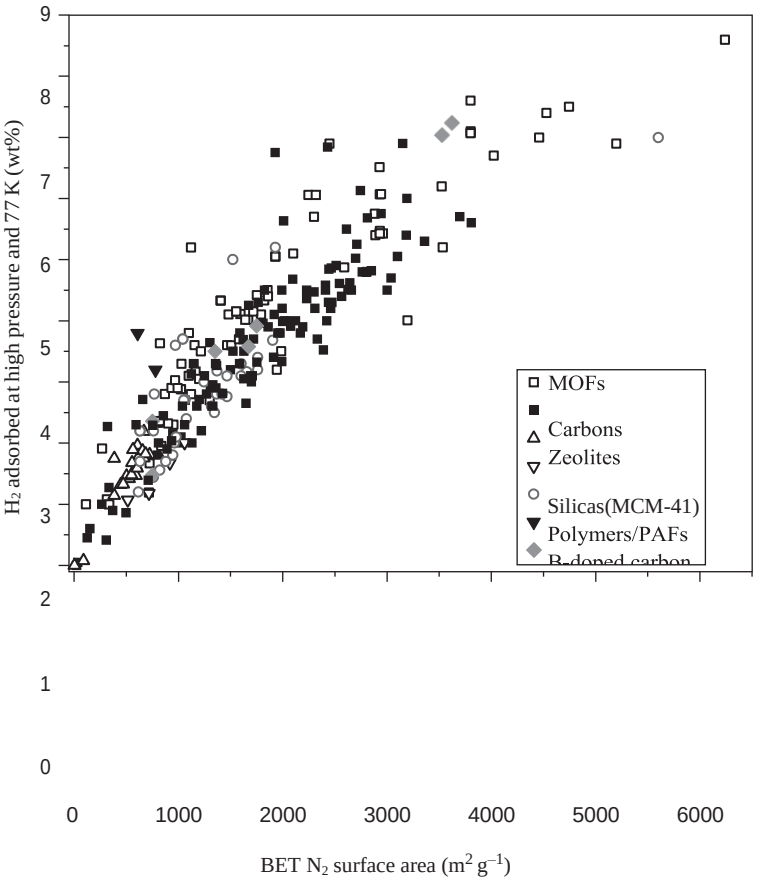
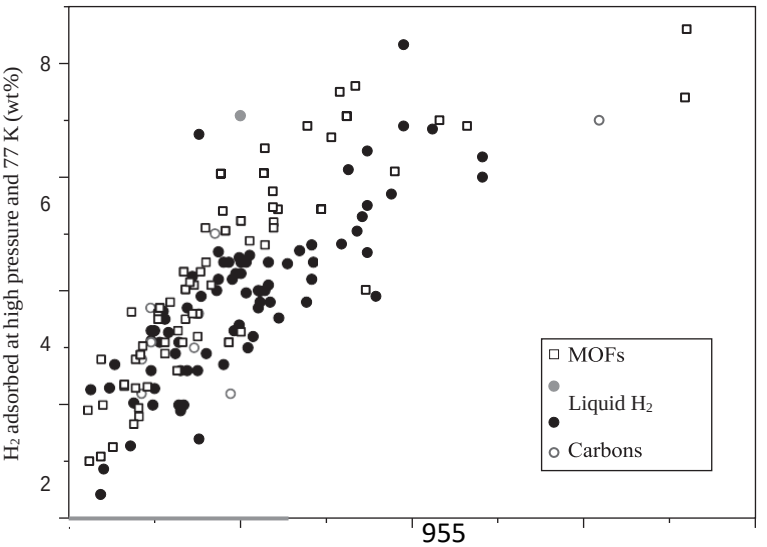


FIGURE 24.9

The variation of H_2 adsorbed (wt%) at saturation at 77 K with BET surface area ($m^2\ g^{-1}$) for porous MOF materials,[26,32,39,42–45,47,49,57,59,62,65,66,69,118,125,127,134,135,137,138,143,144,191–193,196,204,205,208,210,212,217,228,231,232,234,236–239,241–244] carbons,[75,80–84,156–174,248,250] boron-doped carbon,[247,256] MCM-41,[176] zeolites,[85,86] polymers,[91,92,94,95,97,182,184,186–188,251–253] and COFs.[98] (Data are taken from the references in Table 24.1.)



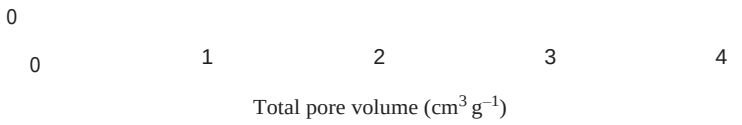


FIGURE 24.10

The variation of H_2 adsorbed (wt%) at saturation at 77 K with total pore volume ($cm^3\ g^{-1}$) for porous MOFs,[32,42,44,45,47,52,57,59,62,65,66,69,110,118,125,128,137,144,191–193,196,199,200,204,206–208,210,211,234,236,238,239,241,244,245] carbons,[75,80–84,157–159,161,163,165,168–174] and polymer[91,97,182,186,188,253] materials. (Data are taken from the references in Table 24.1.)

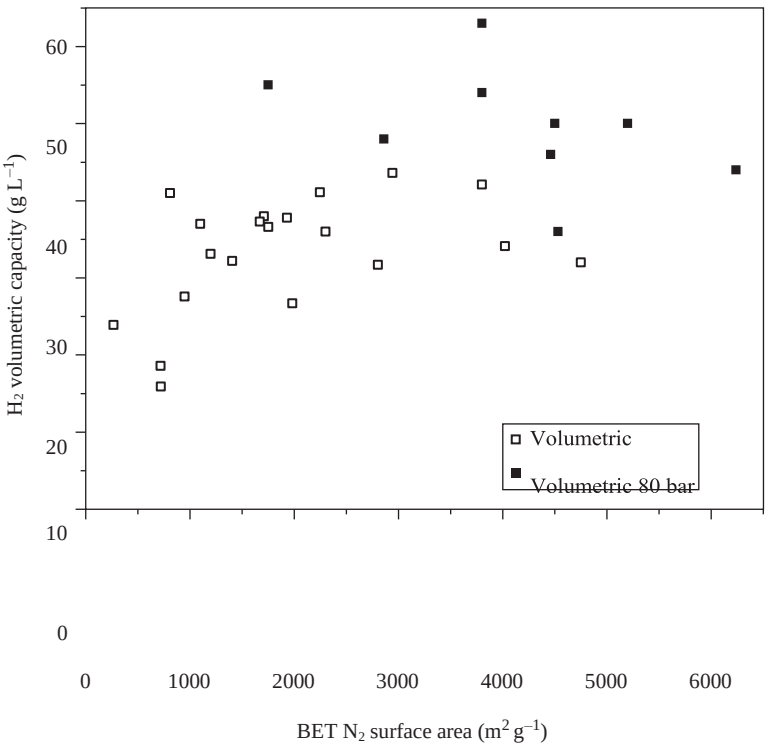


FIGURE 24.11

The variation of H_2 excess volumetric capacity[39,43,45,57,65,118,122,125,127,143,144,205,234,239,241] and volumetric capacity at 80 bar (crystal density was applied to the gravimetric density)[57] versus BET surface area for selected MOFs.

line corresponding to liquid hydrogen filling the pores for comparison with hydrogen uptake data at or close to saturation with total pore volume. The hydrogen saturation uptake values are usually lower than the line for liquid hydrogen filling the pores. The adsorbed hydrogen phase at 77 K is similar to an incompressible fluid with a slightly lower density than liquid hydrogen (critical temperature 32.98 K).[4] MOFs usually have narrower pore size distributions than other porous materials and are usually closer to the line for liquid hydrogen.

Hydrogen storage on a volumetric basis is generally considered to be the most significant characteristic for vehicle applications. These data are mainly available for MOFs. The clear correlations of H_2 excess adsorption on a mass basis with porous structure characterization parameters are no longer observed when the H_2 excess adsorption on a volumetric basis is compared with porous structure characteristics. Figure 24.11 shows the variation of hydrogen adsorbed versus BET surface area. There is an initial improvement up to ~2000 $m^2 g^{-1}$, but above these values, there is a great deal of scatter and there is no clear correlation with BET surface area.

24.9 Temperature Dependence of Hydrogen Physisorption

Physisorption decreases markedly with increasing temperature and H_2–surface interactions are weak, limiting hydrogen adsorption above cryogenic temperatures. This is the major limitation to the use of hydrogen storage using physisorption on porous materi- als. The temperature dependence of hydrogen physisorption is illustrated in Figure 24.12, which shows normalized hydrogen adsorption isobars for 1 bar pressure for an AC, MOF $Ni_3(btc)_2(3\text{-pic})_6(pd)_3$ (C), and the ethanol (**E)-** and methanol (**M)-**templated polymorphs of

$Ni_3(bpy)_3(NO_3)_4$.[200] The shapes of the isobars in the low-pressure region for **E** and **M** are

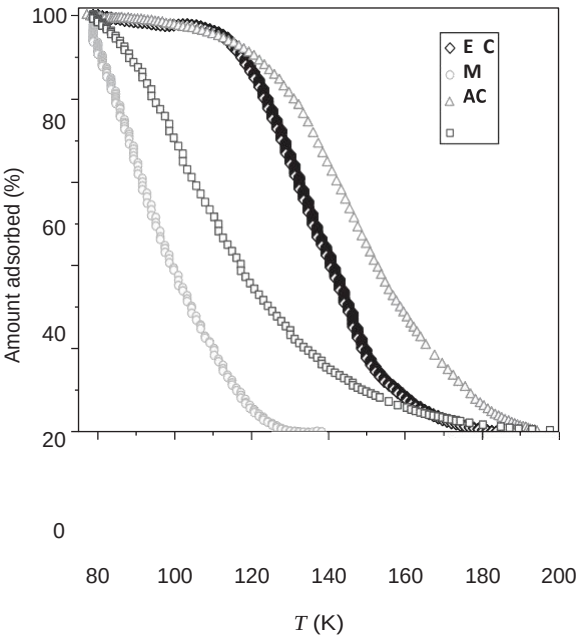


FIGURE 24.12

Isobars for desorption of hydrogen at 1 bar with heating rate 0.3 K min (only every 45th point included for clarity) from AC (∀), $Ni_3(btc)_2(3\text{-pic})_6(pd)_3$ (○), **E** polymorph of $Ni_2(bpy)_3(NO_3)_4$ (M), and **M** polymorph of $Ni_2(bpy)_3(NO_3)_4$ (Δ). (Zhao, X., Xiao, B., Fletcher, A. J., Thomas, K. M., Bradshaw, D., Rosseinsky, M. J., *Science*, 306, 1012, 2004. Copyright Science.)

different from the chiral framework; $Ni_3(btc)_2(3\text{-pic})_6(pd)_3$ and AC are due to hysteretic adsorption in **E** and **M** and this is discussed later. There is little or no conclusive evi- dence for significant quantities of H_2 being physisorbed above temperature of 195 K for a hydrogen pressure of 1 bar. The amounts of hydrogen adsorbed at ambient temperature conditions and high pressure reported in the literature[42,62,69,110,118,128,191,192,196–201,204–206,210,212,217] are usually < 1% and average ~0.5 wt% as shown in Table 24.1.[19] Hydrogen–surface interactions and surface chemistry are major factors under ambient temperature conditions. However, experimental uncertainties in high-pressure measurements under ambient temperature conditions make it difficult to establish correlations with characterization parameters. The low uptakes under these conditions are consistent with low enthalpies for hydrogen adsorption on porous materials.[13,19,200]

24.10 Hydrogen–Surface Interactions in Pores

Adsorption is enhanced by interactions with specific surface sites and in narrow pores by overlap of potential energies from pore walls. Smaller pore sizes enhance adsorption at low pressures, whereas larger pores are necessary for high hydrogen capacity. Hydrogen–surface interactions may be electrostatic and dispersive (van der Waals) forces and Kubas coordination to a transition metal.[254,255] The possible hydrogen interactions with surface sites are

1. Hydrogen coordination to unsaturated metal centers via Kubas coordination
2. Quadrupole moment interaction with the local electric field gradient

3. Electron cloud polarization by a charge center
4. Dispersive forces (van der Waals)
5. Quadrupole moment between neighboring hydrogen molecules

The interaction between hydrogen and surface sites is a critical aspect for improving hydrogen adsorption at temperatures above cryogenic temperatures. MOFs have a wider range of possible surface chemistry than other porous materials since the surface chemistry may vary from open metal centers to hydrophobic surface associated with linker ligands and also may include functional groups on the ligands. It has been estimated that an interac- tion energy in the range of 20–40 kJ mol^{-1} is required for hydrogen storage applications.[254] Porous carbons with high oxygen, nitrogen, and boron contents have also been synthe- sized to investigate the effect on hydrogen adsorption characteristics.[46,157–159,161,163,168,247,256]

The synthesis and structure of the first stable organometallic complex with a H_2-coordinated side-on (η^2) to the metal were reported by Kubas et al. in 1984.[257] Subsequently, many similar complexes have been reported, mainly for second- and third-row transition metals, and some of these complexes are stable under ambient con- ditions.[258,259] H_2-coordinated side-on (η^2) to metals involves nonclassical two-electron three-center bonds with longer H-H bond length than gas-phase H_2 bond length (0.74 Å). Kubas[258,259] has divided the η^2–hydrogen coordination to metals into the following catego- ries based on the H-H bond length:

1. True H_2 complexes (H-H, 0.8–1.0 Å)
2. Elongated H_2 complexes (H-H, 1.0–1.3 Å)
3. Compressed dihydrides (H-H, 1.3–1.6 Å)
4. True dihydrides (H-H, ~1.6 Å)[258]

Hydrogen binding in Kubas complexes is often reversible. Changes in substitution on diphosphine ligands in $[RuCl(\eta^2\text{–}H_2)(pp_2)][BF_4]$ result in the H-H bond length increasing systematically from 0.97 to 1.03 Å with increasing substituent electron-donor ability indicating that varying the substitution in ligands influences the coordination of H_2 to metals.[260]

These η^2–hydrogen–metal complexes are of interest in relation to a strategy of changing surface chemistry in MOFs by the inclusion of open or unsaturated metal centers for Kubas coordination of hydrogen. In principle, the hydrogen–metal interaction strength in MOFs can be varied from very weak physisorption interactions, through elongated coordinated H_2 to dihydrides by changing the metal, ligand, and substitution on the ligand. The aim is to bind hydrogen weakly to metals via nondissociative chemisorption so that enhanced hydrogen adsorption occurs at higher temperatures well above cryogenic temperatures. If the hydrogen–metal interaction is sufficiently strong so that stable hydrides are formed, it will be detrimental for hydrogen storage applications because of difficulty in desorbing the H_2. In principle, fine-tuning the hydrogen–metal–η^2 coordination interaction may pro- vide materials with facile hydrogen adsorption and desorption characteristics. A correla- tion between coordinatively unsaturated metal centers and enhanced hydrogen–surface density in many MOFs has been proposed.[208]

Studies of η^2–hydrogen coordination in Kubas organometallic molecules indicate that bulky ligands inhibit H_2 splitting. This suggests confinement in pores may have an effect on coordination.[259] The interaction of η^2–H_2 coordinated to a metal with the surrounding pore structure is likely to have a significant influence on stability and bonding. Hydrogen interaction with open metal sites in MOFs has been observed but, for the systems studied

so far, it is much weaker than found in Kubas complexes. Only a relatively small number of Kubas complexes of first-row transition metals are known, whereas the MOFs that have been synthesized mainly contain first-row transition metals.[258,259] Further work is required to develop new MOFs incorporating unsaturated metal centers with stronger interactions with hydrogen for storage applications above cryogenic temperatures.

Theoretical studies of H_2 adsorption on porous materials suggest that inclusion of metal ions, such as Li^+, Na^+, or Mg^{2+}, might increase hydrogen adsorption by nondissociative H_2 binding. Mulfort et al. observed increases in both the overall H_2 adsorbed and the isosteric enthalpy for a Li-doped interpenetrated MOF $Zn_2(ndc)_2(diPyNi)$ via chemical reduction with lithium metal.[130] The increases were ascribed to H_2–lithium interactions most likely enhanced by increased ligand polarizability and framework structural changes during chemical reduction.

H_2 adsorption in $(Me_2NH_2)[In(bptc)]$ is enhanced by exchange of $Me_2NH_2^+$ for Li^+ cations.[261] The Li^+-exchanged material had a lower isosteric enthalpy for H_2 adsorption than the parent material. Cation exchange results in increased H_2 capacity due to increased accessible pore volume and lower adsorption enthalpy due to increased pore size.[261]

24.10.1 Isosteric Enthalpies of Hydrogen Adsorption

The isosteric enthalpy of hydrogen adsorption (Q_{st}) at zero surface coverage is a fundamental measurement of the interaction of hydrogen with surfaces.[46,262] Adsorbate–adsorbate and other interactions are factors that influence the adsorption enthalpies at higher surface coverage. The isosteric enthalpy of adsorption is very sensitive to the accuracy of experimental data, the methods used for interpolating between isotherm points to calculate ln(p) values for specific amounts adsorbed for the temperatures used, and the methods for determining Henry's law constant from the low-pressure data. Hydrogen adsorption is normally measured above the critical temperature (33 K) where a saturated vapor pressure cannot be used to compare isotherms at different temperatures. Therefore, isotherm equations that do not use a saturated vapor pressure, for example, virial equation methods[263,264] and Langmuir–Freundlich isotherm methods, have been used. The latter does not reduce to Henry's law and therefore cannot be used at low pressure. Virial parameters can be used for comparisons of H_2–surface and H_2–H_2 interactions in pores.[46,51,52] Comparison of these methods for hydro- gen and deuterium adsorption on $Zn_3(bdc)_3Cu(pyen)$ has shown that the virial methods give a more accurate description of hydrogen and deuterium isotherms at low surface coverage due to the fact that the Langmuir–Freundlich isotherm does not reduce to Henry's law at zero surface coverage.[52]

The isosteric enthalpies of adsorption of hydrogen on a wide range of porous materials have been reported.[39,42,44,46,52,59,66,67,69,98,110–112,118,120,121,147–149,161,177,182–184,191,192,195,196,202,206,214–226,228,244,247–249,256,265–280] The hydrogen adsorption enthalpies for porous materials at cryogenic temperatures are given in Table 24.2 and have the following ranges:

1. Carbons: 1.4–12.5 kJ mol^{-1} [46,147–149,161,247–249]; Boron-doped carbon, 10–20 kJ mol^{-1} [247,256]
2. Zeolites: 5.9–18.2 kJ mol^{-1} [148,177,267–271,274–280]
3. Silicas, siloxanes: 5.4–10.4 kJ mol^{-1} [89,90,148]
4. MOFs: 5.1–13.5 kJ mol^{-1} [39,42,44,52,59,66,67,69,110–112,118,120–123,127,128,133,190–192,195,196,202,214–226,228,235,237,244,245,247,271,281,282]
5. COFs: 2.7–8.8 kJ mol^{-1} [98,103]
6. Porous polymers: 5.7–10.0 kJ mol^{-1} [182–184]

TABLE 24.2

Selected Literature Values for Experimental Values for Isosteric Enthalpies of Adsorption of H_2 on Porous Materials from Gas Adsorption Measurements over a Range of Temperatures and Microcalorimetry

Porous Materials	Isosteric Enthalpy of Adsorption (Q_{st}/kJ mol^{-1})	Temperature Range (K)	References
Metal organic framework			
$Zn_4O(bdc)_3$ (MOF-5, IRMOF-1)	4.9–4.4	77–87	[66]
	4.1	77–298	[191]
	3.8	77–298	[192]
	5.2–4.7	77–87	[215]
$Zn_4O(ndc)_3$ (IRMOF-8)	6.1	77–298	[191]
$Zn_4O(hpdc)_3$ (IRMOF-11)	9.1–5.1	77–87	[66]
Zn_3O_3(dhbdc) (MOF-74)	8.3–5.6	77–87	[66]
Zn_4O(btb) (MOF-177)	11.3–5.8	273–323	[196]
	4.4	77–87	[39]
$Zn_3(bpdc)_3$(bpy)	7.1–5.1	77–87	[120]
$Zn_3(bdt)_3$	8.7–6.8	77–87	[67]
Zn_2(abtc)$(dmf)_2$ (SNU-4)	7.24–5.91	77–87	[245]
Cu_2(bptc) (NOTT-100)	6.3	77–87	[44,45]
Cu_2(tptc) (NOTT-101)	5.35	77–87	[44,45]
Cu_2(qptc) (NOTT-102)	5.4	77–87	[45,244]
$Cu_2(C_{26}O_8H_{12})$ (NOTT-103)	5.7	77–87	[44]
$Cu_2(C_{22}O_8H_8F_2)$ (NOTT-105)	5.77	77–87	[44]
$Cu_2(C_{24}H_{14}O_8)$ (NOTT-106)	6.34	77–87	[44]
$Cu_2(C_{26}H_{20}O_8)$ (NOTT-107)	6.70	77–87	[44]
Cu_2(pddip)$(H_2O)_2(DMF)_{7.5}$ $(H_2O)_5$ (NOTT-110)	5.68	77–87	[244]
[Cu_2(dhpddip)$(H_2O)_2$](DMF) $_{7.5}$ $(H_2O)_5$ (NOTT-111)	6.21	77–87	[244]
Cu_3(dcbplb) (NOTT-112)	5.64–4.74	77–87	[59]
$Cu_3(btc)_2$ (HKUST-1)	6.6–6.0	77–87	[66]
	4.5	77–87	[192]
	7–6	77–87	[216]
Cu_2(abtc)$(H_2O)_2$·3dma (PCN-10)	7–4	77–300	[118]
Cu_2(abtc)$(dmf')_2$ (SNU-5′)	6.53–5.91	77–87	[245]
Cu_2(abtc) (SNU-5)	11.6–4.43	77–87	[245]
Cu_2(sbtc)$(H_2O)_2$·3dma (PCN-11)	7–4	77–300	[118]
Cu_2(adip) (PCN-14)	8.6–5.9	77–87	[241]
Cu_2(bdi) (PCN-46)	7.2	77–87	[237]
[Cu_2(bpndc)(bpy)]n (SNU-6)	7.74	77–87	[134]
$Cr_3OF(btc)_2$ (MIL-100(Cr))	6.3–5.6^{MC}	77	[69]
$Cr_3OF(bdc)_3$ (MIL-101(Cr))	10.0–9.3^{MC}	77	[69]
$H_2[Co_4O(tatb)_{8/3}]$ (PCN-9)	10.1	77–87	[214]
$Co_3(bpdc)_3$(bpy)	6.8–5.7	77–87	[120]
$Mg_3(ndc)_3$	9.5–7.0	77–87	[195]

$Mn_3(bdt)_3$	8.4–6.3	77–87	[67]
$Mn_2(bdt)Cl_2$	8.8–6.0	77–87	[67]

TABLE 24.2 (continued)

Selected Literature Values for Experimental Values for Isosteric Enthalpies of Adsorption of H_2 on Porous Materials from Gas Adsorption Measurements over a Range of Temperatures and Microcalorimetry

Porous Materials	Isosteric Enthalpy of Adsorption (Q_{st}/kJ mol^{-1})	Temperature Range (K)	References
$Mn_3[(Mn_4Cl)_3(btt)_8]_2$	10.1–5.5	77–87	[42,121]
$Cu_3[(Cu_4Cl)_3(btt)_8]_2$	9.5–6	77–87	[122]
$Fe_3[(Mn_4Cl)_3(btt)_8]_2$ $FeCl_2$	10.2–5.5	77–87	[121]
$Co_3[(Mn_4Cl)_3(btt)_8]_2$·1.7 $CoCl_2$	10.5–5.6	77–87	[121]
$Ni_{2.75}Mn_{0.25}[(Mn_4Cl)_3(btt)_8]_2$	9.1–5.2	77–87	[121]
$Cu_3[(Cu_{2.9}Mn_{1.1}Cl)_3(btt)_8]_2$·2$CuCl_2$	8.5–6.0	77–87	[121]
$Zn_3[(Zn_{0.7}Mn_{3.3}Cl)_3(btt)_8]_2$·2$ZnCl_2$	9.6–5.5	77–87	[121]
$Li_{3.2}Mn_{1.4}[(Mn_4Cl)_3(btt)_8]_2$·0.4LiCl	8.9–5.4	77–87	[121]
$Mn_3[(Mn_4Cl)_3(btt)_8]_2$·0.75$CuPF_6$	9.9–5.6	77–87	[121]
$Fe_3[(Fe_4Cl)_3(btt)_8(MeOH)_4]_2$·(Fe-btt)	11.9	77–87	[273]
$Mn_3[(Mn_4Cl)_3(tpt\text{-}3tz)_8(DMF)_{12}]_2$	7.6	77–87	[217]
$Cu_3[(Cu_4Cl)_3(tpb\text{-}3tz)_8]_2$·1.1$CuCl_2$	8.2	77–87	[217]
$Mn_3[Co(CN)_6]_2$	5.9–5.3	77–87	[215]
$Fe_3[Co(CN)_6]_2$	6.6–6.3	77–87	[215]
$Co_3[Co(CN)_6]_2$	6.8–6.5	77–87	[215]
$Ni_3[Co(CN)_6]_2$	7.4–6.9	77–87	[215]
$Cu_3[Co(CN)_6]_2$	7.0–6.7	77–87	[215]
	7.2	77–87	[218]
$Zn_3[Co(CN)_6]_2$	6.5–6.3	77–87	[215]
$Ni[Fe(CN)_5NO]$	7.5–5.7	77–87	[218]
$Co[Fe(CN)_5NO]$	6.5–5.0	77–87	[218]
	8.5–5.5		[219]
$Zn_3K_2[Fe(CN)_6]_2$	8.3–7.1	75–85	[220]
	9.0–7.9	77–87	[221]
$Zn_3Rb_2[Fe(CN)_6]_2$	6.8	75–85	[220]
	7.9–7.3	77–87	[221]
$Zn_3Cs_2[Fe(CN)_6]_2$	6.3	75–85	[220]
$Zn_3Na_2[Fe(CN)_6]_2$	7.7–7.0	77–87	[221]
$Zn_3[Co(CN)_6]_2$-R	6.1	75–85	[220]
$Zn_3[Co(CN)_6]_2$	6.5–6.3	77–87	[221]
$Zn_3Li_2[Fe(CN)_6]_2$·2H_2O	7.9–6.1	77–87	[221]
H_2 Zn_3 $[Fe(CN)_6]_2$·2H_2O	8.2–7.8	77–87	[221]
$NaNi_3(OH)(sip)_2$	10.4–9.4	77–87	[112]
$Co(pyz)[Ni(CN)_4]$	7.2	77–87	[222]
$Co(pyz)[Pd(CN)_4]$	7.8	77–87	[222]
$Co(pyz)[Pt(CN)_4]$	7.6	77–87	[222]
$Ni(pyz)[Ni(CN)_4]$	7.2	77–87	[222]
$Ni(bpy)[Ni(CN)_4]$	7.5	77–87	[222]

$Ni(bpy)[Pd(CN)_4]$	7.0	77–87	[222]
$Ni(dpac)[Ni(CN)_4]$	6.0	77–87	[222]
$Ni_2(dhtp)(H_2O)_2 \cdot 8H_2O$	13.5^{VTIR}	92–150	[110,223]

(*continued*)

TABLE 24.2 (continued)

Selected Literature Values for Experimental Values for Isosteric Enthalpies of Adsorption of H_2 on Porous Materials from Gas Adsorption Measurements over a Range of Temperatures and Microcalorimetry

Porous Materials	Isosteric Enthalpy of Adsorption (Q_{st}/kJ mol^{-1})	Temperature Range (K)	References
Cd(2-pmc)$_2$ *rho*-ZMOF	8.7	77–87	[190]
$Cu_6O(tzi)_3(NO_3)$	9.5–4.7	77–87	[123]
$Cu(bdc)(ted)_{0.5}$	6.1–4.9	77–87	[128]
$Cu_3(bhtc)_2$ (UMCM-150)	7.2–4.9	77–87	[127]
$In_3O(abtc)_{1.5}(NO_3)$	6.5	77–87	[225]
In(4,6-pmdc)$_2$ *sod*-ZMOF	8.4	77–87	[190]
$((CH_3)_2NH_2)$[In(bptc)]	7.6	77–87	[228]
$((CH_3)_2NH_2)$[In(bptc)]Li^+	6.1	77–87	[228]
Y(btc)(H_2O)	7.3	77–87	[202]
$Zn_3(bdc)_3Cu(pyen)$(M′MOF1)	12.29–9.5	77–87	[52]
	12.44–9.5 (D_2)	77–87	[52]
$Zn(bdc)(ted)_{0.5}$	5.3–5	77–87	[128]
$Zn_2(ndc)_2$(diPyNi)	5.7–3.3	77–87	[130]
$Zn_2(ndc)_2$(diPyNi) $^-Li^+$	6.1–5.1	77–87	[130]
Zn(mim)$_2$ (ZIF-8)	4.5	30–300	[210]
Zn(tbip)	6.7–6.4	77–87	[226]
$Zn_3(OH)$ (*p*-cdc)$_{2.5}$	7.2–3	77–87	[224]
$Zn_4O(t^2dc)(btb)_{4/3}$(UCMC-2)	6.4–4.2	77–87	[232]
$Zn_2(cnc)_2$(dpt)	7.85–6.4	77–87	[243]
$Co_4O(tatb)_{8/3}\cdot 2H_3O^+\cdot 5H_2O\cdot 8$dmso (PCN-9(Co))	10.1–6	77–87	[235]
$Fe_4O(tatb)_{8/3}\cdot 5H_2O\cdot 10$dmso (PCN-9(Fe))	6.4–4	77–87	[235]
$Mn_4O(tatb)_{8/3}\cdot 2H_3O^+\cdot 5H_2O\cdot 8$dmso (PCN-9(Mn))	8.7–5.5	77–87	[235]
Mg formate	7–6.5	77–87	[272]
$[Cd_5(Tz)_9](NO_3)_3\cdot 8H_2O$	13.3–6	77–87	[281]
Mg-MOF-74	9.4^{VTIR}	77–97	[271]
Co-MOF-74	11.2^{VTIR}	77–97	[271]
Cr-bdc nanostructures	8	77–87	[282]
Cu-bdc nanostructures	4	77–87	[282]
Carbon materials			
Graphene-like nanosheets	5.9–4	77–87	[250]
Functionalized ACs from coconut and polyacrylonitrile	5.2–3.9	77–114	[46]
Carbon (charcoal)	7.3–1.4	17–90	[147]
Carbons (charcoal)	7.9–6	77–90	[148]
AC AX-21	6.4–5.0	77–273	[149]
Carbons from biomass	4.1–7.5	77–87	[81]
Carbon (wood derived + KOH activation)	10.9	298–333	[248,249]
	17–20	298–333	[248,249]
Carbide-derived carbons	11–6	77–87	[265]

Carbons zeolite β-templated	8.2–4	77–87	[161]

TABLE 24.2 (continued)

Selected Literature Values for Experimental Values for Isosteric Enthalpies of Adsorption of H_2 on Porous Materials from Gas Adsorption Measurements over a Range of Temperatures and Microcalorimetry

Porous Materials	Isosteric Enthalpy of Adsorption (Q_{st}/kJ mol^{-1})	Temperature Range (K)	References
Boron-doped carbon	12.47–10.8	77–298	[247]
BC_6	20–10	77–87	[256]
Zeolites			
Zeolite Na-A	10.7–6.2	40–120	[177]
Zeolites 4A, 5A, 13X	7.9–5.9	75–90	[148]
Aluminophosphates	9.2–3.7	77–87	[266]
Mg exchanged faujasite, Na/K-ZSM-5, (Mg,Na)-Y, (Ca,Na)-Y, Ca-X, Mg-X,	18.2–3.5^{VTIR}	120–150	[267–269,271,274–280]
Li-FER, Na-FER, K-FER, Li-ZSM-5, Na-ZSM-5		79–95	
Silicas			
Silica gel	7.3–5.4	75–90	[148]
Functionalized cubic	7.2		[89]
Siloxane cages			
Poly(ethynylene aryleneethenylene silsesquioxane	8	77–87	[90]
Polymers			
Hyper-cross-linked porous polymers	7.5–6	77–87	[184]
Hyper-cross-linked polyaniline polymers	9.3–5.7	77–87	[182]
Hyper-cross-linked materials	7.8–5.2	77–87	[93]
Polyporphyrins	7.6–5.8	77–298	[186]
Polymers POPs1–4	9–5	77–87	[188]
PAF-1	4.6	77–87	[97]
COFs 1,5,6,8,10, 102, 103	8–3.9	77–87	[103]

MC, Low surface coverage microcalorimetry method; VTIR, variable temperature IR method. All other measure- ments are from hydrogen adsorption isotherm studies.

A correlation has been observed between ΔH_0 and ΔS_0 for hydrogen adsorption on Mg-MOF-74, Co-MOF-74, and cation-exchanged zeolites.[271] This suggests that the opti- mum value of ΔH_0 for hydrogen delivery at room temperature is likely to be in the range of 22–25 kJ mol^{-1}. Other estimates have suggested that an enthalpy of adsorption of 15 kJ mol^{-1} is optimum for hydrogen storage applications,[283] while a range of 20–40 kJ mol^{-1} has also been proposed for hydrogen storage applications.[254] The Q_{st} values obtained for hydro- gen adsorption on porous materials are much higher than the enthalpy of vaporization of 0.9 kJ mol^{-1} for H_2 at 20.28 K.[4] The surface chemistry in MOFs can be varied to a greater extent than in case of other porous materials. Some MOFs have open metal centers that have been proposed as sites for η^2–H_2 coordination similar to that found in Kubas com- pounds. There is some evidence for stronger interactions, but the enthalpies of hydrogen adsorption at zero surface coverage for MOFs with open metal centers are often not appre- ciably higher than for other porous materials (see Table 24.2). This is shown by enthalpies of hydrogen adsorption in the range of 5.3–6.7 kJ mol^{-1} observed for the copper tetracar- boxylate series.[44] The highest enthalpies of hydrogen adsorption so far obtained for MOFs

are 12.3 kJ mol^{-1} for $Zn_3(bdc)_3 \cdot Cu(pyen)$ (gas adsorption method, 77–87 K), 13.5 kJ mol^{-1} for desolvated $Ni_2(dhtp)(H_2O)_2 \cdot 8H_2O$ (variable temperature infrared (IR) method), and 13.3 kJ mol^{-1} for $[Cd_5(Tz)_9](NO_3)$. These enthalpies of hydrogen adsorption at cryogenic temperatures compare with the following maximum values: boron-doped carbon (>7%) (~12.5 kJ mol^{-1} and (BC_6) 20 kJ mol^{-1}),[247,256] ~11 kJ mol^{-1} for carbide-derived carbons,[265] <8.2 kJ mol^{-1} for other carbons,[161] 18.2 kJ mol^{-1} for zeolites,[268] 8 kJ mol^{-1} for COFs,[103] and

10.0 kJ mol^{-1} for porous polymers.

Recent results for H_2 adsorption on an ultramicroporous carbon showed that the main process, physisorption with an enthalpy of adsorption of 9–11 kJ mol^{-1}, was accompanied by a slow process. The latter involves slow uptake at high pressures with a high enthalpy of adsorption (17–20 kJ mol^{-1}) and hysteresis on desorption. The combined result is relatively high levels of hydrogen uptake at near-ambient temperatures and pressures (e.g., up to 0.8 wt% at 298 K and 2 MPa). These unusual adsorption characteristics were attributed to contributions from polarization-enhanced physisorption induced by residual traces of alkali metals from chemical activation.

Currently, the Q_{st} values reported for hydrogen adsorption on porous materials are too low for significant adsorption at ambient temperatures. An intermediate weak nondissociative η^2 coordination or other weak chemisorption with Q_{st} values in excess of values observed so far and probably in the range of 20–40 kJ mol^{-1} with facile adsorption and desorption characteristics is required for storage applications. If the hydrogen is strongly chemisorbed H_2 desorption, it would require desorption temperatures that are too high.

24.10.2 Diffraction Studies of Hydrogen in Pores

X-ray diffraction studies have provided direct evidence of hydrogen adsorption.[284,285] Dense aggregates of adsorbed H_2 were observed in MOF $[Rhbza)_4(pyz)]_n$ at 90 K.[285] Hydrogen adsorbate molecules were located near a corner of rectangular nanochannels in $[Cu_2(pzdc)_2(pyz)]$n coordination polymer. These results are consistent with adsorption due to overlap of potential energy fields from the pore walls.[284]

Neutron diffraction provides direct evidence for the position of hydrogen adsorption sites. Spencer et al. used variable-temperature single-crystal neutron diffraction to investigate hydrogen-loaded MOF-5 $[Zn_4O(bdc)_3]$.[286] The sites for hydrogen adsorption were the nodal regions with one site located over the shared vertex of the ZnO_4 units at the center of the node and the other over the face of ZnO_4. The hydrogen adsorption sites of MOF-5 were also determined using deuterium loading and powder neutron diffraction meth- ods.[287] The initial adsorption sites were identified as the center of three ZnO_3 triangular faces followed by the top of single ZnO_3 triangles. At higher loading, ZnO_2 sites and sites on the hexagonal linkers were occupied. 3D interlinked nanoclusters of hydrogen mol- ecules were observed at high loading.

Six D_2 adsorption sites were observed in HKUST-1 ($Cu_3(btc)_2$) using neutron powder diffraction techniques. Adsorption occurred initially on coordinatively unsaturated axial sites of the dinuclear Cu center [Cu–D_2 = 2.39(1) Å].[288] This distance is much larger than that observed for σ-bonded η^2–H_2 complexes, but it represents a significant interaction. Competitive adsorption on other D_2 sites proceeded with increasing pore size. Neutron powder diffraction studies showed that adsorbed D_2 is associated with the Mn center (Mn–D_2 = 2.27 Å) in $Mn_3[(Mn_4Cl)_3(btt)_8 \cdot (CH_3OH)_{10}]_2$.[42] One of the strongest D_2 adsorption sites was 2.47 Å from the Cu^{2+} ions in $HCu_3[(Cu_4Cl)_3(btt)_8]_2 \cdot 3.5HCl$.[122]

Neutron powder diffraction studies on D_2-loaded $Cu_3(dcbplb)$ (NOTT-112) showed that the axial sites of exposed Cu(II) ions in the smallest cuboctahedral cages are the initial,

strongest binding sites with a Cu–D_2 distance of 2.23 Å. This allows discrimination between the two types of exposed Cu(II) sites at the paddle wheel nodes.[289]

Studies have shown that in Zn_2(dhbdc) (MOF-74), the first site occupied had a longer Zn–D_2 distance (2.6 Å).[208] Powder neutron diffraction studies[273] of $Fe_3[(Fe_4Cl)_3(btt)_8(MeOH)_4]_2$ (Fe-btt), under various deuterium loadings at 4 K, showed 10 different adsorption sites. The strongest binding site was 2.17(5) Å from the Fe^{2+} in the framework.

Neutron diffraction and inelastic neutron scattering (INS) studies have shown that hydrogen (deuterium) adsorption on Cr MIL-53 at low temperature involves the occupation of four different adsorption sites. Adsorption sites near the Cr–O clusters had the highest occupations, while adsorption occurs in the corners formed by the linker ligands. Significant breathing of the framework occurred and this was pronounced above the boiling point of hydrogen.[290]

High-resolution neutron powder diffraction studies of hydrogen adsorption on $Cu_3[Co(CN)_6]_2$ at 1, 2, and 2.3 H_2/Cu loadings showed that adsorption occurred on two sites.[291] The strongest adsorption site was an interstitial location within the structure. The second adsorption type of site was exposed Cu^{2+} ion coordination sites resulting from the presence of $[Co(CN)_6]^{3-}$ vacancies.

Neutron diffraction studies revealed four distinct D_2 adsorption sites in Y(btc). The strongest adsorption sites identified were the aromatic rings in the organic linkers rather than the open metal sites, as reported for other MOFs.[202] At high H_2 loadings, highly symmetric novel nanoclusters of H_2 molecules with relatively short H_2–H_2 contact distances were formed.

Hydrogen interactions in MOF materials are complex and a variety of factors influence adsorption interactions when H_2 is confined in pores. The metal–H_2 and D_2 distances observed earlier are in the range of 2.17–2.6 Å, which is significantly longer than the range of 1.6–1.92 Å reported[257,260,292] for Kubas compounds, but the shorter distances represent a significant interaction. Comparison of the metal–H_2 (or M–D_2) distances with corresponding isosteric enthalpy data suggests that other factors may also influence H_2–surface interactions.

24.10.3 Spectroscopic Studies of Hydrogen–Surface Interactions

INS measurements on porous nickel phosphateVSB-5[293] and porous hybrid inorganic/organic framework material $NaNi_3(OH)(sip)_2$ [112,293] showed that initially, adsorption occurred on unsaturated Ni(II) sites in the latter. Binding sites consistent with physisorption were occupied as hydrogen loading increased and finally, at higher loading interactions between H_2 adsorbate molecules occurred. Studies of unsaturated metal centers in metal cyano[68,107,215,294] and MOF materials suggest that H_2 interactions with surface sites in these materials are weaker.[26,291,294]

INS studies[295] of D_2 adsorption on HKUST-1 were consistent with previous neutron powder diffraction studies. Three binding sites for H_2 loading <2.0 H_2/Cu were identified and these were progressively populated with increasing loading. The variation of INS peaks with temperature showed that the peak corresponding to population at H_2/Cu ratio <0.5 had the highest enthalpy (6–10 kJ mol^{-1}), while the peaks for the other sites had lower enthalpies.

Zhou et al. proposed[296] that hydrogen binding in $(Mn_4Cl)_3(btt)_8$-MOF[42] is not of the expected Kubas type because there is (a) no significant charge transfer from metal to H_2, (b) no evidence of any H_2–σ^* Mn-d orbital hybridization, (c) no significant H-H bond elongation, and (d) no significant shift in ν(H-H) stretching vibration.[296] The short metal–H_2

distances and relatively high binding energies were explained by an enhanced classical coulombic interaction. This effect is unlikely to be sufficient to increase the hydrogen storage temperature to ambient conditions.

INS spectra of $Fe_3[(Fe_4Cl)_3(btt)_8(MeOH)_4]_2$ (Fe-btt) were consistent with the strong rotational hindering of adsorbed H_2 molecules at low loadings.[273] Catalytic conversion of *ortho* to *para* hydrogen by the paramagnetic iron centers was also observed.

IR spectroscopic studies of H_2 adsorption on various MOF materials at 300 K and high pressures (27–55 bar) have shown that ν(H-H) stretching vibration at 4155 cm^{-1} for *ortho* H_2 is shifted (30–40 cm^{-1}) to lower energy.[297] H_2 molecules interact with the organic ligands of MOFs $M(bdc)(ted)_{0.5}$ (M = Ni, Cu, Zn.) instead of the saturated metal centers located at the corners of the unit cell. Density functional calculations showed that for the induced dipole associated with the trapped H_2 in $M(bdc)(ted)_{0.5}$ systems, the strongest dipole moment is for the site in the unit cell corner dominated by the interaction with the benzene ligand rather than the metal center. A weak dependence of ν(H-H) on cations was observed for 1D pore structures $M_3[HCOO]_6$ (M = Mn, Co, Ni)-type formate structures, and this was attributed to a small change in pore size rather than a direct interaction with the metal centers. No correlation was observed between H_2 binding energies (determined by isotherm measurements) and the ν(H-H) stretch shift, indicating that these shifts are dominated by the environment (organic ligand, metal center, and structure) rather than the strength of the interaction.[297]

Interaction between adsorbed hydrogen and the coordinatively unsaturated Mg^{2+} and Co^{2+} cationic centers in Mg-MOF-74 and Co-MOF-74, respectively, has been investigated using variable temperature infrared (VTIR) spectroscopy.[271] The H_2 molecule is perturbed by the cationic adsorption center making the ν(H-H) stretching mode IR active at 4088 and 4043 cm^{-1} for Mg-MOF-74 and Co-MOF-74, respectively. The correspond- ing enthalpies of adsorption were 9.4 and 11.2 kJ mol^{-1} for Mg-MOF-74 and Co-MOF-74, respectively. The ν(H-H) IR bands for zeolites were in the range of 4056–4111 cm^{-1}. These IR band shifts are consistent with only very weak interactions with unsaturated metal centers.

The ν(H-H) stretching vibration in H_2 becomes IR active when adsorbed on surfaces due to lowering of symmetry. However, the IR spectra are complex because of the pres- ence of *ortho* and *para* forms of H_2, and in situ evidence for a single-site catalyzed con- version of adsorbed H_2 was obtained.[298] The IR bands shift to lower energy relative to the gas-phase spectrum and the intensity is proportional to the strength of the H_2–sur- face interaction. IR spectroscopy studies have shown that unsaturated copper sites in HKUST-1 are preferential adsorption sites for H_2 and the ν(H-H) band is ~70 cm^{-1} lower than the corresponding gas-phase band.[298] Smaller shifts (37–45 cm^{-1}) in ν(H-H) have been observed for H_2 adsorption on a cross-linked polymer. It was proposed that this shift was primarily due to specific interactions of the H_2 molecule with the electron-rich part of the polymer.[299] The H_2 adsorption energy estimated from the temperature depen- dence of IR spectral features was 10 kJ mol^{-1}. This is similar to the highest value obtained from INS measurements.[295]

The shifts to lower energy in low-temperature-stable η^2–H_2 complexes are much larger with ν(H-H) typically in the range of 2600–3250 cm^{-1} [258] (ν(H-H) for H_2 in gas phase is 4160 cm^{-1} [298]). The IR spectrum of $W(CO)_3(PCy_3)_2(\eta^2–H_2)$ gives ν(H-H) of 2690 cm^{-1}, while the H-H bond length in $W(CO)_3(P\mathit{i}Pr_3)_2(\eta^2–H_2)$ was 0.84 Å as determined by neutron diffraction studies compared with 0.74 Å in H_2 gas.[257] Raman spectroscopy has also been used to study the adsorbed H_2 phase in porous materials at room temperature and under cryogenic conditions.[300–302] The results confirm that the interaction strength for adsorption

of molecular hydrogen is small and consistent with physisorption for single-walled nanotubes, MOF-5, and HKUST-1.

Overall, the spectroscopic evidence currently available indicates that interactions of molecular hydrogen with surfaces in pores are weak. This is consistent with crystallographic diffraction studies that show longer distances than those observed for Kubas compounds and low enthalpies for hydrogen adsorption on porous materials. The inclusion of Kubas-type motifs in MOFs has the greatest potential for developing materials for hydrogen storage under ambient conditions.

24.10.3.1 Framework Flexibility and Hysteretic Adsorption in MOFs

Some MOFs have framework flexibility and structural change may occur during the adsorption process. MOF framework flexibility may occur either without any bond breaking or some materials undergo bond breaking and reforming reactions. The latter are much rarer and the former have possible applications in storage applications. The flexibility in the MIL series is an example of large structural changes during adsorption.[12] Structural change without bond breaking occurs with a scissoring motion leading to an increase in crystallographic cell volume of ethanol and methanol templated phases E and M of on $Ni_2(bpy)_3.(NO_3)_4$ during adsorption of the templates.[303,304] Hysteretic adsorption was observed initially for hydrogen adsorption on $Ni_2(bpy)_3.(NO_3)_4$[200] (see Figure 24.13) and several further systems have been identified.[207,227,305] This is thought to be a kinetic trapping effect. The corresponding isobars are shown in Figure 24.12. It is apparent that hydrogen desorption does not start until higher temperatures (~110 K).[200] These materials have windows and pore cavities and the diffusion through the very nar- row windows and framework flexibility are probably factors in hysteretic adsorption. Hysteretic hydrogen adsorption was subsequently observed in a related system for desolvated $[Co_2(bpy)_3(SO_4)_2(H_2O)_2](bpy)(CH_3OH)$.[306]

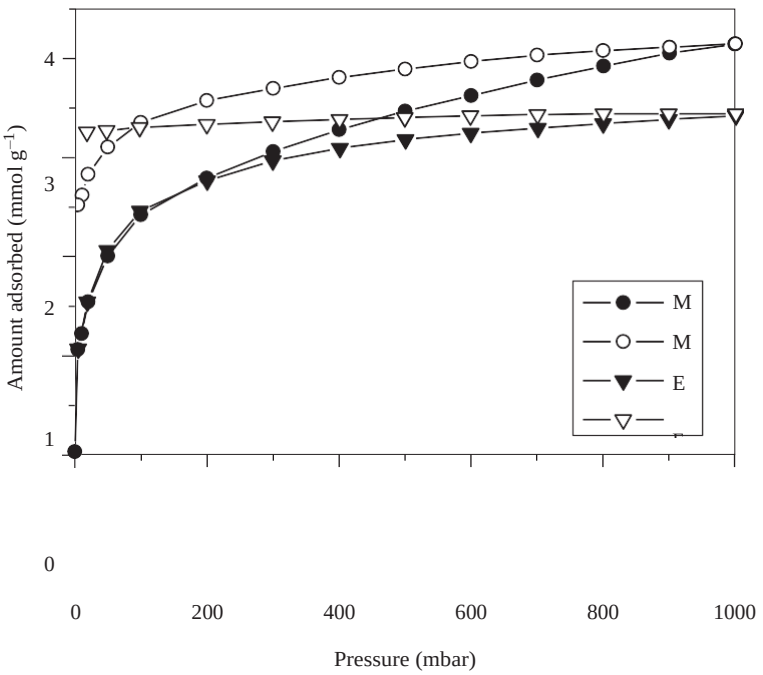


FIGURE 24.13

Adsorption/desorption isotherms for H_2 adsorption (filled symbols) and desorption (open symbols) isotherms on MOF adsorbents at 77 K: **M** polymorph of $Ni_2(bpy)_3(NO_3)_4$ (●, ○); **E** polymorph of $Ni_2(bpy)_3(NO_3)_4$ (▼, ▽). (Zhao, X., Xiao, B., Fletcher, A.J., Thomas, K.M., Bradshaw, D., Rosseinsky, M.J., *Science*, 306, 1012, 2004. Copyright Science.)

Cation-induced kinetic trapping and enhanced hydrogen adsorption in a modulated anionic MOF (In(III) centers and tetracarboxylic acid) have been observed.[307] The framework exhibits hysteretic hydrogen adsorption with piperazinium dications in pores, but on exchange of these dications with lithium cations, no hysteresis is observed.

Ferey et al. have developed the MIL series of MOFs where the changes in structure during adsorption are much larger.[229,308] Hysteresis has been observed for hydrogen adsorption on the MIL-53, ($M = Al^{3+}, Cr^{3+}$) at high pressure and 77 K.[125]

Choi et al. studied[207] H_2 adsorption on a MOF Co(bdp) that showed temperature-dependent broad hysteresis loops over the temperature range of 50–87 K. The results suggested a pressure-, temperature-, and gas-dependent pore-opening mechanism with the hysteretic behavior governed by phase transitions with energies comparable to the H_2 adsorption enthalpy. Some high-pressure H_2 hysteresis has also been observed for FMOF-1, which was formed by reaction of Ag(I) with 3,5-bis(trifluoromethyl)-1,2,4-triazolate.[305] The fluorolined channels and cavities of the framework show hysteretic adsorption of H_2.

There are now a number of examples of hysteretic adsorption of hydrogen[125,200,207,305] and other gases.[309–311] Hysteretic H_2 adsorption has been observed in several MOFs and may have applications for hydrogen storage. A microscopic theory has been proposed showing that enhanced adsorption hysteresis of H_2-activated diffusion along the small-pore channels is a dominant equilibration process. The sensitivity of gas adsorption to tempera- ture changes is explained by thermodynamics. Analysis of transient adsorption dynamics reveals that the hysteretic H_2 adsorption is an intrinsic adsorption characteristic in diffusion-controlled small-pore systems, but this has not yet been realized.[312]

24.10.3.2 Kubas-Type Compounds Doped in Porous Materials

Kubas-type compounds have been doped into mesoporous materials to produce potential hydrogen storage materials. The problem is getting high enough loadings. Low-coordinate Ti(III) fragments with controlled geometries designed specifically for σ–H_2 binding have been dispersed on mesoporous silica using tri- and tetrabenzyl Ti precursors. The optimal loading level of 0.2 mol equivalents of tetrabenzyl Ti gave a material with total hydrogen storage capacity at 77 K of 21.45 wt% (including compressed gas at 100 atm). The binding adsorption enthalpies increased with increasing surface coverage to a maximum of 22.15 kJ mol^{-1}. A quantum increasing chemical computational model of the titanium–H_2 binding sites of a mesoporous silica is in agreement with experimental results that average Ti–H_2 interaction energies increase as the number of bound H_2 molecules. These findings suggest that η^2–H_2 binding to unsaturated metal centers may possibly be exploited for hydrogen storage. The silica-supported systems have 5–10 wt% of organometallic Ti, V, and Cr grafted onto mesoporous silica.[313–315] These materials are of interest because high H_2/metal ratios and enthalpies increase with increasing adsorption. In general, the H_2 storage ability of the materials decreases in the order Ti > V > Cr and $M^{2+} > M^{3+}$.

24.10.3.3 Hydrogen Spillover on Porous Materials

Hydrogen spillover is well established in catalysis where hydrogen atoms are formed on metal particles by dissociative chemisorption and diffuse from the particles onto pore surfaces where further diffusion may occur. The use for hydrogen storage on porous materials was first proposed by Yang and coworkers.[316,317] The hydrogen atoms react with surface sites, and therefore, surface chemistry and surface area are important. Studies have been undertaken for hydrogen spillover on carbon nanotubes,[316,318,319] graphite nanofibers,[318,320]

ACs,[321–323] nitrogen-doped carbons,[324] zeolites,[87] Al-doped MCM-41 mesoporous silica,[325] COFS,[326] and MOFs.[327,328] The adsorption isotherms are reversible with acceptable desorption characteristics at ambient temperature. Isotope tracer studies have been undertaken on IRMOF-8 bridged to Pt/C to understand the mechanism. Studies of hydrogen spillover on MOF-5,[329] HKUST-1, and MIL-101[326] showed that H_2 storage capacity at 298 K and high pressure correlated with the surface area and pore volume. Hydrogen uptake at room tem- perature in composite MIL-100(Al)/Pd(10%) is ~2× that of the MIL-100. This is accounted for by Pd hydride formation and a spillover mechanism.[330]

Sample-to-sample consistency in storage capacity on the bridged MOF samples is difficult to achieve unlike Pt/C sorbents. However, significant storage enhancements are still observed.[331] The effect of Pd nanoparticles on the rate of hydrogen adsorption provides supporting evidence for the hydrogen spillover mechanism in Pd/ultramicroporous carbon systems.[249] Although this method may enhance storage capacities by ~3 compared with physisorption under ambient temperature conditions, it is still well below the hydrogen storage capacities required for applications.

24.10.3.4 Comparison of H_2 and D_2 Adsorption

Both H_2 and D_2 have bond lengths of 0.7416 Å, but different zero point energies.[332] Small differences in physical properties (density, boiling point, amplitudes of vibration, dissociation energy, etc.) and adsorption characteristics are observed.[46,51,52,333–335] Comparison of H_2 and D_2 adsorption at 77 and 87 K shows that D_2/H_2 molar ratios in the range of 1.06–1.15 are typical for porous MOF,[45,47,52,143] carbons,[46,51] and zeolite materials.[177]

When differences between H_2 or D_2 sizes and pore size are similar to the de Broglie wavelength, quantum effects occur and this leads to molecular sieving of H_2 and D_2.[336–338] Quantum effects lead to higher amounts of deuterium adsorbed than hydrogen under the same experimental conditions.[46,47,51,52,334,335,338] Kinetic quantum molecular sieving was first observed experimentally for adsorption and desorption of H_2 and D_2 on a carbon molecular sieve (Takeda 3a), and a microporous carbon[51] and typical adsorption/desorption kinetic profiles for D_2 and H_2 are shown in Figure 24.14. This figure shows that D_2 adsorption is faster than H_2 for both adsorption and desorption contrary to the trend expected based on mass. Analysis of the H_2 and D_2 adsorption isotherms using a virial equation shows that the D_2–D_2 interactions are smaller than the H_2–H_2 interactions, and this is consistent with the smaller amplitude of vibration of D_2 compared with H_2.[51,52]

Similar observations of faster deuterium adsorption kinetics compared with hydro- gen were reported subsequently for $Zn_3(bdc)_3 \cdot Cu(pyen)$[52] and zeolites.[88] The MOF $Zn_3(bdc)_3 \cdot Cu(pyen)$ has two types of pores present in the material and independent quantum effects were observed for these pores.[52] The activation energies for hydrogen were slightly greater than for deuterium for both types of pores. The difference between the adsorbate dimensions and the minimum pore dimension needs to be close to the de Broglie wavelength for quantum effects to be observed. The faster adsorption kinetics for D_2 compared with H_2 is contrary to that expected on a mass basis. The larger amplitude of vibration of hydrogen atoms leads to an effective larger cross section for hydrogen leading to slower hydrogen adsorption and desorption kinetics when the pore size is similar to the de Broglie wavelength. Theoretical studies of quantum kinetic molecular sieving have been reported.[339,340] These kinetic effects have only been observed at low temperature in materials with narrow pores. This effect would not be an issue for storage in materials with larger pores. Kinetic quantum molecular sieving has possible applications for isotope separation.

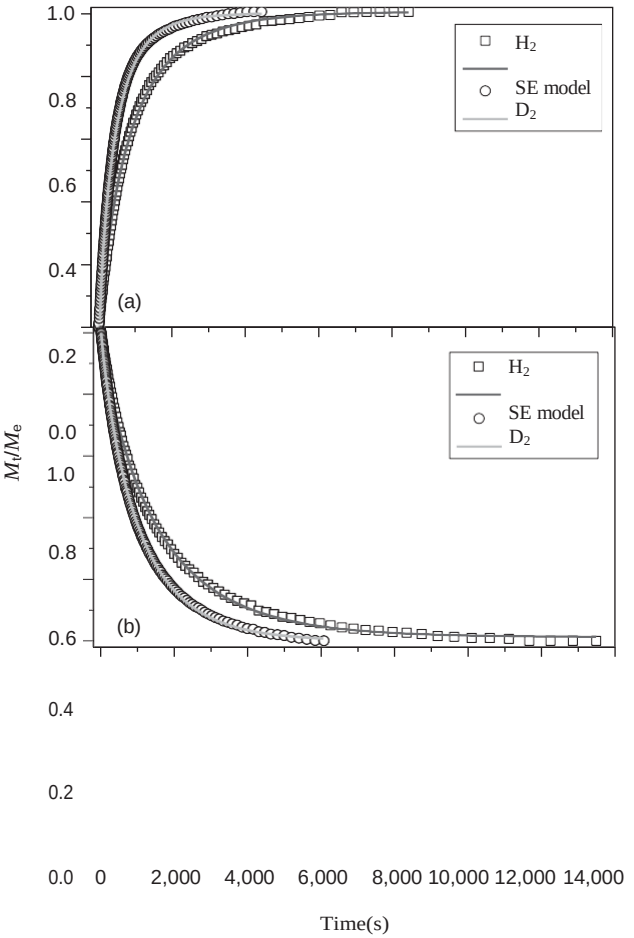


FIGURE 24.14

Typical H_2 and D_2 adsorption and desorption kinetic profiles and fitting of the stretched exponential kinetic model for pressure increments (1–2 kPa) and decrements (2–1 kPa) on CMS T3A at 77 K (a) adsorption and

(b) desorption. (Reproduced with permission from the American Chemical Society.)

24.11 Applied Electric Field and Hydrogen Adsorption

It has been proposed that an applied electric field may increase hydrogen adsorption. Density functional theory has been used to show that an applied electric field may improve the hydrogen storage properties of polarizable substrates. The adsorption of a layer of hydrogen molecules on several nanomaterials was investigated.[341]

The effect of an applied electric field on the hydrogen physisorption isotherm of platinum-supported carbon sorbents has shown that sorption enhancement was obtained by applying a positive electrical potential of 2000 V, and this was ascribed to stronger hydrogen–surface interactions. The interaction was van der Waal type between the σ-bonds of hydrogen and the π-bonds of the aromatic rings. However, the interaction between electrically charged carbon and hydrogen might involve stronger orbital interactions between hydrogen and carbon.[342]

The synthesis of porous materials for hydrogen adsorption and desorption with capacities at cryogenic temperatures that meet the US DOE targets has recently been the focus of a great deal of research. Several groups have reported experimental measurements showing

maximum excess adsorption of ~6.5 to 8.6 wt% of hydrogen at 77 K and < 100 bar on MOF (MOF-200, MOF-210, NOTT-112),[57,59] polymers (PAF-1),[97] and various porous carbon materials.[168,169] It is apparent that similar adsorption uptakes are observed for the best performing porous materials. Total hydrogen uptakes for MOF-200 (16.3 wt%), MOF-210(17.6 wt%),[57] NOTT-112(10 wt%),[59] and UMCM-2(12.4 wt%)[232] at 80 bar have been observed at 77 K.[57] However, for storage applications, hydrogen capacity on a volume basis is more important. The materials with highest adsorption capacities on a volumetric basis are PCN-14(55 g L^{-1}) and NOTT-112 (54 g L^{-1}).[57,59,241]

Hydrogen maximum surface excess capacity (wt%) and BET N_2 surface area at 77 K have a strong correlation for a wide range of porous materials. Similar correlations are observed for all porous materials for maximum surface excess hydrogen adsorbed with other pore structure characterization parameters, such as pore volume. However, when the hydrogen maximum excess adsorption is expressed on a volumetric basis for the adsorbent, the correlations are much less clear for surface areas >2000 $m^2 g^{-1}$. Hydrogen adsorbate can be considered as an incompressible fluid with a density similar to liquid hydrogen, and the maximum surface excess adsorbed is limited by the available total pore volume of the adsorbent. The amounts of hydrogen adsorbed on a wide range of porous materials under high pressure and ambient temperature conditions are small (less than ~1 wt%).

The maximum enthalpies of hydrogen adsorption obtained experimentally over the temperature range of 77–87 K are MOFs (12–13.5 kJ mol^{-1}), boron-doped carbon (20 kJ mol^{-1}), carbons (20 kJ mol^{-1}), polymers (9 kJ mol^{-1}), and zeolites (18 kJ mol^{-1}). However, most reports have isosteric enthalpy adsorption measurements <13 kJ mol^{-1} (see Table 24.2). Currently, the highest isosteric enthalpies of hydrogen adsorption for MOFs have been observed for $Zn_3(bdc)_3 \cdot Cu(Pyen)$,[52] $Ni_2(dhtp)$,[223] and $[Cd_5(Tz)_9](NO_3)_3$.[281] These materials have open metal centers. The thermodynamic results and structural and spectroscopic observations of H_2 adsorbed in pores with open metal centers in MOFs show that the interactions observed so far are much weaker than those observed for η^2–H_2 bonding in Kubas compounds. Higher enthalpies of adsorption probably in the range of 20–40 kJ mol^{-1} are required for increased adsorption for storage applications at temperatures higher than 77 K.

Adsorption of hydrogen on porous materials is currently limited to cryogenic temperatures (77 K), and this limits the use of the technique in real practical transport application situations. The design of porous materials with enhanced adsorption capacity under ambient conditions involves increasing hydrogen–surface interactions. The stability of η^2-type hydrogen–metal complexes suggests that, in principle, unsaturated metal centers in MOFs may act as sites for η^2-type hydrogen coordination and this is potential development route for materials with enhanced hydrogen–surface interactions. Also, the doping of Kubas compounds into porous materials is also a possible option. The effect of confinement in pores on hydrogen–metal interactions is less clear. Structural studies of Kubas (η^2–H_2) coordination compounds provide evidence for a wide variation in H_2 interaction strength with metals. This suggests that modification of the hydrogen–metal interaction can be achieved by varying the metal, ligand, and ligand substitution in MOFs. The ability to fine-tune the hydrogen–metal specific interactions involving weak nondissociative chemisorption rather than nonspecific physisorption is important. However, open metal centers only rep- resent a small fraction of the internal surface area of MOFs. Coordination of multiple H_2 molecules per unsaturated metal is necessary for storage applications. However, only a few stable solid bis-H_2 organometallic complexes are known.[258,259] Multiple coordination of H_2 to copper centers has been proposed for $Zn_3(bdc)_3 \cdot Cu(Pyen)$ based on the variation in enthalpy of adsorption with surface coverage. Interaction of H_2 molecules with both sides

of copper in the Cu(Pyen) pillar increases the influence of open metal centers.[52] However, confinement in pores may influence the primary H_2 interactions with open metal sites by interactions from other pore surfaces. Secondary interactions influence framework flexibility and window opening in MOFs, which control hysteretic adsorption characteristics, and these may also be useful in the design strategies for storage applications. An improved understanding of surface chemistry and framework flexibility will lead to porous materials with improved hydrogen adsorption characteristics for storage applications under high pressure and ambient temperature conditions.

8. Conclusion

25

Hydrogen Storage in Hollow Microspheres

Laurent Pilon
University of California, Los Angeles

CONTENTS

25.1 Introduction 764
25.1.1 Hydrogen Storage Technologies 764
25.1.2 Hydrogen Storage in Hollow Glass Microspheres 765
25.2 Design Parameters for Hydrogen Storage in Hollow Microspheres 769
25.2.1 Principles 769
25.2.2 Hydrogen Properties 769
25.2.2.1 Density 769
25.2.2.2 Compressibility Factor 771
25.2.3 Burst Pressure 771
25.2.4 Buckling Pressure 773
25.2.5 Hydrogen Permeation Processes 773
25.2.6 Geometric Considerations 774
25.2.7 Material Considerations 775
25.2.7.1 Mechanical and Thermal Properties 776
25.2.7.2 Hydrogen Permeability 776
25.2.7.3 Hydrogen Diffusion Coefficient and Solubility in Glass 779
25.2.7.4 Optical Properties 780
25.3 Performance Assessment 781
25.3.1 Gravimetric and Volumetric Energy Densities 781
25.3.2 Loading and Unloading Times 784

25.3.3 Filling and Discharging Energy Requirements 786
25.4 Experiments 789
25.5 Synthesis of Hollow Glass Microspheres 791
25.5.1 Hollow Microspheres in Fly Ash 791
25.5.2 Spray Pyrolysis Process 791
25.5.2.1 Blowing Process 792
25.5.2.2 Semiproduct Production 792
25.5.3 Liquid-Droplet Method 794
25.5.4 Hollow Glass Microspheres by Solgel Process 795
25.5.5 Hollow Silica Aerogel Spheres 795
25.5.6 Porous Wall Glass Hollow Microspheres 796
25.5.7 Surface Treatment and Additional Functionality 797
25.5.8 Other Materials and Shapes 798
25.6 Conclusions and Perspectives 799
Nomenclature 800
References 801

25.1 Introduction

The element hydrogen is the most commonly found element in the universe. However, hydrogen molecules (H_2) are not readily available. As such, it is an energy carrier as opposed to a fuel. It can be used in various mobile applications such as (1) in proton exchange membrane (PEM) fuel cell for transportation systems or mobile devices (e.g., laptops and cell phones) where it catalytically reacts with oxygen to produce water and electricity, (2) in internal combustion engines for surface transportation where it can be mixed with liquid fuel [1,2], or (3) in rocket propulsion [3]. Akunets et al. [2] also suggested using a mixture of liquid oxygen and hydrogen in polymer microballoons for jet engine fuel [2].

Hydrogen storage for such mobile applications is arguably one of the main technological challenges for a viable hydrogen economy. This chapter focuses on hydrogen storage in hollow glass microspheres or microcapsules in general. First, various power sources and fuels for mobile applications are compared based on their energy densities. Then, competing hydrogen storage technologies are reviewed. Moreover, principles, design parameters, material considerations, and performances associated with hydrogen storage in hollow glass microspheres are discussed in detail. Processes for synthesizing hollow glass microspheres are also reviewed.

25.1.1 Hydrogen Storage Technologies

In order to compare different fuels and energy carriers as well as hydrogen storage solutions, it is useful to remember that (1) energy contained in 1 kg of hydrogen is equivalent to that in 1 gal (3.78 L) of gasoline and that (2) current gasoline or diesel tanks contain between 10 and 30 gal. However, fuel cells are more efficient than internal combustion engines, thus reducing the required amount of hydrogen on board to 5–8 kg. In addition, a midsize fuel cell car cruising at 100 km/h (62 mph) consumes about 400 mg of H_2/s, which needs to be delivered on demand [4].

The US Department of Energy (DOE) has developed a technology roadmap for hydrogen storage. It sets quantitative targets that would ensure vehicle autonomy greater than 300 miles as well as safe and flexible driving, fast refueling time, procedure, and retail sales comparable to existing ones [5]. The technical criteria for selecting a specific hydrogen storage technology for transportation applications and the associated 2015 US DOE targets have been identified as follows [5]:

1. *Safe operation under all circumstances* including road accidents since hydrogen reacts explosively with oxygen above the ignition temperature of 450°C at atmospheric pressure
2. *Large gravimetric energy density* defined as the mass of H_2 (or energy) stored per unit mass of storage systems, which should be larger than 9 wt.% or 10.8 MJ/kg
3. *Large volumetric energy density* defined as the mass of H_2 or energy stored per unit volume of storage systems, which should be larger 81 g of H_2/L or 9.72 MJ/L
4. *Refueling time* of hydrogen tanks as short as refueling with current fuels such as diesel or gasoline (2.5 min for 5 kg of H_2)
5. *Reversibility of uptake and release* so that the storage system can be used numerous times (1500 cycles from 1/4 to full) for reliability and cost-effectiveness

6. On-demand availability with a minimum mass flow rate of 0.02 g/s/kW
7. Operating temperatures between −40°C and 60°C to work in any weather conditions
8. *Low energy requirements* for loading and unloading H_2 in order to achieve maxi- mum energy efficiency
9. *Safe dormancy properties*, that is, at room temperature, very little hydrogen should leak out from the storage solution making the storage safe while not in use for extended periods of time
10. Low fabrication and operation costs for a pretax cost of $2/kW/h

Gaseous hydrogen at room temperature without its storage tank has gravimetric energy density of 143 MJ/kg and therefore exceeds by far DOE's target. Unfortunately, gaseous hydrogen at standard temperature and pressure has volumetric energy density of 0.01079 MJ/L. Such a very low value requires that hydrogen be compressed drastically. Numerous techniques have been proposed and can be grouped as (1) compressed hydrogen gas, (2) liquid hydro- gen, (3) cryoadsorption, and (4) [6–8]. High-pressure H_2 storage solutions at room temperature include gas cylinders, underground reservoirs, and hollow glass microspheres [9–11]. Hydrogen can also be stored in liquid phase at cryogenic temperatures ($\leq$20 K). Low-temperature cryoad- sorption of hydrogen is achieved in (1) carbon nanotubes [12], (2) activated carbon [13], (3) carbon aerogels [13], (4) metal-organic framework [14], and (5) zeolite. Chemical hydrogen storage includes (1) metal hydrides [8,15], (2) liquid (organic) hydrides, and (3) ammonia and methanol. Unfortunately, none of the current technologies meet the aforementioned 2015 performance and cost targets set by the US DOE by a wide margin [16,17].

As an energy carrier for transportation systems and portable applications, hydrogen storage performances should be compared with other fuels or power systems including (1) liquid fuels (e.g., gasoline, diesel, biodiesel, ethanol, and methanol), (2) batteries (e.g., lithium ion, fluoride ions, and zinc–air) used in hybrid and all-electric cars, (3) solid fuel (e.g., Al, Zn, and Li) used in rocket propulsion, (4) compressed or liquified natural gas already widely used for public transportation, and (5) compressed air. To do so, it is useful to define the gravimetric and volumetric energy densities representing the amount of energy stored in a system per unit mass or unit volume, respectively. Figure 25.1 plots the gravimetric versus volumetric energy densities for each fuel or energy storage technologies and the associated container as reported in the literature [11,18]. It is evident that gasoline or diesel or biodiesel has outstanding performances that explain their widespread use. These performances are only matched by those of solid fuels, which cannot be consid- ered for surface transportation. Performances of battery technologies, however, remain an order of magnitude smaller than liquid fuels.

Figure 25.2 also compares the best reported performances of the various hydrogen storage technologies [8,11]. It is evident that metal hydrides offer large volumetric energy density but relatively low gravimetric density. Liquid H_2 storage at 20 K and atmospheric pressure as well as cryoadsorption and cryocompressed storages show good performance but require large energy for liquefaction (27.9% of the stored energy [8]). They also feature poor dormancy properties.

25.1.2 Hydrogen Storage in Hollow Glass Microspheres

As previously discussed, the volumetric energy density of gaseous hydrogen at room temperature is very small and falls short of the DOE targets [5]. One strategy to increase its

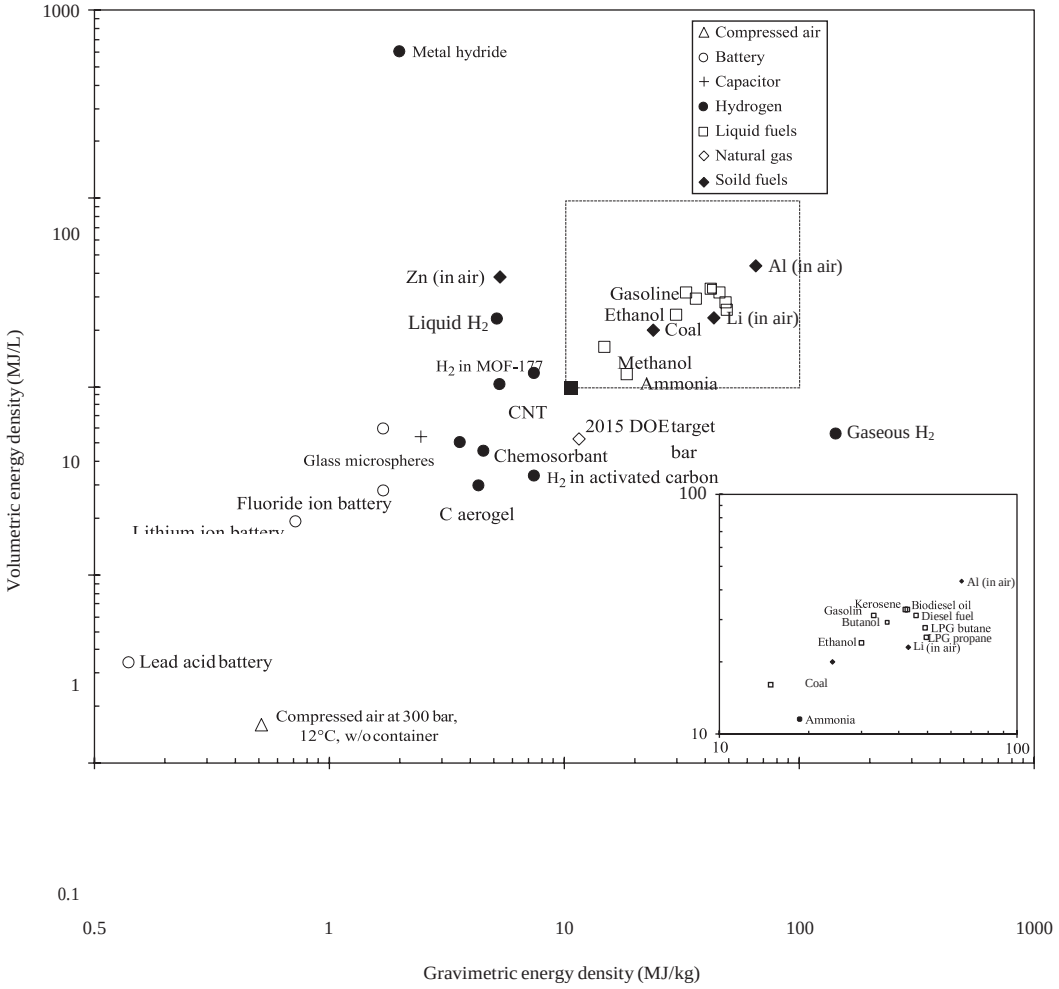


FIGURE 25.1

Comparison of gravimetric and volumetric energy densities for different fuels and hydrogen storage technolo- gies. (From Yartys, V.A. and Lototsky, M.V., An overview of hydrogen storage methods, in *Hydrogen Materials Science and Chemistry of Carbon Nanomaterials*, Veziroglu, T.N., Zaginaichenko, S.Y., Schur, D.V., Baranowski, B., Shpak, A.P., Skorokhod, V.V., and Kale, A., eds., Kluwer Academic Publishers, Dordrecht, the Netherlands; Herr, M. and Lercher, J.A., Hydrogen storage in microspheres—Final report, ET-TN-03-628, September 9, 2003; Teitel, R.J., Microcavity hydrogen storage final progress report, Prepared for US Department of Energy and Environment, Report BNL 51439, 1981.)

volumetric energy density is to compress H_2 inside hollow glass microspheres or microcapsules in general. Loading and unloading of hydrogen gas in and out is based on the fact that gas permeation through the solid shell is a thermally activated process, that is, gas permeation increases exponentially with temperature. Hollow microspheres are also called microcapsules, microcavities, microbubbles, or microballoons. This was first proposed by Teitel in 1980 [9,10]. The initial thought was to use it in combination with a metal hydride storage system designed to store hydrogen released by hollow glass microspheres during cooldown and able to provide hydrogen during cold starts and accelerations. Moreover, "the addition of a metal hydride to the system would increase its hydrogen volumetric energy density and reduce the gravimetric energy density" [9]. Since then, hollow glass microspheres have been considered as stand-alone H_2 storage solutions [19]. Geometries other than microspheres have

also been considered including microcylinders [4,20] and foams [21].

Figure 25.3 illustrates the typical life cycle of hollow microspheres for H_2 storage including (1) hydrogen loading, (2) storage and distribution, (3) onboard H_2 unloading,

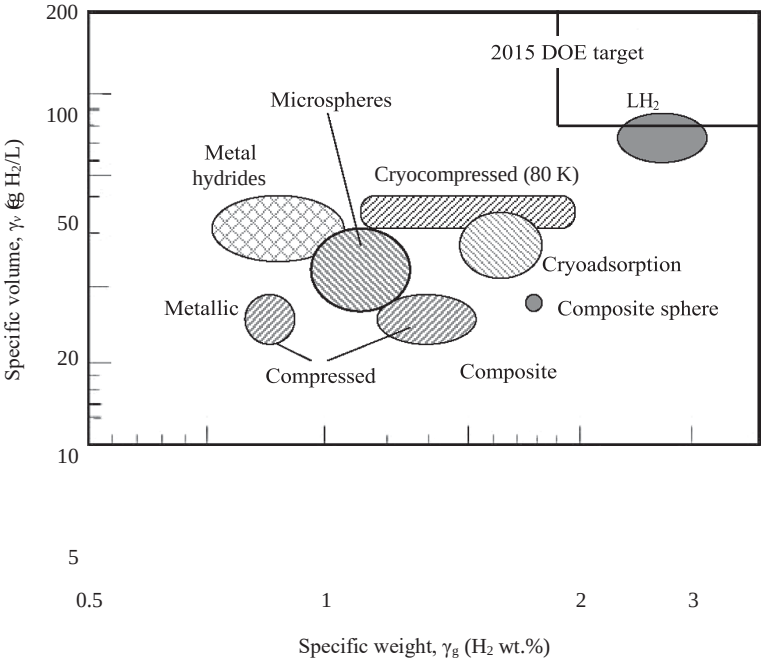
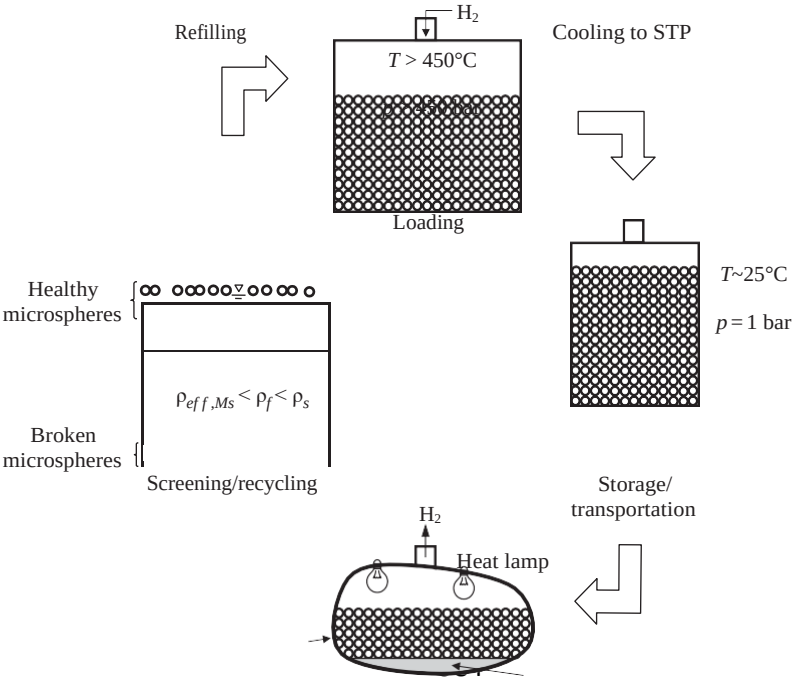


FIGURE 25.2

Comparison of gravimetric and volumetric energy densities for hydrogen storage technologies. (From Herr, M. and Lercher, J.A., Hydrogen storage in microspheres—Final report, ET-TN-03-628, September 9, 2003.)



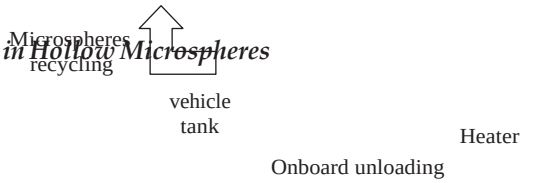


FIGURE 25.3

Life cycle of hollow microspheres from hydrogen loading and microsphere storage to vehicle refueling and microsphere recycling.

and (4) screening and recycling of healthy microcapsules. Practically, hydrogen loading in hollow microspheres can be performed at industrial scale in a batch process off vehicle in an autoclave at high temperatures (≈400°C) and pressures (>450 bar) to accelerate hydrogen permeation through the container's shell. Then, the hollow micro- spheres are cooled to room temperature so that hydrogen gas remains trapped inside due to significant reduction in the H_2 permeation with decreasing temperature (see Section 25.2.7.2). The hollow microspheres, then, can be safely transported to distri- bution points at room temperature and atmospheric pressure. Hydrogen refueling of a vehicle would consist of sucking the spent microspheres out of the tank and pour- ing loaded ones in the tank in a manner very similar to current gasoline or diesel refueling. On-demand hydrogen release from the microspheres would be induced by an onboard electric heater or a heat lamp integrated in the tank. Alternatively, unload- ing could also be achieved by mechanically or thermally destroying the microspheres, thus releasing their H_2 content. This strategy would still require removing the broken microspheres before tank refueling to be remelted or discarded. However, small pieces of broken microspheres could constitute a health hazard [22]. Empty microspheres removed from the tank would be screened for cracks and sorted by size and recycled to undergo the same sequence of H_2 loading, distribution, and unloading. Separation of broken microspheres from reusable ones can be achieved by the sink–float method [23,24]. This consists of placing all microspheres in a fluid whose density ρ_f is smaller than that of the shell materials ρ_s but larger than the effective density of the micro- spheres ρ_{MS}, that is, $\rho_{MS} < \rho_f < \rho_s$. Thus, pieces of broken microspheres will sink while *healthy* microspheres will float.

Hydrogen storage in hollow glass microspheres presents the following advantages over the previously reviewed storage technologies. First, hollow microspheres have high gravimetric energy density [11]. Hydrogen can be stored under internal pressure higher than that inside conventional cylinders [11]. Hydrogen-filled hollow glass micro- spheres are also easy and safe to handle at atmospheric pressure and ambient tempera- ture and can be poured or pumped in tanks of any arbitrary geometries and made of lightweight materials (e.g., plastic) [11,19]. The technology is inexpensive and requires low energy consumption for producing large quantities of microcontainers [7]. In addi- tion, this technology has good dormancy characteristics [7]. It is also resistant to con- tamination by atmospheric gases, unlike metal hydrides. Similarly, the microspheres are expected to remain stable and intrinsically safe under accident or fire conditions thanks to the small volume of hydrogen stored in each microspheres and their con- formation or ability of the bed to change shape caused by potential deformation of the outside container [7,19,25]. Finally, the technical risks are minimal [7] and scaling from benchtop to full-scale utilization appears to be straightforward as hollow microspheres are already produced at industrial scale albeit for other applications and without the desired mechanical properties required for H_2 storage [26,27].

The challenges of hydrogen storage in microcontainers are [11,28] (1) the low vol- umetric energy density, (2) the relatively low fraction of recoverable hydrogen [29], (3) the fact that one needs to heat the microcapsules at temperatures above the operating temperature of PEM fuel cells, (4) the small H_2 release rate, (5) the large amount of energy required to compress hydrogen to very high pressures used during H_2 loading (25% of storage energy [8]), and (6) the cost of disposing or recycling glass microspheres. Table 25.1 summarizes the different advantages and disadvantages of hydrogen storage in microcapsules.

TABLE 25.1

Established and Potential Advantages and Disadvantages Associated with Current Hydrogen Storage in Hollow Microcapsules

Advantages	Disadvantages
High gravimetric energy density	Low volumetric energy density
Handling at room temperature and atmospheric pressure	Requires hydrogen loading under very high pressures
Inexpensive and high-throughput manufacturing process	Requires heating for loading or unloading
Intrinsically safe	Potentially high loading energy cost
Good dormancy characteristics	Requires reprocessing of spent microcapsules
Resistant to contamination/poisoning by atmospheric gases	Potential health hazard from broken microcapsules
Can be poured and fit in any container solution	Uncertain consumer acceptance of refueling conditions
Easily scalable from lab to industrial scale	Large uncertainty in achieving desired performances
Minor technical risks	

Source: Robinson, S.L. and Handrock, J.L., Hydrogen storage for vehicular applications: Technology status and key development areas, Sandia National Laboratory Report SAND94-8229-UC-406, 1994.

25.2 *Design Parameters for Hydrogen Storage in Hollow Microspheres*

25.2.1 Principles

The amount of hydrogen gas stored inside a capsule and its permeation rate depends on the inner and outer pressures, the temperature, and the shell material and thick- ness. To achieve the maximum storage capacity, pressure inside the microcapsules should be as large as possible. Similarly, for fast H_2 release, the outside pressure should be reduced and the temperature increased while the shell should be as thin as possible. However, the operating temperatures and pressures during loading and unloading and the handling of the hollow microcontainers should not threaten their mechanical integrity. The shell material should have the proper permeation properties but also the mechanical properties able to stand large pressures and temperatures as well as the thermal cycling associated with successive loading and unloading. Consequently, microcapsules' geometry and material as well as the operating temperatures and pres- sures must be optimized to minimize the loading and unloading times and to maxi- mize the energy densities, the permeation rate, the hold time, and the number of life cycles. To do so, concepts of burst and buckling pressures, gas permeation, as well as geometric and material considerations are reviewed.

25.2.2 Hydrogen Properties

25.2.2.1 Density

At temperatures and pressures of interest for hydrogen storage, gaseous hydrogen cannot be considered as an ideal gas. Instead, a more complex equation of state must be used to

account for repulsion forces between H_2 molecules. The Beattie–Bridgeman equation gives the hydrogen pressure P as a function of temperature T and density ρ [30]:

$$P = \rho^2 RT\left(1 - \frac{c\rho}{T^3}\right)\left[\frac{1}{\rho} + B_0(1 - b\rho)\right] - A_0\rho^2(1 - a\rho) \quad (25.1)$$

where

R is the ideal gas constant (=8.314 J/mol K) the pressure P is expressed in Pa

ρ is expressed in kg/m^3

T is expressed in K

the parameters a, b, and c are equal to -5.06×10^{-6} m^3/mol, -43.56×10^{-6} m^3/mol, and 5.04 m^3 K^3/mol, respectively

the coefficients A_0 and B_0 are equal to 0.02 Pa m^3/mol^2 and 20.96×10^{-6} m^3/mol, respectively [30]

Figure 25.4 compares the actual density of hydrogen ρ with that predicted by the ideal gas law $\rho = PM/RT$ for temperature and pressure ranging 48–398 K and 1–1000 bar (14.5–14,500 psi), respectively. It shows that H_2 deviates from ideal gas law for values of PM/RT larger than 10, that is, for low temperatures and/or high pressures.

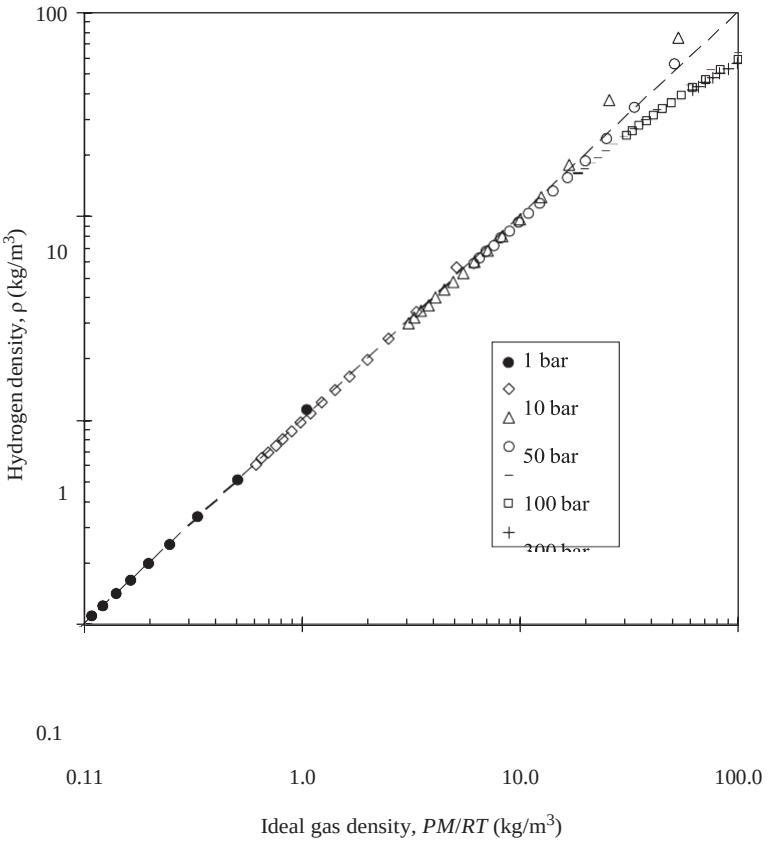


FIGURE 25.4

Actual hydrogen density versus ideal gas density ($\rho = PM/RT$) for pressure ranging from 1 to 1000 bar and temperatures between 48 and 398 K. (From Lemmon, E.W. et al., NIST reference fluid thermodynamic and trans- port properties database (REFPROP): Version 8.0, National Institute of Standards and Technology, Boulder, CO, http://www.nist.gov/srd/nist23.htm, 2007.)

25.2.2.2 Compressibility Factor

Alternative to the previous equation of state, one can define the compressibility factor as

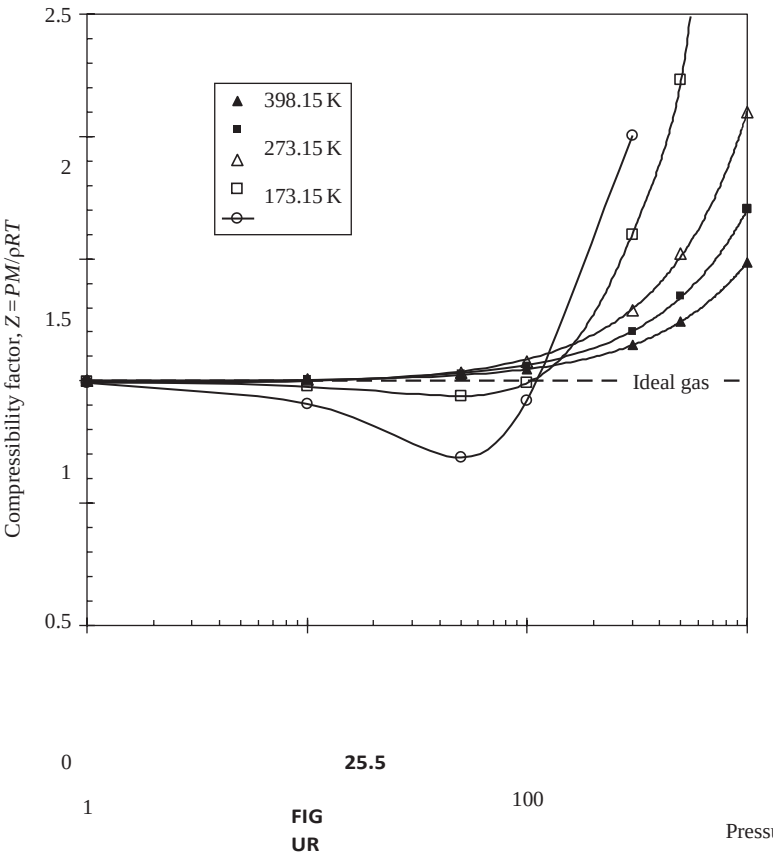
$$Z(T, P) = \frac{PM}{\rho RT} \tag{25.2}$$

Figure 25.5 shows the compressibility factor of hydrogen as a function of pressure P between 1 and 1000 bar for different values of temperature T between 48 and 398 K. Within this range, the compressibility factor $Z(T,P)$ of H_2 varies between 0.68 and 2.23. It is nearly equal to unity (ideal gas) for pressure less than 10 bar and temperatures larger than 48 K.

25.2.3 Burst Pressure

The volumetric energy density of hollow microspheres filled with hydrogen depends strongly on the differential pressure it can sustain. The maximum pressure of H_2 inside a hollow microsphere depends on the inner and outer radii denoted by r_i and r_o, respectively and on the biaxial tensile strength of the shell materials denoted by $\sigma_{s,max}$. For thin-walled microspheres (i.e., $r_o > 5(r_o - r_i)$), the burst pressure denoted by P_{max} is expressed as [31]

$$P_{max} = \frac{2\sigma_{s,max}(r_o - r_i)}{S_f r_0} \quad \text{for hollow microspheres} \tag{25.3}$$



25.5

FIG UR E

100 100

0

Compressibility factor of hydrogen as a function of pressure for temperature ranging from 48 to 398 K and pressure between 1 and 1000 bar. (From Lemmon, E.W. et al., NIST reference fluid thermodynamic and trans- port properties database (REFPROP): Version 8.0, National Institute of Standards and Technology, Boulder, CO, http://www.nist.gov/srd/nist23.htm, 2007.)

A safety factor S_f, typically ranging from 1.5 to 10, must also be considered for the actual design and fabrication of the storage system [32]. It is often taken as 1.5 for H_2 storage applications since the breaking of one microsphere does not endanger the integrity of the entire hydrogen storage solution [32]. Equation 25.3 indicates that the internal pressure increases as the tensile strength $\sigma_{s,max}$ and the shell thickness $(r_o - r_i)$ increase and as the outer radius r_o decreases.

For cylindrical thin-walled containers, the burst pressure is expressed as [31]

$$P_{max} = \frac{\sigma_{s,max}(r_o - r_i)}{S\, r_{f0}} \quad \text{for cylinders} \tag{25.4}$$

Here, $\sigma_{s,max}$ is the maximum strength in the radial direction also called hoop stress σ_h. For cylindrical geometry, a longitudinal stress σ_l exists but is only half the hoop (radial) stress, that is, $\sigma_l = \sigma_h/2$ [31]. It is evident from Equations 25.3 and 25.4 that hollow microspheres are, a priori, preferable to cylinders with the same inner and outer diameters as they can sustain burst pressures twice as large. However, synthesis of hollow microspheres is more challenging than microcylinders [4] (see Section 25.5).

Achieving large burst pressure first guided the search for the best shell materials that could stand large tensile stress. Teitel [9,10] suggested using glass for their outstanding mechanical properties under a wide range of temperatures. Indeed, the tensile strength of glasses is reported to be above 4 GPa and can reach up to 6.9 GPa for quartz (SiO_2) at room temperature compared with 460 MPa for steel [33,34]. Figure 25.6 shows the burst pressure predicted by Equation 25.3 for thin-walled microspheres as a function of radii ratio r_o/r_i

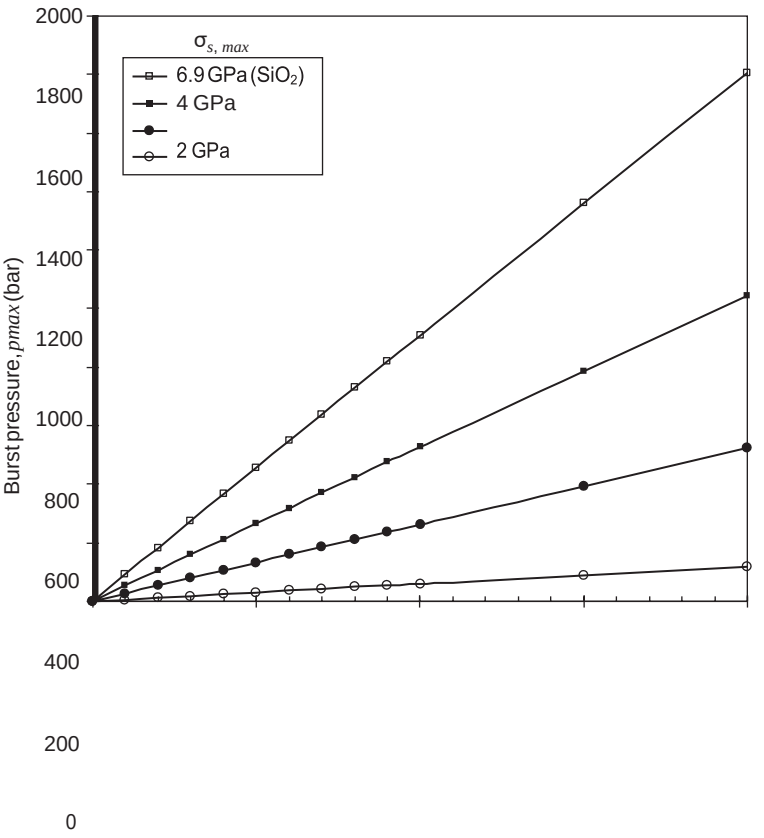


FIGURE 25.6

Burst pressure of thin-walled microspheres predicted by Equation 25.3 for different values of tensile strength $\sigma_{s,max}$ and S_f = 1.5. Burst pressure for cylinders with the same r_o/r_i ratio is half of that shown.

for tensile strength σ_{max} varying from 460 MPa (steel) to 6.9 GPa (quartz) and safety factor equal to 1.5. The radii ratio r_o/r_i is kept smaller than 1.02, beyond which Equation 25.3 is no longer valid [31].

For either microspheres or microcylinders, the absence of defects in the sphere membrane (or shell) and the close-to-perfect sphericity or cylindricity are essential elements in order to achieve large burst pressure. Imperfection may exist and scratches can appear at the surface of the microcapsules during manufacturing and handling, which can result in decrease in the tensile strength [35]. To prevent scratches from occurring, the microcapsule surface can be acid etched or coated with a hard coating material as discussed in Sections 25.4 and 25.5.7.

25.2.4 Buckling Pressure

During hydrogen loading, the external pressure should be controlled to prevent the microspheres from collapsing when the difference between inner and outer pressures exceeds the buckling pressure. The classical expression for the static buckling pres- sure P_{cr} for isotropic thin-walled and shallow spherical shell under uniform pressure is given by [36,37]

$$P_{cr} = \frac{2E_s(r_o - r_i)^2}{r_o^2\sqrt{3(1-\nu_s^2)}} \tag{25.5}$$

where E_s and ν_s are the Young's modulus and Poisson's ratio of the shell material, respectively. The previous expression provides an upper limit for the pressure under which the hollow microspheres can be exposed [27]. In general, thin-walled micro- spheres can stand very large buckling loads [36]. In addition, numerous studies have also investigated dynamic buckling and how it is affected by shell defects, nonspheric- ity, nonuniformity in shell thickness, as well as coaxial loads [37–39]. However, experi- mental study for hollow microspheres were found to be more reliable to estimate the buckling pressure [37,39].

Rambach and Hendricks [27] experimentally investigated the buckling pressure of silicate glass microspheres 45 μm in average diameter and wall thickness of 0.9 μm. The buckling pressure predicted by Equation 25.5 was 1172 bar (17,000 psi) using E_s = 62.0 GPa and ν_s = 0.22. Experimentally, however, more than 20% of the microspheres collapsed for loading pressures larger than 500 bar at room temperature. Failure rate exceeded 80% for external pressure larger than 800 bar. No significant failure occurs for external pressure smaller than 414 bar (6000 psi) at the loading temperature up to 350°C thus setting practical limits of operations.

25.2.5 Hydrogen Permeation Processes

Gas permeability refers to the steady flow rate of gas across a specimen per unit of differential pressure and per unit thickness [40]. It is denoted by K and expressed in mol/Pa m s. The mass transfer rate of hydrogen entrapped in a single microsphere is expressed as [29]

$$\frac{dm_i}{dt} = \pm \frac{4\pi r^2 MK(T)}{(r_o - r_i)}(P_o - P_i) \tag{25.6}$$

where P_i and P_o are the inner and outer pressures, respectively. The ± sign depends whether hydrogen is loaded (+) ($P_o > P_i$) or released (−) ($P_o < P_i$) from the microspheres. Here, changes in the surface area for diffusion were ignored, and the inner surface area $4\pi r_i^2$ was chosen since it is the smallest and therefore controls the hydrogen permeation [29]. The mass of H_2 contained inside the microspheres is given by [41,42]

$$m_i = \rho_i \frac{4\pi r_i^3}{3} = \frac{4\pi r_i^3}{3} \frac{P_i M}{Z(T, P_i)RT} \tag{25.7}$$

Similarly, for a single microcylinder, the mass transfer rate and the mass of H_2 entrapped are, respectively, expressed as

$$\frac{dm_i}{dt} = \pm \frac{2\pi r_i L M K(T)}{(r_o - r_i)} (P_o - P_i) \quad \text{and} \quad m_i = \frac{P_i M}{Z(T, P_i)RT} \pi r_i^2 L \tag{25.8}$$

where

L is the length of the cylinder
r_i and r_o are the inner and outer diameters, respectively

25.2.6 Geometric Considerations

Several geometric parameters should be optimized for hydrogen storage in microcapsules, namely, (1) the shape (spherical or cylindrical), (2) the inner and outer diameters r_i and r_o of the microspheres or microcylinders, (3) the shell thickness ($r_o - r_i$), and (4) the volume fraction or packing fraction of microcapsules in the storage tank, which depends on their size distribution. Each of these design parameters are discussed in the following sections.

25.2.6.1 Shape

Most studies have focused on hydrogen in hollow glass microspheres by virtue of the fact that microspheres have the highest burst pressure and smaller release time constant. In addition, glass was the material of choice for its high tensile strength and permeability. However, their synthesis can be more complex and costly than those of cylinders [4,20]. Yan et al. [20] manufactured hollow silica fibers with outer diameter ranging from 160 to 260 μm and wall thickness between 16 and 35 μm. The authors also discussed sealing and strengthening of the microcylinders (see Section 25.4)

25.2.6.2 Size

Commercially available hollow glass microspheres feature outer diameter between 5 and 500 μm and shell thickness between 0.5 and 20 μm [11]. Increasing the shell thickness increases the burst and buckling pressures and extends the hold time of the microspheres. However, it also reduces the volume available for hydrogen storage and the volumetric energy density while increasing the loading and unloading times. Thus, there exist an optimum values for outer and inner radii associated with operating temperature and pressure.

25.2.6.3 Packing Fraction

The maximum theoretical packing of monodisperse spheres is 74% corresponding to a body-centered (BCC) and face-centered (FCC) cubic face-centered arrangement as illustrated in Figure 25.7. However, this highly ordered arrangement is not achieved in practice

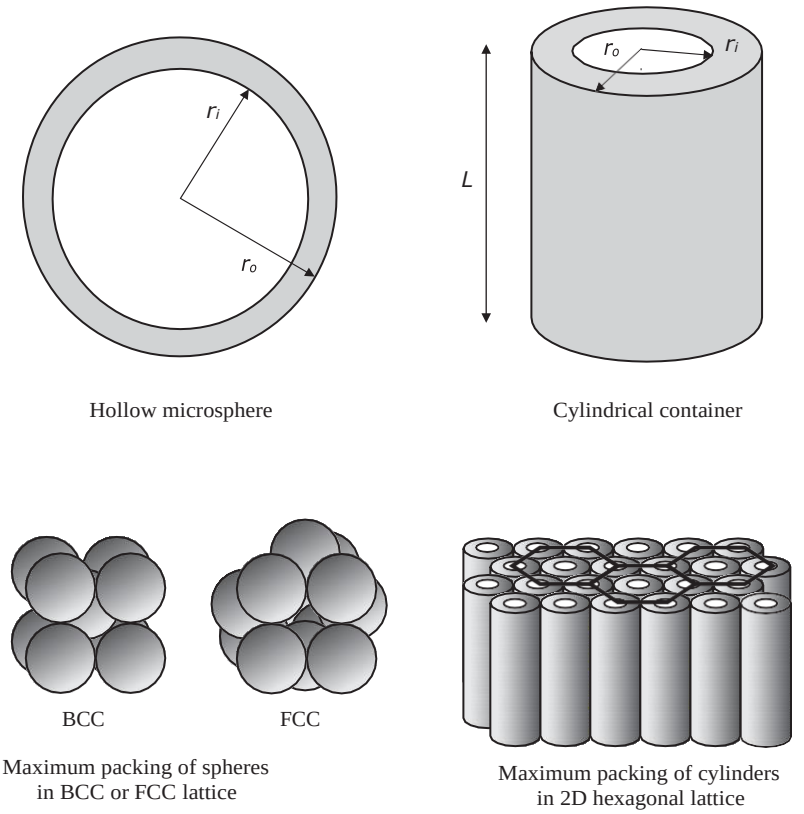


FIGURE 25.7

Schematic and dimensions of microspheres and microcylinders along with their spatial arrangement.

and maximum random packing of 63.7% is more realistic [43]. Larger packing can be achieved if polydisperse spheres are used [43], but this can also complicate the handling, sorting, and recycling of the microspheres [11] since the microsphere density will vary with size, which is incompatible with the sink–float method [23,24].

Further increase in packing fraction can be obtained if the spheres are deformed or if polymeric or glass foams are used [21,44]. Pientka et al. [44] showed that extruded polystyrene foams can be used for hydrogen separation from CO_2 and N_2 as well as for hydrogen storage. Metallic foams can stand larger pressure than polymeric foams but have much larger density and may become brittle when exposed to H_2. Banyay et al. [21] concluded that metallic foams meet the volumetric energy density DOE target but not the gravimetric one and vice versa for polymeric foams. The authors suggested that composite foams might satisfy both targets. In the case of closed-cell foams for H_2 storage, Equation 25.6 is not valid and modeling mass transfer through foams has been discussed in the literature [45].

Finally, the maximum packing fraction of monodisperse and aligned cylinders ordered in 2D hexagonal lattice is 90.7% [4], while it is 0.82–0.83 if they are randomly packed [46].

25.2.7 Material Considerations

The shell material is selected for its tensile strength and permeability as a function of

temperature along with the specific heat and optical properties depending on the heating process. These properties are reviewed in the following sections.

25.2.7.1 *Mechanical and Thermal Properties*

Mechanical and thermal properties of glass depend on compositions, sample history, and temperature. Glass is brittle and much stronger under compression than tensile loads [47,48]. Table t-mechanics provides of range of realistic values for $\sigma_{s,max}$, E_s, ν_s, ρ_s, k_s, and $c_{p,s}$ [47]. Note that tensile strength is significantly affected by surface imperfections or flaws [47–49]. Strength of glass decreases as temperature increases [49]. It is also size depen- dent and strength of glass fibers increases sharply as the fiber diameter decreases, for example [48]. Attempts to correlate glass strength and composition were typically unsuc- cessful [48] and experimental data showed very large variations mainly due to the fact that surface flaws determine the glass strength and are difficult to observe directly [49]. The ultimate tensile strength $\sigma_{s,max}$ is expressed as [49,50]

$$\sigma_{s,max} = \sqrt{\frac{E_s \alpha}{a}} \tag{25.9}$$

where

E_s is the shell material Young's modulus
a is the interatomic distance
α is the surface energy

For commercial oxide glass, a is not significantly affected by the compositions [50] and is of the order of 2×10^{-10} m [49,50] while α varies from 3.5 J/m^2 for soda-lime glass to 5.2 J/m^2 for vitreous silica [49]. Thus, the ultimate tensile strength is 16 GPa for soda-lime silicate and 24 GPa for vitreous silica, for example. These values are much higher (up to 60% for silica [49]) than experimental measurements due to the unavoidable presence of surface flaws [49,50]. Thus, experimentally measured values of $\sigma_{s,max}$ should be used in estimating the burst pressure from Equation 25.3 (Table 25.2).

25.2.7.2 *Hydrogen Permeability*

The first mechanism for hydrogen dissolution in glass consists of physical dissolution when H_2 molecules occupy the interstices of the glass. The second mechanism involves

TABLE 25.2

Summary of Mechanical and Thermal Properties of Glasses Considered for Hydrogen Storage

Property	Vitreous Silica	Soda-Lime Glass	Borosilicate Pyrex
$\sigma_{s,max}$ (GPa)	24	16	14
E_s (GPa)	72.9–77.2	70–72	64
ν_s (-)	0.165–0.177	0.25	0.2
ρ_s (kg/m^3)	2200	2520	2230
$c_{p,s}$ (J/kg K)	712	754	750
$k_{c,s}$ (W/m K)	1.46–1.71	1.2–1.78	1.2–1.78

Source: Bansal, N.P. and Doremus, R.H., *Handbook of Glass Properties*, Academic Press, Inc., Orlando, FL, 1986.

chemical reactions between H_2 and the glass resulting in the formation of OH groups. For example, hydrogen causes the reduction of variable-valence ions such as Fe^{3+}, Ce^{4+}, and Sn^{4+} [51]. In particular, Fe^{3+} can be reduced almost completely to Fe^{2+} according to the following reaction [51]:

$$H_2 + 2(\equiv Si - O)^- + 2Fe^{3+} = 2(\equiv Si - OH) + 2Fe^{2+} \quad (25.10)$$

The reaction rate is much faster than the diffusion rate. Thus, the process is diffusion limited and can be accounted for through standard mass diffusion model with some effective diffusion coefficient, permeability, and solubility [52]. Several empirical relationships for temperature dependence of gas permeability $K(T)$ have been suggested and are of the following general form:

$$K(T) = K_0 T^n \exp\left(\frac{-Q_K}{T}\right) \quad (25.11)$$

where K_0, n, and Q_K are constants determined empirically. Souers et al. [53] identified K_0 and Q_K while n was set equal to 1 as suggested by Doremus [54] and Shelby [40]. Alternatively, other researchers [2,4,29,42,55–59] used the standard Arrhenius law for which $n = 0$. The values of K_0 and Q_K are sometimes expressed in terms of (1) the content of glass network formers such as SiO_2, B_2O_3, and P_2O_5 denoted by G and expressed in mol.% or (2) the content of modifier oxide such as CaO, Na_2O, MgO, SrO, and NaO denoted by M. Table 25.3 summarizes values of K_0 and Q_K as reported in literature for vitreous silica, silicate, soda-lime, and borosilicate glasses [29,53,55–58,60,61]. In general, hydrogen permeability increases with G and decreases with M as suggested by the expressions for Q_K reported in Table 25.3. In addition, the permeability has been reported in different units such as molecules/cm s atm and mol/cm s when measured with 1 atm pressure difference across the sample. Thus, conversion was sometimes nec- essary to compare the different studies according to

$$K\,(\text{in mol/Pam s}) = \frac{100}{P_{atm} N_A} K\,(\text{in molecules/cm s atm}) = \frac{100}{P_{atm}} K\,(\text{in mol/cm s}) \quad (25.12)$$

where

N_A is the Avogadro number (=6.022 × 10^{23} molecules/mol)

P_{atm} is the atmospheric pressure (=1.013 × 10^5 Pa) or the pressure difference at which the measurements were performed

Note that H_2 permeability in glass can be considered to be independent of pressure up to 1000 bar [47]. Figure 25.8 shows the evolution of permeability as a function of temperature for the different glasses and references summarized in Table 25.3. It shows that H_2 permeability increases significantly with temperature and can vary widely with glass composition. It is also evident that permeability is systematically larger in vitreous silica or quartz than in glasses with other compositions.

TABLE 25.3

Empirical Constants for the Permeability of Various Glasses Used in Equation 25.11

Composition	n	$K_0 \times 10^{17}$ (mol/Pa m s)	Q_K(K)	References	Reported in
Soda-lime glass (72% ≤ G ≤ 100%)	0	8,100	17,330 − 127.8 G	[29]	mol/Pa m s
Silicate glasses	1	3.4 + 8 × 10^{-4} M^3	3,600 + 165 M	[53]	mol/Pa m s
Soda-lime glasses (M = 19%)	1	20	5,600	[53]	mol/Pa m s
Vitreous silica (see Ref. [40])	0	58.1	4,234	[55]	[a]
Vitreous silica (quartz)	0	8,688	4,469	[56]	molecules/cm s
Vitreous silica (quartz)	0	7,409	4,539	[57]	molecules/cm s
Pyrex (borosilicate) (D_2)	0	10.7	4,529	[58]	mol/cm s
Pyrex (borosilicate)	1	2.8	4,026	[60]	molecules/cm s atm
Pyrex (borosilicate) (D_2)	0	23.1	4,199	[61]	mol/cm s

[a] cc(STP)/s cm^2 area/mm thickness/cm Hg.

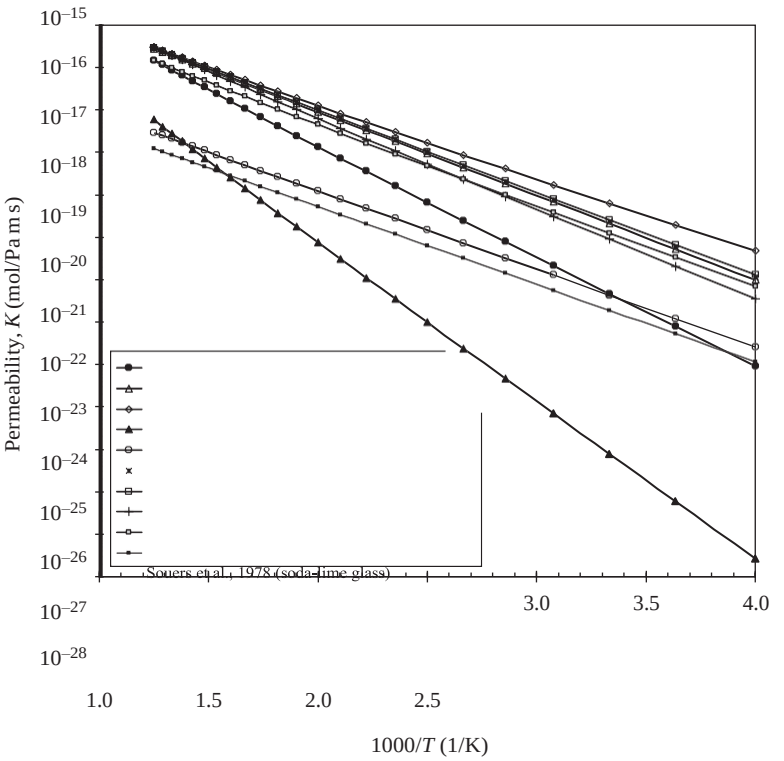


FIGURE 25.8
Hydrogen permeation through soda-lime, silicate, vitreous silica, and Pyrex as a function of 1000/T as reported in the literature and summarized in Table 25.3.

25.2.7.3 *Hydrogen Diffusion Coefficient and Solubility in Glass*

Diffusion coefficient $D(T)$ (in m²/s) and solubility $S(T,P)$ (in mol/m³ Pa) of hydrogen have also been reported in the literature for Pyrex [58,60], quartz [56–58], and silicate glass [59]. They are related to the permeability through [40]

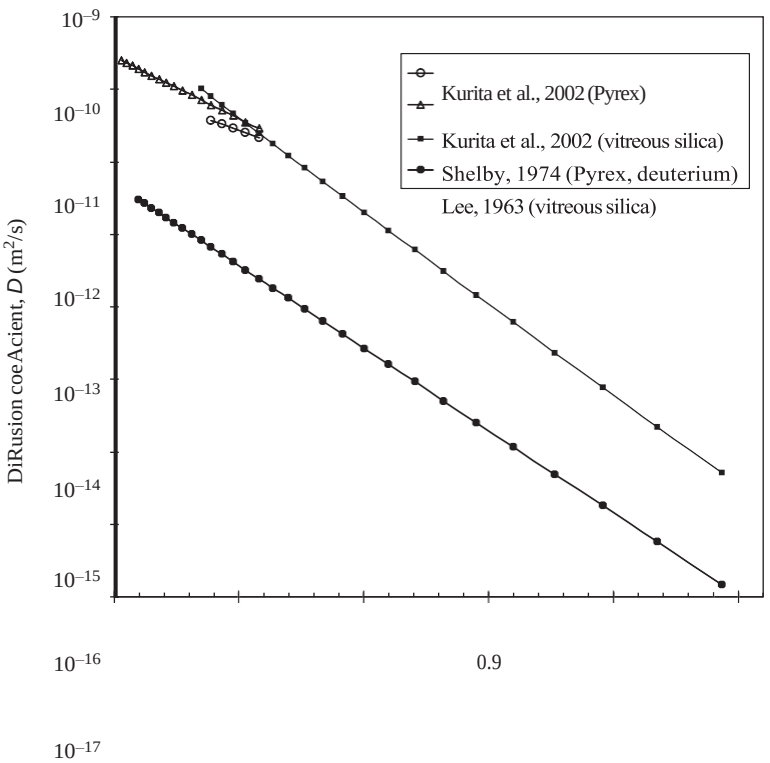
$$K(T) = D(T)S(T) \tag{25.13}$$

They can be assumed to be independent of pressure below 1000 bar [47]. To be consistent with Equations 25.11 and 25.13, diffusion coefficient and solubility are expressed as

$$D(T) = D_0 T^n \exp\left(\frac{-Q_D}{T}\right) \quad \text{in m}^2/\text{s} \tag{25.14}$$

$$S(T, P) = \frac{K(T, P)}{D(T)} = S_0 \exp\left(\frac{Q_S}{T}\right) \quad \text{in mol/Pam}^3 \tag{25.15}$$

where D_0, Q_D, S_0, and Q_S are empirical constants such that $K_0 = D_0 S_0$ and $Q_K = Q_D - Q_S$. Figure 25.9 shows the diffusion coefficient of vitreous silica and borosilicate Pyrex as a function of temperature as reported in the literature [40,57,61] and summarized in Table 25.4.



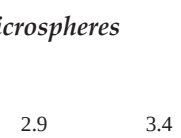


FIGURE 25.9

Hydrogen diffusion coefficient through vitreous silica and borosilicate Pyrex as a function of 1000/T as reported in the literature [40,57,61] and summarized in Table 25.3.

TABLE 25.4

Empirical Constants for the Permeability of Various Glasses Used in Equation 25.14

Composition	n	$D_0 \times 10^{10}$ (m^2/s)	Q_D (K)	References	Gas
Vitreous silica	0	5.65	5237	[57]	H_2
Pyrex 7740	1	1.06	5385	[60]	D_2
Borosilicate Pyrex	0	14.0	2820	[61]	H_2
Vitreous silica	0	96.0	3928	[61]	H_2

Recently, Shelby et al. [62–65] presented experimental study of what they called *photo-induced hydrogen outgassing* from borosilicate glass doped with various metal oxides especially Fe_3O_4. The authors observed that [62–65] (1) hydrogen release from a slab of doped borosilicate glass placed in a vitreous silica tube was accelerated when exposed to an incandescent heating lamp compared with heating in a furnace at 400°C, (2) the onset of outgassing was observed immediately with lamp heating but was slower for furnace heating, (3) increasing the lamp intensity accelerated the H_2 release rate and the over- all H_2 released from the sample, (4) borosilicate glass CGW 7070 demonstrated the best H_2 release response, and (5) increasing the Fe_3O_4 doping level increases the H_2 release rate. The authors suggested that "infrared radiation is contributing the activation energy necessary for hydrogen diffusion." To the best of our knowledge, this would constitute a new physical phenomenon [66]. It remains unclear, however, how the total irradiance and the spectral nature of radiation would be accounted for in an Arrhenius type of rela- tion for the diffusion coefficient or permeability. Moreover, the reported experimental data do not isolate the proposed mechanism from the well-known thermally activated gas diffusion. In fact, Kitamura and Pilon [67] numerically showed that the experimental observations can be qualitatively explained based on conventional thermally activated gas diffusion and by carefully accounting for the participation of the silica tube to radia- tion transfer along with the spectral properties of the silica tube and the glass samples. In brief, the radiation emitted by the incandescent lamp has a peak emission between 1 and 2 μm and reaches directly the sample since the silica tube is nearly transparent up to 3.5 μm. On the contrary, for furnace heating at 400°C, the silica tube absorbs a large fraction of the incident radiation, which reduces the heating rate and the H_2 release rate. However, between 0.8 and 3.2 μm, undoped borosilicate does not absorb signifi- cantly. Coincidentally, Fe_3O_4 doping increases the absorption coefficient and also reacts with H_2 to form ferrous ions, which increase the absorption coefficient of the sample by two orders of magnitude. Thus, doped and reacted samples heat up much faster when exposed to the heating lamp resulting in the observed faster response time and larger H_2 release rate.

25.2.7.4 *Optical Properties*

In the case when heating of microcapsules is achieved by infrared lamp heating, the optical properties of the glass shell are essential to predict the heating rate and the tem- perature on which hydrogen permeability depends. Optical properties of fused quartz (vitreous silica) from ultraviolet to infrared at room temperature have been reviewed by

Kitamura et al. [68]. Those of soda-lime silicate glass can be found in Ref. [69] while De Sousa Meneses et al. [70] reported the optical properties of borosilicate glass at room temperature over the spectral range beyond 4.0 μm.

As a first-order approximation, one can assume that glass optical properties do not change significantly with temperature (see Ref. [69], Fig. 2). However, they may change with ions doping and due to reaction with hydrogen. For example, in soda-lime silicate glass, Johnston and Chelko [51] established that reduction of Fe^{3+} by H_2 into Fe^{2+} results in significant increase in the absorptance of the glass sample in the spectral range from 0.4 to 2.5 μm. The changes were apparent with the unaided eye. Similarly, Shelby and Vitko [71] observed (1) an increase in absorptance beyond 0.8 μm and (2) a reduction in absorptance between 0.4 and 0.8 μm for soda-lime silicate. Rapp [65] confirmed Shelby and Vitko's results for Fe_3O_4-doped borosilicate glass showing an increase in the Fe^{2+}/Fe^{3+} ratio as the duration of exposure to hydrogen gas increases [64]. This was attributed to the fact that the absorption band around 380 nm corresponds to the ferric state (Fe^{3+}) while a peak around 1.1 μm corresponds to the ferrous state Fe^{2+}. In addition, the formation of OH groups results in a strong absorption band at wavelengths around 2.73–2.85, 3.5, and 4.5 μm [64,72,73]. The refractive and absorption indices of vitreous silica and borosilicate glass used in this study are presented in Figure 25.10.

25.3 Performance Assessment

Several parameters are useful in assessing and comparing the performances of hydrogen storage solutions including hollow glass microspheres. Parameters of particular interest are (1) gravimetric and volumetric energy densities, (2) loading and unloading times, as well as (3) the energy required to store the hydrogen gas.

25.3.1 Gravimetric and Volumetric Energy Densities

The gravimetric energy density η_g of a bed of monodisperse hollow microspheres is expressed in MJ/kg and given by

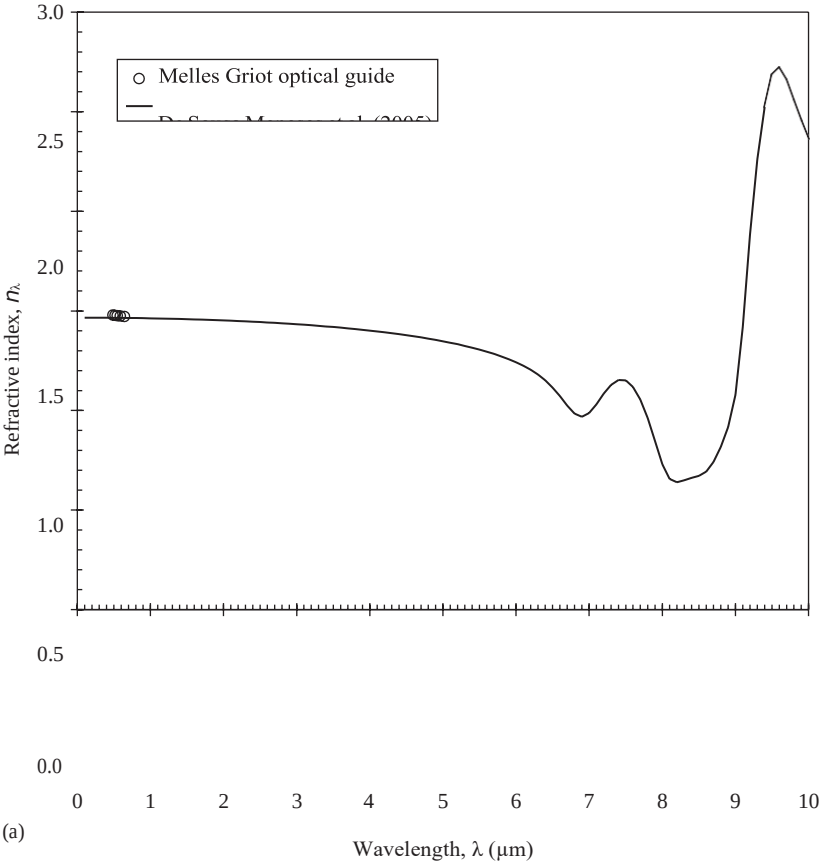
$$\eta_g = \frac{N_T m_{H_2} \Delta H_L}{N_T (m_s + m_{H_2})} = \frac{\rho r_i^3 \Delta H_L}{\rho r_i^3 + \rho_s (r^3 - r_i^3)} \tag{25.16}$$

where

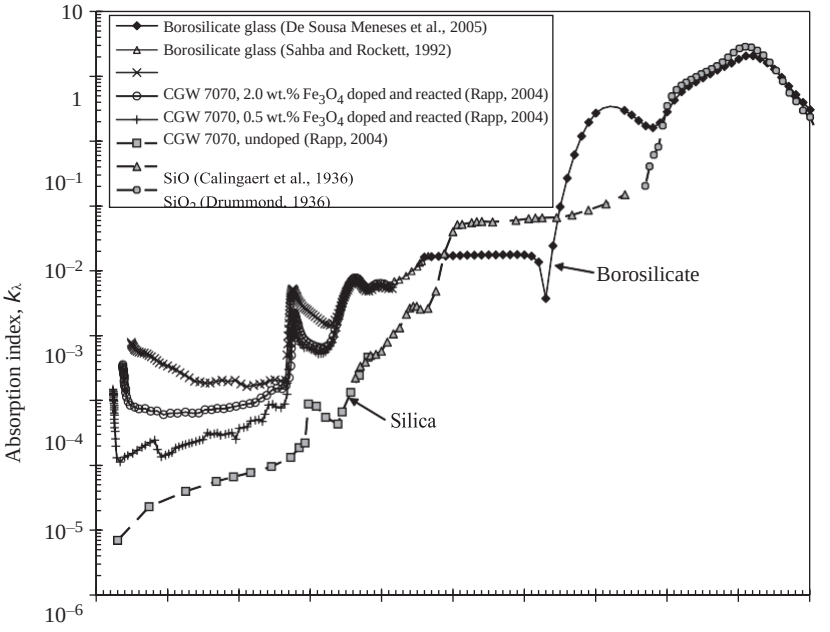
N_T is the total number of microspheres in the container

m_s and m_{H_2} are the mass of the solid shell and of the entrapped H_2 in a single microsphere

The densities of H_2 and of the glass shell are denoted by ρ and ρ_s. The lower heating value (LHV) denoted by ΔH_L represents the amount of heat released from combusting a unit mass of H_2 at 25°C and returning the combusting products (H_2O) to 150°C. It is equal to 120 MJ/kg, which exceeds that of all conventional fuels including gasoline (42 MJ/kg), ethanol (27 MJ/kg), natural gas (47 MJ/kg), and coal (23 MJ/kg) [8]. Note that the mass of the container is not considered here since it can be a lightweight plastic whose mass is negligible compared with that of the microspheres.


Melles Griot optical guide
Refractive index, n_λ
Wavelength, λ (μm)
3.0
2.5
2.0
1.5
1.0
0.5
0.0
0
1
2
3
4
5
6
7
8
9
10

(a)


Borosilicate glass (De Sousa Meneses et al., 2005)
Borosilicate glass (Sahba and Rockett, 1992)
CGW 7070, 2.0 wt.% Fe_3O_4 doped and reacted (Rapp, 2004)
CGW 7070, 0.5 wt.% Fe_3O_4 doped and reacted (Rapp, 2004)
CGW 7070, undoped (Rapp, 2004)
SiO (Calingaert et al., 1936)
SiO_2 (Drummond, 1936)
Borosilicate
Silica
Absorption index, k_λ
10
1
10^{-1}
10^{-2}
10^{-3}
10^{-4}
10^{-5}
10^{-6}

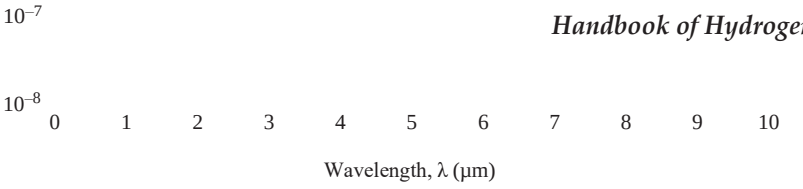


FIGURE 25.10

The (a) refractive and (b) absorption indices of undoped and Fe_3O_4 borosilicate glass obtained or retrieved from various sources. (From Rapp, D.B., Photo-induced hydrogen outgassing of glass, PhD thesis, Alfred University, Alfred, NY, 2004; De Sousa Meneses, D. et al., *J. Non-Crystal. Solids*, 351, 124, 2005; Sahba, N. and Rockett, T.J., *J. Am. Ceramic Soc.*, 75(1), 209, 1992.)

Similarly, the volumetric energy density η_v for monodisperse spheres is expressed in MJ/m^3 and given by

$$\eta_v = \frac{N_T m_{H_2} \Delta H_L}{N_T V_{total}} = \rho \varepsilon \Delta H_L \left(\frac{r_i}{r_o}\right)^3 \tag{25.17}$$

where

V_{total} is the total volume of the storage solution

is the packing fraction of the hollow glass microspheres

Alternatively, the storage capacity and the hydrogen relative weight content have been used extensively to assess the performance of storage solutions [2,11]. The relative weight percent of hydrogen in the microsphere, expressed in kg of H_2 per kg of microspheres or wt.%, is defined as

$$\gamma_g = \frac{m_{H_2}}{m_s} = \frac{\rho r_i^3}{\rho_s (r_o^3 - r_i^3)} \tag{25.18}$$

Making use of the equality $(r_o^3 - r_i^3) = (r_o - r_i)(r_i^2 + r_i r_o + r_o^2) \approx 3r_o^2 (r_o - r_i)$, γ_g simplifies to [2]

$$\gamma_g \approx \frac{3\rho r_i}{\rho_s (r_o - r_i)} \tag{25.19}$$

Based on Equation 25.19, γ_g can be expressed in terms of burst pressure and tensile strength of the shell materials:

$$\gamma_g = \frac{2\rho\sigma_{s,max}}{3\rho_s S_f P_{max}} \tag{25.20}$$

On the other hand, the effective density of hydrogen stored in a bed of monodisperse hollow microspheres, expressed in kg of H_2/m^3 of bed, is given by [35]

$$\gamma_v = \frac{\eta_v}{\Delta H_L} = \rho \varepsilon \left(\frac{r_i^3}{r_o^3}\right) \tag{25.21}$$

Note that because the shell thickness is relatively thin, $r_i^3 \approx r_o^3$ and γ_v depend essentially on the internal hydrogen pressure.

Figure 25.11 shows the gravimetric and volumetric energy densities of hydrogen stored at 300 K in randomly packed $(\varepsilon = 0.63)$ monodisperse hollow glass microspheres 50 μm

in diameter with shell thickness of 1 μm. The glass tensile strength $\sigma_{s,max}$ was taken as 1 GPa. It indicates that even for a conservative value of $\sigma_{s,max}$, hollow glass microspheres can achieve the 2015 DOE target for gravimetric energy density. Unfortunately, the volu- metric energy density falls short of the 2015 DOE target by a wide margin unless the internal pressure greatly exceeds 1000 bar, which would require a large amount of energy for compressing H_2.

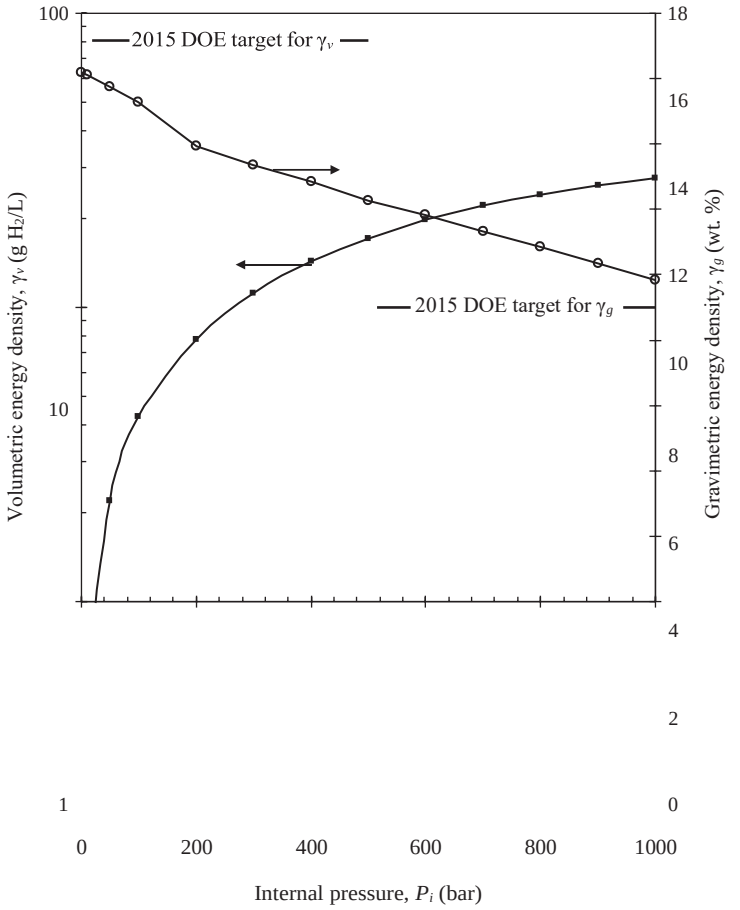


FIGURE 25.11

Gravimetric and volumetric energy densities of hydrogen stored in monodisperse hollow glass microspheres with r_o = 25 μm, $r_o - r_i$ = 1 μm, S_f = 1.5, $\sigma_{s,max}$ = 1 GPa, ε = 0.63, and ρ_s = 2230 kg/m³.

Finally, if the storage bed consists of monodisperse microcylinders with inner and outer diameters r_o and r_i, the gravimetric and volumetric energy densities are expressed as

$$\gamma_g = \rho_{so}\left(1 - \frac{r_i^2}{r_o^2}\right) \quad \text{and} \quad \gamma_v = \rho_g\left(1 - \frac{r_i^2}{r_o^2}\right) \tag{25.22}$$

25.3.2 Loading and Unloading Times

Combining Equation 25.6 with equation of state (25.2) yields the following governing equation for the inner H_2 pressure:

$$\frac{d}{dt}\left(\frac{P_i}{Z(T,P_i)T}\right) = -\frac{3RK(T)}{r_o(r_o - r_i)}(P_o - P_i) \tag{25.23}$$

Then, assuming that the temperature T and the outer pressure P_o remain constant dur- ing the loading or unloading processes while the compressibility factor $Z(T,P_i)$ is approximately constant for pressure varying between $P_i(0)$ and $P_i(t)$ yields expression for the pressure inside the microcontainers:

$$P_i(t) = P_i(0) \pm [P_i(0) - P_o] exp\left(-\frac{t}{\tau}\right) \quad (25.24)$$

where the time constant τ is expressed as

$$\tau = \frac{r_i(r_0 - r_i)}{Z(T,P_i)RTK(T)} \quad \text{for hollow spheres} \quad (25.25)$$

The time needed for the pressure difference ($P_i - P_o$) to decrease by 63% and 95% from its initial value is equal to τ and 3τ, respectively. The presence of the compressibility factor Z in the denominator suggests that H_2 release is faster for large temperatures and pressures when Z is greater than 1 (see Figure 25.5). Treating hydrogen as an ideal gas at temperature T and pressure P_i gives $Z(T,P_i) = 1.0$ and $\tau = r_o(r_o - r_i)/3RTK(T)$ as often encountered in the literature [11,29,53]. Similarly, Equation 25.24 is valid for cylindrical containers with a time constant given by

$$\tau = \frac{2 r_i(r_o - r_i)}{Z(T,P_i)RTK(T)} \quad \text{for cylinders} \tag{25.26}$$

Note that τ is independent of the cylinder length L [4]. In addition, assuming that the container wall is thin, the time constant for a sphere is 33% smaller than that for a cylinder with the same inner and outer diameters. In other words, loading and unloading times are shorter for spheres than for cylinders. The maximum shelf time of loaded microcapsules can be estimated from Equations 25.25 and 25.26 using T = 300 K. If the temperature of the microcontainer is not constant during the loading or unloading processes, the energy conservation equation must also be solved giving the temperature distribution within the container shell or within the packed bed. Heat transfer in packed beds has been studied extensively [74–85]. Models accounted for combined heat conduction through the wall of the hollow microspheres as well as for absorption, scattering, and emission of radiation models found in the literature can be adapted to predict the temperature inside a bed of hollow glass microspheres heated by a resistive heater or an incandescent lamp.

Figure 25.12 shows the evolution of the time constant τ as a function of temperature predicted by Equation 25.25 using permeation $K(T)$ reported by Lee et al. [56] for hollow vitreous silica microspheres 50 μm in diameter with shell thickness equal to 1 μm, that is, r_o = 25 μm and $r_o - r_i$ = 1 μm. It also shows the time constant τ if the gas is assumed to be ideal, that is, $Z(T,P) = 1$. Note that for pressure less than 100 bar (1450 psi), the loading and unloading time is independent of pressure as observed experimentally with soda-lime glass [29]. However, when the initial hydrogen pressure is large ($Z(T,P) > 1$), the time con- stant depends on pressure and is shorter than that predict assuming ideal gas behavior.

Figure 25.13 shows the loading and unloading characteristic time τ as a function of the microsphere radius r_o at temperatures corresponding to (1) storage and handling temperature (25°C) and (2) the loading and unloading temperatures of 200°C and 400°C assuming that the shell is 1 μm thick and made of vitreous silica. It establishes that the loading and unloading time decreases significantly with decreasing microsphere radius and increas- ing temperature.

As previously mentioned, permeation is associated with the steady-state transport of hydrogen through the glass shell. Thus, it does not account for the time necessary for H_2 to diffuse through the shell of the microspheres before reaching a steady-state mass flux. This lag time denoted by τ_l corresponds to the time needed to establish the glass solubility in the microspheres wall. As a first-order approximation, τ_l can be expressed as [29]

$$\tau_l = \frac{(r_o - r_i)^2}{6D(T)} \tag{25.27}$$

where the lag time depends only on the shell thickness. It is typically much smaller than the unloading or loading time at low temperatures (i.e., $\tau_l \ll \tau$). For example, for hollow

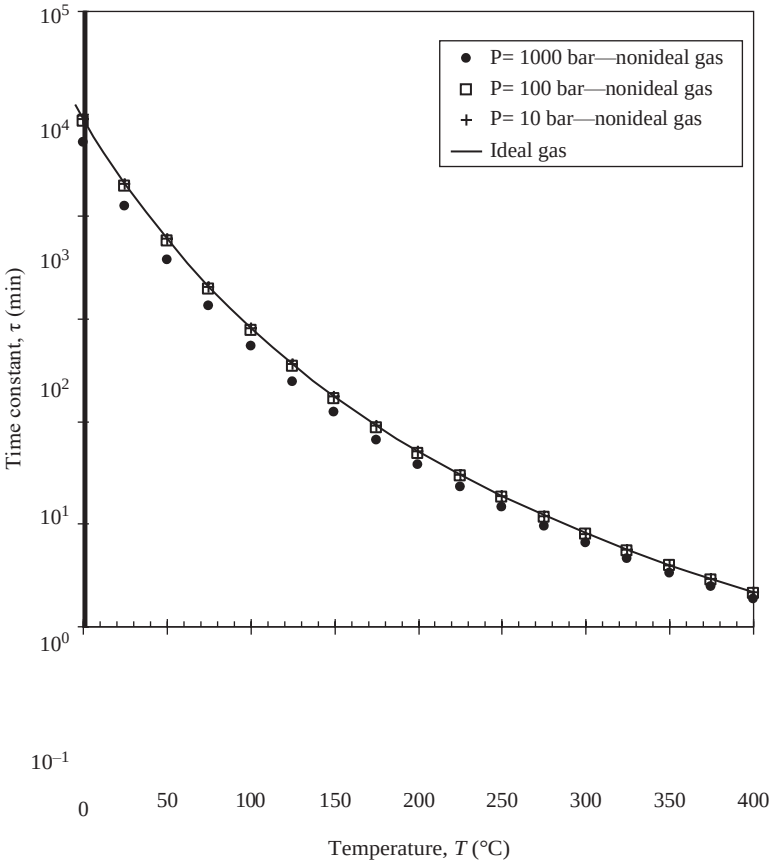


FIGURE 25.12

Loading and unloading time constant τ predicted by Equation 25.25 for vitreous silica glass microspheres with r_o = 25 μm, ($r_o - r_i$) = 1 μm, $Z(T,P)$ = 1.0, $K_0 = 8.688 \times 10^{-14}$ mol/Pa m s, and Q_K = 4469 K. Time constant for microcylinders can be found by multiplying the results shown by 3/2. (From Lee, R.W. et al., *J. Chem. Phys.*, 36(4), 1062, 1962.)

vitreous silica microspheres with r_o = 25 μm and ($r_o - r_i$) = 1 μm, the time constant τ is 0.9 days, 3.8 min, and 11 s compared with the corresponding time lag τ_l of 6.2 min, 0.3 s, and 7 ms at temperature of 25°C, 200°C, and 400°C, respectively. Nonetheless, this suggests that 95% of the hollow glass microspheres content is released in 33 s at 400°C and in 2.7 days at 25°C.

25.3.3 Filling and Discharging Energy Requirements

Another key element is assessing that the performance of hydrogen storage solution is (1) the energy required to compress the hydrogen gas to pressures in excess of 450 MPa during loading and (2) the thermal energy provided to heat up the microspheres and their content around 400°C to achieve high permeation rates.

Because of repulsion forces between H_2 molecules, hydrogen gas deviates significantly from an ideal gas under loading conditions and requires large compression work. Energy-efficient and cost-effective hydrogen compressors operating at high pressure are critical components of the envisioned hydrogen economy [86]. Hydrogen gas has also small molecules and low viscosity, which renders sealing of the compressors challenging. In addition, at high temperatures and pressures, hydrogen permeates through steel and causes embrittlement resulting in material failure, high maintenance costs, and safety concerns.

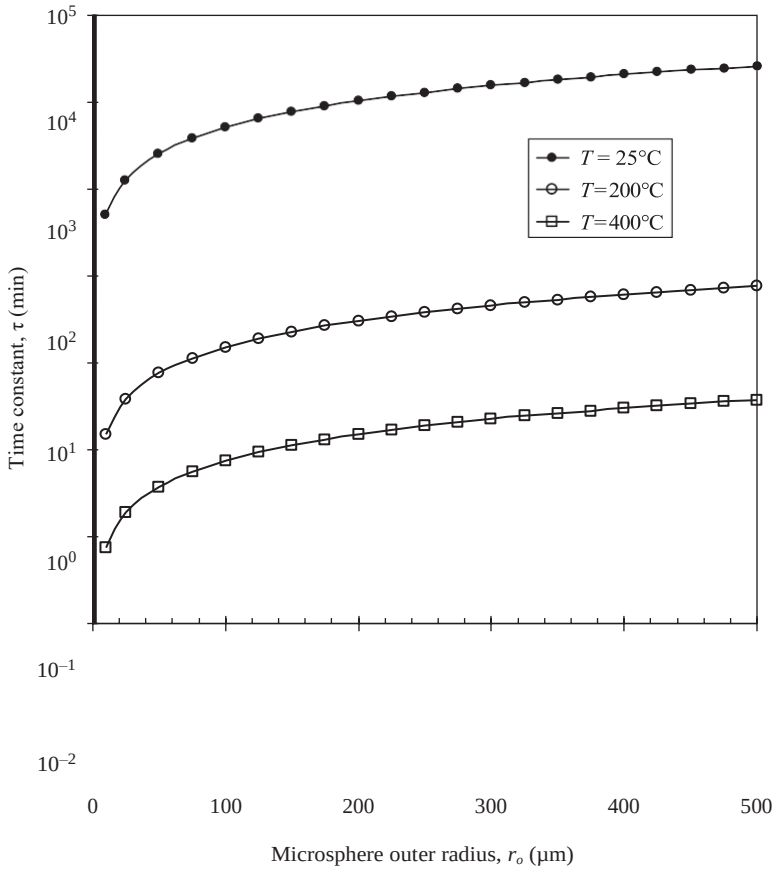


FIGURE 25.13

Loading and unloading time constant τ predicted by Equation 25.25 for vitreous silica glass microspheres as a function of r_o assuming ($r_o - r_i$) = 1 μm, $Z(T,P)$ = 1.0, $K_0 = 8.688 \times 10^{-14}$ mol/Pa m s, and Q_K = 4469 K. (From Lee, R.W. et al., *J. Chem. Phys.*, 36(4), 1062, 1962.)

Material embrittlement can be addressed by using more expensive material alloys such as chromium/molybdenum/vanadium alloys.

The total specific energy E_t required per loading and unloading cycle of 1 kg of microspheres with H_2 is the sum of (1) the specific work done for pressurizing the hydrogen during loading denoted by W_p and (2) the specific thermal energy for heating both the microspheres and the hydrogen to desired temperatures denoted by Q_u, that is,

$$E_t = W_p + 2Q_u \tag{25.28}$$

where the factor 2 accounts for thermal energy required for both loading and unloading.

The compression work required for pressurizing H_2 depends on the thermodynamic process, the number of stages, the compressor efficiency β, and the initial and final hydrogen pressures denoted by P_1 and P_2, respectively. For isothermal compression and assuming ideal gas behavior, the specific compression work W_p (in J/kg) is given by [86]

$$\int_{\rho_1}^{\rho_2} \frac{P(T,\rho)}{\rho}$$

$$W = \int_{\rho_1}^{\rho_2} d\rho = ZRT \ln\left|\frac{\rho_1}{\rho_2}\right| \quad (25\text{-}29)$$

For isentropic compression, the specific compression work is expressed as [86]

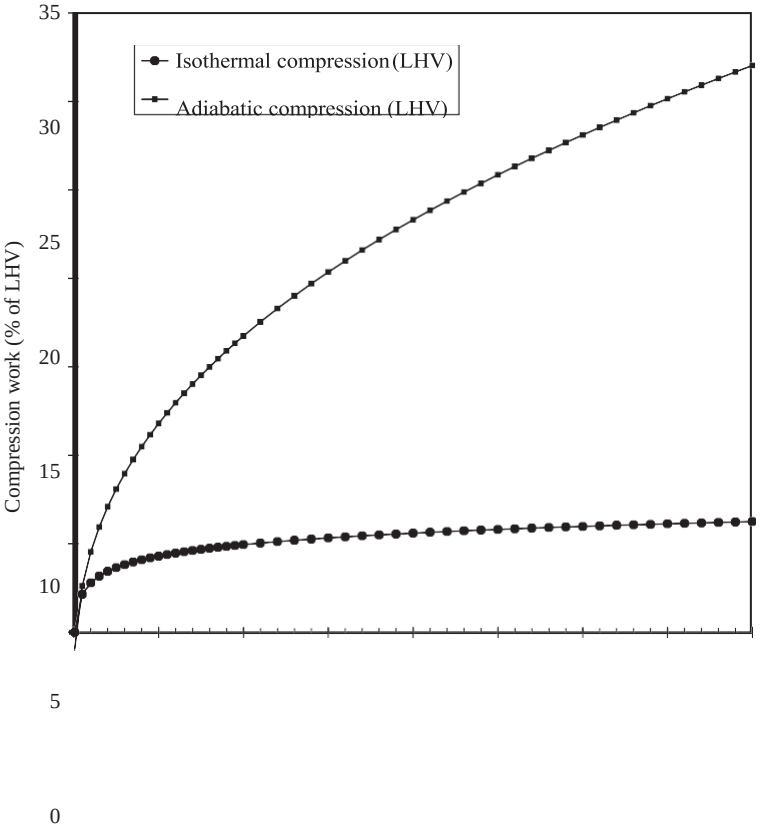
$$\beta W^{p} = \frac{k}{(k-1)\,\rho_1}\frac{P_1}{}\left[\left(\frac{P_2}{P_1}\right)^{(k-1)/k} - 1\right] \tag{25.30}$$

where

k is the specific heat ratio ($k = c_p/c_v$)

ρ_1 is the density at T_1 and P_2

Assuming hydrogen is compressed from standard temperature and pressure $\rho_1 = 0.09$ kg/m^3 and $k = 1.41$. Multistage compressors with cooling between stages operate between these two limiting cases albeit closer to isothermal [86]. Figure 25.14 shows the work W_p required for adiabatic and isothermal hydrogen compressions as a fraction of the hydrogen LHV as a function of final pressure P_2. For example, multistage compression from atmospheric pressure to 200 and 800 bar requires 11.9% and 19.1% of the LHV of hydrogen, respectively. It can reach 20% if one accounts for mechanical and electrical losses. These results are in good agreement with analysis by Ramback et al. [26,27,32]. The authors estimated the specific compression work for temperatures up to 400°C and pressure less than 620 bar to range between 10% and 20% of the LHV of H_2 assuming a three-stage compressor with 75% efficiency (Fig. 7 in Ref. [32]). However, Ramback [32] noted that it is less than the energy needed to liquify hydrogen, and therefore, hydrogen storage in hollow glass



0 100 200 300 400 500 600 700 800

Final pressure, P_f (bar)

FIGURE 25.14

Energy required for adiabatic and isothermal compressions as a fraction of the hydrogen LHV.

TABLE 25.5

Expression of Design Parameters for Thin-Walled Monodisperse Hollow Microspheres and Microcylinders

Parameters	Symbol	Microspheres	Microcylinders
Burst pressure	P_{max}	$P_{max} = \frac{2\sigma_{s,max}(r_o - r_i)}{S_f r_0}$	$P_{max} = \frac{\sigma_{s,max}(r_o - r_i)}{S_f r_0}$
Buckling pressure	P_{cr}	$P_{cr} = \frac{2E_s(r_o - r_i)}{r_o\sqrt{3(1-\nu_s^2)}}$	$P_{cr} = \frac{E_s(r_o - r_i)}{r_o\sqrt{3(1-\nu_s^2)}}$
Maximum packing		74%	90.7%
Random packing Loading		63%	82%–83%
time constant	T	$\tau = \frac{Z(T, P_i)RTK(T)}{3}$	$\tau = \frac{2Z(T, P_i)RTK(T)}{r_i(r_o - r_i)}$
Gravimetric density	γ_g	$\gamma_g = \rho\varepsilon\frac{r_i^3}{r_s^3 - r_o^3}$	$\gamma_g = \rho\varepsilon\frac{r_i^2}{r_s^2 - r_o^2}$
Volumetric density	γ_v	$\gamma_v = \rho\varepsilon r_i^3 / r_o^3$	$\gamma_v = \rho\varepsilon r_i^2 / r_o^2$

microsphere can be economically competitive. On the contrary, Robinson and Iannicci [87] concluded that compressing H_2 at high pressures in excess of 1000 bar appears unpractical from an energy consideration point of view despite the fact that hollow glass microspheres could sustain such pressures [11]. Similar conclusions were reached by Bossel [86] and was identified as one of the reasons why the hydrogen economy *will never make sense*.

The specific thermal energy required to heat up the microspheres and the hydrogen from T_1 to T_2 can be expressed as

$$Q_u\,(\text{J/kg}) = \int_{T_1}^{T_2} c_{eff}\,(T)\,\mathrm{d}T \tag{25.31}$$

where c_{eff} is the effective specific heat of the microcontainer bed defined as $c_{eff} = \varepsilon[c_p r_i^3/r_o^3 - c_{s,p}(1 - r_i^3/r_o^3)]$. As a first-order approximation, one can assume c_{eff} to be constant so Q_u is proportional to the temperature difference $(T_1 - T_2)$. Ramback [27] showed that it represents between 2% and 6% for monodisperse soda-lime silicate hollow microspheres 50 μm in diameter with a 0.9 μm thick shell for = 0.63 and $(T_1 - T_2)$ between 100°C and 400°C and pressures between 248 and 620 bar.

Table 25.5 summarizes expressions for design parameters and assessing performances of thin-walled monodisperse hollow microspheres and microcylinders.

Only a few experimental studies focusing on H_2 storage in glass microcontainers have been performed over the last three decades and are summarized in Table 25.6. Teitel [9,10] performed crush tests and loading tests with different commercial hollow microspheres made of soda-lime silica glass with outer radius ranging from 14 to 55 μm and wall thickness from 0.4 to 2.2 μm. They showed that the survival rate varied from 30% to 90% depending

TABLE 25.6

Summary of Experimental Studies on Hydrogen Storage in Microcapsules

				Loading				
				$(r_o - r_i)$	P (bar)/T	Outgassing	η_g	η_v
References	**Composition**	**Shape**	r_o (μm)	**(μm)**	**(°C)**	T**(°C)**	**(wt.%)**	**(g/L)**
[29]	Soda-lime	Microspheres	40–45	1	104	100–300	2	
[18]	Soda-lime	Microspheres	14–55	0.4–2.2	551/350	N/A	5.3	12
[20]	Fused quartz	Microcylinders	160–260	16–35	N/A	N/A	2	N/A
[35]	S60/1000 (3M)	Microspheres	5–15	200	350	4	14	
[27]		Microspheres	25.5	0.9	581/350			
[34]	Soda-lime	Microcylinders	100–500	2–10	100–250	200–250	15–17	10–15

2015 DOE targets are η_g = 9 wt.% and η_v = 81 g H_2/L.

on the glass composition, the microsphere radii, and the loading gas. The authors suggested an aspect ratio $r_o/(r_o - r_i)$ of at least 30. Loading tests were performed at up to 551 bar (8000 psi) at 350°C. The author reported a gravimetric energy density of 4%–5% and a volumetric energy density of 20 g of H_2/L. Pressure would need to be significantly increased to reach the 2015 DOE target of 9 wt.% and 81 g of H_2/L. Microspheres breakage rate during the loading and unloading cycle was about 15%.

Tsugawa et al. [29] loaded soda-lime silicate microspheres 40–45 μm in outer diameter with a 1 ± 0.1 μm thick shell. The microspheres were placed in a highly impermeable beryllium container and heated at 763 K. Then, hydrogen was introduced and pressurized for 24 h until pressure reached 103 atm. The microspheres were quenched for 1 min in liquid nitrogen. The gravimetric energy density was reported as 2 wt.%. Finally, outgassing was performed at constant temperature ranging from 373 to 573 K. The authors also established experimentally that soda-lime glass microspheres pressurized with H_2 fill to only 82 vol.% instead of 100% with helium and 2% of H_2 remained inside the microspheres after outgassing.

Duret and Saudin [35] performed crush and burst tests on commercial hollow glass microspheres, provided from 3M and Saint Gobain, with outer diameter between 2 and 80 μm and a mean diameter between 12 and 30 μm. Hollow glass microsphere effective density was between 0.57 and 1.5 g/cm^3. The crush test was performed in water at 1000 bar for a few hours followed by a float test. Survival rate as low as 10% was recorded. Unbroken microspheres underwent a burst test at 200 bar and 400°C. 3M microspheres could sustain the crush test and achieved gravimetric and volumetric energy density of 4 wt.% and 14 g/L, respectively.

Recent studies have explored the use of hydrogen storage in microcylinders. First, Yan et al. [20] drew fused quartz hollow fibers (or microcylinders) 15 cm in length and with outer diameter ranging from 160 to 260 μm and wall thickness between 16 and 35 μm. They also subjected the fibers to chemical strengthening through hydrofluoric acid (HF) etching [88]. In addition, fiber coating with Shellac was performed. This reduced significantly the frequency of breakage and protected the fibers' surfaces from the effects of aging and handling. Different end sealing techniques were also tested including (1) heat treating the tip of fiber bundles in a furnace, (2) individual fiber sealing with an open flame, and (3) end plugging the fibers with colloidal silica. Flame sealing method provided the best sealing. The authors also performed hot static and dynamic fatigue tests and burst tests as well as hydrogen loading and unloading tests. They established that liquid-phase HF etching

significantly increases the tensile strength of the microcylinders and enables further control of the wall thickness. Finally, a gravimetric energy density of 2 wt.% was reported.

Kohli et al. [34] loaded soda-lime silicate glass hollow microspheres with aspect ratio $r_o/(r_o - r_i)$ ranging from 80 to 180 at outside pressure up to 250 bar and temperature of 200°C–250°C. They estimated the gravimetric energy density at 15–17 wt.% and volumetric energy density between 10 and 15 g/L (Fig. 4 in Ref. [34]).

Based on the previous discussion, it is evident that hollow glass microspheres are the microcapsules offering the best mechanical and gas permeation properties, which maximize gravimetric and volumetric energy densities and minimize loading and unloading times. The next section presents manufacturing processes for producing hollow glass microspheres.

25.5 Synthesis of Hollow Glass Microspheres

Extensive efforts have been devoted to the fabrication of hollow glass microspheres for applications ranging from thermal insulation and fire retardant to lightweight composite materials for flotation and reinforced materials. They have also been used for viscosity modification, shrinkage reduction, and chemical resistance enhancement of plastics or paints, as well as for radiation shield [89]. Hollow microspheres made of materials other than glass have also been used to encapsulate drugs for controlled drug delivery or colorant or artificial flavor in food science. Thus, there exist numerous synthesis methods with different levels of control in the size distribution, shell thickness, material composi- tion, mechanical properties, and throughput. The different synthesis processes have been reviewed extensively elsewhere [90–93] and this section is meant to give a relatively brief overview. In addition, numerous patents have been claimed for manufacturing, functionalizing, or strengthening hollow glass microspheres [94–110].

25.5.1 Hollow Microspheres in Fly Ash

Hollow glass microspheres have been observed in fly ash emanating from coal-fired power plants [90,111]. Indeed, coal particles injected in the furnace contain silica, sulfates, and other inorganic matter. As coal particles burn from the outside inward, carbon gets oxidized, and the remaining matter forms a molten glassy outer shell. The inner coal continues burning and releases gases such as carbon dioxide and sulfur oxides resulting from the oxidation of carbon and sulfates at high enough temperatures. These gases are entrapped in the molten glassy shell and blow it to produce a hollow microsphere, which solidifies as it exits the furnace. However, the hollow microspheres formed in this pro- cess (1) may not be perfectly spherical, (2) feature a wide size distribution (from a few to hundreds of microns), and (3) have nonuniform wall thickness [90]. Moreover, impurities and particles are often present in the shell along with tiny bubbles [90]. The nature of the process offers very little control except for the size of the initial coal particles [111].

25.5.2 Spray Pyrolysis Process

Several processes aimed to emulate hollow microspheres formation in coal burning but in a controlled manner have been developed over the last 50 years. The most widely used

processes can be reduced to two consecutive stages: (1) fabrication as semiproducts in the form of coarse or fine irregular particles or spheres and (2) blowing (or molding) of the semiproducts into hollow glass microspheres [92]. The main differences in the fabrication of hollow microspheres lie in the fabrication of the micropowder, which determines the dimensions and properties of the hollow glass microspheres. Formation of the semiproduct can include (1) glass frit, (2) liquid-droplet process, (3) solgel process, and (4) rotating and electric arc methods. The second stage consists of spray pyrolysis in flame or hot gas or a rotating electric arc plasma. Microspheres with porous walls have also been synthesized using spray pyrolysis [112,113].

25.5.2.1 Blowing Process

Glass frits, microspheres, or micropowders can be transformed in hollow microspheres using flame spray pyrolysis process [114]. It consists of spraying the semiproducts containing a blowing agent (e.g., sulfates) into an oxy-fuel flame at temperature between 1000°C and 1200°C. Upon rapid heating, the frit assumes spherical shape thanks to reduced viscosity and large surface tension. Beyond a certain temperature, the blowing agent undergoes thermal decomposition releasing gases (e.g., SO_2 and O_2), which results in the formation of a cavity that expands over time. Then, the resulting spherical hollow glass microspheres are rapidly cooled from the outside, which provides enough mechanical strength to retain their sphericity. The glass composition as well as the microsphere size and wall thickness can be controlled by changing the size, shape, and composition of the initial glass frit including the blowing agent [101,115,116]. Further control can be achieved through process parameters such as the residence time and the temperature history. Figure 25.15 shows the history of the semiproduct (e.g., glass frit or spherical particles) undergoing flame spray pyrolysis.

Other blowing processes have been proposed such as replacing flames by high-temperature gases. Similarly, Bica [117] formed hollow glass microspheres from glass frit introduced in a rotating electric arc plasma. The author reported that 85% of the glass frit was transformed into hollow microspheres with diameters between 2 and 24 μm and wall thickness between 0.4 and 1.6 μm.

25.5.2.2 Semiproduct Production

Glass frits are the simplest semiproducts used to produce hollow glass microspheres. They are obtained by mechanically crushing glass or by rapidly cooling hot glass, which shatters under thermal stress. Glass beads can also be produced from a stream of molten glass using (1) a horizontal rotating paddle wheel [118] to mechanically break

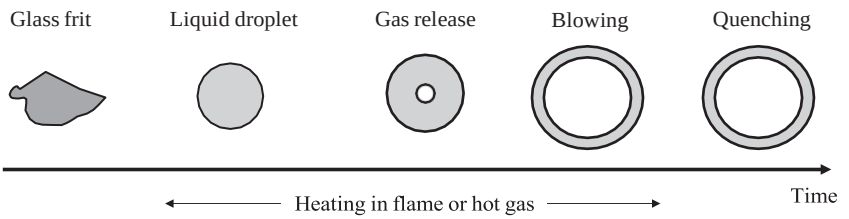


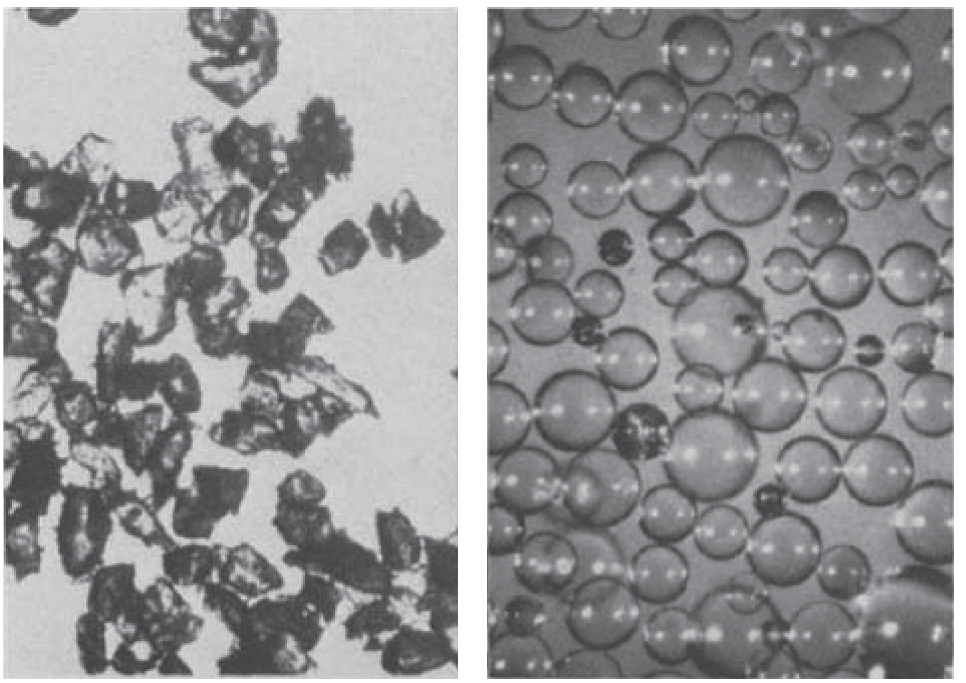
FIGURE 25.15

Schematic of a spray pyrolysis process to produce hollow glass microspheres.

the vertically flowing stream or (2) under electric field in the longitudinal direction of the stream and a temporally variable magnetic field perpendicular to the stream [119]. However, the resulting glass frit has irregular shape and wide mass and size distri- butions. Consequently, the resulting hollow microspheres produced after the blow- ing process have also a widespread size distribution and shell thickness. Thus, a more advanced process has been conceived to produce semiproducts with controlled size and composition.

In dried-gel process, a gel having the desired glass composition is formed, dried, and ground into fine particles. Then, spray pyrolysis of the sieved gel powder (as opposed to glass frit) is performed. For example, Downs and Miller [120] claimed a solgel process resulting in a glass shell composed of at least 99% silica that does not suffer from inhomogeneities and phase separation associated with multiple component glass shells. A blowing agent such as urea may also be added to produce large hollow microspheres with thin wall [121]. Figure 25.16 shows micrographs of dried-gel particles and the resulting hollow glass microspheres after

However, dried-gel process tends to produce hollow microspheres with a wide range of diameter and wall thickness as illustrated in Figure 25.16. This drawback has been addressed by pressing the gel powder into mold to form cylindrical pellets of uniform and arbitrary size [122]. Moreover, Schmitt et al. [123] produced iron-doped sodium borosilicate



(a) (b)

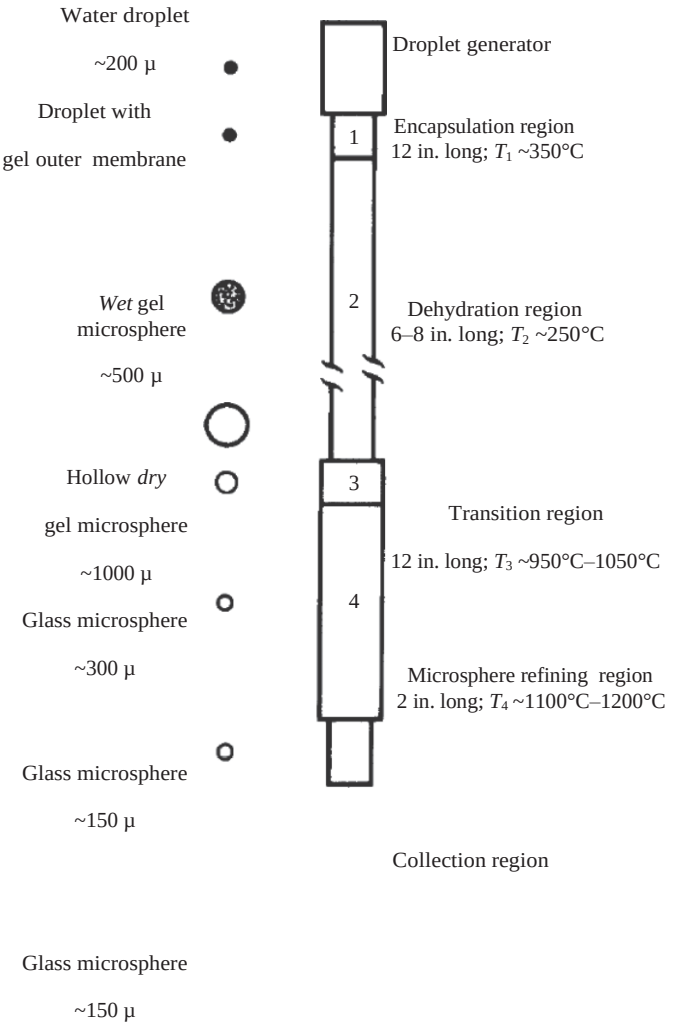
FIGURE 25.16

Micrographs of (a) dried-gel particles and (b) resulting hollow glass microspheres after spray pyrolysis. (Reproduced from Hendricks, C.D., *J. Nuclear Mater*., 85–86(1), 107–111, 1979; Rosencwaig, A. et al., Laser fusion hollow glass microspheres by the liquid-droplet method, Lawrence Livermore Laboratory Report UCRL-81421, June 5, 1978.)

granules doped by spray drying an aqueous suspension of crushed xerogel powder with iron chloride or iron sulfate and surfactants. They investigated the effects of heat treatment of the gel, spray drying parameters, and blowing agents.

25.5.3 Liquid-Droplet Method

Liquid-droplet process to produce glass beads to be blown into hollow microspheres was developed for producing laser fusion targets [121,124–126]. Figure 25.17 shows a schematic of the vertical-drop tower along with the different zones and thermal stages undergone by the liquid droplets. First, glass-forming components are dissolved and mixed in an aqueous solution. An in-line stream made of a large quantity of uniform-size droplets is generated by a Rayleigh–Taylor droplet generator [121,124,125] or a vibrating nozzle [121] at the top of a vertical-drop furnace. Air is drawn in the column in a controlled manner from the top to the bottom of the furnace. The generated droplets travel downward through a region of moderate temperature (region 1) to remove the water from the outer surface and to create an elastic gel membrane that encapsulates the rest of the droplet. Then, in region 2, water evaporates from the droplet and diffuses through the membrane resulting in dry solid gel particles. Upon further heating at higher temperatures (region 3), the gel



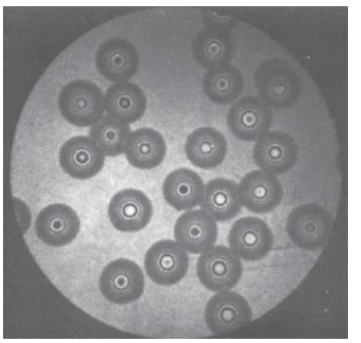


FIGURE 25.17

Schematic of a vertical-drop furnace used in liquid-droplet process and interference micrograph of the pro- duced hollow glass microspheres. The column was 5 m high and made of quartz tube 7.5 cm in diameter. (Reproduced from Hendricks, C.D., *J. Nuclear Mater*., 85–86(1), 107–111, 1979; Rosencwaig, A. et al., Laser fusion hollow glass microspheres by the liquid-droplet method, Lawrence Livermore Laboratory Report UCRL-81421, June 5, 1978.)

microspheres fuse to glass and collapse to form denser glass microspheres. In region 4, gases are released and diffuse through the shell whose wall becomes uniform thanks to lower viscosity caused by higher temperatures and to the action of surface tension forces. The hollow glass microspheres are then rapidly quenched and collected. This process produces nearly monodisperse microspheres with excellent sphericity, wall uniformity, and concentricity. It also offers control of the microspheres' diameter and shell thickness by controlling the liquid solution composition, the droplet formation process, the tem- perature profile in the column, and the liquid flow rate [91]. The microsphere size can be increased by increasing the drop tower height [121]. However, it requires that the glass- forming compounds be in solution. Unfortunately, some compositions form a gel so rap- idly that droplets cannot be produced. In addition, the produced microspheres are small, spherical, monodisperse, and concentric as illustrated in Figure 25.17 [121]. However, the throughput is relatively small. Dried-gel process addresses the limitations in terms of composition, microsphere size, and throughput but has its own drawbacks as previously discussed [121,125].

25.5.4 Hollow Glass Microspheres by Solgel Process

The synthesis of hollow glass microspheres by solgel process has been described by Ding and Day [127]. The starting aqueous solution is prepared with a precursor solution of metal alkoxide (e.g., tetraethyl orthosilicate [TEOS]) with ethanol and hydrochloric acid (HCl). Partial hydrolyzation (or polymerization) of the metal alkoxide, catalyzed by the acid, takes place over time. The solution is used to produce droplets with a droplet generator such as a vibrating nozzle [127]. The falling droplets are rapidly transformed into solid gel microspheres upon drying at temperatures less than 250°C. Finally, water, ethanol, and HCl are removed from the gel microspheres by thermal treatments at 500°C to 700°C to form hollow glass microspheres. Ding and Day [127] produced microspheres 60–81 μm in diameter. The advantages of this process include uniform sphere size, high chemical purity, low processing temperatures, and controllable microstructures along with the possibility of achieving compositions that cannot be made by conventional melting. Finally, hollow glass microspheres can also be synthesized using colloidal tem- plating of sacrificial polystyrene latex microspheres removed by calcination [128] as well as miniemulsions [129].

25.5.5 Hollow Silica Aerogel Spheres

Hollow silica aerogel spheres have been synthesized by combining a droplet-generation method with solgel processing [130,131]. The process starts with preparation of TEOS, ethanol, and HNO_3 aqueous solution at pH 2. The solution is flown through the outer nozzle of a dual-nozzle hollow droplet generator. The hollow droplets are briefly injected in a gelation chamber where, upon contact with the gelation agent, they transform into rigid alcogel spheres. Two methods were proposed, namely, [130] (1) the levitation method where the droplets fall in an upward stream of NH_3–N_2 gas mixture acting as a gelation agent and (2) the NH_4OH vapor column techniques where the droplets fall through the saturated vapor above liquid NH_4OH. Both approaches are illustrated in Figure 25.18.

They are then collected and aged for 24 h in ethyl alcohol before being dried with supercritical CO_2. The process results in hollow silica aerogel spheres with a hollow core surrounded by a shell of silica aerogel and a thin outer membrane as shown in Figure 25.18. Spheres thus formed were several hundreds of microns in diameters and as large as 2 mm.

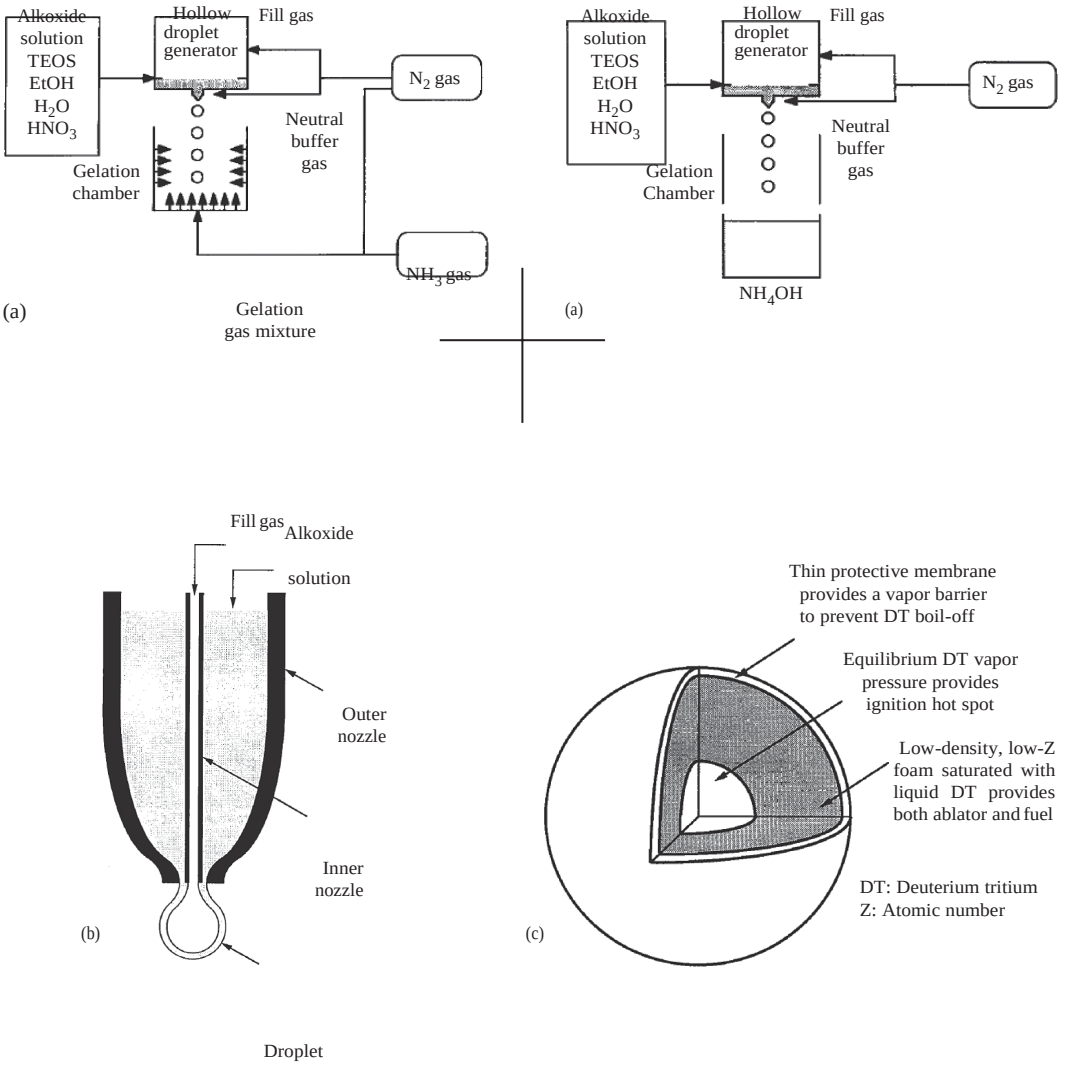


FIGURE 25.18

Illustration of hollow silica aerogel spheres synthesis method by (a) levitation in NH_3–N_2 gas mixture or (b) free fall in NH_4OH vapor column along with (c) dual-nozzle hollow droplet generator and resulting (d) hollow silica aerogel spheres. (Reproduced from Kim, K.K., *J. Am. Ceramic Soc.*, 74(8), 1987, 1991.)

Porosity of the aerogel ranged from 90% to 97% with pore diameters between 9 and 60 nm. The porosity and pore size could be controlled by varying (1) the solution composition (and its viscosity), (2) the gelation time, and (3) the gelation method. Optimization of the process parameters were later investigated [131]. The overall diameter can be controlled through the design of the dual nozzle and the solution viscosity.

25.5.6 Porous Wall Glass Hollow Microspheres

More recently, porous wall glass microspheres made of silica glass containing boron oxide, alkaline earths, and alkali have been synthesized with diameters from 2 to 100 μm and shell thickness from 10 to 300 nm [112]. The first step of the process consists of flame spray

pyrolysis to form conventional hollow glass microspheres. The shell is made porous through heat treatment and acid leached [112,113]. The heat treatment induces phase separation between a continuous silica-rich phase interconnected with an alkali- and borate-rich phase. Acid leaching with 3 M HCl at 80°C–85°C dissolves away the alkali–borate phase, thus making the wall porous with pore size between 1 and 100 nm. Figure 25.19 shows a schematic of the porous wall glass hollow microspheres along with an SEM

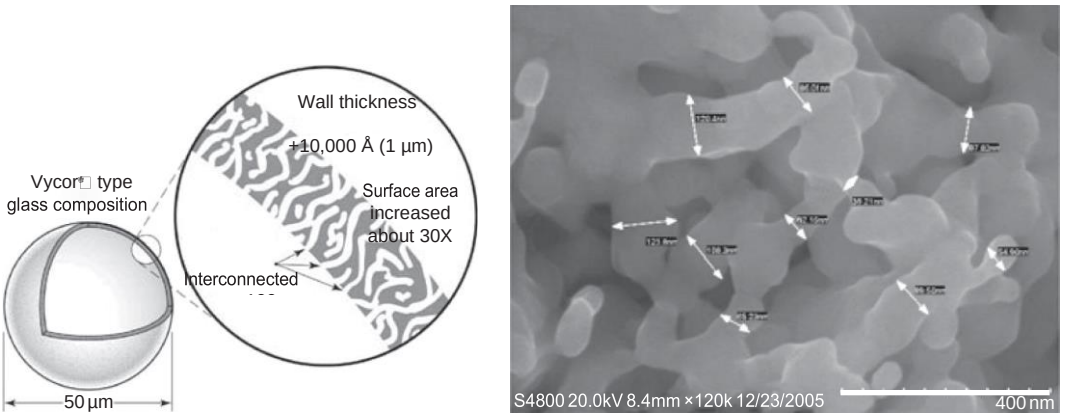


FIGURE 25.19

Schematic and SEM image of porous wall glass hollow microspheres. (Reproduced from Heung, L.K. et al., Hollow porous-wall glass microspheres for hydrogen storage, Patent Application No. US 2006/0059953 (October 21, 2005) and International Application No. PCT/US2006/040525 (October 17, 2006); Wicks, G.G. et al., *ACerS Bull.*, 23–28, June 2008.)

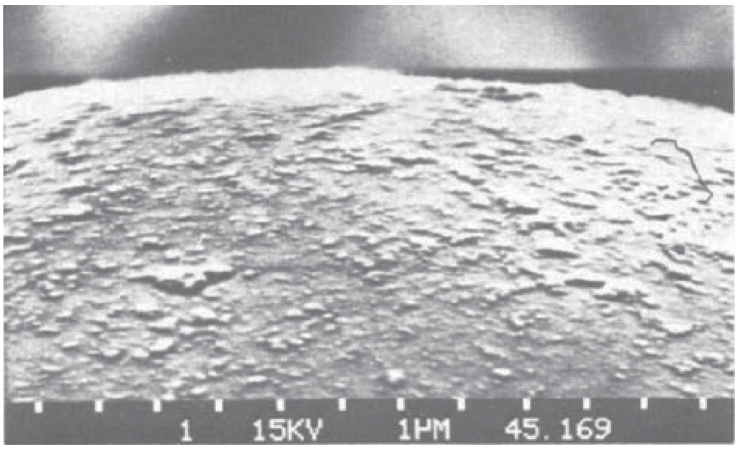
picture of the porous wall. The porosity of the wall can be controlled by selecting different glass compositions and silica/alkali/borate ratios. The hollow microspheres can then be sorted by flotation techniques. Their density ranged from 0.1 to 0.7 g/cm^3. The authors were also able to fill the microspheres with palladium through the porous wall [113]. Thus, the microspheres could potentially be filled with various hydrogen adsorbent materials [113]. The porous wall would enable faster loading and release of the hydrogen.

Finally, alternative processes have been developed to synthesize hollow glass microspheres with porous wall combining (1) colloidal templating of polystyrene latex microspheres, to form a large microcavity with (2) solgel method to form the mesoporous wall after calcination of both the micelles and the microsphere [132–135]. Similarly, a combination of emulsions (e.g., oil/water) and the solgel method has been demonstrated by the self-assembly of silica and surfactants at the oil/water droplet interface [136,137]. In addition to pursuing these synthesis efforts, mechanical and thermal testing of these novel microspheres are needed including cycling under realistic pressures and temperatures expected during hydrogen loading and unloading.

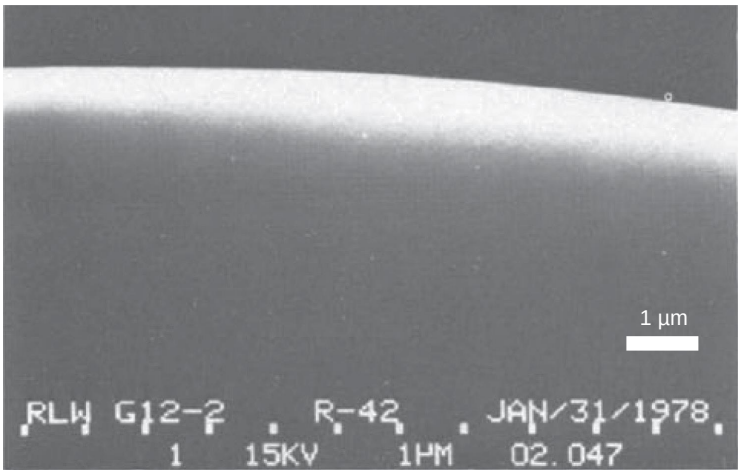
25.5.7 Surface Treatment and Additional Functionality

As discussed in Section 25.2.7.1, tensile strength of the glass shell strongly depends on imperfection or flaws at the shell surface. Such flaws must be removed to strengthen and to improve the durability of the glass shell. Surface treatment by heat polishing [138] and chemical hardening [88] can be used to smoothen the microspheres' surface and strengthen their shell. Hendrick et al. [121] used a mixture of HNO_3 and NH_4F at 90°C followed by washes with water, acetone, and alcohol. Figure 25.20 compares SEM images of the surface of hollow glass microsphere commercially available with those synthesized and acid etched by Hendricks et al. [121,125].

The authors established that this etching process results in a 100–200 Å surface finish and no sign of surface deterioration after exposure to humid air compared with a few days when using conventional HCl or HF wash. Acid etching also provides further control of the shell thickness. In addition, processes have been developed for coating the hollow glass



(a)



(b)

FIGURE 25.20

SEM images of the surface of hollow glass microsphere (a) commercially available and (b) synthesized by liquid droplet method and chemically etched. (From Hendricks, C.D., *J. Nuclear Mater.*, 85–86(1), 107–111, 1979.)

microspheres with a thin layer of materials to strengthen the thin glass shell [20,34,125,139]. For example, hollow glass microspheres have been coated with nickel [140], TiO_2, AlN [141], or with a gel [142] to name a few. Processes have also been developed to form a multilayer shell [143,144]. However, this protective coating should be thin and nonreactive with H_2 to limit potential barrier to hydrogen permeation. Acid etching and coatings of the shell of the hollow glass microspheres could be repeated between consecutive uses albeit at an additional cost.

25.5.8 Other Materials and Shapes

Hollow microspheres have also been made of polymers. They can be produced by emulsion processes as well as by coating solid template particles (e.g., polystyrene or silica) in liquid suspensions or in fluidized beds [91]. The solid particles act as sacrificial cores and

are removed by thermolysis [91] or chemical etching. Hollow microspheres have also been synthesized with various polymeric materials and various size distributions [145–148].

As previously discussed, synthesis of cylindrical glass capillaries or hollow glass fibers is much more straightforward as they can be produced by simply drawing hollow fibers [149–151]. These products are inexpensive and commercially available as capillary tubes. For hydrogen storage, both cylinder ends must be sealed as described in details in Ref. [20].

25.6 Conclusions and Perspectives

This chapter has reviewed the principles, advantages, and challenges of hydrogen stor- age in hollow glass microspheres. Glass, and in particular vitreous silica, appears to be the material of choice for its superior tensile strength and good hydrogen permeability. In addition, hollow microspheres can sustain larger pressures and feature larger hydrogen permeation rate than cylinders with the same inner and outer radii and internal pressure. Significant progress has been made in synthesizing monodisperse hollow glass micro- spheres with controlled diameter and shell thickness. Strategies have been developed to further strengthen the shell through acid etching, heat polishing, or coating with hard material. Hollow glass microspheres feature excellent gravimetric energy density and can be safely handled at room temperature and atmospheric pressure and poured in any con- tainer solution. They are relatively inexpensive to make and the associated technology can be scaled up and present little risks. However, their volumetric energy density falls short of the 2015 DOE target. Moreover, the energy cost for compressing hydrogen at high pressure during loading is very high. Detailed cost analysis for this technology could not be found in the open literature. However, it has been stated that "the use of commercial grade hollow- glass microspheres for high pressure hydrogen storage has been shown to be cost ineffec- tive" [7]. This conclusion was reached based on experimental tests performed by Teitel [18] and due to (1) material and synthesis cost, (2) the low volumetric energy density achieved, (3) high microsphere breakage rate, (4) the low fraction of recoverable hydrogen, and (5) the fill and release energy requirements. On the other hand, Akunets et al. [2] suggested that hydrogen storage in hollow glass microspheres could be used in applications when storage lifetime, safety, and weight are major concerns and where cost is not the determining factor. Similarly, Robinson and Handrock [7] suggested the use of hollow glass microspheres for fleet applications where volume and refueling concerns are not critical.

Based on the previous discussion and in order to make this technology competitive with other hydrogen storage technologies, the following technical recommendations are made [11,28]:

1. Develop energy-efficient, reliable, cost-effective, and clean 1000 bar hydrogen compressors [28]. Technologies to reduce energy requirement for H_2 compres- sion would have no moving parts and be oil- and lubricant-free thus reducing the risk for contamination of hydrogen. They include metal hydride hydrogen com- pressors [152,153], for example. This effort would also benefit other high-pressure hydrogen storage technologies.
2. Develop inexpensive and high-throughput processes to produce high-quality monodisperse microspheres with large tensile strength and uniform shell thickness

able to withstand high internal pressures. The shell material should also feature adequate permeability to achieve long dormancy time as well as short unloading times for on-demand delivery.

3. Optimize existing or develop new coating and etching techniques to strengthen the shell and reduce breakage rate during loading and handling. This would increase reliability and the number of loading and unloading cycles hollow glass microspheres can withstand.
4. Develop materials and strategies to unload H_2 at temperature below 100°C. Then, heating could be achieved by using waste heat generated by the fuel cell or a sim- ple heater powered by a battery during fuel cell start-up.
5. Develop novel approaches to control H_2 permeability through nonthermal meth- ods such as magnetic, electric, or electromagnetic [28].
6. Assess the financial and energy costs associated with reprocessing the spent microspheres.

9. References

References

1. Hirsch, R. L., Bezdek, R., Wendling, R. *Peaking of World Oil Production*. www.netl.doe.gov/publications/others/pdf/Oil_Peaking_NETL.pdf, 2005.
2. phttp://www.eere.energy.gov/hydrogenandfuelcells/hydrogen/storage. html#objectives.
3. Schlapbach, L., Zuttel, A. *Nature* **2001**, *414*, 353–358.
4. David, R. L. (ed). *CRC Handbook of Chemistry and Physics*, 74th edn., The Chemical Rubber Co., Boca Raton, FL, **1993**.
5. Eddaoudi, M., Kim, J., Rosi, N., Vodak, D., Wachter, J., O'Keeffe, M., Yaghi, O. M. *Science* **2002**, *295*, 469–472.
6. Reid, C. R., Thomas, K. M. *J. Phys. Chem. B* **2001**, *105(33)*, 10619–10629.
7. Chagger, H. K., Ndaji, F. E., Sykes, M. L., Thomas, K. M. *Carbon* **1995**, *33*, 1405–1411.
8. Jiang, S. Y., Gubbins, K. E., Balbuena, P. B. *J. Phys. Chem.* **1994**, *98*, 2403–2411.
9. Britt, D., Tranchemontagne, D., Yaghi, O. M. *Proc. Natl. Acad. Sci. (USA)* **2008**, *105(33)*, 11623–11627.
10. Davis, M. E. *Nature* **2002**, *417*, 813–821.
11. Corma, A. *Chem. Rev*. **1997**, *97*, 2373–2419.
12. Fletcher, A. J., Thomas, K. M., Rosseinsky, M. J. *J. Solid State Chem*. **2005**, *178*, 2491–2510.
13. Thomas, K. M. *Catalysis Today* **2007**, *120*, 389–398.
14. Felderhoff, M., Weidenthaler, C., von Helmolt, R., Eberle, U. *Phys. Chem. Chem. Phys*. **2007**, *9*, 2643–2653.
15. Morris, R. E., Wheatley, P. S. *Angew. Chem. Int. Ed*. **2008**, *47*, 4966–4981.
16. van den Berg, A. W. C., Arean, C. O. *Chem. Commun*. **2008**, 668–681. 17.

Collins, D. J., Zhou, H. C. *J. Mater. Chem*. **2007**, *17*, 3154–3160.

18. Dinca, M., Long, J. R. *Angew. Chem. Int. Ed*. **2008**, *47*, 6766–6779.
19. Thomas, K. M. *Dalton Trans*. **2009**, 1487–1505.
20. Lin, X., Jia, J., Hubberstey, P., Schroder, M., Champness, N. R. *Cryst. Eng. Commun*. **2007**, *9*, 438–448.
21. Ma, S. Q., Zhou, H. C. *Chem. Commun*. **2010**, *46*, 44–53.
22. Thomas, K. M. In *Energy Materials*, Bruce, D. W., O'Hare, D., Walton, R. I., Eds., Wiley, New York, **2011**, pp. 245–281.
23. Kinoshita, Y., Matsubara, I., Hibuchi, T., Saito, Y. *Bull. Chem. Soc. Jpn*. **1959**, *32*, 1221–1226. 24.

Hoskins, B. F., Robson, R. *J. Am. Chem. Soc*. **1989**, *111*, 5962–5964.

25. Kondo, M., Yoshitomi, T., Seki, K., Matsuzaka, H., Kitagawa, S. *Angew. Chem. Int. Ed*. **1997**, *36*, 1725–1727.
26. Chen, B., Ockwig, N. W., Millward, A. R., Contreras, D. S., Yaghi, O. M. *Angew. Chem. Int. Ed*. **2005**, *44*, 4745–4749.
27. Kitagawa, S., Kitaura, R., Noro, S. *Angew. Chem. Int. Ed*. **2004**, *43*, 2334–2375.
28. Ferey, G., Mellot-Draznieks, C., Serre, C., Millange, F., Dutour, J., Surble, S., Margiolaki, I. *Science* **2005**, *309*, 2040; *Science* **2005**, *310*, 1119.
29. Ferey, G. *Chem. Soc. Rev*. **2008**, *37*, 191–214.
30. Kitagawa, S., Matsuda, R. *Coord. Chem. Rev*. **2007**, *251*, 2490–2509.
31. Huang, X.-C., Lin, Y.-Y., Zhang, J.-P., Chen, X.-M. *Angew. Chem. Int. Ed*. **2006**, *45*, 1557–1559.
32. Park, K. S., Ni, Z., Cote, A. P., Choi, J. Y., Huang, R., Uribe-Romo, F. J., Chae, H. K., O'Keeffe, M., Yaghi, O. M. *Proc. Natl. Acad. Sci. (USA)* **2006**, *103*, 10186–10191.
33. Broom, D. P. *Int. J. Hydrogen Energy* **2007**, *32*, 4871–4888.
34. Harding, A. W., Foley, N. J., Norman, P. R., Francis, D. C., Thomas, K. M. *Langmuir* **1998**, *14*, 3858–3864.
35. Fuller, E. L., Poulis, J. A., Czanderna, A. W., Robens, E. *Thermochim. Acta* **1979**, *29*, 315–318.
36. Sing, K. S. W., Everett, D. H., Haul, R. A. W., Moscou, L., Pierotti, R. A., Rouquerol, J., Siemieniewska, T. *Pure Appl. Chem*. **1985**, *57*, 603–619.

37. Broom, D. P., Moretto, P. *J. Alloys Compd*. **2007**, *446–447*, 687–691.

38. Anson, A., Benham, M., Jagiello, J., Callejas, M. A., Benito, A. M., Maser, W. K., Zuettel, A., Sudan, P., Martinez, M. T. *Nanotechnology* **2004**, *15*, 1503–1508.
39. Furukawa, H., Miller, M. A., Yaghi, O. M. *J. Mater. Chem*. **2007**, *17*, 3197–3204.
40. Zlotea, C., Moretto, P., Steriotis, T. *Int. J. Hydrogen Energy* **2009**, *34*, 3044–3057.
41. Sircar, S. *Ind. Eng. Chem. Res*. **1999**, *38*, 3670–3682.
42. Dinca, M., Dailly, A., Liu, Y., Brown, C. M., Neumann, D. A., Long., J. R. *J. Am. Chem. Soc*. **2006**, *128*, 16876–16883.

43. Kaye, S. S., Dailly, A., Yaghi, O. M., Long, J. R. *J. Am. Chem. Soc*. **2007**, *129*, 14176–14177.

44. Lin, X., Telepeni, I., Blake, A. J., Dailly, A., Brown, C. M., Simmons, J. M., Zoppi, M. et al. *J. Am. Chem. Soc*. **2009**, *131*, 2159–2171.
45. Lin, X., Jia, J., Zhao, X., Thomas, K. M., Blake, A. J., Walker, G. S., Champness, N. R., Hubberstey, P., Schroder, M. *Angew. Chem. Int. Ed*. **2006**, *45*, 7358–7364.
46. Zhao, X. B., Xiao, B., Fletcher, A. J., Thomas, K. M. *J. Phys. Chem. B* **2005**, *109*, 8880–8888.
47. Xiao, B., Wheatley, P. S., Zhao, X., Fletcher, A. J., Fox, S., Rossi, A. G., Megson, I. L., Bordiga, S., Regli, L., Thomas, K. M., Morris, R. E. *J. Am. Chem. Soc*. **2007**, *129*, 1203–1209.
48. Hafizovic, J., Bjorgen, M., Olsbye, U., Dietzel, P. D. C., Bordiga, S., Prestipino, C., Lamberti, C., Lillerud, K. P. *J. Am. Chem. Soc*. **2007**, *129*, 3612–3620.
49. Liu, J., Culp, J. T., Natesakhawat, S., Bockrath, B. C., Zande, B., Sankar, S. G., Garberoglio, G., Johnson, J. K. *J. Phys. Chem. C* **2007**, *111*, 9305–9313.
50. Nelson, A. P., Farha, O. K., Mulfort, K. L., Hupp, J. T. *J. Am. Chem. Soc*. **2009**, *131*, 458–460.
51. Zhao, X., Villar-Rodil, S., Fletcher, A. J., Thomas, K. M. *J. Phys. Chem. B* **2006**, *110*, 9947–9955.
52. Chen, B., Zhao, X., Putkham, A., Hong, K., Lobkovsky, E. B., Hurtado, E. J., Fletcher, A. J., Thomas, K. M. *J. Am. Chem. Soc*. **2008**, *130*, 6411–6423.
53. Marsh, H. *Carbon* **1987**, *25*, 49–58.

54. Rouquerol, F., Rouquerol, J., Sing, K. *Adsorption by Powders and Porous Solids*, Academic Press, London, U.K., 1999.

55. Walton, K. S., Snurr, R. Q. *J. Am. Chem. Soc*. **2007**, *129*, 8552–8556.

56. Mertens, F. O. *Surf. Sci*. **2009**, *603*, 1979–1984.

57. Furukawa, H., Ko, N., Go, Y. B., Aratani, N., Choi, S. B., Choi, E., Yazaydin, A. O. et al. *Science* **2010**, *329*, 424–428.

58. Juan-Juan, J., Marco-Lozar, J. P., Suarez-Garcia, F., Cazorla-Amoros, D., Linares-Solano, A. *Carbon* **2010**, *48*, 2906–2909.

59. Yan, Y., Lin, X., Yang, S. H., Blake, A. J., Dailly, A., Champness, N. R., Hubberstey, P., Schroder, M. *Chem. Commun*. **2009**, 1025–1027.

60. Rosi, N. L., Eckert, J., Eddaoudi, M., Vodak, D. T., Kim, J., O'Keeffe, M., Yaghi, O. M. *Science* **2003**, *300*, 1127–1129.

61. Yaghi, O. M., O'Keeffe, M., Ockwig, N. W., Chae, H. K., Eddaoudi, M., Kim, J. *Nature* **2003**, *423*, 705–714.
62. Rowsell, J. L. C., Millward, A. R., Park, K. S., Yaghi, O. M. *J. Am. Chem. Soc*. **2004**, *126*, 5666–5667.
63. Rowsell, J. L. C., Spencer, E. C., Eckert, J., Howard, J. A. K., Yaghi, O. M. *Science* **2005**, *309*, 1350–1354.
64. Rowsell, J. L. C., Yaghi, O. M. *Angew. Chem. Int. Ed*. **2005**, *44*, 4670–4679.
65. Wong-Foy, A. G., Matzger, A. J., Yaghi, O. M. *J. Am. Chem. Soc*. **2006**, *128*, 3494–3495. 66.
Rowsell, J. L. C., Yaghi, O. M. *J. Am. Chem. Soc*. **2006**, *28*, 1304–1315.
67. Dinca, M., Yu, A. F., Long, J. R. *J. Am. Chem. Soc*. **2006**, *128*, 8904–8913.

68. Prestipino, C., Regli, L., Vitillo, J. G., Bonino, F., Damin, A., Lamberti, C., Zecchina, A., Solari, P. L., Kongshaug, K. O., Bordiga, S. *Chem. Mater*. **2006**, *18*, 1337–1346.
69. Latroche, M., Suble, S., Serre, C., Mellot-Draznieks, C., Llewellyn, P. L., Lee, J. H., Chang, J. S., Jhung, S.

H., Ferey, G. *Angew. Chem. Int. Ed.* **2006**, *45*, 8227–8231.

70. Gogotsi, Y., Dash, R. K., Yushin, G., Yildirim, T., Laudisio, G., Fischer, J. E. *J. Am. Chem. Soc.* **2005**, *127*, 16006–16007.

71. Armandi, M., Bonelli, B., Arean, C. O., Garrone, E. *Microporous Mesoporous Mater*. **2008**, *112*, 411–418.
72. Nijkamp, M. G., Raaymakers, J. E. M. J., van Dillen, A. J., de Jong, K. P. *Appl. Phys. A Mater. Sci. Process*. **2001**, *72*, 619–623.
73. Pang, J., Hampsey, J. E., Wu, Z., Hu, Q., Lu, Y. *Appl. Phys. Lett*. **2004**, *85*, 4887–4889.
74. Parra, J. B., Ania, C. O., Arenillas, A., Rubiera, F., Palacios, J. M., Pis, J. J. *J. Alloys Compd*. **2004**, *379*, 280–289.
75. Texier-Mandoki, N., Dentzer, J., Piquero, T., Saadallah, S., David, P., Vix-Guterl, C. *Carbon* **2004**, *42*, 2744–2747.
76. Schimmel, H. G., Nijkamp, G., Kearley, G. J., Rivera, A., de Jong, K. P., Mulder, F. M. *Mater. Sci. Eng. B Solid State Mater*. **2004**, *B108*, 124–129.
77. Schimmel, H. G., Kearly, G. J., Nijkamp, M. G., Visser, C. T., de Jong, K. P., Mulder, F. M. *Chem. Eur. J*. **2003**, *9*, 4764–4770.
78. Takagi, H., Hatori, H., Yamada, Y., Matsuo, S., Shiraishi, M. *J. Alloys Compd*. **2004**, *385*, 257–263.
79. Takagi, H., Hatori, H., Soneda, Y., Yoshizawa, N., Yamada, Y. *Mater. Sci. Eng. B* **2004**, *108*, 143–147.
80. Gadiou, R., Saadallah, S. E., Piquero, T., David, P., Parmentier, J., Vix-Guterl, C. *Microporous Mesoporous Mater*. **2005**, *79*, 121–128.
81. Cheng, F., Liang, J., Zhao, J., Tao, Z., Chen, J. *Chem. Mater*. **2008**, *20*, 1889–1895.
82. Zubizarreta, L., Gomez, E. I., Arenillas, A., Ania, C. O., Parra, J. B., Pis, J. J. *Adsorption* **2008**, *14*, 557–566.
83. Zubizarreta, L., Arenillas, A., Pis, J. J. *Int. J. Hydrogen Energy* **2009**, *34*, 4575–4581.
84. Guo, H. L., Gao, Q. M. *Int. J. Hydrogen Energy* **2010**, *35*, 7547–7554.
85. Langmi, H. W., Book, D., Walton, A., Johnson, S. R., Al-Mamouri, M. M., Speight, J. D., Edwards, P. P., Harris, I. R., Anderson, P. A. *J. Alloys Compd*. **2005**, *404–406*, 637–642.
86. Langmi, H. W., Walton, A., Al-Mamouri, M. M., Johnson, S. R., Book, D., Speight, J. D., Edwards, P. P., Gameson, I., Anderson, P. A., Harris, I. R. *J. Alloys Compd*. **2003**, *356–357*, 710–715.
87. Li, Y., Yang, R. T. *J. Phys. Chem. B* **2006**, *110*, 17175–17181.
88. Chu, X. Z., Zhou, Y. P., Zhang, Y. Z., Su, W., Sun, Y., Zhou, L. *J. Phys. Chem. B* **2006**, *110*, 22596–22600.
89. Chaikittisilp, W., Sugawara, A., Shimojima, A., Okubo, T. *Chem. Mater*. **2010**, *22*, 4841–4843.
90. Chaikittisilp, W., Sugawara, A., Shimojima, A., Okubo, T. *Chem. Eur. J*. **2010**, *16*, 6006–6014.
91. Lee, J. Y., Wood, C. D., Bradshaw, D., Rosseinsky, M. J., Cooper, A. I. *Chem. Commun*. **2006**, 2670–2672.
92. McKeown, N. B., Gahnem, B., Msayib, K. J., Budd, P. M., Tattershall, C. E., Mahmood, K., Tan, S., Book, D., Langmi, H. W., Walton, A. *Angew. Chem. Int. Ed*. **2006**, *45*, 1804–1807.
93. Germain, J., Hradil, J., Frechet, J. M. J., Svec, F. *Chem. Mater*. **2006**, *18*, 4430–4435.
94. Ghanem, B. S., Msayib, K. J., McKeown, N. B., Harris, K. D. M., Pan, Z., Budd, P. M., Butler, A., Selbie, J., Book, D., Walton, A. *Chem. Commun*. **2007**, *1*, 67–69.
95. Ghanem, B. S., Hashem, M., Harris, K. D. M., Msayib, K. J., Xu, M. C., Budd, P. M., Chaukura, N. et al. *Macromolecules* **2010**, *43*, 5287–5294.
96. Zhang, W., Li, C., Yuan, Y. P., Qiu, L. G., Xie, A. J., Shen, Y. H., Zhu, J. F. *J. Mater. Chem*. **2010**, *20*, 6413–6415.
97. Ben, T., Ren, H., Ma, S. Q., Cao, D. P., Lan, J. H., Jing, X. F., Wang, W. C. et al. *Angew. Chem. Int. Ed*. **2009**, *48*, 9457–9460.
98. Han, S. S., Furukawa, H., Yaghi, O. M., Goddard, W. A. *J. Am. Chem. Soc*. **2008**, *130*, 11580–11581.
99. Tilford, R. W., Mugavero, S. J., Pellechia, P. J., Lavigne, J. J. *Adv. Mater*. **2008**, *20*, 2741–2746.
100. Weber, J., Antonietti, M., Thomas, A. *Macromolecules* **2008**, *41*, 2880–2885.
101. El-Kaderi, H. M., Hunt, J. R., Mendoza-Cortes, J. L., Cote, A. P., Taylor, R. E., O'Keeffe, M., Yaghi, O. M. *Science* **2007**, *316*, 268–272.
102. Cote, A. P., El-Kaderi, H. M., Furukawa, H., Hunt, J. R., Yaghi, O. M. *J. Am. Chem. Soc*. **2007**, *129*, 12914–12915.
103. Furukawa, H., Yaghi, O. M. *J. Am. Chem. Soc*. **2009**, *131*, 8875–8883.

104. Lee, E. Y., Suh, M. P. *Angew. Chem. Int. Ed*. **2004**, *43*, 2798–2801.

105. Dybtsev, D. N., Chun, H., Yoon, S. H., Kim, D., Kim, K. *J. Am. Chem. Soc*. **2004**, *126*, 32–33.
106. Dybtsev, D. N., Chun, H., Kim, K. *Angew. Chem. Int. Ed*. **2004**, *43*, 5033–5036.
107. Chapman, K. W., Southon, P. D., Weeks, C. L., Kepert, C. J. *Chem. Commun*. **2005**, *26*, 3322–3324.
108. Perles, J., Iglesias, M., Martin-Luengo, M. A., Monge, M. A., Ruiz-Valero, C., Snejko, N. *Chem. Mater*. **2005**, *17*, 5837–5842.
109. Chun, H., Dybtsev, D. N., Kim, H., Kim, K. *Chem. Eur. J*. **2005**, *11*, 3521–3529.

110. Dietzel, P. D. C., Panella, B., Hirscher, M., Blom, R., Fjellvag., H. *Chem. Commun*. **2006**, *9*, 959–961.
111. Guo, X., Zhu, G., Li, Z., Sun, F., Yang, Z., Qiu, S. *Chem. Commun*. **2006**, 3172–3174.
112. Forster, P. M., Eckert, J., Heiken, B. D., Parise, J. B., Yoon, J. W., Jhung, S. H., Chang, J. S., Cheetham, A. K. *J. Am. Chem. Soc*. **2006**, *128*, 16846–16850.
113. Jia, J., Lin, X., Blake, A. J., Champness, N. R., Hubberstey, P., Shao, L., Walker, G., Wilson, C., Schroeder, M. *Inorg. Chem*. **2006**, *45*, 8838–8840.
114. Moon, H. R., Kobayashi, N., Suh, M. P. *Inorg. Chem*. **2006**, *45*, 8672–8676.
115. Navarro, J. A. R., Barea, E., Salas, J. M., Masciocchi, N., Galli, S., Sironi, A., Ania, C. O., Parra, J. B. *Inorg. Chem*. **2006**, *45*, 2397–2399.

116. Rood, J. A., Noll, B. C., Henderson, K. W. *Inorg. Chem*. **2006**, *45*, 5521–5528.
117. Ma, S., Wang, X. S., Yuan, D., Zhou, H. C. *Angew. Chem. Int. Ed*. **2008**, *47*, 4130–4133.

118. Wang, X. S., Ma, S. Q., Rauch, K., Simmons, J. M., Yuan, D. Q., Wang, X. P., Yildirim, T., Cole, W. C., Lopez, J. J., Meijere, A. d., Zhou, H. C. *Chem. Mater*. **2008**, *20*, 3145–3152.

119. Chun, H., Jung, H., Koo, G., Jeong, H., Kim, D. K. *Inorg. Chem*. **2008**, *47*, 5355–5359.

120. Lee, J. Y., Pan, L., Kelly, S. P., Jagiello, J., Emge, T. J., Li, J. *Adv. Mater*. **2005**, *17*, 2703–2706. 121. Dinca, M., Long, J. R. *J. Am. Chem. Soc*. **2007**, *129*, 11172–11176.

122. Dinca, M., Han, W. S., Liu, Y., Dailly, A., Brown, C. M., Long, J. R. *Angew. Chem. Int. Ed*. **2007**, *46*, 1419–1422.
123. Nouar, F., Eubank, J. F., Bousquet, T., Wojtas, L., Zaworotko, M. J., Eddaoudi, M. *J. Am. Chem. Soc*. **2008**, *130*, 1833–1835.
124. Choi, S. B., Seo, M. J., Cho, M., Kim, Y., Jin, M. K., Jung, D. Y., Choi, J. S., Ahn, W. S., Rowsell, J. L. C., Kim, J. *Cryst. Growth Des*. **2007**, *7*, 2290–2293.
125. Férey, G., Latroche, M., Sérre, C., Millange, F., Loiseau, T., Percheron-Guegan, A. *Chem. Commun*. **2003**, *24*, 2976–2977.

126. Kramer, M., Schwarz, U., Kaskel, S. *J. Mater. Chem*. **2006**, *16*, 2245–2248.
127. Wong-Foy, A. G., Lebel, O., Matzger, A. J. *J. Am. Chem. Soc*. **2007**, *129*, 15740–15741.

128. Lee, J. Y., Olson, D. H., Pan, L., Emge, T. J., Li, J. *Adv. Funct. Mater*. **2007**, *17*, 1255–1262. 129. Chun, H., Moon, J. *Inorg. Chem*. **2007**, *46*, 4371–4373.

130. Mulfort, K. L., Hupp, J. T. *J. Am. Chem. Soc*. **2007**, *129*, 9604–9605.

131. Park, H., Britten, J. F., Mueller, U., Lee, J. Y., Li, J., Parise, J. B. *Chem. Mater*. **2007**, *19*, 1302–1308. 132. Lee, E. Y., Jang, S. Y., Suh, M. P. *J. Am. Chem. Soc*. **2005**, *127*, 6374–6381.

133. Humphrey, S. M., Chang, J. S., Jhung, S. H., Yoon, J. W., Woo, P. T. *Angew. Chem. Int. Ed*. **2007**, *46*, 272–275.

134. Park, H. J., Suh, M. P. *Chem. Eur. J*. **2008**, *14*, 8812–8821.

135. Park, M., Moon, D., Yoon, J. W., Chang, J. S., Lah, M. S. *Chem. Commun*. **2009**, *15*, 2026–2028. 136. Ma, S. Q., Yuan, D. Q., Wang, X. S., Zhou, H. C. *Inorg. Chem*. **2009**, *48*, 2072–2077.

137. Sabo, M., Henschel, A., Froede, H., Klemm, E., Kaskel, S. *J. Mater. Chem*. **2007**, *17*, 3827–3832.
138. Saha, D. P., Wei, Z. J., Deng, S. G. *Sep. Purif. Technol*. **2009**, *64*, 280–287.
139. Zhang, Y. B., Zhang, W. X., Feng, F. Y., Zhang, J. P., Chen, X. M. *Angew. Chem. Int. Ed*. **2009**, *48*, 5287–

5290.

140. Shu-Hao, H., Chia-Her, L., Wei-Chang, W., Sue-Lein, W. *Angew. Chem. Int. Ed*. **2009**, *48*, 6124–6127.
141. Duriska, M. B., Neville, S. M., Lu, J. Z., Iremonger, S. S., Boas, J. F., Kepert, C. J., Batten, S. R. *Angew. Chem. Int. Ed*. **2009**, *48*, 8919–8922.
142. Gedrich, K., Senkovska, I., Baburin, I. A., Mueller, U., Trapp, O., Kaskel, S. *Inorg. Chem*. **2010**, *49*, 4440–4446.

143. Jia, J. H., Lin, X., Wilson, C., Blake, A. J., Champness, N. R., Hubberstey, P., Walker, G., Cussen, E. J., Schroder, M. *Chem. Commun*. **2007**, 840–842.
144. Yang, W., Lin, X., Jia, J., Blake, A. J., Wilson, C., Hubberstey, P., Champness, N. R., Schroeder, M. *Chem. Commun*. **2008**, 359–361.

145. Huang, S.-H., Lin, C.-H., Wu, W.-C., Wang, S.-L. *Angew. Chem. Int. Ed*. **2009**, *48*, 6124.
146. Li, A., Lu, R. F., Wang, Y., Wang, X., Han, K. L., Deng, W. Q. *Angew. Chem. Int. Ed*. **2010**, *49*, 3330–3333.
147. van Dingenen, W., van Itterbeek, A. *Physica (Hague)* **1939**, *6*, 49–58.
148. Basmadjian, I. D. *Can. J. Chem*. **1960**, *38*, 141–148.

149. Benard, P., Chahine, R. *Langmuir* **2001**, *17*, 1950–1955.

150. Gundiah, G., Govindaraj, A., Rajalakshmi, N., Dhathathreyan, K. S., Rao, C. N. R. *J. Mater. Chem*. **2003**, *13*, 209–213.

151. Zhou, Y., Feng, K., Sun, Y., Zhou., L. *Chem. Phys. Lett*. **2003**, *380*, 526–529.

152. Kayiran, S. B., Lamari, F. D., Levesque, D. *J. Phys. Chem. B* **2004**, *108*, 15211–15215.
153. Shiraishi, M., Takenobu, T., Kataura, H., Ata, M. *Appl. Phys. A* **2004**, *78*, 947–953.
154. Zhou, L., Zhou, Y., Sun, Y. *Int. J. Hydrogen Energy* **2004**, *29*, 475–479.
155. Poirier, E., Chahine, R., Tessier, A., Bose, T. K. *Rev. Sci. Inst*. **2005**, *76*, 055101.
156. Panella, B., Hirscher, M., Roth, S. *Carbon* **2005**, *43*, 2209–2214.
157. Pacula, A., Mokaya, R. *J. Phys. Chem. C* **2008**, *112*, 2764–2769.
158. Pacula, A., Mokaya, R. *Microporous Mesoporous Mater*. **2007**, *106*, 147–154.

159. Yang, Z. X., Xia, Y. D., Sun, X. Z., Mokaya, R. *J. Phys. Chem. B* **2006**, *110* 18424–18431.

160. Hu, Q. Y., Lu, Y. F., Meisner, G. P. *J. Phys. Chem. C* **2008**, *112*, 1516–1523.

161. Yang, Z., Xia, Y., Mokaya, R. *J. Am. Chem. Soc*. **2007**, *129*, 1673–1679.

162. Jorda-Beneyto, M., Suarez-Garcia, F., Lozano-Castello, D., Cazorla-Amoros, D., Linares-Solano, A. *Carbon* **2007**, *45*, 293–303.

163. Xia, Y., Walker, G. S., Grant, D. M., Mokaya, R. *J. Am. Chem. Soc*. **2009**, *131*, 16493–16499.

164. Mendez-Linan, L., Lopez-Garzon, F. J., Domingo-Garcia, M., Perez-Mendoza, M. *Energy Fuels* **2010**, *24*, 3394–3400.

165. Balathanigaimani, M. S., Shim, W.-G., Kim, T.-H., Cho, S.-J., Lee, J.-W., Moon, H. *Catalysis Today* **2009**, *146*, 234–240.

166. Meisner, G. P., Hu, Q. *Nanotechnology* **2009**, *20*, 204023/1–204023/10.

167. Gogotsi, Y., Portet, C., Osswald, S., Simmons, J. M., Yildirim, T., Laudisio, G., Fischer, J. E. *Int. J. Hydrogen Energy* **2009**, *34*, 6314–6319.

168. Zheng, Z., Gao, Q., Jiang, J. *Carbon* **2010**, *48*, 2968–2973.

169. Wang, H., Gao, Q., Hu, J. *J. Am. Chem. Soc*. **2009**, *131*, 7016–7022.

170. Gao, F., Zhao, D. L., Li, Y., Li, X. G. *J. Phys. Chem. Solids* **2010**, *71*, 444–447.
171. Weinberger, B., Lamari, F. D. *Int. J. Hydrogen Energy* **2009**, *34*, 3058–3064.
172. Suarez-Garcia, F., Vilaplana-Ortego, E., Kunowsky, M., Kimura, M., Oya, A., Linares-Solano, A. *Int. J. Hydrogen Energy* **2009**, *34*, 9141–9150.

173. Bonilla, M. R., Bae, J. S., Nguyen, T. X., Bhatia, S. K. *J. Phys. Chem. C* **2010**, *114*, 16562–16575.
174. Lee, S.-Y., Park, S.-J. *Int. J. Hydrogen Energy* **2010**, *35*, 6757–6762.
175. Bianco, S., Giorcelli, M., Musso, S., Castellino, M., Agresti, F., Khandelwal, A., Russo, S. L., Kumar, M., Ando, Y., Tagliaferro, A. *J. Nanosci. Nanotechnol*. **2010**, *10*, 3860–3866.

176. Sheppard, D. A., Buckley, C. E. *Int. J. Hydrogen Energy* **2008**, *33*, 1688–1692.
177. Stephanie-Victoire, F., Goulay, A. M., de Lara, E. C. *Langmuir* **1998**, *14*, 7255–7259.
178. Kayiran, S. B., Darkrim, F. L. *Surf. Interface Anal*. **2002**, *34*, 100–104.
179. Dong, J., Wang, X., Xu, H., Zhao, Q., Li, J. *Int. J. Hydrogen Energy* **2007**, *32*, 4998–5004.
180. McKeown, N. B., Budd, P. M. *Chem. Soc. Rev*. **2006**, *35*, 675–683.
181. Budd, P. M., Butler, A., Selbie, J., Mahmood, K., McKeown, N. B., Ghanem, B., Msayib, K., Book, D., Walton, A. *Phys. Chem. Chem. Phys*. **2007**, *9*, 1802–1808.
182. Germain, J., Frechet, J. M. J., Svec, F. *J. Mater. Chem*. **2007**, *17*, 4989–4997.
183. Jiang, J. X., Su, F., Trewin, A., Wood, C. D., Niu, H., Jones, J. T. A., Khimyak, Y. Z., Cooper, A. I. *J. Am. Chem. Soc*. **2008**, *130*, 7710–7720.

184. Wood, C. D., Tan, B., Trewin, A., Niu, H., Bradshaw, D., Rosseinsky, M. J., Khimyak, Y. Z. et al. *Chem. Mater*. **2007**, *19*, 2034–2048.

185. Germain, J., Svec, F., Frechet, J. M. J. *Chem. Mater*. **2008**, *20*, 7069–7076.
186. Xia, J., Yuan, S., Wang, Z., Kirklin, S., Dorney, B., Liu, D.-J., Yu, L. *Macromolecules* **2010**, *43*, 3325–3330.
187. Wood, C. D., Tan, B., Trewin, A., Su, F., Rosseinsky, M. J., Bradshaw, D., Sun, Y., Zhou, L., Cooper, A. I. *Adv. Mater*. **2008**, *20*, 1916-+.
188. Yuan, S. W., Dorney, B., White, D., Kirklin, S., Zapol, P., Yu, L. P., Liu, D. J. *Chem. Commun*. **2010**, *46*, 4547–4549.

189. Yoon, J. H., Choi, S. B., Oh, Y. J., Seo, M. J., Jhon, Y. H., Lee, T. B., Kim, D., Choi, S. H., Kim, J. *Catalysis Today* **2007**, *120*, 324–329.

190. Sava, D. F., Kravtsov, V. C., Nouar, F., Wojtas, L., Eubank, J. F., Eddaoudi, M. *J. Am. Chem. Soc.* **2008**, *130*, 3768–3770.

191. Dailly, A., Vajo, J. J., C. Ahn, C. *J. Phys. Chem. B* **2006**, *110*, 1099–1101.

192. Panella, B., Hirscher, M., Puetter, H., Mueller, U. *Adv. Funct. Mater*. **2006**, *16*, 520–524.

193. Panella, B., Hones, K., Muller, U., Trukhan, N., Schubert, M., Putter, H., Hirscher, M. *Angew. Chem. Int. Ed*. **2008**, *47*, 2138–2142.

194. Millward, A. R., Yaghi, O. M. *J. Am. Chem. Soc*. **2005**, *127*, 17998–17999.

195. Dinca, M., Long, J. R. *J. Am. Chem. Soc*. **2005**, *127*, 9376–9377.

196. Li, Y., Yang, R. T. *Langmuir* **2007**, *23*, 12937–12944.

197. Kesanli, B., Cui, T., Smith, M. R., Bittner, E. W., Brockrath, B. C., Lin, W. *Angew. Chem. Int. Ed*. **2005**, *44*, 72–75.

198. Fang, Q. R., Zhu, G. S., Xue, M., Zhang, Q. L., Sun, J. Y., Guo, X. D., Qiu, S. L., Xu, S. T., Wang, P., Wang, D. J., Wei, Y. *Chem. Eur. J*. **2006**, *12*, 3754–3758.
199. Chen, B., Ma, S., Zapata, F., Lobkovsky, E. B., Yang, J. *Inorg. Chem*. **2006**, *45*, 5718–5720.
200. Zhao, X., Xiao, B., Fletcher, A. J., Thomas, K. M., Bradshaw, D., Rosseinsky, M. J. *Science* **2004**, *306*, 1012–1015.

201. Pan, L., Sander, M. B., Huang, X., Li, J., Smith, M., Bittner, E., Bockrath, B., Johnson, J. K. *J. Am. Chem. Soc*. **2004**, *126*, 1308–1309.
202. Luo, J., Xu, H., Liu, Y., Zhao, Y., Daemen, L. L., Brown, C., Timofeeva, T. V., Ma, S., Zhou, H. C. *J. Am. Chem. Soc*. **2008**, *130*, 9626–9627.

203. Xue, M., Zhu, G., Y. Li, X. Zhao, Jin, Z., Kang, E., Qiu, S. *Cryst. Growth Des*. **2008**, *8*, 2478–2483.
204. Liu, J., Lee, J. Y., Pan, L., Obermyer, R. T., Simizu, S., Zande, B., Li, J., Sankar, S. G., Johnson, J. K. *J. Phys. Chem. C* **2008**, *112*, 2911–2917.

205. Takei, T., Kawashima, J., Li, T., Maeda, A., Hasegawa, M., Kitagawa, T., Ohmura, T., Ichikawa, M., Hosoe, M., Kanoya, I., Mori, W. *Bull. Chem. Soc. Jpn*. **2008**, *81*, 847–856.
206. Surble, S., Millange, F., Serre, C., Duren, T., Latroche, M., Bourrelly, S., Llewellyn, P. L., Ferey, G. *J. Am. Chem. Soc*. **2006**, *128*, 14889–14896.

207. Choi, H. J., Dincă, M., Long, J. R. *J. Am. Chem. Soc*. **2008**, *130*, 7848–7850.

208. Liu, Y., Kabbour, H., Brown, C. M., Neumann, D. A., Ahn, C. C. *Langmuir* **2008**, *24*, 4772–4777.
209. Autie-Castro, G., Autie, M., Reguera, E., Santamaria-Gonzalez, J., Moreno-Tost, R., Rodriguez-Castellon, E., Jimenez-Lopez, A. *Surf. Interface Anal*. **2009**, *41*, 730–734.
210. Zhou, W., Wu, H., Hartman, M. R., Yildirim, T. *J. Phys. Chem. C* **2007**, *111*, 16131–16137.
211. Fang, Q. R., Zhu, G. S., Jin, Z., Ji, Y. Y., Ye, J. W., Xue, M., Yang, H., Wang, Y., Qiu., S. L. *Angew. Chem. Int. Ed*. **2007**, *46*, 6638–6642.
212. Lin, X., Blake, A. J., Wilson, C., Sun, X. Z., Champness, N. R., George, M. W., Hubberstey, P., Mokaya, R.,

Schroder, M. *J. Am. Chem. Soc*. **2006**, *128*, 10745–10753.
213. Comotti, A., Bracco, S., Sozzani, P., Horike, S., Matsuda, R., Chen, J., Takata, M., Kubota, Y., Kitagawa, S. *J. Am. Chem. Soc*. **2008**, *130*, 13664–13672.
214. Ma, S., Zhou, H. C. *J. Am. Chem. Soc*. **2006**, *128*, 11734–11735.
215. Kaye, S. S., Long, J. R. *J. Am. Chem. Soc*. **2005**, *127*, 6506–6507.
216. Lee, J. Y., Li, J., Jagiello, J. *J. Solid State Chem*. **2005**, *178*, 2527–2532.
217. Dinca, M., Dailly, A., Tsay, C., Long, J. R. *Inorg. Chem*. **2008**, *47*, 11–13.

218. Culp, J. T., Matranga, C., Smith, M., Bittner, E. W., Bockrath, B. *J. Phys. Chem. B* **2006**, *110*, 8325–8328.
219. Reguera, L., Balmaseda, J., Krap, C. P., Reguera, E. *J. Phys. Chem. C* **2008**, *112*, 10490–10501.
220. Reguera, L., Balmaseda, J., Castillo, L. F. d., Reguera, E. *J. Phys. Chem. C* **2008**, *112*, 5589–5597.
221. Kaye, S. S., Long, J. R. *Chem. Commun*. **2007**, 4486–4488.

222. Culp, J. T., Natesakhawat, S., Smith, M. R., Bittner, E., Matranga, C., Bockrath, B. *J. Phys. Chem. C* **2008**, *112*, 7079–7083.
223. Vitillo, J. G., Regli, L., Chavan, S., Ricchiardi, G., Spoto, G., Dietzel, P. D. C., Bordiga, S., Zecchina, A. *J. Am. Chem. Soc*. **2008**, *130*, 8386–8396.

224. Farha, O. K., Spokoyny, A. M., Mulfort, K. L., Hawthorne, M. F., Mirkin, C. A., Hupp, J. T. *J. Am. Chem. Soc*. **2007**, *129*, 12680–12681.
225. Liu, Y., Eubank, J. F., Cairns, A. J., Eckert, J., Kravtsov, V. C., Luebke, R., Eddaoudi, M. *Angew. Chem. Int. Ed*. **2007**, *46*, 3278–3283.
226. Pan, L., Parker, B., Huang, X., Olson, D. H., Lee, J. Y., Li, J. *J. Am. Chem. Soc*. **2006**, *128*, 4180–4181.
227. Burrows, A. D., Cassar, K., Duren, T., Friend, R. M. W., Mahon, M. F., Rigby, S. P., Savarese, T. L. *Dalton Trans*. **2008**, 2465–2474.

228. Yang, S., Lin, X., Blake, A. J., Thomas, K. M., Hubberstey, P., Champness, N. R., Schroder, M. *Chem. Commun*. **2008**, 6108–6110.

229. Liu, Y., Her, J. H., Dailly, A., Ramirez-Cuesta, A. J., Neumann, D. A., Brown, C. M. *J. Am. Chem. Soc*. **2008**, *130*, 11813–11818.
230. Gao, C. Y., Liu, S. X., Xie, L. H., Sun, C. Y., Cao, J. F., Ren, Y. H., Feng, D., Su, Z. M. *CrystEng. Comm.* **2009**, *11*, 177–182.
231. Xiang, Z., Lan, J., Cao, D., Shao, X., Wang, W., Broom, D. P. *J. Phys. Chem. C* **2009**, *113*, 15106–15109.

232. Koh, K., Wong-Foy, A. G., Matzger, A. J. *J. Am. Chem. Soc*. **2009**, *131*, 4184–1485.

233. Kanoo, P., Matsuda, R., Higuchi, M., Kitagawa, S., Maji, T. K. *Chem. Mater*. **2009**, *21*, 5860–5866.

234. Ma, S. Q., Simmons, J. M., Yuan, D. Q., Li, J. R., Weng, W., Liu, D. J., Zhou, H. C. *Chem. Commun*.

2009, 4049–4051.

235. Ma, S., Yuan, D., Chang, J.-S., Zhou, H.-C. *Inorg. Chem*. **2009**, *48*, 5398–5402.

236. Park, H. J., Suh, M. P. *Chem. Commun*. **2010**, *46*, 610–612.

237. Zhao, D., Yuan, D. Q., Yakovenko, A., Zhou, H. C. *Chem. Commun*. **2010**, *46*, 4196–4198. 238. Yang, C., Wang, X. P., Omary, M. A. *J. Am. Chem. Soc*. **2007**, *129*, 15454-+.

239. Wang, Y., Cheng, P., Chen, J., Z. Liao, D., Yan, S. P. *Inorg. Chem*. **2007**, *46*, 4530–4534.
240. Ma, S. Q., Eckert, J., Forster, P. M., Yoon, J. W., Hwang, Y. K., Chang, J. S., Collier, C. D., Parise, J. B., Zhou, H. C. *J. Am. Chem. Soc*. **2008**, *130*, 15896–15902.
241. Ma, S. Q., Simmons, J. M., Sun, D. F., Yuan, D. Q., Zhou, H. C. *Inorg. Chem*. **2009**, *48*, 5263–5268.
242. Wang, X. S., Ma, S. Q., Yuan, D. Q., Yoon, J. W., Hwang, Y. K., Chang, J. S., Wang, X. P., Jorgensen, M. R., Chen, Y. S., Zhou, H. C. *Inorg. Chem*. **2009**, *48*, 7519–7521.
243. Xue, M., Liu, Y., Schaffino, R. M., Xiang, S. C.,, Zhao, X. J., Zhu, G. S., Qiu, S. L., Chen, B. L. *Inorg. Chem*. **2009**, *48*, 4649–4651.
244. Yang, S. H., Lin, X., Dailly, A., Blake, A. J., Hubberstey, P., Champness, N. R., Schroder, M. *Chem. Eur. J*. **2009**, *15*, 4829–4835.
245. Lee, Y. G., Moon, H. R., Cheon, Y. E., Suh, M. P. *Angew. Chem. Int. Ed*. **2008**, *47*, 7741–7745.
246. Yang, J., Zhao, Q., Li, J., Dong, J. *Microporous Mesoporous Mater*. **2010**, *130*, 174–179.
247. Chung, T. C. M., Jeong, Y., Chen, Q., Kleinhammes, A., Wu, Y. *J. Am. Chem. Soc*. **2008**, *130*, 6668–6669.
248. Bhat, V. V., Contescu, C. I., Gallego, N. C., Baker, F. S. *Carbon* **2010**, *48*, 1331–1340.
249. Bhat, V. V., Contescu, C. I., Gallego, N. C. *Carbon* **2010**, *48*, 2361–2364.
250. Srinivas, G., Zhu, Y. W., Piner, R., Skipper, N., Ellerby, M., Ruoff, R. *Carbon* **2010**, *48*, 630–635.
251. McKeown, N. B., Budd, P. M., Book, D. *Macromol. Rapid Commun*. **2007**, *28*, 995–1002.
252. Makhseed, S., Samuel, J. *Chem. Commun*. **2008**, *36*, 4342–4344.
253. Yuan, S. W., Kirklin, S., Dorney, B., Liu, D. J., Yu, L. P. *Macromolecules* **2009**, *42*, 1554–1559.

254. Lochan, R. C., Head-Gordon, M. *Phys. Chem. Chem. Phys*. **2006**, *8*, 1357–1370.
255. Reguera, E. *Int. J. Hydrogen Energy* **2009**, *34*, 9163–9167.

256. Jeong, Y., Chung, T. C. M. *Carbon* **2010**, *48*, 2526–2537.

257. Kubas, G. J., Ryan, R. R., Swanson, B. I., Vergamini, P. J., Wasserman, H. J. *J. Am. Chem. Soc*. **1984**, *106*, 451–452.

258. Kubas, G. J. *Chem. Rev*. **2007**, *107*, 4152–4205.

259. Kubas, G. J. *Proc. Natl. Acad. Sci. (USA)* **2007**, *104*, 6901–6907.

260. Dutta, S., Jagirdar, B. R., Nethaji, M. *Inorg. Chem*. **2008**, *47*, 548–559.
261. Yang, S., Lin, X., Blake, A. J., Thomas, K. M., Hubberstey, P., Champness, N. R., Schröder, M. *Chem. Commun*. **2008**, 6108–6110.

262. Cerny, S. *Chem. Phys. Solid Surf. Heterog. Catal*. **1983**, *2*, 1–57.
263. Cole, J. H., Everett, D. H., Marshall, C. T., Paniego, A. R., Powl, J. C., Rodriguez-Reinoso, F. *J. Chem. Soc. Faraday Trans*. **1974**, *70*, 2154–2169.

264. Czepirski, L., Jagiello, J. *Chem. Eng. Sci*. **1989**, *44*, 797–801.
265. Yushin, G., Dash, R., Jagiello, J., Fischer, J. E., Gogotsi, Y. *Adv. Funct. Mater*. **2006**, *16*, 2288–2293.
266. Jhung, S. H., Kim, H. K., Yoon, J. W., Chang, J. S. *J. Phys. Chem. B* **2006**, *110*, 9371–9374.

267. Palomino, G. T., Carayol, M. R. L., Arean, C. O. *J Mater. Chem*. **2006**, *16*, 2884–2885.
268. Arean, C. O., Palomino, G. T., Carayol, M. R. L. *Appl. Surf. Sci*. **2007**, *253*, 5701–5704.
269. Arean, C. O., Delgado, M. R., Palomino, G. T., Rubio, M. T., Tsyganenko, N. M., Tsyganenko, A. A., Garrone, E. *Microporous Mesoporous Mater*. **2005**, *80*, 247–252.
270. Palomino, G. T., Carayol, M. R. L., Arean, C. O. *Catalysis Today* **2008**, *138*, 249–252.
271. Areán, C. O., Chavan, S., Cabello, C. P., Garrone, E., Palomino, G. T. *ChemPhysChem* **2010**, *11*, 3237–3242.
272. Schmitz, B., Krkljus, I., Leung, E., Hoeffken, H. W., Mueller, U., Hirscher, M. *ChemSusChem* **2010**, *3*, 768–761.

273. Sumida, K., Horike, S., Kaye, S. S., Herm, Z. R., Queen, W. L., Brown, C. M., Grandjean, F., Long, G. J., Dailly, A., Long, J. R. *Chem. Sci*. **2010**, *1*, 184–191.
274. Arean, C. O., Manoilova, O. V., Bonelli, B., Delgado, M. R., Palomino, G. T., Garrone, E. *Chem. Phys. Lett*. **2003**, *370*, 631–635.
275. Palomino, G. T., Delgado, M. R., Tsyganenko, N. M., Tsyganenko, A. A., Garrone, E., Bonelli, B., Manoilova, O. V., Arean, C. O. In *Molecular Sieves: From Basic Research to Industrial Applications, Pts a and B*, Cejka, J., Zilkova, N., Nachtigall, P., Eds., Elsevier Science Bv, Amsterdam, the Netherlands, **2005**, Vol. 158, pp. 853–860.
276. Arean, C. O., Palomino, G. T., Garrone, E., Nachtigallova, D., Nachtigall, P. *J. Phys. Chem. B* **2006**, *110*, 395–402.

277. Nachtigall, P., Garrone, E., Palomino, G. T., Delgado, M. R., Nachtigallova, D., Arean, C. O. *Phys. Chem. Chem. Phys*. **2006**, *8*, 2286–2292.

278. Arean, C. O., Palomino, G. T., Carayol, M. R. L., Pulido, A., Rubes, M., Bludsky, O., Nachtigall, P. *Chem. Phys. Lett*. **2009**, *477*, 139–143.

279. Palomino, G. T., Bonelli, B., Arean, C. O., Parra, J. B., Carayol, M. R. L., Armandi, M., Ania, C. O., Garrone, E. *Int. J. Hydrogen Energy* **2009**, *34*, 4371–4378.
280. Palomino, G. T., Arean, C. O., Carayol, M. R. L. *Appl. Surf. Sci*. **2010**, *256*, 5281–5284. 281.
Zhong, D. C., Lin, J. B., Lu, W. G., Jiang, L., Lu, T. B. *Inorg. Chem*. **2009**, *48*, 8656–8658.
282. Xin, Z. F., Bai, J. F., Shen, Y. M., Pan, Y. *Crystal Growth Des*. **2010**, *10*, 2451–2454.

283. Bhatia, S. K., Myers, A. L. *Langmuir* **2006**, *22*, 1688–1700.

284. Kubota, Y., Takata, M., Matsuda, R., Kitaura, R., Kitagawa, S., Kato, K., Sakata, M., Kobayashi, T. C. *Angew. Chem. Int. Ed*. **2005**, *44*, 920–923.

285. Takamizawa, S., Nakata, E. *Cryst. Eng. Commun*. **2005**, *7*, 476–479.
286. Spencer, E. C., Howard, J. A. K., McIntyre, G. J., Rowsell, J. L. C., Yaghi, O. M. *Chem. Commun*.

2006, 278–280.

287. Yildirim, T., Hartman, M. R. *Phys. Rev. Lett.* **2005**, *95*, 215504.
288. Peterson, V.K., Liu, Y., Brown, C. M., Kepert, C. J. *J. Am. Chem. Soc.* **2006**, *128*, 15578–15579.
289. Yan, Y., Telepeni, I., Yang, S. H., Lin, X., Kockelmann, W., Dailly, A., Blake, A. J. et al. *J. Am. Chem. Soc.* **2010**, *132*, 4092-+.
290. Mulder, F. M., Assfour, B., Huot, J., Dingemans, T. J., Wagemaker, M., Ramirez-Cuesta, A. J. *J. Phys. Chem. C* **2010**, *114*, 10648–10655.

291. Hartman, M. R., Peterson, V. K., Liu, Y., Kaye, S. S., Long, J. R. *Chem. Mater*. **2006**, *18*, 3221–3224.
292. Kubas, G. J., Burns, C. J., Eckhert, J., Johnson, S. W., Larson, A. C., Vergamini, P. J., Unkefer, C. J., Khalsa, G. R. K., Jackson, S. A., Eisenstein, O. *J. Am. Chem. Soc*. **1993**, *115*, 569–581.
293. Forster, P. M., Eckert, J., Chang, J.-S., Park, S.-E., Férey, G., Cheethem, A. K. *J. Am. Chem. Soc*. **2003**, *125*, 1309–1312.

294. Chapman, K. W., Chupas, P. J., Maxey, E. R., Richardson, J. W. *Chem. Commun*. **2006**, 4013–4015.
295. Liu, Y., Brown, C. M., Neumann, D. A., Peterson, V. K., Kepert, C. J. *J. Alloys Compd*. **2007**, *446–447*, 385–388.

296. Zhou, W., Yildirim, T. *J. Phys. Chem. C* **2008**, *112*, 8132–8135.

297. Nijem, N., Veyan, J.-F. o., Kong, L., Li, K., Pramanik, S., Zhao, Y., Li, J., Langreth, D., Chabal, Y. J. *J. Am. Chem. Soc*. **2010**, *132*, 1654–1664.

298. Bordiga, S., Regli, L., Bonino, F., Groppo, E., Lamberti, C., Xiao, B., Wheatley, P. S., Morris, R. E., Zecchina, A. *Phys. Chem. Chem. Phys*. **2007**, *9*, 2676–2685.
299. Spoto, G., Vitillo, J. G., Cocina, D., Damin, A., Bonino, F., Zecchina, A. *Phys. Chem. Chem. Phys*. **2007**, *9*, 4992–4999.

300. Panella, B., Hirscher, M. *Phys. Chem. Chem. Phys*. **2008**, *10*, 2910–2917.
301. Centrone, A., Siberio-Perez, D. Y., Millward, A. R., Yaghi, O. M., Matzger, A. J., Zerbi, G. *Chem. Phys. Lett*. **2005**, *411*, 516–519.
302. Centrone, A., Brambilla, L., Zerbi, G. *Phys. Rev. B* **2005**, *71*, 245406.
303. Fletcher, A. J., Cussen, E. J., Prior, T. J., Rosseinsky, M. J., Kepert, C. J., Thomas, K. M. *J. Am. Chem. Soc*. **2001**, *123*, 10001–10011.
304. Fletcher, A. J., Cussen, E. J., Bradshaw, D., Rosseinsky, M. J., Thomas, K. M. *J. Am. Chem. Soc*. **2004**, *126*, 9750–9759.

305. Yang, C., Wang, X., Omary, M. A. *J. Am. Chem. Soc*. **2007**, *129*, 15454–15455.

306. Bradshaw, D., Warren, J. E., Rosseinsky, M. J. *Science* **2007**, *315(5814)*, 977–980.
307. Yang, S., Lin, X., Blake, A. J., Walker, G. S., Hubberstey, P., Champness, N. R., Schröder, M. *Nat. Chem*. **2009**, *1*, 487–493.
308. Llewellyn, P. L., Maurin, G., Devic, T., Loera-Serna, S., Rosenbach, N., Serre, C., Bourrelly, S., Horcajada, P., Filinchuk, Y., Férey, G. *J. Am. Chem. Soc*. **2008**, *130* 12808–12814.
309. Humphrey, S. M., Oungoulian, S. E., Yoon, J. W., Hwang, Y. K., Wise, E. R., Chang, J. S. *Chem. Commun*. **2008**, 2891–2893.
310. Ma, S., Wang, X. S., Manis, E. S., Collier, C. C., Zhou, H. C. *Inorg. Chem*. **2007**, *46* 3432–3434.
311. Culp, J. T., Smith, M. R., Bittner, E., Bockrath, B. *J. Am. Chem. Soc*. **2008**, *130*, 12427–12434. 312.
Kang, J., Wei, S.-H., Kim, Y.-H. *J. Am. Chem. Soc*. **2010**, *132*, 1510–1511.
313. Hamaed, A., Trudeau, M., Antonelli, D. M. *J. Am. Chem. Soc*. **2008**, *130*, 6992–6999.
314. Hamaed, A., Hoang, T. K. A., Trudeau, M., Antonelli, D. M. *J. Organometal. Chem*. **2009**, *694*, 2793–2800.
315. Hamaed, A., Van Mai, H., Hoang, T. K. A., Trudeau, M., Antonelli, D. *J. Phys. Chem. C* **2010**, *114*, 8651–8660.
316. Lueking, A., Yang, R. T. *J. Catal*. **2002**, *206*, 165–168.

317. Yang, F. H., T. Yang, R. *Carbon* **2002**, *40*, 437–444.

318. Lueking, A. D., Yang, R. T. *Appl. Catal. A General* **2004**, *265*, 259–268.
319. Yang, F. H., Lachawiec, A. J., Yang, R. T. *J. Phys. Chem. B* **2006**, *110*, 6236–6244.
320. Lueking, A. D., Yang, R. T., Rodriguez, N. M., Baker, R. T. K. *Langmuir* **2004**, *20*, 714–721.
321. Lachawiec, A. J., Qi, G. S., Yang, R. T. *Langmuir* **2005**, *21*, 11418–11424. 322. Li,
Y. W., Yang, R. T. *J. Phys. Chem. C* **2007**, *111*, 11086–11094.

323. Wang, L. F., Yang, R. T. *J. Phys. Chem. C* **2008**, *112*, 12486–12494.

324. Wang, L. F., Yang, R. T. *J. Phys. Chem. C* **2009**, *113*, 21883–21888.

325. Ramachandran, S., Ha, J. H., Kim, D. K. *Catal. Commun*. **2007**, *8*, 1934–1938. 326.
Li, Y., Yang, R. T. *AIChE J*. **2008**, *54*, 269–279.

327. Li, Y., Yang, R. T. *J. Am. Chem. Soc*. **2006**, *128*, 726–727.

328. Li, Y., Yang, R. T. *J. Am. Chem. Soc*. **2006**, *128*, 8136–8137.

329. Lachawiec, A. J., Yang, R. T. *Langmuir* **2008**, *24*, 6159–6165.

330. Zlotea, C., Campesi, R., Cuevas, F., Leroy, E., Dibandjo, P., Volkringer, C., Loiseau, T., Férey, G. r., Latroche, M. *J. Am. Chem. Soc*. **2010**, *132*, 2991–2997.

331. Stuckert, N. R., Wang, L., Yang, R. T. *Langmuir* **2010**, *26*, 11963–11971. 332. Stoicheff, B. P. *Can. J. Phys*. **1957**, *35*, 730–741.

333. Fletcher, A. J., Thomas, K. M. *J. Phys. Chem. C* **2007**, *111*, 2107–2115.

334. Tanaka, H., Kanoh, H., El-Merraoui, M., Steele, W. A., Yudasaka, M., Iijima, S., Kaneko, K. *J. Phys. Chem. B* **2004**, *108*, 17457–17465.

335. Noguchi, D., Tanaka, H., Kondo, A., Kajiro, H., Noguchi, H., Ohba, T., Kanoh, H., Kaneko, K. *J. Am. Chem. Soc*. **2008**, *130*, 6367–6372.

336. Beenakker, J. J. M., Borman, V. D., Krylov, S. Y. *Phys. Rev. Lett*. **1994**, *72*, 514–517.
337. Beenakker, J. J. M., Borman, V. D., Krylov, S. Y. *Chem. Phys. Lett*. **1995**, *232*, 379–382. 338. Yaris, R., Sams, J. R. J. *J. Chem. Phys*. **1962**, *37*, 571–576.
339. Kumar, A. V. A., Bhatia, S. K. *Phys. Rev. Lett*. **2005**, *95*, 245901.

340. Kumar, A. V. A., Jobic, H., Bhatia, S. K. *J. Phys. Chem. B* **2006**, *110*, 16666–16671.

341. Zhou, J., Wang, Q., Sun, Q., Jena, P., Chen, X. S. *Proc. Natl. Acad. Sci. (USA)* **2010**, *107*, 2801–2806.

342. Shi, S. Z., Hwang, J. Y., Li, X., Sun, X., Lee, B. I. *Int. J. Hydrogen Energy* **2010**, *35*, 629–631.